Advances in Science, Technology & Innovation
IEREK Interdisciplinary Series for Sustainable Development

Mustapha Meghraoui · Narasimman Sundararajan · Santanu Banerjee · Klaus-G. Hinzen · Mehdi Eshagh · François Roure · Helder I. Chaminé · Said Maouche · André Michard *Editors*

Advances in Geophysics, Tectonics and Petroleum Geosciences

Proceedings of the 2nd Springer Conference of the Arabian Journal of Geosciences (CAJG-2), Tunisia 2019

IEREK RESEARCH & KNOWLEDGE ENRICHMENT

Springer

Advances in Science, Technology & Innovation

IEREK Interdisciplinary Series for Sustainable Development

Advances in Science, Technology & Innovation (ASTI) is a series of peer-reviewed books based on important emerging research that redefines the current disciplinary boundaries in science, technology and innovation (STI) in order to develop integrated concepts for sustainable development. It not only discusses the progress made towards securing more resources, allocating smarter solutions, and rebalancing the relationship between nature and people, but also provides in-depth insights from comprehensive research that addresses the **17 sustainable development goals (SDGs)** as set out by the UN for 2030.

The series draws on the best research papers from various IEREK and other international conferences to promote the creation and development of viable solutions for a **sustainable future and a positive societal** transformation with the help of integrated and innovative science-based approaches. Including interdisciplinary contributions, it presents innovative approaches and highlights how they can best support both economic and sustainable development, through better use of data, more effective institutions, and global, local and individual action, for the welfare of all societies.

The series particularly features conceptual and empirical contributions from various interrelated fields of science, technology and innovation, with an emphasis on digital transformation, that focus on providing practical solutions to **ensure food, water and energy security to achieve the SDGs.** It also presents new case studies offering concrete examples of how to resolve sustainable urbanization and environmental issues in different regions of the world.

The series is intended for professionals in research and teaching, consultancies and industry, and government and international organizations. Published in collaboration with IEREK, the Springer ASTI series will acquaint readers with essential new studies in STI for sustainable development.

ASTI series has now been accepted for Scopus (September 2020). All content published in this series will start appearing on the Scopus site in early 2021.

More information about this series at https://link.springer.com/bookseries/15883

Mustapha Meghraoui ·
Narasimman Sundararajan ·
Santanu Banerjee · Klaus-G. Hinzen ·
Mehdi Eshagh · François Roure ·
Helder I. Chaminé · Said Maouche ·
André Michard
Editors

Advances in Geophysics, Tectonics and Petroleum Geosciences

Proceedings of the 2nd Springer Conference of the Arabian Journal of Geosciences (CAJG-2), Tunisia 2019

Springer

Editors
Mustapha Meghraoui
EOST - Institut Terre et Environnement de Strasbourg
University of Strasbourg, CNRS - UMR
Strasbourg, France

Santanu Banerjee
Department of Earth Sciences
Indian Institute of Technology Bombay
Mumbai, Maharashtra, India

Mehdi Eshagh
University West
Trollhättan, Västra Götalands Län, Sweden

Helder I. Chaminé
Laboratory of Cartography and Applied Geology
School of Engineering (ISEP), Polytechnic of Porto
Porto, Portugal

André Michard
Paris-Sud University
Paris, France

Narasimman Sundararajan
Department of Earth Sciences
Sultan Qaboos University
Muscat, Oman

Klaus-G. Hinzen
University of Cologne
Bergisch Gladbach
Nordrhein-Westfalen, Germany

François Roure
Géosciences
IFP Energies Nouvelles
Rueil-Malmaison, France

Said Maouche
Center for Research in Astronomy
Astrophysics and Geophysics
Alger, Algeria

ISSN 2522-8714 ISSN 2522-8722 (electronic)
Advances in Science, Technology & Innovation
IEREK Interdisciplinary Series for Sustainable Development
ISBN 978-3-030-73025-3 ISBN 978-3-030-73026-0 (eBook)
https://doi.org/10.1007/978-3-030-73026-0

About the 2nd Springer Conference of the Arabian Journal of Geosciences (CAJG-2), Tunisia 2019

The Arabian Journal of Geosciences (AJG) is a Springer journal publishing original articles on the full range of Earth sciences in partnership with the Saudi Society for Geosciences. The journal focuses on, but is not limited to, research themes which have regional significance for the Middle East, the Euro-Mediterranean, Africa, Asia and some other regions of the world. The journal receives on average 4000 submissions a year and accepts around 1000 papers for publication in its 24 annual issues (acceptance rate around 25%). It benefits from the participation of an editorial team of 100 international Associate Editors who generously help in evaluating and selecting the best papers.

In 2008, Prof. Abdullah Al-Amri, in close partnership with Springer, founded the Arabian Journal of Geosciences (AJGS). In 2018, the journal celebrated its 10th anniversary. To mark the event, the founder and Editor-in-Chief of the AJGS organized the 1st Conference of the Arabian Journal of Geosciences (CAJG) in close collaboration with Springer on 12–15 November 2018. The conference was an occasion to endorse the journal's long-held reputation

and brought together 450 authors from 70 countries, who work in the wide-ranging fields of Earth sciences. The dynamic four-day conference in a stimulating environment in Hammamet, Tunisia provided attendees with opportunities to share their latest unpublished findings and learn about the latest geosciences studies. The event also allowed attendees to meet and talk to the journal's editors and reviewers. Three field trips were organized alongside the conference, and many participants enjoyed the wonders of the geology of Tunisia.

In a continuation of the successful 1st CAJG, the 2019's conference aimed to bring geoscientists from all over the world to present and discuss their most recent findings. The 2nd CAJG was an occasion to publish the newest findings in its proceedings by Springer and a special issue in the AJGS, with a clear mission to drive greater North-South (Europe-Africa) scientific cooperation and to open doors to new and enriching collaborations with geoscientists based in Asia and the Americas. The 2nd CAJG devoted a special session (workshop) to studies focusing on unraveling the undiscovered oil and gas resources in the Mediterranean and North Africa. Many international experts took part in the discussion.

The conference covered all cross-cutting themes of geosciences and focused principally on the following 15 tracks:

- Track 1. Atmospheric Sciences, Meteorology, Climatology, Oceanography
- Track 2. Biogeochemistry, Geobiology, Geoecology, Geoagronomy
- Track 3. Earthquake Seismology and Geodesy
- Track 4. Environmental Earth Sciences
- Track 5. Exploration & Theoretical Geophysics, Seismic & Well Logging Methods, Mathematical Geosciences
- Track 6. Geo-Informatics and Remote Sensing
- Track 7. Geochemistry, Mineralogy, Petrology, Volcanology
- Track 8. Geological Engineering, Geotechnical Engineering
- Track 9. Geomorphology, Geography, Soil Science, Glaciology, Geoarchaeology, Geoheritage
- Track 10. Hydrology, Hydrogeology, Hydrochemistry
- Track 11. Marine Geosciences, Historical Geology, Paleoceanography, Paleoclimatology
- Track 12. Numerical and Analytical Methods in Mining Sciences and Geomechanics
- Track 13. Petroleum and Energy Engineering, Petroleum Geochemistry
- Track 14. Sedimentology, Stratigraphy, Paleontology, Geochronology
- Track 15. Structural Geology, Tectonics and Geodynamics, Petroleum Geology

The dynamic four-day conference provided more than 400 attendees with opportunities to share their latest unpublished findings and learn the newest geosciences studies. The event also allowed attendees to meet and discuss with the journal's editors and reviewers.

More than 710 short contributing papers to the conference were submitted by authors from more than 74 countries. After a pre-conference peer review process by more than 500 reviewers, 462 papers were accepted. These papers are published as chapters in the conference proceedings which consist of four edited volumes, each edited by the following group of Arabian Journal of Geosciences (AJGS) editors and other guest editors:

Proceedings Volume 1: New Prospects in Environmental Geosciences and Hydrogeosciences

Haroun Chenchouni: University of Tebessa, Tebessa, Algeria
Helder I. Chaminé: School of Engineering—ISEP, Polytechnic of Porto, Porto, Portugal
Md Firoz Khan: Department of Chemistry, Faculty of Science, University of Malaya, Kuala Lumpur, Malaysia

Proceedings Volume 2: Advances in Geophysics, Tectonics and Petroleum Geosciences

Proceedings Volume 3: Recent Research on Geomorphology, Sedimentology and Geochemistry

Proceedings Volume 4: Research developments in Geotechnics, Geo-Informatics and Remote Sensing

About the Conference Steering Committee

General Chair

Abdullah Al-Amri
Founder and Editor-in-Chief
Arabian Journal of Geosciences
King Saud University, Saudi Arabia

Conference Supervisor

Nabil Khélifi
Senior Publishing Editor, MENA program
Journal Publishing Manager
Arabian Journal of Geosciences
Springer, a part of Springer Nature, Germany

Advisory Co-chair

Walter D. Mooney
Guest of Editorial Board
Arabian Journal of Geosciences
United States Geological Survey Western Region, USA

Advisory Co-chair

Dorrik Stow
Guest of Editorial Board
Arabian Journal of Geosciences
Heriot-Watt University, Edinburgh, Scotland

Scientific Committee Co-chair

François Roure
Chief Editor—Track 15
Arabian Journal of Geosciences
IFP—Energies Nouvelles, France

Scientific Committee Co-chair

Biswajeet Pradhan
Chief Editor—Track 6
Arabian Journal of Geosciences
University of Technology Sydney, Australia

Local Organizing Co-chair

Mohamed Soussi
Former Associate Editor
Arabian Journal of Geosciences
Tunis El Manar University, Tunis, Tunisia

Local Organizing Co-chair

Samir Bouaziz
Former Associate Editor
Arabian Journal of Geosciences
University of Sfax, Sfax, Tunisia

Publications Co-chair

Beatriz Bádenas
Chief Editor—Track 14
Arabian Journal of Geosciences
University of Zaragoza, Zaragoza, Spain

Publications Co-chair

Marina Rabineau
Chief Editor—Track 11
Arabian Journal of Geosciences
University of Brest, Brest, France

Program Co-chair

Amjad Kallel
Chief Editor—Track 4
Arabian Journal of Geosciences
ENIS, University of Sfax, Tunisia

Program Co-chair

Sami Khomsi
Former Associate Editor
Arabian Journal of Geosciences
King Abdulaziz University, Jeddah, Saudi Arabia

Proceedings Editorial Manager

Mourad Amer
Editor of Springer/IEREK ASTI Series
Guest of Editorial Board of AJGS
IEREK, Alexandria, Egypt

Communication Chair

Zakaria Hamimi
Associate Editor
Arabian Journal of Geosciences
Benha University, Benha, Egypt

Public Relations Chair

Faïez Gargouri
Director of the Higher Institute of Computer Science and Multimedia
President of the AIG
University of Sfax, Tunisia

Conference Manager

Mohamed Sahbi Moalla
Journal Coordinator
Arabian Journal of Geosciences
ISET, University of Sfax, Tunisia

Preface

The diversity of the geological and geophysical structures and its components are major markers of the evolution of our planet. Field and laboratory studies leading sometimes to discoveries are a necessary step to unveil the outstanding variety of rocks, their transformation and deformation that may enhance our understanding of the Earth's formation. Previously forming a large part of the Pangea, the African continent and its conterminous domains such as the Arabian Plate, the Mediterranean and Indian Ocean regions conceal a wealth of indicators on the plate tectonics and mineral resources. The continent that seems stable displays seismic ruptures, active tectonics and volcanoes as a testimony of the still alive telluric activity and as a warning for the building of proper mitigation plans against catastrophes mainly due to anthropic occupations. The development of research programs in geology and geophysics is becoming a real challenge for the Earth environmental settings.

Four sections spanning a large spectrum of geological and geophysical topics form the content of conference tracks presented during the 2nd CAJG. The proceedings volume presents here a series of research methods that are nowadays in use for measuring, quantifying and analyzing the targeted geological domains. Remote sensing with high-resolution satellite imagery, seismology, geochemistry, theoretical geophysics and related profiles with tomographic images, earthquake geology with times series radar interferometry and related geodetic-GPS campaigns, well-logging contribute to scrutinizing the Earth tectonic architecture. Several contributions are from young researchers that often benefited from training sessions during previous meetings. Fundamental questions that address the genesis and evolution of our planet are built upon data collection and experimental investigations under physical constitutive laws which are the conditions for a successful scientific research. These multidisciplinary approaches combined with the geodynamics of tectonic provinces and investigations of potential zones of natural resources (petroleum reservoirs) provide the basis for the economic development.

Strasbourg, France	Mustapha Meghraoui
Muscat, Oman	Narasimman Sundararajan
Mumbai, India	Santanu Banerjee
Bergisch Gladbach, Germany	Klaus-G Hinzen
Trollhättan, Sweden	Mehdi Eshagh
Rueil-Malmaison, France	François Roure
Porto, Portugal	Helder I. Chaminé
Alger, Algeria	Said Maouche
Paris, France	André Michard

Contents

Geodesy and Exploration & Theoretical Geophysics

Layout: T3_Grey | Book ID: 502827_1_En | Book ISBN: 978-3-030-73025-3
Chapter No.: FM 1 | Date: 10-5-2024 | Time: 3:11 pm | Page: 28/35

About the Editors

Mustapha Meghraoui (Ph.D.) is a senior research scientist (Physicien 1ère Classe) at the IPG Strasbourg (France). He leads the "Active Tectonics and Paleoseismology" group of IPG Strasbourg and develops programs in the study of earthquake faulting, seismotectonics, paleoseismology, paleotsunami and geological hazards. He has played a significant role in the identification of earthquake faulting in intraplate and interplate tectonic domains. He teaches active tectonics and paleoseismology to Master I and II degree students and conducted more than 12 Ph.D. theses at the University of Strasbourg. He has been a coordinator and PI in previous and current scientific projects in Europe and Middle East (EC-funded PALEOSIS ENV4-CT97-0578; SAFE EVG1-2000-22005, RELIEF EVG1-2002-00069, APAME ICA-CT-2002-10024, TRANSFER EC GOCE Contract No. 037058, FP7-ENV.2013.6.4-3-ASTARTE), in Algeria (PNE, ACI, CMEP) and in Africa (IGCP-601, IGCP-659 Seismic Hazard and Risk in Africa). He is elected President of the African Seismological Commission, Freeman of the city of Chlef (ex El Asnam, Algeria), Honor Medalist of Aristoteles University (Thessaloniki, Greece), Merit Medalist of the Italian Ministry of Interior and Honor Medalist of the Turkish Geological Society. He is a founding member of the Algerian Academy of Science and Technology and author and co-author of about 98 peer-reviewed scientific publications in international journals, with 2967 citations and an H-index of 37 (ISI Web of Science).

Prof. Dr. Narasimman Sundararajan graduated in Mathematics from the University of Madras followed by a M.Sc. (Tech) and Ph.D. in Geophysics from Osmania University, India. He began a career as Research Scientist in the National Laboratory under Council of Scientific & Industrial Research and later switched over to teaching in Osmania University where he became Professor in 2004. Currently, he is Professor Geophysics in the Department of Earth Sciences, Sultan Qaboos University, Oman. He has published more than 90 research papers in the leading international journals. He has authored a book and a couple of chapters besides edited volume for Springer Publishers. He supervised successfully several Ph.Ds in Geophysics as well as Mathematics. He brought out a few innovative tools for processing and interpreting of various geophysical data besides a mathematical concept called "Sundararajan Transform." He implemented several research projects including one on Uranium exploration. He is Member of XIV Indian Scientific Expedition to Antarctica during 1994–1995. He introduced a valid and viable approach to multidimensional Hartley transform in contrast to the definition of Prof. R. N. Bracewell from Stanford University, USA. For his overall significant research contribution, the Government of India has conferred upon him the National Award for Geosciences in 2007. His research interests are varied and wide including geophysical data processing, mineral and ground water exploration, earth quake hazard assessment studies, etc. In 2015, he has joined the editorial board of *Arabian Journal of Geophysics* as Associate Editor. Currently, he is working as Chief Editor responsible for evaluating submissions in the field of theoretical and applied geophysics.

Prof. Santanu Banerjee is associated with Indian Institute of Technology Bombay since 1999. He supervised several research projects on sedimentology and stratigraphy of Indian sedimentary basins. Along with his collaborators, he attempted a correlation of Precambrian sedimentary successions across the world. He also carried out several research projects on petroleum geology sponsored by oil companies. His research interests include and petroleum geology, microbial mat structures in Precambrian siliciclastics, origin of glauconite and sequence stratigraphy. He has published more than 120 papers in peer-reviewed journals and books and edited two books. He is currently country Ambassador of Society for Sedimentary Geology (SEPM). He is one of the Topical Chief Editors in *Arabian Journal of Geosciences* and Associate Editor-in-Chief of the *Journal of Palaeogeography*. He also serves the editorial board of the *Journal of Earth Systems Science* and *Journal of Indian Association of Sedimentologists*.

Klaus-G. Hinzen's main interests are local earthquake seismology, engineering and particularly archaeoseismology; he worked on source mechanisms of induced and teleseismic earthquakes at the Ruhr-University, Bochum (Ph.D. thesis). During 11 years at the Federal Institute for Geosciences and Natural Resources (BGR), Hannover, he gained experience in seismic in situ testing methods and the modeling of the dynamic behavior of underground openings. In several projects, he developed methods to reduce environmental effects of blast vibrations. In 1995, he became director of the Earthquake Geology Division of the Institute for Geology and Mineralogy of University of Cologne (BNS). The division runs a local seismic network in the northern Rhine area (NRA) which he expanded to 40 seismic stations including a strong motion network and monitoring of Cologne Cathedral. In several projects, the first instrumental earthquake catalog of the NRA was published, historical and palaeoseismological studies were made and a ground amplification model for the southern Lower Rhine Embayment was developed. Since two decades quantitative archaeoseismic studies based on laser scan surveys and discrete element modeling in the Rhine area, Turkey, Greece, Italy, Israel and Tunisia are in the focus of his work which continues after his retirement in 2018.

Mehdi Eshagh received his B.Sc. in Surveying Engineering in 1999 from Islamic Azad University, Iran, his M.Sc. in Geodesy in 2002 from K. N. Toosi University of Technology, Iran, and his Ph.D. in Geodesy in 2009 from the Royal Institute of Technology (KTH) in Sweden. In October 2010, he was appointed as Docent/Associate Professor of Physical Geodesy/Space Geodesy at KTH and, since 2013, has been Professor of Geodesy at University West, Sweden. He has taught a variety of courses in surveying engineering at different levels of education, from high school to Ph.D. programs, since 1999. His research interests are mainly in the fields of physical geodesy, in particular geoid and gravity field determination, satellite gravimetry and gradiometry, adjustment theory, satellite orbit determination, geodetic network optimization and design, theories of isostasy, Moho and density contrast determination and sub-lithospheric stress modeling using gravimetric data. He has published and co-authored over 150 original articles, monographs, text-books, edited books, special issues and conference abstracts. He is Founder and Editor-in-Chief of the *Journal of Geodetic Science* and is currently Editor of the *Journal of Geodesy and Geomatics Engineering*and the *Arabian Journal of Geosciences*.

François Roure is a graduate of the Ecole Normale Supérieure of St-Cloud, France, and holder of Doctorate in Sciences from the University of Paris VI. He joined the IFP's GeologyGeochemistry-Geophysics Division in 1984, following a 4-year career at the CNRS. His research is predominantly focused on the study of sedimentary basins (architecture and geodynamics, thermicity, oil-bearing systems, fluid/rock interactions and reservoir characterization). He was selected as an extraordinary professor from IFP at the Free University of Amsterdam (VU) and then in Utrecht. He is former Editor of Tectonics, and he also chaired for 10 years the working group on sedimentary basins in the International Lithosphere Program (ILP). He has contributed more than 100 articles and published in prestigious international journals. In 2010, François Roure was honored by the European Association of Geoscientists and Engineers (EAGE), which selected him as the winner of the2010 Wegener Award, as a recognition of his contribution to the geoscientific research in the area of petroleum exploration of frontier areas and the search for new reserves, particularly in mountain belts. He is the current chief editor for Track 15 of the *Arabian Journal of Geo-Sciences*.

Helder. I. Chaminé is skilled Geologist and Professor of Engineering Geosciences at the School of Engineering (ISEP) of the Polytechnic of Porto, with over 32 years' experience in multidisciplinary geosciences research, consultancy and practice. He studied geological engineering and geology (B.Sc., 1990) at the Universities of Aveiro and Porto (Portugal), respectively. He received his Ph.D. in geology at the University of Porto in 2000 and spent his postdoctoral research in applied geosciences at the University of Aveiro (2001–2003). In 2011, he received his Habilitation (D.Sc.) in geosciences from Aveiro University. Before joining academy, he worked over a decade in international projects for mining, geotechnics and groundwater industry and/or academia related to geodynamics and regional geology, hard-rock hydrogeology and water resources, engineering geosciences and applied geomorphology, rock engineering and georesources. His research interests span over fundamental to applied fields: GIS mapping techniques for applied geology, structural geology and regional geology, engineering geosciences and rock engineering, slope geotechnics, mining geology and hydrogeomechanics, hard-rock hydrogeology, exploration hydrogeology, urban groundwater and hydromineral resources. He has interests on mining geoheritage, history of cartography, military geosciences and higher-education dissemination, skills and core values. Presently, he is Head of the Laboratory of Cartography and Applied Geology (LABCARGA|ISEP), Senior Researcher at Centre GeoBioTec| U.Aveiro and Centre IDL| U.Lisbon, as well as belongs to the executive board of the M.Sc.+B.Sc. Geotechnical and Geoenvironmental Engineering (OE+EUR-ACE Label) and the Department of Geotechnical Engineering (ISEP). Currently, he

belongs to the board of the Technical Committee of Environmental Geotechnics of the Portuguese Geotechnical Society (SPG) and IAH—Portuguese Chapter. He was a board member of the APGeom—Portuguese Association of Geomorphologists (2009–2013), APG - Portuguese Association of Geologists (2020), and SPG (2016–2020). He was a consultant and was responsible over 70 projects of rock engineering, applied geology, hydrogeomechanics, slope geotechnics, mining geology, exploration hydrogeology, hard-rock hydrogeology, water resources, urban groundwater and applied mapping (Mozambique, Portugal and Spain). He has been co-authored over 220 publications in indexed journals, conference proceedings/full papers, chapters, technical and professional papers. He co-edited over 15 special volumes, as well as is presently evolved in editing themed issues for three international journals (Geotechnical Research ICE, Springer Nature Applied Sciences and Water MDPI). He has a wide activity as a referee for several international journals. He served as invited Expert Evaluator of Bologna Geoscience Programme for DGES (Portugal) and Scientific Projects Evaluation for NCST, 2017–2019 (Kazakhstan) and NRF|RISA, 2019 (South Africa), as well as Coordinator of "Geology on Summer/Ciência Viva" program at ISEP, since 2005, for geosciences dissemination. He has been also active with teaching and supervising of many Ph.D., M.Sc. and undergraduate students. He has been on the editorial board, among others of *Arabian Journal of Geosciences* (SSG +Springer), *Hydrogeology Journal* (IAH+Springer), *Euro-Mediterranean Journal for Environmental Integration* (Springer), *Springer Nature Applied Sciences* (Springer), *Mediterranean Geoscience Reviews* (Springer), *Geotechnical Research* (ICE), *Geosciences* (MDPI), *Revista Geotecnia* (Portugal) and *Geología Aplicada a la Ingeniería y al Ambiente* (Argentina). He integrates as moderator or session chair in several conferences, workshops and meetings. Currently, is in organizing/scientific committee of the 3rd International Workshop on Natural Hazards—NATHAZ'22 (Terceira Island, Azores, May 2022).

Dr. Said Maouche is currently Professor of structural geology and earthquake geology at the Centre de Recherche en Astronomie, Astrophysique et Geophysique (CRAAG) in Algeria. He is the author of more than 50 publications peer-reviewed journals. He serves as reviewer in several international journals. His research falls in different areas of interest: currently works on active tectonics, earthquakes, neotectonics and coastal tectonics, geology and geomorphology, tsunami deposits, floods and environment.

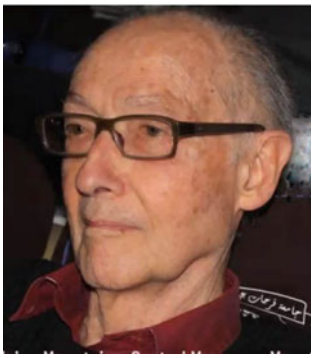

André Michard is a graduate of the Ecole Normale Supérieure, holder of the Agrégation of Natural Sciences (1955) and holder of a doctorate in Earth Sciences from the University of Paris Sorbonne (1966). He is an emeritus professor from the University of Paris-Sud (Orsay) since 1999. He began his academic career in the latter university, just launched, in 1958, after a Ph.D. thesis in the Western Alps, and kept working in the Alpine belts (Alps, Oman, Taurus, Cuba) until the early 2000s. He discovered Morocco in 1966 as a professor at Mohamed-V University, Rabat, and immediately fell in love of the geology of the country. His first works concerned the Variscan metamorphic domains of the Western Meseta. Once appointed professor at the University of Strasbourg (1968), he extended his Moroccan works to the Rif belt in connection with the Spanish geologists of the Betics. He published a first overview of Moroccan Geology in 1976 ("Eléments de Géologie marocaine"; 3rd edition in 2001, also translated in Japanese) and a second one co-authored by a large panel of Moroccan or European specialists, in 2008 ("Continental evolution: the Geology of Morocco"). In the meanwhile, he collaborated with several Moroccan academics in research programs targeting the High Atlas, Anti-Atlas and the Saharan domains. Based on this experience, he was the linchpin of the editing program of the "Nouveaux Guides géologiques et Miniers du Maroc" (2011, vol. 1–9). In the last decade, he co-authored also some 20 articles dealing with the structural geology, geodynamics, stratigraphy, paleontology or geoheritage of the various regions of Morocco. From the beginning of his academic activity, he has contributed more than 100 articles published in prestigious international journals. The first West African Craton and Margins International Workshop (Dakhla, Apr. 2017) has been dedicated to André as a tribute for his jubilee of works in Morocco.

Dr. Abdullah Al-Amri holds a B.Sc. in Geology (1981) from King Saud University (KSA), a M.Sc. in Applied Geophysics (1985) from the University of South Florida (USA) and a Ph.D. degree in Earthquake Seismology (1990) from the University of Minnesota (USA). He is currently Professor of Earthquake Seismology at King Saud University (KSU) and Director of the Seismic Studies Center at KSU, the Chairman of KSU's Geology and Geophysics Department and the President of the Saudi Society for Geosciences (SSG). He has received several international prizes and awards for scientific excellence and innovation. His research interests focus on crustal structures and seismic microzoning of the Arabian Peninsula. He has conducted more than 45 research projects, the most recent of which involved EM and MT applications in deep groundwater exploration of the Empty Quarter, and geothermal prospecting of volcanic Harrats in the Arabian shield. He has co-published 65 research articles in international indexed and refereed

journals and authored several books. In 2008, he, in close partnership with Springer, founded the Arabian Journal of Geosciences (AJGS) on behalf of the SSG. In 2018, Marquis Who's Who, the world's premier publisher of biographical profiles, proudly presented to him with the Albert Nelson Marquis Lifetime Achievement Award.

Earthquake Seismology and Geodesy (T3): IGCP-659 Meeting—Seismic Hazard and Risk Assessment in Africa

Tsunami Hazard Along the Eastern African Coast from Mega-Earthquake Sources in the Indian Ocean

Amir Salaree and Emile A. Okal

Abstract

The catastrophic 2004 Indonesian tsunami reached the shores of Eastern Africa, where it affected at least 12 countries and caused several hundred casualties, principally in Somalia. Significant variations in run-up were documented by various post-tsunami surveys (note that the latter remain incomplete, especially in Southern Tanzania and Mozambique). In a previous study, Okal et al. (Okal et al. South Afr. J. Geol. 112:343–358, 2009) it has been suggested that these variations could depend on the precise location of the tsunami sources, as a result of the combined effect of source directivity and refraction by irregular bathymetry. In this context, we present the results of a significantly enhanced study, which considers a total of twelve potential sites of mega-earthquakes, along both the Sunda Arc, and the Makran subduction zone. Numerical simulations are carried out at a total of 25 virtual gauges, spanning the East African coast from Socotra in the north to Port Elizabeth in the south, as well as adjoining islands (Madagascar, Comoros, Mascarenes). In particular, we identify locations where the 2004 tsunami (which to a large extent awakened the awareness of the continent to tsunami danger) may not have represented the worst-case scenario.

Keywords

Tsunami • Indian Ocean • Eastern Africa • Earthquake

1 Introduction

The Sumatra-Andaman tsunami of 26 December 2004 was the first in modern history to export death and destruction across the Indian Ocean Basin. It affected the coastlines of Eastern Africa, where it caused an additional ∼300 casualties, principally in Somalia, but also all the way to South Africa. In a previous study, Okal et al. (2009; hereafter Paper I) used numerical simulations to investigate a number of credible scenarios for future large Indonesian tsunamis impacting the Western Indian Ocean shorelines. In this context, we present here an update of the Paper I, which is enhanced in several aspects. First, we increase the number of virtual gauges from 19 to 25, by targeting additional shorelines in Tanzania and Northern Mozambique (Fig. 1). Second, we fine-tune the position of all virtual gauges to ensure a commonality of water depth, chosen as 1000 m for all the locations, thus allowing more meaningful comparison between gauges. Finally, we add sources in the Makran subduction zone, the only other region with known earthquakes having generated large tsunamis in the Indian Ocean Basin.

2 Earthquake Sources and Hydrodynamic Simulations

We use sources located at both the Sumatra and Makran Trenches, similar to those used in Paper I. Source **S.I** models the 2004 event as a composite rupture. Source **S.II** uses Okal and Synolakis (2008) model of the 1833 earthquake. Source **S.III** models the main 2007 Bengkulu earthquake, using Borrero et al. (2009) simple source. Source **S.IV** releases the strain left over on the 1797 and 1833 ruptures after the 2007 Bengkulu event, as detailed in Okal and Synolakis (2008); it is representative of the widely expected Padang earthquake which should close that seismic gap in the next decades (McCloskey et al. 2010). Finally, Source **S.V** is similar to **S.**

A. Salaree (✉)
University of Michigan, Ann Arbor, MI 48109, USA
e-mail: salaree@umich.edu

E. A. Okal
Northwestern University, Evanston, IL 60208, USA

M. Meghraoui et al. (eds.), *Advances in Geophysics, Tectonics and Petroleum Geosciences*,
Advances in Science, Technology & Innovation, https://doi.org/10.1007/978-3-030-73026-0_1

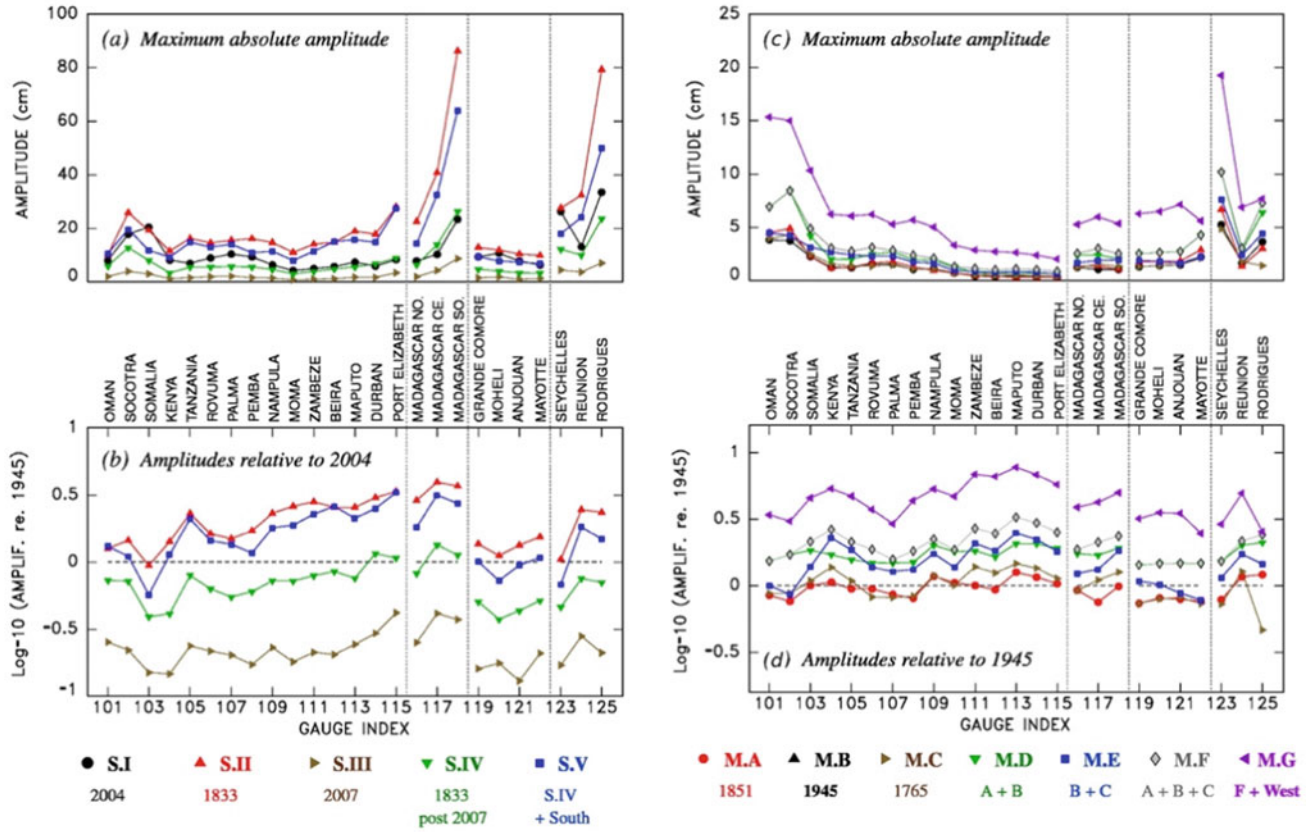

Fig. 1 (Left) Summary of Sumatra simulations at the 25 virtual gauges. **a** Maximum absolute amplitude recorded at each gauge, color-coded according to source model. **b** Amplitudes relative to 2004, plotted on a logarithmic scale. See text for discussion. (Right) Same as the left panel in the case of the Makran simulations. Note the different vertical scale in (**c**).In **d** amplitudes are taken relative to the quantified event of 1945

IV, but it extends south toward the Sunda Straits, and reproduces Okal and Synolakis (2008) speculative Model 2a.

Historical records (e.g., Ambraseys and Melville 1982) suggest the occurrence of tsunamigenic earthquakes on either side of the 1945 rupture (our Model **M.B**), in 1851 (and possibly 1864) to the west, and in 1765 to the east. Following Okal and Synolakis (2008), we use such scenarios as models **M.A** and **M.C**, respectively. We then use the concept of fault fragmentation along a subduction zone to build three additional models in which two or more of the three blocks (A, B, C) rupture simultaneously. Here, we consider Models **M.D**, **M.E**, and **M.F** as combined ruptures of [A-B], [B-C], and [A-B-C], respectively. We also consider prolonging Model **M.F** $\sim$450 km to the fest as a very large and highly speculative scenario as Model **M.G**. As initial conditions for the vertical displacements of the sea surface, $\eta(t = 0_+)$, we use the field of static deformations resulting from the seismic dislocation, computed through the algorithm of Mansinha and Smylie (1971) in the geometry of a homogeneous half-space. We adopt this algorithm over the more recent versions as it has been extensively tested and validated through detailed tsunami studies (e.g., Borrero et al. 2009).

We then use the extensively validated MOST algorithm (Titov et al. 2016) which solves the full non-linear equations of hydrodynamics under the shallow-water approximation. The simulations use the 2–arcmin grid ETOPO, a time step of 5 s satisfying the CFL stability condition and are carried on for 24 h. We do not compute the interaction of the wavefield with very shallow bathymetry or initially dry land, but rather stop the computation at the 20-m isobath in the vicinity of coastlines. This procedure still allows the comparison, at a given site, of tsunamis emanating from neighboring but distant provinces.

3 Results

The locations of the 25 virtual gauges are indexed starting at 101. The left and right panels in Fig. 1 show the profiles of maximum amplitude at the gauges, as a function of their index for Sumatra and Makran, respectively. Along the coast

of East Africa, maximum amplitudes are generally contained under 20 cm (with a couple exceptions), and their lateral variations are limited. Due to directivity (Ben-Menahem and Rosenman 1972), Models **S.II** and **S.V** produce amplitudes larger than the 2004 event (Model **S.I**), even though the moments of the parent earthquakes are smaller. This constitutes a major observation, namely that the 2004 tsunami did not amount to a "worst-case scenario". Our results are particularly critical in the case of Madagascar, where all models show a regular increase in amplitude form north to south, this trend being generally confirmed by the dataset of 2004 surveyed run-up values (Okal et al. 2006). In this respect, Fig. 1 suggests that the Mascarene Plateauacts as a barrier effectively sheltering Northern Madagascar, while waves can reach its southern coast by skirting the Mascarene Islands (Rodrigues, Mauritius and Réunion). We also note that while the largest amplitudes in Fig. 1 are below 1 m due to the excitation and propagation characteristics of tsunamis, such amplitudes correspond to extremely large amounts of energy compared to regular oceanic waves, especially while running up the coastal slopes (Okal and Synolakis 2003).

With the exception of the speculative Model **M.G**, simulations for the Makran sources yield generally much smaller amplitudes at our virtual gauges than for the Sumatra models. This a combined reflection of the generally smaller size of the seismic sources, and of their orientation, which results in directivity lobes beaming SSE, away from Africa and its neighboring islands. As would be expected under this particular geometry, moving the source west (**M.A**) to east (**M.B** to **M.C**) leaves the far-field amplitude pattern essentially unchanged, while the composite sources (**M.B**, **M.E**, **M.F**) feature values enhanced by an average factor of two, which could lead to significant run-up values in the Seychelles and Rodrigues. Only the extreme, speculative model **M.G** produces decimetric amplitudes approaching those simulated for Sumatran sources.

4 Conclusions

The distribution of off-shore tsunami amplitudes varies significantly with the location of mega-earthquakes along the Sumatra Trench, as a result of the combination of directivity effects and refraction by irregular bathymetry. Consequently, and despite its extreme moment (1.2×10^{30} dyn*cm), which may not be duplicated in future Sumatran large earthquakes, the 2004 Sumatra-Andaman event does not always constitute the worst-case scenario for tsunami hazard at various sites on the East African shoreline or its neighboring islands. We regard this as a crucial result, since the exceptional size of the 2004 event could give a false sense of security from a disastrous basin-wide tsunami following great earthquakes which may not match its seismic moment.

In general, tsunami hazard from large events in the Makran remains relatively low, mainly due to unfavorable directivity at the source, the only potential exception being the highly improbable model **M.G**, which could occasionally give rise to amplitudes comparable to those observed in 2004. Given the continuing level of speculation surrounding the nature of the plate convergence in the Western Makran, it is clear that a program of multidisciplinary research is warranted in that region, including monitoring of sea-floor deformation through underwater geodesy, as well as paleo-tsunami investigations.

References

Ambraseys, N.N., Melville, C.P.: A History of Persian Earthquakes. Cambridge Univ. Press, Cambridge, 219 p (1982)

Ben-Menahem, A., Rosenman, M.: Amplitude patterns of tsunami waves from submarine earthquakes. J. Geophys. Res. **77**, 3097–3128 (1972)

Borrero, J.C., Weiss, R., Okal, E.A., Hidayat, R., Arcas, D., Titov, V. V.: The tsunami of 12 September 2007, Bengkulu Province, Sumatra, Indonesia: post-tsunami survey and numerical modeling. Geophys. J. Intl. **178**, 180−194 (2009)

Mansinha, L., Smylie, D.E.: The displacement fields of inclined faults. Bull. Seismol. Soc. Amer. **61**, 1433–1440 (1971)

McCloskey, J., Lange, D., Tilmann, F., Nalbant, S.S., Bell, A.F., Natawidjaja, D.H., Rietbock, A.: The September 2009, Padang earthquake. Nat. Geosci. **3**, 70–71 (2010)

Okal, E.A., Synolakis, C.E.: A theoretical comparison of tsunamis from dislocations and landslides. Pure Appl. Geophys. **160**(10–11), 2177–2188 (2003)

Okal, E.A., Synolakis, C.E.: Far-field tsunami hazard from mega-thrust earthquakes in the Indian Ocean. Geophys. J. Intl. **172**, 995–1015 (2008)

Okal, E.A., Fritz, H.M., Raveloson, R., Joelson, G., Pančošková, P., Rambolamanana, G.: Madagascar field survey after the December 2004 Indian Ocean tsunami. Earthq. Spectra **22**, S263–S283 (2006)

Okal, E.A., Fritz, H.M., Sladen, A.: 2004 Sumatra tsunami surveys in the Comoro Islands and Tanzania and regional tsunami hazard from future Sumatra events. South Afr. J. Geol. **112**, 343–358 (2009)

Titov, V., Kanoglu, U., Synolakis, C.: Development of MOST for real-time tsunami forecasting. J. Waterway Port Coast Oc. Eng. **142** (6), 03116004, 16 pp (2016)

Preliminary Tsunami Hazard Map for Africa

Asem Salama, Mohamed ElGabry, Mustapha Meghraoui, and Hesham Hussein Moussa

Abstract

Tsunami worst-case scenarios were modelled for some tsunamigenic sources towards the coasts of African cities. These tsunamigenic sources are the ones known with our present knowledge from the historical and recent records. Mirone software version 2.10 update: the 11th of July 2018 (Luis 2007) was used to model the wave height and travel time. The data of bathymetry used in this study were 1-min arc per second for a source distance greater than 1000 km and 30 arc per second for source distances less than 1000 km and high resolution for the nearby shoreline coastal area as available. 2–4 m was the calculated maximum wave height resulted from the scenario (1) which arrived to the coasts of Tanzania, South Africa, and South Madagascar, while scenario (2) resulted in a maximum wave height of 1–2 m towards the Somalian coast. The scenarios (3) and (4) were responsible for maximum wave height of 2–4 m at the Egyptian and Libyan coasts.

Keywords

African tsunamis • Modelling • Tsunami hazard map

1 Introduction

Tsunamis are natural hazards that can trigger severe disasters. In the last 30 years, more than 290 tsunamis were observed worldwide. Around 250 thousand deaths resulted from two transoceanic tsunamis: 2004 Indian Ocean and 2011 Tohoku (Gusiakev et al. 2019). Many lessons were gained from these two significant events, aiming to provide understanding, detecting and mitigation of the impacts of tsunamis. Large earthquakes and tsunamis have affected the coastal areas along the African continent (Okal and Hartnady 2009). Few studies were conducted to model the worst-case scenarios and the effects of the far-field tsunamigenic sources of the whole African coastal areas as a key for tsunami hazard issues. Although Løvholt et al. (2009) used numerical modelling to predicate the sources, amplitude which could affect the South African zone and the results of the study were published as a tsunami hazard map of Africa UNISDR report (2009).

The tsunamigenic sources of large earthquakes and mega-tsunamis that impacted the African coastal cities were: (1) Andaman and Sumatra subduction zone [2004 Sumatra earthquake (Mw 9.1; Duputel et al. 2012)], (2) Makran [1945 Arabian sea (Mw 8.1; Byrne et al. 1992)], (3) Eastern Crete Island [1303 east Crete island (Mw 9.0; Ambraseys 2009)] (4) Western Crete Island [21 July 365, (Mw = 8.2; Shaw et al. 2008)] (5) Sicily and Calabria [1908 Messina and Reggio earthquake, (Mw = 7.0; Pino et al. 1908)], (6) Alboran Sea [1755 earthquake, (Mw = 8.5; Baptista et al. 2003)], (7) Gloria transform fault zone and Atlantic tectonic regions [1941 earthquake, (Mw = 8.4; Baptista et al. 2016)], (8) South Atlantic subduction zone, (9) Caribbean subduction zone, and (10) volcanic islands nearby the African coastlines. Highly dangerous tsunamigenic sources had chosen that affect the East Africa part as a starting point to create models to define maximum wave heights for the tsunami hazard map of Africa. Different scenarios have been tested with parametric study for the fault geometry for four

A. Salama (✉) · M. ElGabry · H. H. Moussa
National Research Institute of Astronomy and Geophysics, Helwan, 11421, Cairo, Egypt
e-mail: asem.mostafa@nriag.sci.eg

M. Meghraoui
EOST - Institut Terre et Environnement de Strasbourg, University of Strasbourg, CNRS - UMR 7063, Strasbourg, France

M. Meghraoui et al. (eds.), *Advances in Geophysics, Tectonics and Petroleum Geosciences*,
Advances in Science, Technology & Innovation, https://doi.org/10.1007/978-3-030-73026-0_2

Table 1 Fault geometry used in this study for modelling four different sources

Tsunamigenic sources	Length (km)	Width (km)	Slip (m)	Depth (km)	Seismic moment (dyne.cm)	Mw	Strike	Dip	Rake	Equivalent historical events	References
Scenario(1) Sumatra-Andaman	500	150	20	30	6.67×10^{25}	9.1	132	84	87	26th of December 2004	https://earthquake.usgs.gov/earthquakes/eventpage/official20041226005853450_30/moment-tensor
Scenario (2) Makran trench	350	100	15	30	2.4×10^{24}	8.8	270	5.5	89	27th of November 1945	Jaiswal et al. (2009)
Scenario (3) Eastern Hellenic arc	124	47	8	57	1.4×10^{28}	8.0	54	55	90	8th of August 1303	Pagnoni et al. (2015)
Scenario (4) Western Hellenic arc	115	45	16	40	2.48×10^{28}	8.2	133.5	45	90	21st of July 365	Stiros (2010)

tsunamigenic sources Sumatra–Andaman, Makran, Eastern Hellenic arc, western Hellenic arc. Mirone software version 2.10 (Luis 2007) was adopted to compute the travel time and the maximum wave height in the eastern Africa of the coastal areas. For the computation; we used workstation with a Quad-core 3.18 MHz processor and 16 Gigabytes of RAM.

2 Methodology

Eight models for the four tsunamigenic sources affecting the African coastal zones have been tested, two models for each tsunamigenic zone. Mirone software has been used (Luis 2007) which was built up a MATLAB code. This software version used the TINTOL (NSWING) code to perform tsunami modelling of the wave's propagation and inundation. For a better computational time optimization, linear inversion was used in the deep sea and non-linear inversion for the shallow waters, according to Luis (2007).

The fault's geometries were tested from previous studies as shown in Table 1. Some modification has been done to the previous studies to the chosen fault geometries to enlarge the historical events with calculations of uncertainties at the wave height. Algorithm of Okada (1985) was applied by the input of seismic parameters including the strike, dip and slip angles, seismic moment and dimensions (length and width) of the rupture area, as well as the earthquake's depth using the Mirone software to calculate the ground deformation for the given tsunamigenic sources.

3 Results

Four main worst-case scenarios were performed out toward the African continent (Table 1; Fig. 1). Scenario (1) models the wave propagation of the Sumatra–Andaman trench. Scenario (2) models the wave propagation from the second tsunamigenic Makran trench between Pakistan and Iran. Scenario (3) models wave propagation from a third tsunamigenic zone, eastern Hellenic arc. Scenario (4) models wave propagation from the fourth tsunamigenic zone western Hellenic arc. Our simulation results are summarized in a tsunami hazard map for the eastern part of the African continent (Fig. 1). This map shows an example of four different scenarios, compiling the maximum wave height grids at the coastal areas. For the northern Africa scenarios, 30 arcs per second (Layer B; IOC, Iho, and BODC 2003) bathymetry data has been used with nested grid 15 arc per second (Layer C; IOC, Iho, and BODC 2003) near the coastal zones. For East Africa scenarios, 1-min arc per second (ETOPO1; Amante and Eakins 2009) has been used as an external layer with nested grid 30 arc per second (layer B) from Tanzania to South Africa coastal areas for scenario (1) and nested grid 15 arc per second (layer c) at Somalia for scenario (2) (Fig. 1c).

The Sumatra–Andaman scenario was the most dangerous tsunami source in east Africa which resulted in a maximum wave height of 2–4 m at Tanzania, South Africa and South Madagascar coasts (Fig. 1c). Farther North Africa, the east Hellenic arc was the most dangerous tsunami source in historical tsunami records (Salama et al. 2018) towards the northern Egyptian coasts. The east Hellenic arc scenario

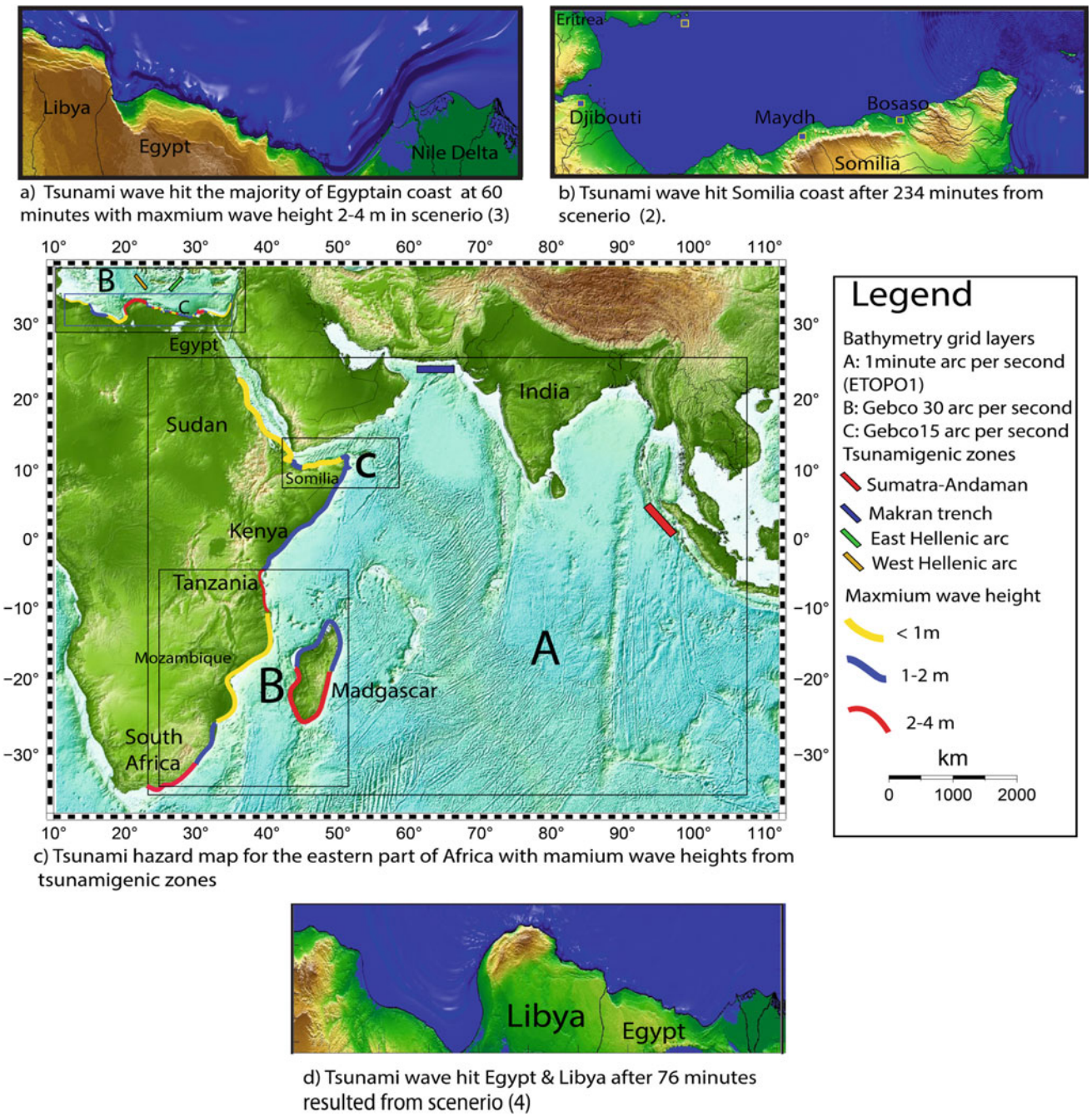

Fig. 1 Tsunami hazard map of the eastern part of Africa continent

created 2–4 m maximum wave height at the Egyptian coast while west Hellenic arc resulted in 2–4 m maximum wave height at Libya coast (Fig. 1c).

4 Discussion

Africa has suffered from the impact of several mega earthquakes associated with mega-tsunamis, for example, the subduction zone at Sunda Trench between Indonesia and Burma Indian Ocean, the subduction zone at Makran trench bordering Pakistan and Iran and far north at the East and west Hellenic arc between African and Eurasia which have an impact on Northern Africa. Our initial results show that some coastal areas will suffer from a maximum wave height 2–4 m considered as a dangerous zone in red colour (Fig. 1c). From a tsunami hazard assessment point of view, these simulations show detailed information about the travel time and maximum wave height of tsunamis. From the western Hellenic source zone, the Egyptian coast can expect

a maximum wave height 1.7 m tsunami at 76 min (Fig. 1a, c). For Eastern Hellenic zone, the Egyptian coast has the maximum wave heights of 2–4 m at 60 min as shown snapshot (Fig. 1c, d). For the Makran scenario, the maximum wave height 2–4 m at 234 min (Fig. 1c, b). The wave height uncertainties are calculated depending on the tested 2 models for each zone resulted in ±2 m in wave height in case of scenario (1) and ±1.5 m in wave height in scenario (2). Scenario (3) has a wave height uncertainty of ±3 m while scenario (4) was ±3 m.

The maximum wave height at the eastern African coastal areas resulted from this study was considered higher than the one estimated in the African tsunami hazard map of Africa (UNSDIR 2009) at the whole east and North African coasts expect for the south Madagascar which shows nearly the same wave height. This is because the used bathymetry is of a high resolution near the coastal areas, in addition to modification done to the fault's geometries to enlarge the events, to predicate the worst-case scenarios.

5 Conclusions

For our future work, a detail work of updated tsunami Africa hazard map is required to examine all possible tsunamigenic sources including the western part of Africa continent. From our tested scenarios, there was enough wave propagation time to reach the coastal zones to save people's lives by preparing early warning systems for the whole African continent.

References

Amante, C., Eakins, B.W.: ETOPO1 1 Arc-Minute Global Relief Model: Procedures, Data Sources and Analysis. NOAA Technical Memorandum NESDIS NGDC-24. National Geophysical Data Center, NOAA (2009). https://doi.org/10.7289/V5C8276M

Ambraseys, N.: Earthquakes in the Mediterranean and Middle East: A Multidisciplinary Study of Seismicity up to 1900, pp. 947 (2009). Cambridge University Press. ISBN: 9780521872928

Baptista, M.A., Miranda, J.M., Chiericci, F., Zitellini, N.: New study of the 1755 earthquake source based on multi-channel seismic survey data and tsunami modeling. Nat. Hazard. **3**, 333–340 (2003)

Baptista, M., Miranda, J., Batlló, J., Lisboa, F., Luis, J., Macià, R.: New study on the 1941 Gloria fault earthquake and tsunami. Nat. Hazards Earth Syst. Sci. 1–17 (2016). https://doi.org/10.5194/nhess-2016-130

Byrne, D.E., Sykes, L.R., Davis, D.M.: Great thrust earthquakes and aseismic slip along the plate boundary of the Makran subduction zone. J. Geophys. Res. **97**, 449–478 (1992)

Duputel, Z., Rivera, L., Kanamori, H., Hayes, G.W.: phase source inversion for moderate to large earthquakes (1990–2010). Geophys. J. Int. **189**(2), 1125–1147 (2012)

Gusiakev, V.K., Dunbar, P.K., Arcos, N.: Twenty five years (1992–2016) of global tsunamis: statistical and analytical overview. Pure Appl. Geophys. (2019). https://doi.org/10.1007/s00024-019-02113-7

https://earthquake.usgs.gov/earthquakes/eventpage/official20041226005853450_30/moment-tensor

IOC, IHO, and BODC.: Centenary edition of the GEBCO digital atlas, published on CD-ROM on behalf of the Intergovernmental Oceanographic Commission and the International Hydrographic Organization as part of the general bathymetric chart of the oceans, British Oceanographic Data Centre, Liverpool (2003), last update 2014 and 2019

Jaiswal, R.K., Singh, A.P., Rastogi, B.K.: Simulation of the Arabian Sea tsunami propagation generated due to 1945 Makran earthquake and its effect on western parts of Gujarat (India). Nat. Hazards **48** (2), 245–258 (2009)

Løvholt, F., Zamora, N., Glimsdal, S., Yetman, G., Smebye, H.: 'Tsunamis', in Global Assessment Report on Disaster Risk Reduction, pp. 31–36 (2009)

Luis, J.F.: Mirone: a multi-purpose tool for exploring grid data. Comput. Geosci. **33**, 31–41 (2007)

Okada, Y.: Surface deformation due to shear and tensile faults in a half space. Bull. Seismol. Soc. America **75**, 1135–1154 (1985)

Okal, E.A., Hartnady, C.J.H.: The South Sandwich Islands earthquake of 27 June 1929: seismological study and interference on tsunami risk for the South Atlantic. South Afr. J. Geol. **112**, 359–370 (2009)

Pagnoni, G., Armigliato, A., Tinti, S.: Scenario-based assessment of buildings' damage and population exposure due to earthquake-induced tsunamis for the town of Alexandria, Egypt. Nat. Hazard. **15**, 2669–2695 (2015)

Pino, N.A., Giardini, D., Boschi, E.: The December 28, 1908, Messina straits, southern Italy, and earthquake: waveform modeling of regional seismograms. J. Geophys. Res. (2000)

Salama, A., Meghraoui, M., El Gabry, M., Maouche, S., Hussein, M. H., Korrat, I.: Paleotsunami deposits along the coast of Egypt correlate with historical earthquake records of eastern Mediterranean. Nat. Hazard. **18**(8), 2203–2219 (2018)

Shaw, B., Ambraseys, N.N., England, P.C., Floyd, M., Gorman, G.J., Higham, T.F.G., Jackson, J., Nocquet, J.-M., Pain, C.C., Piggott, M. D.: Eastern Mediterranean tectonics and tsunami hazard inferred from the AD 365 earthquake. Nat. Geosci. **1**, 268–276 (2008). https://doi.org/10.1038/ngeo151

Stiros, S.C.: The 8.5+ magnitude, AD365 earthquake in Crete: coastal uplift, topography changes, archaeological and historical signature. Quatern. Int. **216**, 54–63 (2010)

UN-ISDR.: Global Assessment Report on Disaster Risk Reduction, p. 207 (2009). ISBN: 9789211320282. http://www.preventionweb.net/english/hyogo/ gar/report/index.php

The AD 365 Crete Earthquake/Tsunami Submarine Impact on the Mediterranean Region

Alina Polonia, Alberto Armigliato, Luca Gasperini, Giulia Giorgetti, Gianluca Pagnoni, Stefano Tinti, and Filippo Zaniboni

Abstract

The Calabrian and Hellenic subduction systems accommodate the African Eurasian plate convergence in the Mediterranean Sea and are the site of large earthquakes in the forearc region facing the northern African coasts. Some of the historical earthquakes were associated with the generation of tsunami waves affecting the entire Mediterranean basin. We investigated the submarine effects of the AD 365 Crete earthquake on the sedimentary records through the integrated analysis of geophysical data, turbidite deposits, and tsunami modelling.

Seismic reflection images show that some turbidite beds are thick and marked by acoustic transparent layers at their top. Radiometric dating of the most recent of such mega-beds, the Homogenite/Augias turbidite (HAT), provide evidence for synchronous basin-wide sedimentation during a catastrophic event which has occurred in the time window of AD 364–415, consistent with the AD 365 Mw = 8.3–8.5 Crete earthquake/tsunamis. The HAT (up to 25 m thick) contains components from different sources, implying remobilization of material from areas very far from the epicentre. Utilizing the expanded stratigraphy of the HAT and the heterogeneity of the sediment sources of the Mediterranean margins, we reconstructed the relative contribution of the Italian, Maltan and African margins to the turbidite deposition. Our sedimentological reconstructions combined with tsunami modelling suggest that the tsunami following the Crete earthquake produced giant turbidity currents along a front over 2000 km long, from northern Africa to Italy. Our cores suggests that during the last 15,000 years, only two similar turbidites have been deposited in the deep basins, pointing to a large recurrence time of such extreme sedimentary events.

Keywords

AD 365 Crete earthquake • Tsunami • Slope failures • Seismo-turbidite • Tsunami modelling

1 Introduction

Extreme submarine geo-hazards, such as strong earthquakes and tsunamis, have repeatedly affected the Mediterranean region. A record of these past events can be provided by large-volume turbidites in the marine sedimentary records as the result of catastrophic failure of submarine slopes. The central Mediterranean Sea is located between the Calabrian and Hellenic subduction systems that were struck repeatedly by strong tsunamigenic earthquakes (Maramai 2014). During the late Quaternary turbidite deposition dominating in the deep basins, the earthquake-triggered mass flows deposits represents more than 90% of the total sedimentation during historical times (Polonia et al. 2013a, 2017, 2021). Some of the turbidites are up to 20 m thick and marked by the acoustic transparency of the upper mud layer in the seismic sections. The most recent of these mega-beds, the Homogenite/Augias turbidite (HAT), is observed over a wide area of the Central and Eastern Mediterranean Sea. The original hypothesis attributed the HAT to the 3500 yr BP Minoan eruption of Santorini and the related tsunamis (Kastens and Cita 1981). However, the turbidite composition and structure, as well as radiometric dating and age modelling, revealed that it was not triggered by the Santorini event, but by the later AD 365 Crete earthquake/tsunami (Polonia et al. 2013b, 2016; Shaw 2008). We present the analysis of seven sediment cores containing the complete

A. Polonia (✉) · L. Gasperini · G. Giorgetti
Institute of Marine Sciences, National Research Council, 40129 Bologna, Italy
e-mail: alina.polonia@cnr.it

A. Armigliato · G. Pagnoni · S. Tinti · F. Zaniboni
Department of Physics and Astronomy, Alma Mater Studiorum—University of Bologna, 40127 Bologna, Italy

M. Meghraoui et al. (eds.), *Advances in Geophysics, Tectonics and Petroleum Geosciences*, Advances in Science, Technology & Innovation, https://doi.org/10.1007/978-3-030-73026-0_3

record of the HAT in different physiographic and oceanographic settings including basins offshore Africa. Sedimentology was integrated by tsunami modelling to verify the possible role of tsunami propagation and its impact on the coastal regions in the destabilization of continental slopes.

2 Materials and Methods

Our high-resolution study combines the interpretation of seismic reflection profiles, multi-beam data and the analysis of sediment cores. Cores were collected with a 1.2 t gravity corer and a 2.3 t piston corer. The cores were analysed through a multi-proxy approach involving X-ray images, texture, geochemistry, organic matter, micropaleontology and mineralogical analysis. Results of radiometric dating obtained from pelagic sediments interbedded between re-sedimented deposits were used to define an age model and a chronological framework.

3 Results

Seismic reflection profiles show that the mega-bed is present in many different basins of the central-eastern Mediterranean Sea. These range from the 4,000 m deep abyssal plain to shallower slope basins, including the Calabrian Arc and the Mediterranean Ridge, the Tyro Basin SE of Crete and the Western Herodotus trough offshore Cyrenaica (Fig. 1). The thickness of the turbidite varies between 0.1 m up to more than 25 m in the different basins.

Radiometric ages obtained from pelagic sediments deposited after the catastrophic event suggest that all the turbidites collected in different physiographic settings were deposited synchronously in the time window AD 364–415. Sedimentology and geochemistry of the cores identified different turbidite units whose composition widely varies as confirmed by geochemical analyses. Further micropaleontological and mineralogical analyses suggest that the sediment sources are compatible with Greece, the Malta escarpment, Southern Italy and Africa.

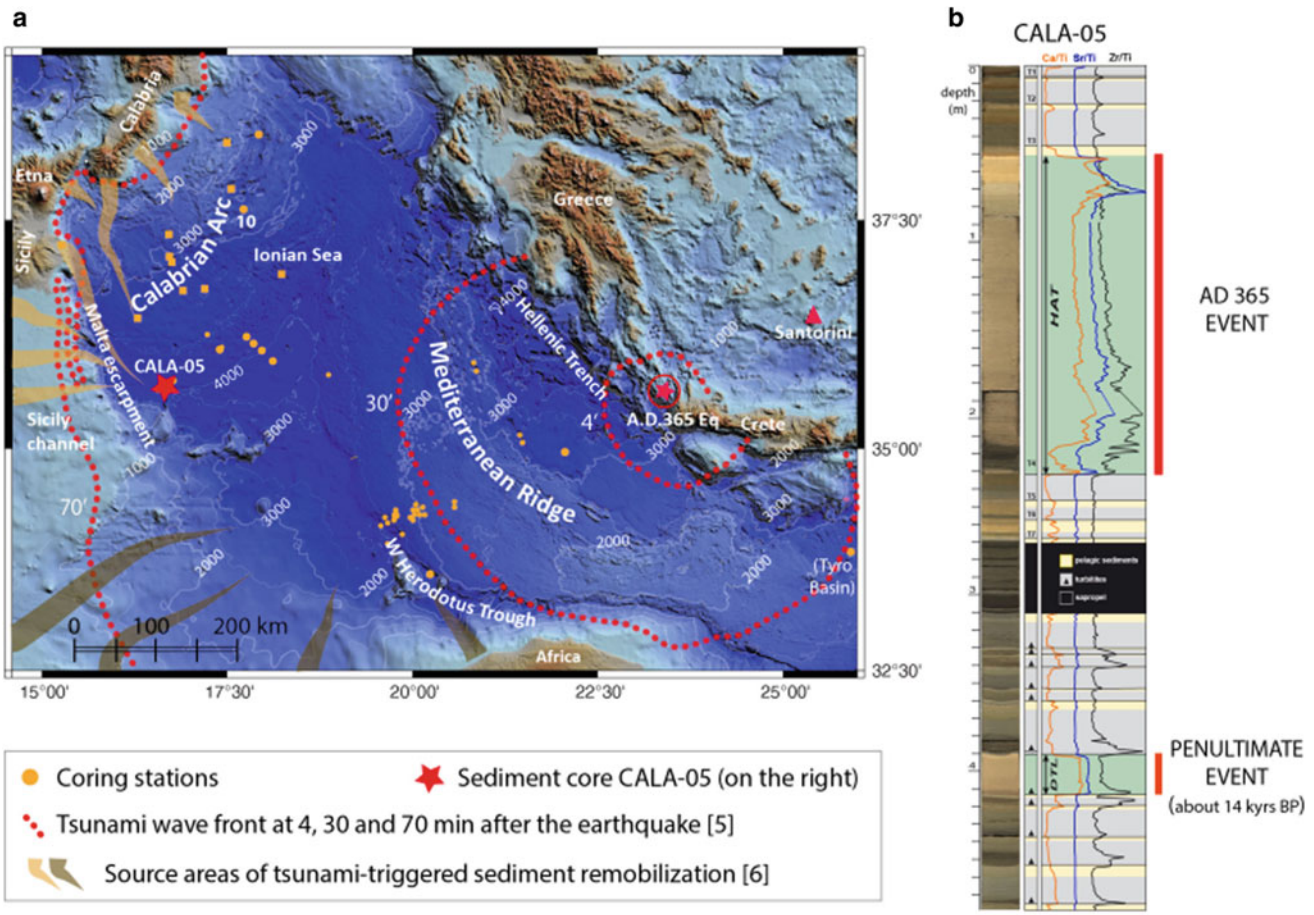

Fig. 1 **a** Shaded relief map of topography/bathymetry of the central and eastern Mediterranean Sea. **b** Photograph of sediment core CALA-05 with sedimentary facies and major XRF geochemical elements. Modified from Polonia (2016)

Tsunami modelling allows verifying a possible correlation between tsunami propagation and the generation of turbidity currents. Starting from some reasonable hypothesis for the parent fault of the 365 earthquake (Shaw 2008), numerical simulations of the tsunami propagation help deduce the main paths of tsunami energy focussing and quantifying the spatial distribution of the extreme particle velocities. The latter can be used to estimate the shear stresses induced by the tsunami on the ocean bottom and along the coastal regions, providing a rough estimation of the destabilisation and transport power of the tsunami waves and currents.

4 Discussion

The HAT was triggered by an event taking place in the time window AD 364–415 which was capable of initiating, simultaneously, sediment transport in widely separated sedimentary basins. The lithology, structure and regional occurrence of the mega-bed place the triggering mechanism within narrow constraints: it affected every basin of the central Mediterranean and its provenance varied in different parts of the basin margins. The only historical earthquake potentially capable of generating such devastating effects from Greece to the African margins during the given time interval, is the exceptionally strong Crete 365 AD earthquake.

The M = 8.3–8.5 AD 365 Crete earthquake (Shaw 2008) occurred on a major reverse fault, dipping beneath Crete. Seismic shaking from this earthquake, although exceptional, was probably unable to trigger mass movements 700 km from the epicentre, in flat and stable areas of the Sicily Channel and Africa's continental shelves. The areal extent of the mega-bed, as shown by our radiometric dating, supports the hypothesis that it was the tsunami following the Crete earthquake that triggered the giant turbidity currents (Fig. 1). The 365 AD Crete tsunami wave caused local reworking during its transit towards the West. When the tsunami hit the shallow continental shelves of Italy and Africa, it has triggered gigantic turbidity flows that transported shallow water detritus to the deep basins along a front from Calabria to Africa. The magnitude of the parent earthquake and the extent of the ensuing tsunami impact make this event comparable, at least as a first approximation, to more recent giant subduction zone earthquake-generated tsunamis (2004 Sumatra and 2011 Tohoku-Oki), whose effects, regarding sediment mobilization, can then be used as terms of comparison for our investigations.

5 Conclusions

The earthquake and tsunami of the 21st of July 365 AD have stimulated discussions between historians, archaeologists and geophysicists, mainly because historical records are not always concordant in chronology and in the extent of reported damages. However, an unusual event with a magnitude > 8.5 was proposed (Stiros 2010) with a tsunami spread across the Mediterranean Sea (Shaw 2008; Tinti 2005). The detailed sedimentological and chronostratigraphic analysis of deep-sea cores allows the reconstruction of sedimentary processes that generated the deposit. Our results suggest that the HAT deposition was related to multiple turbidity currents triggered by the tsunami waves hitting the continental shelves of Italy, Malta and Africa along the continental margins for more than 2000 km.

The synchronous deposition of the HAT over an area larger than 150,000 km^2 implies an exceptional event triggering catastrophic failure of submarine slopes in the Mediterranean Sea basins including the African coasts.

References

Kastens, K.A., Cita, M.B.: Tsunami-induced sediment transport in the abyssal Mediterranean Sea. Geol. Soc. Am. Bull. **92**(I), 845–857 (1981)

Maramai, A., et al.: The Euro-mediterranean tsunami catalogue. Ann. Geophys. v.57, **4** (2014)

Polonia, A., et al.: Turbidite paleoseismology in the Calabrian arc subduction complex (Ionian Sea). Geochem. Geophys. Geosyst. **14**, 112–140 (2013a)

Polonia, A., et al.: Mediterranean megaturbidite triggered by the AD 365 Crete earthquake and tsunami. Scientific Reports, 3. Article number 1285 (2013b). https://doi.org/10.1038/srep01285

Polonia, A., et al.: Did the AD 365 Crete earthquake/tsunami trigger synchronous giant turbidity currents in the Mediterranean Sea? Geology (2016). https://doi.org/10.1130/G37486.1

Polonia, A., Nelson, H.C., Romano, S., Vaiani, S.C., Colizza, E., Gasparotto, G., Gasperini, L.: A depositional model of seismoturbidites in confined basins based on Ionian Sea deposits. Mar. Geol. **384**, 177–198, ISSN 0025-3227, (2017). https://doi.org/10.1016/j.margeo.2016.05.010

Polonia, A., Bonetti, C., Bonetti, J., Çağatay, M.N., Gallerani, A., Gasperini, L., Nelson, C.H., Romano, S.: Deciphering coseismic sedimentary processes in the Mediterranean Sea using elemental, organic carbon and isotopic data. Geochem. Geophys. Geosyst. (2021). https://doi.org/10.1029/2020GC009446

Shaw, B., et al.: Eastern Mediterranean tectonics and tsunami hazard inferred from the AD 365 earthquake. Nat. Geosci. **1**, 268–276 (2008)

Stiros, S.C.: The 8.5+ magnitude, AD365 earthquake in Crete: coastal uplift, topography changes, archaeological and historical signature. Quatern. Int. v. 216, **1**, 54–63 (2010)

Tinti, S., et al.: Scenarios of giant tsunamis of tectonic origin in the Mediterranean. ISET J. Earthq. Technol. **42**(4), 171–188 (2005)

The AD 365 Alexandria (Egypt) Tsunami, Revisited

Stathis C. Stiros

Abstract

Earthquake and tsunami hazards along the Mediterranean coast of Africa are essentially constrained by historical data, and especially a notorious description of the AD365 tsunami by Ammianus Marcellinus, a historian of the Roman period. This report was used to constrain geophysical models, for example, the modeling of inundation of Alexandria by a tsunami generated by a fault offshore Crete. This approach, however, has some limitations. The AD365 tsunami models predict major impact in Libya (for which no clear evidence exists), limited impact in Alexandria (in which major damage is reported by Ammianus), and no retreat of the sea preceding the flooding in contrast to the ancient report. Furthermore, minor flooding is predicted for Methoni (SW Greece mainland), for which major inundation is reported. For this reason, the available historical information was examined through a comparative historical approach, and it was investigated whether the postulated tsunami damage is compatible with the political, religious, cultural, etc., history of Alexandria. The overall conclusion is that Ammianus reported a tsunami which was destructive probably in the lowlands of the Nile Delta, but not in Alexandria. Such a tsunami is unlikely to originate from Crete.

Keywords

Historical seismology • Fault • Tsunami • Alexandria • Crete • Libya

1 Introduction

A famous report by the fourth century's writer Ammianus Marcellinus (*Amm. 26.10.15*) provides a fascinating description of a tsunami, and this information has been readily adopted by earth scientists. The basic points of Ammianus are

(i) Retreat of the sea after an earthquake, and then flooding, with thousands of drowned people in Alexandria, Egypt, in the morning of the 31st of July AD365.
(ii) Tsunami effects also in Mothone, a priori assigned to Methoni in SW Greece.

The AD365 tsunami has been correlated with impressive coastal uplift in Crete (Pirazzoli 1982) and destructions derived from archaeological evidence in this island (Stiros 2001), and there have been proposed fault models for coastal uplift in Crete (Stiros and Drakos 2006; Shaw et al. 2008) and for tsunami generation and propagation (Shaw et al. 2008) (Fig. 1).

In the last years, however, it has been shown that in many cases, ancient sources may report true catastrophic events, but with errors in their dating and/or location, or exaggerations, sometimes deliberate, to justify political and religious ideas. Is this the case with the Ammianus report? Should it be taken word-by-word, or does it need some decoding?

This paper is a first contribution in the solution of this problem, with two specific aims:

First, to examine whether the proposed tsunami model is consistent with the ancient report.
Second, to re-evaluate the ideas for damage in Alexandria and Mothone (Methoni) based on literal sources.

S. C. Stiros (✉)
Patras University, 26500 Patras, Greece
e-mail: stiros@upatras.gr

M. Meghraoui et al. (eds.), *Advances in Geophysics, Tectonics and Petroleum Geosciences*,
Advances in Science, Technology & Innovation, https://doi.org/10.1007/978-3-030-73026-0_4

2 Evaluation of the Tsunami Model Predictions

Assuming a fault SW of Crete, the tsunami model of Fig. 1 predicts major flooding in the Libyan coast, for which no evidence exists. For Alexandria, on the contrary, it predicts minor flooding, of the order of half a meter, and no retreat of the water prior to flooding. Hence, the main points of the Ammianus story *are not satisfied*. For Methoni (SW continental Greece), no significant tsunami flooding is predicted (Fig. 1).

If instead of the fault model of Shaw et al. (2008), the fault model of Stiros and Drakos (2006) is adopted, no major changes in the tsunami modeling are expected.

Another piece of evidence is that sedimentological analyses along the Egyptian coast, in two sites west of Alexandria, provided evidence of several cycles of tsunami deposits, but their time bracketing is broad (Salameh 2018).

3 Revisiting Historical Sources

3.1 Alexandria

Tsunami damage in Alexandria is reported *only* by Ammianus, while a later source reports a yearly festivity for the Day of Fear on the 21st of July, giving no further details (*Sozomen 6.2*).

This is quite surprising, because Alexandria was a leading political, cultural, religious, and financial center in the wider region and a major calamity would NOT have been ignored. In addition, during this critical period, Alexandria was marked by a religious debate with high-level political dimensions, especially since Athanasius, the local bishop (Patriarch) in AD365, was one of the main figures and saints of Christianity and one of the main spiritual leaders fighting Arianism. In fact, Arianism was an emperor-supported dogma which subsequently shaped the Coptic Orthodox Church in Africa and the Middle East. For this reason, Athanasius was exiled several times; especially after the spring of AD365, he was hiding in the outskirts of Alexandria and he was permitted to return from his exile to Alexandria in September AD365.

This means that the memories of the postulated tsunami damage would have been fresh, but nothing is noticed in the religious and political history of Alexandria. On the contrary, a later source reported that St Athanasius made a miracle and saved Alexandria from rising waters (*John Nikiu, 82.19*).

The available information indicates that perhaps there was a tsunami *which only marginally affected Alexandria*, but it had destroyed other areas, probably east of the Nile Delta. This is consistent with the reports of John Cassian, Bishop of Alexandria in the AD420s, who reported inundation in the lowlands of the Nile Delta (Panephysis area).

3.2 Methoni

Ammianus reported ships pushed inland, and he specifies an area in which such a ship was observed. His Latin text,

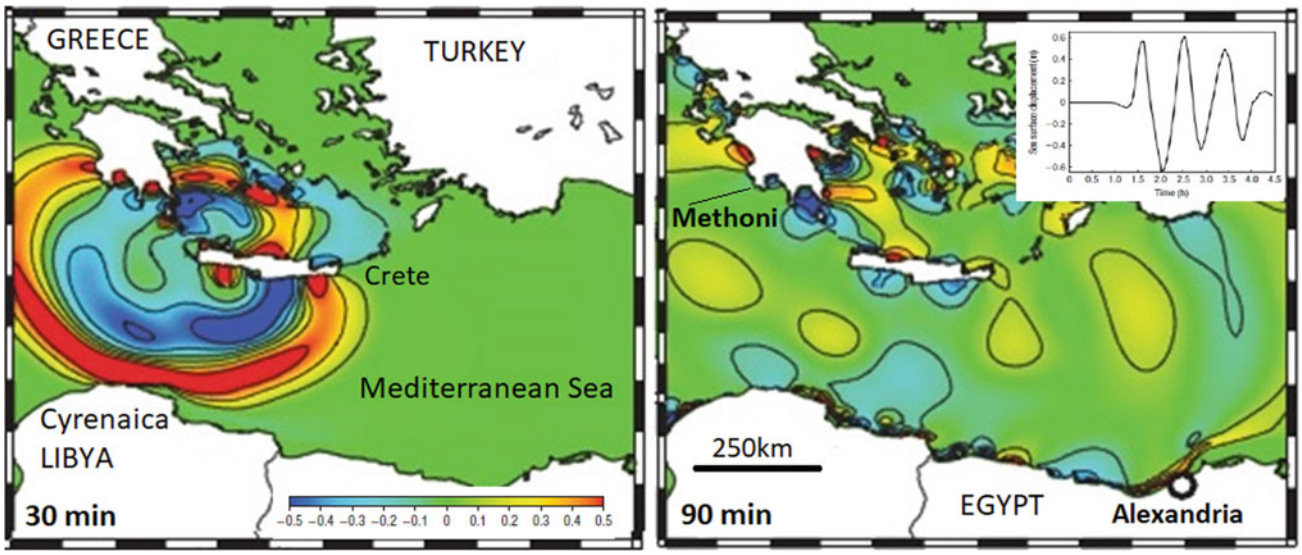

Fig. 1 Predictions of tsunami height by an earthquake in Crete. Major tsunami flooding is predicted for Cyrenaica (Libya) and minor only for Alexandria. Minor flooding is also predicted for Methoni. In the inset, predicted sea-level oscillations during the arrival of the tsunami waves at Alexandria, not consistent with the retreat of waters before flooding. Shaw et al. After (2008), modified

however, contains an ambiguous expression which can be translated either as "a ship in the Laconian (Spartan) Mothone" which clearly indicates a site in modern Greece (Fig. 1), or as "a Laconian ship at Mothone," which is less clear.

Ammianus Mothone has been a priori associated with Methoni in SW Greece (Fig. 1), but this is dubious, since there existed several towns with this name in other parts of Greece and in the Middle East.

Another difficulty in accepting the Peloponnesian Mothone as an area strongly inundated by a tsunami is that the local topography excludes the possibility of a ship to be brought at a large distance inland, as mentioned by Ammianus.

There is however another possibility, Mothone to reflect a site in Egypt, with its name, deriving from the pharaonic Egyptian word *mtwn*, indicating an arena for bullfights; an old practice which had survived in the Roman times.

4 Discussion

The report of Ammianus clearly provides information for a tsunami which is usually interpreted to have destroyed Alexandria in 365, on a specific day, but there are two main problems.

First, the tsunami modeled to be generated by a Crete earthquake (Fig. 1) predicts serious inundation in Libya, for which there is no evidence, while it is hard to explain inundation at Methoni (if located in SW Greece), and especially of Alexandria, with thousands of victims. Furthermore, the *critical* polarity of tsunami attack (first water retreat and then flooding) is *not* reproduced by the geophysical model (Fig. 1 inset).

Second, the postulated destruction of Alexandria, built on low-land and hence vulnerable to inundation, occurred during a politically turbulent period, covered by numerous reports, but *all* sources except for Ammianus are silent about a tsunami destruction. On the contrary, a later report describes a miracle of St Athanasius, local bishop (Patriarch) which saved Alexandria from flooding (*John Nikiou LXXXI*).

A likely explanation is that there was a tsunami, probably destructive in the Nile Delta, but *not* in Alexandria. It was assigned to Alexandria because it was the major town, or to impress people. This is not unreasonable; for example, Ambraseys (1971) in a benchmark publication for Historical Seismology has noticed that historical earthquakes seem to be confined (shifted?) to major ancient towns.

The source of this tsunami seems not to be seismic faulting near Crete, but probably faulting or secondary seabed deformation farther east (e.g., Yalciner 2014).

This has important implications for modeling tsunami hazards in Egypt and Libya. A more detailed analysis is made elsewhere.

Acknowledgements Comments of three anonymous reviewers are appreciated.

References

Ambraseys, N.: Value of historical records of earthquakes. Nature **232**, 375–379 (1971)

Pirazzoli, P., et al.: Crustal block movements from Holocene shorelines: Crete and Antikythira (Greece). Tectonophysics **68**, 27–43 (1982)

Salameh, A., et al.: Paleotsunami deposits along the coast of Egypt correlate with historical earthquake records of eastern Mediterranean. NHESS **18**, 2203–2219 (2018)

Shaw, B., et al.: Eastern Mediterranean tectonics and tsunami hazard inferred from the AD365 earthquake. Nat. Geosci. **1**, 268–276 (2008)

Stiros, S.: The AD 365 Crete earthquake and possible seismic clustering during the 4–6th centuries AD in the Eastern Mediterranean: a review of historical and archaeological data. J. Struct. Geol. **23**, 545–562 (2001)

Stiros, S., Drakos, A.: A fault model for the tsunami-associated magnitude > 8.5 Eastern Mediterranean, AD 365 earthquake. Z. Geomorphol. **146**, 125–137 (2006)

Yalciner, A., et al.: A possible submarine landslide and associated tsunami at the northwest Nile Delta, Mediterranean Sea. Oceanography **27**, 68–75 (2014)

Seismotectonics of the Easternmost Cyprus Arc: Implications for Tsunami Hazard Assessment

Ryad Darawcheh, Adnan Hasan, and Mohamad Khir Abdul-wahed

Abstract

Analysis of multiple data based on historical earthquakes, instrumental seismicity, bathymetric data, and geophysical marine surveys for assessing the seismotectonic setting of the northeast corner of the Mediterranean Sea has led to the construction of a seismotectonic map of the area. The easternmost Cyprus arc, which is the eastern part of Sinai-Anatolian plate boundary, includes two active marginal faults and a third active one in between. The easternmost Cyprus arc is characterized by two different seismic regions: the first one is located southeast of Cyprus Island with dense and moderate events, whereas the second one is located north of Latakia City with lower magnitude events. A reasonable match between the fault plane solutions and the thrust faulting system southeast of Cyprus has been observed. The results also show spatial variations of S_{Hmax} orientation in concordance with the movements of the tectonic plates. The easternmost Cyprus arc could be the source of a large earthquake causing a probable sea wave along the coasts of the region.

Keywords

Seismotectonics • Tsunami hazard • Landslide • Cyprus arc

1 Introduction

The African-Eurasian plate boundary in the northeast corner of the Mediterranean Sea, i.e., Cyprus arc (CA), is a wide zone of complex crustal deformation (Benkhelil et al. 2005). The seismotectonic investigation is of importance for this area in the context of earthquake and tsunami hazard assessment. The present study is aimed to construct a seismotectonic map of the northeast corner of the Mediterranean between the Syrian and Cypriot coasts, in an area that has very few attempts to study its seismotectonic setting (Salamon et al. 2003).

2 Materials and Methods

Our procedure to establish the targeted seismotectonic map is to collect the relevant studies published partially and completely in the study area. This includes studies of the historical earthquakes (Sbeinati et al. 2005) and the marine geophysical surveys (Benkhelil et al. 2005; Tahchi et al. 2010; Hübscher et al. 2009). Also, a list of earthquakes for the period 1906–2015 has been mainly collected from the International Seismological Center (ISC) (http://www.isc.ac.uk), published papers and earthquake data centers for other periods. The list includes for each event its date, origin time, coordinates, focal depth, different magnitude values (M_L, mb, Ms, and Mw), and the quality factor of the event. The fault plane solutions (FPS) of the reliable events were adopted from International Seismological Centre Homepage (http://www.isc.ac.uk), Harvard Centroid Moment Tensor Catalog Homepage (https://www.globalcmt.org/). These FPS were inverted to stress (S_{Hmax}) using the program (Meca3) developed by Abdul-Wahed and Alissa (2020). We used the data available at the European Marine Observation and Data Network (EMODnet) (http://www.emodnet.eu/) to produce a bathymetric map with 225 m spatial resolution (Fig. 1).

3 Results

Figure 2 shows the seismotectonic map of the easternmost Cyprus arc. It includes the main active faults at seabed and inland, the historical tsunamigenic earthquakes that

R. Darawcheh (✉) · A. Hasan · M. K. Abdul-wahed
Department of Geology, Atomic Energy Commission of Syria, Damascus, Syria
e-mail: rdarawcheh@aec.org.sy

M. Meghraoui et al. (eds.), *Advances in Geophysics, Tectonics and Petroleum Geosciences*,
Advances in Science, Technology & Innovation, https://doi.org/10.1007/978-3-030-73026-0_5

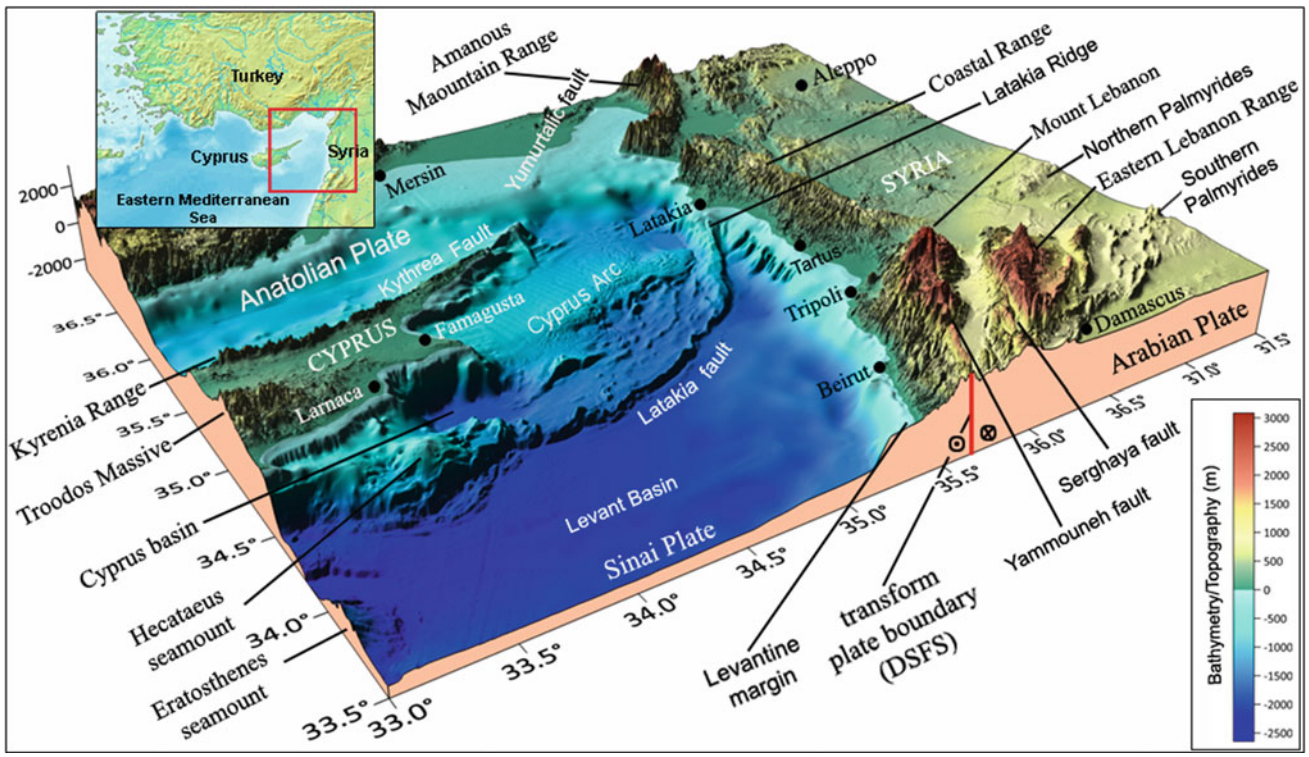

Fig. 1 Bathymetric 3D map of the northeast corner of the Mediterranean Sea showing the crustal deformation front of the CA between the Syrian and eastern Cypriot coasts. Topography data are from the United States Geological Survey (USGS) with 90 m spatial resolution (http://www.usgs.gov)

originated from the central and the northern Dead Sea fault system (DSFS) in Lebanon and western Syria, the instrumental seismicity with (Ms $\geq$ 4.0) that occurred between 1906 and 2015, FPS of reliable seismic events and distribution of maximum horizontal stress field (S_{Hmax}).

Based on the bathymetric map and results of the studies mentioned above (Benkhelil et al. 2005; Tahchi et al. 2010; Hübscher et al. 2009), we delineate the zone of the CA (Fig. 2). As known, this zone separates two minor plates, northward moving Sinai and westward-moving Anatolian. It is bounded by two regional faults, Latakia fault (LAF) in the south and the fault extending between Kythrea (KYF) and Yumurtalik (YUF) faults in the north. Also, in the middle of CA, there is a fault which we called it Famagusta fault (FAF). These three regional faults are active since they pierce the seafloor of Pliocene–Quaternary sediments.

The epicentral distribution of the earthquakes shows that CA is seismically active, which is attested by low to moderate events. The most notable feature of the epicentral distribution is the presence of a dense cluster of seismic activity along the local fault trends southeast of Cyprus. In general, the easternmost Cyprus arc is characterized by two different seismic regions: the first one is located southeast of Cyprus Island with dense and moderate events, whereas the second one is located north of Latakia City with lower magnitude events. The depth of these events lies between 4 and 60 km.

An overall look of the FPS at the CA, southeast of Cyprus in particular, indicates a dominant thrust faulting component with greater than 60% (earthquakes of 1961, 1975, 1982, 1984, and 1993). We can observe a reasonable agreement between the FPS and the thrust faulting system southeast of Cyprus. The results also reveal spatial variations of S_{Hmax} orientation which are agreed with the movements of the tectonic plates along the regional faults.

4 Discussion

The seismotectonic setting of the easternmost CA has been investigated using multiple data. The instrumental seismic activity could be classified as low to moderate, which might be regarded as accumulating the stress along the CA faults.

Some large historical earthquakes that originated along the DSFS such as 1157 AD., 1170, 1202, 1408, and 1759 (Fig. 2) have caused the occurrence of sea waves along the Syrian, Lebanese, and Cypriot coasts. These earthquakes have probably induced landslides of unstable sedimentary masses (evaporites) distributed along the Levantine margin according to Ambraseys and Barazangi (1989). In this

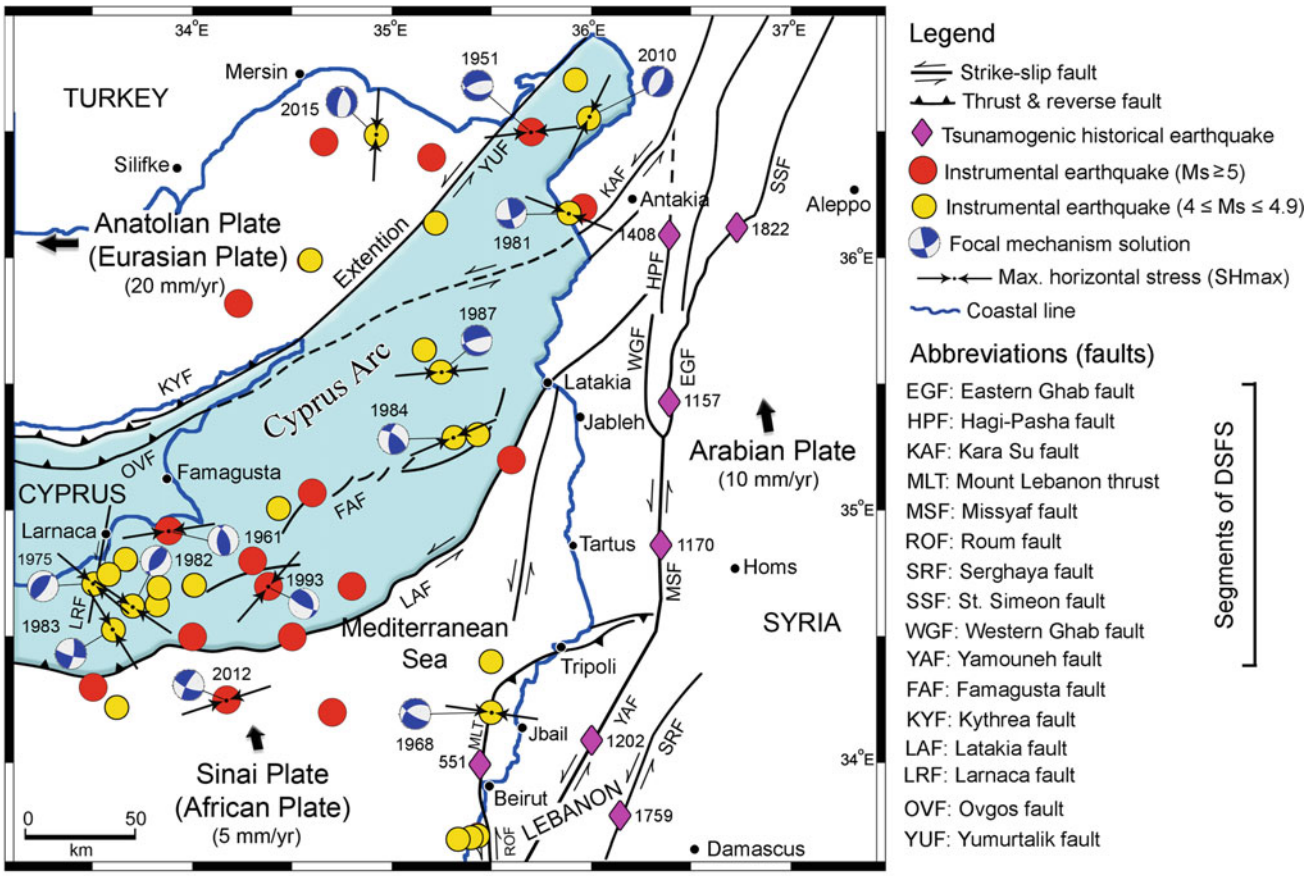

Fig. 2 Seismotectonic map of the easternmost Cyprus arc (light blue zone). Large black arrows present relative plate motions (Jackson and McKenzie 1988; McClusky et al. 2000)

regard, (Tahchi et al. 2010) identified a probable future landslide of 11 km^3 to occur at the northern Latakia ridge (see Fig. 1) south of Latakia City. Our results suggest that CA in the study area represents a seismogenic source to generate a large earthquake and trigger such a landslide which, in turn, produces probable sea waves. Also, large future DSFS events should not be neglected to trigger slumps along the Levantine margin.

5 Conclusions

This work has led to the assessment of the seismotectonic features of the easternmost CA with the possible tsunamigenic sources and the seabed topography. We see that CA has reasonable specifications to generate tsunamogenic earthquakes. We recommend the tsunami numerical modeling in this area, which could be a suitable tool for the engineering planning of the coasts.

References

Abdul-Wahed, M.K. and ALISSA, M.: Present-day stress state in northwestern Syria. Geofísica Internacional. 59, 4, 299-316 (2020). https://doi.org/10.22201/igeof.00167169p.2020.59.4.2038

Ambraseys, N.N., Barazangi, M.: The 1759 earthquake in the Bekaa Valley: implications for earthquake hazard assessment in the eastern Mediterranean region. J. Geophys. Res. **94**, 4007–4013 (1989)

Benkhelil, J., Bayerly, M., Branchoux, S. et al.: The Cyprus Arc eastern bend. Morphostructural characteristics at plates boundary from data of the BLAC survey (2003). C. R. Geoscience **337**, 1075–1083 (2005). https://doi.org/10.1016/j.crte.2005.05.002

European Marine Observation and Data Network Homepage. http://www.emodnet.eu/

Harvard Centroid Moment Tensor Catalog Homepage. https://www.globalcmt.org/

Hübscher, C., Tahchi, E., Klaucke, I., et al.: Salt tectonics and mud volcanism in the Latakia and Cyprus basins, Eastern Mediterranean. Tectonophysics **470**, 173–182 (2009)

International Seismological Centre Homepage. http://www.isc.ac.uk

Jackson, J., McKenzie, D.: The relationship between plate motions and moment tensors, and the rates of active deformation in the Mediterranean and Middle East. Geophys. J. Inter. **93**, 45–73 (1988)

McClusky, S., Balassanian, S., Barka, A., et al.: Global positioning system constraints on plate kinematics and dynamics in the eastern Mediterranean and Caucasus. J. Geophys. Res. **105**, 5695–5719 (2000)

Salamon, A., Hofstetter, A., Garfunkel, Z., et al.: Seismotectonics of the Sinai subplate-the eastern Mediterranean region. Geophys. J. Int. **155**, 149–173 (2003)

Sbeinati, M.R., et al.: The historical earthquakes of Syria: an analysis of large and moderate earthquakes from 1365 BC. to 1900 AD. Ann. Geophys. **48**, 347–436 (2005)

Tahchi, E., Urgeles, R., Hübscher, C., et al.: Mass wasting at the easternmost Cyprus Arc, off Syria, Eastern Mediterranean. In submarine mass movements and their consequences. Adv. Nat. Technol. Hazards Res. **28**, 323–334 (2010)

United States Geological Survey Homepage. http://www.usgs.gov.

Seismic Hazard and Risk in Africa, a Hidden Hazard in an Extreme Vulnerable Context

Mustapha Meghraoui

Abstract

The IGCP-659 "*SEISMOSHAF*" project addresses the seismic hazard and risk mitigation, using the IGCP-601 project database on the seismotectonics of Africa. The seismic hazard assessment and risk mitigation will be conducted to comply with the proposals of the Sendai Framework for Disaster Risk Reduction 2015–2030 (http://www.unisdr.org/we/inform/publications/43291. Last accessed 30.07.2019). Studies of seismic hazard are vital in terms of understanding potentially damaging earthquakes, which may cause loss of life, injury or other health impacts, property damage, social and economic disruption, or environmental degradation. Seismic hazard assessment is based on the information about the features of excitation of seismic waves at the source, seismic wave propagation (attenuation), and site effect in the region under consideration and combines the results of seismological, geomorphological, geological, geodetic, tectonic investigations, and modeling.

Keywords

Earthquakes • Seismic hazard • Seismotectonics • Vulnerability • Africa

1 Introduction

The assessment of seismic hazards and disaster risks in Africa is one of the most important scientific, engineering, and political issues. Although the seismic hazard in Africa is moderate in terms of significant magnitude earthquakes, the vulnerability of African countries even to a moderate event can be high; hence, integrated risks could be high. In 2011, a project on development of the seismotectonic map of Africa (Meghraoui et al. 2016) was initiated with the financial support of the UNESCO-IUGS International Geoscience Program (IGCP-601), was successfully completed in 2016, and the map was released to the scientific community at the 35th International Geological Congress held in Cape Town, South Africa (August 27, 2016–September 4, 2016).

Challenges posed by disasters due to earthquakes can result in negative impacts for the sustainable development. Since the beginning of the twenty-first century, the impacts of earthquake-related disasters have rapidly risen, e.g., the 2004 Sumatra–Andaman earthquake and induced tsunamis, the 2005 Kashmir earthquake, the 2010 Haiti earthquake was associated with tremendous damage to the capital city Port-au-Prince, the 2011 Tohoku earthquake and induced tsunamis and flooding, and the 2015 Nepal earthquake and landslides. The disasters affect developed and developing countries and almost all sectors of economy at local, national, and regional levels. The vulnerability of our civilization to seismic events is still growing in part because of the increase in the number of high-risk objects, the clustering of populations, and the infrastructure in the areas prone to earthquakes. Today, an earthquake may affect several hundred thousand lives and cause significant damage costing up to hundred billion dollars. A large earthquake may trigger an ecological catastrophe. Reducing disaster risk using scientific knowledge is a foundation for sustainable development.

Our knowledge on seismic hazard and its interaction with human systems is lacking in some important areas and is being challenged by the unforeseen or unknown repercussions

Mustapha Meghraoui—Coordinator of SEISMOSHAF Project IGCP-659 and President of the African Seismological Commission

M. Meghraoui (✉)
EOST - Institut Terre et Environnement de Strasbourg, University of Strasbourg, CNRS - UMR 7063, Strasbourg, France
e-mail: m.meghraoui@unistra.fr

Algerian Academy of Science and Technology, Algiers, Algeria

M. Meghraoui et al. (eds.), *Advances in Geophysics, Tectonics and Petroleum Geosciences*, Advances in Science, Technology & Innovation, https://doi.org/10.1007/978-3-030-73026-0_6

Table 1 Results and deliverables' summary of the SEISMOSHAF project

Expected results and output/deliverables	Output/deliverables
Capacity building in hazard and risk assessment: workshops and summer schools	Lectures and practical classes
Seismic hazard analysis	Maps for selected regions
Risk analysis and mitigation plans	Assessment maps in selected sites (large cities)
Outreach and dissemination	Conferences, meetings, articles, video courses

of a rapidly changing and increasingly interdependent world. In such a tightly coupled world, a disaster not only affects the immediate area where it occurs, but also may have cascading impacts that can affect other near and far nations.

2 The SEISMOSHAF Project

The SEISMOSHAF project is prepared to assess the seismic hazard and risk mitigation, with the background knowledge and experience of the IGCP-601 project on the seismotectonics and seismic hazards in Africa. The seismic hazard and risk mitigation will be assessed to comply with the priorities of the Sendai Framework for Disaster Risk Reduction 2015–2030 (Sendai Framework 2015).

Previous works were devoted to the building of a databank (satellite images, tectonic and geophysical background, major active faults, active volcanoes, historical and instrumental seismicity, earthquake focal mechanisms, geomorphology and topographic data, geodetic data, tsunamis and their coastal impacts, lithospheric and crustal structures, tomographic data) with harmonization and homogenization of catalogues' parameters, represented by means of a GIS platform under an ArcGIS subproject for all African countries.

The IGCP-659 annual meeting in Sousse–Tunisia will provide the opportunity to present, discuss, and program scientific activities associated with the Seismic Hazard and Risk Assessment in Africa. Table 1 summarizes the activities.

3 Implementation Strategy

The SEISMOSHAF project and commitment with the EARS conference is planned and implemented in agreement with the relevant UNESCO national or regional office, the International Union of Geological Sciences (IUGS), the International Association of Seismology and Physics of the Earth's Interior (IASPEI), the African Seismological Commission (AfSC), the UNESCO Natural Sciences Sector's Section of Earth Sciences and Geo-hazards Risk Reduction and African Partners, with the scientific and coordinating support of the Institute of Physics of the Earth (IPG) in Strasbourg (France).

These activities are conducted in close collaboration with the African national partners, as well as with other agencies and programs of the United Nations. Among the African partners, the Council for Geoscience (Pretoria) and the Organization of African Geological Surveys in South Africa, the Atomic Energy Commission in Accra (Ghana), the National Research Institute in Astrophysics and Geophysics in Cairo (Egypt), the University of Addis Ababa, the University of Dar Es Salam, and the African Union Scientific, Research and Technology Commission have expressed strong interest in seeing the project move forward.

Their commitment and engagement to the reduction of disaster risks in Africa could be beneficial for the implementation of the UNESCO-IGCP-659 project and could provide critical information for decision makers.

The users and beneficiaries of the outcome of the SEISMOSHAF project and our participation in the international conference are broad and include all those who make decisions based on earthquake hazard and risk:

- National governments,
- Municipal authorities,
- Engineers,
- Organizations in charge of standards in all the countries (for seismic guidelines),
- Insurance and financial industries,
- Emergency service departments,
- Disaster management professionals (risk professionals),
- National research organisations.
- Scientific community users (Including academic institutions).
- The population at large.

References

Meghraoui, M., Amponsah, P., Ayadi, A., Ayele, A., Ateba, B., Bensuleman, A., Delvaux, D., El Gabry, M., ernandes, R.-M., Midzi, V., Roos, M., Timoulali, Y.: The seismotectonic map of Africa. Episodes **39**(1). https://doi.org/10.18814/epiiugs/2016/v39i1/89232

Sendai Framework.: Sendai Framework for Disaster Risk Reduction 2015–2030 (2015). http://www.unisdr.org/we/inform/publications/43291. Last accessed 30.07.2019

Seismotectonics of the Khurutse Region, Botswana

Thifhelimbilu Mulabisana, Mustapha Meghraoui, and Vunganai Midzi

Abstract

An earthquake of magnitude M_W 6.5 occurred on the evening of the April 3, 2017 in Central Botswana, southern Africa. Although it is located in the continental interior of the African plate, the seismogenic area was previously considered as a stable region revealing a background seismicity associated with long-term deformation and faulting. The intraplate seismic activity and mainshock area are studied using the database of the Seismotectonic Map of Africa. The mainshock (25.156° E, 22.678° S, 28 km in depth) and aftershocks are located in a sparsely populated national park. The aftershock sequence, which is the largest event of M_W 4.5 magnitude, followed the mainshock on the April 5, 2017. The analysis of Sentinel-1 interferogram shows 4–6 cm coseismic surface slip on a NW–SE elongated and ~30 km long surface deformation consistent with the mainshock and aftershock distribution, normal faulting mechanism, and source time function. Here, we study the faulting geometry and rupture characteristics using more than 1000 recorded aftershocks of magnitude $M_L \geq 0.5$. All seismic events are located at the eastern edge of the Central Kgalagadi Park near the mainshock location in two clear seismicity clusters. The NW–SE trending seismic clusters imply that a segmented fault is the source of these earthquakes, similar to the inferred direction from the normal faulting solution of the main shock. The earthquake rupture geometry results from an active normal fault that agrees with the aftershock locations at surface and at depth and confirms the thickness of ~28 km seismogenic layer.

Keywords

Seismotectonics • Seismogenic • Mainshock • Aftershock • Magnitude

1 Introduction

A major (M_W 6.5) earthquake (shown in Fig. 1) occurred on the April 3, 2017 at 17:40:13.4, Greenwich Mean Time (GMT), in the Central Province of Botswana (25.156° E, 22.678° S). The intraplate seismicity experienced in the country, like elsewhere in the rest of southern Africa, is characterized by a diffuse pattern of few moderate-to-large events per century, with a few concentrated clusters of modern-day seismicity (Graham et al. 1995). Although Botswana is not well-known as an earthquake-prone country due to the relatively low levels of local seismicity, the country has experienced unexpected moderate to large earthquakes, especially in the Okavango Delta Region where an earthquake of magnitude 6.7 was observed on the October 11, 1952 (Hutchins et al. 1976). In this intraplate tectonic domain, other earthquakes with relatively large magnitudes have occurred, such as the 2006 MW 7.0 earthquake which was located at Machaze, about 900 km to east.

2 Results

The studies of the intraplate seismic activity and mainshock area were conducted using the seismotectonic data of the recent published map of Africa and the Archean Limpopo–

T. Mulabisana (✉)
Institut de Physique du Globe, CNRS-UMR 7516, University of Strasbourg, 4 Rue René Descartes, 67084 Strasbourg, France
e-mail: mulabisana@etu.unistra.fr

AEON-ESSRI, Nelson Mandela University, University Way, Summerstrand, Port Elizabeth, 6019, South Africa

T. Mulabisana · V. Midzi
Council for Geoscience, 280 Pretoria road, Silverton, Pretoria, 0184, South Africa

M. Meghraoui
EOST - Institut Terre et Environnement de Strasbourg, University of Strasbourg,CNRS - UMR 7063, Strasbourg, France

M. Meghraoui et al. (eds.), *Advances in Geophysics, Tectonics and Petroleum Geosciences*,
Advances in Science, Technology & Innovation, https://doi.org/10.1007/978-3-030-73026-0_7

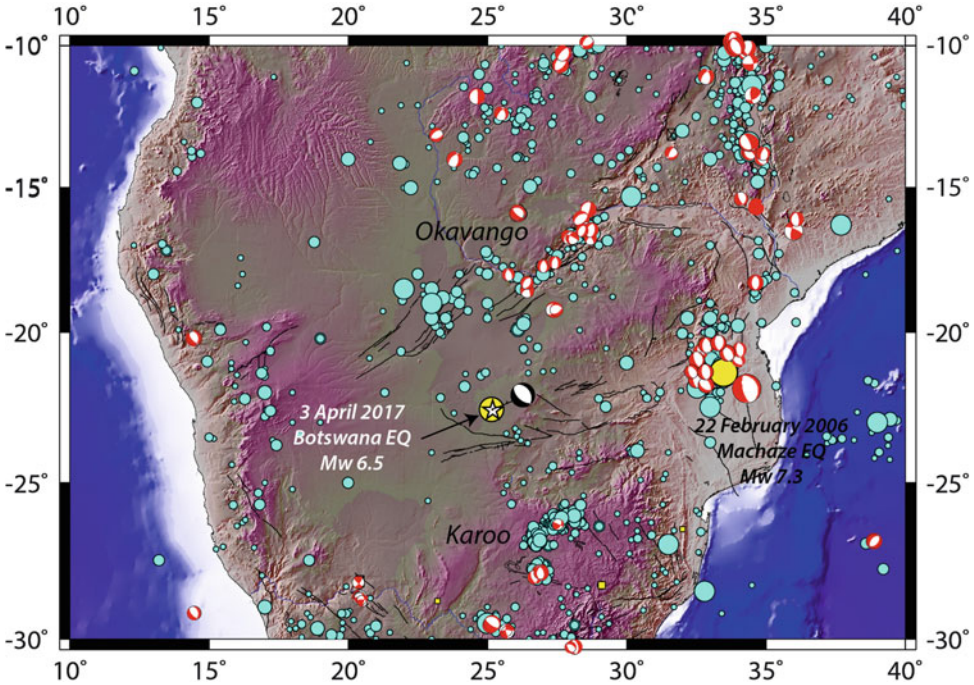

Fig. 1 Excerpt of the Seismotectonic Map of Africa (Meghraoui et al. 2016) and the Botswana earthquake location (star and related CMT-Harvard mechanism). The background seismicity and faulting indicate an intraplate active interior in Africa

Shashe Tectonic Belt (ALSTB), the geodetic (InSAR) analysis and seismological (aftershock data) were determined from a post-earthquake local seismic array. The seismotectonic setting of the ALSTB shows a significant recent background seismicity reaching M_L 4.5 in 2009 along the ENE-WSW trending shear zones associated with NW–SE striking dip-slip fault system. The analysis of Sentinel-1 interferogram (images from ascending orbit) shows 4–6 cm coseismic slip on a NW–SE elongated and 30-km-long surface deformation consistent with the mainshock location, normal faulting mechanism, and source time function (http://geoscope.ipgp.fr/index.php/en/catalog/). The Khurutse fault scarp is visible southeast of the main shock location and dipping NW–SE direction (see Fig. 2). The earthquake rupture dimension at depth was also investigated from the inversion of surface deformation and slip distribution on a fault plane striking 315°, dipping 45° and −80° rake, and with Mo 7.12 e18 Nm. The earthquake rupture geometry agrees with the $\geq$1000 aftershock locations at surface and depth and confirms the ~28 km seismogenic layer thickness. Fault plane solutions of the April 3, 2017 event were determined independently with the FOCMEC algorithm (Snoke 2003) and the FPFIT code (Reasenberg and Oppenheimer 1985) from 42 first motion P-phase arrivals using a 2° increment search. The solutions show that the event occurred on a normal fault oriented in a NW–SE direction.

3 Discussion and Conclusion

The M_W 6.5 Botswana earthquake is one of the largest instrumentally recorded events to occur within the Botswana territory. The distribution of the aftershock activity exhibits a clear NW–SE orientation in two clusters. The two clusters suggest that the fault source of these events, and possibly the main event, constitute two fault segments. The earthquake rupture geometry resulted from an active normal fault, which agrees with the aftershock's surface and depth locations and confirms the thickness of ~28 km seismogenic layer. Although the seismic strain rate is of low level at $\geq$1 nanostrain yr^{-1} (Malservisi et al. 2013), the characteristics of the 2017 earthquake rupture and related seismotectonic

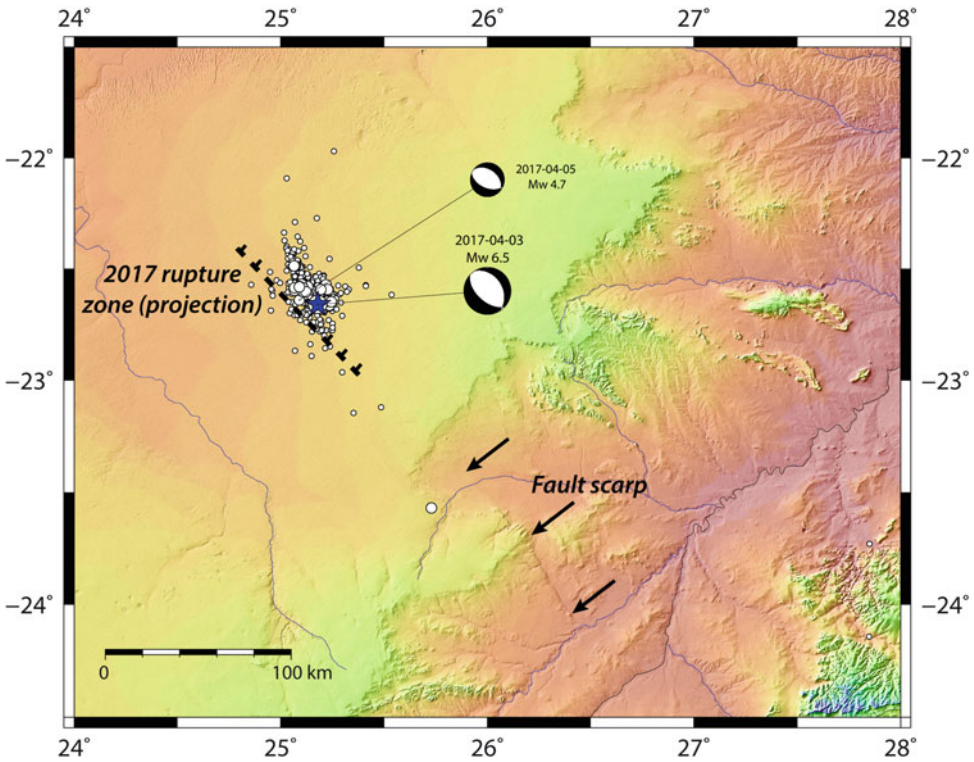

Fig. 2 Botswana earthquake (blue star) and aftershocks' location with focal mechanism and rupture zone projection. The Khurutse fault scarp is indicated by the black arrows

framework classify the intraplate region as an active plate interior.

References

Graham, G., Brandt, M.B.C., Ford, M., Saunders, I., Brink, L.: Catalogue of Earthquakes in Southern Africa and Surrounding Oceans for 1990. Council for Geoscience, Pretoria, South Africa, p. 21 (1995)

Hutchins, D.G., Hutton, L.G., Hutton, S.M., Jones, C.R., Loenhert, E. P.: A summary of the geology, seismicity, geomorphology and hydrogeology of the Okavango Delta. Bulletin 7, Botswana Geological Survey Department (1976)

Malservisi, R., Hugentobler, U., Wonnacott, R., Hackl, M.: How rigid is a rigid plate? Geodetic constraint from the TrigNet CGPS network, South Africa. Geophys. J. Int. **192**, 918–928 (2013)

Meghraoui, M., Amponsah, P., Ayadi, A., Ayele, A., Ateba, B., Bensuleman, A., Delvaux, D., El Gabry, M., Fernandes, R.M., Midzi, V., Roos, M., Timoulali, Y.: The seismotectonic map of Africa. Episodes **39**(1), 9–18 (2016)

Reasenberg, P., Oppenheimer, D.: Fp_t, fpplot, and fppage: Fortran computer programs for calculating and displaying earthquake fault plane solutions. Technical report, U.S. Geological Survey (1985)

Snoke, J.A.: FOCMEC: focal mechanism determinations. In: Lee, W.H. K., Kanamori, H., Jennings, P.C., Kisslinger, C. (Eds.) International Handbook of Earthquake and Engineering Seismology. Academic Press, San Diego, California, p. 994 (2003)

Kinematic and Elastic Modeling of Fault-Related Folds: Examples from Active Structures of the Tell Atlas (Northern Algeria)

Souhila Bagdi-Issaad, Mustapha Meghraoui, Jugurtha Kariche, and Ahmed Nedjari

Abstract

Active folds are tectonic structures with seismogenic potential, able to generate large magnitude earthquakes with Mw > 6.5. Here, we compare the elastic modeling with the kinematic modeling of active folds. This research is based on characterization of geological and geomorphic features using field observations and remote sensing approaches. We also use seismic parameters of main earthquakes recorded in the Tell Atlas of Algeria. In this work, we focus on three tectonic structures; El Asnam (responsible of the 1980 Mw 7.1 earthquake with surface faulting and considered as a reference tectonic and seismogenic structure for comparison), Sahel and Tenes-Abou Al Hassen (Meghraoui, 1988).

This work is part of a research program of the identification of active and seismogenic structures, with a particular attention to blind faults to allow a better seismic hazard assessment in the region.

Keywords

Tell Atlas • Quaternary geology • Tectonic geomorphology • Fault-related fold • Kinematic-elastic model • Seismic hazard and assessment

1 Introduction

The Algerian Tell Atlas is characterized by NE-SW trending "en-echelon" active fault-related folds. They are generated by a transpressive tectonic regime with NNW-SSE to NW–SE shortening directions which is estimated to be of 2.2 ± 0.5 mm/yr (Meghraoui 1988). This regime is related to the 4–6 mm/yr, oblique convergence along the Africa–Eurasia plate boundary (Serpelloni et al. 2007). The estimated uplift rate across the Tell Atlas is 0.7 ± 0.2 mm/yr in agreement with the geological, geomorphological, and paleoseismological results (Bagdi et al., submitted paper). The Tell fault-related folds' structures show structural geometries that may generate shallow moderate and large earthquakes with magnitudes Mw ≥ 5.5. Although some of these tectonic structures already generated seismic events such as: Cavaignac 1922 (Ms 5.9), El Asnam 1980 (Mw 7.1), and Zemmouri 2003 (Mw 6.8), other active fault-related folds such as the Sahel structure have not been yet associated with a significant seismic event (Fig. 1).

2 Materials and Methods

Geological maps (1/50,000 scale) and related stratigraphic analysis from wells combined with high-resolution panchromatic 'Pleiades' tri-stereo-satellite images (0.5 m resolution) and field observations are used as a database.

The collected geological data allowed the kinematic modeling using Trishear 4.5 algorithms as described in Allmendinger (1999).

The fold dislocation modeling is based on the linear elastic, uniform, and isotropic Okada method (1992) and the seismotectonic background results of past significant earthquakes' studies of the Tell Atlas.

3 Analysis and Results

The Sahel and El Asnam structures are ~60 and ~40 km long asymmetrical folding that affects Mio-Plio-Quaternary deposits. They display a comparable lithostratigraphic section in Mitidja and Chelif basins, respectively. Geological

S. Bagdi-Issaad (✉) · M. Meghraoui · J. Kariche
EOST - Institut Terre et Environnement de Strasbourg, University of Strasbourg, CNRS - UMR 7063, Strasbourg, France

S. Bagdi-Issaad · J. Kariche · A. Nedjari
Faculté Des Sciences de La Terre FSTGAT, USTHB, Bab Ezzouar, Algeria

M. Meghraoui et al. (eds.), *Advances in Geophysics, Tectonics and Petroleum Geosciences*, Advances in Science, Technology & Innovation, https://doi.org/10.1007/978-3-030-73026-0_8

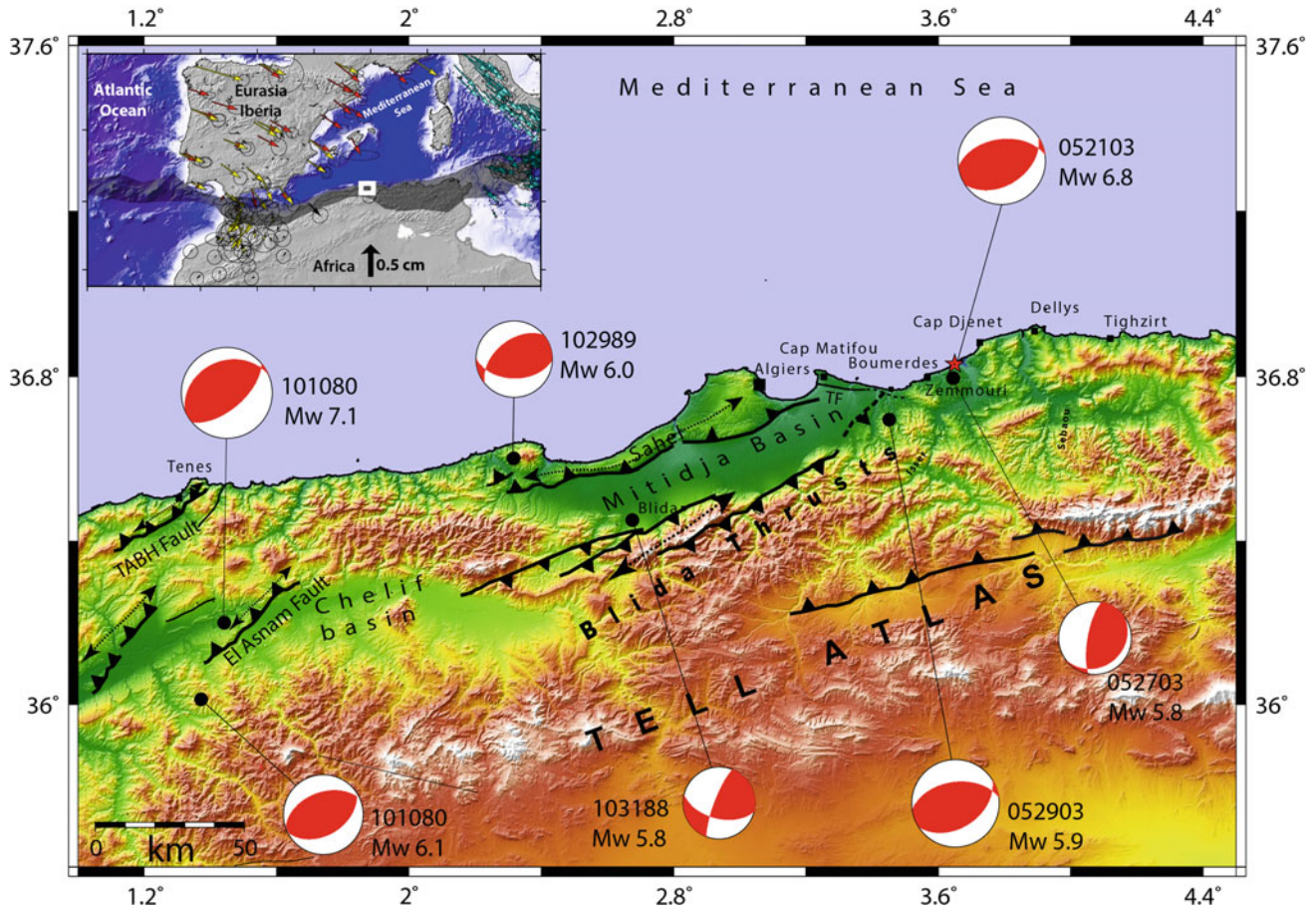

Fig. 1 Morphotectonic and recent large to moderate earthquakes of the central Tell Atlas (Bagdi et al., submitted paper). Shaded relief is SRTM 3″ posting digital elevation model. Focal mechanisms are CMT-Harvard solutions

and balanced cross sections through the Sahel and El Asnam tectonic structures reveal thick (>5000 m),

El Asnam, Sahel, and TAEH fault-related folds form active margins of Quaternary basins. In all case studies, progressive unconformities visible along fold flank affect the Pleistocene and Holocene deposits of marine (Sahel) or fluvial terraces (El Asnam, Sahel, and TAEH).

Folding structures show geometrical unconformities and triangular facets near active faults that allow a subdivision in 2–3 distinct segments. Abandoned river beds and river channel deviations of the Mazafran, Fodda-Chelif, and Allalah indicate river damming and migrations due to recurrent fold-related fault activity. In coastal areas, we also observe exposed abrasion platforms and notches that denote successive uplift during past earthquakes. Most of the modeling results are in agreement with our geological and geomorphic descriptions.

The kinematic modeling reveals changes in the reverse fault dip, ranging from 30° to 65°. The elastic model based on results of the 1980 El Asnam earthquake implies reverse faults taking origin from decollement plans located at 8–10 km depth, in agreement with the seismicity distribution in the brittle crustal structure. On Fig. 2, we show an example of kinematic modeling (Fig. 2a) and elastic modeling (Fig. 2b) of the central segment of Sahel structure.

4 Discussion and Conclusion

The Sahel and TAEH structures are faults propagation folds, and their seismic potential is important when compared to the El Asnam structure and related major past earthquakes. Our geomorphological analysis shows that the studied threefold-related structures reveal several similarities. They show geological and geomorphological features which are common to active zones with thrust and reverse faults.

Kinematic models applied to El Asnam, Sahel, and TAEH fault-propagation folds explain the difference in thickness between deposits in hanging and footwall block and there active margins that form fold-related faults. In the

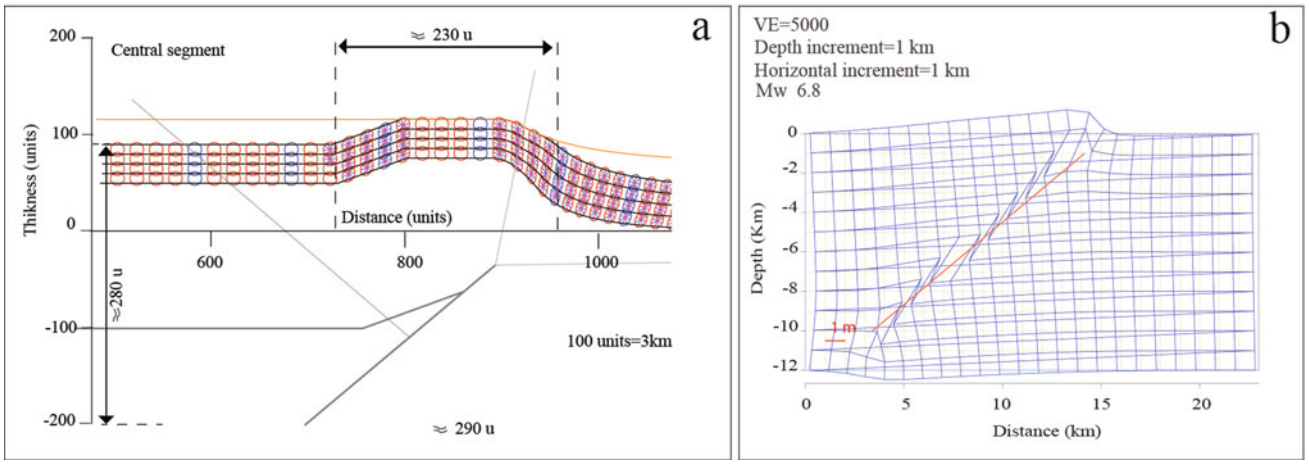

Fig. 2: **a** Kinematic modeling and **b** elastic modeling of the central segment of Sahel fault-related fold (Bagdi et al., paper in progress)

Tell Atlas, reverse faults take origin from decollement plan located at an average of 8–10 km of depth (Fig. 3), in agreement with seismic events recorded along active tectonic structures.

In each structure, the fold morphology observed at the surface shows different widths. The difference between hanging and footwall blocks along active faults is also visible in kinematic and elastic modeling as it is often related to fault deep variations. Fault dips that exceed 45° are likely related to past tectonic normal faults heritage accompanied post-nappes Neogene basins extension.

From the fold modeling, a fault activity close to the surface gives a higher relief, and a low-angle dip gives a wider folding structure. The kinematic modeling approach provides satisfactory results for horizontal and large vertical dimensions (seismogenic crust) but exaggerates small vertical dimensions (thickness of deposits on fold and its height in relation to horizontal level of sedimentary basins). The

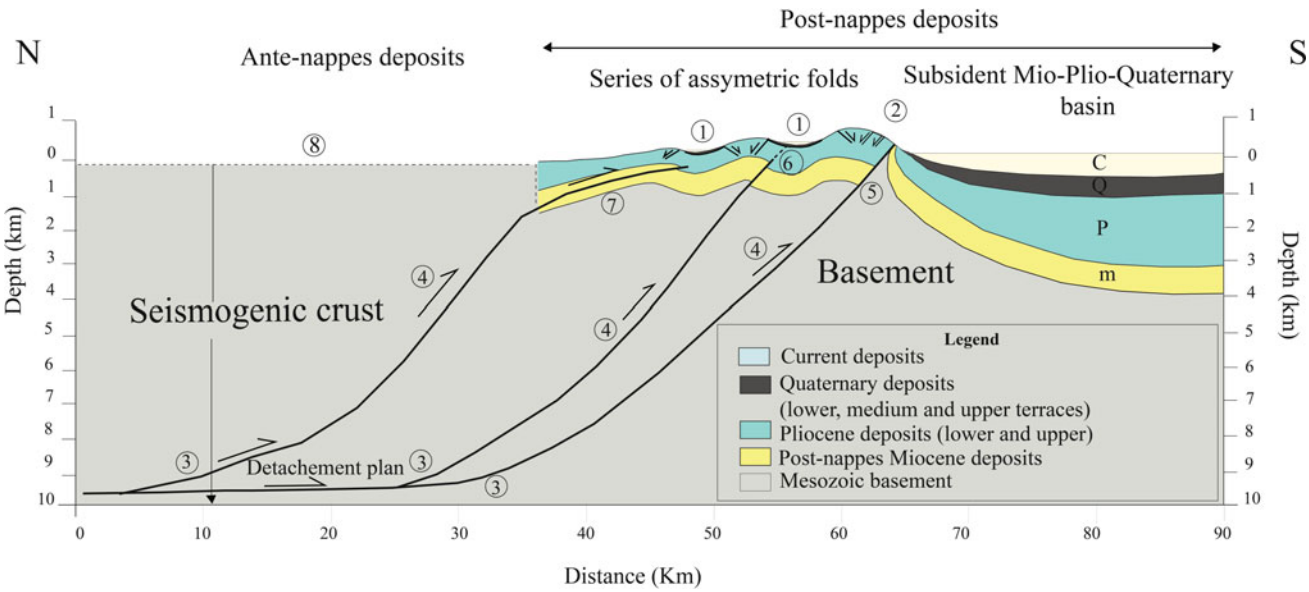

Fig. 3 Proposed model for fault-related folds in the Tell Atlas (Algeria), according to geology, geomorphology descriptions, kinematic and elastic models (Bagdi et al., paper in progress). 1—small basins occupied by quaternary, recent and current deposits; 2—normal extrado faults; 3—thrust faults (10°–30° dip); 4—reverse fault (>45° dip); 5—reverse fault with visible scarp on surface (e.g., El Asnam model, segment 2); 6—reverse fault without visible carp on surface (e.g., Tenes model, segment 1); 7—thrust fault without visible scarp on surface (e.g., Sahel model, segment 3); 8—ante-nappes deposits (basement), where geology and topography are different from one structure to another; c—current and recent deposits; Q—quaternary deposits; P—Pliocene units; m—post-nappes Miocene units

elastic modeling approach gives better results on the coseismic deformation at depth but it requires detailed knowledge on seismic event parameters.

Kinematic and elastic modeling may infer that blind fault geometries are appropriate tools for explaining surface active deformation and obtaining a virtual image of the substratum, especially in the absence of seismic profiles.

References

Allmendinger, R.W.: Propagation-to-slip ratio and fold style in fault-propagation folds: perspectives gained from trishear modeling. In: Geological Society of America Abstracts with Programs (1999)

Meghraoui, M. : Géologie des zones sismiques du nord de l'Algérie (Paléosismologie, Tectonique active et synthèse sismotectonique), Thèse de doctorat d'Etat, Université de Paris-Sud, Centre d'Orsay (France), 356 pages (1988)

Okada, Y.: Internal deformation due to shear and tensile faults in a half-space. Bull. Seismol. Soc. America **82**(2), 1018–1040 (1992). http://dx.doi.org/

Serpelloni, E., Vannucci, G., Pondrelli, S., Argnani, A., Casula, G., Anzidei, M., Baldi, P., Casperini, P.: K nematics of the western Africa-Eurasia plate boundary from focal mechanism and GPS data. Geophys. J. Int. **169**, 1180–1200 (2007)

Magmatic Rifting and Seismicity in Afar and Northern Main Ethiopian Rift (MER)

Atalay Ayele

Abstract

Over 20 volcano-tectonic earthquake sequences have occurred in Afar and the northern main Ethiopian rift for the last couple of decades and the corresponding seismic data are recorded by temporary and permanent broadband seismic networks. The Dabbahu sequence is the most notable of all, as it spanned over a long period of activity and covered a wide spatial extent, which rarely happens. A wide range of seismic signals is recorded from high-frequency microfractures to tilt signals during volcano-tectonic sequences, which all explain the various dynamics underway around the volcanic source regions. The tectonic stress release mechanism in the area is associated with the interplay between crustal deformation and magma emplacement. In all the aforementioned activities, it is quite common to observe hybrid events that commence with a high-frequency onset with long period tail, while typical long period (LP) events with emergent onset are least common. This kind of volcano-seismicity is observed even when there were no eruptions observed. A significant part of seismic energy in the area is released as sequences/swarms with the prints of diking or magma emplacement except for the Ankober area in the western plateau, where the typical tectonic type of earthquakes occurs.

Keywords

Ethiopia • Afar • Magmatic rifting

1 Introduction

Hundreds of years have elapsed since earthquakes started to be instrumentally recorded. However, our understanding of magmatic rifting and other complicated source features that we observe today was limited due to the absence of digital seismic records at epicentral distances of interest. After the advent of digital broadband instrumentation with wide dynamic range, volcano-seismology has become one of the strongest disciplines contributing to the study of magmatism and assessment of volcanic unrest for disaster mitigation. The Afar Depression is one of the world's best tectonic domains for the study volcano-seismology (Fig. 1).

Rifting between the Arabia, Somalia, and Nubia plates during the past ~30 Ma produced the ~300-km-wide and ~600-km-long Afar depression (Fig. 1) formed within the Palaeogene flood basalt province (e.g., Hofmann et al. 1997). The largest dike opening event ever measured occurred along part of the Manda-Harraro rift segment of Afar in September 2005 and was the first event of this kind observed using satellite geodetic methods. Interferometric Synthetic Aperture Radar (InSAR) showed that an up to 8 m of opening has occurred on a ~60-km-long, ~10-km-deep dike (Wright et al. 2006; Ayele et al. 2007), but it could not determine either the location of the source of the dike filling magma or the time history of the event.

To this date, various properties of the magma source region and its dynamics are being captured on broadband stations and spectral analysis is performed to distinguish low-frequency earthquakes with one or more spectral peaks below 5 Hz, following the Seismic signals are diagnostic tools for identifying whether the local earthquakes that are recorded on a routine basis are of tectonic type or if the event is issued from a volcanic source region (Chouet 2003). This demonstrates that there are several active volcanic and fissure eruptive centers in the Afar region which need monitoring in order to study continental rift mechanifsms and for

A. Ayele (✉)
Institute of Geophysics Space Science and Astronomy, Addis Ababa University, P.O. Box 1176 Addis Ababa, Ethiopia
e-mail: atalay.ayele@aau.edu.et

M. Meghraoui et al. (eds.), *Advances in Geophysics, Tectonics and Petroleum Geosciences*,
Advances in Science, Technology & Innovation, https://doi.org/10.1007/978-3-030-73026-0_9

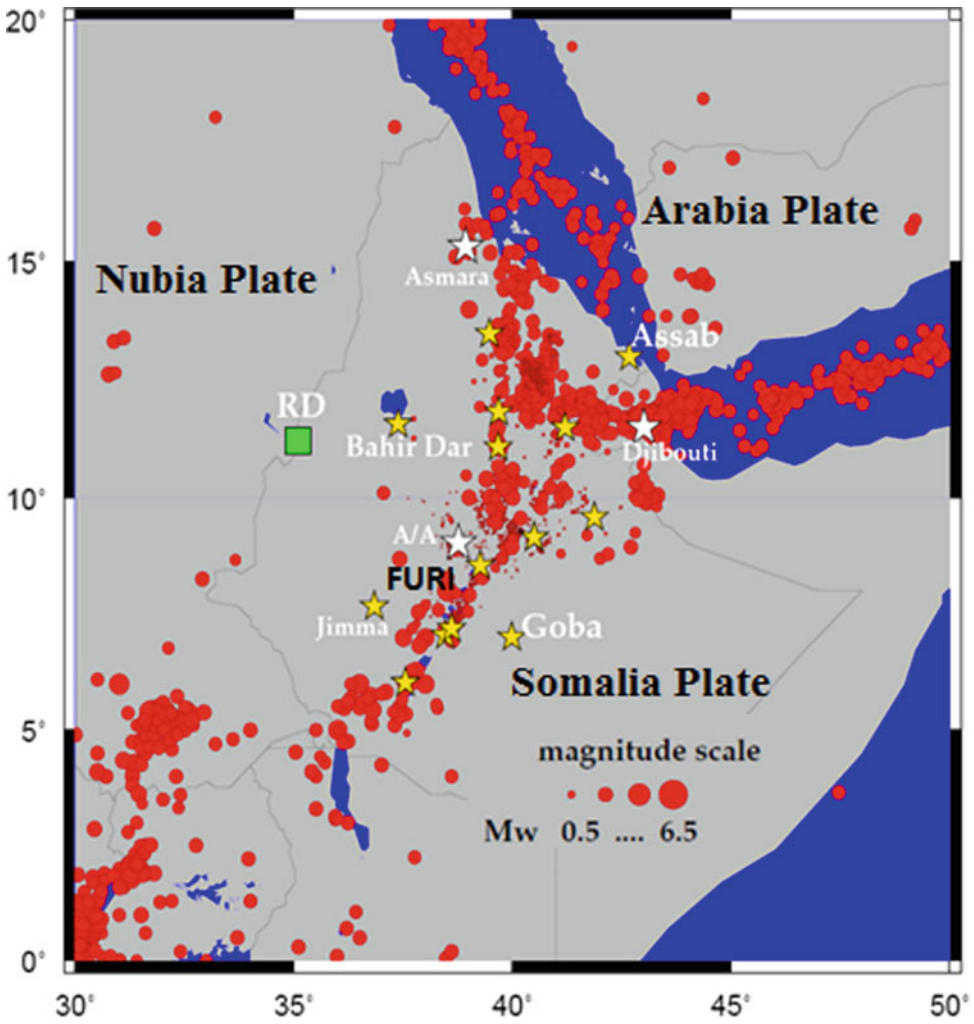

Fig. 1 Seismicity in Ethiopia and the neighboring region. The red dots show locations of earthquakes where circle size is proportional to magnitude in the range 0.5–6.5 Mw. The white stars show capital cities in the region and the yellow stars show major towns in Ethiopia. AA—Addis Ababa and RD (green box) is the Ethiopian Renaissance Dam. FURI is the station used for the volcano-seismology data analysis

mitigating volcano and earthquake disasters. To better capture and understand episodic magmatic activities in Afar and the neighborhood, deploying a limited number of very-broadband seismic stations (to be followed by dense and short period network in time of volcanic unrest), is advisable for the interested researchers in the region.

ssification of Lahr et al. (1994) and McNutt (2005).

2 Methods

Seismicity is plotted using Generic Mapping Tools (GMT) of Wessel and Smith (1998) to produce both Figs. 1 and 2. Figure 3 is produced using existing scientific third-party packages, such as (http://pypi.python.org/pypi/MLPY) to perform a continuous wavelet transform with a Morlet wavelet, using jupyter Notebook.

3 Results

3.1 Results (Earthquake Swarms)

A closer look at Fig. 1 shows the clustering of earthquake activity in the Afar region, which is dominated by distinct magmatic and dike intrusions in the region as displayed in Fig. 2. As a result, it is tantamount to say that magmatism or magma is the mother of seismicity in the region (Ayele et al. 2015).

3.2 Results (Frequency Time Analysis)

Figure 3 shows broadband seismograms recorded at FURI station and the corresponding wavelet plot of amplitude on a

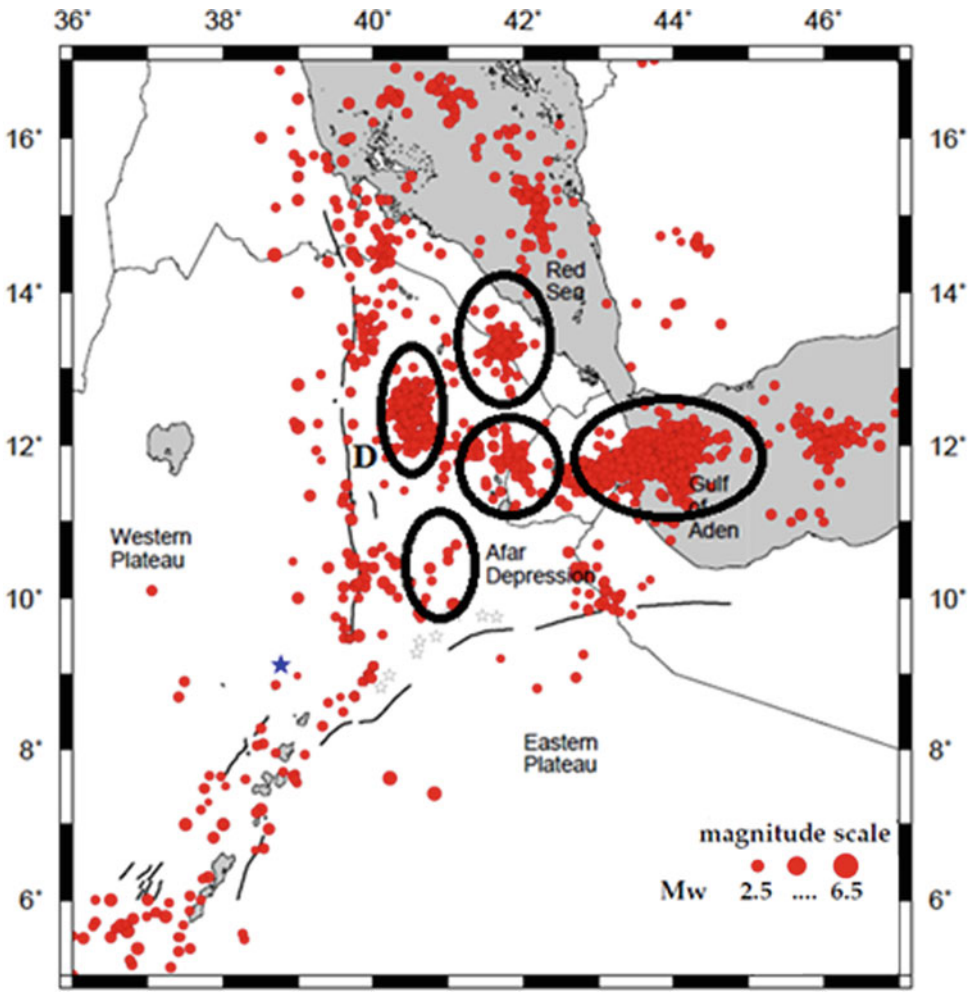

Fig. 2 Seismicity around the Afar depression. The ellipses mark distinct volcanic centers in the region. The letter D shows Dabbahu mega dike intrusion that sustained over a period of 10 years starting from 2005 to 2014. Black lines are faulting. The blue star shows the location of Addis Ababa

frequency versus time axes. Both records are from the 2005 Dabbahu major dike intrusion in the Afar region. Figure 3a is a resonating low frequency signature trailing a local earthquake of magnitude 4.5 ML while Fig. b is a very long period signal recorded on the horizontal components and probably shows the deeper magma pumping system beneath the dike source. The first high-frequency signal on Fig. 3b is probably associated with the felsic explosion observed on September 26, 2005. Instrument response is removed in both cases.

.

4 Discussion

The advent of digital seismology and other contemporary data analysis techniques paved the way for a better understanding of the active volcanic regions. Volcano-tectonic dynamics have been recorded with analog seismographs in the predigital era, but it was difficult to treat the full waveform features other than picking the ordinary P- and S-wave arrivals for earthquake locations. With the current status of seismograph networks all over the globe, we can record different features and extract the desired information by investigating the fingerprints of different source regions using the frequency band of interest.

5 Conclusions

Volcano-seismology can tell us a lot on the different features of the source region, while models for low-frequency seismicity offer insight into magma (or other fluid) compositions. If assisted by InSAR techniques, we can better understand dike intrusions and active volcano-source regions.

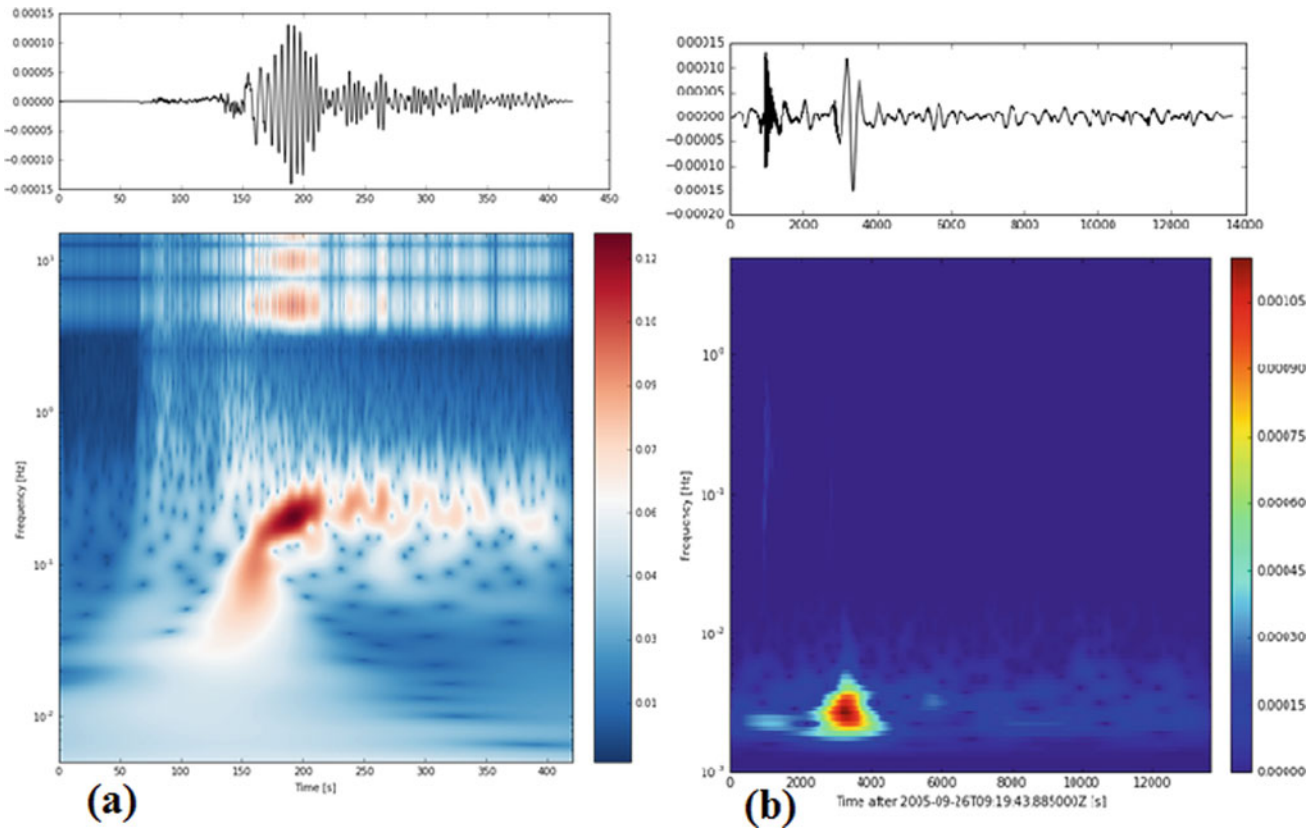

Fig. 3 **a** Seismogram for an earthquake in the Dabbahu sequence and the corresponding frequency time analysis using continuous wavelet transform. **b** Time–frequency analysis but for a longer time span showing very long period from possibly deep seated magma source. Bluish colors represent low energy while reddish colors represent high energy

References

Ayele, A., Jacques, E., Kassim, M., Kidane, T., Omar, A., Tait, S., Nercessian, J., Chabalier, J.-B., King, G.: The volcano-seismic crisis in Afar, Ethiopia, starting September 2005. Earth Planet. Sci. Lett. **255**, 177–187 (2007)

Ayele, A., Ebinger, C., Van Alstyne, C., Keir, D., Nixon, C., Belachew, M., Hammond, J.: Seismicity of the central Afar rift and implications for Tendaho dam hazards, Magmatic Rifting and Active Volcanism. In: Wright, T.J., Ayele, A., Ferguson, D.J., Kidane, T., Vye-Brown, C. (Eds.) Geol. Soc., Spec. Publ., vol. 420, pp. 341–354 (2015)

Chouvet, B.: Volcano seismology. Pure Appl. Geophys. **160**, 739–788 (2003)

Hofmann, C., Courtillot, V., Fe´raud, G., Rochette, P., Yirgu, G., Ketefo, E., Pik, R.: Timing of the Ethiopian flood basalt event and implications for plume birth and global change. Nature **389**, 838–841 (1997)

Lahr, J.C., Chouet, B., Stephens, C.D., Power, J.A., Page, R.A.: Earthquake classification, location, and error analysis in a volcanic environment: Implications for the magmatic system of the 1989–1990 eruptions at Redoubt Volcano, Alaska. J. Volcanol. Geotherm. Res. **62**, 137–151 (1994)

McNutt, S.R.: A review of volcanic seismology. Ann. Rev. Earth Planet. Sci. **33**, 461–491 (2005)

Wessel, P., Smith, W.H.F.: New, improved version of the generic mapping tools released. EOS Trans. AGU **79**, 579 (1998)

Wright, T.J., Ebinger, C., Biggs, J., Ayele, A., Yirgu, G., Keir, D., Stork, A.: Magma maintained rift segmentation at continental rupture in the 2005 Afardyking episode. Nature **442**, 291–294 (2006)

Architecture and Evolution of the Kivu Rift Within the Western Branch of the East African Rift System: Implications for Seismic Hazard Assessment

Damien Delvaux, Gloire Bamulezi Ganza, Silvanos Bondo Fiama, and Hans-Baalder Havenith

Abstract

The Kivu rift, in the middle of the western branch of the East African Rift system, has a particular setting within the African continent. It represents the most recent (late Cenozoic) evolution of the Mesoproterozoic Karagwe-Ankole Belt of the Great Lakes Region in Central Africa. Its architecture and evolution have been profoundly influenced by the tectonic framework inherited from the Kibaran and Pan-African orogenic events. In order to build a new detailed seismic hazard map, we have compiled regional geological and neotectonic maps, re-examined the tectonic evolution, investigated the brittle structures, and determined the paleo-stress field evolution. The Kivu rift appears heterogeneous and complex. It probably started as an isolated segment that progressively linked with the adjacent segments of the Western Rift Branch. Its architecture and structural inheritance are reflected in the seismic activity and the current stress field. This results in a marked lateral variability of the Gutenberg–Richter parameters and seismic hazard estimates.

Keywords

East African rift • Kivu rift • Tectonic structure • Neotectonics • Seismic hazard assessment

D. Delvaux (✉)
Department of Earth Sciences, Royal Museum of Central Africa, Tervuren, Belgium
e-mail: damien.delvaux@africamuseum.be

G. B. Ganza
Department of Geology, Université Officielle de Bukavu, Bukavu, DR, Congo

S. B. Fiama
Department of Geophysics, Centre de Recherche en Sciences Naturelles (CRSN), Lwiro, DR, Congo

H.-B. Havenith
Department of Geology, University of Liège, Liège, Belgium

1 Introduction

The Kivu rift, in the middle of the western branch of the East African Rift system, has a particular setting within the African continent. It represents the most recent (late Cenozoic) evolution of the Mesoproterozoic Karagwe-Ankole orogenic belt of the Great Lakes Region in Central Africa (Fig. 1). Its architecture and evolution have been profoundly influenced by the tectonic framework inherited from the Kibaran and Pan-African orogenic events.

2 Geological and Neotectonic Evolution

In order to build a new detailed seismic hazard map for the Kivu rift region, we first compiled regional geological and neotectonic maps of the region surrounding the Kivu rift and re-examined the tectonic evolution, investigated the brittle structures, and determined the paleo-stress field evolution.

The neotectonic setting, related to the evolution of the late Cenozoic rifting, has been highlighted by mapping the fault pattern from combined interpretation of the topography from the NASA Shuttle Radar Topography Mission (SRTM) at 30 m resolution, existing geological maps and additional field work (Smets et al. 2016). We also added the known thermal springs, quaternary volcanic centers, and seismic epicenters (Delvaux et al. 2017). The Kivu rift appears heterogeneous and complex, influenced by prerift tectonic heterogeneities (faults and shear zones, shown in black in Fig. 2).

It probably started as an isolated segment that progressively linked with the adjacent segments of the Western Rift Branch. Two dominant fault trends have been recognized: an older NE-SW almost rectilinear trend with the Rutshuru basin, Virunga volcanic province, Kivu basin and Kamituga failed rift (in yellow in Fig. 2) and a younger N-S S-shaped trend trend connecting the Kivubasin to the North Tanganyika basin trough the Rusizi valley and plain (in red).

M. Meghraoui et al. (eds.), *Advances in Geophysics, Tectonics and Petroleum Geosciences*,
Advances in Science, Technology & Innovation, https://doi.org/10.1007/978-3-030-73026-0_10

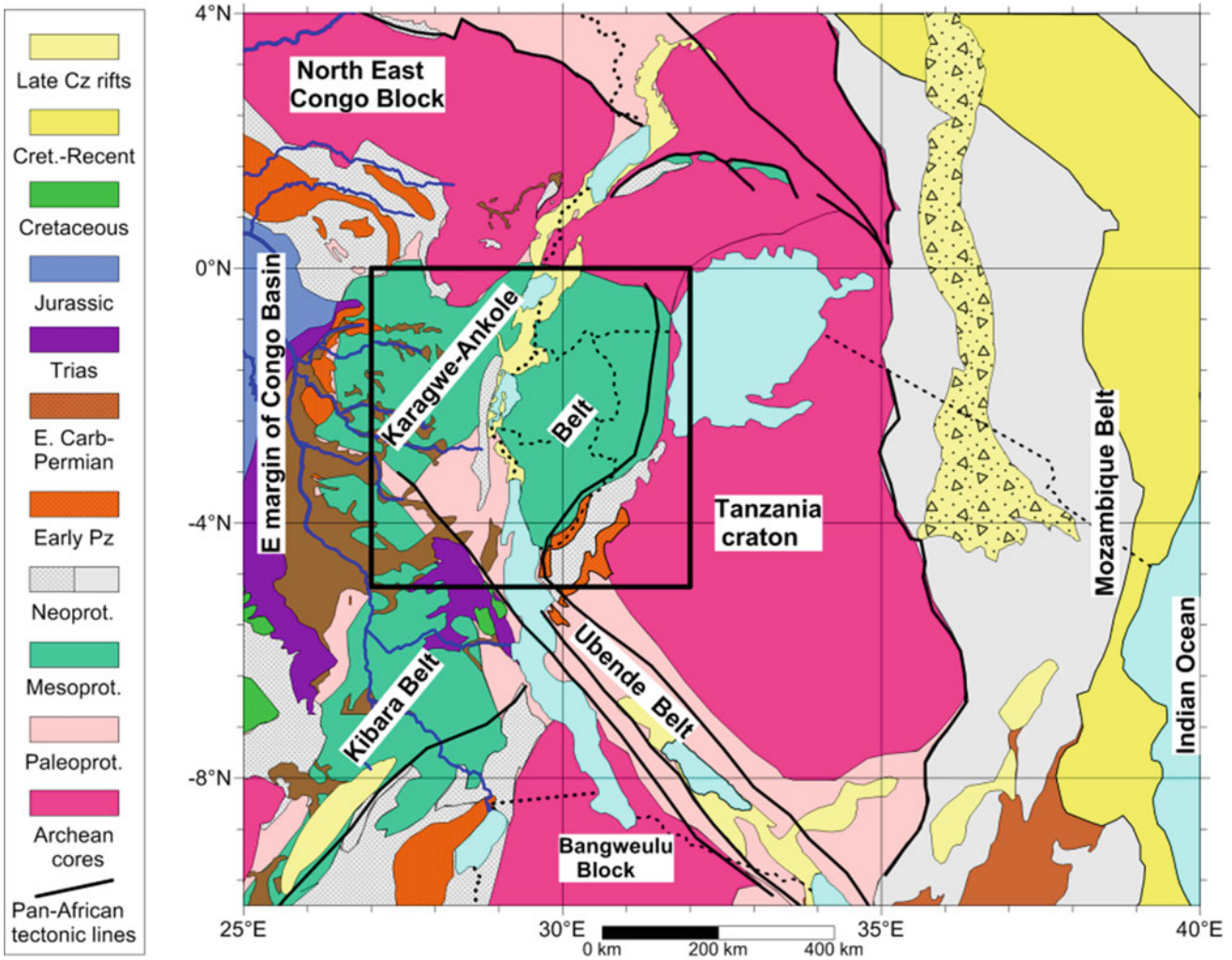

Fig. 1 Location of the Kivu rift region within the Mesoproterozoic Karagwe-Ankole orogenic belt. It forms the central part of the western branch of the East African rift system (adapted from Delvaux et al. 2017)

In the Kivu rift basin, the two directions are superimposed while south of it, the older NE-SW trend formed the Kamituga rift which is now abandoned (but still seismically active) and was connected to the central part of Lake Tanganyika by the Namoya-Kalemie NW-SE depression. More recently, probably in the quaternary, the active rift migrated eastward to connect directly the northern tip of the Kivu basin with the northern extremity of the Tanganyika rift basin (Fig. 2). Its architecture and structural inheritance are reflected in the seismic activity and the current stress field.

3 Seismic Hazard Evaluation

The detailed methodology used for the seismic hazard evaluation is explained in Delvaux et al. (2017), and we will in this section only summarize the most important points. To evaluate the seismic hazard for the Kivu rift region, we compiled a regional seismic catalogue based on the ISC reviewed earthquake catalogue, completed by data from BUL (until 1990), EAF (since 1991), ENT, NAI, PRE, LSZ, CGS, NEIC, and GSHAP catalogues, spanning 126 years, with one thousand and sixty eight (1068) events. The magnitudes have been homogenized to Mw and aftershocks removed. It was subdivided into four subcatalogues with a total of seven hundred and seventeen (717) data from 1931 to 2015 with various magnitudes of completion. The catalogue used for the seismic hazard assessment contains three hundred and fifty nine (359) data for the homogeneous part with a completion magnitude Mw = 4.4 between the years of 1956 and 2015 (60 years) (Fig. 3).

The region of the Kivu rift was subdivided into seven seismic source areas based on the regional geological structure, neotectonic fault systems, basin architecture and distribution of thermal springs and earthquake epicenters (Fig. 3).

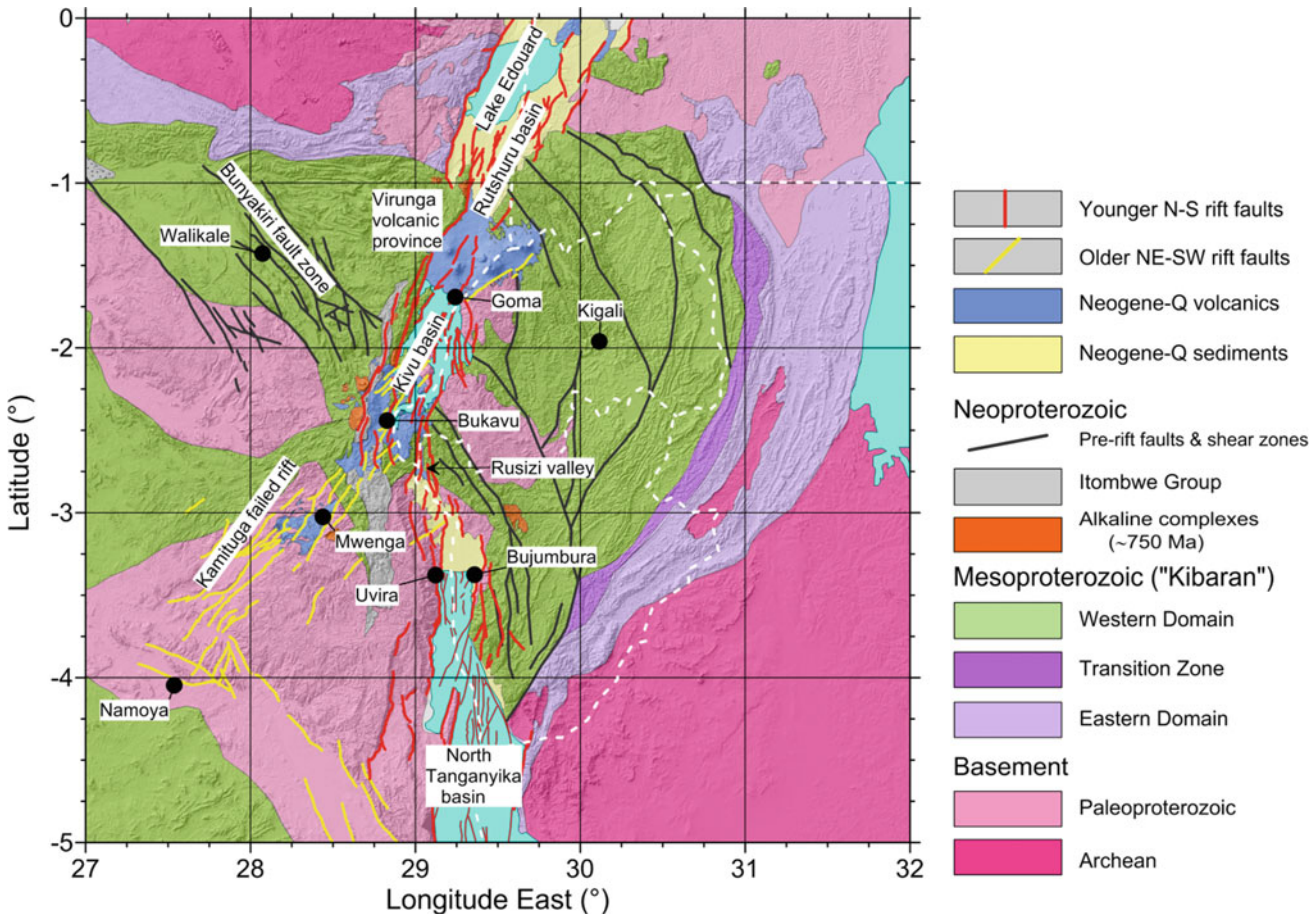

Fig. 2 Geology and neotectonics of the Kivu rift region, showing the older NE-SW rift trend with the Kamituga failed rift branch between Bukavu and Namoya, and the new N-S rift trend linking the Kivu basin to the North Tanganyika basin trough the Rusizi valley (adapted from Delvaux et al. 2017)

The seismic hazard map (Fig. 3) was computed using the Gutenberg–Richter seismic hazard parameters determined by the maximum likelihood method and existing attenuation laws with the Crisis 2012 software (details in Delvaux et al. 2017). The PGA values obtained (475 years return period) are higher than previous estimates (Mavonga and Durrheim 2009). They vary laterally in function of the geological setting, being highest in the non-magmatic part of the rift (Southern Lake Kivu and Rusizi zones), intermediate in the volcanically active Virunga zone, and lowest in the rift flanks.

4 Discussion/Conclusion

Compared with the previous estimations, our model provides a finer seismic zonation using a longer earthquake catalogue, but it can still be improved using more realistic attenuation laws in a logic tree approach. We observed a marked lateral variability of the Gutenberg–Richter parameters and seismic hazard estimates which reflect the heterogeneity of the rift and its location within the African continental plate. The same region has been incorporated in the new seismic hazard

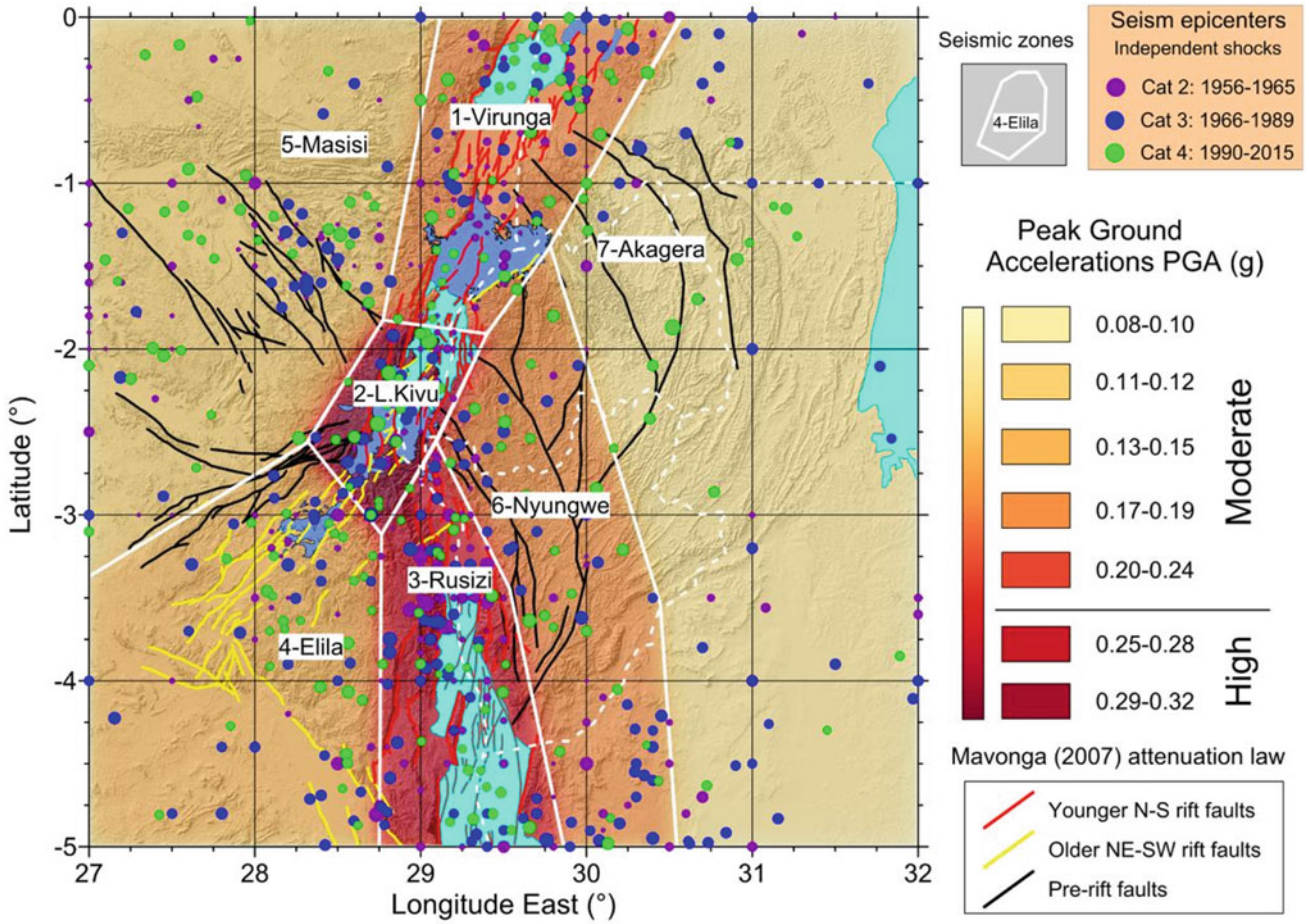

Fig. 3 Seismic hazard map

model for the East African Rift (Poggi et al. 2017), overlying five (5) different seismic zones.

References

Delvaux, D., Mulumba, J.-L., Sebagenzi, M.N.S., Fiama Bondo, S., Kervyn, F., Havenith, H.-B.: Seismic hazard assessment of the Kivu rift segment based on a new seismotectonic zonation model (Western Branch, East African Rift system). J. Afr. Earth Sci. **134**, 831–855 (2017)

Mavonga, T., Durrheim, R.J.: Probabilistic seismic hazard assessment for the Democratic Republic of Congo and surrounding areas. South Afr. J. Geol. **209**, 329–342 (2009)

Poggi, V., Durrheim, R., Mavonga Tuluka, G., Weatherill, G., Pagani, M., Nyblade, A., Delvaux, D.: Assessing seismic hazard of the East African rift: a pilot study from GEM and Africa array. Bull. Earthq. Eng. **15**(11), 4499–4529 (2017)

Smets, B., Delvaux, D., Ross, K.A., Poppe, S., Kervyn, M., d'Oreye, N., Kervyn, F.: The role of inherited crustal structures and magmatism in the development of rift segments: Insights from the Kivu basin, western branch of the East African rift. Tectonophysics **683**, 62–76 (2016)

Stress Transfer and Poroelasticity Associated to Major Earthquakes: From the East African Rift to the African–Eurasian Plate Boundary

Jugurtha Karciche and Mustapha Meghraoui

Abstract

This study focuses on the stress transfer and the related poroelastic effect of four major earthquake sequences that occurred in the Northern and East African rift system: the May–July 1990 Sudan earthquake sequence, the May 2018–June 2019 Mayotte–Comores earthquake swarm sequence, the 1980–2003 El Asnam-Zemmouri (Algeria) earthquake sequence, and the 2016 Alboran sea earthquake sequence. We observe a causative relationship between the stress transfer caused by mainshock fault ruptures and the post-seismic deformation controlled by the aftershock distribution. Also, all seismic sequences are apparently controlled by the poroelastic properties of the seismogenic zone that depend on the undrained and drained fluid conditions.

Keywords

Seismicity and tectonics • Stress transfer • Elasticity • Poroelasticity

1 Introduction

The active tectonics along the East African rift system and the African–Eurasian plate boundary in the western Mediterranean is associated with shallow strong earthquakes (Mw > 6.5) and stress redistribution on nearby fault often following major seismic events. To understand the mechanism of stress transfer caused by earthquake slip and related stress redistribution on nearby faults, we use a computational method based on the change in Coulomb failure function (ΔCFF) made on varied fixed fault planes.

In the previous work, we provide a clear example from the Tell Atlas of Algeria, where the effect of major earthquakes of El Asnam (1980, Mw 7.1) and Zemmouri (2003, Mw = 6.9) on the nearby Sahel fold-related fault illustrates a stress transfer with mechanical and elastic diffusion with crustal deformation that implies earthquake triggering through time (Kariche et al. 2017). Here, we explore the effect of the stress redistribution and the poroelastic effect caused by the May–July 1990 Sudan earthquake sequence (Ms 7.2, 7.1, 6.4, 6.4; Fig. 1), the 2003 Zemmouri earthquake (Mw 6.8), the Mayotte–Comores earthquake swarm sequence from May 2018 to June 2019, and the 1994–2016 Alboran sea earthquake sequence (Fig. 1). The Coulomb modeling procedure using elastic and viscoelastic characteristics of the crust (Wang et al. 2006; Toda et al. 2011) is intended to be generalized on major earthquake sequences of the African plate.

2 Stress Modeling and Fault Interaction

To compute a stress change caused by major earthquakes on nearby fault ruptures, we use a concept of stress change on fixed receiver fault. The static stress change (of the Coulomb failure function ΔCFF) can be expressed by (Reasenberg and Simpson 1992)

$$\Delta \mathrm{CFF} = \Delta\tau - \mu\prime\, \Delta\sigma n \qquad (1)$$

in which (τ) is the shear stress, (σn) is the normal stress, and (μ') is the effective friction coefficient (Beeler et al. 2000). The apparent (of effective) friction coefficient used in triggered seismicity is defined as the combination of fluid pressure and internal friction coefficient (Kariche et al. 2018)

J. Karciche (✉)
Institut de Physique du Globe, CNRS-UMR7516, EOST, F-´ 67084 Strasbourg, France
e-mail: kariche@unistra.fr

J. Karciche
Laboratoire de Geophysique, FSTGAT, USTHB, Algiers, Algeria

M. Meghraoui
EOST - Institut Terre et Environnement de Strasbourg, University of Strasbourg, CNRS - UMR 7063, Strasbourg, France

M. Meghraoui et al. (eds.), *Advances in Geophysics, Tectonics and Petroleum Geosciences*,
Advances in Science, Technology & Innovation, https://doi.org/10.1007/978-3-030-73026-0_11

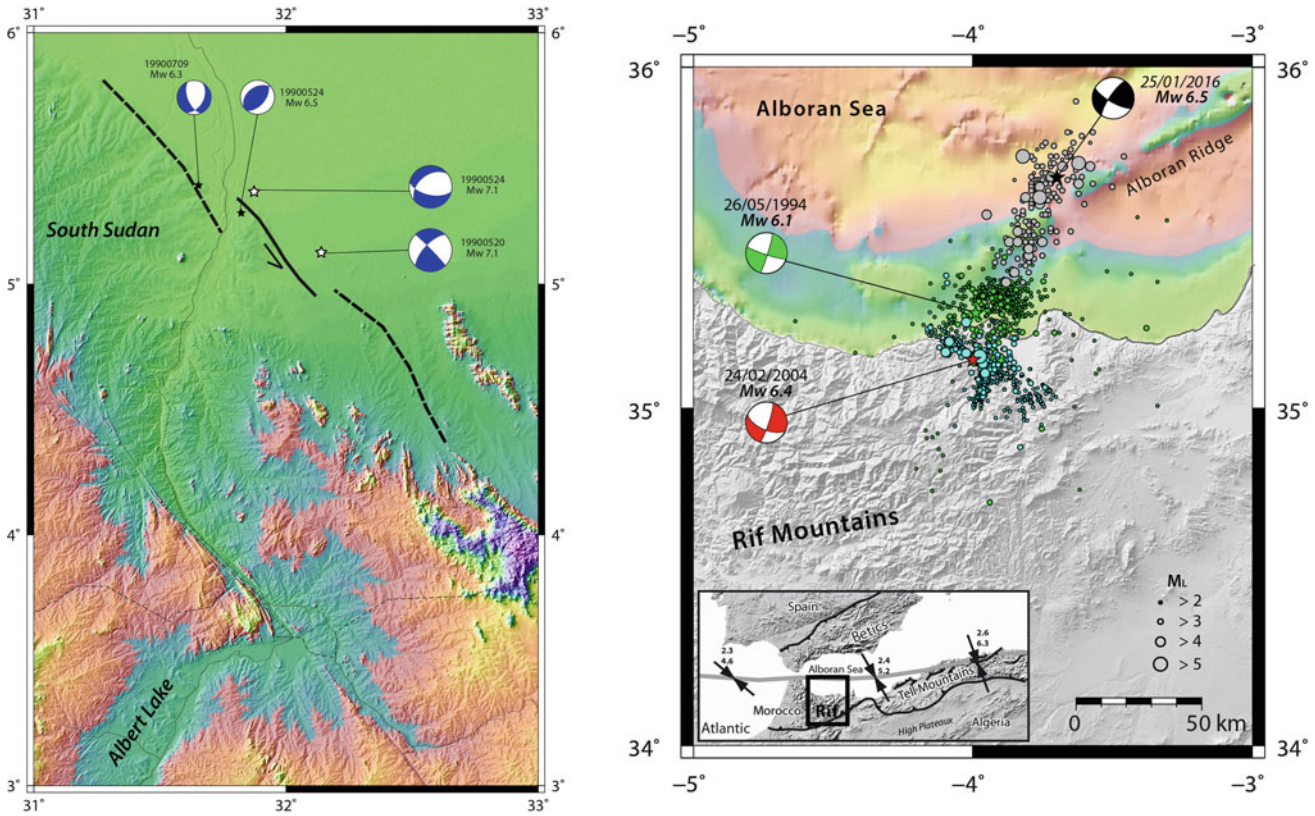

Fig. 1 Left: 1990 Seismic sequence in South Sudan that implies earthquake stress transfer. Black lines are inferred fault zones. Focal mechanisms and earthquake data are from Girdler and Mc Connell (1994). Right: Seismic sequence in northern Morocco and Alboran Sea, colored circles represent the aftershock distribution following each sequence. Focal mechanisms are from Harvard-CMT, and earthquake data are in Kariche et al. (2018)

$$\mu\prime = \mu(1 - \Delta P/\Delta\sigma n) \tag{2}$$

The coupling between the pore pressure change and the mean stress change in undrained condition (no fluid flow) can be replaced by the known Skempton coefficient (B) (Beeler et al. 2000).

$$B = \Delta P/\Delta\sigma m \tag{3}$$

Substituting Eqs. (1) and (2) in Eq. (3), we obtain (Kariche et al. 2018)

$$\Delta\mathrm{CFF} = \tau + \mu(\Delta\sigma n - B\Delta\sigma m)$$

In this work, we compute the fault rupture interactions using Coulomb modeling on both fixed planes and optimally oriented faults, based on the conversion of DC3D subroutines (Okada 1992) to calculate the ΔCFF. The static stress change is computed using an effective coefficient of friction $\mu' = 0.4$ taking into account that the stress distribution and seismicity rate change often suggest a pore fluid effect correlated with elastic dislocation in undrained and drained conditions.

3 Results

Our ΔCFF calculation shown in Fig. 2 includes the poroelastic and the visco-poroelastic physical process with stress redistribution caused by the different earthquakes that contribute to the stress loading, for instance in the case of the Zemmouri earthquake and Mitidja region with implications especially on the Sahel fold-related fault (see Fig. 2; Kariche et al. 2017). The computation is obtained by linear elasticity theory with appropriate values of undrained and drained Poisson ratio by means of full poroelastic relaxation due to the fault ruptures with a typical sedimentary undrained and drained Poisson ratios. The stress change exceeds a value of 0.4 bar along the Sahel rupture when we consider a complex rheology of the materials (see Fig. 2). From the tectonic

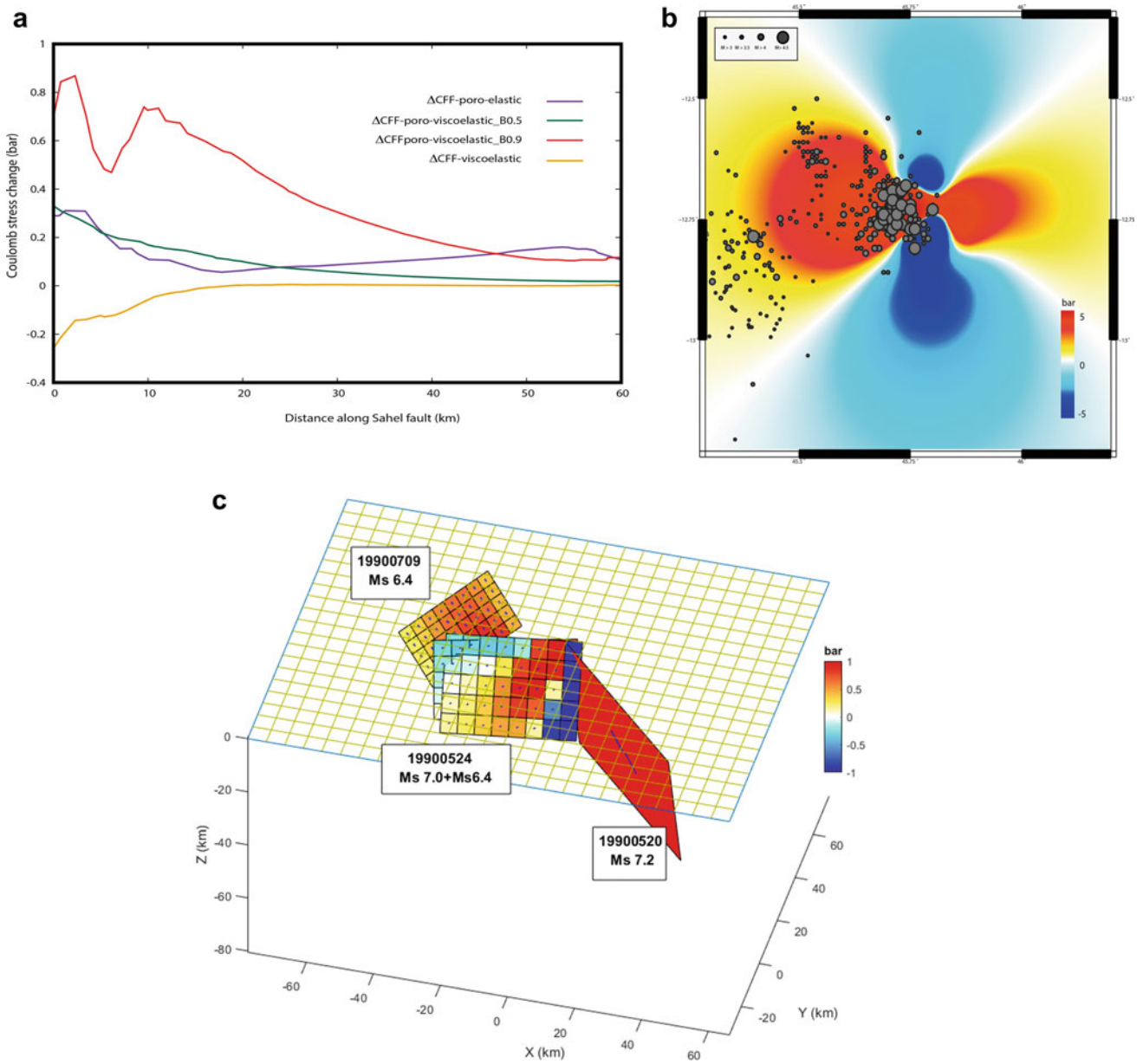

Fig. 2 **a** Stress loading on the Sahel fault as calculated from the 2003 earthquake using different values of the Skempton coefficient *B*. The fault dip of the receiver plane is fixed on 55°, the mean strike of the receiver Sahel fault is 250°, and the mean rake is equal to 70° (Kariche et al. 2017). **b** Poroelastic stress change caused by pressurized volume as source linked to the May 2018–June 2019 Mayotte–Comores earthquake swarm sequence on fixed fault planes (strike/dip/rake = 350°/68°/ − 6°) at variable depth. c Poroelastic stress change caused by the 24/05/1990 earthquake (Mw7.2) on major nearby fault planes

point of view, the 2003 epicentral region limits to the east the Kabylia block, to the west the Mitidja basin and Sahel anticline (Ayadi et al. 2008). Note that a sufficient value promoting failure in the central Tell Atlas obtained by previous studies is estimated to be between 0.1 and 0.8 bar (Kariche et al. 2017).

The four case studies, namely May–July 1990 Sudan earthquake sequence, the Mayotte–Comores earthquake swarm sequence, the 1980–2003 El Asnam-Zemmouri (Algeria) earthquake sequence, and the 1994–2016 Alboran sea earthquake sequence, present a physical process of fault interaction comparable to the 2003 Zemmouri earthquake (Mw 6.8; Kariche et al. 2017), with a short-term coupled poroelastic deformation and a full poroelastic relaxation of the earthquake zones from the undrained to the fully drained state. For all active zones, Fig. 2 illustrates the stress transfer distribution and zones of tectonic loading with respect to areas of stress relaxation. The cumulative seismic moment that ranges between 10^{18} N.m. and 10^{20} N.m. implies a seismic strain release tested on a fault network with

a low effective coefficient of friction on coseismic fault ruptures (≤ 0.2). The May–July 1990 Sudan earthquake sequence shows a fault interaction with the northwestern migration within 4 days to about 3 months of major seismic events, which suggest the effect of a pore fluid migration. Although the main seismic event reached Mw = 5.9 on May 15, 2018, the May–June 2019 Mayotte–Comores earthquake sequence appears to follow the stress transfer physical process on the fault ruptures and related volcanic structures, with a likely deflation of magma reservoir producing a new seamount visible in the differential bathymetric profiles (Lemoine et al. 2019). The modeling of the 1994–2016 Alboran Sea earthquake sequence suggests a static stress change with poroelastic relaxation (under drained fluid conditions) and a coupled short-term (10–12 years recurrence) poroelastic stress transfer consistent with the seismic migration (Kariche et al. 2018). It is important to note that for all sequences, a clear causative relationship is established between the stress loading of fault plane, the progression of pore pressure, and the fluid migration across the fault zone.

4 Conclusion

Our stress change modeling shows a causative relationship between the observed migration of earthquakes, the triggered seismic events, the pore fluid effect, and positive stress load on target faults. In our study, the stress transfer analysis using the earthquake sequence and related fault parameters constrained from field investigations provides a better constraint on fault interactions and related failure threshold. This approach, based primarily on combined geologic and seismological data, is critical for the seismic hazard evaluation (Kariche et al. 2017; Meghraoui 2018).

References

Ayadi, A., Dorbath, C., Ousadou, F., Maouche, S., Chikh, M., Bounif, M.A., Meghraoui, M.: Zemmouri earthquake rupture zone (Mw 6.8, Algeria): Aftershocks sequence relocation and 3D velocity model. J. Geophys. Res. Solid Earth **113**(B9) (2008)

Beeler, N.M., Simpson, R.W., Hickman, S.H., Lockner, D.A.: Pore fluid pressure, apparent friction, and Coulomb failure. J. Geophys. Res. Solid Earth **105**(B11), 25533–25542 (2000)

Girdler, R.W., McConnell, D.A.: The 1990 to 1991 Sudan earthquake sequence and the extent of the East African Rift System. Science **264**, 67–70 (1994)

Kariche, J., Meghraoui, M., Ayadi, A., Boughacha, M.-S.: Stress change and fault interaction from a two century-long earthquake sequence in the central tell Atlas, Algeria. Bull. Seismol. Soc. Am. **107**(6), 2624–2635 (2017)

Kariche, J., Meghraoui, M., Timoulali, Y., Cetin, E., Toussaint, R.: The Al Hoceima earthquake sequence of 1994, 2004 and 2016: Stress transfer and poroelasticity in the Rif and Alboran Sea region. Geophys. J. Int. **212**(1), 42–53 (2018). https://doi.org/10.1093/gji/ggx385

Lemoine, A., Bertil, D., Roullé, A., Briole, P.: The volcano-tectonic crisis of 2018 east of Mayotte, Comoros islands, submitted to Geophys. J. Intern. (2019)

Meghraoui, M.: Earthquake faulting and their implications for the seismic hazard assessment along the plate boundary in North Africa. In: Kallel, A., Ksibi, M., Ben Dhia, H., Khélifi, N. (éds.) Recent Advances in Environmental Science from the Euro-Mediterranean and Surrounding Regions, pp. 37–40 (2018). https://doi.org/10.1007/978-3-319-70548-4_15

Reasenberg, P.A., Simpson, R.W.: Response of regional seismicity to the static stress change produced by the Loma Prieta earthquake. Science **255**(5052), 1687–1690 (1992)

Toda, S., Stein, R.S., Sevilgen, V., Lin, J.: Coulomb 3.3 graphic rich deformation and stress-change software for earthquake, tectonic, and volcano research and teaching, User guide, U.S. Geol. Surv. Open-File Rept. 2011–1060, p. 63 (2011). Available at: http://pubs.usgs.gov/of/2

Wang, R., Lorenzo-Martín, F., Roth, F.: PSGRN/PSCMP—a new code for calculating co- and post-seismic deformation, geoid and gravity changes based on the viscoelastic-gravitational dislocation theory. Comput. Geosci. **32**(4), 527–541 (2006)

Seismic Risk in Ghana: Efforts and Challenges

Paulina Amponsah and Irene Opoku-Ntim

Abstract

Since 1939, Ghana has experienced its severest earthquake with a magnitude of 6.5 on the Richter scale, which killed seventeen people and caused a lot of damages to property. There have been reported occurrences of earth tremors in recent times, though the region is generally considered a stable continental area with few active tectonic features. Three recent earth tremors were recorded in the country in March and December 2018 and March 2019 with magnitudes ranging from 3.0 to 4.8 on the Richter scale. These tremors caused a lot of panics to the inhabitants of the most affected areas. Earthquake occurrence and observation surveys were conducted in March 2019 in the southern part of the country where the events were most felt. The main objective of the survey was to assess the perception, experiences and adaptation strategies of randomly sampled residents of the area to seismic events. Questionnaires were administered for the survey in the Awutu Senya East and Weija-Gbawe Municipalities. There were divergent views from the inhabitants on their perception, experiences and adaptation strategies to earth tremors in the area. We realized that most of the people were aware that they live in an earthquake prone area, but have no measures in place to mitigate the seismic risk. Therefore, the responsible government agencies need to conduct geological and geophysical investigation on every land acquired before releasing them to developers.

Keywords

Seismic risk • Coastal boundary fault • Akwapim fault zone • Awareness creation • Ghana

1 Introduction

The seismicity of Ghana is attributed to possible recent movements along the Togo, Birimian and Dahomeyan thrust faults (Bondessen and Schmidt 1972). Sykes (1978) emphasized the role of these faults in the high seismic activity in the region. The relative intense seismicity in the region is attributed to the resurgence of movement along ancient tectonic boundaries. Bacon and Banson (1979), Amponsah (2002), attributed the seismicity of Southeastern Ghana to the level of activity of the Akwapim fault zone with little activity along the Coastal boundary fault.

There have been reported occurrences of earth tremors in recent times in parts of southern Ghana namely Awutu Senya East and Weija-Gbawe Municipalities (Amponsah et al. 2012; Amponsah 2004; Akoto and Anum 1992). These events have thrown residents into fear and panic. Table 1 shows magnitudes and earthquakes recorded in Ghana from 1615 to 2019.

Earthquake occurrence and observation surveys were conducted in March 2019, to assess the perception, experiences and the adaptation strategies for the residents of these areas regarding the seismic events. Figure 1 is a map of Awutu Senya East and Weija-Gbawe Municipalities. The purpose of the survey was to disseminate information on seismic hazard to ensure that effective measures are taken in land development. Information was also sought for policy-making as well as advising the government on geo-scientific issues related to seismic events.

The questionnaire which was prepared by the staff of **the Ghana Atomic Energy Commission (GAEC)** had two sections. One section had to do with the socioeconomic background of the people and the other part dealt with the perceptions, experiences and adaptation strategies of the people to earthquakes.

P. Amponsah (✉) · I. Opoku-Ntim
National Nuclear Research Institute, Ghana Atomic Energy Commission, Accra, Ghana

M. Meghraoui et al. (eds.), *Advances in Geophysics, Tectonics and Petroleum Geosciences*,
Advances in Science, Technology & Innovation, https://doi.org/10.1007/978-3-030-73026-0_12

Table 1 Earthquakes recorded in Ghana from 1615 to 2019

Magnitude/Richter scale	Number of earthquakes
Less than or equal to 2	47
2.1–3.0	117
3.1–4.0	49
4.1–5.0	66
5.1–6.0	4
Greater than 6.0	2
Total	285

Source Amponsah et al. 2012; Doku 2013; CTBTO Sel 1

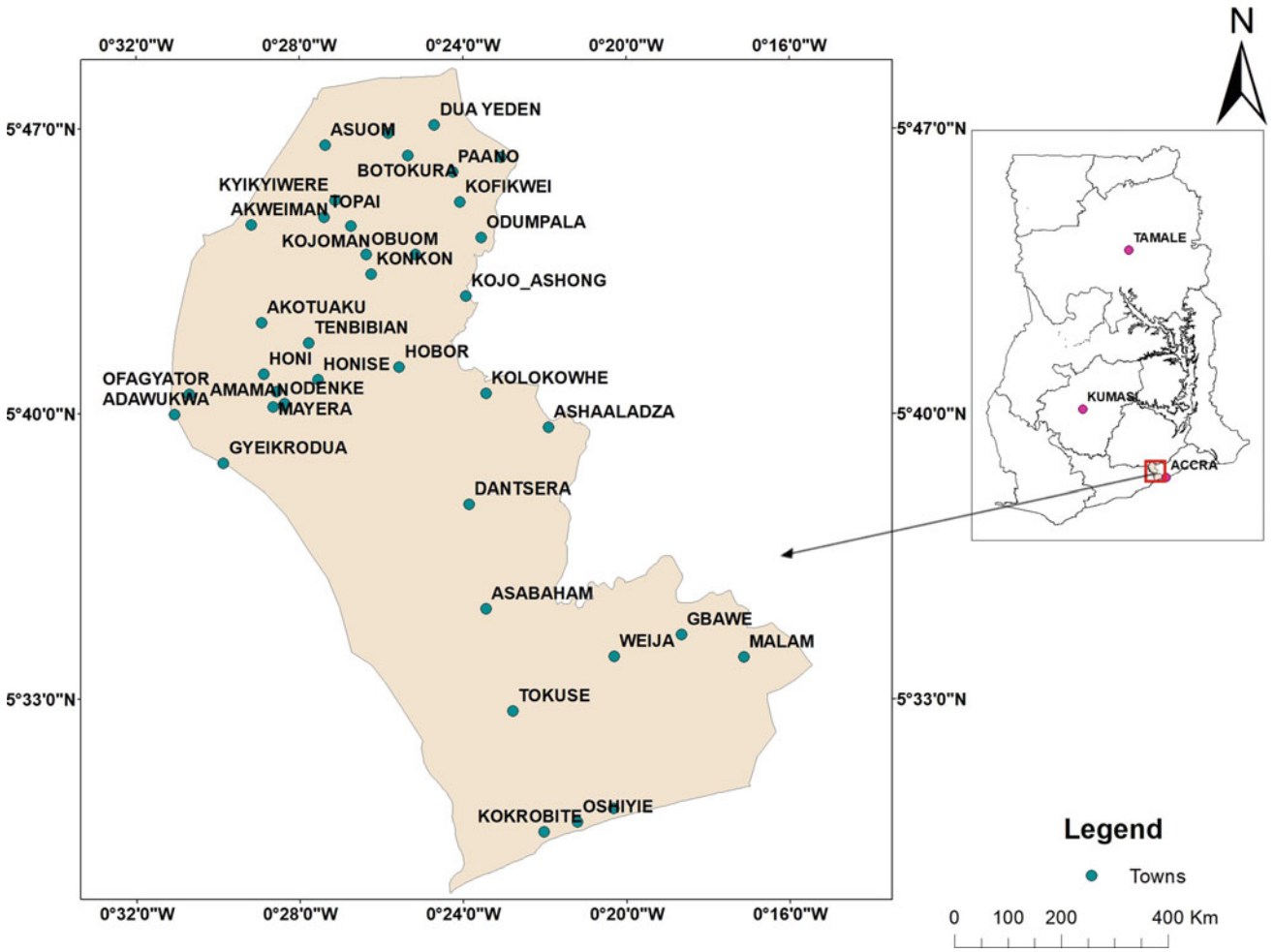

Fig. 1 Map of the study area

2 Materials and Methods

Questionnaires were administered by staff of GAEC and NADMO. Residents who could not read were assisted. The elite completed the questionnaires themselves. Three days were allotted for the interview as indicated in Table 2 at Awutu Senya East and Weija-Gbawe Municipalities, respectively.

A total of two hundred and twenty-one (221) residents in the area were interviewed. There were divergent views from the inhabitants on their perception, experiences and adaptation strategies to earth tremors in the area.

Table 2 Earthquake occurrence and observation survey in the Awutu Senya East and Weija-Gbawe Municipalities

	Awutu Senya East Municipality	Weija-Gbawe Municipality
Day 1	Introductory visit to the National Disaster Management Organization (NADMO) office Planning of fieldwork, locations and schedule of personnel to administer questionnaire	Introductory visit to the National Disaster Management Organization (NADMO) office Planning of fieldwork, locations and schedule of field personnel
Day 2	Training of NADMO staff on seismic events and questionnaire administration	Training of NADMO staff on seismic events and questionnaire administration
Day 3	Administration of questionnaires and interview session	Administration of questionnaires and interview session
	Ninety-seven questionnaires were administered	One hundred and twenty-four questionnaires were administered

Through the briefing and interview sessions, the realization was that:

- Most of the people were aware that they live in an earthquake prone area but had no measures put in place to mitigate it in any form.
- The agencies and institutions responsible for permitting and regulating building activities in the area do not emphasize the need for geophysical investigation of their sites before development.
- There is the need to involve the chiefs and opinion leaders, real estate developers and the people themselves in the mitigation process since they are the custodians of the land.

3 Discussions

During the interview session, it was observed that most of the inhabitants are aware that the area is prone to earthquakes but have no other place to move to, so they have decided to live with the menace. Others were ignorant and felt it was a common occurrence, so it did not bother them much. There is, therefore, the need for the responsible government agencies to conduct geological and geophysical investigation on every land acquired before releasing them to developers. There should be intensive and consistent public awareness creation on the need for geophysical investigation on all sites before development.

4 Conclusions

It is important to recognize that the southern part of Ghana has the highest concentration of strategic assets and human population. Therefore, strategies must be devised to minimize the risks posed by some of these natural disasters that can strike the area. Seismologists have warned that the continuous earth tremors should not be taken for granted. As a precautionary measure, it is recommended that all residents of the earthquake prone areas should seek professional advice for a seismic and geotechnical evaluation of the sites where their structures are located in order to determine the hazards and possible solutions.

The Geological Survey Authority is mandated to monitor seismic activities in the country and advice accordingly. This is supported by other agencies such as the National Data Centre of the Ghana Atomic Energy Commission.

For Ghana to become resilient to natural, manmade and technological hazards, we must be proactive in our planning and development strategies.

References

Akoto, M.A., Anum, S.A.: Monitoring recent microseismic activity in Ghana. Tectonophysics **209**(1–4), 43–46 (1992)

Amponsah, P.E.: Seismic activity in relation to fault systems in southern Ghana. J. Afr. Earth Sci. **35**, 227–234 (2002)

Amponsah, P.E.: Seismic activity in Ghana: past, present and future. Ann. Geophys. **47**(2/3), 239–543 (2004)

Amponsah, P.E., Leydecker, G., Muff, R.: Earthquake Catalogue of Ghana for the Time Period 1615–2003 with Special Reference to the Tectono-Structural Evolution of South-East Ghana. J. Afr. Earth Sci. **75**, 1–13 (2012)

Bacon, M., Banson, J.K.A.: Recent Seismicity of Southeastern Ghana. Earth Planet. Sci. Lett. **44**, 43–46 (1979)

Bondessen, E., Schmidt, A.F.J.: Holocene tectonic activity in West Africa dated by archaeological methods: Discussion. Geol. Soc. Am. Bull. **83**, 1193–1196 (1972)

Doku, M.R.S.: Seismological and Geological investigation for Earthquake hazard in the Greater Accra Metropolitan Area. MPhil theses, University of Ghana, Legon (2013)

Sykes, R.L.: Intraplate seismicity, reactivation of pre-existing zones of weakness, alkaline magmatism and other tectonism postdating continental fragmentation. Rev. Geophys. Space Phys. **16**(4), 621–682 (1978)

Toward an African Seismological Data Center

Mohamed Elgabry, Islam Hamama, Mahmoud Salam, Adel Sami, Asem Salama, and Mohamed Maklad and AfSC executive Committee

Abstract

In recent years, Africa was hit by several severe earthquakes. Although the seismic monitoring in Africa has been evolving during the last decade, there has been no joint effort to collect, archive, and process the data, in order to publish earthquake bulletins at the continental or world level. Scientific projects (e.g., IGCP-601–659) dedicated to the seismotectonics and seismic hazard assessment of Africa allowed for the compilation of a database at the continental and regional levels. These research projects have exposed conspicuous aspects of the seismic activity, but also uncovered a severe deficiency of seismic and geophysical equipment and limited capacity throughout the continent. The newly established African Seismological Commission (established in 2014; https://www.afsc-web.org.za/) has highlighted the importance of having an African Seismological Data Center (Meghraoui et al., in Episodes 39:9, 2016) in its first General Assembly in Luxor, Egypt, and the second one in Hoceima Morocco. Many scientific, logistic, and financial challenges face this goal. An experiment has been initiated to collect and process data from seismological stations with open access located within Africa and to provide a platform for supplying a generic seismological bulletin using a SeisComp3-based system. The system is a real-time processing server at the Egyptian National Data Center. This system is currently under alpha testing utilizing internal auditing. The second stage will be in the first quarter of 2020 through beta testing after selecting a closed group to test the system's efficiency and stability to be ready for the validation phase and then commissioning.

Keywords

Africa • Seismological data center • Earthquakes • AFSC

1 Introduction

Earthquakes are natural phenomena which can trigger severe disasters. Losses and causalities from earthquakes have been increasing since the beginning of the 20th century due to risk-blind development which has affected many physical, social, economical, and environmental aspects which in turn increase the susceptibility to the impacts of hazards such as population growth, unplanned urbanization, underdevelopment/poverty, and climate change. These cascading factors are called vulnerability, and they could result in increased frequency, complexity, and severity of disasters. Global economic statistics (Fig. 1) for natural disasters show a trend for a decrease in the economic losses in the last decade. This decrease may be related to the ongoing efforts of integrating and mainstreaming risk reduction into development policies and processes on the heels of the Sendai Framework for Disaster Risk Reduction and the previous Hyogo Framework for Action 2005–2015. Furthermore, the causality rates are decreasing since the 1920s of 20th century.

AFSC executive Committee: Mustapha Meghraoui, Paulina Amponsah, Georges Mavonga Tuluka, Michelle Grobbelaar, and Atalay Ayele.

M. Elgabry (✉) · I. Hamama · M. Salam · A. Sami · A. Salama · M. Maklad
National Research Institute of Astronomy and Geophysics, Helwan, Cairo, 11421, Egypt
e-mail: elgabry@nriag.sci.eg

M. Meghraoui et al. (eds.), *Advances in Geophysics, Tectonics and Petroleum Geosciences*, Advances in Science, Technology & Innovation, https://doi.org/10.1007/978-3-030-73026-0_13

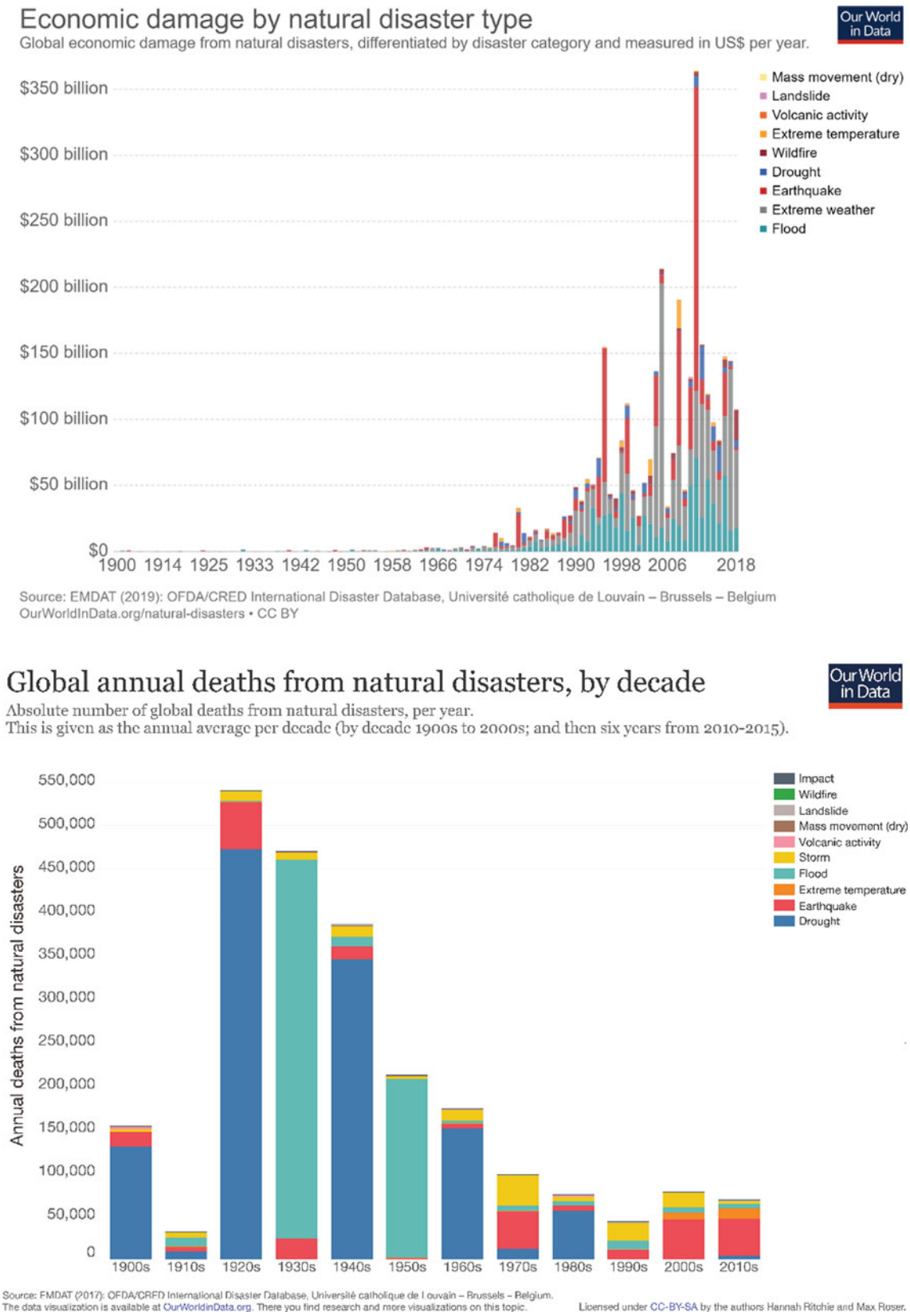

Fig. 1 Economic damage by natural disaster type, EMDAT 2019

2 Methodology

Although the casualties from disasters triggered by natural hazards globally decreased, African countries still claim the majority of deaths due to environmental causes. In recent years, Africa was vulnerable to several severe earthquakes. The rapid urbanization, development of critical engineering works and lifelines, such as dams, oil facilities, industrialization of cities with modern types of buildings, and the concentration of populations living or settling in hazardous areas are matters of growing concern. Indeed, the recent social and economic development exposed to the earthquake

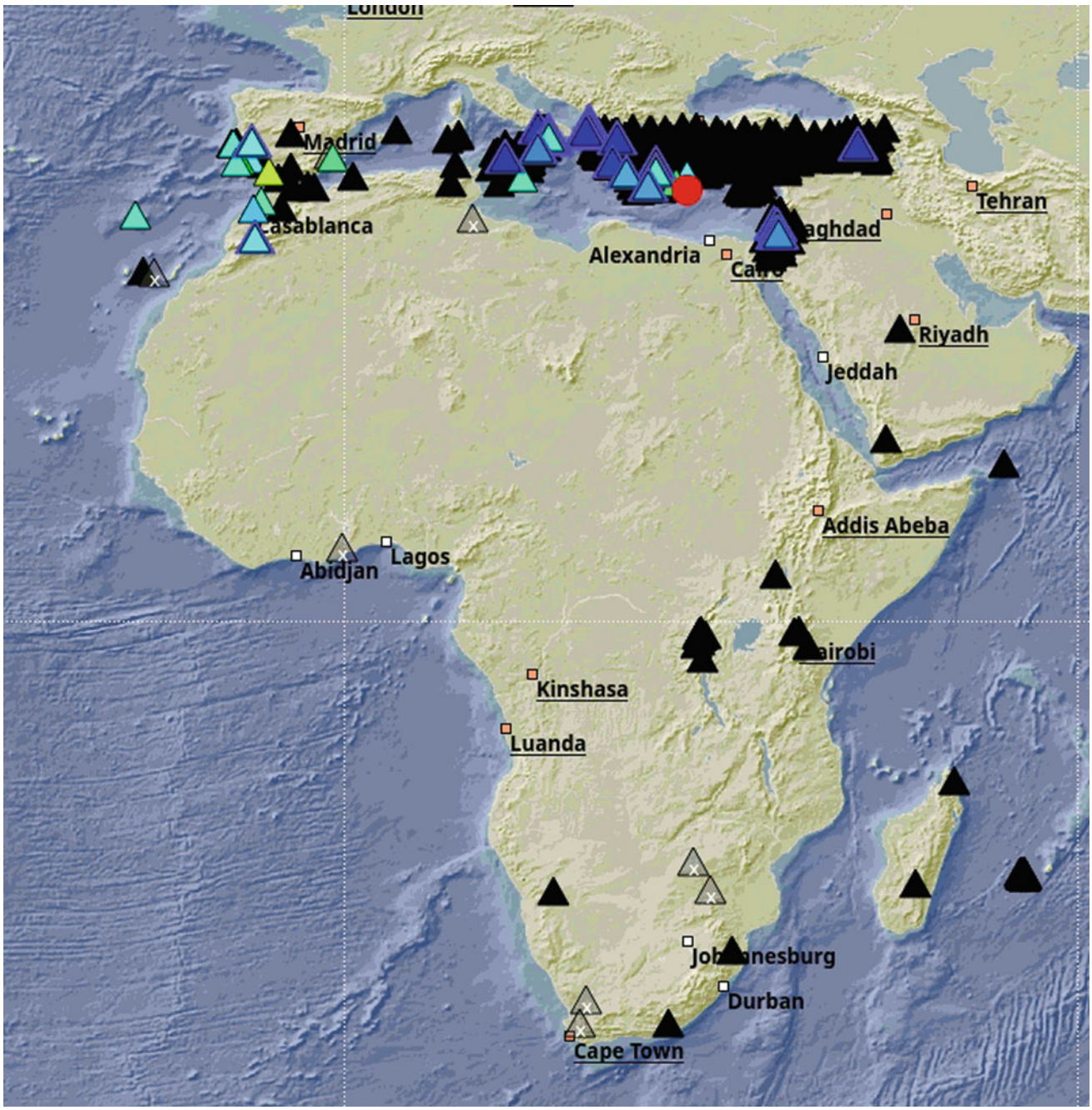

Fig. 2 Location map showing stations streaming online data to the prototype system

hazards implies heavier losses of life and considerable cost of economic damage. The environmental concerns and an increased official and public awareness of earthquake hazards have, since the 80s, led to a rapid rise of interest in seismicity and seismic hazard and risk evaluations in Africa. On the other hand, there has been no joint effort to collect, process, and publish earthquake bulletins at the continental level. Scientific projects (e.g., IGCP-601–659) dedicated to the seismotectonics and seismic hazard assessment of Africa allowed for the compilation of a database at the continental and regional levels. The research projects have exposed conspicuous aspects of the seismic activity, but also uncovered a severe deficiency of seismic and geophysical equipment and limited human capacity throughout the continent.

In order to meet the demands to have an African Seismological Data Center, an experiment has been initiated to collect, process data from seismological stations with open access located within Africa and to provide a platform for supplying a generic seismological bulletin using a SeisComp3-based system. The system is a real-time processing server at the Egyptian National Data Center at NRIAG. The data is received through a seed-link connection to open access data servers of GFZ Geofone and IRIS (Fig. 2). Automatic algorithms analyze the data and automatically detect arrival. When several arrivals are coincident, they are associated to declare an event. This system is currently under alpha testing utilizing internal auditing.

3 Discussion

Several stations were successfully connected to a data server in the Egyptian National Data Center with data flowing in real time. The system is working automatically to detect arrivals and associate events. The system is under alpha testing. This system would accumulate data for two months of operations that will provide opportunity to optimize the system. After optimization, the second system will be ready for the second stage of testing in the first quarter of 2020 through beta testing after selecting a closed group to test the system's efficiency and stability to be ready for the validation phase and then commissioning. All results and documentation will be presented during the African Seismological Commission General Assembly in June 2020.

References

EMDAT: Number of reported natural disasters. Retrieved from International Disaster Database, Université catholique de Louvain, Brussels, Belgium (2019). http://www.emdat.be/

Global Platform for Disaster Risk Reduction, Mexico. (2017, May 22–26). Retrieved from unisdr: https://www.unisdr.org/conferences/2017/globalplatform/en

Meghraoui, M., Amponsah, P., Ayadi, A., Ayele, A., Ateba, B., Bensuleman, A., Delvaux, D., El Gabry, M., Fernandes, R.-M., Midzi, V., Roos, M., Timoulali, Y.: The Seismotectonic Map of Africa. Episodes **39**(1), 9 (2016)

An Overview of the Seismic Hazard in Sudan

Nada El Tahir and Vunganai Midzi

Abstract

In this paper, we present the probabilistic seismic hazard analysis for Sudan. The seismic database used consists of a regional catalog compiled from the earthquake catalog for East and Southern Africa, NOAA, ISC and PDE. The catalog was checked for completeness with respect to time, and it was homogenized to a surface wave magnitude (Ms). Areal seismic zones were selected based on present day seismotectonic knowledge. The hazard calculations are done for rock sites, and a new ground motion predictive relation, SEA96, has been applied. In the results, regional hazard maps for a 50-year period, 100-year return periods and 10% probability of excess have been presented. High seismic hazard is found in Southern Sudan and slightly less values in the central part of the country. Furthermore, induced seismicity in some different parts of Sudan has been evaluated.

Keywords

Tectonic • Sudan • Seismicity • Hazard

1 Introduction

Sudan is largely a stable intra-plate region characterized by relatively low levels of seismic activity. However, earthquakes whose effects caused major damage and even deaths, include, the Suakin graben earthquake (Ms = 5.8) of May 12, 1938, located on the western margin of the Red Sea, the Jebel Dumbier event located in Central Kordofan (Ms = 5.6), which occurred on the 9th of October 1966 and the Khartoum event (Ms = 5.5) of the 1st of August 1993 (Fig. 1). The later earthquake is of special interest because it occurred away from the unstable belt of the East African Rift system, and the source is not fully understood. In addition, the largest of these earthquakes was probably the largest earthquake in Africa in the twentieth century. It occurred on the 20th of May 1990 (Ms = 7.1–7.4,), near Juba in the Southern Sudan Republic.

There are several rifts and fault lines that are potential places for strain energy release, therefore, earthquakes. Figure 2 shows the major rifts and corresponding faults in Sudan which are the Central African Rift system, East African Rift system, Southern Rift system, White Nile Rift system, Blue Nile Rift system and Atbara Rift system. It is not known whether these basins are the product of crustal extensions and attenuations that accompanied the opening of the South Atlantic during the Neocomian to early Aptian (Burke and Dewey 1974) and (Guiraud and Maurin 1992) or controlled by older pre-existing zones of weakness from the Pan-African orogeny or later, and rejuvenated during the cretaceous times (Klitzsch 1986). However, it is noteworthy that Africa has experienced major episodes of rifting since the Proterozoic through the Mesozoic to the tertiary and quaternary times.

2 Method

The seismic database used consists of a regional catalog compiled from the earthquake catalog for East and Southern Africa, NOAA, ISC and PDE. The catalog was checked for completeness with respect to time, and it was homogenized to a surface wave magnitude (Ms).

Areal seismic zones were selected based on present day seismotectonic knowledge. The hazard calculations are done for rock sites. Since there are no ground motion prediction models for Sudan, we selected the SEA96 model, which was derived for extensional tectonic regimes similar to Sudan.

N. El Tahir (✉)
University of Khartoum, Khartoum, Sudan

V. Midzi
Council for Geoscience, Pretoria, South Africa

M. Meghraoui et al. (eds.), *Advances in Geophysics, Tectonics and Petroleum Geosciences*,
Advances in Science, Technology & Innovation, https://doi.org/10.1007/978-3-030-73026-0_14

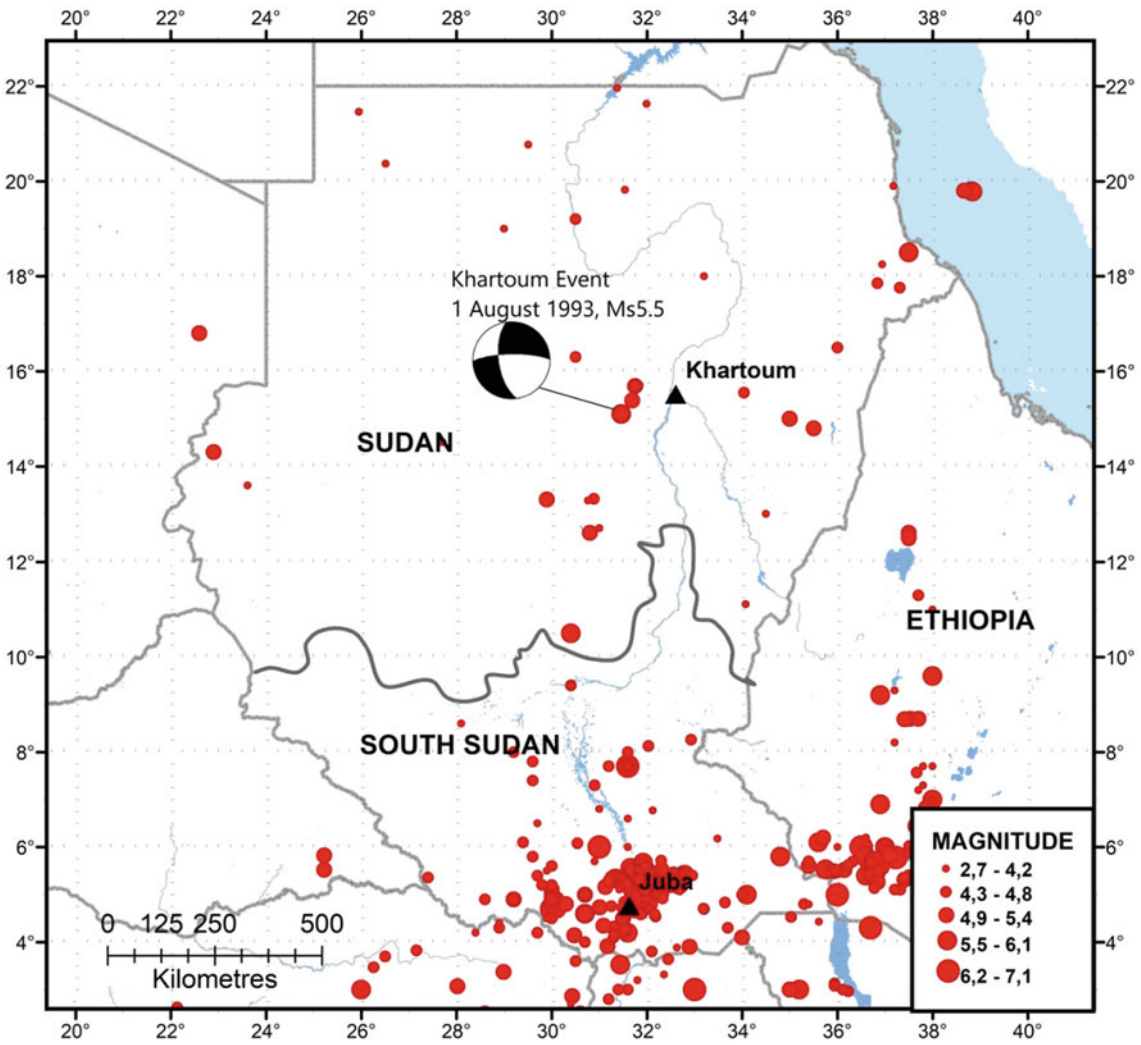

Fig. 1 Significant earthquakes in Sudan and the focal mechanism of the Khartoum

3 Results

Hazard maps for return periods 50 years, 100 years and 10% probability of excess in 50 years (475) were obtained. The unit of ground motion is "g." For all return periods, the highest peak of ground acceleration (PGA) is located in the south of Sudan Republic along the Aswa shear zone. A maximum ground motion value of about 0.2 g was observed near the city of Juba for the hazard map for 10% probability of excess in 50 years and about 0.14 g for the return period of 100 years (Fig. 3).

4 Discussion and Conclusion

Based on the results obtained here, the southern part of Sudan is the most susceptible to earthquake effects and preventive measures are necessary. Furthermore, central and northern parts of Sudan are quite interesting, since many earthquakes have been recorded after the establishment of the Sudanese Seismic Network (SSN) in 2001 (Alhassan et al. 2007). These events will help in determining the earthquake generating faults in the region, thus improving the source zones used in the future seismic hazard studies.

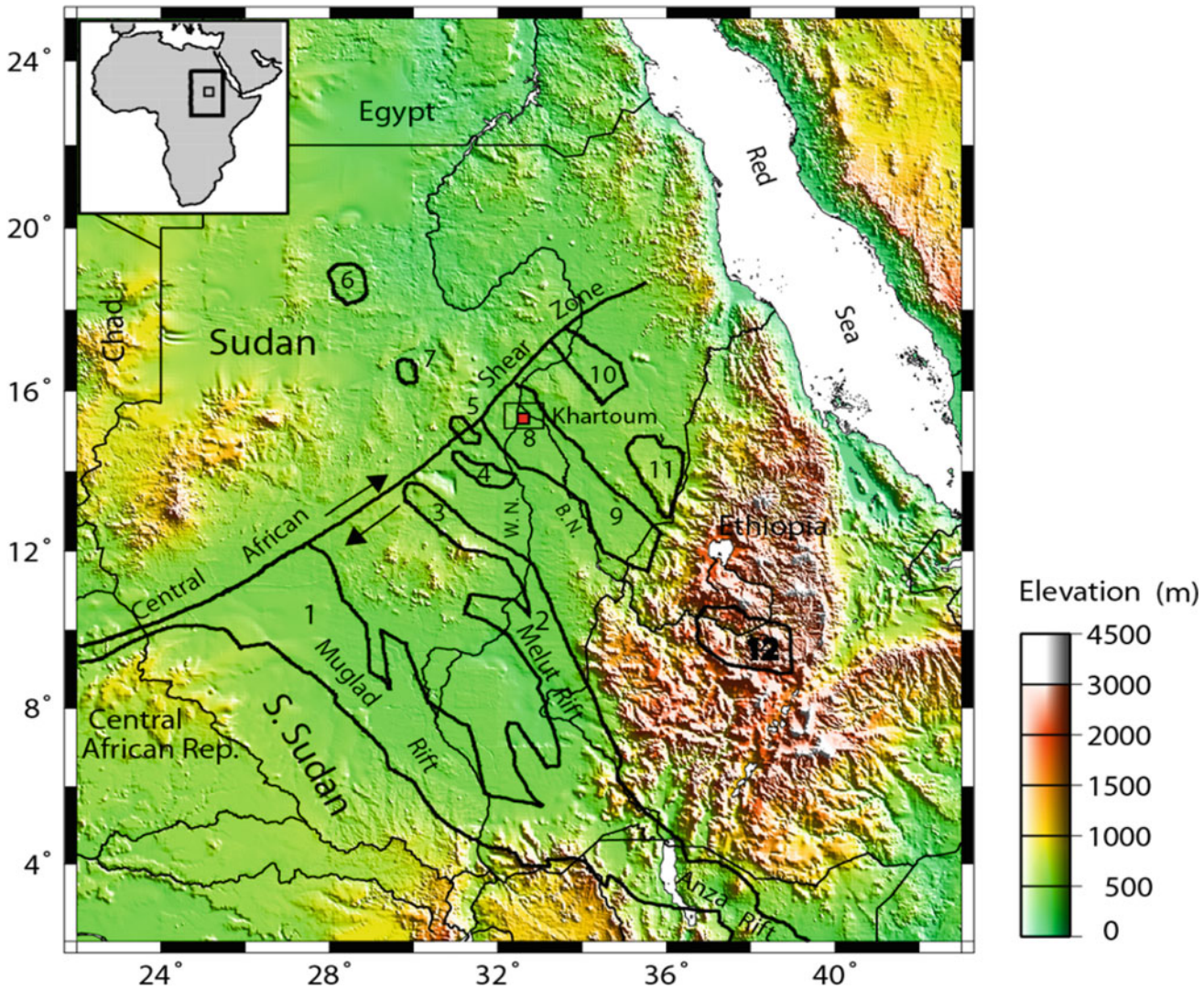

Fig. 2 Topographic map showing the locations of Mesozoic rift basins of Central Sudan and the Central African shear zone

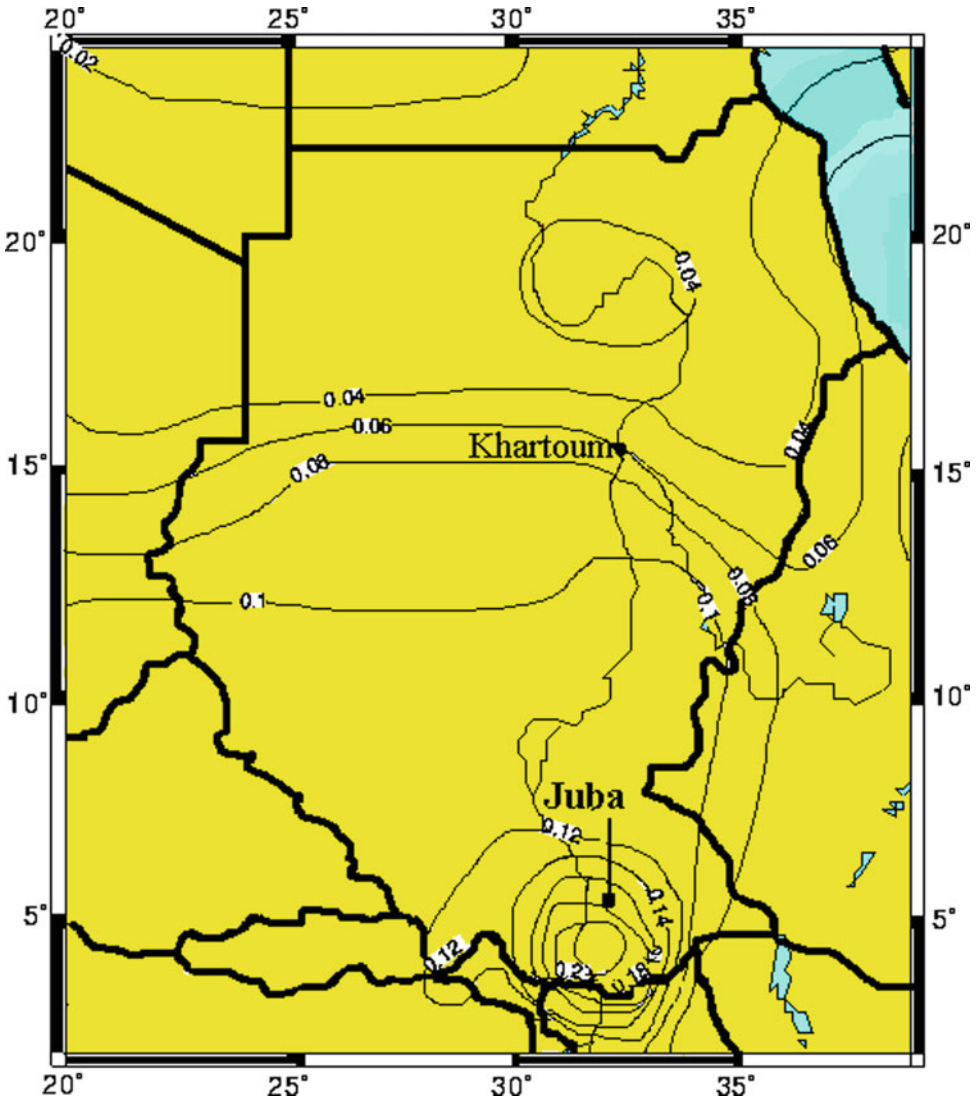

Fig. 3 Contour map showing peak ground acceleration in g, for 10% probability of excess in 50 years, respectively

Recently, induced geo-hazard is of a great importance in Sudan. For example, Marawi Dam was built in 2009. The reservoir is located not far from tectonically active areas of the Red Sea Rift and the Central African shear zone. However, low to moderate seismic activity has been recorded in the northern part of Sudan as a result of the reservoir's load on the ground. In addition, mining and oil extraction locations have created an imbalance in the tectonic setting of these areas. Thus, identifying the geo-hazard map for Sudan is widely of a significant concern.

References

Alhassan, A.I., Belail, A.E., Elbashir, H.S.H., Mohamed, I.A.R., Mohammed, M.B., Eltahir, N.B., Havskov, J.: The Sudanese seismic network. Seismol. Res. Lett. **78**(5), 498–501 (2007)

Burke, K., Dewey, J.F.: Two plates in Africa during the Cretaceous? Nature **249**, 313–316 (1974)

Guiraud, R., Maurin, J.C.: Early Cretaceous rifts of western and central Africa. Tectonophysics **213**, 153–168 (1992)

Klitzsch, E.: Plate tectonic and cratonal geology in Northeast Africa (Egypt/Sudan). Geol. Rundsch **3**, 755–768 (1986)

Seismic Hazard Assessment in Kenya and Its Vicinity

Sophie J. Kipkwony, Justus. O. Barongo, Edwin. W. Dindi, Josphat. K. Mulwa, and Georges. T. Mavonga

Abstract

According to the seismicity and the historical records of the previous considerably large magnitude earthquakes, Kenya can be regarded as a country of low to medium seismicity. Tectonically, the country is, however, cut longitudinally by the seismically active East Africa Rift. The most significant earthquakes have occurred along the rift and adjoining areas causing minor to major damages in the region. Based on seismicity records and the seismotectonics of the region, the current work presents a probabilistic assessment of seismic hazard in Kenya with the aim of bringing into focus the cities/towns that are more prone to seismic hazard due to ground shaking occasioned by earthquakes along the region. The potential seismic source zones are identified, and the resultant seismic ground motion parameters are evaluated. An appropriate ground motion prediction attenuation equation is adopted. The seismic hazard has been computed using the probabilistic approach under "Openquake Version 2.0.1" program. The results show that the seismic hazard levels in PGA range from 0.32 to 0.02 g and 0.176 to 0.016 g for the 2% and 10% probability of exceedance in 50 years, respectively. Cities/towns located in south-western regions are more vulnerable to high seismic hazards than the cities located in the north-eastern part of the study area. The results from this research have shown that the high hazard levels are associated with very active tectonic activity within the region.

Keywords

Seismicity • East Africa Rift • Seismic Hazard • Seismic source • Ground motion prediction equation • Probabilistic • OpenQuake • PGA

1 Introduction

According to the seismicity and historical records of the previous considerably large magnitude earthquakes, Kenya can be viewed as a low to medium seismicity country. Tectonically, the country is cut longitudinally by the seismically active East Africa Rift. The most significant earthquakes, for example the Mw7.1 Subukia earthquake in 1928, have occurred along the rift causing minor to major damages in the region. Based on seismicity records and seismotectonics of the region, the current work presents a probabilistic assessment of seismic hazard in Kenya with the aim of bringing into focus the cities/towns that are more prone to seismic hazard due to the ground shakings occasioned by earthquakes along the region.

2 Material and Method

The earthquake catalogue used for this study includes both historical and instrumental data compiled from various sources to cover the area of interest bounded by latitudes 5°S and 5°N and longitudes 32°–42°E, for the period ranging from 1900 to 2015. The main sources include data from the University of Nairobi Seismic Network, International Seismological Centre (ISC), Incorporated Research Institutions for Seismology (IRIS) and United States Geological Survey (USGS).

Probabilistic seismic hazard assessment developped by Cornel (1968), later revised by McGuire (1976) and utilized by many subsequent analysts, was used in this study. This

S. J. Kipkwony (✉) · Justus. O. Barongo · Edwin. W. Dindi · Josphat. K. Mulwa
Department of Geology, University of Nairobi, Nairobi, Kenya

Georges.T. Mavonga
Goma Volcano Observatory, Goma, Democratic Republic of Congo

M. Meghraoui et al. (eds.), *Advances in Geophysics, Tectonics and Petroleum Geosciences*,
Advances in Science, Technology & Innovation, https://doi.org/10.1007/978-3-030-73026-0_15

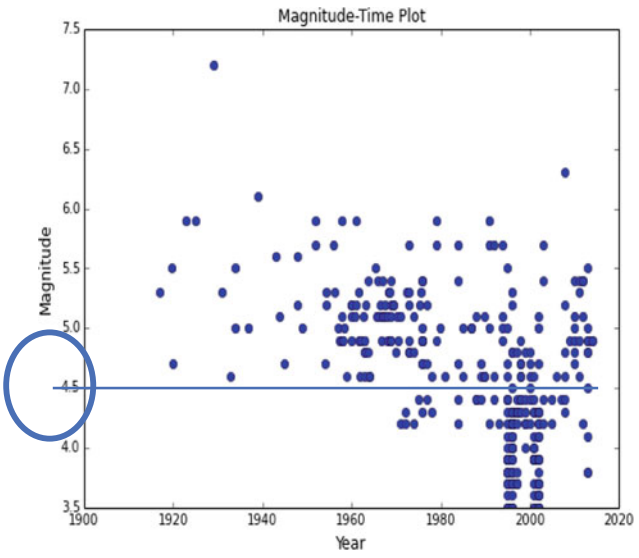

Fig. 1 Magnitude completeness of the study area

method is a mathematical approach to performing seismic hazard calculations in terms of ground motion (e.g., PGA). A Poisson model of earthquake occurrence was adopted, which assumes that events are independent. Therefore, aftershocks, foreshocks and earthquake swarms were removed from the catalogue of the 1554 events, leaving a sub-catalogue of 874 events. Declustering was performed using Gardner and Knopoff (1974) in OpenQuake Program Version 2.0.1. Magnitude completeness was found to be 4.5 (Fig. 1). The seismic source zone was defined based on seismic data as expression of tectonic activity of East Africa rift, Aswa-Nyangia fault and Anza rift shear zone, and geology. Source parameters (b-value in Eq. 1 by Gutenberg and Richter (1954), activity rate, the $M_{\min}$ and $M_{\max}$) were computed using the MATLAB program "AUE" developed by Kijko and Smit (2012).

$$Log(N)M = a - bM \tag{1}$$

The ground motion prediction equation of active shallow crust by Boore and Atkinson (2008) was adopted from global database. The seismic hazard analysis for Kenya was computed using the OpenQuake software Version 2.0.1. The input parameters used for hazard computation are listed in Table 1.

3 Results and Discussion

The obtained results show considerable high PGA values along the rift and the highest observed value is in the southern region, near Kenya-Tanzania border (Figs. 2 and 3). These high PGA values were found to be 0.32 g and 0.176 g with 2475 years and 475 years return period, respectively. The elevated hazard levels can be associated with many active faults/swarm activities (Ibs-von Seht et al. 2001 and Kuria 2011), active magmatic processes related to the rifting (Ritter and Kaspar 1997), located near the active main rift (Ambraseys 1928) and some may be more or less related to the reactivated rift zones of Aswa-Nyangia fault and Anza rift.

4 Conclusion

Results of a probabilistic seismic hazard assessment carried out for the Kenya region are presented in terms of ground motion (PGA). The uncertainties in this study were not considered. The results show that the seismic hazard level is moderate with expected bedrock horizontal PGA in the range 0.176–0.016 g for 474 years return period and 0.32–0.02 g for 2475 years return period with slightly higher values in the cities in proximity to the seismically active rift. These findings generally agree with recent seismic hazard studies carried out for Eastern and Southern Africa (Midzi et al. 1999) and East Africa (Poggi et al. 2017). Seismic data are still a big challenge as it is evident from this study. So, efforts should be put in place to improve seismic coverage, especially that of the vulnerable parts of the country. With more data, further study's results can be improved and it would be more reliable.

Table 1 Input parameters for the area source zones

Source Id	Evens	a-value	b-value	$M_{\min}$	$M_{\max}$	Mmaxob	Activity rate (λ)	Beta-value (β)
1	29	3.5	0.93	4.5	7.2	7.7	0.223	2.13
2	39	3.2	0.94	4.5	5.9	6.4	0.115	2.17
3	100	3.3	0.74	4.5	6.3	6.8	0.945	1.71
4	19	3.6	0.94	4.5	5.9	6.4	0.235	2.17
5	52	3.9	0.95	4.5	6.1	6.6	0.518	2.18
6	8	2.9	0.93	4.5	4.6	5.1	0.062	2.13

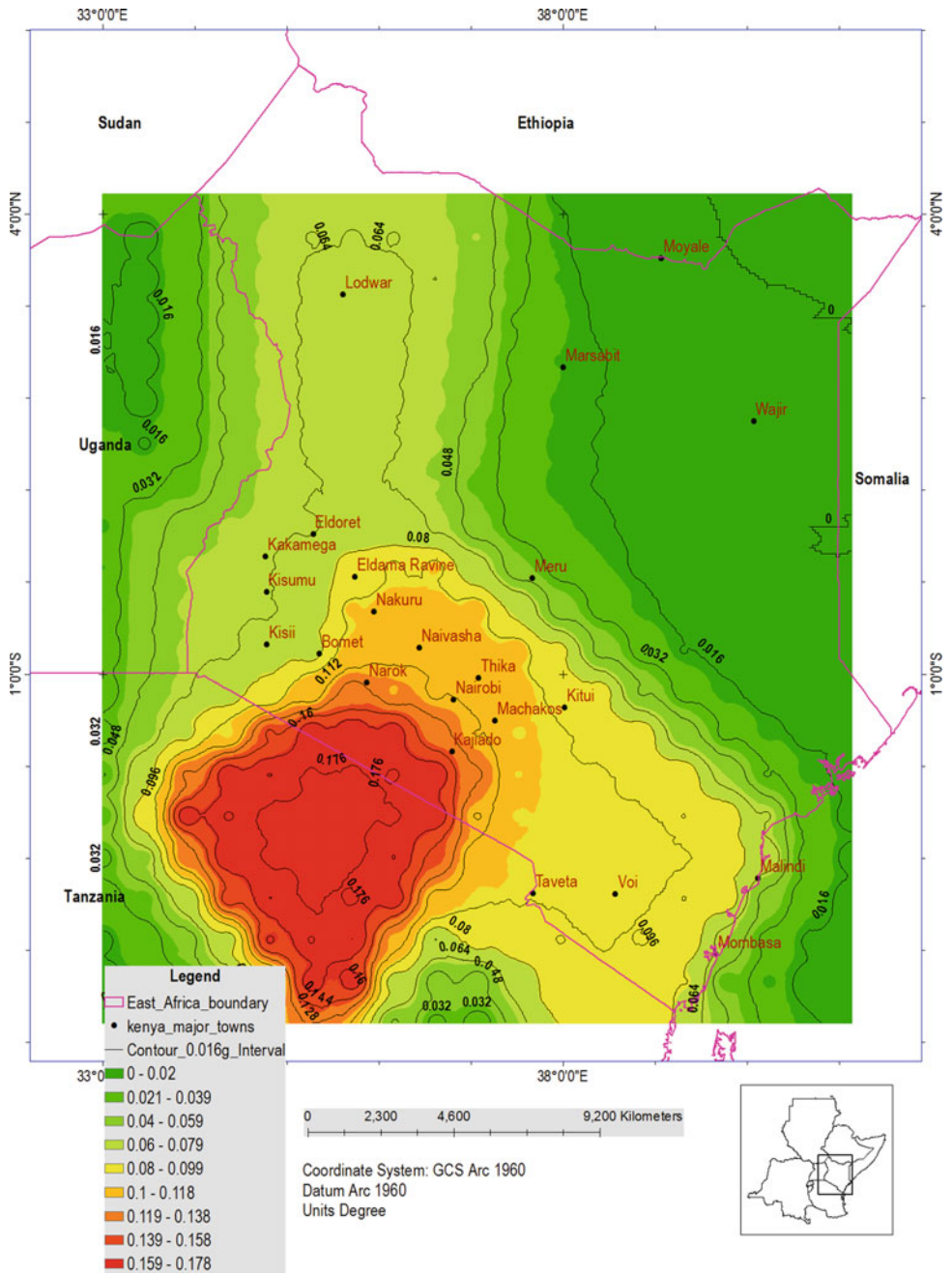

Fig. 2 The distribution of mean PGA values (in unit g) in Kenya and major cities/towns computed at 10% chance of exceedance in 50 years

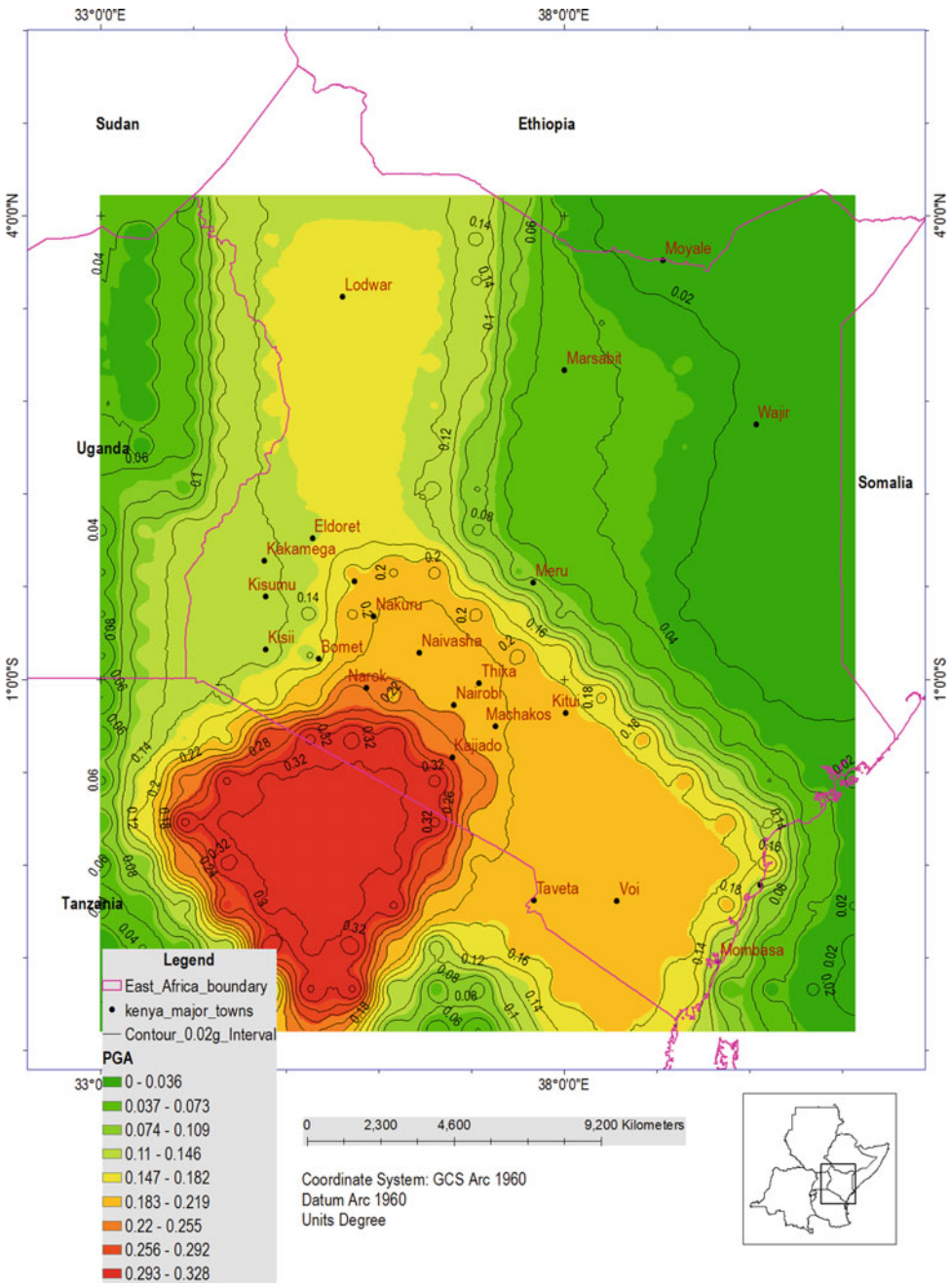

Fig. 3 The distribution of mean PGA values (in unit g) in Kenya and major cities/towns computed at 2% chance of exceedance in 50 years

References

Ambraseys, N.: Earthquake hazard in the Kenya Rift: the Subukia earthquake 1928. Dep. Civ. Eng. Coll. Sci. Technol. Med. Lond. SW72BU UK **105**, 243–269 (1991)

Boore, D.M., Atkinson, G.M.: Ground-Motion Prediction Equations for the average horizontal component of PGA and 5%—damped PSA at spectral period between 0.01s and 10s. Earthq. Spectra **24**, 99–134 (2008)

Cornel: Engineering seismic risk analysis. Bull. Seisol. Soc. Am. **58**, 1583–1606 (1968)

Gardner, J., Knopoff, L.: Is the sequence of earthquake in Southern California, with aftershocks removed, Poissonian. Bull. Seismol. Soc. Am. **64**, 1363–1367 (1974)

Gutenberg, B., Richter, C.F.: Seismicity of the Earth and related phenomena, 2nd edn. University Press, Princeton U.S.A (1954)

Ibs-von Seht, M., Blumenstein, S., Wagner, R., Hollnack, D., Wohlenberg, J.: Seismicity, seismotectonics and crustal structure of the southern Kenya Rift—new data from the Lake Magadi area. Geophys. J. Int. **146**, 439–453 (2001)

Kijko, A., Smit, A.: Extension of the Aki-Utsu b-Value estimator for incomplete catalogs. Bull. Seism. Soc. Am. **102**, 1183–1287 (2012)

Kuria, Z.: Seismotectonics of active faults: Magadi fault system, southern Kenya rift. University of Twente (2011)

McGuire, R.K.: Evaluation of Earthquake risk to site. U.S. GeolSuev open-file, pp. 76–77 (1976)

Midzi, V., Hlatywayo, D.J., Chapola, L.S., Kebede, F., Atakan, K., Lombe, D.K., Turyomurugyendo, G., Tugume, F.A.: Seismic hazard assessment in Eastern and Southern Africa. Annli di Geofisica **42**(6) (1999)

Poggi, V., Durrheim, R., Tuluka, G.M., Weatherill, G., Gee, R., Pagani, M., Nyblade, A., Delvaux, D.: Assessing seismic hazard of the East African Rift: a pilot study from GEM and Africa Array. Bull. Earthq. Eng. (2017). https://doi.org/10.1007/s10518-017-0152-4

Ritter, R.R., Kaspar, T.: A tomography study of the Chyulu Hills, Kenya. Tectonophysics **278**, 146–169 (1997)

Probabilistic Seismic Hazard Assessment for the Main Cities Along the Continental Section of the Cameroon Volcanic Line

Delair Etoundi Ndibi, Ferdinand Eddy Mbossi, Bekoa Ateba, and Pauline Nguet Wokwenmendam

Abstract

The Cameroon Volcanic Line (CVL) is located in the Gulf of Guinea. It is an alignment of volcanic islands and continental volcanoes that extend over a distance of nearly 1600 km. One of the hypotheses of its origin suggests that volcanism was guided by faults that are covered by lava flows, making it difficult to identify them. Moderate seismicity is associated with CVL, especially at the level of Mt Cameroon, an active volcano where damage has often been observed on buildings due to the earthquakes. To date, no studies have been carried out to evaluate the seismic risks in this area. This is the main reason behind conducting the current study using a probabilistic approach. Geology, tectonics geophysics and local seismicity were used to map three seismic source zones. The recurrence model is that of Gutenberg and Richter; and choosing ground motion prediction equations corresponding to an active continental crust, we were able to calculate the occurrence probability if the intensity of the ground motion is greater than a precise value for a given period. So for a return period of 475 years, we calculated the PGA for eleven (11) cities, spreading along the CVL. The results show that Buea, located at the foot of Mt. Cameroon, has a PGA of 10% g. This value decreases as one moves away from it, such that at Bamenda-Bafoussamabout 200 km northeast of Buea, the PGA is of the order of 5% g.

Keywords

Cameroon Volcanic Line • Earthquakes • Probabilistic seismic hazard assessment • Ground motion prediction equation

1 Introduction

The CVL in West Africa is a chain of volcanic islands of the Atlantic Ocean, and Cenozoic to Quaternary intraplate volcanic massifs that extend over a distance of approximately 1600 km (Fitton and Dunlop 1985). Volcanism is active along the CVL from Eocene to the Present on Mt Cameroon (Déruelle et al. 2007; Njonfang et al. 2011). Several hypotheses were suggested on the origin of the CVL, including the one that proposes that the alignment of volcanoes could be guided by the presence of faults masked by lava flows (Moreau et al. 1987).

Fertile volcanic lands attract farmers, such that the Highlands Western region has the highest population density. The recent seismicity of the CVL has been studied by several authors which include Ambeh et al. (1989), Ateba and Ntepe (1997), Eloumala et al. (2014), and Tabod et al. (1992). The studies concluded that seismicity is distributed along the CVL with Mount Cameroon as the most active center. Outside the crisis period (seismic swarm or volcanic eruption), the monthly frequency of recorded earthquakes varies between 20 and 30 events in Mt Cameroon region. Building damage has been recorded during the Mt Cameron 1999 eruption. Despite the risk, people build houses without any respect to the building code. This is why, for the first time, seismic hazard assessment is performed on the main cities along the CVL, to assist in mitigation efforts.

D. E. Ndibi · F. E. Mbossi · B. Ateba (✉) · P. N. Wokwenmendam
Institute of Geological and Mining Research (IRGM), P.O Box 4110 Yaounde, Cameroon

D. E. Ndibi · F. E. Mbossi
Department of Physics, Faculty of Science, University of Yaoundé 1, P.O Box 812 Yaoundé, Cameroon

M. Meghraoui et al. (eds.), *Advances in Geophysics, Tectonics and Petroleum Geosciences*, Advances in Science, Technology & Innovation, https://doi.org/10.1007/978-3-030-73026-0_16

2 Data and Methods

Mainly two methods are used to assess seismic hazard: the deterministic approach and the probabilistic approach. The probabilistic seismic hazard assessment (PSHA) used in this study was developed by Cornell (1968). It expresses the probability that ground motion (acceleration, velocity or displacement) exceeds certain amplitude values within a specified time interval. Three steps are needed before the calculation: the definition of seismotectonic source zones, a model of earthquake recurrence with respect to the magnitude, and a ground motion prediction equation (GMPE). Then the occurrence probability if the ground motion intensity exceeds a certain value was computed for different time frames, using CRISIS software (Ordaz et al. 2015).

3 Results

3.1 Earthquake Catalogue of CVL

A catalogue of earthquakes was compiled from those given by the international seismological data distribution centers such as the International Seismological Center (ISC), National Earthquake Information Center (NEIC), at the United States Geological Survey (USGS). It is enriched by data from local networks of the Institute of Geological and Mining Research (IRGM), as well as the locations given in some publications and doctoral theses. For the period from 1900 to 2010, we compiled data for one thousand (1000) earthquakes with magnitudes ranging between 1.0 and 4.5 (Fig. 1).

The catalogue underwent several refinements: de-cluster, determine Mc the magnitude for which one considers that the catalogue is complete, as well as the maximum magnitude, and the uncertainties of these values.

3.2 Seismic Source Zones and Seismicity Models

On the basis of seismicity, geology and geophysical studies, we identified three (3) seismic area sources: the region of Mount Cameroon, the NE of Mt Cameroon and finally the West Cameroon (Fig. 2). At this stage, we consider as seismicity model that of Gutenberg and Richter (Gutenberg and Richter 1954) which states that the appearance of earthquakes obeys the Poisson's law. Thus, the occurrence of events is distributed exponentially as expressed by Gutenberg and Richter law (Eq. 1):

$$\text{Log } N = a - bM \tag{1}$$

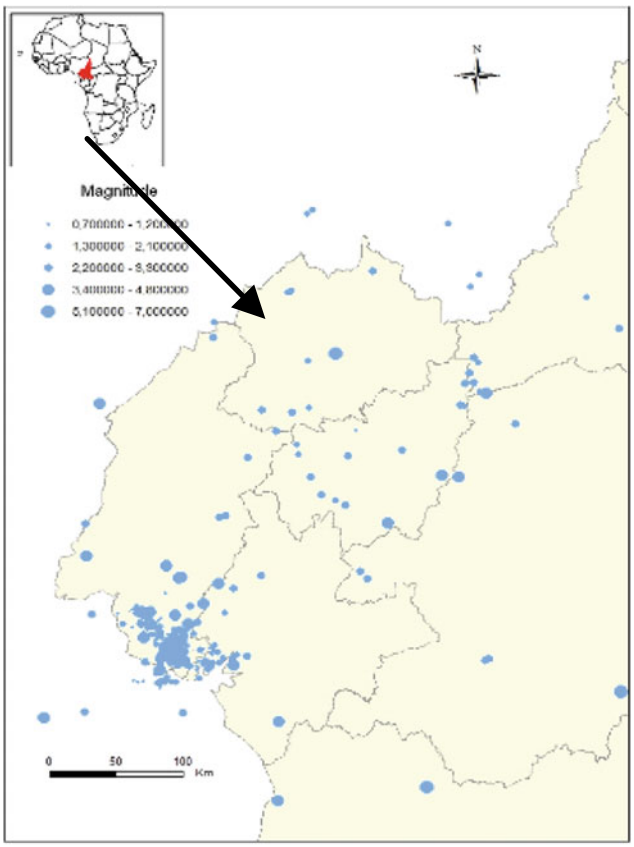

Fig. 1 Seismicity of W Cameroon

where N is the number of earthquakes whose magnitudes are greater than or equal to M. a and b are constants that were determined for each of the seismic source zones, referred to as the (a) value and the (b) value. They are used to characterize source zones that are used as input in the hazard calculation.

3.3 Ground Motion Prediction Equations (GMPE)

A GMPE has not yet been developed for Central and West Africa. We chose according to the geodynamic context. For this study, we selected the equations given by Abrahamson et al. (2014) and Boore et al. (2014).

3.4 Seismic Hazard Along the CVL

Eleven (11) major cities were selected along the CVL continental section to calculate seismic hazard for different return periods. For a return period of 475 years that serves as a reference, the average PGA for both GMPE is around 10% of g at Buea in the Mount Cameroon region (Fig. 2). It

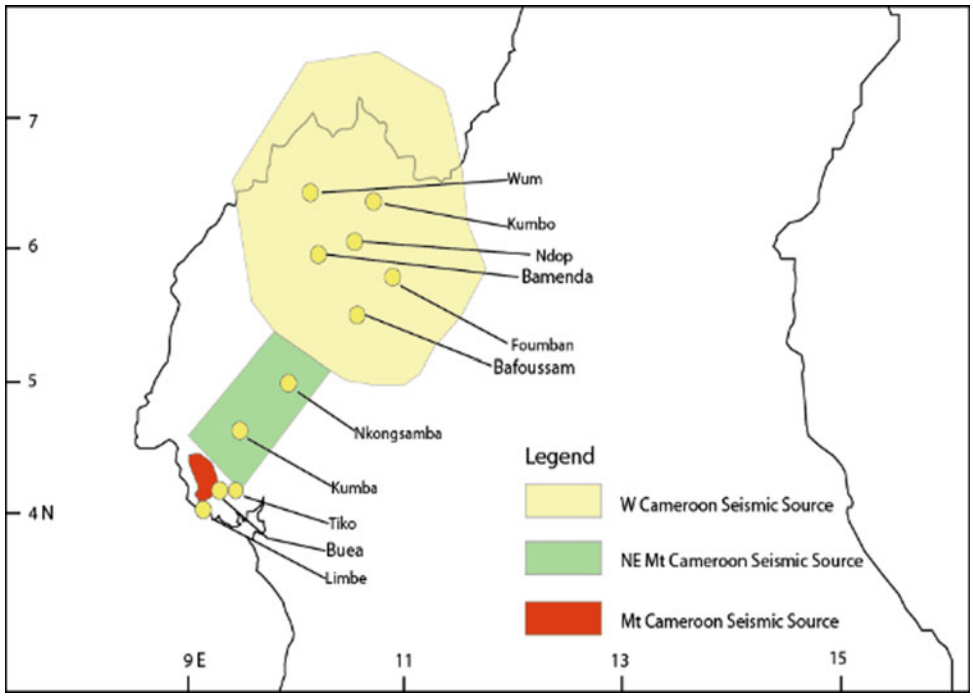

Fig. 2 Seismic Sources and main Cities along CVL

Table 1 PGA of main cities along the CVL

City	Latitude N	Longitude E	Altitude (m)	PGA
Buea	4.2097	9.3823	720.0	0.11
Limbe	4.0891	9.3026	90.0	0.07
Tiko	4.1626	9.4483	35.0	0.04
Kumba	4.6367	9.4517	224.0	0.07
Nkongsamba	4.9533	9.9410	827.0	0.07
Bafoussam	5.5205	10.5620	1430.0	0.06
Foumban	5.7650	10.9172	1072.0	0.06
Bamenda	5.9794	10.2263	1280.0	0.06
Ndop	6.0570	10.5083	1188.0	0.06
Kumbo	6.3521	10.6966	1866.0	0.06
Wum	6.4000	10.1633	1014.0	0.06

decreases appreciably to values of 5% of g, as one moves away from the main focus, in the NE direction (Table 1). The SA increases with the period, up to about 0.2 s, before starting to decrease as the period increases.

4 Discussion

Sub-Saharan Africa has a weak coverage in terms of seismographs. Earthquake catalogues are also fragmented which sometimes requires special treatment. Our results differ from those of the Global Earthquake Model (GEM) for which the hazard around Mt Cameroon is around 0.03 g for a return period of 475 years. On the other hand further North, in the region of Bamenda-Wum, it would be null [https://hazard.openquake.org/gem/models/WAF/]. The main difference is on the selection of the seismic source; that of GEM being larger.

The lack of accelerometers and strong ground motion data in the country does not allow the development of a local empirical GMPE. The uncertainties associated with this lack of useful data can be managed by adopting alternative models that cover the uncertainty and can be implemented in the calculation using the logical tree methodology (Coppersmith and Youngs 1986).

The hypothesis on the presence of faults along the CVL which are covered by lava flows was made. However, currently no evidence exists to prove this and studies are

ongoing to obtain such evidence. This will allow the use of faults as independent sources in the hazard analysis.

5 Conclusions

The assessment of the seismic hazard of the main cities located in the continental part of the CVL was carried out using the probabilistic approach. For a return period of 475 years, the PGA is of the order of 10% of g at Mt Cameroon. This value is almost reduced to the half for towns further away from Mt Cameroon, in the region of West Cameroon. Thus the seismic risk is not to be neglected along the CVL.

In perspective, we will study the influence of tectonic faults located in the near vicinity of the CVL.

References

Abrahamson, N.A., Silva, W.J., Kamai, R.: Summary of the ASK14 ground motion relation for active crustal regions. Earthq. Spectra. **30**, 1025–1055 (2014)

Ambeh, W.B., Fairhead, J.D., Francis, D.J., Nnange, J.M., Soba, D.: Seismicity of the Mount Cameroon region, West Africa. J. Afr. Earth Sci. **9**, 1–7 (1989)

Ateba, B., Ntepe, N.: Post-eruptive seismic activity of Mount Cameroon (Cameroon, West Africa): A statistical analysis. J. Volcanol. Geotherm. Res. **79**(1–2), 25–45 (1997)

Boore, D.M., Stewart, J.O., Seyhan, E., Atkinson, G.M.: NGA-West2 equations for predicting PGA, PGV, and 5% damped PSA for shallow crustal earthquakes. Earthq. Spectra. **30**, 1057–1085 (2014)

Coppersmith, K.J., Youngs, R.R.: Capturing uncertainty in probabilistic seismic hazard assessments within intraplate tectonic environments. Proceedings of the Third U.S. National Conference on Earthquake Engineering, Charleston, South Carolina, vol. 1, pp. 301–312 (1986)

Cornell, C.A.: Engineering seismic risk analysis. Bull. Seismol. Soc. Am. **58**(5), 1583–1606 (1968)

Déruelle, B., Ngounouno, I., Demaiffe, D.: The Cameroon Hot Line (C H L): A unique example alkaline activity of intraplate structure in both oceanic and continental lithospheres. C. r. Geosci. **339**, 589–600 (2007)

Eloumala, O.P.N., Mouzong, P.M., Ateba, B.: Crustal structure and seismogenic zone of cameroon: integrated seismic, geological and geophysical data. Open J. Earthq. Res. **3**, 152–161 (2014)

Fitton, J.G., Dunlop, H.M.: The Cameroon Line, West Africa and its bearing on the origin of oceanic and continental alkali basalts. Earth Planet Sci. Lett. **72**, 23–38 (1985)

Gutenberg, B., Richter, C.F.: Seismicity of the earth and associated phenomena. Princeton University Press, Pinceton (1954)

Moreau, C., Regnoult, J.M., Deruelle, B., Robineau, B.: A new tectonic model for the Cameroon Line, Central Africa. Tectonophysics **13**, 317–334 (1987)

Njonfang, E., Nono, A., Kamgang, P., Ngako, V., Tchoua, F.M.: Cameroon Line alkaline magmatism (central Africa): a reappraisal. Geol. Soc. Lon. Spec. Pap. **478**, 173–191 (2011)

Ordaz, M., Faccioli, E., Martinelli, F., Aguilar, A., Arboleda, J., Meletti, C., D'Amico, V.: CRISISversion 2.2: Computer program for computing seismic hazard. Instituto de Ingenieria, UNAM, Mexico (2015)

Tabod, C.T., Fairhead, J.D., Stuart, G.W., Ateba, B., Ntepe, N.: Seismicity of the Cameroon Volcanic Line, 1982–1990. Tectonophysics **212**, 303–320 (1992)

Assessing Seismic Hazard for the Democratic Republic of Congo and Its Vicinity Based on New Seismic Zoning Source Model

Georges Mavonga Tuluka, Jeanpy Lukindula, and Raymond J. Durrheim

Abstract

The DRC encompasses both intra-plate and active tectonic areas associated with the Congo Craton and the western branch of the East African Rift System, respectively. The seismic hazard assessment is based on the new Sub-Saharan-Global Earthquake Model earthquake catalogue (SSA–GEM) with homogeneous magnitude representation. The final declustered catalogue spans 55 years (from 1960 to 2015) with 398 events and a magnitude of completeness of about 4.5. The maximum credible magnitude of earthquakes was determined using the entire catalogue from 1900 to 2015. The seismotectonic zonation into 15 seismic source zones was done on the basis of the regional geological structure, neotectonic fault systems, distribution of thermal springs, regional strain rate model developed for the East African Rift by Saria and earthquake epicenters. The Gutenberg Richter parameters were determined using Aki's maximum likelihood method Aki (Bulletin of the Earthquake Research Institute, Tokyo University, 43, 237-239, 1965) and Weichert's method Weichert (Bulletin of the Seismological Society of America, 70, 1337-1346, 1980), which were compared with extension of the Aki-Utsu b value estimator for incomplete catalogues by Kijko and Smit. Hazard computations were performed using the Open Quake engine (version 2.7.0-1). The peak Ground Acceleration and spectral acceleration at periods of 0.05, 0.1, 0.2, 0.5, 1 and 2s were calculated using 4 Ground Motion Prediction Equations: two for active shallow crust and two for stable continental conditions for soil sites corresponding to V_{s30} = 600, 760 and 1500 m/s at 11 cities of the DRC and surrounding areas. The results are consistent with those obtained using the regional frequency-independent attenuation law using Crisis 2012 software.

Keywords

OpenQuake engine • Earthquake catalogue • Probabilistic seismic hazard assessment • Seismic zonation source model • D.R. Congo

1 Introduction

The DRC encompasses both intra-plate and active tectonic areas associated with the Congo Craton and the Western branch of the East African rift system, respectively (Fig. 1). In this study, a combination of seismic zoning source models from Mavonga and Durrheim (2009), Delvaux et al. (2016) and Poggi et al. (2017) was compiled and the SSA–GEM earthquake catalogue with homogeneous magnitude representation (Mw) was used to assess the seismic hazard for the DRC and surrounding areas.

2 Methodology

2.1 Declustering and Assessment of the Completeness of the Earthquake Catalogue

SSA–GEM earthquake catalogue with homogeneous magnitude representation Mw was used in this study. The necessary steps to setup the SSA–GEM catalogue (main assumptions, earthquake location solution preference and magnitude conversion rules) are described in Poggi et al. (2017). The catalogue was declustered using the declustering algorithm of Gardner and Knopoff (1974), implemented in

G. M. Tuluka (✉)
Department of Seismology, Goma Volcanic Observatory, Goma, DR, Congo

J. Lukindula
Departments of Geology, University of Goma, Goma, DR, Congo

R. J. Durrheim
School of Geosciences, University of the Witwatersrand, Johannesburg, South Africa

M. Meghraoui et al. (eds.), *Advances in Geophysics, Tectonics and Petroleum Geosciences*, Advances in Science, Technology & Innovation, https://doi.org/10.1007/978-3-030-73026-0_17

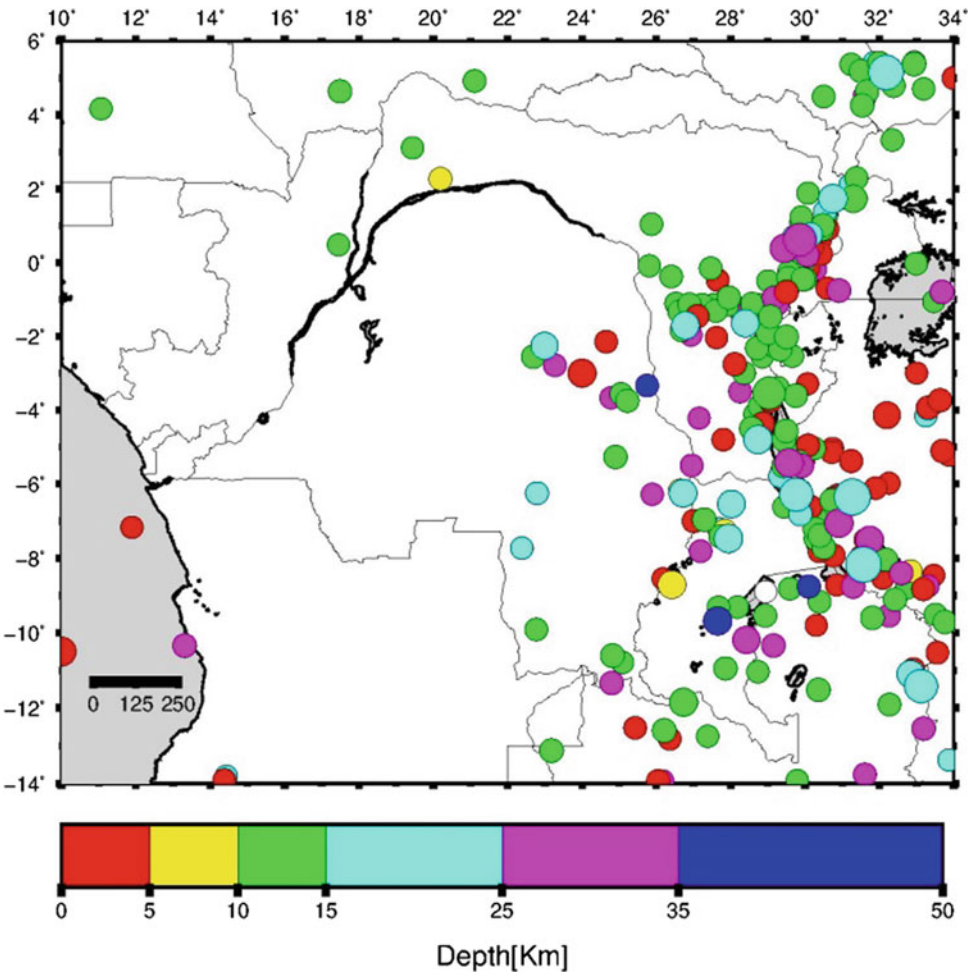

Fig. 1 Epicenters in the DRC of magnitude from 4.5 to 7.5 and surrounding areas for the time period 1910–2015 that were used in the seismic hazard analysis

the AFTERAN program (Musson 1999), which is distributed in OpenQuake software. After the declustering, the catalogue had 782 events. The completeness of the catalogue was determined using Stepp (1971) algorithm. The catalogue is complete for magnitude Mw $\geq$ 4.5 for the period 1960–2015. Thus, any events with Mw < 4.5 were excluded from the working catalogue to remain with 398 events.

2.2 Seismic Source Zoning and Seismicity Analysis

The identification and delineation of source zones was based on observed seismicity, geologic/tectonic characteristics from the database of Mac Gregory (2015) and the plate boundary model by Saria et al. (2014). The area is discretized into area source zones of supposed uniform temporal and spatial earthquake occurrence (Fig. 2). Seismicity in each zone is assumed to follow a double truncated Gutenberg Richter magnitude. Following Cornel (1968), each seismic source is described by 3 parameters: the mean seismic activity rate (λ), the Gutenberg-Richter parameter (b) and the maximum expected magnitude (M_{max}). MATLAB program "AUE" by Kijko and Smit (2012) was used to compute b and λ. M_{max} was obtained by adding 0.5 to the maximum magnitude observed in the source zone.

2.3 Ground Motion Prediction Equations and Hazard Computation

The ground motion logic-tree model included four GMPEs, two for active shallow crust (Chiou and Youngs 2014—CY; Akkar et al. 2014—AK) and two for stable continental conditions (Atkinson and Boorek 2006—AB; Pezeshk et al. 2011—PZ). We assigned all of the selected GMPEs to each source zone, but allowing the corresponding weights to vary in agreement with the likelihood of each specific tectonic type.

Hazard computations were performed using the OpenQuake engine (Version 2.7.0–1) through the available classical calculator for distributed seismicity. The investigation area consists of a mesh of sites with 10 km resolution. For each site of the mesh, soil conditions were assumed, with a

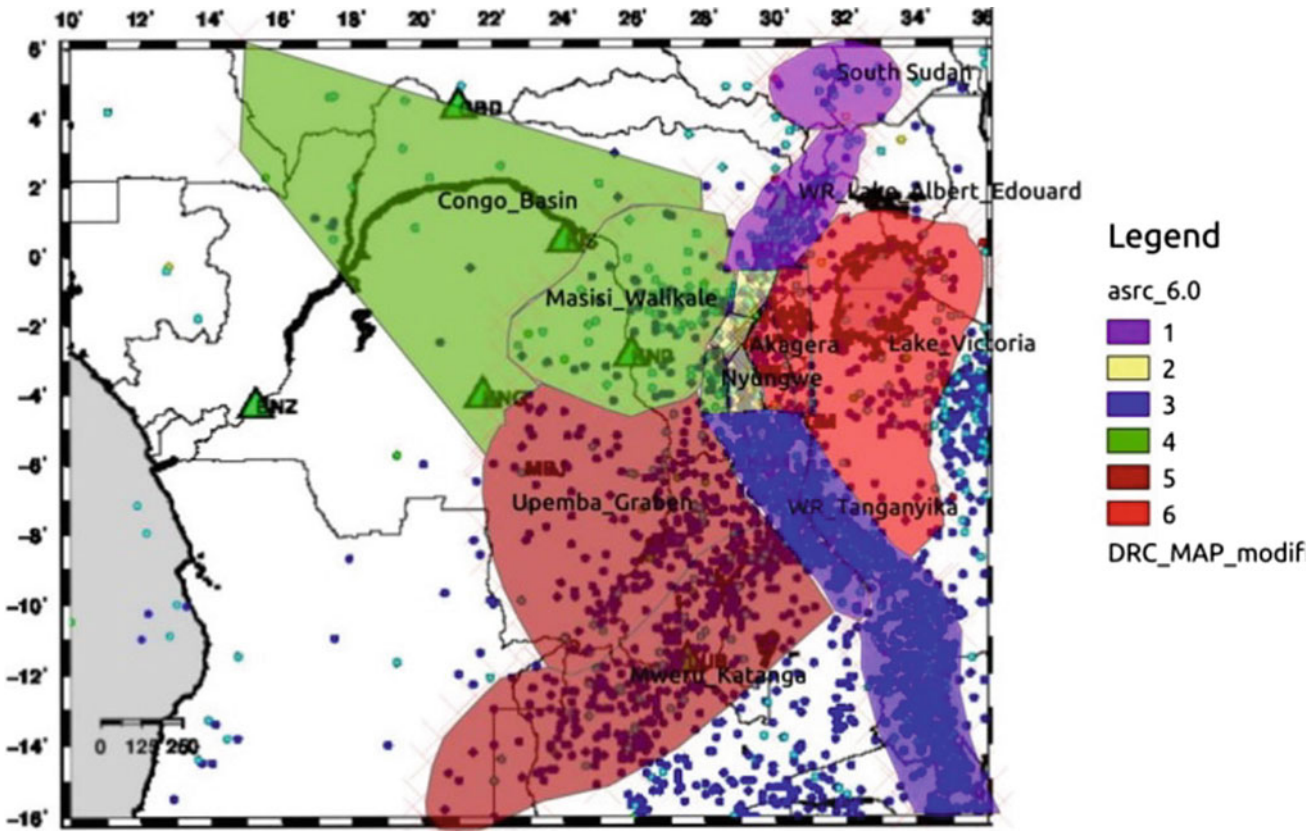

Fig. 2 Source zonation model used in this study

fixed V_{s30} value according to the National Earthquake Hazard Reduction Program (NEHRP) classification of soil in the European Building Code.

3 Results

Uniform Hazard Spectra (UHS) indicates, for a fixed annual probability of exceedance (return period), the value of the ground motion parameter versus the structural periods (PGA, T = 0.05 s, 0.1 s, 0.2 s, 0.5 s, 1.0 s, 2.0 s). In this study the 5%-damped UHRS on soft rock/very dense soil, rock and hard rock, corresponding to V_{s30} = 600 m/s, 760 m/s and 1500 m/s, respectively, were computed for a return period of 475 years (probability of 10% probability of exceedance in the next 50 years) at eight cities in DRC and three in adjacent countries in the East African region. Spectral acceleration for four main cities (Bukavu, Goma, Kigali and Bujumbura) was computed. In this short paper, we show only the results obtained for Bukavu (Fig. 3). This representation is useful to highlight those periods during which larger spectral acceleration is expected and is useful for structural engineers to design safe structures.

4 Discussion, Conclusion and Recommendations

Spectral acceleration maps produced for different structural periods for 10% probability of exceedance in 50 years show that the largest accelerations are found for periods of 0.1 s and 0.2 s along the Western Branch of the EARS (0.6–0.8 g for structural period T = 0.1 s). This is due to residual effect of local soil conditions, which are likely to affect the predicted ground motion in this frequency band (5–10 Hz). This frequency range is significant from the engineering perspective, as it matches the resonance response of common buildings in urban environments. Spectral acceleration is dependent on structural period and soil site. Therefore, a micro-zoning or site response investigation is very important for critical infrastructure.

As a conclusion, we recommend that seismic hazard assessment should be improved by maintaining and expanding seismic monitoring networks, supplementing historical and paleoseismic catalogues, and mapping active faults and the near-surface soil structure. Building codes should be formulated and enforced.

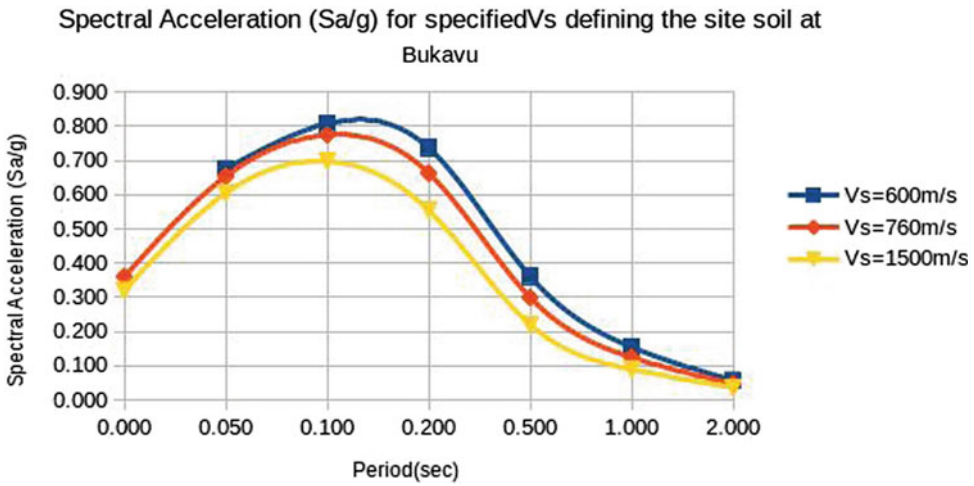

Fig. 3 Mean Uniform Hazard Spectra computed for Bukavu City

References

Aki, K.: Maximum likelihood estimate of b in the formula log N =a − bM and its confidence limits. Bulletin of the Earthquake Research Institute, Tokyo University, vol. 43, pp. 237–239 (1965)

Akkar, S., Sandikkaya, M.A., Bommer, J.J.: Empirical ground-motion models for point and extended-source crustal earthquake scenarios in Europe and the Middle East. Bull. Earthq. Eng. **12**, 359–387 (2014)

Atkinson, G., Boorek, D.: Earthquake ground-motion prediction equations for eastern North America. Bull. Seismol. Soc. Am. **96**, 2181–2205 (2006)

Chiou, B.S.-J., Youngs, R.R.: Update of the Chiou and Youngs NGA model for the average horizontal component of peak ground motion and response spectra. Earthq. Spectra **30**, 1117–1153 (2014)

Cornell, C.A.: Engineering seismic risk analysis. Bull. Seism. Soc. Am. **18**, 1583–1606 (1968)

Delvaux, D., Mulumba, J.-L., Fiama Bondo, S., Kervyn, F., Havenith, H.-B. Seismic hazard assessment of the Kivu rift segment based on a new seismotectonic zonation model (Western Branch, East African Rift system). J. Afr. Earth Sci. AVCoR (2016). https://doi.org/10.1016/j.jafrearsci.2016.10.004

Gardner, J.K., Knopoff, L.: Is the sequence of earthquakes in Southern California, with aftershocks removed, Poissonian? Bull. Seism. Soc. Am. **64**, 1363–2136 (1974)

Kijko, A., Smit, A.: Extension of the Aki-Utsu b-Value estimator for incomplete catalogs. Bull. Seism. Soc. Am. **102**, 1183–1287 (2012)

Mac Gregor, D.: History of the development of the East African Rift System: a series of interpreted maps through time. J. Afr. Earth Sci. **101**, 232–252 (2015)

Mavonga, T., Durrheim, R.J.: Probabilistic seismic hazard assessment for the Democratic Republic of Congo and surrounding areas. S. Afr. J. Geol. **112**, 329–342 (2009)

Musson, R.M.W.: Probabilistic seismic hazard maps for the north Balkan region. Ann. Geofis. **42**, 1109–1124 (1999)

Pezeshk, S., Zandieh, A., Tavakoli, B.: Hybrid empirical ground-motion prediction equations for eastern North America using NGA models and updated seismological parameters. Bull. Seism. Soc. Am. **101**, 1859–1870 (2011)

Poggi, V., Durrheim, R., Mavonga, T.G., Weatherill, G., Gee, R., Pagani, M., Nyblade, A., Delvaux, D.: Assessing seismic hazard of the East African Rift: a pilot study from GEM and Africa Array. Bull. Earthq. Eng. **15**, 4499–4529 (2017)

Saria, E., Calais, E., Stamps, D.S., Delvaux, D., Hartnady, C.J.H.: Present-day kinematics of the East African Rift. J. Geophys. Res. **119**, 3584–3600 (2014)

Stepp, J.C.: An investigation of earthquake risk in the Puget Sound area by use of the type I distribution of largest extremes. Ph.D. thesis, Pennsylvania State University (1971)

Weichert, D.H.: Estimation of the earthquake recurrence parameters for unequal observation periods for different magnitudes. Bull. Seismol. Soc. Am. **70**, 1337–1346 (1980)

AEON Transdisciplinary Natural Baseline in the Karoo (South Africa)

Moctar Doucouré

Abstract

Given the fracking debate in South Africa, AEON initiated a transdisciplinary baseline research ahead of fracking related to possible exploration and shale gas development in the Karoo. Aspects of the natural baseline in relation to subsurface geometry and connectivity within the critical zone are presented, and geophysical results, with emphasis on ambient seismic noise and magneto-telluric, are summarised.

Keywords

Natural Baseline • Karoo • Subsurface • Transdisciplinary • AEON

1 Introduction

AEON stands for Africa Earth Observatory Network and is linked to Earth Stewardship Science as a Research Institute at Nelson Mandela University. Its activities are aiming at making an impact on the way Africa manages its resources and how it responds to the many pressures on diversity, the environment, and society (Doucouré and De Wit 2018).

Baseline data enable the establishment of knowledge and relevant information on key attributes or characteristics of the natural environment prior to the commencement of exploration/exploitation. As it stands, today, the Karoo of South Africa is a unique natural laboratory where near-pristine baseline data can be extracted and used as a global standard (De Wit and Doucouré 2018). International energy companies have been allowed exploration licences. Here, we report on an extensive, experimental, ongoing transdisciplinary baseline research programme initiated in 2014. The transdisciplinary context of the baseline research can be seen in the various themes involved including Earth, Water, Life, People, Data, and Citizen Science. We highlight below the baseline research as it relates to geophysics and present some of the preliminary findings, many of which will evolve through collaborative work amongst researchers.

2 Transdisciplinary Baseline in the Karoo

The Shale Gas debate in South Africa largely revolved around the impact of hydraulic fracturing (fracking) on future water needs for the ecosystem, human health, and food security. AEON initiated a transdisciplinary baseline research project ahead of fracking related to possible exploration and shale gas development in the Karoo (see Fig. 1 for location). The project had 35 Master and Doctoral students, all from different backgrounds, registered in nine different departments from four different faculties. The main resource targeted by exploration companies is unconventional gas in the Whitehill shale rocks. The gas potential predicted for the Whitehill shale in the Karoo Basin (40–260 trillion cubic feet) is similar to that of the largest unconventional gas-field in the USA—the Marcellus shale in the Appalachian Basin across Pennsylvania.

Central to the motivation for the baseline is thus groundwater and the subsurface connectivity between natural water reservoirs throughout the Critical Zone (CZ) of the Earth's upper crust. The CZ is a vast network of conduits that controls many important physical and chemical life enabling processes. It is the zone in which soils and the deep biosphere are hosted; and where fracture systems are found to play an important role in defining regions prone to greater degree of interconnectivity (De Wit and Doucouré 2018).

M. Doucouré (✉)
AEON, Nelson Mandela University, Port Elizabeth, South Africa
e-mail: Moctar.doucoure@mandela.ac.za

M. Meghraoui et al. (eds.), *Advances in Geophysics, Tectonics and Petroleum Geosciences*,
Advances in Science, Technology & Innovation, https://doi.org/10.1007/978-3-030-73026-0_19

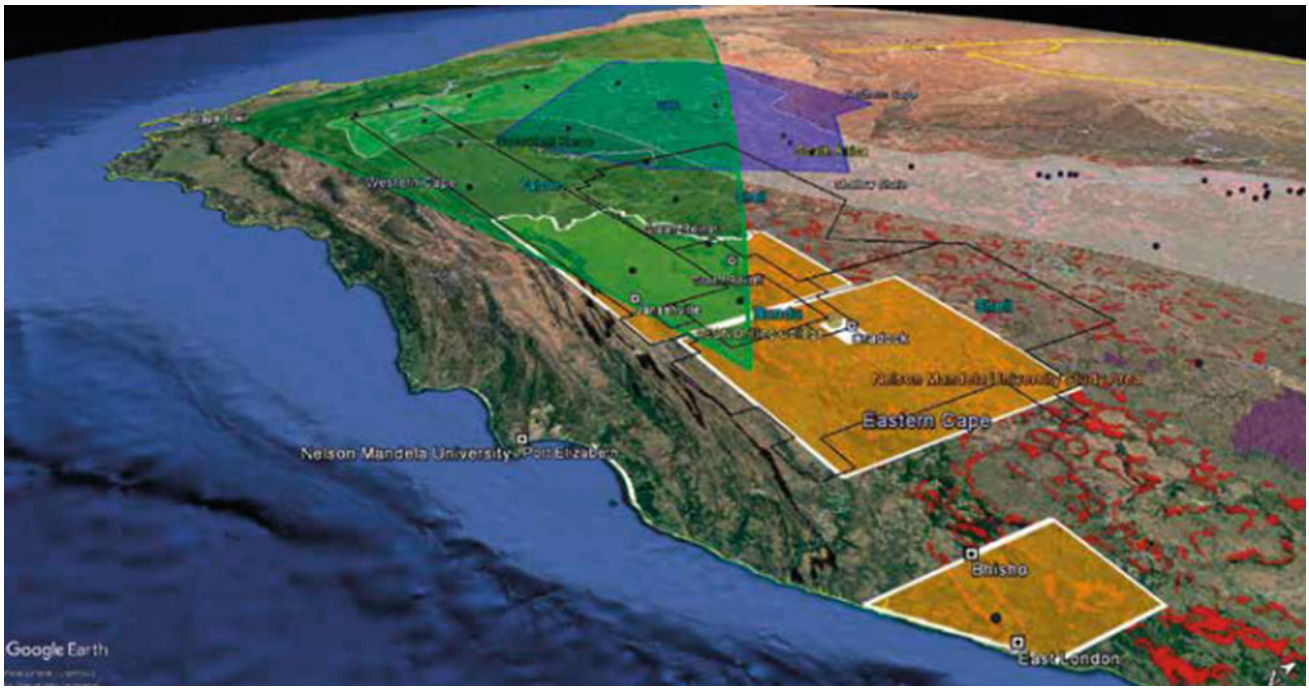

Fig. 1 Google view across southernmost Africa, showing areas most likely to be explored for Shale Gas (De Wit and Doucouré 2018)

3 Deep and Shallow Aquifer Connectivity as Early Warning Systems

Exploration typically affects resources confined to within the highly interconnected region of the CZ. This region is likely to experience an increase in fracture-controlled interconnectivity and subsequently a growing number of induced environmental feedback mechanisms with potential negative ecosystem services. Water quality has extreme spatial and temporal variability linked to both natural and human activities, and thus detecting contamination is difficult if not near impossible to document if there are no natural baseline data available. Parameters that characterise groundwater including conductivity, depth and aquifer yield are measured (De Wit and Doucouré 2018). Whilst fractal characterisation can be used to define regions of the CZ prone to a greater environmental feedback and/or potential concentration of fracture-dependent natural resources, the depth extent of these fractures, the geometry of deep aquifers, and shale gas bearing rock formations are probed using geophysical methods.

4 Geophysical Probing of the Critical Zone

4.1 Airborne Magnetic Mapping of Subsurface Structures

The airborne survey is designed to acquire magnetic and radiometric data together with digital terrain model and is expected to expose the detailed configuration of the baseline area and its fault and fracture patterns, as well as intrusive rocks which influence both surface topography and groundwater movement (De Wit and Doucouré 2018). The presence of dolerite sills in particular could significantly have an impact on groundwater flow in the form of aquitards. The survey is currently ongoing and preliminary work based on adjacent coverage, and using multi-scale tilt depth and forward modelling, suggests magnetic sources at varying depths up to few hundred metres. Pervasive faulting is also exposed.

4.2 Ambient Noise Imaging and Micro-Earthquake Monitoring

Non-invasive, cost-effective ambient seismic noise technique is suitably used to map and monitor within a natural baseline environment. This technique is based on the cross-correlation of microseismic surface waves recorded from a network of three-component data-cubes with built-in GPS and external antenna. The portable seismic array is made of temporary stations placed in the study area where there are no known other seismic network. An example of such stations and array measurement is shown in Fig. 2. Cross-correlations between pairs of stations are used to determine the approximate source azimuth of the ambient seismic noise. It is found that most of the (Eastern Cape Karoo) ambient noise is generated near the coast of South Africa. Group velocities of the Rayleigh and Love waves

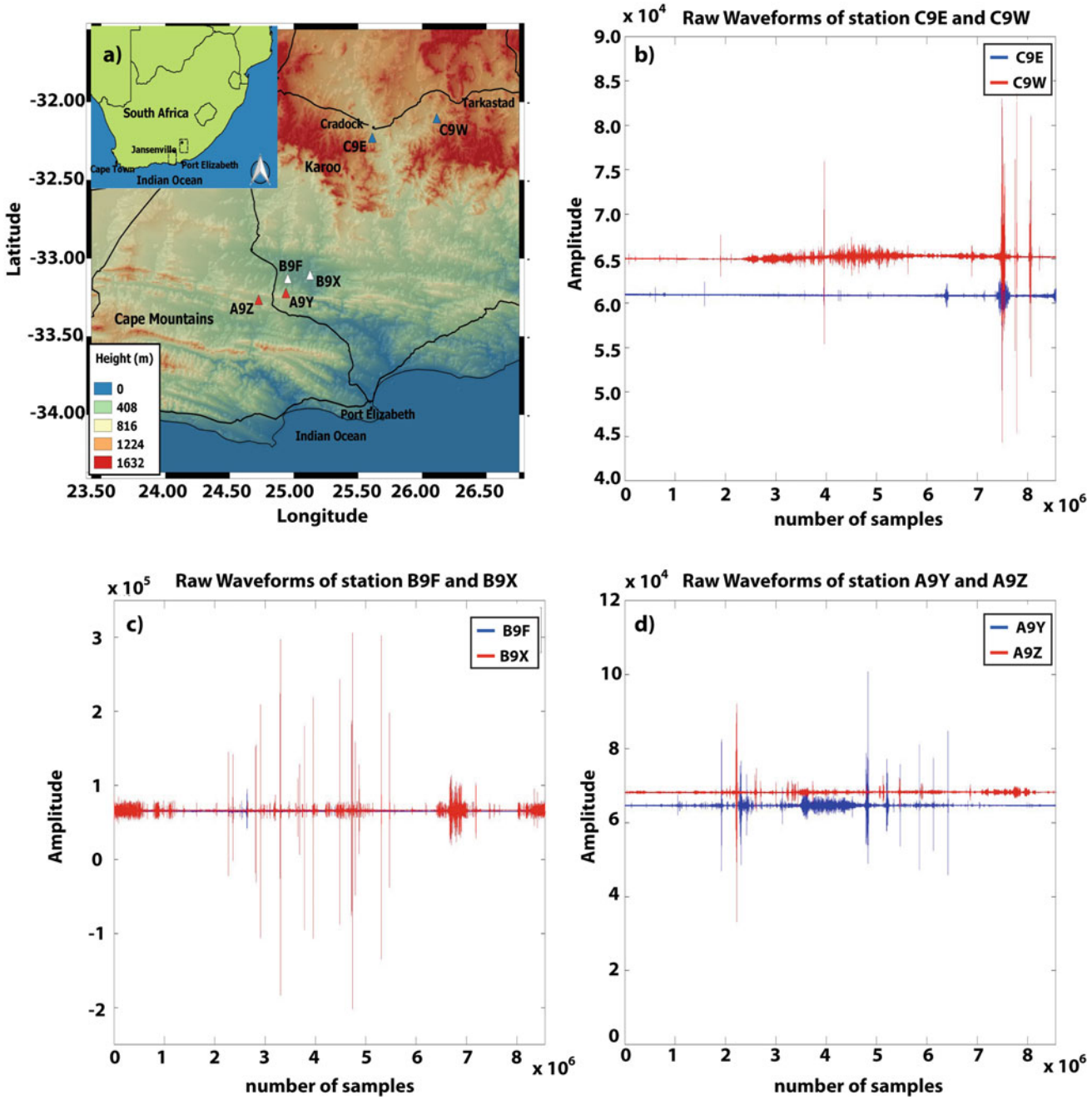

Fig. 2 **a** Station location of ambient noise raw waveforms; **b** raw waveforms from station C9E and C9W; **c** raw waveforms from stations B9F and B9X; **d** raw waveforms from stations A9Y and A9Z (Bezuidenhout 2017)

were inverted to produce 2-D group velocity images at different periods (e.g. Fig. 3), showing high velocity anomalies associated with denser, thick sedimentary basin of the Karoo compared to the adjacent geological domain (Bezuidenhout et al. 2017; Bezuidenhout and Doucouré 2019).

4.3 Deep Conductive Horizons Imaging Using Natural Earth's Electrical Currents and Magnetism

The magneto-telluric (MT) imaging uses natural sources to better define the geometry of the conductive hydrocarbon-bearing

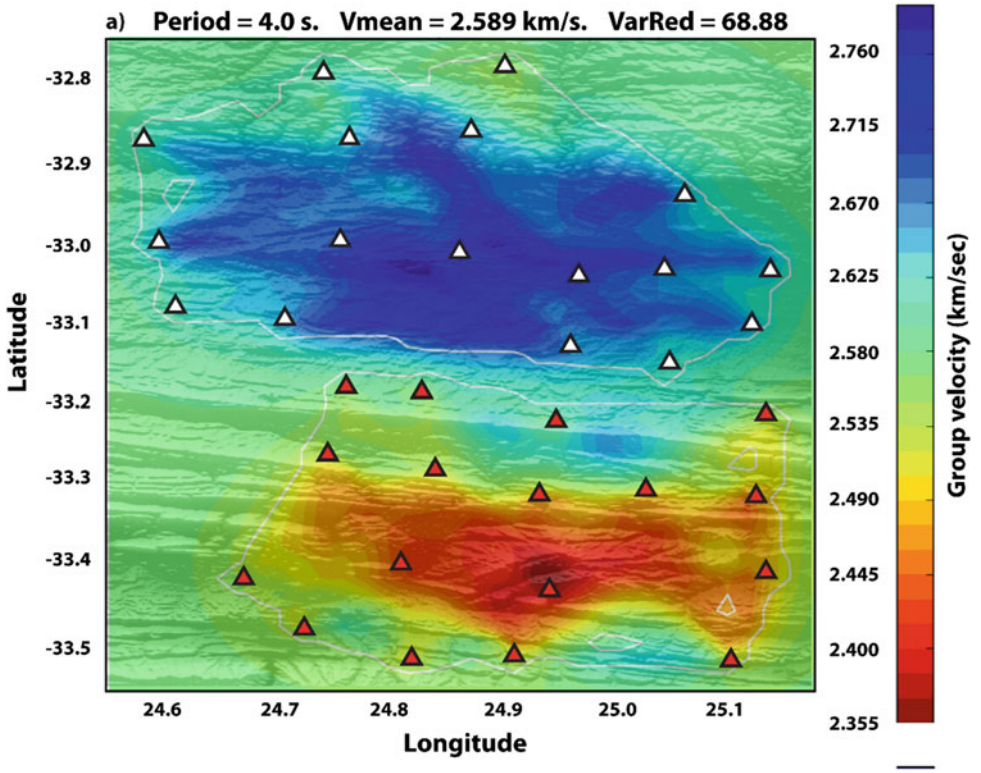

Fig. 3 Group velocity map using ambient seismic noise wavefield at 4 s period (De Wit and Doucouré 2018)

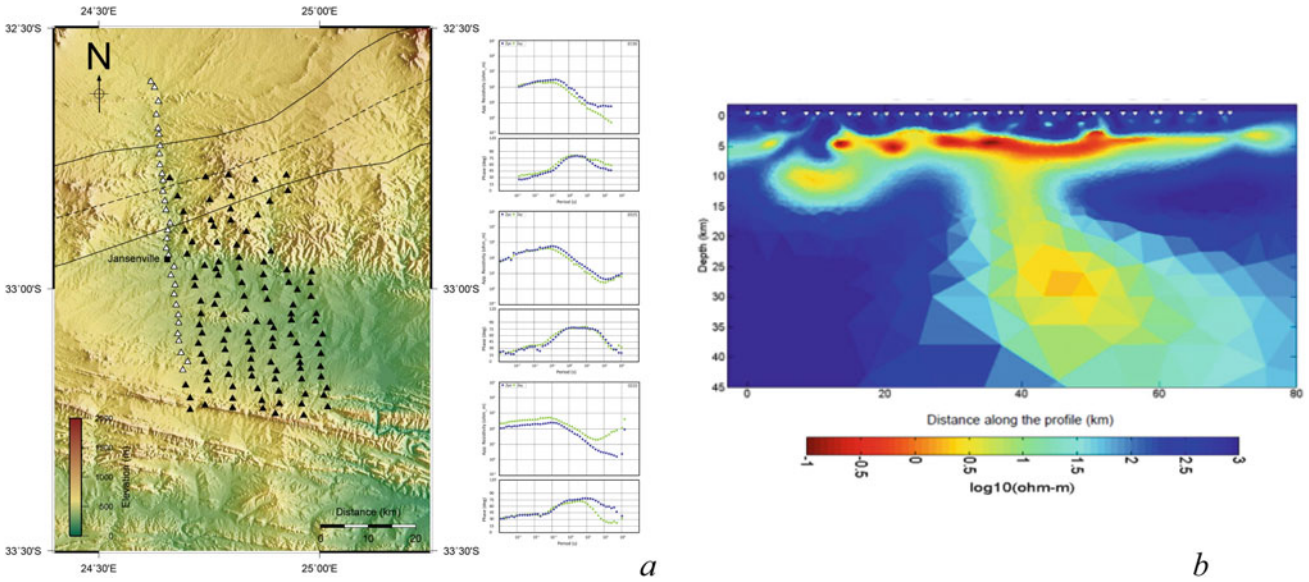

Fig. 4 **a** Location map of the MT stations where the stations (black triangles) are arranged in ~NS 2D profiles and form a 50 km by 30 km block used to produce the model images (profile 1 to the west is ~70 km long). The dotted black line indicates the maximum axis of the Beattie Magnetic Anomaly, whilst the solid black lines demarcate the extent of this feature. Representative stations from the south (station 0210, bottom right), centre (station 0315, middle right) and north (station 0130, top right) of the array indicate the three trends most commonly observed in the data across the array, as well as the high data quality achieved after data processing. **b** 2D subsurface resistivity inversion model vertical slice of survey profile 1 (westernmost profile) with station locations indicated by the white triangles. From (De Wit and Doucouré 2018)

shales and aids in the identification of deep saline water reservoirs. The data collection was through the deployment of broadband MT stations (location in Fig. 4a) to characterise the conductivity structure at depth. Shallow and sub-horizontal high-conductivity is found to be correlated with the exploration targeted shale formations. Processing and modelling of the MT data show that a sub-horizontal high-conductivity layer is associated with the Whitehill Formation at upper/middle crust depths (De Wit and Doucouré 2018); the surface of the conductive horizon is found to undulate between 1.6 and 5.9 km (Fig. 4b).

5 Discussion and Conclusions

This significance of the transdisciplinary baseline investigations should be seen in the broader context of shale gas development in South Africa, for which the Department of Science and Technology has commissioned the Academy of Science of South Africa to develop a national research programme referred to as the Science Action Plan for Shale Gas. This national action plan proposes flagship programmes of which "geology, gas resources, seismicity, exploration, and electromagnetic interference" form the foundation. The results from multidisciplinary datasets analysis and interpretation will have bearing on both the potential shale gas potential targeted by exploration. Transdisciplinary integration of the results together with borehole measurements and socio-economic data will provide the basis for strategies to be designed in context of new challenges linked to energy, climate change, and development.

References

Bezuidenhout, L.: Ambient noise tomography towards imaging the south-eastern Cape-Karoo and Karoo region, South Africa. PhD Thesis, Nelson Mandela University (2017)

Bezuidenhout, L., Doucouré, M.: Source azimuth determination of ambient seismic noise in the Eastern Cape Karoo, South Africa. J. Afr. Earth Sci., accepted (2019)

Bezuidenhout, L., Mordret, A., Doucouré, M., Lecocq, T., Brenguier, F., Wagener, V., de Wit, M.: Rayleigh group velocity extraction from ambient seismic noise to map the south Eastern Cape Karoo region, South Africa. SA J. Geol. **120**(3), 341–350 (2017)

De Wit, M., Doucouré, M.: The Baseline Research Team. (T)(C)raking the shale gas debate. AEON Report Series No 4, p. 123 (2018)

Doucouré, M., De Wit, M.: AEON Phase-2 Report, p. 31 (2018)

Earthquake Geodesy

Active Deformation in Tunisia from Continuous GPS Data

Nejib Bahrouni, Mustapha Meghraoui, Frederic Masson, Mohamed Saleh, Reda Maamri, and Fawzi Dhaha

Abstract

The plate boundary in the western Mediterranean includes the Tunisian Atlas Mountains. We study the active deformation of this area using continuous Global Positioning System (GPS) data collected from 2014 to 2018. WNW to NNW trending velocities express the crustal motion and geodetic strain field from the Sahara platform to the Tell Atlas, consistent with the African plate convergence. To the south, the velocities and trajectories indicate a nearly WNW–ESE trending right-lateral motion of the Sahara fault-related fold belt with respect to the Sahara Platform. Further north and northeast, the significant decrease in velocities between the Eastern Platform and Central—Tell Atlas marks the NNW trending shortening deformation associated with local ENE–WSW extension visible in the Quaternary grabens. The velocity field and strain distribution associated with the active E–W trending right-lateral faulting and NE–SW fault-related folds sustain the existence of three main tectonic blocks and related transpression tectonics. The velocity field and pattern of active deformation document the convergence of the oblique plate of Africa toward the oblique plate of Eurasia.

Keywords

Permanent GPS • Geodynamics • Strain deformation • Active tectonics • Tunisia

N. Bahrouni · R. Maamri · F. Dhaha
Office National Des Mines, Tunis, Tunisia

M. Meghraoui (✉)
EOST - Institut Terre et Environnement de Strasbourg, University of Strasbourg, CNRS - UMR 7063, Strasbourg, France
e-mail: m.meghraoui@nistra.fr

F. Masson · M. Saleh
IPGS (CNRS-UMR 7516), EOST, Université de Strasbourg, Strasbourg, France

M. Saleh
NRIAG, Helwan, Cairo, Egypt

1 Introduction

Large and moderate earthquakes attest for a significant crustal deformation across continental Tunisia (Fig. 1). Although the present-day background seismicity shows low-level activity, the seismic catalog (Guidoboni et al. 1994; Ambraseys 2009; Kharrat et al. 2018) shows the continuous occurrence of damaging earthquakes that affected Utique Roman city in AD 412, Kairouan region in 859, Tunis in 856, Mahdia in 981, Tunis in 1758, Gabes in 1881, Jemmel in 1887, El Guettar in 1889, Souk El Khemis in 1920, Gafsa in 1992, Tozeur in 1997, and more recently an Mw reaching 5 in 2018 in Tunis-Bizerte region. This seismicity appears as diffuse across the continental tectonic domain of Tunisia, but it also shows the extent of the active deformation from the Tell Atlas in the north to the Sahara Atlas in the south.

In this paper, we present Global Positioning System (GPS) results with new data, well distributed across Tunis and collected between 2014 and 2018 (six days of data per year). A previous study provides the details of the GPS data and results (Bahrouni et al., in press). Horizontal GPS coordinates' time series and velocities are presented along with the deformation field. The data analysis reveals a subdivision in complex block tectonics and related crustal motion with regards to the Eurasia reference system. The active tectonics and related strain field in Tunisia are discussed in the frame of the seismotectonics of the western and central Mediterranean regions.

2 Neotectonic Setting

Continental Tunisia shows various geological structures and tectonic blocks mainly limited by E–W trending strike-slip and NE–SW thrust faulting and folding with diapyr outcrops, and NW–SE striking normal faulting with depressions (Frizon de Lamotte 2000; Bouaziz et al. 2002; El Ghali et al.

M. Meghraoui et al. (eds.), *Advances in Geophysics, Tectonics and Petroleum Geosciences*,
Advances in Science, Technology & Innovation, https://doi.org/10.1007/978-3-030-73026-0_20

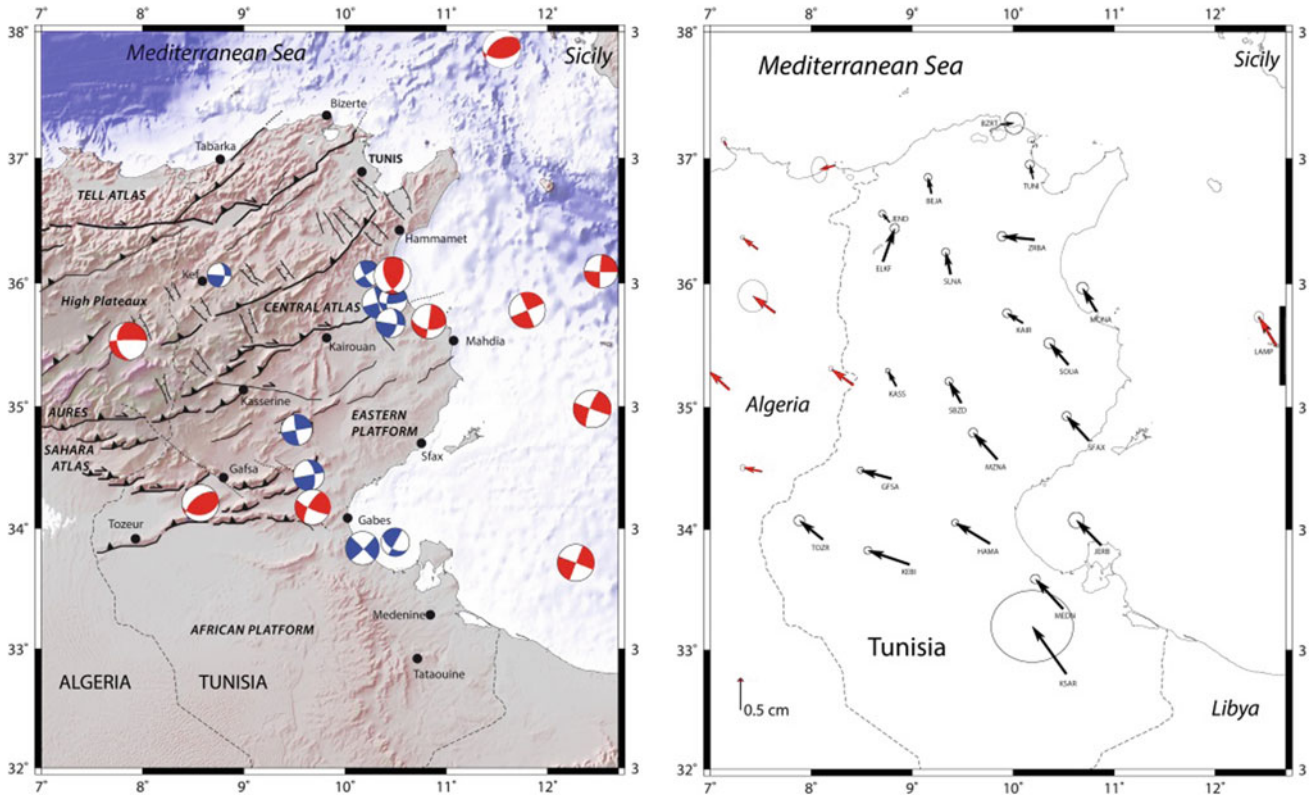

Fig. 1 Left—Seismotectonic map of Tunisia. Neotectonic faulting is from Bahrouni et al. (2013), and focal mechanism solutions are CMT-Harvard (red) and National Institute of Meteorology of Tunisia (blue). Topography and bathymetry are from Gebco**1**' grid data (Smith and Sandwell 1997). Right—GPS trend and velocities (black arrow) across continental Tunisia; red arrows are data from Algerian GPS network (Bougrine et al. 2019) and Italian GPS network (Serpelloni et al. 2007)

2003). Local and regional tectonic studies on the stress distribution determined from fault plane kinematics and earthquake focal mechanisms indicate the persistence of the N–S to NNE–SSW shortening direction during the Plio-Quaternary period over the Tell Atlas and central Atlas of Tunisia (Rebai et al. 1992; Ghribi and Bouaziz 2010; Bahrouni et al. 2013).

Evidences of E–W trending right-lateral faults with NE–SW faulting and folding of Quaternary formations are visible throughout the Maghrebides tectonic blocks of northern and southern Tunisia (Mejri et al. 2010; Saïd et al. 2011; Bahrouni et al. 2013). The active NW–SE trending grabens in the southern and central Atlas of Tunisia and partly in Algeria attest for the E–W to NE–SW extension (Philip et al. 1986). However, focal mechanism solutions of earthquakes display strike-slip and thrust faulting with NW–SE trending P axes. The study of instrumental seismicity such as the 1989 Metlaoui earthquake (Mw 5.4) (Dlala and Hfaiedh 1989) and the 1995 Sahraoui earthquake (Mw 5.3) (National Institute of Meteorology 1996) and their focal mechanisms (CMT—Harvard) shows the predominance of thrust and strike-slip tectonic faulting that characterize the transpressive character of the active deformation in Tunisia Atlas Mountains.

3 Results

The velocities in the Eurasia fixed reference frame are obtained using the Euler pole of Eurasiadetermined by Altamimi et al. (2017) and GAMIT-GlobK (King et al. 2009). In order to estimate a realistic margin of standard deviations, we applied MIDAS tool for permanent sites, while for the epoch sites, we scaled the standard deviations by the ratio of the formal error and repeatability estimated by the Kalman filter step (Hollenstein et al. 2003; Saleh and Becker 2015; Alothman et al. 2016). The uncertainties with 95% confidence level are fairly low except for the KSAR and BZRT stations. The vertical component is not taken into account due to the large uncertainties of the measurements and the relatively low deformation signal. From this velocity field of Fig. 1, we evaluate the strain rate tensor using the (Strain Tensor from Inversion of Baseline) STIB method (Masson et al. 2014). We also project North and East

velocities along a NS profile and point out that the ZRBA and ELKF stations appear as outliers (in red in Fig. 1). The two velocities at the ELKF and ZRBA stations are significantly different compared with their neighbours to be integrated into tectonic interpretation. It will be necessary to check the stability of the sites. Therefore, we did not discuss this issue and include it in the calculation of the deformation tensor.

The velocity vectors of the Tunisian territory mainly ranging between 2 and 7 mm/yr have a general WNW to NNW trend consistent with the active tectonics and plate convergence rate in nearby Algeria and Sicily (D'Agostino and Selvaggi 2004; Meghraoui and Pondrelli 2012; Bougrine et al. 2019). A first analysis of the Tunisian velocity field makes it possible to separate all the sites into three main areas, the south (Sahara Atlas and African Platform), the center-east (Eastern Platform) and the center-west/north (Tell and Central Atlas; Fig. 1).

Using the GPS velocities, we have calculated the strain distribution and rate based on a 100 km correlation length and a standard error of 0.5 mm/yr. The deformation field indicates the distribution of active deformation with transpression in the Sahara Atlas and eastern platform. A striking deformation is the ENE–WSW trending extensional field to the eastern central Atlas at the boundary between Algeria and Tunisia. The NNW–SSE trending shortening affects the Tell Atlas in agreement with the transpression tectonics along the plate boundary.

4 Discussion and Conclusion

The Global Positioning System (GPS) data in Tunisia bring new insights into the deformation rate of the eastern region of the Maghrebides Mountain range. The crustal motion with higher velocities of the African Platform to the south with regards to the fold and thrust belt to the north is here critical and attests for the amount of plate convergence. The decrease in the GPS velocities with up to 4 mm/yr shortening across mainly the Sahara Atlas, Central Atlas and Tell Atlas outlines the significant crustal deformation across this part of the Africa-Eurasia plate boundary.

The rate of crustal shortening and compression across the mountain ranges in Tunisia are comparable to the rates obtained from GPS in eastern Algeria (Bougrine et al. 2019) and in southern Italy (Serpelloni et al. 2007). The NNW trend with mainly 2–5 mm/yr velocities of GPS results in Tunisiapresent similar pattern of active deformation in Algeria (Bougrine et al. 2019) and in Sicily (D'Agostino and Selvaggi 2004). The WNW to NW trend and velocities across the Sahara Atlas in Tunisia and the Aures Mountains in Algeria show a remarkable consistency.

References

Alothman, A.O., Fernandes, R.M., Bos, M.S., Schillak, S., Elsaka, B.: Angular velocity of Arabian plate from multi-year analysis of GNSS data. Arab. J. Geosci. **9**(8) (2016). https://doi.org/10.1007/s12517-016-2569-5

Altamimi, Z., Métivier, L., Rebischung, P., Rouby, R., Collilieux, V.: ITRF2014 plate motion model. Geophys. J. Int. **209**(3), 1906–1912 (2017). https://doi.org/10.1093/gji/ggx136

Ambraseys, N.N.: Earthquakes in the Mediterranean and Middle East: A Multidisciplinary Study of Seismicity up to 1900, p. 947. Cambridge University Press, Cambridge, United Kingdom (2009)

Bahrouni, N., Bouaziz, S., Soumaya, A., Ben Ayed, N., Attafi, K., Houla, Y., El Ghali A., Rebai, N.: Neotectonic and seismotectonic investigation of seismically active regions in Tunisia: a multidisciplinary approach. J. Seismol. **18**(2) (2013). ISSN 1383–4649. https://doi.org/10.1007/s10950-013-9395-y

Bahrouni, et al.: GPS constraints on the active deformation in Tunisia: Implications for the geodynamics of the Western Mediterranean, submitted to Geology

Bouaziz, S., Barrier, E., Soussi, M., Turki, M., Zouari, H.: Tectonic evolution of the northern African margin in Tunisia from paleostress data and sedimentary record. Tectonophysics **357**, 227–253 (2002)

Bougrine, A., Yelles-Chaouche, A., Calais, E.: Active deformation in Algeria from continuous GPS measurements. Geophys. J. Int. **217** (1), 572–588 (2019). https://doi.org/10.1093/gji/ggz035

D'Agostino, N., Selvaggi, G.: Crustal motion along the Eurasia-Nubia plate boundary in the Calabrian Arc and Sicily and active extension in the Messina Straits from GPS measurements. J. Geoph. Res. **109** (B11), 11402 (2004). https://doi.org/10.1029/2004JB002998

Dlala, M., Hfaiedh, M.: Le séisme du 7 novembre 1989 à Metlaoui (Tunisie méridionale): une tectonique active en compression. C. R. Acad. Sci. Paris Série II **317**(10), 1297–1302 (1993)

El Ghali, A., Bobier, C., Ben Ayed, N.: Rôle du système de faille E–W dans l'évolution géodynamique de l'avant-pays de la chaîne alpine de Tunisie. Exemple de l'accident de Sbiba-Chérichira en Tunisie centrale. Bull. Soc. Geol. Fr. **174**(4), 373–381 (2003)

Frizon de Lamotte, F.D., Saint Bezar, B., Bracene, R., Mercier, E.: The two main steps of the Atlas building and geodynamics of the western Mediterranean. Tectonics **19**, 740–761 (2000)

Ghribi, R., Bouaziz, S.: Neotectonic evolution of the Eastern Tunisian platform from paleostress reconstruction. J. Hydrocarb. Mines Environ. Res. **1**(1), 14–25 (2010)

Guidoboni, E., Comastri, A., Traina, G.: Catalogue of Ancient Earthquakes in the Mediterranean Area up to the 10th Century, Istituto Nazionale di Geofisica, Rome, p. 504 (1994)

Hollenstein, Ch., Kahle, H.-G., Geiger, A., Jenny, S., Goes, S., Giardini, D.: New GPS constraints on the Africa-Eurasia plate boundary zone in southern Italy. Geophys. Res. Lett. **30**, 1935 (2003). https://doi.org/10.1029/2003GL017554

Institut National de la Météorologie, Annual Internal Seismicity Reports (1996)

Kharrat, S., Harbi, A., Meghraoui, M., Bouaziz, S.: The Tunisian homogenized macroseismic database (second century to 1981): first investigations. Seismol. Res. Lett. **90**(1), 347–357 (2018). https://doi.org/10.1785/0220180237

King, R.W., Mc Clusky, S., Herring, T.: Documentation of the GAMIT GPS Analysis Software, Release 10.3, Massachusetts Institute of Technology (2009)

Masson, F., Lehujeur, M., Ziegler, Y., Doubre, C.: Strain rate tensor in Iran from a new GPS velocity field. Geophys. J. Int. (2014). https://doi.org/10.1093/gji/ggt509

Meghraoui, M., Pondrelli, S.: Active faulting and transpression tectonics along the plate boundary in North Africa. Ann. Geophys. **55**(5) (2012). https://doi.org/10.4401/ag-4970

Mejri, L., Regard, V., Carretier, S., Brusset, S., Dlala, M.: Evidence of Quaternary active folding near Utique (northeast Tunisia) from tectonic observations and a seismic profile. Comptes Rendus Geosci. **342**(11), 864–872 (2010)

Philip, H., Andrieux, J., Dlala, M., Chihi, L., Ben Ayed, N.: Evolution tectonique mio-plio-quaternaire du fossé de Kasserine (Tunisie centrale): implications sur l'évolution géodynamique récente de la Tunisie. Bull. Soc. Geol. France **8**(II), 559–568 (1986)

Rebaï, S., Philip, H., Taboada, A.: Modern tectonic stress field in the Mediterranean region: evidence for variation in stress directions at different scales. Geophys. J. Int. **110**(1), 106–140 (1992). https://doi.org/10.1111/j.1365-246X.1992.tb00717.x

Said, A., Chardon, D., Baby, P., Ouali, J.: Active oblique ramp faulting in the Southern Tunisian Atlas. Tectonophysics **499**(1–4), 178–189 (2011)

Saleh, M., Becker, M.: New constraints on the Nubia-Sinai-DeadSea fault crustal motion. Tectonophysics **651–652**, 79–98 (2015)

Serpelloni, E., Vannucci, G., Pondrelli, S., Argnani, A., Casula, G., Anzidei, M., Baldi, P., Gasperini, P.: Kinematics of the western Africa-Eurasia plate boundary from focal mechanisms and GPS data. Geophys. J. Int. **169**(3), 1180–1200 (2007)

Smith, W.H.F., Sandwell, D.T.: Global sea floor topography from satellite altimetry and ship depth soundings. Science **277** (1997)

Active Deformation in Northern Algeria from Continuous GPS Measurements and Recent Seismic Data

Abdel Karim Yelles-Chaouche, Amina Bougrine, Eric Calais, and Mohamed Hamdache

Abstract

Recent installation of GPS (Global Positioning System) network in northern Algeria (the REGAT REseau Geodesique de l'ATlas Project), combined with the seismic ADSN (Algerian Digital Seismic Network) data network, fills an important gap in our knowledge of the present-day Nubian–Eurasian plate boundary in the western Mediterranean where likely most of the oblique plate convergence concentrates. From ten years of continuous measurements, the first geodetic velocity field shows variations from west to east. In western Algeria, GPS velocities are uniform and collinear to the N50W NU–EU convergence trend while in the east they indicate that the deformation involves a broader region. These results are consistent with the recorded seismicity in northern Algeria and the geophysical investigations held in the Algerian offshore basin. GPS data show that the deformation in Algeria is accommodated in the west along an offshore reverse fault system that runs along the toe of the Algerian margin with a slip rate decreasing from west to east. To the east, the deformation is accommodated by an E–W-trending strike-slip fault and a shortening component distributed along a reverse fault system offshore and between the Saharan platform and the Aures range in southeastern Algeria.

Keywords

GPS • Seismicity • Active deformation • Northern Algeria

1 Introduction

The present-day kinematics of plate boundary deformation in the western Mediterranean is now well described by space geodetic measurements (Nocquet and Calais 2004), except for the Algerian–Tunisian part of northern Africa where information is still lacking. Yet, that portion of the Nubian–Eurasian Plate boundary likely concentrates most of the oblique plate convergence with an on-going debate on the role of offshore versus on-land active and seismogenic structures (Nocquet 2012) where important earthquakes (El Asnam, 1980, Boumerdes, 2003) have recently occurred (Fig. 1).

Two competing models of the deformation process exist. For some authors (Meghraoui and Pondrelli 2012; Soumaya et al. 2018), this region is a transpressional system, with large east–west-trending strike slip faults in western and eastern Algeria. In this view, the Nubia–Eurasia oblique convergence is partitioned solely by onshore fault systems. For others (Domzig et al. 2006; Leprêtre et al. 2013; Hamai et al. 2015), the recent Maradja and Spiral surveys along the Algerian margin display a significant shortening at the bottom slope. In that view, the Algerian margin is the location of an inversion process leading to an incipient subduction zone. This point of view is also reinforced by the inverse focal mechanism of the many recent offshore earthquakes along the margin (Fig. 1).

From 10 years of continuous GPS data of the Algerian REGAT ("REseau Géodésique de l'ATlas") network, we discuss the active deformation pattern in northern Algeria integrating the first geodetic velocity field in Algeria with recent seismic activity of the different seismogenic zones.

2 Data Acquisition and Processing

The REGAT geodetic network is composed of 54 continuously recording GPS stations distributed in the Algerian Atlas (Yelles-Chaouche et al. 2019). The network spans the whole

A. K. Yelles-Chaouche (✉) · A. Bougrine · M. Hamdache
Centre de Recherche en Astronomie Astrophysique et Géophysique (CRAAG), Bouzareah, Algiers, Algeria

E. Calais
Department of Geosciences, Ecole Normale Superieure, Université PSL, Paris, France

M. Meghraoui et al. (eds.), *Advances in Geophysics, Tectonics and Petroleum Geosciences*,
Advances in Science, Technology & Innovation, https://doi.org/10.1007/978-3-030-73026-0_21

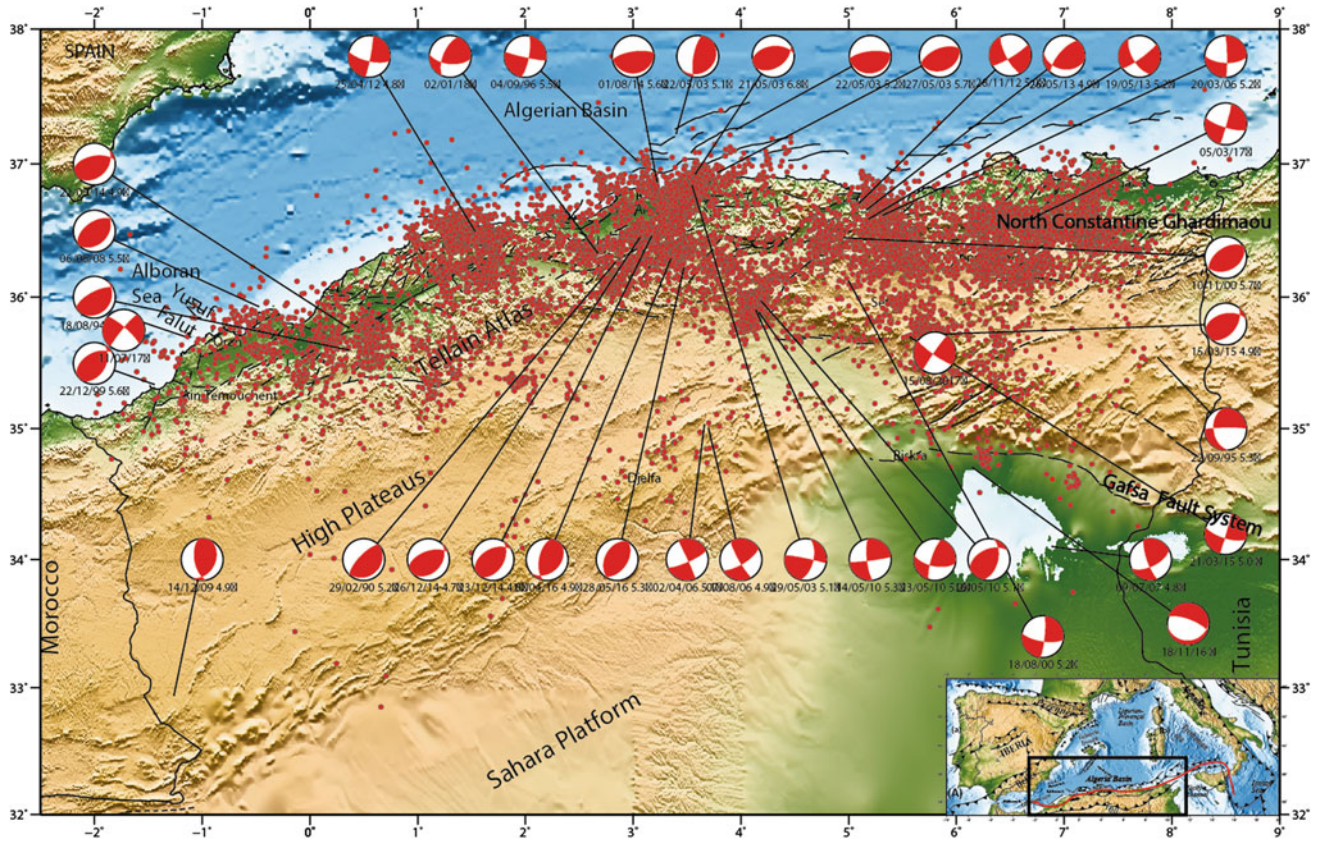

Fig. 1 Seismotectonic map of northern Algeria. Bathymetry and topography are from ETOPO1 Global relief (www.ngdc.noaa.gov). Solid black lines show the major tectonic features from Rabaute and Chamot-Rooke (2014). Red dots show instrumental seismicity from the CRAAG catalog ($M > 2$, 01/2000 to 12/2018). Earthquakes' focal mechanisms are from Yelles-Chaouche et al. (2017). Inset shows the broader Western Mediterranean region with simplified Eurasian–Nubian plate boundary (Aidi et al. 2018)

width of the Algerian coast and reaches 300 km inland, with an inter-sites distance of about 100 km. One additional site is located in Tamanrasset in the southernmost part of the country. The network, whose oldest stations started operating in 2007, encompasses the main active tectonic features of the most seismically active segment of the Nubian–Eurasian plate boundary in the Western Mediterranean.

The recorded GPS data from the REGAT network sites are all controlled for quality using the TEQC routine (Estey and Meertens 1999) before archival storage and processing. The data at all sites passed the quality test successfully.

We processed data from REGAT stations together with 34 sites from the International GNSS Service (IGS) located in Europe and Africa using the GAMIT-GLOBK software package (Herring et al. 2015). We compute the daily position time series which we analyze visually for discontinuities, position offsets or data gaps. Among the 54 GPS sites, 8 of them show low-quality position time series signal with non-tectonic behavior. We noticed that some of them are from sites located in vicinity of water dams, and for the others their behavior is probably due to soil conditions and or monument construction. We use the First-Order Gauss–Markov Extrapolation (FOGMEx) algorithm to compute station-dependent variance scaling factors to be applied to formal errors in order to obtain velocity uncertainties that account for the level of colored noise present in the time series. We combine our solutions into a single position/velocity solution while accounting for the FOGMEx variance factors which we tie to the ITRF by minimizing position and velocity deviations from the globally distributed set of core IGS reference sites common to our solution via a 12-parameter Helmert transformation, as described in details in Yelles-Chaouche et al. (2019).

For the seismic events (Fig. 1), data from the National Algerian seismic network ADSN (Yelles-Chaouche et al. 2013) are analyzed.

To define earthquake source parameters, we use the Hypoinverse software package with RMS < 2 and GAP < 180 and a horizontal and vertical errors ERH and ERZ < 0.2 km. To improve the location of events, we proceed with the HypoDD software for the relocation of the seismic events. In order to calculate the seismic moment, the moment magnitude Mw and the focal mechanism, we use the waveform modeling method which is implemented in the

SEISAN software package. Focal mechanism has also been determined from P-wave first motion polarities using the program FOCMEC. The velocity models are in general issued from the geophysical studies made previously or obtained by trial and error approach.

Several studies (Ousadou et al. 2014; Beldjoudi 2011; Kherroubi 2011; Abacha 2015; Yelles-Chaouche et al. 2017) discussed parameters (location, magnitude, FMS) of the recent seismic events.

3 Results

The resulting Velocity field in the study area shows oblique convergence between EU and NU (Fig. 2). In the west, velocities are uniform and collinear to the plate's convergence trend, with a sharp gradient at the coast, while in the east they indicate that the deformation involves a broader region. Using a simple block kinematic approach (Bougrine et al. 2019), we show that the velocities are consistent with the presence of an active, reverse, offshore fault system that runs along the toe of the Algerian margin, with a slip rate decreasing from west to east. In the western half of Algeria, the GPS data do not require additional on-land fault systems. In the eastern half, GPS velocities require an E–W-trending strike-slip fault separating two blocks that accounts for the strike-slip component of the overall plate motion. We also observe significant shortening between the Saharan platform and the Aures range in southeastern Algeria.

This first velocity field associated with the seismicity of northern Algeria displays a first-order zoning of the seismogenic zones (Fig. 2) with the role of the main offshore and onshore active structures. From this study, the role of the main right lateral strike slip GNC (Ghardimaou–North Constantine fault) fault system is outlined.

Along these main active structures, many recent moderate events occurred as the 2012–2013 Bejaia sequence, the 2015 Ain Azel sequence or the 2017 North Constantine sequence.

4 Implication to Seismic Hazard Assessment

Identified active fault sources are increasingly integrated into, and the practice is growing in popularity (Valentini et al. 2017; Visini et al. 2019).

In this context, the estimated slip rate derived in this study is distributed along the known active faults. Combined to other fault parameters such as the length, the type of fault, the mean return period of the characteristic earthquake is thus obtained. Different models can be used, although dependent (based on Brownian passage time) or independent (mainly Poissonian) temporal model, to analyze the

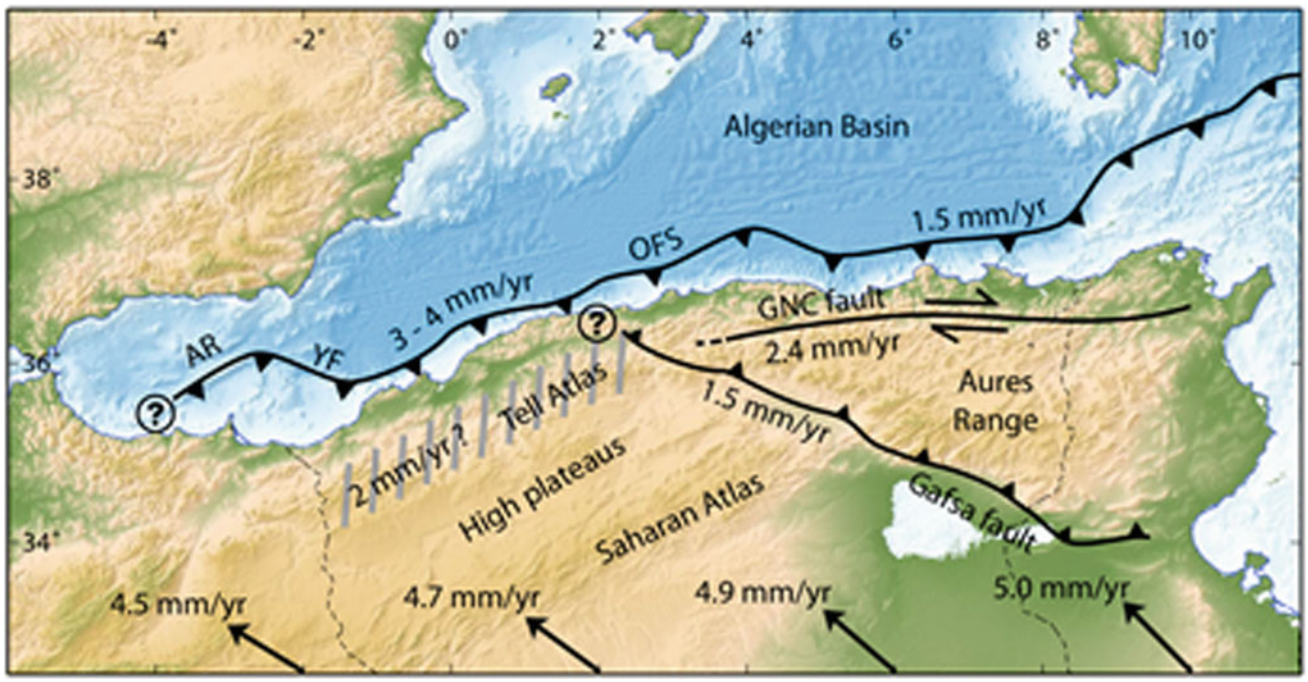

Fig. 2 Tectonic interpretation of the GPS velocity field (Bougrine et al. 2019). Solid black lines show the major tectonic active faults required by the data. Numbers show horizontal displacement rates along faults in mm yr^{-1}. Arrows at the bottom of the map show the NU–EU relative plate motion derived from this work. The hatched area over the Tell Atlas represents the possible ~2 mm of oblique shortening across that structure. OFS = offshore fault system, AR = Alboran Ridge, YF = Yussuf fault, GNC = Ghardimaou–North Constantine fault

probability of occurrence of the characteristic earthquake during the next T years knowing the elapsed time. In this study, the attempt to perform such analysis is developed for northern Algeria as the one made by Hamdache et al. (2019).

5 Discussion-Conclusion

The new data recorded from the GPS REGAT network allow us to obtain the first velocity field in northern Algeria. Combined to the data from the ADSN seismological network's major active, features in northern Algeria are identified. Several earthquakes that struck the country in the past can be now linked to these new identified active features, such as the historical 1856 Djidjeli earthquake that triggered a tsunami on the Algerian coast along the eastern segment of the offshore fault and recently the 2003 Boumerdes earthquake. Combining the resulted kinematic model to earthquake epicenter's locations and focal solutions, we delineate the Nubia–Eurasia convergence boundary showing a broader area in the east than the one in the west. The Nubia–Eurasia oblique convergence is accommodated mostly by offshore compression in the western half of Algeria and in its eastern half by onshore strike-slip combined with shortening both offshore as in the west and inland across the Atlas domain. Accounting for the slip rate, we can now compute new seismic hazard models in order to improve the several previous models already proposed.

References

Abacha, I.: Etude de la sismicité de la région de Constantine. PhD Thesis, Ferhat Abbas University, Setif (2015)

Aidi, C., Beslier, M.O., Yelles-Chaouche, A.K., Klingelhoefer, F., Bracene, R., Galve, A., Djellit, H.: Deep structure of the continental margin and basin off Greater Kabylia, Algeria—new insights from wide-angle seismic data modeling and multichannel seismic interpretation. Tectonophysics **728**, 1–22 (2018)

Beldjoudi, H.: Etude de la sismicité du Nord Algérien. PhD Thesis, Tlemcen University (2011)

Bougrine, A., Yelles-Chaouche, A.K., Calais, E.: Active deformation in Algeria from continuous GPS measurements. Geophys. J. Int. **217**, 572–588 (2019). https://doi.org/10.1093/gji/ggz035

Domzig, A., et al.: Searching for the Africa-Eurasia Miocene boundary offshore western Algeria (Maradja'03 cruise). Compt. Rend. Geosci. **338**(1–2), 80–91 (2006)

Estey, H.H., Meertens, C.M.: TEQC: the multi-purpose toolkit for GPS/GLONASS data. GPS Solut. **3**, 42–49 (1999)

Hamai, L., Petit, C., Abtout, A., Yelles-Chaouche, A.K., Deverchere, J.: Flexural behaviour of the north Algerian margin and tectonic implications. Geophys. J. Int. **201**, 1426–1436 (2015)

Hamdache, M., Pelaez, J.A., Yelles-Chaouche, A., Castro, M., Monteiro, R., Beldjoudi, H., Kherroubi, A.: Progress in seismic hazard modeling in Northern Algeria. In: 2nd Conference of the Arabian Journal of Geosciences (CAJG), Sousse, Tunisia, 25–28 Nov 2019

Herring, T.A., King, R.W., Floyd, M., McClusky, S.C.: Introduction to GAMIT/GLOBK, Release 10.6. Technical Report. Massachusetts Institute of Technology (2015)

Kherroubi, A.: Etude de la sismicité de la région offshore. PhD Thesis, Tlemcen University (2011)

Leprêtre, A., Klinglhoefer, F., Graindorge, D., Schnurle, P., Beslier, M. O., Yelles, K., Deverchere, J., Bracene, R.: Multiphased tectonic evolution of the Central Algerian margin from combined wide angle and reflection seismic data off Tipaza, Algeria. J. Geophys. Res. Solid Earth **118**, 3899–3916 (2013)

Meghraoui, M., Pondrelli, S.: Active faulting and transpression tectonics along the plate boundary in North Africa. Ann. Geophys. **55**, 5 (2012). https://doi.org/10.4401/ag-4970

Nocquet, J.M.: Present-day kinematics of the Mediterranean. A comprehensive overview of GPS results. Tectonophysics **578**, 220–242 (2012)

Nocquet, J.M., Calais, E.: Geodetic measurements of crustal deformation in the western Mediterranean and Europe. Pure Appl. Geophys. **161**(3), 661–681 (2004)

Ousadou, F., Dorbath, L., Ayadi, A., Dorbath, C., Gharbi, S.: Stress field variations along the Maghreb region derived from inversion of major seismic crisis fault plane solutions. Tectonophysics **632**, 261–280 (2014)

Rabaute, A., Chamot-Rooke, N.: Active tectonics of the Africa-Eurasia boundary from Algiers to Calabria. Contributor: S. Bouaziz (2014)

Soumaya, A., Ben Ayed, N., Rajabi, M., Meghraoui, M., Delvaux, D., Kadri, A.: Active faulting geometry and stress pattern near complex strike-slip systems along the Maghreb region: constraints on active convergence in the western Mediterranean. Tectonics **37** (2018). https://doi.org/10.1029/2018TC004983

Valentini, A., Visini, F., Pace, B.: Integrating faults and past earthquakes into a probabilistic seismic hazard model for peninsular Italy. Nat. Hazards Earth Syst. Sci. **17**, 2017–2039 (2017)

Visini, F., Valentini, A., Chartier, T., Scotti, O., Pace, B.: Computational tools for relaxing the fault segmentation in probabilistic seismic hazard modelling in complex fault systems. Pure Appl. Geophys. (2019). https://doi.org/10.1007/s00024-019-02114-6

Yelles-Chaouche, A.K., Allili, T., Alili, A., Messemen, W., Beldjoudi, H., Semmane, F., Kherroubi, A., Djellit, H., Larbes, Y., Haned, S., Deramchi, A., Amrani, A., Chouiref, A., Chaoui, F., Khellaf, K., Nait Sidi Said, C.: The new Algerian Digital Seismic Network (ADSN): towards an earthquake early-warning system. Adv. Geosci. **36**, 31–38 (2013). https://doi.org/10.5194/adgeo-36-31

Yelles-Chaouche, A.K., Kherroubi, A., Beldjoudi, H.: The large Algerian earthquakes (267 AD-2017). Fisica De La Terra **29**, 159–182 (2017)

Yelles-Chaouche, A.K., Lammali, K., Bellik, A., Bougrine, A., Mahsas, A., Bacha, W., Terki, T., Meliani, O., Ouzzani, F., Lakehal, Y., Ait Amir, A., Khellaf, K., Khentar, S., Chouiref, A., Bendekkan, A., Calais, E.: REGAT: a permanent GPS network in Algeria, configuration and first results. Helyon **5** (2019). https://doi.org/10.1016/j.heliyon.2019.e01435

How InSAR Can Help on the Seismic Hazard Assessment

Esra Cetin

Abstract

Interferometric synthetic aperture radar (InSAR) is a geodetic technique, particularly utilized to reveal the surface deformation according to its phase differences of two SAR images. Persistent scatterer techniques are a recent development from conventional InSAR and rely on studying pixels, which remains coherent over a sequence of interferograms. These methods can potentially measure mm-scale changes of deformation over spans of ranging from days to years. Accordingly, it allows us to study the spatial and temporal evolution of the crustal deformations. The main contributions of InSAR within the coseismic and interseismic stages of the seismic cycle are particularly in the determination of fault parameters, the distribution and partitioning of strain along faults. Besides, it has also significant contributions to investigate the seismic cycle-related slow crustal deformations, such as postseismic transients and aseismic creep. Postseismic transient signals exhibit characteristic time scales ranging from weeks to decades, which can release ~70% of the moment of the main event. Moreover, some faults slip freely, accumulating little or no strain called as fault creep. Knowledge of the extent and rate of these slow motions of the fault plane are critical for reliable seismic hazard assessments as it effectively reduces the capable area of rupture in earthquakes. Therefore, InSAR has important implications for forecasting the potential earthquakes and for understanding the fault behavior.

Keywords

InSAR • Persistent scatterers • Earthquake cycle • Postseismic • Aseismic creep

1 Introduction

Crustal deformation observations by satellite geodesy have significantly contributed to our understanding of tectonics. Measurements of surface deformation are routinely used to constrain the subsurface geometry of active faults and the spatial distribution of interseismic, coseismic, postseismic and aseismic creeps. Recent developments in InSAR have led to a dramatic improvement in the quantity and quality of deformation measurements of the earthquake cycle (e.g., Wright 2002; Akoglu et al. 2006; Peyret et al. 2011; Cakir et al. 2012). Since its application to the 1992 Landers earthquake (Massonnet et al. 1993), the conventional InSAR technique has been widely used for measuring the coseismic and interseismic displacements associated with continental earthquakes. But, recent advanced techniques of InSAR, called persistent scatterers, also allow us examine and constrain postseismic and aseismic slips according to its possibility to produce time series and capability of mapping subtle surface deformation. Earthquake cycle-related slow crustal motions' contributions to the seismic hazard assessments are emphasized in this study relying on the case studies within the Africa-Eurasia Convergence Zone.

2 Methods

InSAR is a powerful technique for measuring surface deformation because of the high spatial resolution achieved and the ability to acquire the data remotely. Conventional InSAR techniques are based on the phase differences of two SAR images acquired before and after the earthquake (Massonnet et al. 1993). On the other hand, recent advanced techniques, relying on the coherent pixels over time, called persistent scatterers (PS), increase the number of locations where a deformation signal can be extracted and reduce the associated error with regard to involve the simultaneous processing of multiple SAR acquisitions in time (Ferretti

E. Cetin (✉)
Mugla Sitki Kocman University, 48000 Mugla, Turkey
e-mail: esracetin@mu.edu.tr

M. Meghraoui et al. (eds.), *Advances in Geophysics, Tectonics and Petroleum Geosciences*,
Advances in Science, Technology & Innovation, https://doi.org/10.1007/978-3-030-73026-0_22

et al. 2000; Hooper 2008; Hooper et al. 2007). Furthermore, subsurface analysis is required to understand the evolution of the crustal deformation. Accordingly, the inverse modeling using 3D elastic dislocations on triangular faults has been utilized to obtain the slip distribution (Maerten et al. 2005).

3 Results

The postseismic deformation of the May 21, 2003, (Mw 6.6) Zemmouri earthquake (Algeria) has been studied using the InSAR method. Figure 1 shows the cumulative surface displacement of seven years obtained from PS-InSAR. Modeling results suggest a shallow after-slip movement and a complementary coseismic and postseismic slip as commonly observed for other moderate–large earthquakes (see Fig. 1) (Reilinger et al. 2000; Cetin et al. 2012). The cumulative postseismic moment is equivalent to an Mw 6.3 earthquake for the 2003 Zemmouri earthquake. Moreover, according to other case studies, the postseismic deformation can release ~70% of the moment of the main event (see Table S1 in Fattahi et al. 2015).

The creeping section of the North Anatolian Fault (NAF) at Ismetpaşa has been studied using InSAR data with elastic dislocation models. According to the InSAR analysis shown in Fig. 2, the creep rate is found to fluctuate along a 100-km-long section of the fault, reaching a maximum of ~20 ± 2 mm/yr, and it is in the range of 8 ± 2 mm/yr at Ismetpaşa. Modeling of the InSAR data reveals a heterogeneous creep distribution confined mostly to the uppermost 5 km portion of the seismogenic crust, releasing annually a 6.2×10^{16} Nm (Mw 5.1) geodetic moment. The analysis suggests that the creep might have started as a postseismic deformation following the 1944 earthquake, and has evolved to a stable fault creep with time (Cetin et al. 2014).

Consequently, postseismic transients have a significant impact on the reducing accumulated strain along the fault rupture. And the creeping sections may accumulate little or no strain and generate no significant earthquakes. Knowledge of the extent and rate of postseismic or aseismic slip on the fault plane is therefore critical for obtaining a reliable assessment of seismic hazard as it effectively reduces the fault surface area capable of rupture in earthquakes.

4 Discussion and Conclusions

Realistic seismic hazard analysis must be able to explain the interaction of aseismic and seismic slips, the segmentation of faults and the strong spatial variations in the intensity of strong shakings. In this study, the InSAR analysis suggested that the cumulative postseismic moment can release 20–30%, max ~70%, of the main event. Additionally, surface creep of the NAF might have started as a postseismic deformation about 70 years ago, after two large earthquakes (Mw 7.3–6.9), and it is annually releasing Mw 5.1 earthquake moment. As a conclusion, postseismic and aseismic slips effectively reduce the fault surface area capable of rupture during earthquakes. Therefore, satellite geodesy observations, particularly InSAR, have significantly contributed to our understanding of the earthquake cycle and build reliable hazard assessments.

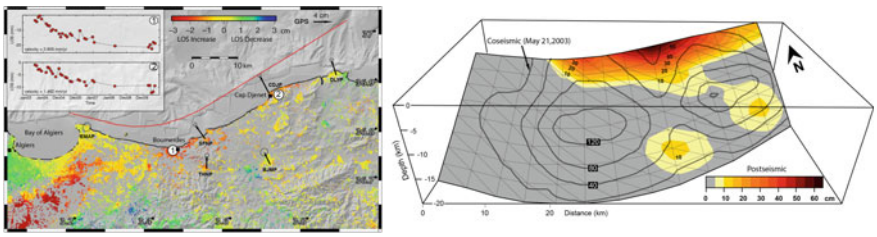

Fig. 1 (Left) Seven-year postseismic cumulative displacements of the 2003 Zemmouri earthquake. Inset shows time series of InSAR data (red circles). (Right) Color codes are after-slip distribution and black dashed lines show the coseismic slip distribution (see related figures in Cetin et al. 2012)

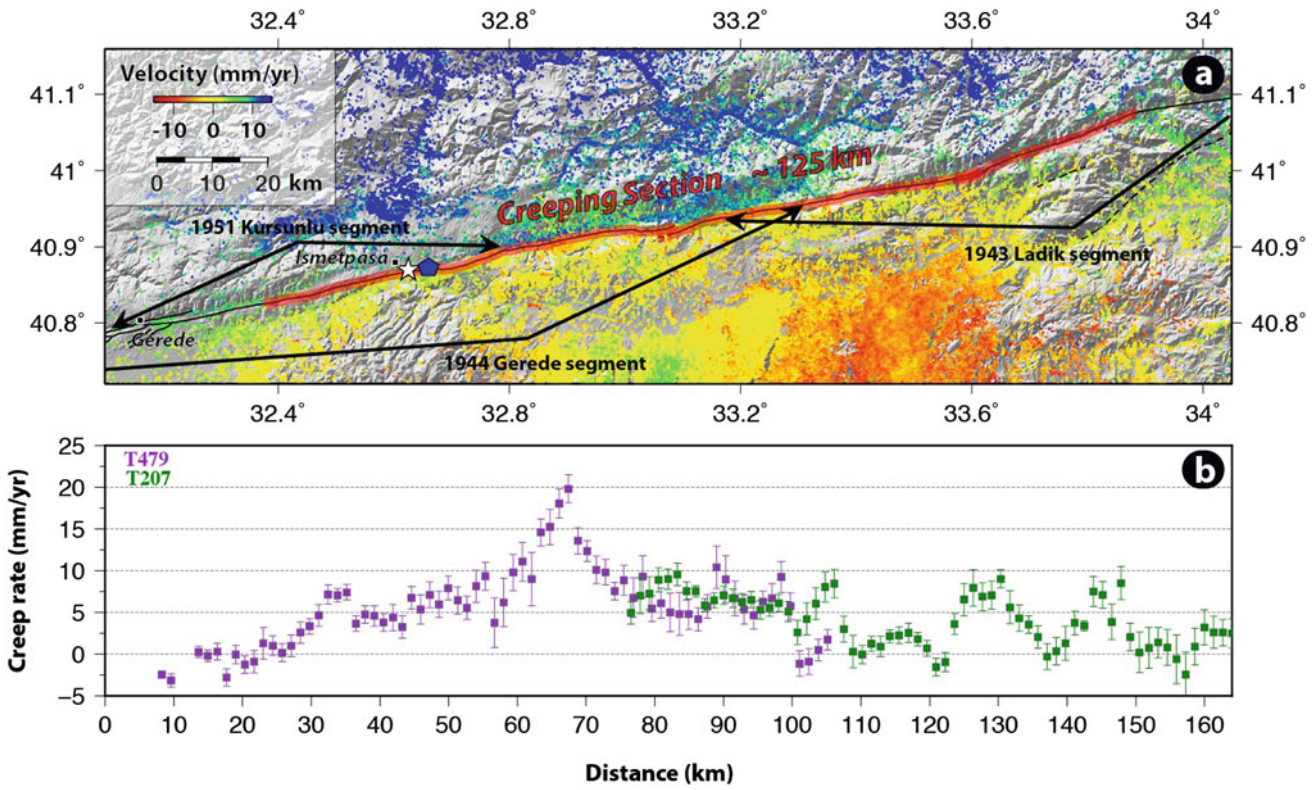

Fig. 2 **a** A "mosaic" map of fault-parallel horizontal velocity field. The red line shows the creeping section of the NAF. **b** Creep rates with error bars along the fault are estimated from the InSAR velocities (see related figures in Cetin et al. 2014)

References

Akoglu, A.M., Cakir, Z., Meghraoui, M., Belabbes, S., El Alami, S.O., Ergintav, S., Akyuz, H.S.: The 1994–2004 Al Hoceima (Morocco) earthquake sequence: conjugate fault ruptures deduced from InSAR. Earth Planet. Sci. Lett. **252**, 467–480 (2006)

Cakir, Z., Ergintav, S., Ozener, H., Dogan, U., Akoglu, A.M., Meghraoui, M., Reilinger, R.: Onset of aseismic creep on major strike-slip faults. Geology **40**(12), 1115–1118 (2012). Bakun, W.H., Aagaard, B., Dost, B., Ellsworth, W.L., Hardebeck, J.L., Harris, R. A., et al.: Implications for prediction and hazard assessment from the 2004 Parkfield earthquake. Nature **437**(7061), 969–974 (2005)

Cetin, E., Meghraoui, M., Cakir, Z., Akoglu, A.M., Mimouni, O., Chebbah, M.: Seven years of postseismic deformation following the 2003 Mw=6.8 Zemmouri earthquake (Algeria) from InSAR time series. Geophys. Res. Lett. **39**, L10307 (2012)

Cetin, E., Cakir, Z., Meghraoui, M., Ergintav, S., Akoglu, A.M.: Extent and distribution of aseismic slip on the Ismetpaşa segment of the North Anatolian Fault (Turkey) from persistent scatterer InSAR. Geochem. Geophys. Geosyst. **15**, 2883–2894 (2014)

Fattahi, H., Amelung, F., Chaussard, E., Wdowinski, S.: Coseismic and postseismic deformation due to the 2007 M5.5 Ghazaband fault earthquake, Balochistan, Pakistan. Geophys. Res. Lett. **42**(9), 3305–3312 (2015)

Ferretti, A., Prati, C., Rocca, F.: Nonlinear subsidence rate estimation using permanent scatterers in differential SAR interferometry. IEEE Trans. Geosci. Remote Sens. **38**, 2202–2212 (2000)

Hooper, A.: A multi-temporal InSAR method incorporating both persistent scatterer and small baseline approaches. Geophys. Res. Lett. **35**(16) (2008)

Hooper, A., Segall, P., Zebker, H.: Persistent scatterer interferometric synthetic aperture radar for crustal deformation analysis, with application to Volcan Alcedo, Galapagos. J. Geophys. Res. **112**, B07407 (2007)

Maerten, F., Resor, P., Pollard, D., Maerten, L.: Inverting for slip on three dimensional fault surfaces using angular dislocations. Bull. Seismol. Soc. Am. **95**(5), 1654–1665 (2005)

Massonnet, D., Rossi, M., Carmona, C., Adragna, F., Peltzer, G., Feigl, K., Rabaute, T.: The displacement field of the Landers earthquake mapped by radar interferometry. Nature **364**, 138–142 (1993)

Peyret, M., Dominguez, S., Cattin, R., Champenois, J., Leroy, M., Zajac, A.: Present-day interseismic surface deformation along the Longitudinal Valley, eastern Taiwan, from a PS-InSAR analysis of the ERS satellite archives. J. Geophys. Res. **116**, B03402 (2011)

Reilinger, R.E., Ergintav, S., Bürgmann, R., McClusky, S., Lenk, O., Barka, A., et al.: Coseismic and postseismic fault slip for the 17 August 1999, M=7.5, Izmit, Turkey Earthquake. Science **289** (5484), 1519–1524 (2000)

Wright, T.: Remote monitoring of the earthquake cycle using satellite radar interferometry. Philos. Trans. R. Soc. Lond. Ser. A Math. Phys. Eng. Sci. **360**(1801), 2873–2888 (2002)

Surface Deformation Monitoring from SAR Interferometry for Seismic Hazard Assessment Around Major Active Faults: Case of Zemmouri Earthquake (Algeria)

Samir Aguemoune, Abdelhakim Ayadi, Aichouche Belhadj-Aissa, and Mourad Bezzeghoud

Abstract

In seismogenic zones, geodetic campaigns are usually used to monitor the ground deformation. Nowadays, satellite imaging became a powerful tool to monitor surface deformation on very large areas using InSAR (Interferometry Synthetic Aperture Radar). To get reliable results, reducing errors became a real challenge. We recently proposed a new phase unwrapping procedure and a new technique to reduce atmospheric errors. These techniques were assembled to develop a new InSAR time series methods named ISBAS (Improved Small BAseline Subsets). We tested our procedure on Zemmouri (Algeria) seismogenic zone struck by an Mw 6.8 earthquake in 2003. Several SAR images from ENVISAT satellite were used in combination with data from MERIS tool embedded on the same satellite to monitor post-seismic deformation. Our analysis highlights the zones of significant deformation due to not only post-seismic seismic movement, but also to other anthropogenic origin. This kind of studies can really help to better assess the seismic hazard around major active fault such as that of Zemmouri and on other active sources that could generates strong seismic events.

Keywords

InSAR • Surface deformation • Atmospheric wet delay • Phase unwrapping • Earthquakes

S. Aguemoune (✉) · A. Ayadi
Centre de Recherche en Astronomie Astrophysique et Géophysique, Algiers, Algeria

S. Aguemoune · A. Belhadj-Aissa
Université des Sciences et de la Technologie Houari Boumedienne, Bab Ezzouar, Algiers, Algeria

M. Bezzeghoud
Universidad de Evora, Evora, Portugal
e-mail: mourad@uevora.pt

1 Introduction

SAR interferometry is now widely used to monitor surface deformation over seismogenic zones. We have implemented a new approach to get better results of ground deformation using a series of images on 7 years' time span. In this study, we have proposed a new approach to implement phase unwrapping and reducing water vapor delay from interferograms. Two steps are necessary in order to obtain reliable results. Recently, the reduction of the atmospheric phase delay using space-based near-infrared water vapor data [e.g., ESA Medium Resolution Imaging Spectrometer (MERIS)] has been successfully demonstrated (Li et al. 2009; Aguemoune et al. 2019). We present in this study the potential of using MERIS water vapor product to correct atmospheric effects on ASAR (Advanced Synthetic Aperture Radar) interferograms. This study provides an inter-comparison of atmospheric correction effects between two methods: The first method is the SBAS (Small BAseline Subsets) classic (Berdino et al. 2002) which uses atmospheric filtering operations model, and the second one is the SBAS integrated with MERIS correction model appalled ISBAS. This work has been evaluated by applying it to an investigation of the post-seismic surface deformation of the 2003 MW 6.8 Zemmouri earthquake (Fig. 1a), using ASAR and MERIS data acquired from 2003 to 2010 by ENVISAT (ENVIronment SATellite).

2 Data Analysis and Processing

The SBAS and ISBAS processing could be divided into two main steps: The pre-processing step represents the core of the SBAS and ISBAS algorithm, which begins from the SAR images pair selection until the phase unwrapping. We note that both SBAS and ISBAS methods have the same pre-processing step. The selection criteria of the SAR images for the interferograms generation are characterized by small

M. Meghraoui et al. (eds.), *Advances in Geophysics, Tectonics and Petroleum Geosciences*,
Advances in Science, Technology & Innovation, https://doi.org/10.1007/978-3-030-73026-0_23

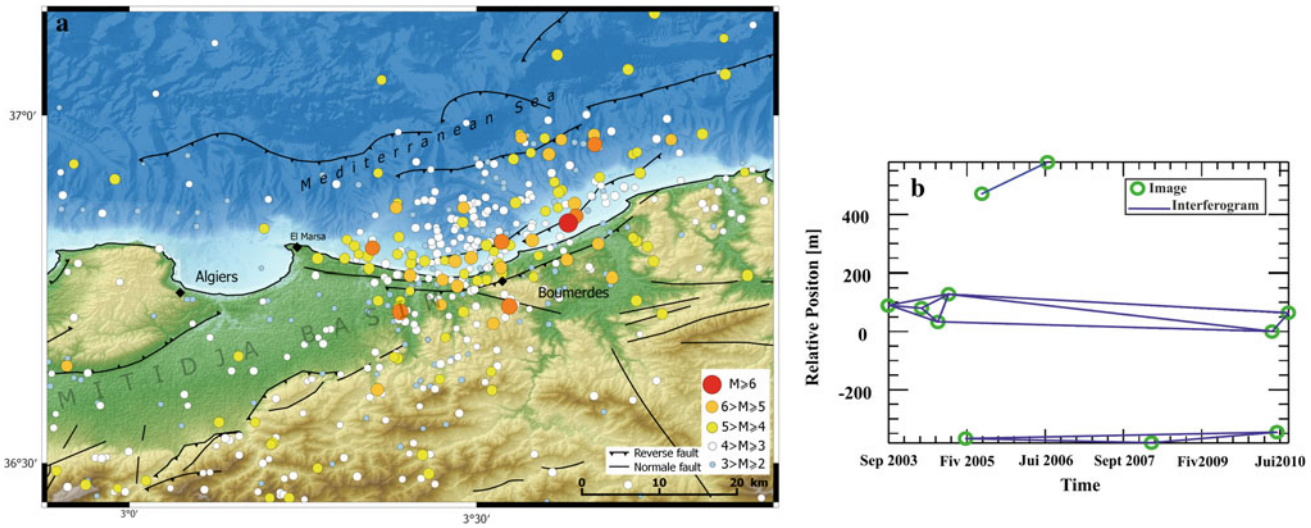

Fig. 1 **a** Seismotectonic map of the study area. **b** Spatial and temporal configuration of interferometric pairs

spatial and temporal base lines (Fig. 1b). The total number of interferograms used in the final analysis is 14 interferograms, which are temporally overlapped to preserve the capability of the system to retrieve 7 years of post-seismic deformation. The unwrapping phases of the multi-look interferograms were determined by using the path unwrapping method proposed by (Aguemoune et al. 2014) to avoid propagation errors. It is important to note that for the ISBAS method; the phase unwrapping is done after the correction of the atmospheric wet delay by the approach developed by Aguemoune et al. (2019).

The post-processing step of both SBAS and ISBAS methods is summarized in three successive steps as following:

a. **SBAS post-processing**

Based on the fact that the atmospheric phase signal component is characterized by high correlation in space but poorly in time, the atmospheric component can be isolated from temporally correlated displacement components of the system using a filtering operation performed on the output of the based procedure. The post-processing of SBAS method is summarized in four successive steps as following:

1. Generate a system of equations of the unwrapping interferograms by assuming a linear model of deformation (Deformation = Velocity × Time).
2. Resolve the system of equations by using SVD method (Singular Values Decomposition) to estimate the average velocity of deformation and the topographical error.
3. Correction of atmospheric delays by a cascade of spatial filtering (low pass) and a temporal filtering (high pass).
4. Final estimation of the corrected surface deformation velocity.

b. **ISBAS post-processing**

The atmospheric wet delay model used in ISBAS method is based on the use of auxiliary water vapor data of each image (MERIS images) to correct all interferograms. We adopted an adequate logarithmic deformation model to assure more accurate results in space and time.

The post-processing of ISBAS method is summarized in two successive steps as following:

1. Generate a system of equations of the unwrapping interferograms by assuming a linear model of deformation (Deformation = Velocity × Log(Time)).
2. Resolve the system of equations by using SVD method to estimate the average velocity of deformation and the topographical error.

3 Results and Discussion

The map of cumulative surface deformation (Fig. 2a) obtained by SBAS method reveals two zones of important subsidence. The first zone spreads over a large area in the Mitidja basin and reaches 45 mm of cumulative surface deformation. The second zones located in the coastal zone in

Zemmouri area (rupture area), which shows a lower cumulative surface deformation, ∼20 mm less than that observed in the Mitidja basin. We note that these results agree with those obtained by Cetin et al. (2012). However, the ISBAS method also shows the existence of two zones of subsidence, but the zones of high value of cumulative surface deformation ∼45 mm is located along the rupture zone (Fig. 2b, area surrounded by a square); while the zone of low value of cumulative surface deformation ∼25 mm is localized in subsiding districts in the Mitidja basin.

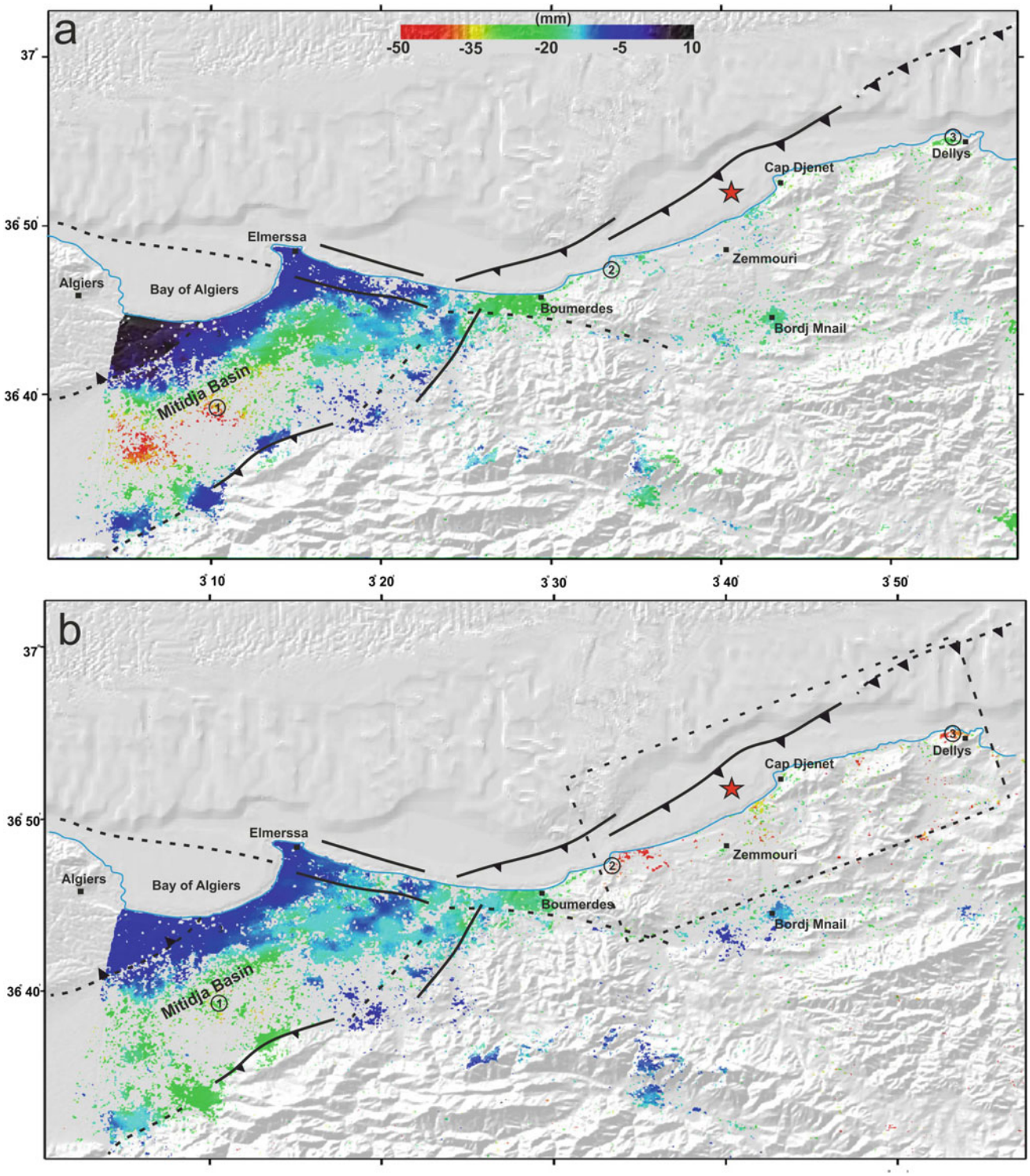

Fig. 2 **a** Cumulative surface deformation obtained by SBAS. **b** Cumulative surface deformation obtained by ISBAS

4 Conclusions

The results show that the ISBAS method has well defined the spatial post-seismic surface deformation. These results confirm the rupture models obtained by Beldjoudi (2017). This study shows that the phase unwrapping method, the atmospheric wet delay and the choice of the deformation model are very important to assure reliable results. The phase unwrapping method used in this study allows us to localize phase unwrapping errors and avoid their propagation over the scene. The atmospheric wet delay model from auxiliary water vapor data of each individual image (MERIS) is used to correct all interferograms. The a priori logarithmic deformation model allows us to assure more accurate results in space and time.

References

Aguemoune, S., Hocine, F., Belhadj-Aissa, A., Ayadi, A.: 2-D phase unwrapping algorithm based on pseudocorrelation quality map. J. Image Graph. **2**(2), 94–99 (2014). https://doi.org/10.12720/joig.2.2.94-99

Aguemoune, S., Ayadi, A., Belhadj-Aissa, A., Bezzeghoud, M.: A novel interpolation method for InSAR atmospheric wet delay correction. J. Appl. Geophys. (2019). https://doi.org/10.1016/j.jappgeo.2019.02.013

Beldjoudi, H.: Modélisation de la source des séismes par inversion des données sismologiques et géodésiques: application aux séismes du Nord de l'Algérie. Université de Côte d'Azur. https://tel.archives-ouvertes.fr/tel-01615648/document (2017)

Berardino, P., Fornaro, G., Lanari, R., & Sansosti, E.: A new algorithm for surface deformation monitoring based on Small Baseline Differential SAR Interferograms. IEEE Transactions on Geoscience and Remote Sensing, 40(11), 2375−2383 (2002)

Cetin, E., Meghraoui, M., Cakir, Z., Akoglu, A.M., Mimouni, O., Chebbah, M.: Seven years of postseismic deformation following the 2003 Mw = 6.8 Zemmouri earthquake (Algeria) from InSAR time series. Geophys. Res. Lett. **39**, L10307 (2012). https://doi.org/10.1029/2012GL051344

Li, Z., Fielding, E.J., Cross, P., Preusker, R.: Advanced InSAR atmospheric correction: MERIS/MODIS combination and stacked water vapour models. Int. J. Remote Sens. (2009)

The Use of an ELMI for Measuring the Movement of the Trougout and the Ajdir-Imzouren Faults—(North East of the RIF) MOROCCO—Between 2017 and 2019

Morad Taher and Taoufik Mourabit

Abstract

Due to the seismic risk in the Al-Hoceima area, many studies have been carried out in order to understand seismicity, seismotectonics and structural geology, especially after the last earthquakes in the years of 1994 (Mw = 5.4), 2004 (Mw = 6.3) and 2016 (Mw = 6.1). To improve seismic risk assessment and to map the velocity field of active faults that affect the region, various techniques and methods must be used. We propose in this study the use of an Electronic Length Measuring Instrument (ELMI) to study and follow the horizontal movement of the Trougout and Ajdir-Imzouren faults. After two years (from 2017 to 2019) of preliminary observation, the determined rate of horizontal movement is 5.5 mm/yr (± 2 mm).

Keywords

Movement • Nekor basin • Station Leica • Topometric • Trougout fault

1 Introduction

The geodynamic activity of the western Mediterranean is very complex (Serpelloni et al. 2007) because of its location on the borders of the two tectonic plates, African and Eurasian. The Rif chain is one of the results of geodynamic activity of the western Mediterranean (Fig. 1), and the Rif is an alpine chain of 300 km length and 100 km width in the northern region of Morocco (Di Bucci et al. 2010), which stretches between 34–36° N latitude and 2–7° W longitude. It is a very contrasting mountain range where the humid forest landscapes in the West are opposed to the semiarid and steppe massifs of the East.

Because the convergence of these two plates (Morel 1989; Meghraoui and Pondrelli 2012) enduring activities along major faults in Nekor basin (Trougout fault, Ajdir-Imzouren fault, Boussekour fault, Rouadi fault) are caused generating strong seismic events. The aim of this study is measuring the horizontal movements of the Trougout fault and the Ajdir-Imzouren fault using ELMI technique for providing the best explanations for these seismic activities that affect the region.

2 Study Area

The study area (Fig. 1) is located between longitudes W3° 55′–3° 45′ and latitudes N35° 15′–N35° 05′, situated in the Rif region, northeast of Morocco. The study area is a lower Nekor basin located southeast of Al-Hoceima, and it is characterized by low slope gradients and low elevation (Taher et al. 2019). This region has been affected by strong seismic events such as the Mw 6.0 earthquake on May 26, 1994, the Mw 6.4 earthquake on February 24, 2004, and the Mw 6.4 earthquake on January 25, 2016 (Taher et al. 2019; El Alami et al. 1998; Tahayt et al. 2009; Medina and El Alami 2006; Van der Woerd et al. 2014; Buforn et al. 2017; Stich et al. 2005; Cakir et al. 2006). The Trougout fault (N–S) (Fig. 2a), which runs along the eastern boundary of the lower Nekor basin (Fig. 2) (Medina 1995), marks the contact between andesitic breccia of the Tortonian-Messinian Ras Tarf formation or Flysch nappes and the Quaternary Nekor deposits (Poujoul et al. 2014). The Trougout Fault corresponds to the main fault separating Al-Hoceima Bay to the west of the Ras Tarf volcanic massif to the east. At the El Hadid site, a 9 m high escarpment (Fig. 2b) shows oblique striations (N5° E/82° W, 60° S pitch) (Poujoul et al. 2014). The speed of vertical displacement along the Trougout fault, estimated from the morphotectonic markers, is 2 mm/year

M. Taher (✉) · T. Mourabit
Abdelmalek Essaadi University, Ziaten, B.P. 416, Tetouan, Morocco

M. Meghraoui et al. (eds.), *Advances in Geophysics, Tectonics and Petroleum Geosciences*,
Advances in Science, Technology & Innovation, https://doi.org/10.1007/978-3-030-73026-0_24

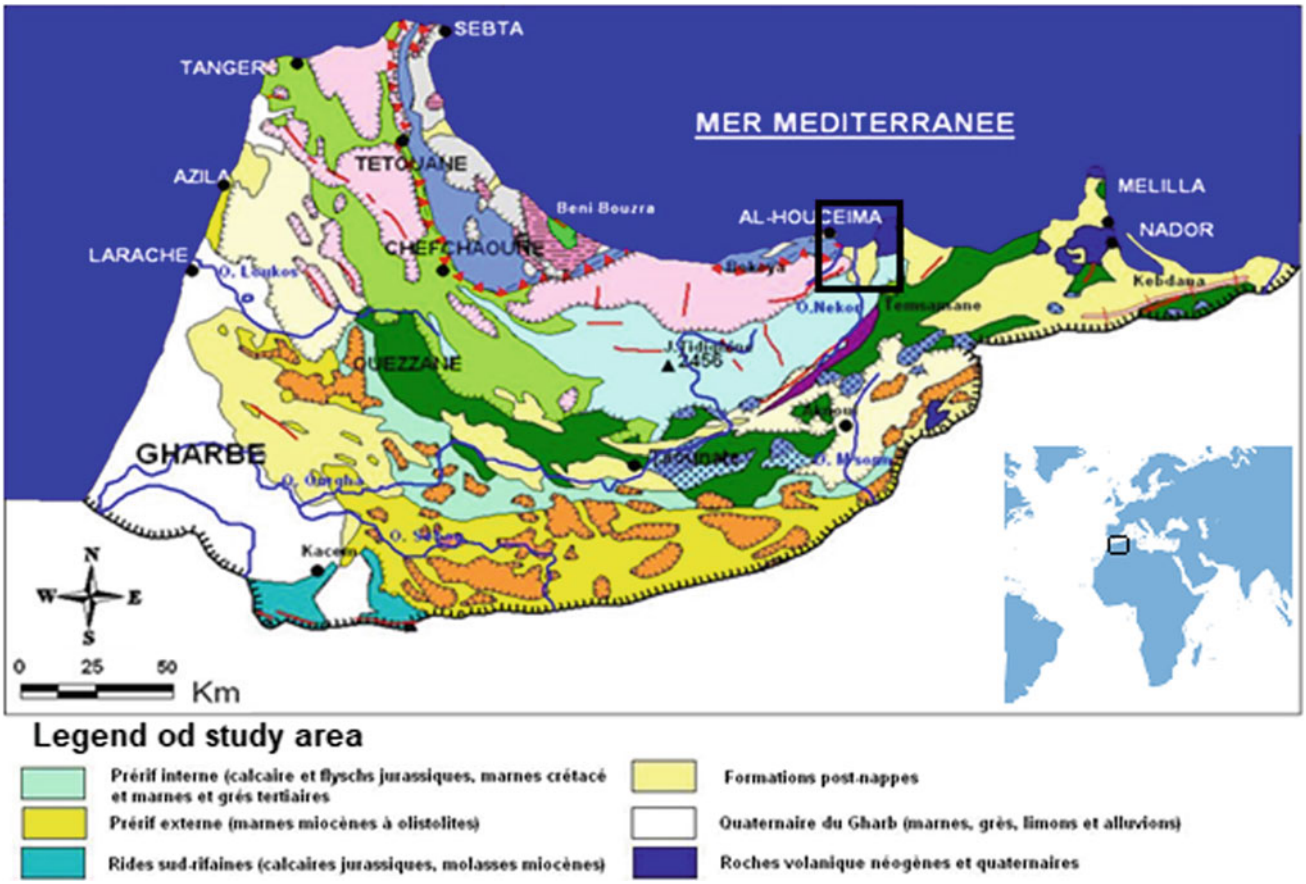

Fig. 1 Geological map of the Rif chain. The square shows study area

(Poujoul et al. 2014). The Ajdir-Imzouren fault (NNW–SSE) (Fig. 2c) runs along the western boundary of the lower Nekor basin; it marks the contact between flysch marno limestone of the Cenomanian-Santonian and the Quaternary Nekor deposits (Taher et al. 2019).

3 Methodology

The objective of our study is to accurately determine the movement of Trougout Fault using IMEL or distance meter; a device that works most often by emission of an electromagnetic wave, allowing the measurement of the phase shift of the echo of this wave returned by a reflector (Milles and Lagofun 1999). The principle adopted in this study is to measure the variations of the exact position (Table 1) of some points located on either side of the Trougout fault and the Ajdir-Imzouren fault. The reference points precisely located by a total station equipped with a laser system (Fig. 3b) are measured periodically with the same station and in close climatic conditions.

4 Result and Discussion

The results (Table 2) show that the horizontal activities of Trougout fault and Ajdir-Imzouren fault are by average 5.5 mm per year. After several attempts to measure, at the first time, we concluded that the incertitude is equal to 2 mm. For the Trougout fault, we have suitable conditions (Fig. 3a) for measurement: Flat ground, solid rocks to install the screws at close distance and absence of human activities. In contrast of Ajdir-Imzouren fault, the results cannot be taken as seriously as we wish because of the lack of perfect conditions, like sloped ground, human activities and installing the screws at a far distance (Fig. 3c), which can affect the measurement.

The obtained results are greater than the estimated rate from the morphotectonic marker which is 1.5 mm/year (Poujoul et al. 2014). These results can be explained by the relatively low convergence between Africa and Eurasia plates with a rate of 3–6 mm/yr (McKenzie 1972; Buforn et al. 2004; Nocquet and Calais 2004) is related to an oblique

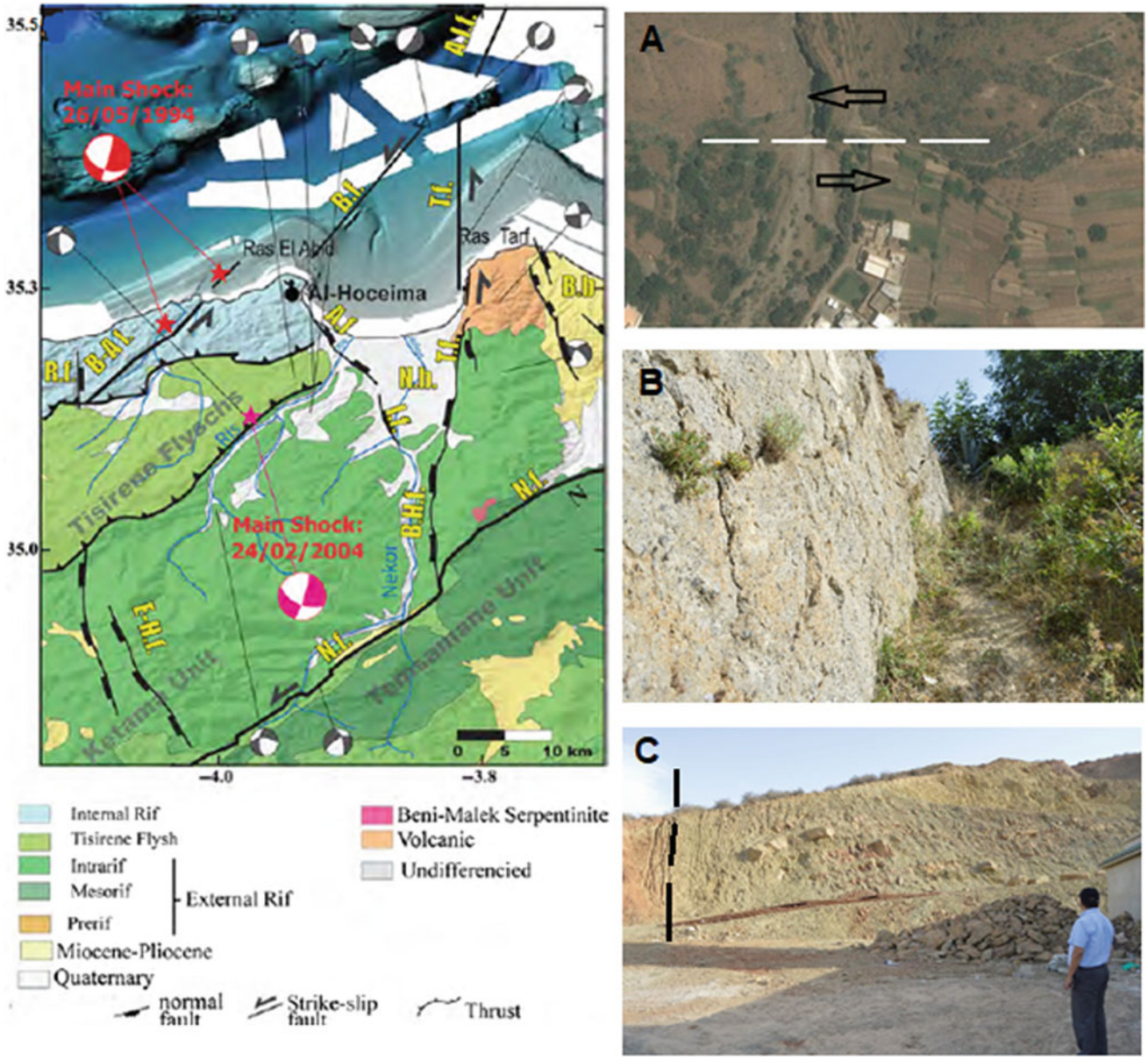

Fig. 2 Regional map of the recent active structures. A.f., Ajdir fault; B.H.f., Bou Haddad fault; R.f., Rouadi fault, B.f, Bokkoya fault, B.-A.f., Bousekkour–Aghbal fault, I.f., Imzouren fault; T.f., Trougout fault; A.I.f., Al-Idrissi fault; N.f., Nekor fault, E-H.f., El-Hammam fault (Lafosse et al. 2016). **a** Trougout fault. **b** Escarpment of Trougout fault. **c** Ajdir-Imzouren fault

Table 1 The geographic coordinates of the measurement points

Point	*X*	*Y*
A	649,055	514,845
B	649,069	514,856
E	637,633	510,828
F	637,671	510,890

Fig. 3 The use of station Leica TS02 equipped with laser. **a** Measurement in the Trougout fault. **b** Laser emitted by station. **c** Measurement in the Ajdir-Imzouren fault

Table 2 Measurement results

			Measured variation	
Fault	Profile	08/2017	08/2018	08/2019
Trougout	AB	0	10 mm ± 2	01 mm ± 2
Ajdir-Imzouren	EF	0	1 mm ± 2	10 mm ± 2

convergence along the western section of North Africa which shows an increasing eastward rate of 3–5 mm/yr (DeMets et al. 1994).

5 Conclusion

The stations offer the advantage of independence, where the precision to the hundredth of a millimeter is sought. The use of this technique for scientific purpose is cheap compared with GPS. But for the sake of obtaining good results, using this technique is better to continue measuring over a longer period of more than two years. Finally, this technique equipped with a laser has proved usefulness of horizontal movement measurement of faults for defining geodynamic activity in Low Nekor basin.

Acknowledgements The authors wish to thank Ben Lkadi Mohammed, technician in "société topographie modern. sarl" TOPO-MOD Al-Hoceima for facilitating the use of total station Leica TS02 to take the measurements.

References

Buforn, E., Bezzeghoud, M., Udias, A., Pro, C.: Seismic sources on the Iberia–African plate boundary and their tectonic implications. Pure Appl. Geophys. **161**, 1–24 (2004)

Buforn, E., Pro, C., Sanz de Galdeano, C., Cantavella, J.V., Cesca, S., Caldeira, B., Udias, A., Mattesini, M.: The 2016 south Alboran earthquake (Mw = 6.4): a reactivation of the Ibero-Maghrebian region? Tectonophysics **712–713**, 704–715 (2017)

Cakir, Z., Meghraoui, M., Akoglu, A.M., Jabour, N., Belabbes, S., Ait-Brahim, L.: Surface deformation associated with the Mw 6.4, 24 February 2004 Al- Hoceima, Morocco, earthquake deduced from InSAR; implications for the active tectonics along North Africa. Bull. Seism. Soc. Am. **96**, 59–68 (2006)

DeMets, C., Gordon, R.G., Argus, D.F., Stein, S.: Effect of recent revisions to the geomagnetic reversal timescale on estimates of current plate motions. Geophys. Res. Lett. **21**, 2191–2194 (1994)

Di Bucci, D., Burrato, P., Vannoli, P., Valensise, G.: Tectonic evidence for the ongoing Africa-Eurasia convergence in central Mediterranean foreland areas: a journey among long-lived shear zones, large earthquakes, and elusive fault motions. J. Geophys. Res. **115**, B12404, P1–17 (2010). https://doi.org/10.1029/2009JB006480

El Alami, S.O., Tadili, B.A., Cherkaoui, T.E., Medina, F., Ramdani, M., Ait Brahim, L., Harnaff, M.: The Al-Hoceima earthquake of May 26, 1994 and its aftershocks: a seismotectonic study. Ann. Geofis. **41**, 519–537 (1998)

Lafosse, M., d'Acremont, E., Rabaute, A., Mercier de Lépinay, B., Tahayt, A., Ammar, A., Gorini, C.: Evidence of quaternary transtensional tectonics in the Nekor basin (NE Morocco). Basin Res. 1–20 (2016). https://doi.org/10.1111/bre.12185

McKenzie, D.P.: Active tectonics of the Mediterranean region. Geophys. J. R. Astr. Soc. **30**, 109–185 (1972)

Medina, F.: Present-day state of stress in northern Morocco from focal mechanism analysis. J. Struct. Geol. **17**(7), 1035–1446 (1995)

Medina, F., El Alami, S.O.: Focal mechanisms and state of stress in the Al-Hoceima area (Central Rif, Morocco). Bull. Inst. Sci. Rabat Sect. Sci. Terre **28**, 19–30 (2006)

Meghraoui, M., Pondrelli, S.: Active faulting and transpression tectonics along the plate boundary in North Africa. Ann. Geophys. **55**(5) (2012). https://doi.org/10.4401/ag-4970

Milles, S., Lagofun, J.: Topographie et topométrie modernes: Techniques de mesure et de représentation 1, pp. 297–300. Éditions Eyrolles (1999). ISBN13: 978-2-212-02287-2

Morel, J.L.: Etats de contrainte et cinématique de la chaîne rifaine (Maroc) du Tortonien à l'actuel. Geodin. Acta **3**, 283–294 (1989)

Nocquet, J.M., Calais, E.: Geodetic measurements of crustal deformation in the western Mediterranean and Europe. Pure Appl. Geophys. **161**, 661–681 (2004). https://doi.org/10.1007/s00024-003-2468-z

Poujoul, A., Ritz, J.F., Tahayt, A., Vernant, P., Condomines, M., Blard, P.H., Billant, J.: Active tectonics of the Northern Rif (Morocco) from geomorphic and geochronological data. J. Geodyn. (2014). https://doi.org/10.1016/j.jog.2014.01.004

Serpelloni, E., Vannucci, G., Pondrelli, S., Argnani, A., Casula, G., Anzidei, M., Baldi, P., Gasperini, P.: Kinematics of the Western Africa-Eurasia plate boundary from focal mechanisms and GPS data. Geophys. J. Int. **169**(3), 1180–1200 (2007). https://doi.org/10.1111/j.1365-246X.2007.03367.x

Stich, D., Mancilla, F., Baumont, D., Morales, J.: Source analysis of the Mw 6.3 2004 Al-Hoceima earthquake (Morocco) using regional apparent source time functions. J. Geophys. Res. **110**, B06306 (2005). https://doi.org/10.1029/2004JB003366

Tahayt, A., Feigl, K.L., Mourabit, T., Rigo, A., Reilinger, R., McClusky, S., Fadil, A., Berthier, E., Dorbath, L., Serroukh, M., Gomez, F., Ben Sari, D.: The Al-Hoceima (Morocco) earthquake of 24 February 2004, analysis and interpretation of data from ENVISAT ASAR and SPOT5 validated by ground-based observations. Remote Sens. Environ. **113**, 306–316 (2009)

Taher, M., Lmourabet, T., Boulaassal, H.: Measuring vertical deformation of the low-Nekor basin due to 2016 Alboran Mw6.4 earthquake by using DInSAR analysis. IREHM **7**(1) (2019)

Van der Woerd, J., Dorbath, C., Ousadou, F., Dorbath, L., Delouis, B., Jacques, E., Tapponnier, P., Hahou, Y., Menzhi, M., Frogneux, M., Haessler, H.: The Al-Hoceima Mw 6.4 earthquake of 24 February 2004 and its aftershocks sequence. J. Geodyn. **77**, 89–109 (2014)

Land and Sea Earthquakes Triggered by Groundwater Fluctuation Due to the Hydrologic Cycle in South Korea

Suk Hwan Jang, Kyoung Doo Oh, Jae-Kyoung Lee, and Jun Won Jo

Abstract

It was hypothesized that groundwater flow could trigger earthquakes both in lands and seas due to its seasonal fluctuation following the Monsoon season in South Korea. An earthquake catalogue compiled by Korea Meteorological Administration from 1978 till 2017 was analyzed to test this hypothesis. For the earthquakes that occurred in lands, a six-month land earthquake active period from August to January was identified following the Monsoon season lasting from June till September in South Korea. One or two month delay between the peak rainy months of July and August and the peak land earthquake energy month of September was supposed to be the time necessary for groundwater recharge and pressure propagation in fault zones. The other six-month period from February to July was inactive for land earthquakes showing a relatively low level of earthquake energy. Meanwhile, for the earthquakes occurred in seas, another six-month sea earthquake active period from February to July, delayed by six months from that of lands, was also identified. Six month delay between earthquake active periods in lands and seas was supposed to be travel time for groundwater to flow from lands to seas. In addition to the seasonal variation of earthquake count and energy, fairly good correlations of them between land and sea earthquakes seem to be a probable indicator of hydro-seismicity in Korean Peninsula. These hypotheses need more thorough study in the future. Considering constant movement of tectonic plates which builds up intra-plate stress in South Korea, cyclic bursts of earthquake energy release, supposed to be triggered by groundwater fluctuation, seem to be playing the role of invisible hands which prevents excessive accumulation of geotectonic energy in the crust. On-going climatic change that might bring about abnormal behavior of hydrologic cycle may change not only the spatial and temporal pattern, but also the magnitude of earthquakes occurring in South Korea in the future.

Keywords

Earthquake trigger • Groundwater • Hydrologic cycle • Monsoon • Hydro-seismicity

1 Introduction

South Korea, which is located in intra-plate seismic zone, has been long believed to be a relatively safe place from earthquake threat. However, the recent M_L 5.8 earthquake occurred in Gyeongju City on the 12th of September 2016 has changed this belief altogether. This research was also stemmed from this changed view of earthquake threat in South Korea. For the cause of the Gyeongju earthquake, there has been no firm conclusion yet. Many research projects have been launched since this earthquake drew national concern about potential catastrophic earthquake hazard. Most researches have focused on active faults, the traditional theme of earthquake research in South Korea.

However, our main theme of the research has been a possible relation between seismicity and hydrological cycle in Korean Peninsula.

Costain and Bollinger (2010) proposed that naturally occurring earthquakes anywhere on Earth belong to one of two types: (1) inter-plate seismicity associated with the dynamics of plate tectonics and (2) intra-plate seismicity associated with the dynamics of the hydrological cycle. This

S. H. Jang · J.-K. Lee · J. W. Jo
Daejin University, 1007, Hoguk-ro, Pocheon-si, Gyeonggi-do 11159, Republic of Korea

K. D. Oh (✉)
Korea Military Academy, Gongreung-dong, Nowon-gu, Seoul, 01780, Republic of Korea
e-mail: okd0629@hanmail.net

M. Meghraoui et al. (eds.), *Advances in Geophysics, Tectonics and Petroleum Geosciences*,
Advances in Science, Technology & Innovation, https://doi.org/10.1007/978-3-030-73026-0_25

paper introduces the hydro-seismicity model proposed by Costain (2016) briefly and then explores possible evidences of the cause-and-effect relation between groundwater flow and seismicity using earthquake data recorded in South Korea.

2 Materials and Methods

Based on his hydro-seismicity model and the data collected worldwide Costain (2016) suggested that only 0.01–0.1 MPa of pore-fluid overpressure was sufficient to trigger intra-plate earthquakes in crusts in the state of the SOC (Self-Organized Criticality) but persistence of pore-fluid overpressure was a key factor in triggering intra-plate seismicity. He also suggested that depending on hydraulic diffusivity of crusts, there were one to six-month time lags between groundwater recharge and the onset of hydro-seismicity.

This paper explores the possible evidences of hydro-seismicity due to groundwater flow using earthquake data recorded in South Korea. A catalogue of 1157 earthquakes, with a minimum threshold of M_L 2.0 that occurred in South Korea from 1978 till 2017, was used. First, we sorted out earthquakes by the place where they occurred. The number of earthquakes occurred in lands and seas were 520 and 637, respectively.

Next, we further sorted out these two groups of earthquakes by the month when they occurred. Then for each month we counted the occurrence of earthquakes and computed the energy of them to find evidences that might support hydro-seismicity in terms of temporal and spatial variation with respect to groundwater fluctuation due to hydrologic cycle, driven mainly by precipitation during the Monsoon season in South Korea.

3 Results

3.1 Comparison of Earthquakes Between Lands and Seas

To explore any pattern of occurrence and energy release from land and sea earthquakes, their monthly count and energies were compared as shown in Figs. 1 and 2 with some time-shifting. In order to facilitate and to grasp some

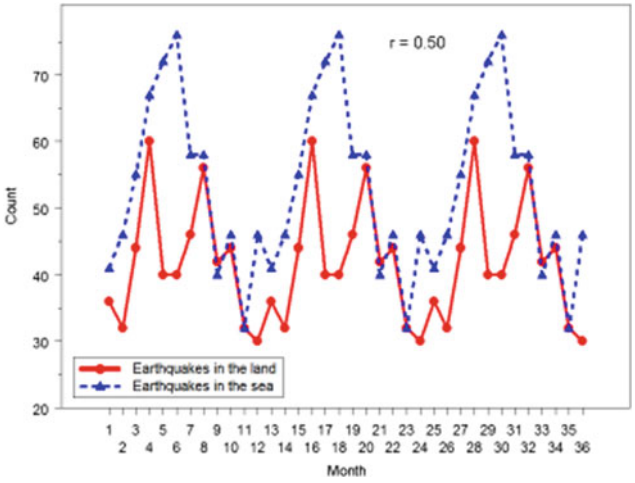

Fig. 1 Monthly earthquake count series after moving the time series for lands backward by 4 months

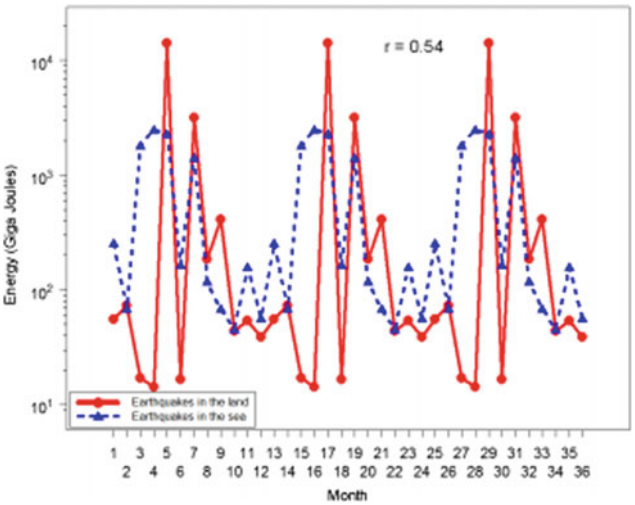

Fig. 2 Monthly earthquake energy series after moving the time series for lands backward by 8 months

patterns of these time series that seem to expand over two years 12-month time series were repeated three times. Correlation coefficients between land and sea earthquakes were 0.50 and 0.54 for monthly earthquake count and energy, respectively.

We divided 12-month energy series into two categories: an active period and an inactive period depending on the level of monthly earthquake energy. For land earthquakes,

6 months from August till January was classified as an active period, while 6 months from February till July was classified as an active period for sea earthquakes.

Figures 3, 4 and 5 compare monthly earthquake energy series between lands and three seas. Monthly earthquake energy series of lands was moved backward by 6 months.

Land earthquakes and earthquakes of the South Sea showed the highest correlation coefficient of 0.93. This high correlation seems to be attributable to relatively uniform characteristics of the contributing watersheds including the travel time of groundwater flow along the coast of the South Sea.

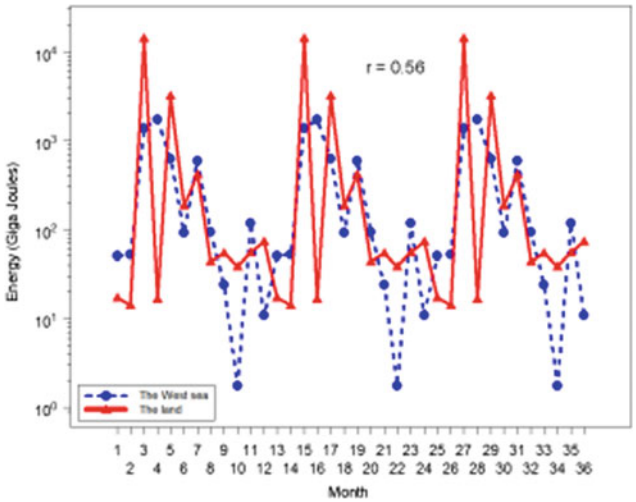

Fig. 3 Monthly energy series for the West Sea and lands

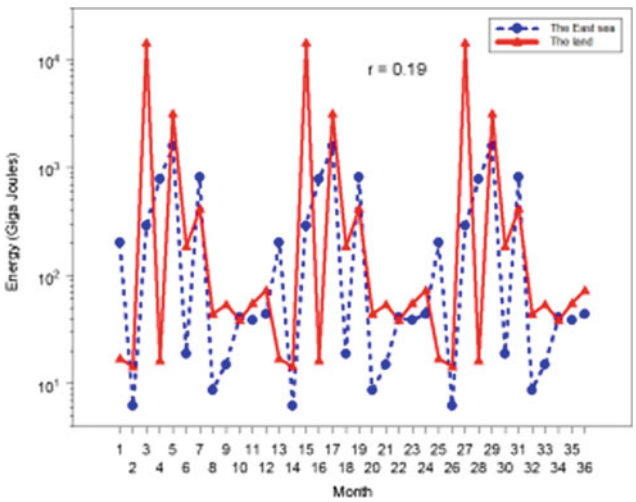

Fig. 4 Monthly energy series for the East Sea and lands

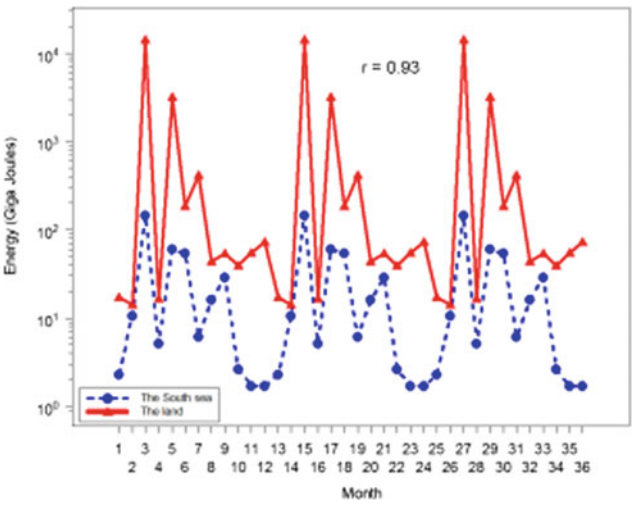

Fig. 5 Monthly energy series for the South Sea and lands

3.2 Rainfall, Groundwater and Earthquakes

Measured nation-wide groundwater table from 108 groundwater monitoring wells represented by a brown solid line in Fig. 6 shows the highest peak in May and the second peak in August, which seems to be influenced by irrigation water supply represented by a red broken line from March through September.

Variation of estimated natural groundwater level, excluding the influence of irrigation water supply is represented by a blue broken line for the irrigation period. As shown in Fig. 6, modified groundwater table shows the higher peaks on July through December which almost coincide with the active period of land earthquakes from September through January of the next year, with one or two month gaps. One or two month delay between the peak rainy months of July and August and the peak land earthquake energy month of September was supposed to be the time necessary for groundwater recharge and pressure propagation in fault zones.

4 Conclusions

Using 1157 earthquakes occurred in South Korea from 1978 till 2017 active and inactive earthquake periods for lands and seas were identified. Comparison of monthly earthquake

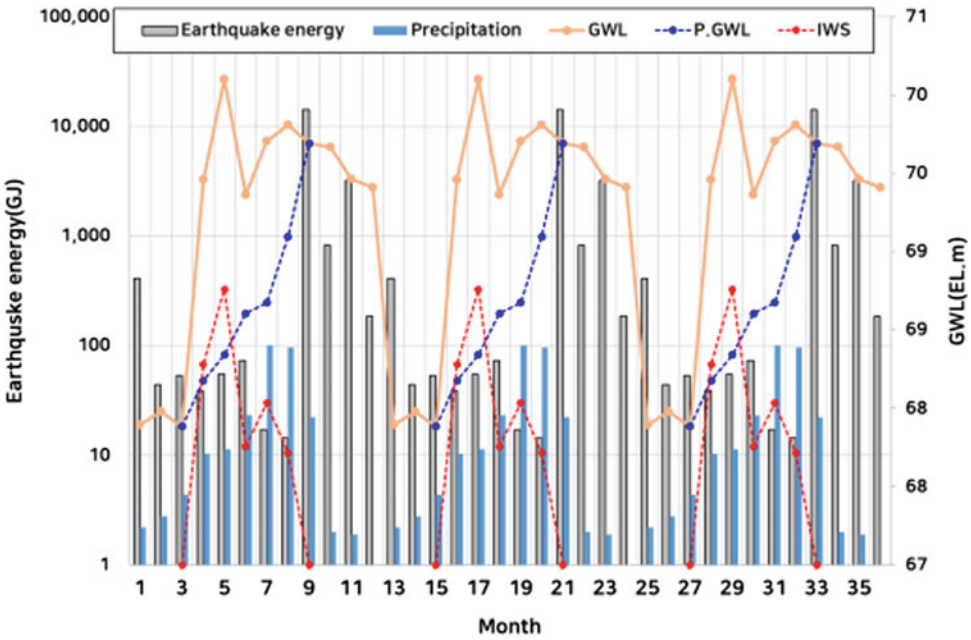

Fig. 6 Monthly precipitation, groundwater table and earthquake energy. GJ: giga-Joules, GWL: measured ground water level, IWS: irrigation water supply, P. GWL: presumed natural ground water level

count and energy series between lands and seas seems to support the hydro-seismicity hypothesis for earthquakes occurring in South Korea.

Acknowledgements This work was supported by grant NFR-2017R1E1A1A01075118 through Basic Science Research Program of National Research Foundation of Korea (NRF).

References

Costain, J.K.: Groundwater recharge as the trigger of naturally occurring intraplate earthquakes. In: Landgraf, A., Kuebler, S., Hintersberger, E., Stein, S. (eds.) Seismicity, Fault Rupture and Earthquake Hazards in Slowly Deforming Regions. Geological Society, London, Special Publications, 432 (2016)

Costain, J.K., Bollinger, G.A.: Review: research results in hydroseismicity from 1987 to 2009. Bull. Seismol. Soc. Am. **100**, 1841–1858 (2010)

Seismotectonics, Archeoseismology and Active Faulting

Advances in Archaeoseismology

Klaus-G. Hinzen and Sharon Kae Reamer

Abstract

Our knowledge of pre-instrumental earthquakes is mainly based on historic reports and palaeoseismological evidence. Under favorable conditions, damage to archaeologically documented structures may quantify earthquake-related parameters, such as the type of ground motions that caused damage. The Mediterranean Region, with a plethora of archaeological sites and one of the highest global seismicity rates, is an ideal place for archaeoseismological research. In addition to basic questions, e.g. whether observed damage is of a co-seismic nature and bracketing ground motion levels, advanced surveying and modelling techniques can also provide additional insights. We show that models of precariously balanced archaeological structures provide natural limits to past ground motion levels and that structures built on active faults may give information on the slip velocity during earthquakes. Quantitative models also provide perspectives for discussions about historical building techniques, such as the existence of ancient earthquake-resistant construction. The results of such investigations can improve efforts to preserve the cultural heritage of a region and can be utilized to avoid future construction mistakes.

Keywords

Archaeoseismology • Mediterranean region • Precariously balanced structures • Adapted building techniques • Earthquake slip velocity

1 Introduction

Research into the nature of pre-instrumental earthquakes, besides being interesting, is also important from several perspectives. First, any seismic risk study, no matter whether deterministic or probabilistic, is only as meaningful as the data it is based on with the catalogue of past events being the most important category of data. Second, knowledge of historic and pre-historic earthquakes, their effects on anthropogenic structures and the subsequent response of past civilizations are a part of our cultural heritage. And last, but not least, improved knowledge of past events, especially that of a quantitative nature, can help to protect this heritage in the future and to avoid contemporary building mistakes.

The study of earthquakes affecting archaeologically excavated buildings and structures or persisting monuments is called Archaeoseismology (Hinzen 2011). While early archaeoseismological investigations were mainly descriptive tools to catalog damage, recent studies also employ modern seismological and engineering tools for a quantitative approach.

The primary data any archaeoseismological study is based on are the damage and deformation patterns of broken or ruined structures. The challenge is the back calculation of the earthquake ground motion parameters which caused the damage. An even greater challenge is to draw conclusions on the nature of the earthquake source responsible for the ground motions. In general, such specific conclusions require information from more than one site, sometimes called a 'territorial approach' (Galadini et al. 2006).

The discipline of Archaeoseismology began with studies in the Mediterranean Region. One of the most active earthquake zones globally, the region is congruent with the oldest human settlements and numerous prospering civilizations which over millennia produced a plethora of structures ranging in size from small to monumental (Fig. 1). However, relatively few studies have been made at sites of the

K.-G. Hinzen (✉) · S. K. Reamer
University of Cologne, 50923 Köln, Germany
e-mail: hinzen@uni-koeln.de

M. Meghraoui et al. (eds.), *Advances in Geophysics, Tectonics and Petroleum Geosciences*,
Advances in Science, Technology & Innovation, https://doi.org/10.1007/978-3-030-73026-0_26

southern shores of the Mediterranean at the northern limit of the African continent.

Favourable conditions for archaeoseismic studies are those where (1) damage can be evaluated during a new and ongoing excavation. At existing archaeological sites, where excavations were carried out more than a century ago, alterations and renovations to the original excavated structures are often obscured and undocumented; this can easily lead to misinterpretations (Hinzen et al. 2018). (2) Sufficient archaeological evidence exists to reconstruct the damaged structures to their state before the damaging event occurred. (3) Archaeological and physical dating techniques allow identifying when the earthquake occurred; this can be crucial to correlate damage at different sites (Galadini et al. 2006). (4) A good database of active faults in the area of interest exists which can be used to estimate strong motion characteristics at the investigated site(s). (5) Circumstances at the site (permissions for sampling and geophysical exploration) allow determination of crucial site effects and material properties. Responsible archaeologists accept the application of natural sciences including engineering seismology.

In this keynote, we briefly present the concept and techniques which have been recently introduced and applied in

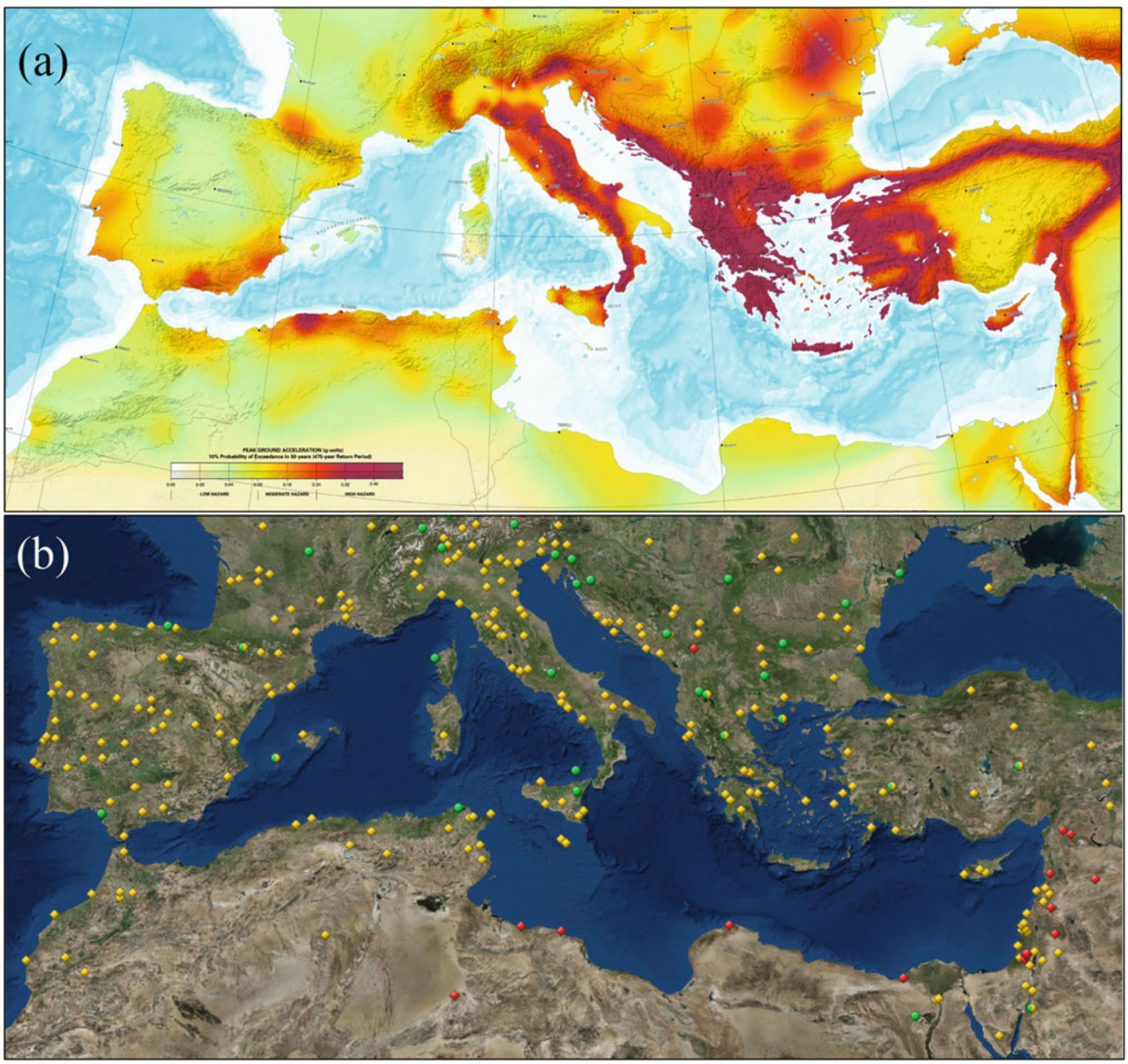

Fig. 1 **a** Seismic hazard of the Mediterranean region, peak ground acceleration of 10% probability of exceedance in 50 years (Jiménez et al. 2003). **b** UNESCO world heritage sites (http://whc.unesco.org/en/interactive-map/)

archaeoseismological studies and show some examples from the Mediterranean region.

2 Concept and Methods

In quantitative archaeoseismology, advanced surveying techniques (e.g. laser scanning, photogrammetry) are used to document the current state of the target structures, analyze and quantify damage patterns, and provide a basis for reconstruction and implementation of numerical models (Fig. 2). These models are often finite element (FE) or discrete element (DE) models which are used to explore the dynamic capacity of the buildings and simulate ground motion scenarios. Common geophysical and geotechnical in situ exploration is used to evaluate seismic site effects, which are essential for quantitative modelling of strong ground motions. Seismological tools enable calculations of the boundary conditions for the FE and DE models in the form of synthetic seismograms for earthquake scenarios based on the seismotectonic situation.

In cases where non-seismic causes of damage cannot be ruled out, alternative scenarios (mass wasting, flooding, rock fall, anthropogenic action such as war, looting, etc.) can be tested in the form of appropriate input forces and/or motions to the numeric models (Fig. 2).

Comparison between the quantified damage (movement of ashlars, topple directions of columns, crack pattern, etc.) and the calculated results of the models provide information to test the plausibility of the various scenarios. However, as in any forensic study, scenarios not taken into account can lead to misinterpretation.

The classical questions asked in archaeoseismic studies are:

- Is the observed damage of co-seismic nature?
- What kind of ground motion caused the damage?
- What can be said about the source of the causing earthquake?
- When did the damage occur?

However, under favorable conditions, advanced problems can be addressed:

- Which limits to ground motions can be inferred from precariously balanced archaeological structures?
- Are certain ancient building techniques earthquake-adapted?
- Do archaeological structures on active faults provide limits to parameters such as earthquake slip velocity?

In the following, three examples, in which the above-mentioned questions were addressed, are briefly described.

3 Examples

3.1 Precariously Balanced Archaeological Structures

In 2017, we introduced the concept of precariously balanced archaeological structures (PBAS) (Schweppe et al. 2017). As an analogue to the study of precariously balanced rocks (PBR), PBAS can be used to estimate critical levels of

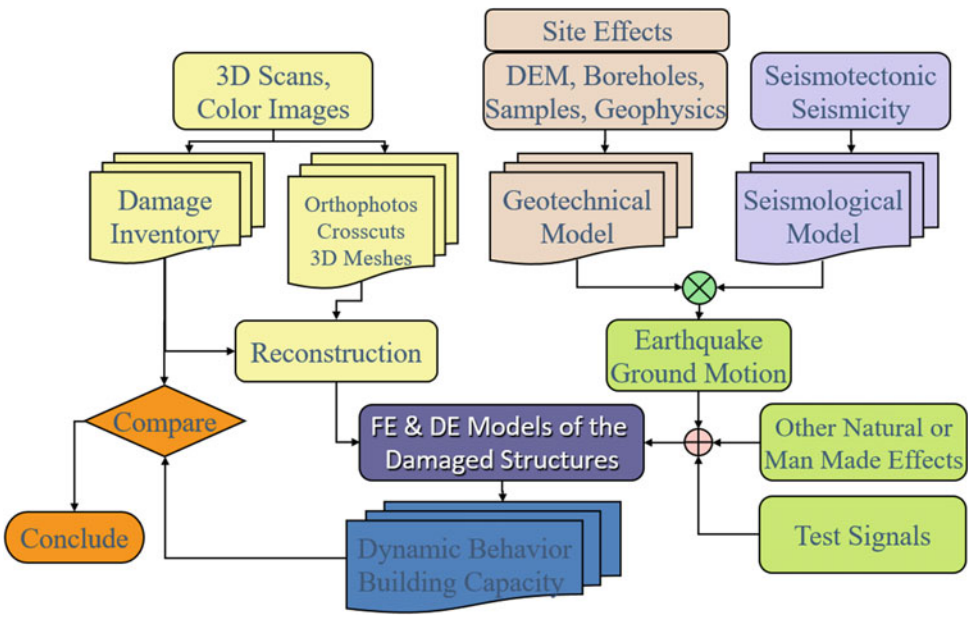

Fig. 2 Schematic workflow of a standard quantitative archaeoseismological study (after Hinzen et al. 2011)

ground motion parameters, specifically, those levels which have not been exceeded since the structure achieved its delicate state. Dynamic tests with FE or DE models provide the corresponding thresholds of ground motion values. The example in Fig. 3 is a ruin of a Roman Temple in Kedesh, Israel (Schweppe et al. 2017). The DE model of the ruin was constructed from a laser scan and tested with analytic ground motion signals and a set of synthetic seismograms of local, historically documented earthquakes. It could be shown that the current knowledge of the size of the historic events is compatible with the fact that the ruin is still standing, as none of the calculated site-specific ground motions toppled the ruin. While PBAS covers a much shorter time span than PBR, they have one decisive advantage: In most cases, the time since they exist can be taken from the historic/archaeologic context, in the case of the Kedesh Temple, an earthquake in 363 C.E. The PBAS method utilizes archaeological structures which cannot be reconstructed with a sufficient degree of confidence, but their current state can be modelled.

3.2 Adapted Building Techniques

The second example in Fig. 3 concerns earthquake-adapted building techniques in ancient cultures, and an issue often discussed in building history (Ferrigni 2005). It is sometimes claimed that polygonal-shaped building blocks (e.g. in Inca constructions) have been used for earthquake safety. Advanced modelling techniques help to test common sense arguments. In a study (Hinzen and Montabert 2017) with four generic wall models, we tested the dynamic stability of a Roman wall with rectangular ashlars, an Inca-type wall, and two polygonal block walls based on a Lycian and a Roman example. While the polygonal walls and particularly the Inca-type wall were more stable than the rectangular ashlars, it turned out that the height to width ratio of the wall is equally important as the block shape. As many other reasons (available material, economic, aesthetic) might influence the block shape used by certain cultures or for certain constructions, it is still not certain in most cases that earthquake safety was a primary consideration, if at all (Meghraoui et al. 2003).

3.3 Earthquake Source Parameters

Sometimes archaeological structures have been built directly on top of or across active faults (Meghraoui et al. 2003; Ellenblum et al. 1998). These structures are perfect markers for co-seismic deformation that occurred when the fault ruptured. Horizontal and vertical offsets are key parameters for estimating the moment magnitude of a pre-instrumental earthquake. In a recent project (Schweppe et al. 2021), we sought to quantify the nature of the earthquakes which had offset the walls of a Crusader fortification in Tell Ateret,

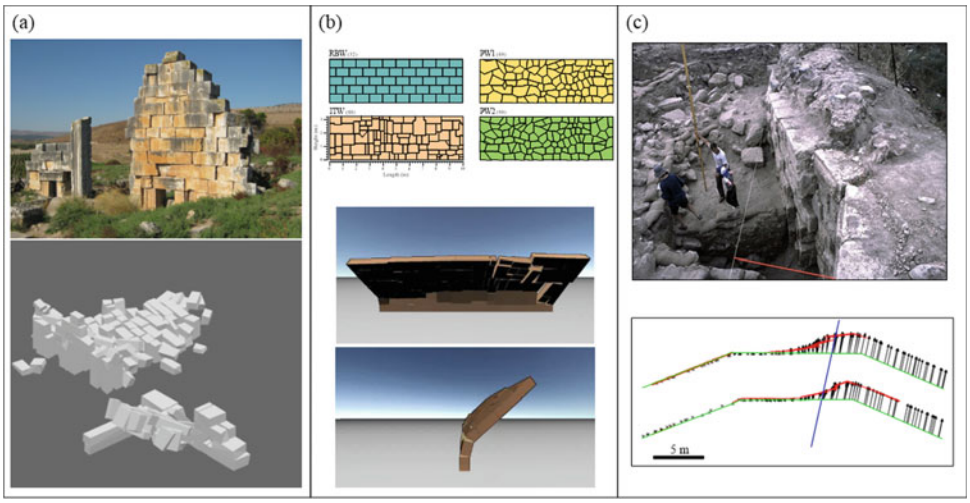

Fig. 3 Three examples of advanced archaeoseismological studies. **a** The use of the precariously balanced archaeological structure of the ruin of a Roman temple in Kedesh, Israel, to determine the toppling ground motion parameters. Top: photo of the ruin; bottom: toppled DE model (after Schweppe et al. 2017). **b** Testing the dynamic behaviour of four differently structured block walls. Top: model of a Roman wall with rectangular ashlars, an Inca-type wall, and two polygonal block walls. Bottom: snapshot from a DE calculation during dynamic loading (after Hinzen and Montabert 2017). **c** Back calculation of plate slip velocity during an earthquake that deformed the fortification wall of the Crusader caste Ateret on the DSTF. Top: excavation photo of the deformed wall (curtsey: Marco). Bottom: green lines indicate the original position of the ashlars of the wall. Black arrows show the dislocation at the end of a numeric experiment compared to the in situ deformation (red); the blue line shows the trend of the DSTF (after Schweppe et al. 2021)

built right on top of the Dead Sea Transform Fault (DSTF). With a laser scan-based DE model, it was possible to estimate the slip velocity during two earthquakes in 1202 and 1759 C.E. and determine that during these events, the Arabian plate moved northward, while the Sinai sub-plate was to a large extent locked. The slip velocity was estimated by comparing the deformation pattern seen in situ with the calculated deformation of the wall during a broad range of slip scenarios applied to the DE model. In particular, inertial forces in the ashlars, especially during the start and stop phase of the slip motion, influence the block movements and their final resting position. Because parts of the walls on the locked side of the fault did not experience the inertial forces, a different dislocation pattern subsequently formed, allowing deduction for a locked western site of the fault.

4 Discussion

In the above-mentioned examples, 3D laser scans of the studied structures are a central piece of the database used in the numeric analysis. The actual 3D laser scanning is fast; with modern equipment, some 20 individual scans with good resolution can be made in a working day. In contrast, the preparatory work for scanning is more time consuming. Targets for the scan registration have to be placed, and often vegetation obscuring a free view to the structure has to be removed. Processing of large scan models can also be time-consuming and requires powerful workstations. The transformation of the scanned point clouds into FE or DE models places large constraints on time and manual operation. In the case of DE models in general, the individual elements are restricted to convex shapes in order to use efficient collision detection algorithms. In the case of the Kedesh Temple (Schweppe et al. 2017), for example, some blocks definitely have concave shapes and each block had to be 'broken' until it was composed only of convex sub-blocks which were then physically treated as a single unit.

In the shown examples, the overall approach was deterministic: The DE model was activated by certain selected ground motion scenarios. The main limitation for the number of scenarios that can be tested is the calculation effort necessary for each iteration. For larger models (as in the Ateret example Schweppe et al. 2021) and depending on the software and boundary conditions used, a single calculation can take over a week of calculation time. However, with increasing calculation power and optimized implementations, it will become possible to use more and more probabilistic approaches in which a large number of calculations can help to better constrain the uncertainties of the results.

For each field case, a unique and suitable method to compare the observed deformations and damage with the outcome of the numerical simulations has to be developed. A perfect match between calculation and observation is not achievable nor is it to be expected; however, quantitative measures of the differences in results, such as median values of the distance between the endpoints of deformation vectors, allow a plausibility ranking for the scenarios to be applied. This resulted in preferring 3.0 m/s as the most appropriate slip velocity in the Ateret example.

5 Conclusions

The plethora of archaeological sites in the Mediterranean Region, one of the most active seismic zones globally can be used to gain information about pre-instrumental seismic activity. Under favourable conditions, advanced techniques of damage documentation and dynamic modelling provide quantitative estimation of ground motion parameters.

More sites at the southern shores of the Mediterranean should be investigated. Results of quantitative archaeoseismological studies can significantly improve seismic hazard analysis, the knowledge on the history of the sites, and help to protect the cultural heritage.

References

Ellenblum, R., Marco, S., Agnon, A., Rockwell, T., Boas, A.: Crusader castle torn apart by earthquake at dawn, 20 May 1202. Geology **26**, 303–306 (1998)

Ferrigni, F.: Ancient Buildings and Earthquakes: Reducing the Vulnerability of Historical Built-Up Environment by Recovering the Local Seismic Culture: Principles, Methods, Potentialities. Edipuglia, Bari (2005)

Galadini, F., Hinzen, K.-G., Stiros, S.: Archaeoseismology: methodological issues and procedure. J. Seismolog. **10**, 395–414 (2006)

Hinzen, K.-G.: Seismology, archaeoseismology. In: Gupta, H. (ed.) Encyclopedia of Solid Earth Geophysics, pp. 11–15. Springer (2011)

Hinzen, K.-G., Montabert, A.: Rectangular blocks vs polygonal walls in archaeoseismology. Ann. Geophys. **60**(4), 1–18 (2017)

Hinzen, K.-G., Fleischer, C., Reamer, S.K., Schreiber, S., Schütte, S., Yerli, B.: Quantitative methods in archaeoseismology. Quatern. Int. **242**(1), 31–41 (2011)

Hinzen, K.-G., Maran, J., Hinojosa-Prieto, H., Damm-Meinhardt, U., Reamer, S.K., Tzislakis, J., Kemna, K., Schweppe, G., Fleischer, C., Demakopoulou, K.: Reassessing the Mycenaean earthquake hypothesis: results of the HERACLES Project from Tiryns and Midea, Greece. Bull. Seismol. Soc. Am. **108**(3), 1046–1070 (2018)

http://whc.unesco.org/en/interactive-map/. Last accessed 29 June 2019

Jiménez, M.-J., Giardini, D., Grünthal, G.: The ESC-SESAME unified hazard model for the European-Mediterranean region. EMSC/CSEM Newsl. **19**, 2–4 (2003)

Meghraoui, M., Gomez, F., Sbeinati, R., Van der Woerd, J., Mouty, M., Darkal, A.N., Radwan, Y., Layyous, I., Najjar, H.A., Darawcheh, R., Hijazi, F., Al-Ghazzi, R., Barazangi, M.: Evidence for 830 years of seismic quiescence from palaeoseismology, archaeoseismology and historical seismicity along the Dead Sea fault in Syria. Earth Planet. Sci. Lett. **210**, 35–52 (2003)

Schweppe, G., Hinzen, K.-G., Reamer, S.K., Marco, S.: Reconstructing the slip velocities of the 1202 and 1759 CE earthquakes based on faulted archaeological structures at Tell Ateret, Dead Sea Fault. J Seismol **25**, 1021–1042 (2021). https://doi.org/10.1007/s10950-021-10009-0

Schweppe, G., Hinzen, K.-G., Reamer, S.K., Fisher, M., Marco, S.: The ruin of the Roman temple of Kedesh, Israel; example of a precariously balanced archaeological structure used as a seismoscope. Ann. Geophys. **60**(4), 1–17 (2017)

Possible Tectonic Styles of Future Earthquakes from Seismic Moment Tensors of Previous Events: An Example in Italy

Silvia Pondrelli, Carlo Meletti, Andrea Rovida, Francesco Visini, Vera D'Amico, and Bruno Pace

Abstract

During the new elaboration of the hazard model for Italy, a study on the indications we may collect concerning the tectonic style of future earthquakes and seismic ruptures has been done. All available seismic moment tensors for relevant seismic events (Mw starting from 4.5) of the last 100 yrs, first arrival focal mechanisms for less recent earthquakes and geological data on activated faults have been collected in a unique database, that includes thousands of data all over the Italian peninsula. After several summation trials, changing parameters, seismogenic thicknesses and taking into account the characteristics of seismicity distribution, a unique computation procedure has been applied to each of the 50 seismic zones of the new seismogenic zoning for Italy. The results for several seismic zones are very stable, for instance, in the southern Apennines we expect mostly extensional earthquakes, although in the outer part of the chain strike-slip events are possible. In the northern part of the Apennines, we also expect different, opposite tectonic styles for different hypocentral depths. In several zones characterised by a low seismic moment release, the next possible tectonic style of future earthquakes is less clear and it has been represented using different combination (total or partial) of random sources. A comparison of our results with recent earthquake moment tensors show a good agreement with the computed possible tectonic style.

Keywords

Seismic moment tensors • Tectonic styles • Future earthquakes

1 Introduction

Italy is a territory prone to earthquakes. At the same time, it is a region where not only great earthquakes, but also those with a moderate magnitude, may produce strong damages and victims. This is typical for a place where a high population density, accompanied by a thousands of years of history, art treasures and a beautiful nature, produce a particular hazard profile. And this description applies for most of territories around the Mediterranean sea.

The seismotectonic setting of Italy shows the presence of all tectonic styles seismically active (Fig. 1). With the purpose of understanding the tectonic style of the future earthquakes in our territory, we used old previous earthquakes. A big database of seismic source parameters information has been collected, including data from the European Mediterranean RCMT Catalog (Pondrelli and Salimbeni 2015 and reference therein; http://rcmt2.bo.ingv.it/), the Italian CMT Dataset (Pondrelli et al. 2006; http://rcmt2.bo.ingv.it/Italydataset.html), the EMMA dataset (Vannucci and Gasperini 2004) and the DISS database (DISS Working Group 2015). This last source of information has been used for a couple of events that occurred in 1905 and 1915 in Southern Italy, where seismological instrumentally recorded data (i.e. first arrival focal mechanisms) were not as much stable as the geological ones. The final dataset is composed of thousands of seismic moment tensors for earthquakes that

S. Pondrelli (✉)
Istituto Nazionale di Geofisica e Vulcanologia, Sezione di Bologna, Bologna, Italy
e-mail: silvia.pondrelli@ingv.it

C. Meletti · V. D'Amico
Istituto Nazionale di Geofisica e Vulcanologia, Sezione di Pisa, Pisa, Italy

A. Rovida
Istituto Nazionale di Geofisica e Vulcanologia, Sezione di Milano, Milano, Italy

F. Visini
Istituto Nazionale di Geofisica e Vulcanologia, L'Aquila, Italy

B. Pace
Dip. di Sc. Pisicologiche, della Salute e del Territorio (DiSPUTer), Un. G. d'Annunzio Chieti-Pescara, Chieti, Italy

M. Meghraoui et al. (eds.), *Advances in Geophysics, Tectonics and Petroleum Geosciences*, Advances in Science, Technology & Innovation, https://doi.org/10.1007/978-3-030-73026-0_27

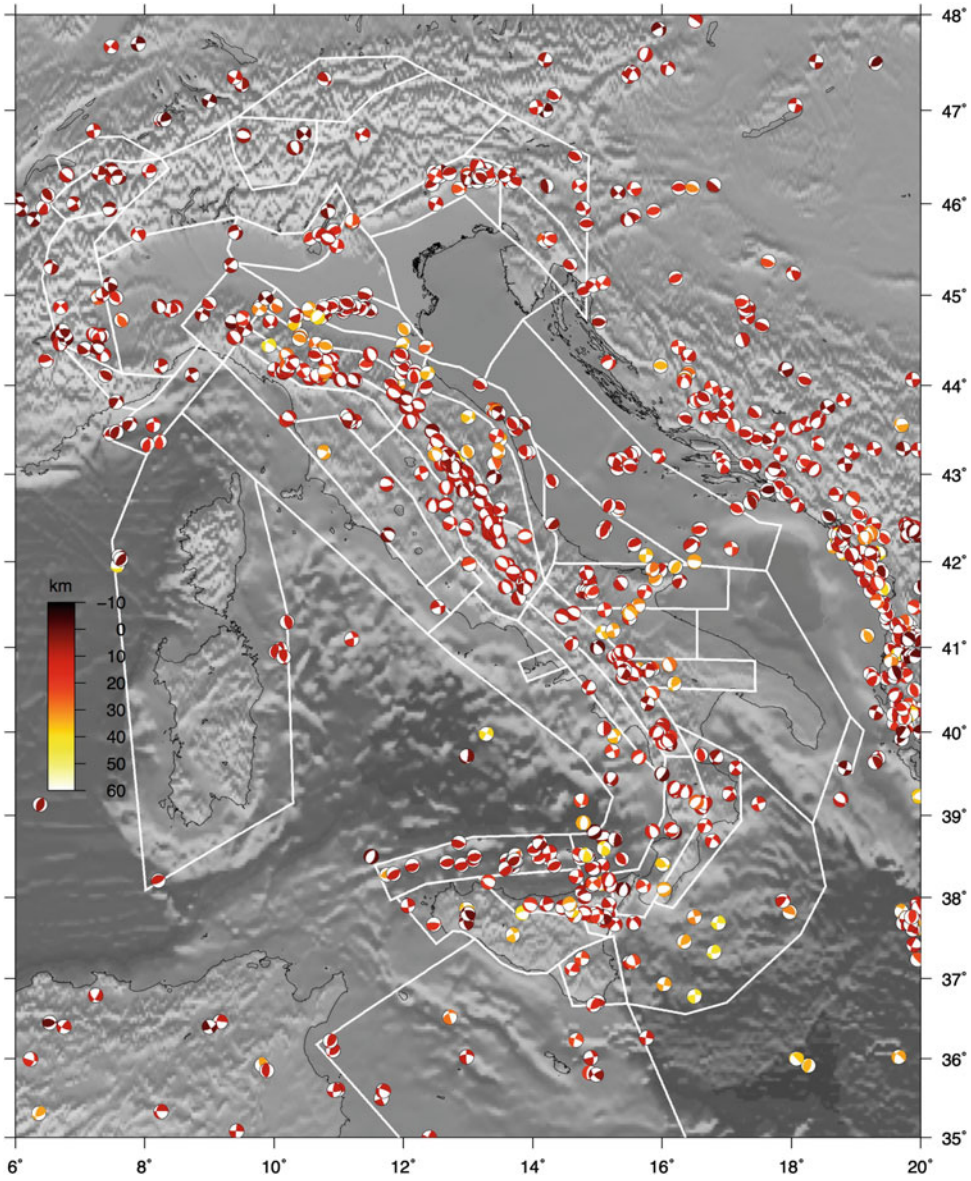

Fig. 1 Map of the entire dataset of seismic moment tensors collected for this work. Different colours follow different hypocentral depths (colour scale on the left). In the background, the new Italian seismic zoning

occurred within 2015, with a Mw greater than 4.5 and a hypocentral depth within 40 km (Fig. 1).

2 Computational Method

Within each seismic zone, all seismic moment tensors included in our dataset have been separated in the three main tectonic style groups (normal, compressive and strike-slip). Over each group we applied the well-known Kostrov Method (1974), i.e. a summation of seismic moment tensors that gives a final cumulative one, considered representative in the volume of crust within which it was obtained. This technique is widely applied and accepted for these purposes (Jackson and Mckenzie 1988; Kiratzi and Papazachos 1992; Pondrelli et al. 1995; Serpelloni et al. 2007). In the summation we took into account only shallow crustal events. In general, in Italy, 40 km of depth is the right hypocentral depth, but in some regions we had to take into account some local variations. For instance, in the Northern Apennines (zones n. 19 and 20, Fig. 2), a tectonic style layering has been found: in the first 15 km of crust an extensional tectonic regime dominates, while at a greater depth an opposite type of deformation is recorded. Consequently, we applied the summation over two different layers of crust, following the characteristic of distribution of seismicity.

Summation procedure gives, for each seismic zone, from one to three cumulative seismic sources, one from each tectonic style (if active in the zone). The final seismic source for each zone is composed by a percentage of each tectonic

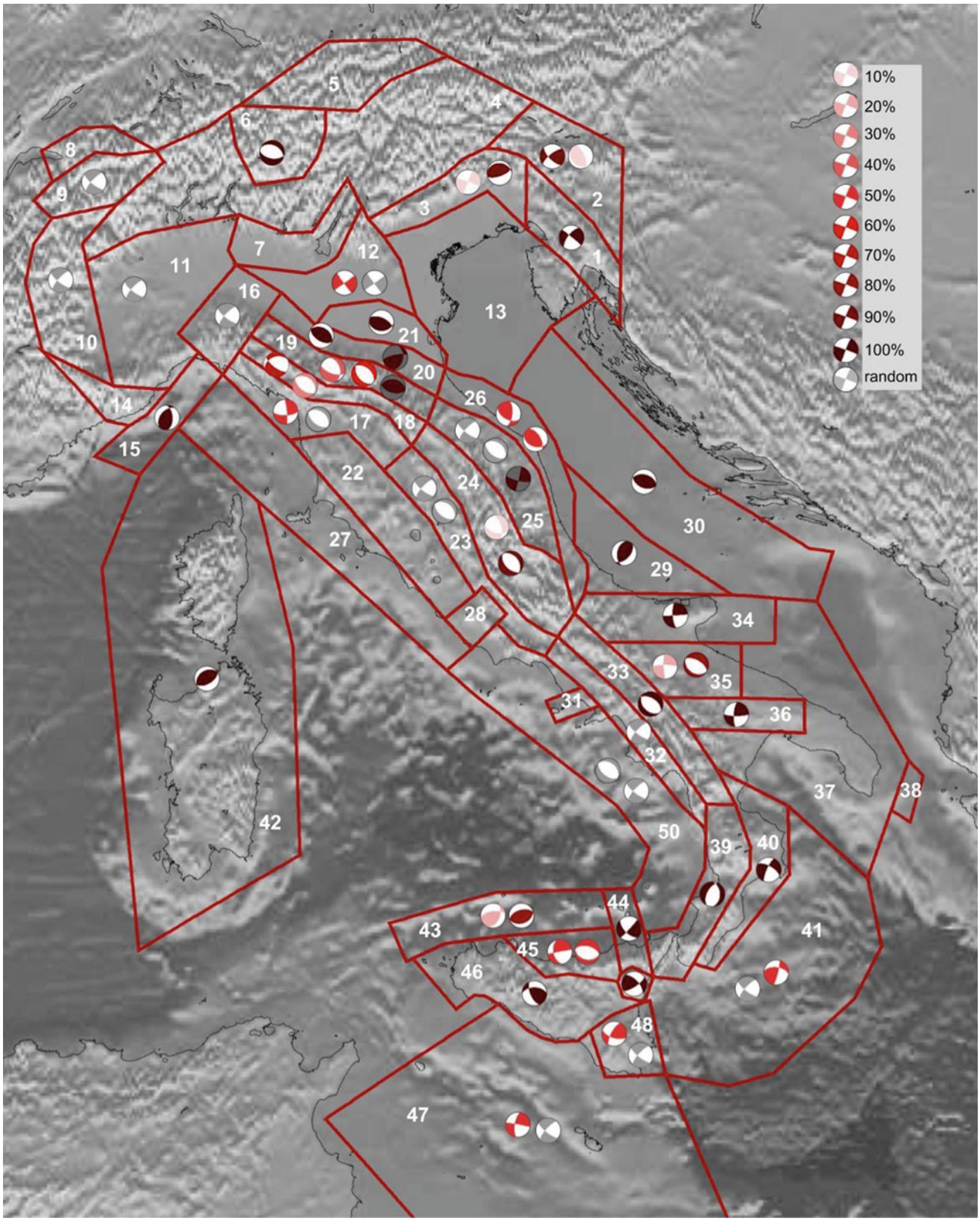

Fig. 2 Map of possible seismic sources obtained for each seismic zone. Top right is reported a colour scale for different percentages of contribution of single tectonic styles. In grey are focal mechanisms that represent seismic sources with random fault plane directions. Grey background of few focal mechanisms is used for cumulative sources obtained for deep seismogenic layers (e.g. between 20 and 40 km)

style, defined on the base of the amount of cumulative seismic moment. For instance, in a zone of Eastern Alps (zone n. 3 in Fig. 2), the cumulative seismic source is composed by a 10% of strike-slip and a 90% of thrust and zero % of normal slip. This result means that, over the total of the cumulative seismic moment of this seismic zone, summed thrust events reach the 90%. Where the amount of seismic moment is very low or just few events with a Mw 4.5 occurred, in the final composite seismic source a part of randomness is included. Where from the past we did not obtain any information, the final source is fully random.

3 Discussion and Conclusions

The preliminary results of this work are shown in Fig. 2. In each seismic zone, we mapped the final composite seismic source we obtained. Along the Apennines chain prevails an extensional style of deformation, but in the outer part of the belt, on the Adria side, thrust and strike slip tectonics are present from north to south, up to the Gargano promontory. Other thrust tectonics prevail in the Eastern Alps and in the off shore of the Northern Sicily coast. In the Western Alps and along the peninsular Thyrrenian coast, seismicity is so weak that random solution (represented by a grey strike slip focal mechanism) are a frequent result.

Most of the seismic zones have more than one tectonic style in its final result. In Fig. 2, the final seismic source is related to the percentage of contribution of seismic moments, reported using different colours. In the n. 1 zone for instance, only strike slip earthquakes occurred, so the final seismic source is represented by only one focal mechanism, with a colour reporting the 100% of seismic moment. For the n. 43 zone, northern coast of Sicily, in Fig. 2, two focal mechanisms are mapped, one representing the summation of strike slip events, reaching the 20% of the contribution, while the other is the thrust 80% contribution to the final result. In some zone, i.e. n. 19 and 20, also a grey background focal mechanism is drawn on map of Fig. 2; this symbol has been used to represent the tectonic style we expect from seismic events with a deeper focal source. In n. 19 zone we then obtain that shallow seismicity (0–15 km of depth) indicates a prevailing extensional tectonic style, with a minor strike slip component. At a depth greater than 15 km, it is active a pure compressive deformation.

The results of this study are in use at present to recompute the new Italian map of seismic hazard. We considered these cumulative seismic moments representative of the possible tectonic style of future earthquakes in Italy after a comparison with previous geological tectonic studies, but most of the capacity of these results to be realistically helpful in seismic hazard is due to the comparison with the focal mechanisms of earthquakes that hit Italy after the 2015 (latest time of the dataset used in computations). An example is the correspondence between the zone n. 24's results and the clearly extensional seismic moment tensors of the central Italy 2016–2017 seismic sequence (Pondrelli et al. 2016). The same confirmation arrived comparing other minor events, in different part of the peninsula, from Northern Apennines to Sicily. These preliminary results are still under review, but up to now, we have confidence in their efficiency. So, our choice to apply a very simple method to obtain information on the tectonic style of future events may be considered good, mainly in regions with good data on previous seismicity coexisting with tectonic complexities.

References

DISS Working Group: Database of Individual Seismogenic Sources (DISS), Version 3.2.0: a compilation of potential sources for earthquakes larger than M 5.5 in Italy and surrounding areas. http://diss.rm.ingv.it/diss/. Istituto Nazionale di Geofisica e Vulcanologia. https://doi.org/10.6092/INGV.IT-DISS3.2.0 (2015)

Jackson, J., Mckenzie, D.: The relationship between plate motions and seismic moment tensors, and the rates of active deformation in the Mediterranean and Middle East. Geophys. J. Int. **93**, 45–73 (1988)

Kiratzi, A.A., Papazachos, C.B.: Active crustal deformation from the Azores triple junction to the Middle East. Tectonophysics **243**, 1–24 (1992)

Kostrov, V.V.: Seismic moment and energy of earthquakes and seismic flow of rocks. Izv. Acad. Sci. USSR Phys. Solid Earth **1**, 23–40 (1974)

Pondrelli, S., Salimbeni, S.: Regional moment tensor review: an example from the European Mediterranean region. In: Encyclopedia of Earthquake Engineering, pp. 1–15. Springer, Berlin, Heidelberg. http://link.springer.com/referenceworkentry/10.1007/978-3-642-36197-5_301-1 (2015)

Pondrelli, S., Morelli, A., Boschi, E.: Seismic deformation in the Mediterranean area estimated by moment tensor summation. Geophys. J. Int. **122**, 938–952 (1995)

Pondrelli, S., Salimbeni, S., Ekström, G., Morelli, A., Gasperini, P., Vannucci, G.: The Italian CMT dataset from 1977 to the present. Phys. Earth Planet. Int. **159**(3–4), 286–303 (2006). https://doi.org/10.1016/j.pepi.2006.07.008

Pondrelli, S., Salimbeni, S., Perfetti, P.: Moment tensor solutions for the Amatrice 2016 seismic sequence. Ann. Geophys. **59**, Fast Track 5 (2016). https://doi.org/10.4401/ag-7240

Serpelloni, E., Vannucci, G., Pondrelli, S., Argnani, A., Casula, G., Anzidei, M., Baldi, P., Gasperini, P.: Kinematics of the western Africa-Eurasia plate boundary from focal mechanisms and GPS data. Geophys. J. Int. (2007). https://doi.org/10.1111/j.1365-246X.2007.03367.x

Vannucci, G., Gasperini, P.: The new release of the database of earthquake mechanisms of the Mediterranean area (EMMA version 2). Ann. Geophy. **47**(1), 307–334 (2004)

Stress Transferred by the May 2010 Beni-Ilmane Seismic Sequence

Hamoud Beldjoudi

Abstract

In this work, we will try to understand the interaction between three moderate earthquakes which occurred in May 2010 in the region of Beni-Ilmane (East of Algeria). We use a seismotectonic model suggested in a previous study for the calculation of the Coulomb Stress Change (ΔCFF). The first shock occurred on the 10th of May, 2010 (Mw = 5.5) either on a dextral plane oriented [Strike, Dip, Rake: 254°, 74°, 175°, respectively] or on sinistral plane oriented [Strike, Dip, Rake: 345°, 85°, 16°, respectively]. We consider that the (254°, 74°, 175°) oriented plane was the seismic source. We confirm also that the plane of the second shock oriented [Strike, Dip, Rake: 250°, 55°, 120°, respectively] is loaded by the first shock, and we record a ΔCFF = 0.19 bar. The plane oriented [Strike, Dip, Rake: 12°, 57°, 12°] for the third shock was also loaded by the two previous shocks and the ΔCFF = 0.04 bar.

Keywords

Stress change • Focal mechanism • Beni-Ilmane • Algeria • Earthquake

1 Introduction

A seismic sequence hits the Beni-Ilmane region between the 10th of May, 2010, and the 23rd of May, 2010. Three moderate shocks were recorded. The first shock is of a moment magnitude Mw of 5.5 and a seismic moment of (Mo) 1.8×10^{17} Nm, occurred on a dextral plane oriented [Strike, Dip, Rake: 254°, 74°, 175°, respectively]. The second shock hits the region with a Mw of 5.1 and Mo of 5.5×10^{16} Nm, occurred on a reverse fault oriented [Strike, Dip, Rake: 250°, 55°, 120°, respectively], and a third shock occurred on a plane oriented [Strike, Dip, Rake: 12°, 57°, 12°, respectively] with a Mw of 5.2 and a Mo of 7.4×10^{16} Nm (Beldjoudi et al. 2016). In this work, we will try to understand the interaction between these three moderate events which occurred on three neighboring unconnected faults. We use the seismotectonic model suggested by Beldjoudi et al. (2016) for this seismic sequence.

2 Coulomb Stress Changes

We calculate Coulomb stress changes (ΔCFF) using the Coulomb3.3 software (Toda et al. 2005; Lin and Stein 2004). The static pattern changes caused by an earthquake rupture are computed using the Coulomb failure assumptions (King et al. 1994; Hodgkinson et al. 1996; Harris 1998; Cocco et al. 2000). The variation of the Coulomb stress changes is computed as in Harris (1998) and Stein et al. (1992) defined as:

$$\Delta\mathrm{CFF} = \Delta\tau + \mu(\Delta\sigma + \Delta P) \tag{1}$$

where $\Delta\tau$ is the change in shear stress, $\Delta\sigma$ is the change I, normal stress (positive for extension), μ is the friction coefficient and ΔP is the change in pore pressure. This latter term can be expressed in terms of the Skempton's coefficient B as follows (Harris 1998; Cocco et al. 2000). Under certain conditions, Eq. (1) is frequently written as:

$$\Delta\mathrm{CFF} = \Delta\tau + \mu'\Delta\sigma_n \tag{2}$$

where μ' is the effective friction coefficient. Equation (2) is commonly used to calculate Coulomb stress changes by assuming different values for μ'.

H. Beldjoudi (✉)
CRAAG, Algiers, Algeria
e-mail: hamoud.beldjoudi@craag.edu.dz

M. Meghraoui et al. (eds.), *Advances in Geophysics, Tectonics and Petroleum Geosciences*,
Advances in Science, Technology & Innovation, https://doi.org/10.1007/978-3-030-73026-0_28

3 Stress Change Following the First Shock

On the 14th of May, 2010, the seismic sequence of Beni-Ilmane region started with a first shock of a magnitude Mw (5.5) and Mo of (1.83×10^{17} Nm) (Beldjoudi et al. 2016). The focal mechanism calculated by waveform inversion (Beldjoudi et al. 2016) shows a strike slip fault for the first plane [strike1, dip1, rake1: 254°, 74°, 175°, respectively] and [strike2, dip2, rake2: 345°, 85°, 16°, respectively] for the second plane (Fig. 1). Tests favor plane 1 as the fault plane (Fig. 1).

We calculate the Coulomb Stress Change (ΔCFF) on the receiver fault which represents the second main shock which occurred on the 16th of May, 2010, with a (Mw = 5.1) and oriented [Strike, Dip, Rake: 250°, 55°, 120°, respectively].

In Fig. 2a, we present the three main shocks of the seismic sequence and their respective assumed fault models. We calculate the ΔCFF at a depth of 6 km, and we assume that the effective coefficient of friction $\mu' = 0.4$. We have four positive lobes where the ΔCFF raised, two in the extremities of the fault 1 (Fault source), and two others in the north and south parts of the fault 1. All other regions show a drop of the ΔCFF. The fault 2 is located where the ΔCFF is raised. On Fig. 2b, we present the cross section (*AB*) which shows the variation of ΔCFF on depth, the red line draws the fault 2; it is located in the region within the ΔCFF > 0. We confirm that the second shock is loaded by the first shock with plane oriented [Strike, Dip, Rake: 254°, 74°, 175°, respectively].

4 Stress Change Following the First and Second Shocks

In this section, we will present the influence of the first (1) and second (2) faults resolved on the third event (3) of the Beni-Ilmane seismic sequence. We confirm that the fault plane (3) is located on a transitional zone with (ΔCFF > 0.04 bar), this means that the third event was loaded by the two previous shocks (Fig. 3).

5 Coulomb Stress Change and Aftershocks' Sequence

5.1 Aftershocks' Sequence Between the Second Shock and the Third Shock

We plot 694 aftershocks which occurred between the 16th of May at 06 h 53 mn and the 23rd of May at 13 h 28 mn

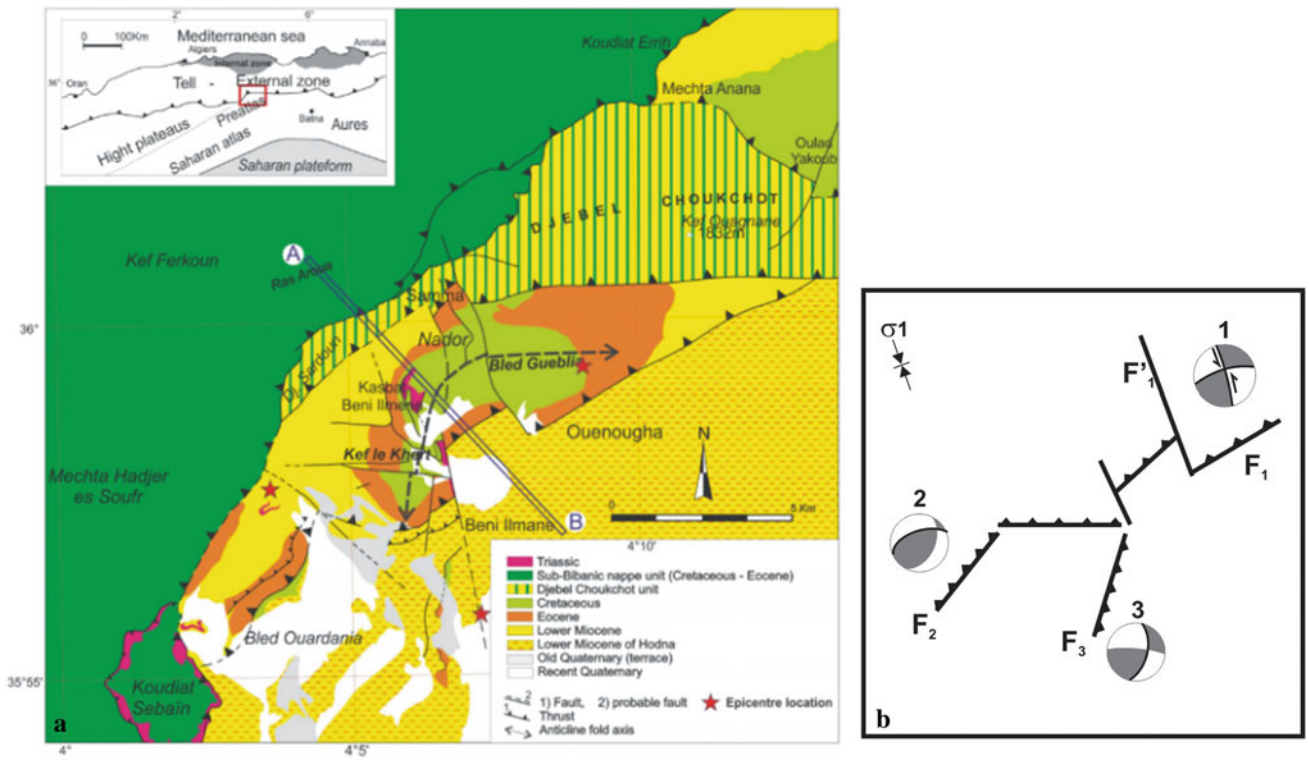

Fig. 1 **a** Geological map of the epicentral area. Red rectangle is an epicentral area. **b** Tectonic model suggested in Beldjoudi et al. (2016). F_1 and F'_1 show the possible faults activated during the first main shock. F_2 and F_3 are the second and third faults of the seismic sequence. The focal mechanisms of each main shock. $\sigma 1$ is the most compressive principal stress axis orientation

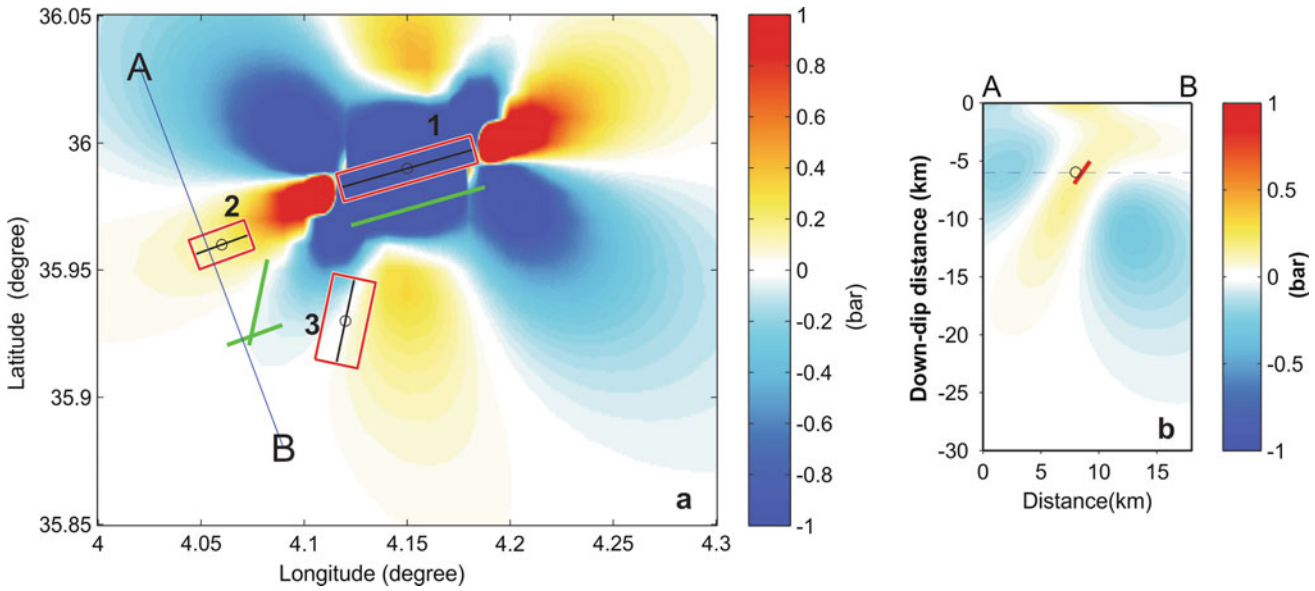

Fig. 2 **a** Stress change associated with the first shock resolved on the plane of the second shock oriented [Strike, Dip, Rake: 250°, 55°, 120°, respectively]. **b** Cross section

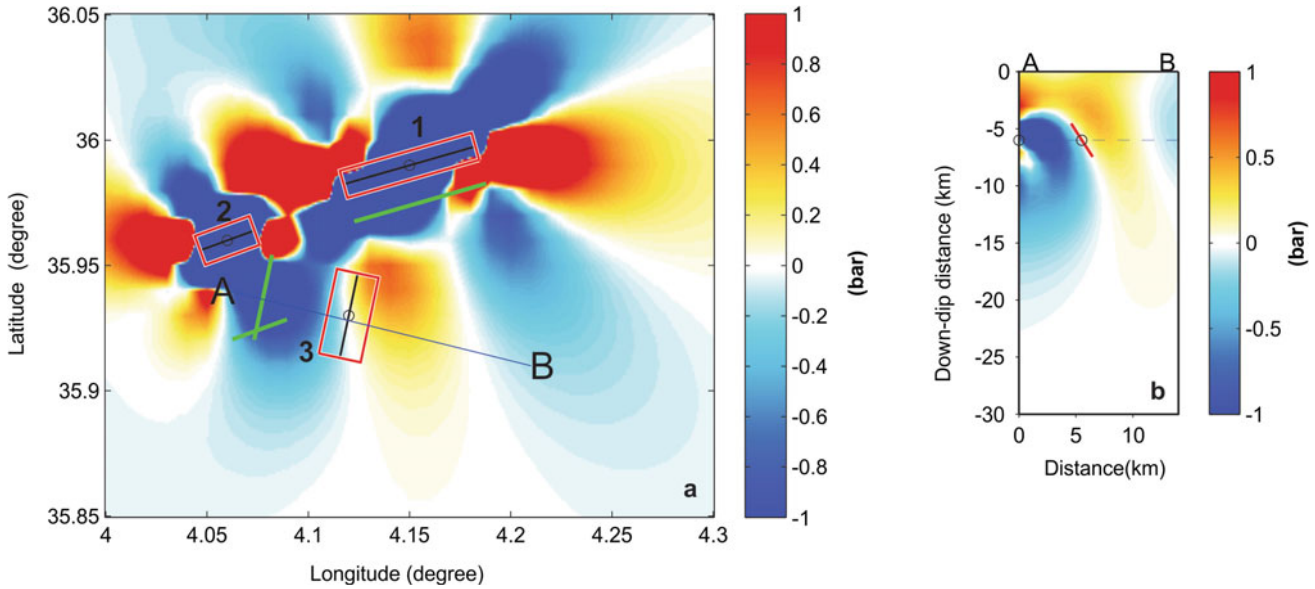

Fig. 3 **a** Stress change associated with the first and the second shock resolved on the third fault plane oriented [Strike, Dip, Rake: 12°, 57°, 12°, respectively]. **b** Cross section

(Beldjoudi et al. 2016). Their duration magnitudes Md vary between 1.7 and 5.0 (including the third shock on 23/05). These aftershocks are located between 1 and 12 km of depth. Three cross sections A1B1, A2B2 and A3B3 (Fig. 4b–d) show the distribution of aftershocks with depth. We can observe that about 95% of aftershocks are located on depth with ΔCFF > 0.1 bar. The same observation can be done when we calculate ΔCFF on optimal strike-slip planes (Table 1).

6 Discussion and Conclusion

We present a case of seismic sequence recorded in the eastern part of Algeria with a maximum Moment magnitude Mo of 5.5. The three main events of the sequence occurred on three disconnected active faults. The first shock loaded fault plane of the second shock with ΔCFF > 0.1 bar. The same happened for the third shock; it was loaded by the

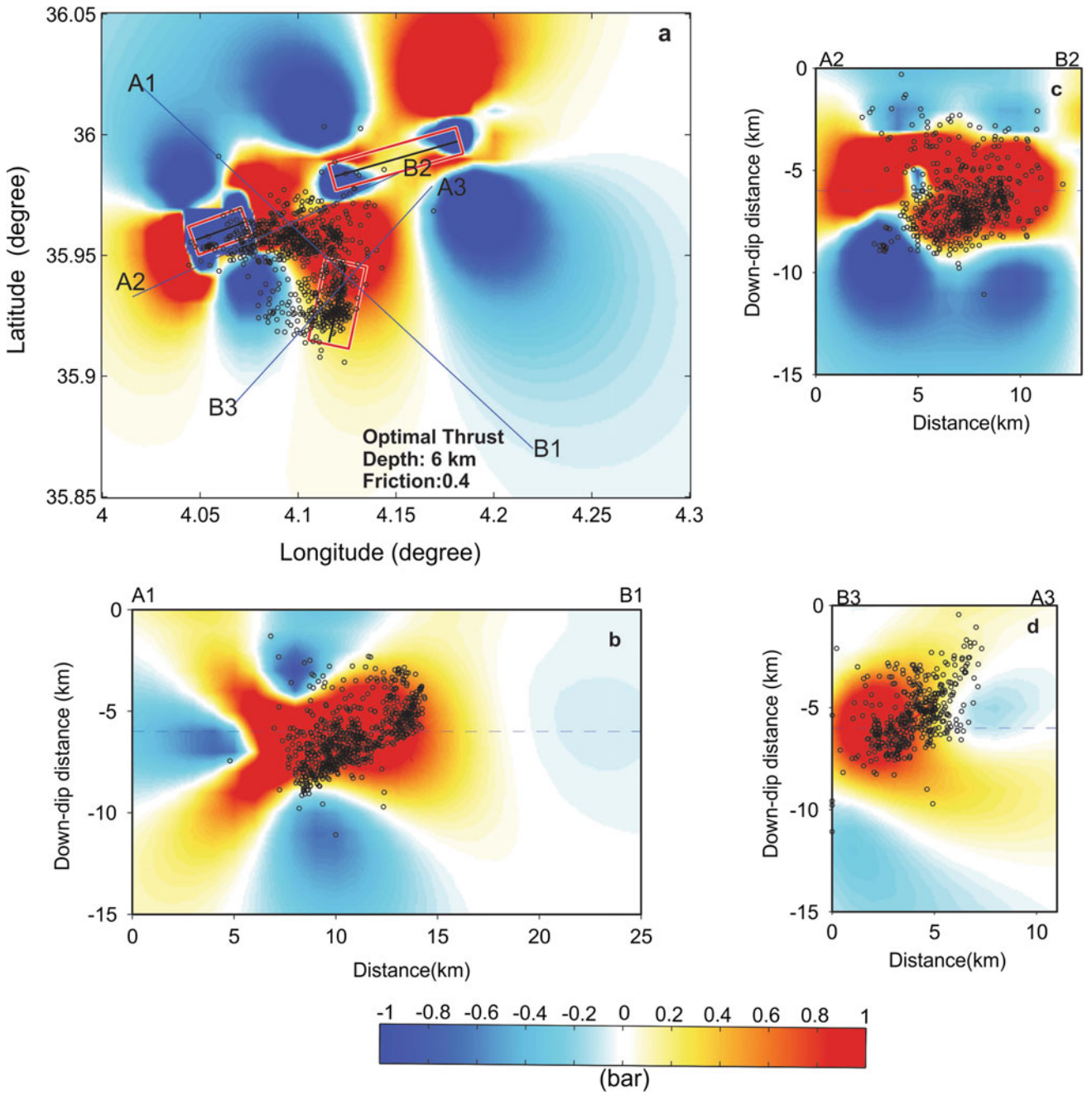

Fig. 4 **a** A1B1, A2B2, A3B3 show the orientation of cross sections. **b–d** Cross sections with different azimuths in correlation with ΔCFF. 95% of aftershocks, which occurred between the second and the third shocks are located where ΔCFF > 0

Table 1 Source parameters of the seismic sequence

Event	Strike dip rake (°)	Mw	Mo (Nm)	Length (km)	Width (km)	Total slip (m)
1	254° 74° 175°	5.5	2.4×10^{17}	6.0	4.5	0.24
2	250° 55° 120°	5.1	5.3×10^{16}	2.6	2.4	0.27
3	12° 57° 12°	5.2	7.4×10^{16}	3.8	3.47	0.17

previous main shocks with a ΔCFF > 0.04 bar. This seismic sequence occurred on a faulted fold with a huge number of ancient faults with various orientations and types, which are active during the actual tectonic phase with a principal most compressive stress $\sigma 1$ oriented NNW–SSE. The seismic sequence influenced the close active faults in the epicentral area of the Biban region. This can be explained by the occurrence of an important number of aftershocks in a proximate area (Beldjoudi et al. 2016).

References

Beldjoudi, H., Delouis, B., Djellit, H., Yelles-Chaouche, A., Gharbi, S., Abacha, I.: The Beni-Ilmane (Algeria) seismic sequence of May 2010: seismic sources and stress tensor calculation. Tectonophysics **670**, 101–114 (2016)

Cocco, M., Nostro, C., Ekström, G.: Static stress changes and fault interaction during the 1997 Umbria-Marche earthquake sequence. J. Seismol. **4**, 501–516 (2000)

Harris, R.A.: Introduction to special section: stress triggers, stress shadows, and implication for seismic hazard. J. Gephys. Res. **10**, 24347–24358 (1998)

Hodgkinson, K.M., Stein, R.S., King, G.C.P.: The 1954 rainbow mountain-fairview peak-dixie valley earthquakes:a triggerednormal faulting sequence. J. Geophys. Res. **101**(25), 459–471 (1996)

King, G.C.P., Stein, R.S., Lin, J.: Static stress changes and the triggering of earthquakes. BSSA **84**(3), 935–953 (1994)

Lin, J., Stein, R.S.: Stress triggering in thrust and subduction earthquakes, and stress interaction between the southern San Andreas and nearby thrust and strike-slip faults. J. Geophys. Res. **109**, B02323 (2004). https://doi.org/10.1029/2003jB002607

Stein, R.S., King, G.C.P., Lin, J.: Change in failure stress on the southern San Andreas fault system caused by the 1992 magnitude = 7.4 Landers earthquake. Science **258**, 1328 (1992)

Toda, S., Stein, R., Reasenberg, P.A., Dietrich, J.H., Yoshida, A.: Stress transferred by the 1995 Mw = 6.9 Kobe, Japan, shock: effects on aftershocks and future earthquake probabilities. J. Geophys. Res. **103**, 24543–24566 (2005)

Contribution of the Pleiade Satellite Image Processing in the Characterization of the Active and Seismogenic Structures in the Tell Atlas (Northern Algeria)

Souhila Bagdi-Issaad, Mustapha Meghraoui, Elise Kali, and Ahmed Nedjari

Abstract

High-resolution data allows the production of accurate maps and precise observations. In our research, we used panchromatic 'Pleiades' tri-stereo-satellite images with 0.5 m of resolution, to identify and characterize active and seismogenic structures in the Tell Atlas. In this study, the Pleiade images processing has simplified the recognition of geomorphological markers related to active tectonics and the highlighting of the cumulative surface deformation. The results obtained are mainly integrated into two research strands. The first one is tectonic geomorphology and quantification of deformation. The second strand is kinematic and elastic modelling of fault-related folds. Our research in its entirety aims to assess seismic hazard in the Tell Atlas.

Keywords

Tell Atlas • Active tectonics • Geomorphological markers • Remote sensing • Pleiades satellite images

1 Introduction

Tell Atlas, a part of the southern Mediterranean margin, is characterized by NE–SW trending "en-echelon" active faults-related folds (Meghraoui 1988) generated by a trans-pressive tectonic regime; the shortening is in the order of 2.2 ± 0.5 mm/yr in NNW–SSE to NW–SE directions. This regime is related to the 4–6 mm/yr oblique convergence along the Africa-Eurasia plate boundary (Serpelloni et al. 2007; Bougrine et al. 2019). This dynamic generates important surface deformation.

2 Materials and Methods

A total of 11 high-resolution (0.5 m) panchromatic "Pleiades" tri-stereo-satellite images were acquired. They cover four (04) zones that correspond to active fault-related folds, namely the Zemmouri uplift area, Sahel, El Asnam and Tenes Abou El Hassen (TAEH).

Raw data is visualized in focus of PCI Geomatica soft. It offered a clear image in a small scale where geomorphological markers are easily recognizable. This allowed mapping the lineaments that we think correspond to active blind faults.

We generated digital elevation models (DEMs) using the three images. The method states that we first generated two epipolar images (2 couples of images). To avoid the problems of artefacts, data loading methods differ according to the number of rows and columns that make up the row data. We obtained accurate DEMs with 1 m uncertainties.

Post-processing was mainly done with ArcGis and Global Mapper softwares using DEMs obtained in previous step. Shaded terrain and slope maps were done with ArcGis.

With Global Mapper, we generated orographic, topographic and hydrographic maps. We made topographic profiles along marine and fluvial deposits. We also obtained longitudinal profiles and cross sections of main rivers. With the same software, we obtained 3D geomorphic models.

Processing was done for the four zones mentioned before.

3 Results (Presentation of Some Examples)

We mapped active faults for the four structures mentioned before. In Fig. 1, we show an example for the central part of El Asnam blind fault that reached the surface during 1980 Mw 7.1 earthquake. Along the fault, we can see triangular

S. Bagdi-Issaad (✉) · M. Meghraoui · E. Kali
EOST - Institut Terre et Environnement de Strasbourg, University of Strasbourg, CNRS - UMR 7063, Strasbourg, France

S. Bagdi-Issaad · A. Nedjari
Faculté des Sciences de la Terre FSTGAT, USTHB, Algiers, Algeria

M. Meghraoui et al. (eds.), *Advances in Geophysics, Tectonics and Petroleum Geosciences*, Advances in Science, Technology & Innovation, https://doi.org/10.1007/978-3-030-73026-0_29

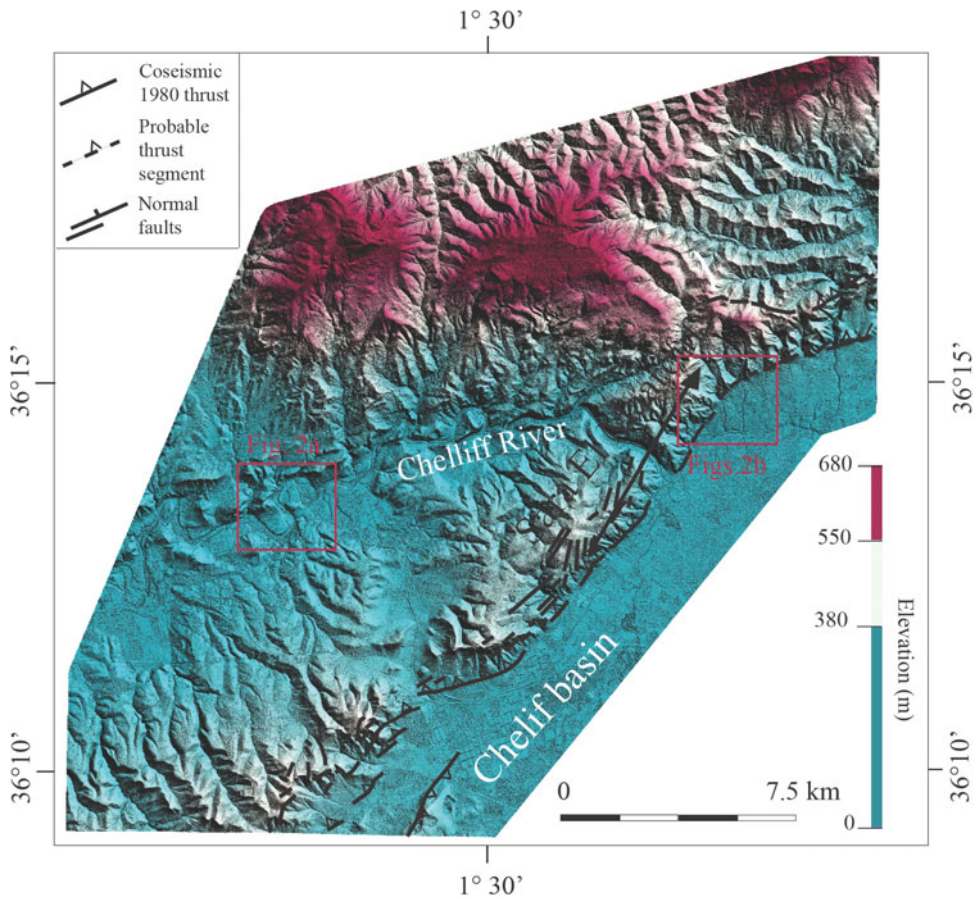

Fig. 1 Orographic map of central part of El Asnam fault-related fold

facets, sharper in Fig. 2b. The geomorphic limit between Chelif basin and south flank of El Asnam fold can be mapped with 1 m uncertainties (Fig. 2b).

Measures of folds (width, length, height and position of hinge) and fault (length) were done using mainly orographic maps. The values obtained have been used in

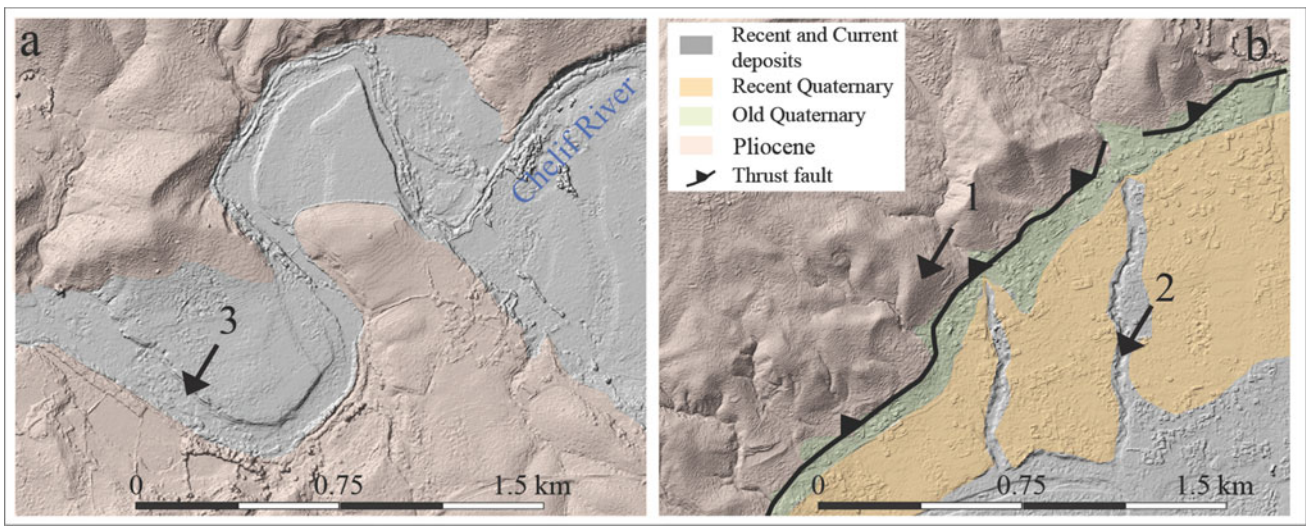

Fig. 2 **a**, **b** Geological maps realized on shaded terrain maps in small areas in El Asnam active structure. 1: Triangular facets; 2: streams; 3: riverbanks

kinematic and elastic modelling, another part of our research.

For each zone, we mapped facies along the active faults with a particular interest of quaternary deposits (Fig. 2b) that shows recent and active deformation.

Drainage is also mapped. Riverbanks of main rivers are sharp, especially on shaded terrain maps and slope maps. Figure 2a shows an example of a very short segment of Chelif River where the narrowest fluvial terraces are visible.

Longitudinal profiles and cross sections of the main rivers, obtained with DEMs-Pleiades, were used to calculate drainage morphometric parameters. That is also another part of our research.

Marine, lacustrine and fluvial terraces are finely mapped. We can see an example in Fig. 3 of the Sahel structure. Topographic profiles reveal their precise altitudes.

4 Discussion and Conclusion

The use of Pleiade images allowed a better recognition of geomorphological markers that reveal the seismic potential of blind zones. In this context, new maps of El Asnam, Zemmouri, Sahel and TABH active structures were realized.

Maps showing distribution of marines, lacustrine and fluvial terraces are accurate, and topographic profiles offer

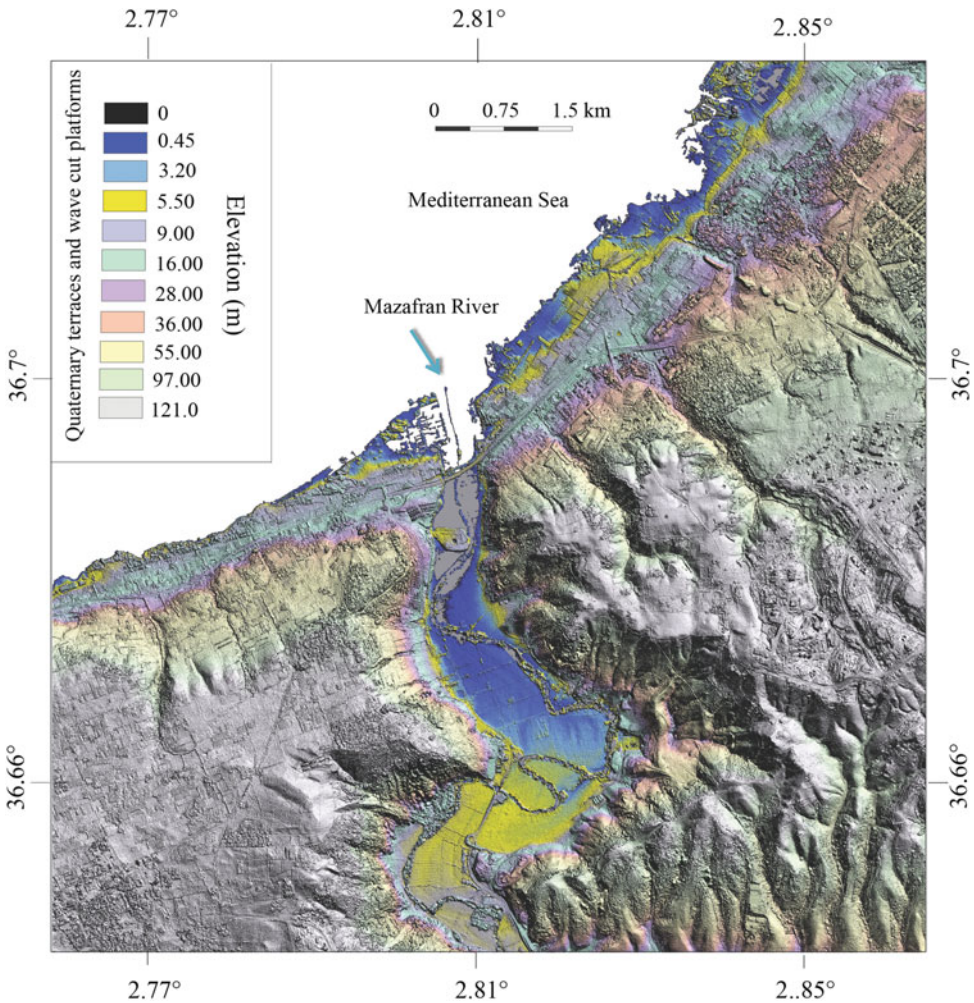

Fig. 3 Distribution of quaternary marine terraces in a segment of eastern Sahel structure and fluvial terraces along Mazafran River

precise altitudes. This is an asset to quantify short- and long-term deformations.

Drainage morphometric parameters obtained are precise too. They determined the more deformed areas of the least deformed.

Precise measurements (x, y and z) of structural elements are good input for kinematic and elastic modelling.

In areas with lack of seismic data, the use of high-resolution (0.5 m) data for a surface study that we have made is decisive for our research.

Identifying active blind structures potentially able to generate large earthquakes proves very important in seismic hazard and assessment.

References

Bougrine, A., Karim Yelles-Chaouche, A., Calais, E.: Active deformation in Algeria from continuous GPS measurements. Geophys. J. Int. **217**, 572–588 (2019). https://doi.org/10.1093/gji/ggz035

Meghraoui, M.: Géologie des zones sismiques du nord de l'Algérie (Paléosismologie, Tectonique active et synthèse sismotectonique). Thèse de doctorat d'Etat, Université de Paris-Sud, Centre d'Orsay (France), 356 pp. (1988)

Serpelloni, E., Vannucci, G., Pondrelli, S., Argnani, A., Casula, G., Anzidei, M., Baldi, P., Casperini, P.: Kinematics of the western Africa-Eurasia plate boundary from focal mechanism and GPS data. Geophys. J. Int. **169**, 1180–1200 (2007)

Historical and Archeoseismic Investigations in Kairouan Region (Central Tunisia): Evidence for the 9 October 859 AD Large Earthquake

Nejib Bahrouni, Mustapha Meghraoui, Klaus Hinzen, Mohamed Arfaoui, Ridha Maamri, and Faouzi Mahfoud

Abstract

The Kairouan city, capital of the Aghlabides Dynasty (800–909 AD), and surrounding region were affected by a large earthquake in 8 Rajab 245 Hijri (9 October 859). Contemporaneous accounts by local travellers to the Abbasides Caliphate (750–1258 AD) and reported by the chroniclers and historians Al-Baghdadi (died 860) and Al-Tabari (838–923 AD) have described the damage to the city and more than 13 villages that suffered severe destructions and left a large number of people homeless. In Kairouan city, the dome and other holy places (Minbar and Mihrab) of the great mosque, the houses, fortifications and bridges suffered damage. The aqueduct that used to supply Kairouan with fresh water from western mountains was badly damaged at about 20 km west of the city. Field investigations of the aqueduct using geodesy and archeoseismology with radiocarbon dating characterize the damage features. Recent field investigations in the region taking into account the construction typology and inferred damage distribution suggest a macroseismic intensity reaching IX–X MSK. The seismotectonic context suggests a seismic source along the major Sbiba E–W trending transpressive fault that includes the Cherichira, Sfaia, El Baten folding system near Kairouan. The active fault system affecting late Quaternary units, made of 30-km-long thrust-related "en-echelon" folds related to the E–W trending fault, is characterized and identified as seismogenic ~20 km west of Kairouan.

N. Bahrouni · M. Arfaoui · R. Maamri
Office National des Mines, Tunis-El Cherguia, Tunisia

M. Meghraoui (✉)
EOST - Institut Terre et Environnement de Strasbourg, University of Strasbourg, CNRS - UMR 7063, Strasbourg, France
e-mail: m.meghraoui@unistra.fr

K. Hinzen
University of Cologne, Cologne, Germany

F. Mahfoud
Institut National du Patrimoine, Tunis, Tunisia

Keywords

Kairouan • Historical earthquake • Archeoseismology • Damage • Aqueduct

1 Introduction

Kairouan city, previously *Fossatum* Roman town, was founded by Okba Ibn Nafî in AD 670 and established as a capital by the Aghlabide Dynasty (AD 801–909). Kairouan, the first established city of the Islamic Maghreb, was considered by the Caliphate of Baghdad and Abbasides Dynasty as the fourth most important holy city after Mecca, Al Medina and Jerusalem. The city is well known for its impressive great mosque built in AD 836 with 31.5 m high minaret and its 3.5-km-long city walls (Golvin 1968). The water supply was provided through rainwater channelling for underground cistern or through the ~35-km-long Cherichira aqueduct bringing fresh water from the Oueslet western mountains.

Studies on the occurrence of the AD 859 earthquake and the related damage in the Kairouan region are primarily based on the examination of contemporaneous documents from the historian-chroniclers Al-Baghdadi, who died in AD 860 (1980), and Al-Tabari AD 838–923 (1967). Field investigations using archeoseismologic approaches (Hinzen et al. 2011; Stiros and Jones 1996) suggest earthquake-induced damage of the Cherichira aqueduct and Kairouan city mosque (Bahrouni et al. 2019). The analysis of historical documents indicates severe damage of mosques, houses, walls and bridges among buildings, and villages in the epicentre area (Younes 2009). What is also observed is that there have been important building reconstructions and renovations beginning from AD 860 (Mahfoudh et al. 2004). However, the instrumental background seismicity is moderate and no major earthquake with Mw > 5 occurred in the past century.

M. Meghraoui et al. (eds.), *Advances in Geophysics, Tectonics and Petroleum Geosciences*,
Advances in Science, Technology & Innovation, https://doi.org/10.1007/978-3-030-73026-0_30

2 The 9th of October, 859 Earthquake

As a holy city, Kairouan was an important urban area linked to the Abbaside Dynasty (750–1258). All reports on the political and economic situation of the region, including natural hazards (i.e. earthquakes, flooding, storms) were regularly sent to Baghdad. Two contemporaneous historians and chroniclers, Al-Baghdadi and Al-Tabari report on the earthquake with descriptions from Maghrebian traders and travellers and related book of merchants. Both historians added that the strong earthquake has affected the city of Kairouan, and Al-Tabari noted the date of 8 Rajab 245 Hijri (H) that corresponds to AD 9 October 859.

We note here that Al-Baghdadi (1980) reported on the earthquake as one of the main catastrophic events that occurred during the 240H decade in the Abbasid Caliphate. Subsequently, this date was erroneously reported as the date of the earthquake by several authors (Ibn al Jawzi 1987; Al Suyuti 1971). However, Ibn Al-Athir 1160–1233 (1872) relied on Al-Tabari who also reports 8th Rajab 245H. The AD 859 historical earthquake of Kairouan and the related damage in the epicentre area were cited two times by Ibn Al Jawzi 1116–1201 (1987, 1997) who quotes the book of Maghrebian merchants as cited by Al-Baghdadi (1980). Furthermore, all details already mentioned by chroniclers and local witnesses are later on repeated by other historians such as Ibn Al-Athir (1160–1233), Ibn Adhari (died 1295), Ibn Taghribirdi (1411–1470), Al Suyuti (1445–1505).

3 Results

Earthquake Damage and Reconstruction

According to Al-Baghdadi (1980), in Kairouan city, the dome and other holy places (Minbar and Mihrab) of the great mosque, the houses, fortifications and bridges suffered severe damage. Golvin (1968) reports after observation of technical failure the important repairs with double arches in the nave of the great mosque beginning from AD 862 to AD 864 (Bahrouni et al. 2019).

In AD 860 and the following years, the local governor, Al Amir Abou Ibrahim Ahmed (who ruled Kairouan from AD 856 to 863), conducted important reconstructions and repairs in Kairouan and neighbouring areas (Mahfoudh et al. 2004; Solignac 1952). As the city suffered severe shortage of fresh water in AD 860, probably due to the AD 859 earthquake and damage to the Cherichira aqueduct, the local governor dedicated 300,000 dirhems (around 700,000 €) to the construction of an open circular water reservoir, a historical masterwork of a large cistern also called "*Feskiya*" of Bab Tounes for the city water supply (Golvin 1968).

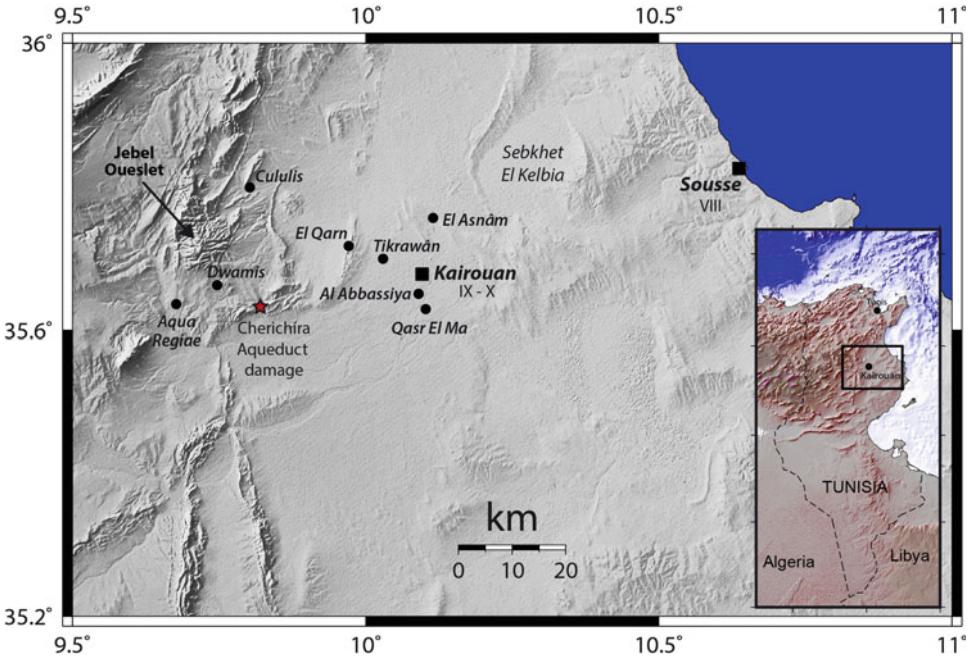

Fig. 1 The Kairouan city (box) in central Tunisia (see inset), the site of the AD 859 earthquake, according to two contemporaneous chroniclers Al-Baghdadi (1980) and Al-Tabari (1967). Severe damage is reported to the city and 13 neighbouring villages (Bahrouni et al. 2019). The black circles represent the location of nine old villages often cited in historical documents and likely damaged by the earthquake. The star indicates the damage location of the Cherichira Aqueduct that was used to bring fresh water from Jebel Oueslet to Kairouan. The intensities IX–X and VIII MSK are attributed to Kairouan and Sousse cities, respectively, based on the reported damage descriptions and important reconstructions beginning from AD 860 (Al-Baghdadi 1980; Al-Tabari 1967; Bahrouni et al. 2019; Golvin 1968; Mahfoudh et al. 2004)

Both Al-Baghdadi (1980) and Al-Tabari (1967) reported that 13 villages were damaged in Kairouan region. Based on local witnesses of local archaeological remains, old buildings and historical documents, we conducted field investigations in order to evaluate the possible earthquake damage extent. The heavy damage of the Roman towns Cululis and Aquae Regia (Fig. 1) and the disappearance of several mediaeval towns (see the 9 old villages in Fig. 1) suggest earthquake effects beyond the Kairouan city and as far as the coastal city of Sousse (ex. Justinianopolis, later on named Susa; Fig. 1). The coincidence between the earthquake date and the AD 860–863s significant reconstruction incidences indicates the level of severity of the seismic damage. In comparison with other reported large earthquakes in the central coastal Tunisia (Kharrat et al. 2018), the size and extent of damage in Kairouan region, nearby 13 villages, and coastal Sousse suggest a maximum intensity of IX–X MSK for the AD 859 earthquake.

The Damaged Cherichira Aqueduct

The Cherichira aqueduct is an ancient Roman structure bringing fresh water from Jebel Oueslet (to the west) to the Kairouan city and its 100,000 inhabitants in the ninth century. The building shows two main superposed canals, the first being Roman and the second Aghlabides. The aqueduct is embedded or carved in bedrock, sometimes built upon the ground, and also elevated as a bridge when crossing river valleys. The ~400-m-long Cherichira bridge reaches an height of about 25 m with basement stones ~1 m long by ~0.5 m wide and height forming ~3 m by ~3 m size pillars. The northern half section of the aqueduct bridge is damaged and collapsed when crossing the valley leaving the two edges quasi-unbroken. Often located upon the Roman structure, the Aghlabides canal can be easily identified with its ~1-m-high arched mortar edges (Bahrouni et al. 2019).

In order to characterize the period of aqueduct collapse and interruption of water supply, we selected further south downhill a damaged and buried canal site filled with sediments ~800 m southeast of the bridge (Fig. 2). The excavation clearly reveals the aqueduct frame made of white mortar and inner part filled with a succession of silty-sandy units mixed with fine and coarse gravel. The accelerator mass spectrometry (AMS) radiocarbon dating of mortar sample collected on the aqueduct wall gives AD 771–AD 965 (2σ 95.4%) which corresponds to a large bracket for the construction time, but in agreement with the aqueduct built in early ninth century (Mahfoudh et al. 2004; Solignac 1952). The filling of the Aghlabide canal with a succession of deposits implies (1) the end of aqueduct function coeval with the early deposits in the canal, and (2) the AMS radiocarbon analysis of a charcoal sample in early deposits

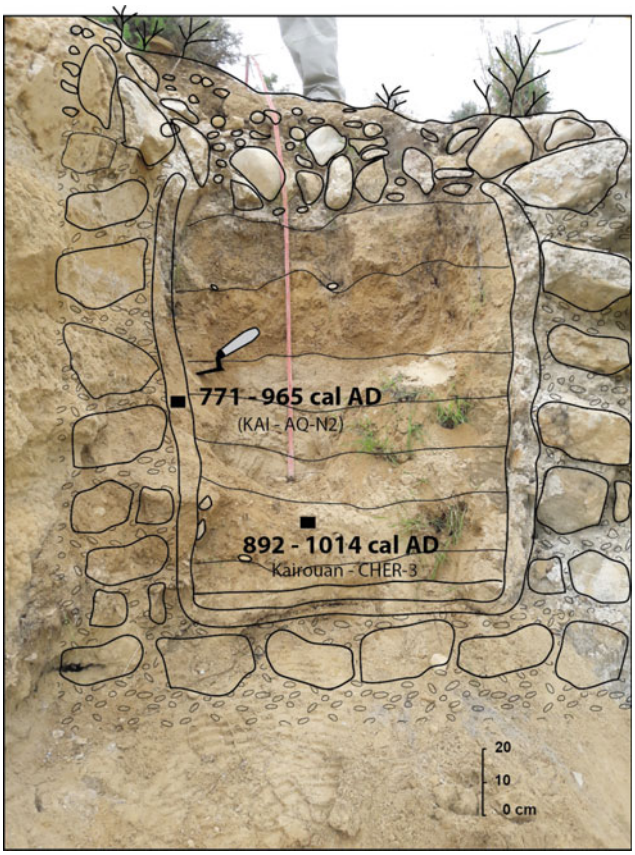

Fig. 2 Section of buried Aghlabides aqueduct filled with alluvial and colluvial deposits. Black box is the location of charcoal sample with the lowermost calibrated radiocarbon date 2σ (Bahrouni et al. 2019)

provides AD 892–AD 1014 (2σ 95.4%) postdates the AD 859 earthquake occurrence by a few tens of years.

4 Conclusions

The Kairouan city and surrounding region were affected by an earthquake in AD 859 that generated significant damage. Several contemporaneous and subsequent chroniclers and historians provided descriptions of the damage of the Kairouan region leaving a large number of people homeless. It is also reported that a sequence of strong earthquakes continued for three days and the homeless villagers requested refuge in the city. Although Guidoboni et al. (1994) and Ambraseys (2009) mention the earthquake occurrence in the Maghreb (i.e. Northwest Africa), the earthquake is reported as doubtful as its related historical effects have not been sufficiently studied by recent seismologists and historians.

Our investigations include indirect account of earthquake damage linked to the important reconstruction projects in Kairouan and Sousse cities from AD 859 to AD 864. Indeed, several more recent authors (Golvin 1968; Laporte 2015;

Mahfoudh et al. 2004; Solignac 1952) provide details on the main reconstructions and their dating that coincide with the AD 859 earthquake aftermath.

The damaged Roman—Aghlabide aqueduct at Cherichira shortly postdates the AD 859 earthquake. Here, the isotopic dating suggests that the aqueduct activity was interrupted during the Aghlabides' ruling. Furthermore, the trace of a NE–SW trending reverse fault can be delineated, with a linear fault scarp at the edge of the Sebkhet El Kelbia. The Kairouan region being an important urban and rural agglomeration, the earthquake activity and related active tectonics should be the focus of a research programme necessary for seismic hazard and risk assessment.

References

Old References

Al-Baghdadi (Abu Ja'far Muhammad ibn Habib Al-Hashimi, died 860): Kitāb al Mukḥabbir, Ed. Dar al-afaq al-jadida, 6752 pp. Beyrut (1980)

Al Suyuti (Jalal al-Din): Kashf al-salsala 'an wasf al-Zalzala, edited by Abd al Latif Saadani. Fez (1971)

Al Tabari, Muhammad Ibn Jarir: Ta'rikh al-rusul wa'l-mulûk, tome 9, p. 212, ed. Dar al Ma'arif. le Cairo (1967)

Ibn Al-Athîr: "al-kâmil fî al-târikh", 12 volumes, Tomberg (ed.). Leiden (1872)

Ibn al-Jawzi: "al-muntadhem fi tarikh al umam wal muluk", tome XI, 372 pp. Dar al–Kutub Al-Ilmia, Beyrouth Lebanon (1987)

Ibn al-Jawzi: Talkih fouhoum ahl al ater fi aouioun eterikh wa esier, pp. 63. Published by Dar Al Arkam Ibn Abi Al Arkam, Beirut (1997)

Recent References

Ambraseys, N.N.: Earthquakes in the Mediterranean and Middle East: A Multidisciplinary Study of Seismicity Up to 1900, p. 947. Cambridge University Press, Cambridge (2009)

Bahrouni et al.: The 9 October 859 AD Kairouan (Tunisia) large earthquake: evidence from historical and archeoseismic investigations. Submitted to SRL (2019)

Golvin, L.: Quelques réflexions sur la grande mosquée de Kairouan à la période des Aghlabides. Rev. Occid. Musul. Méditerr. **5**, 69–77 (1968)

Guidoboni, E., Comastri, A., Traina, G.: Catalogue of Ancient Earthquakes in the Mediterranean Area Up to the 10th Century, p. 504. Istituto Nazionale di Geofisica, Rome (1994)

Hinzen, K.-G., Fleischer, C., Reamer, S.K., Schreiber, S., Schütte, S., Yerli, B.: Quantitative methods in archaeoseismology. Quatern. Int. **242**, 31–41 (2011)

Kharrat, S., Harbi, A., Meghraoui, M., Bouaziz, S.: The Tunisian homogenized macroseismic database (second century to 1981): first investigations. Seismol. Res. Lett. **90**(1), 347–357 (2018)

Laporte, J.P.: D'Hadrumète à Sousse, des années 350 à 859. RM2E. Rev. mediterr. ed. électron. **II**(1), 3–34 (2015)

Mahfoudh, F., Baccouch, S., Yazidi, B.: L'histoire de l'eau et des installations hydrauliques dans le bassin de Kairouan, éd. International Water Management Institute, Tunis (2004)

Solignac, M.: Recherches sur les installations hydrauliques de Kairouan et des basses steppes tunisiennes du VIe au XIe siècle, pp. 1–273. A.I.E.O., Alger (1952)

Stiros, S., Jones, R.E.: Archaeoseismology (Fitch Laboratory Occasional Paper), 268 pp. British School at Athens (1996)

Younes, K.: Akhbar El Zalazel fel Maghreb El Arabi (Reports on earthquakes in the Maghreb). Rev. univ. islam. (in Arabic) **13**(1), 67–92. Ghaza, Palestine (2009)

Algerian's Seismic Catalogue Completeness from Historical Instrumental Monitoring, Archeoseismological and Paleoseismological Studies

Abdelhakim Ayadi, Farida Ousadou, Kahina Roumane, Assia Harbi, Said Maouche, Mourad Bezzeghoud, and Mustapha Meghraoui

Abstract

For any seismic hazard study, a reliable, homogenized and complete seismic catalogue is required. The Algerian seismicity catalogue has been recently updated by retrieving and reappraising many historical events. The Algerian seismic network has also been densified up to about 80 seismic stations covering the Tell Atlas which is the most active area of northern Algeria for monitoring of the seismic activity reducing the magnitude threshold. Recently, we have launched archeoseismological studies to retrieve past strong earthquakes that have affected Roman sites located along the Tell Atlas. Here, we proceed with tectonic investigations around selected sites where significant observed damage was identified. On the other hand, paleoseismological investigations were conducted along the El Asnam fault (now Chlef) following the large Ms 7.3 earthquake of 1980. Paleoseismic studies combined with archeoseismological results provide the dating of past earthquakes and contribute to the completeness of the seismicity catalogue.

Keywords

Historical seismicity • Archeoseismicity • Paleoseismicity • Earthquake catalogue • Seismic hazard

A. Ayadi (✉) · F. Ousadou · A. Harbi · S. Maouche
Centre de Recherche en Astronomie Astrophysique et Géophysique, Algiers, Algeria

K. Roumane
University of Algiers 2 Abou el Kacem Saadallah, Algiers, Algeria

M. Bezzeghoud
Escola de Ciencias e Tecnologia (ECT), University of Evora, Evora, Portugal

M. Meghraoui
EOST - Institut Terre et Environnement de Strasbourg, University of Strasbourg, CNRS - UMR 7063, Strasbourg, France

1 Introduction

The Tell Atlas of Algeria experienced strong seismic events which caused heavy damage left behind a significant number of victims. Prior to 1900, several destructive earthquakes were reported by Algerian seismological catalogues (Ayadi and Bezzeghoud 2015; Harbi et al. 2015) such as those of Algiers (1365, 1716), Oran 1790, Djidjelli 1856 (Table 1), cited as documented events. Other events have occurred, but no information is available so far except that their effects could be recognized on archeological structures. The aim of our study is to complete the Algerian seismicity catalogue with past strong events retrieved from the analysis of damage on archeological sites and from paleoseismological investigations. A recent study on Roman sites in the Tell Atlas of Algeria revealed the existence of damage related to strong earthquakes that affected the archeological remains (Roumane and Ayadi 2019).

2 Historical and Archeoseismological Investigations

An update of the historical seismicity has been recently made by adding more than 200 new events in the north central and eastern Algeria to the Algerian catalogue (Harbi et al. 2015). An ongoing project is investigating the historical seismicity in the remaining western parts of the country. Most of the retrieved events were found in archives (journals, periodicals, unpublished documents and old books) and epigraphic documents (Table 2). More efforts are needed to check and analyze the huge quantity of unread documents. The second part of our study concerns the archeoseismological investigations on the Roman sites. Most of those in the eastern and central Algeria were investigated and resulting in interesting observations. They are probably related to the action of strong past earthquakes. The third part of our study concerns the paleoseismological

M. Meghraoui et al. (eds.), *Advances in Geophysics, Tectonics and Petroleum Geosciences*, Advances in Science, Technology & Innovation, https://doi.org/10.1007/978-3-030-73026-0_31

Table 1 List of strong seismic events in the Tell Atlas of Algeria

Date	Location	Io/Ms
January 3, 1365	Algiers	X
October 9, 1790	Oran	X
March 2, 1825	Blida	X
August 22, 1856	Djidjelli	IX
June 24, 1910	Aumale	X/6.4
September 9, 1954	Orléansville	IX/6.7
October 9, 1980	El Asnam	IX/7.3
May 21, 2003	Zemmouri	X/6.8

Io is MSK

Table 2 List of new retrieved events that occurred in the Tell Atlas of Algeria

Date	Location	Effects
1637	Algiers	Destructive
June 23, 1849	Constantine	Damaging
May 25, 1861	Hammam Debagh (Guelma)	Felt with aftershocks
November 30, 1863	Bougie	Largely observed
January 15, 1870	Philippeville	Strong

investigations which will give us indications about strong event by dating samples from specified trench.

3 Results

3.1 New Historical Seismic Events

According to Harbi et al. (2015), 286 events were retrieved from archives by analyzing periodicals, historical books, unpublished manuscripts, military reports, chronicles, testimonies and newspapers. 54 were determined with intensity Io $\geq$ VI (MSK scale). These unpublished events concern the northern, central and eastern Algeria (Fig. 1). A seismic database for historical seismicity is now available on the website of the North African Group for Earthquake and Tsunami Studies "NAGET" (http://naget.ictp.it/PUBLICATIONS/resources/AMD.pdf).

Table 1 displays the strongest and damaging seismic events that have occurred in the Tell Atlas.

Table 2 displays examples of the new earthquakes retrieved from archives and other unpublished documents. For some retrieved events, intensity (MSK scale) was not assigned because of the limited amount of information.

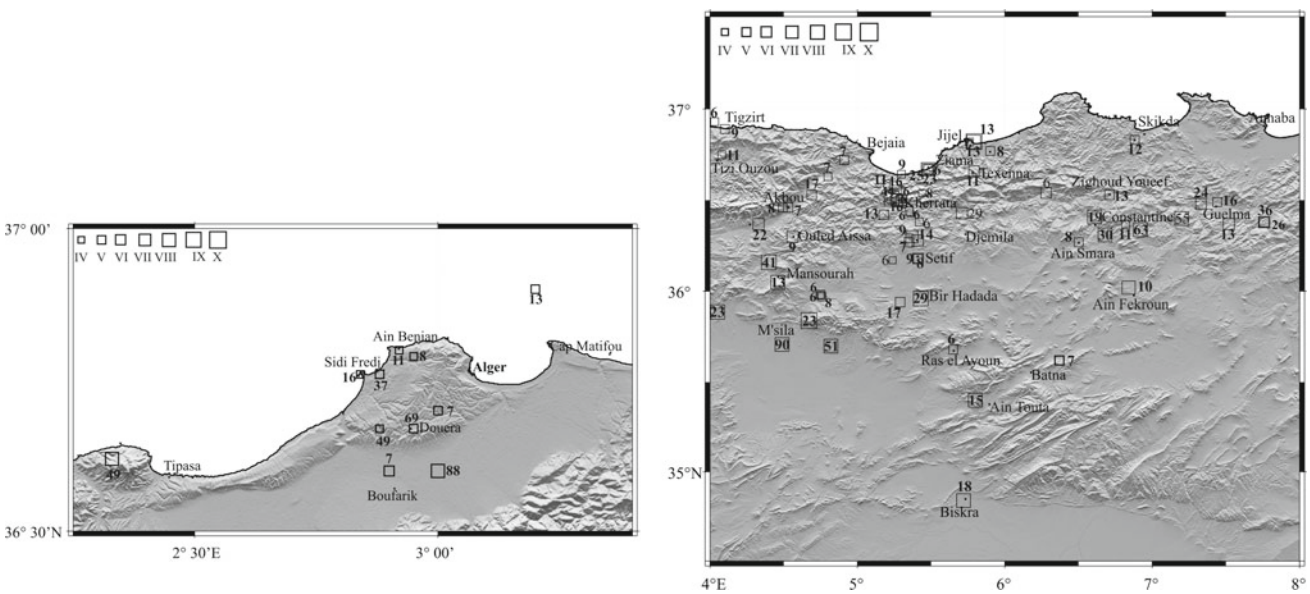

Fig. 1 Map of the distribution of new historical events retrieved from archives and other historical documents

3.2 Damage Observed on Archeological Structures

Damage was also observed on archeological structures and analyzed regarding that it could be attributed to earthquakes, human activities or any other cause (Fig. 2). Comparable damages observed on different sites worldwide have been identified on several Roman sites of northern Algeria. It has been suggested that they were caused by earthquakes (Roumane and Ayadi 2019).

3.3 Paleoseismological Observations

The application of paleoseismological method is an important tool using trenches dug across a fault zone for the identification of successive large earthquakes that affect a selected area. Dating would be useful to determine the earthquake occurrence chronology. This was conducted following the El Asnam earthquake of October 10, 1980, Ms 7.3 (Meghraoui 1988). An example of such investigation is given in Fig. 3.

4 Conclusion

The completeness of seismic catalogue is necessary for seismic hazard assessment. The Algeria catalogue is considered complete for strong and moderate events since 1960 due to the installation of seismological stations (Bezzeghoud et al. 1994). The study of historical seismicity helped to complete several gaps in the catalogue for the period between 1365 and 1960, and 286 new events that occurred in central and eastern part of the country were retrieved from historical documents and archives. Archeoseismological and paleoseismological studies will help to assure more

(a)

(b)

(c)

Fig. 2 Damage observed on Algerian Roman sites: **a** fallen columns in Timgad, **b** displaced blocks in lintel in Djemila, **c** displaced block observed in Caracalla Temple in Tebessa

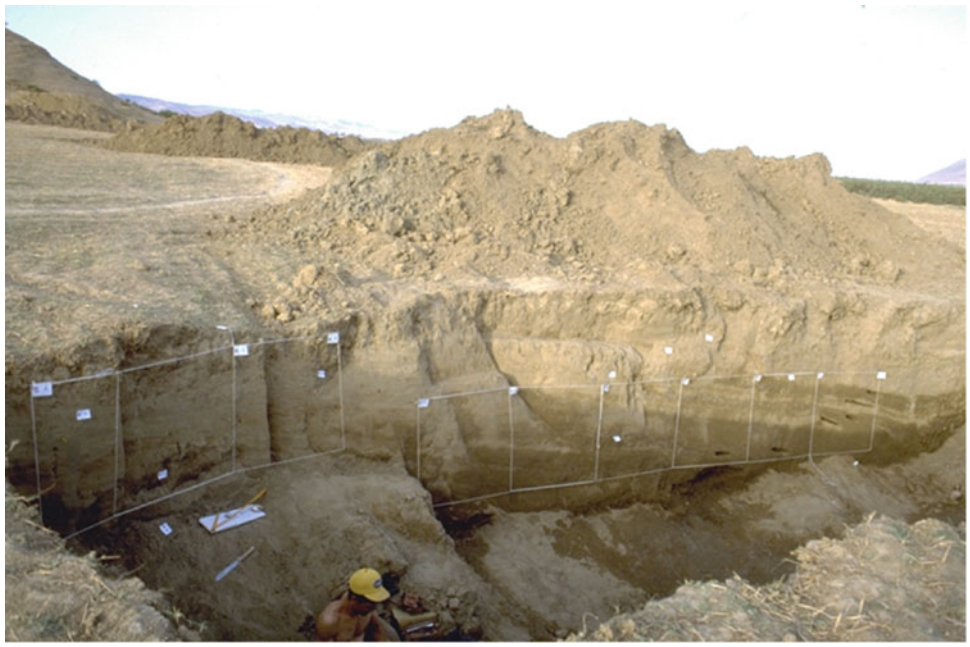

Fig. 3 Trench exposure (view to east) across the El Asnam fault trace near the dammed Chelif River (Meghraoui 1988)

completeness to the seismic database. Archeoseismological investigations have recently been launched on Roman sites and should be followed by paleoseismological studies to precisely locate and date damaging seismic events.

References

Ayadi, A., Bezzeghoud, M.: Seismicity of Algeria from 1365 to 2013: maximum observed intensities map (MOI_{2014}). Seismol. Res. Lett. **86**(1), 236–244 (2015)

Bezzeghoud, M., Ayadi, A., Sebaï, A., Benhallou, H.: Seismogenic zone survey by Algerian telemetred seismological network: case-study of Rouina earthquake, 19 January 1992. Phys. Earth Planet. Inter. **84**, 235–246 (1994)

Harbi, A., Sebaï, A., Benmedjber, M., Ousadou, F., Rouchiche, Y., Grigahcene, A., Aïni, D., Bourouis, S., Maouche, S., Ayadi, A.: The Algerian homogenized macroseismic database (267–1989): a deeper insight into the Algerian historical seismicity. Seismol. Res. Lett. **86** (6), 1705–1716 (2015)

Meghraoui, M.: Géologie des zones sismique du nord de l'Algérie, paléosismologie, tectonique active et synthèse sismotectonique. Thèse de Doctorat de l'Université Paris-Sud, France (1988)

NAGET webpage, http://naget.ictp.it/PUBLICATIONS/resources/AMD.pdf

Roumane, K., Ayadi, A.: Archaeoseismology in Algeria: observed damage related to probable past earthquakes on archaeological remains on Roman sites (Tell Atlas of Algeria). In: Geology of the Arab World—An Overview, pp. 318–339. Springer Geology (2019)

Analysis of the Bejaia Seismic Sequence of 2012–2013, Northeastern, Algeria

Oualid Boulahia, Issam Abacha, Abdelkarim Yelles-Chaouche, Hichem Bendjama, and Abdelaziz Kherroubi

Abstract

The Bejaia region in northeastern Algeria experienced three seismic sequences in November 2012, February 2013 and May 2013. The first started on the November 28, 2012, with a main shock of M_w = 5.1. Further, the second has begun on the February 22, 2013, with M_w = 4.3 and was preceded by three foreshocks. Finally, the last sequence occurred on the May 19, 2013, with M_w = 5.2 followed on the May 26, 2013, by an event of M_w = 5.0. Precise relative locations show a cluster of 196 accurately relocated events. The focal mechanisms are consistent with NW–SE striking near vertical right-lateral strike-slip fault, which extends from inland, the Babors chain, to the Gulf of Bejaia offshore on about 30 km long. It is known as the "Kherrata transversal accident," and found to be segmented in four parts S1, S2, S3 and S4, respectively. From the space–time evolution, the rupture seems to have gone through three stages. The area looked like activating an earthquake triggering process which started from S1, migrated progressively to S2, and terminating on S3 and S4. The release of energy has been distributed over four segments of the fault, apparently a disaster was avoided through an earthquake of bigger magnitude. Focal mechanisms, aftershocks distribution, isoseismic maps and the trends of offshore lineaments confirmed the activity of the NW–SE transversal accident, likely responsible for the recent seismicity in the region.

Keywords

The Babors chain • Seismicity and tectonics • Strike-slip fault • Focal mechanisms

1 Introduction

The 2012–2013 Bejaia seismic sequence occurred in a moderate seismic activity region spreading from the chains of Babors to the Bejaia gulf. The tectonics of the region is more complicated due to the junction of several seismogenic zones (the Soummam basin, the Lesser and Greater Kabylia) (Fig. 1a). The only detailed seismological study in the region concerns a significant earthquake which has recently affected the Laâlam region, with a moderate magnitude in 2006 (Beldjoudi et al. 2009), which is a property that characterizes all events in the region (see Table and Fig. 1). The characteristics of faulting related to the studied sequence have been revealed through a relative location of events, focal mechanisms, space–time evolution and Coulomb stress variations.

2 Seismotectonic Settings

The chain of Babors is located to the North of Setif and East of the Soummam valley. It represents the manifestation of the oblique collision between the tectonic plates of Africa and Eurasia, with local crustal shortening apparent of about 1.5 mm/year (Bougrine et al. 2019). The chain belongs to the external domain of the Alpine belt shown in this area by the Tellian units and embedded between two internal domains of the Lesser and Greater Kabylia (Fig. 1a). The present belt is one of the most seismically active regions, where we highlight the presence of several active faults, particularly the Kherrata thrust fault, known to be active for the earthquake of the February 19, 1949, which generated surface ruptures offset of about 50 cm. This fault has a total

O. Boulahia (✉) · I. Abacha · A. Yelles-Chaouche · H. Bendjama · A. Kherroubi
CRAAG, Route de l'Observatoire, B.P.63, Algiers, Algeria
e-mail: o.boulahia@craag.dz

M. Meghraoui et al. (eds.), *Advances in Geophysics, Tectonics and Petroleum Geosciences*,
Advances in Science, Technology & Innovation, https://doi.org/10.1007/978-3-030-73026-0_32

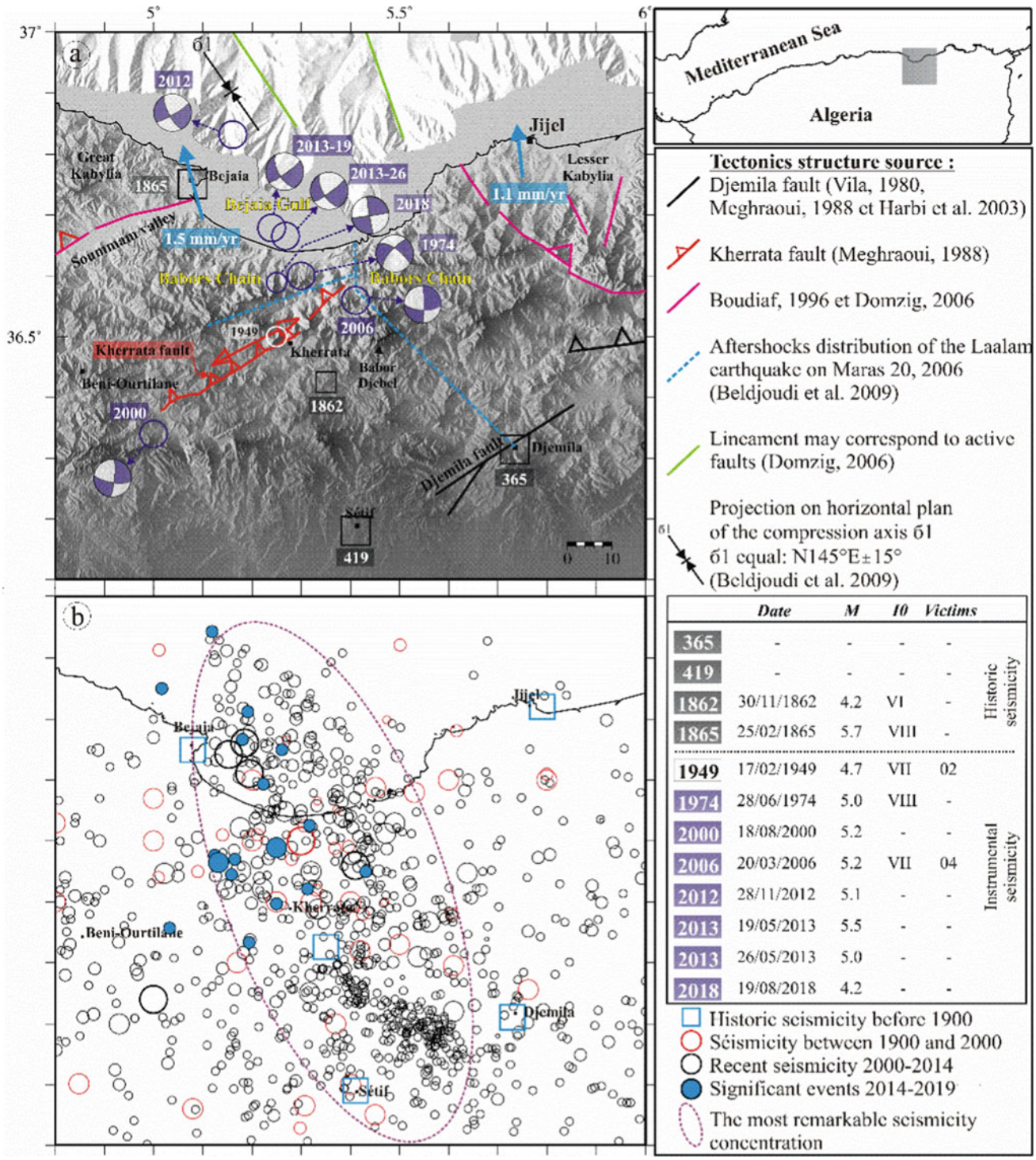

	Date	M	I0	Victims	
365	-	-	-	-	Historic seismicity
419	-	-	-	-	
1862	30/11/1862	4.2	VI	-	
1865	25/02/1865	5.7	VIII	-	
1949	17/02/1949	4.7	VII	02	Instrumental seismicity
1974	28/06/1974	5.0	VIII	-	
2000	18/08/2000	5.2	-	-	
2006	20/03/2006	5.2	VII	04	
2012	28/11/2012	5.1	-	-	
2013	19/05/2013	5.5	-	-	
2013	26/05/2013	5.0	-	-	
2018	19/08/2018	4.2	-	-	

Fig. 1 **a** Seismotectonic map of Babors zone and Setif region, including GPS velocities from (Bougrine et al. 2019). **b** Seismicity of the region from 1900 to 2014 and significant events during 2014–2019

length of 40 km, oriented N70° with a southward dip (Meghraoui 1988; Rothé 1950). The seismicity distribution (Fig. 1b) shows a cluster oriented along NW–SE, which includes several recent events (e.g., Laâlam earthquake of March 2006), the present studied sequence in Bejaia (2012–2013), and the significant events that occurred between 2014 and 2019. All these earthquakes show a strike-slip dominated movements along NW–SE direction.

3 Aftershocks Relocation and Focal Mechanisms' Determination

Applying the widely used HypoDD (Waldhauser and Ellsworth 2000), we relocated 207 earthquakes selected according to both horizontal and vertical uncertainties of less than 2 km. An event must have eight links with neighbors, which is why 95% of the events are kept. The horizontal distribution of the relocated events (Fig. 2a) shows a main cluster, oriented along NW–SE, a fault zone of about 30 km long and 3 km wide. Cross sections A1–A2 and B1–B2 (Fig. 2a) indicate that the foci are distributed on a near-vertical plane, mainly along a band at a depth of 5–11 km. The space–time evolution differentiates three main clusters: C1, C2 and C3 (Fig. 2a, b). It appears that each cluster is likely generated by a segment fault; S1 for C1, S2 for C2, C3 is a V-shaped structure which gives the segments S3 and S4, while all segments belong to the NW–SE Kherrata transverse accident. Focal mechanisms were computed from the first motion polarities using SPHERA (Rivera and Cisternas 1990). The groups of mechanisms are colored and separated according to their appropriate clusters. All focal mechanisms show a strike-slip faulting consistent with right-lateral motion on fault plane, oriented along NW–SE. The mean fault orientation has an azimuth of 136° and it is nearly vertical, in perfect coincidence with the orientation of the whole sequence.

4 Discussion

The aftershock data analysis and the focal mechanisms' determination of the 2012–2013 Bejaia earthquake sequences showed a main cluster of 196 accurately relocated events, generated by a NW–SE near-vertical right-lateral strike-slip fault, extending from the Babors Chain to the offshore of Bejaia Gulf for 30 km long. Analysis of the epicenters' locations and the focal solutions of the events that occurred in the region such as: Darguinah 1974, Laâlam 2006, Aokas 2018 and earthquakes between 2014 and 2019, then the trends of isoseismic maps of Laâlam 2006 and Bejaia 2012 earthquakes and finally the offshore lineament identified during MARADJA project lead us altogether to confirm the relationship between this NW–SE fault and the seismicity of the region.

The relocated events exhibited four sub-clusters C1, C2, C3 and C4, probably generated by four fault segments S1, S2, S3 and S4, respectively. The space–time distribution of the seismicity also shows some interesting features as, for two months after the main shock of the November 28, 2012, the aftershocks remained confined along the S1 segment. The area seems to be activating an earthquake triggering process. The triggering process is supported by small variations in the static stress, even lower than 1 bar, which are able to induce the reactivation of nearby faults that are close to failure (Toda et al. 1998). It may involve the generation of aftershocks or major shocks (Stein 1999). The chronological distribution progressively went through the segment S2 to finish on S3 and S4. The preliminary results of the computed Coulomb stress changes do explain the spatial distribution of stress-triggered aftershock seismicity, considering the lobes of high stress increase which perfectly matches the fault segments.

5 Conclusions

The Bejaia earthquake sequence (2012–2013) revealed for the first time a new tectonic feature known as the "Kherrata transverse fault," which is likely responsible for the seismic activity of the region. Further, the conclusion by the authors in Beldjoudi et al. (2009) may be incorrect, it cannot be excluded that the 2006 Laâlam earthquake was also associated with a NW–SE direction.

The triggered aftershock seismicity observed during the sequence can have a mechanical implication; fluids may control the space–time evolution of the seismicity, through the non-stationary migration of pore pressure disturbances. When pore pressure slightly increases, the effective Coulomb shear stress increases so that local failure conditions are reached. The role of fluids in the observed seismicity pattern has already been suggested for a few specific cases (Bourouis and Cornet 2009).

The sequence analysis contributes to the knowledge of seismic hazard since the possibility of large slip is not excluded, because the step-over between segments are not exceeding 3 km, taking into account the total width of the fault zone.

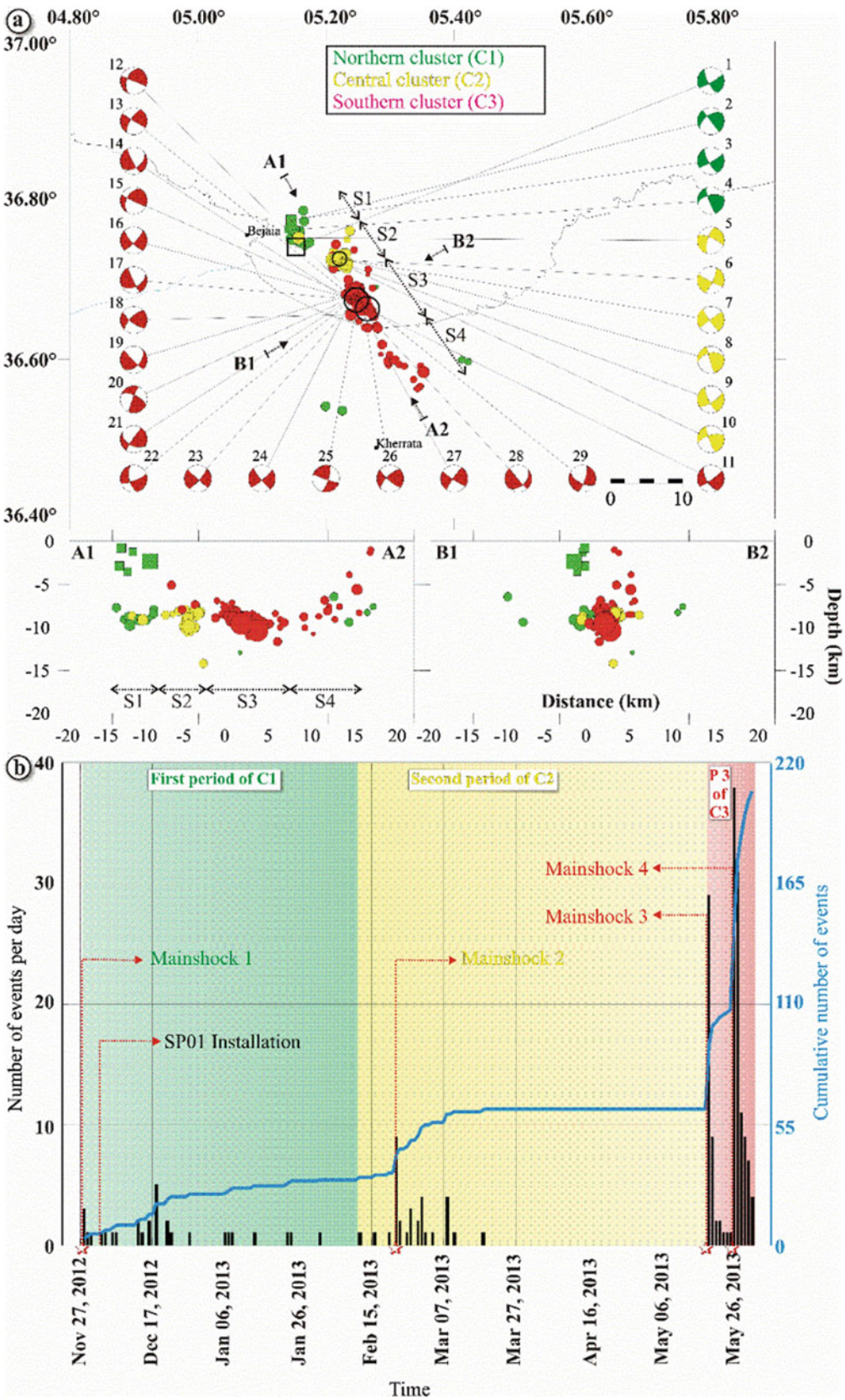

Fig. 2 **a** Horizontal and vertical distributions of the 196 relocated events, showing focal mechanisms of events with $M \geq 3.0$. **b** Cumulative number of seismic events versus time and number of events per day of cluster 1 (C1), cluster 2 (C2) and cluster 3 (C3)

References

Beldjoudi, H., Guemache, M.A., Kherroubi, A., Semmane, F., Yelles-Chaouche, A.K., Djellit, H., Amrani, A., Haned, A.: The Laâlam (Béjaïa, North-East Algeria) moderate earthquake (Mw = 5.2) on March 20, 2006. Pure Appl. Geophys. **166**(4), 623–640 (2009)

Bougrine, A., Yelles-Chaouche, A.K., Calais, E.: Active deformation in Algeria from continuous GPS measurements. Geophys. J. Int. **217** (1), 572–588 (2019)

Bourouis, S., Cornet, F.H.: Microseismic activity and fluid fault interactions: some results from the Corinth Rift Laboratory (CRL), Greece. Geophys. J. Int. **178**(1), 561–580 (2009)

Meghraoui, M.: Géologie des zones sismiques du Nord de l'Algérie (paléosismologie, tectonique active et synthèse sismotectonique). Ph.D. thésis, Université de Paris-sud, Orsay, France (1988)

Rivera, L., Cisternas, A.: Stress tensor and fault plane solutions for a population of earthquakes. Bull. Seismol. Soc. Am. **80**(3), 600–614 (1990)

Rothé, J.P.: Les séismes de Kherrata et la séismicité de l'Algérie. Bull Serv Cart Geol Algérie, 4 èmesérie, Géophysique, N. 3 (1950)

Stein, R.S.: The role of stress transfer in earthquake occurrence. Nature **402**, 605–609 (1999)

Toda, S., Stein, R.S., Reasenberg, P.A., Dieterich, J.H., Yoshida, A.: Stress transferred by the 1995 Mw = 6.9 Kobe, Japan, shock: effect on aftershocks and future earthquake probabilities. J. Geophys. Res. **103**(B10), 24543–24565 (1998)

Waldhauser, F., Ellsworth, W.L.: A double-difference earthquake location algorithm: method and application to the northern Hayward fault California. Bull. Seismol. Soc. Am. **90**(6), 1353–1368 (2000)

The Hammam Melouane Seismic Sequences (North Algeria) 2014–2016

Abdel Karim Yelles-Chaouche, Chafik Aidi, Mohamed Fedl Elah Khelif, Abderahmene Haned, Hamoud Beldjoudi, Fethi Semmane, Adel Chami, and Athman Belheouane

Abstract

During the last decade, many moderate earthquakes occurred in the central part of the Tell-Atlas belt of northern Algeria. Along the southern limit of the Mitidja basin bordered by the Blidean Atlas (30 km south of Algiers, the capital of Algeria), a number of seismic sequences with several moderate events occurred from 2013 to 2014. On the 17th of July 2013, a first event of magnitude Mw 5.0 occurred at 6.4623° N, 3.0426° E, 24 km south-east of the village of Hammam Melouane. Two years later, on the 23rd of December 2014, a seismic activity picked up in the same city by the occurrence of two successive moderate earthquakes of magnitude Ml 5.0 and Ml 4.8 at 8:00 and 8:59, respectively. A third sub-sequence occurred on the 10th of February 2016, south-east of the previous sub-sequence with a number of events having magnitude M < 5. The present study aims to understand this activity in the tectonic context of the southern limit of Mitidja basin which is subjected to compressive stresses, similar to other Neogene basins in northern Algeria (e.g. Mleta, Chlef, Tizi Ouzou basins). Study of these sequences integrating aftershocks' analysis and focal solution parameters determination indicates that the Hammam Melouane seismic activity occurred on three sub-faults located along the southern limit of the Mitidja basin. The occurrence of this sequence demonstrates the complexity of the rupture of one of the main seismogenic structure of the Mitidja basin.

Keywords

Hammam Melouane • Mitidja basin • Sequence • Active faults

A. K. Yelles-Chaouche (✉) · C. Aidi · M. F. E. Khelif · A. Haned · H. Beldjoudi · F. Semmane · A. Chami · A. Belheouane
Centre de Recherche en Astronomie, Astrophysique et Géophysique, Algiers, Algeria
e-mail: k.yelles@craag.dz

1 Introduction

North central Algeria is the location of a moderate-to-strong seismic activity. The occurrence of this seismicity is related to the instantaneous deformation of the inter-plate zone between the African and Eurasian plates. On the 17th of July 2013, a moderate event of Mw 5.0 occurred close to Hammam Melouane, one of the small villages of the Neogene Mitidja basin (north central Algeria) located south of Algiers, the capital of Algeria. The epicentre was precisely located at 6.4623° N, 3.0426° E, 24 km at the foot of the northern boundary zone of the Tell belt of northern Algeria (Yelles-Chaouche et al. 2017). This event is related to a NW–S strike-slip fault crosscutting the main NE–SW reverse active fault system of the southern boundary of the Mitidja Neogene basin. Two years later, on the 23rd of December 2014, the seismic activity picked up in the same region by the occurrence of two successive moderate earthquakes of magnitudes ML 5.0 ML 4.8 at 08:00 and 08:59, respectively. The first event was located at 3.0480° E and 36.4867° N; the second event was located at 3.0551° E and 36.4858° N. These two events triggered a seismic activity that continued until March 2015 with numerous aftershocks. A third sub-sequence was observed on the 10th of 2016, south-east of the location of the previous sub-sequence with a considerable number of earthquakes with M < 5 (Fig. 1 and Table 1). Nevertheless, an important number of minor events characterized this sub-sequence (Fig. 2 and Table 1).

2 Data Acquisition and Processing

Following the occurrence of the two earthquakes of the 23rd of December 2014, we installed four temporary stations to reinforce the CRAAG's permanent network (Fig. 1). These four portable stations were equipped with digitizers, coupled with passive sensors L22-D (f0 = 2 Hz) similar to those

M. Meghraoui et al. (eds.), *Advances in Geophysics, Tectonics and Petroleum Geosciences*, Advances in Science, Technology & Innovation, https://doi.org/10.1007/978-3-030-73026-0_33

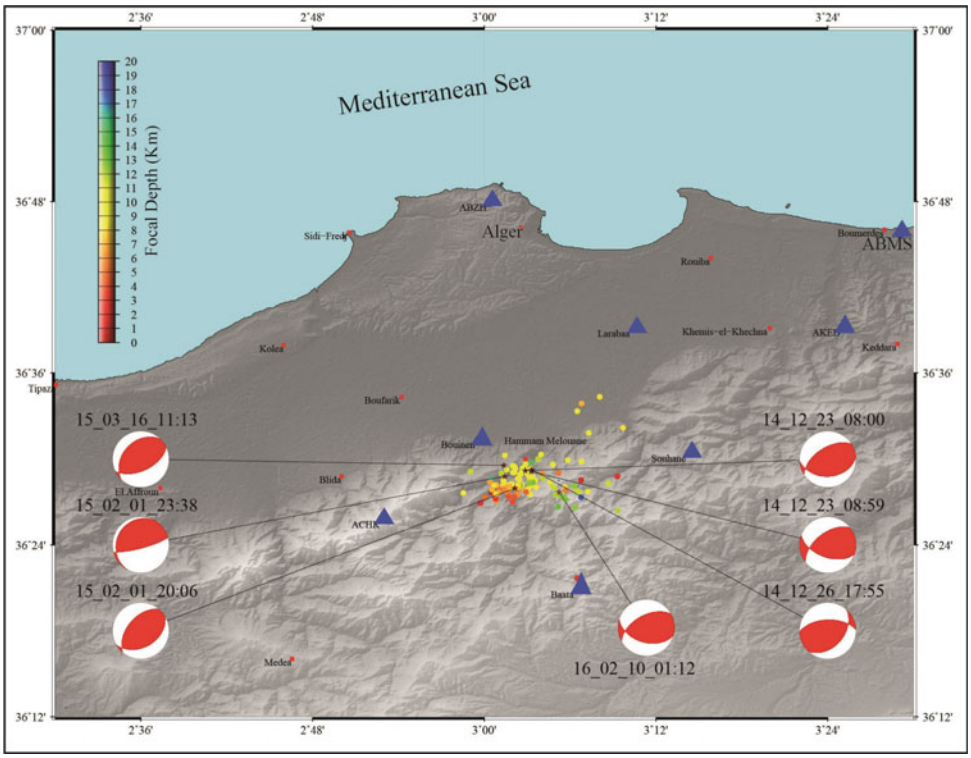

Fig. 1 A map showing distribution of the events (of the sub-sequences), and focal mechanisms of the seven most important aftershocks. Blue triangles represent the seismic stations used

Table 1 List of the most important earthquakes (M > 4) produced during the second and third sub-sequence of Hammam Melouane, with their magnitudes and focal mechanisms

Date dd/mm/yy	Origin times hhmm	Longitude	Latitude	Focal depth (km)	M_L	Str (°)	Dip (°)	Slip (°)
23/12/2014	08h00	3.0480	36.4867	10.90	5.0	237	56	72
23/12/2014	08h59	3.0551	36.4858	11.26	4.8	232	55	47
26/12/2014	17h55	3.0555	36.4880	9.21	4.5	268	58	119
01/02/2015	20h06	3.0358	36.4663	12.87	4.5	220	51	77
01/02/2015	23h38	3.0240	36.4798	11.36	4.6	209	14	45
16/03/2015	11h13	3.0228	36.4928	12.12	4.6	224	36	73
10/02/2016	01h12	3.0867	36.4750	11.14	4.8	241	54	59

installed for the July 2013 sub-sequence (Yelles-Chaouche et al. 2017). A total of 202 events were recorded during 4 months. Analysis of the recorded data to determine the earthquake source parameters was done using the Hypoinverse software package (Klein 1978) to obtain 134 events with RMS < 2 and GAP < 180 and a horizontal and vertical error ERH and ERZ < 0.2 km. To improve the relative location, the events were relocated using HypoDD (Waldhauser and Ellsworth 2000) to obtain 67 events well relocated (Fig. 1). In order to calculate the seismic moment M_0, the moment magnitude Mw and the focal mechanism of the 08:00 a.m. earthquake of the 23rd of December 2014, we use (Dreger 2003) waveform modelling method, which is implemented in the SEISAN software package (Havskov and Ottemoller 1999). Waveform inversion was performed at relatively low frequencies (0.02–0.07 Hz) using waveform from six broadband stations (18 components) that showed the best fit between observed and synthetic waveforms.

2.1 Aftershocks' Analysis of the Sub-sequences

The horizontal distribution of the events of the whole Hammam Melouane 2013–2016 (Fig. 2) shows that the main events with magnitude Ml > 4 occurred during the second and third sub-sequence, those events are characterised by reverse motion with minor strike-slip component (Fig. 1). In order to get more details about the relation between the sub-sequences, we represent the events of different sub-sequences with different colours. The first sub-sequence of July 2013 is presented in black; the second

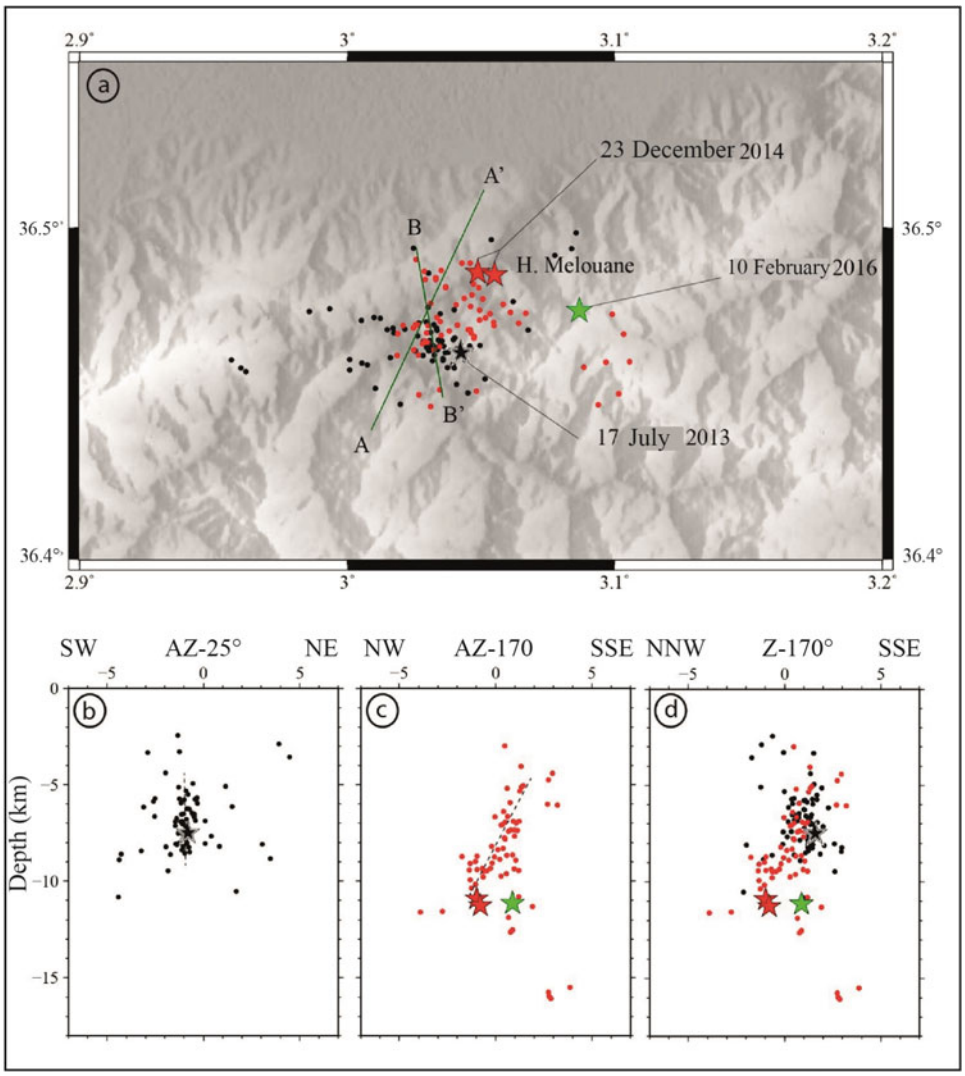

Fig. 2 A distribution of **a** all relocated events in the Hammam Melouane sequence, **b** vertical section of the events occurred during the first sub-sequence, **c** vertical section of the events occurred during the second and third sub-sequences, **d** superposition of the two sections AA′ and BB′. The black star represents the event of the 17th of July 2013, the red stars represent the events of the 23rd of December 2014 and the green star represents the event of the 10th of February 2016. The red dotted lines indicate the interpretation of the best alignment of events

and third sub-sequences are represented in red (Fig. 2). The red cloud of events (north-east) can easily be distinguished from the black point cloud of events located to the south-west. In order to see what happened in depth, we made cross sections, perpendicular to the two fault planes of the two focal mechanisms of the main shocks (Fig. 2). The two cross sections AA′ and BB′ correspond to the black cloud of events and red cloud of events, respectively. The third CC′ cross section is for all events. The first cross section AA′ (Fig. 2a) shows an almost vertical alignment of the hypocentres, which is related to the fault highlighted in Yelles-Chaouche et al. (2017). The second section BB′ of N170° direction, perpendicular to the N232° plane of the ML5.0 event of the 23rd of December 2014 (Fig. 2c), displays the best alignment of the hypocentres; this section shows an almost east–west alignment of the events, with (N80°) direction dipping 60° to the north. One other fact that needs to be pointed out is that the event of the 10th of February 2016 (green star in Fig. 2) occurred in the small swarm located to the south-east.

3 Results and Discussion

From this analysis, and taking into account the depth distribution of the events and the focal mechanism solutions of the main events, we can assume that the Hammam Melouane sequence occurred on three sub-faults. The first is a vertical dextral strike-slip fault oriented in a N115° direction; the second fault has reverse faulting along plane in a direction of N80°, dipping 60° towards the north-west. The third is a NE–SW reverse fault. Unfortunately, due to the limited number of aftershocks in the third sub-sequence, we were not able to give more detailed parameters of the third sub-fault.

4 Conclusions

The whole aftershocks' analysis with focal solution parameters of the main events of the Hammam Melouane sequences demonstrated that these sequences occurred on

three sub-faults. The occurrence of these events along the southern limit of the Mitidja basin indicates that the rupture along this limit is complex and happening along several minor faults. It indicates that the capital of Algeria and other small cities such as Tipaza, Blida and Boumerdès are highly exposed to seismic risk.

References

Dreger, D.S.: TDMT_INV: time domain seismic moment tensor inversion. Int. Geophys. **81**, 1627 (2003). Academic Press

Havskov, J., Ottemoller, L.: SEISAN earthquake analysis software. Seismol. Res. Lett. **70**(5), 532–534 (1999). https://doi.org/10.1785/gssrl.70.5.532

Klein, F.W.: Hypocenter Locations Program HYPOINVERSE, Users Guide to Versions 1, 2, 3, and 4. Part II. Source Listings and Notes (No. 78-694). US Geological Survey (1978)

Waldhauser, F., Ellsworth, W.L.: A double-difference earthquake location algorithm: method and application to the northern Hayward fault. Bull. Seism. Soc. Am. **90**, 1353–1368 (2000)

Yelles-Chaouche, A.K., Haned, A., Aidi, C., Beldjoudi, H., Kherroubi, K., Semmane, F., Benabdeloued, B.Y.N., Larbes, Y., Alili, A., Khelif, M.F., Belhouane, A.: The Mw 5.0 Hammam Melouane earthquake (North Central Algeria) of 17 July 2013 in the context of the Tellian Atlas seismicity. Pure Appl. Geophys. **174**(4), 1601–1614 (2017)

Statistical Study of Earthquake Swarms in Northeastern Algeria with Special Reference to the Ain Azel Swarm; Hodna Chain, 2015

Issam Abacha, AbdelKarim Yelles-Chaouche, and Oualid Boulahia

Abstract

Northeastern Algeria is known by its high seismic activity as reflected by several hundreds of events occurring every year. Recently, this area has been the seat of several seismic sequences such as the 2010 Beni-Ilmane earthquake sequence and the 2012–2013 Bejaia earthquake sequences. On the other hand, it is also observed that the seismic activity of this part of Algeria is dominated by swarms, with high concentrations in time and space, from a few days to several months, ranging from a few kilometers to ten kilometers, and sometimes showing a migration of several kilometers in several weeks. The earthquake swarms are related to the increase in the water body of the reservoir after a heavy precipitation (Beni-Haroun (B-H) dam on 2012), and to the increase in the interstitial pressure due to the fluid injection (the 2007 Mila crisis and Grouz reservoir crisis) or due to the water circulation in hydrothermal systems (Ain Azel, El-Hachimia, Azzaba and Djemila swarms). Here, 10 swarms occurring in the region were analyzed using statistical laws, and finally the results have been discussed.

Keywords

Earthquake swarms • Statistical laws • Time clustering • Induced seismicity

1 Introduction

Earthquake swarms are earthquake sequences without a discernible main-shock. Swarms can last weeks and produce many thousands of earthquakes within a relatively small volume (Miller 2013). Swarms are observed in volcanic environments, hydrothermal systems, and other active geothermal areas. Also, numerous examples of the microseismic activity generated by the increase in interstitial pressure have been described in the literature and probably concern with the filling of dam reservoirs (Gupta 1983) or the injection of fluids at depth (Cornet et al. 2007). This induced seismicity is related to the increase in water in the reservoir causing the increase in the interstitial pressure due to the fluid diffusion. In contrast, earthquake swarms may confine to the fluid-filled fractured rock matrix (Kayal et al. 2002; Mishra and Zhao 2003; Mishra et al. 2008). Changes in the water pressure once exceeded the effective pore pressure at shallow layers that lead to seismogenesis in swarms. Percolation of continuous rain water during monsoon season through the active faults or cracks may also lead to genesis of earthquake swarms as observed in Talala source zone of Gujarat, India (Singh and Mishra 2015). But here we have studied the statistical behavior of earthquake swarms occurred in northeastern Algeria in between 2000 and 2018 using the Algerian catalogue, including those and some seismic events recorded by portable stations installed after the occurrence of several shocks.

We identify 10 possible swarms (Fig. 1), and we applied some statistical tests on the size of seismic events and on the time intervals between successive earthquakes, which have made it possible to identify the existence of forcing linked either to creep processes, to a fluid percolation phenomenon, or to the coupled action of these two processes.

2 Scientific Background, Data and Methodology

The seismic data were collected by the Algerian seismic network, and from several seismic studies carried out after the occurrence of several moderate shocks. Then, the identified earthquake swarms as stated above have been analyzed

I. Abacha (✉) · A. Yelles-Chaouche · O. Boulahia
CRAAG, Route de l'Observatoire BP 63, Bouzaréah, Algiers, Algeria
e-mail: i.abacha@craag.dz

M. Meghraoui et al. (eds.), *Advances in Geophysics, Tectonics and Petroleum Geosciences*,
Advances in Science, Technology & Innovation, https://doi.org/10.1007/978-3-030-73026-0_34

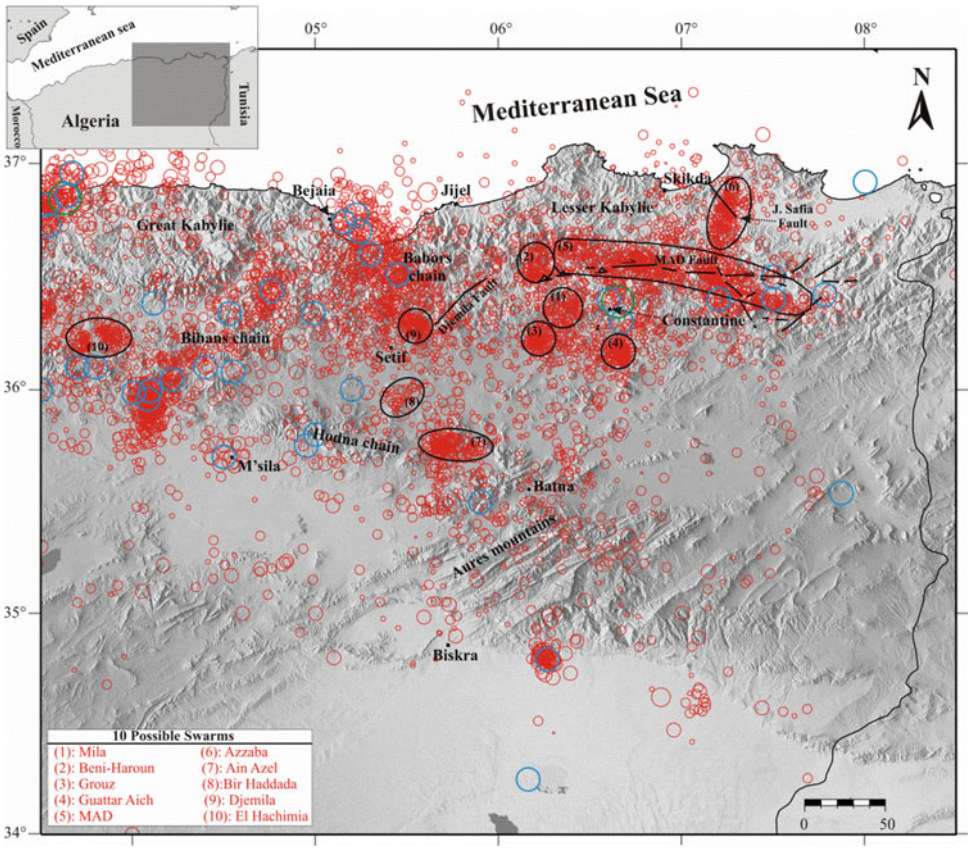

Fig. 1 Seismicity map of Algeria (2000–2018) (red circle) along with location of the large events of M $\geq$ 5 recorded in between 1900 and 2018 (blue circle) and identified 10 earthquake swarms

and interpreted using well-known statistical laws of earthquake occurrence as described below:

(1) *Gutenberg–Richter Law (G-R Law)*: Defines the frequency of the seismic event distribution and was determined for the California earthquakes (Gutenberg and Richter 1944). This is written as below:

$$\log(N_{\geq M}) = a - bM \tag{1}$$

With $N_{\geq M}$ is the number of magnitude greater than M. (a) and (b) are constants.

(2) *Gamma Law*: It states that the seismic event's distribution of the same block can usually be approximated by the function whose parameters are related to the proportion of independents earthquakes (Hainzl et al. 2006):

$$\Gamma(\tau) = C\tau^{\gamma-1}\mathrm{e}^{-\tau/\beta} \tag{2}$$

where (τ) is the ratio between the time intervals of successive microseisms $\Delta t(\Delta t_i = t_i - t_{i-1})$ and the average time intervals of the entire Δt_0. C, (γ) and (β) are constants.

(3) *Omori Law*: This one relates with the decrease in the average rate of events per unit of time and is generalized as below (Utsu 1961):

$$\left\langle \frac{\mathrm{d}n}{\mathrm{d}t} \right\rangle = \frac{K}{(t+c)^p} \tag{3}$$

The coefficient (K) depends on the time unit chosen to calculate the event's rate, the (t) is the origin time and the exponent (p) is different from one earthquake sequence to another. This law provides information on the decay rate of a number of earthquakes with lapse of time (Mishra et al. 2007).

Besides the methodology followed for assessing the statistical parameters, the results showed concern about only one swarm, the remainders are listed in Table 1. We have tried to clarify the nature of swarms based on these results and the field observations.

3 Analysis and Results

The chosen specific event for analysis relates to Ain Azel's earthquake swarm located in the Hodna chain (N°8 Fig. 1). It was marked by the appearance of two important events on the 15th and 21st of March, 2015 with magnitudes Mw = 4.7 and 4.9, respectively.

It is conspicuously observed that maximum number of events in swarms (Fig. 2a) is confined to the almost same

Table 1 Results for above Ain Azel earthquake swarm and 9 earthquake swarms

Swarm	*b* value	γ value	*P* value	Description and interpretation
1	1.0	0.74	0.64	Induced seismicity caused by the water infiltration in the Jebel Akhal, a small rocky hill between the B-H dam and the Oued Athmania reservoir
2	1.4	0.73	0.80	The earthquake swarm is related to the increase in the water body of the B-H dam after a heavy precipitation on January–February 2012
3	1.2	0.77	0.74	Induced seismicity caused by the water infiltration in the Grouz dam
4	0.9	0.45	1.02	Tectonic seismicity
5	1.1	0.73	0.72	Intense seismicity along of MAD fault with low magnitudes, which can be explained by the geological and tectonic nature of this fault that composed by small segments surrounded by numerous thermal sources
6	2.1	0.67	0.68	Induced seismicity linked to the circulation of the waters thermal in Jebel Safia fault
8	0.9	0.55	1.01	Tectonic seismicity
9	2.3	0.80	0.71	Induced seismicity linked to the circulation of the waters thermal in Djemila fault
10	1.7	0.76	0.79	Induced seismicity linked to the waters thermal

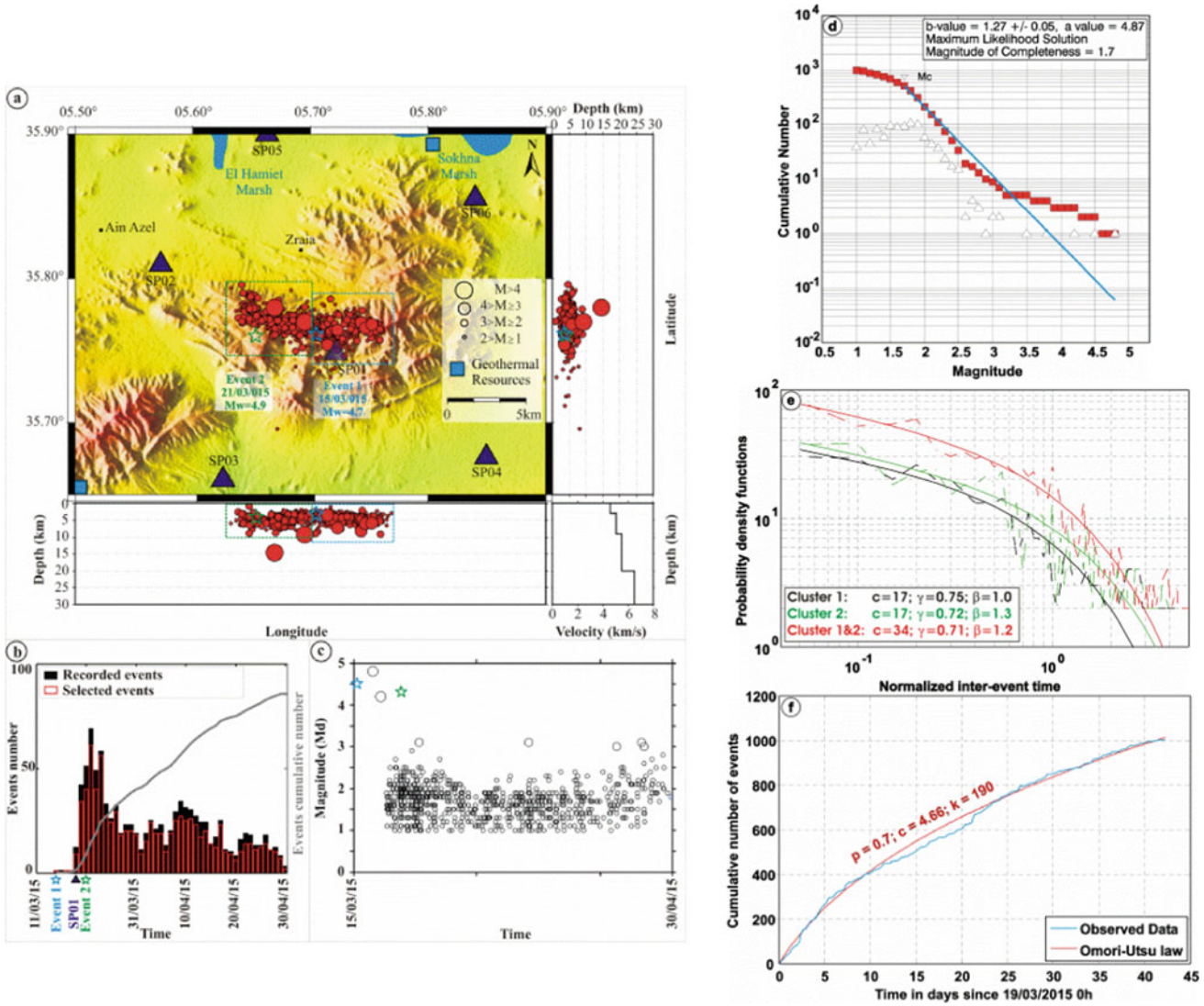

Fig. 2 Ain Azel earthquake swarm (N°8 Fig. 1). **a** Spatial distribution of 862 events with nearby thermal sources. **b** Events' number/cumulative number of events per time. **c** The magnitude evolution per time. **d** Gutenberg–Richter law. **e** Gamma law. **f** Omori law

layer and this observation is corroborative to an earlier study carried out by Paul and Sharma (2011). The spatial distribution (Fig. 2a, b) and the statistical analysis show a high concentration in time and space for these earthquake swarms with the following results: b value equal 1.27; γ value equal 0.71 and P value equal 0.7 (Fig. 2d–f respectively).

4 Discussion

The study shows distributions in power law characterized by their exponents in the two domains of the seismic events' size (G-R law, exponent b) and temporal (Omori law, exponent P and gamma law, exponent γ) using the maximum likelihood method and for the G-R law using the best combination Mc (Mc95-Mc90-max curvature).

Ain Azel swarm (N°8 Fig. 1): The Gutenberg–Richter law gives a b value equal to 1.27. Indeed, the b value is proportional to the rock's heterogeneity degree or the density of faults and inversely proportional to the effective normal stress. This suggests that the region is relatively inhomogeneous, where the effective normal stress is low and suitable for triggering the earthquakes swarms.

The block of events gives a high γ value ($\gamma = 0.71$) (i.e., 71% of independent events) (Bernard et al. 2007). Suggested that if γ greater is than 0.5, the events are independent where the triggering is due to the forcing mechanism (creep or fluid pressure).

Finally, $P = 0.7$ indicates that the seismic activity is generated by the increase in the interstitial pressure by the fluid circulation. This assumption is all the more credible due to the existence of several geothermal resources along the Hodna chain with one being at a distance close to the epicenter area ($\sim$12 km) (Fig. 2a). This phenomenon is based on the physics of seismogenesis through fracturing of fluid-filled rock matrix (Mishra and Zhao 2003). In the same way we analyzed the other earthquake swarms and results have been tabulated here (Table 1).

5 Conclusions

In order to understand the physical correlation between the seismic events of the similar block and the origin of their fluctuations, we performed statistical tests on the time intervals as stated between successive earthquakes and the size–frequency seismic event distribution. Based on the analysis, it is concluded that the earthquake swarms are related either to the increase in the charge done water body of the reservoir after a heavy precipitation (B-H dam on 2012), to the increase in the interstitial pressure due to the fluid injection (the 2007 Mila crisis and Grouz reservoir swarm) or to the water circulation in hydrothermal systems (Ain Azel, El Hachimia, Azzaba and Djemila swarms).

References

Bernard, P., Boudin, F., Bourouis, S., Patau, G.: Transitoires de déformation dans le Rift de Corinthe. Communication orale, 3F Workshop, Nancy, France (2007)

Cornet, F.H., Berard, Th., Bourouis, S.: How close to failure is a natural granite rock mass at 5 km depth? Int. J. Rock Mech. Min. Sci. **44** (1), 47–66 (2007)

Gupta, H.K.: Induced seismicity hazard mitigation through water level manipulation at Koyna, India: a suggestion. Bull. Seismol. Soc. Am. **73**, 679–682 (1983)

Gutenberg, B., Richter, C.F.: Frequency of earthquakes in California. Bull. Seismol. Soc. Am. **34**, 185–188 (1944)

Hainzl, S., Scherbaum, F., Beauval, C.: Estimating background activity based on interevent-time distribution. Bull. Seismol. Soc. Am. **96** (1), 313–320 (2006)

Kayal, J.R., Zhoa, D., Mishra, O.P., Reena, D., Singh, O.P.: The 2001 Bhuj earthquake: tomographic evidence for fluids at the hypercenter and its implications for rupture nucleation. Geophys. Res. Lett. **29** (2002). https://doi.org/10.1029/2002GL015177

Miller, S.A.: The role of fluids in tectonic and earthquake processes. Adv. Geophys. **54**, 1–46, Chap. 1 (2013)

Mishra, O.P., Zhao, D.: Crack density, saturation rate and porosity at the 2001 Bhuj, India, earthquake hypocenter: a fluid-driven earthquake? Earth Planet. Sci. Lett. **212**, 393–405 (2003)

Mishra, O.P., Kayal, J.R., Chakrabortty, G.K., Singh, O.P., Ghosh, D.: Aftershock investigation in Andaman-Nicobar of the 26 December 2004 earthquake (Mw 9.3) and its seismotectonic implications. Bull. Seismol. Soc. Am. **97**(1A), S71–S85 (2007)

Mishra, O.P., Zhao, D., Wang, Z.: The genesis of the 2001 Bhuj, India, earthquake (Mw 7.6): a puzzle for Peninsular India. J. Indian Miner. Spec. Issue **61**(3–4) & **62**(1–4), 149–170 (2008)

Paul, A., Sharma, M.L.: Recent earthquake swarms in Garhwal Himalaya: a precursor to moderate to great earthquakes in the region. J. Asian Earth Sci. **42**, 1179–1186 (2011). https://doi.org/10.1016/j.jseaes.2011.06.015

Singh, A.P., Mishra, O.P.: Seismological evidence for Monsoon induced micro to moderate earthquake sequence. Tectonophysics **661**, 38–48 (2015)

Utsu, T.: A statistical study on the occurrence of aftershocks. Geophys. Mag. **30**, 521 (1961)

Deep Rupture Process of the 3rd of April, 2017 Earthquake in Stable Continental Region, Botswana

Jima Asefa and Atalay Ayele

Abstract

On April 3, 2017; an earthquake of magnitude Mw 6.5 has occurred in Botswana in a region where there were no recent tectonic activity and where present-day deformation is believed to be negligible. The event was followed by several aftershocks distributed along NW–SE direction with NE–SW extension direction. We focused on the determination of a reliable source parameter for the Mw 6.5 earthquake using moment tensor inversion both in time and frequency domains from broadband waveform data. We obtained the hypocentral depth value which is of 38.4 km, deeper than the previous results. The estimated hypocentral depth of this study is approximately estimated at the boundary between lower crust and Moho depth beneath the region, reflecting a deep source that is relatively rare in stable continental regions. The result may suggest that the continental-rift initiation between weak upper mantle and weak lower crust or due to a reactivation of the pre-existing faults at deep region. The resulted focal mechanism of the event shows normal faulting with NE–SW extension. The results of this study will provide useful information about the future seismicity in this region, a stable area where rare large magnitude and relatively deep earthquakes occur.

Keywords

East African Rift System • Okavango Delta Region • Okavango Rift Zone

J. Asefa (✉)
School of Earth Science, Addis Ababa University, Box 1176 Addis Ababa, Ethiopia

J. Asefa
College of Natural and Computational Sciences, Wolkite University, Box 07, Wolkite, Ethiopia

A. Ayele
Institute of Geophysics, Space Science and Astronomy, Addis Ababa University, Box 1176 Addis Ababa, Ethiopia

1 Introduction

The African continent is a tectonic plate with diverse geological domains that include seismically active and aseismic regions. The continent is mainly characterized by earthquakes with shallow depths of 0–70 km (Adagunodo et al. 2018). The East African Rift System (EARS) has been the site occurrence of small to large magnitude earthquakes (Foster and Jackson 1998). The Botswana region in particular has been the site of several small to moderate earthquakes (Nthaba et al. 2018). The April 3, 2017 Botswana earthquake struck the central Botswana, and the shaking was felt in different neighboring countries, and Modified Mercalli intensities of VI (Midzi et al. 2018) were estimated. Major historical earthquakes recorded in Botswana are mainly located near Okavango Delta Region (ODR) where young arm of the EARS is developing. Previously, the region has been rocked by the 11th of September and 11th of October 1952 earthquakes whose magnitudes are of 6.1 and 6.7 ML (Nthaba et al. 2018), respectively.

The April 3, 2017 Botswana earthquake has been investigated by different researchers. The geometric and kinematic characteristics of the causative fault were estimated from the modeling of InSAR interferograms (Albano et al. 2017). The deep fluid injection has been expected to induce the event (Gardonio et al. 2018). On the other hand, a result from an integrated geophysical study suggests that the event may be a sign of future activity, controlled by the collocation of a weak upper mantle and weak crustal structure (Moorkamp et al. 2018). Moreover, Materna et al. (2019) used teleseismic broadband waveform data to generate synthetic waveforms in the time domain. Studying such a large earthquake in the region helps to refine the estimate of source parameters and expands our understanding of reliable hypocentral depth of the event in a region where there is no direct evidence for observed surface deformation related to a fault. The April 3, 2017 Botswana earthquake is relatively deep, which has never been observed before. Hypocentral

M. Meghraoui et al. (eds.), *Advances in Geophysics, Tectonics and Petroleum Geosciences*,
Advances in Science, Technology & Innovation, https://doi.org/10.1007/978-3-030-73026-0_35

depth estimation of an earthquake is usually the most difficult to nail down with great accuracy. Thus, techniques used in order to determine earthquakes' depths (Maggi et al. 2000) should be improved. Therefore, we applied moment tensor inversion using regional broadband waveform data that provides reliable source parameters of the event.

2 Data and Method

Three-component broadband waveform data and instrument response information were obtained from the IRIS DMC for all of the stations at regional distances which successfully recorded the April 3, 2017 Botswana earthquake (Fig. 1).

In this study, we applied the approach developed by Cesca et al. (2010) to estimate source parameters of the event using moment tensor inversion in both frequency and time domains. We selected six broadband seismic stations with high quality waveform data located at various azimuths and distances from the source. We generated synthetic seismograms both in time and frequency domain and fitted synthetic seismograms with the observed seismograms. The reliable source parameters of the event were extracted at the best fits using the band-pass filtering in the range of 0.02–0.05 Hz.

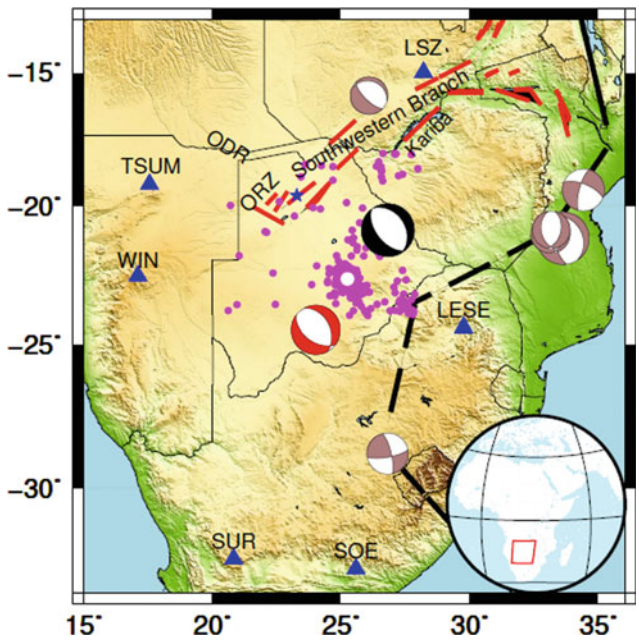

Fig. 1 Focal mechanism of the April 3, 2017 Botswana main shock (black and white color beach ball) and its aftershocks distribution. The white dot represents the location of the main shock, and magenta dots represent the epicenter location of the aftershocks. The blue triangles represent the seismic stations used, and the blue star is the location of the historical earthquake of 1952. The red and white beach ball is focal mechanism for 2017 Botswana mainshock from GCMT solution, while pink and white are for some earthquakes from GCMT solutions. Broken red lines represent the fault system of the Okavango Rift Zone (ORZ) and the Southwestern Branch, ODR represents Okavango Delta Region (modified from Kinabo et al. 2007). Heavy black lines represent plate boundaries (modified from Bird 2003). Inset map shows the study area

3 Results

After conducting the moment tensor inversion for the April 3, 2017 Botswana earthquake, the hypocentral depth, which is of 38.4 km (Fig. 1), has been estimated with an error misfit of 0.296 (L2 norm misfit which is equal to sqrt((*d* − *s*) **2), where *d* are data, and *s* are synthetics). Moment magnitude Mw 6.5 is estimated for the event. A good waveform fit is obtained for the observed and synthetic seismograms in both cases (Figs. 2, 3 and 4).

4 Discussion

The distribution of aftershocks (Fig. 1) of the April 3, 2017 Botswana earthquake show NW–SE trending, consistent with the trend of focal mechanism of the main shock (purely normal faulting). The southward propagation of the EARS extends to the Southwest into Botswana, where it forms a Southwestern branch (Modisi 2000) toward the Okavango Rift Zone (ORZ) and weakness zones initiate strain, when coupled to favorable plate kinematics can lead to continental break-up. The ORZ has several rift related faults and a zone of extension (Kinabo et al. 2007). Thus, the extension of EARS toward Botswana may be the main cause of the 2017 Botswana earthquake occurrence.

The well-constrained hypocentral depth is estimated to be 38.4 km, which is near to be the lower crust and upper mantle boundary, reflecting relatively a deep hypocentral depth, which is rare in the earthquake occurrence tradition of the EARS. The ORZ serves as the stage development of continental rifts, and the structures bounding and linking rift basins are strongly controlled by pre-existing rift structures (Ring 1994). Therefore, the relatively deep hypocentral depth of this study may suggest the reactivation of a deep weak pre-existing NW–SE trending geological structure or from the early rift faults within the stress region during rift initiation beneath the area.

5 Conclusions

We applied moment tensor inversion techniques from regional waveform data to determine reliable source parameters of the April 3, 2017 Mw 6.5 Botswana earthquake. The moment magnitude of Mw 6.5 is estimated

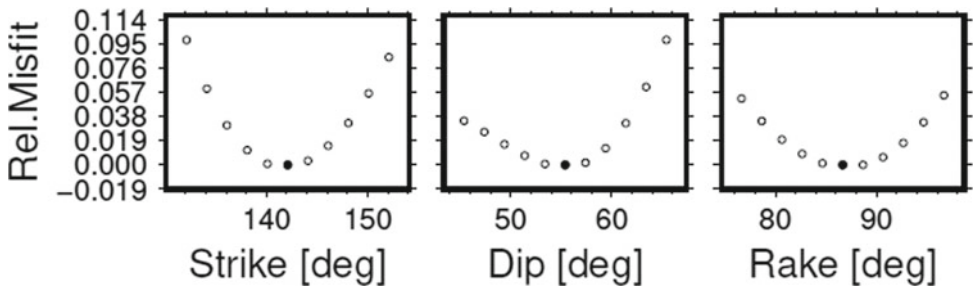

Fig. 2 The relative misfits (illustrate how our misfit increases when we perturb one single parameter) versus Strike, Dip and Rake angles for fault plane solution estimated using moment tensor inversion and obtained at a hypocentral depth of 38.4 km. The bold black dots represent the value at which three angles are selected from the minimum variance

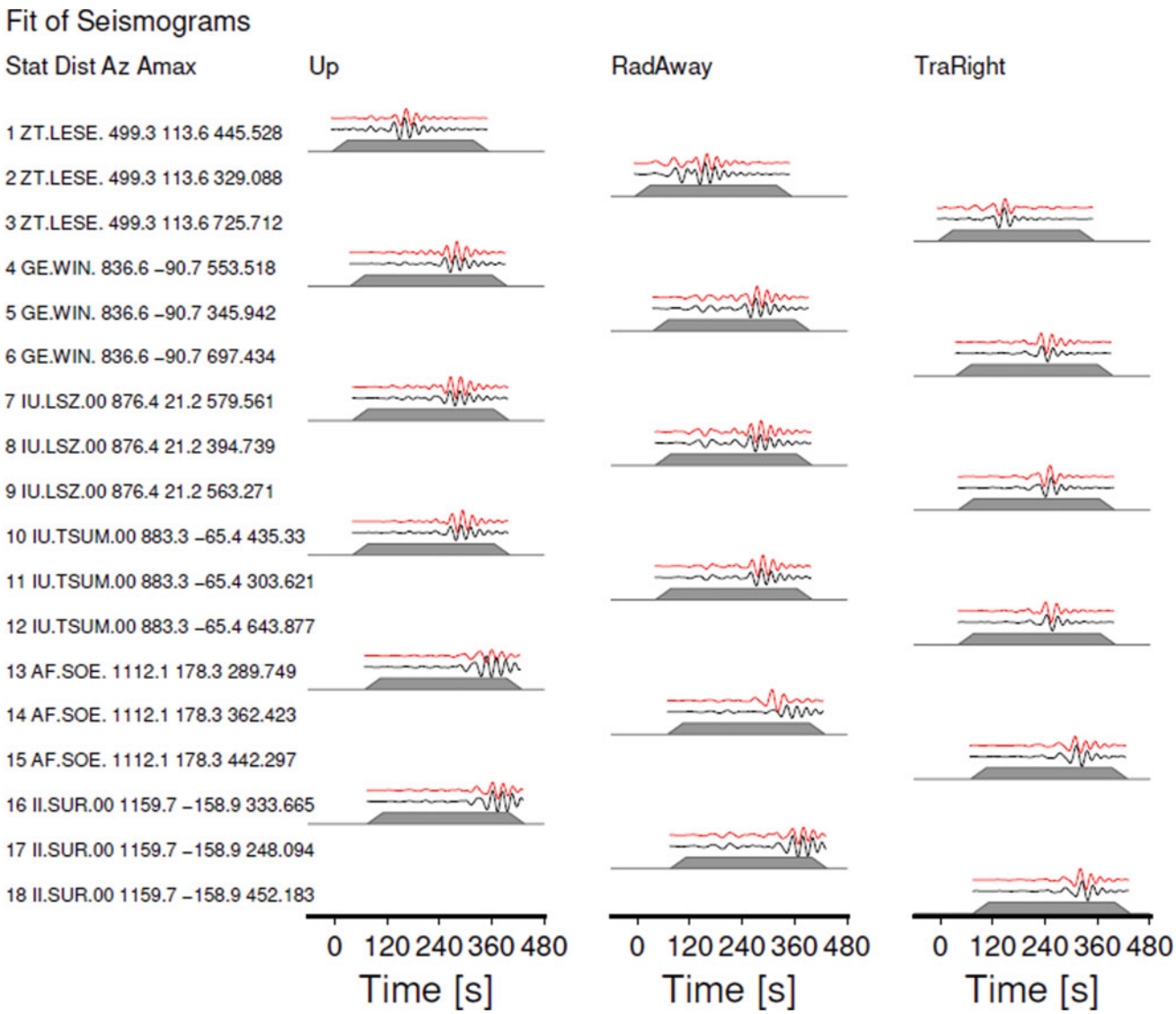

Fig. 3 Regional waveform fits of the April 3, 2017 Botswana main shock using moment tensor inversion in the time domain. The panel is dedicated to waveform comparison (red color is for data, black is for synthetics). Stations are sorted according to epicentral distances, with station name, distance, azimuth and maximal amplitudes provided on the left side

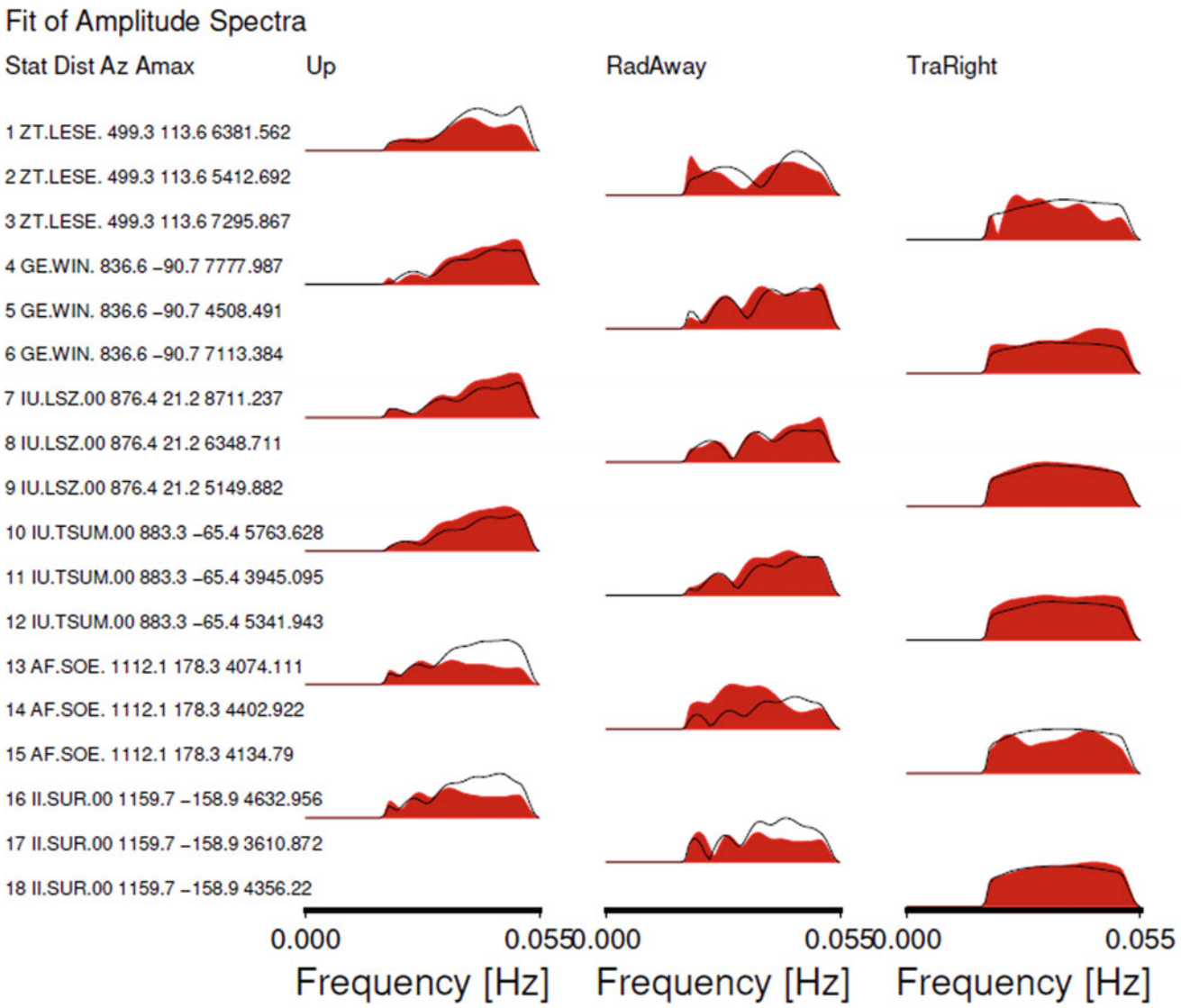

Fig. 4 Spectra amplitude fits of the April 3, 2017 Botswana main shock using moment tensor inversion in frequency domain. The panel is dedicated to spectra comparison (red color is for data, black is for synthetics). Stations are sorted based on epicentral distances, with station name, distance, azimuth and maximal amplitudes provided on the left side

using broad band-pass frequency range of 0.02–0.05 Hz in contrast to the GCMT solution relatively narrow frequency range of 0.02–0.025 Hz. Our fault plane solution shows normal faulting on a NW–SE trending fault and NE–SW extension direction. Thus, the propagation of southwestern branch of EARS toward Botswana (Fig. 1) may be the main cause for the occurrence of this rare event. We obtained the hypocentral depth of 38.4 km, which is relatively deeper than the previous results. The relatively deep hypocentral depth, which is near to the lower crust and the upper mantle boundary, may suggest the reactivation of preexisting fault.

References

Adagunodo, T.A., Lüning, S., Adeleke, A.M., Omidira, J.O., Aibeokhai, A.P., Oyeyemi, K.D., Hammed, O.S.: Evaluation of $0 \leq M \leq 8$ earthquake data sets in African–Asian region during 1966–2015. Data Brief **17C**, 588–603 (2018)

Albano, M., Polcari, M., Bignami, C., Moro, M., Saroli, M., Stramondo, S.: Did anthropogenic activities trigger the 3 April 2017 Mw 6.5 Botswana earthquake? Remote Sens. **9**, 1–12 (2017)

Bird, P.: An updated digital model of plate boundaries. Geochem. Geophys. Geosyst. **4** (2003)

Cesca, S., Heimann, S., Stammler, K., Dahm, T.: Automated procedure for point and kinematic source inversion at regional distances. J. Geophys. Res. Solid Earth **115**, 1–24 (2010)

Foster, A.N., Jackson, J.A.: Source parameters of large African earthquakes: implications for crustal rheology and regional kinematics. Geophys. J. Int. **134**, 422–448 (1998)

Gardonio, B., Jolivet, R., Calais, E., Leclère, H.: The April 2017 Mw6.5 Botswana earthquake: an intraplate event triggered by deep fluids. Geophys. Res. Lett. **45**, 8886–8896 (2018)

Kinabo, B.D., Atekwana, E.A., Hogan, J.P., Modisi, M.P., Wheaton, D. D., Kampunzu, A.B.: Early structural development of the Okavango rift zone, NW Botswana. J. Afr. Earth Sci. **48**, 125–136 (2007)

Maggi, A., Jackson, J.A., McKenzie, D., Priestley, K.: Earthquake focal depths, effective elastic thickness, and the strength of the continental lithosphere. Geology **28**, 495–498 (2000)

Materna, K., Wei, S., Wang, X., Heng, L., Wang, T., Chen, W., Salman, R., Bürgmann, R.: Source characteristics of the 2017 Mw 6.4 Moijabana, Botswana earthquake, a rare lower-crustal event within an ancient zone of weakness. Earth Planet. Sci. Lett. **506**, 348–359 (2019)

Midzi, V., Saunders, I., Manzunzu, B., Kwadiba, M.T., Jele, V., Mantsha, R.: The 03 April 2017 Botswana M6.5 earthquake: preliminary results. J. Afr. Earth Sci. **143**, 187–194 (2018)

Modisi, M.P.: Fault system at the southeastern boundary of the Okavango Rift, Botswana. J. Afr. Earth Sci. **30**, 569–578 (2000)

Moorkamp, M., Fishwick, S., Walker, R.J., Jones, A.G.: Geophysical evidence for crustal and mantle weak zones controlling intraplate seismicity—the 2017 Botswana earthquake sequence. Earth Planet. Sci. Lett. **506**, 175–183 (2019)

Nthaba, B., Simon, R.E., Ogubazghi, G.M.: Seismicity study of Botswana from 1966 to 2012. Int. J. Geosci. **09**, 707–718 (2018)

Ring, U.: The influence of preexisting structure on the evolution of the Cenozoic Malawi rift (East African rift system). Tectonics **13**, 313–326 (1994)

Moho Depth Variation and Crustal Velocity Structure in Northern Algeria by Teleseismic Receiver Function Analysis

Billel Melouk, Abdelkrim Yelles-Chaouche, Juan Jose Galiana-Merino, Chafik Aidi, and Fethi Semmane

Abstract

In order to map the Moho depth variations in the north of Algeria, we use the teleseismic receiver function (RF) technique to estimate the crustal thickness and Vp/Vs ratios beneath the Algerian seismic network. We used 12 broadband stations, installed throughout the northern part of the country from east to west. For now, we selected the data of 34 earthquakes from the entire dataset with (Mw $\geq$ 6.0) between January 2016 and June 2017 in an epicentral distance of 30°–90°. All the selected 3C seismograms show a good signal-to-noise ratio. We calculated the P-wave RFs by deconvolving the radial component of the seismogram by the vertical component to obtain the PS converted waves. We used the *H–k* staking method to transform the time domain waveforms into the depth domain, which usually gives the best estimations for both the crustal thickness and Vp/Vs ratios. In addition, we used the inversion of all the RFs to get the S-wave velocity model beneath each station starting from the continental AK135 model for teleseisms. We obtained the Moho depth (20–25 km near the shoreline and 38–42 km in the High Plateau) and the 1D velocity model beneath each station. Our results agree with those obtained during the SPIRAL (Sismique Profonde et Investigation Regionale en Algerie) project using a tomographic inversion of travel times along a wide-angle seismic profile. Finally, a joint inversion of RFs and surface wave dispersion curves is in progress for a better-constrained model, in addition to the application of the common-conversion-point technique to generate a 2D map of the study area.

B. Melouk (✉) · A. Yelles-Chaouche · C. Aidi · F. Semmane
Centre de Recherche en Astronomie Astrophysique et Géophysique (CRAAG), Algiers, Algeria
e-mail: b.melouk@craag.dz

B. Melouk · J. J. Galiana-Merino
University Institute of Physics Applied to Sciences and Technologies, University of Alicante, Alicante, Spain

Keywords

Receiver function • Crustal thickness • Mohorovicic discontinuity (Moho) • Inversion • Velocity model

1 Introduction

The Mohorovicic discontinuity (Moho), which separates the Earth's crust from the underlying upper mantle, represents a major change in seismic velocities, chemical compositions and rheology. The depth of Moho is an important parameter to characterize the overall structure of the crust; it can often be related to geology and tectonic evolution of the region. In northern Algeria, recent studies were conducted in the offshore Algerian margin (SPIRAL) particularly to estimate the Moho depth using different geophysical methods, as for example the wide-angle seismic reflection. The results show that the continental Moho discontinuity is ranging, for example for the central part of northern Algeria, between 20 and 25 km depth. To better constrain the Moho depth, we use the teleseismic receiver function (RF) technique to estimate the crustal thickness and Vp/Vs ratios beneath the Algerian broadband seismic network.

2 Data and Methodology

Receiver function analysis requires three-component seismic stations. In the last ten years, the number of digital stations in northern Algeria has increased following the installation of a new network. There are now about 70 stations, 17 of which are broadbands (Yelles-Chaouche et al. 2013). This provides a unique opportunity to map out the lateral variations of Moho depth using the receiver function method. For this work, we selected the data from 34 earthquakes from those with (Mw $\geq$ 6.0) that occurred between January 2016

M. Meghraoui et al. (eds.), *Advances in Geophysics, Tectonics and Petroleum Geosciences*, Advances in Science, Technology & Innovation, https://doi.org/10.1007/978-3-030-73026-0_36

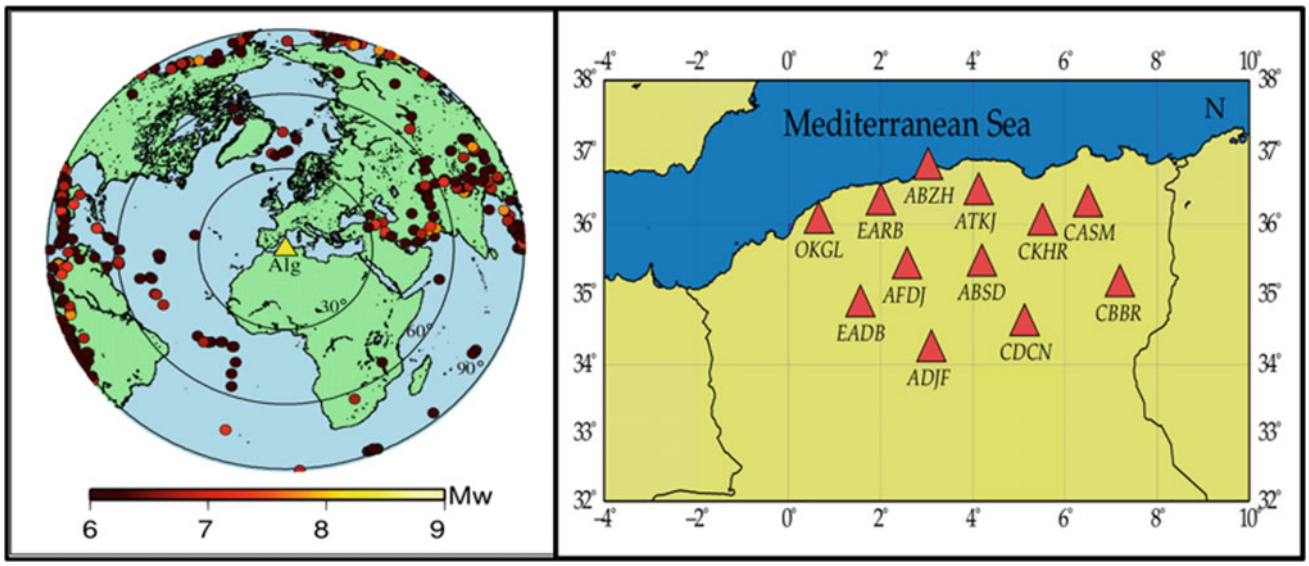

Fig. 1 Locations of the teleseismic events (colored dots) and the broadband stations (red triangles) used in this study

and June 2017 and were recorded by 12 broadband stations at an epicentral distance of 30°–90° (see Fig. 1).

We first rotate the original *ZNE* coordinate system to isolate the energy from the different wave types. The vertical component (*Z*) remains the same, while the two horizontal components (*N* and *E*) were rotated to get the radial (*R*) and tangential (*T*) components. We calculated the P-wave RFs by deconvolving the radial component of the seismogram by the vertical component to obtain the PS converted waves (Ligorria and Ammon 1999; Gurrola et al. 1995; Park and Levin 2000).

$$\begin{pmatrix} R \\ T \\ Z \end{pmatrix} = \begin{pmatrix} -\cos\gamma & -\sin\gamma & 0 \\ -\sin\gamma & -\cos\gamma & 0 \\ 0 & 0 & 1 \end{pmatrix} \begin{pmatrix} N \\ E \\ Z \end{pmatrix}$$

where *N*, *E* and *Z* are the original north–south, east–west, and vertical components, respectively, and γ is the back-azimuth of the incident wave.

In order to estimate the Moho depth and the Vp/Vs ratio, we use the *H*–*k* stacking method introduced by Zhu and Kanamori (2000) as a grid search over crustal thickness (*H*) and average crustal Vp/Vs ratio (*k*). This method sums the weighted receiver functions conversion phase (Ps) and multiples (PpPs and PpSs + PsPs) of all recorded events at the predicted differential arrival times respecting to direct *P*, for different pairs of *H* and *k*. The maximum summation represents the best estimation for the crustal model.

In our study, we choose the same weights that Zhu and Kanamori (2000) used and a value of 7 km/s for the average crustal Vp in the study area.

In addition to *H*–*k* stacking method, we used the inversion of all the receiver functions (Ammon et al. 1990) to get the crustal structure and the velocity model beneath each station starting from the continental AK135 model for teleseisms.

3 Results

Table 1 and Fig. 2 show the first estimation of the Moho depth and the Vp/Vs ratio under each station obtained by the *H*–*k* staking method.

The inversion of all the receiver functions has allowed us to generate a 1D S-wave velocity model for each station as shown in Fig. 3.

Table 1 Moho depth, Vp/Vs ratio and Poisson ratio under 12 stations

Stations	Moho depth (km)	Vp/Vs ratio	Poisson ratio
ABZH	26.2 ± 0.6	1.70 ± 0.03	0.235 ± 0.012
ABSD	38.3 ± 02	1.75 ± 0.04	0.248 ± 0.017
OGJS	38.1 ± 4.1	1.76 ± 0.12	0.261 ± 0.041
CASM	29.5 ± 3.4	1.76 ± 0.09	0.260 ± 0.033
EADB	33.6 ± 1.6	1.82 ± 0.05	0.283 ± 0.017
EARB	30.1 ± 0.4	1.76 ± 0.02	0.264 ± 0.008
ATKJ	28.6 ± 0.9	1.73 ± 0.02	0.248 ± 0.010
CDCN	36.8 ± 1.2	1.68 ± 0.03	0.228 ± 0.014
ADJF	38.2 ± 2.0	1.81 ± 0.05	0.248 ± 0.015
AFDJ	32.2 ± 3.2	1.77 ± 0.06	0.260 ± 0.16

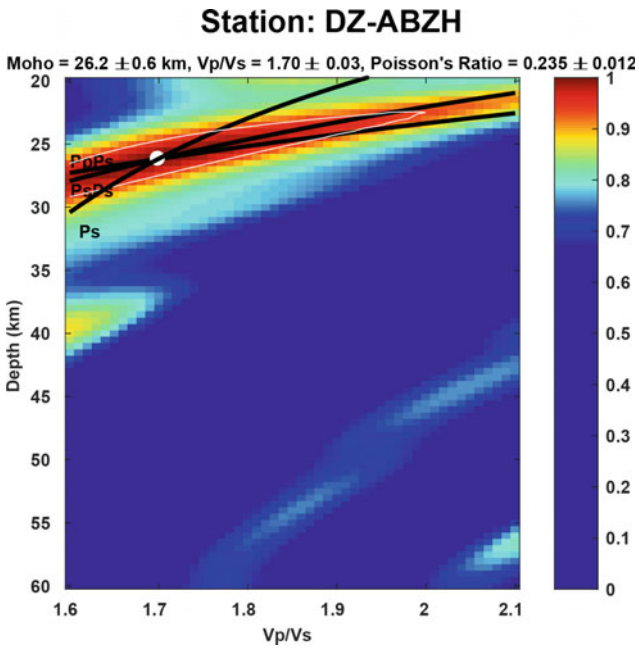

Fig. 2 *H–k* grid for ABZH station obtained from *H–k* stacking method

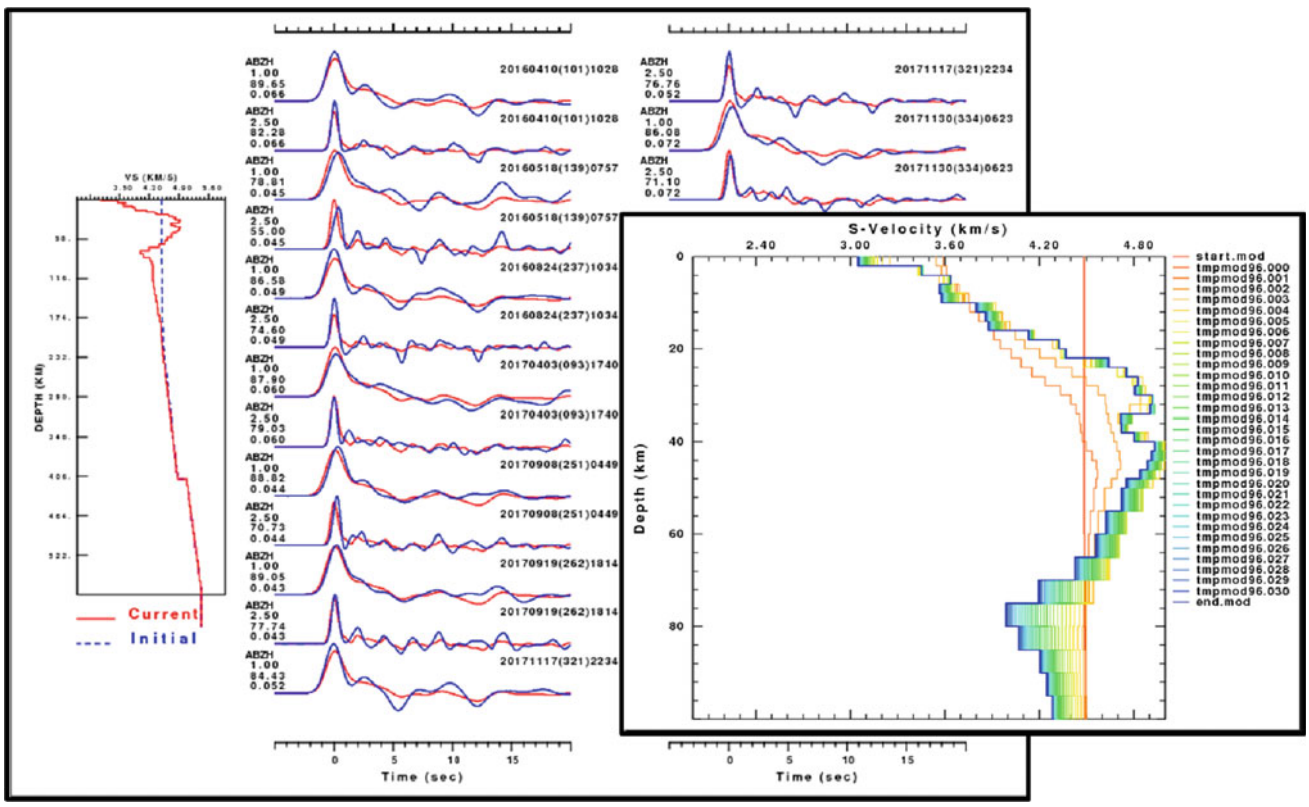

Fig. 3 An example that shows the results obtained by the inversion of the receiver function recorded at the ABZH. The observed RFs are in blue and the synthetic RFs are in red. The 1D profile, (right) shows the evolution of the model from the starting AK 135 model in orange to the final model in blue

4 Discussion and Conclusion

The results presented in this study suggest that the Moho depth in north of Algeria increases from 20 and 25 km near the shoreline to 38 and 42 km for the most southern stations. These findings are in agreement with the recent results obtained during the SPIRAL project using a tomographic inversion of travel times along a wide-angle seismic profile (Badji et al. 2014; Aïdi et al. 2018). In a next step of this study, the joint inversion of surface waves and receiver functions (Julià et al. 2000), as well as the common-conversion-point technique (CCP stacking) (Frassetto et al. 2010) will be applied for all available stations to better constrain our velocity models and to increase the resolution, which allow us to generate a 2D map of the Moho depth variations in northern Algeria.

References

Aïdi, C., Beslier, M., Yelles-Chaouche, A., Klingelhoefer, F., Bracene, R., Galve, A., Bounif, A., Schenini, L., Hamai, L., Schnurle, P., Djellit, H., Sage, F., Charvis, P., Déverchère, J.: Deep structure of the continental margin and basin off Greater Kabylia, Algeria—new insights from wide-angle seismic data modeling and multichannel seismic interpretation. Tectonophysics **728–729**, 1–22 (2018)

Ammon, C.J., Randall, G.E., Zandt, G.: On the nonuniqueness of receiver function inversions. J. Geophys. Res. Space Phys. **95**, 303–315 (1990)

Badji, R., Charvis, P., Bracene, R., Galve, A., Badsi, M., Ribodetti, A., Benaissa, Z., Klingelhoefer, F., Medaouri, M., Beslier, M.: Geophysical evidence for a transform margin offshore Western Algeria: a witness of a subduction-transform edge propagator? Geophys. J. Int. **200**(2), 1029–1045 (2014)

Frassetto, A., Zandt, G., Gilbert, H., Owens, T., Jones, C.: Improved imaging with phase-weighted common conversion point stacks of receiver functions. Geophys. J. Int. **182**, 368–374 (2010)

Gurrola, H., Baker, G.E., Minster, J.B.: Simultaneous time-domain deconvolution with application to the computation of receiver functions. Geophys. J. Int. **120**, 537–543 (1995)

Julià, J., Ammon, C.J., Herrmann, R.B., Correig, A.M.: Joint inversion of receiver function and surface wave dispersion observations. Geophys. J. Int. **143**, 99–112 (2000)

Ligorria, J.P., Ammon, C.J.: Iterative deconvolution and receiver-function estimation. Bull. Seismol. Soc. Am. **89**(5), 1395–1400 (1999)

Park, J., Levin, V.: Receiver functions from multiple-taper spectral correlation estimates. Bull. Seismol. Soc. Am. **90**(6), 1507–1520 (2000)

Yelles-Chaouche, A., Allili, T., Alili, A., Messemen, W., Beldjoudi, H., Semmane, F., Kherroubi, A., Djellit, H., Larbes, Y., Haned, S., Deramchi, A., Amrani, A., Chouiref, A., Chaoui, F., Khellaf, K., Nait Sidi Said, C.: The new Algerian Digital Seismic Network (ADSN): towards an earthquake early-warning system. Adv. Geosci. **36**, 31 (2013)

Zhu, L.P., Kanamori, H.: Moho depth variation in southern California from teleseismic receiver functions. J. Geophys. Res. Solid Earth **105**(B2), 2969–2980 (2000)

Shear Velocity Structure of the Crust and Upper Mantle of North Algeria from Rayleigh Wave Dispersion Analysis

Zohir Radi, Abdelkrim Yelles-Chaouche, and Salim Guettouche

Abstract

There are few scientific works about the crust and the upper mantle in northern Algeria because of the complexity of the formations and its particular position between the African and the Eurasian plates. The present study is motivated by targeting eventual subduction traces or hotspots deduced from previous works. After the installation of seventeen permanent broadband seismic stations deployed over this area, we used earthquake data recorded between 2007 and 2016, to define shear wave velocities' structure as a function of depth, using surface Rayleigh waves' dispersion curves fundamental mode inversion. The phase-velocity measurements for periods of 5–200 s are used to generate the first 3D shear-velocity model for north Algeria velocity structure. We observed a variation in shear velocity in the first ten kilometers. These results are in good agreement with the crustal thickness depth of the Moho discontinuity because our area is located in a collision zone. Beyond 30 km depth, the failed subduction slab traces can be clearly observed in the eastern part.

Keywords

Inversion • Rayleigh wave • Shear velocity • Lithosphere • North Algeria

1 Introduction

Northern Algeria is part of the Mediterranean basin. This region is experiencing slow deformation on a relatively large area due to its location between the African and Eurasian plates, which is the main cause of seismic hazards in this area (Stich et al. 2006). Our region is known to have a moderate to strong seismic activity in the west. There were some scientific works conducted on northern Algeria such as the SPIRAL (Sismique Profonde et Investigations Régionale du Nord de l'Algérie) (Yelles et al. 2010), studies of seismic anisotropy of northeast Algeria (Radi et al. 2015) and crust and upper mantle shear wave structure of northeast Algeria from Rayleigh wave dispersion analysis (Radi et al. 2017) that help us to constrain the geodynamic evolution of the Algerian domain. Surface waves are particularly sensitive to the structure of the crust and uppermost mantle, and thus, to the depth of the Moho discontinuity. Dispersion curve analysis of Rayleigh waves at fundamental modes is a well-established method for resolving earth structure.

2 Data and Methods of Analysis

In the present study, we use teleseismic data recorded by 17 broadband permanent stations of the ADSN (Algerian Digital Seismic Network) (Fig. 1a). This network was installed in 2007 in response to the 2003 Boumerdes earthquake (Yelles-Chaouche et al. 2013). Other stations have been added more recently. Each station is equipped with a three-component broadband sensor (Kinemetrics STS-2 or Geodevice BBVS-60). Our data set consists of a few hundreds of teleseisms with Mw $\geq$ 5 at epicentral distances of roughly 30°–90°, recorded by the broadband network between 2007 and 2016 (Fig. 1b). This magnitude threshold was chosen to ensure a high signal/noise ratio over a wide range of periods. These records are considered suitable for this study because the broadband seismographs have relatively flat instrument response curves between 1 and 200 s (Dziewonski et al. 1969). This range of periods is well suited to studying earth structure at depths up to 500 km, which is the main objective of this work.

Z. Radi (✉) · A. Yelles-Chaouche · S. Guettouche
Centre de Recherche en Astronomie Astrophysique et Géophysique, Route de l'Observatoire, BP 63, Bouzaréah, Algiers, Algeria

M. Meghraoui et al. (eds.), *Advances in Geophysics, Tectonics and Petroleum Geosciences*,
Advances in Science, Technology & Innovation, https://doi.org/10.1007/978-3-030-73026-0_37

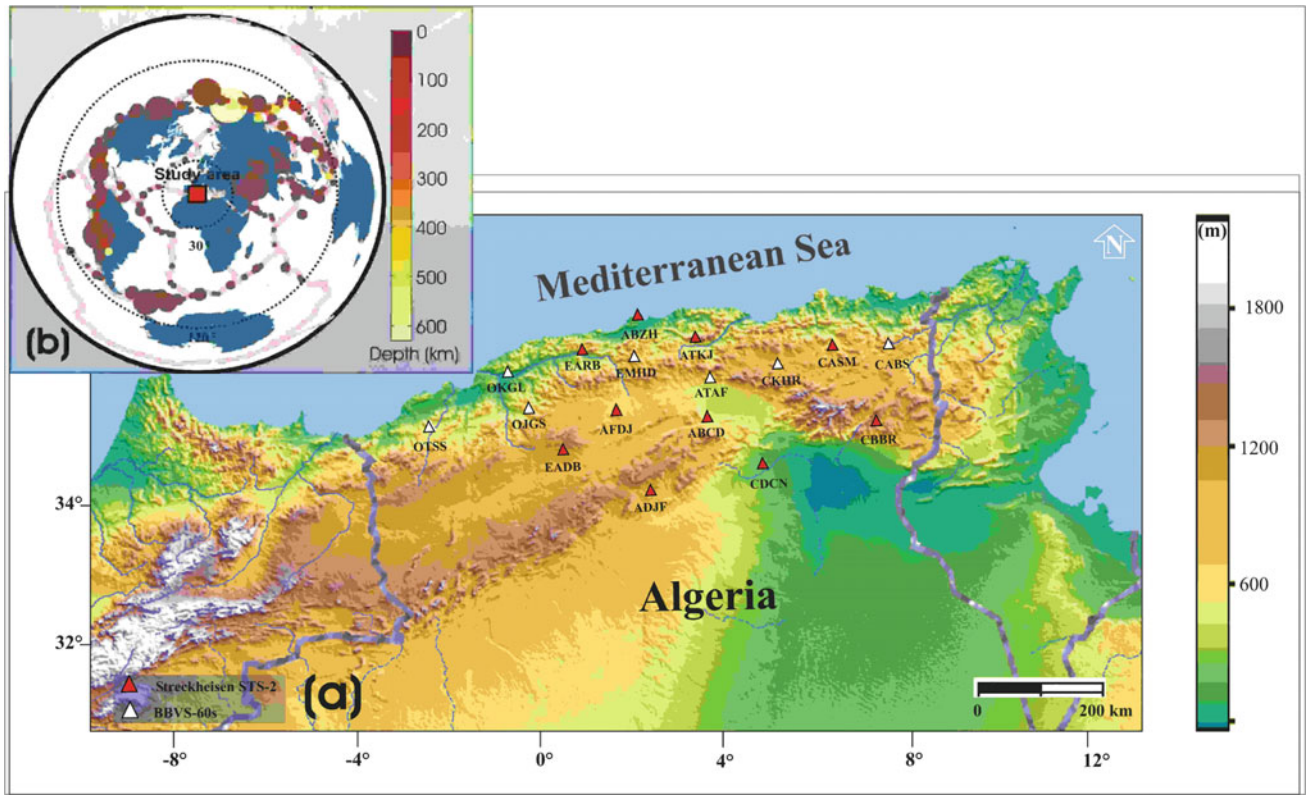

Fig. 1 **a** Geographic distribution of permanent stations of the Algerian seismic network in northeast Algeria (BB = broadband). **b** (inset) Spatial distribution of earthquakes (Mw > 5) used in the present study

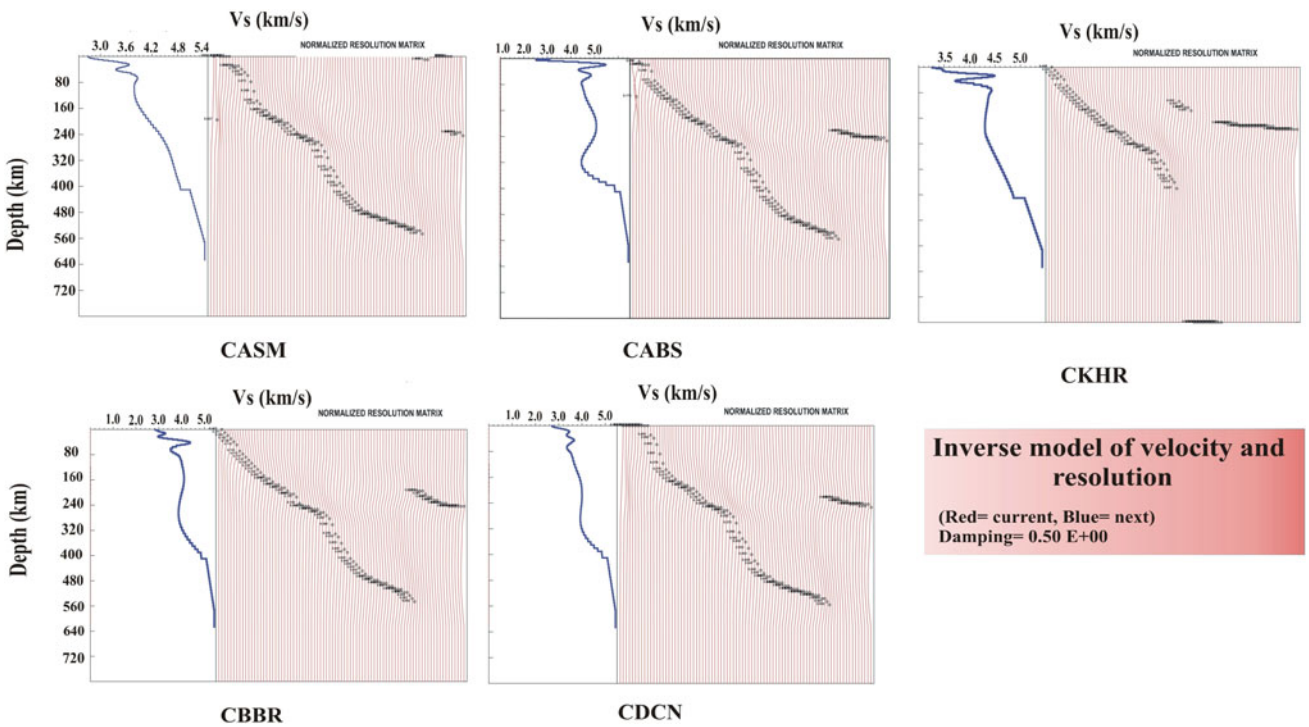

Fig. 2 Variations of Vs with depth

For each teleseismic recording, we first extract the Rayleigh wave dispersion curve using the multiple filter technique of Corchete (2013). First is applied the TVF filtering technique, on a pre-processed seismogram (without instrumental response) to minimize the noise effects, obtaining a smoothed signal. After that, we applied the MFT filtering technique (Dziewonski et al. 1969) on the data set to obtain the dispersion curve of group velocity. We then use the surf 96 program to invert for three-dimensional velocity structure (Hermann and Ammon 2002). The S-wave velocity structure is estimated from the frequency-dependent velocities of Rayleigh waves.

3 Results and Discussion

In Fig. 2, we present some examples of one-dimensional velocity dispersion curves. We compute the shear wave velocity below each station. After that, we calculate the mean shear wave velocity of the seventeen stations. Then, we deduce the relative shear wave velocity variation from the relation (ΔVs/Vs) so in 1D for each station and depth. We plot them for each layer of depth separately in 2D from 10 to 110 km.

The curves in Fig. 3 show relative variations of Vs from 0 to 70 km, which are in good agreement with crustal thickness depth of Moho because our area is located in a collision zone.

At depths of 80–110 km, in Fig. 4, we note negative relative variations of Vs, at the eastern region. This could be interpreted as an evidence of the existence of a failed subduction slab traces. This suggestion is even accepted in comparison with the values found in the regional study (Koulakov et al. 2009) where the anomalies are located between 55 km and around 200 km over our study area. Also, Wortel and Spakman (1992) studied the structure and dynamics of subducted lithosphere in the Mediterranean region. They suggested a slab detachment over the Calabrian Arc until northern Africa.

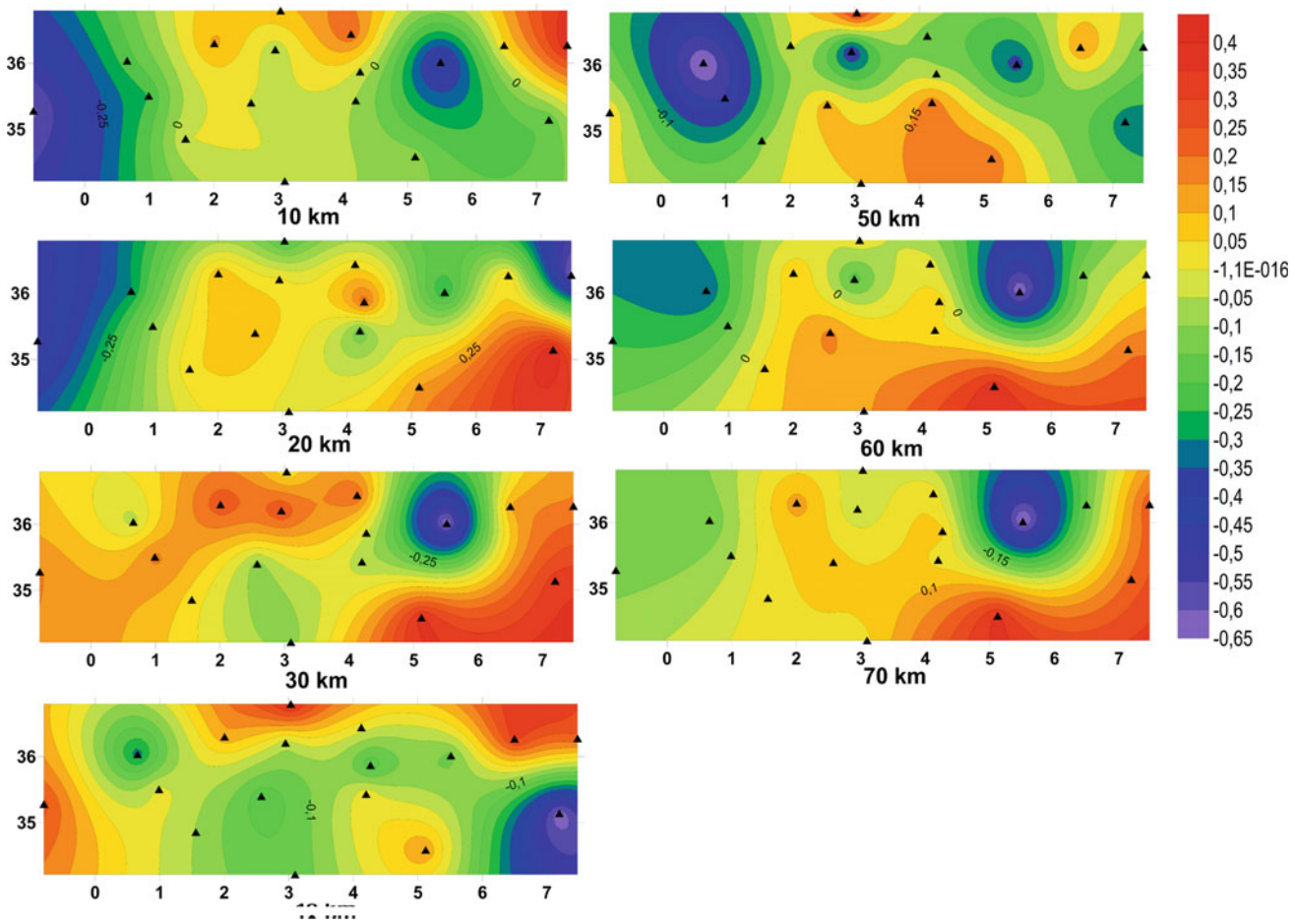

Fig. 3 Relative variations of Vs at depth slices of 10, 20, 30, 40, 50, 60 and 70 km

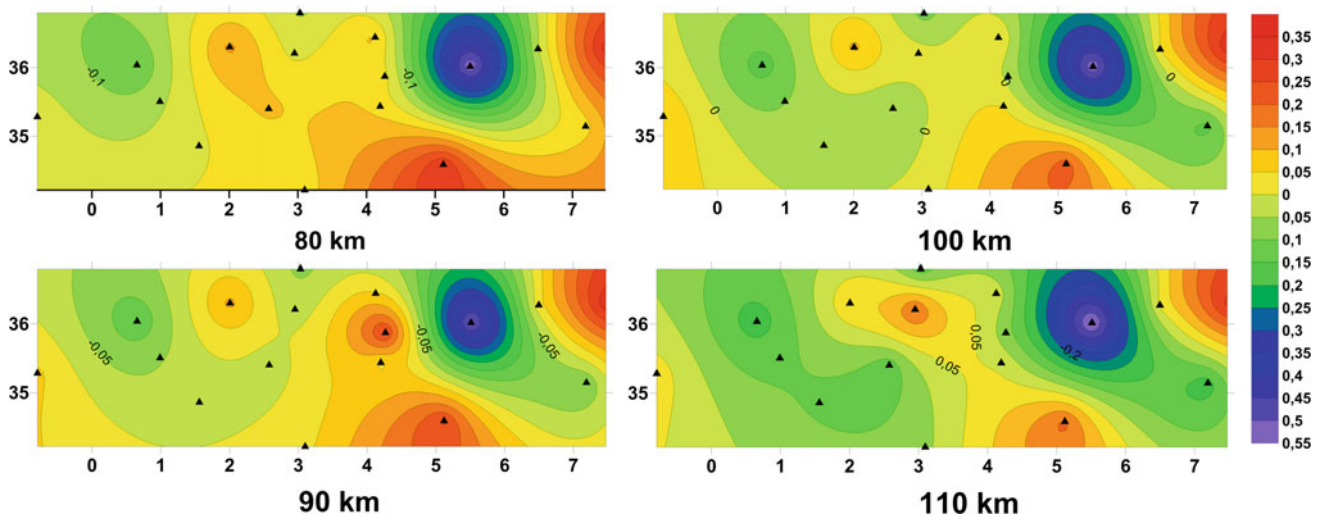

Fig. 4 Relative variations of Vs at depth slices 80–110 km

4 Conclusions

We obtained a high-resolution Vs model of the lithosphere under North Algeria by analyzing surface waves' data recorded by ADSN broadband stations network, using the inversion of fundamental mode Rayleigh wave dispersion curves. We obtained a good agreement between the current results and the regional variations in seismic anisotropy orientations reported by Radi et al. (2015), where the transition of lithospheric thickness is consistent with the general trends of the topographic profile at the surface, corresponding to the changes of fast shear-wave polarization directions. Furthermore, at depth sections of 80, 100 and 110 km, we notice velocity anomalies at the eastern area. Further research is required to investigate the possibility of a failed subduction zone in this region.

References

Corchete, V.: Shear-wave velocity structure of Africa from Rayleigh-wave analysis. Int. J. Earth Sci. **102**, 857–873 (2013)

Dziewonski, A.M., Bloch, S., Landisman, M.: A technique for the analysis of transient seismic signals. Bull. Seism. Soc. Am **59**, 427–444 (1969)

Hermann, R.B., Ammon, C.J.: Computer Programs in Seismology: Surface Wave, Receiver Function and Crustal Structure. Saint Louis University, St. Louis, MO (2002)

Koulakov, I., Kaban, M.K., Tesauro, M., Cloetingh, S.: P- and S-velocity anomalies in the upper mantle beneath Europe from tomographic inversion of ISC data. Geophys. J. Int **179**, 345–366 (2009)

Radi, Z., Yelles-Chaouche, A.K., Bokelmann, G.: Seismic anisotropy of northeastern Algeria from shear-wave splitting analysis. Phys. Earth Planet. Inter. **248**, 73–82 (2015)

Radi, Z., Yelles-Chaouche, A., Corchete, V., Guettouche, S.: Crust and upper mantle shear wave structure of northeast Algeria from Rayleigh wave dispersion analysis. Phys. Earth Planet. Inter. **270**, 84–89 (2017)

Stich, D., Serpelloni, E., de Lis Mancilla, F., Morales, J.: Kinematics of the Iberia-Maghreb plate contact from seismic moment tensors and GPS observations. Tectonophysics 99–110 (2006)

Wortel, M.J.R., Spakman, W.: Structure and dynamics of subducted lithosphere in the Mediterranean region. Proc. Kon. Ned. Akad. v. Wetensch **95**, 325–347 (1992)

Yelles, A., Déverchère, J., Bracene, R., Cattaneo, A., Gaullier, V., Geli, L., Graindorge, D., Kherroubi, A., Klingelhoefer, F., Mercier de Lépinay, B.: From Maradja to Spiral surveys: recent and active deformation of the Algerian margin: evidence for its contractional reactivation. In: ESC 32nd General Assembly, Montpellier, France, 6–10 Sept 2010

Yelles-Chaouche, A.K., Allili, T., Alili, A., Messemen, W., Beldjoudi, H., Semmane, F., Kherroubi, A., Djellit, H., Larbes, Y., Haned, S., Deramchi, A., Amrani, A., Chouiref, A., Chaoui, F., Khellaf, K., Nait Sidi Said, C.: The new Algerian Digital Seismic Network (ADSN): towards an earthquake early-warning system. Adv. Geosci. **36**, 31–38 (2013)

S-Wave Velocity Structure in the City of Oued Fodda, Northern Algeria, by Inversion of Rayleigh Wave Ellipticity

Abdelouahab Issaadi, Fethi Semmane, Abdelkrim Yelles-Chaouche, Juan José Galiana-Merino, and Khalissa Layadi

Abstract

The city of Oued Fodda is located in north-central Algeria in the margins of the middle Cheliff basin. This region has suffered several destructive earthquakes, and the strongest was the 1980 El-Asnam earthquake (Ms 7.3). The causative fault of this earthquake is located at about 1 km north of the city of Oued Fodda. It is well known that a good knowledge of the soil characteristics in a city may lead to better evaluate the seismic risk and therefore help to minimize damages in the future. For this purpose, we used ambient vibration data with the application of the horizontal-to-vertical spectral ratio (HVSR) method to estimate the soil's fundamental frequencies (f_0) and the corresponding amplitudes (A_0). We also applied the random decrement technique method (RayDec) to calculate the ellipticity of the Rayleigh waves. Two measurement campaigns were carried out in the city of Oued Fodda with a set of 102 measurement points. From the visual analysis of the calculated HVSR curves, we divided the study area into four different zones. Thirty Rayleigh wave ellipticity curves were then inverted to characterize the S-wave velocity structures in Oued Fodda city. In the central part of the city, the frequency values (12.5–15 Hz) correspond to the impedance contrast at shallow depth (0–20 m), between the Miocene blue marls (950–1350 m/s) and the ante-Neogene basement (2000–2600 m/s). In the surrounding plain, the frequencies vary between 1.8 and 3.5 Hz, and the existence of a second frequency peak (7.5–11 Hz) is due to the contrast between the Holocene (280–330 m/s) and the Pleistocene (615–710 m/s) deposits.

Keywords

Oued Fodda • Cheliff basin • Ambient vibrations • Fundamental frequencies • Rayleigh wave ellipticity • Shear-wave velocity

1 Introduction

The Cheliff basin is a Neogene basin located in northern Algeria, between the septentrional and meridional Tellian Atlas mountain belts and lying parallel to the Mediterranean coast in an E–W direction. The city of Oued Fodda is situated in the western margins of the middle Cheliff basin. Over the past 200 years, this region has experienced several destructive earthquakes; the strongest one is the 1980 El-Asnam earthquake (Ms 7.3) (Ouyed and Hatzfeld 1981), with an intensity of IX (MSK) attributed to the Oued Fodda city. The El-Asnam fault trace is situated at about 1 km north of the city of Oued Fodda. After the El-Asnam earthquake, the Woodward and Clyde consultants conducted a microzonation study in the city of Oued Fodda (Woodward Clyde Consultants (WCC) Report 1984), with a set of eight shallow geotechnical boreholes. The study assumed that the city was built on and around a bedrock knoll. The main result of the study was the making of geotechnical, hydrogeological and hazard maps in the city. Our work carries on the one made by the WCC in order to minimize potential building damages in the future by estimating the soil fundamental frequencies and also the S-wave velocity structure using more recent experimental techniques for ambient vibrations (Layadi et al. 2018).

A. Issaadi (✉) · F. Semmane · A. Yelles-Chaouche · K. Layadi
Centre de Recherche en Astronomie, Astrophysique et Géophysique (CRAAG), Algiers, Algeria
e-mail: A.Issaadi@craag.dz; Ia30@alu.ua.es

A. Issaadi · J. J. Galiana-Merino
University Institute of Physics Applied to Sciences and Technologies, University of Alicante, Alicante, Spain

M. Meghraoui et al. (eds.), *Advances in Geophysics, Tectonics and Petroleum Geosciences*,
Advances in Science, Technology & Innovation, https://doi.org/10.1007/978-3-030-73026-0_38

2 Methodology

2.1 The Horizontal-to-Vertical Spectral Ratio (HVSR) Method

Introduced by Woodward Clyde Consultants (WCC) Report (1984) and developed by Nakamura (1989), the horizontal-to-vertical spectral ratio (HVSR), most commonly known as the H/V method, links between the HV frequency peak and the fundamental resonance frequency of the soil. The H/V frequency peak is obtained by calculating the average between the Fourier amplitude spectra of the horizontal and vertical components of the recorded signal (Bonnefoy-Claudet et al. 2006). Although this method has proven its reliability in estimating the fundamental resonance frequency of the soil, it appears to under-estimate the amplification factor (Lachet and Bard 1996). Nonetheless, the methodology has wide-scale applicability to address several intricate geological fractions to discriminate the physical property contrasts among different layers that may help in determining the soil/sedimentary thicknesses at the site under study (Chowdhuri and Mishra 2012; Chowdhuri et al. 2008). The equipment used for the recording was a couple of TROMINO seismographs with a sampling rate of 512 samples per second.

2.2 The Rayleigh Wave Ellipticity Inversion

We used the random decrement technique (Hobiger et al. 2009) to calculate the ellipticity of the Rayleigh waves. The ellipticity curves were then inverted to estimate the shear-wave velocity structure and the sediments' thickness in Oued Fodda city. Since the HVSR curve is mainly controlled by Rayleigh and Love waves in case of a large impedance contrast (Bonnefoy-Claudet et al. 2006), the proportion between both surface waves must be assumed before the inversion process. The random decrement technique allows us to extract only the Rayleigh waves (Hobiger et al. 2009). The Rayleigh wave ellipticity inversion is a nonlinear problem, which means that there is no single solution for this problem. A large number of models are then generated. For each generated model, we obtain a Vs profile and a calculated fundamental-mode Rayleigh wave ellipticity curve, which are linked to the experimental curve by a misfit value.

3 Results

3.1 The Resonance Frequencies

The fundamental frequencies obtained from the H/V analysis at each measurement site are shown in Fig. 1. The frequency values vary from 1.8 to 15 Hz. This wide frequency range is due to the different outcropping formations within the study area. The fundamental frequency values range from 1.8 to 3.5 Hz in the western and southern parts of Oued Fodda city and from 2 to 6 Hz in its eastern and northern parts. The frequency values increase considerably towards the central part of the city to reach a maximum value of 15 Hz on the most elevated point of the city, where the bedrock is at a very shallow depth (Woodward Clyde Consultants (WCC) Report 1984). Some flat H/V curves had been also observed in this area. Most of the obtained H/V curves show a secondary peak at frequencies between 7 and 11 Hz, and this frequency peak corresponds to shallow impedance contrasts in the soil column.

3.2 Shear-Wave Velocity Models

Once the H/V curves are obtained and the fundamental frequencies are identified for each site, a zonation map of the HVSR curves has been performed before the inversion in order to facilitate the process. Four distinct zones have then been identified based on the degree of similarity of the HVSR curves. The random decrement technique was applied to the selected HVSR curves using the Raydec code of Hobiger et al. (2009). The ellipticity of Rayleigh waves' fundamental mode was then calculated. The obtained curves were inverted using Dinver software from Geopsy package (www.geopsy.org). The shear-wave velocity for the topmost layer of the zone Z1, which consists of Holocene alluviums, ranges between 280 and 330 m/s, with a maximum thickness of 10 m. The velocity contrast between this layer and the underlying Pleistocene formation is responsible for the second peak at higher frequencies. Within the city area, the topmost layer consists of Pleistocene deposits; the thickness varies between 2 and 13 m in the centre, where the bedrock is believed to be at very shallow depths (Woodward Clyde Consultants (WCC) Report 1984). In the rest of the study area, the thickness varies between 13 and 58 m. The shear-wave velocity ranges between 615 and 710 m/s. The Vs values for the bottom sediment layer range between 960 and 1350 m/s. The thickness varies from 13 to 16 m in the zone Z4 and from 40 to 126 m in the surrounding plain. The Vs values for the ante-Neogene basement vary between 2000 and 2600 m/s. The velocity models for the four zones are plotted in Fig. 2.

4 Discussion

The spatial distribution of the H/V curves with only one clear peak shows that these sites are located only in the central part of the Oued Fodda city, while H/V curves with two frequency peaks are located all around the city centre.

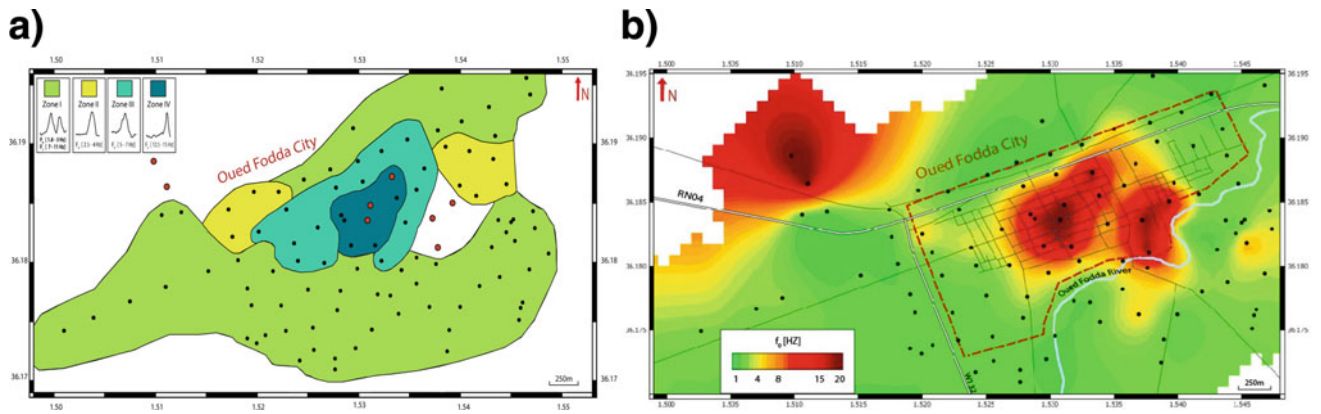

Fig. 1 **a** Zonation map of the HVSR curves. **b** Fundamental frequencies' map (interpolated) obtained from the H/V analysis

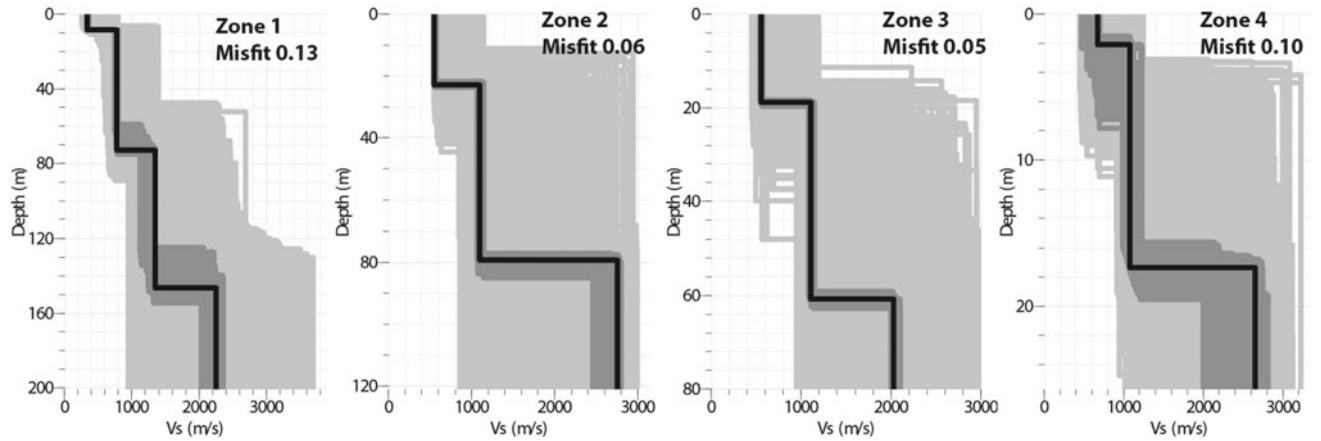

Fig. 2 Velocity models obtained from the inversion of the Rayleigh wave ellipticity curves. Black line represents the minimum misfit model. The dark grey represents the minimum misfit + 10%

By plotting the H/V results on the geological map of the area, we notice that the curves with one clear frequency peak are located on Pleistocene formation, while curves with two frequency peaks are on Holocene alluviums. The secondary peak at higher frequencies appears to be related to a shallow impedance contrast between the Holocene alluviums and the Pleistocene red clays. The higher depths to bedrock are observed in the western and southern parts with a maximum value of 181 m.

5 Conclusions

We used the horizontal-to-vertical spectral ratio (HVSR) technique and the inversion of the Rayleigh wave ellipticity to characterize the subsurface structure in the city of Oued Fodda. The fundamental frequencies range between 1.8 and 15 Hz, and this large variation is due to local geology. The high frequencies (12.5–15 Hz) obtained on the knoll situated in the centre of the city along with the flat H/V curves confirm the assumption made by the WCC (1984) that this knoll is a bedrock outcrop. The results of the inversion show clearly the existence of lateral variations of the shear-wave velocities and the sediments' thickness in the plain of Oued Fodda. The city of Oued Fodda is growing southward, where the largest thickness of the sedimentary cover is obtained. Site effect investigations should be considered, especially for growing cities on seismic zones, in order to minimize potential building damages due to earthquakes.

References

Bonnefoy-Claudet, S., Cornou, C., Bard, P.Y., Cotton, F., Moczo, P., Kristek, J., Fäh, D.: H/V ratios: a tool for site effects evaluation. Geophys. J. Int. **167**, 827–837 (2006)

Chowdhuri, S.N., Mishra, O.P.: Oblate particle motion for high site response characteristics in Agartala city, India. Indian J. Geosci. **66** (4), 225–232 (2012)

Chowdhuri, S.N., Singh, O.P., Mishra, O.P., Kayal, J.R.: Microzonation study from ambient noise measurement for assessing site effects

in Krishnagar area and its significance with damage pattern of Ms = 4.3 24 September 1996 earthquake. J. Indian Miner. Spec. Issue **61** (3–4) & **62**(1–4), 183–192 (2008)

Hobiger, M., Bard, P.-Y., Cornou, C., Le Bihan, N.: Single station determination of Rayleigh wave ellipticity by using the random decrement technique (RayDec). Geophys. Res. Lett. **36**(14), L14303 (2009)

Lachet, C., Bard, P.Y.: Numerical and theoretical investigations on the possibilities and limitations of Nakamura's technique. J. Phys. Earth **42**(4), 377–397 (1996)

Layadi, K., Semmane, F., Yelles-Chaouche, A.: S-wave velocity structure of Chlef City, Algeria, by inversion of Rayleigh wave ellipticity. Near Surf. Geophys. **16**(3), 328–339 (2018)

Nakamura, Y.: A method for dynamic characteristics estimation of subsurface using ambient noise on the ground surface. Q. Rep. **30**, 25–33 (1989)

Ouyed, M., Hatzfeld, D.: Etude seismotectonique. In: Proceedings of des Journees Scientifiques sur le Seisme d'El Asnam, Oct 1980 (1981)

Woodward Clyde Consultants (WCC) Report: Seismic microzonation of Ech-Chellif region—Algeria. Report prepared for Organisme de Contrôle Technique de la Construction (CTC), vol. I/II, Algiers (1984)

Studying the Evolution of Earthquake Network Measures for the Main Shock of the 24th of June 2015 in Egypt

Khaled Omar and Dimitris Chorozoglou

Abstract

The monitoring of network measures, such as degree centrality, betweenness centrality, and clustering coefficient is performed, aiming to identify the periods during which the earthquake network has distinct evolution before the main shock of the 24th of June 2015 in Egypt. As nodes the 42 square cells that constitute a normal grid superimposed onto the study area are considered and the connections are drawn whenever earthquake succession is observed between the node areas of seismic activity of the corresponding nodes. The data are taken from a seismic catalog comprising crustal earthquakes (focal depth less than 50 km) of magnitude $M \geq 2.5$ that occurred in the territory of Egypt during the period 1998–2015. The earthquake network is formed on sliding windows of 90 days and then the values of 9 network measures on each sliding window are computed before the main shock of the 24th of June 2015. The investigation of network measures revealed that more of their values exhibit an abrupt jump just before the main shock's occurrence.

Keywords

Nodes • Connections • Network measures • Seismicity in Egypt

1 Introduction

Another way to approach the study of the spatial and temporal complexity of seismicity, for the seismic hazard assessment is through the construction of earthquake networks. Network (graph) theory provides a framework to investigate the structure and dynamics of a complex system. The network nodes are usually assumed to represent distinct subsystems and the connections represent the interactions among them. In recent years, network theory was successfully applied in different disciplines, such as economics (Emmert-Streib and Dehmer 2010; Papana et al. 2017), neuroscience (Rubinov and Sporns 2010; Kugiumtzis and Kimiskidis 2015; Bullmore et al. 2016), physiology (Porta and Faes 2016) and transportation (Wang et al. 2017; Aydin et al. 2017). In Seismology, the complex network analysis was introduced by Abe and Suzuki (2004) to study seismicity as a spatiotemporal complex system. The aim of this study is to investigate whether the earthquake network constructed for the area of Egypt presents any distinct structure before the main shock of the 24th of June 2015. A similar study was performed for the Greek area (Chorozoglou et al. 2018) based on time series. We first present in Sect. 2 the construction of the earthquake networks as well as the network measures which are used. In Sect. 3, the monitoring of the 9 network measures for the Egypt seismicity is presented and discussed. The concluding remarks are given in Sect. 4.

2 Methodology

In the following, we present first the construction of the earthquake network and then the network measures that were used for their monitoring.

K. Omar (✉)
National Research Institute of Astronomy and Geophysics (NRIAG), Helwan, Cairo, Egypt
e-mail: khaled.abdellah@nriag.sci.eg

D. Chorozoglou
Department of Geophysics, School of Geology, Aristotle University of Thessaloniki, 54124 Thessaloniki, Greece
e-mail: chorozod@geo.auth.gr

M. Meghraoui et al. (eds.), *Advances in Geophysics, Tectonics and Petroleum Geosciences*, Advances in Science, Technology & Innovation, https://doi.org/10.1007/978-3-030-73026-0_39

2.1 Building the Earthquake Network

For the earthquake network construction, we first create the nodes. We divide the study area into a grid of $K = 42$ two-dimensional (2D) seismicity cells. A connection is drawn whenever successive earthquakes occur at a pair of cells. If an earthquake occurs in a site i and the next earthquake in the catalog occurs at the site j, there is a connection between the pair of nodes (i, j). In this way, asymmetric adjacency matrix $A = \{aij\}$, $i, j \in \{1, \ldots, K\}$ is formed with ones and zeros, where the entry one in aij indicates that a succession of earthquakes from sites i and j has occurred in the study period. Multiple successive occurrences at a site pair (i, j) still suggest $aij = 1$.

2.2 Network Measures

Nine (9) network measures are considered and computed on the adjacency matrix. The mathematical definitions are given in Table 1. The network measures are described below.

Table 1 The mathematical definitions of the network measures with simple undirected connections

Network measures	Mathematical type
Clustering coefficient	$C = \frac{1}{K}\sum_{i=1}^{K} c_i = \frac{1}{K}\sum_{i=1}^{K} \frac{\sum_{j,h\in K} a_{ij}a_{ih}a_{jh}}{k_i(k_i-1)}$
Degree centrality	$\overline{k} = \sum_{i=1}^{K} k_i, \quad k_i = \sum_{j=1}^{K} a_{ij}$
Global efficiency	$E = \frac{1}{n}\sum_{i\in N} E_i = \frac{1}{n}\sum_{i\in N} \frac{\sum_{j\in N, j\neq i} d_{ij}^{-1}}{N-1}$
Eigenvector centrality	$X_i = \lambda^{-1}\sum_{j\in N} a_{ij}x_j$
Characteristic path length	$L = \frac{1}{K}\sum_{i=1}^{K} L_i = \frac{1}{K}\sum_{i=1}^{K} \frac{\sum_{j\in K, j\neq i} d_{ij}}{K-1}$
Assortativity	$r = \frac{E^{-1}\sum_{(i,j)\in E} k_i k_j - \left[E^{-1}\sum_{(i,j)\in E} \frac{1}{2}\left(k_i^2 + k_j^2\right)\right]^2}{E^{-1}\sum_{(i,j)\in E} \frac{1}{2}\left(k_i^2 + k_j^2\right) - \left[E^{-1}\sum_{(i,j)\in E} \frac{1}{2}\left(k_i^2 + k_j^2\right)\right]^2}$
Betweenness centrality	$b_i = \frac{1}{(N-1)(N-2)} \sum_{\substack{h,j\in \\ h\neq j, h\neq i, j\neq i}} \frac{\rho_{hj}(i)}{\rho_{hj}}$
Diameter	$d_G = \max_{i\in N} e_i$
Eccentricity	$e_i = \max_{x\in N}\{d(i,x)\}$

3 Application

The investigation of the network measures evolution before the main shock of the 24th of June 2015 is performed. The data and the application of the methodology are described, and then the results are given.

3.1 Data and Computational Setting

Earthquake data are gathered from the catalog of El-Eraki et al. (2015) and from the earthquakes recorded by the Egypt National Seismic Network (ENSN) and presented in the bulletin of the National Research Institute of Astronomy and Geophysics (www.nriag.sci.eg). Crustal earthquakes (focal depth less than 50 km) that occurred during 1998–2015 (Fig. 1) are only considered for a magnitude threshold of $M \geq 2.5$, for the status of the catalog completeness to be fulfilled (Fig. 2). The aim of this study is to investigate whether the earthquake network which was constructed for Egypt presents a distinct structure before the main shock of the 24th of June 2015. The sampling time is 90 days for the period 1998–2015, and the earthquake network is formed on sliding windows, then the values of 9 network measures on each sliding window are computed. Regarding the network nodes, the study area is divided into = 45 2D square seismic cells with side 0.7°. For the network connections formed from the succession of earthquakes, the adjacency matrix A is simply formed having ones when at least one succession occurs between two nodes.

3.2 Results

In Fig. 3, the values of the nine network measures before the main shock of the 24th of June 2015 on the sliding windows are shown. Five out of nine network measures, namely clustering coefficient, global efficiency, eigenvector centrality, betweenness centrality, and eccentricity, are quite stable with small fluctuations before the main shock, before increasing abruptly just before its occurrence. These network measures can be regarded as indexes of the level of seismicity and may be a useful tool in earthquake forecasting.

In Fig. 4, the structure of the earthquake network is shown on different time windows before the main shock of the 24th of June 2015. The network structure is different on each time window (Fig. 4). In the first panel of Fig. 4, the network has a few connections and the seismic activity was weak in the middle of 1998 (second-time window). Then, the seismicity is increased (second panel of Fig. 4) in the middle of 2007 (35th-time window), because the connections on network are more than the previous windows. A few days before the main shock (67th-time window), the connections are increased (third panel of Fig. 4). Therefore, this constitutes an indication that a high level of seismicity appears and the main shock is likely to occur.

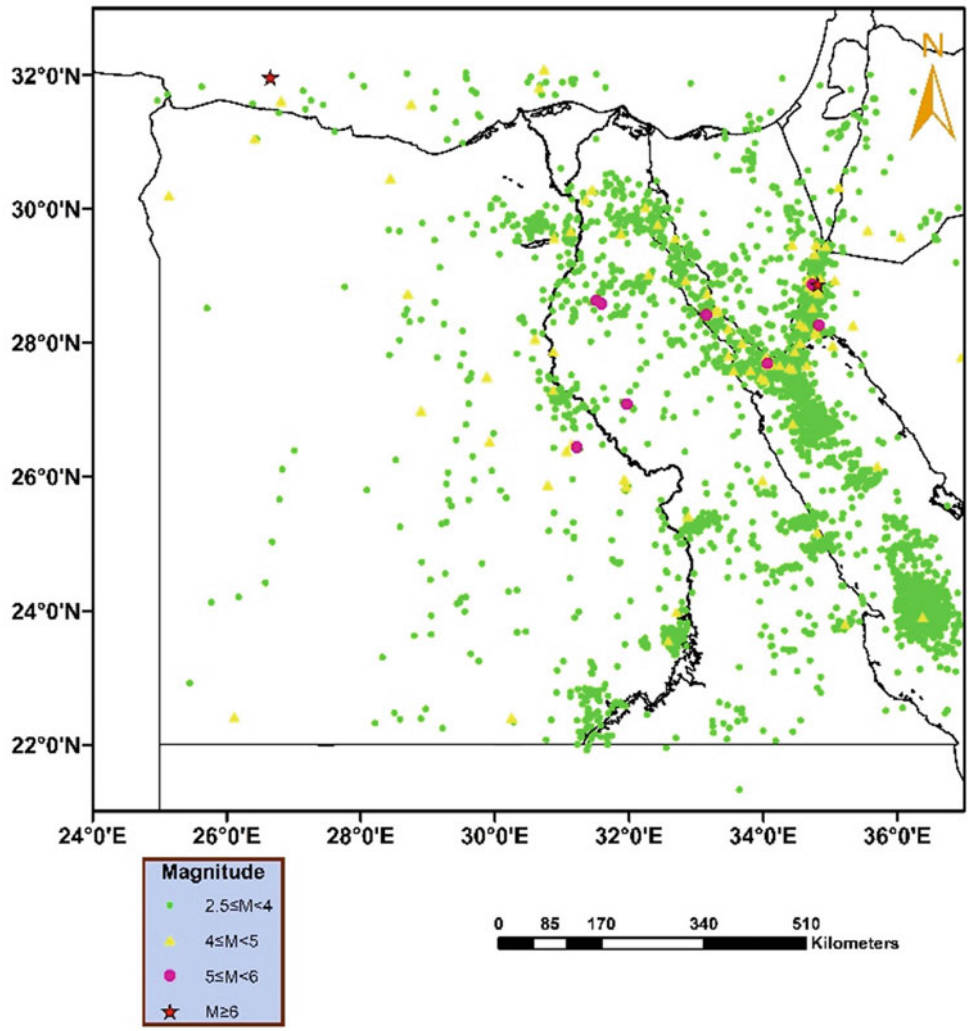

Fig. 1 The epicentral distribution of the earthquakes spanning the period 1998–2015

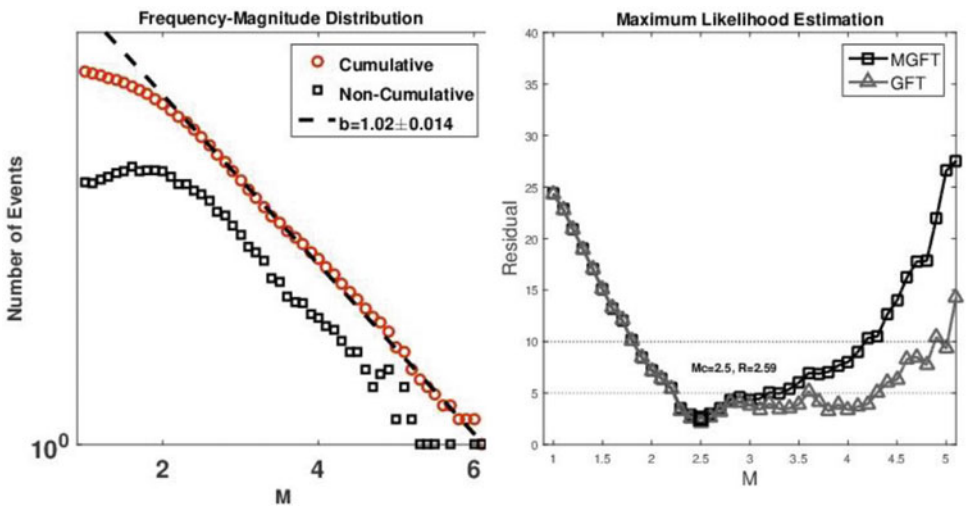

Fig. 2 Completeness of data of the period 1998–2015

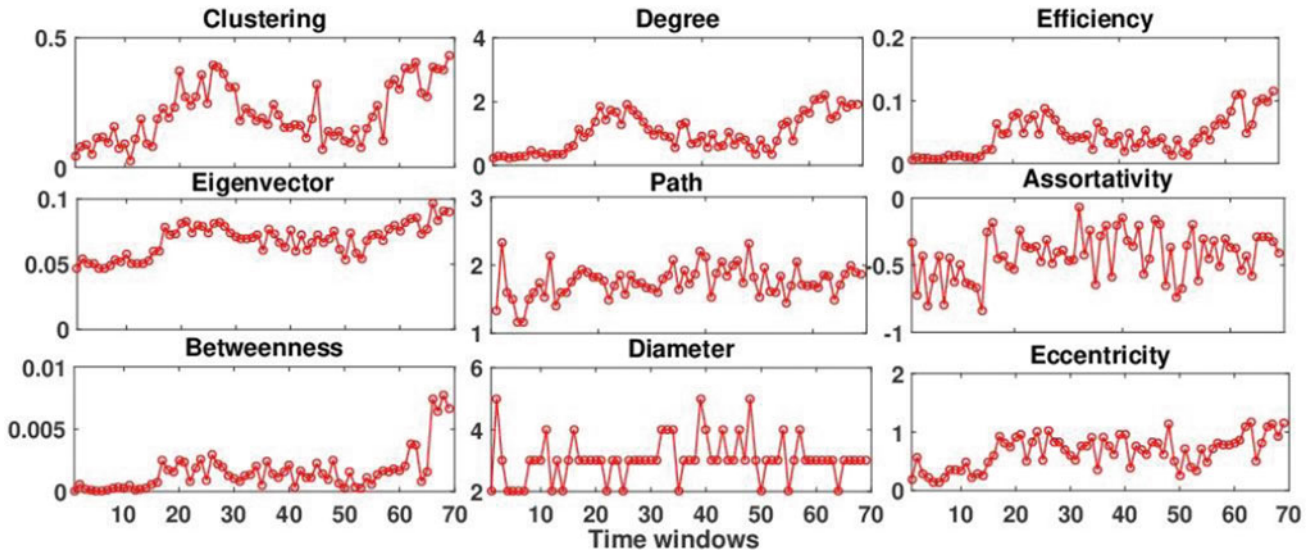

Fig. 3 The values of nine network measures on each of the 70 sliding windows before the main shock of the 24th of June 2015

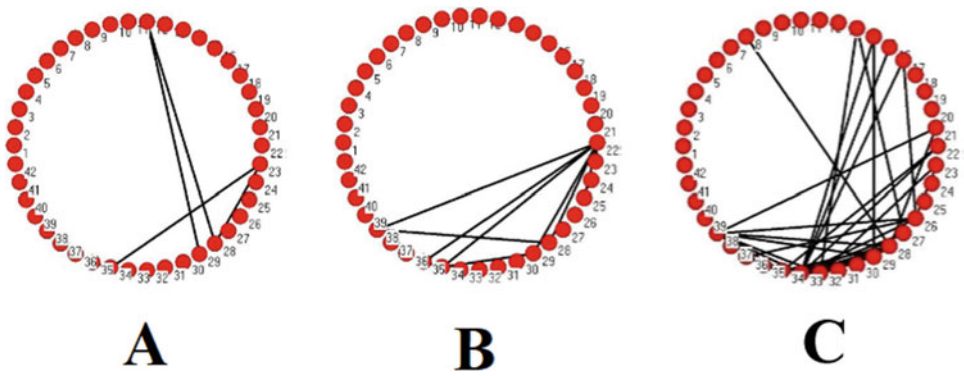

Fig. 4 The earthquake network structure in the second time window (**a**), in 35th (**b**) and in the 67th time window. The red cycles are the 42 nodes of earthquake network and the black lines are the connections among the nodes

4 Discussion and Concluding Remarks

An analysis was performed aiming to identify whether the earthquake networks for the Egypt seismicity exhibit any distinct structure before the main shock of the 24th of June 2015. The application of the network theory is found to be a powerful tool for the investigation of these structures of complex phenomena. Such network properties may signify the distinct evolution of complex networks before the occurrence of main shocks (strong earthquakes). For example, the changes in the network structure, i.e., the transition from random to small-world structure, can reveal certain seismicity behavior a few days before a strong earthquake occurrence (Abe and Suzuki 2009; Chorozoglou et al. 2017).

In this study, the network nodes were represented by $2D$ square seismicity cells and the connections were binary as defined by the succession of earthquakes. The earthquake networks constructed for the period 1998–2015 and for a certain magnitude cut-off for the catalog to be complete show a distinct structure for five network measures, clustering coefficient, global efficiency, eigenvector centrality, betweenness centrality, and eccentricity. We found that earthquake networks possess hierarchical organizations. The five network measures can track changes in the evolution of networks, computed on sliding time windows of 90 days duration, associated with the main shock. We acknowledge that the analysis in this work can be extended in the future to include directed connections (causality networks) and possibly increase the number of nodes.

References

Abe, S., Suzuki, N.: Small-world structure of earthquake network. Phys. A **337**, 357–362 (2004)

Abe, S., Suzuki, N.: Main shocks and evolution of complex earthquake networks. Braz. J. Phys. **39**(2A), 428–430 (2009)

Bullmore, E.T., Fornito, A., Zalesky, A.: Fundamentals of Brain Network Analysis. Academic Press, Elsevier (2016)

Chorozoglou, D., Kugiumtzis, D., Papadimitriou, E.: Application of complex network theory to the recent foreshock sequences of Methoni (2008) and Kefalonia (2014) in Greece. Acta Geophys. **65** (3), 543–553 (2017). https://doi.org/10.1007/s11600-017-0039-4

Chorozoglou, D., Kugiumtzis, D., Papadimitriou, E.: Testing the structure of earthquake networks from multivariate time series of successive main shocks in Greece. Phys. A **499C**, 28–39 (2018). https://doi.org/10.1016/j.physa.2018.01.033

El-Eraki, M.A., Abd El-Aal, A.K., Mostafa, S.I.: Multiseismotectonic models, present-day seismicity and seismic hazard assessment for Suez Canal and its surrounding area, Egypt. Bull. Eng. Geol. Environ. **75**(2), 503–517 (2015). https://doi.org/10.1007/s10064-015-0774-1

Emmert-Streib, F., Dehmer, M.: Influence of the time scale on the construction of financial networks. PLoS One **5**(9), e12884 (2010)

Kugiumtzis, D., Kimiskidis, V.K.: Direct causal networks for the study of transcranial magnetic stimulation effects on focal epileptiform discharges. Int. J. Neural Syst. **25**, 1550006 (2015)

Papana, A., Kyrtsou, C., Kugiumtzis, D., Diks, C.: Financial networks based on Granger causality: a case study. Phys. A **482**, 65–73 (2017)

Porta, A., Faes, L.: Wiener-Granger causality in network physiology with applications to cardiovascular control and neuroscience. Proc. IEEE **104**, 282–309 (2016)

Rubinov, M., Sporns, O.: Complex network measures of brain connectivity: uses and interpretations. NeuroImage **52**, 1059–1069 (2010)

Wang, X., Koç, Y., Derrible, S., Ahmad, S.N., Pino, W.J.A., Kooij, R. E.: Multi-criteria robustness analysis of metro networks. Phys. A **474**, 19–31 (2017)

On Detecting Changes in Earthquake Occurrence Rates Through Trend Reversal

Moinak Bhaduri

Abstract

Earthquakes, like several other rare events, strike at random times and predicting the next one remains daunting despite today's scientific advances. An unchanged rate of occurrence signifies stationarity when the shocks may be taken to occur purely at random, while an elevated (or reduced) rate is usually accompanied by higher (or lower) frequencies. This work imposes a point (Poisson) process structure on these shocks and seeks to discover statistically significant changes, especially increases in these rates. Preventive measures such as relocating inhabitants or arranging relief can then be undertaken to minimize the loss of lives and property. We achieve this through switching the traditional flow of time from the left to the right and from the right to the left, thereby bringing about an apparently minor change in the way, an established trend statistic (termed the forward statistic), is formulated, paving the way for a backward version of it. Extensive simulations document smooth and rough intensities, deterministic or randomly mixed, under which the backward proposal outperforms the traditional forward or other competitors like the Laplace test through achieving better detection power. We finally outline a way to estimate the number of earthquakes in a given period of time.

Keywords

Earthquake forecasts • Point process • Poisson distribution • Step intensities • Time reversal • Change point detection

1 Introduction

At this writing, the state of California in the USA is struggling to recover from the 7.1 magnitude earthquake that shook Ridgecrest barely a few days ago on July 6, with tremors felt as far as in Mexico. Collecting historical records from the neighboring Parkfield, we predicted in one of our previous works (Ho and Bhaduri 2015) such a shock around 2025. The notion of Empirical Recurrence Rates was used, which, through a sequence of other papers (Tan et al. 2014; Ho et al. 2016; Ho and Bhaduri 2017; Bhaduri and Zhan 2018; Bhaduri and Ho 2018); was generalized to construct Empirical Recurrence Rates Ratio. While such proximity between the predicted and the actual time remains tolerably close, the mentioned analysis was left at the mercy of a fitted time-series model, choosing which, as modelers would doubtlessly agree, remains, at times, problematic, and subjective. The present work, therefore, offers an alternative. It examines the backward statistic introduced by Ho (1993) in the context of checking possible changes in earthquake occurrence rates. Some unavoidable mathematical preliminaries are elaborated next.

With the continuous time, discrete space stochastic process $\{N(t)\}_{t>0}$ counting the number of earthquakes in a time interval $(0, t]$, it is often convenient to require a Poisson law explaining the event generation. Probabilistically, thus, the chances of observing n shocks in the said interval are given by

$$P[N(t)=n]=\exp\left(-\int_0^t \lambda(x)\mathrm{d}x\right)\frac{\left\{\int_0^t \lambda(x)\mathrm{d}x\right\}^n}{n!}, \quad \forall t>0,\ n=0,1,2,3,\ldots \tag{1}$$

where $\lambda(.)$, known as the governing intensity, controls the frequency of occurrences. These frequencies will be high (suggesting process deterioration, meaning more earthquakes) over a period on which $\lambda(.)$ is inflated and low over

M. Bhaduri (✉)
Department of Mathematical Sciences, Bentley University, 175 Forest St, Waltham, MA 02452, USA
e-mail: mbhaduri@bentley.edu

M. Meghraoui et al. (eds.), *Advances in Geophysics, Tectonics and Petroleum Geosciences*,
Advances in Science, Technology & Innovation, https://doi.org/10.1007/978-3-030-73026-0_40

one on which it is not. A constant $\lambda(.)$ implies roughly the same number of shocks over different periods of the same length (termed homogeneity or stationarity), while a departure from such constancy insinuates a preference of the shocks to cluster in pockets on the time axis. We will work with different choices of $\lambda(.)$ in Sect. 3.

2 Methodology

We let $t_1 < t_2 < \ldots < t_n$ represent the global occurrence times and note the way Rigdon and Basu (2000), among others, define what, from now on, we will term the forward statistic:

$$Z = -2\sum_{i=1}^{n} \log\left(\frac{t_i}{t_n}\right) \tag{2}$$

Under process deterioration (when $\lambda(.)$ is high), the t_is will hover around t_n, lowering the value of Z. Ho (1993) proposed a modification

$$Z_B = -2\sum_{i=1}^{n} \log\left(1 - \frac{t_i}{t_n}\right) \tag{3}$$

where the trend got switched, hence, the name backward statistic. Under deterioration, thus, Z_B, unlike Z, will be inflated.

Another established option is the Laplace statistic defined by

$$L = \sum_{i=1}^{n} \frac{t_i}{t_n}$$

It can be proved (Rigdon and Basu 2000; Ho 1993) that the distributions of Z and Z_B under the assumption of stationarity are both chi-square with $2(n-1)$ degrees of freedom where n is the sample size. Ho (1993) discovered a special class of intensities (step functions) and scenarios (late jumps in these steps) under which Z_B detects changes in $\lambda(.)$ more efficiently than Z. This work generalizes that study, finding other situations relevant in an earthquake context (such as mixture intensities) under which that supremacy is retained. The Poisson process provides a scope of understanding earthquake genesis and conflict analysis (Dutta et al. 2013a).

3 Results

Using different forms of the intensity function $\lambda(.)$ in the subsections to follow, we will simulate 10^4 non-stationary Poisson processes (according to (1)), measure the proportion of times Z and Z_B, and correctly identify them as being non-stationary. Following the discussions in the previous section, the classification will be based on chi-square thresholds, i.e., deterioration, for instance, through the backward version will be flagged if the observed value of Z_B exceeds the upper α point of a chi-square density. α controls the Type-I error probability and is set at 0.05 in this study.

3.1 Rough Intensities

p-step intensities of the form

$$\lambda(t) = \sum_{i=1}^{p} k_i I_{(\tau_{i-1},\tau_i]}(t), \quad t > 0 \tag{4}$$

where $I_A(.)$ represents the usual indicator function on a set A, allowing the switch from stationarity to non-stationarity to happen abruptly and, hence, are ideal to model sudden changes in a geological context.

Table 1 demonstrates how Z_B performs better in detecting deterioration than Z at various sample sizes in case the intensity shoots up through steps of three. At sample size 45, for instance, Z_B is able to correctly identify around 67% of the simulation cases as deteriorating. The corresponding number for Z is around 59%. Although not extremely crucial since a decreasing intensity is favorable in this context; Table 2 shows how Z_B performs marginally better than Z even in detecting process improvement. This is evidenced through the slight increase of Z_B's power which is of 0.7238, over Z's which is of 0.7227.

As the last level of complexity, we explore a random mixing of steps. To incorporate our lack of complete knowledge about the nature of the underlying intensity, we adopt a simulation framework where an increasing step intensity $k_1 = 1$, $k_2 = 3$ will be sampled 50% of the times, and a decreasing step intensity $k_1 = 3$, $k_2 = 1$ will be sampled the remaining 50%. The sample size was held at 40, and the jumps were placed late into the process $\tau_{inc} = 27$, $\tau_{dec} = 27/3$ to highlight the power differences.

Table 3 records the results. Z_B emerges as the best classifier even under this hybrid setting.

3.2 Earthquake Applications

We initiated this work with an observation of the recent earthquake in Ridgecrest, California. In this section, we revisit this problem with the goal of implementing the forward and backward versions to detect changes in earthquake intensity over this geographic location. The USGS repository reveals five other recent earthquakes in this region that clocked more than 6.7 on the Richter scale. They occurred

Table 1 Power comparison between the forward and backward tests with sampling frequency = 1:1:1 and $k_1 = 1$, $k_2 = 2$, $k_3 = 3$

Sample size	Sampling frequency = 1:1:1		Average counts		Knot placements	
	Z power	Z_B power	$E(0, \tau_1]$	$E(\tau_1, \tau_2]$	τ_1	τ_2
$n = 15$	0.2623	0.2352	5.0088	4.8811	5	7.5
$n = 30$	0.4378	0.4719	10.0435	9.9387	10	15
$n = 45$	0.5886	0.6693	15.0238	14.9823	15	22.5

Table 2 Power comparison between the forward and backward tests with sampling frequency = 1:2:1 and $k_1 = 3$, $k_2 = 2$, $k_3 = 1$

Sample size	Sampling frequency = 1:2:1		Average counts		Knot placements	
	Z power	Z_B power	$E(0, \tau_1]$	$E(\tau_1, \tau_2]$	τ_1	τ_2
$n = 24$	0.2925	0.2963	5.9738	11.7766	2	8
$n = 48$	0.5434	0.5387	12.0093	23.8463	4	16
$n = 72$	0.7227	0.7238	18.0263	35.9533	6	24

Table 3 Power comparison under random mixing of increasing and decreasing step intensity

Classifier	Estimated power
Forward Z	0.5441
Backward Z_B	0.7218
Laplace L	0.7069

on April 18, 1906, the July 21, 1952, June 28, 1992, January 17, 1994, and October 16 ,1999. Treating the 1906 occurrence as the time origin, the global times (in days) are $t_1 = 16{,}896$, $t_2 = 31{,}484$, and $t_3 = 32{,}052$, $t_4 = 34{,}150$. We invoke (2) and (3) to find that the observed values of the forward and backward versions are $Z = 1.697$, $Z_B = 12.045$. At 10% type-I error, the lower and upper alpha points of a chi-square density with $(2 \times 4 - 2 =)$ 6 degrees of freedom are 2.204 and 10.645, respectively. Thus, at any point prior to the latest strike, we find that both these statistics would have signaled process deterioration, suggesting an increased likelihood of an imminent shock with $1.697 < 2.204$ and $12.045 > 10.645$.

We have next analyzed three other earthquake sequences that originated in Ogata, North China, and Phuket to analyze sequences of various sample sizes.

Data on these other earthquake sequences can be had from the PtProcess package in the software R (Harte 2010). Due to space constraints, we direct readers interested in the background to this resource. Table 4 records our findings. We may note that in all the examples considered, we have agreement between Z and Z_B. This, however, need not be always true. In view of its superior power performance, as evidenced in the previous subsections, if there is ever a disagreement between the two, we will have more faith in Z_B to sound a deterioration alarm, which can also be achieved through trust validation using the concept of decision analysis for earthquakes (Dutta et al. 2012, 2013b).

4 Discussion and Conclusions

Rarity of occurrence, though desirable from a pragmatic viewpoint, poses a formidable challenge in data-based earthquake modeling. By employing a Poisson process framework to describe these events, we have shown how a minor switch in the way trend is analyzed and understood (left–right to right–left) that can generate a new statistic capable of sounding timely alarms. Extensive simulations conducted with small sample sizes to better emulate these scenarios and with different forms of underlying intensities (deterministic and random, smooth, and rough) not considered in previous works, demonstrate its superior power compared to similar competitors. These simulations were essential since an exact closed-form theoretic expression for power does not exist under step intensities of the form (4). Unlike some of our previous work mentioned in the introduction, here we have not partitioned the time axis into separate blocks to create a discrete domain time series. Valuable information about the exact occurrence time is, thus, retained. This work, thus, helps to check whether Poissonian earthquakes are occurring more or less frequently in a given geographical neighborhood, so that inhabitants may be removed from or brought in from other potentially hazardous regions to minimize the loss of lives and property. This analysis also lays the foundation of aftershock modeling through tools such as self-exciting Hawkes processes.

Table 4 Earthquake rate change detection through forward and backward tests

Earthquake	Z	Z_B	Lower crit. point	Upper crit. point	Deterioration?
Ogata (n = 100)	226.31	178.29	172.96	223.89	Z: No, Z_B: No
N. China (n = 65)	129.24	133.37	107.97	148.88	Z: No, Z_B: No
Phuket (n = 1248)	2749.05	1732.00	2403.93	2584.93	Z: No, Z_B: No
Ridgecrest (n = 4)	1.697	12.045	2.204	10.645	Z: Yes, Z_B: Yes

The point process we have worked with turns out to be simple in the sense that each earthquake is similar to the other once a magnitude threshold of say 6.7 is exceeded. In contrast, a marked point process may be employed where the time stamps would remain the same, but each earthquake would possess some distinguishing feature such as its Richter scale value, the amount of damage it inflicted, or anything that quantifies its enormity or seriousness. Finally, we have worked under a failure truncated setup, i.e., we follow the process till a given number of shocks is attained, regardless of how long it takes to go that far. Similar analyses may be carried out under the time truncated scenario too, where a process is observed over a predetermined time horizon, no matter how many observations occur over it. However, the process of earthquake genesis is deciphered using finite element analysis (Dutta and Mishra 2017).

References

Bhaduri, M., Ho, C.: On a temporal investigation of hurricane strength and frequency. J. Environ. Model. Assess. (2018)

Bhaduri, M., Zhan, J.: Using empirical recurrence rates ratio for time series data similarity. IEEE Access **6**, 30855–30864 (2018)

Dutta, P.K., Mishra, O.P.: Identification of collision mechanism at seismogenic fault interface using finite element analysis involving plate bending applications using ant colony optimization. J. Appl. Eng. Sci. (JAES) **7**(20), 15–20 (2017). https://doi.org/10.1515/jaes-2017-0002

Dutta, P.K., Naskar, M.K., Mishra, O.P.: Decision analysis for earthquake prediction methodologies: fuzzy inference algorithm for trust validation. Int. J. Comput. Appl. **45** (2012)

Dutta, P.K., Naskar, M.K., Mishra, O.P.: A Poisson process hidden Markov cellular automa model in earthquake genesis and conflict analysis: a physical approach. J. Seismol. Earthq. Eng. SS320 **14**(2), 81–90 (2013a)

Dutta, P.K., Mishra, O.P., Naskar, M.K.: Evaluation of seismogenesis behavior in Himalayan belt using data mining tools for forecasting. Cent. Eur. J. Geosci. (CEJG) **5**(2), 236–253 (2013b)

Harte, D.: PtProcess: an R package for modelling marked point processes indexed by time. J. Stat. Softw. **35**(8), 1–32 (2010)

Ho, C.-H.: Forward and backward tests for an abrupt change in the intensity of a Poisson process. J. Stat. Comput. Simul. **48**, 245–252 (1993)

Ho, C., Bhaduri, M.: On a novel approach to forecast sparse rare events: applications to Parkfield earthquake prediction. Nat. Hazards **78**(1), 669–679 (2015)

Ho, C., Bhaduri, M.: A quantitative insight into the dependence dynamics of the Kilauea and Mauna Loa volcanoes, Hawaii. Math. Geosci. **49**(7), 893–911 (2017)

Ho, C., Zhong, G., Cui, F., Bhaduri, M.: Modeling interaction between bank failure and size. J. Finance Bank Manage. **4**(1), 15–33 (2016)

Rigdon, S.E., Basu, A.P.: Statistical Methods for the Reliability of Repairable Systems. Wiley Series in Probability and Statistics. Wiley (2000)

Tan, S., Bhaduri, M., Ho, C.: A statistical model for long term forecasts of strong dust sand storms. J. Geosci. Environ. Prot. **2**, 16–26 (2014)

High-density Seismic Network for Monitoring Alentejo Region (Portugal) and Mitidja Basin Region (Algeria)

Marco Manso, Mourad Bezzeghoud, José Borges, Bento Caldeira, João Fontiela, and Abdelhakim Ayadi

Abstract

The seismic sensor network Alentejo (SSN-Alentejo) developed by the Earth Sciences Institute (*Instituto de Ciências da Terra*, University of Évora) brings the largest high-density seismic sensor network ever deployed in Portugal. This novel network aims to improve the characterization of seismic activity in the region, through a high-resolution mapping of seismic clusters and known faults. Over the next two years, SSN-Alentejo will deploy a monitoring network of 300 sensors, combining high-sensitive sensors with low-cost sensors. SSN-Alentejo augments existing sensing and monitoring capabilities, enabling the opportunity to observe, for the first time in Portuguese territory, live seismic activity in high resolution. Moreover, seismogenic zones such as the Mitidja or Chleff basins in Algeria will also benefit from having a high-density network.

Keywords

High-density seismic network • Seismic sensors • Seismology

M. Manso (✉) · M. Bezzeghoud · J. Borges · B. Caldeira · J. Fontiela
Instituto de Ciências da Terra, Universidade de Évora, Évora, Portugal
e-mail: marco@marcomanso.com

M. Bezzeghoud · J. Borges · B. Caldeira
Departamento de Física, Escola de Ciências e Tecnologia da Universidade de Évora, Évora, Portugal

A. Ayadi
Centre de Recherche en Astronomie Astrophysique et Géophysique, Algiers, Algeria

1 Introduction

Seismic events can be extreme and severe to humanity, causing a heavy death toll and serious destruction and damage. Being no exception, the Iberian Peninsula and the North of Africa (part of the Ibero-Maghrebian region between the Gulf of Cadiz and Algeria) share the Eurasian–Nubian plate boundary that corresponds to a well-defined narrow band of seismicity, where large earthquakes occur (Ousadou and Bezzeghoud 2019).

Helping to understand these phenomena, seismic networks have been deployed in increasing number, filling in gaps in the global coverage and improving our understanding of the physical processes that cause earthquakes. Portugal, in particular, has made a significant effort to develop the broadband Portuguese seismic network integrating seismological stations from various institutions supporting real-time monitoring of the earthquake activity (Caldeira et al. 2007). Between 2010 and 2012, the WILAS (West Iberia Lithosphere and Asthenosphere Structure) project integrated a temporary network of 20 sensors in the Portuguese national network resulting in a total of 55 stations spaced on average by 50 km. These stations continuously recorded measurements at frequencies up to 100 Hz, and thus gathering an unprecedented volume of high-quality data of densely distributed broadband stations that can be used to image the Earth's inner structure with unprecedented resolution (Palomeras et al. 2014). More recently, the Arraiolos seismic network (in Alentejo) was deployed comprising 14 broadband stations (CMG 6TD, 30 s) of the ICT (Institute of Earth Sciences, Évora) and temporarily extended with 21 short-period stations (CDJ, 2.0 Hz) of the IDL (Instituto Dom Luiz) within a 20 km radius (Wachilala et al. 2019).

Continuing the trend to increase seismic monitoring resolution by deploying more seismic stations, the United States deployed several very high-density seismic networks obtaining the capacity to generate high-resolution images. This methodology allowed displaying seismic wave

M. Meghraoui et al. (eds.), *Advances in Geophysics, Tectonics and Petroleum Geosciences*,
Advances in Science, Technology & Innovation, https://doi.org/10.1007/978-3-030-73026-0_41

propagations in space and time (i.e., dynamic shake maps): in 2001 and 2002, the California Institute of Technology (CalTech) deployed more than 5200 stations spaced by 100 m for the main purpose of better defining the Long Beach Oil Field (Inbal et al. 2015). In addition, CalTech's established the community seismic network (CSN), an earthquake monitoring system based on a dense array of low-cost acceleration sensors (more than 1000), aiming to produce block-by-block measurements of strong shaking during an earthquake (see http://csn.caltech.edu/about/). The University of Southern California's (USC) Quake Catcher Network (QCN) began rolling out in the San Francisco Bay Area comprising 6000 tiny sensors, being part of the densest networks of seismic sensors ever devoted to studying earthquakes in real time (Science 2.0 Homepage 2011).

High-density networks also present several challenges for the state-of-the-practice in seismology. According to Addair et al. (2014), the traditional techniques used in seismology use a processing paradigm that was developed in the 1980s when average computer processing power was a tiny fraction of what is commonly available now. The huge data volume generated by high-density networks demands for research on the application in seismology of data intensive processing techniques like big data and artificial intelligence (e.g., clustering, pattern-matching and correlation).

2 SSN-Alentejo: High-density Seismic Networks

In the last years, sensors and sensing network technology evolved at a strong fast pace, resulting in improved performance (resolution, bandwidth, sensitivity, dynamic range and data processing capacity), operation (energy efficiency, operation time) and connectivity (broadband communications), at a significant cost reduction. Low-cost microelectromechanical (MEM) accelerometers, in particular, demonstrated the capability to generate relevant data for seismic analysis in dense deployment contexts (Lainé and Mougenot 2014).

Inspired by successful study cases in United States as cited above, the seismic sensor network Alentejo (SSN-Alentejo) developed by the Earth Sciences Institute (*Instituto de Ciências da Terra*, University of Évora) brings the largest high-density seismic sensor network ever deployed in Portugal. This novel network aims to improve the characterization of seismic activity in the region through the development of high-resolution mapping of seismic clusters and known faults and the rapid assessment of ground shaking, and to improve geohazard assessments. Moreover, the high-density network will enable knowledge advances of the Earth's crustal and upper structure, as well as of earthquake rupture processes.

Over the next two years, SSN-Alentejo will deploy a monitoring network of 300 sensors to generate significant volumes of live data and advance seismology knowledge. The sensors will be distributed in a mesh configuration and covering an area of several square kilometers, with only hundreds of meters distancing each neighboring sensing node. The density proposed for the network abides to the findings of Clayton et al. (2011). Furthermore, as recommended by Evans et al. (2003), the project opts for a cost-effective network configuration, combining high-performing broadband stations and low-cost sensors.

Figure 1 shows an illustrative example for the SSN-Alentejo high-density network complementing the existing Arraiolos seismic network. As it can be visualized in figure, SSN-Alentejo brings a significant increase in the monitoring of seismic activity in the area of interest.

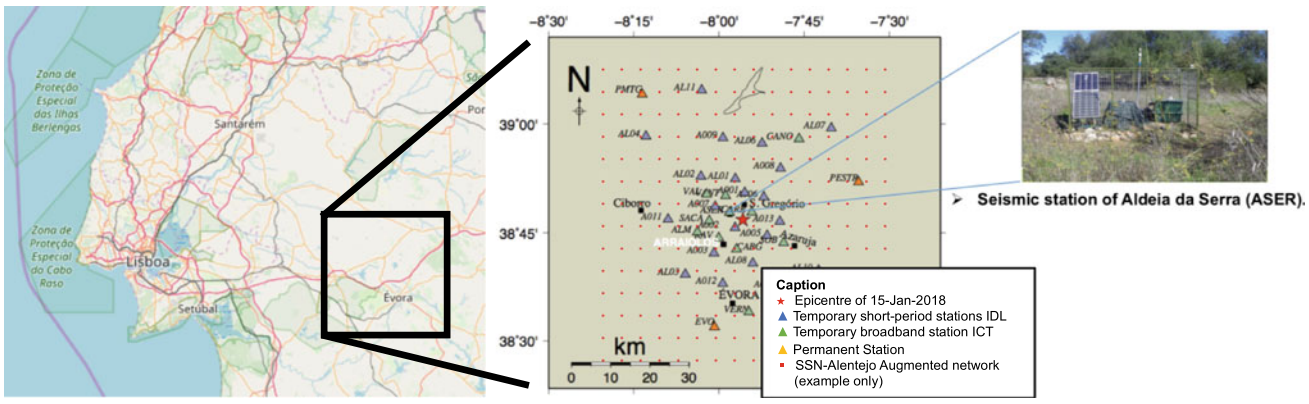

Fig. 1 SSN-Alentejo complementing the Arraiolos temporary seismic network (based on (Wachilala et al. 2019))

The developed prototypes demonstrated the feasibility of the sensor network that will now be deployed in real environment.

The following scientific advances are expected with SSN-Alentejo: (1) Enhancement of the knowledge on the characterization of the seismic activity in the region through high-resolution mapping of clusters and faults; (2) Creation of an organized database populated with live data from the high-density seismic network; (3) Rapid assessment of ground shaking movements (e.g., earthquake); (4) Improvement of geohazard assessments; (5) Application of novel computational-intensive techniques to the seismology domain and comparison of results with the traditional methods.

3 Conclusion

SSN-Alentejo represents a reinforcement of sensing and monitoring capabilities, enabling the opportunity to explore, for the first time in Portuguese territory, the high-resolution observation of seismic activity. It is also expected to significantly enhance the understanding of environmental risks associated with extreme phenomena.

SSN-Alentejo, and high-density seismic sensor networks in general, bring enormous potential to better understand seismogenic zones such as the Mitidja or Chleff basins in Algeria. It is our aim to explore a deployment resorting to our close relationship with several Algerian institutions such as the Algiers and Oran universities as well as some institutions such as CGS and CRAAG.

Acknowledgements The SSN-Alentejo project is funded by the Science Foundation of Portugal (FCT) under grant number ALT20-03-0145- FEDER-031260.

References

Addair, T.G., Dodge, D.A., Walter, W.R., Ruppert, S.D.: Large-scale seismic signal analysis with Hadoop. Comput. Geosci. **66**, 145–154 (2014)

Caldeira, B., Carrilho, F., Miranda, M., Bezzeghoud, M., Alves, P.M., Silveira, G., Villalonga, F., Pena, J.A., Matias, L., Borges, J.F., Vales, D., Corela, C., Madureira, G.: Recent improvements in the Broadband seismic networks in Portugal. EMSC Newslett. Spec. Iss. **22**, 18–19 (2007)

Clayton, R.W., Heaton, T., Chandy, M., Krause, A., Kohler, M., Bunn, J., Guy, R., Olson, M., Faulkner, M., Cheng, M., Strand, L., Chandy, R., Obenshain, D., Liu, A., Aivazis, M.: Community Seismic Network. Ann. Geophys. **54**, 6 (2011)

Evans, J.R., Hamstra, R.H., Spudich, P. Jr., Kündig, C., Camina, P., Rogers, J.A. TREMOR: A Wireless, MEMS Accelerograph for Dense Arrays. U.S. Department of the Interior, U.S. Geological Survey. Open-file Report 03–159 (2003)

Inbal, A., Clayton, R., Ampuero, J.: Imaging widespread seismicity at midlower crustal depths beneath Long Beach, CA, with a dense seismic array: Evidence for a depth-dependent earthquake size distribution. Geophys. Res. Lett. **42**(15), 6314–6323 (2015)

Lainé, J., Mougenot, D.: A High-Sensitivity MEMS-Based Accelerometer. The Leading Edge. November 2014. Special Section: Sensor technology and nanotechnology. https://doi.org/10.1190/tle33111234

Ousadou, F., Bezzeghoud, M.: Seismicity of the Algerian Tell Atlas and the impacts of major earthquakes. In: Bendaoud, A. et al. (Eds.) The geology of the Arab world—an overview, Springer Geology, pp. 401–426 (2019)

Palomeras, I., Thurner, S., Levander, A., Liu, K., Villasenor, A., Carbonell, R., Harnafi, M.: Finite-frequency Rayleigh wave tomography of the western Mediterranean: mapping its lithospheric structure. Geochem. Geophys. Geosyst. **15**(1), 140–160 (2014)

Science 2.0 Homepage.: Quake Catcher Network—Citizen Science Tackles Seismology (2011). http://www.science20.com/news_articles/quake_catcher_network_citizen_science_tackles_seismology-80887, Last accessed 28 July 2019

Wachilala, P., Borges, J., Caldeira, B., Matias, L., Rio, I., Bezzeghoud, M.: Characterization of the Region of Arraiolos, South Portugal—Period of January—May 2018. Ass. IUGG 2019, Montreal, Canada (2019)

Seismic Sources and Their Statistics: An Application to Kachchh Rift Basin (India)

Sandeep Kumar Aggarwal and Prosanta Kumar Khan

Abstract

Kachchh Rift Basin (KRB) is India's highest seismically active region after the Himalaya, having 2727 events of $M_c \geq 3$ with a homogenous catalog from 2002 to 2012. These events are statistically analyzed to assess the seismic potential in KRB. The Narmada Dam Seismic Network works steadily since 1980s, and its phase data were used to assess the homogeneity and completeness. The seismicity is analyzed statistically for a, *b*, p, z and D values. The magnitude and the time histogram depict the distribution of activity. The cumulative seismic magnitudes and moment release with time depict the seismicity in the region and can be characterized of epidemic type. The space/time clustering obeys the epidemic-type model, and z-value significant level ~ 50% occurs before $M_w \geq 5$ mainshock. The decay rate $p = 0.75$ describes slow decaying, and the activity rate $a = 6$ implies that the seismicity will continue for a long time in the future. The study region is divided into 25 grid cells of dimension $0.2° \times 0.2°$ each, with overlapping window of 0.1°. Fractal dimension (D) and *b*-value of each grid cell are computed, and contour maps are prepared. The estimated fractal dimension varies from 0.45 to 1.93, whereas *b*-value varies from 0.71 to 1.31. The results show a higher fractal dimension and *b*-value along the KMF, Wagad faults and lower corresponds to the Gedi fault. The *b*-value, fractal dimension D distribution and Aki's D/b ratio across the Kachchh region imply significant differences in the rate of deformation along the Wagad and Gedi faults, and hence implicate toward relative hazard assessment.

Keywords

Kachchh • Seismicity • Fractal dimension • *b*-value • Correlation

1 Introduction

Statistics of any time series has the ability to describe complex natural processes with scale invariant property. Tectonic processes, such as folding, faulting as extreme complex process, satisfy the fractal statistics. Fractals in seismicity have the capability to characterize that self-similarity. The fractal dimension (D) characterizes the degree to which earthquake phenomenon follows with respect to space, time and magnitude (Legrand 2002) and is often correlated with the slope-b of the Gutenberg-Richter law, independently of the size of an earthquake. Similarly, the Gutenberg and Richter (1956) relation for frequency versus magnitude is a power law involving magnitude. In this, the aftershock decay follows another power law involving time. Hence, earthquakes are represented by self-similar mathematical construct. Fractal dimension gives vital information about the stability of a region. Hence, the scale invariant is an efficient statistical parameter to quantify the dimensional distribution of seismicity with proportion of randomness and clusterization. In this study, an attempt has been made to map the spatial distribution of fractal dimension (D) and *b*-value in Kachchh region, Gujarat, India, which is one of the most seismically active regions in the world.

The seismicity in the approximately 200 × 200 km wide Kachchh region having salt plains and sedimentary basin in the north (called Rann) and high lands (called uplift) in the south with intervening grassland (called Banni plains) basically originates from a single seismogenic zone whose master fault is the Kachchh Mainland Fault (KMF) and other faults such as Nagar-Parkar (NPF), Wagad, Island belt and

S. K. Aggarwal (✉) · P. K. Khan
Indian Institute of Technology (ISM), Dhanbad, India

S. K. Aggarwal
Institute of Seismological Research, Gandhinagar, India

M. Meghraoui et al. (eds.), *Advances in Geophysics, Tectonics and Petroleum Geosciences*,
Advances in Science, Technology & Innovation, https://doi.org/10.1007/978-3-030-73026-0_42

Katiawar are interacting with each other to report to principal fault as KMF. The rocks in the region of the highest epicenters concentration (Fig. 1) are of Mesozoic (135–65 Ma) and younger, Cenozoic, age; overlying a granite basement (Biswas, 1987). The (60–65 Ma) Deccan volcanic formation is exposed in southern Kachchh. The KRB started being formed 135 Ma ago, at the time of the breakup of Gondwanaland and lies between two extensional faults, i.e., the south-dipping NPF and the north-dipping Kathiawar fault in the south (Fig. 1). The subsurface N-S basement ridge-Median high as KMF crosses the basin. Acting as a hinge, it divides the basin into a deeper western part and a shallower more tectonized eastern part. During the late Cretaceous pre-collision stage of the Indian plate, these major faults acted as thrust faults, although later on, due to plate movement induced horizontal stress, they presented strike-slip movement. The right-lateral slip shifted the uplifts eastward with respect to Kachchh mainland, and in this sense, KRB is an incomplete diffused rift basin. Igneous plutons have extensively intruded in Mesozoic sediments during rifting and post-rift hotspot-related Deccan volcanism occurred. Studies on intrusive bodies and seismological data of Mandal et al. (2006) suggest the presence of an ultramafic magmatic body in the 2001 epicentral zone (Fig. 1). The present compressive stage of KMF sets it as principle active fault in the study area.

The 2001 Bhuj earthquake of M_w 7.7 is supposed to have activated blindly the North Wagad Fault adjacent to KMF as a main constituent and right laterally uplifted the eastern margin of KMF. Subsequently, a mainshock of M_w 5.7 was triggered on Gedi Fault during 2006 (Fig. 1), and this region is supposed to be the most active and hazardous due to its shallow seismicity and weak rheological strength in the area of KRB. We analyze *b*-value and D-value on these active faults.

2 Data and Analysis

KRB hosted an earthquake of M_w 7.7 on the 26th of January 2001, which was scarcely recorded at close distances but well recorded by analog NDSN telemetry. We used the phase data of Narmada Dam Seismic Network (NDSN) to compile the homogeneous and magnitude complete (M_c 3) catalog of the sequence for the period 2002–2012 and plotted the amount of data as a function of magnitude (Fig. 2a) and time (Fig. 2b). The fractal dimension (D) is mapped for a degree of clustering in space of 0.2° × 0.2° wide cells, with an overlap of 0.1°. This attempt generated 25 grid cells (Fig. 2c). The grid cells that include less than 50 events (G4, G8, G9, G10, G11, G12, G14, G15, G16, G17, G15, G22 and G25) have been discarded, and only grid cells containing 50–258 events were considered for subsequent analysis.

The widely used correlation dimension $D_{wr} = \lim_{r \to 0} \frac{\log(C_r)}{\log(r)}$ of Grassberger and Procaccia (1983) is applied to analyze the spatial distribution of the studied seismicity. The Gutenberg-Richter (G-R) magnitude-frequency relationship,

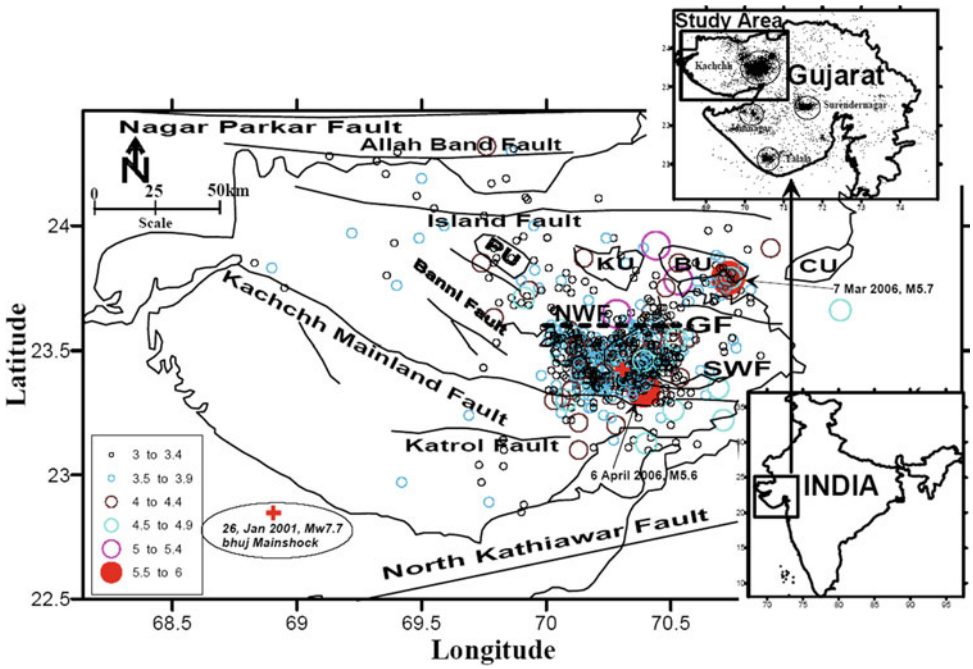

Fig. 1 Seismicity and tectonic settings in KRB with sublet of Gujarat and India (after Aggarwal et. al. 2015)

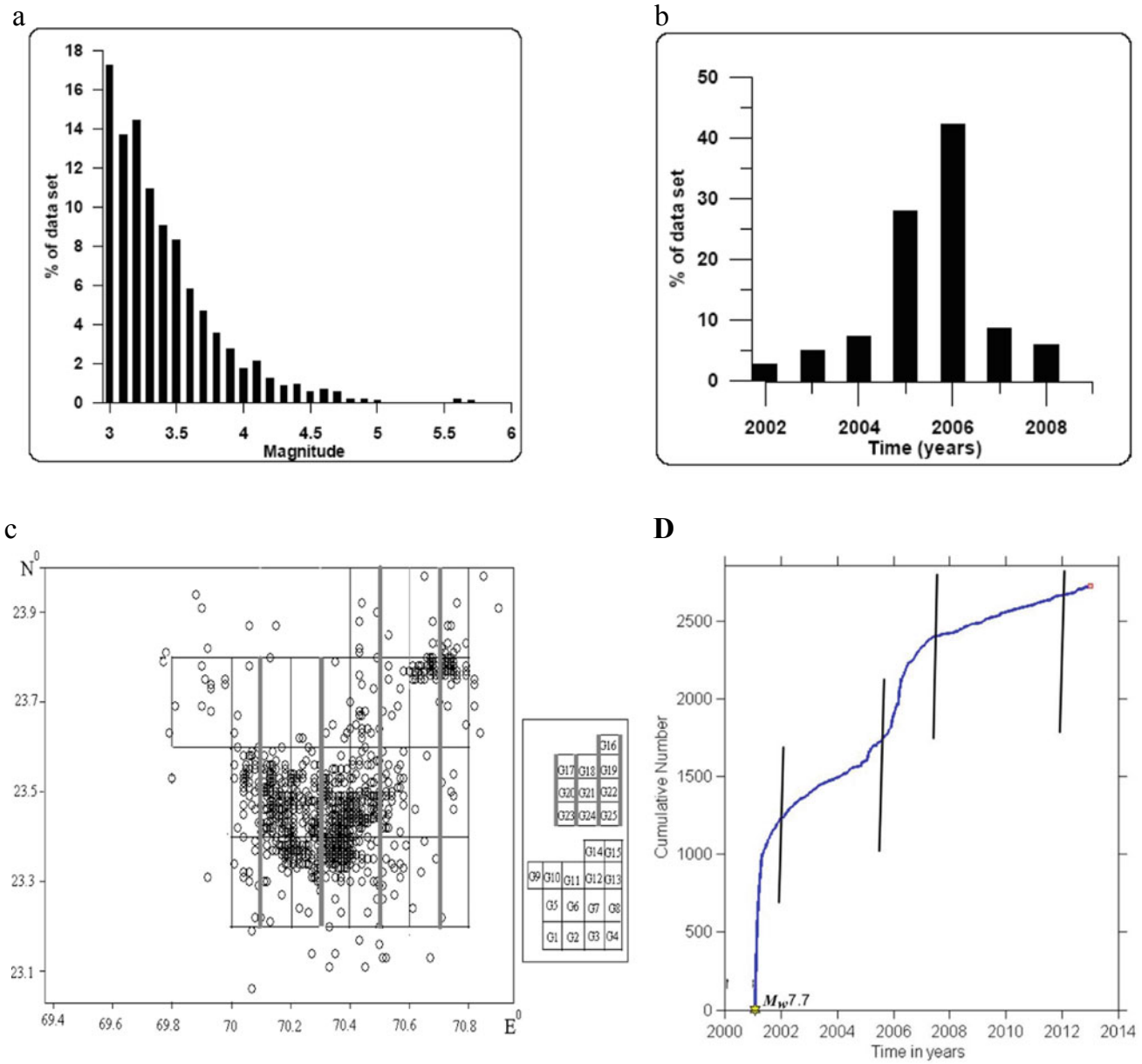

Fig. 2 Distribution of Kachchh seismicity in **a** Magnitude bins **b** Time and **c** Space. **d** *Z*-value graph for KRB seismicity rate for $M_c \geq 3$

log $N = a - b$M, which exhibits scale invariability applied and maximum likelihood function, is used to estimate *b*-values. To analyze the seismicity rate with time, the *Z*-value graph (Habermann 1983) is evaluated. The analysis of *Z*-values (Fig. 2d) shows that after the 2001 M_w 7.7 Bhuj earthquake, there is a lowering in the rate of seismicity for a period of 3–4 years. But again in 2006, seismicity increases during the M_w 5.7 event on the Gedi fault. This cycling of the seismicity rate presents a repetition time of three to four years, including an earthquake of $M_w \geq 5.0$.

3 Results and Discussion

The fractal dimension D, ranging between 0 and 2 (Tosi 1998), illustrates the possible information in embedded space (Fig. 2c). A value close to 0 indicates events clustered in space at a shallow depth, whereas values close to 2 indicate events that are distributed randomly in space. Idziak and Teper (1996) suggested that D $\sim$ 2 is an evidence of multiple external forces acting on a tectonic regime. The

fractal dimension D in KRB seismic sequence implies a similar behavior with average fractal dimension D = 1.42 (Fig. 3a). The slope of the Gutenberg-Richter relation (*b*-value; Fig. 3b) appears self-similar and obeys the power law. The *b*- and D-values are often positively correlated, independently of the earthquake size. We find a positive correlation between *b*- and D-values in most of the examined grid cells covering KRB (Fig. 3c). This implies the absence of a characteristic event size. Throughout the examined cells, the *b*-value ranges from 0.7 to 1.2, and the D value ranges from 0.45 to 1.95 depending on the tectonic setting in different parts of the KRB active region. Higher *b*-values are attributed to higher degree of heterogeneity, and lower *b*-values are attributed to increased rheological strength in the crust. The average *b*-value of the study region is 1.02, which is higher in comparison to that of the Peninsular India (0.54); also, indicating that Kachchh is a more active seismic regime. The simple relationship between the b-value and the fractal dimension with a positive correlation $D = 3b/c$ (where c is the slope of the relation between the logarithm of seismic moment versus magnitude and is about 1.5) has been used in the text. In general, both positive (Legrand 2002) and negative (Wang and Lee 1996) correlations between these two scaling exponents have been reported. In some cases (Mandal et al. 2005), the correlation could even change from a negative one to a positive one. Our results support Aki's relation ($D = 3b/c$), which could be attributed to a single fracturing process and its related aftermath.

The temporal distribution of aftershocks widely accepted to follow the law: $N = K/(1 + t)^p$ (N is the decay of the number of aftershocks with time t after the mainshock, p is the decay rate and K is a constant) (Fig. 3d) defines the KRB sequence decay rate as slow with $p = 0.75$, while the activity rate is estimated at $a = 6$ implying that the sequence will continue for a long time in the future. The cumulative seismic moment (dyn * cm) release (Fig. 3e) shows a two-step evolution: one in 2001, corresponding to the Bhuj mainshock of M_w 7.7 near Wagad area and a second one in 2006, corresponding to the M_w 5.7 event near Gedi area. The space/time clustering appears to obey the epidemic-type aftershock model. The earthquakes' cumulative number plot (Fig. 3f) shows three changes in slope in years 2003, 2006 and 2009, i.e., every three to four years, also indicating that the epidemic-type aftershock model works in KRB.

Since the seismicity in the KRB region is dynamic in terms of space, time and magnitude (Aggarwal et al. 2015, 2017; Telesca et al. 2015, 2016), its related statistical parameters such as b and D are also dynamic and present near similar behavior with corresponding parameters in different parts of the world (Tuncay et al. 1991; Serken 2012; Kumar et al. 2013). The 2001 Bhuj earthquake occurred in the KMF and Wagad regions (G1, G2, G3, G5, G6, G7, G20, G21, G23, G24) and the 2006 earthquake in Gedi region (G13, G19). The faults in KRB are constituent of Kachchh mainland region in terms of a unique chamber of stress field and interact with each other in terms of seismicity distribution. This feature can be clearly seen in terms of variation in *b*- and D-values graphs (Fig. 3c) and maps (Fig. 3g, 3h). In 0.2° mapping, the higher D contours are most prominent along the KMF and Wagad area, whereas lower D contours are most prominent along Gedi area. The *b*-value map (Fig. 3g) clearly depicts the spatial variation of earthquake frequency in the region, showing a higher *b*-value contours in the KMF and Wagad region and lower value contours in Gedi region. The higher b-value contours are comparable with the higher fractal dimension D contours. The high *b*-value obtained in the present study could be associated with the relaxation state of the medium in KMF and Wagad in comparison to low *b*-value in Gedi region. The *b*-value and the fractal dimension mapping in KRB also clearly identify the seismogenic structures along the KMF and Gedi area.

4 Conclusions

The high *b*-value in grid cells G5, G6, G7 on KMF and Wagad faults means that the region has lost its strength of producing large magnitude earthquakes, although small shocks are going to occur regularly. However, low *b*-values at G19, G20, G21 and extreme lowest at G13 imply the potential for the area of producing large magnitude earthquakes on the recently activated Gedi faults system. The fractal dimension D's analysis with the lowest dip confirms this argument. This zone is also inferred to be a fluid-filled heterogeneous rock mass with high-density fractures (Mandal et al. 2006) and according to Hirata (1989) if $D \sim 1.6$ is an upper limit to the fractal dimension of the fracture geometry that can be explained by the Griffith (1921) energy balance concept. The estimated fractal dimensions range from 0.45 to 1.94, and thus, this study suggests that active faults are spatially distributed in the whole region and interacting with each other. Higher fractal dimension (1.6–1.9) is estimated along the east–west direction on Wagad faults in Wagad region, indicating higher heterogeneity, possibly due to the highly fractured maffic plutonic body. Low fractal dimension (0.45) in Gedi faults system favors a super-strength region capable to produce the next big earthquake.

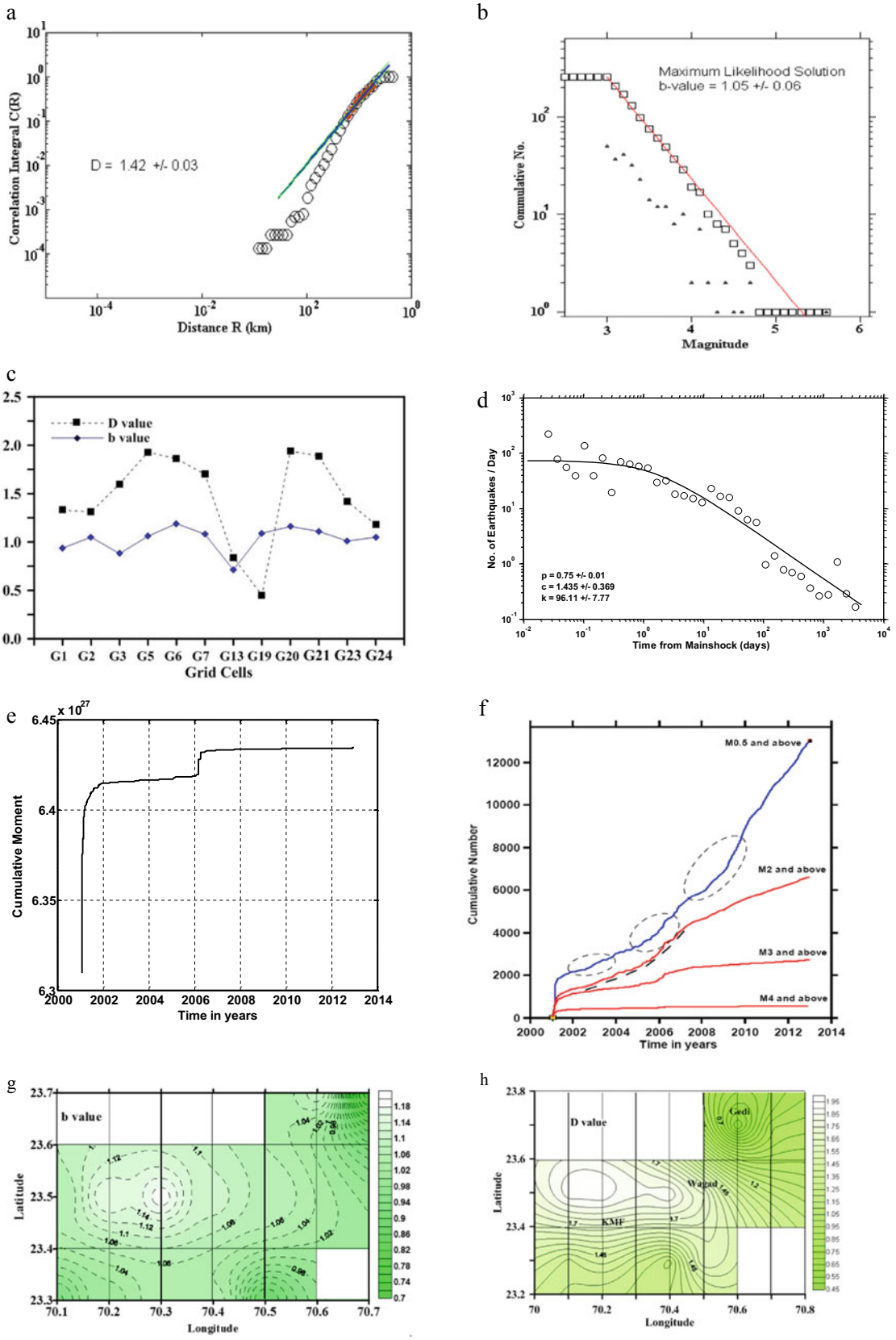

Fig. 3 Results for **a** Map of fractal dimension D **b** Mean *b*-value of the entire study region (black triangle shows the number of events for each magnitude) **c** Fractal dimension D and *b*-value in each grid cell (see Fig. 2c for grid cell coding) **d** Seismicity decay **e** Cumulative moment (dyn * cm) release **f** Cumulative number of earthquakes with time **g** Map of *b*-value for entire space **h** Map of fractal dimension D for entire space

References

Aggarwal, S.K., Lovallo, M., Khan, P.K., Rastogi, B.K., Luciano T.: Multifractal detrended fluctuation analysis of magnitude series of seismicity of Kachchh region, Western India. Physica A **426**, 56–62 (2015)

Aggarwal, S.K., Pasten, D., Khan, P.K.: Multifractal analysis of 2001 Mw7.7 Bhuj earthquake sequence in Gujarat, Western India. Physica A. **488**, 177–186 (2017)

Biswas, S.K.: Regional framework, structure and evolution of the western marginal basins of India. Tectonophysics **135**, 302–327 (1987)

Grasseberger, P., Procaccia, I.: Measuring the strangeness of strange attractors. Physica D **9**, 189–208 (1983)

Griffith, A.A.: The phenomena of rupture and flow in solids. Philos. Trans. R. Soc. Lond. **221**, 163–198 (1921)

Gutenberg, B., Richter, C.F.: Earthquake magnitude, intensity, energy and acceleration. Bull. Seismol. Soc. Am. **46**(2), 105–145 (1956)

Hirata, T.: A Correlation Between the b- value and the fractal dimension of earthquakes. J. Geophys. Res. **94**, 7507–7514 (1989)

Habermann, R.E.: Teleseismic detection in the Aleutian Island Arc. J. Geophys. Res **88**(B6), 5056–5064 (1983)

Idziak, A., Teper, T.: Fractal dimension of faults network in the upper Silesian coal basin Poland: Preliminary studies. Pure and Appl. Geophys. **147**, 239–247 (1996)

Kumar, A., Rai, S.S., Joshi, A., Mittal, H., Sachdeva, R., Kumar, R., Ghangas, V.: The b value and fractal dimension of local seismicity around Koyna dam (India). Earthq. Sci. **26**(2), (2013)

Legrand, D.: Fractal dimensions of small, intermediate, and large earthquakes. Bull. Seismol. Soc. Am. **92**(8), 3318–3320 (2002)

Mandal, P.: Sedimentary and crustal structure beneath Kachchh and Saurashtra regions Gujarat, India. Phys. Earth Planet. Int. **155**, 286e299 (2006)

Mandal, P., Mabawonku, A.O., Dimri, V.P.: Self-organized fractal seismicity of reservoir triggered earthquakes in the Koyna-Warna seismic zone, western India. Pure Appl. Geophys. **162**, 73–90 (2005)

Serken, O.: Statistical correlation between b-value and fractal dimension regarding Turkish epicentre distribution. Earth Sci. Res. J. **16** (2), (2012).

Telesca, L., Lovallo, M., Aggarwal, S.K., Khan, P.K.: Precursory signature in the visibility graph analysis of seismicity: An application to the Kachchh (Western India) seismicity. Phys. Chem. Earth, Parts A/b/c **85**, 195–200 (2015)

Telesca, L., Lovallo, M., Aggarwal, S.K., Khan, P.K.: Visibility graph analysis of the 2003–2012 earthquake sequence in the Kachchh region of western India. Pure Appl. Geophys. **173**(1), 125–132 (2016)

Tosi, P.: Seismogenic structure behaviour revealed by spatial clustering of seismicity in the Umbria-Marche region (Central Italy). Ann.De Geofisica **41**(2), 215–224 (1998)

Tuncay, T., Jackson, J., McKenzie, D.: Active tectonics of the north and central Aegean Sea. Geophys. J. Int. **106**(2), 433–490 (1991)

Wang, J.H., Lee, C.W.: Multifractal measures of earthquakes in west Taiwan. Pure Appl. Geophys. **146**, 131–145 (1996)

Source and Path Characteristics of Chamoli Region, India

Neetu Goswami, S. C. Gupta, Ashwani Kumar, and M. L. Sharma

Abstract

The digital time histories of 149 local earthquakes ($0.6 \leq M_L \leq 5.1$) that occurred in Chamoli region of the Garhwal Himalaya, recorded by a 12-station digital telemetry seismological network around Tehri region, have been analyzed to estimate source parameters using Brune's (1970) point source circular model (Brune, J Geophys Res 75:4997–5009, 1970) and path characteristics by estimating the quality factor, Q_c, applying the single back scattering model given by Aki and Chouet (J Geophys Res 80(23):3322–3342, 1975). Two data sets composed of 86 local earthquakes (data set 1) in the magnitude range ($0.6 \leq M_L \leq 3.3$) recorded during the period from January 2009 to December 2014, and 63 local earthquakes (data set 2) ($0.7 \leq M_L \leq 5.1$) recorded during the period from January 2017 to December 2017 have been analyzed. The source parameters viz., seismic moment, source radii, stress drop, and moment magnitude are computed from the displacement spectra of SH component of S-wave, whereas the quality factor, Q_c, is estimated from the coda waves of 30 s of vertical component. The source parameters are estimated as 1.2×10^{11} to 7.9×10^{13} Nm, 132 and 317 m, 0.05–42.9 bars, and 1.4–3.2, respectively, for the cluster 1 and from 2.5×10^{11} to 2.1×10^{15} Nm, 45.7 and 365 m, and 0.234–663.5 bars, 1.5–4.2, respectively, for the cluster 2. Besides that, the high stress drops have been observed for two small size earthquakes, 660 bars ($M_w \sim 5.1$) and 663 bars ($M_w \sim 4.7$). The frequency dependent average attenuation relationship $Q_c = 137f^{0.87}$ has been obtained for the region using both the data sets.

Keywords

The Garhwal Himalaya • Brune's model • Seismic moment • Stress drop • Single backscattering model

1 Introduction

According to New Global Tectonics, the origin of the Himalayan mountain belt is considered due to continental collision among the Indian and Eurasian tectonic plates (Seeber and Armbuster 1981; Khattri 1987). Recently, a number of moderate to large-sized earthquakes have occurred in the part of Himalaya region, namely the April 25, 2015, Gorkha earthquake ($M_w = 7.8$) and May 12, 2015, Kodari earthquake ($M_w = 7.3$) in central Nepal occurred in the region.

The Chamoli region of the Garhwal Himalaya in Uttarakhand state of India, the area of present study, is located in the N–W part of the Himalaya. The region lies in seismic zone V, the highest seismic zone, as per the seismic zoning map of India (IS 1893 (Part 1): 2002). The frequent occurrence of moderate to large-sized earthquakes in this region of the Garhwal Himalaya has led us to study the source and path characteristics of local seismicity in the region. The seismogenic potential of the region is well understood due to occurrence of the March 29, 1999, Chamoli earthquake ($M_w = 6.8$).

The three component digital time histories of 149 local earthquakes, recorded at the sampling rate of 100 samples/s by the triaxial short-period seismometer (CMG 40 T-1) and the data acquisition system (DAS 130-01/03) for data set 1 and data set 2, have been analyzed (Fig. 1).

N. Goswami · S. C. Gupta (✉) · A. Kumar · M. L. Sharma
IIT Roorkee, Roorkee, Uttarakhand, India

M. Meghraoui et al. (eds.), *Advances in Geophysics, Tectonics and Petroleum Geosciences*,
Advances in Science, Technology & Innovation, https://doi.org/10.1007/978-3-030-73026-0_43

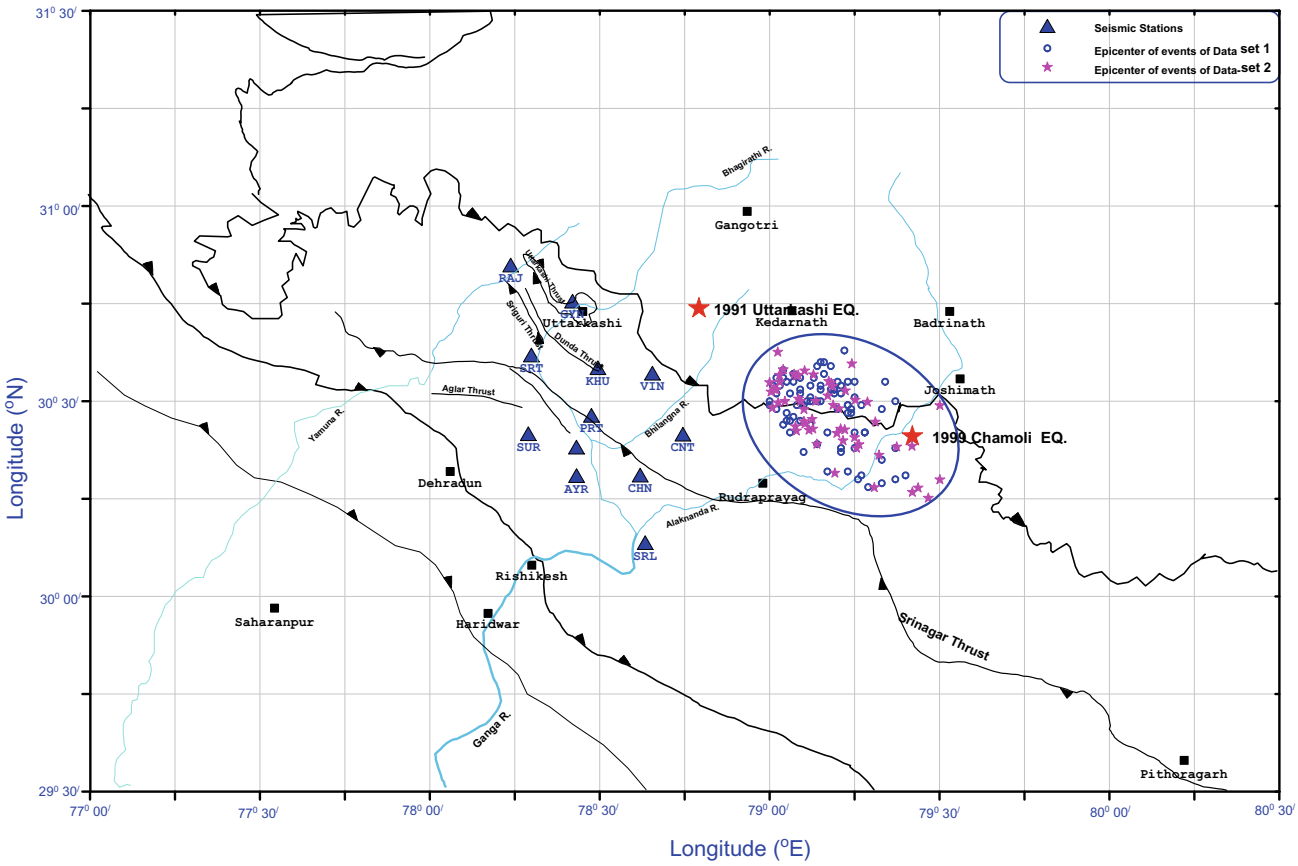

Fig. 1 Epicenters of local earthquakes of data set 1 and data set 2, along with 12-station local seismological network. Tectonic features after Geological Survey of India (GSI, 2000)

2 Methods

In order to estimate the source parameters of local earthquakes, the digital time history of transverse component of S-wave, i.e., SH-wave has been used to obtain the displacement spectra of local earthquakes employing Brune's circular source model (Brune, 1970) using mathematical expressions: seismic moment, $M_o = 4\pi\rho\beta^3 R\Omega/R_{\theta\Phi}S_a$ (Nm), source radius, $r = 2.34\beta/2\pi f_c$ (m), and stress drop, $\Delta\sigma = 7\ M_o/16\ r^3$ (bars).

To estimate the quality factor of coda waves Q_c, the single backscattering model (Aki and Chouet 1975) has been used. Steps for computation of Q_c at different frequencies are discussed by many authors, e.g., (Gupta et al. 1995; Jain et al. 2015). To apply near surface attenuation correction, the best fit regression line showing variation of Kappa with distance developed for the region by Sen (2016) as, $\kappa = (0.000153 \pm 0.000038)R + (0.0188 \pm 0.0042)$, has been used for the study.

3 Results

The following results have been obtained on the estimation of source parameters and quality factor (Table 1).

Table 1 Estimation of source parameters and quality factor for both data sets

Parameter	Data set 1	Data set 2
Seismic moment	1.2×10^{11}–7.9×10^{13} Nm	$2.5 \times 10^{11} - 2.5 \times 10^{15}$ Nm
Source radius	132–317 m	45.7–365 m
Stress drop	0.05–42.9 bars	0.2 bars to 149.4 bars
Moment magnitude	1.4–3.2	1.5–4.2
Quality factor	$Q_c = 137f^{0.87}$	

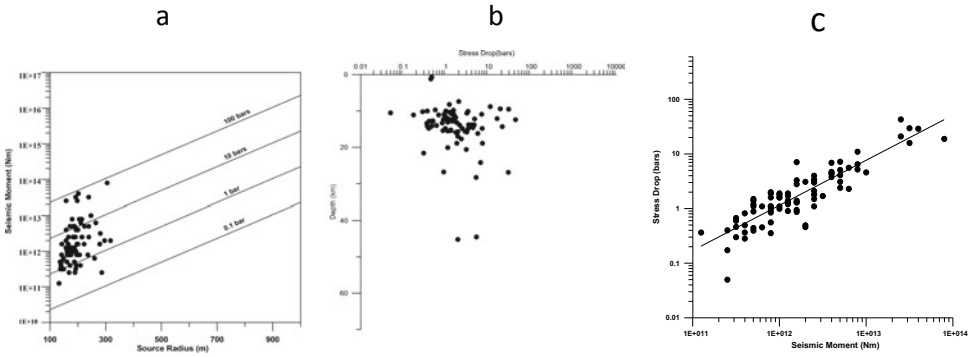

Fig. 2 Plots of seismic moment and source radius (**a**), stress drop and focal depth (**b**), and stress drop and seismic moment (**c**) for data set 1

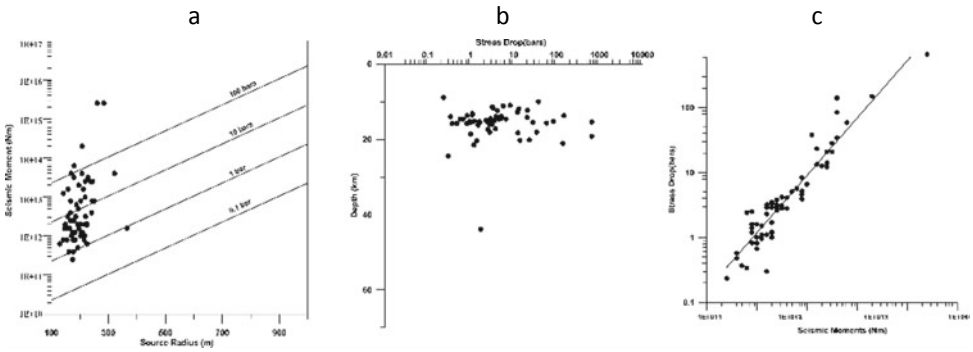

Fig. 3 Plots of seismic moment and source radius (**a**), stress drop and focal depth (**b**), and stress drop and seismic moment (**c**) for data set 2

4 Discussion

Out of 86 local events of data set 1, we have observed that the majority of events fall in stress drop range from 1 to 10 bars. Only 10 events showed stress drops range between 10 and 100 bars, which clearly depicts the seismic potential of the region Fig. 2a. The plot between stress drop and focal depth, Fig. 2b, shows that the majority of events occurred in between 1.2 to 20.6 km. The trend of earthquakes depicts the presence of active seismic fault in the region. Only six events fall between the focal depth range of 20 and 30 km, whereas only two events occurred in a depth range between 40 and 50 km. The plot between stress drop and seismic moment, Fig. 2c, shows a linear increasing trend. The empirical relation between stress drop and seismic moment is obtained as $\Delta\sigma = 2.09 \times 10^{-23} M_o^{0.82}$.

The result of data set 2 is present in Fig. 3. Out of 63 local events, almost half of the events fall in stress range between 1 and 10 bars, Fig. 3a. Only one event has stress drop below 1 bar, and a total of three events have stress drop values above 10 bars, as it has been observed. Two of the events, Rudraprayag earthquake February 06, 2017, (~5.1 mag) and Rudraprayag earthquake December 06, 2017, (~4.7 mag) show exceptional higher stress drop values, i.e., 660 bars and 663 bars, respectively.

The plot between stress drop and focal depth, Fig. 3b, shows that the majority of events occurred in between 8.9 and 20.4 km. The trend of earthquakes depicts the presence of active seismic fault in the region. Only three events fall in the focal depth range 20 and 25 km, and only one event occurred at a focal depth of 43.9 km. The plot shows a horizontally scattered pattern. The plot between stress drop and seismic moment, Fig. 3c, shows a linear increasing trend. The empirical relation between stress drop and seismic moment is obtained a $\Delta\sigma = 5.7 \times 10^{-25} M_o^{0.80}$.

5 Conclusions

The trend of stress drop shows that the majority of events have found low stress drop for both data sets. The high stress drops have been obtained only for two earthquakes that occurred on February 06, 2017, (~5.1 mag) and December 06, 2017 (~4.7 mag.), i.e., 660 and 663 bars, respectively.

Low stress drop observed in the present study is similar to low stress drop obtained in the part of Himalaya (Sharma and Wason 1994).

The linear trend has been observed between stress drop and seismic moment for both data sets.

The frequency dependent Q_c relation, $Q_c = 137f^{0.87}$, shows that the region is heterogeneous and seismically active.

References

Aki, K., Chouet, B.: Origin of coda waves: source, attenuation, and scattering effects. J. Geophys. Res. **80**(23), 3322–3342 (1975)

Brune, J.N.: Tectonic stress and the spectra of seismic shear waves from earthquake. J. Geophys. Res. **75**, 4997–5009 (1970)

Geological Survey of India (GSI): In: Narula, P.L., Acharya, S.K., Banerjee, J. (eds.) Seismotectonic Atlas of India and its environs. Geol. Surv. India, Sp. Pub., p. 86 (2000)

Gupta, S.C., Singh, V.N., Kumar, A.: Attenuation of coda waves in the Garhwal Himalaya, India. Phys. Earth Planet. Inter. **87**(3–4), 247–253 (1995)

Jain, S.K., Gupta, S.K., Kumar, A.: Attenuation of coda waves in Garhwal Lesser Himalaya. J. Seismol. **19**, 355–369 (2015)

Khattri, K.N.: Great earthquakes, seismicity gaps and potential for earthquake disaster along the Himalaya plate boundary. Tectonophysics, **138**(1), 79–92 (1987)

Seeber, L., Armbuster, J.G.: Great detachment earthquakes along the Himalayan arc and long term forecasts. In Simpson, D.W., Richards, P.G. (eds.) Earthquake prediction: an international review. Maurice Ewing series 4, Am. Geophys. Union, Washington, pp. 259–279 (1981)

Sen, A.: Seismotectonics of main frontal thrust and Indo-Gangetic plains around Roorkee, a Ph.D. Thesis, IIT Roorkee, p. 192, (2016)

Sharma, M.L., Wason, H.R.: Occurrence of low stress drop earthquakes in the Garhwal Himalaya region. Phys. Earth Planet. Interiors **85**(3–4), 265–272 (1994)

Seismic Hazard and Risk

Earthquake Early Warning Systems: Methodologies, Strategies, and Future Challenges

Gaetano Festa, Aldo Zollo, Matteo Picozzi, Simona Colombelli, Luca Elia, and Alessandro Caruso

Abstract

Earthquake early warning systems are able to issue an alert just after the start of the seismic rupture on the fault plane, but before the ground shaking reaches the sites to be protected. The available lead-time for security actions is very short (seconds to several dozens of seconds), requiring fast and robust methods to make these systems operational. Here, general principles about the two paradigms of early warning systems are presented: the regional and the on-site systems. When these methods are applied to data recorded by very dense networks, such as in near-fault observatories, the blind zone can be shortened to 15–25 km. Next generation of early warning systems should reduce the epistemic variability by implementing modeling of finite-source and site effects. Finally, the combination of on-site and regional systems may lead to a real-time estimation of the ground-shaking maps, overcoming the problem of computing the event location, and magnitude.

Keywords

Earthquake early warning • Source parameters • Event location • Real-time risk reduction

1 Introduction

Earthquake early warning systems (EEWSs) are real-time systems that analyze the radiation emitted by a propagating rupture and predict the incoming ground shaking at target sites to be protected. The issued warning can be then used to pilot security actions for people, lifelines, and machineries. EEWSs analyze the P waveform as it is recorded by a seismic network and forecast the following shaking associated with S or surface waves. An important parameter in EEWSs is the lead-time; the time available for triggering security actions, which depends on the distance between the event source and the site to protect. The higher the lead-time, the better the success rate of an EEWS.

EEWSs are usually classified in two paradigms: regional and on-site systems. A regional system records the P (and sometimes the early S) wave at a dense network surrounding the faults that can potentially generate a large earthquake in the area. They provide an event detection, location, and magnitude estimation. These parameters are later used to predict the ground motion at farther sites through Ground Motion Prediction Equations (GMPEs) (Allen and Kanamori 2003; Zollo et al. 2006).

In regional systems, there is no time available for security actions in a wide area around the event's epicenter: the corresponding blind zone, whose size depends on geometrical and technological parameters, can be as large as 30 km for dense networks in near-fault observatories (Satriano et al. 2011). Nevertheless, several regional EEWSs are operational or under testing worldwide (e.g., in Romania, United States, Mexico, Taiwan, and Japan for operation and Italy, Switzerland, India, Israel, and Spain for testing).

On-site systems are based on one or more seismic sensors installed at the same site where the warning is issued. These systems process the early portion of P-wave signals and forecast the following shaking owing to S and surface waves through empirical amplitude-scaling relationships (Zollo et al. 2010). In these systems, the information about source location and magnitude is very poor, but they provide a ground-motion estimation constrained by information recorded at the same site and they may in principle furnish non-negative, albeit small lead-time also for sites in the neighborhood of the earthquake's epicenter. Such systems operate in trigger mode, issuing the alert from predefined thresholds, calibrated on the ground-motion intensity (Colombelli et al. 2015).

G. Festa (✉) · A. Zollo · M. Picozzi · S. Colombelli · L. Elia · A. Caruso
Università di Napoli Federico II, Naples, Italy
e-mail: gaetano.festa@unina.it

M. Meghraoui et al. (eds.), *Advances in Geophysics, Tectonics and Petroleum Geosciences*,
Advances in Science, Technology & Innovation, https://doi.org/10.1007/978-3-030-73026-0_44

2 Regional Systems

A standard regional EEWS provides earthquake detection, location, and magnitude estimation of a seismic event running on the fault plane. An example of such a system is the platform PRESTo—Probabilistic and Evolutionary early warning System (Satriano et al. 2011). A regional system processes in real time the continuous data stream from a seismic network and, after the event detection, it promptly provides probabilistic and evolutionary estimates of location and magnitude, as well as the ground-shaking prediction at target sites through GMPEs. A typical timeline of the methods associated with a regional EEWS is shown in Fig. 1. In the case of PRESTo, the location is performed through the algorithm RTLoc (Satriano et al. 2008) that exploits both triggered and not-yet triggered stations and provides a probabilistic description of the hypocenter coordinates with uncertainties; the magnitude is based on an evolutionary Bayesian approach grounded on the peak displacement measured on the first 2–3 s of P wave and for the close stations on the first 2 s of S wave, which are empirically correlated with the final earthquake size (Lancieri and Zollo 2008); and GMPEs are finally used for estimating the peak ground motion at target sites accounting for uncertainties in location and magnitude estimations.

PRESTo is currently running in real time, on the Irpinia near-fault observatory. Real-time testing is also ongoing in South Korea, Romania, in the Marmara region, in the central Italy, and in a transnational region including Italy, Slovenia, and Austria.

In the case of the very dense seismic network displaced in Central Italy, during the 2016–17 earthquake sequence, the success rate of the regional system is 90% for the main event and $\sim$80% when considering all the events with magnitude larger than M_w 5.0 in the whole epicentral distance. The lead-time increases from 5 s at 30 km to 15 s at 55 km, allowing triggering automatic security actions. The size of the blind zone is about 20 km, while for the M 6.5 earthquake, damage was reported up to 60 km from the event's epicenter (Festa et al. 2018).

3 On-Site Systems

An on-site EEWS is based on estimations built on the early P-wave recorded at the same site where the ground shaking will be predicted. The structure of an on-site EEWS with associated timeline is shown in Fig. 2. An example of an on-site system is the platform SAVE (Caruso et al. 2017). The system is based on the measurement of the peak displacement and the predominant period over time windows of variable length (i.e., 1, 2, and 3 s) after the P-phase arrival.

Thus, it provides the expected ground-shaking intensity at the site, and a local alert level, based on a matrix of values for the peak displacement and the predominant period.

Using the same catalog of Central Italy's events, performances of on-site systems range between 80 and 90%. A positive, less than 3 s lead-time, has been reported in the blind zone of the regional system, and it is almost halved at 50 km of epicentral distance when compared to the regional system (Festa et al. 2018).

4 Discussion and Future Challenges

Performances of regional systems evaluated using data from a very dense network indicate a large success rate (> 80%), while limiting the percentage of missed/false alerts and

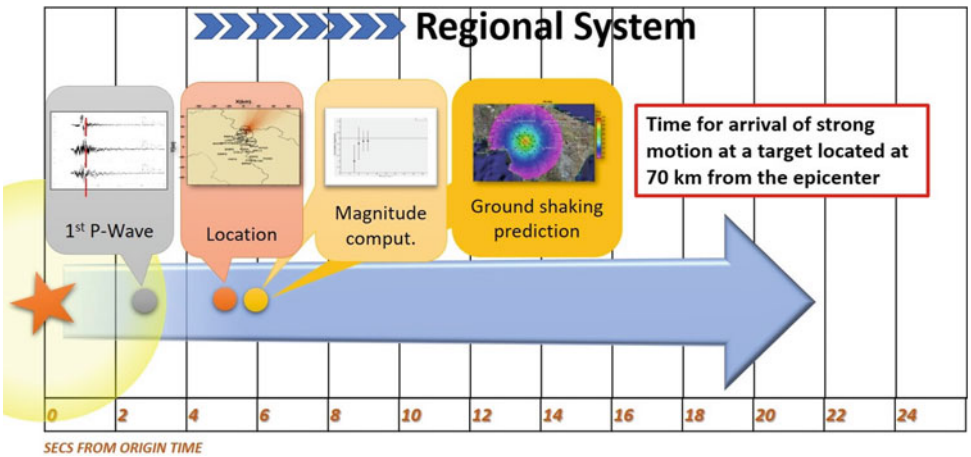

Fig. 1 A typical regional EEWS with the timeline at which the information is available in a dense seismic network. Usually, the first P wave is detected within 2–3 s from the origin time; first estimations of location and magnitude are available within 4–8 s from the event origin. Available lead-time is usually 10–15 s at a target located at 70 km from the event epicenter

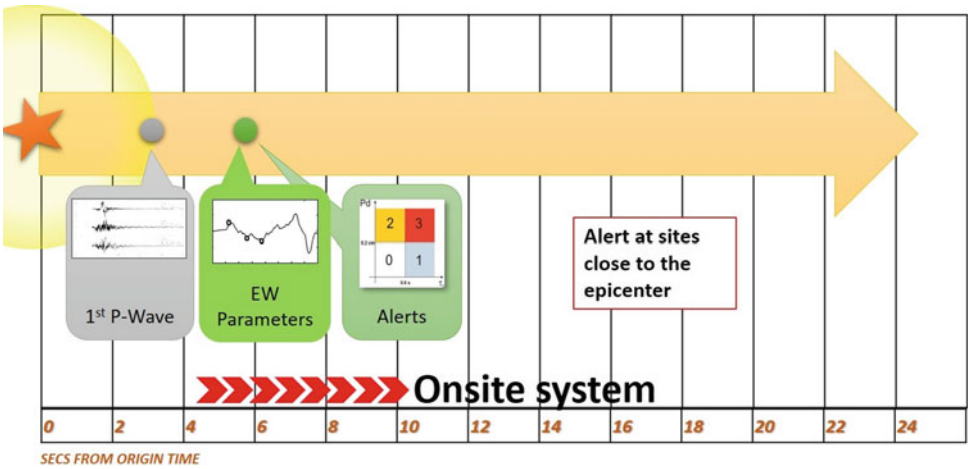

Fig. 2 The structure of an on-site EEWS with the timeline at which the information is available at a site close to the epicenter. Alert levels can be issued very soon after the P wave's arrival and detection, leaving a positive albeit small lead-time

opening the possibility to make these systems operational at a large scale.

However, a very limited number of infrastructures are nowadays technologically ready to support an EEWS. Data transmission has to be performed using dedicated wi-fi antennas and internet connection, while satellite connection should be avoided since its latency is comparable with the available lead-time in the event damage area. In addition, most of these networks do not release continuous data with a controlled delay to support a decision module based on the available lead-time. Few softwares are able to present a robust estimation of the ground shaking with a very limited computational time. In order to provide fair software comparison and performance evaluation, the CREW (the EU Testing Centre for Early Warning and Source Characterization) has been developed in the framework of the EPOS project.

Also, scientific limitation prevents from increasing the accuracy of the ground-motion prediction. When using a fixed size for the P-wave time window, the earthquake size estimation may saturate. Saturation can be avoided when expanding the P-wave time window or following the growth of the strong motion data from the P-wave onset (Colombelli et al. 2014).

To improve the characterization of the ground motion, a combination of regional and on-site systems has been developed in the testing platform QuakeUp. In this case, the system aims to build the potential damage zone around an earthquake. Such a system should initially combine GMPE-based regional estimates of ground-motion parameters with on-site predictions to define the areal distribution of the ground-motion severity. Then, the maps should be continuously updated as the effective ground motion starts to be collected at the stations close to the epicenter.

Also, improvement of site models can reduce epistemic variability in the ground-shaking prediction of regional systems, accounting for velocity, attenuation, and nonlinear rheology in the shallow layering beneath the station, and offsets in the ground-motion parameters at the site with respect to the selected GMPEs. The real-time evaluation of source parameters such as fault geometry, size, directivity, and focal mechanism requires the development of new methodologies, for the evolutionary inversion of the extended source properties. Some techniques were already proposed to improve the source description while the earthquake is still ongoing.

Some effort is also ongoing in the instrumental improvement. Specifically, the use of a huge number of low-cost instruments has started to be tested for early warning applications. In this direction, few strategies have been developed for mems in smartphones, to extract a seismic event from normal actions that provide large accelerations, either based on time–frequency analysis, or on coherency within a smartphone network. While the improvement of the rapid-response and shake map definition is obvious because it is based on the S wave characterization, low-frequency P waves are poorly resolved by low-cost accelerometers and new techniques and/or proxies for strong motion characterization are required to make these instruments of service for EEWS. There is a possibility to couple the early shape map in the source vicinity with the ground-motion prediction beyond the actual S wavefront in order to improve the characterization of the event potential damage zone.

5 Conclusions

In this paper, the two strategies adopted for earthquake early warning systems have been presented: the regional and the on-site ones. Large rate of success in Central Italy (> 80%) opens the possibility to make the systems operational, providing that the seismic networks will be technologically improved.

References

Allen, R.M., Kanamori, H.: The potential for earthquake early warning in southern California. Science **300**, 786–789 (2003). https://doi.org/10.1126/science.1080912

Caruso, A., Colombelli, S., Elia, L., Picozzi, M., Zollo, A., An on-site alert level early warning system for Italy. J. Geophys. Res. **122** (2017). https://doi.org/10.1002/2016JB013403

Colombelli, S., Zollo, A., Festa, G., Picozzi, M.: Evidence for a difference in rupture initiation between small and large earthquakes. Nat. Commun. **5**, 3958 (2014). https://doi.org/10.1038/ncomms4958

Colombelli, S., Caruso, A., Zollo, A., Festa, G., Kanamori, H.: A P wave-based, on-site method for earthquake early warning. Geophys. Res. Lett. **42**, 1390–1398 (2015). https://doi.org/10.1002/2014GL063002

Festa, G., Picozzi, M., Caruso, A., Colombelli, S., Cattaneo, M., Chiaraluce, L., Elia, L., Martino, C., Marzorati, S., Supino, M., Zollo, A.: Performance of earthquake early warning systems during the 2016–2017 Mw 5–6.5 Central Italy Sequence. Seism. Res. Lett. **89**, 1–12 (2018). https://doi.org/10.1785/0220170150

Lancieri, M., Zollo, A.: Bayesian approach to the real-time estimation of magnitude from the early P and S wave displacement peaks. J. Geophys. Res. **113**, B12302 (2008). https://doi.org/10.1029/2007JB005386

Satriano, C., Lomax, A., Zollo, A.: Real-time evolutionary earthquake location for seismic early warning. Bull. Seismol. Soc. Am. **98**(3), 1482–1494 (2008). https://doi.org/10.1785/0120060159

Satriano, C., Elia, L., Martino, C., Lancieri, M., Zollo, A., Iannaccone, G.: PRESTo, the earthquake early warning system for southern Italy: Concepts, capabilities and future perspectives. Soil Dynam. Earthq. Eng. **31**(2), 137–153 (2011). https://doi.org/10.1016/j.soildyn.2010.06.008

Zollo, A., Lancieri, M., Nielsen, S.B.: Earthquake magnitude estimation from peak amplitudes of very early seismic signals on strong motion. Geophys. Res. Lett. **33**, L23312 (2006). https://doi.org/10.1029/2006GL027795

Zollo, A., Amoroso, O., Lancieri, M., Wu, Y.M., Kanamori, H.: A threshold-based earthquake early warning using dense accelerometer networks. Geophys. J. Int. **183**, 963–974 (2010). https://doi.org/10.1111/j.1365-246X.2010.04765.x

Status of Seismic Hazard Modeling of Active Faults in Oran City, (Northwestern Algeria)

Mohamed Hamdache, Jose Antonio Pelaez, Abdelkrim Yelles Chaouch, Miguel Castro, Ricardo Monteiro, Hamoud Beldjoudi, and Abdel Aziz Kherroubi

Abstract

This work, as a stage of the collaborative project Smarter between CRAAG and FEUP, aiming to mitígate the seismic risk in Oran city, leading to update the seismic design regulations, will address some recent progresses and considerations made toward a further improvement of the component of seismic risk related to the probabilistic quantification of seismic hazard. The study focuses on the case of Oran city, where several identified active faults are modeled, and their characteristic parameters are turned as input to probabilistic seismic hazard. Site-specific seismic hazard analysis is then performed at Oran, and the derived results are presented in terms of different ground motion parameters, i.e., PGA and uniform hazard spectra (UHS) for a return period of 475 years. Moreover, seismic disaggregation for the same return period is performed to derive the contribution of the different seismic scenarios. Also, based on these results, we compute the so-called control earthquake, that is, the most contributing earthquake to seismic hazard at Oran city from a probabilistic point of view.

Keywords

Peak ground acceleration • Hazard curves • Uniform hazard spectra • Disaggregation • Earthquake design • Northwestern Algeria • Smarter project

M. Hamdache (✉) · A. Y. Chaouch · H. Beldjoudi · A. A. Kherroubi
Dépt Etudes et Surveillance Sismique. CRAAG, BP 63 16348 Bouzareah, Algeria
e-mail: mohamed.hamdache@craag.edu.dz

J. A. Pelaez
Department of Physics, University of Jaén, Jaen, Spain

M. Castro
FEUP, Facultade de Engenharia, Universidade Do Porto, Porto, Portugal

R. Monteiro
University School of Advanced Studies IUSS, Pavia, Italy

1 Introduction

According to Misha et al. (2014), the challenge of urban mapping is to predict the ground motion effects related to various sources' path and site characteristics, not just a single site but at all the places with an acceptable level of reliability. This study is an attempt in seismic hazard modeling of active faults at Oran city in the northwestern Algeria. Thus, the previously estimated seismic hazard values at Oran city (Hamdache et al. 2019) are revisited. The improvements introduced correspond to recent efforts made to implement fault rupture model into the previously proposed source-zone model for the Algeria-Morocco region by Peláez et al. (2018). Initially, the model is a set of area sources, delineated with care and including both the well-known tectonic structures and the known seismicity. Oran city is located into the delineated source-zone T1 of the proposed zone model (Peláez et al. 2018), where several active fault sources are identified and characterized. According to Pace et al. (2016) and Visini et al. (2019), the fault parameters are then turned into seismic hazard input. Site-specific seismic hazard analysis is performed using OpenQuake Engine (Pagani et al. 2014) in terms of PGA and UHS. The contribution of the different scenarios to seismic hazard values and the so-called control earthquake (Berneuter 1992) or modal earthquake (Chapman, 1995) is derived through disaggregation analysis.

2 Earthquake Data File and Fault Source Model

The earthquake data file used to perform this study is analyzed in Peláez et al. (2007) and Hamdache et al. (2010). Overall, the final catalog is presented and used in previous works (Peláez et al. 2016; Hamdache et al. 2019). The main tectonic structures and the epicentral distribution of event

M. Meghraoui et al. (eds.), *Advances in Geophysics, Tectonics and Petroleum Geosciences*, Advances in Science, Technology & Innovation, https://doi.org/10.1007/978-3-030-73026-0_45

magnitudes above *Mw* 4.0 are shown in Fig. 1a, and on Fig. 1b, the identified active faults are displayed.

The identified active faults are denoted F1 for the Off-shore fault, F2 for Oran fault or Sebkha north, F3 for Arzew fault, F4 for South East Mleta fault, F5 South West Mleta fault, F6 South Habra fault, F7 Beni-Chougrane fault, and F8 Ghriss fault. The Off-shore fault F1 is an interpreted fault.

3 Results

Probabilistic seismic hazard analysis can be adopted into new insight, which has already been done for central India (Mandal et al. 2013). High site response may be characterized on studying oblate particle motion (Chowdhari et al. 2012). Identified active fault sources are increasingly integrated into probabilistic seismic hazard assessment, and the practice is growing in popularity. In this section, we use the approach developed by Pace et al. (2016) and Visini et al. (2019) to turn fault data into seismic hazard model. Using the slip range and the rupture fault length, the procedure allows the estimation of four magnitudes. The magnitude denoted MM0 is from the standard formula (ISAPEI, 2005); the magnitude named MRLD derived from the maximum subsurface fault length and the magnitude named MRA derived from the maximum rupture area are deduced from the empirical relationship of Wells and Coppersmith (1994). The obtained results for the fault F2 are displayed on Fig. 2, showing the plot of the probability curve for each magnitude by following normal distribution. M_{obs} corresponds to the largest observed moment magnitude.

The following plots show (a) the activity rate of magnitude in the range $M_{max} - \sigma_{Mmax}$ to $M_{max} + \sigma_{Mmax}$, (b) plot of the Brownian Passage Time (BPT) (black line) and the time-dependent probability of occurrence for the next 50 years given the elapsed time.

The earthquake rate derived from the fault parameters, using the approach introduced by Pace et al. (2016) and Visini et al. (2019), allows preparing the input file for OpenQuake Engine to perform site-specific seismic hazard at Oran city. Performed seismic hazard curve in terms of PGA and UHS for 475 years return period as shown in Fig. 4a, b. The quantile at 0.05, 0.5, and 95% are also displayed.

Disaggregation of seismic hazard for a return period of 475 years is displayed on Fig. 4**c** which gives the contribution of the different scenarios to the estimated seismic hazard values. The modal and mean scenarios in terms of magnitude and distance obtained according to Berneuter (1992), Chapman (1995) are given on the plots.

4 Discussion

From the attributed parameters (length, dip, thickness, slip range, and the last earthquake) to the fault F2, as displayed on Fig. 2a, the maximum magnitude is estimated to 7.0 ± 0.3, and the mean recurrence time T_{mean} is about 5287 years. The coefficient of variation of T_{mean}, defined as the ratio between the uncertainty of T_{mean} and T_{mean}, is equal to 1.09. The seismic moment rate obtained equals $7.5299.\ 10^{15}$ N m/year. Using the Gutenberg–Richter Truncated relationship, Fig. 2b displays the annual cumulative rate for magnitude range 4.0–7.0 M*w*. Using these results as input and considering that the fault F2 follows the model of the so-called characteristic Gaussian model, the cumulative annual rate as a function of magnitude for the case of characteristic Gaussian model is displayed in Fig. 3a. The frequency-magnitude distribution oscillates exclusively between $M_{max} \pm \sigma_{Mmax}$, which is 6.7–7.3 M*w*, with no earthquakes outside this interval. The cumulative annual number of earthquakes above the given magnitude appears on the ordinates axis. The plot on the graph Fig. 3b shows

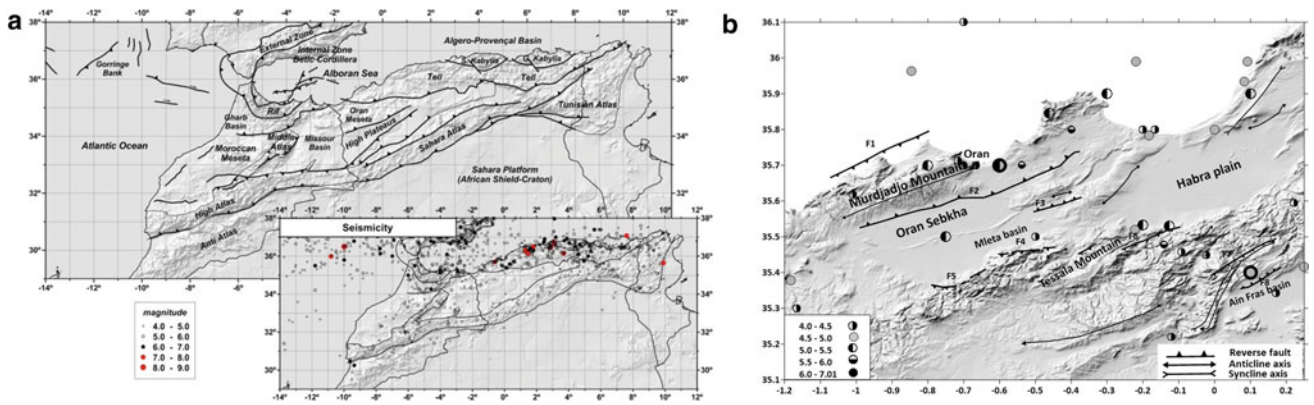

Fig. 1 **a** Global tectonic sketch for the studied region including seismicity (Hamdache et al. 2019). **b** Active faults around the Oran city (modified from Bouhadad et al. 2002)

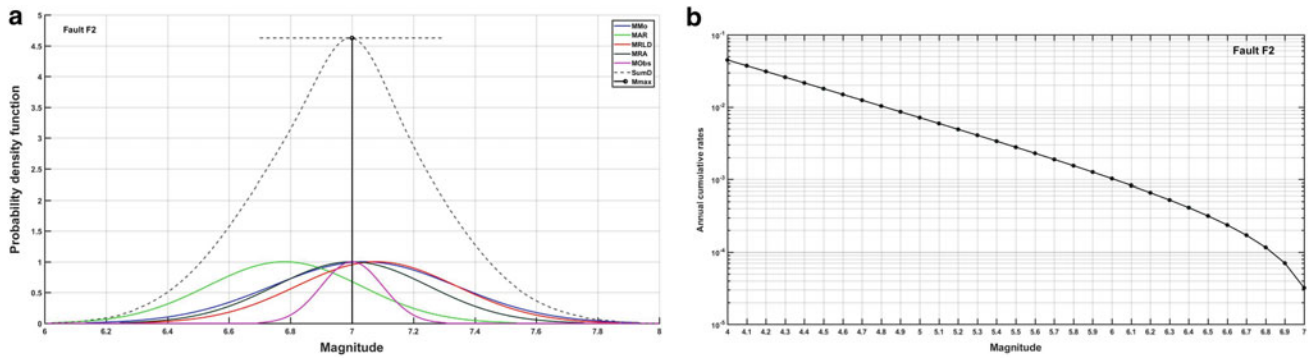

Fig. 2 **a** Summed probability density (PDF) curve in dashed line. **b** Truncated magnitude-frequency distribution of the Gutenberg–Richter for fault F2

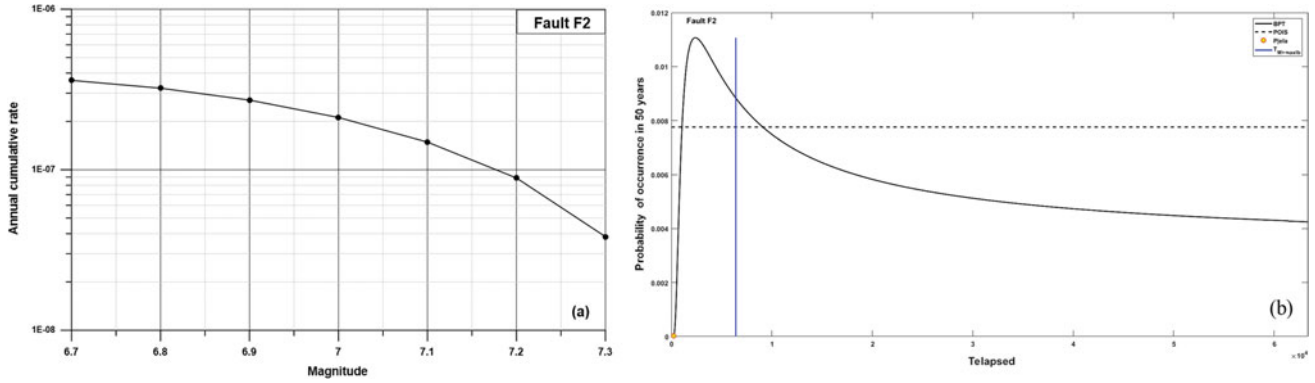

Fig. 3 **a** Plot of the activity rate for magnitude in the range $M_{max} \pm \sigma_{Mmax}$. **b** Probability of occurrence in the next 50 years given the elapsed time

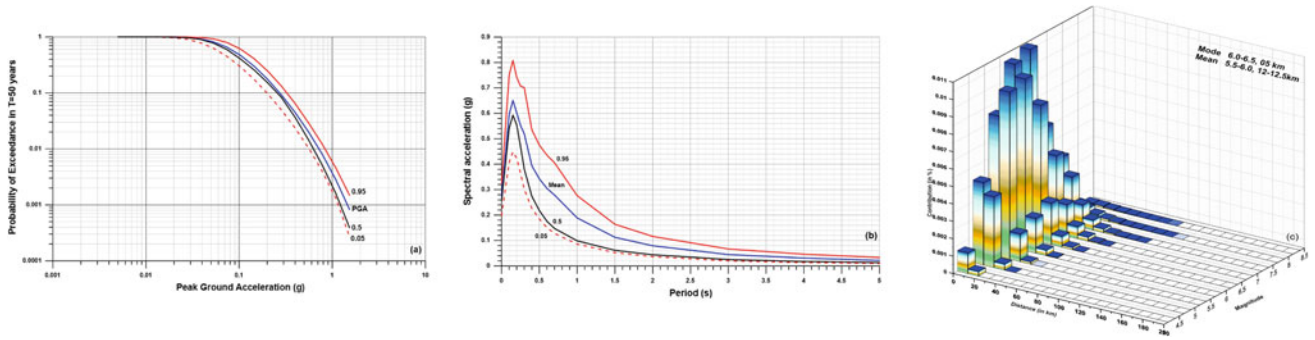

Fig. 4 Hazard curve in terms of **a** PGA and **b** UHS for 475 years return period. **c** Disaggregation for a return period of 475 years

the computed probability of occurrence for the next 50 years of an earthquake in the interval $M_{max} \pm \sigma_{Mmax}$ given the elapsed time (P_{elap}) since the last event (229 years in the case of the fault F2). In dashed line, assuming that the behavior is Poissonian, that is, model independent of the elapsed time, we obtain $P = 0.0077577$. In a continuous line, assuming that the behavior is that of the so-called characteristic Gaussian model, given an elapsed time since the last event, in red circle, the probability is given by the Brownian Passage Time (BPT) displaying the time-dependent model on the elapsed time. The vertical blue line represents the average recurrence time of an earthquake of magnitude $M_{max} - \sigma_{Mmax}$ (in our case 6.7 M*w*). Figure 4a–c displays the seismic hazard values derived using this approach, for a return period of 475 years, in terms of PGA, UHS, and the contribution of the different couple of

(M, R) to seismic hazard. The modal scenario is 6.0–6.5 at 5–10 km for the estimated PGA that is equal to 0.27 g at Oran city.

5 Conclusions

This note presents some new challenges in seismic hazard assessment in northern Algeria by introducing fault rupture modeling. The recent works by Pace et al. (2016) and Visini et al. (2019) allow us in a first stage to turn the fault parameters into seismic hazard input and then to build the appropriate input file to perform seismic hazard evaluation using OpenQuake Engine (Pagani et al. 2014) providing the estimate values at Oran site in terms of PGA and UHS, for different return periods. The disaggregation analysis performed for different return periods allows the estimation of the so-called control earthquake (Berneuter 1992) or modal earthquake (Chapman 1995), which corresponds to the magnitude-distance group that gives the largest contribution to the hazard (Barani et al. 2009) as shown in Fig. 4c for a return period of 475 years. This new perspective in seismic hazard modeling is still under the study to improve substantially the seismic hazard assessment in northern Algeria by using more reliable fault data.

Acknowledgements We would like to thank the anonymous reviewers for their valuable comments and suggestions that greatly contributed to the improvement of this note.

References

Barani, S., Spallarossa, D., Bazzuro, P.: Disaggregation of probabilistic ground-motion hazard in Italy. B.S.S. America **99**, 2638–2661 (2009)

Berneuter, D.L.: Determining the control earthquake from probabilistic hazards for the proposed Appendix B. In: L.L.N.L. Report UCRL-JC-111964, Livermore California (1992)

Bouhadad, Y., Laouami, N.: Earthquake hazard assessment in the oran region (Northwest Algeria). Nat. Hazards **26**(227–243), 2002 (2002)

Chapman, M.C.: A probabilistic approach to selection of ground motions for engineering design. Bull. Seismol. Soc. Am. **85**, 937–942 (1995)

Chowdhuri, S.N., Mishra, O.P.: Oblate particle motion for high site response characteristics in Agartala city, India. Ind. J. Geosci. **66**(4), 225–232 (2012)

Hamdache, M., Peláez, J.A., Talbi, A., López Casado, C.: A unified catalog of main earthquakes for Northern Algeria from A.D. 856 to 2008. S. Res. Lett. **81**, 732–739 (2010)

Hamdache, M. Peláez, J.A., Yelles-Chaouche, A., Monteiro, R., Marques, M., Castro, M., Beldjoudi, H., Kherroubi, A.: A preliminary seismic hazard modelling in Northern Algeria. Springer Nature Switzerland AG 2019. In: Sundararajan, N. et al. (eds.) On Significant Applications of Geophysical Methods, Advances in Science, Technology & Innovation (2019). https://doi.org/10.1007/978-3-030-01656-2_53

ISAPEI: Recommendations and standard procedures for determining earthquake magnitude from digital data (2005)

Pace, B., Visini, F., Peruzza, L.: FiSH: MATLAB tools to turn fault data into seismic-hazard models. S.R. Letters **87**(2A) (2016)

Pagani, M., Monelli, D., Weatherill, G., Danciu, L., Crowley, H., Silva, V., Henshaw, P., Butler, L., Nastasi. M., Panzeri. L., Simionato. M., Vigano, D.: OpenQuake engine: an open hazard (and risk) software for the global earthquake model. Seismol. Res. Lett. **85**(3), 692–702 (2014). https://doi.org/10.1785/0220130087

Peláez, J.A., Chourak, M., Tadili, B.A., Brahim, L.A., Hamdache, M., López Casado, C., Martínez Solares, J.M.: A catalog of main Moroccan earthquakes from 1045 to 2005. Seismol. Res. Lett. **78**, 614–621 (2007)

Peláez, J.A., Hamdache, M., Sanz de Galdeano, C., Sawires, R., García Hernández, M.T.: Forecasting moderate earthquakes in Northern Algeria and Morocco. In: D'Amico, S. (ed.) Earthquake and Their Impact on Society, pp. 81–95. Springer, Natural Hazards (2016)

Peláez, J.A., Henares, J., Hamdache, M., Sanz de Galdeano, C.: An updated seismic model for the northwestern Africa. 16 E.C.E. Eng. Thessaloniki, 18–21 June 2018 (2018)

Mandal, H.S., Shukla, A.K., Khan, K., Mishra, O.P.: A new insight into probablistic seismic hazard analysis for Central India. Pure Appl. Geophys. (PAGEOPH) (2013). https://doi.org/10.1007/s00024-013-0666-x,2013

Mishra, O.P.: Intricacies of Himalayan seismotectonics and seismogenesis: need of an integrated research. Current Sci. **106**(2), 176–187 (2014)

Visini, F., Valentini, A., Chartier, T., Scotti, O., Pace, B.: Computational tools for relaxing the fault segmentation in probabilistic seismic hazard modeling in complex fault system. Pure Appl. Geophys. (2019) https://doi.org/10.1007/s00024-019-02114-6

Wells, D.L., Coppersmith, K.L.: New empirical relationship among magnitude, rupture length, rupture width, rupture area, and surface displacement. B.S S.A. **84**, 74–1002 (1994)

Large Earthquakes and Active Faulting in the Gafsa-Metlaoui Region (South Tunisia): Implications on the Seismic Hazard Assessment

Malak Athmouni, Mustapha Meghraoui, Nejib Bahrouni, and Ahmed Ksentini

Abstract

The main purpose of this work is to estimate the seismic hazard and earthquake occurrence rates from the characterization and modeling the active fault parameters in southern Tunisia. The aim is to determine the slip rate of faults which are capable of generating large magnitude earthquakes ($M_w > 6$) and to characterize the annual occurrence rates generated by these faults. This is considered as an alternative to standard models based on seismicity catalogs.

Keywords

Metlaoui • Earthquakes • Mechanical and elastic modeling • Shortening rate • Seismic hazard model

1 Introduction

The Metlaoui and Gafsa regions in southern Tunisia have been the site of shallow and damaging earthquakes in 1989 (M_w 4.9) and 1992 (M_w 4.7) related to the Africa—Eurasia plate convergence (Fig. 1 and Table 1). The seismic activity of this region is generated not only on the NW–SE trending and right-lateral Gafsa strike-slip fault, but also on E–W striking fold-related faults that also mark the limit between the Maghrebian Mountain ranges and the African platform of the Nubian plate. Although this region was in focus of several neotectonic and seismotectonic studies (Bahrouni et al. 2014), the active fold-related faults received limited attention, and the rate of active deformation of seismogenic structures was poorly explored.

2 Materials and Methods

We conducted geological earthquake investigations along with structural and neotectonic studies including mechanical and elastic modeling of the active folds of southern Tunisia. Our approach consists in the study of active tectonic structures at the crustal level (seismogenic layer) using kinematic-mechanical and elastic modeling. The comparison between these two methods may provide some constraints on the characterization of seismogenic structures and their rate of active deformation.

The local geology with detailed stratigraphic log (mostly from wells), the geophysical results (seismicity distribution and gravity), and its structural characteristics provide the tectonic background for the preparation of balanced cross sections. The tectonic structures visible at the surface and inferred at depth are used for the kinematic and mechanical modeling using the Trishear software (Allmendinger 1998).

The elastic modeling is performed based on the constitutive formula of dislocation of Okada (1992). It allows the characterization of the parameters of coseismic ruptures such as the fault dimensions, the coseismic displacement, the seismic moment M_o ($M_o = \mu * LW * \bar{U}$), and, thus, the associated moment magnitude M_w. Field observations associated to the mechanical and elastic modeling allow better estimation of the size of potential future large earthquakes (with $M > 6$) and constrain their occurrence rate, the seismic zoning, and seismic hazard assessment.

M. Athmouni (✉)
Institut de Physique du Globe, CNRS-UMR, 7516 Strasbourg, France

M. Athmouni · A. Ksentini
University of Sfax, 3029 Sfax, Tunisia

M. Meghraoui
EOST - Institut Terre et Environnement de Strasbourg, University of Strasbourg, CNRS - UMR 7063, Strasbourg, France

N. Bahrouni
Office National des Mines, 24,2035 La Charguia, Rue de l'énergie, 2035 Tunis, Tunisia

M. Meghraoui et al. (eds.), *Advances in Geophysics, Tectonics and Petroleum Geosciences*,
Advances in Science, Technology & Innovation, https://doi.org/10.1007/978-3-030-73026-0_46

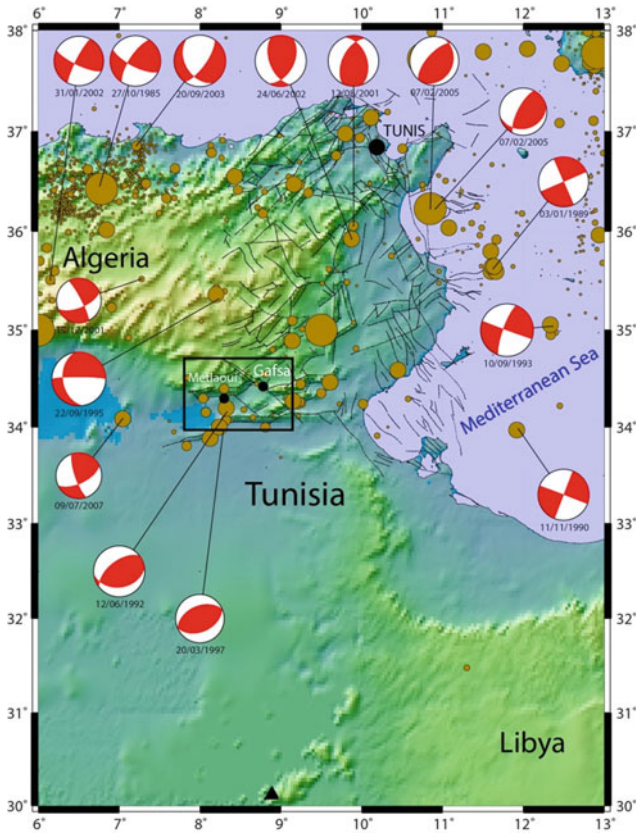

Fig. 1 Seismotectonic map of Tunisia (Bahrouni et al. 2014). Black lines are for faults, and topography is from ASTER-DEM (1 m resolution). Box is the study area

3 Results

The E-W trending fold structures in northern Africa are associated with transpressive tectonic movements that associate right-lateral slip with NE-SW shortening (Meghraoui and Pondrelli 2012). Active folds are asymmetrical with southern vergence along fault segments that may reach 40 km in length and ~550 m topographic offset.

The balanced cross sections of the Metlaoui fold-related fault with thick sedimentary units on the hanging block indicate the evolution of pre-Miocene normal faulting (Fig. 2). The modeling proceeds with the high-angle (~50° north dipping) reverse fault segments and its evolution during the Plio-Quaternary.

The kinematic and mechanical modeling of fold-related faults using the Trishear code (Allmendinger 1998) allowed the modeling of active deformation during the Plio-Quaternary, taking into account the stratigraphic succession, tectonic characteristics, and fault geometry (Bahrouni et al. 2014; Saïd et al. 2011; Zargouni 1985). The modeling of successive fault displacement and folding deformation lead to a 0.7 ± 0.1 mm/year shortening rate, which is in agreement with the results of recent GPS surveys (Bahrouni et al., submitted).

4 Discussion

Active folds in southern Tunisia and South Eastern Algeria may generate strong crustal movements and tectonic deformations such as the Gafsa–Metlaoui earthquakes. These earthquakes are controlled by the movements of the fold-related faults. The active zone of Metlaoui presents transpressive tectonics which associates NW–SE to E–W trending, right-lateral strike-slip faults with fold-related fault. The high-angle reverse faulting confirms the assumption of the tectonic inversion of the pre-Miocene normal faults during the Plio-Quaternary. This is also attested by the uplifting of alluvial terraces with artefacts (tools) dated at Mousterian (~150–350 ka). The Metlaoui fault length, estimated at ~ 40 km, implies an earthquake magnitude of $M_w > 6.5$, according to Wells and Coopersmith empirical relation (Wells and Coppersmith 1994).

Unfortunately, the historical seismicity catalog does not mention any earthquakes in the Gafsa region. The estimation

Table 1 List of significant earthquakes in southern Tunisia from 1989 to 2018

Date (M, D, Y)	Long	Lat	Depth (km)	M (INM M_L, CMT M_w)	Reference
110,789	8.4	34.33	12	4.4	INM
061,292	8.44	34.21	15	5.2	CMT
091,093	12.44	34.99	26	5.3	CMT
051,194	8.45	34.22	5	4.6	INM
032,996	9.53	34.82	10	4.4	INM
010,598	10.18	33.85	16	4.7	INM
050,698	9.25	34.22	15	4	INM
050,901	10.5	33.9	14	4	INM
052,118	9.69	34.19	12	5	CMT

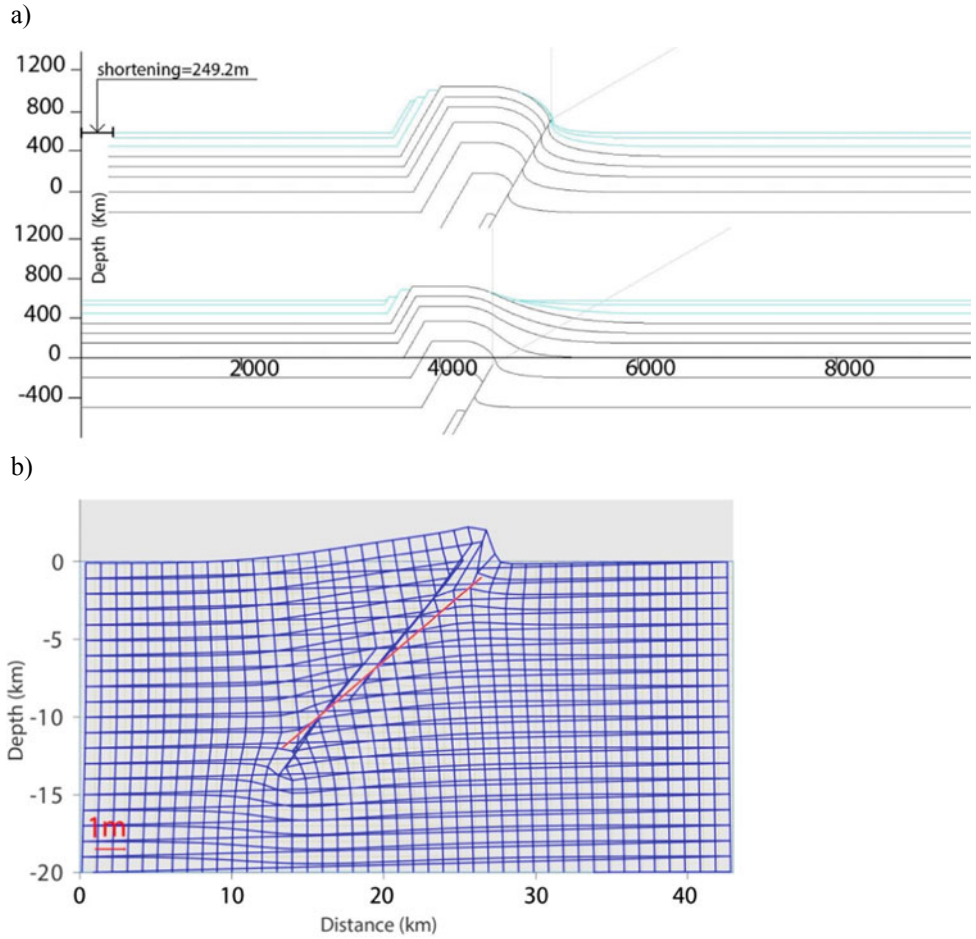

Fig. 2 **a** Balanced cross sections of the Metlaoui fault-related fold. The comparison of the cross sections allows the determination of the ~ 249.2 m of shortening. The folded and faulted tectonic structures involve alluvial terraces dated 300 ± 50 ka (Saïd et al. 2011) and imply a minimum 0.7 mm/year shortening rate. **b** Elastic modeling based on 1992 earthquake data (Table 1 and Fig. 1). The modeling of geological units suggests an estimation of the late Quaternary shortening rate

of the earthquake occurrence rate is still uncertain in the Gafsa-Metlaoui region. In order to better refine our estimated 0.7 ± 0.1 mm/year shortening rate and return period of large earthquakes ($M_w > 6$), the elastic and mechanic modeling needs to be combined with investigations in tectonic geomorphology and paleoseismology.

In order to establish the relationship between the earthquake generation at depth and surface deformation, we also proceed with the elastic deformation using the elastic dislocation modeling (Okada 1992). Using previous seismological studies of past earthquakes, we observe that coseismic rupture initiation may occur at 6–8 km depth in agreement with the mechanical properties of the upper crust. The elastic modeling also conforms with the seismic parameters such as the fault dimensions, average coseismic slip, seismic moment, and estimated maximum moment magnitude M_w 7 on the active fold-related folds.

5 Conclusions

Our study of active folds in the Gafsa-Metlaoui region combines kinematic and elastic modeling using geological, geophysical, tectonic, and seismological data. The seismic and tectonic parameters obtained from earthquake studies and field observations on the deformation of Quaternary deposits allow us to determine the 0.7 ± 0.1 mm/year Shortening rate across the Metlaoui active fold. Field observations, seismotectonic and geodetic results, and modeling of the active deformation constrain the size and

rate of large earthquake generation and lead to a new model of seismic hazard assessment in Tunisia.

References

Allmendinger, R.W.: Inverse and forward numerical modeling of Trishear fault-propagation folds. Tectonics **17**(4), 640–656 (1998)

Bahrouni, N., Masson, F., Meghraoui, M., Saleh, M., Maamri, R., Dhaha, F., Arfaoui, M.: GPS constraints on the active deformation in Tunisia, Geology, submitted

Bahrouni, N., Bouaziz, S., Soumaya, A., Ben Ayed, N., Attafi, K., Houla, Y., El Ghali, A., Rebai, N.: Neotectonic and seismotectonic investigation of seismically active regions in Tunisia: a multidisciplinary approach. J. Seismol. **18**(2). https://doi.org/10.1007/s10950-013-9395-y.2014

Meghraoui, M., Pondrelli, S.: Active faulting and transpression tectonics along the plate boundary in North Africa. Ann. Geophys. 55(5). https://doi.org/10.4401/ag-4970.2012

Okada, Y.: Internal deformation due to shear and tensile faults in a half-space. Bull. Seismol. Soc. Am. **82**(2), 1018–1040 (1992)

Saïd, A., Chardon, D., Baby, P., Ouali, J.: Active oblique ramp faulting in the Southern Tunisian Atlas. Tectonophysics **499**(1–4), 178–189 (2011)

Wells, D.L., Coppersmith, K.J.: Updated empirical relationships among magnitude, rupture length, rupture area, and surface displacement. Bull. Seismol. Soc. Am. **84**, 974–1002 (1994)

Zargouni, F.: Tectonique de l'Atlas méridional de Tunisie, évolution géométrique et cinématique des structures en zone de cisaillement, vol. 3, 302p. Thèse Doct. ès-Sc., Univ. Louis Pasteur (Strasbourg). Ed. Mem. INRST.5, Tunisie (1985)

Is the Seismic Hazard in Tunisia Underestimated? An Archaeoseismological Study

Miklós Kázmér

Abstract

The recent seismicity of Tunisia is considered sparse and moderate. A number of historical studies are available, but the archaeological evidence has not been properly used. Pilot studies were carried out at three sites in the less seismic middle part of Tunisia: Roman Thysdrus (Arabic El-Jem), and the Islamic *medina* (old town) of El-Jem, Sousse and Monastir. A selection of earthquake archaeological effects observed is shown (dropped keystones, fractured or extruded masonry blocks, columns displaced from plinth), marking the potential minimum intensity of shaking. To create this level of damage, local intensity IX is hypothesized. This is certainly higher than the 2007 seismic hazard map produced by WHO, where only medium intensities are indicated for the region. It is suggested that a systematic archaeoseismological study of Tunisia will contribute in improving seismic hazard assessment.

Keywords

Archaeoseismology • Earthquake • Seismic hazard • Tunisia

1 Introduction

The recent seismicity of Tunisia is considered sparse and moderate, mostly based on instrumental data. A number of historical studies are available. Utilizing the information hidden in archaeological objects has started only recently: Bahrouni et al. (2019) offered a glimpse in their studies on the archaeological evidence of the AD 859 earthquake in Kairouan.

Recently, the author carried out pilot studies in three sites in the less seismic middle part of Tunisia: Roman Thysdrus (Arabic El-Jem), and the Islamic *medina* (old town) of El-Jem, Sousse and Monastir. Short list of observed earthquake's archaeological effects is shown below, marking the potential minimum intensity of shaking (after Rodriguez-Pascua et al. 2011).

2 Methods

Sites were documented by visual observation, photography, and hand drawings. Measurements were taken by a Laser Disto 8 range finder, which allowed quick measuring of horizontal and vertical distances. Observed damage must be interpreted within the context of the building. Work on the details of the history of construction, destruction, and restoration of each site by literature studies is in progress.

3 Results

3.1 El-Jem, Roman Amphitheatre

- Dropped keystones—VII—frequent in radial arches, rare in tangential arches
- Dropped arch sectors (Fig. 1a)—VII. This is the highest, 'severe' damage category of arches, as understood by Hinzen et al. (2016).
- Collapsed arches/vaults—IX
- Extruded blocks (Fig. 1b)—IX(?)
- Penetrating fracture in arch masonry (Fig. 1c)—parallel to stress—VII. 'Severe' damage category of Hinzen et al. (2016).

M. Kázmér (✉)
Department of Palaeontology, Eötvös University & MTA-ELTE Geological, Geophysical and Space Science Research Group, Budapest, Hungary

M. Meghraoui et al. (eds.), *Advances in Geophysics, Tectonics and Petroleum Geosciences*,
Advances in Science, Technology & Innovation, https://doi.org/10.1007/978-3-030-73026-0_47

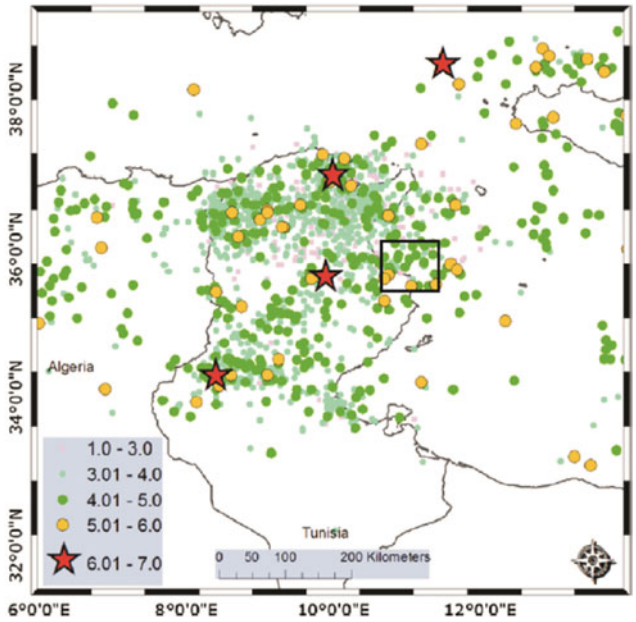

Fig. 1 Seismicity of Tunisia (after Ksentini and Romdhane 2014, modified). Sites in El-Jem, Sousse, and Monastir are within the rectangle. This is where a possibly $M > 6.0$ earthquake occurred within the last millennium, additionally to the already known three marked by stars

3.2 Sousse, Ribat and Kasbah (Islamic)

- Twisted walls (Fig. 2f)—VIII
- Broken corners of columns: axial and oblique (Fig. 1d)—VII
- Shift between column and capital (Fig. 2e)—IX
- Penetrating fracture through capital or plinth (Fig. 1d)—VII
- Extruded masonry block (Fig. 2g)—IX(?)
- Displaced arch sector (fallen keystone) (Fig. 2h)—VII
- Axial fracture in tower
- Column displaced from plinth—IX.

3.3 Monastir, Ribat (Islamic)

- Column displaced from plinth—IX
- Broken corners of columns: axial and oblique—VII.

4 Discussion and Conclusion

The current instrumentally recorded seismic activity nearby Sousse produced up to M 4.5 earthquakes (Bahrouni et al. 2014). Historical M 6–7 earthquakes are known in Tunisia (Ksentini and Romdhane 2014). However, their epicentres are more than 200 km away from Sousse: These probably did not cause major damage in public buildings and nearby the city. The archaeoseismic damage outlined above was certainly caused by at least one other major earthquake nearby, during the past millennium. It is suggested that a systematic archaeoseismological survey of Tunisia will change our perception of the seismic hazard of the country.

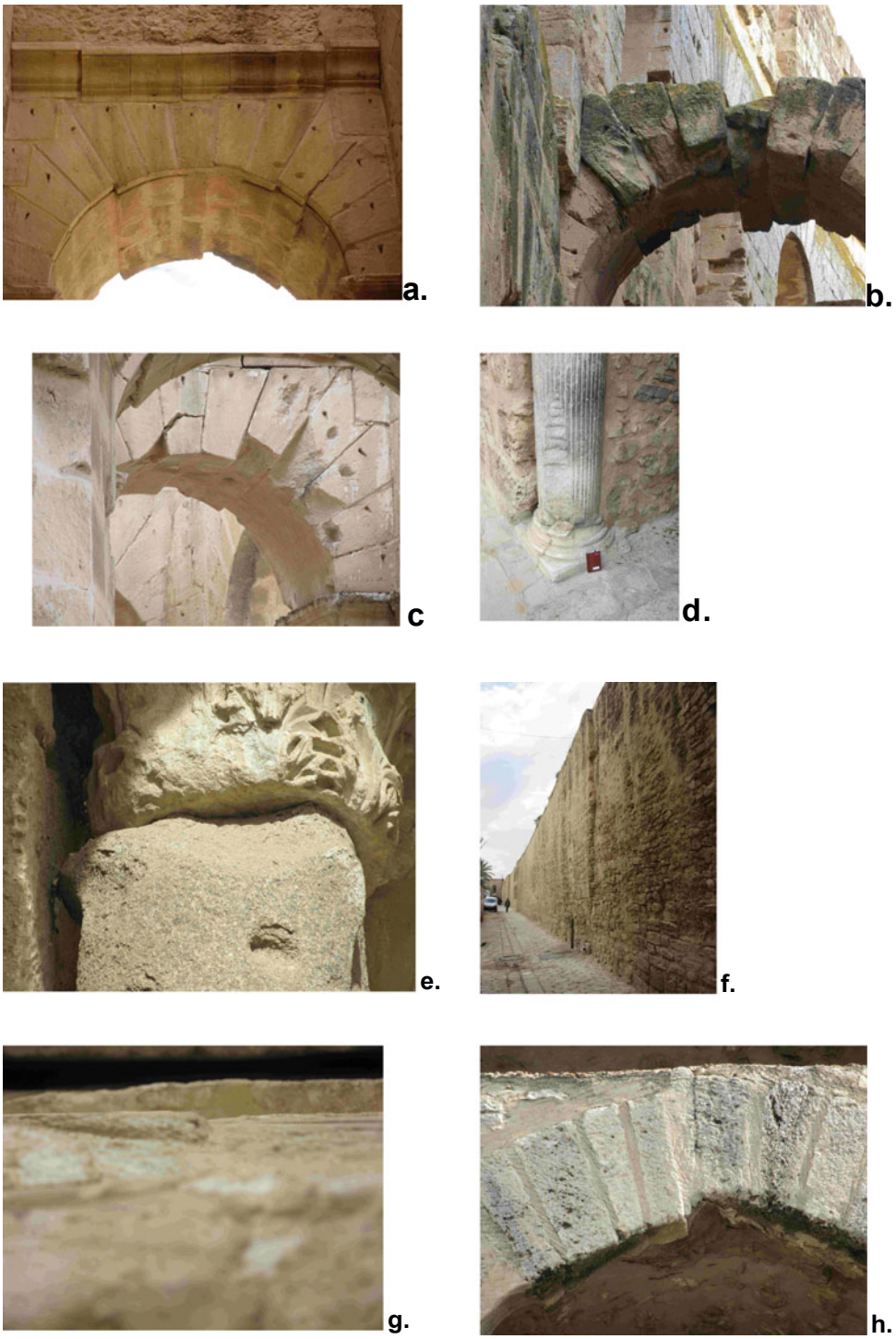

Fig. 2 Archaeoseismological evidence for damaging earthquakes in the middle part of Tunisia. **a** Dropped arch sectors. El-Djem amphitheatre. #6085. **b** Extruded blocks. El-Djem amphitheatre. #6062. **c** Penetrating fracture in arch masonry—parallel to stress. El-Djem amphitheatre. #6098. **d** Broken corners of columns: axial and oblique. Sousse, Ribat. #5794. Serial numbers refer to images in the archaeoseismological database (Moro and Kázmér 2019). **e** Shift between column and capital. Sousse, Ribat. #5800. **f** Twisted walls. Sousse. #5897. **g** Extruded masonry block. Sousse. #5805. **h** Displaced arch sector (fallen keystone). Sousse. #5867

References

Bahrouni, N., Bouaziz, S., Soumaya, A., Ben Ayef, N. Attafi, K., Houla, Y., El Ghali, A., Rebai, N.: Neotectonic and seismotectonic investigation of seismically active regions in Tunisia: a multidisciplinary approach. J. Seismol. **18**, 235–256 (2014)

Bahrouni, N., Meghraoui, M., Hinzen, K., Arfaoui, M., Maamri, R., Mahfoud, F.: Historical and archeoseismic investigations in Kairouan region (central Tunisia): evidence for the 9 October 859 AD large earthquake. In: 2nd Conference of the Arabian Journal of Geosciences, 25–28 November 2019, Sousse, Tunisia (this volume) (2019)

Hinzen, K.-G., Schwellenbach, I., Schweppe, G., Marco, S.: Quantifying earthquake effects on ancient arches, example: the Kalat Nimrod fortress, Dead Sea Fault Zone. Seismol. Res. Lett. **87**(3), 751–764 (2016)

Ksentini, A., Romdhane, N.B.: Updated seismic hazard assessment of Tunisia. Bull. Earthquake Eng. **12**, 647–670 (2014)

Moro, E., Kázmér, M.: Damage in ancient buildings—towards an archaeoseismological database (2019). (In preparation)

Rodríguez-Pascua, M.A., Silva, P.G., Peérez-López, R., Giner-Robles, J.-L., Martín-González, F., Perucha, M.A.: Preliminary intensity correlation between macroseismic scales (ESI07 and EMS98) and Earth-quake Archaeological Effects (EAEs). In: Proceedings of the 4th International INQUA Meeting on Paleoseismology, Aachen, pp. 221–224 (2011)

WHO: World Health Organization. Seismic Hazard Distribution Map, Tunisia (2007)

Preliminary Fault Instability Analysis of Mw 6.5 Pidie Jaya, Aceh 2016 Earthquake (Indonesia)

David Prambudi Sahara, Dian Kusumawati, Sri Widiyantoro, Andri Dian Nugraha, Zulfakriza, and Nanang Tyasbudi Puspito

Abstract

The Mw 6.5 Pidie Jaya strike-slip earthquake struck Pidie Jaya, Aceh, on December 7, 2016. The aftershocks lasted until January 2017. The aftershocks, which were recorded by Indonesia's Meteorological, Climatological, and Geophysical Agency (BMKG) network on December 7–19, 2016, depicted northwest–southeast cluster orientation. While the aftershocks, which were recorded by the local Aceh aftershock network on December 14, 2016–January 15, 2017, depicted northeast–southwest, perpendicular to the BMKG aftershocks. In many cases, fault plane orientation can be determined from focal mechanism's nodal planes. However, in the Pidie Jaya earthquake, the perpendicular aftershocks clusters observed by regional BMKG and local Aceh network may complicate this task. Fault instability concept was brought in this study to interpret Pidie Jaya fault plane's orientation. We used focal mechanism solutions from three institutions: BMKG, German Research Centre for Geosciences (GFZ), and United States Geological Survey (USGS). We analyzed each nodal plane instability values. Our results showed that the nodal plane, which has northeast–southwest orientation, is the most unstable in Sumatra regional stress tectonic condition. Therefore, we concluded that the northeast–southwest fault orientation is the likely Pidie Jaya fault plane orientation. Further study is conducted to quantify the interactions of the mainshock-aftershocks of Pidie Jaya earthquake.

Keywords

Fault instability • Mw 6.5 Pidie Jaya 2016 earthquake • Mohr diagram

D. P. Sahara (✉) · D. Kusumawati · S. Widiyantoro · A. D. Nugraha · Zulfakriza · N. T. Puspito
Global Geophysics Research Group, Faculty of Mining and Petroleum Engineering, Institut Teknologi Bandung, Bandung, Indonesia
e-mail: david.sahara@gf.itb.ac.id

1 Introduction

Fault instability method explains which surface is more likely to fail or undergo a slip in a given stress field (Morris et al. 1996; Lund and Slunga 1999; Vavryčuk et al. 2013). This concept is based on Mohr failure criterion (Lund and Slunga 1999; Vavryčuk et al. 2013). In a strike-slip earthquake mechanism, one can use aftershock spatial distribution as a constraint to determine the fault plane orientation out of two nodal planes. However, for the Mw 6.5 Pidie Jaya, Aceh 2016 earthquake, the station coverage is limited, and the aftershock distribution depicted an ambiguous trend.

Aceh earthquake (Mw = 6.5) shook the Pidie Jaya district on December 7, 2016 at 5:05 local time. There was no tsunami generated by this earthquake. Twelve days into the earthquake, the National disaster Management Agency of Indonesia (BNPB) reported that this event caused 104 deaths, 395 injuries, and thousands of infrastructures damaged. The aftershocks lasted until a month after the earthquake occurred.

Two perpendicular aftershock clusters shown in Fig. 1 complicate the focal mechanism fault plane interpretation. Fault plane interpretation is indeed important for seismic hazard input. Thus, in this study, we applied fault instability method to interpret Pidie Jaya 2016 earthquake focal mechanism fault plane. We used fault instability method calculation procedure that was proposed by Vavryčuk et al. (2013).

2 Methods and Data

We referred to fault instability calculation procedure from Vavryčuk et al. (2013), because their calculation approach is independent of absolute regional stress magnitude. The Pidie Jaya earthquake focal mechanism data were obtained from three institutions: BMKG, GFZ, and USGS. We calculated mean and standard deviations for each solution. The regional stress magnitude used in this study is referred from well stress

M. Meghraoui et al. (eds.), *Advances in Geophysics, Tectonics and Petroleum Geosciences*, Advances in Science, Technology & Innovation, https://doi.org/10.1007/978-3-030-73026-0_48

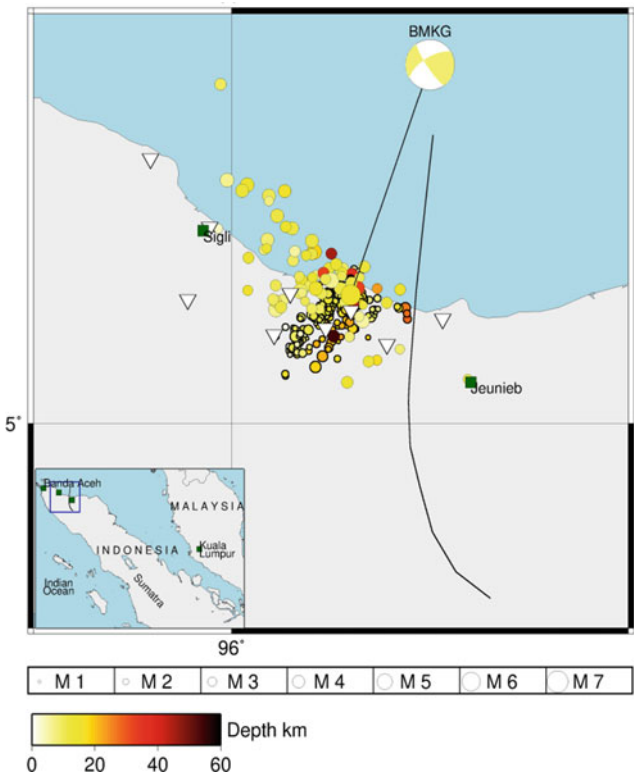

Fig. 1 Distribution of the mainshock and the aftershocks of the Pidie Jaya 2016 earthquake, as well as the focal mechanism from BMKG. The relocated BMKG aftershocks (December 7–19, 2016) are plotted with a thin outline (Supendi et al. 2016). Aftershocks recorded using local station networks from December 14, 2016–January 15, 2017 are plotted with a thick outline (Muzli et al. 2016). Color gradation depicts focal depths. The local station network is plotted with a white inverted triangle symbol. The BMKG stations are not plotted due to out of map boundaries. The black line shows Samalanga-Sipopok fault (SSF) (Barber et al. 2005)

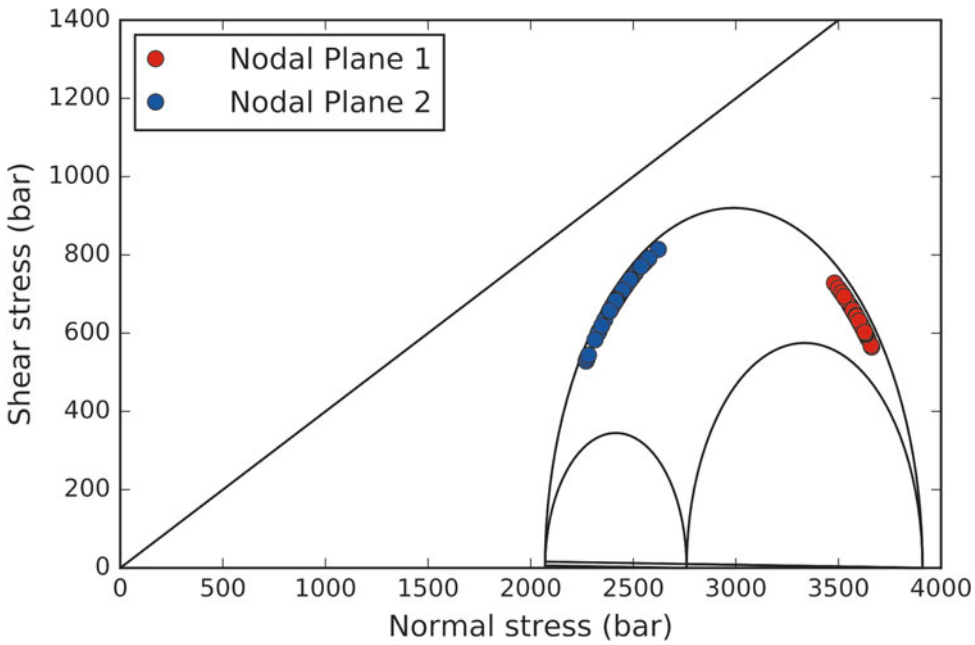

Fig. 2 Normal and shear stresses of planes with different strike values, plotted in Mohr diagram. The friction coefficient is chosen to be 0.4. Normal and shear stresses were calculated at a depth of 11.5 km

Table 1 Pidie Jaya 2016 earthquake focal solutions from various institutions

Institutions	Nodal plane 1			Nodal plane 2		
	Strike	Dip	Rake	Strike	Dip	Rake
BMKG	145°	80°	155°	239°	66°	10°
GFZ	148°	79°	170°	240°	80°	11°
USGS	147°	57°	170°	243°	81°	33°
Mean	146.7°	72°	165°	240.7°	75.7°	18°
Std. deviation	2.16°	18.4°	12.2°	2.9°	11.9°	18.4°

profile in Suban field, South Sumatra (Hennings et al. 2012), i.e., 34 MPa/km for horizontal maximum stress, 24 MPa/km for vertical stress and 18 MPa/km for horizontal minimum stress. The horizontal maximum stress orientation is referred from borehole breakouts and hydraulic fracture tests in central Sumatra region and also focal mechanism inversion in the central part of Sumatra; that is N39° ± 3.9°E (Mount and Suppe 1992; Sahara et al. 2018; Tingay et al. 2010).

3 Results

Fault instability values were mapped into Mohr circle diagram in Fig. 2. The straight line in the figure is called failure envelope. Points, which are near to the failure envelope, are exposed to failure. We could see that the points were clustered into two clusters: red-mark cluster which was further from the failure envelope and blue-mark cluster which was closer to the failure envelope. The red-mark cluster and the blue-mark cluster are the groups of instability values for nodal plane 1 and 2, respectively. Hence, the nodal plane 2, which has northeast–southwest orientation, is more susceptible to failure than nodal plane 1 in this stress condition.

4 Conclusion

In this study, we calculated fault instability (Vavryčuk et al. 2013) values for the M 6.5 Pidie Jaya 2016 earthquake to find the most likely fault plane orientation out of the two focal mechanisms' nodal planes orientations. We used focal solutions from three institutions: BMKG, GFZ, and USGS; by utilizing their mean and standard deviation, the fault instability of several planes was calculated. We also used regional stress magnitude and orientation from South Sumatra (Hennings et al. 2012) and Central Sumatra (Mount and Suppe 1992; Sahara et al. 2018), respectively. Although the locations are different from our study area, the data are still relevant.

We plot the planes in Mohr diagram. Each plane was clustered in the diagram; creating two clusters: one which was far and one which was close to the Mohr's failure envelope. The 'far' cluster has an average instability value of 0.518, while the 'near' cluster has average instability value of 0.932. The 'near' cluster is the group of second nodal planes (nodal plane 2). The higher instability value the more likely it is to fail. Hence, we concluded that nodal plane 2, which has northeast–southwest orientation, is most likely the Pidie Jaya fault plane's orientation. Our result is in agreement with (Muzli et al. 2016)'s finding that is the sinistral fault with northeast–southwest orientation.

References

Barber, A.J., Crow, M.J., Milsom, J.: Sumatra: geology, resources and tectonic evolution, 1st edn. Geological Society of London, London (2005)

Hennings, P., Allwardt, P., Paul, P., Zahm, C., Reid, R., Jr., Alley, H., Kirschner, R., Lee, B., Hough, E.: Relationship between fractures, fault zones, stress, and reservoir productivity in the Suban gas field, Sumatra. Indonesia. AAPG Bull. **96**(4), 753–772 (2012)

Lund, B., Slunga, R.: Stress tensor inversion using detailed microearthquake information and stability constraints: application to Ölfus in southwest Iceland. J. Geophys. Res. Solid Earth **104** (B7), 14947–14964 (1999)

Morris, A., Ferrill, D.A., Henderson, D.B.: Slip-tendency analysis and fault reactivation. Geology **24**(3), 275–278 (1996)

Mount, V.S., Suppe, J.: Present-day stress orientations adjacent to active strike-slip faults: California and Sumatra. J. Geophys. Res. Solid Earth **97**(B8), 11995–12013 (1992)

Muzli, M., Umar, M., Nugraha, A.D., Bradley, K.E., Widiyantoro, S., Erbas, K., Jousset, P., Rohadi, S., Nurdin, I., Wei, S.: The 2016 Mw 6.5 Pidie Jaya, Aceh, North Sumatra, earthquake: reactivation of an unidentified Sinistral fault in a region of distributed deformation. Seismol. Res. Lett. **89**(5), 1761–1772 (2018)

Sahara, D.P., Widiyantoro, S., Irsyam, M.: Stress heterogeneity and its impact on seismicity pattern along the equatorial bifurcation zone of the Great Sumatran Fault, Indonesia. J. Asian Earth Sci. **164**, 1–8 (2018). https://doi.org/10.1016/j.jseaes.2018.06.002

Supendi, P., Nugraha, A.D., Wijaya, T.A.: Relocation and focal mechanism of aftershocks Pidie Jaya earthquake (Mw 6.5) Dec 7th, 2016 using BMKG network. J. Geofisika **15**(03), 19 (2017)

Tingay, M., Morley, C., King, R., Hillis, R., Coblentz, D., Hall, R.: Present-day stress field of Southeast Asia. Tectonophysics **482**(1), 92–104 (2010)

Vavryčuk, V., Bouchaala, F., Fischer, T.: High-resolution fault image from accurate locations and focal mechanisms of the 2008 swarm earthquakes in West Bohemia. Czech Republic. Tectonophys. **590**, 189–195 (2013)

The Perturbation of Background Stress Field Along Sunda Subduction Margin During 2004 Mw 9.1 Off-Sumatra Earthquake

Muhammad Taufiq Rafie, David Prambudi Sahara, Sri Widiyantoro, Wahyu Triyoso, and Andri Dian Nugraha

Abstract

The Sumatra Island, which is close to the active subduction zone between the Indo-Australian and Eurasian plates, experienced numerous earthquakes in the historical past. One of those earthquakes is the 2004 Mw 9.1 off-Sumatra earthquake, considered to be the second largest event ever recorded in history after the 1960's Chilean earthquake (Mw 9.5). To analyze the impact of 2004 Sumatra earthquake in the background stress field along the Sunda margin, we retrieve the principal stress orientations of background seismic activities based on focal mechanisms' solutions. Co-seismic slip data were also being used to compute the static stress changes in the study area. We found a significant counterclockwise rotation of maximum compressive stress axis of around 25° following the 2004 event. This perturbation corresponds to a moderate difference between the mainshock and the background principal stress orientations. This result indicates that the 2004 event caused a redistribution of stress field around the Sunda subduction margin.

Keywords

2004 Sumatra earthquake • Sunda margin • Stress field • Stress changes

1 Introduction

Earthquakes occur as a consequence of stress-releasing processes in the lithosphere. It could alter the pre-state/background stress field during the earthquake cycle when the stress drop for mainshock is near complete or large enough relative to the background stress (Hardebeck and Okada 2018; Hardebeck 2012). Sumatra Island is located around the active ocean-continent plate boundary, and it experienced one of the largest earthquakes in history and is the second largest earthquake after the 1960's Chilean earthquake (Mw 9.5) (Mishra et al. 2004, 2007) that occurred on the December 26, 2004, with a of Mw 9.1 (Ammon et al. 2005). This mega-event occurred by cyclic stress loading from slab pull and buoyancy forces' interaction that caused brittle failure phase around the descending lithosphere (Khan 2007; Khan and Chakrabortty 2009). By understanding the in situ stress evolution due to a significant earthquake, we could reveal the physical processes of earthquake generation and stress rotation using stress perturbation phenomena (Hardebeck and Okada 2018; King et al. 1994).

We have analyzed the stress parameters by inverting the stress orientations before and after the 2004 event to understand how the earthquake modulated the background stress regime.

2 Methods

We used focal mechanisms data with Mw $\geq$ 5.0 and focal depth < 100 km which were compiled from Global Centroid Moment Tensor (GCMT) (Dziewonski et al. 1981; Ekström et al. 2012) and International Seismological Centre (ISC Homapage, 2017) catalogs from June 1976 to December 2014. Those data represent the background seismicity and aftershocks of the 2004 off-Sumatra earthquake. The distribution of those focal mechanisms is explained in Fig. 1. These data are used to generate principal stress orientation

M. T. Rafie (✉)
Geophysical Engineering Program, Faculty of Mining and Petroleum Engineering, Institut Teknologi Bandung, Ganesha 10, Bandung, 40132, Indonesia
e-mail: taufiqrafie@students.itb.ac.id

D. P. Sahara · S. Widiyantoro · W. Triyoso · A. D. Nugraha
Global Geophysics Group, Faculty of Mining and Petroleum Engineering, Institut Teknologi Bandung, Ganesha 10, Bandung, 40132, Indonesia

M. Meghraoui et al. (eds.), *Advances in Geophysics, Tectonics and Petroleum Geosciences*,
Advances in Science, Technology & Innovation, https://doi.org/10.1007/978-3-030-73026-0_49

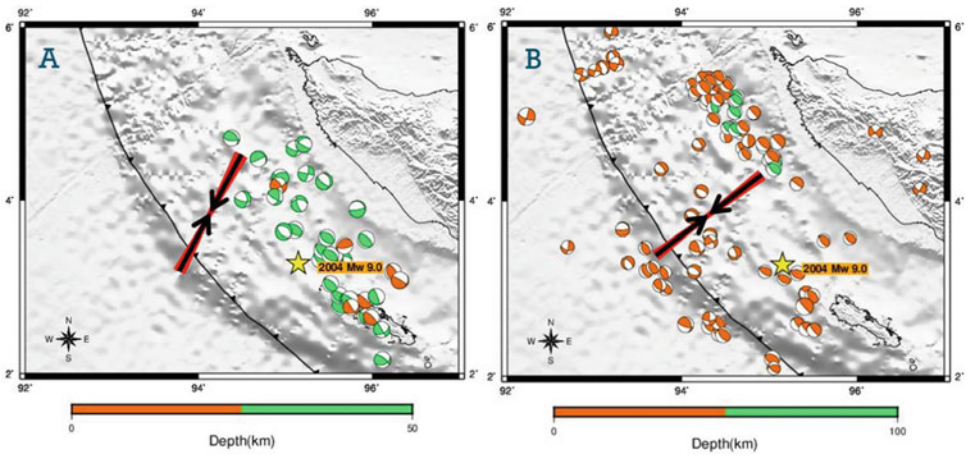

Fig. 1 Map illustrating the focal mechanisms embedded with the orientation of compressive stress axis (σ_1) obtained by stress inversion before the 2004 Sumatra earthquake (**a**) and aftershocks of 2004 Sumatra earthquake (**b**). The red lines indicate the 95% confidence interval of σ_1. The centroid depths are indicated by orange color for shallower depth and green color for deeper depth. The location of 2004 mainshock is marked by the yellow star and background topography from GEBCO with grayscale color palette

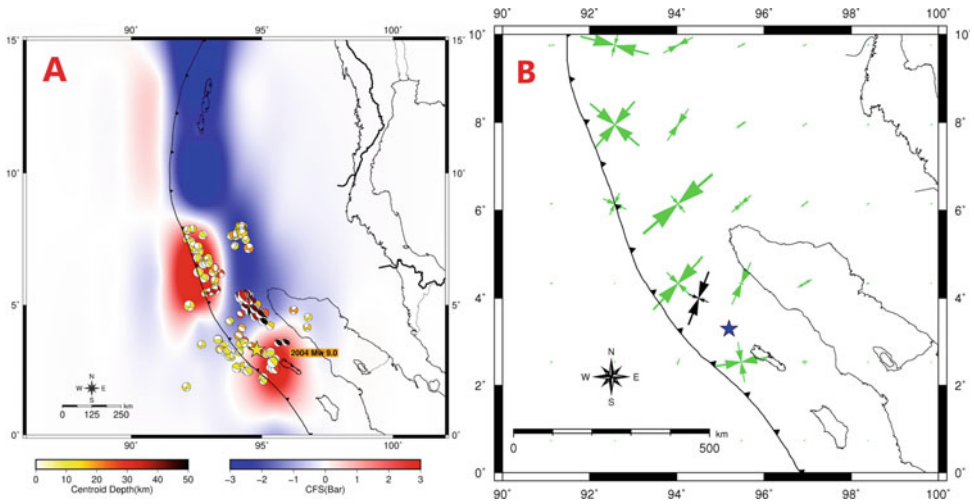

Fig. 2 Co-seismic ΔCFS model of 10 km depth overlapped with focal mechanisms data (**a**) and principal stress orientation pattern of co-seismic slip model (green arrow) embedded with orientation of principal stress before the 2004 event (black arrow) (**b**). The blue star mark indicates the location of 2004 mainshock

through stress inversion (Vavryčuk 2014) which modified the methods from Michael (1984) by applying fault instability constrain approach (Lund and Slunga 1999). Additionally, the co-seismic slip data from Ammon et al. (2005) were used to model static Coulomb-Failure Stress (ΔCFS). The slip data were generated by applying finite fault inversion from waveform data, and ΔCFS was calculated using Coulomb-failure criterion of optimally oriented fault approach (King et al. 1994) with apparent friction coefficient assumed to be 0.4 due to average value based on (Parsons et al. 1999).

3 Results

3.1 Stress Orientation

The 37 focal parameters of background seismicity and 109 focal parameters of aftershocks of the 2004 event were used for stress inversion. The azimuths/plunges of maximum stress axis (σ_1) were found to be around N209° ± 1.3° E/18.5° prior to the 2004 earthquake (Fig. 1a) and N233.5° ± 1.3°E/33.2° for post-2004 events (Fig. 1b) with 95% confidence interval of σ_1. The results, thus, show a rotation of about 25° during the incidence of the 2004 mega-event.

3.2 Coulomb-Failure Stress (ΔCFS) Model

The modeling of ΔCFS is carried out to analyze the effect of large earthquake to the stress changes emphasizing the mechanisms of stress rotation. Figure 2 displays the co-seismic ΔCFS model (a) and principal stress orientation pattern derived from mainshock slip data (b). Figure 2a illustrates the stress transferred into almost northern direction close to Andaman-Nicobar Island.

4 Discussion

Our results show a maximum principal stress rotation of around 25° directed along NNE (see Fig. 1). The results are apparently correlated well with the results performed by Khan et al. (2004) and (Shamim et al. 2019), exhibiting the maximum change of stress field around the vicinity of the 2004 event rupture. Static ΔCFS model of the 2004 event describes stress changes and corresponding accumulation around Nias Island and Northwest Sumatra around ~ 5°N to ~ 8°N, which was correlated with high seismic moment observed by Gui et al. (2019). Also, the latest study by Sengupta et al. (2018) demonstrated that low-b value and low fractal dimension in and around the Sumatra–Andaman earthquake source zone correspond to high stress which is further corroborated by the findings of other studies using different seismological methodologies (Mukhopadhyay et al. 2018; Mishra et al. 2011). From Fig. 2a, the distribution of focal mechanisms with shallow centroid depths (>20 km) is found to be dominantly located in the area of positive ΔCFS value of 10 km depth and few focal mechanisms occurred on stress shadow zone, corresponds with the approach of Coulomb-failure criterion used in this model. Stress assessment based on the assessment of strain-positioning in and around the 2004 and 2005 events demonstrated that both mainshocks were occurred in the locked subduction interface because of inactive trench-parallel strike slip stress components (Ghosh and Mishra 2008).

In order to analyze the influence of the 2004 event in terms of perturbation of the background stress field, we calculated the stress orientation of the 2004 event based on a constitutive equation of stress–strain Hooke's Law. It can be inferred from Fig. 2b that the stress orientation of background stress compared to the 2004 event stress orientation pattern yields a moderate difference, which might have altered the spatial variation of stress condition around Sumatra subduction margin (Hardebeck 2012).

5 Conclusions

We have investigated the perturbation of background stress field due to the 2004 Sumatra earthquake through qualitative and quantitative stress properties interpretations. Our study reveals that the difference of background stress orientation and the 2004 event's stress orientation is around 25°. It advocates a stress rotation which could redistribute the stress condition that has built up during inter-seismic process. This result could contribute in understanding the earthquake-stress interaction, constraining the heterogeneity of stress field due to post-seismic stress reloading and improving seismic hazard evaluation by integrating other results independently obtained from the use of different seismological tools and methods applied to the assessment of earthquake hazard.

References

Ammon, C.J., Ji, C., Thio, H.K., Robinson, D., Ni, S., Hjorleifsdottir, V., Kanamori, H., Lay, T., Das, S., Helmberger, D., Ichinose, G.: Rupture process of the 2004 Sumatra-Andaman earthquake. Science **308**(5725), 1133–1139 (2005)

Dziewonski, A.M., Chou, T.A., Woodhouse, J.H.: Determination of earthquake source parameters from waveform data for studies of global and regional seismicity. J. Geophys. Res. **86**(B4), 2825–2852 (1981)

Ekström, G., Nettles, M., Dziewonski, A.M.: The global CMT project 2004–2010: Centroid-moment tensor for 13,017 earthquakes. Phys. Earth Planet. Inter. **200**, 1–9 (2012)

Ghosh, D., Mishra, O.P.: Possible causes of 12 May 2008 Wenchuan earthquake at Longmenshan collision front, western Sichuan province, central China. Indian Miner **61**, 213–222 (2008)

Gui, Z., Bai, Y., Wang, Z., Li, T.: Seismic b-value anomalies in the Sumatran region: seismotectonic implications. J. Asian Earth Sci. **173**, 29–41 (2019)

Hardebeck, J.L.: Coseismic and postseismic stress rotation due to great subduction zone earthquakes. Geophys. Res. Lett. **39**(21), 1–6 (2012)

Hardebeck, J.L., Okada, T.: Temporal stress changes caused by earthquake: a review. J. Geophys. Res. Solid Earth **123**(2), 1350–1365 (2018)

ISC Homapage. http://www.isc.ac.uk. Last accessed 10 Jan 2017

Khan, P.K.: Lithospheric deformation under pre- and post-seismic stress fields along the Nicobar-Sumatra subduction margin during 2004 Sumatra mega-event and its tectonic implication. Gondwana Res. **12**, 468–475 (2007)

Khan, P.K., Chakrabortty, P.P.: Bearing of plate geometry and rheology on shallow-focus mega-thrust seismicity with special reference to 26 December 2004 Sumatra event. J. Asian Earth Sci. **34**, 480–491 (2009)

Khan, P.K., Shamim, S.k., Mohanty, S.P., Aggarwal, S.K.: Change of stress patterns during 2004 Mw 9.3 off-Sumatra mega-event: Insights from ridge-trench interaction for plate margin deformation. Geol. J. (in press, 2018). https://doi.org/10.1002/gj.3419

King, G.C.P., Stein, R.S., Lin, J.: Static stress changes and triggering of earthquake. Bull. Seismol. Soc. Am. **84**(3), 935–953 (1994)

Lund, B., Slunga, R.: Stress tensor inversion using detailed microearthquake information and stability constrains: application to Ölfus in southwest Iceland. J. Geophys. Res. **104**(B7), 14947–14964 (1999)

Michael, A.J.: Determination of stress from slip data: faults and folds. J. Geophys. Res. **89**, 11517–11526 (1984)

Mishra, O.P., Chakrabortty, G.K., Singh, O.P., Kayal, J.R., Ghosh, D.: Aftershock investigation in Andaman-Nicobar Islands: an antidode to Public Panic? Seismol. Res. Lett. **78**, 591–600 (2007)

Mishra, O.P., Zhao, D., Ghosh, C., Wang, Z., Singh, O.P., Ghosh, B., Mukherjee, K.K., Saha, D.K., Chakrabortty, G.K., Gaonkar, S.G.: Role of crustal heterogeneity beneath Andaman-Nicobar Islands and its implication for coastal hazard. Nat. Hazards **57**, 51–64 (2011)

Mishra, O.P., Kayal, J.R., Chakrabortty, G.K., Singh, O.P., Ghosh, D.: Aftershock investigation in Andaman-Nicobar of the 26 December

2004 earthquake (Mw 9.3) and its seismotectonic implications. Bull. Seismol. Soc. Am. **97**, 71–85 (2007)

Mukhopadhyay, B., Mukhopadhyay, M., Mishra, O.P., Sengupta, D., Dasgupta, S., Elawadi, E., Mondal, P.K., Gonnade, G.D.: Constraining the seismic potentiality analysis for Andaman arc system, NE Indian Ocean. J. Geol. Soc. India **91**, 523–534 (2018)

Parsons, T., Stein, R.S., Simpson, R.W., Reasenberg, P.A.: Stress sensitivity of fault seismicity; a comparison between limited-offset oblique and major strike-slip faults. J. Geophys. Res. **104**, 20183–20202 (1999)

Sengupta, D., Mukhopadhyay, B., Mishra, O.P.: Seismic cycles and trend predictions of earthquakes in Sumatra-Andaman and Burmese subduction zones using temporal b-value and hurst analysis. J. Geol. Soc. India **92**, 661–670 (2018)

Shamim, S.k., Khan, P.K., Mohanty, S.P.: Stress reconstruction and lithosphere dynamics along the Sumatra subduction margin. J. Asian Earth Sci. **170**, 174–187 (2019)

Vavryčuk, V.: Iterative joint inversion for stress and fault orientations from focal mechanisms. Geophys. J. Int. **199**(1), 69–77 (2014)

Azimuth Dependence in Topographical Site Effects: Case of ABZH Broadband Station (North of Algeria)

Khalissa Layadi, Fethi Semmane, and Abdelkarim Yelles-Chaouche

Abstract

Azimuthal variations of site response are observed in ABZH station installed in the topographical irregularity of Bouzeréah Massif (North of Algeria). It is due to the utilization of two groups of seismicity with different azimuth, southeast (Group 1) and southwest (Group 2) of ABZH site. Using the local seismicity of Group 1, ABZH site has a fundamental frequency around 3 Hz with an amplitude of 5 times, using the receiver function technique. Applying this technique on the seismicity of Group 2, ABZH site showed three main peaks at 1, 2 and 3.5 Hz, with amplitudes between 3 and 5 times. Similar curves shape of site response using earthquakes and ambient vibration is obtained around the fundamental frequency, with an underestimation of its amplitude.

Keywords

Topographical site effects • Seismicity • Seismic source • Azimuth

1 Introduction

In site effects study, the same site of investigation can present variations in the fundamental frequency peak, f_0, and its corresponding amplitude using different seismic events. These variations are due to several earthquake parameters such as the frequency content of the incident waves, azimuth, magnitude, seismic source, epicentral distance… or the site itself.

In this study, we focus on ABZH station (Fig. 1a) from the Algerian Digital Seismological Network (ADSN, Yelles et al. 2013) to show one of the cases of dependence between site effects and the incidence angles (azimuth) using different local earthquakes. In Fig. 1b, we show the topographical elevation variation around ABZH station. It is installed on the top of the Bouzaréah massif, and it consists of a metamorphosed gneissic basement of Paleozoic. The obtained results will be compared with H/V curves from ambient noise (HVSRN; Nakamura 1989) to show the relationship between the broad peak and the azimuth dependence in site effects.

2 Data and Methodology

2.1 Earthquake Data

ABZH is a permanent broadband station of ADSN, equipped with QUANTERRA (Q330) digitizer and STS-2 sensor (120 s). In order to estimate the site response at this station using receiver function (RF) technique (Lermo and Chavez-Garcia 1994), we considered a local seismicity from 2010 to 2018 of magnitude (M_L) ranging between 2.8–5.3, with a good signal–noise ratio. The location of the 29 selected events is shown in Fig. 1a.

2.2 Ambient Vibration Data

2-h of ambient vibration data are selected during a calm period in order to estimate the site response of the ABZH station using HVSRN technique.

2.3 RF Technique

To estimate the site effects in ABZH site using RF technique, we used a 50-s window beginning with the S-wave's arrival. After computing the fast Fourier transform (FFT) of

K. Layadi (✉) · F. Semmane · A. Yelles-Chaouche
Centre de Recherche en Astronomie Astrophysique Et Geophysique (CRAAG), Bouzareah, Algeria
e-mail: k.layadi@craag.dz

M. Meghraoui et al. (eds.), *Advances in Geophysics, Tectonics and Petroleum Geosciences*,
Advances in Science, Technology & Innovation, https://doi.org/10.1007/978-3-030-73026-0_50

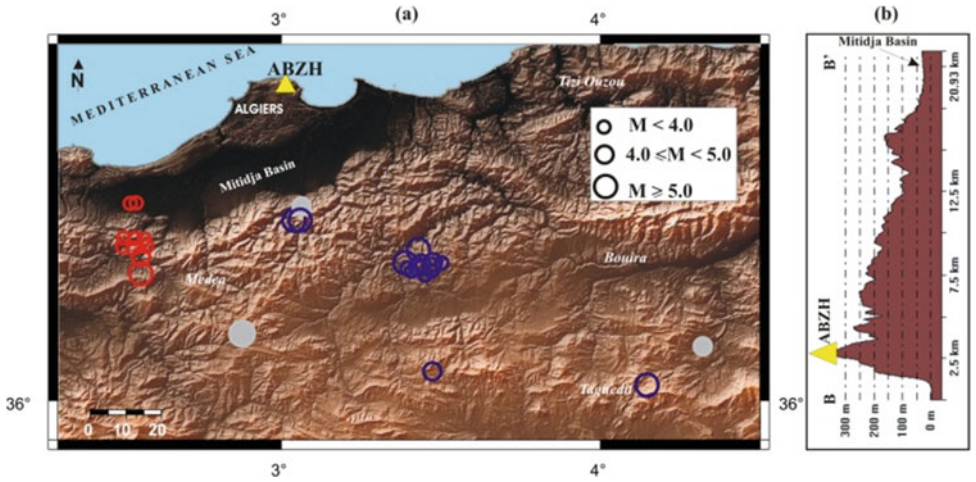

Fig. 1 **a** Localization of ABZH station and the used local seismic events for estimating site response by receiver function (RF) technique in Fig. 2. Three groups of seismic events: blue circles (Group 1), red circles (Group 2) and gray-filled circles (Group 3). **b** Elevation variation of the Bouzaréah massif around ABZH station

each individual window of the three components (east–west [EW], north–south [NS], and vertical [Z]), the amplitude spectrum, $A(f)$, was smoothed using the Konno–Ohmachi algorithm (Konno and Ohmachi 1998), with a b-value of 40. The spectral ratio was calculated in the RF technique using Eq. (1).

$$RF = \frac{\frac{1}{\sqrt{2}}\sqrt{A(f)_{EW}^2 + A(f)_{NS}^2}}{A(f)_Z} \quad (1)$$

2.4 HVSRN Technique

In this technique, for data analysis, we used the Geopsy code (Wathelet 2005). Using the auto-window selection module of the software, a number of time windows with durations of 50-s each were processed for the [EW], [NS] and [Z] components with the same manner as in the RF technique.

3 Results

The computations of the individual RF curves of each event were conducted to separate them into three groups (Fig. 2): curves with clear f_0 at $\sim$ 3 Hz (Group 1); curves with three peaks at 1, 2 and 3.5 Hz (Group 2) and unclear curves (Group 3). The seismic events used in each group are shown in Fig. 1a, blue, red and gray circles for Group 1, 2 and 3, respectively. The mean RF curve of each group (RF_GRP1, RF_GRP2 and RF_GRP3) is computed and plotted in Fig. 2, with $\pm$ standard deviation (σ).

To explain this difference in site response, principally between Group 1 and 2, according to Fig. 1a, the azimuth played the main role, whatever the magnitude and the epicentral distance of the selected seismic events. The Group 2 dataset is seismic events coming from the southwest of ABZH site, whereas those of Group 1 are coming from south and southeast. About the seismic events of Group 3, they are coming from the same direction as Group 1. The unclear curve using earthquakes of Group 3 is independent of magnitude, epicentral distance and azimuth.

In the second part of this study, we gathered all the seismic events of Fig. 1a to estimate the site response in ABZH station by RF technique. The averaged or global obtained RF curve (RF_GLB) is plotted in Fig. 3 and compared to the HVSRN curve of ABZH site (broad peak at $\sim$ 3 Hz). According to this figure, the shape of RF_GLB curve is similar to the HVSRN one, but with more important amplitudes (2 times), we talk about the irregularities before f_0 of RF_GLB and HVSRN, compared to RF_GRP1 which is a clear curve (Fig. 2).

4 Discussion

Our obtained results at ABZH site using all earthquakes plotted in Fig. 1a with different azimuths (RF_GLB curve in Fig. 3) agree well with the HVSRN curve with a broad peak at 3 Hz, where the ambient vibrations come from all directions. The seismic events of Group 2 are responsible for the irregularities before 3 Hz (f_0) in the RF_GLB curve, while the seismic events of Group 1 are responsible for the appearance of f_0 in RF_GLB (Fig. 3). According to

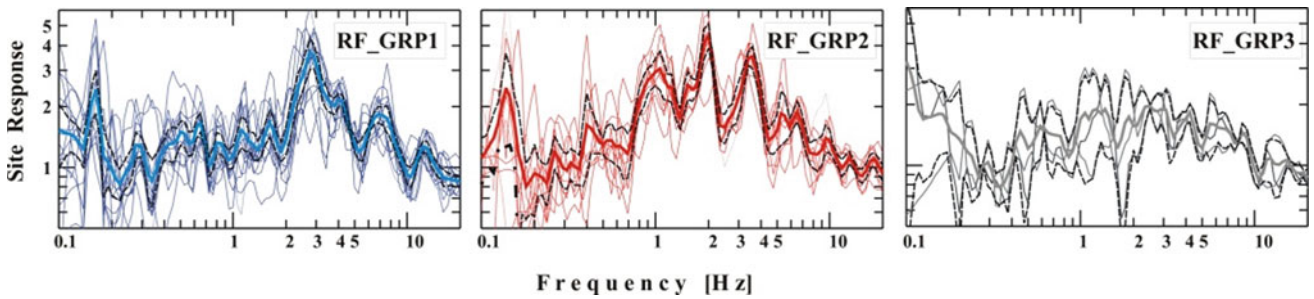

Fig. 2 Individual (thin lines) and mean (thick lines) RF curves obtained for each group using earthquake data of Fig. 1a. Group1: clear curve with f_0 at $\sim$ 3 Hz (RF_GRP1); Group 2: 3 peaks at 1, 2 and 3.5 Hz (RF_GRP2); Group 3: unclear curve (RF_GRP3). Dashed lines are $\pm$ σ

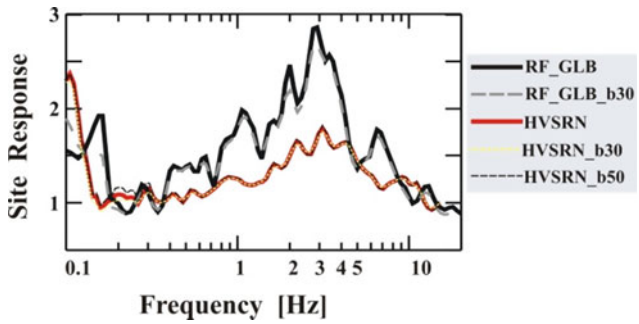

Fig. 3 Comparison between HVSRN (red line) and RF_GLB (black line) curves considering all the seismicity in Fig. 1a. Dashed lines are site responses using the Konno–Ohmachi algorithm with 30 and 50 of b-values

Uebayashi et al. (2012) and Bonnefoy-Claudet et al. (2008), the broad peak obtained by HVSRN technique is due to the local irregular topography of sediment-bedrock interface, and the low impedance contrast between them, respectively. In our case, it can be explained by the influence of the azimuth. The site effects can be influenced by the seismic source location and focal mechanism (Parvez et al. 2006), since the active tectonics in the northern part of Algeria are variable from a geological and a seismological point of view.

Regarding the influence of the smoothing on the irregularities in the site response estimated by RF and HVSRN techniques, we considered a b-value of 30 in the spectral analysis. Results are plotted in Fig. 3. The obtained curves are not changed considerably, which can explain that the irregularities before 3 Hz are caused by the geological and/or topographical contexts. We considered a b-value of 50 in HVSRN technique, and the obtained curve is not changed strongly (Fig. 3).

The underestimated frequency peak amplitude using ambient vibration data, compared with earthquake data (Fig. 3), is well known and was already discussed (e.g., Layadi et al. 2016). In this study, it can be explained by the limited data of seismic events of Group 3 (three events) which give unclear curve (Fig. 2). The amplitude of f_0 identified by the seismic events of Group 1 (Fig. 2) is higher than thus of RF_GLB curve (Fig. 3) and is due to consideration of the seismic events of Group 3 (unclear curves) and the messing of f_0 at 3 Hz in the RF_GRP2 curve (Fig. 2).

5 Conclusions

According to this study, in the ABZH station, the estimated site effects can be influenced by the azimuth of the recorded earthquake, and it can modify the shape of the site response curve around and near f_0. Our results are confirmed by the HVSRN technique, where irregularities are shown in a broad peak independent of the used smoothing. The origin of the amplification at ABZH station can be explained by a topographical site effect, regarding to its geological formation (metamorphic rock) and the complex topography of Bouzeréah Massif. This preliminary analysis on the azimuthal dependence in site effects can be completed by the influence of the seismic sources responsible for the used seismicity.

References

Bonnefoy-Claudet, S., Baize, S., Bonilla, L.F., et al.: Site effect evaluation in the basin of Santiago de Chile using ambient noise measurements. Geophys. J. Int. **176**, 925–937 (2008)

Konno, K., and T. Ohmachi.: Ground-motion characteristics estimated from spectral ratio between horizontal and vertical components of microtremor, Bull. Seismol. Soc. Am. 88, 228–241 (1998)

Layadi, K., Semmane, F., Yelles-Chaouche, A.K.: Site-effects investigation in the city of Chlef (formerly El-Asnam), Algeria, using earthquake and ambient vibration data. Bull. Seismol. Soc. Am. **106** (5), 2185–2196 (2016)

Lermo, J., Chavez-Garcia, F.J.: Site effect evaluation at Mexico City: dominant period and relative amplification from strong motion and microtremor records. Soil Dynam. Earthq. Eng. **13**, 413–423 (1994)

Nakamura, Y.: A method for dynamic characteristics estimation of subsurface using ambient noise on the ground surface. Q. Rep. **30**, 25–33 (1989)

Parvez, I.A., Vaccari, F., Panza, G.F.: Influence of source distance on site-effects in Delhi city. Current Science (2006)

Uebayashi, H., Kawabe, H., Kamae, K.: Reproduction of microseism H/V spectral features using a three-dimensional complex topographical model of the sediment-bedrock interface in the Osaka sedimentary basin. Geophys. J. Int. **189**, 1060–1074 (2012)

Yelles-Chaouche, A., Allili, T., Alili, A., et al.: The new Algerian Digital Seismic Network (ADSN): towards an earthquake early-warning system. Adv. Geosci. **36**, 31–38 (2013)

Wathelet., M.: Array recordings of ambient vibrations: Surface-wave inversion, Ph.D. thesis, University of Liège, Belgium. (2005)

Seismic Site Response Assessment Using Predominant Periods and Shear Wave Velocity Estimation in Nador (N-E of Morocco)

Aboubakr Chaaraoui, Mimoun Chourak, José A. Peláez, and Seif-eddine Cherif

Abstract

Local seismic hazard is influenced by the variation of soil parameters which modulates the propagation of seismic waves through soil. Nador is one of the cities in Morocco which is located in a seismically hazardous region. Investigations using ambient noise and SPT-N values were conducted in order to characterize site effects in the urban area of Nador. The predominant period values obtained vary between 0.2 and 0.5 s; whereas shear wave velocity in superficial soft sediment varies from 156 to 212 m/s. The geotechnical conditions are also used to identify the areas of high impedance contrast. It is found that soil with high predominant period undergoes significant amplification. This is observed in the center and near to the shore of Nador city which is underlaying deep soils with clay and sandy clay deposits. The provided results can be useful for seismic risk studies in the region.

Keywords

Nador Urban area • Predominant period • Shear wave velocity • Sediment deposits • Impedance contrast

1 Introduction

Study of local seismic hazard is necessary for Earth sciences and urbanism. It is linked to site effects, which can be influenced by the characteristics of soils, possibly resulting in the amplification of seismic waves during earthquakes (Parolai 2012). Many studies use dynamic parameters (predominant period and shear wave velocities) to determine the site response in different areas (Panjamani and Parihar 2011; Pilz et al. 2009; Sil and Sitharam 2013; Lachet et al. 1996).

Nador is located in northeastern Morocco within a geological basin. The geology of the basin is made up of sedimentary deposits of quaternary age with different thicknesses and a volcanic substratum in the Gourougou Mountain (Achalhi 2016). The Moroccan seismic code (Le Reglement Marocain de Construction Parasismique 2002) classifies the region as a high seismicity area, with a PGA value typically of 0.17 g for a return period of 475 years. The main goal of this study is to prepare a map of local seismic hazard for Nador city in terms of predominant period.

2 Data and Methodology

The geotechnical characteristics of the Nador region was obtained from the analysis of fifty three different geotechnical boreholes, providing the lithology and the thickness of shallow layers (Fig. 1).

Shear wave velocity V_s: Seven SPT-N measurements were conducted to determine the N-value (Number of blows), and therefore, we used Eq. (1) given by Hanumantharao and Ramana (2008) to estimate values of shear wave velocities (V_s) in the basin:

$$V_s = 82.6\,N^{0.43}\ \text{m/s} \quad (1)$$

A. Chaaraoui (✉)
Laboratory of Applied Geosciences, Faculty of Sciences, Mohamed Premier University, Oujda, Morocco
e-mail: a.chaaraoui@ump.ac.ma

M. Chourak
Department of Mechanics and Applied Mathematics, National School of Applied Sciences, Mohamed Premier University, Oujda, Morocco

J. A. Peláez
Department of Physics, University of Jaén, Jaén, Spain

S. Cherif
Laboratoire Géoressource, Géo-environnement et Genie Civil, Faculty of Sciences and Technologies of Marrakech, Cadi Ayyad University, Marrakech, Morocco

M. Meghraoui et al. (eds.), *Advances in Geophysics, Tectonics and Petroleum Geosciences*, Advances in Science, Technology & Innovation, https://doi.org/10.1007/978-3-030-73026-0_51

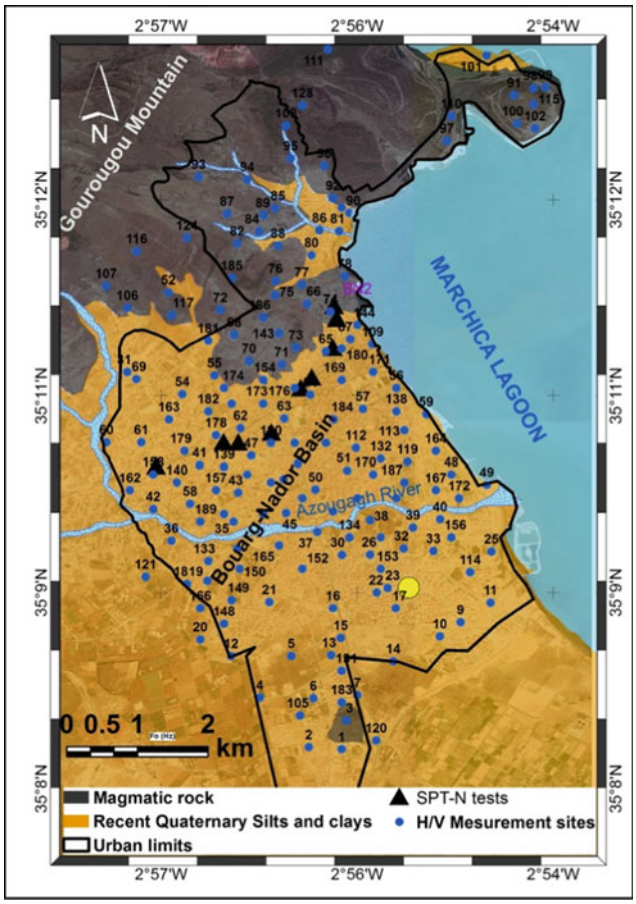

Fig. 1 Lithology at Nador city and location of boreholes and H/V measurements

where:

V_s = shear wave velocity at a particular depth.

N = SPT-N value at the same depth.

The average shear wave velocity is calculated using the formula (NEHRP 2003):

$$V_{Sd} = \Sigma d_i / \Sigma (d_i V_{Si}) \quad (2)$$

where:

V_{sd} = the shear wave velocity,

Vsi = the shear wave velocity of any layer in m/s,

di = the thickness of any layer (between 0 and 30 m).

Geological units in Nador give a first knowledge on the shear wave velocity. Many studies (Pitilakis et al. 2013; Wills and Clahan 2006) and several Building codes (NEHRP, EC8) give correlation between shear wave velocities and geology. The soil in the basin contains soft sediments of fluvial and littoral origin dating from a recent quaternary age down to a depth of 20 m. This formation has V_s values ranging from 150 to 360 m/s.

On the foot of the Gourougou Mountain (Fig. 1a) in the west and north-west of the region, the soil is composed of two layers, including the sedimentary rocks, and from a depth of 6.5 m basaltic volcanic rocks, constituting the basement. The Vs value for the basalts is larger than 760 m/s. The origins and properties of the two layers are different, showing strong impedance contrast between them.

The H/V technique (Nakamura 1989): H/V spectral ratios using ambient vibration data are widely used to characterize site response, particularly in urban areas (Parolai 2012). About 190 background noise recordings were conducted in the urban center and surrounding area of Nador town (Fig. 1b). Ambient vibrations were recorded with a three components material: a CMG-6TD seismometer, a laptop allowing the visualization of the records in the field, and in situ verification. The H/V analysis of the recorded noise was conducted using the SESAME guideline (Bard et al. 2004) and the Geopsy software (Fig. 2). The two types obtained from analysis of H/V spectrum, (a): a clear peak with amplification values superior than 2.5 and (b) a flat curve which there is a non-exhibition of amplification in the measurement's sites.

3 Results and Discussion

Using the correlation of shear wave velocity with N-values obtained from standard penetration, the mean of shear wave velocity values of soil for the different depths are computed using the formula given by Hanumantharao and Ramana (2008). The mean of superficial V_s values for the different depths is varying from 156 to 212 m/s, and these areas correspond to the central part of the city characterizing the recent quaternary formation. The soil is classified as a very dense soil and soft rocks depending on the classification of Moroccan seismic code (Le Reglement Marocain de Construction Parasismique 2002).

The analysis of H/V curves allow us to estimate the predominant period values in Nador city, the distribution of predominant period values range between 0.2 and 0.5 s (Fig. 3), approximately. The predominant period values describe the surface lithology, which is covered by sediments of loose sands, limestone, and sandy clay materials. Borehole data in soft soils show that the thickness of silt and clay are over 40 m near the shoreline, and decreases as we move away to the west and to the Gourougou Mountain.

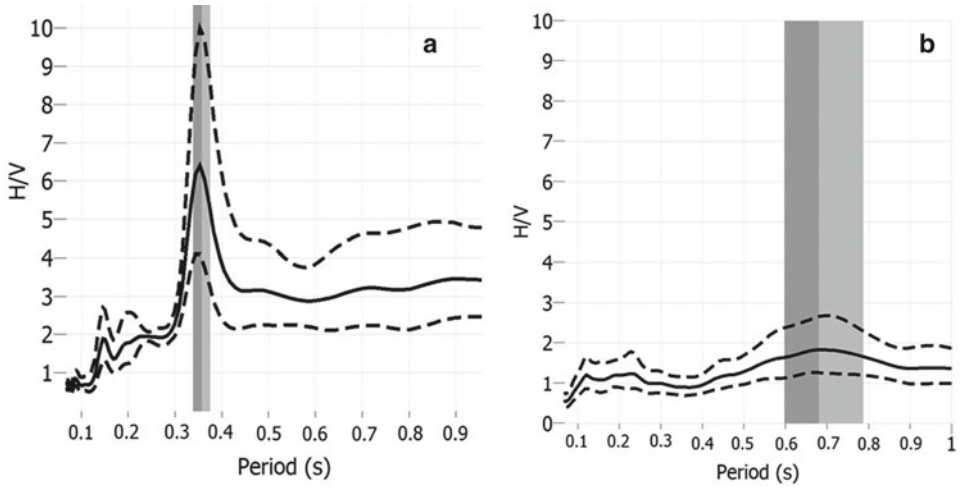

Fig. 2 Site responses (H/V curves) with mean and standard deviations obtained for ambient noise measurements, **a** a clear peak, **b** a non-clear peak

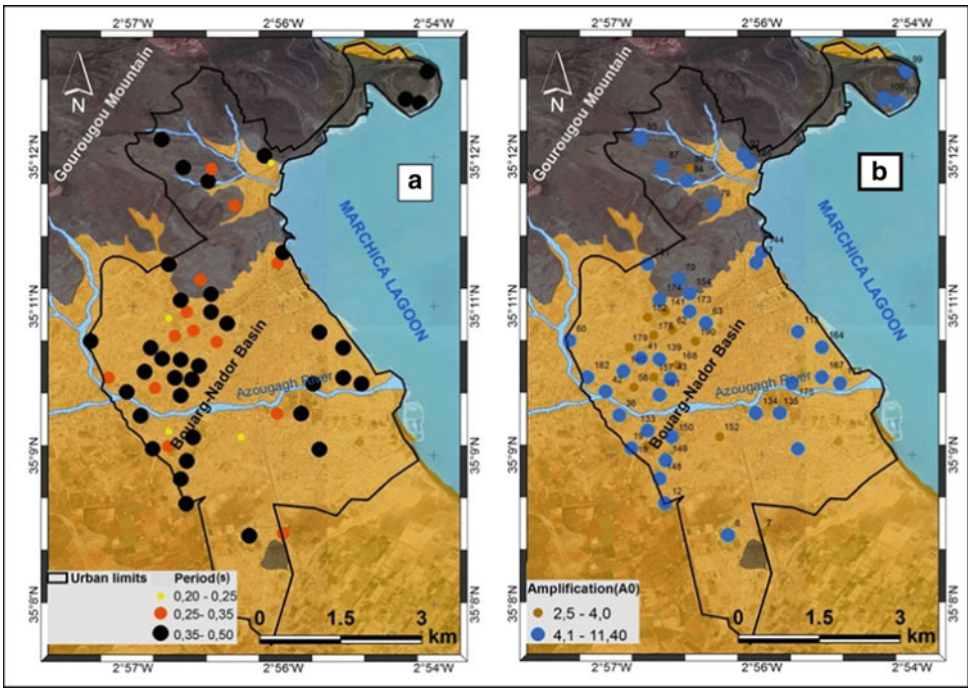

Fig. 3 **a** Distribution of predominant obtained periods (T_0). **b** Distribution of amplification factors A_0

High period values are observed on the Eastern part (near to the lagoon). These values are gradually decreasing to the west along the river. The same formation contains a large range of period values, which could be related to the complex geological setting of the area. The results of predominant period obtained in Melilla (Casado et al. 2017) (14 km from Nador) are ranging from 0.12 to 0.5 s which approximately corresponds to the same ranges obtained in this study.

The variation of the observed periods around the Azougagh River (Fig. 3), and in some mountainous regions, is due to several factors such as the composition of soil layers affecting the impedance contrast due to soil density, velocity, and thickness of sediments.

4 Conclusions

This study gives a first quantification of the site response in Nador city. It provides predominant periods and shear wave estimation for the different existing types of soil. These parameters are important to assess the local seismic hazard.

The obtained predominant periods in the urban area range between 0.2 and 0.5 s, with an amplification factor, obtained from H/V curves, ranging from 2.5 to 11.4 (Fig. 3). Even the amplification obtained does not reflect the real amplification that can be exhibited in a seismic action. The values of predominant periods are important in term of spectral

coincidences with the building period of the different structures in Nador.

The shallow shear wave velocity in Nador city was calculated through analyzing the standard penetration test for seven measurements. The estimation of shear wave velocity gives information about soil classification. All values in the basin are in range of: 150 m/s < V_s < 360 m/s, which corresponds to a stiff and soft soil, and this classification is very important for engineers in order to make a good building concept.

References

Achalhi, M.: Chronostratigraphie et sédimentologie des bassins néogènes de Boudinar et d'Arbaa Taourirt, Rif oriental, Morocco (2016)

Bard, P.Y., Duval, A.M., Koehler, A., Rao, S.: Guidelines for the implementation of the H/V spectral ratio technique on ambient vibrations measurements. Proc. Interpret. Bull. Earthq. Eng. **169**, 1–62 (2004)

Casado, C.L., Henares, J.G., Delgado, J., Pelaez, J.A., Henares, J.: HVSR estimation of site effects in Melilla (Spain) and the damage pattern from the 01/25/2016 Mw 6.3 Alborán Sea earthquake. Nat Hazards. (2017)

Hanumantharao, C., Ramana, G.: Correlation between shear wave velocity and N value for Yamuna sand of Delhi. J. Earth Syst. Sci. **117**, S2 (2008)

Lachet, C., Hatzfeld, D., Bard, P.Y., Theodulidis, N., Papaioannou, C., Savvaidis, A.: Site effects and microzonation in the city of Thessaloniki (Greece) comparison of different approaches. Bull. Seismol. Soc. Am. **86**, 1692–1703 (1996)

Le Reglement Marocain de Construction Parasismique, Ministère de l'Habitat et de la Politique de la Ville (2002 version 2011)

Nakamura, Y.: A Method for Dynamic Characteristics Estimation of Subsurface Using Microtremors on the Ground Surface. Railwai Technical Researtch Institute Report (1989)

NEHRP: Recommended Provisions for Seismic Regulations for New Buildings and Other Structures (FEMA). National Institute For Building Sciences, Washinton (2003).

Panjamani, A., Parihar, A.: Amplification based on shear wave velocity for seismic zonation: comparison of empirical relations and site response results for shallow engineering bedrock sites. Geomech. Eng. 189–206 (2011)

Parolai, S.: Investigation of Site Response in Urban Areas by Using Earthquake Data and Seismic Noise, pp. 1–34. GFZ, German Research Centre for Geosciences (2012)

Pilz, M., Parolai, S., Felipe, L., Campos, J.: A comparison of site response techniques using earthquake data analysis and ambient seismic noise in large urban areas of Santiago de Chile. Geophys. J. Int. 713–728 (2009)

Pitilakis, K., Riga, E., Anastasiadis, A.: New code site classification, amplification factors and normalized response spectra based on a worldwide ground-motion database. Bull. Earthq. Eng. 925–966 (2013)

Sil, A., Sitharam, T.G.: Dynamic site characterization and correlation of shear wave velocity with standard penetration test 'N' values for the city of Agartala, Tripura State, India. Pure Appl. Geophys. (2013)

Wills, C.J., Clahan, K.B.: Developing a map of geologically defined site-condition categories for California. Bull. Seismol. Soc. Am. 1483–1501 (2006)

On the Influence of Earthquakes and Soil Characteristics on the Seismic Response and the Performance of Isolated Bridges

Nastaran Cheshmehkaboodi and Lotfi Guizani

Abstract

Seismic isolation technology is an effective mean of reducing seismic risk and enhancing the structural seismic performance. However, some parameters affect and mitigate the efficiency of this technology: earthquake inputs and soil characteristics. The main purpose of this study is to investigate the simultaneous effects of different records and flexible soils on isolated bridges. For this reason, an isolated bridge is assumed to be at different distances from the ruptured fault (Rrup) to represent the near-fault (NF) and far-field (FF) situations. These records are extracted on different soils which are categorized based on their shear velocity to represent different soils' behaviors and characteristics. Nonlinear time history analyses (NTHAs) are carried out on a typical isolated bridge model with the SAP2000 software. Responses in terms of deck acceleration, base shear, displacement and the performance of the isolation units are studied. Results demonstrate that for NF zones, the consideration of the soil effects is imperative. In soft soils, all seismic responses are amplified, leading to higher force and displacement demands. In such zones, not considering this fact during the design, results in largely insufficient displacement and force capacities of the isolated bridge system are seriously harming its seismic performance.

Keywords

Seismic isolation • Earthquake characteristics • Near-fault • Far-field • Soil effects • Seismic response • Bridges

1 Introduction

Seismic isolation technology is based on decreasing the fundamental frequency of the structural vibration to a value less than the predominant energy-containing frequencies of the earthquake in order to reduce the seismic force demand to or near the elastic capacity of the structural members, thereby eliminating or drastically reducing inelastic deformations (Soneji 2008). According to the recent studies and based on the evidences from past earthquakes, record characteristics and soil effects are two among the most important parameters impacting the seismic performance of the isolated structures (Roussis 2003; Jonsson 2010). Ground motion records obtained in major earthquakes have shown that the characteristics of NF are particularly different from FF records. NF records often contain strong and long period velocity pulses that could cause severe structural damages (Galal and Naimi 2008; Choi 2010). These records change drastically in their frequency contents by passing through the different soils and can be more destructive for infrastructures located on soft soils leading to higher demand in terms of displacements and shear forces by negatively influencing the isolated system (Worku 2014; Castaldo and Ripani 2016; Castaldo and Tubaldi 2018). Different methods and software programs were used to provide reliable soil models and structural behaviors to help researchers and designers attain more dependable predictions of bridges' seismic performances. Soil materials exhibit a diverse range of complex constitutive behaviors, which makes the development of numerical models quite challenging (Beresnev 1996; Neethu and Das 2018). Some soils exhibit nonlinear behavior with gradual softening, which manifests as a decrease in shear modulus with increasing strain. Previous studies have demonstrated the effects of soft soils on seismic responses of bridges, and they showed that neglecting the soil effects leads to underestimating the bridge damage potential (Soneji 2008; Castaldo and Ripani 2016; Chouw and Hao 2005). According to few studies, seismically isolated bridges are

N. Cheshmehkaboodi (✉) · L. Guizani
University of Québec, École de technologie supérieure, Montreal, Canada
e-mail: nastaran.cheshmehkaboodi.1@ens.etsmtl.ca

M. Meghraoui et al. (eds.), *Advances in Geophysics, Tectonics and Petroleum Geosciences*,
Advances in Science, Technology & Innovation, https://doi.org/10.1007/978-3-030-73026-0_52

very sensitive to NF records and soft soil effects (Castaldo and Ripani 2016; Liao 2004). The objective of this study is to investigate the simultaneous effects of record characteristics including NF and FF on different soils with the changing of the frequency of records based on their characteristics according to the Canadian Standards Association (CSA 6-14) (CHBDC 2014).

2 Selected Records and Case Study Bridge Model

Twenty-one (21) records of Northridge (1994), Kobe (1995) and Parkfield (2004) earthquakes were extracted from the PEER database Web site (PEER Homepage 2019). These earthquakes were chosen because they are among the most destructive earthquakes. Additionally, there is a rich database of these records at different distances from the epicenter, Rrup, to represent NF and FF situations as well as soil types to represent the soil effects. Records were chosen nearly at the same distances and soil classes for all three earthquakes. The purpose of using real measured records is to better take into account the observed changes in the records' characteristics by passing through the different soil layers instead of software predictions. Records and site classes are classified according to the CSA 6–14. Nine (9) of the 21 records are in a distance of 10 km from the epicenter (R_{rup} less than 10 km) and are considered as NF records. NF records have higher characteristic values especially in terms of peak ground velocity (PGV), specific energy density and damage index. These features cause higher seismic responses, and such signals impose a very high input energy to the structure at the early stages of the records (Liao 2004). As the main purpose of this study is to investigate the simultaneous effects of NF and FF on different soils, the effect of different source mechanisms is not considered. Spectral accelerations of Northridge earthquake, as an illustration of the effects of different soil classes on records' characteristics extracted from PEER, are shown in Fig. 1. Drastic changes in the maximum response acceleration and period elongation in soft soils are observed and point out the importance of considering soil classes for the seismic analysis of bridges.

The selected case study bridge with conventional and isolated designs is chosen from Alper Ucak's research work (Ucak and Tsopelas 2008). The bridge has two equal spans supported on a circular 30 MPa concrete pier with 5.2-m height and 1.1-m diameter. The deck is a uniform solid slab with a total mass of 265 KN. The isolation system is designed for a period $T = 2.0$ s, and the displacement capacity of the isolator is 7.0 cm. Assuming the bridge is in Montreal, Canada, the hysteresis parameters, the behavior of the isolation system and the bridge 3D model are shown in Fig. 1. The isolation system is lumped at the central pier (free moving bearings at abutments and fixed base of the pier), and only the longitudinal direction is studied. NTHAs were conducted in SAP2000 (Wilson 2017). The results are discussed in the following section.

3 Results

The isolation hysteresis loops, obtained from NTHA, are shown in Fig. 2. They illustrate that the isolator displacement and energy dissipation allocate the highest amounts on soft soils and NF records. The dissipated energies within the hysteresis loops as well as shear forces are higher for the mentioned condition. In FF areas, the farther the distance

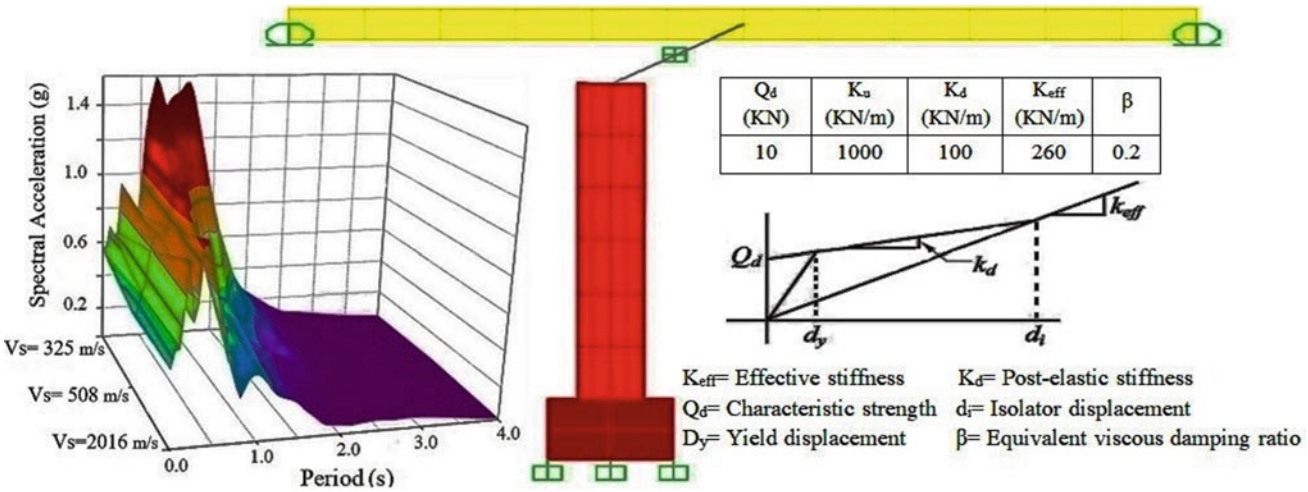

Fig. 1 Left side—spectral acceleration of Northridge records on different soils, R_{rup} = 7 km; right side—isolated bridge model and hysteresis primary curve parameters

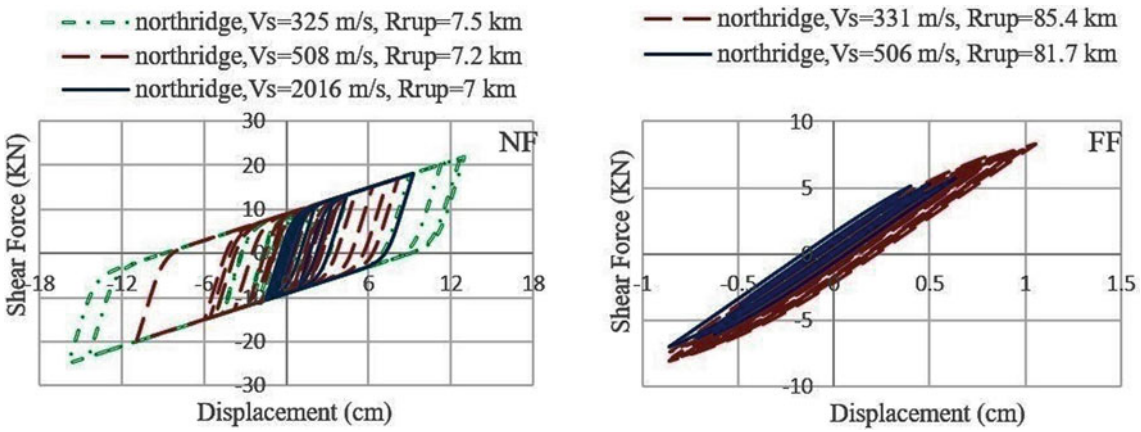

Fig. 2 Isolation hysteresis loops: left side—NF records (R_{rup} < 10 km), right side—FF records

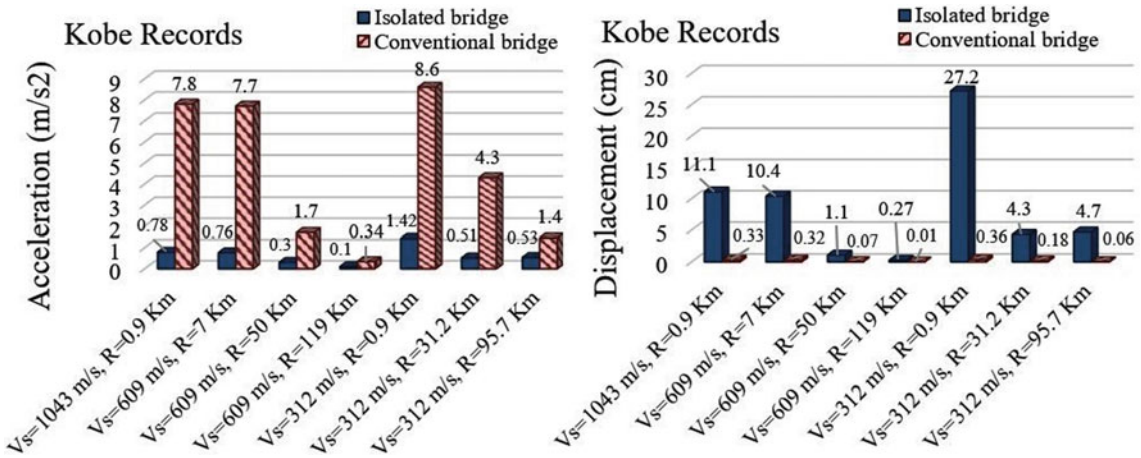

Fig. 3 Left—maximum acceleration responses, right—maximum deck displacements

away from a ruptured fault results in higher responses and displacement demands on soft soils. The maximum acceleration and isolation displacement responses for Kobe records are presented in Fig. 3. It is obvious that the seismic isolation has considerably reduced the seismic acceleration forces by a factor up to 10 in stiff soils, while this factor is only 2 in soft soils for FF records which shows that maximum reduction is obtained for stiff soils.

The maximum deck displacements for isolated bridges are 27.2, 15.9 and 6.7 cm for Kobe, Northridge and Parkfield records, respectively, and they are related to NF on soft soils' records. It should be mentioned that more than 95% of the deck displacement takes place within the seismic isolation system. In the case of Kobe and Northridge records, the isolator displacements are nearly 4 and 2 times more than the isolator displacement capacity, which is 7 cm. This shows that the amount of isolation displacement demand is higher in NF zones, especially on soft soils. This trend is the same for base shear responses, and the maximum responses are related to NF records on soft soils. As it is shown in Table 1, in NF zone (R = 0.9 km), the base shear force increased nearly 3 times (28,000 N vs. 10,500 N) in soft soils (V_s = 312 m/s) compared to stiff soils (V_s = 1045 m/s) in the case of Kobe records. For the other two earthquakes, the trend is the same by a factor of 2.

4 Conclusions

The seismic responses of an isolated bridge subjected to NF and FF records on different soils by NTHA were compared, and the following results were obtained:

1. In NF records, all mentioned seismic responses are amplified for the isolated and conventional bridges. These increasing trends are more severe on soft soils, and this effect should be considered in the design steps for the bridges under these circumstances.

Table 1 Base shear forces for isolated bridge and Kobe records

Record	1	2	3	4	5	6	7
V_s (m/s)	1045	609	609	609	312	312	312
Rrup (Km)	0.9	7	50	119	0.9	31.2	95.7
Shear force (N)	10,500	16,200	3100	500	28,000	9900	4700

2. In the case of the isolated bridge, NF records and soft soils lead to the higher demands in terms of displacements, 4 and 2 times more than the designed displacement in the case of Kobe and Northridge records. Ignoring this issue during the design leads to a large underestimation and possible failure of the isolation system and the bridge during a strong NF earthquake on soft soil sites.
3. In soft soils, the amount of the reduction in acceleration responses of the isolated bridge was limited. The reduction factor is (8–10) for all records in NF located on stiff soils, while it dropped to the factor of 2 for FF records on soft soils. It shows that seismic isolation is more efficient for firm or rock soils than soft soils. A careful attention and scrutiny are required for designing these technologies, depending on the structure distance from active faults and the type of soil where it is located.

References

Association, Canadian Highway Bridge Design Code (CHBDC), CSA Standard S6–14 (2014)

Beresnev, I.A., et al.: Nonlinear soil response—a reality? Bull. Seismol. Soc. Am. **86**(6), 1964–1978 (1996)

Castaldo, P., Ripani, M.: Optimal design of friction pendulum system properties for isolated structures considering different soil conditions. Soil Dyn. Earthq. Eng. **90**, 74–87 (2016)

Castaldo, P., Tubaldi, E.: Influence of ground motion characteristics on the optimal single concave sliding bearing properties for base-isolated structures. Soil Dyn. Earthq. Eng. **104**, 346–364 (2018)

Choi, H., et al.: Experimental study of reinforced concrete bridge columns subjected to near-fault ground motions. ACI Struct. J. **107** (1), 3–12 (2010)

Chouw, N., Hao, H.: Study of SSI and non-uniform ground motion effect on pounding between bridge girders. Soil Dyn. Earthq. Eng. **25**(7–10), 717–728 (2005)

Galal, K., Naimi, M.: Effect of soil conditions on the response of reinforced concrete tall structures to near-fault earthquakes. Struct. Design Tall Spec. Build. **17**(3), 541–562 (2008)

Jonsson, M., et al.: Earthquake response of a base-isolated bridge subjected to strong near-fault ground motion. Soil Dyn. Earthq. Eng. **30**(6), 447–455 (2010)

Liao, W., et al.: Comparison of dynamic response of isolated and non-isolated continuous girder bridges subjected to near-fault ground motions. Eng. Struct. **26**(14), 2173–2183 (2004)

Neethu, B., Das, D.: Effect of dynamic soil–structure interaction on the seismic response of bridges with elastomeric bearings. Asian J. Civil Eng. **20**, 1–11 (2018)

PEER Homepage, https://ngawest2.berkeley.edu/. Last accessed 10 Jun 2019.

Roussis, P., et al.: Assessment of performance of seismic isolation system of Bolu Viaduct. J. Bridg. Eng. **8**(4), 182–190 (2003)

Soneji, B.: Influence of soil–structure interaction on the response of seismically isolated cable-stayed bridge. Soil Dyn. Earthq. Eng. **28** (4), 245–257 (2008)

Ucak, A., Tsopelas, P.: Effect of soil–structure interaction on seismic isolated bridges. J. Struct. Eng. **134**(7), 1154–1164 (2008)

Wilson, E.L.: CSI analysis reference manual for SAP 2000, ETABS, SAFE and CSI bridge. Computer & Structures Inc., Berkeley (2017)

Worku, A.: A potential tool to consider for economical seismic design of buildings. J. South Afr. Inst. Civil Eng. **56**(1), 54–62 (2014)

Dynamic Stability of Anchored Retaining Walls

Fatima Zohra Benamara, Oussama Boutahir, and Farhi Ramzi

Abstract

The anchored retaining walls are structures designed to support different loading applied in static and dynamic cases. We applied Mononobe-Okabe theory for the evaluation of seismic earth pressures developed behind the anchored wall. The purpose of this work is to design and study the stability of anchored retaining wall loaded with different seismic actions to obtain minimal anchor lengths. This analysis was carried out using Kranz's failure model, which is generally used to research the critical angle failure performed iteratively until the necessary horizontal anchor length is determined for a minimum safety factor. The results of this study confirmed the effect of the seismic load on the design of anchored retaining wall and its stability, which had an influence on the estimation of anchor lengths.

Keywords

Anchored wall • Safety factor • Pseudo static • Seismic earth pressure

1 Introduction

Anchored retaining walls are used to stabilize excavations and slopes. Stability analysis of anchored retaining walls under static and dynamic loading is a necessary step to design the structure (Costet and Sanglerat 1988). Estimation of the seismic earth pressure is important for the safe design of anchored retaining walls in a seismic zone. Mononobe-Okabe is still (Mononobe and Et matsuo, 1929) the most used method to determine the lateral seismic earth pressure of cohesionless soils and rigid retaining walls (Saran and Prakash 1968). Using the pseudo-static approach, several researchers have developed different methods to determine the seismic earth pressure considering $c - \varphi$ backfill soil on rigid retaining wall, without considering the roughness of the wall and also without taking into account the effect of tension crack, while adopting the planar single wedge method in the seismic analysis (Shukla et al. 2009).

In the current study, an analytical solution procedure predicting the seismic earth pressures in $c - \varphi$ soils is proposed for the seismic design and stability of anchored retaining walls (Whitlow 1995). The effect of tension crack was adopted, and the roughness of the retaining anchored wall was taken into consideration (Ghosh and Sharma 2010). In addition, the rigid double-wedge failure mechanism was used to analyze the stability of anchored retaining walls (Kranz 1953).

The design of the anchored retaining wall and its stability checks was carried out under different seismic loadings by varying the seismic coefficients k_h using Kranz's failure model (Corfdir 2008).

2 The Design of the Anchored Retaining Wall

In the present study, an analytical solution procedure including a pseudo-static method for predicting the seismic earth pressures in $c - \varphi$ soils is proposed for the seismic design of the anchored retaining wall. The free earth support method was adopted for deducing the wall embedment depth (f), the anchor force (T), and the maximum moment as presented in Table 1. The geometry, soil conditions, and surcharge adopted in the present analysis are given in Fig. 1.

According to Règles Parasismiques Algériennes RPA99/ Version2003 (2003), the horizontal and vertical seismic

F. Z. Benamara (✉) · O. Boutahir · F. Ramzi
Civil and Hydraulic Engineering Department,
8 Mai 1945 University, 24000 Guelma, Algeria
e-mail: benamara.fatimazohra@univ-guelma.dz

F. Z. Benamara
Laboratory of Civil and Hydraulic Engineering (LGCH),
8 Mai 1945 University, 24000 Guelma, Algeria

M. Meghraoui et al. (eds.), *Advances in Geophysics, Tectonics and Petroleum Geosciences*,
Advances in Science, Technology & Innovation, https://doi.org/10.1007/978-3-030-73026-0_53

Table 1 Results of the calculations of anchor force (T), the wall embedment depth (f), and the moment $M(z)$ for the case (k_h; $+k_v$)

k_h	0.05	0.10	0.15	0.20
k_v	0.015	0.03	0.045	0.06
f (m)	2.35	2.95	3.80	5.20
T (kN)	115.8	130.41	153.07	184.85
M (z) (kN m)	134.12	168.36	217.83	275.23

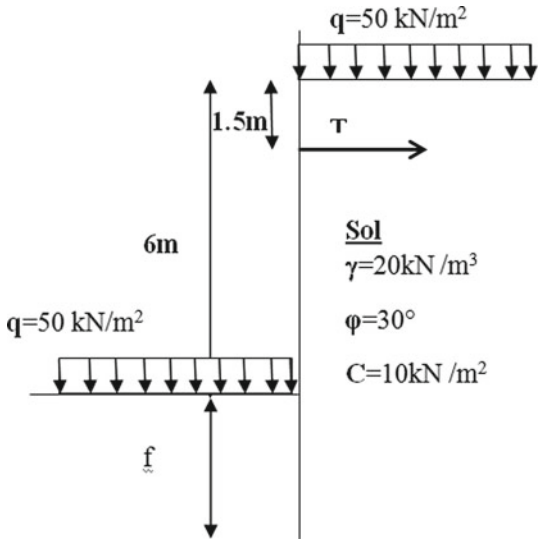

Fig. 1 Standard anchored wall profile

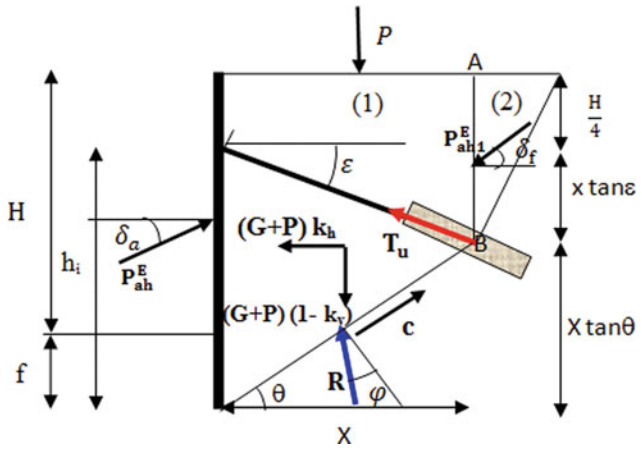

Fig. 2 Applied forces on the rigid body in the Kranz model under dynamic loading

coefficients (k_h, k_v) are to be taken into account as following: k_h = A(%g) and k_v = $\pm$ 0.3k_h, with (A) the zone acceleration coefficient. Table 1 presents a detailed calculation of different seismic accelerations k_h = (0.05, 0.10, 0.15, 0.20) (g). The roughness of the anchored retaining wall is the friction angle between the wall and soil as (δ_a = 2/3 φ) for the evaluation of active earth pressure.

3 Dynamic Stability Study with the Kranz Model

Kranz model was used to check the stability of the anchored retaining wall. The failure mechanism is defined by the principal failure line that cuts the bond length (L_0) at the center and divides it into two secondary sliding surfaces. This model is characterized by a rigid wedge (1), in which the following forces are applied: the reaction of the anchor (T), the reaction of the wall on that wedge ($\mathbf{P^E_{ah}}$), the friction of the soil on the main failure line (R), the cohesion force (C), the overload (P), and the weight of the wedge (1) (G). The seismic active earth pressure ($\mathbf{P^E_{ah1}}$) replaces the wedge action (2) on the wedge (1) through the secondary slip surface considered as a fictitious vertical wall. The inter-wedge friction angle (δ_f = φ) be used (Benamara et al. 2019) (see Fig. 2).

The safety factor defined by Kranz was given by (Eq. 1).

$$F_s = \frac{T_u}{T} \tag{1}$$

where T_u = the ultimate pullout capacity of the anchor
T = the mobilized capacity of the anchor.

The forces applied to the models are calculated according to the anchor length (X) given by Eq. (2).

$$X = \frac{3H/4 + f}{\tan\varepsilon + \tan\theta} \tag{2}$$

The equilibrium study of vertical and horizontal forces gives us, after algebraic transformation (Eq. 3).

$$T_{uh} = \frac{\left[(G+P)(1-k_v+k_h) - P^E_{ah}\tan\delta_a - C\sin\theta\right]}{\tan(\theta-\varphi) - P^E_{ah} + P^E_{ah1} - C\cos\theta \over \tan\varepsilon\tan(\theta-\varphi) - 1} \tag{3}$$

The failure angle (θ) is varying iteratively to find the horizontal anchor length (X) corresponding to a minimum safety factor (F_s) given by Eq. (1). The forces of Eq. (3) are calculated according to the anchor length (X) given by Eq. (2). The anchor lengths are determined for the different values of k_h. The comparative results of studies for different failure angles are presented in Table 2.

Table 2 Results of the calculations of the safety coefficients F_s and anchor lengths

k_h	T (kN)	f (m)	θ (°)	G (kN)	P (kN)	P^E_{ah}(kN)	P^E_{ah1}(kN)	C (kN)	T_{uh} (kN)	F_S	L (m)
0.05	115.8	2.35	38	805	344	282.6	78.12	85.8	179.0	1.52	7.12
0.10	130.4	2.95	40	823.9	336	389.9	78.51	87.7	204.3	1.56	6.95
0.15	153.0	3.80	52	900.6	313	505.0	93.14	101.6	238.7	1.56	6.48
0.20	184.8	5.20	55	813.4	205.5	709.8	87.36	99.5	290.2	1.57	5.91

3.1 Results

The wall embedment depth and the moment increase with the increase of the seismic coefficient (k_h).

The anchor force (T_{uh}) increases with the increase of the seismic coefficient. As shown in Table 1, the active earth pressures developed behind the anchored wall are higher; the more the earthquake is powerful, the same is for the seismic active earth pressures developed behind the fictitious vertical wall (AB). The anchor lengths decrease with the increase of the seismic load. This is due to the increase of the failure angle (θ) which reduces the vertical loads (G) and (P). Safety factors decrease with the increasing seismic load. However, the anchor lengths decrease.

4 Conclusions

The purpose of this study is to design an anchored retaining wall and to verify its stability by estimating dynamic earth pressures for four horizontal seismic coefficients (k_h) to determine the wall's embedment depth, and the anchor force and the maximum moment are developed in the wall. The Kranz failure mechanism was the failure model used to verify the stability for different seismic loadings. The study of the stability of the anchored retaining wall has shown that the anchor force (T_{uh}) increases with the increasing earthquake intensity, which influences the estimation of the anchor lengths.

References

Benamara, F.Z., Belabed, L., Rouaiguia, A.: Proposed improvements to analytical models of anchored retaining walls. Environ. Eng. Geosci. **25**(2), 115–126 (2019)

Corfdir, A.: Kranz's method from yesterday to day: a critical review. Rev. Fr. Géotech. **124**(3), 19–30 (2008)

Costet, J., Sanglerat, G.: Cours pratique de mécanique des Sol 2 calcul des ouvrages, 3rd edn. Dunod, Paris (1988)

Ghosh, S., Sharma, R.P.: Pseudo-dynamic active response of non-vertical retaining walls upporting c–φ backfill. Geotech. Geol. Eng. **28**(5), 633–641 (2010)

Kranz, E.: Über die Verankerung von Spundwänden. Mitteilungen aus dem Gebiet des Wasserbaues und der Baugrundforschung. Ernst & Sohn (1953), p. 11

Mononobe, N., Et matsuo, H.: On the determination of earth pressure during earthquake. In: Proceedings of World Engineering congress , pp. 177–185 (1929)

Règles Parasismiques Algériennes RPA99/Version2003. Centre National de Recherche Appliquée en Génie Parasismique. Algérie (2003)

Saran, S., Prakash, S.: Dimensionless parameters for static and dynamic earth pressures behind retaining walls. Indian Geotechnical J. **7**(3), 295–310 (1968)

Shukla, S. K., Gupta, S. K., Sivakugan, N.: Active earth pressure on retaining wall for c–φ soil backfill under seismic loading condition. J. Geotech. Geoenviron. Eng. **135**(5) (2009)

Whitlow, R.: Basic soil mechanics. 3rd edn. Wesley Longman, England (1995)

Seismic & Well Logging Methods, Geodesy and Exploration & Theoretical Geophysics (T5): Seismic & Well Logging Methods

Thermal Anomaly and Land Surface Temperature Associated with the Abuja, Nigeria Earth Tremor of 7th September 2018

Abayomi Osotuyi, Ayomiposi Falade, Abraham Adepelumi, and Samson Onibiyo

Abstract

Satellite thermal infrared has proven to be a veritable tool in earthquake studies and has recorded anomalies in association with fault systems and prior to major earthquakes perhaps where ground seismic data are not available. This study aims at verifying if TIR anomalies can be found in association with low-magnitude events which took place in a basement complex geological terrain with medium- to high-density local fault system. This is carried out by systematically applying remote sensing analysis techniques to imagery recorded prior to, during, and immediately after the earth tremors, such as recorded in Abuja and environ in 5–7 September 2018 in Nigeria. MODIS satellite thermal images were used to study the relation between thermal anomalies and seismic activity while the remotely sensed aeromagnetic data was used to decipher the fault system and also provide information about the lineament juxtaposition of the terrain. A NE distribution of the TIR around the major faults was observed before the mainshock and showed that the spatial temperature rose by 10–13°C and suddenly attenuated on the day after the aftershock. It was inferred that reactivation of faults in the weak/sheared zones of the FCT, triggered by strain energy released and propagated through the seismically active NE-SW Romanche fault from the Gulf of Guinea, could be the most plausible causative factor of the tremor.

Keywords

Satellite thermal infrared • Anomaly • Fault system • Mainshock • Seismic

A. Osotuyi (✉) · A. Falade · A. Adepelumi
Seismological Research Laboratory, Obafemi Awolowo University, Ile-Ife, Nigeria

S. Onibiyo
Department of Geosciences, Georgia State University, Atlanta, GA, USA

1 Introduction

One of the most significant and most important natural geological hazards is earthquakes. Hence, the need for the continuous study and research into earthquake prediction and forecasting.

From 5 to 7th September 2018, sequences of low-magnitude earth tremors were reported in the capital city of Nigeria and mainly felt at the Northeastern Federal Capital Territory (FCT), in Mpape and environs, Abuja. The Mpape, FCT tremor was recorded on the 6th September 2018. In the area, there are many mountains, hills, and valleys. Though no human casualty was reported, human and economic activities were disrupted, and so on. This event has further drawn attention to a series of earthquakes reported on a stable intraplate region, contrary to previous assumptions that Nigeria is located within an aseismic zone (Adepelumi 2009; Akpan and Yakubu 2010). Hence, this is bringing renewed attention to earthquakes as a potent natural hazard in the western African region.

Land surface temperature (LST) from thermal infrared (TIR) instruments, which is a key parameter in the physics of land surface processes on both regional and global scales, containing the scientific data sets in the MOD11A1 product include LST data, was adopted to investigate and answer some questions around thermal variations, if there are any, that are associated with the Federal Capital Territory, Nigeria event.

2 Settings, Theories, and Methods

2.1 Geology and Tectonic Settings of the Area

The Federal Capital Territory (FCT) is mainly underlain by rocks of the crystalline basement complex within the northcentral part of the Nigeria, which forms part of the Pan-African mobile belt in the west African Congo cratons

M. Meghraoui et al. (eds.), *Advances in Geophysics, Tectonics and Petroleum Geosciences*, Advances in Science, Technology & Innovation, https://doi.org/10.1007/978-3-030-73026-0_54

(Black 1980). The rock units are made up of granites, mica schists, hornblende and feldspathic schists and migmatites. They are highly fractured and jointed showing essentially three (3) lineaments patterns in the NE-SW, N-S, and NW-SE orientation (Fig. 1) Avci (1983). There is the presence of dense fracture network which may be interconnected and linked to the regional NE-SW trending Ifewara-Zungeru fault line and takes the form of cracks and tensional joint resulting from stresses occasioned by alternating heating-up and cooling sequence of rocks. Both horizontal and vertical fractures are very common with the width of the fractures generally decreasing with depth. This may be an indication that the fracture systems are young and maybe evolving structures.

Of note is the detailed geological report of the study carried out on the Federal Capital Territory by Julius Berger in 1979 which gives an in-depth and comprehensive background insight into the geologic and tectonic settings of the FCT. It was reported that the most evident structural features in the basement complex rocks of the FCT are northerly to northeasterly–southwesterly trends of the basement complexes near the eastern and western boundaries; and the easterly trends in the central part. These reflect the presence of a north-trending shear zone along the eastern limb of the FCT. A smaller north-trending shear zone appears just west of Abuja. Many faults and fractures

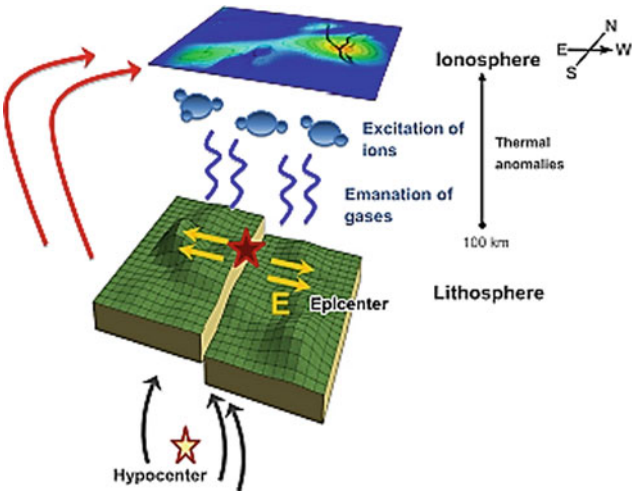

Fig. 2 Schematic of the formation of thermal anomalies in the atmosphere as shown by interaction between the emanation of gases and the excitation of ions between the lithosphere and the ionosphere, respectively, as presented by Pulinets and Ouzounos (2011)

trending NW cut these structures and must, therefore, be of younger origin (JBCC Report 1979). These show the young tectonic growths may still be developing. The eastern shear zone represents a major regional tectonic feature persisting for many tens of kilometers. Near the

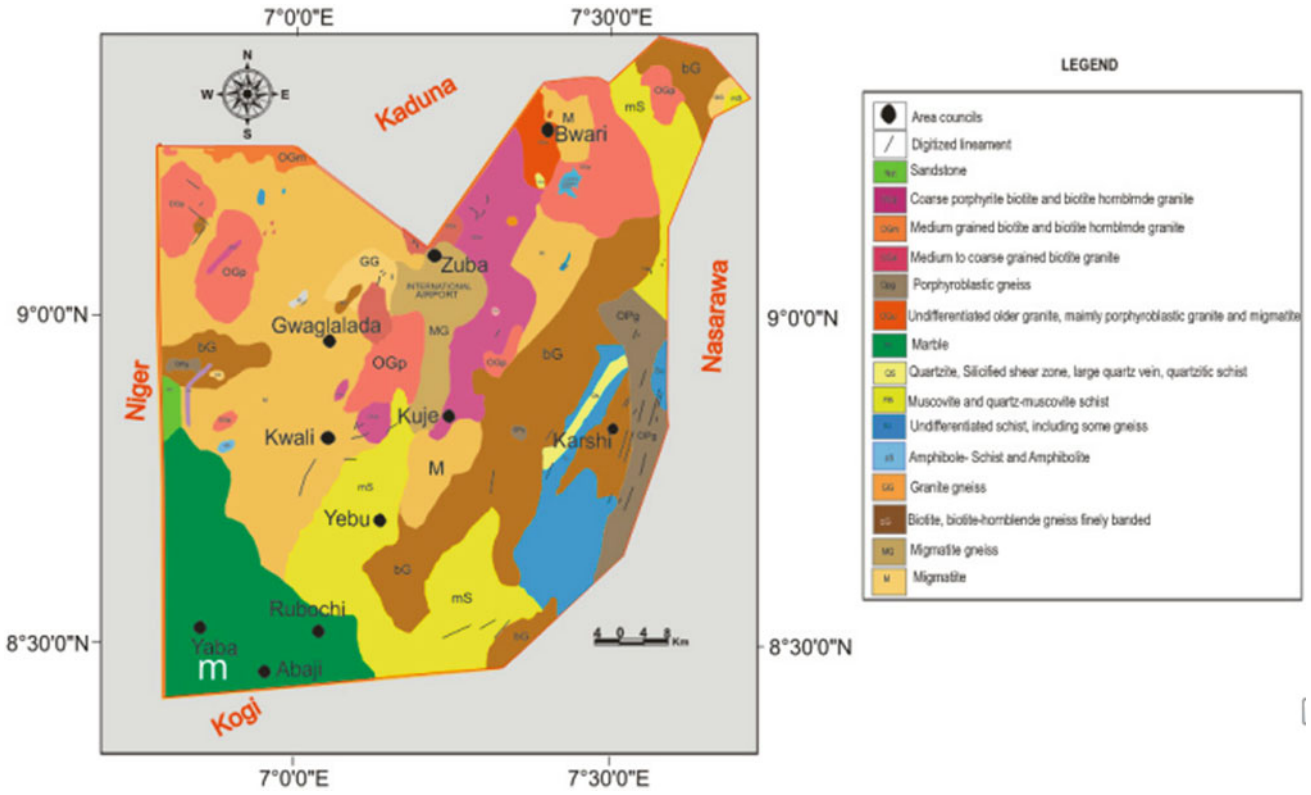

Fig. 1 Geological map of Federal Capital Territory, Abuja (modified from NGSA 2006)

northeast corner of the FCT the shear zone is only a few kilometers wide. In the southern part of the eastern shear zone, there are at several places individual shear zones in schists or granitic gneisses cutting other minor rocks such as amphibolites. Therefore, it is supposed that there have been some tectonic movements causing regional metamorphosis which took place in Precambrian times (JBCC 1979). Shear zones are known to be weak zones which as reported from the study abundantly underlie the FCT, hence, parts of the FCT may not be immune to tectonic movements and activities which may have caused the reported earth tremor of 6th September 2018.

2.2 Theories of Thermal Infrared Anomalies

Thermal infrared anomalies come in along with earthquakes. Figure 1 was an idea from previous researches of Huang et al. (2008), Shah et al. (2015) defined the earthquake-induced anomalies as "the generation of hole charges on the lithospheric surface and the intensification of the lower atmosphere by the hole charges". Though several theories and models have been presented to shed light on thermal anomalies emanating from earth lineaments as a result of stress build-up and subsequent release along these structures due to tectonic activities. It is an established fact that thermal anomalies are due to the release of built-up stresses in rocks, thereby producing hole charges. Increase in land surface temperature observed by spatial analysis is suggested to be as a result of the ions from the earthquake breeding zone.

Some attendant signals preceding earthquakes are changes in land and air surface temperature (days or even weeks prior to strong, even moderate earthquakes), gas emissions (including methane, radon, etc.), water level and quality (in wells), and electric and magnetic (electromagnetic) fields of the earth (Freund 2011; Varotsos et al. 2011). Advances in Space technology have made the measurement of surface geophysical parameters and related quantities associated with ground deformation around tectonic plate boundaries, active faults, and shear zones possible. Zoran et al. (2014) stated that earthquake pre-signals for which clear geophysical anomalies are observable can be remotely sensed using different criteria. Also, local and regional airborne measurements, and traditional in-situ and ground-based seismological sensor monitoring networks can be complemented with satellite data information from established space observatories.

Guangmeng (2008) reported that "Russian scientists discovered short-lived thermal anomalies from satellite image before earthquake in central Asia" in Gorny et al. (1988) work. After that, several researchers have studied and reported this thermal anomaly phenomenon with satellite information in Japan, China, India, Iran, and Algerian earthquakes (Ouzounov and Freund 2004; Saraf et al. 2004). The thermal anomalies have been reported to be short-lived and typically appear 7–14 days before an earthquake, cutting across thousands or tens of thousands square kilometers, showing a positive rise of 2–4 k or more from the background temperature and disappearing a few days after the event. This method is not without its attendant limitation, as satellite thermal sensors are limited in penetrating thick clouds to acquire land surface temperature data. Hence, continuous temperature data could not be obtained and some component of thermal anomaly would be lost. This forms a major challenge to predicting earthquake using satellite thermal infrared data (Guangmeng 2008). Lei et al. (2018) submitted that seasonal variation (i.e., rainy and dry seasons) and vegetation cover (dense vegetation and barren surfaces) contribute to and influences LST accuracy. Build-up of stresses due to shearing or compression in the rocks or tectonic plates creates fractures and fissures that would cause trapped gases to evolve out of the rocks and enter into aquifers or underground water or the lower atmosphere. The gases would add to the already present gases to increase the pressure in the lithosphere, thus rising above the atmosphere along the faults which subsequently raises the atmospheric temperature. This phenomenon would cause water vapor to be released which soaks-in the infrared as indicated by MODIS LST changes (Xiong et al. 2010; Shah et al. 2015).

2.3 Research Data and Methodology

MODIS data derived from the NASA official network (NASA's Land Processes Distributed Active Archive Center (DAAC) https://lpdaac.usgs.gov/products/mod11a1v006/) were analyzed for this study. Surface temperature was obtained from MODIS data, and the remote sensing imagery has 1 km spatial resolution. Land surface temperature (LST) was extracted from the MODIS. NASA LST data provided are precise and have errors less than 1 k, though it is complex and not easy to use. It was possible to predicate earthquakes and tremors using this data. The scientific data sets in the MOD11A1 product include LST 1 km Day/Night, QC Day/Night, View Time Day/Night, View Angle Day/Night, Emissivity Band 31/Band 32, Clear Sky Coverage Day/Night. The daytime data were used. According to the acquired data, some preprocesses were done. The original data contain land surface temperature (LST) imagery, but the map projection is sinusoidal; i.e., LST product is provided in intergerized sinusoidal projection. MODIS reprojection tool (MRT) was used in order to reproject and mosaic the tiles of the product.

3 Results

The Mpape, FCT tremor was recorded on the 6th September 2018 and the data acquired included the 4th September, 5th September, 6th September, 7th September, and 8th September 2018. This is to incorporate the LST for days before, during, and after the events were reported to establishing spatial thermal infrared variation and temporal anomaly. Hence, the LST data sets for each day considered were processed, and the spatial anomaly maps are produced. The LST data are presented as maps (Figs. 3, 4, 5, 6, and 7), and averaged temperature value for each day were plotted (Fig. 8) to observe the trend of temperature fluctuation over the days under review.

4 Discussions

The vast area within the FCT was thermally quiet, and there was no significant observable thermal energy spread across the area the 4th September 2018 on the first day of data observation except the southern boundaries that began to pick up some specks of temperature increase relative to the environment (Fig. 3). On 5th September 2018, noticeable thermal anomaly began to emerge and build up at the northwestern area of the FCT with respect to the surrounding environment picking up an increase in temperature (Fig. 4). There was significant energy dissipation across the most northern parts of the FCT, and most significantly the entire northeastern and eastern parts where Mpape, identified as the epicenter, is specifically located. This trend spreads eastward on 6th September 2018 which is just the day before the mainshock as reported. There is a rise in temperature across the northern part on 6th September 2016 with the sharp increase in thermal anomaly in the NE. Hence, it can be deduced that there was a W-E movement of increasing

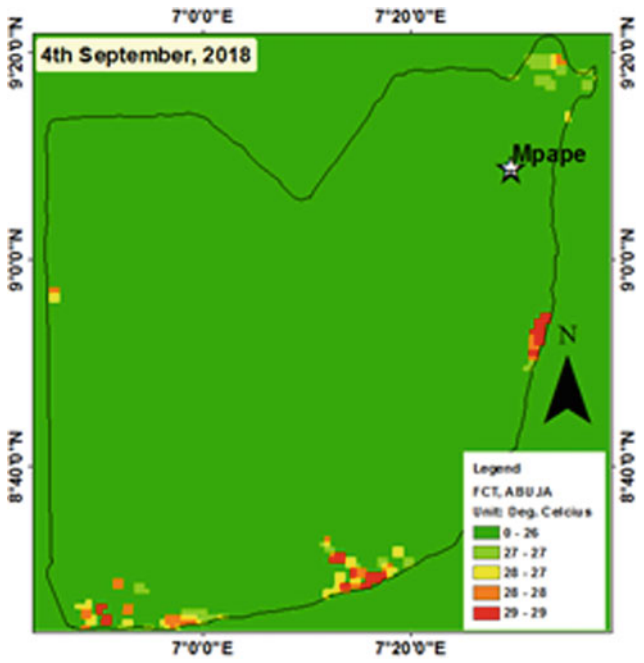

Fig. 3 Spatial anomaly image of 4th Sept. 2018

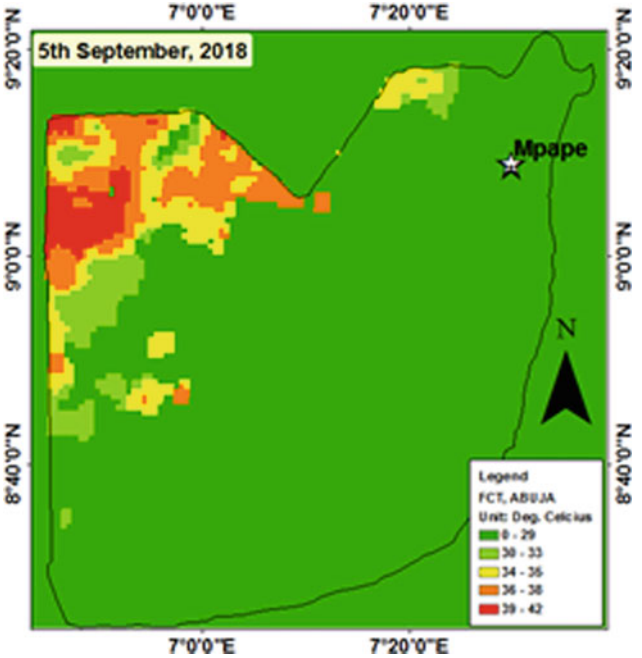

Fig. 4 Spatial anomaly image of 5th Sept. 2018

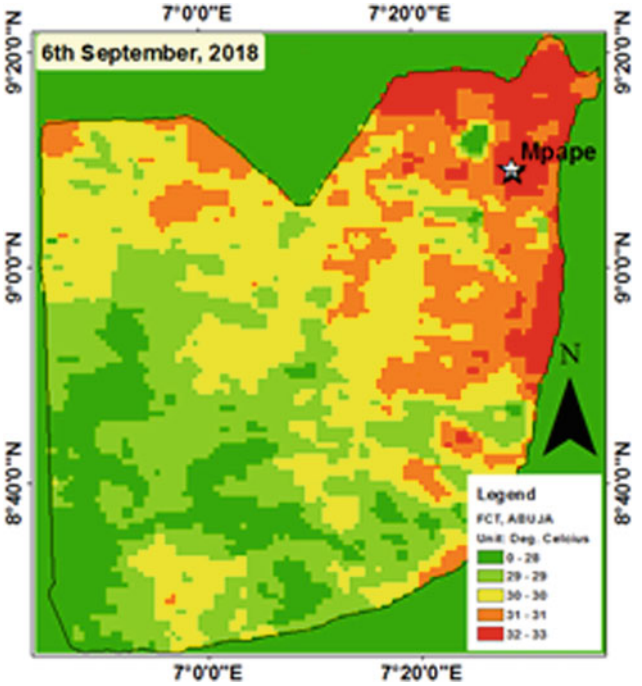

Fig. 5 Spatial anomaly image of 6th Sept. 2018

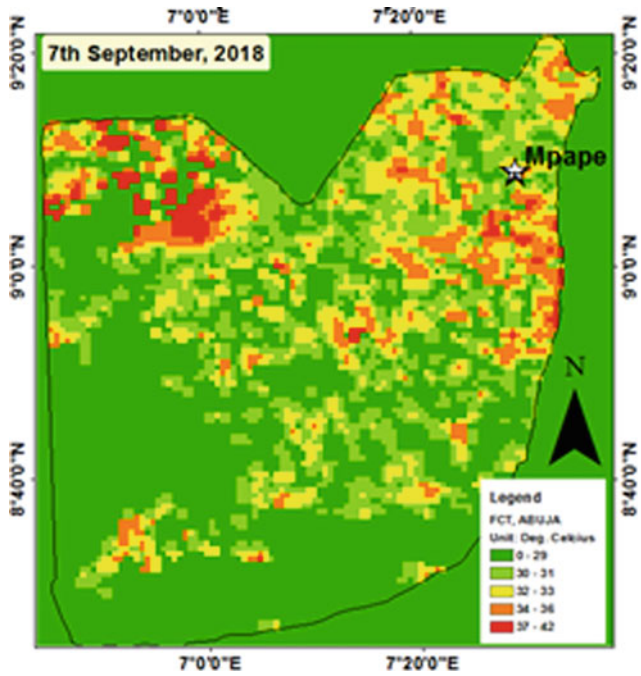

Fig. 6 Spatial anomaly image of 7th Sept. 2018

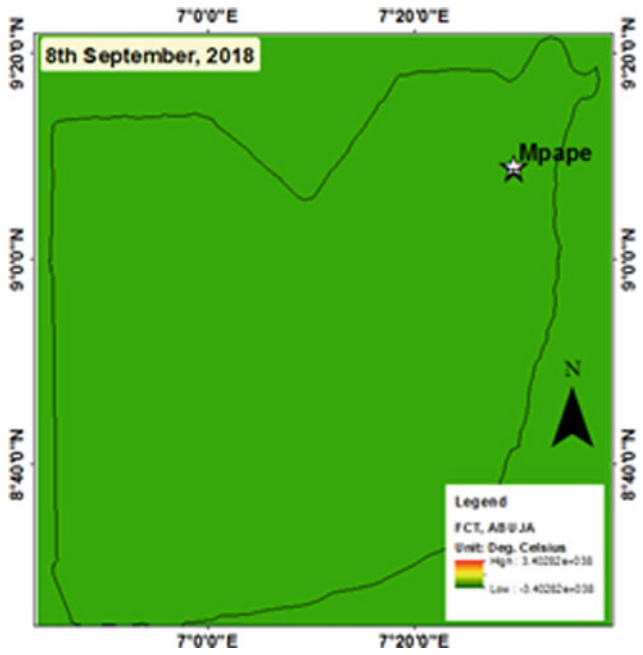

Fig. 7 Spatial anomaly image of 8th Sept. 2018

thermal flux from the 5th through to 6th September 2018 (Figs. 4 and 5). On 7th September 2018, there is energy dissipation across the entire FCT relative to the two previous days (Fig. 6). Energy loss and attenuation are observed across the area when compared to the 6th September data, though patches of high thermal anomaly were observed on the day the event was recorded. There is complete energy attenuation and there was no observable anomaly on 8th September 2018 which coincided with the day after the tremor was reported (Fig. 7). The NE of FCT covering about 3,176 Square Kilometers across Gwagalada, Bwari, and Abuja areas recorded the highest observable thermal anomaly, with Mpape, where the aftershock of the tremor was most felt lying in Bwari area. Maximum temperature ranging between 29–42 °C was recorded on 7th September in the anomalous zone and shows temperature rise ranging between 3–13 °C across this vast area. After the tremor, the temperature was lower than other days (Figs. 7 and 8). This suggests that the TIR anomalies existed in association with tectonic activities/plate movement/earth tremor/earthquake that occurred between 5 to 7th September 2018.

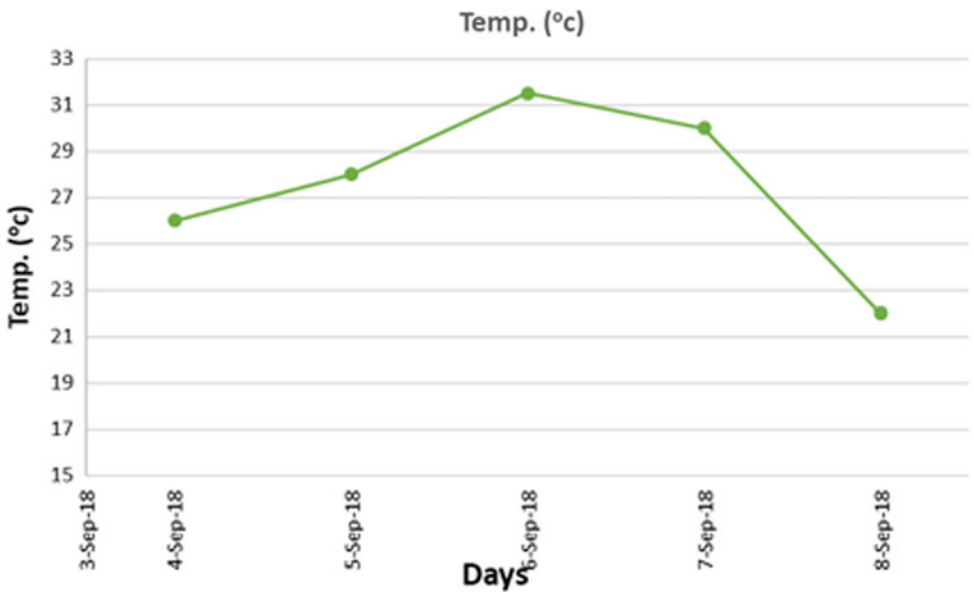

Fig. 8 Daily average temperature anomaly from 4 to 8th September 2018

5 Conclusions

Earthquakes are natural events which happen all the time. There is no current technology to avert them. Hence, emphasis is placed on monitoring, identifying, and cataloging their locations as accurately as possible so as to make improvements on future forecasts in time and space. The study revealed the gradual progressive changes involving the increase and attenuation of thermal flux across the FCT, Abuja from the NW to NE parts respectively, prior to and during the periods of the reported seismic events. Maximum temperature ranging between 29–42 °C was recorded on 7th September in the anomalous zone, which coincided with the day the major event was reported. Also, temperature rise ranging between 3–13 °C across the vast area was recorded. After the tremor, the temperature was lower than other days. TIR should be adopted for continuous monitoring in earthquake-prone areas and regions where such events have been reported in the past.

References

Adepelumi, A.A.: Short-term probabilistic forecasting of earthquakes occurrence in South-Western Nigeria. Technical Report Submitted to the Centre for Geodesy and Geodynamics, Toro, Nigeria (2009)

Akpan, O.U., Yakubu, T.A.: A review of earthquake occurrences and observations in Nigeria. Earthq. Sci. **23**, 289–294 (2010). https://doi.org/10.1007/s11589-010-0725-7

Avci, M.: Photogeology and structural interpretation of the Southern section of the New Federal Capital City site, Abuja, Nigeria. Nig. J. Min. Geol. **20**(1 & 2), 51–56 (1983)

Black, R.: Precambrian of West Africa. Episodes **4**, 3–8 (1980)

Freund, F.: Seeking out Earth's warning signals. Nature **473**(7348), 452 (2011). https://doi.org/10.1038/473452d

Gorny, V.I., Salman, A.G., Tronin, A.A., Shilin, B.B.: The Earth outgoing IR radiation as an indicator of seismic activity. Proc. Acad. Sci. USSR **301**, 67–69 (1988)

Guangmeng, G.: Studying thermal anomaly before earthquake with NCEP data. In: The International Archives of the Photogrammetry, Remote Sensing and Spatial Information Sciences, Vol. XXXVII, Part B8. Beijing (2008)

Huang, J., Mao, F., Zhou, W., Zh, X.: Satellite Thermal IR Associated with Wenchuan Earthquake in China Using Modis Data. The 14th World Conference on Earthquake Engineering, October 12–17, 2008, Beijing, China (2008)

JBCC Technical Report: Unpublished geological and environmental mapping technical report of Julius Berger construction company. Archived in the Federal Capital Development Authority (FCDA), Federal Republic of Nigeria (1979)

Lei, L., Tingjun, Z., Tiejun, W., Xiaoming, Z. (2018): Evaluation of collection-6 MODIS land surface temperature product using multi-year ground measurements in an arid area of Northwest China. Remote Sens. **2018**(10), 2018 (1852). https://doi.org/10.3390/rs10111852

NASA Land Processes Distributed Active Archive Center (DAAC). https://lpdaac.usgs.gov/products/mod11a1v006/

Nigeria Geological Survey Agency, NGSA: Nigeria Geological Map (2006)

Ouzounov, D., Freund, F.: Mid-infrared emission prior to strong earthquakes analyzed by remote sensing data. Adv. Space Res. **33**, 268–273 (2004)

Pulinets, S., Ouzounov, D.: Lithosphere–Atmosphere–Ionosphere Coupling (LAIC) model—an unified concept for earthquake precursors validation. J. Asian Earth Sci. **41**, 371–382 (2011)

Saraf, A.K., Choudhury, S.: Satellite detects surface thermal anomalies associated with the Algerian Earthquakes of May, 2003. Int. J. Remote Sens. **26**(13), 2705–2713 (2004)

Shah, M., Khan, M., Ullah, H., Ali, S.: Thermal Anomalies Prior to the 2015 Gorkha (Nepal) Earthquake from MODIS Land Surface Temperature and Outgoing Longwave Radiations. Institute of the Earth's Crust, Siberian Branch of Russian Academic of Sciences. 2018, vol. 9, Issue 1, pp. 123–138 (2018)

Varotsos, P.A., Sarlis N.V., Skordas, E.S.: Scale-Specific order parameter fluctuations of seismicity in natural time before main shocks. Europhys. Lett. **96**, 59002 (2011). https://doi.org/10.1209/02955075/96/59002

Xiong, P., Shen, X.H., Bi, Y.X., Kang, C.L., Chen, L.Z., Jing, F., Chen, Y.: Study of outgoing longwave radiation anomalies associated with Haiti earthquake. Nat. Hazards Earth Syst. Sci. **10**, 2169–2178 (2010). https://doi.org/10.5194/nhess-10-2169-2010

Zoran, M.A., Savastru, R.S., Savastru, D.M.: Satellite thermal infrared anomalies associated with strong earthquakes in the Vrancea area of Romania. De Gruyter Open, Open Geosci. **2015**(1), 606–617 (2014)

Porosity Model Construction Based on ANN and Seismic Inversion: A Case Study of Saharan Field (Algeria)

Said Eladj, Mohamed Zinelabidine Doghmane, Leila Aliouane, and Sid-Ali Ouadfeul

Abstract

The seismic data inversion provides litho-stratigraphic information necessary for the reservoir characterization and new traps discoveries. However, uncertainties inherent in seismic data inversion and nonlinear relationship between petrophysical parameters pose a challenge for reliable reservoir characterization. In this study, a multilayer feed-forward neural network (MLFN) is designed to overcome the non-uniqueness of the seismic inversion solution. MLFN learning was based on the logging data. The 3D seismic acoustic was inverted using the colored inversion. The resulting acoustic impedance volume was then used as an input for model-based inversion method designed for calculating the porosity volume using the trained artificial neural network. The effectiveness of the proposed algorithm was demonstrated using Algerian hydrocarbons field.

Keywords

MLFN • Non-uniqueness of solution • Seismic inversion • Reservoir characterization • 3D porosity volume • Algerian hydrocarbons' field

1 Introduction

The feed-forward algorithm consists of propagating the error committed by a neuron at its synapses and its related neurons. In the learning step, the gradient error is recalculated for each iteration by taking the dominant synaptic weights that have contributed more to the previously calculated error (Bhatt and Helle 2002; Sagar et al. 2016). In this study, we have performed an inversion technique on seismic data using a conventional algorithm to obtain acoustic impedance volume (Elkatatny et al. 2018; Ahmadi et al. 2014). This volume was introduced as an external attribute and used as input to the multilayer feed-forward network (MLFN) technique to generate a porosity volume (Hatampour et al. 2016). The network was trained by the logging data where the input was acoustic impedance obtained from Sonic logs, and the target was the porosity logs. The main challenge was to find the optimum parameter of the MLFN, and it was one of the main objectives of this study. The trained MLFN algorithm has been tested by comparing the log porosities of the three existing wells with values in the porosity map. The use of this neural network allows us to improve the prediction of porosity in a Saharan oil field under exploration (Naeem et al. 2015).

2 MLFN Algorithm Steps

In the first step, the total iteration number was set to 15 and the gradient-conjugate iteration number was 120. The hidden layer neuron number (HLNN) was then varied from 20 to 100. The validation error for each network was then calculated.

As demonstrated in Table.1, it is remarkable that the best configuration of the network is in row four, where the correlation of validation is 0.38 with good learning correlation value. The selected number of hidden layers was then 94 because the maximum learning correlation (0.93) did not provide a good correlation value in the validation. In the

S. Eladj (✉) · L. Aliouane
University M'hamed Bougara of Boumerdes, LABOPHYT, 35000 Boumerdes, Algeria
e-mail: s.eladj@univ-boumerdes.dz

M. Z. Doghmane
Department of Geophysics, FSTGAT, , University of Sciences and Technologies Houari Boumediene, 16000 Bab Ezzaour, Algeria

S.-A. Ouadfeul
The Algerian Petroleum Institute, 35000 Boumerdes, Algeria

M. Meghraoui et al. (eds.), *Advances in Geophysics, Tectonics and Petroleum Geosciences*,
Advances in Science, Technology & Innovation, https://doi.org/10.1007/978-3-030-73026-0_55

Table 1 Hidden layer neuron number variation

HLNN	TIN	GCIN	Learning	Correlation	Validation	Correlation
20	15	120	6.12	0.78	10.15	0.24
50	15	120	5.72	0.87	10.88	0.15
80	15	120	4.30	0.93	11.97	0.22
94	15	120	5.21	0.91	11.17	0.38
100	15	120	5.60	0.89	12.24	0.31

Table 2 Gradient-conjugate iterations number variation

GCIN	TIN	HLNN	Learning	Correlation	Validation	Correlation
80	15	94	3.84	0.89	12.35	0.28
90	15	94	4.33	0.83	12.89	0.23
100	15	94	4.82	0.88	13.92	0.15
120	15	94	5.21	0.91	11.17	0.38
130	15	94	5.28	0.89	13.57	012

Table 3 Total number iterations variation

TIN	GCIN	HLNN	Learning	Correlation	Validation	Correlation
10	120	94	5.43	0.82	12.25	0.19
12	120	94	5.13	0.9	13.20	0.17
15	120	94	5.21	0.91	11.17	0.38
18	120	94	5.25	0.89	14.23	0.15
20	120	94	4.10	0.92	14.60	0.08

second step, the HLNN was fixed to 94, and the total iteration number (TIN) was set to 15. The gradient-conjugate iterations number (GCIN) was then varied from 80 to 130 with a step length of 10.

As demonstrated in Table.2, the best configuration of the network where the two correlations are maximized together was in row four with optimized GCIN value of 120.

The final step of the architecture optimization phase was to determine the total iterations number. As shown in Table3, the best configuration of the network where the validation correlation was maximized with good learning correlation was in row three with optimized TIN equal 15.

3 Optimization Results

Based on the minimum prediction error and the correlation coefficient, the optimum configuration of the MLF Network can be chosen to obtain the best correlation between the predicted values and the real values of the porosity logs (HLNN = 94, TIN = 15, and GCIN = 120) (Hatampour et al. 2016; Naeem et al. 2015). The parameters' tests performed during the learning step allowed us to predict the real porosity values using the three wells' attributes of the logging inputs curve (Baouche 2017). Based on the values mentioned above, a better correlation was obtained between the calculated porosity and the porosity logs (Baouche et al. 2017).

4 Generalization in Seismic Data

After setting the network parameters for the MLFN algorithm, it has been trained and validated on porosity logs of wells 1, 2, and 3. Then, the process has been applied for the entire seismic volume using acoustic impedance cube generated from seismic inversion and upscaling process for the trained MLFN algorithm (Elkatatny et al. 2018; Ahmadi et al. 2014). The learning phase of the algorithm was realized by using real data where the maximum obtained correlation was 0.91 (well-1), and the average error did not exceed 5.26%. Well-3 is located near the two wells in the same reservoir; the correlation of network validation was 0.38, and the average error was 11.67%. The obtained validation results allowed us to generate the MLFN network for the whole region. A porosity map has been generated as shown in Fig. 1; this map can be used as a guideline for hydrocarbons estimation, reservoir model construction and monitoring, and it is an original map that helps geomodelers to have a more precise reservoir evaluation instead of correlating porosities between wells (Lashin and Din 2013; Singh 2016). Moreover, the obtained porosity map has been generated using three wells, which means that it is advantageous in the absence of enough data of drilled wells, and it can be used to optimize a number of wells to drill in this under-exploration reservoir.

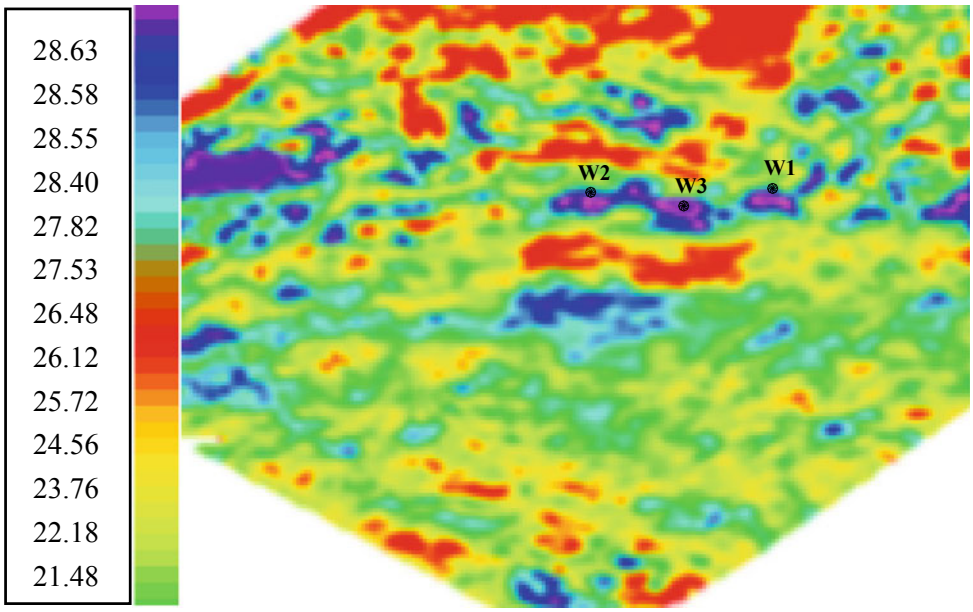

Fig. 1 Porosity values (in %) map generalized using MLFN inversion algorithm

5 Conclusions

The use of MLFN allowed us to build a porosity volume of the studied hydrocarbons' field. The inversion of real seismic data by MLFN gave acceptable results even with only three wells used in the training phase. Network learning based on three wells did not reflect all reservoir heterogeneities, but it predicts the porosity parameter with moderate precision. Moreover, the model can be useful to give a general view of petrophysical parameters variation and to guide geomodelers and reservoir engineers into a better understanding of the reservoir under study. Other newly drilled wells can be inserted in the training phase to improve the obtained results. Therefore, the accuracy of the network will be improved, and the validation region of the algorithm will be expanded.

References

Ahmadi, M.-A., Ahmadi, R.-A., Hosseini, S.M., Ebdi, M.: Connectionist model predicts porosity and permeability of petroleum reservoirs by means of petro-physical logs: application of artificial intelligence. J. Petrol. Sci. Eng. **123**, 183–200 (2014). https://doi.org/10.1016/j.petrol.2014.08.026

Baouche, R., Aïfa, T., Baddari, K.: Intelligent methods for predicting nuclear magnetic resonance of porosity and permeability by conventional well-logs: a case study of Saharan field. Arab. J. Geosci. **10**, 545 (2017). https://doi.org/10.1007/s12517-017-3344-y

Bhatt, A., Helle, H.B.: Committee neural networks for porosity and permeability prediction from well logs. Geophys. Prospect. **50**(6), 645–660 (2002)

Doghmane, M.Z., Belahcene, B., Kidouche, M.: Application of improved artificial neural network algorithm in hydrocarbons' reservoir evaluation. In: Hatti, M. (eds.) Renewable Energy for Smart and Sustainable Cities, pp. 129–138, Lecture Notes in Networks and Systems 62. Springer, Cham (2019). https://doi.org/10.1007/978-3-030-04789-4_14

Elkatatny, S., Tariq, Z., Mahmoud, M., Abdulraheem, A.: New insights into porosity determination using artificial intelligence techniques for carbonate reservoirs. Petroleum **4**(4), 408–418 (2018). https://doi.org/10.1016/j.petlm.2018.04.002

Hatampour, A., Schaffie, M., Jafari, S.: Estimation of NMR total and free fluid porosity from seismic attributes using intelligent systems: a case study from an iranian carbonate gas reservoir. Arab J. Sci. Eng. **42**(1), 315–326 (2016)

Lashin, A., El Din, S.S.: Reservoir parameters determination using artificial neural networks: Ras Fanar field, Gulf of Suez, Egypt. Arab. J. Geosci. **6**(8), 2789–2806 (2013). https://doi.org/10.1007/s12517-012-0541-6

Naeem, M., El-Araby, H.M., Khalil, M.K., et al.: Integrated study of seismic and well data for porosity estimation using multi-attribute transforms: a case study of Boonsville Field, Fort Worth Basin, Texas, USA. Arab. J. Geosci. **8**(10), 8777–8793 (2015). https://doi.org/10.1007/s12517-015-1806-7

Sagar, S., Ismet, K.A., Sevgen, S.: A general approach for porosity estimation using artificial neural network method: a case study from Kansas gas field. Stud. Geophys. Geod. **60**(1), 130–140 (2016)

Singh, Y., et al.: Prediction of gas hydrate saturation throughout the seismic section in Krishna Godavari basin using multivariate linear regression and multi-layer feed forward neural network approach. Arab. J. Geosci. **9**, 415 (2016). https://doi.org/10.1007/s12517-016-2434-6

The Study of the Regional Seismic Line of the Western Desert (Iraq)

Ezzadin Baban, Basim Al-hijab, and Hamid Al-sadi

Abstract

A seismic reflection regional line (Reg124) was built in the Western Desert of Iraq using local seismic lines of several seismic reflection surveys. Nine reflectors (named H1–H9) were picked on the regional seismic line which represents the top of Jurassic, Triassic, Permian, Carbo/Devonian, Silurian, Ordovician, top of Cambrian, Middle Cambrian, and Basement formations, respectively. The reflectors show dipping and deepening toward the east. Two sequences of reflectors can be recognized on the regional seismic line. The first sequence consists of Jurassic, Triassic, Permian, Carbo/Devonian, and Silurian reflectors which are sub-parallel and dip toward the east. The second sequence is composed of Ordovician to Basement reflectors. The Ordovician reflector makes angular unconformity surface with Silurian reflector. The reflectors of this group are thicker at the western part and thinner toward the eastern part. A Paleohigh (Anbar uplift) is found on the regional line which might have been formed during the Caledonian orogeny.

Keywords

Seismic reflection • Western Desert • Iraq • Regional line • *Anbar uplift*

1 Introduction

The studied line is located within the Western Desert part of Iraq, west and southwest of Euphrates River. The Arabian Shelf, which lies to the east of the Arabian Shield, consists of stable and unstable shelves. The Iraqi part of the Arabian Shelf is divided into stable shelf and unstable shelf. The Stable Shelf in Iraq bounded by (south Sinjar, east of Hatra, and Hit) zones at the N and NE parts and generally, the structural axes of the Shelf trending N–S, E–W, NW–SE, and SW–NE. The boundary between the two parts of the platform is taken along Anah–Abu Jir fault zones. The Western Desert is a part of the northern Arabian platform, where relatively thin Phanerozoic sediments cover the Precambrian N–S and NW–SE fractured continental basement complex. The Paleozoic sequence is dominated by silica-clastic sediments deposited in a shallow epicontinental sea in relatively stable conditions. In contrast, the Mesozoic sequence shows a significant change in the depositional system from a primary silica-clastic Paleozoic regime to a significant carbonate deposition with interspersed clastic episodes. However, the Cenozoic sequence displays a gradual retreat of the sea and the final transition to the continental conditions (Fouad 2007). Sedimentary rocks, which range in age from Cambrian to Quaternary, dip gently toward the Arabian Gulf in the east and the depression of Rub Al Khali in the south. These sedimentary rocks are mostly limestone, sandstone, siltstone, and shales (Poulos 2018).

2 Construction of the Regional Seismic Line

Construction of the regional seismic line from those local seismic lines of areas where the regional seismic line passed through is the most crucial step in regional geological studies. For constructing a regional line firstly, we selected a group of local lines from local areas to be component lines

E. Baban (✉)
University of Sulaimani, Sulaymaniyah, Kurdistan Region, Iraq
e-mail: ezadin.mohamed@univsul.edu.iq

B. Al-hijab
University of Baghdad, Baghdad, Iraq

H. Al-sadi
Iraqi Oil Company (formerly), Baghdad, Iraq

M. Meghraoui et al. (eds.), *Advances in Geophysics, Tectonics and Petroleum Geosciences*,
Advances in Science, Technology & Innovation, https://doi.org/10.1007/978-3-030-73026-0_56

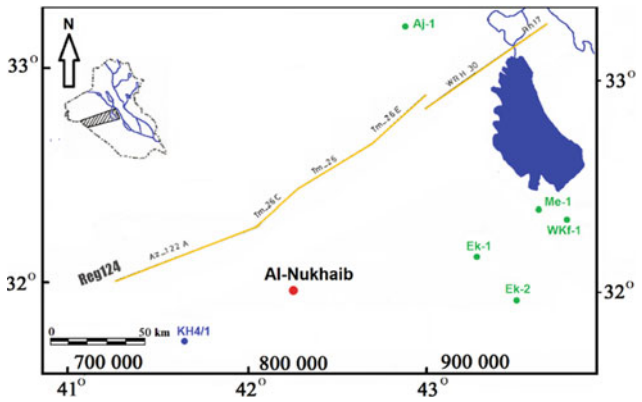

Fig. 1 Local seismic sections used to construct the regional line (Reg124)

of a regional line, as shown in Fig. 1. These local areas are of different topographical and geological natures. Therefore, the final stacked lines have been of different quality ranges between good in western and eastern parts and poor in the central part. The selected local lines are merged at intersecting adjacent points, which make up one line forming a regional line called Reg124 (Fig. 1).

3 Results

After constructing the regional seismic line, we applied several necessary processing steps to get the best quality reflectors of time and depth sections. We try to describe the results as the following.

3.1 Interpretation of the Regional Time Section

Nine reflectors on the regional seismic line are identified as follows:

H1 represents the Najmah and Gotnia formations of Jurassic age.
H2 represents the Kurra Chini, Mallusa, and Zor Houran of Triassic age.
H3 represents the Ga'ara (in the western part).
H4 represents one of these formations: Ora, Kaista, or Harur of Carbo/Devonian times.
H5 represents the Akkas formation of Silurian time.
H6 represents the Khabour quartzite formation of Ordovician age (strong reflector, sometime is composed of three succession cycles).
H7 represents the "bottom of Khabour quartzite" or perhaps the "top of the Cambrian" rocks.
H8 represents the top of Burj limestone formation of Middle Cambrian age which is identified in the Jordanian territory.

Finally, we tried to identify (or estimate) the basement surface (H9) (see Table 1).

A Paleotime high (*Anbar uplift*) appears at the southwestern part of the area. The amplitude of the Paleotime decreases toward the south. The top and the northeastern part of the line is highly deformed and fractured, and more faults are detected. The upper part of the reflectors (H1–H5) is dipping regionally toward the northeast. The reflectors of the western side of the Paleotime high "*Anbar uplift"* (H6–H9) are dipping toward the southwest. In general, all the reflectors are dipping steeply toward the NE.

3.2 Depth Section of the Regional Line

The depth sections (Fig. 2) show regional dipping trends toward the east. All the formations deepen more steeply toward the east (the southeastern part is steeper than the northeastern part of the regional lines). The Mesozoic and Upper Paleozoic formations thicken, while the Lower Paleozoic formations are becoming thinner.

Structurally, the eastern flank of the Anbar uplift appears on the southwestern part of the line sloping toward the northeast gently. The maximum amplitude of the uplift at this line is less than one kilometer and may be formed through the Caledonian and Hercynian orogenies. The formations from the Jurassic down to the basement appear at depths approximately 783, 1304, 1913, 2565, 3043, 3565, 4696, 6087, and 7391 m, respectively. Many vertical or sub-vertical faults of small displacements are observed on

Table 1 Reflectors and the represented formation

R	Formation	Age	R	Formation	Age	R	Formation	Age
H1	Najmah and Gotnia	Jurassic	H4	Ora, Kaista, or Harur	Carbo/Devonian	H7	Bottom of Khabour quartzite	Top of the Cambrian
H2	Kurra Chini, Mallusa, and Zor Houran	Triassic	H5	Akkas	Silurian	H8	Top of Burj limestone	Middle Cambrian
H3	Ga'ara (in the western part)	Triassic	H6	Khabour quartzite	Ordovician	H9	Basement	

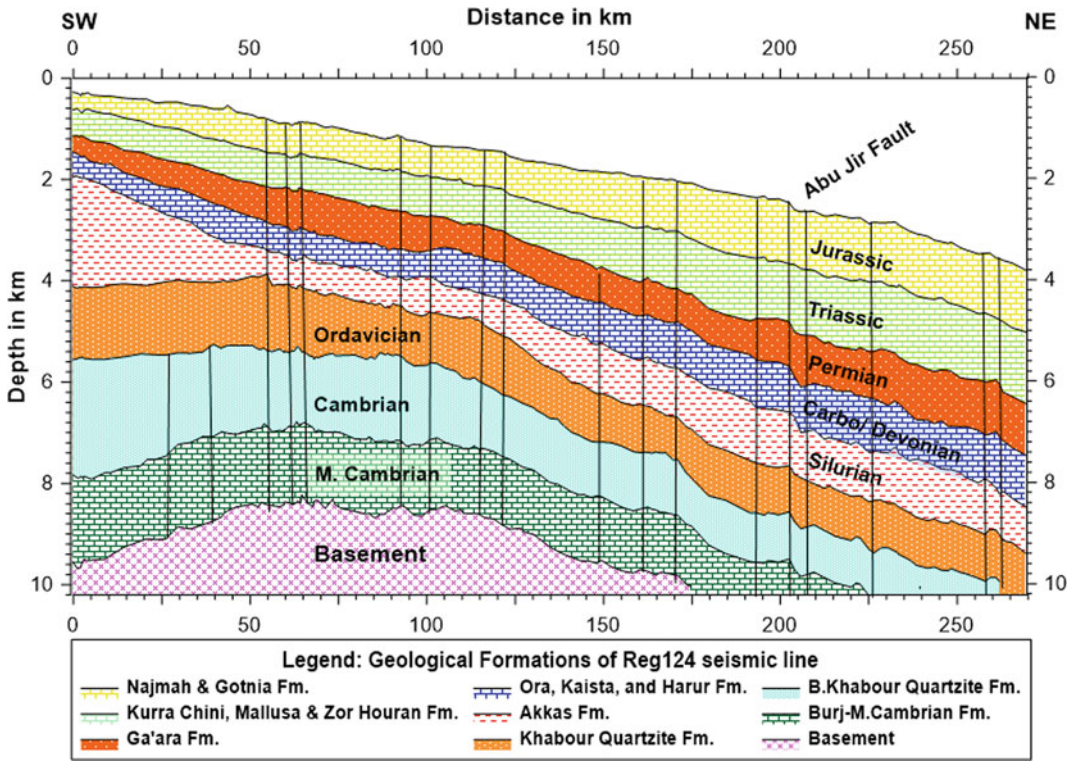

Fig. 2 Depth cross section of Reg124 line with picking faults

the regional line (Fig. 2), especially on the northeastern part of the line. Most of these faults come out from basement or deeper, penetrating most of the Paleozoic and the Mesozoic sediments. Some of them reach the surface, especially in Abu Jir fault zone.

Stratigraphically, the formations are divided into two sequences. The basement to Ordovician rocks represents the lower sequence, parallel to sub-parallel, thicker at the western part and thinner toward the east (convergence). The rocks of the Silurian to Jurassic times appear as the upper sequence, thinning in the west and thickening toward the east (divergence). Each sequence may be representing one cycle of depositions. The dipping, thickness, and deepening of the beds of the lower group are significantly different from those of the upper sequence. The stratigraphic traps can be expected in the eastern part of the line due to the transition from the platform to the Mesopotamian sedimentary basin. All the formations are dipping and deepening toward the northeast.

3.3 Flattening of the Regional Line Reflectors

The flattening technique is applied to Jurassic, Silurian, and top of Ordovician reflectors to remove the effect of other formations (back strip thickness, by removing the reflectors from the basin gradually). Generally, the volcanic activity, deformation, and uplifting of the rocks occur due to the Caledonian orogeny which caused uplifting the deposits beneath the Late Silurian.

Flattening of the Ordovician reflector shows that the whole studied area is nearly flat during the deposition of the Cambrian and Ordovician sediments. No any indication or trace of the Paleohighs (Anbar uplifts) is observed on the flattening basement, Cambrian, and Ordovician reflectors of the regional seismic lines. The reflectors are parallel and horizontal; this means that the depositions occurred in a quiet and calm environment, and no tectonic movements have affected the area during those times. Flattening of the Silurian reflector shows the effect of Anbar uplift and appears that it was uplifted at the end of Late Silurian–Early Devonian. This uplift is caused by the Caledonian orogeny. After that, the erosion of these rocks began. Although the effect of this erosion was clearly revealed in the center of the Anbar uplift where the Silurian deposits are very thin, it thickens on both sides of the uplift, especially on the western side.

Flattening of the Jurassic reflector: It seems that through the deposition of the Jurassic formations, the two sequences of the reflectors can be noticed. On the flattening lines, thus the Anbar uplift also appears on the regional line. This means that the uplifting in the area has occurred before. The surface of the reflector is faultier and more undulate.

The on-lap phenomena between the Silurian and Ordovician reflectors are manifest. At any rate, the transgression of the sea has covered all the central and eastern parts of the studied area, while the western and southwestern parts are positive areas.

4 Discussion

Al-Bassam et al. (1997) believed that the Anbar uplift is a part of the Hail Rutba Arch in Iraq. We believe that this uplift has occurred during the Caledonian orogeny then it was subjected to erosion relatively for a short period, then the subsidence occurred again, it might be stable, or the transgression of the sea might be continued in this region. Most workers who are studying the Saudi Arabian part of the arch believed that the uplift occurred during the Hercynian orogeny (Late Devonian–Early Carboniferous). However, the formation from Cambrian to Lower Devonian ages can be noticed on the arch, while the formations of post-Devonian till Cenozoic are missing (Fig. 2). The wells, drilled in Saudi Arabia near the southwestern part of the studied area, penetrated all the formations from the Paleozoic to Mesozoic and show that there is no indication that uplifting occurred in that area after these two orogenies. Also, many vertical or sub-vertical faults of small displacements are observed on the regional line (Fig. 2). Most of the faults come out from the basement or deeper, penetrating most of the Paleozoic and the Mesozoic sediments. Some of them reach the surface mainly at Abu Jir fault zone. Thus, it seems that most of them bound the sub-blocks forming features like horst and grabens, which may be referred to the acting of the vertical movements in the area too. Tamar-Agha (1899) believed that the vertical movements are a translation of the lateral movements, which are induced as a sequence of the interaction and differential movements of the adjacent basement blocks. However, we thought that the source of the movements is mostly vertical movements or isostatic.

5 Conclusions

a. Two major groups of reflectors can be recognized on the regional seismic line sections. The first group consists of Jurassic, Triassic, Permian, Carbo/Devonian, and Silurian reflectors. The second group consists of Ordovician, bottom of Ordovician (top of Cambrian), Middle Cambrian, and basement reflectors.
b. Anbar uplift is situated at the western and central parts of the studied area. It seems that it has been formed during the Caledonian orogeny at Late Silurian–Early Devonian.
c. Most of the observed faults are vertical or sub-vertical, generated from the basement and cutting most of the Paleozoic and Mesozoic rocks.

References

Al-Bassam, K.S., Al-Bdaiwi, J.M., Al-Kadhimi, J.A: A study about the extending of the Ha'il arch inside Iraq: a new data from Nukhaib area at southern Iraq. Geosci. Arab Dev. **1–2**, 12–23 (1997)

Fouad, S.F.A.: Tectonic and structural evolution. Iraqi Bull. Geol. Min. Special Issue, 2007: Geology of Iraqi Western Desert, pp. 29−50 (2007)

Poulos, H.G.: A review of geological and geotechnical features of some Middle Eastern countries. Springer, Innovative Infrastructure Solutions (2018)

Tamar-Agha, M.Y.: Exploration, and processing in the Ga'ara depression, part one, general geology, GEOSURF, Report No. 1899, Baghdad. 145p (1993)

Fusion of Seismic Attributes Using Evidence Theory

Noomane Drissi and Ahmed Labidi

Abstract

Seismic attributes are derived from the seismic data in order to help the interpreter to explore and monitor the reservoir. Since the introduction of the first instantaneous attributes, the number of seismic attributes is becoming more and more critical, and each attribute has a specific significance. In the vicinity of a well, it is easy to correlate the data to the geology. However, when there is no well data available, which is usually the case; interpreters have to extract the best attribute(s) that have a geological significance. The proposed method in this paper is to integrate two instantaneous attributes using the evidence theory (also called Dempster Shafer theory) to generate a map of hydrocarbon distribution in order to delineate the reservoir better and to find new well locations.

Keywords

Seismic attributes • Fusion • Evidence theory

1 Introduction

The objective of this work is the delineation of the main reservoir and the detection of infill areas near the producing wells using the evidence theory by combining the instantaneous amplitude and the instantaneous frequency (Shafer 1976). Two unsupervised approaches are proposed where the basic probability assignments (BPAs) are derived after the application of a fuzzy c-means clustering. The decision map, which gives the hydrocarbon distribution of the field, is made based on the maximum belief. In the first section, seismic attributes are presented. After that, a brief introduction to the evidence theory is done. In Sect. 4, the two methods are presented. Finally, conclusions are given in the last section.

2 Seismic Attributes

Instantaneous attributes were introduced by Taner et al. (1977, 1979). Let $f(t)$ be the real trace in function of time. The complex trace is defined as $F(t) = f(t) + jf^*(t)$ where the quantity f^* is the Hilbert transform of f (Layer and Tomczyk 2015). The complex trace can also be written $F(t) = e(t).\exp(j\varphi(t))$. The instantaneous amplitude is then defined as the magnitude of the complex trace $e(t) = |F(t)| = \sqrt{f(t)^2 + f^*(t)^2}$. Similarly, the instantaneous phase φ and the instantaneous frequency ν are defined by $\varphi(t)=\arctan\left(\frac{f^*(t)}{f(t)}\right)$ and $\nu(t) = \frac{d\varphi(t)}{dt}$. Instantaneous attributes have many applications in reservoir characterization and reservoir monitoring (Quincy and Steve 1997; Sønneland and Barkved 1990). In this work, we will focus only on the instantaneous amplitude and instantaneous frequency for the delineation of the reservoir and the detection of infill locations and explorable areas. The seismic volume was used to extract the instantaneous amplitude and the instantaneous frequency than the two attributes were extracted along the top reservoir surface (time map). The instantaneous amplitude is generally low except in the vicinity of faults and discontinuities (south-western region) where the seismic signal is not coherent. However, it cannot distinguish between the reservoir and non-reservoir areas. Similarly, the instantaneous frequency map cannot distinguish between the reservoir and non-reservoir areas.

Clustering method is applied to the cross plot of the two attributes to calculate the membership degree in order to compute the mass function using two different methods (Celikyilmaz and Türksen 2009). The fusion of the two attributes is then performed using the evidence theory (Mordeson et al. 2013).

N. Drissi (✉)
SEREPT, 8 Avenue Slimen Ben Slimen BP 46, 2092 Manar 2, Tunis, Tunisia

A. Labidi
Faculty of Science of Tunis, 2092 Manar 2, Tunis, Tunisia

M. Meghraoui et al. (eds.), *Advances in Geophysics, Tectonics and Petroleum Geosciences*,
Advances in Science, Technology & Innovation, https://doi.org/10.1007/978-3-030-73026-0_57

3 Introduction to the Evidence Theory

The hypothesis set θ is called the frame of discernment. It is the set of the mutually exclusive and exhaustive propositions $\theta = \{w_1, w_2, \ldots, w_N\}$. Evidence on a subset $B \subset \theta$ is represented by a basic probability assignment BPA: $m(B) \geq 0$ (called also mass function). Subsets with non-zero BPA are called focal elements. PBA must verify some conditions. Let $A_i \in 2^\theta$, we have $0 \leq m(A_i) \leq 1$; $m(\varnothing) = 0$ and $\sum A_i \in 2^\theta m(A_i) = 1$.

The BPA presents the advantage (compared to probability) that it assigns a mass value to the union $w_1 \cup w_2$ when the information source cannot distinguish between the two propositions. Also, BPAs from different sources can be combined using the following Dempster's orthogonal rule

$$m(A_k) = \frac{1}{1-K} \times \sum_{A_1 \cap A_2 \ldots A_N = A_k} \prod_{1 \leq j \leq N} m_j(A_j);\ k = \sum_{A_1 \cap A_2 \ldots A_N = \emptyset} \left(\prod_{1 \leq j \leq N} m_j(A_j) \right)$$

where m is the new mass function and k is a scaling factor often interpreted as a measure of the conflict between sources.

The most important and most challenging part is the derivation of the BPA because it represents the knowledge about the uncertainty incorporated in the source (Boudraa et al. 2004). The decision rule used in this paper is the maximum belief among simple hypothesis (Bloch 1996; Mordeson et al. 2013). In the next section, we will use evidence theory to integrate the two attributes using two unsupervised methods.

4 Unsupervised Approaches

4.1 Method 1

In this section, the BPAF is defined using the method introduced in Boudraa et al. (2004). Let $\beta = \max_{i=1,2} \mu_i$, $\alpha = \beta - \min_{i=1,2} \mu_i$.

if $|\mu_k - \mu_l| \leq \xi$ then $m(\theta) = \alpha$ and $m(W_i) = (1 - \alpha) \times \mu_i$.

else $m(\theta) = 0$, $m(W_1) = \mu_1 \times (\mu_2 - \mu_1)$ and $m(W_2) = 1 - m(W_1)$.

Where ξ is a threshold value (a 0.7 value is used).

The fusion result is shown in Fig. 1. In addition to the main producing area in the central part, this method confirmed the prospectivity of two leads: lead one (the footwall area of the main fault) and lead two (the western region delimited by two faults).

4.2 Method 2

This method defines the non-normalized basic probability assignments as equal to the membership functions (Bentabet et al. 2000) and the quantity of uncertain is approximated by:

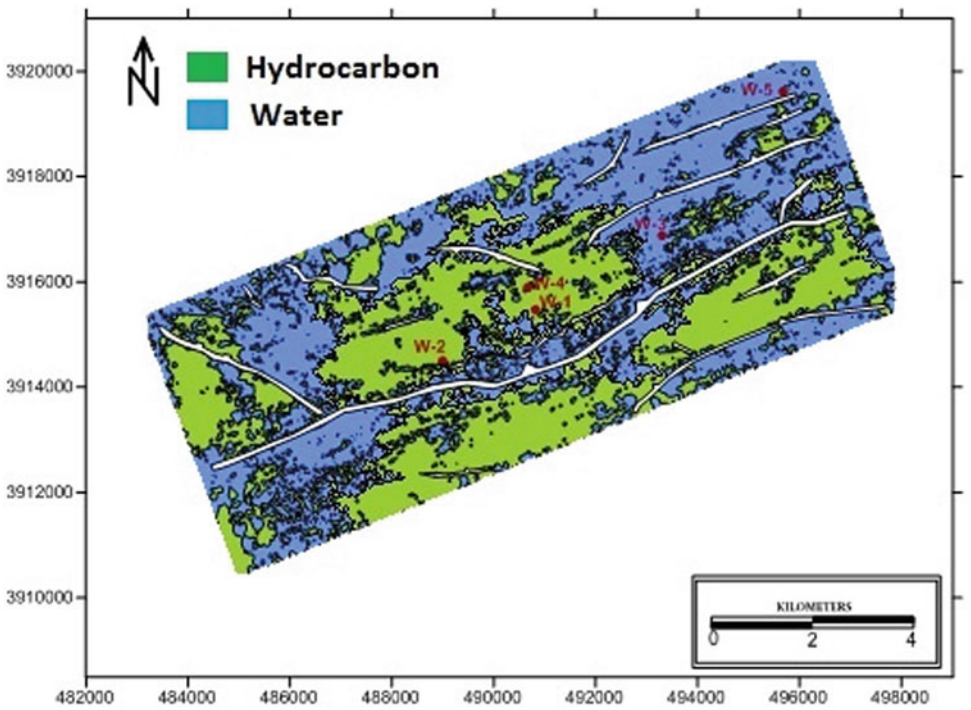

Fig. 1 Fusion using method1: Hydrocarbon (green) and water (blue)

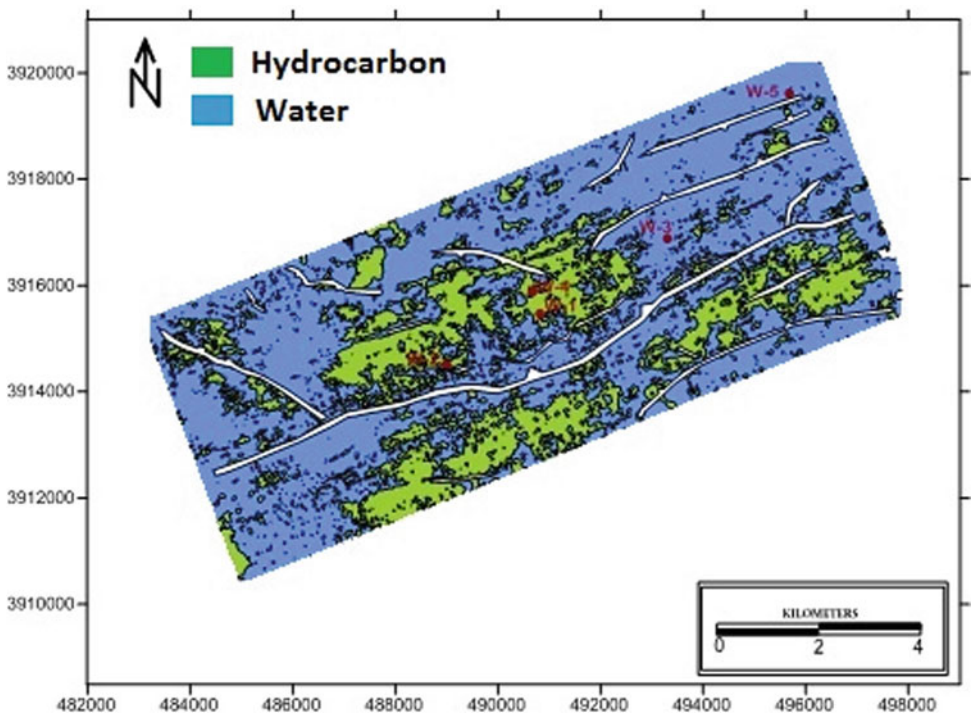

Fig. 2 Fusion using method 2: Hydrocarbon (green) and water (blue)

$$\tilde{m}(H_1 \cup H_2) = \frac{2\mu_1\mu_2}{\mu_1 + \mu_2}, \tilde{m}_1 = \mu_1 \text{ and } \tilde{m}_2 = \mu_2$$

In this case, the normalized BPAs are given by

$$\begin{aligned} m(H_1) &= \frac{\tilde{m}_1}{\tilde{m}_1 + \tilde{m}_2 + \tilde{m}(H_1 \cup H_2)}, m(H_2) \\ &= \frac{\tilde{m}_2}{\tilde{m}_1 + \tilde{m}_2 + \tilde{m}(H_1 \cup H_2)} \\ \text{and } m(H_1 \cup H_2) &= 1 - m(H_1) - m(H_2), \end{aligned}$$

The same decision criteria are applied, and the resulting fusion map is shown in Fig. 2. This map confirms the main reservoir area and the lead one. However, the prospect of lead two is not confirmed. This method also shows less possible hydrocarbon area (total green area). The difference between the two methods is in quantity and the interval of uncertainty in the BPA construction. In fact, in method 1, the mass of uncertainty depends on the ability to discriminate the two clusters and masses are defined based on this, i.e. if the discrimination between clusters is clear, the mass affected to uncertainty is null. In the other hand, method 2 defines the uncertainty for different values of membership functions. For this reason, method 1 gives a low mass in the zones where the ambiguity is low, contrary to method 2, which gives a greater mass of uncertainty. Thus, method 1 is more optimistic for explorations and method two is more pessimistic for production geoscientists.

5 Conclusion

In this paper, we introduced different methods of fusion of instantaneous attributes based on the evidence theory. They are based on the membership computation and then the construction of the basic probability assignment functions. These methods show interesting results in the detection of the reservoir area for new infill well locations and the detection of new explorable areas. The added value of the unsupervised methods is to bring different optimistic and pessimistic views to the interpretation.

References

Bentabet, L., Zhu, Y., Dupuis, O., Kaftandjian, V., Babot, D., Rombaut, M.: Use of fuzzy clustering for determining mass functions dempster-shafer theory. In: 5th international Proceeding in Signal Processing, pp.1462–1470. 16th World Computer Congress 2000, Beijing, China (2000)

Bloch, I.: Some aspect of dempster-shafer evidence theory for classification of multimodality medical images taking partial volume effect into account. Pattern Recogn. Lett. **17**, 905–916 (1996)

Boudraa, A., Bentabet, A., Salzenstein, F., Guillon, L.: Dempster-shafer's basic probability assignment based on fuzzy membership functions. Electron. Lett. Comput. vis. Image Anal. **4**, 1–9 (2004)

Celikyilmaz, A., Türksen, I.B.: Improved fuzzy clustering. In: Modeling Uncertainty with Fuzzy Logic. Studies in Fuzziness and Soft Computing, vol. 240. Springer, Heidelberg (2009)

Layer, E., Tomczyk, K.: Hilbert transform. In: Signal Transforms in Dynamic Measurements. Studies in Systems, Decision and Control. Springer, Cham (2015)

Mordeson, J., Wierman, M., Clark, T., Pham, A., Redmond, M.: Evidence theory. In: Linear Models in the Mathematics of Uncertainty. Studies in Computational Intelligence. Springer, Heidelberg (2013)

Quincy, C., Steve, S.: Seismic attribute technology for reservoir forecasting and monitoring. Lead. Edge **16**(5), 445–448 (1997)

Shafer, G.: A Mathematical Theory of Evidence. Princeton University Press (1976)

Sønneland, L., Barkved, O.: Use of Seismic Attributes in Reservoir Characterization. In: Buller, A.T., Berg E., Hjelmeland O., Kleppe J., Torsæter O., Aasen J.O. (eds.) North Sea Oil and Gas Reservoirs—II. Springer, Dordrecht (1990)

Taner, T., Koehler, F., Sheriff, R.: Complex seismic trace analysis. Geophysics **6**(44), 1041–1063 (1979)

Taner, T., Sheriff, R., Koehler, F., Frye, D.: Extraction and interpretation of complex seismic trace. In: 6th Annual Convention Proceedings, vol. 2, pp. 305–316 (1977)

Seismic Data Compression: A Survey

Hilal Nuha, Mohamed Mohandes, Bo Liu, and Ali Al-Shaikhi

Abstract

With the advent of robust computing power, any sophisticated algorithm for data compression is becoming a trivial task. With more than petabytes of seismic data produced every day and the trend toward 4D survey, it is becoming essential to develop robust algorithms for the seismic data compression. This led to significant research efforts in data compression for field implementation, as shown by the research trends. The study of seismic data compression techniques is the main focus of this paper. In particular, we provide a short survey of different seismic data compression methods. This survey covers several categories of compression techniques, namely transformation, prediction, quantization, run length, and sampling. This paper can be deemed an initial attempt to provide an up-to-date overview of the research work carried in this all-important field of seismic data processing.

Keywords

Seismics • Data compression • Survey

1 Introduction

Along with the rising demand for oil and gas, it is desirable to produce a higher quality of seismic images, which in turn requires the acquisition of more seismic data. The emergence of more advanced seismic data acquisition techniques has led to the production of datasets capable of burdening network capacities of the latest communication technologies. The development of networked and distributed computing environment has aggravated most problems of dealing with seismic data that can approach or even exceed petabyte levels (Boman 2017). It is advisable to reduce the volume of data to be stored and transmitted as long as this can be achieved without loss of significant accuracy (Ergas et al. 1998). For that purpose, data compression is considered as an essential solution to handle sizeable seismic data volume (Rosten et al. 2000) efficiently.

The idea of seismic data compression was initiated in 1974 (Wood 1974), but the idea did not gain much attention from researchers and practitioners—Figure 1 shows the yearwise publications since 1974 for different types of seismic data compression. The data is collected from Scopus using a combination of search keyword seismic data compression (i.e., seismic, data compression). Overall, we notice a significant increase in early 1990, but the trend does not show any annual increase in this field. However, this area is still active as new geophysical acquisition techniques like 3D and 4D schemes arise along with rapidly growing computing power in the geophones or sensors. This paper attempts to summarize the efforts from past decades of seismic data compression scheme by presenting a short survey in the area.

2 Methodologies

In this section, we list and describe the methods used for seismic data compression and its classification. Herein, the current works are classified based on the compression technique utilized for seismic data. We use a similar classification of data compression presented in Salomon (2007) for seismic data case. The major categories of seismic data compression include sampling, run length, prediction, quantization, and transformation-based techniques. Table 1 summarizes the overall characteristics of each approach. Run length-based technique is typically used for lossless

H. Nuha · M. Mohandes (✉) · B. Liu · A. Al-Shaikhi
King Fahd University of Petroleum and Minerals (KFUPM), Dhahran, 31261, Saudi Arabia
e-mail: mohandes@kfupm.edu.sa

M. Meghraoui et al. (eds.), *Advances in Geophysics, Tectonics and Petroleum Geosciences*,
Advances in Science, Technology & Innovation, https://doi.org/10.1007/978-3-030-73026-0_58

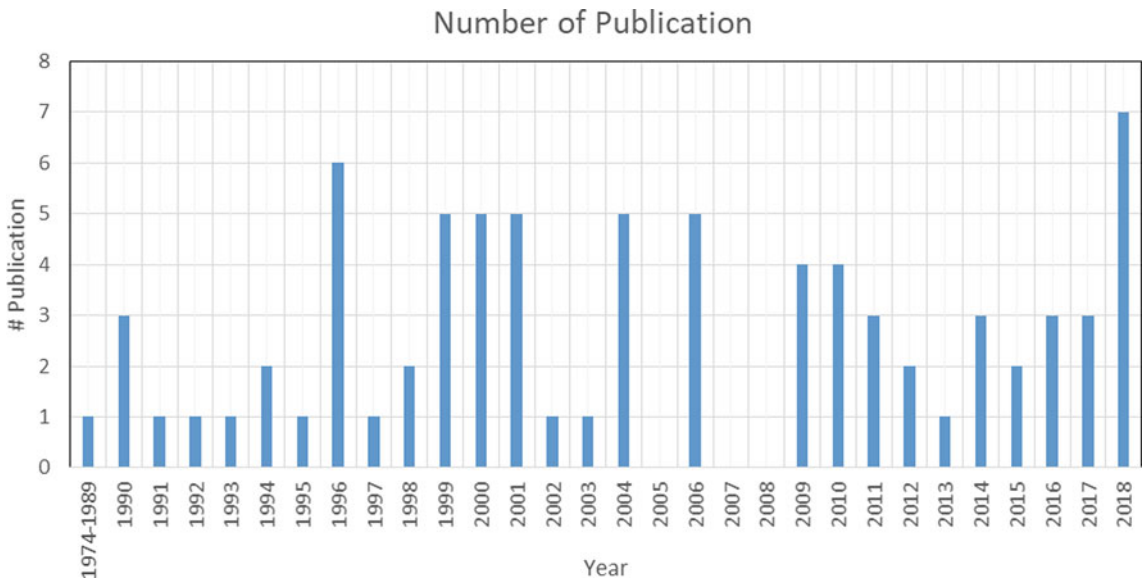

Fig. 1 Total number of yearwise publications since 1974 (Scopus)

Table 1 Characteristics of each approach

Aspect	Sampling	Quantization	RLE	Prediction	Transformation	Machine learning
Lossy/less	Lossy	Lossy	Lossless	Lossy	Lossy	Lossy
Overhead	None	Quantization steps	List of symbol frequency	Predictor coefficients	Transformation weights	Model weights

compression while other techniques are utilized for lossy compression to achieve higher compression ratios. From the types of overhead perspective, sampling-based compression has no overhead. However, for sampling-based compression, the overhead may be in the form of coefficients for data recovery using interpolation. For transformation with a fixed basis, the transform weights can be disregarded since the coefficients are fixed for all data.

2.1 Sampling-Based Compression

A seismic trace is a continuous signal sampled with a fixed sampling period. Intuitively, it is evident that a high sampling rate leads to a better signal representation. However, such signal contains much more samples and has larger file sizes. Therefore, the major problem is how often to sample a given wave. The solution to such problem is to sample seismic wave with slightly above the Nyquist frequency, which is represented by twice the highest frequency contained in the wave (Salomon 2004, 2007).

2.2 Quantization-Based Compression

Quantization is a simple technique to achieve lossy compressions. The technique starts by creating a finite list of symbols, called quantizer, and maps each of the actual samples to the closest symbol. For instance, if a sample is a real number located within a specific interval, then the number can be replaced by the nearest integer. Since integers require fewer bits, the data volume is smaller. However, such technique yields the lossy technique since it is impossible to obtain the actual value from the integers (Salomon 2007; Failed 1995).

2.3 Run Length Encoding

The basic idea of run length encoding (RLE) is that in many types of data, adjacent samples are often correlated; therefore, it easy to find sequences of identical symbols which can be used for data compression. Each sequence of samples with the same value is represented as a pair consisting of run

length and sample value. The sample value can be encoded using original encoding style like integer or characters. This technique and its variants have been implemented in many works on seismic data compression to encode quantized samples (Averbuch et al. 2001).

2.4 Prediction-Based Compression

Statistical model-based data predictions or prediction-based compression (PBC) are encouraging ways of time-series compression, such as seismic data. In PBC, the inherent temporal correlation samples in a trace predict missing or future observations based on the statistical model and existing observations. The statistical model and its prediction accuracy are the core of the PBC (Razzaque et al. 2013) where the models rely mainly on auto-regression.

2.5 Transformation-Based Compression

Data compression algorithms commonly have two main steps to achieve higher compression ratios. The first step is the decorrelation stage to exploit the redundancy in the data, and the second is an encoding which takes advantage of the reduced entropy in the data as indicated by lower entropy. Transformation-based compression approaches are prevalent for data decorrelation stage. The transformation techniques are designed to reduce data redundancy by identifying and removing the less important parts of the data. Transformation may use different types of basis; to name a few, cosine, wavelet, eigenvector from a covariance matrix. (Failed 1990; Spanias et al. 1991; Jones 1985; Liu et al. 2016).

2.6 Machine Learning and Other Techniques

Machine learning approaches may dominate other unclassified techniques in the above categories. Huang et al. (2003) proved that neural networks could be used to obtain principal components for dimensionality reduction of seismic data. The neural networks with multiple hidden layers for dimensionality reduction of seismic data are presented in Reddy et al. (2012). Nuha et al. (2019) investigated a deep neural network (DNN) and extreme learning machine (ELM) for the same purpose.

3 Conclusions

In this paper, we presented a brief discussion of different types of seismic data compression methods. We classified a large number of compression techniques proposed for seismic data to several classes. It is worth mentioning the transformation approaches, especially the wave-based, dominate the compression methods proposed for seismic data. This approach is intuitive since a seismic signal is a wave that we can exploit for compression and should we be able to model the signal.

Acknowledgement This work is supported by the Center for Energy and Geo Processing (CeGP) at King Fahd University of Petroleum and Minerals (KFUPM), Dhahran, Saudi Arabia, under Project GTEC1801.

References

Averbuch, A.Z., Meyer, F., Stromberg, J.-O., Coifman, R., Vassiliou, A.: Low bit-rate efficient compression for seismic data. IEEE Trans. Image Process. **10**, 1801–1814 (2001)

Boman, K.: RigZone [Online]. Available: https://www.rigzone.com/news/oil_gas/a/140418/big_data_growth_continues_in_seismic_surveys/?all=hg2. Accessed 10 Oct 2017

Donoho, P., Ergas, R., Villasenor, J.: High-Performance Seismic Trace Compression. Houston (1995)

Ergas, R.A., Donoho, P.L., Villasenor, J.: Method for reducing data storage and transmission requirements for seismic data. Google Patents (1998)

Huang, K.-Y.: Seismic principal components analysis using neural networks. In: Geophysical Applications of Artificial Neural Networks and Fuzzy Logic, Springer, pp. 103–122 (2003)

Jonsson, S.B., Spanias, A.S.: Seismic data compression. In: Ninth Annual International Phoenix Conference on Computers and Communications, 1990. Conference Proceedings (1990)

Jones, I.F.: Applications of the Karhunen-Loeve Transform in Reflection Seismology (1985)

Liu, B., Nuha, H., Mohandes, M., Deriche, M., Fekri,F.: Disributed principal component analysis for data compression of sequential seismic sensor arrays. In: SEG Technical Program Expanded Abstracts 2016, Society of Exploration Geophysicists, 2016, pp. 250–254

Nuha, H., Balghonaim, A., Liu, B., Mohandes, M., Deriche, M., Fekri, F.: Deep neural networks with extreme learning machine for seismic data compression. Arab. J. Sci. Eng. **45**, 1–11 (2019)

Razzaque, M.A., Bleakley, C., Dobson, S.: Compression in wireless sensor networks: a survey and comparative evaluation. ACM Trans. Sens. Netw. (TOSN) **10**, 5 (2013)

Reddy, T.A., Devi, K.R., Gangashetty, S.V.: Nonlinear principal component analysis for seismic data compression. In: 2012 1st International Conference on Recent Advances in Information Technology (RAIT) (2012)

Rosten, T., Ramstad, T.A., Amundsen, L.: Lossless compression of seismic trace headers. In: 62nd EAGE Conference and Exhibition (2000)

Salomon, D.: Data Compression: The Complete Reference. Springer Science & Business Media (2004)

Salomon, D.: A Concise Introduction to Data Compression. Springer Science & Business Media (2007)

Spanias, A.S., Jonsson, S.B., Stearns, S.D.: Transform methods for seismic data compression. IEEE Trans. Geosci. Remote Sens. **29**, 407–416 (1991)

Wood, L.C.: Seismic data compression methods. Geophysics **39**, 499–525 (1974)

Edge Detector Radon Transform for Seismic Multiple Attenuation

Meysam Zarei and Hosein Hashemi

Abstract

Multiple attenuations are a critical and essential step in processing marine data. Radon transform is widely applicable for multiple attenuations with different functions (parabolic, linear or hyperbolic). The most critical challenge in radon domain is separating primary from multiples for filtering. We propose a new method based on pattern recognition and mathematical operation in offset domain to initialized input data for parabolic radon transform for separating primary and multiple in the transformed domain. Based on this idea, the multiple can be modelled accurately and subtracted from the original data. Result of applying this method on real data shows the power of this method to separate primaries from multiples in comparison to standard parabolic radon transform.

Keywords

Multiple attenuation • Parabolic radon • Edge detection • Pattern recognition

1 Introduction

Multiples are one of the significant forms of noise mostly visible in marine seismic data. Different methods are introduced for multiple attenuations based on multiple properties: periodicity (Peacock and Treitel 1969), coherency (Kneib and Bardan 1994), Wavefield extrapolation (Verschuur et al. 1992), move out and dip discrimination. The parabolic radon transform (RT) was introduced by to map different events in the CMP domain to radon domain. Hampson applied the parabolic radon transform to NMO-corrected gathers. Primaries in parabolic RT map to zeros move out part and multiples map to nonzero move out part of radon domain. The band-limited nature of seismic data, near offset energy sharing and far offset truncation in seismic data due to blurring effects on radon domain. This implies that distinguishing primaries and multiples in radon domain are a very crucial step. Some methods introduced for solving this problem and de-blurring radon domain. The reduction of resolution as a result of the limited aperture is less critical now using stochastic inversion with zero-order regularization, initially proposed by Thorson and Claerbout (1985), leading to the high-resolution time-domain RT. Sacchi and Ulrych (1995) implemented the sparse RT in the frequency domain using Bayes rule using a Cauchy form probability-density functions (PDFs), which is now generally applicable in seismic processing. Since then, some other variants of the sparse RT have been developed. Gholami (2017) developed the deconvolution RT (DecRT) as a generalization of conventional RT and to increase the temporal resolution. We introduced a new approach for de-blurring radon domain and achieved high-resolution radon panel to distinguish multiple areas in radon domain. The results of applying this method for initializing input for radon transform illustrate that the new approach for parabolic radon transform can lead to discrimination of the multiples area in radon domain.

2 Method

The direct forward parabolic Radon transform is defined as follows:

$$m(q,\tau) = \sum_{n=1}^{N} d(x_n, t = \tau + \theta x_n^2) \qquad (1)$$

M. Zarei · H. Hashemi (✉)
Institute of Geophysics, University of Tehran, Tehran, Iran
e-mail: hashemy@ut.ac.ir

M. Meghraoui et al. (eds.), *Advances in Geophysics, Tectonics and Petroleum Geosciences*,
Advances in Science, Technology & Innovation, https://doi.org/10.1007/978-3-030-73026-0_59

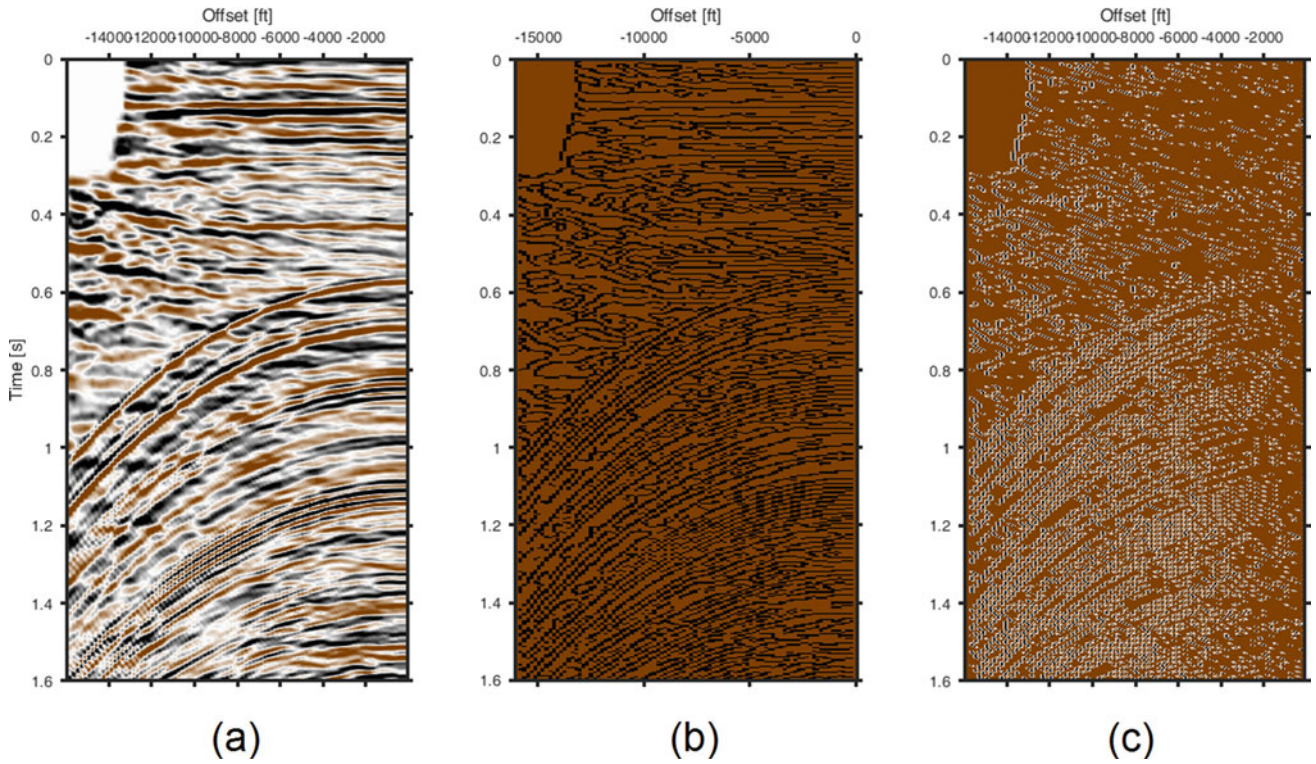

Fig. 1 **a** Input seismic data from Gulf of Mexico, **b** edge detection output using canny approach, **c** section b after mathematical operation for removing primaries

where $d(x_n, t)\ldots$ is the data in the offset (x)–time (t) domain, N is the number of traces, θ is ray parameter or slowness and $m(q, \tau)$ … is the data in the parabolic radon domain. In parabolic radon domain, primaries map to near-zero residual move out axis and multiples map to far from zero residual move outs. Nevertheless, separating multiples and primary area in radon panel is very critical and usually dependent on the knowledge and sense of processor. Canny (1986) developed a mathematical form with two criteria (low error rate and localization of the edge point) which can be used to design detectors for arbitrary edges. Canny assumed that the edge is centred at $x = 0$ and the filter has a finite response bounded between $[-w, w]$ around x. Using numerical optimization, Canny derives optimal operators for ridge and roof edges. He then specifies the criteria for step edges and gives a parametric closed form for the solution. Equations (2) and (3) are mathematical forms for the two criteria used in edge detection. Canny method is widely used in image processing techniques.

$$\mathrm{SNR} = \frac{\left|\int_{-w}^{+w} G(-x)f(x)\mathrm{d}x\right|}{n_0\sqrt{\int_{-w}^{+w} f^2(x)\mathrm{d}x}} \tag{2}$$

$$\text{Localization} = \frac{\left|\int_{-w}^{+w} G'(-x)f'(x)\mathrm{d}x\right|}{n_0\sqrt{\int_{-w}^{+w} f'^2(x)\mathrm{d}x}} \tag{3}$$

Which the impulsive response of the filter be $f(x)$ and denote the edge itself by $G(x)$.We used edge detection with canny approach to initialize input data for parabolic radon transform to obtain radon panel with higher resolution and better identifying of multiple area. At the first step, gain will be applied on data for better separation that appears between events in offset domain followed by applying the edge detection using Canny approach. The result of applying edge detection is shown in Fig. 1b. We use mathematical operation for removing primaries from edge detection output (Fig. 1b) and use this section as an input for parabolic radon transform. The mathematical operations consist of derivation along of offset axis. After derivation along the offset axis, primaries are suppressed and only multiples are modelled. The resultant section contains only ± 1 and zero value. Edge section after removing primaries is shown in Fig. 1c where the multiples remain mostly in edge section with some additional random noise which fade in radon transformation and distributed evenly in the radon domain.

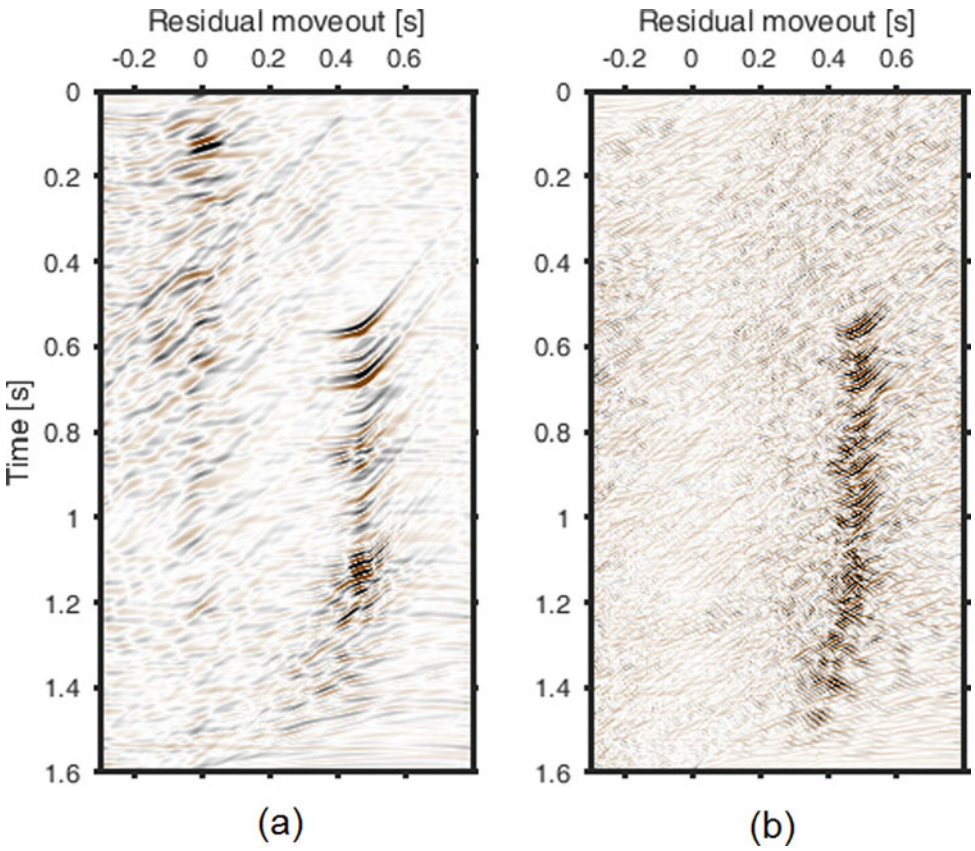

Fig. 2 **a** Parabolic radon transforms of input seismic data (Fig. 1a), **b** parabolic radon transform of Fig. 1c

After removing primary from edge section, we apply parabolic radon transform on data. The impact of applying radon transforms on real seismic data (the nmo-corrected marine gather from Gulf of Mexico (seismic lab toolbox)) and edge section is shown in Fig. 2. As you can see, only multiples map to radon domain and can identify multiples area without any problem. Using this method not only is the radon panel with higher resolution achieved but the range of multiples are also identified more accurately.

3 Discussion and Conclusion

In this paper, we presented the ground for the problem of separation primaries and multiples in radon domain and introduced a solution for solving this problem. We used edge detection with Canny approach for initializing input data for parabolic radon transform. By using this method, only multiples are mapped in radon domain. For better accuracy, the multiples range should be identified with more precision.

We use this method to localize multiple energy and avoid scattering in radon domain. So multiples can be found accurately, and then multiple suppression is performed using original seismic data and its parabolic RT. The result of applying this method to read data shows the advantages of this approach in multiple attenuation step in the marine seismic data processing. The most important achievement is increasing the resolution of the radon domain as the variance of amplitudes is highly attenuated, and only, the skeleton of seismic events is considered for radon computations. Moreover, we found that in future studies, it is feasible to mathematically have a criterion function to find the remnant NMO per events and find decision margin with higher precision and automatize the process as an adaptive one using machine learning technologies.

References

Canny, J.: A computational approach to edge detection. IEEE Trans. Pattern Anal. Mach. Intell. **PAMI-8**(6), 679–698 (1986)

Gholami, A.: Deconvolutive Radon transform. Geophysics **82**(2), V117–V125 (2017)

Kneib, G., Bardan, V.: Targeted multiple attenuation. 56th Mtg., Eur. Assn., Expl. Geophys., Extended Abstracts, H034 (1994)

Peacock, K., Treitel, S.: Predictive deconvolution-theory and practice. Geophysics **34**, 155–169 (1969)

Sacchi, M., Ulrych, T.: High-resolution velocity gathers and offset space reconstruction. Geophysics **60**, 1169–1177 (1995)

Thorson, R., Claerbout, J.: Velocity-stack and slant-stack stochastic inversion. Geophysics **50**, 2727–2741 (1985)

Verschuur, D., Berkhout, A., Wapenaar, C.: Adaptive surface-related multiple elimination. Geophysics **57**, 1166–1177 (1992)

A Comparison Between Distributed Fiber Optic Sensing and Geophone Detection for Passive Seismic Monitoring

Xun Luo, Ludovic Richard, and Joey Duan

Abstract

An investigation of seismicity differences between distributed optical fiber sensing (DOFS) and geophone detection was conducted in the laboratory in order to assess the applicability of DOFS for passive seismic monitoring in mining and civil engineering. The experiments used commercially available fiber cables, geophones and associated data acquisition instruments. The results obtained from the experiments have shown that DOFS can acquire passive seismic data with quality that is comparable to geophones. It has been proven that DOFS can achieve higher spatial resolution for seismicity sensing and higher accuracy for locating events than a customarily distributed geophone network. These characteristics are particularly useful for using DOFS to monitor ground vibrations associated with civil engineering and rock fracturing events induced by mining. It was also found that far more additional seismic events were recorded by the fibers than by the geophones. Automated data discrimination and processing methods must be developed in order to utilize DOFS for real-time civil and mining applications.

Keywords

Passive seismic • Distributed optic fiber sensing • Comparison experiments • Mining and civil engineering

1 Introduction

Distributed optical fiber sensing (DOFS) is an emerging technique over the past 20 years for monitoring ground vibration. This technique allows the sensing with a high spatial resolution at many locations using a single fiber. The concept of DFOS for vibration sensing is described in detail by Hartog (2017) and Domingues and Radwan (2017). In recent years, DOFS has been tested and used in many applications that are related to active and passive seismic sources, such as sensing ground vibration for border control (Owen et al. 2012), and ground movement for dam stability assessments (Thévenaz et al. 1999). For passive seismic applications, DOFS has been used for mapping microseismic events induced by hydraulic fracturing (Karrenbach et al. 2018). In mining, DOFS has been tested in underground conditions for temperature sensing (Willett et al. 1995) and rock deformation induced by strain changes (Naruse et al. 2007). However, few studies have been done on using DOFS to monitor microseismicity in mining and civil engineering. In this study, a comprehensive experiment was conducted to investigate seismicity characteristics obtained by DOFS and to compare the characteristics with those detected by conventional geophones. This study aims to find whether DOFS can replace expensive geophones in microseismic monitoring.

2 Experiment Settings

The experiments were carried out at the CSIRO Geophysical Laboratory in Brisbane. The fibers for trials were stretched out and laid on concrete slabs behind several work-shop buildings (Fig. 1). The total sensing length of the ground is 71 m which is sufficient for a fiber to detect arrival-time differences from a vibration source. Next to the fibers, four triaxial geophones (G1–G4) were installed at 15 m spacing to record seismic signals for comparing with those captured by the fibers.

The weight of sandbags achieved the coupling of the fibers with the concrete slabs. Forty-eight sandbags each weighing 10–15 kg were placed on the fiber cables, at

X. Luo (✉) · L. Richard · J. Duan
CSIRO Energy, Newcastle, Australia
e-mail: xun.luo@csiro.au

M. Meghraoui et al. (eds.), *Advances in Geophysics, Tectonics and Petroleum Geosciences*,
Advances in Science, Technology & Innovation, https://doi.org/10.1007/978-3-030-73026-0_60

Fig. 1 Hardware set-ups. On the left: Installation of the sensors (two fiber cables and a geophone) and coupling methods for the sensors. On the right: Laboratory installation of signal recorders (fiber interrogator and seismic recorder)

spacings of 1.5 m. The coupling of the geophones with the concrete was made by plaster of Paris.

The fiber interrogator, Silixa iDASTM made in the UK was used in this experiment for acquiring the fiber data. The signals from the four geophones were recorded simultaneously on a 12 channel microseismic recorder, manufactured in China. The time synchronization between the two instruments was made using GPS.

A military-level fiber with 4 single-mode cores and an ordinary communication fiber with multiple cores were used in the experiment. The geophones used were composed of 4.5 Hz geophone elements manufactured by GeoSpace Technologies, USA.

The experiments were conducted over three days for both active and passive seismic detections, from January 15th to 17th, 2019. During the day-time, active seismic detection experiments were carried out using hammer tapping on the concrete as a seismic source. During the nights, both DOFS and geophone instruments were left on to record ground vibrations from unknown passive seismic sources. All the geophones recorded some passive seismic events.

3 Results

The geophones over the nights recorded several passive seismic events from unknown source locations. Reviewing the continuous data recorded by the fiber interrogator against the geophone observations, these events were also captured by the fibers.

Figure 2 shows the seismic arrival times of a passive event that was recorded by both the geophones and the

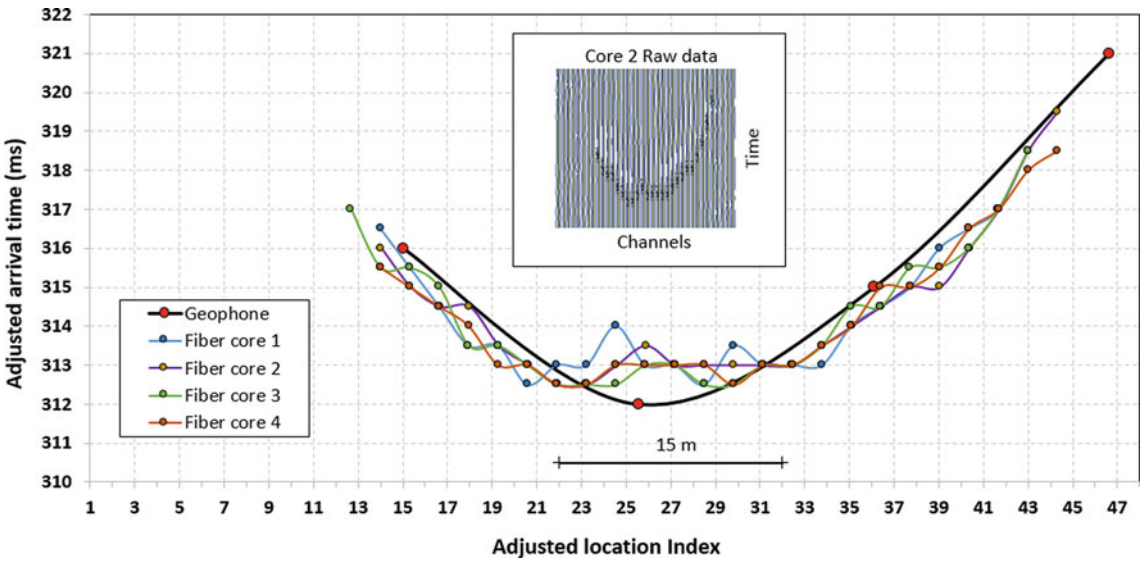

Fig. 2 Curves of the seismic arrival times of a passive event, obtained from the waveforms recorded by the geophones and four cores of the military-grade fiber cable. Insert: raw seismic waveforms captured by the second fiber core

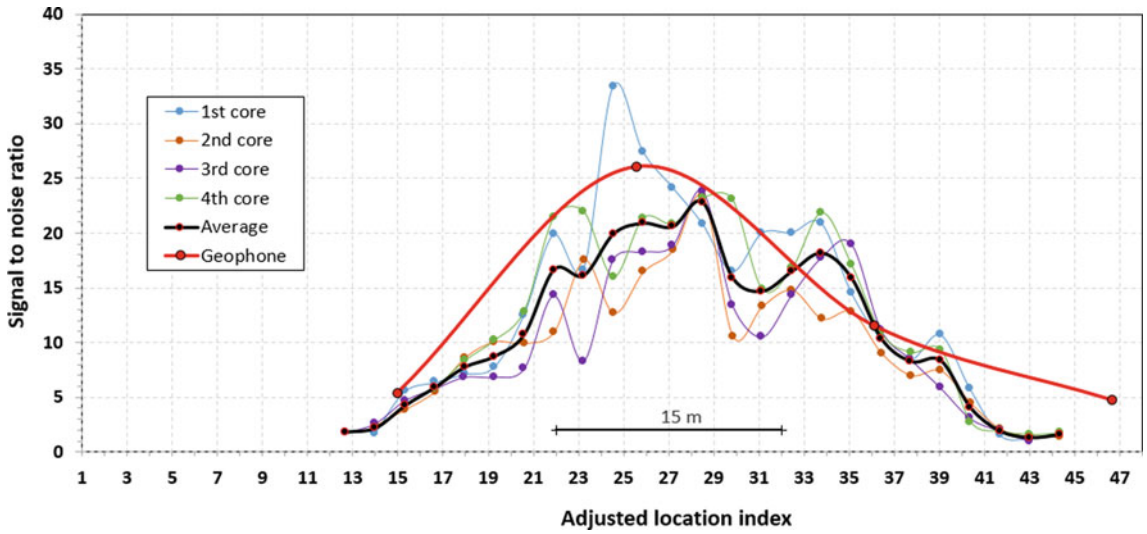

Fig. 3 The signal-to-noise ratio of the geophone and fiber data associated with the passive event. The black curve is the averaged result of the data of the four fiber cores

single-mode military-grade fiber. In general, the trends of the seismic arrival times obtained by the geophone record and four fiber cores are similar.

The reliability of the fibers for seismic detection was assessed using the signal-to-noise ratio (SNR). The SNR curves corresponding to the geophone and fiber data were obtained to the same passive event (Fig. 3). Based on the chart, the SNR values of the geophones are comparable to those obtained by the fibers. The seismic detection sensitivity of the fibers appears similar to that of the geophones. We can also observe the SNR data may be used to estimate the source location.

4 Conclusions

The results obtained from the experiments have shown that DOFS can acquire passive seismic data with quality that is comparable to geophones. It has been proven that DOFS can achieve high spatial resolution for seismicity sensing and high accuracy for locating events. These characteristics are particularly useful for using DOFS to monitor ground vibrations associated with civil engineering and rock fracturing events induced by mining.

During the passive monitoring periods, far more additional seismic events were recorded by the fibers than by the geophones. As it is impracticable to process all of the fiber data manually, automated data discrimination and processing methods must be developed in order to utilize DOFS for real-time civil and mining applications.

Acknowledgements The authors would like to thank Silixa, especially Michael Mondanos for providing us with the opportunity to use the iDAS system in this experiment.

References

Domingues, M.F.F., Radwan, A.: Optical Fiber Sensors for loT and Smart Devices. Springer International Publishing (2017)

Hartog, A.: An Introduction to Distributed Optical Fiber Sensors. Taylor & Francis Group, USA (2017)

Karrenbach, M., Cole, S., Ridge, A., Boone, K., Kahn, D., Rich, J., Silver, K., Langton, D.: Fiber-optic distributed acoustic sensing of microseismicity, strain and temperature during hydraulic fractur-ing. Geophysics **84**(1), D11–D23 (2018)

Naruse, H., Uehara, H., Deguchi, T., Fujihashi, K., Onishi, M., Espinoza, R., Guzman, C., Pardo, C., Orte-ga, C., Pinto, M.: Application of a distributed fibre optic strain sensing system to monitoring changes in the state of an underground mine. Meas. Sci. Technol. **18**, 3202–3210 (2007)

Owen, A., Duckworth, G., Worsley, J.: Fiber optic distributed acoustic sensing for border monitor-ing. IEEE 2012 European Intelligence and Security Informatics Conference, pp. 362–364 (2012)

Thévenaz, L., Facchini, M., Fellay, A., Robert, P., Inaudi, D., Dardel, B.: Monitoring of large struc-ture using distributed Brillouin fibre sensing. In: Proceedings of the 13th International Conference on Optical Fiber Sensors, Kyongju, Korea, 12–16 April 1999, pp. 5–8 (1999)

Willett, M.J., Wykes, J.S., Powell. G.A., Gibson, M.J., Cooke, A.: The use of a distributed optical fi-bre temperature sensing system to monitor underground mine roadways for spontaneous combustion. Mining Technol. **77**, 301–306 (1995)

A Weighted Metric for Semi-blind Seismic Data Quality Assessment

Hilal Nuha, Bo Liu, M. Mohandes, and Ali Al-Shaikhi

Abstract

Seismic data may undergo many types of distortions. However, the effect of distortion on raw data may not be apparent until the end of the standard processing of seismic reflection data. This paper presents a semi-blind metric for seismic data quality assessment, namely weighted normalized mean squared error (wNMSE). A weighting scheme is utilized on the data to shift more emphasis on the samples that are received later. Compared with conventional metrics, the proposed metric exhibits a higher correlation to the signal quality after standard processing steps for all tested noise types. This high correlation indicates that our proposed metric is suitable to quantify stacked seismic trace distortion level.

Keywords

Seismic data • Quality assessment • Mean squared error

1 Introduction

Seismic data acquisition is an essential part of a geophysical survey to discover the subsurface structure of the Earth. However, the acquisition system or data processing may introduce different types of distortions like white noise due to environmental condition or loss of information due to compression. Moreover, to obtain final subsurface images, each seismic trace in the data must undergo several processing steps which may magnify the effect of the distortion and eventually result in inaccurate subsurface images. Among different types of distortions, lossy compression is the most commonly notable one, due to the demand of reducing seismic data volume for storage and transmission (Zheng et al. 2019; Qureshi et al. 2016). Lossy compression can achieve high compression ratios (CR) with a reasonable error energy level. Therefore, researchers recently are focusing on this area (Failed 2018). Wood (Wood 1974) proposed two schemes of compressing seismic data, namely the Walsh transform method and time-domain interpolation technique. Transform methods like discrete cosine transform (DCT) were utilized for seismic data compression by Spanias et al. (Failed 1990). Principal component analysis (PCA) and its derivatives have been proposed for compressing seismic data (Liu et al. 2016; Failed 2003). More recently, modeling was utilized to represent seismic data with a significantly smaller representation by Liu et al. (2018). A generalized lapped orthogonal transform (GenLOT) was reported to achieve low signal reconstruction errors with high compression ratios (Duval and Nguyen 1999). Deep learning methods are also used for data compression in seismology by Nuha et al. (2019).

Despite its importance, seismic data quality assessment (SDQA) is still in an infancy stage. L2-norm-based metrics like the mean squared error (MSE), normalized MSE (NMSE), and signal-to-noise ratio (SNR) are typically used to represent the error energy level of such lossy compression. The major flaw of such metrics is its inability to measure information loss on signal segments with a lower magnitude. This paper proposes a weighted metric for SDQA. The weighting scheme is developed based on the gain correction procedure to magnify low-magnitude oscillation that may contain important information. This metric is considered a semi-blind metric since it uses raw seismic data as a reference but is expected to represent the final data quality without obtaining it. The metric is tested to quantify distortion level generated by a transform-based lossy compression and white Gaussian noise. The detailed proposed

H. Nuha · B. Liu · M. Mohandes (✉) · A. Al-Shaikhi
King Fahd University of Petroleum and Minerals (KFUPM), Dhahran, 31261, Saudi Arabia
e-mail: mohandes@kfupm.edu.sa

H. Nuha
School of Computing, Telkom University, Bandung, Indonesia

M. Meghraoui et al. (eds.), *Advances in Geophysics, Tectonics and Petroleum Geosciences*,
Advances in Science, Technology & Innovation, https://doi.org/10.1007/978-3-030-73026-0_61

metric is discussed in Sect. 2. We further use Pearson's linear correlation coefficient (PLCC) to measure the accuracy of the proposed metric, as shown in Sect. 3.

2 Proposed Metric

Seismic data may be distorted due to lossy compression. Typically, a higher compression ratio leads to a higher level of distortion. L2-norm-based MSE and SNR are two most popular metrics to measure the distortion level which represents the signal error energy. MSE is expressed as

$$\mathrm{MSE} = \frac{1}{\mathrm{MN}} \sum_{i=1}^{M} \|\hat{x}_i - x_i\|^2, \tag{1}$$

where M is the number of traces, $\boldsymbol{x_i} \in \boldsymbol{R^N}$ denotes the ith trace and the corresponding distorted seismic trace is $\hat{\boldsymbol{x}}_i$. Due to the high dynamic range of each seismic trace, MSE may not be relevant, therefore NMSE is proposed to represent the error energy relative to its original signal energy. NMSE is given by:

$$\mathrm{NMSE} = \frac{\sum_{i=1}^{M} \|\hat{x}_i - x_i\|^2}{\sum_{i=1}^{M} \|x_i\|^2}. \tag{2}$$

NMSE is related to SNR in decibel (dB) as follows

$$\mathrm{SNR}_{\mathrm{dB}} = -10 \log_{10} \frac{\sum_{i=1}^{M} \|\hat{x}_i - x_i\|^2}{\sum_{i=1}^{M} \|x_i\|^2} = -10 \log_{10} \mathrm{NMSE}. \tag{3}$$

In this paper, we introduce a weighted scheme for NMSE-based metric, namely weighted NMSE (wNMSE) where the metric is given by:

$$\mathrm{wNMSE} = \frac{\sum_{i=1}^{M} \|\mathbf{w} \circ (\hat{\boldsymbol{x}}_i - \boldsymbol{x}_i)\|^2}{\sum_{i=1}^{M} \|\boldsymbol{x}_i\|^2}. \tag{4}$$

where the operator $\circ\sim$ notes the element-wise vector multiplication. The weighting vector $\boldsymbol{w}$ is given by:

$$\boldsymbol{w} = \left[0\Delta t^2 2\Delta t^2 3\Delta t^2 \ldots (N-1)\Delta t^2\right] \tag{5}$$

where Δt and N denote the sampling period and number of sampling points of the seismic signal, respectively. This weighting scheme is to enlarge the amplitude of the errors from the later received part. The later a sample is received, the heavier weight is put on. The justification of this weighting scheme can be described as follows. The later received samples represent the reflected wavelet have traveled a longer distance; the signal energy has significantly waned when they arrive at the geophones. However, the L2-norm evaluation lays a more significant penalty on the higher errors more than, the smaller error. This diminishes the contribution of the later received samples, although they are equally crucial for revealing the geophysical structure.

The weighting vector magnifies the amplitude of the signal concerning time. The more extensive the signal time index, the more significant the multiplication factor. This weighting scheme yields a similar scale of the regular NMSE since other normalized metrics use denominator to compare the magnitude of the distortion energy concerning its original signal energy. If the distortion energy is larger than the original signal energy, then both metrics yield a ratio larger than unity.

2.1 Experimental Results

In this section, we test the performance of the proposed metric on the East Texas dataset (Mousa and Al-Shuhail 2011) and compare it with the performance of the conventional metrics. We introduce signal distortion from two resources, one is from the lossy DCT compression, and the other is merely adding white Gaussian noise. We first implement a standard seismic data processing to the original dataset obtaining the stacked traces. Stacked traces are the closest version of seismic trace before reaching the final subsurface image. The same procedure is then applied to those two sets of distorted seismic data, one is from lossy compression, and the other is from adding white noise, to evaluate the effect of different types of distortions to the final data. We apply the proposed metric along with the conventional one to measure the distortion level between the original and the distorted data. The metrics are accurate when the value of the metrics is measured before and after the stacking.

The standard seismic data processing consists of several steps namely: trace editing, gain correction, filtering, common midpoint (CMP) sorting, velocity analysis, normal move-out (NMO) correction, and stacking. We apply the steps to the data, both original and distorted ones, to obtain the stacked data. Figure 1 shows the effect of distorted raw data concerning the stacked trace.

Despite having the same level of raw data error energy, one can notice that different types of distortions lead to different error energy levels as shown in Table 1. For example, 5 dB of SNR for DCT compressed raw data yields a very low NMSE of stacked traces (whereas the same level of SNR for white noise leads to a relatively high NMSE of stacked traces).

Table 2 summarizes the Pearson's linear correlation coefficient (PLCC) comparison of the proposed metric and NMSE. We calculate the coefficient to determine the correlation between the metrics measure on the raw seismic trace and the error energy of the stacked trace. One can see that

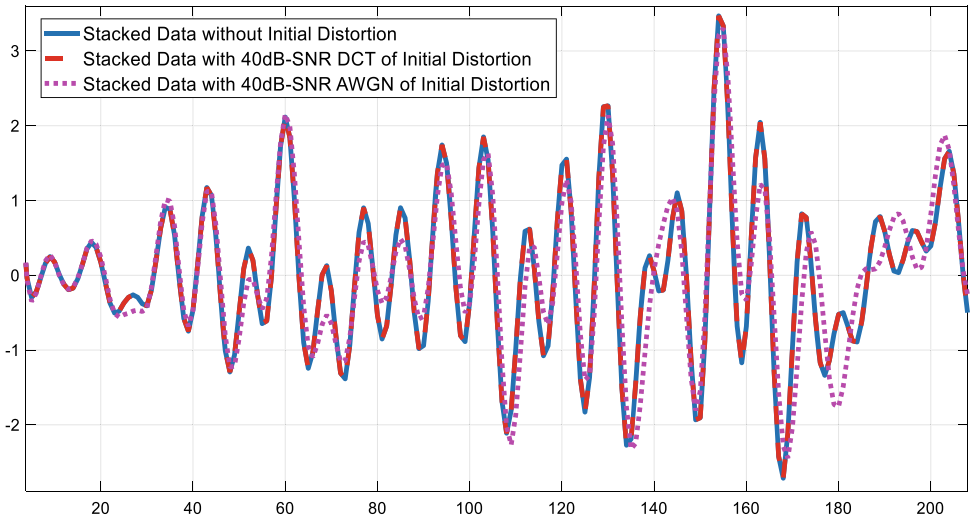

Fig. 1 Comparison of stacked data samples

Table 1 Results for different types of distortions

Raw data SNR (dB)	DCT			White noise		
	NMSE	wNMSE	Final NMSE	NMSE	wNMSE	Final NMSE
10	3.13e−5	6.94e−6	9.03e−07	3.152e−05	0.0005106	0.140366
20	0.00030	4.91e−5	9.77e−07	0.000316	0.0051475	0.3104859
30	0.03126	0.01824	0.003735	0.0031546	0.0511998	0.5700002
40	0.03126	0.01824	0.003735	0.0315653	0.5113124	0.8975484
50	0.31472	0.16840	0.287695	0.315713	5.1295847	1.1162313

Table 2 Linear correlation coefficients for different types of distortions

DCT PLCC		AWGN PLCC	
NMSE	wNMSE	NMSE	wNMSE
0.9397	0.9805	0.7046	0.7394

wNMSE shows higher correlations than that of standard NMSE for both types of distortion. This result indicates that the proposed metric better evaluates information loss than NMSE.

3 Conclusions

In this work, we presented a metric for seismic data quality assessment called the weighted normalized mean squared error (wNMSE). The weighting scheme enhances the energy of the later signal part, which usually has attenuated amplitudes. The metric was compared with NMSE on raw data distorted with DCT lossy compression and white noise. The performance is evaluated by taking stacked original data as a reference. The proposed metric exhibited a higher correlation for both types of distortions than that of the conventional metrics.

Acknowledgements This work is supported by the Center for Energy and Geo Processing (CeGP) at King Fahd University of Petroleum and Minerals (KFUPM), Dhahran, Saudi Arabia, under Project GTEC1801.

References

Duval, L.C., Nguyen, T.Q.: Seismic data compression: a comparative study between GenLOT and wavelet compression. In: Proceedings of SPIE—The International Society for Optical Engineering, 1999

Huang, K.-Y.: Seismic principal components analysis using neural networks. In: Geophysical Applications of Artificial Neural Networks and Fuzzy Logic, pp. 103–122. Springer, 2003

Liu, B., Nuha, H., Mohandes, M., Deriche, M., Fekri, F.: Disributed principal component analysis for data compression of sequential seismic sensor arrays. In: SEG Technical Program Expanded Abstracts 2016, pp. 250–254. Society of Exploration Geophysicists, 2016

Liu, B., Mohandes, M., Nuha, H.: Seismic model estimation using particle-swarm optimization. In: SEG Technical Program Expanded Abstracts 2018, Anaheim, 2018

Mousa, W., Al-Shuhail, A.: Processing of seismic reflection data using MATLAB, Morgan Claypool, 2011

Němcová, A., Smíšek, R., Maršánová, L., Smital, L., Vítek, M.: A comparative analysis of methods for evaluation of ECG signal quality after compression. BioMed. Res. Int. (2018)

Nuha, H., Balghonaim, A., Liu, B., Mohandes, M., Deriche, M., Fekri, F.: Deep neural networks with extreme learning machine for seismic data compression. Arabian J. Sci. Eng. 1–11 (2019)

Qureshi, M., Deriche, M., Beghdadi, A.: Quantifying blur in colour images using higher order singular values. Electron. Lett. **52**(21), 1755–1757 (2016)

Spanias, A.S., Jonsson, S.B., Stearns, S.D.: Transform coding algorithms for seismic data compression. In: IEEE International Symposium on Circuits and Systems (1990)

Wood, L.C.: Seismic data compression methods. Geophysics **39**, 499–525 (1974)

Zheng, F., Ling, Y., Tang, Y., Hui, S., Yang, H.: A fidelity-restricted distributed principal component analysis compression algorithm for non-cable seismographs. J. Appl. Geophys. (2019)

Reservoir Properties of Source Rocks from Well and Seismic Data: A Case Study of Geca Field, Onshore Niger Delta (Nigeria)

George-Best Azuoko, Amobi C. Ekwe, Chigozie J. Eze, Olufemi V. Omonona, and Amarachukwu A. Ibe

Abstract

The reservoir properties of source rocks from an onshore field in the Niger Delta basin in Nigeria have been investigated using well and 3D seismic data from the study area. This involved well log conditioning and analyses, well to seismic tie, acoustic impedance model building, model-based acoustic impedance inversion and generation of attribute slices of selected petrophysical parameters. The analyses of two wells—A and B having density, resistivity, gamma-ray and p-wave, porosity, shale volume and water saturation logs revealed four source rock intervals, A6115 and A7440 in well A, B5485 and B7205 in well B. Horizons (H1-H4) corresponding to the tops of these intervals were further generated. Intervals A7440 (with H2 at the top) and B7205 (with H3 at the top) having respective thicknesses of 80 and 25 ft were selected for a post-inversion attribute slice generation involving three key petrophysical parameters—porosity, resistivity and water saturation. Analyses of the attribute slices revealed that for H2, well B sits in an area of moderate to high values of porosity, resistivity and water saturation, while well A sits in an area of low values of these petrophysical parameters. For H3, we observed moderate to high values of the selected petrophysical parameters around well B location, as well as low to shallow values around well A location. Predominantly high values of these petrophysical parameters were also observed encapsulating the well locations. Thus, investigated source rocks (shale intervals) in the study area are viable reservoir rocks, holding shale hydrocarbon prospects.

Keywords

Niger Delta • Source rock • Reservoir rock • Well log • 3D seismic • Shale hydrocarbon

1 Introduction

Considering the overall decline in the production of conventional hydrocarbon, the need to explore the prospects inherent in shale reservoir hydrocarbons using available data previously used for conventional hydrocarbon prospecting arises. Jarvie et al. (2007) identified unconventional oil and gas as oil and gas exploitable by directly drilling and fracturing of low permeability fine-grained rocks acting as both source and reservoir. In the Nigerian inland basins, interests have been sparked lately in the prospect of basins concerning shale oil and gas (Avbovbo and Ayoola 1978; Idowu and Ekweozor 1993; Obaje and Abaa 1996; Ayodele 2013; Onuoha and Dim 2016). The Niger Delta basin is not excluded from this, as a significant advantage stems from the fact that extensive, conventional hydrocarbon exploration in the basin has made available, much seismic and well log data that will significantly be useful in unconventional hydrocarbon exploration. This current study using well and seismic data from GECA field onshore Niger Delta involves a combination of well log analyses and acoustic impedance inversion in the assessment of the hydrocarbon potentials of conventional source rocks, with the probability of hydrocarbon occurrence.

2 Materials and Methods

Well log data from the location of the study were used in this study. Two wells well A and B, each comprising of a suite of logs were analyzed using Hampson Russel's software. Well A comprised of density, resistivity, gamma-ray and

G.-B. Azuoko (✉) · A. C. Ekwe · C. J. Eze · O. V. Omonona
Department of Physics/Geology/Geophysics, Alex Ekwueme Federal University, Ndufu Alike, Nigeria

A. A. Ibe
Nigerian Maritime University, Okerenkoko, Delta State, Nigeria

M. Meghraoui et al. (eds.), *Advances in Geophysics, Tectonics and Petroleum Geosciences*,
Advances in Science, Technology & Innovation, https://doi.org/10.1007/978-3-030-73026-0_62

p-wave logs. In addition to these logs in well A, well B had more logs: porosity and shale volume logs. Transform porosity (from density) and subsequently water saturation logs (from porosity and resistivity logs) were generated for well A. Markers (A6115 and A7440 for well A; B5485 and B7205 for well B) were used to identify shale intervals of interest. The selection of these shale intervals was made on the basis that viable shale reservoirs are typically characterized by lower clay volumes, higher effective porosity and low water saturation (Holden et al. 2012).

Horizons (H1, H2, H3 and H4), at constant times corresponding, respectively, to the tops of the markers (A6115, A7440, B7205 and B5485), were next picked at constant times on 3D Post Stack Seismic. A well to seismic tie preceded a first model building for an acoustic impedance inversion. The acoustic impedance model was used first for an initial acoustic impedance inversion, followed by targeted advanced inversions involving selected rock properties—resistivity, water saturation and porosity. Considering their more exceptional thickness when compared to the other intervals (A6115 and B5485), attribute slices of these selected rock properties were ultimately extracted at constant times corresponding to the intervals A7440 (80 ft thick) and B7205 (25 ft thick) and their horizons. These slices were further analyzed to ascertain the viability of A7440 and B7205 as source rocks with the probability of unconventional hydrocarbon occurrence.

3 Results

3.1 Presentation of Results

Figure 1 is a suite of logs for well A, containing density, gamma ray, resistivity, porosity and P-wave logs. The highlighted intervals are shale intervals—A6115, A7440, B5485 and B7205**.** Also shown in Fig. 1 are the true vertical depths (TVD) in feet to the left and their corresponding two-way time (TWT) in milliseconds to the right. Figure 2 shows attribute slices for petrophysical parameters (porosity, resistivity and water saturation) from Horizon 2 and Horizon 3 (H2 and H3), corresponding to the top of markers A7440 and B7205.

In Fig. 1, A7440 covers a TVD range from 7440 to 7520 ft within well A. Relatively high value (as high as 150 API) is observed at about 7492 ft, while intercalations of low gamma-ray values are seen at TVDs between 7424 and 7484 ft. Low water saturation values are also observed within A7440 as well as high resistivity values. The useful porosity values range from about 38% at 7451 ft to about 18% at 7510 ft. Also observed are low values of density and low to intermediate *p*-wave velocities (in ft/s). Also within well A, the rock properties analyzed in interval A6115 (from 6115 to 6135 ft) have lower values of gamma-ray value, water saturation and resistivity, porosity, density and *p*-wave velocity.

Within B5485, the API value of the gamma-ray is relatively high (as high as 111API on a scale of 0–150 API). Low water saturation values ranging from about 0.1 to 0.2 on a scale of 0–1 are also observed within B5485, as well as high shale volume readings of 100%, with a little drop to about 76% recorded at about 5488 ft. Also observed are intermediate resistivity values, low *P*-wave values and porosity values ranging between 19 and 32%.

Interval B7205 shows gamma-ray units tending toward the shale line, reaching only as high as about 94 API, unlike the previously examined intervals that had much higher gamma-ray value. Low water saturation values range from 0.2 to about 0.3 within this interval (B7205), and the *P*-wave velocity, resistivity and porosity are consistent with the observations in the other markers within well B. However, intermediate shale volume values are observed in B7205**,** unlike the very high shale volume units observed in B5485**.**

Attribute slices taken at the top of Interval A7440 presented as horizon 2 (H2) in Fig. 2 show well B situated in an area of moderate to high values of porosity, resistivity and water saturation and well A situated in an area of low values of porosity, resistivity and water saturation. The slice, taken at Horizon 3(H3), marks the top of interval B7205 and also reveals moderate to high values of the selected petrophysical parameters in well B location, as well as low to shallow values in well A location. However, predominantly high values of these petrophysical parameters are observed bordering the well locations.

4 Discussion

A combination of petrophysical well log analysis and acoustic impedance inversion of 3D seismic data has been utilized in the investigation of reservoir properties of source rocks. The low resistivity values observed within the selected intervals correspond to one of the requirements for the occurrence of low resistivity hydrocarbon in formations when integrated with other petrophysical properties. This is because resistivity readings are high for hydrocarbon fluids and lower for high clay or pyrite presence (Bandyopadhay et al. 2012; Hamada et al. 2001). More so, in highly mature reservoirs resistivity can be significantly lower than what is obtainable in that same formation at lower thermal maturities (Holden et al. 2012). Low to shallow water saturation values, as seen in the intervals, are characteristic of hydrocarbon-bearing shale intervals.

The moderate to high porosity values in the porosity slices fall within the range of viable hydrocarbon-bearing

Fig. 1 Suite of logs for wells A and B, showing shale intervals (Markers)

shale interval in conformity with the assertion that at higher porosity, organic matter dominated samples have better permeability than comparable samples with lower porosity (Walls et al. 2011). It is worthy of mention, however, that for unconventional shale plays, permeability (and of course porosity) is very low and such plays act as both trap and seal. These shallow porosity values are also observed in the studied shale intervals, an observation which validates them as viable shale plays that could act as both trap and seal for a reservoir. Holden et al. (2012) also stated that shale sweet spots are typically characterized by low water saturation and higher porosity values. Thus, a hybrid of high and low porosity values which are required to validate source and reservoir potentials of shale unconventional shale plays is observed in this study. Observations on the petrophysical slices corroborate inferences drawn from the petrophysical well log analysis, further validating the reservoir status of the selected source rock intervals within the study location. Incidences of high acoustic impedance contrast were observed in the field, which is suggestive of hybrid shale play involving clean shale and organic-lean sandstone and siltstone intervals that are intimately intercalated. This hybrid system as identified by Raji et al. (2015) can contain a higher volume of oil due to a larger storage capacity resulting from larger matrix porosities of the sand-silt intercalations, and a lower adsorptive affinity inherent in the interbedded sandstone. These observations are in line with the petrophysical attribute slice analyses in this study and further validate the hydrocarbon-bearing possibilities of the source rock intervals under investigation. Total organic carbon (TOC) logs or core studies if available will further calibrate the findings in this study.

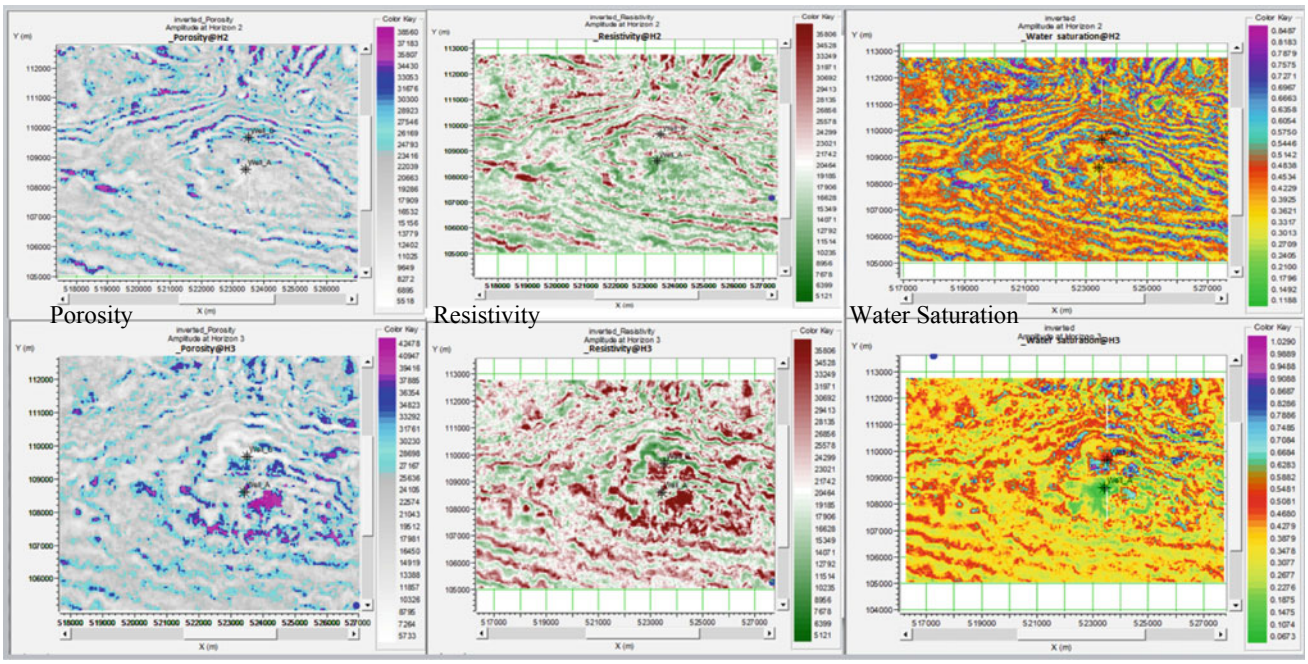

Fig. 2 Attribute slices for petrophysical parameters (*porosity, resistivity and water saturation*) from Horizon 2 and Horizon 3 (H2 and H3), corresponding to the top of markers A7440 and B7205

5 Conclusions

From the previous, we can infer that source rocks in this field of study have also had possibilities of hydrocarbon occurrence. Furthermore, possibilities exist in utilizing already existing conventional reservoir characterization well and seismic data set, as they can be further assessed not just qualitatively, but quantitatively for viability in terms of unconventional hydrocarbon exploration.

References

Avbovbo, A.A.: Tertiary lithostratigraphy of Niger Delta. Bull. Am. Assoc. Pet. Geol. **62**, 297–306 (1978)

Ayodele, O.R.: On Unconventional Gas in Nigeria" Featured article in Nigeria World. https://nigeriaworld.com/articles/2013/sep/253.html. Retrieved on June 14, 2018 (2013)

Bandyopadhyay, K., Sain, R., Liu, E., Harris, C., Martinez, A., Payne, M., Zhu, Y.: Rock Property Inversion in Organic-Rich Shale: Uncertainties, Ambiguities, and Pitfalls. SEG 2012 Abstract (2012)

Hamada, G.M., Al-Awad, M.N.J., Almalik, M.S.: Log evaluation of low resistivity sandstone reservoirs. In: Society of petroleum Engineers: SPE Permian Basin Oil and Gas Recovery Conference Midland Texas (2001). https://doi.org/10.2118/70040MS

Holden, T., Pendrel, J., Jenson, F., Mesdag, P.: Rock Properties for Success in Shales. In: Jascon CGG, p. 1–11 (2012). https://www.cgg.com/data/1/rec_docs/3035_Rock-Properties-for-Success-in-Shales

Idowu, J.O., Ekweozor, C.M.: Petroleum potential of Cretaceous shales in the Upper Benue trough, Nigeria. J. Petrol. Geol. **16**(3), 249–264 (1993)

Jarvie, M.D., Hill, R.J., Rubble, T.E., Pollastro, R.M.: Unconventional shale-gas systems: the Mississippian Barnett shale of north-central Texas as one model for thermogenic shale-gas assessment'. AAPG Bull. **91**(4), 475–499 (2007)

Obaje, N.G., Abaa, S.I.: Potential for coal-derived gaseous hydrocarbons in the Middle Benue trough of Nigeria. J. Petrol. Geol. **19**(1), 77–94 (1996)

Onuoha, K.M., Dim, C.I.P.: Prospects and challenges of developing unconventional petroleum resources in the Anambra Inland Basin of Nigeria. In: Africa Energy and Technology Conference, 2016 Copyright ©2017. American Association of Petroleum Geologists (AAPG) and Society of Petroleum Engineers (SPE)

Raji, M., Grocke, D.R., Greenwell, H.C., Gluyas, J.G., Cornford, C.: The effect of interbedding on shale reservoir properties. Mar. Pet. Geol. **67**(2015), 154–169 (2015)

Walls, J.D., Sinclair, S.W.: Eagle Ford shale reservoir properties from digital rock physics. EAGE **29**(6), 97–101 (2011). www.firstbreak.org

Porosity and Permeability Prediction in Triassic Reservoirs of HassiR'mel Field (Algeria) from Well Logs Data Using Fuzzy Logic

Abdelbassit Sridi, Leila Aliouane, Sid-Ali Ouadfeul, and Amar Boudella

Abstract

In this study, we applied fuzzy logic to estimate the porosity and permeability in theshaly Triassic reservoir. Application on real data in the Algerian Sahara has been realized exploiting recordings of several petrophysical parameters and recordings crossed shaly Triassic reservoirs of one well from HassiR'mel. The application of the proposed approach on well data of the studied reservoirs allowed us to compare the obtained porosity and permeability values to the results measured in laboratory by using cores. Furthermore, the correlation between the obtained results and laboratory data has improved the fuzzy model predictability degree far from the well.

Keywords

Porosity • Permeability • Well logs • Shaly sand reservoir • Fuzzy logic

1 Introduction

Reservoir characterization by logging data is a practical way of describing reservoirs in oil fields. In the 1960s, Dr Lotfi Zadeh of the University of California at Berkeley first advanced the idea of fuzzy logic (Zadeh 1965). For the last years, several studies have been carried out in the fields of oil engineering, applying artificial intelligence such as fuzzy logic. (Lim 2005) applied Fuzzy logic to choose the best logging increments that affect the porosity and the permeability of the carrots. (Ouenes 2000) used this technique to classify the effect of structure, layer thickness, and lithology in fractures. This technique is an approach that enables researchers to compute based on "degrees of truth" rather than the usual "true or false" (1 or 0) in boolean logic' (Mamdani 1974). The truth values of variables may be any real number between 0 and 1 inclusive (Godjevac 1999), The main objective of this case study is to design a methodology for estimating porosity and permeability with minimal acceptable errors, based on fuzzy logic in Hassi R'mel.

2 Materials

The HassiR'mel Triassic has been recorded with a deferred logging suite. One oil production well, namely HR189, were studied to characterize the formation. The record of the well (HR189 are the natural gamma rays (GR), resistivity of deep latero log (RLLD), the transit time (DT), bulk density (RHOB), the neutron porosity (NPHI), The output datasets include FUZZY POR(fuzzy porosity) and FUZZY PERM (fuzzy permeability).

3 Methods

The method used is based on work flow in Fig. 1.The steps necessary to establish this process are as follows:

(1) Data normalization Where The Min-Max Normalizer linearly resizes each function at interval [0.1], resizing at interval [0.1] is done by shifting the values of each function so that the minimum value is 0, then dividing by the new one. maximum value
(2) Organization of data: into input datasets including GR, DT, RHOB, LLD, NPHI and output datasets including

A. Sridi (✉) · A. Boudella
Laboratory of Earth's Physics, Department of Geophysics, University of Science and Technology Houari Boumediene (FSTGAT-USTHB), Bab Ezzouar, Algiers, Algeria
e-mail: abseraidi@usthb.dz

L. Aliouane
Laboratory of Earth's Physics, Faculty of Hydrocarbons, University M'hamed Bougara of Boumerdes, Boumerdes, Algeria

S.-A. Ouadfeul
Geoscience and Mine Department, Algerian Petroleum Institute, IAP, Boumerdes, Algeria

M. Meghraoui et al. (eds.), *Advances in Geophysics, Tectonics and Petroleum Geosciences*,
Advances in Science, Technology & Innovation, https://doi.org/10.1007/978-3-030-73026-0_63

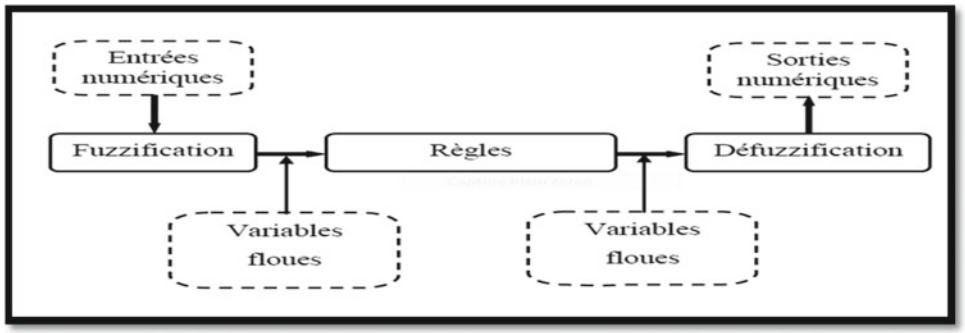

Fig. 1 Basic structure of a fuzzy logic (Hamabalek and Gonzales 2003)

fuzzy permeability (FUZZY PERM) and fuzzy porosity (FUZZY POR).

(3) Fuzzy clustering: During fuzzy classification, it is necessary to classify the sets of input and output data into groups (Tano et al. 1996; Fullér et al. 1996) using in this study a subtractive classification method.

(4) Fuzzy Inference System Construction (FIS):
The fuzzy inference is the process of formulating a mapping from a given input to an output using fuzzy logic. The fuzzy inference process involves putting the membership functions and setting fuzzy rules Tano et al. (1996), In this study, a Gaussian distribution function

$$\mathbf{F}(\mathbf{x}) = \frac{e^{-(x-\mu)^2/\sigma^2}}{\sigma\sqrt{2\pi}}$$

where μ and σ are normal distribution parameters showing mean and standard deviation, respectively, fuzzy inference (FIS) and output membership functions are linear equations, for example:

$$\text{Output MF1} = C1 \times \text{GR} + C2 \times \text{LLD} + C3 \times \text{RHOB} + C4 \times \text{DT} + C5 \times \text{NPHI} + C6$$

The rules for formulating petro-physical entry data of fuzzy permeability and fuzzy porosity:

For the fuzzy porosity (Fuzzy corpor):

- If GR is Low and LLD is Lowand RHOB is Low and DT is low and NPHI is low Then FUZZYPOR is Low.
- If GR is Moderate and LLD is Moderate and RHOB is Moderate and DT is Moderate and NPHI is Moderate Then FUZZYPOR is Moderate.
- If GR is High and LLD is High and RHOB is High and DT is High and NPHI is High Then FUZZYPOR is High.

For the Fuzzy permeability (Fuzzy cperm):

- If GR is Low and LLD is Low andRHOB is Low and DT is Moderate and NPHI is Moderate Then FUZZYPERM is Low.
- If GR is Low and LLD is Moderate and RHOB is High and DT is Moderate and NPHI is Moderate Then FUZZYPERM is Moderate
- If GR is Low and LLD is Moderate RHOB is High DT is High and NPHI is High Then Fuzzy cperm is High

The Mamdani model has been applied to test the data. The membership functions and the "If–Then" rules are generated by the fuzzy Matlab program through the subtractive classification method. Therefore, the porosity and permeability results were compared to the porosity and permeability measured on cores. To test the performance of the inference system, the prediction (R^2) that represents the squared correlation coefficient is used in the range of 0–1 according to the following equation (Bai et al.):

SS Error: Sum of squares of errors due to unexplained variability in the data is:

$$\text{SS Error} = \sum_i \left((Y_i - Y_i^{\wedge})\right)^2$$

SS regression: The sum of the squares of the errors in regression is expressed by

$$\text{SS regression} = \sum_i \left((Y_i - Y_i^{\wedge})\right)^2$$

SS Total = sum total of least squares errors.

R^2 = coefficient defined as the ratio of the sum of squares explained by the regression model and the total sum of the squares.

R^2 = SS regression/SS Total.

(5) Deffuzification

A weighted average method was used in this work based on these weight values and the degree of fuzziness for the output, and the exact output value is determined by the following formula (Cox 1994):

$$Z_0 = (\Sigma\mu(x)_i.w_i)/\Sigma\mu(x)_I$$

μ_i is the degree of Membership of the single production i.

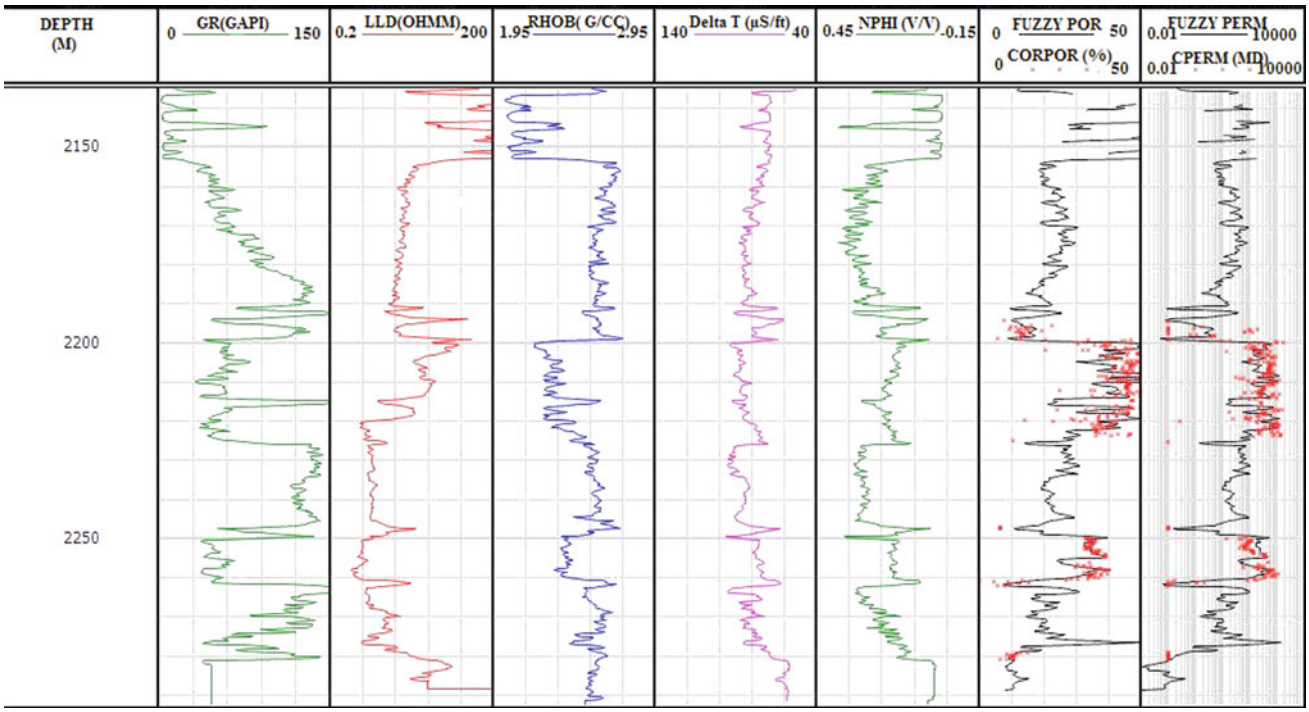

Fig. 2 Prediction of porosity and permeability in Triassic reservoirs of Hassi r'mel

w_i is the weight value of the fuzzy output for the output singleton i.

4 Results

The results obtained by the methods described above are explained in Fig. 2.

5 Discussion

We represent the core porosity and the core permeability by a dotted curve and the results obtained by the fuzzy logic for the porosity and the permeability by a continuous curve to facilitate the comparison between the two curve. The last two columns on the right contain the two parameters we are obtained for, and in the same columns there are the Core Porosity (CORPOR) and the Core Permeability (CPERM) in order to make a comparison between the two curves and to measures the efficiency of fuzzy logic in determining the properties of reservoirs, In general, the results obtained by the fuzzy logic compared to the core data of this study, show that the fuzzy logic is able to estimate the parameters of the reservoir, mainly the porosity and the permeability. However, we notice that by comparison between the measured values (CPERM, CORPOR) and the values predicted by the fuzzy logic (FUZZYPOR, FUZZYPERM) showed a good agreement which means that the curves generated by the fuzzy logic are very close to the real curves (measured) especially in the intervals: [2195m-2225m] and [2250m-2260m] for porosity and permeability with a good correlation coefficient (R^2 = 0.85) for prdicted porosity and the predicted permeability processed using fuzzy logic showed good results with a good correlation coefficient (R^2 = 0.81).

A left deflexion of GR at the interval of (2250–2261.5 m) with a sharp decrease in resistivity LLD shows that the sandstone interval is water.

References

Bai, Y., Zhuang, H., Wang, D.: Springer-Verlag, London, 325 p.

Cox, E.: The Fuzzy Systems Handbook, A Practitioner's Guide to Building Using and Maintaining Fuzzy Systems, 615 pp. Academic Press (1994)

Godjevac, J.: Idées nettes sur la logique Floue, Presses Polytechniques et Universitaire Romandes (PPUR), 1ere édition, Suisse, 125 pp. (1999)

Hamabalek, N., Gonzales, R.: Fuzzy logic applied to lithofacies and permeability forecasting. In: Proceedings of the SPE-81078 Latin American and Caribbean Petroleum Engineering Conference, pp. 1–10, Apr 27–30. Trinidad, West Indies (2003)

Lim, J. S.: Reservoir properties determination using fuzzy logic and neural networks from well data in offshore Korea. Journal of Petroleum Science and Engineering, 49(3-4), 182-192 (2005)

Mamdani, E.H.: Application of fuzzy algorithms for control of simple dynamic plant. Proc. Inst. Electr. Eng. **121**, 1585–1588 (1974)

Ouenes, A. (2000). Practical application of fuzzy logic and neural networks to fractured reservoir characterization. Computers & Geosciences, 26(8), 953-962.

Tano, S., Oyama, T., Arnould, T.: Deep combination of fuzzy inference and neural network in fuzzy inference. Fuzzy Sets Syst. **82**(2), 151–160 (1996)

Zadeh L.A.: Fuzzy sets information and control **8**, 338–353 (1965)

Fuzzy Clustering Algorithm for Lithofacies Classification of Ordovician Unconventional Tight Sand Reservoir from Well-Logs Data (Algerian Sahara)

Amina Cherana, Leila Aliouane, Mohamed Doghmane, and Sid-Ali Ouadfeul

Abstract

In this paper, we present an approach based on a fuzzy clustering algorithm applied for lithofacies classification in an unconventional tight sand reservoir from well-logs data. In some cases, these kinds of reservoirs are radioactive due to the presence of non-clayey radioactive minerals. Thus, conventional lithology classification methods can provide poor results. For that, artificial intelligence, such as Fuzzy logic, can be suitable to solve the problem. Fuzzy clustering is an unsupervised machine learning technique where a given set of data is classified. It is a more general logic then classical logic because it does not ignore uncertainties and accepts the implicit consideration of the inherited error associated with any physical measurement. This technique has been applied to real data of one well in an unconventional tight sand reservoir in the Algerian Sahara. Predicted results are compared to lithofacies obtained from conventional methods and spectral mineralogical well-logs data.

Keywords

Well-log • Unconventional tight reservoir • Lithofacies • Fuzzy logic • Clustering

1 Introduction

Lithofacies determination is a critical step in reservoir characterisation. The main product of lithofacies determination is the primary geological model of the subsurface used further in the construction of a 3D reservoir model. Lithofacies in unconventional tight sand is mandatory for the design of the hydraulic fracturing. Most classical methods in lithofacies determination are time-consuming, and the coring is considerably expensive. Usually, lithofacies is identified using the natural gamma log, which can give unreliable results in case of presence of non-clayey radioactive minerals in the reservoir such as some unconventional tight sand reservoir. For that reason, the interpretation can be enhanced by core data, or advanced well-logs such as spectral mineralogical recordings (Everett 2014). In case theses lasts are not available, we suggest the use of artificial intelligence.

In the last two decades, several methods of artificial intelligence have been introduced in reservoir characterisation from well-log data. The most remarkable is the integration of neural network (Aliouane et al. 2017, 2018; Ma 2011) and Fuzzy logic. The fuzzy logic technique has been applied for lithofacies classification using different algorithms (Cuddy 2000; Hambalek and Gonales 2003). In the same context, we suggest the use of fuzzy clustering algorithm to determine the lithology model of a tight sand reservoir from the well logging data. Application to real data has been established where the petrophysical recordings crossed the Ordovician Tight sand reservoir of one well, from Algerian Sahara, and have been exploited as an input of the fuzzy machine. The output is the different classes of the lithology of the unconventional tight sand reservoir. In the end, the predicted lithofacies are compared to lithofacies obtained from conventional methods and of spectral mineralogical data (ECS) which can give better shale volume providing the percentage of Aluminium (Al) which is the common element of all clay minerals (Everett 2014).

A. Cherana (✉) · L. Aliouane
Laboratoire de Physique de la Terre, Faculté des hydrocarbures et de la chimie, Université M'hamed Bougara de Boumerdes, 35000 Boumerdes, Algeria
e-mail: a.cherana@univ-boumerdes.dz

M. Doghmane
Division Exploration, Sonatrach, Hydra, Algeria

S.-A. Ouadfeul
UKM University, Khemis Miliana, Algeria

M. Meghraoui et al. (eds.), *Advances in Geophysics, Tectonics and Petroleum Geosciences*, Advances in Science, Technology & Innovation, https://doi.org/10.1007/978-3-030-73026-0_64

2 Lithofacies Derived from Fuzzy Clustering Algorithm

In this study, the subtractive clustering algorithm has been used to extracts the natural groupings of data from a large data set. It is a cluster estimation method combined with linear least-squares estimation procedure to identify fuzzy models from numerical data (Chiu 1994).

When the cluster estimation method is applied to a collection of input/output data, each cluster centre is, in essence, a prototypical data point that exemplifies a characteristic behaviour of the fuzzy system (Chiu 1994). Hence, each cluster centre can be used as the basis of a fuzzy rule that describes the system behaviour. The equivalent of these fuzzy rules is the Takagi–Sugeno type (Takagi and Sugeno 1985). Finally, the linguistic rules applied to the set of clusters are selected based on the potential lithofacies derived from the conventional methods, and also modified with knowledge acquired on the geology of the field. Given the geological setting of the Ordovician stratigraphy of the region of our well, four Lithofacies were defined in our geological interval: Clay, Sandstone, Sandy Clay and Clayey Sand.

The set of raw well-logs data of Ordovician Tight sand reservoir of one well, located in Illizi field in the south-east

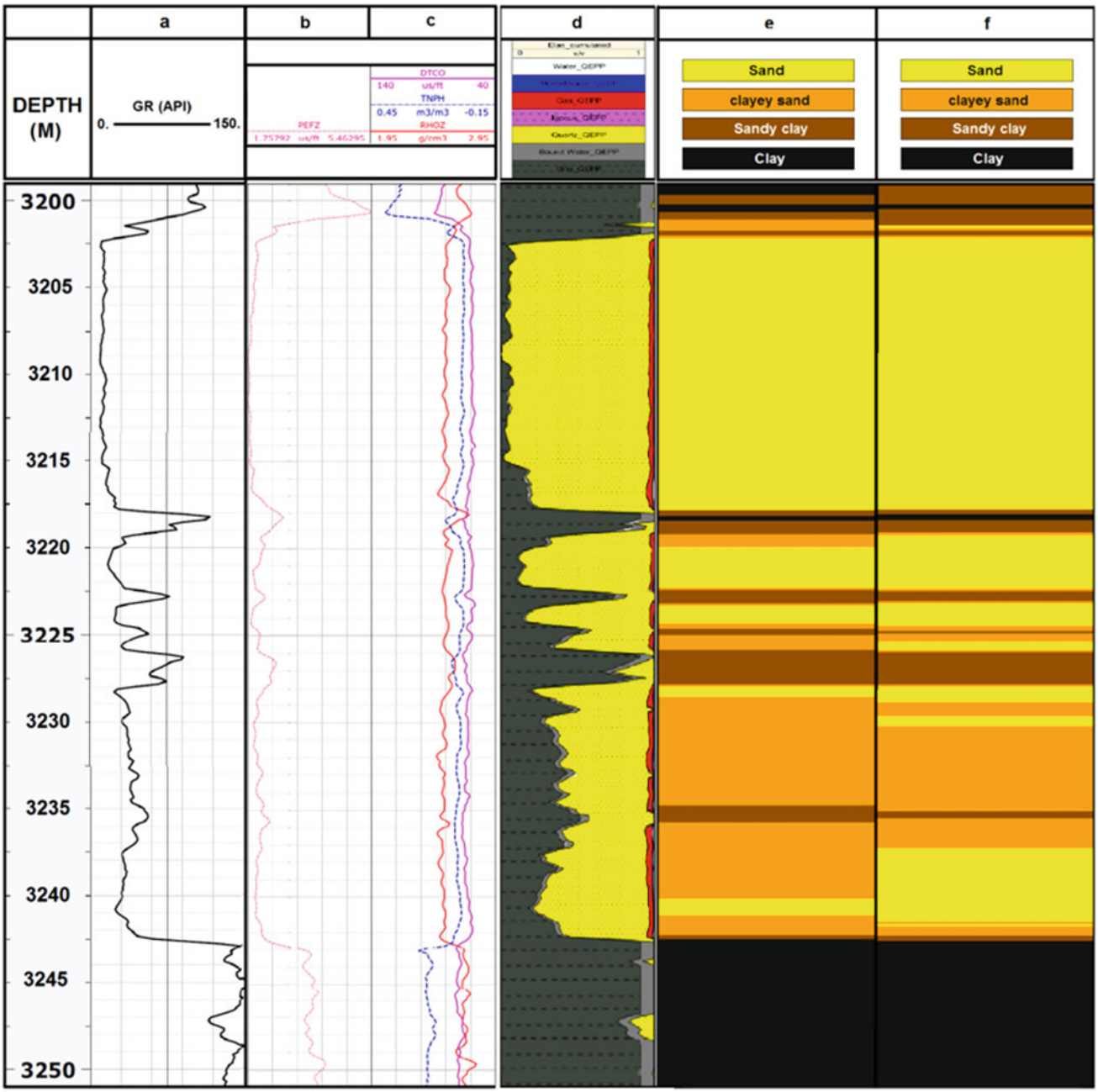

Fig. 1 Raw well-logs data (**a**, **b** and **c**) and lithofacies classification from conventional methods (**d** and **e**) and from fuzzy clustering (**f**)

of the Algerian Sahara, have been used as an input: Gamma Ray log (GR), photoelectric absorption coefficient (PEFZ), Transit time of P wave (DTCO), Neutron porosity (TNPH) and bulk Density (RHOZ).

The output corresponds to different volumes of the four lithological classes cited below. Figure 1 presents both the raw well-logs data and the results of lithofacies of the reservoir.

3 Results, Analysis and Conclusions

Results obtained from fuzzy clustering (Fig. 1f) show that the application of this method could give an excellent lithofacies model which is very similar to the lithofacies model derived from the shale volume using the conventional methods (Fig. 1e) and from of spectral mineralogical (Fig. 1d). Also, the clustering prediction shows an even better correlation when compared to the results that represent the mineral components of the reservoir (Fig. 1d). In this case, Ordovician reservoirs are not radioactive, but in some cases, unconventional tight sand reservoirs are known by their high radioactivity due to the presence of non-clayey radioactive minerals in the reservoir. Consequently, the use of machine learning algorithms on geophysical data is promising and can lead to increased accuracy in automated reservoir characterisation, mainly, when core data and advanced mineralogical well-logs are not available.

References

Aliouane, L., Ouadfeul, S.D., Boudella, A.: Back propagation and hidden weight optimization algorithms neural network for permeability estimation from well-logs data in Shaly sandstone petroleum reservoirs: application to Algerian sahara. Adv Petroleum Eng. Petroleum Geochem. Proc. 1st Springer Conf. Arabian J. Geosci. (CAJG-1), 25–27 (2018)

Aliouane, L., Ouadfeul, S., Boudella, A.: Caractérisation de réservoir par l'analyse neuronale et fractale. Edition Universitaire Européenne, Allemagne (2017)

Chiu, S.L.: Fuzzy model identification based on cluster estimation. J. Intell. Fuzzy Syst. **2**(3), 267–278 (1994)

Cuddy, S.J.: Litho-Facies and permeability prediction from electrical logs using fuzzy logic. SPE Reservoir Eval. Eng. **3**(4) (2000)

Everett, R.V.: Three methods for log-derived mineralogy primarily used for shales (silts) and tight formations SWLS, pp. 19–35. Springer (2014)

Hambalek, N., Gonales, R.: Fuzzy logic applied to lithofacies and permeability forecasting. Society of Petroleum Engineering Inc. (2003)

Ma, Y.Z.: Lithofacies clustering using principal component analysis and neural network: applications to wireline logs. Math. Geosci. **43**, 401–419 (2011)

Takagi, T., Sugeno, M.: Fuzzy identification of systems and its application to modeling and control. IEEE Trans. Syst. Man Cybern. **15**, 116–132 (1985)

Integrated Well Log Analysis and 1D PS Modeling in Assessment of Maturity and HC Generation Potential of the Sources Rocks in Wichian Buri Sub-Basin, Thailand

Chaiyaphruk Chaiyasart and Pham Huy Giao

Abstract

The Wichian Buri sub-basin is located in the southern Phetchabun basin, Thailand. It is reported to have significant recoverable hydrocarbon from fractured igneous rock reservoirs, but until now no detailed research has been done on the effect of igneous intrusion on the maturation of the shallow fractured source rocks and their HC generation. In this study, well logging analysis and petroleum system modeling (PSM) were integrated to evaluate potential source rock of Wichian Buri sub-basin. The study was conducted based on the data from the public domain of the petroleum industry in Thailand, including vertical well sections, well logs, regional geological sections, base maps, and geochemical data. The results of well log analysis found intervals of fractured igneous rock reservoirs with low gamma-ray of 20–30 API and porosity around 8–12%. TOC determined by the ΔlogR technique was further used in one-dimensional (1D) petroleum system modeling (PSM) considering the effect of igneous intrusion, and based on which maturity (Ro) and hydrogen index (HI) of the source rock were found as 0.62% and 222 mg HC/gTOC, respectively. Hydrocarbon generation had started in the late Miocene basalt and Permo–Triassic Nam Duk formation and is estimated around 1392.4–2489.7 MMSTB.

Keywords

Wichian Buri sub-basin • Fractured igneous rock reservoir • Petroleum system modeling (PSM) • Well log analysis

Abbreviations

1D	One Dimensional
HC	Hydrocarbon
HI	Hydrogen Index
LOM	Level of organic metamorphism
LLD	Deep induction log
MMbbl	Million barrels
Ma	Million years ago
OI	Oxygen index
PI	Production index
PSM	Petroleum system modeling
Ro	Vitrinite reflectance
S1	Free hydrocarbon
S2	Generated hydrocarbon
S3	Cracking CO2 peak
TOC	Total organic carbon
TMax	Maximum pyrolysis temperature

1 Introduction

Hydrocarbon in the fractured igneous rock reservoir has been mainly discovered by accident (Petford et al.2003), and it could be found in different types of igneous rock. In Wichian Buri sub-basin, there are both clastic and fractured igneous reservoirs (Remus et al. 1993). One of the critical issues for a fractured igneous rock reservoir is to understand the petroleum system in which it is found, and how the HC was generated and migrated into it. The main objective of this study is to perform well log analysis and one-dimensional petroleum system modeling (PSM) to assess maturity and hydrocarbon generation of Wichian Buri source rock. The results are expected to aid further hydrocarbon exploration in the Wichian Buri sub-basin.

C. Chaiyasart · P. H. Giao (✉)
Geoexploration and Petroleum Geoengineering (GEPG) Program, Asian Institute of Technology (AIT), Bangkok, Thailand
e-mail: hgiao@ait.asia

M. Meghraoui et al. (eds.), *Advances in Geophysics, Tectonics and Petroleum Geosciences*, Advances in Science, Technology & Innovation, https://doi.org/10.1007/978-3-030-73026-0_65

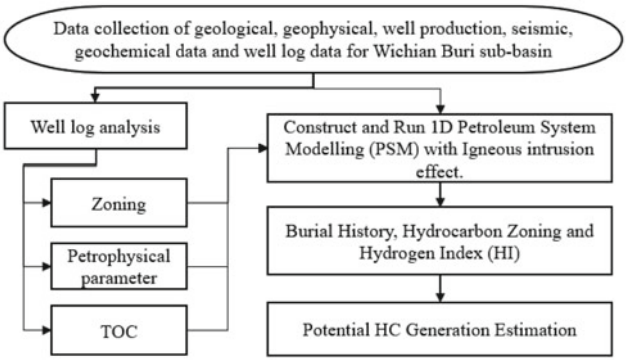

Fig. 1 Flowchart of this study

2 Methods

The flowchart of the study is shown in Fig. 1. The results of well log analysis such as lithological zoning, petrophysical parameter, and TOC were utilized as input data for 1D PSM. The ΔlogR technique (Passey et al. 1990) was used to determine the TOC and HI that was further used for calculation of HC generation by such methods Schmoker (1994), Claypool's communication as mentioned in Peters et al. (2015), and Sheikh and Giao (2017). The hydrocarbon retained in the shale layer is calculated using the following equation:

$$HC_{ret} = \left[(HI^{\circ} - HI) \times TOC - 1000 \times \frac{(TOC^{\circ} - TOC)}{(0.8333 - TOC)} \right] \times M_{rock} \times C_1$$

where HCret (kg) is the amount of hydrocarbon retained within the shale; HI° (mgHC/gTOC) is the original hydrogen index; HI (mgHC/gTOC) is the average hydrogen index; TOC° (fraction) is the initial total organic carbon content; TOC (fraction) is the average total organic carbon content; and M_{rock} (g) is the mass of the source (shale).

3 Geological Setting

The Phetchabun Basin is a Cenozoic rift basin, located in the central Thailand (see Fig. 2a), and is comprised of 5 sub-basins, i.e., North Phetchabun sub-basin, Chai Mongkhon half graben, Khon Khwang graben, Nong Chaeng half graben, and Wichian Buri sub-basin that are elongated and distributed along the N-S trend (Remus et al. 1993). The lithostratigraphic column of the Wichian Buri sub-basin is shown in Fig. 2b, in which the syn-rift sequence is unconformably overlying Permo-Triassic basement by the West-dipping low angle fault (a listric fault). Barr and Cooper (2013) suggested tectonic and igneous activity around 11–16 Ma during Miocene based on a study of well cuttings from 15 exploration wells. A recent study by Pongwapee et al. (2018) reported a stratigraphic revision in Cenozoic section of Wichian Buri sub-basin based on well data and seismic interpretation results.

4 Results and Discussion

Based on well log analysis results (see Fig. 3a), some fractured igneous reservoirs were found by lower gamma-ray (20–30 API) and high density. Average porosity was estimated as 20–30% for sandstone reservoir and 8–12% for fractured igneous rock reservoirs. TOC of source rocks was found around 1.84 wt%, and level of maturity (LOM) about 10–12 as shown in Fig. 3b presented an excellent source rock like oil shale (LOM around 10.5). The results of 1D PSM

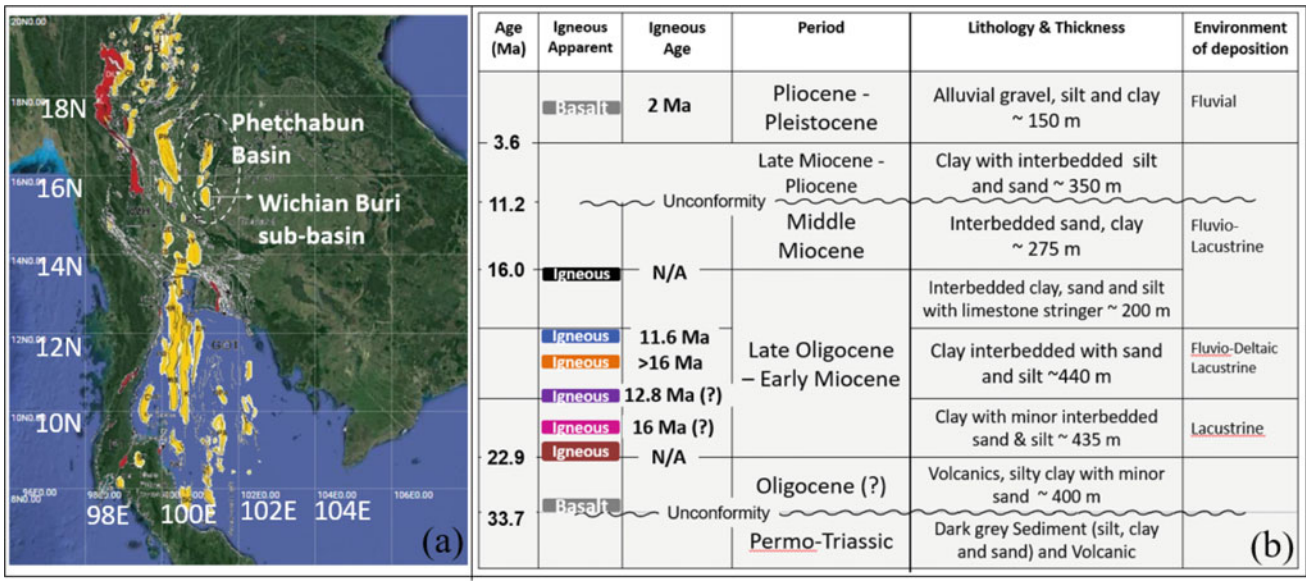

Fig. 2 Location of the Wichian Buri sub-basin (**a**) and the lithostratigraphic column (**b**)

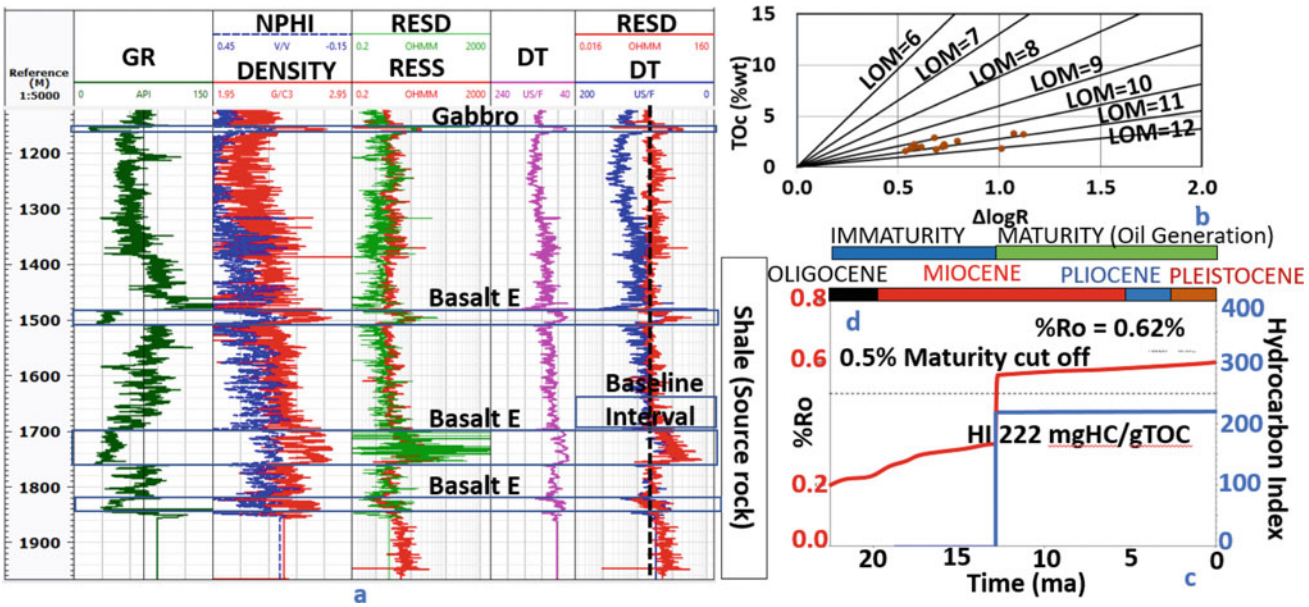

Fig. 3 Well log data and results of the ΔlogR calculation (**a**); level of maturity LOM (**b**); %Ro and HI (mgHC/gTOC) of source rock shale unit IV calculated by using Tegelaar (1994)'s kinetic model considering the igneous intrusion effect (**c**)

plotted in Fig. 3c show that the rifting started from late Oligocene to the late Middle Miocene and continued to Pleistocene. The Wichian Buri sub-basin was formed in this period. In the late Middle Miocene, when post-rift started, the uplifting and erosion occurred, and the subsidence rate had decreased with time. The temperature gradient was found to range from 2.5 to 5.50 °C/100 m, with a high gradient of 4.5–5.50 °C/100 m being found in the fractured igneous layer. The % of Ro had rapidly increased to 0.62%, which supported oil generation. The hydrogen index (HI) value of 222 mg HC/gTOC was used in the calculation of hydrocarbon generation that was around 1392.4–2489.7 MMSTB with a net to gross of 0.5–0.75 and HI° 550–600 mg HC/gTOC. The results from 1D PSM could indicate the effect of shallow igneous intrusion on the maturity of source rock.

5 Conclusions

Well logging analysis and one-dimensional petroleum system modeling (PSM) were successfully integrated and applied for the case of the Wichian Buri sub-basin, in which the petrophysical and geochemical parameters from the well log analysis were used as input data for the PSM that was conducted considering the effect of igneous intrusion results to maturity source rock. Based on the PSM, the retained hydrocarbon generation in the study shale layer of Wichian Buri sub-basin was estimated as 1392.4–2489.7 MMSTB. The approach employed in this study can be applied widely for the study of a shallow fractured igneous rock petroleum system in other sub-basins in the Phetchabun basin of Thailand.

References

Barr, S.M., Cooper, M.A.: Late Cenozoic basalt and gabbro in the subsurface in the Phetchabun Basin, Thailand: implications for the Southeast Asian Volcanic Province. J. Asian Earth Sci. **76**, 169–184 (2013)

Passey, Q.R., Creaney, S., Kulla, J.B., Moretti, F.J., and Stroud, J.D.: A practical model for organic richness from porosity and resistivity logs. Am. Assoc. Pet. Geol. Bull. **74**, 1777–1794 (1990)

Peters, K.E., Walters, C.C., Moldowan, J.M.: The Biomarker Guide: Biomarkers and Isotopes in the Environment and Human History, vol. 01. Cambridge University Press, Cambridge, New York (2005)

Petford, N., McCaffrey, K.J.W.: Hydrocarbons in crystalline rocks. Geol. Soc. London Special Publ. **214**, 35–68 (2003)

Pongwapee, S., Morley, C.K., Won-in, K.: Impact of pre-existing fabrics and mlti-phase oblique extension on Cenozoic fault patterns, Wichian Buri sub-basin of the Phetchabun rift, Thailand. J. Struct. Geol. **118**, 340–361 (2018)

Remus, D., Webster, M., Keawkan, K.: Rift architecture and sedimentology of the Phetchabun Intermontane Basin, central Thailand. J. SE Asian Earth Sci. **8**, 421–432 (1993)

Schmoker, J.W.: Volumetric calculation of hydrocarbons generated. In: Magoon, L.B, Dow, W. (eds.) The petroleumsystem from source to trap. American Association of Petroleum Geologists Memoir, vol. 60, pp. 323 (1994)

Sheikh, N., Giao, P.H.: Evaluation of shale gas potential in the lower Cretaceous Sembar formation, the Southern Indus basin, Pakistan. J. Nat. Gas Sci. Eng. **44**, 162–176 (2017)

Tegelaar, E.W., Noble, R.A.: Kinetics of hydrocarbon generation as a function of the molecular structure of kerogen as revealed by pyrolysis-gas chromatography. Org. Geochem. **22**, 543–574 (1994)

Geodesy and Exploration & Theoretical Geophysics

Gravity Data Assessment as Support to Explore Surface and Subsurface Structural Elements of a Challenged Area Case Study: Northern East Tunisia

Benen Sarsar Naouali, Imen Hamdi Nasr, Rihab Ghallali, and Mohamed Hadi Inoubli

Abstract

Northeast of Tunisia is part of the Maghrebides orogenic belt characterized by a complex geology. The geodynamic of this area has long been challenging because of the deficiency of seismic and geological data. In this respect, we intend to use gravity land data to understand the subsurface geology of the study area. The gravity assessment of the complete Bouguer gravity anomaly is mainly based on the use of many filters applied to decipher fault patterns by enhancing near structures and approximating edges of the sources bodies on the one hand, and to estimate the burial depths of delineated structures on the other hand. The compilation of the detailed gravity analysis confronted to geological data and well data helps clarify the structural distribution in the study area. Our compiled maps reveal the presence of several gravity lineaments and some structures that are well-known surface geology as well as buried structures with different geometries not expressed by surface geology. Results from a regional NNW compressive, the updated structural pattern is conformal to the classic analogical Riedel model of which the interference of both extensive and compressive geologic elements is highlighted. The proposed structural architecture is controlled by E–W major rooted faults, which are linked to a regional EW transcurrent shear zone induced by the African and European plate convergence.

Keywords

Central Mediterranean • Gravity field • Data filtering • Northern East of Tunisia • Structures • Sub-Triassic structures

1 Introduction

The extreme northern area of Tunisia constitutes the eastern end of the Maghrebides that extends from the Moroccan Rif in the west to Sicily and Calabria in Italy to the east (Fig. 1a). This Atlas fold-thrust belt results from the collision of the African and Eurasian plates occurred during the Langhian (Frizon de Lamotte et al. 2000; Carminati et al. 1999). The study area is characterized by few outcrops of the foreland belt and vast plains. The stratigraphic column is ranging from the Triassic to the Quaternary (Fig. 1a, b). Many caps and hiatus intercept it owing to the geodynamic evolution of the region, which have been controlled by the Triassic accession since Jurassic stage (Ben Ayed 1994). The structural assessment of structural element, Triassic outcrops and the depressions are still a subject of discussion (Perthuisot 1978; Rouvier 1977; Ben Ayed 1986; Boukadi 1994). The limitations are the shortage of data, the few number wells, the scarcity of deep wells, and the limited quantity and inconsistent of recorded 2D seismic data. Furthermore, many drilled wells have never encountered the totality of the lithostratigraphic column (Fig. 1b). The thickest Neogene typifies the subsurface series blanked that can attend in several wells more than 2000 m.

Through analysis, the present work intends to investigate deep faults and their eventual role in the tectonic evolution, to detect Triassic salt structures and explain the depression genesis.

B. S. Naouali (✉)
ETAP: Entreprise Tunisienne Des Activités Pétrolières, Tunis, Tunisia

B. S. Naouali · I. H. Nasr · R. Ghallali · M. H. Inoubli
Faculty of Science of Tunis, URGAMM, Tunis, Tunisia

I. H. Nasr
Faculty of Sciences of Bizerte, Bizerte, Tunisia

R. Ghallali
Centre de Recherches Technologiques des eaux, CERTE, Borj Cedria, Tunisia

M. Meghraoui et al. (eds.), *Advances in Geophysics, Tectonics and Petroleum Geosciences*,
Advances in Science, Technology & Innovation, https://doi.org/10.1007/978-3-030-73026-0_66

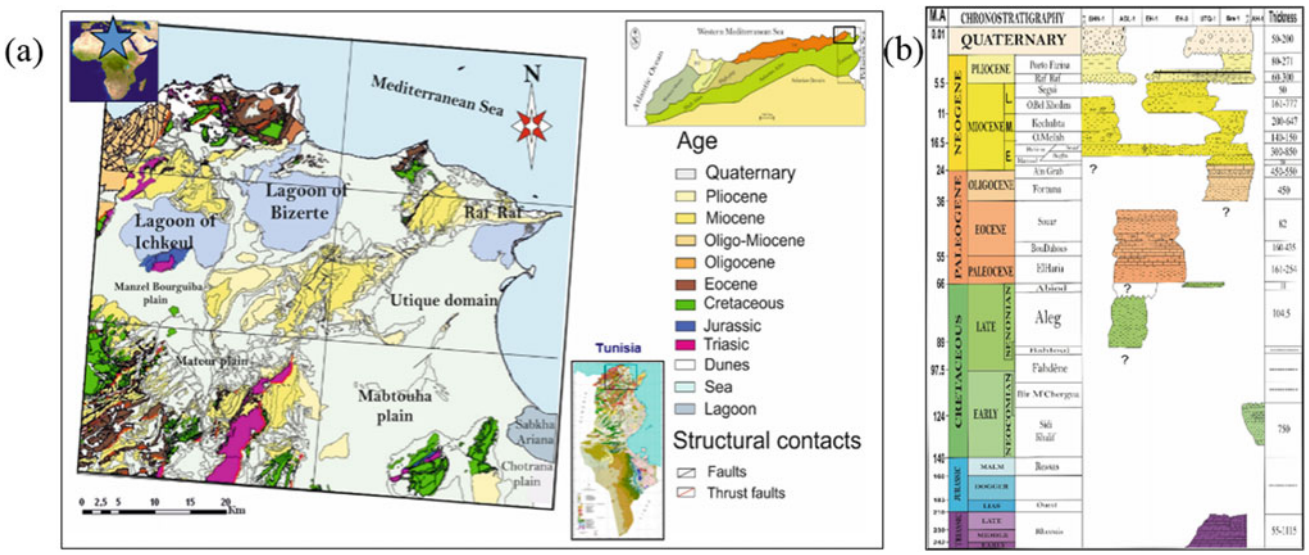

Fig. 1 **a** Geological map of the Northern east of Tunisia; **b** subsurface chart of the study zone

2 Methodology

In this present work, the potential analysis would allow more implication to explore this underexplored zone; a big land gravity data of 2836 measurement points covering the area, with an average grid of 1 km by 1 km. The Acquired data was obtained from the "Office National des Mines" (ONM) of Tunisia. Free-air and Bouguer gravity corrections were applied using a reduction density of 2.32 g/cm^3. The accuracy of the survey is around 0.02 mGal for gravity measurements and 0.1 m for topographic positioning, taking into account the quality of the gravity and positioning measurements. The complete Bouguer anomaly map was elaborated using minimum curvature technique (Briggs 1974).

Residual, upward continuation, vertical derivative, total horizontal derivative and total derivative of the tilt angle maps were computed from the complete Bouguer gravity anomaly to decipher fault patterns by enhancing near structures and approximating edges of the sources bodies (Carminati and Di Donato 1999; Frizon de Lamotte et al. 2000). Euler deconvolution and spectrum analysis were also performed to estimate the burial depths of delineated structures (Keating and Pilkingston 2004; Salem et al. 2007). A compilation map (Fig. 2c) resumes all results acquired through used gradient methods.

3 Results

The integrated data of the detailed gravity analysis confronted to geological data aids clarifying the structural architecture in the study area by the identification of new structural elements (Hamdi Nasr et al. 2009, 2010; Sarsar Naouali 2011). The compilation gradient map (Fig. 2c) discloses, on the one hand, new faults beneath, the Quaternary series: Circular faults, dome structures; NW and EW strike-slip faults, en echelon faults and thrust faults. The principal direction of the detected faults has being controlled by the geodynamic evolution of the basin (Ben Ayed 1994). Moreover, the existence of buried structures with different geometries is not expressed by surface geology. The superposition of the Triassic outcrops on the vertical derivative map explains the conjugate NE and NW gravity lineaments. It seems that these lineaments let interpreting the positive anomaly in many places as being caused by the presence of Triassic material ascension and movement under a Plio-Quaternary series.

4 Discussion and Conclusions

Gravity assessment provides new dimensions for subsurface characterization. The identified features provide new constraints to evolve the geological architecture of the studied area by the proposition of a new structural pattern of the Northeast of Tunisia.

The general kinematics shows that an NE-thrusting component characterizes the detected new faults corresponding to the direction of the significant dislocations drawn by the Triassic outcrops in Northern Tunisia (Perthuisot 1978; Boukadi 1996).

The arrangement of the disclosed NW directed faults bordering the hidden horst in Mabtouha plain allows identifying two grabens in the study area disposed of parallel to the Atlas shortening constraint perpendicular to the Thrust

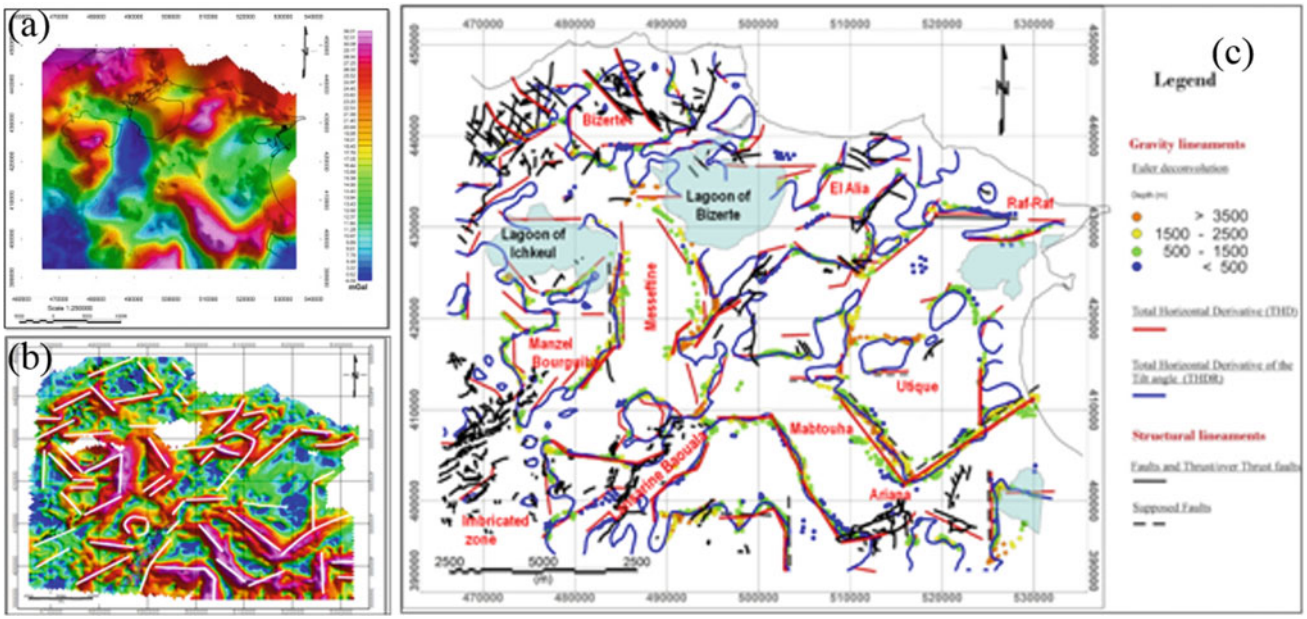

Fig. 2 **a** Complete Bouguer anomaly of the Northern east Tunisia, **b** THD map of the Northern east of Tunisia, **c** completion gradient map of the Northern east Tunisia

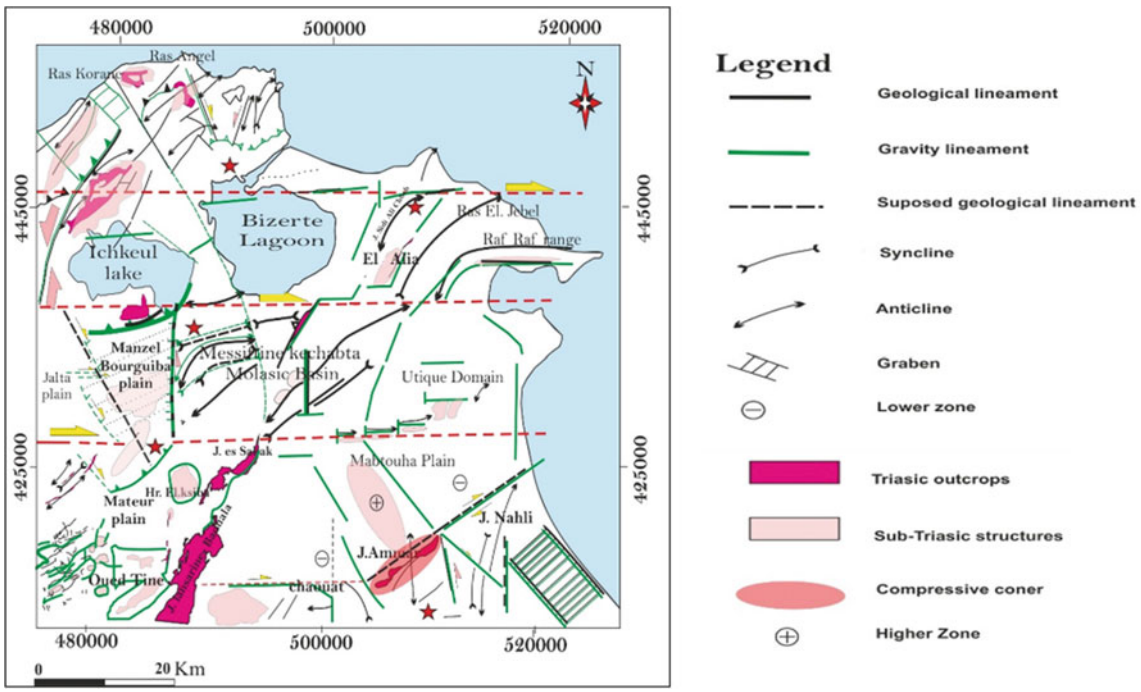

Fig. 3 Structural updated map of the Northern east of Tunisia

structures (Sarsar Naouali et al. 2011). In Mateur and Manzel Bourguiba plains, the circular anomalies are interpreted as Diapir Triassic material beneath the quaternary deposits (Sarsar Naouali et al. 2016).

The complex disposition expressed by the coexistence of compressive and extensive structures is due to the occurrence of a compressive regime in the overall area; the study area is guided by conjugated strike-slip dextral deep faults reactivated during the Upper Miocene to the current shortening. Despite the geological complexity and the sparse control data in the Northern East of Tunisia, the Structural appraisal of Gravity maps through gradient methods

discloses a new structural pattern, which is integrated within the global tectonic setting of Northern Africa.

References

Ben Ayed, N.: Evolution tectonique de l'avant-pays de la chaîne alpine de Tunisie du début du Mésozoïque à l'Actuel. Thèsed'EtatUniversité DePaisSud, Centre d'Orsay (1986)

Ben Ayed, N.: Les décrochements – chevauchements EW et NS convergents de la Tunisie septentrionale. géométrie et essai de reconstitution des conditions de déformations. ETAP 1994 (1994)

Boukadi: Schéma structural nouveau pour le Nord de la Tunisie (1996)

Briggs, I.: Machine contouring "using minimum curvature." Geophysics **39**, 39–48 (1974)

Carminati, E., Di Donato, G.: Separating natural and anthropogenic vertical movements in fast subsiding areas: the Po plain (N. Italy) case. Geophys. Res. Lett. **26**, 2291–2294 (1999)

Frizon de Lamotte, D., SaintBezar, B., Bracène, R., Mercier, E.: The two main steps of the Atlas building and geodynamics of the western Mediterranean. Tectonics **194**, 740–761 (2000)

Hamdi-Nasr, I., Inoubli, M.H., Ben Salem, A., Tlig, S., Mansouri, A.: Gravity contributions to the understanding of salt tectonics from the Jebel Cheid area (dome zone, Northern Tunisia). Geophys. Prospect. **57**, 719–728 (2009)

Hamdi, N.I., Amiri, A., Inoubli, M.H., Ben Salem, A., Chaqui, A., Tlig, S.: Structural setting of Northern Tunisia Insights from gravity data analysis, Jendouba case study. Pure Appl. Geophys. **168**(10), 1835–1849 (2010)

Keating, P., Pilkingston, M.: Euler deconvolution of the analytic signal and its application to magnetic interpretation. Geophys. Prospect. **52**, 165–182 (2004)

Perthuisot, V.: Dynamique et pétrogenèse des extrusions triasiques en Tunisie septentrionale, thèse d'État, École normale supérieure, 312 p. Paris (1978)

Rouvier, H.: Géologie de l'extrême Nord Tunisien .tectonique et paléogéographie superposées à l'extrême orientale la chaîne nord maghrébine. Thèsees—Sciences, VI.898 p. Univ. Paris (1977)

Salem, A., Williams, S., Fairhead, J.D., Ravat, D., Smith, R.: Tilt-depth method: a simple depth estimation method using first-order magnetic derivatives. Lead. Edge **26**, 1502–1505 (2007)

Sarsar Naouali, B., et al.: Gravity data contribution for petroleum exploration domain: Mateur case study (Saliferous Province, Northern Tunisia). Arabian J. Sci. Eng. (2016)

Sarsar Naouali, B., Inoubli, M.H., Amiri, A., Chaqui, A., Hamdi, I.: Subsurface geology of the Ariana region (Diapir Zone, northern Tunisia) by means of gravity analysis. Geophys. Prospect. **59**, 983–997 (2011)

The Relationship Between Surface Atmospheric Potential Gradient Drop and Earthquake Precursors

Xiaobing Jin, Junwei Bu, Jingxuan Tian, Xiaoxiao Wu, Guilan Qiu, and Liang Zhang

Abstract

Abnormal variations of the surface atmospheric potential gradient (SAPG, hereafter) in pre-earthquake earthquake preparation area have been observed many times around the world. On March 27, 2017, in Yangbi county, China, 5.1 earthquakes occurred, and there are 11 SAPG observation stations in the earthquake preparation area. After excluding lightning, heavy precipitation and other factors that may cause interferences on the SAPG during the observation period, the analysis of the SAPG data from 33 days before earthquake shows that the daily means of the SAPG before the earthquake generally decreased. The mechanism of radon emission enhancement can explain this phenomenon before earthquakes. Therefore, the general decrease in SAPG before the earthquake may be a kind of earthquake precursor.

Keywords

Earthquake • Surface atmospheric potential gradient (SAPG) • Lightning • Fair weather (FW) • Earthquake preparation area (EPA)

X. Jin (✉) · J. Bu · L. Zhang
Heavy Rain and Drought-Flood Disasters in Plateau and Basin Key Laboratory of Sichuan Province, Chengdu, 610000, Sichuan, China
e-mail: xiaobingjin@sina.com

G. Qiu
Sichuan Earthquake Prediction Research Center, Chengdu, 610000, Sichuan, China

J. Tian · X. Wu
Department of Mechanical Engineering, The University of Hong Kong, Hong Kong, China

1 Introduction

Among a variety of lithosphere–atmosphere–ionosphere coupling (LAIC) models, it is generally believed that the seismogenic electric field generated in the pre-earthquake at earthquake preparation area can be coupled to the ionosphere through the atmosphere and cause abnormal changes of the total electron content and the electric field in the F2 region of the ionosphere (Ouzounov 2018; Pulinets 2009). Therefore, when LAIC passes through the surface atmosphere, the seismogenic electric field will also cause abnormal changes in the SAPG (Mizuno and Takashima 2013; Li et al. 2016; Choudhury and Guha 2013). The combination of global electrical circuit (GEC) (Williams 2018) model and LAIC (Ouzounov 2018; Pulinets 2009; Hugo Gonçalves Silva 2012) makes it possible to find earthquake precursors through SAPG. There are 11 SAPG stations in the earthquake preparation area (EPA, hereafter) of Yangbi. It is found that the daily mean value of SAPG in fair weather before earthquake generally decreases with the earthquake coming near (Harrison and Nicoll 2018). It is found that the daily mean value of SAPG in fair weather (FW, hereafter) before the earthquake generally decreases with the advent of the earthquake after the possible interference factors are eliminated from the synchro-meteorological data (Harrison and Nicoll 2018). This decrease in pre-earthquake SAPG may be explained by a mechanism focusing on the increasing ionization capacity of the surface atmosphere due to the general increase in radon emissions before earthquakes (Vadim 2015; Hugo Gonçalves Silva 2012; Ghosh et al. 2009). Therefore, this phenomenon may be a kind of earthquake precursor.

2 Observation Methods and Data Processing

On March 27, 2017, 07:55, an M5.1 earthquake struck Yangbi in Yunnan, China (E99.8°, N25.9° M5.1, 12 km depth). The radius of the earthquake preparation area

M. Meghraoui et al. (eds.), *Advances in Geophysics, Tectonics and Petroleum Geosciences*,
Advances in Science, Technology & Innovation, https://doi.org/10.1007/978-3-030-73026-0_67

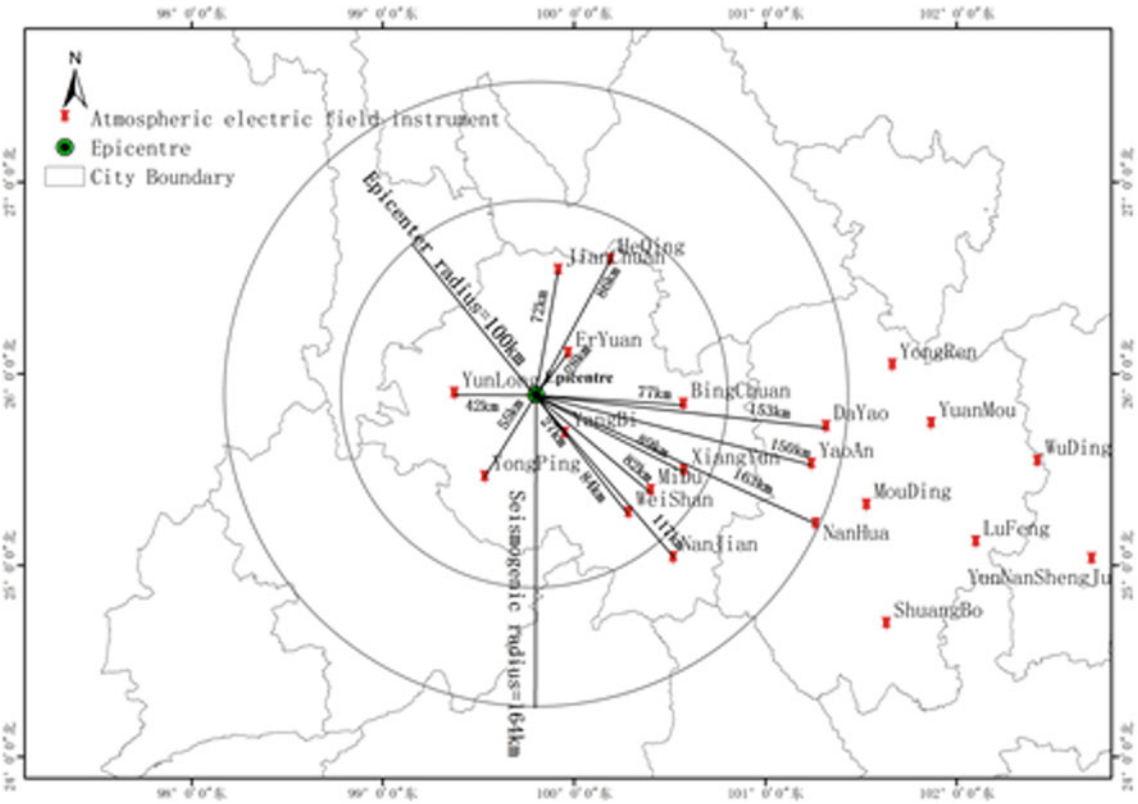

Fig. 1 Distribution of SAPG instruments in the Yangbi earthquake. (There were 11 SAPG instruments within a radius of 164 km. The epicenter of the east, north, west, southwest has an instrument, respectively. The epicenter of the northeast has two instruments. There are five instruments southeast of the epicenter.)

(EPA) is 164 km ($R = e^{M}$ = 164 km) (By and V. I. MIACHKIN. 1979). As shown in Fig. 1, in order to ensure the reliability of data, 11 effective SAPG observation stations and synchronous meteorological data within the EPA were selected as data sources. In order to obtain the SAPG data with less interference, we used the fair weather (FW) SAPG condition in the GEC mechanism to select the obtained SAPG data (Harrison and Nicoll 2018). The selecting conditions of SAPG in FW are as follows: (1) The number of lightning within a radius of 40 km of the SAPG observation stations is less than 4 times/day. (2) No precipitation. (3) Cloud cover is no low cloud (Ghosh et al. 2009). (4) Wind speed is 0.3– m/s (Ghosh et al. 2009). (5) During the observation period, there was no significant change in aerosol concentration. Since the observation period was 33 days, the seasonal change of PG was not considered. The diurnal variation of SAPG caused by global lightning activities and solar radiation can be effectively eliminated by calculating the daily mean value of SAPG obtained in FW.

3 Results

According to the fair weather conditions, the average daily changes over time of SAPG at 11 PG observation stations 33 days before the earthquake (from February 22 to March 27) were obtained, and linear fittings were carried out, respectively. The results are shown in Fig. 2a–k.

As shown in Fig. 2, from 33 days before the earthquake until the time of the earthquake (March 27), 10 out of 11 (91%) observation stations in the EPA near the epicenter showed downward trends in PG linear fittings. As there are 11 SAPG stations distributed in the EPA near the epicenter (see Fig. 1), it indicates that SAPG generally showed a decreasing trend before the earthquake in the EPA.

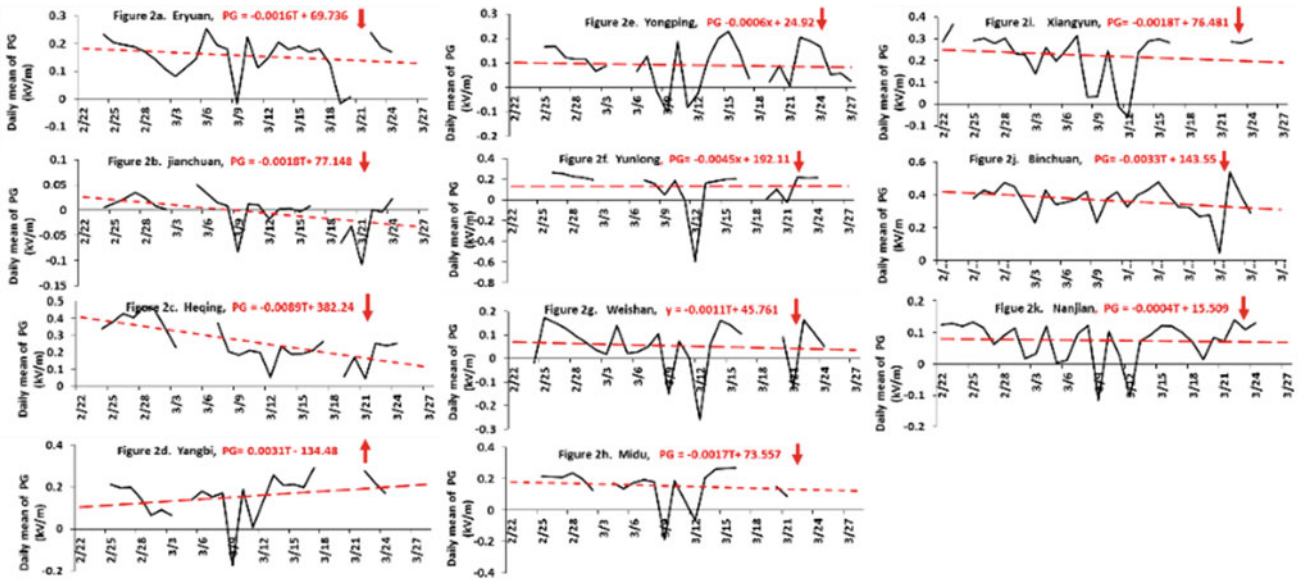

Fig. 2 Daily mean value of SAPG over time and linear trend fitting of 11 observation stations in the EPA. The horizontal axis represents the observation date (M/D), and the vertical axis represents the daily mean value of SAPG. The black solid line represents the daily mean value of SAPG changing with the date, and the data gap indicates that interference factors are excluded. Red dotted lines and arrows represent the trend of linear fitting of SAPG

4 Discussion

Before the earthquake, although the Yangbi station (27 km from epicenter) which is nearest to the epicenter showed an upward trend of SAPG, the SAPG of other stations within the EPA showed a downward trend. Among them, Heqing, Yunlong and Binchuan stations showed the most obvious SAPG declines. As the earthquake approaches, the overall SAPG in the PEA decreased, which can be explained by the radon emission mechanism. Before the earthquake, the radon emission in the EPA increases and spills into the surface atmosphere, increasing the ionization capacity of surface air, increasing the rate of small ions with high migration speed, causing the increase in surface air conductivity, thus causing the decrease in SAPG. Although the radon ionization mechanism can explain the drop of SAPG pre-earthquake, as there are few stations for gas radon observation that can match with the SAPG observation station. In this case, pre-earthquake radon emissions can only be assumed to increase according to conventional methods (Vadim 2015; Hugo Gonçalves Silva 2012; Ghosh et al. 2009). Although we have tried our best to exclude various interference factors, nevertheless, the factors, methods and reference values still need further discussion and researches.

5 Conclusions

Before this earthquake, researchers found that the SAPG generally decreases in the earthquake preparation area and is explained by the mechanism of the increasing emission of radon before the earthquake. If radon emission can be confirmed to increase before the earthquake, the general downward trend of SAPG in the EPA may be a kind of earthquake precursor. We believe that future research should focus on setting up simultaneous SAPG, meteorological conditions, and radon observation projects, as well as on "fair" weather conditions. In particular, interference factors from lightning which was not considered in previous references are also proposed. Only in this way can it be more reliable to study earthquake precursors by using SAPG. Our research also provides ground evidence for abnormal changes in the ionosphere before the earthquake and improves the LAIC mechanism (Ouzounov 2018; Pulinets 2009).

References

Choudhury, A., Guha, A., De, B.K., Roy, R.: A statistical study on precursory effects of earthquakes observed through the atmospheric vertical electric field in northeast India. Ann. Geophys. **56**(3), R3301-3310 (2013)

Dobrovolsky, I.P., Zubkov, S.I., Miachkin, V.I.: Estimation of the size of earthquake preparation zones. PAGEOPH **117**, 1025–1026 (1979)

Ghosh, D., Deb, A., Sengupta, R.: Anomalous radon emission as precursor of earthquake. J. Appl. Geophys. **69**, 67–81 (2009)

Harrison, R.G., Nicoll, K.A.: Fair weather criteria for atmospheric electricity measurements. J. Atmos. Solar Terr. Phys. **179**, 239–250 (2018)

Li, Y.D., Zhang, L., Zhang, K., Jin, X.B.: Research on the atmospheric electric field abnormality near the ground surface before "5.12" Wenchuan Earthquake. Plateau Mountain Meteorol. Res. **37**(1), 49–54 (2016). (in Chinese)

Mizuno, A., Takashima, K.: Continuous measurement of current in air and possible relation with intense earthquake. J. Electrostat. **71**, 529–532 (2013)

Ouzounov, D., Pulinets, S., Hattori, K., Taylor, P.: Pre-Earthquake Processes a Multidisciplinary Approach to Earthquake Prediction Studies. Chapter 6, pp. 79–98. ISBN: 9781119156932, 2018

Pulinets, S.A.: Physical mechanism of the vertical electric field generation over active tectonic faults. Adv. Space Res. **44**, 767–773 (2009)

Silva, H.G., Oliveira, M.M., Serrano, C.: Influence of seismic activity on the atmospheric electric field in Lisbon (Portugal) from 1955 to 1991. Ann. Geophys. **55**(1), 193–197 (2012)

Surkov, V.V.: Pre-seismic variations of atmospheric radon activity as a possible reason for abnormal atmospheric effects. Ann. Geophys. **58** (5), A0554 (2015)

Williams, E.R.: Electricity in the Atmosphere: Global Electrical Circuit, pp. 1–10. Elsevier Inc. (2018)

Key Issues in the Research on Loess Flow Slides Under Hydraulic and Gravitational Soil Erosion

Aidi Huo, Jianbing Peng, Yuxiang Cheng, Xiaolu Zheng, and Yiran Wen

Abstract

Loess flow slides can have catastrophic consequences and have, therefore, become a critical research topic in engineering geology. Recent occurrences have revealed severe problems in the prevention of these events due to imperfect understanding of the effects of hydraulic and gravitational erosion and how these factors can intensify a loess flow slide. In this study, we reviewed studies on the effects of hydraulic and gravitational erosion with particular focus on the erosion resistance of loess landslide deposits and the sliding mechanism of loess flow slides. Additionally, landslide initiation and movement mechanisms of the loess flow slides that occur at the interface between loess and underlying mudstone are discussed. Three typical loess landslides caused by static liquefaction were used as examples, and their possible pore pressure generation modes were proposed. It is recommended that characteristics of the basin (watershed), critical zone (tableland edge), and the dynamic variation of underground water level should be included in the comprehensive evaluation of the potential contributions of the different position and intensity of hydraulic and gravitational erosion to loess flow slide events. This study has important scientific and strategic significance for the implementation of the sustainable development strategy of loess plateau in China.

Keywords

Hydraulic and gravitational Erosion • Loess Flow slide • Research progress • Prospect

1 Introduction

The loess area has long been a critical area of interaction between human and nature in North China (Peng et al. 2017). The loess sediments record the history of environmental change and the civilization and provide a valuable reference focus of past environmental changes allowing prediction of future trends (Li et al. 2013). The loess plateau is one of the most vulnerable areas, with severe soil erosion and a delicate ecological environment, but is also a common area used in arid and semi-arid farming and animal husbandry and provides vital energy and chemical base for China (Huo et al. 2016). Additionally, it is the core area of the implementation of the Belt and Road (abbreviated B and R) strategic layout. Which is also known as One Belt, One Road (abbreviated OBOR) or the Belt and Road Initiative is a development strategy and framework that focuses on connectivity and cooperation among countries primarily between the People's Republic of China and the rest of Eurasia (Yu et al. 2018). There are several published studies concerning loess landslide characteristics, formation mechanism, movement mechanism, stability evaluation, and ideas for prevention and control measures (Sassa 1984; Hatchinson 1988). However, there have been relatively few studies that investigate how intensive hydraulic and gravitational erosion interact with each other to induce loess flow slides and affect the landscape. The geologic environment, causes, movement process, movement mechanism, and disasters-causing characteristics of loess flow slides can contribute to the development and severity of landslides and the resulting flow slide. Loess flow slides exhibit characteristics of landslides and soil erosion.

A. Huo · X. Zheng · Y. Wen
Key Laboratory of Subsurface Hydrology and Ecological Effects in Arid Region (Chang'an University), Ministry of Education, Xi'an, 710054, Shaanxi, China

A. Huo · X. Zheng · Y. Wen
School of Environmental Science and Engineering, Chang'an University, Xi'an, 710054, Shaanxi, China

J. Peng (✉) · Y. Cheng
College of Geology Engineering and Geometrics, Chang'an University, Xi'an, 710054, Shaanxi, China
e-mail: dicexy_2@126.com

M. Meghraoui et al. (eds.), *Advances in Geophysics, Tectonics and Petroleum Geosciences*,
Advances in Science, Technology & Innovation, https://doi.org/10.1007/978-3-030-73026-0_68

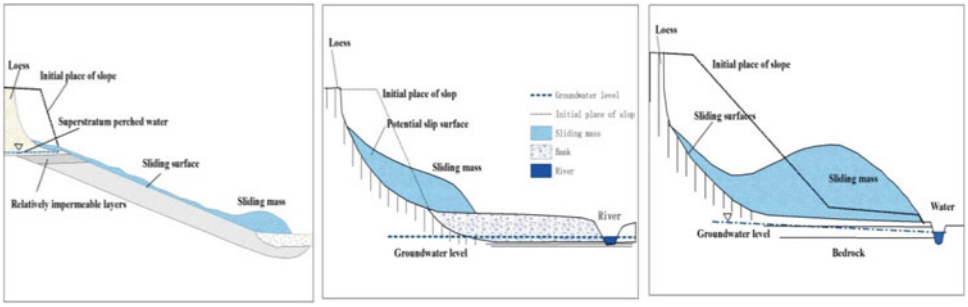

Fig. 1 Schematic diagram of the formation of a loess landslide for three different underground water levels

(a) Deep underground water level

(b) Middle underground water level

(c) Higher underground water level

Loess is widely distributed in the world, accounting for 1/10 of the global land area. It is mainly distributed in China, Iran, Central Asia of the Soviet Union, Argentina, etc. There have been significant advancements in the study of the loess plateau environment and loess flow slide disasters. However, some key issues remain unclear. In particular, the contribution of coupled hydraulic and gravitational erosion effects on loess flow side events are poorly understood. Forecasting and preventing loess flow slides requires a comprehensive analysis of the mechanisms of loess flow slide based on the geological types, disaster degrees, and inducing conditions. Overall, it is of outstanding scientific value and strategic significance to understand the action of the hydraulic and gravitational erosion coupling effect on loess stability for building the regional early warning system for disaster reduction and prevention. These efforts are essential to safeguard regional security and to promote sustainable development in loess areas.

2 Methods

According to satellite imagery, the geological disasters of loess landslides were investigated on a macroscopic scale. On this basis, a field survey was conducted to analyze the effects of hydraulic and gravitational erosion on loess landslides. The formation mechanism of loess landslide is identified combined with relevant literature for analysis.

3 Results

Because loess has pore structure and particles, it is a kind of soil that can easily undergo liquefaction. Studies of liquefaction of loess are needed. Liquefaction is a vitally important component of the slip mechanism but is difficult to study. Terzaghi et al. (1996) and Sassa (1984) proposed models of slip liquefaction in which the vibration force of the sliding body caused liquefaction. Hatchinson (1988) proposed a flow slide mechanism who emphasizes that the soil of the side slope must be an originally loose structure. Three geological conditions are proposed for this kind of landslide based on the large amounts of field investigation, sampling, and analysis: (1) Long-distant high slope with deep groove cutting; (2) Loose loess layer with saturated moisture content over the liquid limit on the top of the slope; (3) Aquifuge that can form upper sluggish water in the lower part of the side slope or gully.

Figure 1a–c shows three various kinds of loess landslides acting on the groundwater level. The major differences between these three are the depth of the groundwater and the eroding position. Figure 1a shows that the glide plane of loess landslide has some angle, and the lower part of loess landslide is a mudstone-water resisting layer. Thus, liquefaction only occurs at the inner part of the loess flow slide. Figure 1b shows that with a low level of groundwater. Figure 1c shows that with a high level of groundwater, the bottom of the landslide mass is close to the groundwater level. If groundwater level is between the levels shown in (a) and (c), sliding on the smaller slope river terrace can occur. Therefore, as shown in Fig. 1b, pore pressure generations are relatively complicated, and the liquefaction mechanism is unclear.

Additional studies are required to explore the effects of landslide mass on the flow slide, effect of the coupling between hydraulic and gravitational erosion on the sliding process and determine the contributions of the loess landslide mass and loess-terrace material mixed liquefaction mechanism. To lower the groundwater level and reduce irrigation on tablelands is a more feasible method for preventing loess landslides.

4 Discussion

Existing research status had provided much insight into loess mechanisms. However, the following questions still exist about loess flow slide due to coupled effects of hydraulic and gravitational erosion: What is the influence of downward water erosion in the valley on slope stability? The

mechanism for rapid infiltration of water-seepage diffusion-Collection-runoff-loess landslide-loess flow slide is deficient, and the characterizations of the above processes are also deficient. In the loess region, an increase in water is generally not sufficient to cause a loess landslide. In some critical areas of the watershed (such as the gully bottom and the margin of the loess platform), the downward erosion plays a vital role to promote the loess landslide in the gully. On-site monitoring or in situ experimental data is necessary to measure the hydrological conditions of hydraulic and gravitational erosion leading to loess flow slides. What is the mutually promoting effect between loess landslide and flow slide? Loess landslides supply the material source for flow slides, and flow slides will further lead to loess landslides, but the mutual effect between these two processes requires further study—hydraulic and gravitational erosion play key driving forces in this process. The main reasons for loess landslide are high and steep loess slope, high water table, rainfall, irrigation, etc. Lowering the groundwater level and reducing irrigation on tablelands is the first thing to do to prevent loess landslides. If it is not possible, we should cut the slope into steps, and do a proper job of slope protection and drainage.

5 Conclusions

Several aspects contribute to the mutual promotion effect of loess landslides and flow slides, including (1) the erosion action of initial and secondary landslides, (2) the mutual promotion and disaster chain evolution mechanism for a loess flow slide, and (3) the evolution mechanism of the loess plateau under effects of gravity and water erosion. Given the coupling effect between hydraulic and gravitational erosion, it is crucial to determine the changing consequences for the stability of loess regions and the potential for a flow slide. At the basin scale, it is necessary to study the mutual promotion effect between loess landslides and flow slides, based on data from unsaturated soil mechanic experiments and extensive monitoring.

References

Hatchinson, J.: Morphological and geotechnical parameters of landslides in relation to geology and hydrology. In: Proceedings of 5th International Symposium on Landslides “Landslides”, pp. 3–35 (1988)

Huo, A.-D., Dang, J., Song, J.-X., Chen, X., Mao, H.-R.: Simulation modeling for water governance in basins based on surface water and groundwater Agric. Water Manage. **174**(22), 29 (2016)

Li, P., Li, T., Wang, A.: In-situ test research on regularities of water migration in loess. Rock Soil Mech. **34**(5), 1331–1339 (2013)

Peng, J., Wang, G., Wang, Q., Zhang, F.: Shear wave velocity imaging of landslide debris deposited on an erodible bed and possible movement mechanism for a loess landslide in Jingyang, Xi’an, China. Landslides **5**, 1–10 (2017)

Sassa, K.: The mechanism starting liquefied landslides and debris flows. In: Proceedings of 4th International Symposium on Landslides, Toronto, pp. 349–354, June 1984

Terzaghi, K., Peck, R.B., Mesri, G.: Soil Mechanics in Engineering Practice. John Wiley & Sons New York (1996)

Yu, Y., Chang, Y.C.: The ‘one belt one road’ initiative and its impact on shipping law in China. Marine Policy **87**, 291–294 (2018)

Determination of Sedimentary Thickness of Parts of Middle Benue Trough, Northeast Nigeria, Using High-Resolution Aeromagnetic Data

Kazeem Adeyinka Salako, Abbass Adebayo Adetona, Abdulwaheed Adewuyi Rafiu, Usman Defyan Alhassan, Aisha Alkali, and Abdulateef Aliyu

Abstract

The sedimentary thickness covering parts of middle Benue Trough, Northeast Nigeria, was determined with the purpose of assessing its hydrocarbon potentials. Longitude 9° E covers the area—10° E, and Latitude 8° N—9.50° N, and with total area coverage of 18,150 km^2. Polynomial fitting method of order one was used to obtain its regional–residual separation. The residual data obtained were analysed using the analytic signal, source parameter imaging (SPI) and spectral depth analytical techniques. Results from the analytic signal technique showed that the area is made up of high and low magnetic anomaly amplitude. The high amplitude anomaly dominates the northern region while the southern region is dominated with low amplitude anomalies. Similarly, results from the SPI revealed a sedimentary thickness ranging between 101.8 and 2550.0 m while that of the spectral analytical method showed that the sedimentary thickness of the study area ranges between 1.20 and 3.20 km. The highest sedimentary thickness from both methods agreed in terms of space. This sedimentary covered could be found around the central and southern parts of the study area, which also agreed with the areas with low amplitude anomalies of the analytical signal results. The estimated depths from the spectral analytical method were contoured to portray the basement isobaths for the study area. The sedimentary thickness of about 3 km ***might*** be sufficient for hydrocarbon maturation in the area.

Keywords

Aeromagnetic data • Polynomial fitting • Source parameter imaging • Spectral analytical • Sedimentary thickness and hydrocarbon maturation

1 Introduction

Exploration of the subsurface Earth has been of particular concern to geoscientists who seeks to investigate the subsurface structures using various means, basically to acquire the knowledge of the subsurface lithology, for exploration activities such as minerals and hydrocarbon (oil/gas) deposits for economic growth of a nation (Azizi et al. 2015; Farhi et al. 2016; Adewumi and Salako 2018).

Efforts are geared towards the exploration of the Cretaceous segment of Nigeria looking for possible hydrocarbon presence and bearing in mind its mineral resources potentialities. The present study seeks to estimate the sedimentary thickness over parts of the middle Benue trough section of the Cretaceous sediments of Nigeria for possible hydrocarbon potentials. If it is probable, it will add to the country's hydrocarbon reserve, however, with the confirmation of other methods.

The magnetic method is **one** of the best geophysical techniques (in terms of coverage and or as a reconnaissance tool) used in delineating or estimating sedimentary thickness and other subsurface structures (Azizi et al. 2015; Farhi et al. 2016; Adewumi and Salako 2018; Salako and Udensi 2015).

1.1 Location and Brief Geology

The study area (Fig. 1) lies in the north-eastern part of Nigeria and lying between Latitudes 8°.00′ N and 9°.50′ N and longitudes 9°.00′ E and 10°.00′ E. It is housed by middle Benue Trough (Fig. 1). (Abdullahi et al. 2014) pointed out that the

K. A. Salako (✉) · A. A. Adetona · A. A. Rafiu · U. D. Alhassan · A. Alkali · A. Aliyu
Department of Geophysics, Federal University of Technology, Minna, Nigeria
e-mail: s.kazeem@futminna.edu.ng

M. Meghraoui et al. (eds.), *Advances in Geophysics, Tectonics and Petroleum Geosciences*, Advances in Science, Technology & Innovation, https://doi.org/10.1007/978-3-030-73026-0_69

Benue Trough generally has been geographically and structurally subdivided into three parts, namely: the "lower Benue Trough", the "middle Benue Trough" and the "Upper Benue Trough". The study conducted by Benkhelil (1989) distinguishes six sedimentary Formations in the middle Benue trough only, which are Asu River Group, Keana Formation, Awe Formation, Ezeaku Formation, Awgu Formation and Lafia Formation. The work of Benkhelil (1989), Offodile (1976), Cratchley and Jones (1965), Burke et al. (1970), Offodile (1984), Osazuwa et al. (1981), Ofoegbu (1985) has more on the geology of the Benue Trough.

2 Materials and Methods

(i) Six aeromagnetic maps with sheets numbers 190, 191, 211, 212, 231 and 232 covering the study area were acquired from the Nigerian Geological Survey Agency (NGSA) Abuja as part of the across the nation aeromagnetic survey carried out in 2009 by Fugro Airborne survey. The survey was conducted along NW–SE flight lines, and tie line along NE-SW direction with 500 m flight line spacing, terrain clearance of 80 m and line spacing of 2 km were used. The magnetic data recording interval during the survey was 0.1 s. All grid data were saved and delivered in Oasis Montaj Geosoft raster file format. Each 1:100,000 topographical sheet covers an area of about 3025 km^2 (i.e. 55 km × 55 km) totalling a superficial area of 18,150 km^2.

(ii) The residual anomaly map was later subjected to three automated processing techniques to determine the depth to magnetic basement. The three automated processing techniques are (i) analytic signal, (ii) source parameter imaging and (iii) spectral analysis.

(iii) Analytical Signal the equation used is (Nabighian 1972):

$$|A(x,y)| = \sqrt{\left(\frac{\partial M}{\partial x}\right)^2 + \left(\frac{\partial M}{\partial y}\right)^2 + \left(\frac{\partial M}{\partial z}\right)^2} \quad (1)$$

where

$A(x, y)$ amplitude of the analytic signal at (x, y) and
M observed magnetic field at (x, y).

(iv) The SPI method (Thurston and Smith 1997) estimates the depth parameter using the local wave number of the analytical signal (Thurston and Smith 1997). The two wave numbers as related by Hilbert transformation (⇔) are given as:

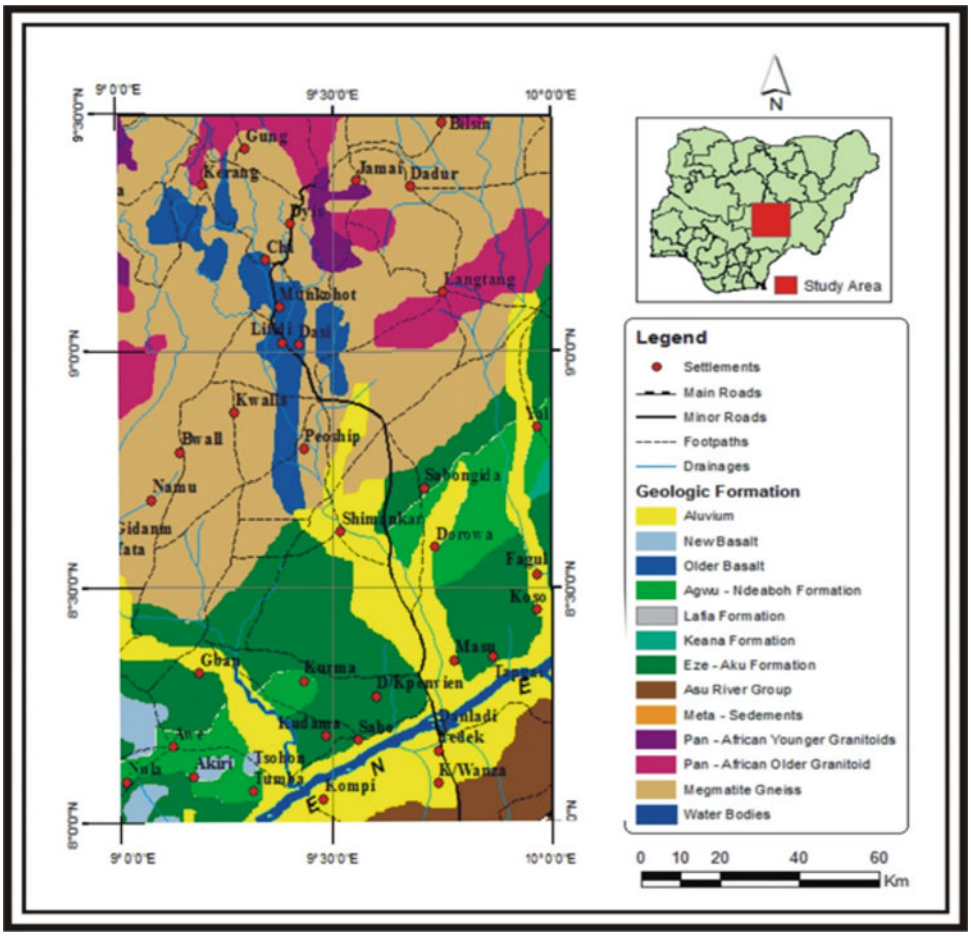

Fig. 1 Geological map of part of middle Benue Trough (Geological Survey of Nigeria 1984)

$$k_1 = \frac{\partial}{\partial x}\tan^{-1}\left[\frac{\partial M}{\partial z}/\frac{\partial M}{\partial x}\right] \quad \text{and}$$
$$k_2 = \frac{\partial}{\partial x}\tan^{-1}\left[\frac{\partial^2 M}{\partial^2 z}/\frac{\partial^2 M}{\partial z \partial x}\right] \tag{2}$$

for analytical signal defined for the first (A_1) and second (A_2) order, respectively.
The k_1 and k_2 are used to determine the most appropriate model and depth estimate of any assumption about a model.

(v) Spector and Grant (1970) demonstrated that the depth could be made using the equation

$$E(r) = e^{-2h}; \tag{3}$$

where

$E(r)$ is the spectral energy,
r the frequency and
h the depth.

The energy or amplitude spectrum is plotted on the logarithmic scale against frequency. The plot shows the straight line segments which decrease in slope with increasing frequency. The slopes of the segments yield estimates of depths to magnetic sources.

3 Results and Discussion

3.1 Results (Analytical Signal)

Figure 2 shows the analytical signal of the study area. The high amplitude magnetic anomalies were very much pronounced in the northern part and at the edges of the study area. The low amplitude magnetic anomalies were located at the central part and trend towards the south-eastern parts. The high amplitude magnetic anomaly is probably due to basement intrusion close to the surface.

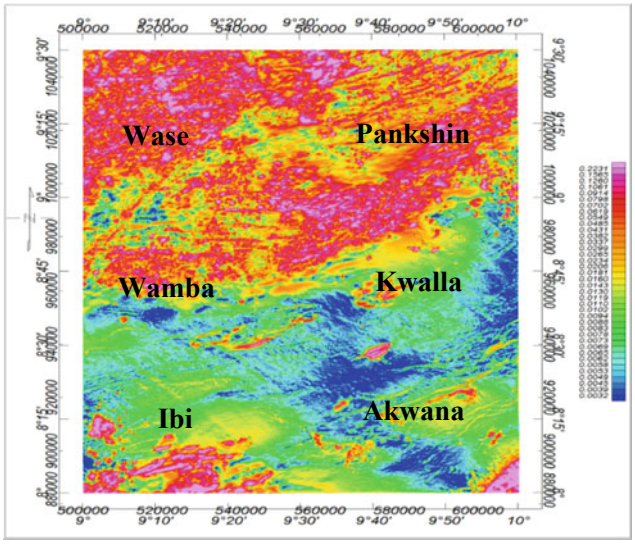

Fig. 2 Analytical signal map of the study area (unit: A/m)

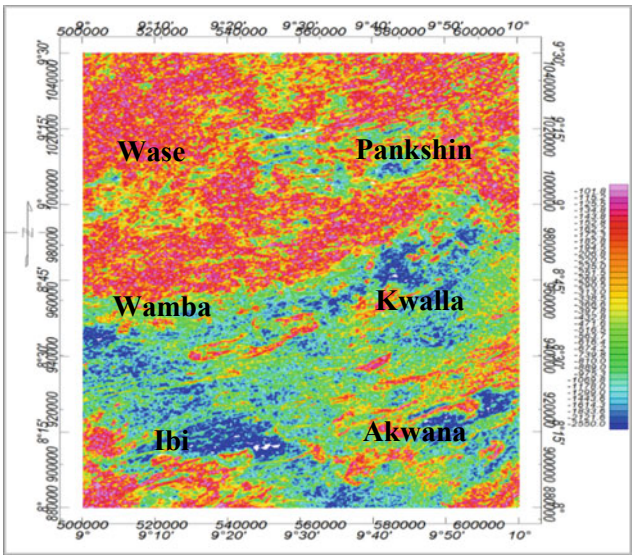

Fig. 3 Source parameter imaging map of the study area (unit: m)

3.2 Results (Source Parameter Imaging)

The source parameter imaging (Fig. 3) of the study area shows that most of the features were aligned in the same manner and trends like the results obtained from the analytic signal map (Fig. 2). The area of highest sedimentary thickness in SPI (Fig. 3) conforms to the area of lower amplitude magnetic anomalies in the analytical signal map (Fig. 2).

From Fig. 3, the depth (below mean sea level) to sedimentary/basement interface varies between 101.8 and 2550.0 m. The highest sedimentary thickness dominates the southern portion of the area while the least basement depth dominates a significant part of the southern portion. However, relatively lower depths are seen scattered around the southern part.

3.3 Results (Spectral Depth Analysis)

The residual map of the study area was divided into fourteen (Blocks A–N) overlapping magnetic sections in which none of the blocks has less than 55 by 55 km data coverage window (Table 1). The sedimentary thickness of 1.20 km to a maximum of 3.20 km were obtained from the spectral analysis

Table 1 Results from spectral plots

Blocks	Longitude (°)	Latitude (°)	Sedimentary thickness Z_t (km)
A	9.25	9.25	2.04
B	9.75	9.25	2.50
C	9.25	8.75	2.14
D	9.75	8.75	1.98
E	9.25	8.25	1.20
F	9.75	8.25	1.40
G	9.5	9.25	2.00
H	9.5	8.75	3.20
I	9.5	8.25	1.70
J	9.5	9.0	1.50
K	9.5	8.0	1.84
L	9.25	8.25	2.08
M	9.75	8.25	1.86
N	9.5	8.25	1.65

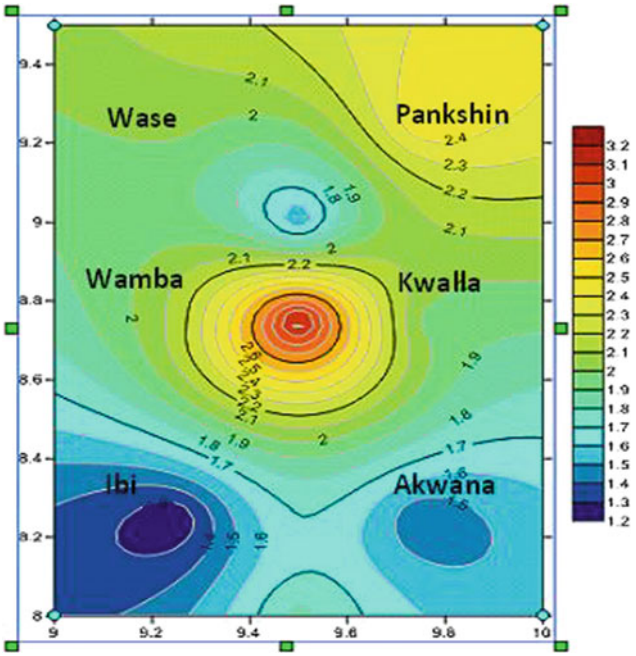

Fig. 5 Residual map of the study area

agrees mostly with the result obtained earlier with SPI, most notably concerning the location (Figs. 4, 5, 6 and 7).

Results from the two depths estimate approach agreed largely with other published works in the studied area. Nwogbo (1997) got 2–2.62 km for deeper source from spectral analysis of upper Benue trough; (Aliyu et al. 2018) obtained two-layer depths with the deeper magnetic sources varying between 1.2 and 4.8 km and the shallower magnetic sources varying between 0.5 and 1 km. (Salako and Udensi 2015) got an average depth of 1079.5 m for shallower source while the deeper magnetic source bodies have an average depth of 4.5 km. Similarly, (Nwogwugwu et al. 2017) using spectral analysis obtained values ranging between 1.22 and 3.45 km for depth to magnetic basement and (Mohammed et al. 2019) and (Salako 2014) got the sedimentary thickness of over 4.0 km while working over upper Benue trough and Bornu Basin, Nigeria, (Ofoha et al.

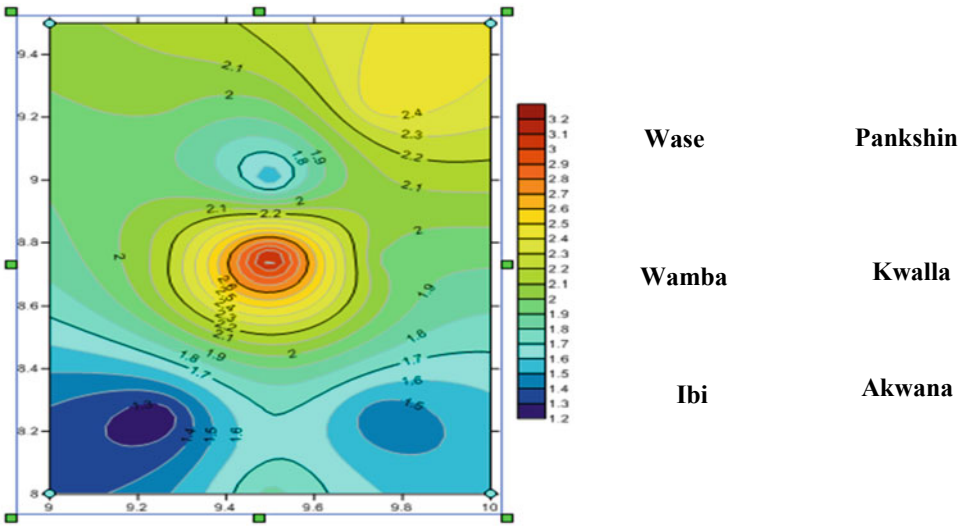

Fig. 4 Contour map of the sedimentary thickness (unit: km)

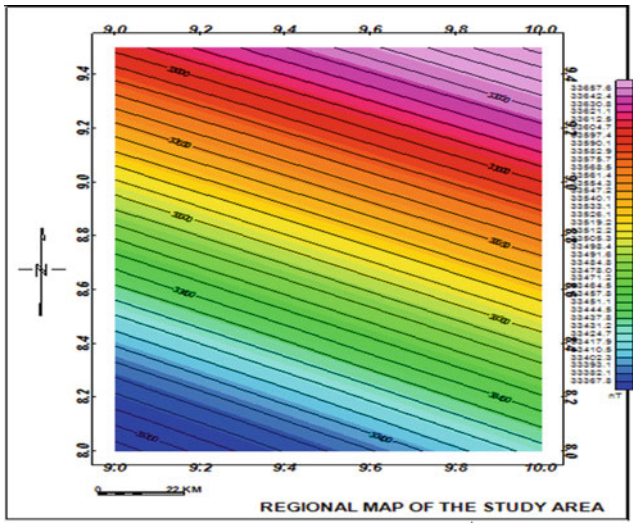

Fig. 6 Regional map of the study area

2016) got sedimentary thickness of less than 3 km while working Sokoto Basin, Nigeria, where the highest sedimentary thickness was obtained from SPI, and spectral methods agreed with the areas with low amplitude anomaly of the analytical signal.

4 Conclusions

The results of this study suggest that the sedimentary thickness of the study area varies between 1.20 and 3.20 km. The highest sedimentary thickness of about 3 km can be obtained from the central part to the south-eastern part of the study area. These areas correspond to areas delineated as low amplitude anomaly of the analytical signal. However, according to Wright et al. (1985), the minimum thickness for the concealment of hydrocarbon is about 2.3 km; hence, the sedimentary thickness of over 3 km might be sufficient for hydrocarbon (at least for gas) maturation in the area.

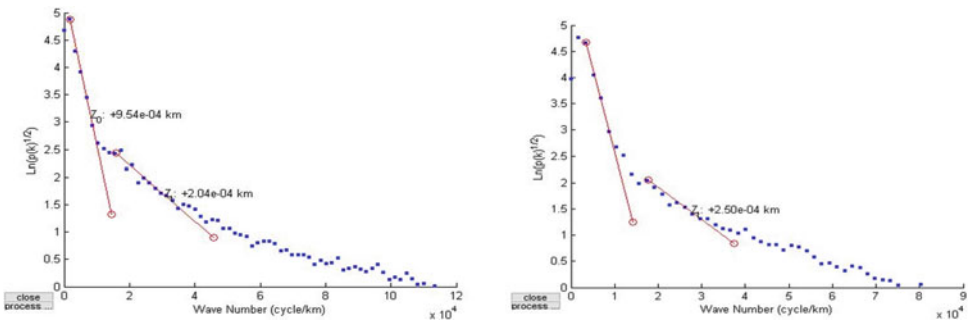

Fig. 7 Typical plots of the logarithm of spectral energies against frequencies obtained for blocks A and B

References

Abdullahi, U.A., Ugwu, G.Z., Ezema, P.O.: Magnetic exploration of the upper and lower Benue trough for metallic deposits and hydrocarbons using 2D/3D. J. Nat. Sci. Res. **4**(20), 41–46 (2014)

Adewumi, T., Salako, K.A.: Delineation of mineral potential zone using high resolution aeromagnetic data over part of Nasarawa State, North Central, Nigeria. Egypt. J. Petrol. **27**, 759–767 (2018). Available at https://doi.org/10.1016/j.ejpe.2017.11.002

Aliyu, A., Salako, K.A., Adewumi, T., Mohammed, A.: Interpretation of high resolution aeromagnetic data to estimate the curie point depth isotherm of parts of middle Benue trough, North-East, Nigeria. Phys. Sci. Int. J. **17**(3), 1–9 (2018)

Azizi, M., Saibi, H., Cooper, G.R.J.: Mineral and structural mapping of the Aynak-Logar Valley (Eastern Afghanistan) from hyperspectral remote sensing data and aeromagnetic data. Arab. J. Geosci. **8**, 10911–10918 (2015)

Benkhelil, J.: The origin and evolution of the cretaceous benue trough (Nigeria). J. Afr. Earth Sci. **8**, 251–282 (1989)

Burke, K.C., Dessauvagie, T.F.J., Whiteman, A.J.: Geologic history of the Benue Valley and adjacent areas. In: Dessauvagie, T.F.J., Whiteman, A.J. (eds.) African geology, pp. 187–206. University of Ibaban Press, Nigeria (1970)

Cratchley, C.R., Jones, G.P.: An interpretation of the geology and gravity anomalies of the Benue Valley, Nigeria. J. Geol. Geophys. **1**, 1–26 (1965)

Farhi, W., Boudella, A., Saibi, H., Bounif, M.O.A.: Integration of magnetic, gravity, and well data in imaging subsurface geology in the Ksar Hirane region (Laghouat, Algeria). J. Afr. Earth Sci. **124**, 63–74 (2016)

Geological Survey of Nigeria: Geological Map of Nigeria (1984)

Mohammed, A., Adewumi, T., Salako, K.A., Rafiu, A.A., Adetona, A. A., Alhassan, U.D.: Assessment of geothermal potentials in some parts of Upper Benue Trough Northeast Nigeria using Aeromagnetic Data. J. Geosci. Eng. Environ. Technol. (JGEET) **4**(1) (2019). https://doi.org/10.25299/jgeet.2019.4.1.2090

Nabighian, M.N.: The analytic signal of two dimensional magnetic bodies with polygonal cross-section. Its properties and use for automated anomaly interpretation. Geophysics **37**, 507–517 (1972)

Nwogbo, P.O.: Mapping the shallow magnetic sources in the Upper Benue Basin in Nigeria from aeromagnetic. Spectra **4**(3/4), 325–333 (1997)

Nwogwugwu, E.O., Salako, K.A., Adewumi, T., Okwokwo, I.O.: Determination of depth to basement rocks over parts of Middle Benue Trough, North Central Nigeria, using high resolution

aeromagnetic data. J. Geol. Min. Res. (JGMR) **9**(3), 18–27 (2017). https://doi.org/10.5897/JGMR2017.0276. Available at http://www.academicjournals.org/journal/JGMR/article-full-text-pdf/8AE382A66043

Offodile, M.E.: The geology of the middle Benue Nigeria. Cretaceous research, paleontological institute: university of uppsala. Special Publ. **4**, 1–166 (1976)

Offodile, M.E.: The geology and tectonics of awe brine field. J. Earth Sci. **2**, 191–202 (1984)

Ofoegbu, C.O.: A review of the geology of the Benue trough, Nigeria. J. Afr. Earth Sci. 283–291 (1985)

Ofoha, C.C., Emujakporue, G., Ngwueke, M.I., Kiani I.: Determination of magnetic basement depth over Parts of Sokoto Basin, within Northern Nigeria, using improved source parameter imaging (ISPI) technique. World Sci. News **50**, 266–277 (2016)

Osazuwa, I.B., Ajakaiye, D.E., Verheiien, P.J.T.: Analysis of the structure of part of the upper Benue rift valley on the basis of new geophysical data. Earth Evol. Sci. **2**, 126–135 (1981)

Salako, K.A.: Depth to Basement Determination Using Source Parameter Imaging (SPI) of Aeromagnetic Data: An Application to Upper Benue Trough and Borno Basin, Northeast, Nigeria, pp 74–86. Academic Research International, 2014. Retrieved from www.journals.savap.org.pk

Salako, K.A., Udensi, E.E.: Two dimensional modeling of subsurface structure over upper Benue trough and Bornu basin in north eastern Nigeria. Nigeria J. Technol. Res. (NJTR) **10**, 94–104 (2015). https://doi.org/10.4314/njtr.v10i1.S11

Spector, A., Grant, F.S.: Statistical models for interpreting aeromagnetic data. Geophysics **35**, 293–302 (1970)

Thurston, J.B., Smith, R.S.: Automatic conversion of magnetic data to depth, dip, and susceptibility contrast using the SPITM method. Geophysics **62**, 807–813 (1997)

Wright, J.B., Hastings, D.A., Jones, W.B., Williams, H.R.: Geology and Mineral Resources of West Africa. George Allen and Unwin (Publishers) Ltd., 40 Museum Street, London WCIA ILU, UK. 187 p. (1985)

Geological and Geophysical Characterization Using Electrical Resistivity Imaging of Certain Landslides at Djimla region (Jijel, Northeast Algeria)

Hassiba Kherrouba, Mohammed Lamara, and Riad Benzaid

Abstract

Slope failure is a complex phenomenon that may cause landslides. Buildings and infrastructure, such as transportation facilities and pipelines, located within the boundaries of a landslide can be damaged or destroyed. The region of Djimla, like all regions of northern Algeria, has several sites affected by these landslides. This work aims to characterize the Tamentout landslides (PK42 + 260 and PK 43 + 050) located in the southeast of the Jijel province. From the geological point of view, this zone belongs to the Tellian domain represented by Senonian formation, mainly composed of marls deposits topped by Numidian flysch formations of Aquitano-Burdigalian age with a topographic slope within a range of 10°–15°. The geophysical approach consists in processing available geophysical data of electrical resistivity by exploiting these data in the form of electrical images of the ground. This geophysical approach aims to delineate lithology and geometry of the formations at the landslide sites, as well as the depth of slip suface associated with these landslides. The results of electrical resistivity tomography, coupled with the data of geological and geotechnical investigations, show a very good correlation of the structure of these studied landslides. The precise determination of the depth of the shear zone is of paramount importance to carry out the stabilization measures of this unstable zone.

Keywords

Djimla • Landslide • Geological context • Electrical resistivity imaging • Slope

1 Introduction

Landslides are complex phenomena whose study necessarily requires a multidisciplinary approach based on a wide range of observations including geological and geomorphological mapping, geotechnical and geophysical investigations. In recent years, the application of geophysics methods to landslide studies has evolved considerably (Lapenna et al. 2005; Meziani et al. 2017, Maameri et al. 2019). Due to the rugged terrain and abrupt topographic changes in the landslide areas, it was difficult to conduct such investigations. Recently, some geophysical imaging techniques based on tomography are commonly used in shallow surveys (Bellanova et al. 2016; Jongmans 2007; Kherrouba et al. 2019). The purpose of geophysical prospecting applied to ground movements is mainly to identify the lateral limits of the mass in motion, the surface of sliding in depth, as well as the imaging of the internal structure of the moving body. Since water is a major factor in the activation of landslides, electrical and electromagnetic techniques are most often used (Lebourg et al. 2005; Nordiana et al. 2018).

The aim of this work is to characterize landslides located in the region of Tamentout (PK42 + 260 and PK43 + 050) which were occured in 2018 during the earthworks of the new penetrating highway.

2 Location of the Study Area

The two unstable zones targeted by our study are located at the level of PK42 + 260 and PK43 + 050 (Fig. 1), located 5.5 km southwest of the Djimla village, north of the locality

H. Kherrouba (✉) · R. Benzaid
Geological Engineering Laboratory (LGG), University of Jijel, Jijel, Algeria

M. Lamara
Laboratoire de Génie Civil et Environnement (LRGCE), University of Jijel, Jijel, Algeria

M. Meghraoui et al. (eds.), *Advances in Geophysics, Tectonics and Petroleum Geosciences*,
Advances in Science, Technology & Innovation, https://doi.org/10.1007/978-3-030-73026-0_70

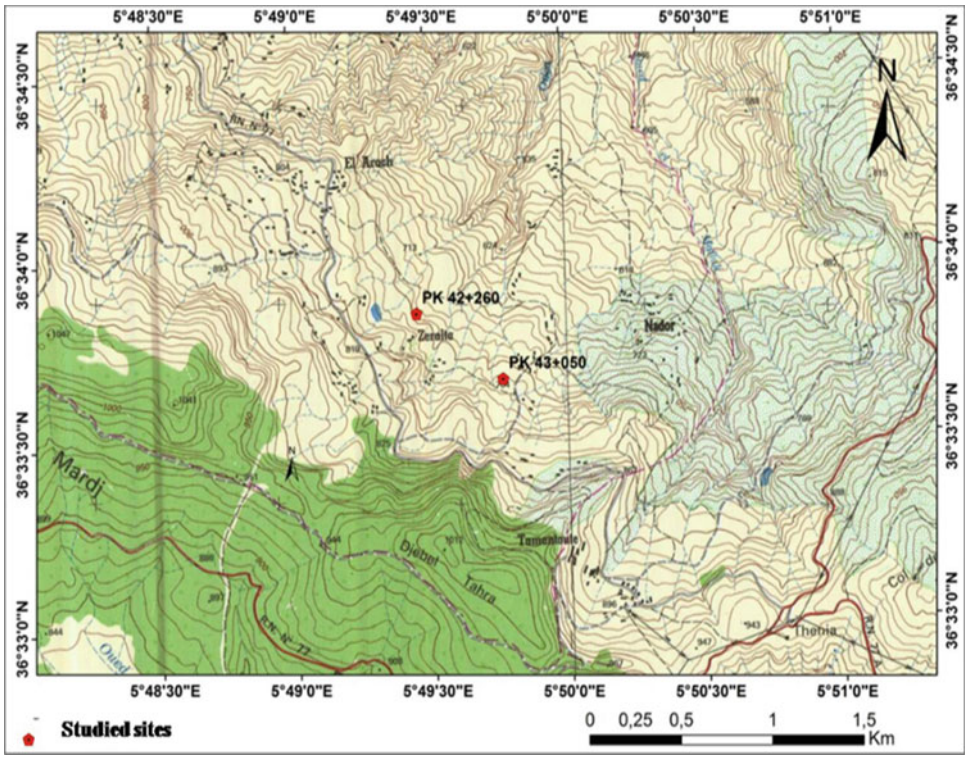

Fig. 1 Location of the studied landslides

of Tamentout, and 2 km NW of the intersection RN 77 and RN77A.

3 Local Geology

Geologically, the region of Tamentout belongs to the tellian domain (Djellit 1987; Kherrouba 2008, Maameri et al. 2019). It is represented by a Senonian formation mainly composed of marls deposits topped by Numidian flysch formations of Aquitano-Burdigalian age (Fig. 2).

4 Geophysical Characterization

Eight profiles of electrical resistivity tomography were made in April 2018 by GeoExplo (2018) on the two areas of landslide. Two electrical profiles (EP2 and EP6) were chosen for the present work and are represented in Figs. 3 and 4.

The pseudo-section of EP2 highlights two compartments of the conductive formation, of resistivity 5–15 Ωm attributed to saturated marly-clay at the flanks of more resistant

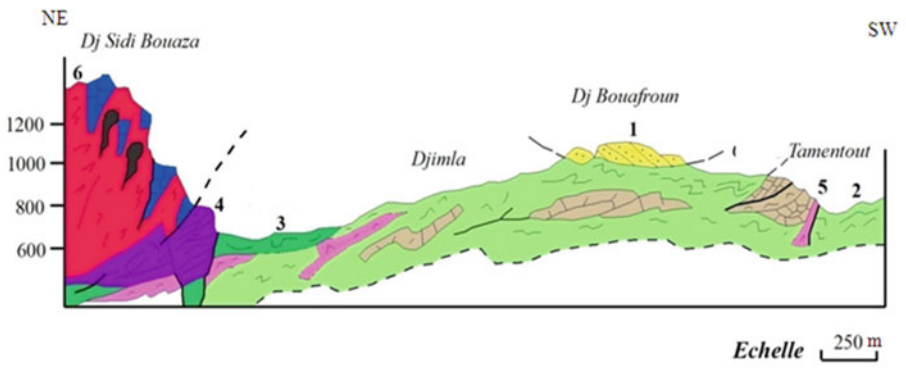

Fig. 2 Geological cross-section of the study region

Legend

1- Numidian series (Aquitano-Burdigalien): clays and sandstones, 2- Tellian series Ypresien-Lutetian , Tellian series :marl and limestone-marl (Paleogene-Senonian), 3- Massylian Flysch (Albo-Aptian):sandstones, shales, 4- VSC: calschists, quartzo-pelitic green-series rocks (presumed Jurassic?), 5- Triassic: clayey sandstone, gypsiferous, 6- Kabyle basement

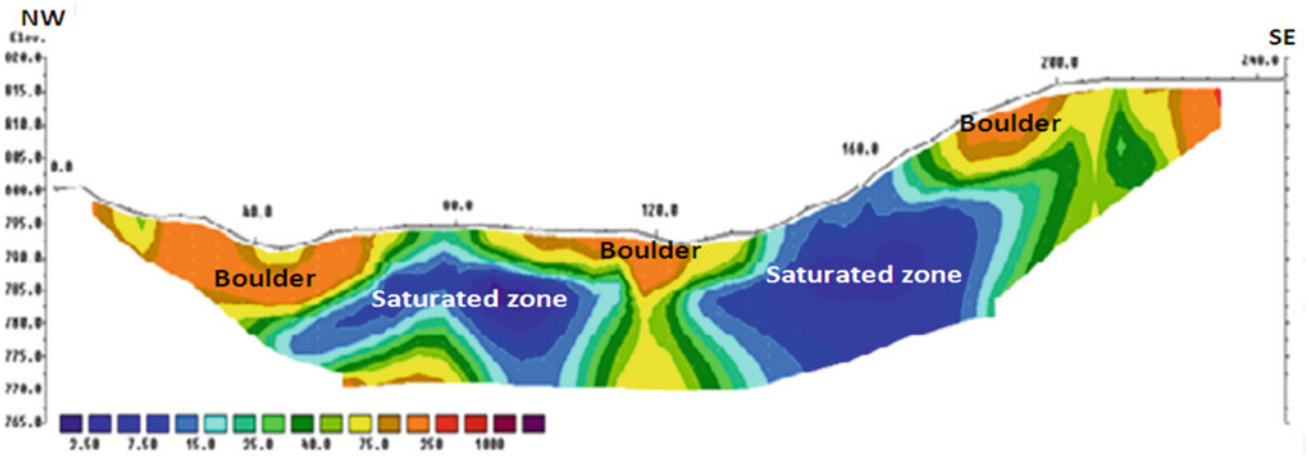

Fig. 3 Pseudo-section of EP2 (GeoExplo 2018)

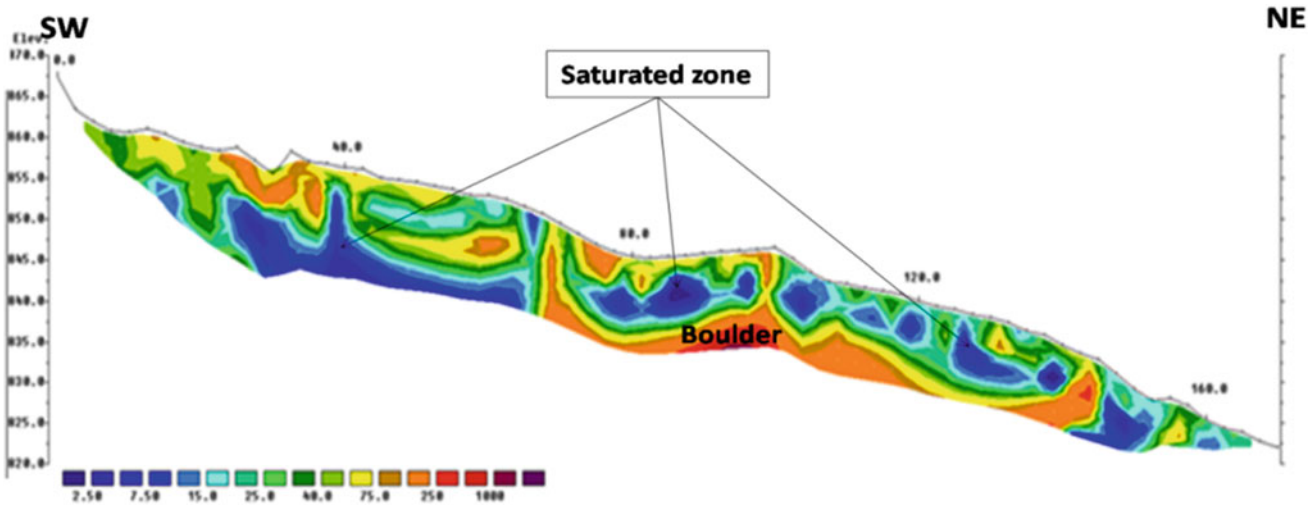

Fig. 4 Pseudo-section of EP6 (GeoExplo 2018)

compact marls/Numidian sandstone of resistivity 20–100 Ωm at the centre of the profile.

The pseudo-section of EP6 shows, contrary to the previous profile, a predominance of the resistant formation, which resistivity values are between 20 and 1000 Ωm. These values are certainly attributed to compact marl for low values (20–100 Ωm) and to the presence of hard Numidian sandstone for higher resistivity values (greater than 100 Ωm).

The results of the electrical resistivity imaging allowed us to characterize the landslides, by combination of the slope with the morphology of conductive and resistant formations. The slip surface can be located in the layer which has a resistivity, varying between 5 and 20 Ωm, which is attributed to saturated formations.

5 Conclusion

Lithology and geometry of the formations constituting the landslide sites at Tamentout were determined. The electrical resistivity pseudo-sections of the sites indicate an alternation of conductive ground strewn with non-resistant and resistant terrain. The distribution of the resistivity in the subsurface indicates highly conductive saturated marly clay formations of resistivity 5–20 Ωm and alternating compact marls and numidian sandstones of resistivity 20–100 and 100–1000 Ωm, respectively.

The pseudo-sections obtained show that the main cause of instability is due to the presence of groundwater at a depth of 4 m combined with the irregular morphology and the geological nature of the sites.

References

Bellanova, J., Calamita, G., Giocoli, A., Luongo, R., Perrone, A., Lapenna, V., Piscitelli1, S.: Electrical resistivity tomography surveys for the geoelectric characterization of the Montaguto landslide (Southern Italy). Natural Hazards Earth Syst. Sci. (2016)

Djellit, H.: Evolution tectono-métamorphique du socle Kabyle et polarité de mise en place des nappes de flyschs en Petite Kabylie occidentale (Algérie). Thèse Doct. Univ d'Orsay, P206, Paris (1987)

Jongmans, D., Garambois, S.: Geophysical investigation of landslides: a review. Bulletin De La Société Géologique De France **178**, 101–112 (2007)

Kherrouba, H.: Etude géologique et géotechnique des zones instables de la région de Texenna-Djimla, wilaya de Jijel, (Algérie), Mém de Magister, 173 p. Univ. Jijel. Algérie (2008). http://dspace.univ-jijel.dz:8080/xmlui/handle/123456789/3619

Kherrouba,H., Lamara,M., Benzaid,R.: Contribution of electrical tomography to the study of landslides in Texenna region (Northeast Algeria).InSundararajan N et al. (eds.), On Significant Applications of Geophysical Methods, Advances in Science, Technology & Innovation. https://doi.org/10.1007/978-3-030-01656-2_11 (2019)

Lapenna, V., Lorenzo, P., Perrone, A., Piscitelli, S., Rizzo, E., Sdao, F.: 2D electrical resistivity imaging of some complex landslides in Lucanian Apennine chain, southern Italy. Geophysics **70**(3), B11–B18 (2005)

Lebourg, T., Binet, S., Tric, E., Jomard, H., El Bedoui, S.: Geophysical survey to estimate the 3D sliding surface and the 4D evolution of the water pressure on part of a deep-seated landslide. Terra Nova **17**, 399–406 (2005)

Maameri, R., et al.: Apport de l'imagerie géophysique à l'étude des glissements de terrain sis au PK42+260 et PK43+050.Pénétrante autoroutière 77-région de Tamentout –Jijel (Nord Est Algérien), Mém de Master.75P., Université de Jijel, Algérie (2019)

Meziani, B., Machane, D., Bendaoud, A., CheikhLounis, G., Oubaiche, E., Chabane, S., Bensalem, R., Moulouel, H.: Geotechnical and geophysical characterization of the Bouira-Algiers Highway (AinTurck, Algeria) landslide. Arab. J. Geosci. **10**, 117 (2017)

Nordiana, M.M., Azwin, I.N., Nawawi, M.N.M., Khalil, A.E., Azwin, I.N., Nawawi, M.N.M., Khalil, A.E.: Slope failures evaluation and landslides investigation using 2-D resistivity method. NRIAG J. Astron. Geophys. **7**, 84–89 (2018)

Rapport de l'étude géophysique des glissements de terrain de Tamentout. Bureau d'engineering, études et équipements en géosciences "GeoExplo", 56 p, Alger, Avr 2018. Source: Agence Nationale des Autoroutes (ANA), Jijel, Algérie (2019)

Computer Technology for Modeling the Sources of Magnetic Anomalies in the Layers of the Earth's Crust

Natalia Fedorova, Peter Martyshko, and Alexey Rublev

Abstract

This paper illustrates new methods to investigate the anomalous magnetic field of the lithosphere and to module sources of anomalies in different layers of the earth's crust. The interpretation consists of three stages: separation of anomalies from sources in different layers of the earth's crust, the transformation of the data to the pole and solution of the inverse problem of finding the surface of the sources. New computer technology was used with an application of parallel computing on multiprocessor computer systems. The results are presented for the Western Ural region, covering the eastern part of the old East-European platform and the Ural orogen. The models of the sources of magnetic anomalies in the granite layer and the surface of the basaltic layer are constructed for magnetization 3 and 4 A/m. Results of the study allowed us the determination of the position of the deep faults in the upper crust of the Western Ural and their connection with the deep **belt of magnetized ultrabasic-basic complexes** projecting above the basalt layer of the earth's crust.

Keywords

Magnetic anomaly • Earth's crust • Modeling

1 Introduction

Magnetic anomalies provide essential information about the structure and history of the earth's lithosphere. We have developed new methods and applied efficient computer technology to study the structure of the anomalous magnetic field and to build sources of anomalies in different layers of the earth's crust. In the study of significant anomalies, it is necessary to process big data; therefore, in our new computer technology, we used parallel computing on multiprocessor computer systems.

N. Fedorova · P. Martyshko (✉) · A. Rublev
Institute of Geophysics UB RAS, 620016 Ekaterinburg, Russia

P. Martyshko
Ural Federal University, 620002 Ekaterinburg, Russia

2 Methods

2.1 Method of Separation of Anomalies from Sources in the Earth's Crust

The anomalous magnetic field has an integral character and contains components from all the sources located in the upper lithosphere. In order to extract the anomaly from the sources in different layers of the earth's crust, a technique based on subsequent upward and downward magnetic data continuation was used (Martyshko et al. 2014). Firstly, the field is continued upwards to level $\boldsymbol{H}$, due to which the effects of the local near-surface sources (up to a depth $\boldsymbol{H}$) are significantly suppressed. In order to get rid of the influence of the local sources located in the horizontal layer between the surface and depth $\boldsymbol{H}$, the field, which was calculated to the height level above the initial surface, was then continued downwards to the depth $\boldsymbol{H}$. Since the downward continuation procedure is an ill-posed problem, the regularization was applied. Finally, the field was continued upwards again to the first surface. The resulting field can be treated as the field of the sources that are located below the $\boldsymbol{H}$ level. Subtraction of this field from the observed one gives the field that is generated by the layer. By repeating this procedure in different heights and depths, we could separate the fields generated by the layers within the corresponding boundaries. The results of using this method are demonstrated for the Western Ural region, covering the eastern part of the old East-European platform and the Western part of the Ural orogen (Fig. 1a). On the platform, the foundation is covered with thick sediments ranging from 4 to 10 km. In the Ural

M. Meghraoui et al. (eds.), *Advances in Geophysics, Tectonics and Petroleum Geosciences*,
Advances in Science, Technology & Innovation, https://doi.org/10.1007/978-3-030-73026-0_71

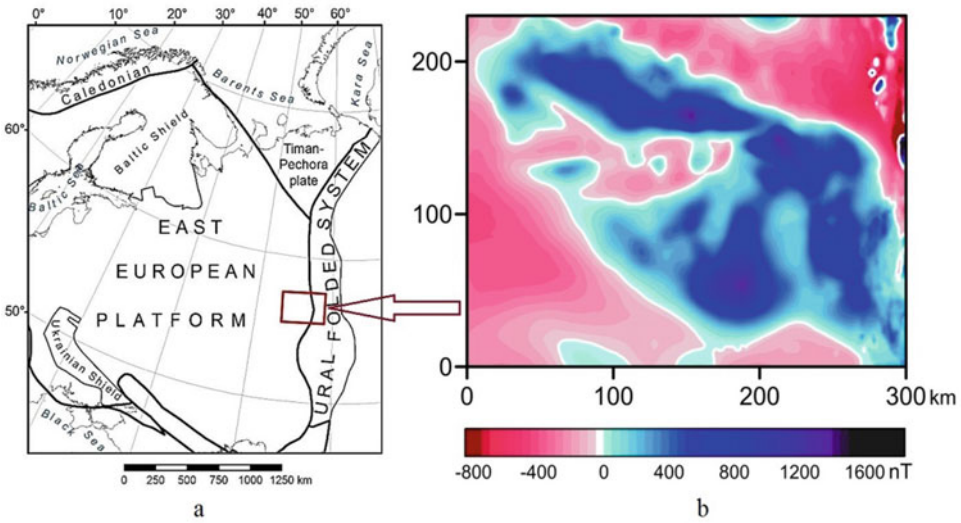

Fig. 1 Tectonic map (**a**) and magnetic anomalies of the Western Ural region (**b**)

region, some basic-ultrabasic massifs are exposed to the surface. In an anomalous magnetic field, five large-scale anomalies are distinguished; these are complicated by the intense local anomalies from intrusions and effusive of the crystalline basement (Fig. 1b).

2.2 Method of Transformation of the Anomalous Field to the Pole

Magnetic surveys are carried out mainly on the specific equipment which measures the absolute values of the geomagnetic induction, and the anomalous magnetic field of the lithosphere is often represented by the module anomalies ΔT. Since ΔT is not a harmonic function, for a correct application of methods to solve the magnetic inverse problems, it is necessary to determine the vertical component of Z. A calculation method for the vertical component of an anomalous magnetic field based on its absolute value was developed (Byzov et al. 2017). The conversion was based on the approximation of the magnetic induction module anomalies by a set of singular sources. A set of rods that are uniformly magnetized were used as a set of modeling singular sources. It is easy to calculate the values ZV for the vertical direction of the magnetization vector using the solution of the direct problem for the singular sources found. It should be noted that the transformation of magnetic anomalies to the pole significantly reduces the computational process of solving the inverse problem.

2.3 Method to Solve the Inverse Problem

The method is designed to solve the magnetic inverse problem for a layered model, and it allows determining the contact surface between two layers with different magnetic characteristics. In order to find points on the surface, it is required to solve the integral equation. A modified method of local corrections was used (Martyshko et al. 2010). The method is based on the assumption that a change in the value of the field at some point is mostly affected by the change of the depth in the nearest point of surface. We used an iterative formula for finding z_{ij}^{n+1}: $\left(z_{ij}^{n+1}\right)^2 = \frac{\left(z_{ij}^{n}\right)^2}{1+\alpha\left(z_{ij}^{n}\right)^2\cdot\left(U_{ij}-U_{ij}^{n}\right)}$, where α is regularization parameter, $\{z_{ij}^{n}\}$ are the values of the unknown surface defining function $z(x, y)$ separating the upper and lower layers, n is the number of iteration, U_{ij}, U_{ij}^{n} are observed and model fields (Martyshko et al. 2010). An iterative method was developed that allows calculating faster the boundaries of three-dimensional sources of anomalies.

3 Modeling Results of the Sources of Magnetic Anomalies

A new computer technology based on parallel computing has been created. Description of the mathematical apparatus and examples of its use are given in Martyshko et al. (2014). For the Western Ural region's study, the separated magnetic anomalies from the granite and basalt layers are shown in Fig. 2a, b. The models of the sources of magnetic anomalies in the granite layer and the surface of the basaltic layer are constructed for the magnetization 3 and 4 A/m (Fig. 2). The magnetization values of 3 and 4 A/m were set based on the results of measuring the magnetic characteristics of rock samples. The basalt layer has five significant elevations in the form of domes, rising from a depth of 20–15 km (Fig. 2c). In the granite layer, magnetized sources form linear belts with a length of 100–200 km (Fig. 2d). Within the Ural, the belts are stretched in a north–south direction.

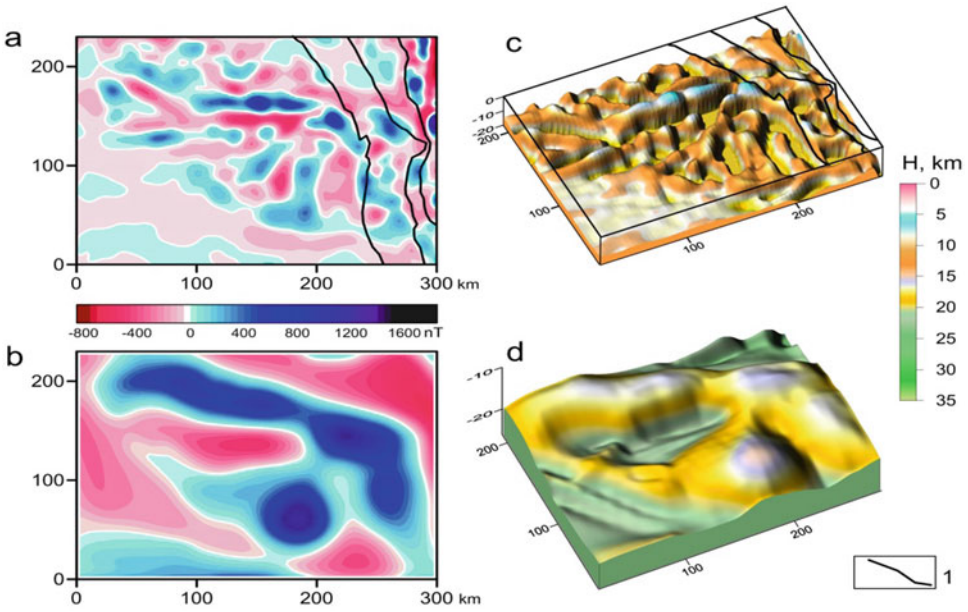

Fig. 2 Separated magnetic anomalies of granite (**a**) and basalt (**b**) layers and the results of modeling sources in the granite layer (**c**) and the surface of the basalt layer (**d**). 1—deep faults identified on the surface according to geological data

On the East-European platform, the strike of the belts varies from sub-latitudinal to sub-meridional, which indicates a lengthy and complicated history of the formation of the ancient platform foundation. The results allow the determination of the position of the deep faults in the upper crust of the Western Ural and their connection with the deep **belt of magnetized ultrabasic-basic complexes** projecting above the basalt layer of the earth's crust.

4 Conclusions

Owing to the new computer technology, the structural features of the anomalous magnetic field for the Western Ural territory were studied. Anomalies from various layers of the earth's crust were identified, and the models of the sources of magnetic anomalies in the granite layer and the surface of the basaltic layer were constructed. The position of the deep faults in the upper crust of the Western Ural was determined. The connection of the faults with the deep basic-ultrabasic belts as projecting above the basalt layer of the earth's crust was also established.

References

Byzov, D., Muravyev, L., Fedorova, N.: The approximation of anomalous magnetic field by array of magnetized rods. AIP Conf. Proc. **1863**, 560051 (2017). https://doi.org/10.1063/1.4992734

Martyshko, P.S., Ladovskiy, I.V., Tsidaev, A.G.: Construction of regional geophysical models based on the joint interpretation of gravitaty and seismic data. Izvestiya Phys. Solid Earth **46**(11), 931–942 (2010). https://doi.org/10.1134/S1069351310110030

Martyshko, P.S., Fedorova, N.V., Akimova, E.N., Gemaidinov, D.V.: Studying the structural features of the lithospheric magnetic and gravity fields with the use of parallel algorithms. Izvestiya Phys. Solid Earth **50**(4), 508–513 (2014). https://doi.org/10.1134/S1069351314040090

Singular Spectral Analysis Applied to Magnetotelluric Time Series Collected at Medea (Algiers, Algeria) to Detect Electromagnetic Signal Signature Associated with Earthquake: First Results

Ahmed Seddik Kasdi, Abderrezak Bouzid, Mohamed Hamoudi, Walid Boukhlouf, Sofiane Saïd Bougchiche, Aboubakr Deramchi, and Abdeslam Abtout

Abstract

Significant changes in amplitude were observed in all five channels of magnetotelluric (MT) recordings, collected at the Observatory of Medea (Algiers, Algeria) on the day of December 23, 2014, during several earthquakes. In this work, we performed a singular spectral analysis (SSA) to magnetotelluric time series to analyze the anomalous electromagnetic (EM) signals associated with some minors to light earthquakes in magnetotelluric signals. We investigate the temporal variation of the eigenvalues. The analysis brought out the existence of a co-seismic electromagnetic signal. The main goal of this work is to implement a practical algorithm for the detection of seismo-electromagnetic signal signature.

Keywords

Singular spectral analysis • Magnetotelluric • Earthquake • Seismo-electromagnetic signal

1 Introduction

Geologically, northern Algeria is an active seismic zone in the Mediterranean region. Several moderate to weak earthquakes have occurred as a result of many active faults in the region (Harbi et al. 2017). Seismo-electromagnetic signals are the result of disturbances in the electric and magnetic fields due to earthquakes, which are the consequence of the conversion between mechanical and electromagnetic energies, more precisely the generation of electromagnetic fields in solids due to stress changes (Nitsan 1977; Ogawa et al. 1985). Various analyses have been applied to this electromagnetic phenomenon (Matsushima et al. 2002; Azeez et al. 2009) to understand the origin and mechanism that generates these electromagnetic disturbances. Magnetotelluric measurements provide an opportunity to observe and analyze these anomalous electromagnetic signals.

In order to discriminate and to detect the electromagnetic signals associated with the seismic activity using magnetotelluric time series, we applied the singular spectrum analysis (SSA) on 4-hour MT recordings on December 23, 2014, from 06:00:00 UT until 10:00:00 UT. Several minor to light, Mw < 5, earthquakes occurred during this recording in the Blida region near the Medea Observatory (Fig. 1).

2 Magnetotelluric Experiment

The Geomagnetic Observatory of Medea, located about 60 km south of Algiers, was chosen to conduct a magnetotelluric experiment (Fig. 1). It consists of quasi-continuous measurement of MT time series using the MT System-2000 device of Phoenix-Geophysics. This experiment aims to measure the temporal variations of the subsurface electrical conductivity as well as EM signals likely to be related to the seismic activity of the region. The time series of the five MT components (two horizontal components of the electric field and three components of the magnetic field) is continuously recorded with a sampling frequency of 15 Hz. In this study, we have chosen the day of December 23, 2014, which is characterized by the occurrence of several minor to light earthquakes (Table 1). To ensure that the observed seismo-electromagnetic signals are not related to external magnetospheric origin, we checked the planetary index of

A. S. Kasdi (✉) · A. Bouzid · W. Boukhlouf · S. S. Bougchiche · A. Deramchi · A. Abtout
Division Géophysique de Subsurface, CRAAG, BP 63, Bouzareah, Algiers, Algeria
e-mail: ahmedseddik.kasdi@craag.edu.dz

A. S. Kasdi · M. Hamoudi
Département de Géophysique, FSTGAT, Université des Sciences et de la Technologie Houari Boumediene (USTHB), BP 32 El Alia, 16111 Algiers, Algeria

M. Meghraoui et al. (eds.), *Advances in Geophysics, Tectonics and Petroleum Geosciences*, Advances in Science, Technology & Innovation, https://doi.org/10.1007/978-3-030-73026-0_72

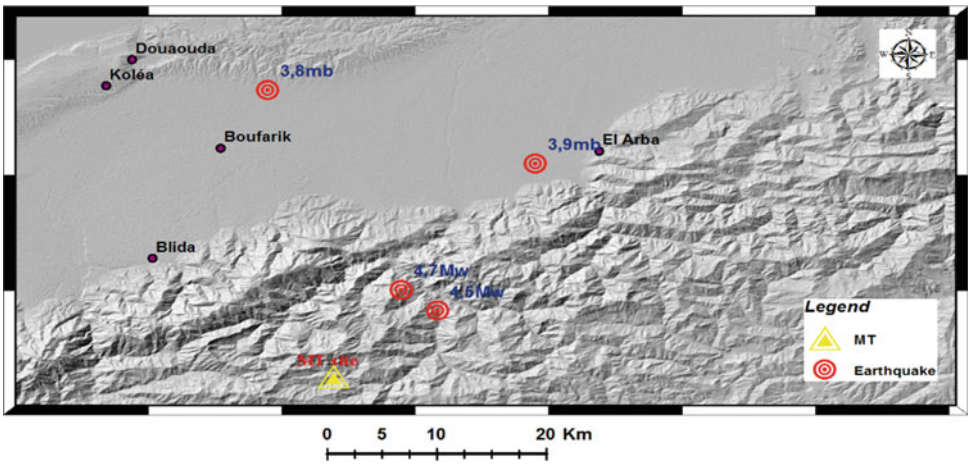

Fig. 1 Map view showing the location of the MT measurement site and distribution of earthquakes epicenters (from https://www.emsc-csem.org) on December 23, 2014, from 06:00:00 until 10:00:00 UT

Table 1 Earthquakes occurred on December 23, 2014, from 06:00:00 until 10:00:00 UT (from https://www.emsc-csem.org)

Origin time (UT)	Magnitude	Magnitude type	Depth (km)	Distance from MT site (km)
23/12/2014 06:33:19	3.8	mb	10	24
23/12/2014 08:00:21	4.7	Mw	8	12
23/12/2014 08:33:54	3.9	mb	30	27
23/12/2014 08:59:04	4.5	Mw	10	14

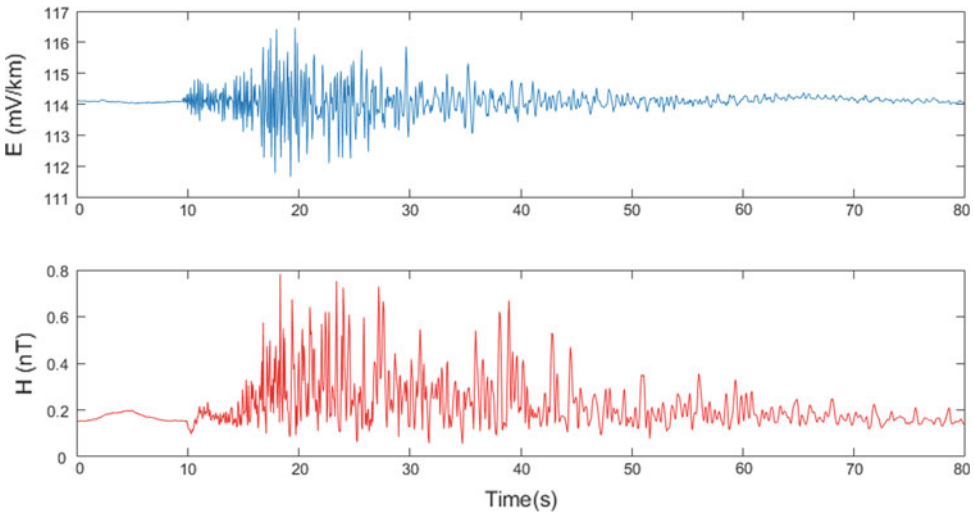

Fig. 2 A closer look at the variation of the horizontal component of the electric and the total component of magnetic fields, respectively, during the 4.7 Mw earthquake

geomagnetic activity level (Kp index) who had a value of 2 indicating a low geomagnetic activity for the 4-hour recording.

3 Singular Spectral Analysis (SSA) Method

Singular spectrum analysis (Vautard and Ghil 1989) is a powerful, nonparametric time series analysis tool for detecting impulsive changes in the time series data (Saito et al. 2011). The procedure of SSA is as follows. We consider one-dimensional time series data $x = \{x_n: n = 1, \ldots, N\}$; The starting point is to embed x into an L-dimensional vector using lagged copies of x_L that are $K = N - L + 1$ elements long. In other words, we form the following Hankel matrix using the $1 - D$ time series:

$$X = \left(x_{ij}\right)_{i,j=1}^{L,K} = \begin{bmatrix} x_1 & x_2 & \cdots & x_K \\ x_2 & x_3 & \cdots & x_{K+1} \\ \vdots & \vdots & \ddots & \vdots \\ x_L & x_{L+1} & \cdots & x_N \end{bmatrix}. \quad (1)$$

The next step consists of performing the singular value decomposition (Golub and Kahan 1965) of the trajectory

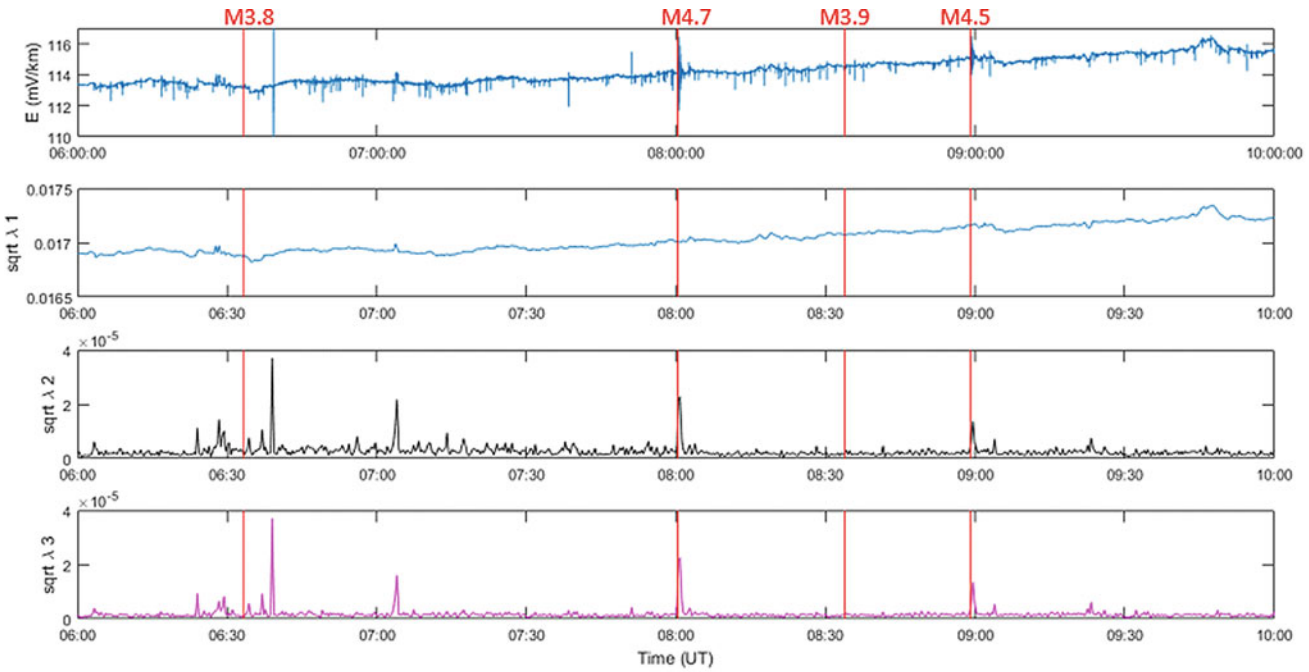

(a)

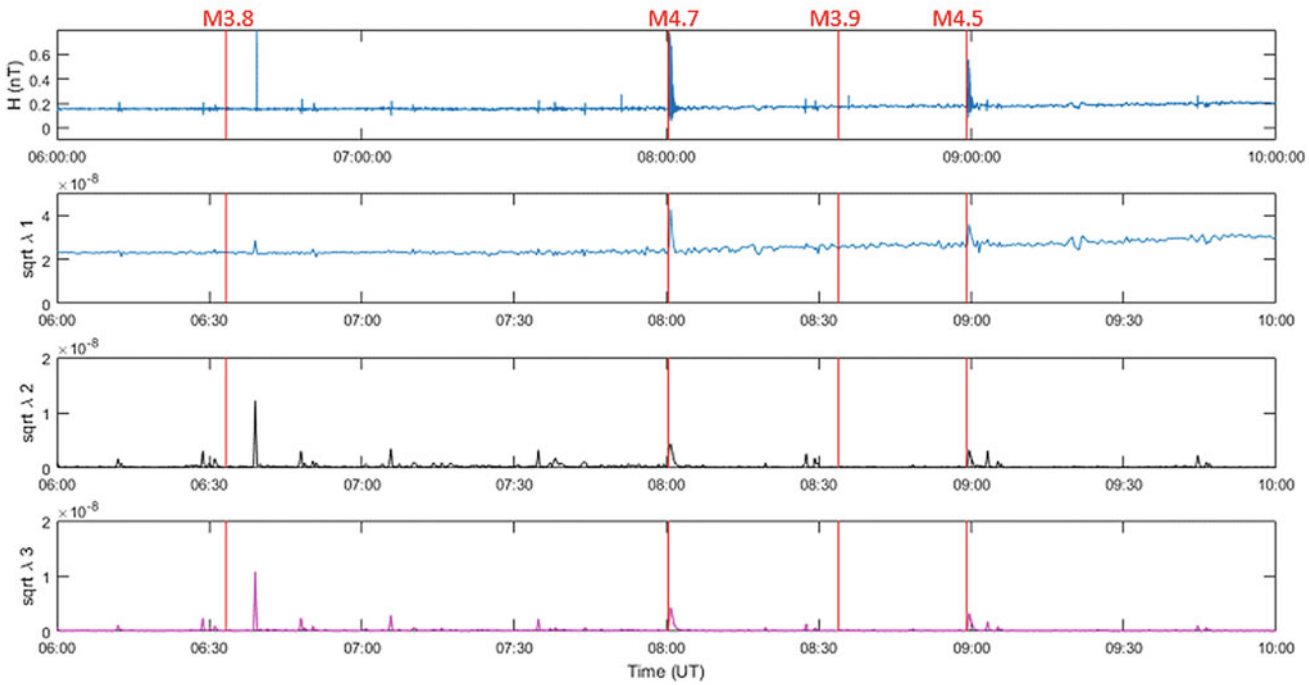

(b)

Fig. 3 Results of SSA at MT site. The top panel indicates the horizontal component of the electric (**a**) and the total component of magnetic (**b**) field variations, respectively, from 6 to 10 am. The second to bottom panel indicates the variations of the first, second and third ($\sqrt{\lambda}\mathbf{1}$, $\sqrt{\lambda}\mathbf{2}$ and $\sqrt{\lambda}\mathbf{3}$) eigenvalues. The red vertical lines indicate the earthquake origin time

matrix $R = XX^T$. We obtain $R = V\lambda V^T$ (λ: diagonal matrix of eigenvalues). Here, T means transpose. The square root of the eigenvalues λi $\{i = 1, \ldots L\}$ is ranked in decreasing order of magnitude ($\sqrt{\lambda}1 \geq \sqrt{\lambda}2 \geq \sqrt{\lambda}3 \geq \cdots \geq \sqrt{\lambda}_L$ 0). In this analysis, we investigate the temporal variations of eigenvalues ($\sqrt{\lambda}i$).

4 Results of Singular Spectral Analysis

Figure 2 shows distinct changes in signal amplitude in the two electromagnetic fields. This relatively high amplitude wave train lasts about 35 s, starting shortly after the first time of the earthquake with a delay of approximately 10 s.

Figure 3 shows the variations of the electric and magnetic fields at the MT site between 6 and 10 am and the results of SSA, respectively. The upper panel shows a distinct change in signal amplitude in both electric and magnetic fields only a few seconds after earthquakes origin time. This relatively high amplitude wave train lasts for several seconds for all earthquakes. The second panel shows that the first eigenvalue is very stable. This stability is caused by the solar–terrestrial interaction (Hattori et al. 2006). We also note the existence of peaks in the magnetic field panel after earthquakes. The third and bottom panel shows the variation of the second and third eigenvalues, and we found several peaks happened after the earthquake origin time. In the absence of more detailed seismological data (in particular, earthquakes with lower magnitude), the other peaks cannot be connected to other earthquakes.

5 Conclusion

Analysis of magnetotelluric time series has revealed the existence of co-seismic electromagnetic signals. After the application of the SSA technique, the variations of the first eigenvalue for the electric fields are stable, but the magnetic field exhibits some peaks during the sequence of December 23, 2014. The variations of the second and third eigenvalues of SSA for both the electric and magnetic fields were found to be very similar to each other by showing the same change during earthquakes. The singular spectrum analysis has allowed us to detect more clearly anomalous changes in magnetotelluric time series that can be correlated with seismic activity.

References

Azeez, K.A., Manoj, C., Veeraswamy, K., Harinarayana, T.: Co-seismic EM signals in magnetotelluric measurement—a case study during Bhuj earthquake (26th January 2001), India. Earth Planets Space **61**(8), 973–981 (2009)

Golub, G., Kahan, W.: Calculating the singular values and pseudo-inverse of a matrix. J. Soc. Indus. Appl. Math. Ser. B Numerical Anal. **2**(2), 205–224 (1965)

Harbi, A., Sebaï, A., Rouchiche, Y., Maouche, S., Ousadou, F., Abbès, K., Benamar, D.A., Benmedjber, M.: Reappraisal of the seismicity of the southern edge of the Mitidja Basin (Blida Region, north-central Algeria). Seismol. Res. Lett. **88**, 1163–1177 (2017)

Hattori, K., Serita, A., Yoshino, C., Hayakawa, M., Isezaki, N.: Singular spectral analysis and principal component analysis for signal discrimination of ULF geomagnetic data associated with 2000 Izu Island Earthquake Swarm. Phys. Chem. Earth Parts A/b/c **31**(4–9), 281–291 (2006)

Matsushima, M., Honkura, Y., Oshiman, N., Baris, S., Tuncer, M.K., Tank, S.B., Pektas, R.: Seismoelectromagnetic effect associated with the Izmit earthquake and its aftershocks. Bull. Seismol. Soc. Am. **92**(1), 350–360 (2002)

Nitsan, U.: Electromagnetic emission accompanying fracture of quartz-bearing rocks. Geophys. Res. Lett. **4**(8), 333–336 (1977)

Ogawa, T., Oike, K., Miura, T.: Electromagnetic radiations from rocks. J. Geophys. Res. Atmosph. **90**(D4), 6245–6249 (1985)

Saito, S., Kaida, D., Hattori, K., Febriani, F., Yoshino, C.: Signal discrimination of ULF electromagnetic data with using singular spectrum analysis–an attempt to detect train noise. Nat. Hazard. **11**(7), 1863–1874 (2011)

Vautard, R., Ghil, M.: Singular spectrum analysis in nonlinear dynamics, with applications to paleoclimatic time series. Phys. D **35**(3), 395–424 (1989)

Migration of GPR Data Based on Phase-Shifting Interpolation Method in Attenuation Media

Jun Chen and Dingkai Chen

Abstract

Because there is conductive current, traditional GPR data migration method imitating seismic data migration of acoustic wave equation is not suitable for that in attenuation media. Here, the phase-shifting interpolation method with the attenuation term from the Helmholtz equation is presented, which is based on the former phase-shifting method. The single-velocity model used in the former method is replaced by the three-parameter models (dielectric constant, electric conductivity, and permeability) together with the frequency. The results of the synthetic model computation and the field GPR data migration show that the attenuation signal can be compensated, and the weak signal can be enhanced after considering the attenuation factor.

Keywords

Ground-penetrating radar (GPR) • Migration • Attenuation media • Phase-shifting interpolation

1 Introduction

The electromagnetic wave propagation equation neglecting the conductive current is similar to the reflection seismic wave equation. So, the processing methods and processes of GPR data migration fully draw on the rich experience of processing seismic reflection data. The processing flow of the transmitted seismic data is applied to the data processing of ground-penetrating radar data (Fisher et al. 1992; Lehmann et al. 2000; Lehmann and Green 2000; Bitri and Grandjean 1998).

However, in many practical applications, the conductivity of the underground medium cannot be ignored entirely. When an electromagnetic wave propagates in underground media, there will be more obvious attenuation, and the reflection signal of the ground-penetrating radar is weak. In this case, the migration method based on acoustic wave equation cannot get ideal results. Therefore, it is meaningful to study a method of GPR section migration considering the attenuation factor of electromagnetic wave (Sena et al. 2006; Di et al. 2006; Zhu and Huang 2016).

Here migration method of ground-penetrating radar data with self-excitation and self-collection (zero offset time section) is studied based on electromagnetic wave equation with current conduction term. It started from the Helmholtz equation with the current conduction term referenced Gazdag's phase-shifting interpolation, which presented the velocity of the plural form using three model parameters (permittivity, conductivity, and permeability) combining with frequency.

2 Methods

Phase-shifting migration method belongs to frequency wavenumber domain migration method, which is based on the Fourier transform. In order to solve the problem of lateral variation of migration velocity, Gazdag improved phase-shifting method, put forward the phase-shifting interpolation method (Gazdag 1978; Gazdag and Sguazzero 1984). Starting from the Maxwell equation, Helmholtz equation of electric field component is as follows:

$$\nabla \times \nabla \times \vec{E} + \mu\sigma \frac{\partial \vec{E}}{\partial t} + \mu\varepsilon \frac{\partial^2 \vec{E}}{\partial t^2} = 0 \qquad (1)$$

J. Chen (✉)
Tongji University, Shanghai, 200092, P. R. China
e-mail: junxianchen@tongji.edu.cn

D. Chen
Institute of Urban Environment, Chinese Academy of Sciences, Xiamen, 361021, P. R. China

M. Meghraoui et al. (eds.), *Advances in Geophysics, Tectonics and Petroleum Geosciences*, Advances in Science, Technology & Innovation, https://doi.org/10.1007/978-3-030-73026-0_73

Here, $\vec{E}$ is electric field, ε is dielectric constant, μ is magnetic permeability, σ is electric conductivity and t is time. For the passive field

$$\nabla \cdot \vec{E} = 0 \tag{2}$$

$$\nabla^2 \vec{E} - \mu\sigma \frac{\partial \vec{E}}{\partial t} - \mu\varepsilon \frac{\partial^2 \vec{E}}{\partial t^2} = 0 \tag{3}$$

If the electric conductivity is neglected, a scalar wave equation is obtained from Eq. (3) for 2D field:

$$\frac{\partial^2 E}{\partial z^2} = \frac{1}{v^2}\frac{\partial^2 E}{\partial t^2} - \frac{\partial^2 E}{\partial x^2} \tag{4}$$

Here, $E = E(x, z, t)$, z is depth, x is horizontal distance, t is time, and $v = 1/\sqrt{\mu\varepsilon}$ is electromagnetic wave velocity. Equation (4) is the basis of former phase-shifting interpolation method.

In many practical applications of ground penetrating radar data, the electromagnetic waves tend to be more attenuated when they conduct in underground media. In this case, the conductive current term plays a more significant role and must not be overlooked. Wavefield continuation formula should be based on Eq. (3). After Fourier transform for Eq. (3), we can get

$$\frac{\partial^2 U(k_x, z, \omega)}{\partial z^2} = -k_z^2 U(k_x, z, \omega) \tag{5}$$

$$k_z = \pm \frac{\omega}{v(\omega)} [1 - (\frac{v(\omega)k_x}{\omega})^2]^{\frac{1}{2}} \tag{6}$$

$$v(\omega) = \frac{1}{\sqrt{\varepsilon\mu - i\mu\sigma/\omega}} \tag{7}$$

Here, $U(k_x, z, \omega)$ is electric field, z is depth, k_x is horizontal wavenumber, ω is angular frequency, ε dielectric constant, μ is permeability and σ electric conductivity. $v(\omega)$ is related with frequency, and it is a complex number. The analytic solutions of Eq. (5) is as follows

$$U(k_x, z + \Delta z, w) = U(k_x, z, \omega) \exp(ik_z \Delta z) \tag{8}$$

$k_z > 0$ denotes downward continuation. From (6) and (8), we can get

$$U(k_x, z + \Delta z, \omega) = U(k_x, z, \omega) \exp\left\{ \frac{i\omega}{v(\omega)} \left[1 - \left(\frac{v(\omega)k_x}{\omega} \right)^2 \right]^{\frac{1}{2}} \Delta z \right\} \tag{9}$$

$$U^*(z) = U(z) \exp(i \frac{\omega}{v(w)} \Delta z) \tag{10}$$

$$U(z + \Delta z) = U^*(z) \exp[i(k_{z1} - \frac{\omega}{v(\omega)'})\Delta z] \tag{11}$$

$$k_{z1} = [1 - (\frac{v(\omega)k_x}{\omega})^2]^{\frac{1}{2}} \tag{12}$$

The selection of reference velocity $v(\omega)'$ is important for phase-shifting interpolation method. It is replaced by $v(z)'$ which is irrelevant to frequency in the former method. But velocity depends on dielectric constant ε and magnetic permeability μ. Here we use three-parameter models (ε, μ and σ) instead of only one velocity model directly. The specific values vary with moisture, material and so on. The values are fixed at fixed locations in underground space. After the combination of three parameters is given for one underground target, the velocity can be calculated from Eq. (7) using the given parameters together with frequency (ω). The detailed parameters table used for the models calculation cannot be presented here due to the page limitation.

3 Results

3.1 Synthetic Data

In order to test and verify the effect of migration processing, three synthetic models were designed, on-point model, two-point model and one-step model. First, the theoretical image is computed using GPR forward software of GPRMax (Warren et al. 2016). The theoretical image was then mixed with noise. Finally, the image before and after mixing noise was separately processed using migration method both considering the attenuation factor and not considering the attenuation factor. After considering the attenuation factor, the migration result can reflect the shape of the underground target more clearly, which proved that the approach here performs in a better way. Because of the page limit, the details are not presented here.

3.2 Field Data Processing

Figure 1 presents the GPR image of one field surveying section. The data were collected on campus, and we aimed to find underground pipeline. The instrument is Canada EKKO-PRO. The frequency of the antenna is 200 MHz.

There are diffractions at 2 m of station and 20 ns of time (Fig. 1), but the signal intensity is weak. The data had been migrated using two shifting-interpolation methods simultaneously. The results are shown in Fig. 2a, b. The former one is the result, not considering the attenuation term, while the latter one is the result considering the attenuation term.

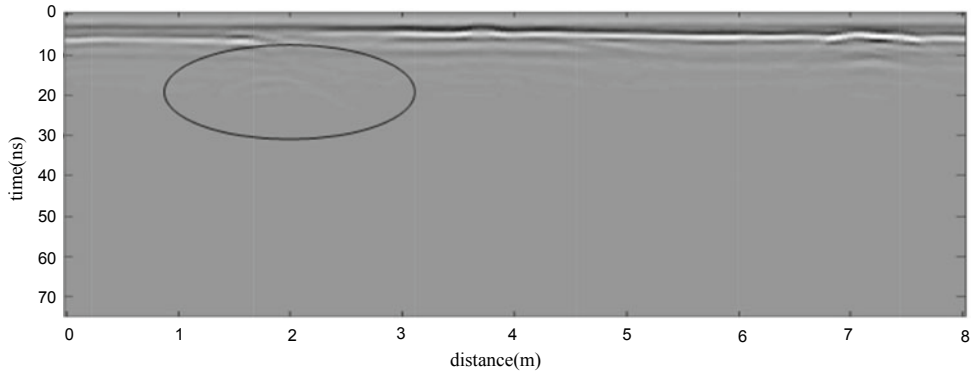

Fig. 1 The field PRG data image

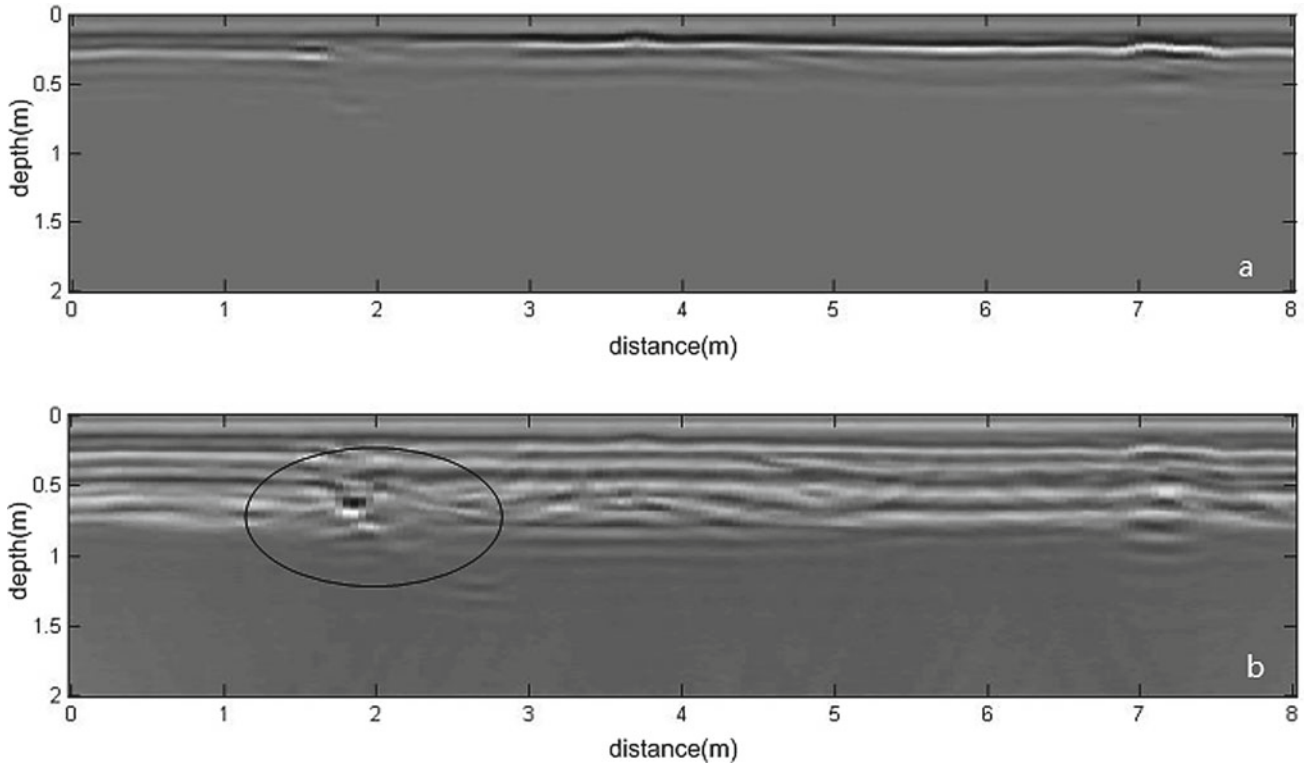

Fig. 2 The results of phase-shifting interpolation migration method **a** not considering attenuation term and **b** considering attenuation term

The migration results show that the diffractions at 2 m of the station are originated from the refraction of one punctate target body, its depth is about 0.7 m. The information of the target body is weak in the result using phase-shifting interpolation without the attenuation term. However, after considering the attenuation term in the phase-shifting interpolation method, the attenuation signal is compensated, then the resulting in image enhancement and more precise identification of the punctate target body. The continuity of the layer is also improved.

4 Conclusions

Here the migration method for self-emitting and self-receiving GPR reflection wave (zero offset time section) is discussed, which considered the electromagnetic wave attenuation factor in subsurface media. Referenced former phase-shifting interpolation method, the phase-shifting interpolation method with the attenuation term is presented, which is derived from Maxwell equation with the

conductive current term. According to the computation results of field data, after considering the attenuation factor in the phase-shifting interpolation method, the attenuation signal can be compensated, and the deep weaker signal of the object can be seen.

Acknowledgements The authors thank Shanghai Survey and Design Institute (Group) Co. Ltd. for providing instrument support. Thanks are also due to the anonymous reviewers for their helpful comments.

References

Bitri, A., Grandjean, G.: Frequency-wavenumber modeling and migration of 2D GPR data in moderately heterogeneous dispersive media. Geophys. Prospect. **46**, 287–301 (1998)

Di, Q., Zhang, M., Wang, M.: Time-domain inversion of GPR data containing attenuation resulting from conductive losses. Geophysics **71**(5), 103–109 (2006)

Fisher, E., McMechan, G.A., Peter Annan, A., et al.: Example of reverse-time migration of single-channel ground-penetrating radar profiles. Geophysics **57**(4), 577–586 (1992)

Gazdag, J.: Wave equation migration with the phase-shift method. Geophysics **43**(7), 1342–1351 (1978)

Gazdag, J., Sguazzero, P.: Migration of seismic data by phase shift plus interpolation. Geophysics **49**(2), 124–131 (1984)

Lehmann, F., Green, A.G.: Topographic migration of georadar data: implications for acquisition and processing. Geophysics **65**(3), 836–848 (2000)

Lehmann, F., Boerner, D.E., Holliger, K.: Multicomponent georadar data: some important implications for data acquisition and processing. Geophysics **65**(5), 1542–1552 (2000)

Sena, A.R., Stoffa, P.L., Sen, M.K.: Split-step Fourier migration of GPR data in lossy media. Geophysics **71**(4), 77–91 (2006)

Warren, C., Giannopoulos, A., Giannakis, I.: gprMax: open source software to simulate electromagnetic wave propagation for ground penetrating radar. Comput. Phys. Commun. **209**, 163–170 (2016)

Zhu, W.Q., Huang, Q.H.: Attenuation compensated reverse time migration method of ground penetrating radar signals. Chin. J. Geophys. **59**(10), 3909–3916 (2016). (in Chinese)

Characterizing the Subsurface Structure Using 3-D Magnetotelluric Inversion: A Case Study of M'rara Basin, Algerian Sahara

Djabir Foudili, Abderrezak Bouzid, Mohamed Chérif Berguig, Said Sofiane Bougchiche, Abdeslam Abtout, and Mehdi A. Guemache

Abstract

The region of M'rara, located in the northeast Algerian Sahara basin, is severely afflicted by several natural perils such as the collapses and fissures around the water borehole situated in the center of the small town of M'rara. The present study was conducted in order to investigate the ground structures under eighteen (18) sites located near the above mentioned water borehole using the magnetotelluric (MT) method to collect the required data. For this reason, the three-dimensional (3-D) inversion method was done using the ModEM package to obtain a realistic 3-D resistivity model of the structures. The preferred model obtained from the 3-D inversion is sufficient to identify the M'rara basin; where reveal the folded resistive structure with an anticline form below the Senonian level and the significant fractures of axial and transverse types that extend in the hinge zone of this structure. As a result, the fissures and collapses at the ground surface may be attributed to a karstic process in the limestone layer in contact with water.

Keywords

Magnetotelluric • 3-D inversion • Anticline • Karst process • M'rara region

1 Introduction

Since the water borehole (H10-42) was drilled in the center of the small town of M'rara, which is located in the Northeastern part of the Algerian Sahara, threats of ground fissures and surface collapses have been of concern. The origin of these menaces remains unknown. This water borehole was originally intended to be used for the exploitation of the continental intercalary (CI) aquifer, for an eventual maximum depth of 1560 m, according to the data of National Agency of the Hydraulic Resources (ANRH). We expect that the fault systems may contribute to the inflow of saline water into the CI aquifer from deeper units up to the limestone beds located at the depth between 57 and 130 m (ANRH). As a result of the above, the limestone beds become prone to form cavities when in contact with brine saturated with CO_2 gas, the so-called karst dissolution process (Gombert 2002). These cavities tend to deform the land surface, which induces ground fissures and collapses.

For this reason, a new magnetotelluric (MT) survey consisting of 18 stations was carried out in this basin around the water borehole in order to investigate the shallow and deep structures (see Fig. 1). The MT measurements allow identifying the structural setting and the different aquifers that may exist in this basin (Cagniard 1953; Chave and Jones 2012). In this contribution, we present the results of Foudili et al. (2019), who proposed a new 3-D resistivity model to collect the MT data on 18 sites.

2 3-D Inversion

The dimensionality of the data was analyzed by the phase tensor method, which revealed that data at periods > 0.5 s are relatively 3-D model (see Foudili et al. 2019).

The 3-D inversion of MT data collected at 18 sites was performed with the ModEM package (Egbert and Kelbert 2012). Our preferred model resulted from the inversion of

D. Foudili (✉) · M. C. Berguig
Department of Geophysics, USTHB University, BP 32 El Alia, Algiers, Algeria

A. Bouzid · S. S. Bougchiche · A. Abtout · M. A. Guemache
CRAAG, Route de l'Observatoire, BP 63 Bouzaréah, 16340 Algiers, Algeria

M. Meghraoui et al. (eds.), *Advances in Geophysics, Tectonics and Petroleum Geosciences*,
Advances in Science, Technology & Innovation, https://doi.org/10.1007/978-3-030-73026-0_74

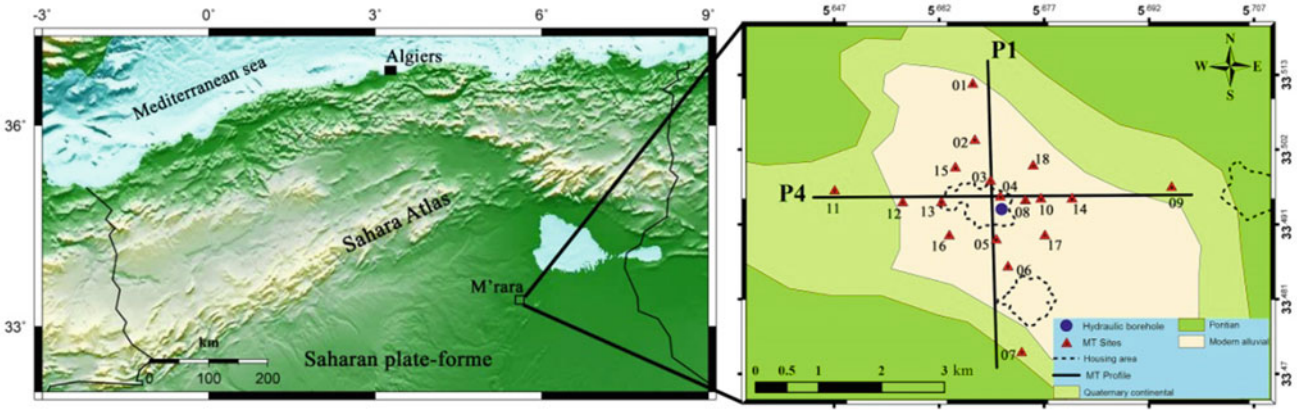

Fig. 1 The M'rara location (left panel) and the MT sites and the water borehole distribution on a simplified geological map (right panel). The black straight lines indicate location of the E-W (P4) and N-S (P1) profiles

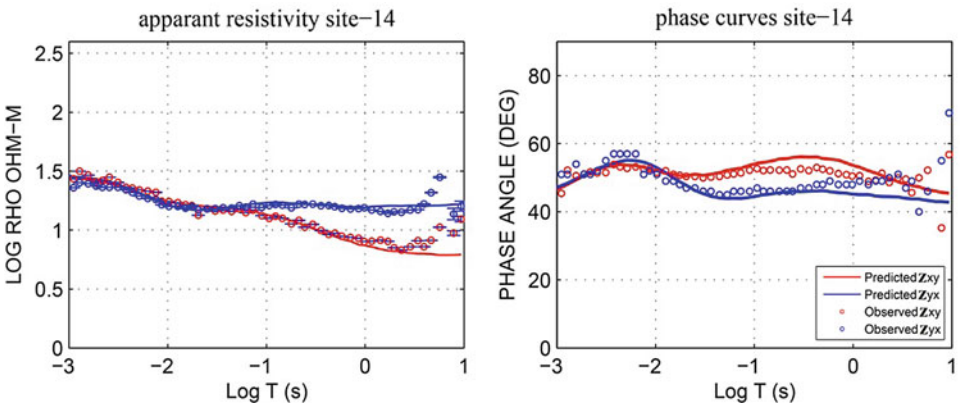

Fig. 2 Apparent resistivity and phase curves of site-14. Red and blue points refer to Z_{xy} and Z_{yx} of the observed data, respectively. The red and blue lines indicate the predicted data from the preferred 3-D inversion model

the total impedance (Z) and the vertical magnetic transfer functions (VTFs). The data of a subset of 16 periods, logarithmically distributed between 0.001 and 10 s, were inverted. The specified error floor was set at 5% of $|Z_{xy} * Z_{yx}|^{1/2}$ for all impedance tensor components and a constant value of 0.1 for VTFs. The inversion began with a 50 Ωm half-space; the NLCG algorithm converged from the normalized RMS Misfit of 9.74 to below 1.57; the example of the resistivity and phase for the Z_{xy} and Z_{yx} of the observed and predicted data are displayed in Fig. 2.

3 Discussion and Conclusion

The representative cross-sections along the N-S and W-E directions (Figs. 3 and 4) are plotted using the final 3-D resistivity model. These cross-sections show the horizontal geoelectrical layer C1 that has specific conductive feature. This low resistivity layer C1, extending from surface to a depth of approximately 150 m, may be interpreted, by comparison with the lithostratigraphic formation, as the Mio-Pliocene and Eocene units. These units consist of clay, sand and sandstone, which confirm the low conductivity. Also, various types of CT aquifers are located in the Mio-Pliocene unit and the fractured limestone beds of the Eocene unit (Guendouz et al. 2003), with high conductivity.

In the cross-section Fig. 3, the key distinguishing feature is the folded resistive structure R1 and low resistivity body F beneath site 06. The folded layers with an anticline form may be interpreted by two astronomical units, both of which have simultaneously resistive and impermeable characteristics. The units are the Senonian and Cenomanian (Busson 1970; Nely 1986). The body F can be interpreted as a fault zone; the rise of saltwater of the CI aquifer along this fault makes it conductive zone. Figure 4 displayed the E-W cross-section, the low resistivity zone C′2, located under sites 12 and 13 and under the white dashed line, may be interpreted as the CI aquifer which contains very salty (1.7 g/l). The conductivity anomalies C2 and C3 can be interpreted as fractures that extend in the hinge zone of the anticlinal structure, and they seem to be in the axial and transverse types, respectively (see Fig. 5). These fractures appeared during the creation of the anticlinal structure. Clearly, from the W-E and N-S cross-sections, the

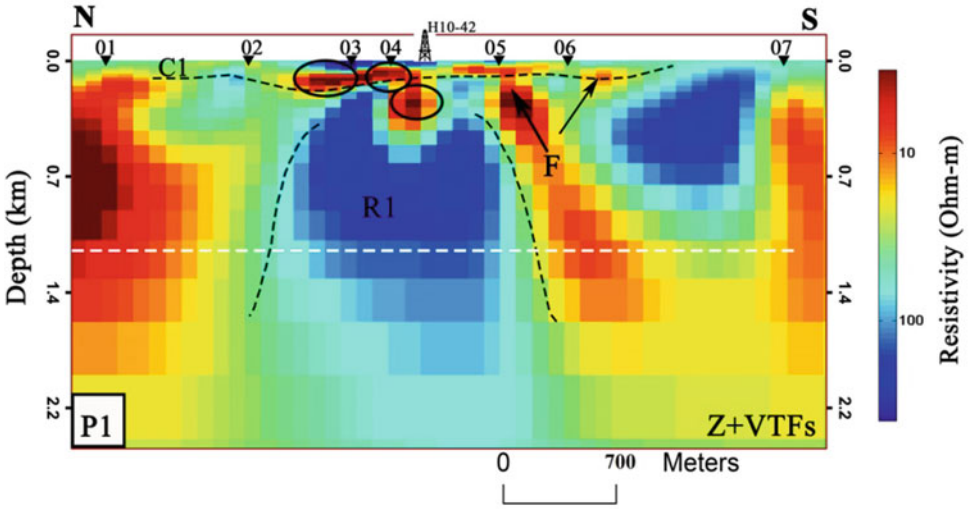

Fig. 3 Vertical section derived from the preferred 3-D model along the N-S profile. The anomaly F represents the fault zone, and the black dashed lines represent the anomalies C1 and R1; C and R denote the conductive and resistive anomalies, respectively. The black arrows represent the flow direction of saline water, and inverted triangles refer to site locations; H10-42 is the water borehole

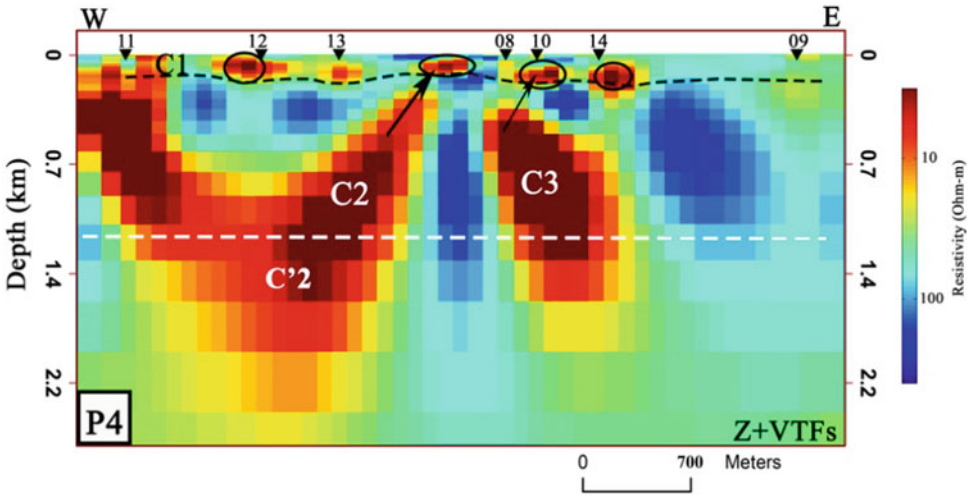

Fig. 4 Vertical section derived from the preferred 3D model along the W-E profile. The white straight dashed line indicates the level of the CI aquifer

geological events in the region of M'rara constitute a reservoir whose permeability and porosity are likely related to significant anticlinal fractures and the fault zone as well. It is clear that the fractures and the fault zone are responsible for the rising saltwater from the Albian unit (the CI aquifer) up to the height of 500 m, and contribute to the contact of the CI aquifer with the limestone layer in the Eocene unit. As a result, the Eocene unit becomes prone to the karst dissolution process and the formation of cavities. Therefore, the small conductivity anomalies detected near the limestone layer of the Eocene unit can be considered as cavities (the black circles in Figs. 3 and 4). These cavities tend to deform the surface through cracks and collapses that have appeared around the water borehole.

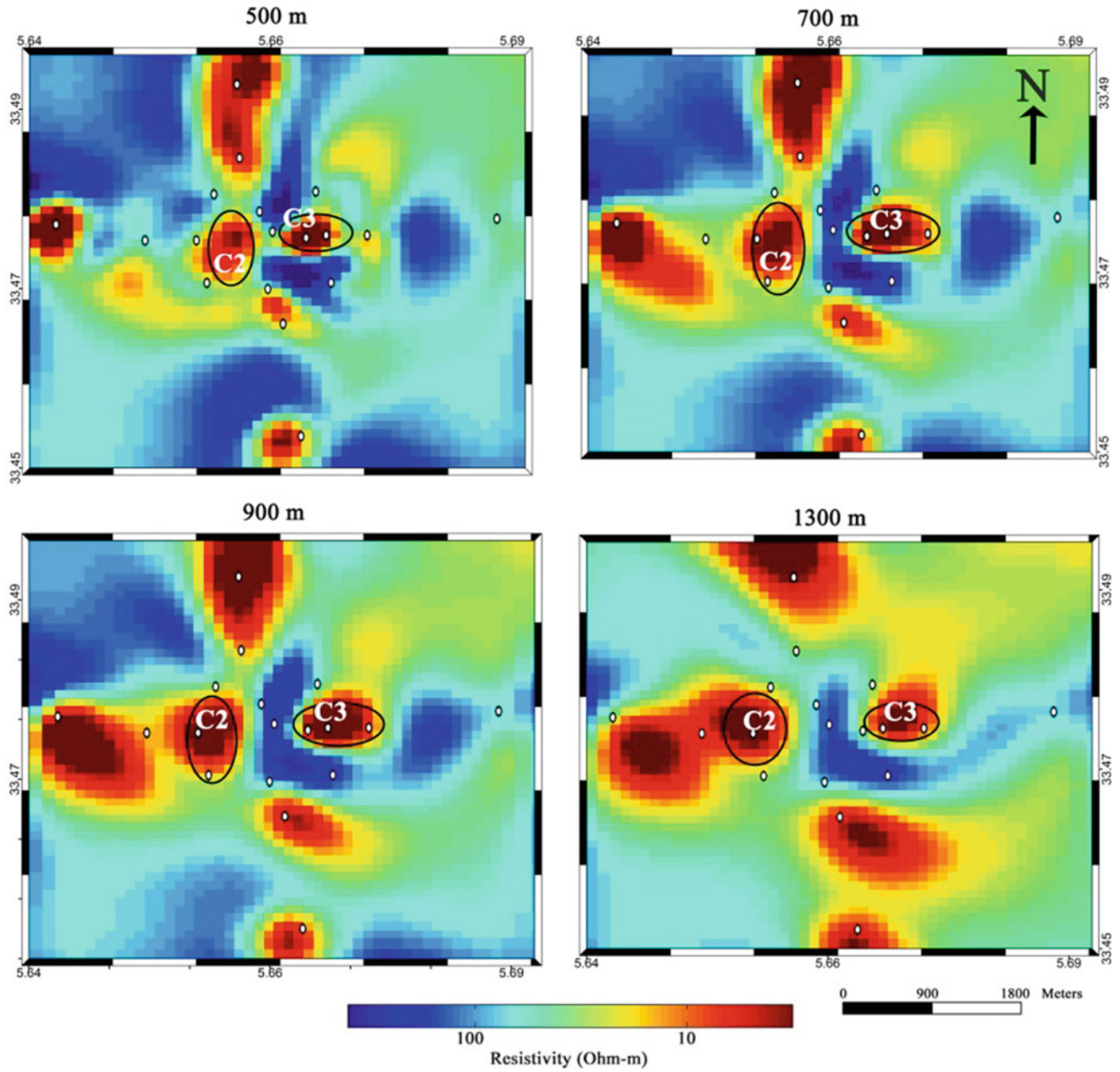

Fig. 5 Horizontal slices through the preferred 3-D resistivity model for different depths. C2 and C3 are the conductive anomalies which are shown in the P4 cross-section (Fig. 4)

References

Busson, G.: Le Mésozoïque Saharien. 2. Essai de synthèse des données des sondages algéro-tunisiens. Centre National de la Recherche Scientifique, Paris (1970)

Cagniard, L.: Basic theory of the magneto-telluric method of geophysical prospecting. Geophysics **18**, 605–635 (1953)

Chave, A.D., Jones, A.G.: The Magnetotelluric Method: Theory and Practice. Cambridge University Press (2012)

Egbert, G.D., Kelbert, A.: Computational recipes for electromagnetic inverse problems. Geophys. J. Int. **189**, 251–267 (2012)

Foudili, D., Bouzid, A., Berguig, M.C., Bougchiche, S.S., Abtout, A., Guemache, M.A.: Investigating karst collapse geohazards using magnetotellurics: a case study of M'rara basin, Algerian Sahara. J. Appl. Geophys. **160**, 144–156 (2019)

Gombert, P.: Role of karstic dissolution in global carbon cycle. Global Planet. Change **33**, 177–184 (2002)

Guendouz, A., Moulla, A.S., Edmunds, W.M., Zouari, K., Shand, P., Mamou, A.: Hydrogeochemical and isotopic evolution of water in the complexe terminal aquifer in the Algerian Sahara. Hydrogeol. J. **11**, 483–495 (2003)

Nely, G.: Méthodes géophysiques, vol. 2. Editions TECHNIP (1986)

Design of New Model for Water Saturation Based on Neural Network for Low-Resistivity Phenomenon (Algeria)

Said Eladj, Mohamed Zinelabidine Doghmane, and Brahim Belahcene

Abstract

This study aims to design a new model for water saturation calculation based on resistivity curves in the case of low-resistivity phenomenon. This model was constructed using artificial neural network combined with support vector machine technique. Low resistivity phenomenon had appeared in a specific field in Algeria, for which many studies have been realized to correct the underestimation of hydrocarbons volume calculated using petrophysical curves, precisely resistivity logs. It has been proven that the presence of heavy minerals is the primary cause of underestimated results. Moreover, some of the researchers have proposed compensator terms in previous studies in pieces of literature. Nonetheless, these terms are generally added empirically and have no mathematical development background, and thus it is so difficult to be generalized for the whole region. Our study aims to design a local compensator model based on artificial neural network and support vector machine (*ANNSVM*), based on field data; the model gives representation that can be more reliable, and the model results match with samples given by modular dynamic testing (MDT) tool.

Keywords

Water saturation calculation • Low-resistivity phenomenon • Support vector machine • Heavy minerals • Modular dynamic testing tool

S. Eladj (✉) · M. Z. Doghmane
Department of Geophysics, University of Science and Technology Houari Boumedienne, FSTGAT, 35000 Bab Ezzaour, Algiers, Algeria
e-mail: s.eladj@univ-boumerdes.dz

M. Z. Doghmane
Exploration Division, Sonatrach, 30500 Hassi Messaoud, Algeria

B. Belahcene
Production Division, Gassi Touil, Sonatrach, Ouergla, Algeria

1 Introduction

Saturated hydrocarbon reservoirs usually have high resistivity values on resistivity logs (Mollajan 2015). However, some hydrocarbon-producing reservoirs could also have low resistivity (Ze et al. 2019; Baziar 2018). The resistivity (R_t) of such oil or gas reservoir could be as low as 5 Ωm (Doghmane 2014). Archie equation is developed to calculate water saturation for clean sand reservoirs; its modified version is then introduced to correct the effect of clay in resistivity logs regardless of its distribution type. Later on, the Indonesian equation has been proposed to consider the distribution of the clay (laminar, dispersed, structural). However, the effect of conductive minerals that may exist in a matrix has not been considered in all the previous equation. The modified *Simandoux* equation given by (1) is designed to compensate for the effect of heavy conductive minerals of the matrix (Hari Kumar 2010) has been proposed to consider the distribution of the clay (laminar, dispersed, and structural). However, the effect of conductive minerals that may exist in matrix has not considered in all the previous equation. The modified *Simandoux* equation given by (1) is designed to compensate the effect of heavy conductive minerals of the matrix (Hari Kumar 2010).

$$\frac{1}{R_t} = \frac{\phi_e^m S_w^n}{(1 - V_{cl} - C_1)aR_w} + \left(\frac{V_{cl}^c}{R_{cl}} + C_2\right) S_w^{n/2} \qquad (1)$$

where R_w is water resistivity, ϕ is the rock porosity, a is the tortuosity factor, m is the cementation exponent, n is the saturation exponent, c is compaction factor, V_{cl} and R_{cl} are the clay volume and resistivity, respectively, and C_1, C_2 are compensation values determined by ANN algorithms. Based thereon, the water saturation computed using such low resistivity values employing Archie's law are not reliable (Doghmane 2014). Tools have been designed to estimate the value of water saturation (S_w) in reservoirs, and hence hydrocarbon saturation can be seamlessly computed without

M. Meghraoui et al. (eds.), *Advances in Geophysics, Tectonics and Petroleum Geosciences*,
Advances in Science, Technology & Innovation, https://doi.org/10.1007/978-3-030-73026-0_75

recourse to the resistivity (Doghmane 2019). In Algeria, the MDT tool is being used to overcome the problem of low resistivity in hydrocarbon reservoirs. Most of the technical problem in reservoir characterization depends on performance and tolerance of laboratory equipment and tools used in the field and situ. Even though these measurements can be reliable, their generalization for the whole reservoir section is not practically justifiable, especially for various fields. In conventional resources, the phenomenon of low resistivity has a considerable influence on interpretation when using classical model (Siddiqui 2015). In conventional logging methods, an increase in conductivity (or decrease of resistivity) is explained by the presence of irreducible water which is not always the case (Ze et al. 2019; Lijun et al. 2017). In clean sand formation, the total resistivity is modelled by Archie equation which is not reliable for various formations with the presence of clay minerals and shale deposit.

2 Proposed Method (ANNSVM)

The classical or analytical models have based on restricted parameters, and sometimes it is not easy to be applied for other fields for the reason that the empirical constants and laboratory data need strong correlation between saturation models, petrophysical and chemicals proprieties of rock (Mode et al. 2015). The intelligently designed model is based on a neural network combined with support vector machine, and it is performed and matched by MDT measured results (Baziar et al. 2018; Zhao et al. 2006). The basic principle of ANN is reposed on input data or signal (neuron input) x_i, weight function w_i and output results (neuron output) y_i. ANNSVM is designed to be able to predict the water saturation model after being trained by logging data, and dynamic tool samples (Mollajan 2015; Doghmane 2014; Lijun et al. 2017). The data sets used in this study belong to five wells in the Algerian field where data of Well-1 have been used for training and testing; validation has been demonstrated using well-2.

3 Case Study: Well-1

Well-1 was drilled to a depth of 5200 m; log data are available over 1–5196 m. The area of interest is 4328–4635 m; an interpretation was performed over this interval. All depths referenced in this manuscript are in meters and MD. It has been supposed that the main reasons for low resistivity of oil reservoirs have been attributed to thin beds, salty water, conductive minerals and a considerable quantity of irreducible water (Ze et al. 2019; Mode et al. 2015). However, the cause of low resistivity of hydrocarbon reservoirs based on a study of over 40 wells in Algeria oil field has been attributed to the presence of heavy minerals and a considerable quantity of irreducible water as a result of excessive surfactant in the sludge [6]. Using the trained ANN algorithm, compensation terms ($C1$) and ($C2$) in the Venezuelan equation were estimated (Hari Kumar 2010). The interpretation of the results of well-1 reservoir gives us water saturation of S_w = 70% and a porosity of 18% (Fig. 1).

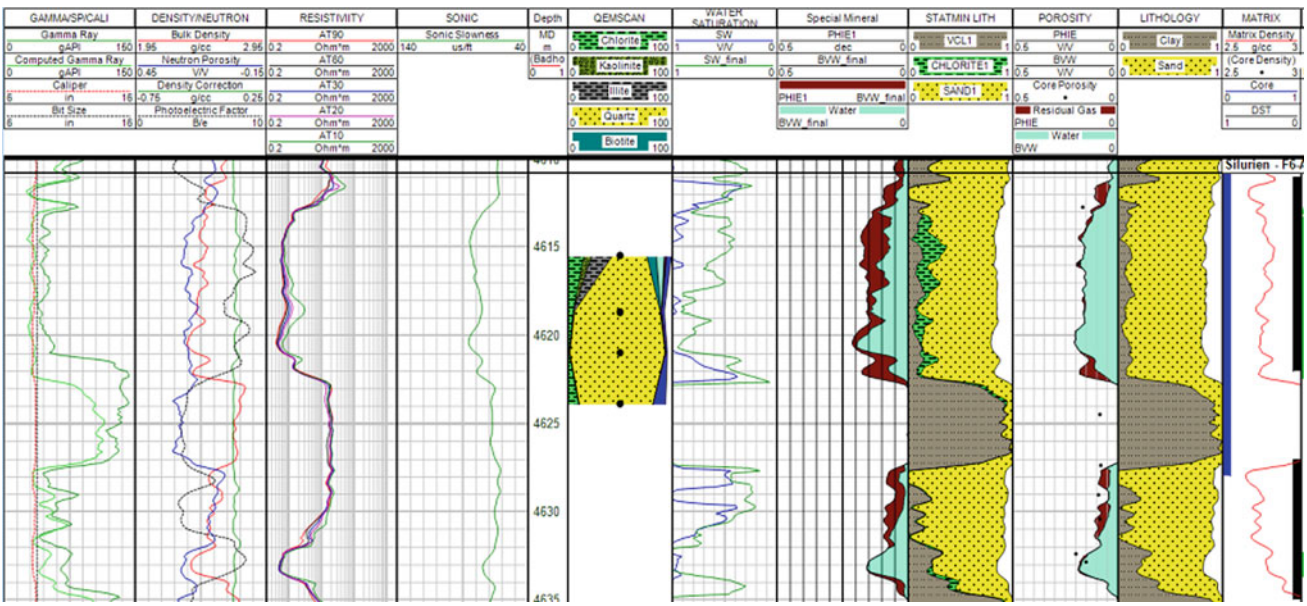

Fig. 1 Effect of using the modified Venezuelan equation

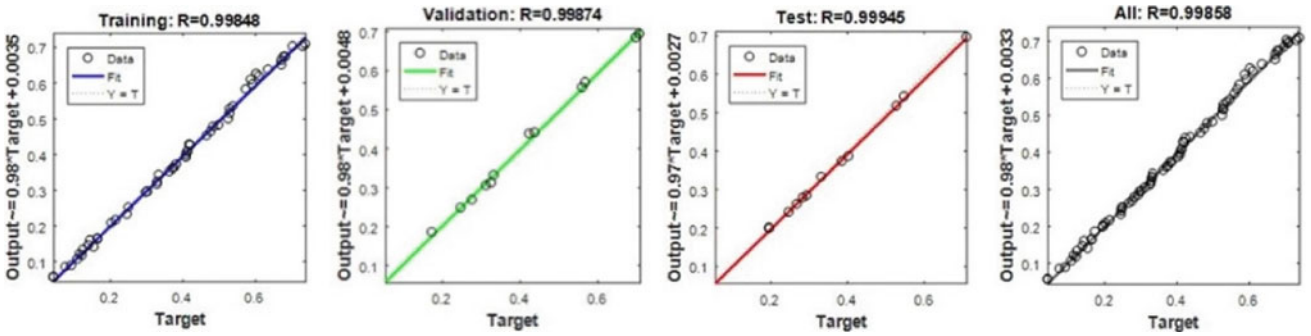

Fig. 2 Results of training and validation of ANNSVM for well-1

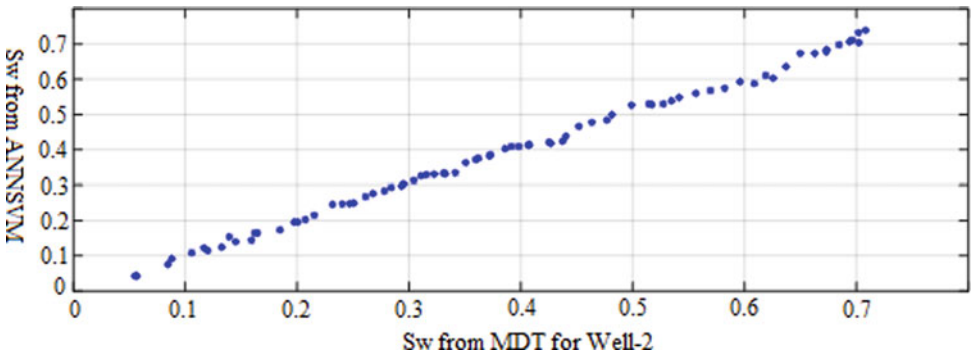

Fig. 3 Results of correlation of ANNSVM with well-2

SVM has been used to classify input log data according to their importance; gamma ray, neutron density, and PEF have set to class 1 (dominant variables); however, resistivity and sonic are set in class 2. The classified data have been used as input for ANN training process denoted by T in Fig. 2a. The ANN has been trained (R = 0.99848), validated (R = 0.99874), and tested (R = 0.99945) using well-1 data as shown in Fig. 2a–c, respectively. The algorithm results have been correlated with Well-2 MDT results (Fig. 3).

4 Conclusions

The study of the petrophysical parameters as well as the determination of the reservoir fluids of well-1 using the classical methods of interpretation proved to be imprecise and led us to an erroneous estimate of the saturation. In the presence of doubts and uncertainties due to the mineralogical study of clays and cuttings, the contribution of the MDT tool by measuring the pressure and carrying out formation tests in front of the reservoir of well-1 was reliable but insufficient for generalization. The ANNSVM model correlated with MDT results reduces the uncertainties of quantitative reservoir evaluation. Moreover, the obtained do not necessitate much laboratory data like conventional models, and its parameters reflect the specifications of local reservoir; thus, it can be useful for deterministic quantitative reservoir evaluation.

References

Baziar, S., Shahripour, H.B., Tadayoni, M., et al.: Prediction of water saturation in a tight gas sandstone reservoir by using four intelligent methods: a comparative study. Neural Comput. Appl. **30**(4), 1171–1185 (2018). https://doi.org/10.1007/s00521-016-2729-2

Doghmane, M.Z.: Classification Automatique des Faciés en Utilisant les Algorithmes d'intelligence Artificiels, Magister Thesis, The Algerian Petroleum Institute Boumerdes, Algeria (2014)

Doghmane, M.Z., Belahcene, B., Kidouche, M.: Application of improved artificial neural network algorithm in hydrocarbons' reservoir evaluation. In: Hatti, M. (eds.) Renewable Energy for Smart and Sustainable Cities. Lecture Notes in Networks and Systems, vol. 62, pp. 129–138. Springer, Cham (2019). https://doi.org/10.1007/978-3-030-04789-4_14

Hari Kumar, K.C.: On the application of simandoux and Indonesian shaly sand resistivity interpretation models in low and high R_w regimes. In: 8th Biennial International Conference & Exposition on Petroleum Geophysics, P-71. Hyderabad, India (2010)

Lijun, G. et al.: Complex resistivity responses explained using LWD laterolog curves and images, LWD propagation resistivity and wireline dielectric measurements. In: International Petroleum Technology Conference, IPTC-19419-MS). Beijing, China (2017). https://doi.org/10.2523/IPTC-19419-MS

Mode, A.W., Anyiam, O.A., Aghara, I.K.: Identification and petrophysical evaluation of thinly bedded low-resistivity pay reservoir in the Niger Delta. Arab. J. Geosci. **8**(4), 2217–2225 (2015). https://doi.org/10.1007/s12517-014-1348-4

Mollajan, A.: Application of local linear neuro-fuzzy model in estimating reservoir water saturation from well logs. A. Arab. J. Geosci. **8**(7), 4863–4872 (2015). https://doi.org/10.1007/s12517-014-1526-4

Siddiqui, F.I., Pathan, D.M., Osman, S.B., et al.: Comparison between regression and ANN models for relationship of soil properties and electrical resistivity. Arab. J. Geosci. **8**(8), 6145–6155 (2015). https://doi.org/10.1007/s12517-014-1637-y

Ze, B., Maojin, T., Gaoren, L., Yujiang, Shi.: Analysis of low-resistivity oil pay and fluid typing method of Chang 8_1 Member, Yanchang Formation in Huanxian area, Ordos Basin, China. J. Petrol. Sci. Eng. **175**, 1099–1111 (2019). https://doi.org/10.1016/j.petrol.2019.01.015

Zhao, B., Zhou, H., Xingong, L., Dehua, H.: Water saturation estimation using support vector machine. In: SEG/New Orleans Annual Meeting, pp. 1693–1697. USA (2006). https://doi.org/10.1190/1.2369848

Change in Streaming Potential with Earthquakes

Naoto Kaneko, Hiroyuki Nagahama, Kan Okubo, and Michiyo Nakashima

Abstract

It is essential to understand the electromagnetic phenomena associated with earthquakes such as ground potential change as a precursor. We theoretically derived the coseismic streaming potential model from the pore water pressure in the ground as a porous medium and the equation of motion. The newly constructed streaming potential model in this study clarified that the ground potential difference 10^{-6} [V] is generated with fluid movement at the time of the Southern Miyagi Pref. earthquakes.

Keywords

Pore water pressure • Porous medium • Ground potential

1 Introduction

Several attempts have been reported in the past to understand the behavior of earthquake potentiality in change of ground potential difference (Myachkin et al. 1972; Corwin and Morrison 1977). However, a mechanism of streaming potential caused by pressure change of pore water passing through the ground as a porous medium has not been proposed based on geological evidences. So based on previous studies (Takeuchi et al. 1997a, b, 1999, 2012), we proposed a new streaming potential model which can estimate shear stress caused by seismic acceleration at any formation depth.

2 Method

Takeuchi et al. (1999) reported the change of ground potential during seismic wave propagation about Southern Miyagi Pref. earthquakes accompanied by numerous aftershocks at 05:24 UTC on September 15, 1998, mainly in Sendai City. The information of this earthquake and Mt. Aobayama observation site (AOB, in Tohoku University) is shown in Figs. 1 and 2 [the data from Takeuchi et al. 1997a; Umino et al. 2002)]. The geological feature of observation site is located in the sand layer through which water flows, and it is easy to measure the flow potential because it is located very close to the groundwater surface as shown in Fig. 2. Takeuchi et al. (1997b) who installed an electrode at this site obtained a ground vertical electric field $\varphi_o = 10^{-5}$ to 10^{-6} [V/Pa] by streaming potential model based on Mizutani et al. (1976). Two electrodes (Takeuchi et al. 1997a) were vertically buried at depths of 0.5 and 2.5 m at the same observation site. The type RE-5 by McMiller Co. consisting copper and a saturated copper sulfate solution was used, and the diameter is 30 mm and length is 15 cm. This device can be avoided error effects by point contact.

3 Results and Discussion

We calculate the streaming potential from a macroscopic stress equation based on the parameters obtained by Takeuchi et al. (1997b). Here, let us derive a new streaming potential model from the view point of the pore water pressure in the ground as follows: The volume change of the ground material is a linear response under undrained condition at the time of the earthquake. The linearly elastic porous medium equation by Roeloffs (1996) as follows:

N. Kaneko (✉) · H. Nagahama
Department of Earth Science, Tohoku University, 6-3 Aoba, Aramaki Aoba-ku, Sendai, Japan
e-mail: naoto.kaneko.t4@alumni.tohoku.ac.jp

K. Okubo
Faculty of System Design, Tokyo Metropolitan University, 6-6 Asahigaoka, Hino, Tokyo, Japan

M. Nakashima
Department of Land Conservation, Osaka Branch Office, Nippon Koei Co., Ltd., 2-5 Nishitenma 1-chome, Kita-ku, Osaka-shi, Osaka, Japan

M. Meghraoui et al. (eds.), *Advances in Geophysics, Tectonics and Petroleum Geosciences*,
Advances in Science, Technology & Innovation, https://doi.org/10.1007/978-3-030-73026-0_76

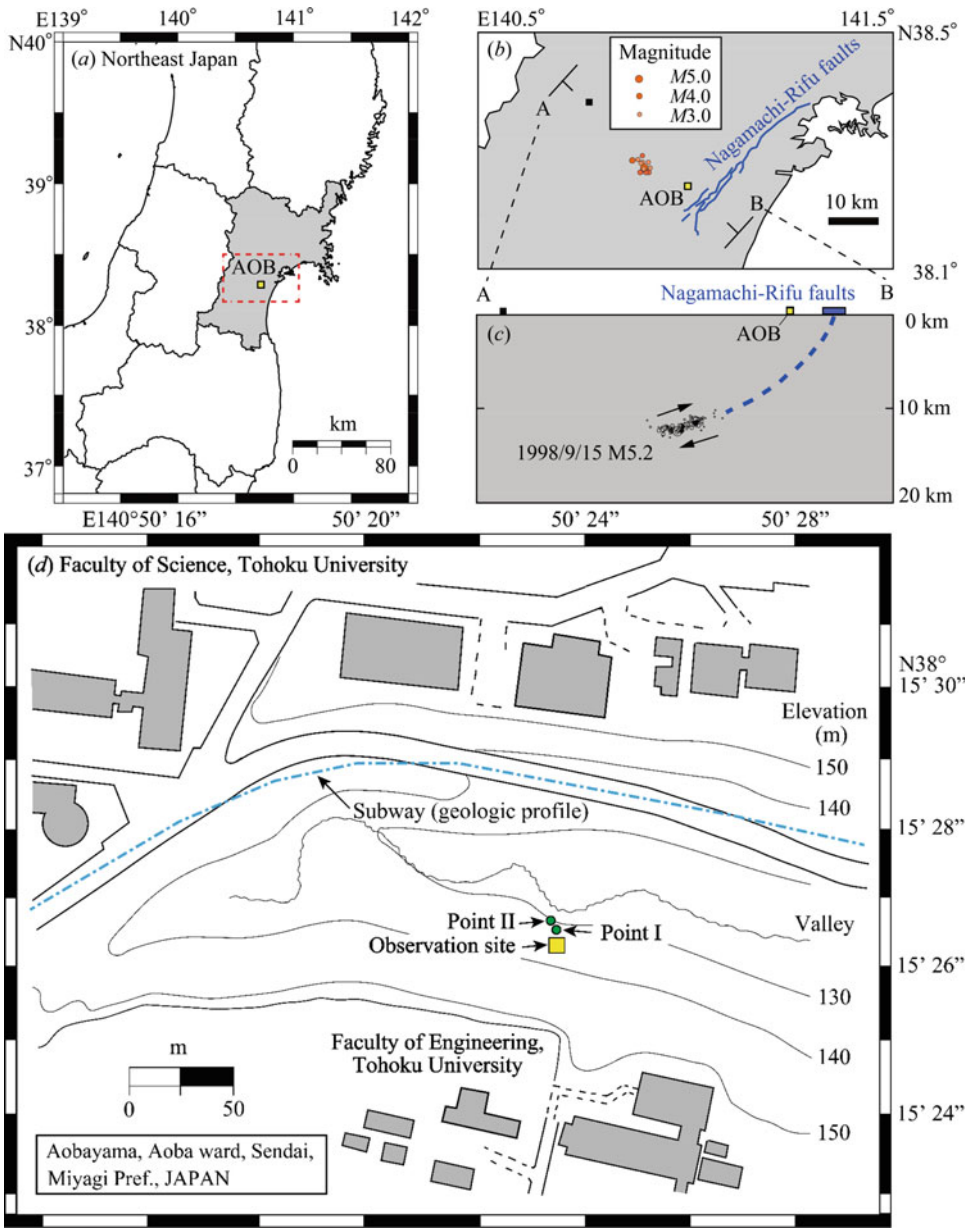

Fig. 1 **(a)** Observation site in Miyagi Pref. **(b)** Epicenters of the mainshock and aftershock (partly modified from Umino et al. (2002). **(c)** Vertical cross section of the events along line AB in **(b)** (partly modified from Umino et al. (2002)). **(d)** Observation site (Takeuchi et al. 1997b). (Point I) Aobayama Formation, (Point II) Boundary of Aobayama and upper Mukaiyama Formation

$\Delta p = \{B(1+v_u)/3(1-v_u)\}\Delta\tau$, where Δp is fluid pressure, v_u Poisson's ratio under undrained condition, B elastic constant of poroelastic medium material, and $\Delta\tau$ stress change in the direction perpendicular to the wavefront. The linearly elastic porous medium equation expresses the propagation of seismic waves accompanied by volume change and stress change at the time of earthquake. The motion equation based on wave motion theory of seismic waves is expressed by Ishihara (1970): $(\partial\tau/\partial x) = \rho_s(\partial^2 y/\partial t^2)$, where displacement at depth x is y and ρ_s is unit volume weight of soil. Moreover, the stress–strain relationship between shear stress τ and shear strain $(\partial y/\partial x)$ for shearing can be expressed by $\tau = \mu_s(\partial y/\partial x)$, where μ_s is the shear modulus. From the motion equation and stress–strain equation for shearing, we can get the wave equation and its general solution, and then, acceleration is given by $\tau = a\rho_s x$. From this equation, shear stress at depth x can be expressed as the product of the mass of the soil above it and the acceleration due to the earthquake acting on it. Based on (Takeuchi et al. 1997b), numerically observed values (a = 1 [Gal]), Δp = 10 [Pa/m] and vertical electric field difference in ground $\Delta\varphi$ = 0.1 [mV/m]) are given to the motion equation and $\tau = a\rho_s x$, and then, we can get $(\Delta\varphi/\Delta p) = 10^{-6}$ [V/Pa]. This value 10^{-6} [V/Pa] is in agreement with the observed values φ_o of Takeuchi et al. (1997b) and laboratory experiment (Jouniaux et al. 1994).

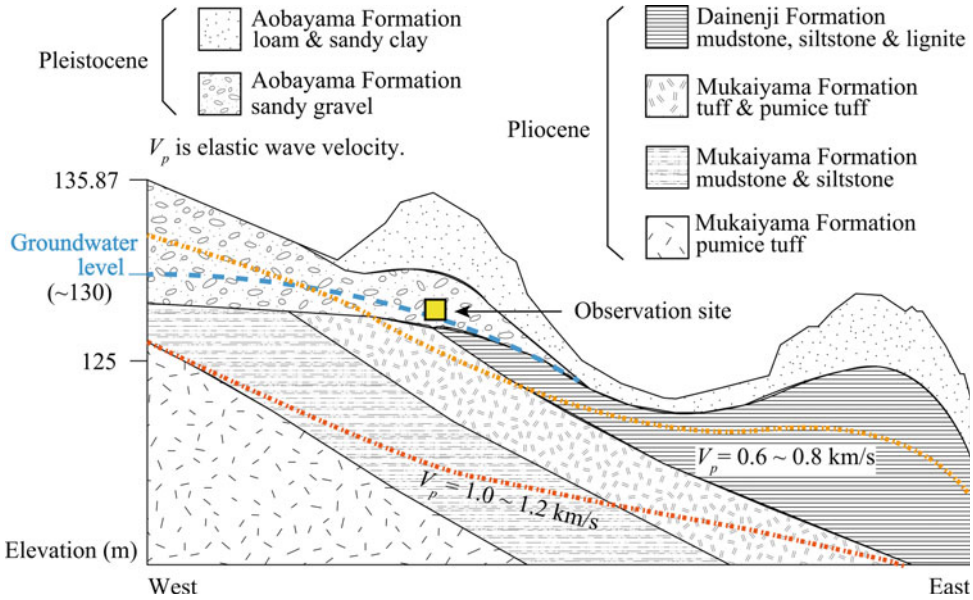

Fig. 2 East–west geological cross section of observation point [partly modified from Japan Railway Construction, Transport and Technology Agency (2008)]. V_p expresses an elastic wave. The permeability coefficient of Aobayama Formation is estimated to be 10^{-3} [cm/s] by (Research Committee of Sendai Castle Ruins Natural Environment 1990, see, pp. 25–26) and is 10^{-2} and 10^{-3} order higher than others (Pliocene)

Acknowledgements This paper is dedicated to Professor emeritus Nobunao Takeuchi.

References

Corwin, R.F., Morrison, H.F.: Self-potential variations preceding earthquakes in central California. Geophys. Res. Lett. **4**(4), 171–174 (1977)

Ishihara, K.: Approximate forms of wave equations for water-saturated porous materials and related dynamic modulus. Soils Found. **10**(4), 10–38 (1970)

Japan Railway Construction, Transport and Technology Agency: Geologic profile of Kameoka Tunnel, Tozai Line of Sendai Municipal Subway (2008). (in Japanese)

Jouniaux, L., Lallemant, S., Pozzi, J.P.: Changes in the permeability, streaming potential and resistivity of a claystone from the Nankai prism under stress. Geophys. Res. Lett. **21**(2), 149–152 (1994)

Mizutani, H., Ishido, T., Yokokura, T., Ohnishi, S.: Electrokinetic phenomena associated with earthquakes. Geophys. Res. Lett. **3**(7), 365–368 (1976)

Myachkin, V.I., Sobolev, G.A., Dolbilkina, N.A., Morozow, V.N., Preobrazensky, V.B.: The study of variations in geophysical fields near focal zones of Kamchatka. Tectonophys. **14**, 287–293 (1972)

Research Committee of Sendai Castle Ruins Natural Environment: Nature of Sendai Castle, Sendai City Board of Education, 295 p. Sendaikyodo Printing Co., Ltd., Sendai (1990). https://doi.org/10.24484/sitereports.3720

Roeloffs, E.: Poroelastic techniques in the study of earthquake-related hydrologic phenomena. Adv. Geophys. **37**, 135–195 (1996)

Takeuchi, N., Chubachi, N., Narita, K.: Observations of earthquake waves by the vertical earth potential difference method. Phys. Earth Planet. Inter. **101**, 157–161 (1997a)

Takeuchi, N., Chubachi, N., Narita, K., Honma, N.: Mechanism of charge appearance on earth surface at earthquake. T. IEEJapan. C **117**(10), 1535–1536 (1997b) (in Japanese)

Takeuchi, N., Ohkubo, K., Sato, M., Honma, N., Narita, K.: Electromagnetic observations of the earthquake occurred in Sendai City. T. IEE Japan. C **119**(8), 979–984 (1999). (in Japanese)

Takeuchi, A., Okubo, K., Takeuchi, N.: Electric signals on and under the ground surface induced by seismic waves. Inter. J. Geophys. **2012**, 1–10 (2012)

Umino, N., Okada, T., Hasegawa, A.: Foreshock and aftershock sequence of the 1998 *M* 5.0 Sendai, northeastern Japan, earthquake and its implications for earthquake nucleation. Bull. Seismol. Soc. Am **92**(6), 2465–2477 (2002)

Radio Direction Finding for Short-Term Crustal Diagnosis (Italy)

Valentino Straser, Gabriele Cataldi, and Daniele Cataldi

Abstract

The radio direction finding (RDF) system is a multi-channel radio receiver prototype capable of working in the SELF–VLF band (0 Hz < $f \leq$ 30 kHz). The detection system, located in Rome (Italy), coupled with a system of directional antennas and software allows measuring the angle of origin of a given electromagnetic emission. The authors compared the electromagnetic emissions detected by the RDF system with the epicenter of earthquakes in Italy and on a global scale. The analysis of the study of the data, referring to the origin of the radio signals, both from Italian geographical areas and from others located at an enormous distance (on a global scale), showed that emissions always precede the mainshocks, whether they occur near at the monitoring station (a few kilometers), whether they are 20,000 km away. The method, started in 2017, is experimental and is a valid tool for the study of potential candidates for seismic precursors of electromagnetic nature of an earthquake. Hence, the higher the proximity to the epicenter, the better the quality of the signal. This is the first trial launched on a European scale.

Keywords

Earthquakes • Seismic precursors • RDF • EM emissions • Crustal diagnosis

1 Introduction

The analysis of the data detected in the RDF experimentation is based on the existence of broadband radio signals, which can be associated from a temporal point of view and azimuth to potentially destructive seismic events. The hypothesized physical mechanism concerns the production of electromagnetic dipoles generated in the microfractures of the earth's crust, in the focal zone of an earthquake in the pre-seismic stage (Varotsos et al. 1986; Gokhberg et al. 1985), i.e., in the moments that precede the seismic triggering following the accumulation of mechanical stress in the fault (Cataldi et al. 2019). This type of emissions can travel thousands of kilometers propagating inside the earth–ionosphere cavity. The intensity of these radio signals could be proportionally related to the earthquake magnitude, considering the amount of mechanical stress accumulated in the fault. In this context, the higher the mechanical stress accumulated on the fault margins, the higher the electromagnetic emission generated and the greater the magnitude of the earthquake associated with these events. The monitoring was developed in Italy and is active 24 h a day, and seven days a week, with continuous data collection and compared in real time with the list of earthquakes published in real time on the website (Straser et al. 2019). To enhance the accuracy of identifying seismic epicenter is under construction, a detection network which will improve the method of triangulation. In this study, the case of the recent earthquake of Ravenna, in Northern Italy, of magnitude M4.6 is presented.

2 The Instruments and Methods of Measure

The monitoring data were acquired through the RDF station of Lariano (Rome, Italy), equipped with radio direction finding technology; it consists of a radio receiver, developed by the Radio Emissions Project and connected to a system of

V. Straser (✉)
Italian Ministry of Education, University and Research, Parma, Italy

G. Cataldi · D. Cataldi
Radio Emission Project, Rome, Italy

M. Meghraoui et al. (eds.), *Advances in Geophysics, Tectonics and Petroleum Geosciences*,
Advances in Science, Technology & Innovation, https://doi.org/10.1007/978-3-030-73026-0_77

spatially oriented antennas in the orthogonal scheme and oriented on the cardinal axes. The data then sent to a PC that processes the signals using software, producing dynamic spectrograms. The bandwidth of the detection system is 32 kHz (0.001–32,000 Hz), with a minimum temporal resolution of 250 ms, but set in this study at 20 s. The system is powered at + 5 V, via the USB socket of the PC to which it is connected, and amplifies the signals received by the square loop antennas (50 turns, 1 × 1 m) a few hundred times, active 24h7, able therefore to continually monitor the terrestrial electromagnetic field.

3 Results

The results of this monitoring (Table 1) showed a close relationship between the appearances of the signals indicated by the RDF station, whose azimuth indicated, with a clear notice in hours, the geographical area where this earthquake occurred.

The indicated azimuth had a phase shift (width) of about 5° in the course of the peaks. However, this width was reduced to about 2°. If we are going to measure the colorimetric variation on the map and the attached spectrogram (Fig. 1), we note that the colorimetric variation decreases when the intensity of the signals increases. This variation indicates that the stronger signals possess a more marked angle of evidence, compared to the less intense signals, which always have a less precise angle of provenance due to the dissipation of the signal itself.

4 Discussion

The working hypothesis was to verify the presence of electromagnetic emissions that had an arrival azimuth able to identify a geographical area that within a few hours had given rise to an earthquake of a certain intensity. In this case, the monitoring system would have highlighted these emissions due to their morphology (intensity, arrival azimuth, duration, electromagnetic frequency, type of appearance and disappearance). The earthquake, of magnitude ML 4.6 recorded on 14-01-2019 at 23:03:56 (UTC) in the area: 11 km E Ravenna (Italy)—GPS (Global Positioning System): 44.37, 12.32, was preceded by the signals highlighted by the monitoring system at least 15 h before indicating the azimuth precisely (Fig. 1).

Table 1 Results of electromagnetic monitoring

Increase time	Bandwidth (kHz)	Azimuth
08:20 UTC—(15 h before)	32	Red color—345°–350°
10:50 UTC—(15 h before)	32	Red color—345°–350°
12:30 UTC—(15 h before)	32	Red color—345°–350°

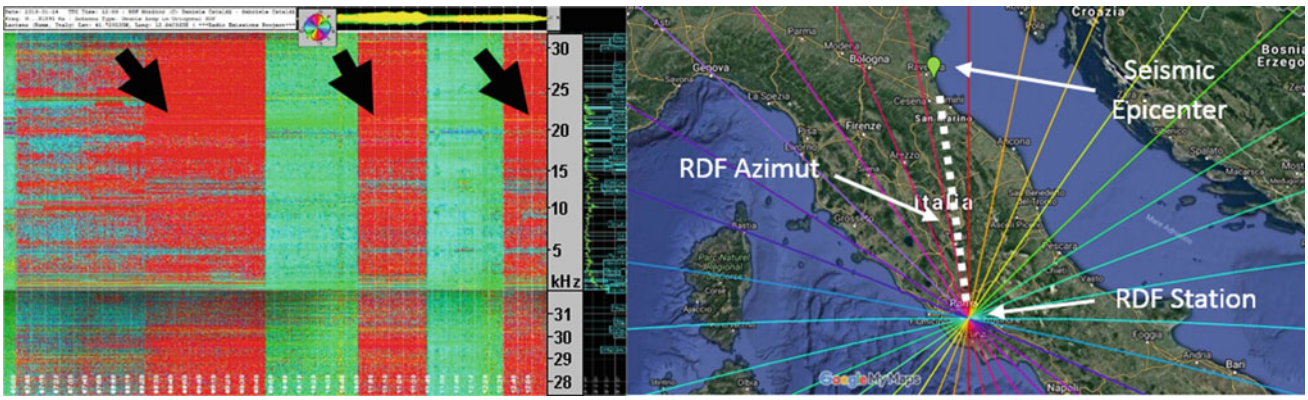

Fig. 1 RDF spectrogram. The image shows a spectrogram recorded by the electromagnetic monitoring system developed by the Radio Emissions Project and, on the right, the relevant worldwide mapping of the RDF system, in which the seismic epicenter is identified: Magnitude earthquake ML4.6 recorded on 14-01-2019 at 23:03:56 (UTC) in the area: 11 km E Ravenna (Italy) GPS 44.37, 12.32 (INGV data). The signals indicated by the black arrows are the electromagnetic increments highlighted by the RDF system having as their object the epicentral azimuth with respect to the position of the detection station. *Credits* Google Maps, Radio Emissions Project, INGV

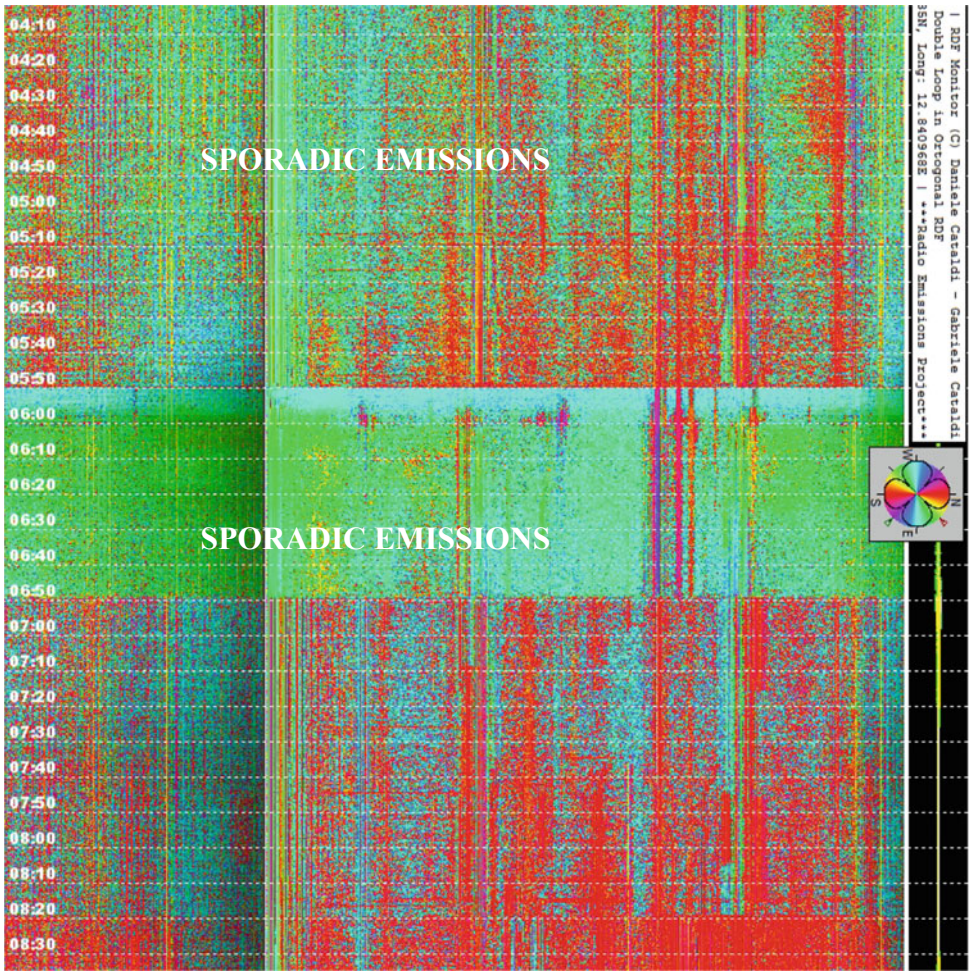

Fig. 2 RDF spectrogram. This shows the beginning of the electromagnetic emissions with the object of the azimuth of the seismic epicenter that within a few hours will appear in the geographical area identified by the RDF system, developed by the Radio Emissions Project

At 08:20 UTC, there was the first explicit appearance of the signals, then again at 10:50 UTC and finally at 12:30 UTC (over 10 h before the seismic event).

Sporadic increases were noted during the first hours of the night of 01-14-2019, and also, in this case, the data indicated the epicentral azimuth (Figs. 2, 3, 4, 5 and 6).

The electromagnetic emissions that appeared suddenly during January 14, 2019, showed necessary and prognostic signals for a seismic trigger on a global scale that would have happened within a short time. These types of emissions were pertinent in full increments, well emerging from the natural electromagnetic background and therefore not to be underestimated. The computerized system had highlighted the arrival azimuth of these signals, highlighting precisely the red azimuth.

5 Conclusions

The monitoring system developed by the Radio Emissions Project, equipped with RDF technology, showed that the electromagnetic signals precede the earthquake by at least 10 h and indicate, in all the cases studied, the direction of the future epicenter.

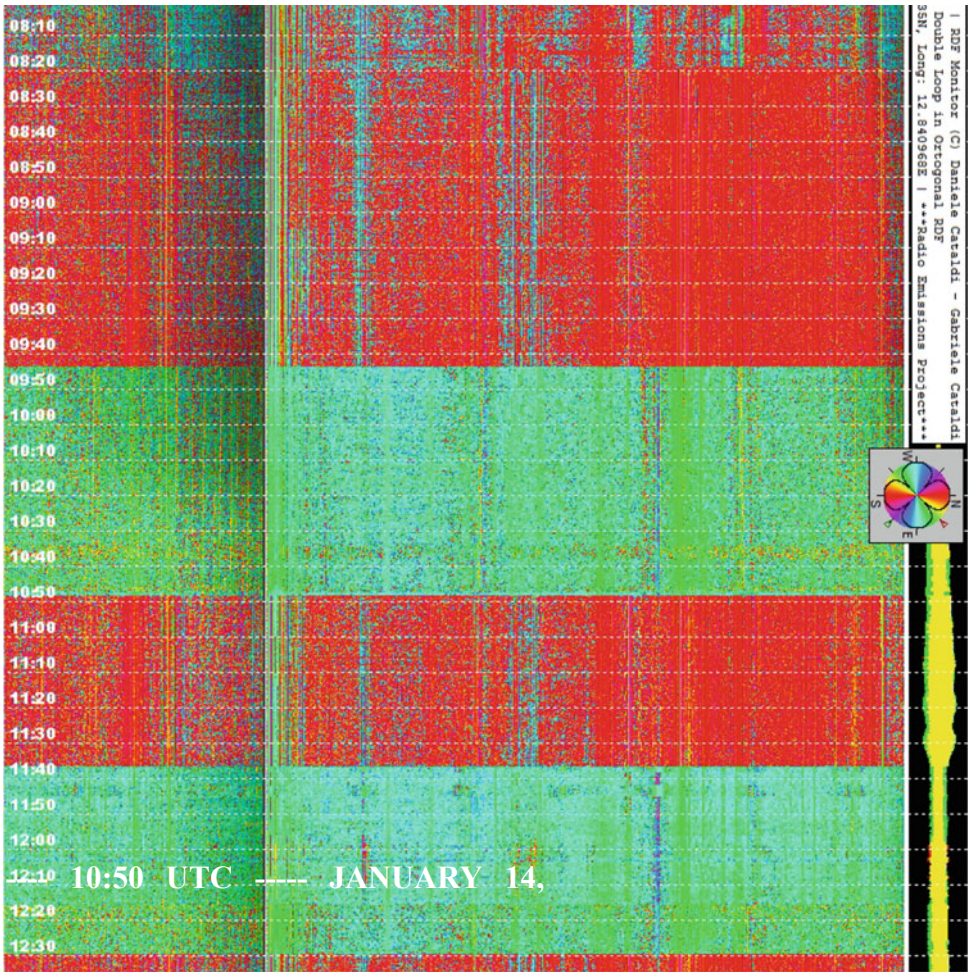

Fig. 3 RDF spectrogram. This highlights the presence of massive electromagnetic emissions with azimuth relative to the seismic epicenter. They are very frequent, separated by a few hours and clearly visible and detached from the natural geomagnetic background

The signals' arrival direction and their morphology identify a restricted portion of azimuth in degrees, out of 360. From a technical point of view, they possess the following characteristics:

- The frequency of each detected electromagnetic signal had a bandwidth of 32 kHz and with a resolution of less than 1 Hz;
- The intensity of each detected electromagnetic signal, expressed in dB (decibel), can be associated with a colorimetric scale;
- The direction/azimuth of origin of the electromagnetic signals expressed in degrees (°) uses a colorimetric scale associated with it;
- The graphical representation (spectrogram) of the intensity of the electromagnetic signals as a function of time and frequency: it allows to obtain a spectrographic impression of the electromagnetic signals received and observe their evolution over time.

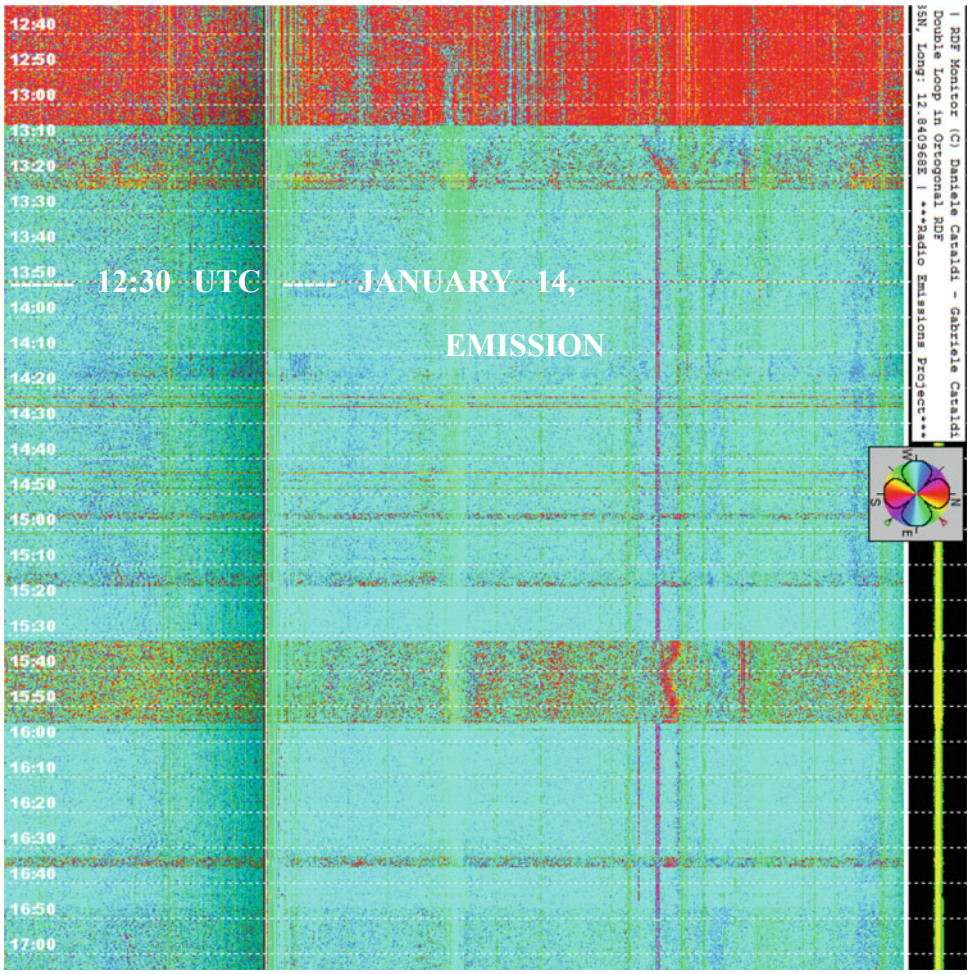

Fig. 4 RDF spectrogram. This highlights how the 12:30 emission represents the last important electromagnetic emission before the earthquake, which will occur on January 14, 2019, at 23:03:56 just under 12 h later

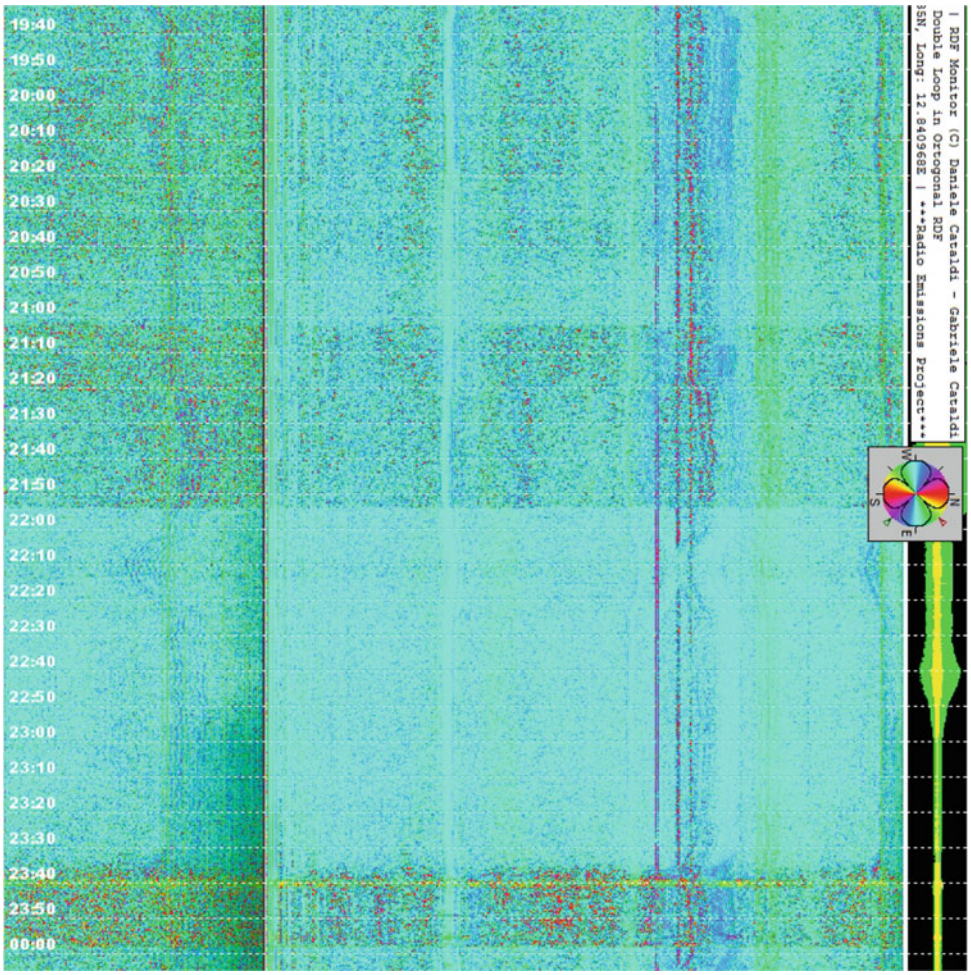

Fig. 5 RDF spectrogram. This highlights the presence of the earthquake timeline, where precursor phenomena are not observed through the monitoring system developed by the Radio Emissions Project. The signals, as evidenced in the previous spectrograms, were evident several hours before the earthquake

Fig. 6 RDF colorimetric map. This shows the colorimetric map developed by the Radio Emissions Project. It highlights the red azimuth signaled by the monitoring system, a few hours before the earthquake occurred in Italy. The earthquake, which then occurred near Ravenna, with a ML 4.6 magnitude 11 km east of Ravenna (Italy) at a precise spatial position (GPS 44.37, 12.32), at a distance of 301 km from the RDF station of Lariano (Rome), Italy

References

Cataldi, D., Cataldi, G., Straser, V.: Radio Direction Finding (RDF)—Pre-seismic Signals Recorded Before the Earthquake in Central Italy on 1/1/2019 west of Collelongo (AQ). European Geosciences Union (EGU) General Assembly 2019, Seismology (SM1.1) General Contributions on Earthquakes, Earth Structure, Seismology, Geophysical Research Abstract, Vol. 21, EGU2019–3124, 2019, Vienna, Austria (2019)

Gokhberg, M.B., Gufeld, I.L., Gershenzon, N.I., Pilipenko, V.A.: Electromagnetic effects in crustal fracturing. In its USSR Rept.: Earth Science (JPRS-UES-85-008) p 34 (SEE N86-12697 03-42) Transl. into English from Izv. Akad. Nauk SSSR: Fiz. Zemli (Moscow), no. 1, Jan 1985 (1985)

Straser, V., Cataldi, D., Cataldi, G.: Registration of pre-seismic signals related to the mediterranean area with the RDF system developed by the radio emissions project. Int. J. Eng. Sci. Invention (IJESI) **8**(03), 26–35 (2019). www.ijesi.org. ISSN (Online): 2319-6734, ISSN (Print): 2319-6726

Varotsos, P., Alexopoulos, K., Nomicos, K., Lazaridou, M.: Earthquake prediction and electric signals. Nature **322**(6075), 120 (1986)

Application of Electrical Imaging and Seismic Tomography in the Study of Viaduct Site in Tabellout, Jijel, Northeast Algeria

Riad Benzaid, Mustapha Tekkouk, and Chahra Yellas

Abstract

The Tabellout Viaduct site is part of the Jijel-El Eulma highway project, located about 8 km southeast of the village of Texenna in the city of Jijel (northeast Algeria). The manuscript reports an integrated geophysical investigation consisting of seismic tomography and electrical resistivity imaging of the studied site. This work aims to confirm the lithology of the different formations and their geometry, the P-wave velocity variation, the variation of the resistivity of the sub-surfaces along the axis of the viaduct as well as potential fault zones including stratigraphic and tectonic contacts between different geological formations characterizing the region.Please check and confirm if the authors and their respective affiliations have been correctly identified. Amend if necessary.Oui, les auteurs et leurs affiliations respectives ont été correctement identifiés.

Keywords

Viaduct • Geophysical surveys • Seismic tomography • Electrical imaging

1 Introduction

The Tabellout Viaduct is located between the village of El Ghdir (Northside) and Tabarkoute (Southside) in the Wilaya of Jijel—Northeast Algeria of a total length of 1238 m. The viaduct has 10 pillars with foundations on 32–48 drilled piles with a diameter of 1.2 m, while the abutments will be made on foundations consisting of 8 to 12 piles (Projet d'exécution du Viaduc Tabellout 2016). In addition to the geological and geotechnical surveys, the results of the geophysical prospection carried out along the axis of the viaduct enabled us to confirm the lithology of the various formations as well as the zones of potential faults and the stratigraphic and tectonic contacts between the different geological formations. This information is valuable in this kind of project.

R. Benzaid (✉) · M. Tekkouk · C. Yellas
Laboratoire de Génie Géologique, Université Mohammed Seddik Benyahia—Jijel, Algérie, BP. 98, Cité Ouled Aissa, Jijel, 18,000, Algérie
e-mail: r_benzaid@univ-jijel.dz

2 Geophysical Surveys

Geophysical work in the study area includes longitudinal and cross sections of seismic tomography and electrical imaging (Projet d'exécution du Viaduc Tabellout 2016; Rapport de l'étude géophysique du Viaduc de Tabellout 2015). The longitudinal profiles were made from the pile P2 to the abutments on C2 of the viaduct, while the cross sections were executed at each support. Geophysical prospecting was performed by surface seismic tomography and electrical imaging methods to determine: - The lithology of the different formations and their geometry. -The velocity variation of the P waves (V_p) as well as the variation of the resistivity of subsurface formations along the axis of the viaduct. - Potential fault zones, including stratigraphic and tectonic contacts between different geological formations.

2.1 Seismic Prospecting

The analysis of the results of the seismic tomography made it possible to reach certain conclusions on the geometrical configuration of the grounds. The profiles made on the axis of the viaduct (Figs. 1 and 2) made it possible to highlight four distinct ranges of velocity, namely (Projet d'exécution du Viaduc Tabellout 2016; Rapport de l'étude géophysique du Viaduc de Tabellout 2015; RAZEL-CMC 2010; RBR 2010):

M. Meghraoui et al. (eds.), *Advances in Geophysics, Tectonics and Petroleum Geosciences*,
Advances in Science, Technology & Innovation, https://doi.org/10.1007/978-3-030-73026-0_78

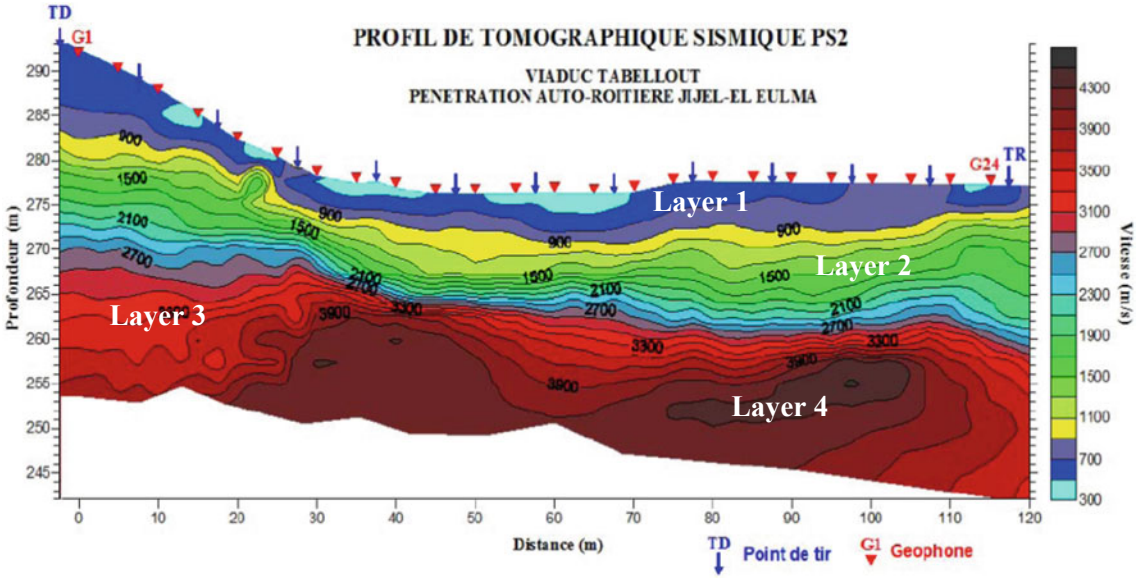

Fig. 1 Axial profile of seismic tomography, at P3 foundation level (Projet d'exécution du Viaduc Tabellout 2016; Rapport de l'étude géophysique du Viaduc de Tabellout 2015)

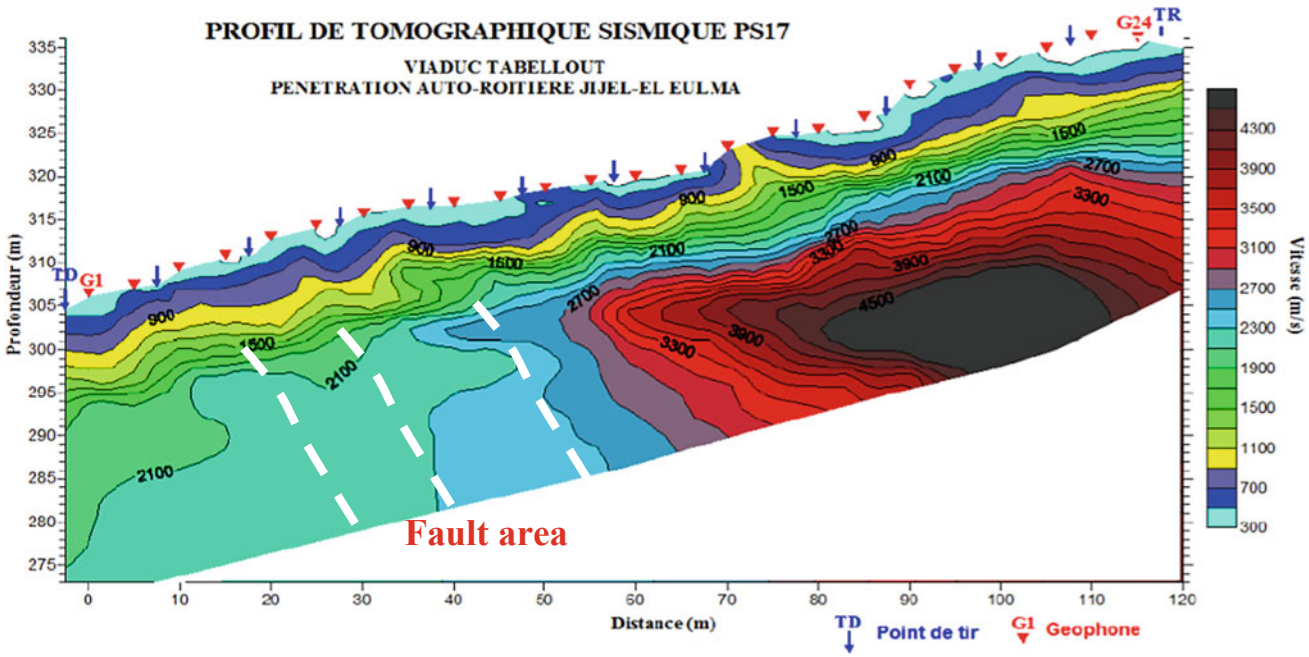

Fig. 2 Transverse profile of seismic tomography, at foundation P10 level (Projet d'exécution du Viaduc Tabellout 2016; Rapport de l'étude géophysique du Viaduc de Tabellout 2015)

- The surface layer, is caracterized with a velocity range of between 300 and 900 m/s. This first layer (whose thickness varies from a few meters to about 10 m) corresponds to quaternary surficial deposits, which include colluvial deposits, alluvial deposits and unconsolidated deposits observed near the P9 and P10 supports.
- The second layer (whose thickness varies between 10 and 15 m), characterized by an intermediate velocity range of 900–2300 m/s, corresponds to an alteration profile of the bedrock. These are the clay, shale, fractured and weathered formations. Besides, this speed interval characterizes the main fault zones.

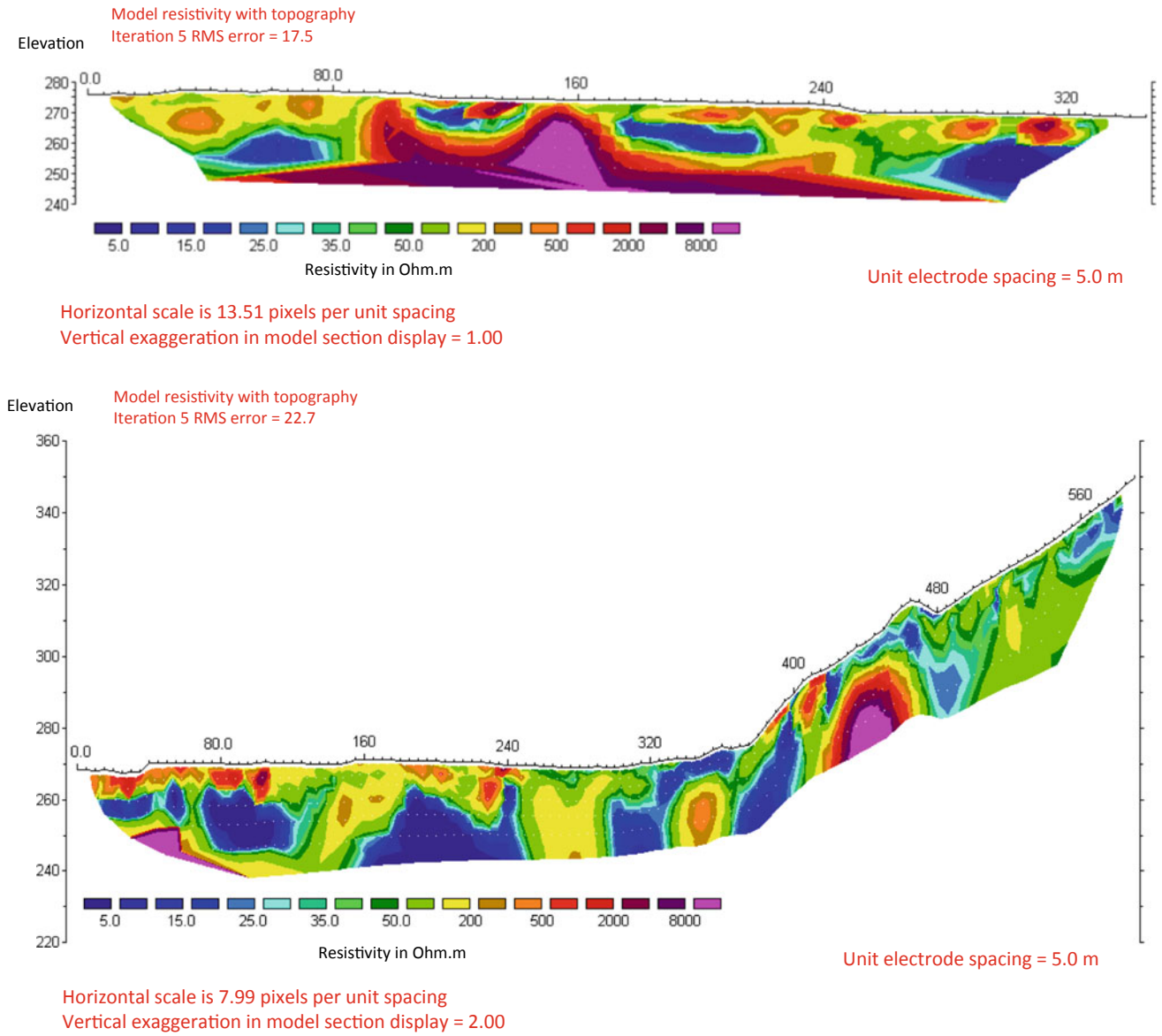

Fig. 3 Geo-electrical profiles in the Viaduct axis (Projet d'exécution du Viaduc Tabellout 2016; Rapport de l'étude géophysique du Viaduc de Tabellout 2015)

- The third range (with a thickness varying between 5 and 10 m approximately), relatively high velocity, is obtained with values between 2300 and 3900 m/s. It corresponds to the bedrock of the Neocomian flysch and the metamorphic complex, characterized, respectively, by flaky marls and marly limestones and by schistose mica schists, more or less fractured.
- The fourth range is obtained with very high velocity whose values are between 3900 and 4500 m/s. These speeds represent areas of the bedrock that are less altered and less fractured.

At the cross section of the seismic tomography PS17 (Fig. 2), a tectonic fault rejection is highlighted. This is an essential zone of deformation or shear that belongs to the overlap of small Kabylie. The interference of the viaduct with this fault zone is mainly located between the P9 and P10 foundations. However, the seismic profiles have also revealed a series of secondary structures (faults) associated with the main thrust that will be crossed by the route from the P5 foundation.

2.2 Electrical Prospecting

The analysis of the electrical imaging results (Fig. 3) made some conclusions about the geometrical configuration of the ground and their resistivity values. In general, the sections of the electrical imaging profiles show three ranges of resistivity (Projet d'exécution du Viaduc Tabellout 2016; Rapport de l'étude géophysique du Viaduc de Tabellout 2015; RAZEL-CMC 2010; RBR 2010):

- The first representing a conductive formation whose resistivity values are between 5 and 30 Ωm.
- The second range represents a relatively resistant formation characterized by values between 50 and 200 Ωm.
- The third range of very high resistivity which varies from 300 and can reach 8000 Ωm.

The variability of the resistivity values and the geometry of the iso-resistivity zones confirm the complexity of the geological modelling in the viaduct sector, which is characterized by the following main elements (Projet d'exécution du Viaduc Tabellout 2016; Rapport de l'étude géophysique du Viaduc de Tabellout 2015; RAZEL-CMC 2010; RBR 2010):

- - The presence of several fault zones with a movement between the blocks of the bedrock.
- - The lateral variability of the degree of fracturing at the level of rock masses between the most deteriorated and crushed zones of low resistivity, and the zones of less deformed rock masses of higher resistivity. - The lateral variability of secondary permeability (fracturing permeability) with the possibility of groundwater circulation at the level of the most fractured rocky horizons.

3 Conclusion

The geophysical methods applied to the site of the Viaduct of Tabellout have come to complete our first works on the fracturing made during our various visits. Indeed, the geometry of the discontinuities, their extensions, their in-depth repercussions and the interconnection between them leads to predicting a very complicated situation concerning the foundation system of this structure. Special attention to the foundation system that will be adopted is recommended.

References

Projet d'exécution du Viaduc Tabellout (Pk30+181–31+419). Annexe E: Reconnaissances géophysiques. 1ère édition le 29/01/2016

Rapport de l'étude géophysique du Viaduc de Tabellout. Bureau d'engineering, études et équipements en géosciences "GeoExplo", 56 p, Alger, Octobre 2015

RAZEL-CMC: Rapport géotechnique- Barrage de Tabellout, Jijel, Algérie (2010)

RBR: Etude géophysique par sismique réfraction sur le site de construction du barrage de Tabellout dans la région de Jijel, Algérie. Rapport final. RBR géophysics. SEA Consulting S.r.l. (2010)

A New Method to Determine In Situ Stress Based on Borehole Cross-Sectional Shape Measuring Technique

Zengqiang Han, Chuanying Wang, Yiteng Wang, and Chao Wang

Abstract

In situ stress played a vital role in the planning, design and decision-making of underground engineering. In this study, we proposed a borehole cross-sectional shape measurement technique. We developed a set of borehole deformation measurement devices using key technologies such as micro-optical imaging measurement technology, multi-contact borehole wall displacement sensing technology and borehole deformation direction measurement technology. Based on these techniques, we put forward a method for calculating in situ stress based on borehole cross-sectional data. The borehole deformation measuring device and the in situ stress calculation method were applied to the in situ stress measurement test in a borehole. The experimental results were concordant with the results of the hydraulic fracturing method, which confirmed the feasibility of this method in in situ stress measurement. This paper introduces a new idea and method for in situ stress measurement.

Keywords

In situ stress • Borehole cross-sectional shape • Micro-optical imaging measurement • Borehole wall displacement • Principal stress

1 Introduction

Since the apparition of the concept of in situ stress, scientists have introduced dozens of in situ stress testing methods (Zang and Stephansson 2010; Amadei and Stephansson 1997; Jaeger et al. 2009). To name a few, Borehole-based method is the most commonly used at present. Under the action of in situ stress, the borehole wall produces a certain degree of deformation, especially in deep boreholes, which is very common. The cross-sectional shape of the deformed borehole is also the corresponding reflection of the magnitude and direction of in situ stress. It is an essential direction of measuring in situ stress based on borehole deformation to develop borehole cross-sectional shape measurement technology and establish the correlation between in situ stress and borehole shape (Wang and Pan 1991; Obara et al. 2010). In this paper, a multi-contact borehole deformation measuring device based on the principle of micro-optical imaging measurement is proposed, which can simultaneously obtain borehole diameter measurement in multiple directions, borehole diameter changes and borehole shape characteristics under in situ stress. The method of rigid contact displacement sensing and micro-optical imaging avoids the influence of traditional electronic sensors in deep borehole high temperature and high-pressure environment.

2 Methods

2.1 Borehole Cross-Sectional Shape Measuring Technique

A symmetrically arranged rigid stylus element is used to sense and reflect the borehole deformation, as shown in Fig. 1. The micro-optical imaging device uses fixed-focus lens and CCD imaging components.

Z. Han · C. Wang (✉) · Y. Wang · C. Wang
State Key Laboratory of Geomechanics and Geotechnical Engineering, Institute of Rock and Soil Mechanics, Chinese Academy of Sciences, Wuhan, 430071, Hubei, China

C. Wang
University of Chinese Academy of Sciences, Beijing, 100049, China

M. Meghraoui et al. (eds.), *Advances in Geophysics, Tectonics and Petroleum Geosciences*, Advances in Science, Technology & Innovation, https://doi.org/10.1007/978-3-030-73026-0_79

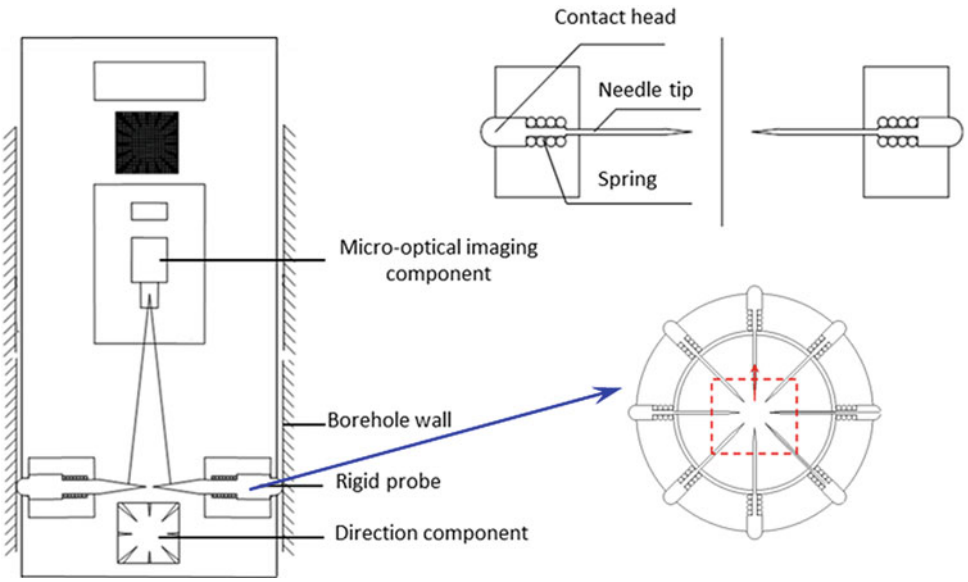

Fig. 1 Schematic diagram of system principle

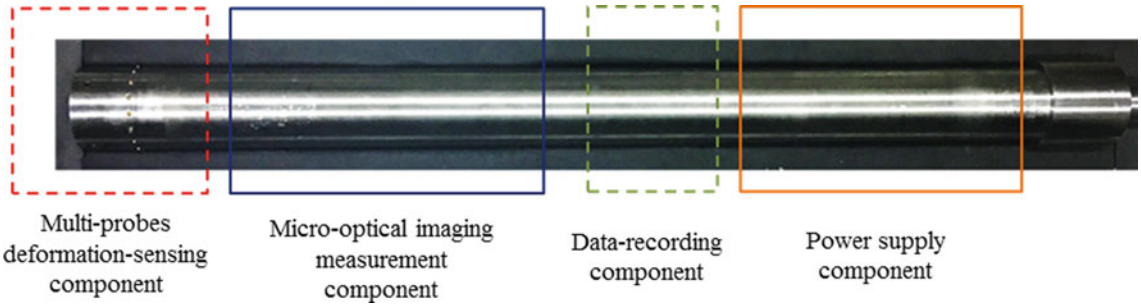

Fig. 2 Borehole cross-sectional shape measuring apparatus

Symmetrically arranged rigid stylus elements reflect the variation in borehole diameter, as shown in Fig. 1. Among them, the contact structure is the sensing part of the borehole wall displacement, that is, the part in contact with the borehole wall. The needle tip structure is the reflection of the borehole diameter deformation, that is, the part reflecting the borehole diameter variation synchronously. In addition, the orientation element (electronic compass) is introduced into the system design to measure the orientation of the aperture deformation.

Through research and development of the above key technologies, a set of measuring device has been developed and completed as shown in Fig. 2. By connecting with drill pipe in drilling site, the borehole deformation measurement in drilling process can be realized, and the obtained borehole deformation data can be analyzed. The magnitude and direction of in situ stress can be calculated.

2.2 In Situ Stress Calculation Based on Borehole Shape Data

Under the action of two-dimensional plane stress, the coordinate from P point to P' point is (x, y), which can be expressed as:

$$\left.\begin{aligned} x &= r\left[1+\frac{1-\mu^2}{E}(3\sigma_1-\sigma_2)\right]\cos\theta \\ y &= r\left[1+\frac{1-\mu^2}{E}(3\sigma_2-\sigma_1)\right]\sin\theta \end{aligned}\right\} \quad (1)$$

σ_1 is the magnitude of the maximum principle stress, σ_2 is the magnitude of the minimum principle stress, E is the elastic modulus and μ is the Poisson's ratio (Fig. 3).

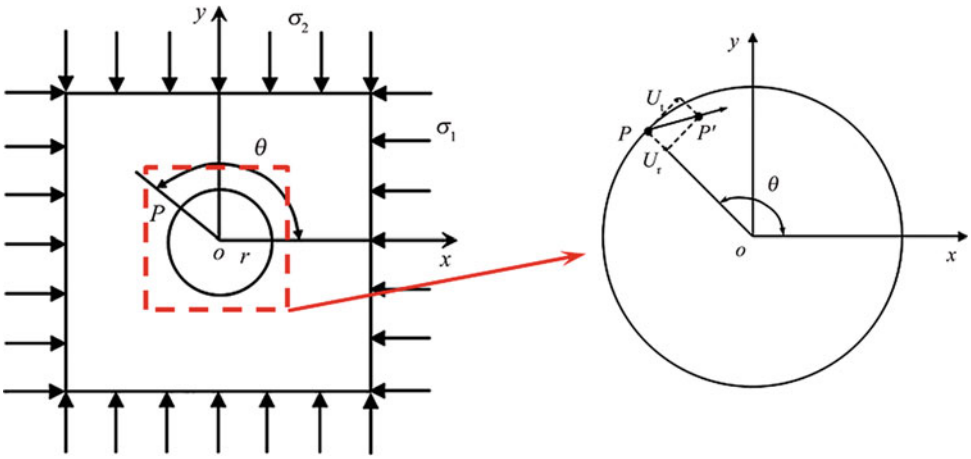

Fig. 3 Sketch of the displacement of borehole wall

Assume $|\sigma_1| > |\sigma_2|$ and we set:

$$\left.\begin{aligned} B &= r\left[1+\frac{1-\mu^2}{E}(3\sigma_1-\sigma_2)\right] \\ A &= r\left[1+\frac{1-\mu^2}{E}(3\sigma_2-\sigma_1)\right] \end{aligned}\right\} \quad (2)$$

A is the length of semi-major axis. B is the length of semi-minor axis of the ellipse. r is the initial radius of the borehole (Wang et al. 2016).

Then, Eq. (1) satisfies:

$$\frac{x^2}{B^2}+\frac{y^2}{A^2}=\cos^2\theta+\sin^2\theta=1 \quad (3)$$

The following equation can also be obtained by Eq. (2):

$$\left.\begin{aligned} \sigma_1 &= \frac{E}{1-\mu^2}\frac{3B+A-4r}{8r} \\ \sigma_2 &= \frac{E}{1-\mu^2}\frac{B+3A-4r}{8r} \end{aligned}\right\} \quad (4)$$

3 Field Test and Results

In situ stress has been tested in scientific drilling in Xishui City, Guizhou Province, China. The diameter of the drilling borehole is 122 mm, and the testing point is located at 636.6 m depth, which belongs to shale formation. Through system software, the change of contact pin is identified and calculated. Combined with rock physical parameters, the principal stress is calculated according to Eq. (4), and the direction of principal stress is calculated. The maximum horizontal principal stress at 636.69 m is 23.14 MPa, the minimum horizontal principal stress is 16.59 MPa, and the azimuth angle of the maximum horizontal principal stress is 181.3°. In this test section, the hydraulic fracturing test was also carried out. Moreover, all the pressure data during the pressurization process were obtained, which can be used to verify the method in this paper. According to the equation of hydraulic fracturing method, the maximum horizontal principal stress is 23.09 MPa, and the minimum horizontal principal stress is 17.6 MPa. The results of in situ stress obtained by borehole deformation method and hydraulic fracturing method are almost the same in magnitude.

4 Conclusions

A borehole cross-sectional shape measurement technique is proposed in this paper. Based on the data of the cross-sectional shape of borehole obtained by this technique, a method of in situ stress measurement based on borehole deformation measurement is proposed. The corresponding testing device is developed and applied in the field test. The experimental results agree well with those of the hydraulic fracturing method, which verifies the correctness and technical feasibility of the method.

References

Amadei, B., Stephansson, O.: Rock Stress and its Measurement. Springer Science & Business Media, UK (1997)

Jaeger, J.C., Cook, N.G.W., Zimmerman, R.: Fundamentals of Rock Mechanics. John Wiley & Sons (2009)

Obara, Y., Shin, T., Yoshinaga, T., et al.: Cross-sectional borehole deformation method (CBDM) for measurement of rock stress change. In: 5th International Symposium on In-Situ Rock Stress, pp. 129–134. Taylor & Francis Group, London (2010)

Wang, L., Pan, L.: Crustal Stress Measurements and their Application in Engineering, pp. 1–31. Geological Publishing House, Beijing (1991)

Wang, C., Han, Z., Wang, J., et al.: Study of borehole geometric shape features under plane stress state. Chin. J. Rock Mechan. Eng. **35** (S1), 2836–2842 (2016)

Zang, A., Stephansson, O.: Stress Field of the Earth's Crust. Springer Science & Business Media, UK (2010)

Geo-Investigations on the Qarat Kibrit Salt Dome Faulting System South of Adam, Oman—In Search of Anomalies Favorable for Uranium and Associated Minerals

Sundararajan Narasimman, Ebrahimy Alaeddin, Bernhard Pracejus, and Talal Al-Hosni

Abstract

The development of salt domes, often arising from depths of some 10 km or more, causes intense faulting of the surrounding host rocks (salt tectonics). The fractured rocks then present ideal space for oil that can migrate and get trapped. If such moving of hydrocarbons passes uranium-carrying rock units (e.g., shales), uranium is collected and enriched by organic carbon compounds. Brines from the salt body is also ideal carriers for oxidized uranium species and will further dislocate uranium when in contact with uranium-enriched oils. Uranium then has the potential to mineralize in the vicinity of the dome (blue halite is evidence for radiation having affected salt deposits). Based on this, the Qarat Kibrit salt dome was investigated by very low-frequency electromagnetic (VLF-EM) and magnetic surveys along five traverses approximately 250 m in length (10 m intervals) in order to identify subsurface fault systems. In-phase and quadrature components of the VLF-EM signal were recorded at two transmitter frequencies (24.0 and 24.9 kHz) along with the total magnetic field. The Karous-Hjelt current density pseudo section delineates the subsurface faults at depths between 10 and 40 m which is substantiated by the Hartley spectral depth from the total magnetic field. The stacked profiles of the line joining the Fraser peaks have brought out two plausible trends/directions of faults. Furthermore, the in situ XRF measurements that were carried out in the field are unable to establish any possible uranium enrichment within the salt-tectonic system, and there seems to be no evidence for an enrichment of uranium.

Keywords

Uranium • Salt tectonics • Fault • Total magnetic field • Very low-frequency electromagnetic signals

1 Introduction

Exploration of radioactive minerals initially involves the identification of a favorable geological setting, followed by geochemical/radiometric surveys and then geophysical techniques to trace structural traps or near-surface anomalies at shallow depth. A geochemical survey based on portable X-ray fluorescence (XRF) device helps to identify target/pathfinder elements or radioactive minerals (Brouwer 2006); however, gamma-ray spectroscopic measurements can yield the concentrations of uranium, thorium, and potassium. Among all the geophysical methods, magnetic survey is a more widespread technique in mineral exploration in addition to conventional geological and structural mapping, because it is simple, rapid, and cost-effective. Integration of geophysical techniques such as very low-frequency electromagnetic (VLF-EM) and magnetic methods was proven to be successful in the case of uranium exploration in other parts of the world including India (Ramesh Babu et al. 2007; Sundararajan et al. 2011). An enrichment of radiogenic elements in the shales of the Tertiary Andhur formation in Oman at depths between 800 and 1000 m is evident (regionally, gamma radiation is highest in the South of Oman, where intense faulting is connected to uranium anomalies; Pracejus et al. 2018), and the shales have been broken and tilted by salt tectonics (Forbes et al. 2010). Uranium transport in brines has been documented in various publications (Richard et al. 2013) which we tried to verify in the present study.

S. Narasimman (✉) · E. Alaeddin · B. Pracejus · T. Al-Hosni
Department of Earth Science, Sultan Qaboos University, Post Box 36 Muscat, 123, Sultanate of Oman
e-mail: visvid12@squ.edu.om

M. Meghraoui et al. (eds.), *Advances in Geophysics, Tectonics and Petroleum Geosciences*, Advances in Science, Technology & Innovation, https://doi.org/10.1007/978-3-030-73026-0_80

2 Methods

Geophysical surveys employing a portable gamma-ray spectrometer, G-859 mining magnetometer, and a VLF-EM receiver in addition to XRF were carried out along five traverses about 25 m apart at a measurement interval of 10 m in the study area. The gamma-ray spectrometer has recorded very weak concentrations of uranium/thorium and potassium as low as less than 4 ppm. The XRF also has shown a similar trend, however, recorded the elements such as CI, S, Ca, and SI in %, as shown in Fig. 1. On the other hand, the total magnetic field along these traverses reveals a subsurface fault that is trending SE-SW. Further, the interpretation of the magnetic data based on Euler deconvolution (ED and Hartley spectral analysis broadly agree well (Fig. 2). The computed amplitude of the analytical signal of total magnetic field delineates boundaries of geologic structures in the vicinity of the subsurface targets.

The very low-frequency electromagnetic (VLF-EM) technique is well established for rapid mapping of structures and veins as well as broader buried conductive targets. Though the in-phase and quadrature components were recorded at two different transmitter frequencies (24.0 and 24.9 kHz), and only the measured in-phase component was subjected to Fraser and Hjelt filtering in order to decipher the nature of subsurface conductors/structures. The computed Fraser filtered responses of the in-phase components yield high positive values which correspond to subsurface conductors/structures. Further, the Fraser and Hjelt filtering (current density maps) responses facilitate the estimation of the depth to subsurface conductors from VLF-EM signals. The line joining the Fraser peaks shown in Fig. 3 reveals the direction/trend of the subsurface fault.

3 Results

The gamma-ray spectroscopic measurements as well as XRF have not shown a considerable concentration of radiogenic elements like uranium, thorium, and potassium; however, the total magnetic field and the VLF-EM signals have established the depth to the subsurface mineralized fault structures in the range 10–60 m (Table 1) by different tools and techniques which is also substantiated by depth obtained from VLF-EM signals.

4 Discussion

Building on the hypothesis of fault-related mobility and mineralization of uranium, this site with salt tectonics had been selected for geo-investigation. All uranium anomalies/mineralization examined in southwestern Dhofar were fault related, however, no evidence of strong uranium anomalies. In the case of VLF-EM signals, the interpretation is confined only to in-phase component since it is sensitive to metal or good conductive bodies, while the quadrature response is sensitive to the variation of the earth electrical properties (Jeng et al. 2007).

5 Conclusions

The geochemical XRF analysis, as well as in-situ measurements, do not reveal any anomalous uranium enrichment and, hence, rule out the presence of any base metal or uranium mineralization in this location. On the other hand, strong magnetic anomalies, as well as the amplitude of the

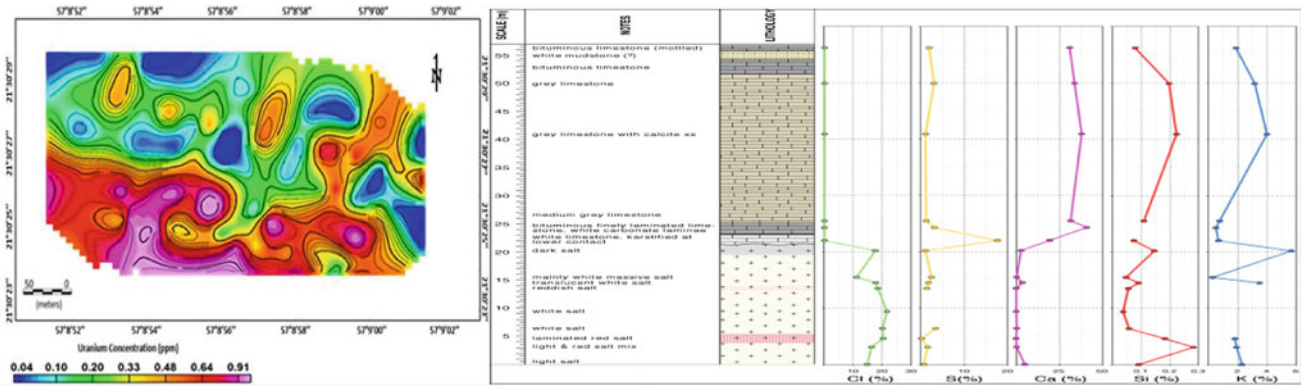

Fig. 1 Uranium concentration by gamma-ray spectrometer (left) and the XRF recorded in the field (right)

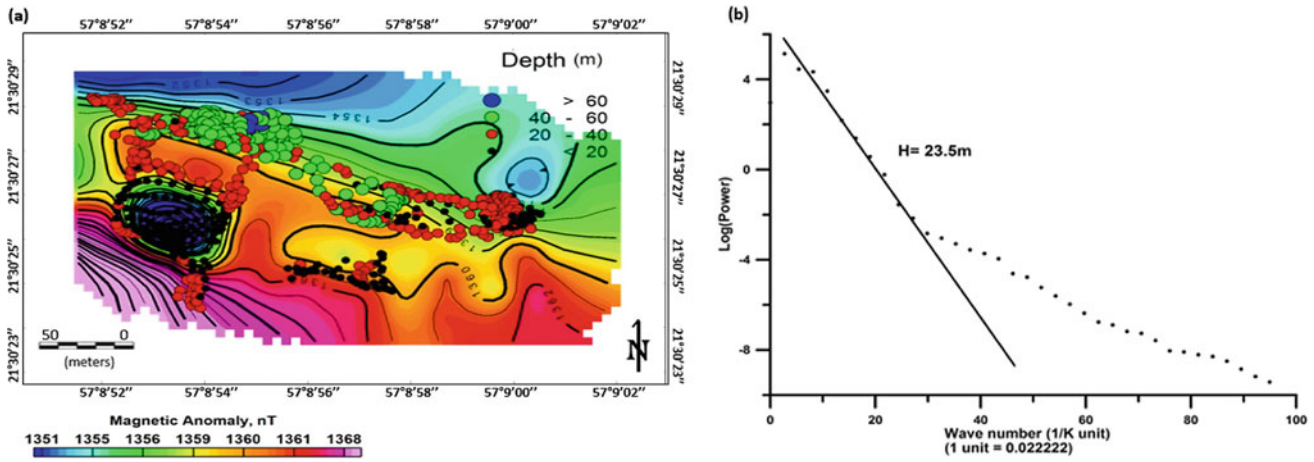

Fig. 2 Depth to subsurface fault structures from total magnetic field by (L) Euler deconvolution and (R) Hartley spectral analysis

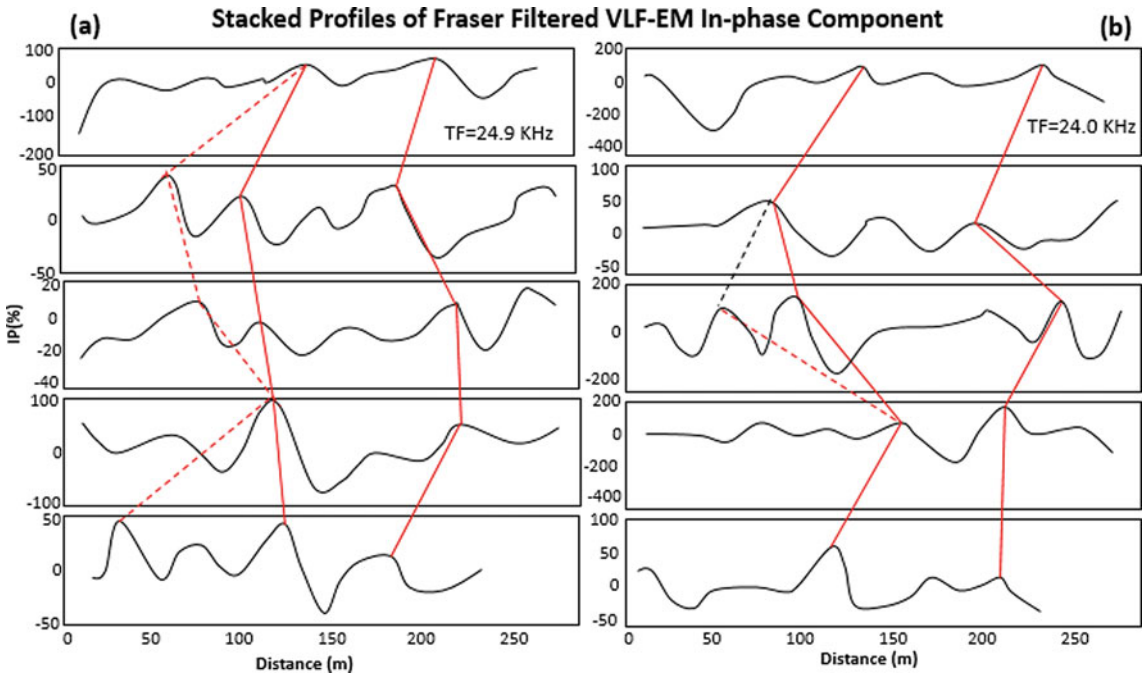

Fig. 3 Trend of the subsurface fault structures based on line joining (in red) the Fraser peaks of the in-phase component of VLF-EM signals at transmitter frequencies 24.9 and 24.0 kHz

Table 1 Estimated depths to subsurface fault by various techniques

Iinterpreted depths in m by	VLF-EM	Magnetics
Euler deconvolution	–	20–60
Hartley spectral analysis	–	23.5
Fraser filtering	–	–
Hjelt filtering	10–40	–

analytical signal, clearly indicates the presence of subsurface salt. The Fraser filtered VLF-EM signal elucidate the probable trend of the subsurface fault at an estimated depth range of 10–40 m derived from different methods are broadly consistent.

References

Brouwer, P.: Theory of XRF. PANalytical BV, Almelo, Netherlands (2006)

Forbes, G.A., Jansen, H.S.M., Schreurs, J.: Lexicon of Oman subsurface stratigraphy. Reference guide to the stratigraphy of Oman's Hydrocarbon Basins. Geoarabia Special Publ. Gulf Petrolink Bahrain **5**, 371 (2010)

Jeng, Y., Lin, M.J., Chen, C.S., Wang, Y.H.: Noise reduction and data recovery for a VLF-EM survey using a nonlinear decomposition method. Geophysics **72**(5), F223–F235 (2007)

Pracejus, B., Sundararajan, N., Al-Khirbash, S., Al-Hosni, T., Ebrahimi, A., Al-Bulushi, S., Al-Maashani, M.: Aspects of U-Th fractionation in tertiary limestones and calcretes of Dhofar, southern Oman. Chem. Erde **78**(4), 479–489 (2018)

Ramesh Babu, V., Ram, S., Sundararajan, N.: Modeling and inversion of magnetic and VLF-EM data with an application to basement fractures: a case study from Raigarh, India. Geophysics **72**(5), B133–B140 (2007)

Richard, A., Boulvais, P., Mercadier, J., Boiron, M.C., Cathelineau, M., Cuney, M., France-Lanord, C.: From evaporated seawater to uranium-mineralizing brines: isotopic and trace element study of quartz–dolomite veins in the Athabasca system. Geochim. Cosmochim. Acta **113**, 38–59 (2013)

Sundararajan, N., Babu, V.R., Chaturvedi, A.K.: Detection of basement fractures favourable to uranium mineralization from VLF-EM signals. J. Geophys. Eng. **8**(2), 330 (2011)

Volume of Clay Estimation Using Artificial Neural Network Case Study: Berkine Basin Southern Algeria

Ouafi Ameur-Zaimeche, Rabah Kechiched, Rima Bouhafs, Abdelnacer Mammeri, Abderrazak Hamdat, and Aziez Zeddouri

Abstract

The estimation of the volume of clay is one of the most important parameters in the characterization of shaly sand reservoirs, by its impact on the estimation of reserves and the production. The estimation of the volume of clay accurately will allow a better determination of the volume of the matrix which will reduce the uncertainty in the evaluation of the reservoir formation through a better estimation of the formation water saturation and the effective porosity for conventional reservoirs. For this reason, the target of this study is to find an efficient solution of this problem in the reservoir of Berkine basin by the application of artificial intelligence methods on logging data: gamma ray, thorium, uranium, potassium, density, and coupled with the volume of clay measured by X-ray diffraction. Due to the topology (5-11-1) of the model multilayer perceptron neural network adopted to estimate the volume of clay and to validate by numerical performance indices between the simulated values and the observed values (R = 0.99, RMSE = 0.0003, and MAE = 0.0001), it was possible to estimate the missing clay volume of 1390 points which corresponds to the 200 m in the well W_A, and this technique allows the gain of cost and time in the laboratory.

Keywords

Volume of clay • Berkine • Artificial neural network • Logging • X-ray diffraction

1 Introduction

The characterization of shaly sand reservoirs is known by its great heterogeneity and among the most important parameters is the estimation of clay volume, and the best source for estimating of volume clay is the results of X-ray diffraction on the cores; however, the recovery of the cores is not always complete due to geological and technical problems during coring operation and the cost and time of the laboratory analysis. Scientists are still looking for techniques for estimating clay volumes (Chegrouche 2016; Jozanikohan et al. 2015; Fertl and Chilingarian 1990; Dresser Atlas 1982; Quirein et al. 1982; Rukhovest and Fertl 1981) with insufficient logging and petrophysical parameters to have the accuracy of the results; they have sought other methods of artificial intelligence that respond to complexity and nonlinearity of relationships between logging and petrophysics. In the purpose study, we applied artificial neural networks, which are a technique inspired by biological neurons to correlate with clay volume (XRD) and logging parameters.

2 Materials and Methods

2.1 Empirical Equations

Empirical equations for estimating the amount of clay from the natural environment, log gamma rays and its spectral component (potassium, thorium and uranium), density, sonic, neutron and resistive diagraph data, respectively, are as follows.

O. Ameur-Zaimeche (✉) · R. Kechiched · A. Zeddouri
Laboratoire des Réservoirs Souterrains: Pétroliers, Gaziers et Aquifères, Université Kasdi Merbah Ouargla, 30000 Ouargla, Algérie
e-mail: ameurzaimeche.ouafi@univ-ouargla.dz

R. Bouhafs · A. Mammeri
Faculté des Hydrocarbures, des Energies Renouvelables et des Sciences de la Terre et de l'Univers, Université Kasdi Merbah Ouargla, 30000 Ouargla, Algérie

A. Hamdat
Enspgroup, BP 83, Hassi-Messaoud, 30500, Algérie

M. Meghraoui et al. (eds.), *Advances in Geophysics, Tectonics and Petroleum Geosciences*,
Advances in Science, Technology & Innovation, https://doi.org/10.1007/978-3-030-73026-0_81

$$I_A = \frac{\mathrm{GR_{log}} - \mathrm{GR_{min}}}{\mathrm{GR_{max}} - \mathrm{GR_{min}}} \quad (1)$$

$$V_{\mathrm{cl}} = I_A \times \left(\frac{\rho b}{\rho b_{\mathrm{cl}}}\right)^3 \quad (2)$$

$$V_{\mathrm{cl}} = \frac{\varphi_{\mathrm{DT}}}{\varphi_{\mathrm{DTcl}}} \quad (3)$$

$$V_{\mathrm{cl}} = \frac{\varphi_N}{\varphi_{N\mathrm{cl}}} \quad (4)$$

$$V_{\mathrm{cl}} = \left(\frac{Rcl}{Rt} \times \frac{R\lim - Rt}{R\lim - Rcl}\right)^{\frac{1}{1.5}} \quad (5)$$

$\boldsymbol{GR_{log}}$: gamma ray read in log, $\boldsymbol{GR_{min}}$: gamma ray minimum, $\boldsymbol{GR_{max}}$ = gamma ray maximum, $\boldsymbol{V_{cl}}$: volume of clay, $\boldsymbol{IA}$: the gradient of gamma ray, $\boldsymbol{\rho b}$: bulk density, $\boldsymbol{\rho b_{cl}}$: density of clay, $\boldsymbol{\Phi_{DT}}$: porosity sonic, $\boldsymbol{\Phi_{DTcl}}$: porosity sonic of the clay, $\boldsymbol{\Phi_N}$: porosity neutron, $\boldsymbol{\Phi_{Ncl}}$: porosity neutron of clay, $\mathbf{R_{cl}}$: resistivity of clay, $\boldsymbol{R_t}$: resistivity true, and $\mathbf{R_{lim}}$: resistivity limited.

2.2 Artificial Neural Network

Over the years, the nonlinear models based on artificial intelligence (AI) approaches have been largely applied in several areas of scientific research, and the artificial neural network (ANN) is the most important among them. By definition, an ANN is nonlinear mathematical model inspired from the function of the human brain and considered as an information-processing system composed of many processing element arranged in several parallel layer (Fausett 1994; Haykin 1999).

In this study, the multilayer perceptron neural network was trained with the Levenberg–Marquardt algorithm. The database is composed in 1390 observations, divided 70% training, 15% validation, and 15% test.

2.3 Performances Criteria

In the present study, the performances of the models were evaluated using the coefficient of correlation (R), the mean absolute error (MAE), and the root mean squared error (RMSE).

$$R = \left[\frac{\frac{1}{N}\sum (O_i - O_m)(P_i - P_m)}{\sqrt{\frac{1}{N}\sum_{i=1}^{n} (O_i - O_m)^2}\sqrt{\frac{1}{N}\sum_{i=1}^{n} (P_i - P_m)^2}}\right] \quad (6)$$

$$\mathrm{MAE} = \frac{1}{N}\sum_{i=1}^{N} |O_i - P_i| \quad (7)$$

$$\mathrm{RMSE} = \sqrt{\frac{1}{N}\sum\nolimits_{i=1}^{N} (O_i - P_i)^2} \quad (8)$$

where N is the number of data points, O_i is the measured, and P_i is the corresponding model prediction. O_m and P_m are the average values of O_i and P_i.

3 Results and Discussion

The clay curve calculated using the empirical equation (GR) from (Eq. 1) does not correspond to the clay volume curve measured by XRD. However, there are intersections between (clay volume measured and calculated) for the same rate, and it is proportional to the percentage of clay and the types of clay (low radioactivity clay; illite, high radioactivity: chlorite).

A negative correlation ($R = -0.72$) between the clay volume was measured and calculated by GR and the large error RMSE and MAE (0.60, 0. 51) between the empirical and XRD methods because of the presence of radioactive clays and radioactivity-leached clays (illite) (Chegrouche 2016); then, this method is very limited in the estimation of the amount of clay in shaly sand reservoirs.

4 Discussion

The amount of clay calculated from gamma ray (Eq. 1) shows that there is a big difference between two graphs in which one can neglect a large reservoir (exceeds the permissible content of clay in the reservoir (cutoff 35%), and it is only the amount of clay obtained by the gamma ray without taking XRD data into consideration (Fig. 1).

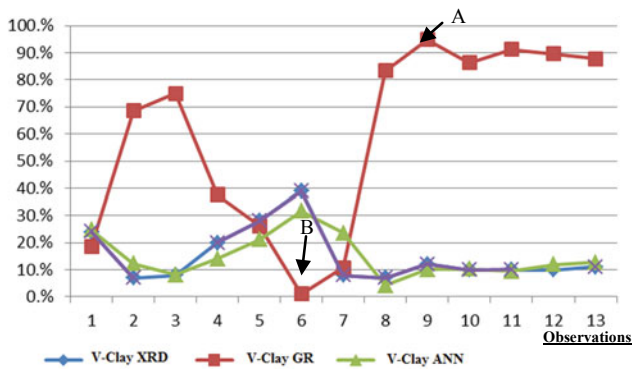

Fig. 1 Comparison between the volume of clay calculated (GR and ANN method) with measured (XRD)

Showing (A) corresponds to the depth: 4676 m, the formation gives a high radioactivity volume of clay gamma ray: 94.8% on the other hand, the analysis of clay volume by XRD (10%) chlorite type clay, 90% quartz; then a small amount of chlorite (10%) distorts the calculation of clay volume by gamma ray. Showing (B) corresponds to the depth 4599 m, volume of XRD clay (40%) and the gamma ray (1%), a great contradiction is linked to the presence of low radioactivity-leached clays (illite).

This method is mostly used to calculate clay volume but with XRD joint-trimming it is very limited and inconvenient: the confusion between reservoirs specific to high radioactivity (plagioclases) and clays leached has low radioactivity (illite) and has false properties and false reserves. To select the optimal transfer function for the network, several types of output transfer functions, including log-sigmoid, sigmoid, triangular base, linear saturation, linear, symmetric hard limit, and hard limit, were tested on a certain network with a fixed topology (5 11-1).

5 Conclusion

The application of artificial neural networks allowed us to define 200 m of volume of clay not measured in the laboratory; this method was used more to correct interference related to contradictions encountered with conventional techniques, or the formation gives a high radioactivity volume of gamma ray clay: 94.8% on the other hand, the analysis of clay volume by XRD (10%) type of clay chlorite, 90% quartz, so a small amount of chlorite (10%) distorts gamma ray's calculation of clay volume, the presence of low-level radioactive clays (illite) and the volume of XRD clay (40%) and GR (1%). This method (GR) is mostly used to calculate the amount of clay, but with the XRD comparison, the confusion between high radioactivity reservoirs (plagioclases) and low radioactivity clays (illite), false properties, false reserves is very limited. The volume was estimated using the topology (5-11-1) of neuron network model adopted to estimate clay volume and validated by numerical performance indices between simulated and observed values ($R = 0.99$, RMSE = 0.0003, and MAE = 0.0001).

Precisely estimating clay volume will allow for better determination of matrix volume (V-matrix), which will reduce uncertainty in the assessment of reservoir formation through better estimation of formation of water saturation (S_w) and actual porosity (φ) for conventional reservoirs.

References

Chegrouche, F.: Procédé pour l'estimation du volume d'argile (Vclay) à partir de la densité de formation, de la porosité et des vitesses acoustiques dans les réservoirs argileux-gréseux. Organisation Mondiale de la Propriété Intellectuelle Bureau international (2016)

Dresser Atlas: Well logging and interpretation techniques. Dresser Atlas Industries, Houston, TX., USA (1982)

Fausett, F.: Fundamentals of Neural Networks: Architectures, Algorithms and Applications. Prentice-Hall, Englewood Cliffs (1994)

Fertl, W.H., Chilingarian, G.V.: Type and distribution modes of clay minerals from well logging data. J. Petrol. Sci. Eng. **3**, 321–332 (1990)

Haykin, S.: Neural Networks: A Comprehensive Foundation, 2nd edn. Prentice Hall, Hamilton (1999)

Jozanikohan, G., Norouzi, G.H., Sahabi, F., et al.: The application of multilayer perceptron neural network in volume of clay estimation: case study of Shurijeh gas reservoir, Northeastern Iran. J. Nat. Gas Sci. Eng. (2015)

Quirein, J.A., Gardner, J.S., Watson, J.T.: Combined natural gamma-ray spectral/litho-density measurements applied to complex lithology. In: 57th Annual Fall Technical Conference and Exhibit, SPE of AIME, New Orleans, USA, Paper SPE 11143 (1982)

Rukhovest, N., Fertl, W.H.: Digital shaly sand analysis based on Waxman-Smith model and log-derived clay typing. In: Trans. SAID/SPWLA 7th European Annual Logging Symposium, pp. 21–37 (1981)

Establishing an Inverse Dependence Between Hawaiian Volcanoes Through Change-Point Detection

Moinak Bhaduri

Abstract

Hawaiian volcanoes Kilauea and Mauna Loa have drawn the attention of researchers since quite some time, and numerous qualitative theories abound hinting at a possible inverse relationship between the two. The present work attempts to address this issue by adopting a more mathematical approach. Several metrics quantifying the distance between two probability distributions are surveyed, and novel change detection techniques are subsequently proposed. The method helps one pinpoint the position in time around which a change corrupts an otherwise stable point process. The existence of such an inverse relationship is established through the proximity of generated change points from the two competing volcanoes. Kilauea has grown exceedingly restless in the recent decade, and the analyses conducted here will predict a safe place to relocate its inhabitants. The method described is general enough to be applicable to other geological hazards such as earthquakes.

Keywords

Hawaiian volcanoes • Point process • Repairable systems • Change-point detection • Non-stationarity

1 Introduction

In geology, computer science, stochastic processes, and industrial engineering, stationarity is often taken to imply a stable, predictable flow of events and non-stationarity; consequently, there is a departure from such a flow. Efficient detection and accurate estimation of such deviations are crucial in understanding the evolution of the governing dynamics. Pragmatic considerations include protecting human lives and property in the context of destructive processes such as earthquakes or hurricanes. Cumulative Sum (CUSUM) charting, the prevalent technique to weed out such non-stationarities, suffers from assumptions on a priori knowledge of the pre- and post-change process parameters and constructs such as time discretization. Surveying a variety of distance metrics, we propose several parametric and nonparametric alternatives that perform better under especially difficult detection scenarios. Simulations (both from deterministic and mixed inter-event time densities), Receiver Operating Characteristic (ROC) curve analyses, and the estimated time of change distributions enable us to track the ideal detection candidate as the non-stationarity environment changes. Incidentally, this study sheds light on the inverse nature of dependence between the Hawaiian volcanoes Kilauea and Mauna Loa and demonstrates how inhabitants of the now-restless Kilauea may be relocated to Mauna Loa to minimize the loss of lives and moving costs.

2 Methodology

Future decisions and plans are made based on the assumptions of an underlying model. The parameters of the underlying statistical model change, and enacting the current plan can cause human and capital loss. In 1913, there was strong statistical evidence suggesting that the rate of a mining accident in the UK was increasing. However, the UK government failed to incorporate new responses which resulted in a mining accident claiming the lives of 439 men and boys. Detecting and estimating the changes in parameters of an underlying model are known formally as the change-point detection and estimation problem. It is cornered with detecting and estimating points in time in which the model for random process changes.

M. Bhaduri (✉)
Department of Mathematical Sciences, Bentley University, 175 Forest St, 02453 Waltham, MA, USA
e-mail: mbhaduri@bentley.edu

M. Meghraoui et al. (eds.), *Advances in Geophysics, Tectonics and Petroleum Geosciences*, Advances in Science, Technology & Innovation, https://doi.org/10.1007/978-3-030-73026-0_82

The most common way to detect such changes is through CUSUM charts (details to be provided in the enlarged version of the paper), where if one of the incoming points falls outside the horizontal bands, the process is thought to have changed. This method, however, suffers from the drawbacks mentioned in the previous section. We thus propose and collect several alternate ways to quantify the distance between the "pre-change" and "post-change" distribution. These alternatives are shown below.

Exp (Ross 2014):

$$M_{k,n} = -2\log(L_0/L_1)$$

Adjusted Exp (Ross2014):

$$M^c_{k,n} = M_{k,n}/E\big(M_{k,n}\big)$$

Mann–Whitney (Hawkins and Deng 2010):

$$U_{k,n} = \sum_i \sum_j \mathrm{sgn}\big(X_i - X_j\big)$$

Mood (Ross et al. 2011):

$$M = \sum_{X_i} \left(\sum_{i \neq j} I(X_i > X_j) - (n + 1/2) \right)^2$$

Lepage (Ross et al.2011):

$$L = U^2 + M^2$$

Kolmogorov–Smirnov (Ross and Adams2012):

$$M_{k,n} = \sup_x |F_{S1}(x) - F_{S2}(x)|$$

Cramer–von Mises (Ross and Adams 2012):

$$\int_{-\infty}^{\infty} |F_{S1}(x) - F_{S_2}(x)| \mathrm{d}F_t(x)$$

E-divergence (Matteson and James 2014):

$$D(X, Y, \alpha) = \int_{R^d} |\phi_X(t) - \phi_Y(t)|^2 (2\pi^{d/2}\Gamma(1 - \alpha/2)|t|^{d+\alpha})/(\alpha 2^\alpha \Gamma((d+\alpha)/2)))\mathrm{d}t$$

For our simulation results to follow, we resorted to two ways we bring non-stationarity in our examples. *Active corruption* occurs when the post-change distribution differs from the pre-change one (to destroy stationarity), and more importantly, it differs in a deterministic way, i.e., the post-change probability distribution (of inter-event times, say) is chosen with absolute certainty. When this is not the case, especially if the post-change density is a non-trivial probabilistic mixture to two or more different fixed densities, *weak corruption* is said to occur. Weak corruptions are, therefore, harder to detect. Owing to space constraints, we refrain from explaining the notations and direct interested readers to Bhaduri (2018) for a thorough description of each.

3 Results

In the analyses to follow, stationary and an equal number of non-stationary cases were generated, and the classification methods described previously were employed to detect these properties. The probability of Type-I error was set at 5%. The mathematical proofs, details, and results are, for now, kept at a minimum. Those will be supplied at a later stage, if and when required. Figure 1 describes how at least one of the newer alternatives comes closer to the actual time of change (the red horizontal line represents the real change point in the boxplots) than the established CUSUM method, regardless of the corruption version implemented—strong or weak.

3.1 Simulation Results

The third option using the Mood statistic, for instance, depends only on the exceedances and not so much on the times of occurrence, providing weaker detection performances. We have constructed a table (to be supplied in the enlarged version of the paper) that collects the best performers under different types of non-stationarities.

3.2 Volcanic Change-Point Detection

Our extensive literature review on volcanic eruption had to be removed in favor of space but will be included in the enlarged version. Eruption data related to dates and lava volumes were collected from the United States Geological Survey (USGS) and the Smithsonian Institute's Global Volcanism Program, spanning the period from 1750 till the present day.

The cumulative eruption times of both volcanoes were next plotted to generate Fig. 2. Here, each spike or step represents the point in time an eruption occurred. The aptest distance metric (for each volcano, details in the graph) was then employed to extract the best estimate of a change point. It is interesting to note that both volcanoes generate change points around similar points in time. As an example, Mauna Loa (represented by the red curve) grew more active around a global time of 50,000 units, with Kilauea becoming less active (i.e., more dormant) around the same time.

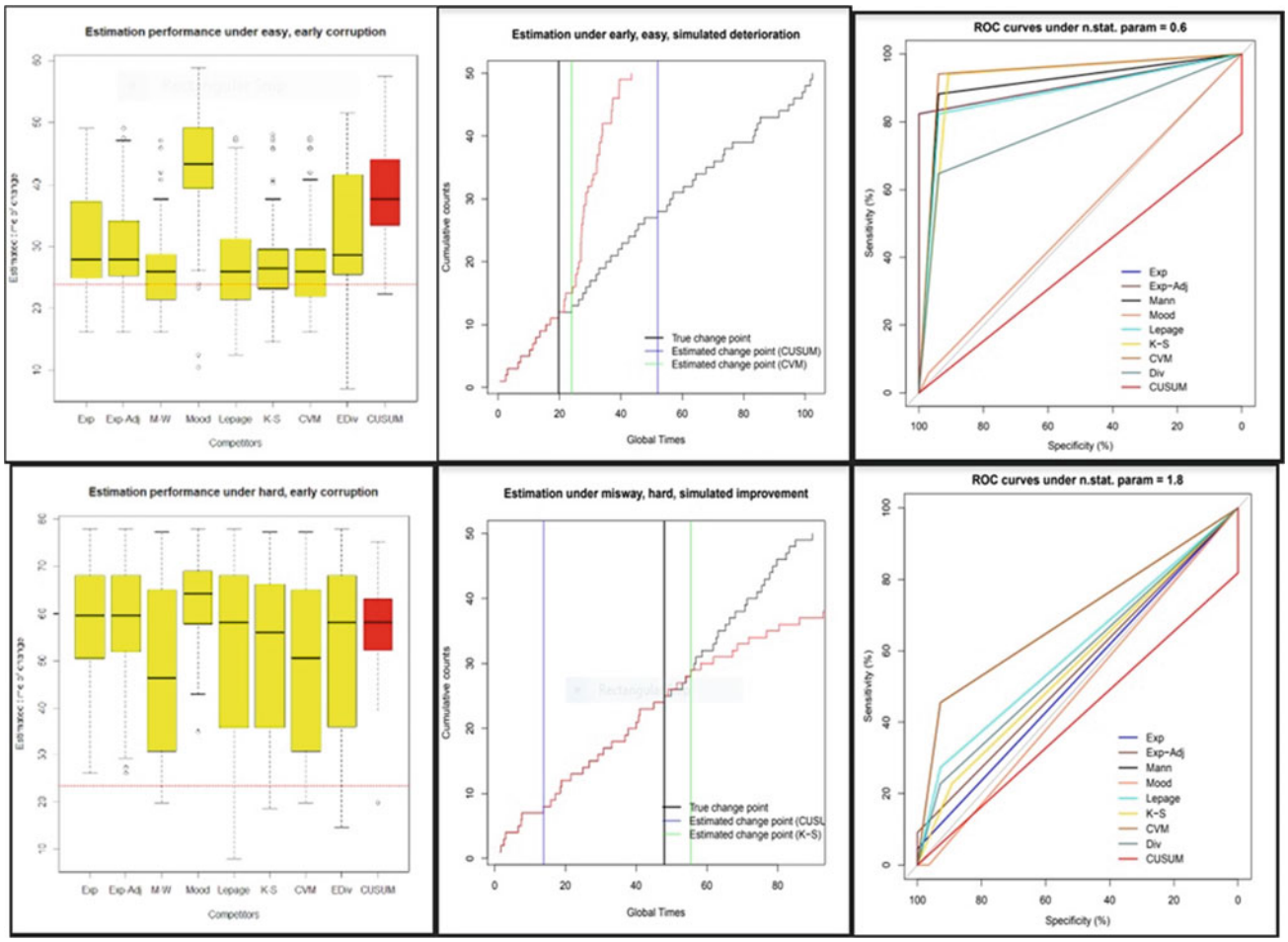

Fig. 1 Superiority of at least one of the recent proposals under strong corruption

This proximity provides credence to their dependence, and the inverse relationship is established through the difference in slopes and the alternate red–black, black–red band patterns among the vertical lines representing these change points, in a spirit similar to the following: if there is a finite amount of food at a given time with two diners at the table, then if one starts to eat more, the other (owing to the finiteness of the food) must eat less. The two volcanoes therefore seem to be competing for the same magma reservoir.

4 Discussion and Conclusion

Noting the drawbacks of CUSUM charting, this work takes stock of a host of statistics, both parametric and nonparametric, and examines their applicability under a wide array of change scenarios. To replicate non-homogeneous environments, we have conducted extensive simulations, both under the deteriorating and improving framework, with the changes placed early midway, and late into the process. To invite further intricacies, within each category, we have generated easily identifiable non-stationarities, when the corrupted parameters are incredibly different from the stable parameters, and difficult-to-identify non-stationarities when they are not. The established CUSUM and our proposals were subsequently employed to address two crucial aspects of instability research: detection—investigating whether a change happened at all, and estimation—guessing the exact time of change, in case it did. This rewarding exercise revealed that in every possible corrupted scenario, at least one of our proposals outperforms CUSUM with regard to both aspects mentioned previously. Large areas under ROC curves imply efficient detection, and distributions for the estimated change times hovering around the actual change suggest accurate estimation. We have constructed a recommendation table, summarizing the apt proposals, for the ease of applicability and the benefit of practitioners. Weak corruptions were then considered, with the non-stationary piece construed as a probabilistic mixture of an improving and a deteriorating system, and the supremacy over CUSUM was observed to be retained.

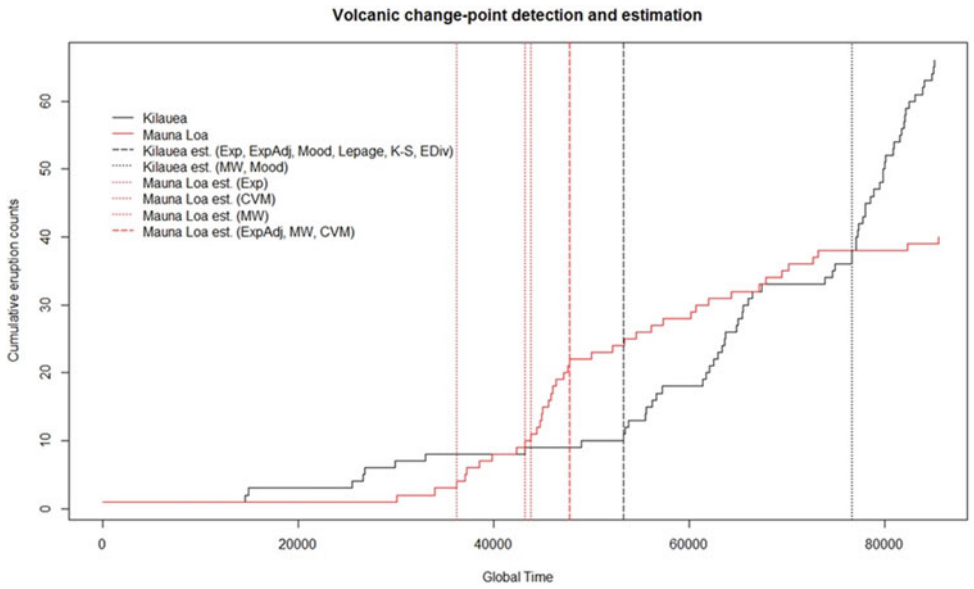

Fig. 2 Close proximity of Kilauea and Mauna Loa change points

Attention was then turned to the harrowing ordeal inhabitants of the Hawaiian volcano, Kilauea, are subject to, and the confidence gained through the simulation studies was channelized both to fuel and resolve an ongoing geological debate—whether Kilauea and its close neighbor Mauna Loa are inversely related. The proximity of the estimated change points of these neighbors provides an answer in the affirmative. Such statistical validation should aid government authorities to relocate Kilauea inhabitants close to Mauna Loa. Lives may be saved, and moving costs may be minimized, owing to the geographical closeness.

This research is still in its infancy, but with its promising prospects, the road ahead looks enticing. Varotsos et al. (2011) introduced the notion of the natural time domain to extract hidden features of a time series through uncertainty reduction and accurate signal drawings. It will be interesting to see how the change detection algorithms will react once the time is measured this way. We are especially excited about ways of putting Bayesian priors on the number of mixture components involved, their biasing intensities, and corruption locations. The author's Ph.D. dissertation (Bhaduri 2018) offers the relevant intricacies. Average run length calculations may be carried out as well, and multiple changes may be detected simply by restarting the algorithm. Our proposals are not tethered to the suffocating CUSUM assumptions brought to the fore and provide better change estimates without paying a hefty price in terms of model complexity. Their computational simplicity and intuitive appeals should also help them find a way into every geologist's arsenal.

References

Bhaduri, M.: Bi-directional testing for change point detection in poisson processes. UNLV Theses, Dissertations, Professional Papers, and Capstones, 3217 (2018)

Hawkins, D.M., and Deng, Q. A.: Nonparametric Change-Point Control Chart. Journal of Quality Technology, 42(2):165-173. (2010)

Matteson, D.S., and James, N.A.: A Nonparametric Approach for Multiple Change Point Analysis of Multivariate Data. ArXiv e-prints. To appear in the Journal of the American Statistical Association, 1306.4933. (2013)

Ross, G.J.: Sequential Change Detection in the Presence of Unknown Parameters. Statistics and Computing, 24(6):1017-1030. (2014)

Ross, G.J., and Adams, N.M.: Two Nonparametric Control Charts for Detecting. Arbitrary Distribution Changes. Journal of Quality Technology, 44(12):102-116. (2012)

Ross, G.J., Tasoulis, D.K., and Adams, N.M.: Nonparametric Monitoring of Data. Streams for Changes in Location and Scale. Technometrics, 53(4):379-389. (2011)

Varotsos, P.A., Sarlis, N.V., Skordas, E.S.: Natural Time Analysis: The New View of Time. Precursory Seismic Electric Signals, Earthquakes and other Complex Time-Series. Springer, Berlin (2011)

Explore the Suitability of Rafah Coastal Aquifers for Sustainable Development Using Geophysics and Remote Sensing

Adel Kotb, Maysa Nabeh, and Alhussein Adham

Abstract

A time-lapse study involving geophysical and remote sensing measurements in 2003, 2013 and 2017 was conducted to investigate changes in groundwater content in the coastal aquifers in El-Arish area where the change rate of the groundwater content reflects the aquifer ability for the success or failure of future development plans. Two multi-temporal Landsat images were used, one from the Multispectral Landsat8-OLI and one from the Enhanced Thematic Mapper ETM+, to calculate the total cultivated land and it is annually changing during the relevant times. In addition to resistivity and TEM measurements to identify the aquifer(s) properties, all data were processed and interpreted. The inferred information from the processed satellite images showed the reclaimed land grows at a rate of about 11 km^2/yr without a noticeable change in the shoreline. Moreover, the geophysical modelling and interpretation elucidate, the study area contains three successive and separated coastal aquifers dunes, old beach, and Kurkar water-bearing layers. These aquifers can be utilized, but the dunes layer is less important than the others. The comparative aquifers thicknesses during the periods indicated were decreased by 4 m during the total period. Finally, the statistical relations between groundwater and cultivated land changing rates confirmed that the groundwater in the relevant area could be in line with the current rate of development process during the current century. Therefore, the Rafah Coastal Aquifers are suitable for sustainable development.

1 Introduction

North Sinai governorate is classified as a Hot spot area for unsustainable land management and water resources scarcity according to the United Nations Environmental Programme (UNEP 2008) and it is under Arid categories. In Arid regions, water resources management is a vital factor in any developmental activities (Elewa et al. 2014), and the majority of usable freshwater on the earth is groundwater (Duda 2017). The agriculture activates growth up before the last decade and still and many authors studied the coastal aquifer for different uses like (Barseem 2016; Abdelaziz and Bakr 2012), but there are no recent research papers that discuss the change in the coastal aquifer with time and its relation with rising the land reclamation. Hence, our study mainly focused on calculating the changes in reclaimed areas and evaluating the main aquifer changes in Rafah-El-Arish area using remote sensing and resistivity methods. The area under study is located in North Sinai governorate within latitudes 31° 09′ and 31° 21′, and longitudes 34° 03′ and 34° 18′ E (Fig. 1).

Remote sensing techniques are deemed among the best solutions for detecting the environmental changes and exploring the new phenomena over the earth surface. Satellite remote sensing has benefit in all fields of earth sciences including the study of changes detection processes (Guneroglu 2015), and the assessment of shoreline change because of the repetitive, synoptic and multispectral coverages of the satellites (Alesheikh et al. 2007; Rao et al. 2009). Change detection is the use of remotely sensed imagery for the same region, acquired on at least two dates, to detect changes that occurred in the interval between the two dates. This approach has several advantages; it is not time-consuming, inexpensive to implement, broad ground coverage, and has the capability for repeat data acquisition and monitoring (Van and Binh 2008). In this study, change detection concerning the use of (LU/LC) has been used to detect threats to groundwater sites due to the expansion of

A. Kotb (✉) · M. Nabeh · A. Adham
Geology Department, Faculty of Science, Helwan University, Cairo, Egypt
e-mail: Adelkotb@Science.helwan.edu.eg

M. Meghraoui et al. (eds.), *Advances in Geophysics, Tectonics and Petroleum Geosciences*,
Advances in Science, Technology & Innovation, https://doi.org/10.1007/978-3-030-73026-0_83

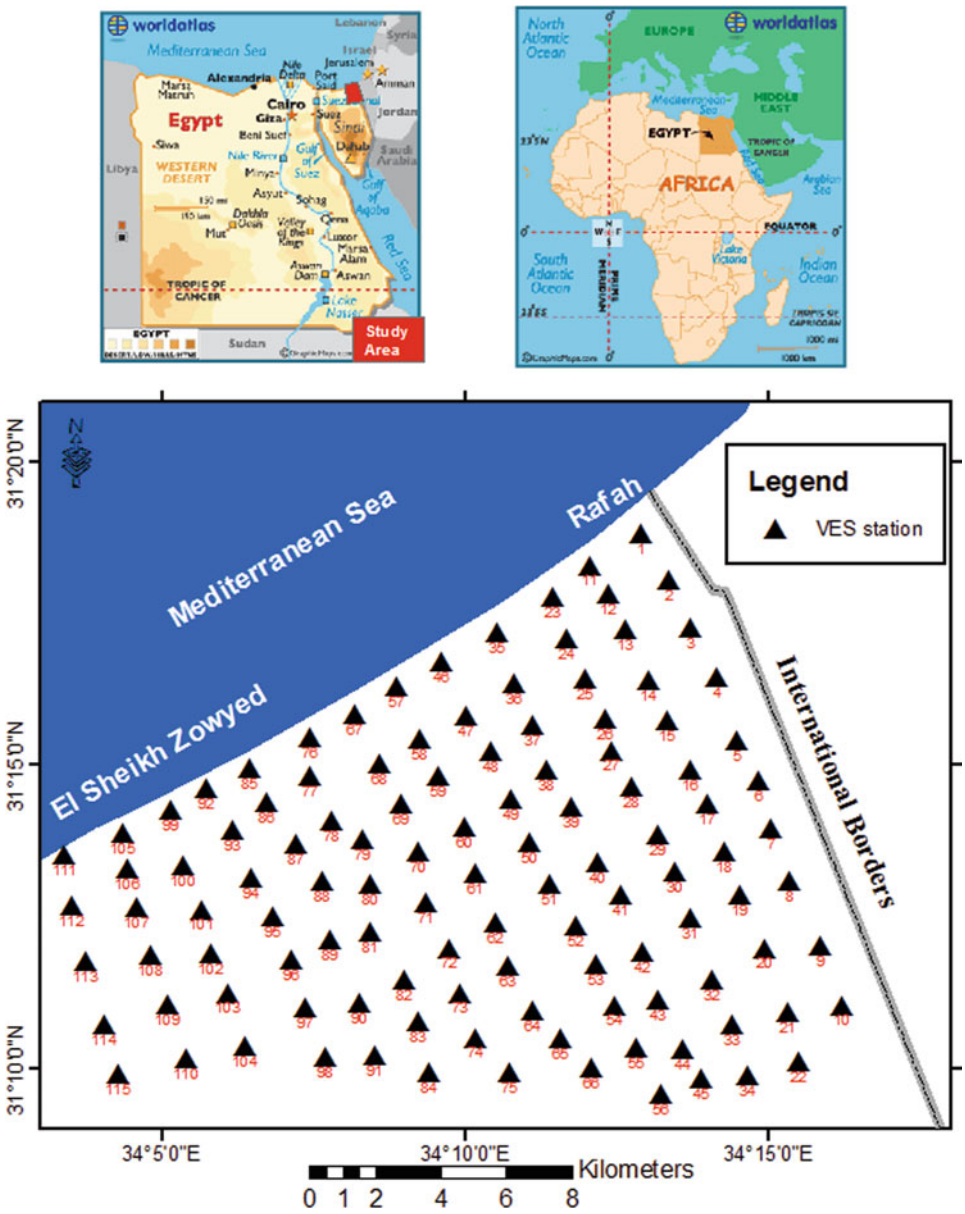

Fig. 1 Location map of the study area

human activities. Change detection also has the potential to provide accurate and time-wisely geospatial information describing changes in land use/land cover (LU/LC) (Guneroglu 2015; Herold et al. 2002; Foody 2003; Yuan et al. 2005). The Rafah coastal zone is mainly vulnerable to land-use changes resulting from increased cultivated area and development pressures. It is necessary to evaluate land cover/use changes to develop efficient management strategies.

The most commonly used methods for the search and evaluation of groundwater are resistivity and time-domain electromagnetic techniques. As the water is the most conducted material, and those techniques measurements attempt to identify the change in the resistivity values in all direction in the relevant area (Loke et al. 2013).

2 Methodology

In order to identify the environmental changes in the research area, two multi-temporal Landsat images (path 175, row 038) were used, one from the Multispectral Landsat8-OLI (dated 30 June 2017) and one from the Enhanced Thematic Mapper ETM+ (dated 20 October 2003 and 15 October 2013). The data were acquired from the GLOVIS and EARTH EXPLORER sites (http://earthexplorer.usgs.

gov/) and maintained by USGS. All image scenes are subjected to image processing using ENVI 5.1 and arc GIS10.3 software. The selected images, based on the criteria of Cloud, cover less than 10% of the data. The change in shoreline is not visible. To observe this, we needed a long and continuous set of data to detect the change in the shoreline. In the present study, a shoreline length of approximately 21 km was examined, and a series of image data is acquired at unequal intervals between 2003 and 2017, that is, covering 14 years. These series include three shorelines: 2003, 2013 and 2017. Photo-interpretation techniques have been used to extract shorelines in different dates then DSAS tool was applied to analyse shoreline change.

Simultaneously, the ground geophysical investigation using vertical electrical sounding and TEM methods were measured in the similar 115 locations to support the interpreted data of the two surveys.

All the 115 of VES with Schlumberger configuration and TEM soundings were measured by **Syscal Pro** and **AIE-2 TDEM**, respectively, processed, and inverted using forward modelling and known geological information in order to reach the final lithological and Geoelectrical model (Baawain et al. 2018). During these three seasons, we used **Res1D**, **IPI2win**, and **ZONDTEM1D** software. Furthermore, the interpreted data from remote sensing and ground geophysical survey were integrated to establish a new relationship between the development of reclamation processes and aquifer parameters to understand the behaviour of the coastal aquifers during the development process.

3 Results

Agriculture is the dominant sector in the economy of the Rafah area and accounts for approximately 80% of the total employment. The processing of satellite images indicated the total area for agriculture was 129.54 km^2 in 2003, approximately 191.81 km^2 in 2013 and about 281. 02 km^2 in 2017, with an average agriculture expansion by about 11 km^2/year (Fig. 2). With little or no change in the shoreline position (Fig. 3).

Modelling and analyses conducted on the resistivity and TEM measurements showed that the study area has three subterranean aquifers (Table 1). The upper aquifer is

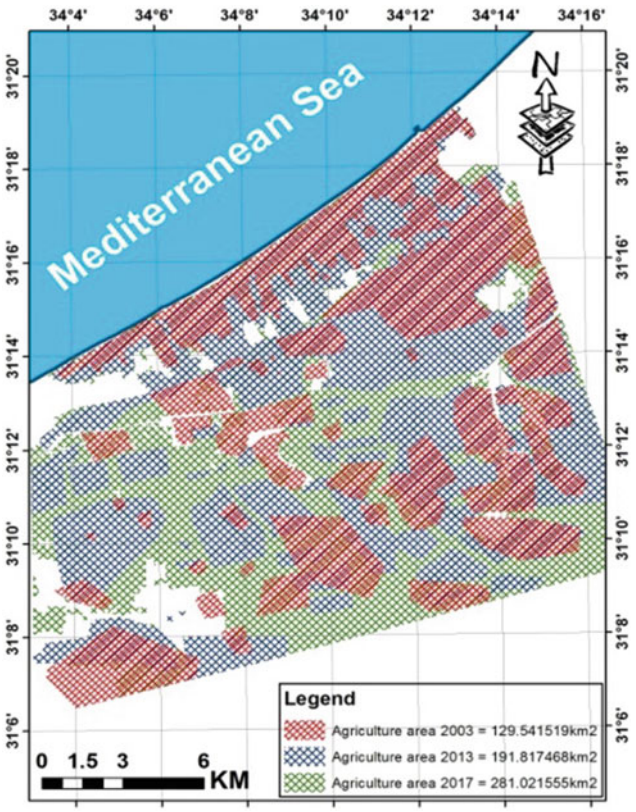

Fig. 2 The growth of cultivated land from 2003 to 2017

water-bearing dune of resistivity values ranging 1–281 Wm covered by dry sediments of the thickness of about 2 m and 30 m at the northern part near the sea and central part, respectively. The middle and lower aquifer represents old beach, and Kurkar formation, respectively, has resistivity values ranging 0–180 Wm. In 2003, the isopach map of dune indicated total thickness decreased southward from 11 m at the northern portion to 1 m at the central portion (Fig. 4a). The isopach map of the old beach indicated that the thickness of the middle aquifer increased from 15 m at the central part to 32 m southwards and northwards (Fig. 4 b). The thickness of Kurkar formation increased from 2 m at the northern portion to 31 m at the southern part (Fig. 4c). In 2013, the dune aquifer has thickness ranging from 1 to 10.5 m (Fig. 4d), the thickness of the middle aquifer increased from 15 m at the central portion to 13 m and 30 m at the northern and southern part, respectively (Fig. 4e),

Table 1 Aquifer parameters

Aquifer	Resistivity (Ωm)	Thickness in 2003 (m)	Thickness in 2013 (m)	Thickness in 2017 (m)
Upper (sand dune)	One -281	1–11	1–10.5	1–10.5
Middle (old beach)	Less than one to -180	15–32	13–30	11–29
Lower (Kurkar)	Less than one to 176	2–31	2–29	2–28

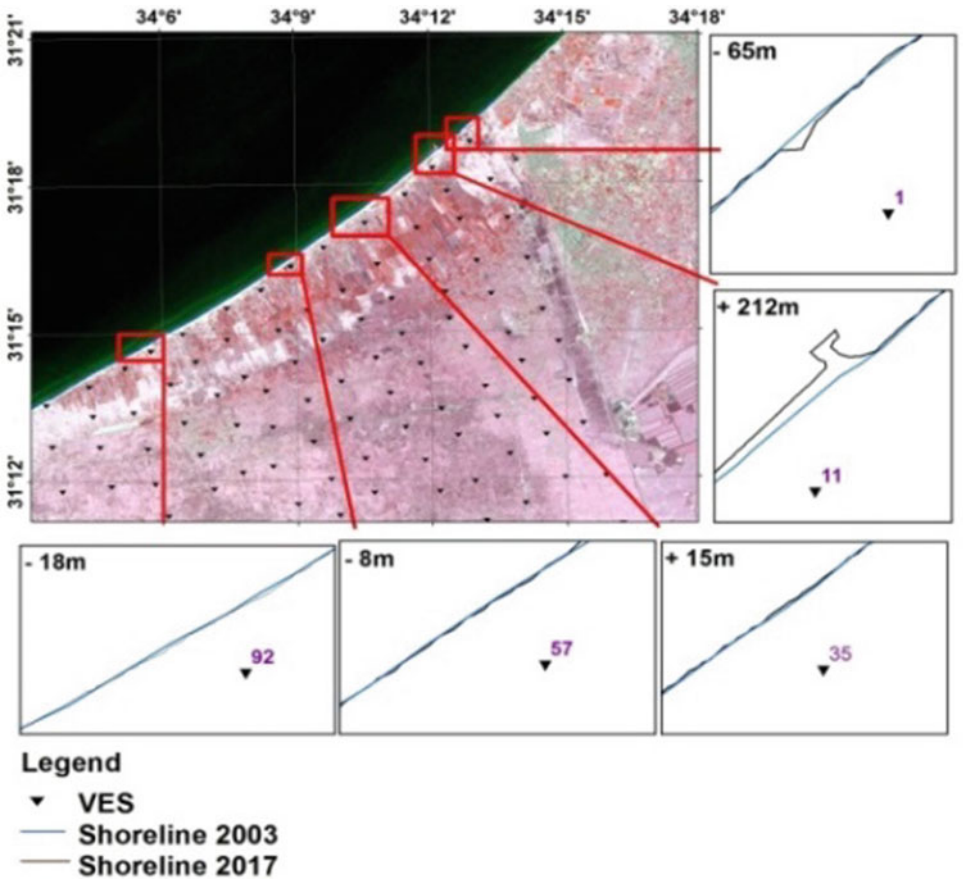

Fig. 3 Changes caused in the shore line from 2003 to 2017

while the most profound Kurkar formation represented by thickness ranging from 2 m at the northern portion to 29 m at the southern part (Fig. 4f). In 2017, the thickness of the upper aquifer ranging from 1 to 10.5 m (Fig. 4g), the thickness of old beach aquifer increased from 15 m at the central portion to 11 m and 28 m, respectively, at the northern and southern portion (Fig. 4h), while the lower aquifer thickness increasing southward from 11 to 28 m (Fig. 4i). These water-bearing layers are isolated by silty sand and clayey silt and the base layer represented by Marl and clay.

In order to evaluate the suitability of the aquifer for sustainable development, a linear empirical relationship between aquifer thickness and results obtained from the irrigated land describing the changes in aquifer thickness with time and growth in cultivated land was established (Fig. 5). The coefficient of correlation calculated using Pearson's equation indicated high and positive coefficient, 0.9994 and 0.9962.

4 Discussion

The stability of shoreline which inverted from remote sensing and general water table indicated that there is only a slight change in surface land quality as it is not affected by seawater salinity. Besides, there was a slight decrease in the thickness of the water-bearing dunes due to the scarcity of wells produced from it. The comparison between seasons in the years 2003, 2013, and 2017 for old beach and kurkar formations was shown, the thicknesses was wane by about two metres from one season to another as a reasonable relation to growth of reclaimed areas, and the total thicknesses of the water-bearing aquifers decreased by 4 m from 2003 till 2017 which equivalent to water table drawdown by rate about 0.28 m per year. Furthermore, the aquifers productivity period under the current conditions became available and predictable from the statistical relations. The same rate still causes the time needed to discharge the total amount of water in the primary aquifer, in case of the rising of cultivated land. According to the empirical relations, the time needed to discharge the total amount of water in the middle aquifer is only 110 years with cultivating the total area about 1418 km^2.

5 Conclusions

Groundwater represents the unique source of water in North Sinai. Furthermore, the main development projects are agricultural. Therefore, these time-lapse studies were needed

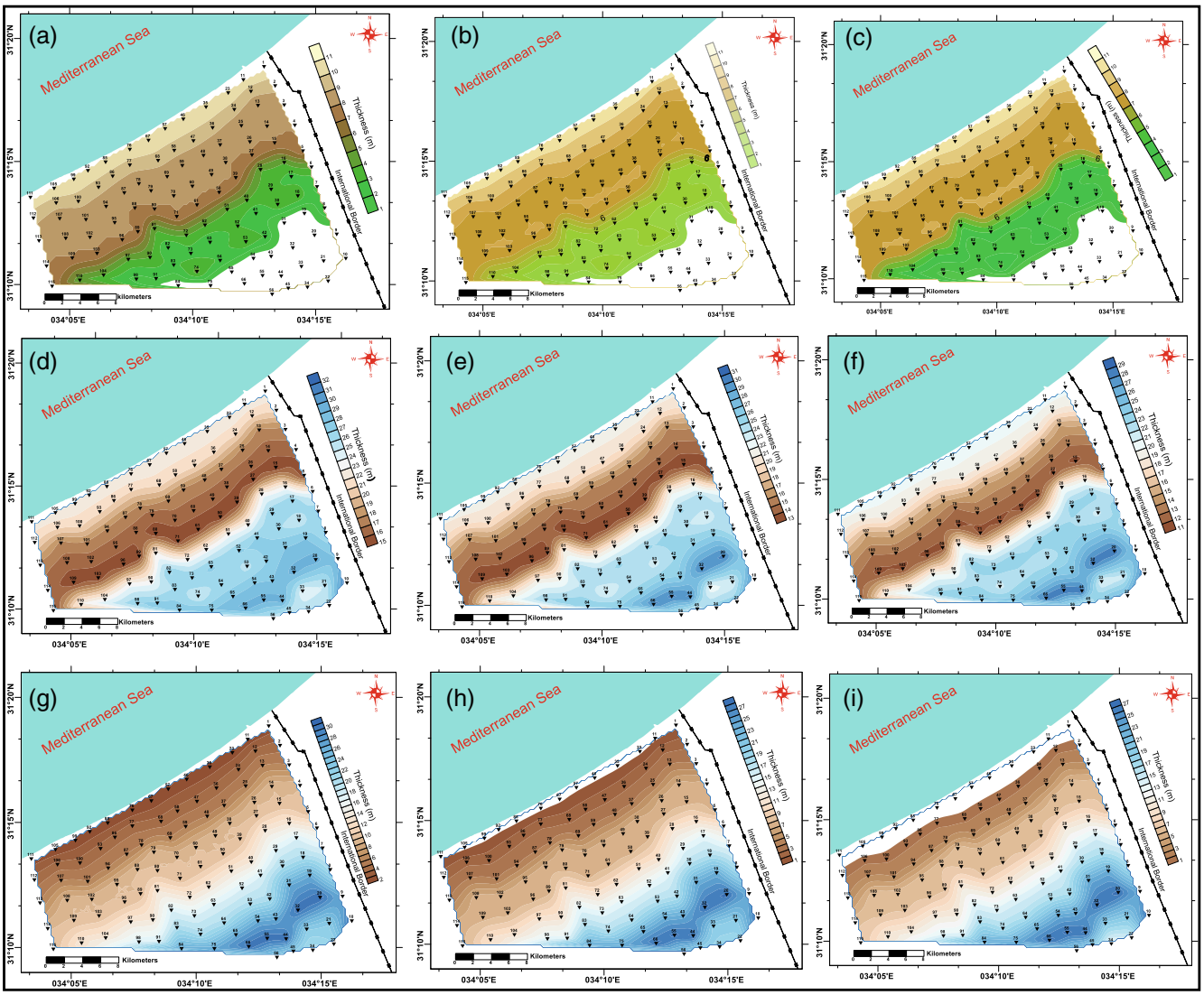

Fig. 4 Isopach maps of the water-bearing formations, in 2003 Sand dune (**a**), Old Beach (**b**), and Kurkar (**c**), in 2013 Sand dune (**d**), Old Beach (**e**), and Kurkar (**f**), and in 2017 Sand dune (**g**), Old Beach (**h**), and Kurkar (**i**)

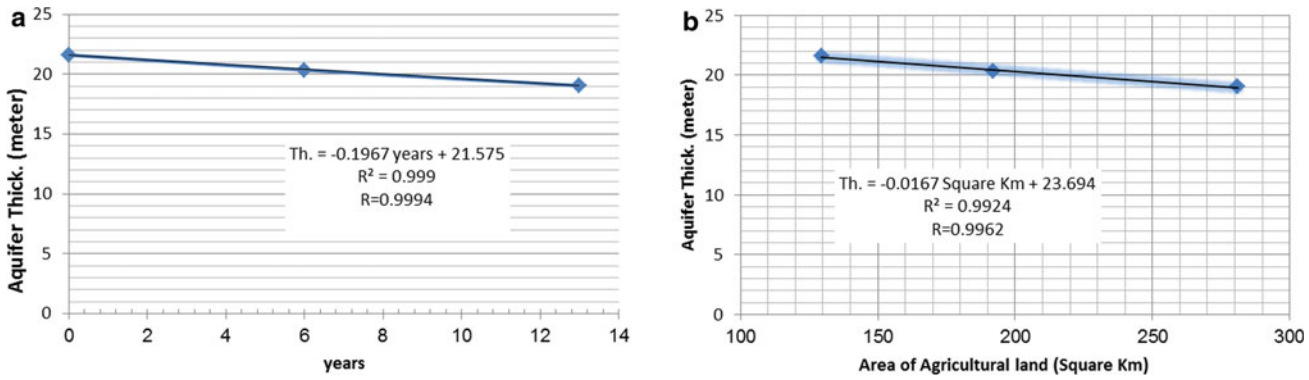

Fig. 5 Linear empirical relation describes the discharge water (**a**) for year, (**b**) for reclaimed square kilometre

in order to assess the efficiency of the groundwater aquifer(s) in the relevant area for the rapid development of land reclamation, the regional changes in agricultural areas and shoreline position were calculated from analyses of Landsat images, the findings showed a high reclamation process by 11km2 per year. Moreover, groundwater quantity changes were calculated in different periods using resistivity and TEM sounding; interpretation of these soundings provided us with the desired information. It showed that there are three separate water-bearing layers, and the thickness is suitable, ranging in the upper one from 1 to 11 m, the middle aquifer has a thickness ranging from 15 to 32 m, while the thickness of the third and deepest one ranges between 1 and 31 m. By integrating the surface and subsurface data gained from remote sensing and ground geophysical measurements, we can conclude that the Rafah coastal aquifer is suitable for the sustainable development at the concerned area. Hence, we ought to pay attention and take into consideration the safety yield at every drilled well.

References

Abdelaziz, R., Bakr, M.I.: Inverse modeling of groundwater flow of delta Wadi El-Arish. J. Water Resour. Protect. **4**, 432–438 (2012). https://doi.org/10.4236/jwarp.2012.47050

Alesheikh, A.A., Ghorbanali, A., Nouri, N.: Coastline change detection using remote sensing. Int. J. Environ. Sci. Technol. **4**(1), 61–66 (2007)

Baawain, M.S., Al-Futaisi, A.M., Ebrahimi, A., Omidvarborna, H.: Characterizing leachate contamination in a landfill site using time domain electromagnetic (TDEM) imaging. J. Appl. Geophys. **151**, 73–81 (2018)

Barseem, M.S.M.: Geoelectrical investigation using 1D and 2D techniques to delineate the groundwater occurrence condition in Al-Gorah and its Vicinities, Northeastern Sinai, Egypt. Egypt. J. Geol. **60**(2016), 61–74 (2016)

Duda, A.M.: Co-Managing Land and Water for Sustainable Development, United Nations convention to combat desertification (UNCCD) Global Land Outlook, Working Paper LAND-WATER NEXUS, 29P (2017)

Elewa, H.H., Ramadan, E.-S.M., Nosair, A.M.: Water/land use planning of Wadi El-Arish watershed, Central Sinai, Egypt Using RS, GIS and WMS techniques. Int. J. Sci. Eng. Res. **5**(9) (2014). ISSN 2229-5518

Foody, G.: Remote sensing of tropical forest environments: towards the monitoring of environmental resources for sustainable development. Int. J. Remote Sens. **24**, 4035–4046 (2003)

Guneroglu, A.: Coastal changes and land use alteration on Northeastern part of Turkey. Ocean Coast. Manag. **118**, 225–233 (2015)

Herold, M., Scepan, J., Clarke, K.C.: The use of remote sensing and landscape metrics to describe structures and changes in urban land uses. Environ. Plan. **34**, 1443–1458 (2002)

Loke, M.H., Chambers, J.E., Rucker, D.F., Kuras, O., Wilkinson, P.B.: Recent developments in the direct-current geoelectrical imaging method. J. Appl. Geophys. **95**, 135–156 (2013)

Rao, V.R., Ramana Murthy, M.V., Manjunath, B., Reddy, N.T.: Littoral sediment transport and shoreline changes along Ennore on the southeast coast of India: field observations and numerical modelling. Geomorphology **112**, 158–166 (2009)

UNEP: Vital Water Graphics—An Overview of the State of the World's Fresh and Marine Waters, 2nd edn. UNEP, Nairobi (2008). ISBN: 92-807-2236-0

Van, T.T., Binh, T.T.: Shoreline change detection to serve sustainable management of coastal zone in Cu long Estuary. In: Proceedings of the International Symposium on Geoinformatics for Spatial Infrastructure Development in Earth (2008)

Yuan, F., Sawaya, K.E., Loeffelholz, B.C., Bauer, M.E.: Land cover classification and change analysis of the Twin Cities (Minnesota) Metropolitan Area by multitemporal Landsat remote sensing. Remote Sens. Environ. **98**, 317–328 (2005)

Petroleum Geochemistry and Engineering (T13): Petroleum Geochemistry

The Application of Glauconite for High-Resolution Stratigraphic Interpretations of Eocene Succession

Santanu Banerjee, Snehasis Chakrabarty, and Tathagata Roy Choudhury

Abstract

This study explores the potential of glauconite for a high-resolution interpretation of Eocene stratigraphic sequences for the correlation of hydrocarbon reservoirs. The authigenic glauconite forms abundantly during the Eocene in shallow marine environments, and its presence indicates a low rate of sediment supply. Glauconite is characteristically associated with transgressive deposits, and its presence reflects marine flooding. The presence of glauconite marks the different orders of marine flooding surfaces in stratigraphic sequences because of the requirement of a low rate of sediment. The glauconitic intervals provide high-resolution sequence stratigraphic interpretations in Kutch, Cambay and Jaisalmer Basins in the onshore basins of western India and in the subsurface Assam-Arakan Basin in northeast India. Because of its highly radioactive nature, the glauconitic rock is useful for subsurface correlation using electrologs.

Keywords

Glauconite • Sequence stratigraphy • Eocene • Maximum flooding surface • Condensed zone

1 Introduction

Glauconite is potassium- and iron-rich sheet silicate and is distinct from other clay minerals by its green colour. Glauconite is an excellent marker of stratigraphic condensation associated with transgressive deposits (Amorosi 1995, 2011; Banerjee et al. 2012, 2016). A recent review reveals the high abundance of glauconite during the Eocene. As global sea-level rise inundated almost all the continents during the Eocene, extensive glauconite formed in marine transgressive deposits. While the authigenic glauconite in recent times forms preferably within outer shelf and slope environments, during the Eocene it forms largely in shallow marine depositional settings (Banerjee et al. 2016).

Although glauconite is an integral part of Eocene shallow marine transgressive deposits, its potential for correlation of stratigraphic sequences remains largely ignored. Because of their high K_2O content, glauconitic rocks are likely to be characterized by its high count of radioactivity. This study discusses the occurrence of glauconite in four Eocene sequences in India and discusses its applications for high-resolution sequence stratigraphic interpretations in subsurface.

2 Samples and Methods

This study investigates the outcrops in three sedimentary basins in western India, viz. Cambay, Kutch and Jaisalmer and subsurface data of the Assam and Assam-Arakan Basin in northeast India. Glauconite is associated with Eocene transgressive events in all four basins. The rock samples were collected from the outcrop for detailed mineralogical and geochemical characterization of glauconites. A few-cm-thick glauconitic shale occurs at upper levels, in association with minor limestone of Harudi and Naredi formations in the ca 70-m-tick Eocene succession of the Kutch Basin. In the Cambay Basin, glauconite occurs as a few-cm-thick layers within ~60-m-thick Eocene succession of Cambay Shale Formation comprised of mostly lignites and shales, with minor sandstone/limestone beds. Cm-scale glauconitic shale occurs within 70-m-thick Eocene succession of the Jaisalmer Basin, consisting of the lower part of

S. Banerjee (✉) · T. R. Choudhury
Department of Earth Sciences, Indian Institute of Technology Bombay, Powai, Mumbai, 400076, India
e-mail: santanu@iitb.ac.in

S. Chakrabarty
Keshav Deva Malaviya Institute of Petroleum Exploration, Oil and Natural Gas Corporation Ltd., 9 Kaulagarh Road, Dehradun, Uttarakhand 248001, India

M. Meghraoui et al. (eds.), *Advances in Geophysics, Tectonics and Petroleum Geosciences*, Advances in Science, Technology & Innovation, https://doi.org/10.1007/978-3-030-73026-0_84

Te Takkar Member of the Khuiala Formation. Thin sections of glauconitic rocks were investigated by Leica DMP4500P polarizing Microscope. Mineral chemical analysis of glauconite was performed by EPMA at the Department of Earth Sciences, Indian institute of Technology, Bombay. Early to Middle Eocene, 170-m-thick Sylhet Formation of the Assam Basin and the Assam-Arakan Basin contains cm-thick glauconitic shale at several intervals within the mixed siliciclastic-carbonate sequence. Basic electrolog data incorporating mainly four conventional logs: gamma-ray, resistivity, neutron and density logs have been calibrated with lithology and the electrolog motifs for regional correlation of glauconitic beds within the Sylhet Formation.

3 Results

3.1 Mineral Chemistry of Investigated Eocene Glauconites

The glauconite forms either by the replacement of faecal pellets or by infillings within the foraminifera and other bioclasts. The content of glauconite in the Eocene Harudi Formation in the Kutch Basin varies between 30 and 50% of the total rock. The K_2O content of the glauconite varies between 6.1 and 7.1 wt%, while its total Fe_2O_3 content ranges between 25.4 and 28.9 wt%. The content of glauconite in the Eocene Cambay Shale Formation in the Cambay Basin varies between 30 and 40% of the total rock. The average K_2O content of glauconite is ca 5%, while its Fe_2O_3 content varies between 16.1 and 21.9 wt%. The average K_2O content of glauconite ranges between 5.8 and 8.7, and 5 to 7% in the Eocene of the Jaisalmer and Assam Basins, respectively.

3.2 Correlation of Subsurface Section

The correlation of electrologs reveals three system tracts of the third order within the second-order TST, viz. a basal TST, represented by limestone and shale, which is followed upwards by a sandy HST and topped by a dominantly shaley TST (Chakrabarty et al. 2019). The HST is further resolved into fourth-order parasequence sets, demarcated by marine flooding surfaces. The glauconite within the Eocene Sylhet Formation represents intervals containing the marine flooding surfaces of third and fourth orders relative to sea-level change. The highly radioactive glauconitic intervals are traced for 30 km in the subsurface using electrolog data (Fig. 1).

4 Discussion

The high-resolution sequence stratigraphic analysis facilitates the exploration for sub-seismic scale reservoirs, which are products of lower order (fourth–fifth orders), relative to sea-level cycles. The study of glauconitic intervals holds promise for the high-resolution analysis of reservoir and source facies of a petroleum system. Although the glauconite may occur anywhere within transgressive systems tract deposits, its abundance and maturity vary systematically. The glauconite is most abundant and most evolved corresponding to the condensed deposits that mark a low rate of sedimentation for a considerable time. The abundance and maturity of glauconite are maximum in sediments corresponding to third- and fourth-order MFS surfaces in all four investigated Eocene successions of India. The content of glauconite usually exceeds 30%, in these intervals and their K_2O content ranges between 5.5 and 8%. A prolonged

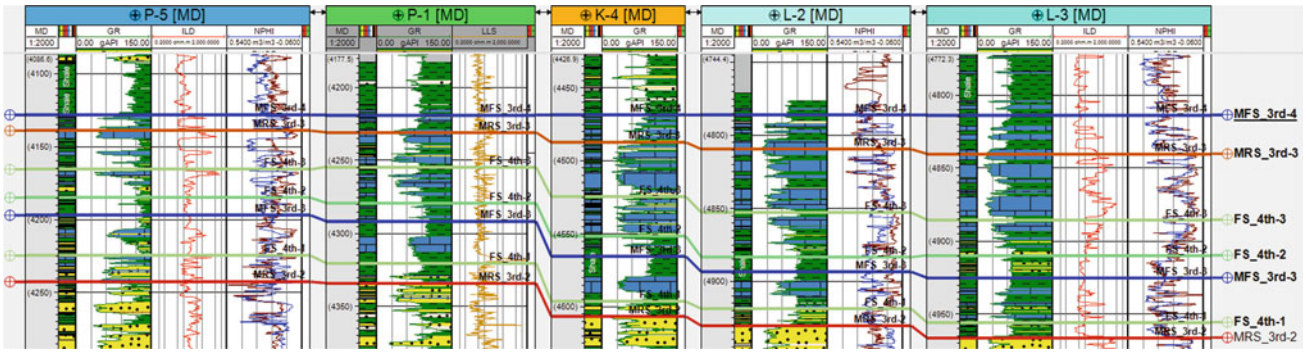

Fig. 1 Electrolog correlation and lithofacies distribution along dip profile in north Assam shelf (yellow = sandstone, green = shale, blue = limestone; MFS = maximum flooding surface, MRS = maximum regressive surface, FS = flooding surface)

residence at or near the sediment–water interface allows the addition of K and Fe from the seawater into the glauconite structure, allowing it to evolve. The glauconitic horizons facilitate the sequence stratigraphic architecture of the Eocene succession in the Assam Basin.

5 Conclusions

The study of Eocene outcrops in the Kutch, Cambay and Jaisalmer Basins in western India and the subsurface sequence in the Assam Basin reveals the usefulness of glauconite for the high-resolution sequence stratigraphic investigations of hydrocarbon-bearing reservoir rocks. The subsurface Sylhet Formation exhibits several glauconitic beds corresponding to marine flooding surfaces of third and fourth orders relative to sea-level changes. The association of glauconite with marine flooding surfaces indicates stratigraphic condensation. Therefore, the glauconitic interval provides crucial inputs for the building up the sequence stratigraphic framework of the Eocene succession. The correlation of glauconitic intervals demarcates the short-term transgressive-regressive cycles and therefore holds potential for the correlation of reservoirs rocks.

References

Amorosi, A.: Glaucony and sequence stratigraphy; a conceptual framework of distribution in siliciclastic sequences. J. Sediment. Res. **65**(4b), 419–425 (1995)

Amorosi, A.: The problem of glaucony from the Shannon Sandstone (Campanian, Wyoming). Terra Nova **23**, 100–107 (2011)

Banerjee, S., Chattoraj, S.L., Saraswati, P.K., Dasgupta, S., Sarkar, U.: Substrate control on formation and maturation of glauconites in the Middle Eocene Harudi Formation, western Kutch, India. Mar. Petrol. Geol. **30**, 144–160 (2012)

Banerjee, S., Bansal, U., Thorat, A.V.: A review on palaeogeographic implications and temporal variation in glaucony composition. J. Palaeogeogr. 43–71 (2016)

Chakrabarty, S., Gorai, D., Shukla, M., Uppal, S.: High-resolution sequence stratigraphy and its implication in mixed siliciclastic-carbonate sequence: a case study from early to middle Eocene Sylhet Formation, Assam and Assam-Arakan Basin, India. AAPG Datapages. https://doi.org/10.1306/30595Chakrabarty2019

Geochemical Evidence for Photic Zone Euxinia During Greenhouse Climate in the Tethys Sea, Egypt

Douaa Fathy, Michael Wagreich, and Mabrouk Sami

Abstract

Upper cretaceous organic-rich sediments are good archives for the paleoceanographic changes. Here, a comprehensive set of geochemical, biological, and mineralogical data have been applied in order to evaluate the role of euxinia on the organic matter during deposition. The total organic matter of these organic-rich sediments reaches up to 23 wt%. They have significant concentrations of redox-sensitive trace elements such as Mo, Cu, Zn, Ni, Cd, U, and V. The values of redox proxies (e.g., U/Mo, V/(V + Ni), V/Ni, Ni/Co, V/Cr, U/Th, U authigenic) and the size of framboids pyrite suggest that the Upper Cretaceous organic-rich sediments were deposited under a euxinic water column environment. The molecular fossils data also point to the predominance of the sulfidic anoxic conditions during deposition. The good correlation between TOC and redox proxies indicates that the oxygen-depleted conditions play a significant role in the preservation of that organic matter.

Keywords

Organic matter • Greenhouse climate • Depositional environment • Cretaceous • Euxinia • Egypt

1 Introduction

The Upper Cretaceous organic-rich sediments in the central part of Egypt were formed in a low paleo-latitude marine environment in the southern Tethyan realm. These sediments are deposited under warm greenhouse climate fluctuating between wet and dry (Fathy et al. 2018b, 2021a). These sediments are located within intracratonic sedimentary basins in a broad northern African empiric sea (Khalil and Mcclay 2009; Tawadros 2011). The organic-rich sediments such as oil shales are suggested to be derived from intermediate igneous rocks (Fathy et al. 2017, 2021b). The formation of organic-rich sediments is a controversial issue. Productivity and preservation models are suggested for their formation (Sageman et al. 2003). The preservation model is dependent on the redox condition and sedimentation rate (Tribovillard et al. 2006). The geochemical behavior of trace metals in the organic-rich sediments can be used to infer the sedimentation conditions under oxygen-deficient bottom water (Calvert and Pedersen 1993). In addition, the size of the framboids pyrite is a valuable tool to reconstruct the oxygen level in the water column (Wilkin et al. 1996). Therefore, we used the geochemical, mineralogical, and biological evidence to evaluate the role of euxinia on the organic matter.

2 Methods

The samples were collected from the Upper Cretaceous organic-rich sediments in the west of the Red Sea coast. The bulk geochemical analyses were done by inductively coupled plasma atomic emission spectrometry and inductively coupled plasma mass spectrometry. The total organic matter was measured by a Leco analyzer. The pyrite size was measured on the backscatter mode using the field emission scanning microscope. The biomarker's analysis was done using gas chromatography–mass spectrometry. The analyses were done at the Bureau Veritas Labs and Vienna University.

3 Results and Discussion

The studied organic-rich sediments have high concentrations of Mo, Ni, Zn, U, V, Cd, and Cu relative to the Post-Archean Australian Shale (PAAS, Taylor and McLennan, 1985 and

D. Fathy (✉) · M. Sami
Department of Geology, Faculty of Science, Minia University, El-Minia, 61519, Egypt
e-mail: douaafathy@mu.edu.eg

M. Wagreich
Department for Geodynamics and Sedimentology, University of Vienna, Althanstrasse 14, 1090 Vienna, Austria

M. Meghraoui et al. (eds.), *Advances in Geophysics, Tectonics and Petroleum Geosciences*, Advances in Science, Technology & Innovation, https://doi.org/10.1007/978-3-030-73026-0_85

1995). The organic-rich sediments have high values of redox proxies such as V/V + Ni (0.98), V/Ni (10.8), Ni/Co (30), V/Cr (6), U/Th (12), $U_{authegenic}$ (35), and U/Mo (0.1). All geochemical redox proxies for the studied sediments are pointing to euxinic conditions during deposition. The average size of the framboids pyrite diameters is ~3.5 μm, reflecting sulphidic anoxic bottom water column. The studied sediments have high concentrations of aryl isoprenoids (~ average = 294 μg/g TOC) and a low content of acyclic isoprenoids (~ average = 0.43). The good correlation between TOC and geochemical proxies (mostly greater than 6) indicates that the formation of these sediments is mainly controlled by the euxinia.

4 Conclusions

All the geochemical proxies, biological, and mineralogical data indicate that the deposition of organic-rich sediments was under euxinic deposition conditions. Additionally, the preservation of the enhanced organic matter is relatively controlled by the expansion of euxinia to the photic zone.

References

Calvert, S.E., Pedersen, T.F.: Geochemistry of recent oxic and anoxic marine sediments: implications for the geological record. Mar. Geol. **113**, 67–88 (1993)

Fathy, D., Wagreich, M., Mohamed, R., Zaki, R.: Sedimentary provenance of Maastrichtian oil shales, Central Eastern Desert, Egypt. In: EGU General Assembly Conference, Geophysical Research Abstracts, vol. 19 (2017)

Fathy, D., Wagreich, M., Gier, S., Mohamed, R., Zaki, R., El Nady, M.: Maastrichtian oil shale deposition on the southern Tethys margin, Egypt: Insights into greenhouse climate and paleoceanography. Palaeogeogr. Palaeoclimtol. Palaeoecol. **505**(15), 18–32 (2018a)

Fathy, D., Wagreich, M., Gier, S., Zaki, R., Mohamed, R.: Geochemical fingerprinting of Maastrichtian oil shales from the Central Eastern Desert, Egypt: Implications for provenance, tectonic setting and source area weathering. Geol. J. **53**(6), 2597–2612 (2018b)

Fathy,D., Wagreich, M., Ntaflos,T., Sami, M.: Paleoclimatic variability in the southern Tethys, Egypt: Insights from themineralogy and geochemistry of Upper Cretaceous lacustrine organic-rich sediments, Cretaceous Research, 126, p.104880 (2021a)

Fathy,D., Wagreich, M., Ntaflos,T., Sami, M.: Provenance Characterization of Campanian Lacustrine Organic-RichMudstones on the Southern Tethyan Margin, Egypt. ACS Earth and Space Chemistry, 5(2), pp.197-209.1. 2021. ProvenanceCharacterization of Campanian Lacustrine Organic-Rich Mudstones on the Southern Tethyan Margin, Egypt. ACS Earth and Space Chemistry, 5(2), pp.197-209 (2021b)

Khalil, S.M., Mcclay, K.R.: Structural control on syn-rift sedimentation, northwestern Red Sea margin, Egypt. Mar. Petrol. Geol. **26**(6), 1018–1034 (2009)

Sageman, B.B., Murphy, A.E., Werne, J.P., Ver Straeten, C.A., Hollander, D.J., Lyons, T.W.: A tale of sediments: the relative roles of production, decomposition, and dilution in the accumulation of organic-rich strata, Middle-Upper Devonian, Appalachian basin. Chem. Geol. **195**, 229–273 (2003)

Tawadros, E.: Geology of North Africa, 931 pp. CRC Press (2011)

Tribovillard, N., Algeo, T.J., Lyons, T., Riboulleau, A.: Trace metals as paleoredox and paleoproductivity proxies: an update. Chem. Geol. **232**, 12–32 (2006)

Wilkin, R.T., Barnes, H.L., Brantley, S.L.: The size distribution of framboidal pyrite in modern sediments: an indicator of redox conditions. Geochima Cosmochima Acta **60**, 3897–3912 (1996)

Molecular Geochemistry of the Mamu Formation Sediments in Anambra Basin, Nigeria

Mutiu A. Adeleye and Omololu E. Okedoyin

Abstract

Mamu Formation sediments that were encountered at depth range of 1015–1185 m in the Akukwa-II well from the Anambra basin were described and subjected to total organic carbon and gas chromatography-mass spectrometry analyses to determine their organic richness, thermal maturity, the source of organic matter and depositional environment. The sediments are composed of fine grained, dark grey shales and medium grained, dark coloured sandy shales. The TOC results ranged from 1.72 to 2.70 wt%. The biomarker results showed relatively low Pristane/Phytane ratios, strong predominance of medium molecular weight n-alkanes and slight predominance of odd numbered n-alkanes, low ratios of Pr/nC_{17} and Ph/nC_{18} and moderate carbon preference index (CPI). The TOC results indicated that the samples have good source rock potential. The n-alkanes isoprenoid, CPI ratios and odd even predominance (OEP) results indicated a marginal to thermally mature organic matter from marine and terrestrial setting. The CPI values of the samples indicate marginal to thermally mature mixed organic matter deposited under relatively anoxic to dysoxic conditions. Pr/nC_{17} and Ph/nC_{18} results also suggested mixed organic matter deposited in dysoxic environment. Pr/Ph data suggested that the samples are within the oxidising field in the mature oil zone. Regular steranes data suggested organic matter within early oil generative window while ternary diagram of steranes shows domination of terrestrial organic matter and a lacustrine environment of deposition for the sediments.

Keywords

Mamu Formation • Biomarkers • Organic source input • Thermal maturity • Depositional environment

1 Introduction

The Maastrichtian Mamu Formation (Reyment 1965) in the Anambra basin consists of rhythmic clastic sequences of sandstones, shales, siltstones, mudstones, sandy shales with interbedded coal seams (Petters 1978). The formation has been identified as hydrocarbon source rock along with Nkporo and Imo formations (Avbovbo and Ayoola 1981). Exposed coal deposits of the Mamu Formation are known in several places within the basin where they have been studied along with their associated lithologies for coal rank, maceral composition, hydrocarbon generation potential and depositional environments (Akande et al. 1992; Adeleye et al. 2017). However there are few studies generally on the geochemical investigation of subsurface sediments of the Mamu Formation. This study evaluates the organic source input, depositional environment and thermal maturity of Mamu Formation from the Akukwa-II well in Anambra basin.

2 Materials and Methods

Ditch cutting and core samples of Mamu Formation encountered at depths of 1015–1185 m in the Akukwa-II well, were examined for their lithology, texture, colour and other features. All samples were finely pulverised, labelled, stored in vials and subjected to total organic carbon (TOC) analysis. Following the TOC results, selected samples were ultrasonically extracted using dichloromethane (DCM) and methanol (CH_3OH) as the solvent mixture in a ratio of (10:0), (5:5) and (0:10). All extractions were repeated thrice and the extracts pooled together. The pooled extracts were reduced by rotavapor machine and separated into the aromatics and saturate fractions. The saturate fractions were analysed for biomarkers by gas chromatography-mass spectrometry (GC-MS).

M. A. Adeleye (✉) · O. E. Okedoyin
Department of Geology, University of Ibadan, Ibadan, Nigeria

M. Meghraoui et al. (eds.), *Advances in Geophysics, Tectonics and Petroleum Geosciences*,
Advances in Science, Technology & Innovation, https://doi.org/10.1007/978-3-030-73026-0_86

3 Results

The sediments of Mamu Formation penetrated by the Akukwa-II are composed of fine grained, dark grey shales and medium grained dark grey sandy shales. The sandy shale unit dominates the studied section with the shale unit overlying the sandy shale. The TOC results of the sediments ranges from 1.72 to 2.70 wt%. This shows that the sediments contained appreciable quantity of organic matter. The biomarker results including n-alkanes, isoprenoids, steranes and terpanes from the sample extracts are presented in Tables 1 and 2.

4 Discussion

4.1 Organic Source Input and Depositional Environment

The distribution of n-alkanes in bitumen and oil has been reported to be good indicator of organic matter source (Duan and Ma 2001). The extracts from Mamu Formation sediments contain a full range of C_{11}-C_{35} n-alkanes and isoprenoids, pristane and phytane maximising at C_{35}. This pattern of distribution indicates organic matter derived from both marine and terrestrial environment (Peters et al. 2005). The carbon preservation index (CPI) which also provides insight into the source input and depositional environment (Peters et al. 2005; Meyers and Snowdon 1993), ranged from 1 to 1.52 in the analysed samples (Table 1). This indicates mixed organic matter deposited under relatively anoxic to dysoxic conditions. Pr/Ph ratios have been used by researchers to predict the prevailing redox conditions of depositional environment (Meyers and Snowdon 1993; Powell and Mckirdly 1973; Didyk et al. 1978). Pr/Ph ratio of 0.62–1.88 (Table 1) in the samples suggests that they are deposited in relatively sub-oxic environments (Peters et al. 2005; Didyk et al. 1978; Peters and Moldowan 1993).

The cross-plot of Pristane/nC_{17} and Phytane/nC_{18} is known for interpreting source rock depositional conditions and organic matter type (Peters et al. 2005; Peters and Moldowan 1993; Koeverden et al. 2011). The cross-plot of Pr/nC_{17} and Ph/nC_{18} (Fig. 1) indicates that the organic matter in the Mamu Formation samples was derived from mixed organic source deposited in a dysoxic environment. In addition, the cross-plot of Pr/Ph and CPI for the samples suggested that the samples are within the oxidising field in the mature oil zone (Fig. 2). However, the ternary diagram for the steranes in the samples shows contribution of terrestrial organic sources with dominance of C_{29} and equally depicts that the sediments were deposited in a lacustrine environment (Fig. 3).

4.2 Thermal Maturity

Alkane and isoprenoids distribution, Pristane/nC_{17}, Phytane/nC_{18}, CPI and improved odd–even preference (OEP) are widely used as indicators of organic maturation (Peters et al. 2005; Peters and Moldowan 1993; Hunt et al. 2002; Bray and Evans 1961; Scalan and Smith 1970). The CPI values for the samples analysed ranging from 1 to 1.52 (Table 1) indicate a marginal thermal maturity rank. The OEP values (0.85–1.52) are quite close to 1.0 except for a sample with value of 1.52, this indicates high maturity to marginal maturity. However, low values of Pr/nC_{17} and

Table 1 N-alkanes, isoprenoids and steranes data of Mamu Formation sample extracts

Depth (m)	TOC (wt%)	Pr/Ph	Pr/nC_{17}	Ph/nC_{18}	CPI	OEP	TAR	20S/20S + 20R C_{29} Steranes	ββ/(ββ αα) C_{29} Steranes
1015–1020	1.97	1.80	0.93	0.42	1.27	1.16	0.25	0.42	0.50
1030–1035	2.07	1.88	0.77	0.29	1.52	1.52	0.29	0.29	0.50
1130–1135	1.78	0.62	0.70	0.81	1.37	0.90	0.10	0.37	0.54
1180–1185	1.77	0.90	0.27	0.31	1.00	0.85	0.13	0.37	0.55

Table 2 Terpanes data of the Mamu Formation sample extracts

Depth (m)	C_{35}ab(S)/C_{34} ab(S)	C_{35}/C_{31}-C_{35}	C_{29}H/C_{30}H	C_{31}R/C_{30}H	Ts/Ts + Tm	Mor/Hop	C_{27}-C_{29}Regular sterane/C_{29}-C_{33}17α(H) hopane	Mor/Hop
1015–1020	0.56	0.07	0.18	0.41	0.42	0.26	0.06	0.26
1030–1035	0.57	0.07	0.002	0.63	0.18	0.48	0.08	0.48
1130–1135	0.42	0.07	0.39	0.99	0.35	0.51	0.06	0.51
1180–1185	0.57	0.09	0.46	0.8	0.34	0.38	0.10	

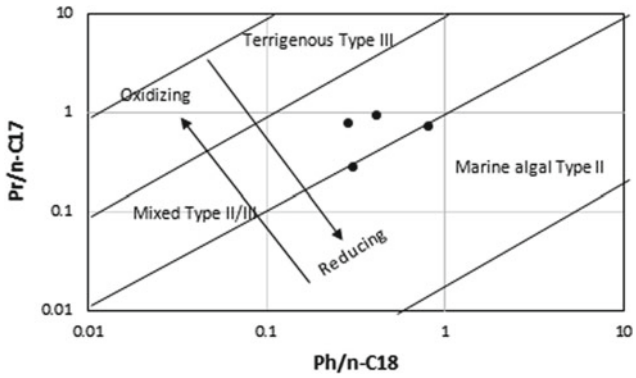

Fig. 1 Plot of Pr/nC_{17} and Ph/nC_{18} for analysed samples

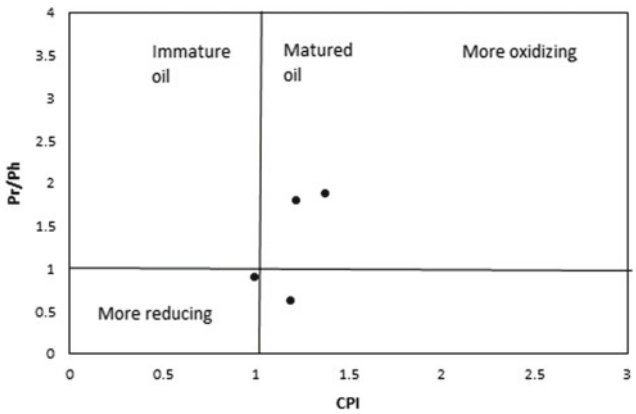

Fig. 2 Plot of Pristane/phytane and CPI for analysed samples

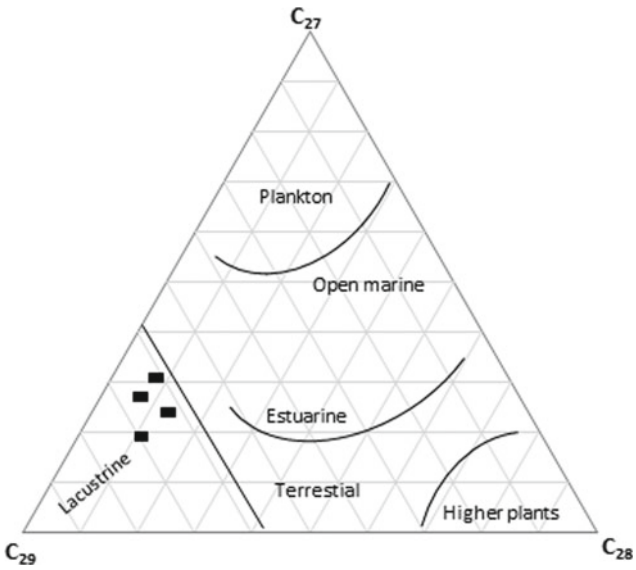

Fig. 3 Ternary diagrams of regular steranes for the analysed samples

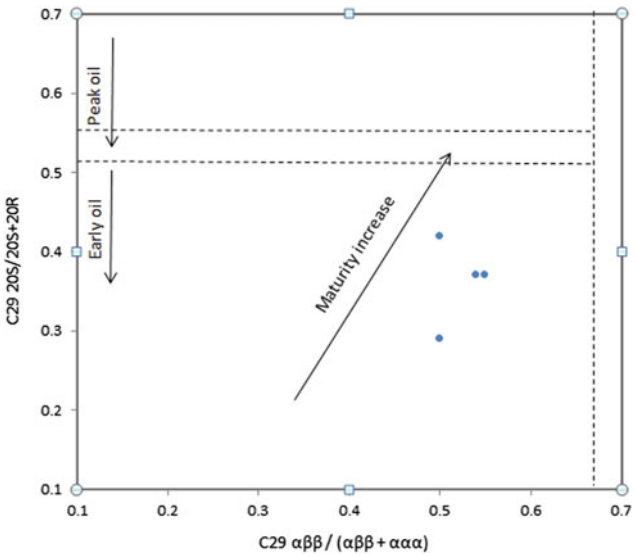

Fig. 4 Plot of C_{29} steranes for the analysed samples

Ph/nC_{18} ratios in Mamu Formation samples (Table 1) suggest a reflection of the marginal maturity of the source rock.

Sterane ratios are equally widely used as maturity parameters in oil and sedimentary organic matter, and the ratio increases with increasing thermal maturity (Peters et al. 2005). In Mamu Formation samples, the C_{29} 20S/(20S + 20R) sterane ratios range from 0.29 to 0.42 (Table 1), this indicates immature to early maturity oil generative window. Furthermore, the C_{29} αββ/αββ + ααα, which is used as a maturity parameter, ranges from 0.50 to 0.55 in the Mamu Formation samples from the Akukwa-II well. All these indicate that the samples are thermally mature or within the oil generative window. However, cross-plot of 20S/(20S + 20R) and αββ/αββ + ααα for the C_{29} steranes revealed that the samples are marginally within the early oil generative window (Fig. 4).

5 Conclusions

The analysed Mamu Formation sediments that range in depth from 1015 to 1185 m in the Akukwa-II well from Anambra basin are composed of fine grained, dark grey shales and medium grained, dark coloured sandy shales. The sediments have good source rock potential and are made up of mixed marine and terrestrial organic matter deposited in anoxic to dysoxic depositional conditions. However, the organic matter in the sediments is predominated by terrestrially derived organic constituents which were deposited in a lacustrine environment. These samples are presently marginally mature for liquid hydrocarbon generation.

References

Adeleye, A.M., Ugboaja, C.Y., Yuhong, L.: Aspects of the hydrocarbon potentials of the coals and associated Shales and mudstones of the Mamu Formation in Anambra basin. J. Environ. Earth Sci. **7**(7), 1–14 (2017)

Akande, S.O., Hoffknecht, A., Erdtmann, B.D.: Upper cretaceous and tertiary coals from Southern Nigeria, composition, rank, depositional environments and their technological properties. NAPE Bull. **7**(1), 26–38 (1992)

Avbovbo, A., Ayoola, E.O.: Petroleum prospects of southern Nigeria's Anambra Basin". Oil Gas J. **79**, 334–348 (1981)

Bray, E.E., Evans, E.D.: Distribution of n-paraffins as a clue to recognition of source beds. Geochim. Chosmochim. Acta **22**, 2–16 (1961)

Didyk, B.M., Simoneit, B.R.T., Brassell, S.C., Eglinton, G.: Organic geochemical indicators of palaeoenvironmental conditions of sedimentation. Nature **272**, 216–222 (1978)

Duan, Y., Ma, L.H.: Lipid geochemistry in a sediment core from Ruoergai Marsh deposit (Eastern Qinghai-Tibet Plateau, China). Org. Geochem. **32**, 1429–1442 (2001)

Hunt, J.M., Philip, R.P., Kvenvolden, K.A.: Early developments in petroleum geochemistry. Org. Geochem. **33**, 1025–1052 (2002)

Meyers, P.A., Snowdon, L.R.: Types and maturity of organic matter accumulated during Early Cretaceous subsidence of the Ex-Mouth Plateau, Northwest Australia Margin. AAPG Stud. Geol. **37**, 119–130 (1993)

Peters, K.E., Moldowan, J.M.: The Biomarker Guide: Interpreting Molecular Fossils in Petroleum and Ancient Sediments. Prentice-Hall Inc., Englewood Cliffs (1993)

Peters, K.E., Walters, C.C., Moldowan, J.N.: The biomarker Guide: Bionarkers and Isotopes in Petroleum Exploration and Earth History, 2nd edn. Cambridge University press, Cambridge (2005)

Petters, S.W.: Stratigraphic evolution of the Benue Trough and its Implications for the Upper Cretaceous Paleogeography of West Africa. J. Geol. **86**, 311–322 (1978)

Powell, T.G., Mckirdly, D.M.: Realtionship between ratio of pristane to phytane, crude oil composition and geological environment in Australia. Nat. Phys. Sci. **243**, 37–39 (1973)

Reyment, R. A.: Aspect of the Geology of Nigeria, 145p. Ibadan University Press (1965)

Scalan, R.E., Smith, J.F.: An improved measure of the odd-even predominance to the normal alkanes of sediments extracts and petroleum. Geochim. Cosmochim. Acta **34**, 611–620 (1970)

Van Koeverden, J.H., Karlsen, D.A., Backer-Owe, K.: Carboniferous non-marine source rocks from Spitsbergen and Bjornoya: comparison with the Western Arctic. J. Pet. Geol. **34**, 53–66 (2011)

Petroleum Potential of Cretaceous Source Rocks in the Levant Basin

Aaron Meilijson, Emily Finkelman, Sarit Ashckenazi-Polivoda, F. Garrett Boudinot, Or M. Bialik, Giovanni Coletti, Josh Steinberg, Kul Karcz, Nicolas D. Waldmann, Julio Sepúlveda, and Yizhaq Makovsky

Abstract

Several oil shows have been reported from offshore and onshore wells of the Levant Basin, which promoted research and exploration as indicators for potential economic discoveries in the yet unpenetrated Mesozoic interval of the basin. In most cases, no definitive source to oil correlation has been established, advocating the need for the fingerprinting of regional source rocks to compare their organic geochemical signatures to those of oils. A summary of known properties of oils sampled from different wells in the region raised several questions regarding source–oil and oil–oil correlation, maturity, and source of the organic matter. In this part of the project we examined the Cretaceous section in the region by conducting a sedimentological and organic geochemical investigation of organic-rich intervals from ODP well material and onshore wells in the Levant region. We show that organic-rich Upper Cretaceous deposits, Turonian OAE2, and lowermost Cretaceous Barremian organic-rich deposits, should be considered as viable candidates for sourcing hydrocarbon formation in the deep basin, where they might have matured.

Keywords

Petroleum source rocks • Cretaceous • Eastern Mediterranean

1 Introduction

Exploration efforts for hydrocarbon reservoirs throughout the Levant Basin of the Eastern Mediterranean are of great interest, especially after the recent discoveries of large Oligo-Miocene gas reservoirs at the margins and center of the Levant Basin offshore Israel, Cyprus, and Egypt (Gardosh and Tannebaum 2014; Daher et al. 2016). The 3D thermal history and maturity models of the basin suggest that oil-prone source rocks might have reached thermal maturity in the offshore localities (Daher et al. 2016; Conway 2002). Structural studies of the offshore Levant indicate a variety of potential structural and stratigraphic petroleum traps. The recent gas discoveries in Tertiary strata also stimulated new interest in potential deeper reservoirs. This report defined the possibility of viable petroleum source rocks of Cretaceous strata in the region.

2 Settings and Methods

Accumulation of the Upper Cretaceous (Coniacian to Maastrichtian) (Almogi-Labin et al. 1993; Meilijson et al. 2014) organic-rich succession in the Levant area was part of an extensive, high-productivity upwelling regime, which operated along the southern margins of the Tethys. Deposition occurred along a regional system of basins containing a unique sequence of chert, porcellanite, phosphorite, and organic-rich sediments (Meilijson et al. 2014; Minster 1996;

A. Meilijson (✉) · O. M. Bialik · N. D. Waldmann · Y. Makovsky
University of Haifa, Mount Carmel, 31905 Haifa, Israel
e-mail: ameilijs@campus.haifa.ac.il

A. Meilijson · F. Garrett Boudinot · J. Sepúlveda
University of Colorado Boulder, Boulder, CO 80309, USA

E. Finkelman
Ben Gurion University of the Negev, 84105 Beer Sheva, Israel

S. Ashckenazi-Polivoda
Dead Sea and Arava Science Center, 86910 Neve Zohar, Dead Sea Mobile Post, Israel

G. Coletti
Milano-Bicocca University, Piazza della Scienza 4, 20126 Milano, Italy

J. Steinberg
Ratio Oil Exploration, Tel Aviv, Israel

K. Karcz
Delek Drilling, Herzelia, Israel

M. Meghraoui et al. (eds.), *Advances in Geophysics, Tectonics and Petroleum Geosciences*, Advances in Science, Technology & Innovation, https://doi.org/10.1007/978-3-030-73026-0_87

Flexer 1968). These OM-rich deposits also appear in different parts of Egypt, Jordan, Syria, and Lebanon (Meilijson et al. 2018). Meilijson et al. (2014, 2018) identified the richest and highest potential interval in the Shefela Basin and presented a stratigraphic control for defining this interval, characterized by the highest TOC (averaging at 15.2 wt%), S1 (2.75), S2 (112), S3 (3.15), GP (1.15), PCI (95.4), and PI (0.02) Rock-Eval values in the section. These, together with the high HI average value (736 mg HC/g TOC), define this interval as an excellent source rock for hydrocarbon generation.

While the Upper Cretaceous is considered an obvious and excellent regional source rock, here we examined other time periods during the Cretaceous that could potentially serve as hydrocarbon sources in the deeper and unknown parts of the Levant Basin. We do this by studying the sedimentology and geochemistry of the Cretaceous section drilled through the Eratosthenes Seamount (ESM) offshore Cyprus (ODP Leg 160) and onshore wells in the Levant.

2.1 The Cenomanian-Coniacian

During the Late Cenomanian-Early Turonian (C/T) Oceanic Anoxic Event (OAE2), organic-rich strata were deposited in rift shelf basins and slopes across North Africa and in deep sea basins of the adjacent oceans (Lüning et al. 2004). Organic-rich C/T strata also occur in parts of the Arabian Peninsula. In the Levantine coastal basins, this interval is represented by up to 50-m-thick bituminous marls and black, laminated shales of the Daliyya Fm, which reach TOC values of up to 4% (Lipson-Benitah et al. 1990). Both, Grohmann et al. (2018) and the current study report considerable organic enrichment (>4% TOC) within the upper Turonian to lower Coniacian interval in well 967E from the ESM, accompanied by an underlying interval of high uranium content. An important open question is the relative role of oxygen and elevated productivity on the preservation of organic matter (OM) in the regional upwelling system during OAE2. The latter would imply a higher probability of source rock deposition around the Eastern Mediterranean and specifically in the Levant Basin.

To address the mechanism for OM preservation in the ESM during OAE2 we inspected the faunal composition within the sediment. A striking and clear dominance of calcispheres is apparent around the C/T boundary. Calcispheres constitute the second-most abundant calcareous microfossils of many Cretaceous rocks and show significant spatial and temporal blooms in places of high nutrient availability, such as upwelling systems (Wendler et al. 2010). Our data indicate that both high-productivity and low oxygen conditions probably prevailed during the C/T OAE2 in the ESM and the Eastern Mediterranean. Upwelling-induced high productivity might imply deposition and/or transport of OM to the deep basins.

2.2 The Barremian-Aptian

Middle Jurassic to Lower Cretaceous source rocks in the region have a high potential for economic oil production in the deep basin, as indicated by the proven oil shown in the Mango-1 well within the El Arish concession (Shaaban et al. 2006). The analysis performed on the Mango-1 oil indicates a non-marine oil source, pointing to a possibly mixed source of deltaic terrestrial or lacustrine OM. Other wells in the Levant Basin also indicate a possible terrestrial source for the oil (e.g., light oil found in Lower Cretaceous sandstone in the Ziv-1 and Tineh-1 wells), which source has not yet been traced. Several examples for terrestrial sources of OM appear in the region [e.g., the Khatatba Fm in Egypt sourcing the Shushan Basin oil; (El-Shahat et al. 2009)].

Here, we report on a sedimentological and organic geochemical investigation of Barremian-Aptian organic-rich sediments from the Manara core in northern Israel with TOC content ranging between 0.5 and 38%. The TOC values in the Aptian upper Hidra Fm black shales are low (0.1–1%), while those in the Barremian Nabi Sa'id cluster vary widely (0.1–38%), with the highest values taken from intervals with visible charcoal flakes. The plotting of Rock–Eval data on a pseudo-van-Krevelen diagram indicates that the OM in the Hidra was sourced from more carbohydrate-rich land plants, while in the Nabi Sa'id it was sourced from a mixed terrestrial-marine setting. Terrestrial contribution of OM is also supported by biomarker analysis including high long- to short-chain *n*-alkane ratios (LCA/(LCA + SCA) = 1.5–4) and high Pr/Ph ratios (2.5–7.8). The relative abundance of $C_{27}\alpha\alpha\alpha R$, $C_{28}\alpha\alpha\alpha R$, and $C_{29}\alpha\alpha\alpha R$ algal steranes reveals an affinity toward the $C_{29}\alpha\alpha\alpha R$ precursor in most samples, which also supports a predominance of terrestrial OM. When compared to previous studies of the Lower Cretaceous Gevar'am Fm in southern Israel (Amit 1978), we may conclude that a terrestrial source for Lower Cretaceous OM is widespread in the region.

3 Conclusions

Our study demonstrated that the Lower, Middle, and Upper Cretaceous periods are viable candidates for sourcing hydrocarbon formation in the deep basin. The Lower Cretaceous (Barremian) was a time period in which source rocks with a terrestrial OM signature were deposited regionally. As several oil samples from offshore wells in the region include terrestrial biomarkers, the Barremian is considered their potential source. Additionally, OAE2 OM-rich deposits are

wider spread than previously considered and probably result from upwelling dynamics. This indicates a strong potential for regional distribution. Together with the OM-rich Upper Cretaceous deposits, we may suggest a high potential for Cretaceous sourced hydrocarbons in the deep Levant Basin.

References

Almogi-Labin, A., Bein, A., Sass, E.: Late Cretaceous upwelling system along the Southern Tethys Margin (Israel): interrelationship between productivity, bottom water environments, and organic matter preservation. Paleoceanography **8**, 671–690 (1993)

Amit, O.: Organochemical evaluation of Gevar'am Shales (Lower Cretaceous), Israel, as possible oil source rock. Am. Assoc. Pet. Geol. Bull. **62**, 827–836 (1978)

Conway, B.H.: The oil-window in the offshore Yam-West 1 borehole as detected by Thermal Alteration Indices (TAI); Jerusalem, 2002

Daher, S.B., Ducros, M., Michel, P., Hawie, N., Nader, F.H., Littke, R.: 3D thermal history and maturity modelling of the Levant Basin and its eastern margin, offshore—onshore Lebanon. Arab. J. Geosci. **9**, 26 (2016)

El-Shahat, W., Villinski, J.C., El-Bakry, G.: Hydrocarbon potentiality, burial history and thermal evolution for some source rocks in October oil field, northern Gulf of Suez, Egypt. J. Pet. Sci. Eng. **68**, 245–267 (2009)

Flexer, A.: Stratigraphy and facies development of Mount Scopus Group (Senonian-Paleocene) in Israel and adjacent countries. Isr. J. Earth Sci. **17**, 85–113 (1968)

Gardosh, M.A., Tannebaum, E.: The petroleum systems of Israel. In: Marlow, L., C. K., L. Y. (ed.) Petroleum Systems of the Tethyan Region. AAPG Memoir 106, 2014, pp. 179–216. ISBN 8230801495

Grohmann, S., Fietz, S.W., Littke, R., Daher, S.B., Romero-sarmiento, M.F.: Source rock characterization of mesozoic to cenozoic organic matter rich marls and shales of the Eratosthenes Seamount, Eastern Mediterranean Sea Source rock characterization of mesozoic to cenozoic organic matter rich marls and shales of the Eratosthene. Oil Gas Sci. Technol. 73 (2018)

Lipson-Benitah, S., Flexer, A., Rosenfeld, A., Honigstein, A., Conway, B., Eris, H.: Dysoxic sedimentation in the Cenomanian-Turonian Daliyya Formation, Israel. AAPG Stud. Geol. (1990)

Lüning, S., Kolonic, S., Belhadj, E.M., Belhadj, Z., Cota, L., Barić, G., Wagner, T.: Integrated depositional model for the Cenomanian-Turonian organic-rich strata in North Africa. Earth-Sci. Rev. **64**, 51–117 (2004)

Meilijson, A., Ashckenazi-Polivoda, S., Ron-Yankovich, L., Illner, P., Alsenz, H., Speijer, R.P., Almogi-Labin, A., Feinstein, S., Berner, Z., Püttmann, W., et al.: Chronostratigraphy of the Upper Cretaceous high productivity sequence of the southern Tethys, Israel. Cretac. Res. 50 (2014)

Meilijson, A., Ashckenazi-Polivoda, S., Illner, P., Speijer, R.P., Almogi-Labin, A., Feinstein, S., Püttmann, W., Abramovich, S.: From phytoplankton to oil shale reservoirs: a 19-million-year record of the Late Cretaceous Tethyan upwelling regime in the Levant Basin. Mar. Pet. Geol. **95**, 188–205 (2018)

Minster, T.: Reconstruction of Sedimentary Basins in the Senonian, Northern Negev—a Contribution to the Understanding of Anoxic Events, Tal-Aviv University, 1996

Shaaban, F., Lutz, R., Littke, R., Bueker, C., Odisho, K.: Source-rock evaluation and basin modelling in NE Egypt (NE Nile Delta and northern Sinai). J. Pet. Geol. **29**, 103–124 (2006)

Wendler, J.E., Wendler, I., Huber, B., Macleod, K.G.: What are calcispheres?—Pristine specimens from the Tanzania Drilling Project provide unprecedented insight into an enigmatic Cretaceous microfossil group. Conf. Pap. GSA, Denver (2010)

Petroleum Generation Potential of the Lower Palaeozoic Organic Matter-Rich Shales in the Central Part of the Baltic Sedimentary Basin

Anna Cichon-Pupienis, Jurga Lazauskienė, Ralf Littke, and Felix Froidl

Abstract

The lower Palaeozoic sedimentary succession of the Baltic Basin forms a petroleum system with several commercial hydrocarbon accumulations predominantly present in Cambrian reservoirs. The main petroleum generation area is situated at the SW part of the basin due to maximum subsidence. The central part of the basin hosts three excellent source rock horizons, each several metres thick, in addition to more than a hundred-metre-thick section with fair and good hydrocarbon generation potential. In this study, a set of organic petrographical and geochemical analyses was applied in order to study the quantity, composition and thermal maturity of the organic matter. A broad spectrum of thermal maturities ranging from immature to the late phase of oil window was determined with corresponding changes in kerogen composition and organic petrological properties.

Keywords

Kerogen • Paleotemperatures • Solid bitumen reflectance • Baltic Basin • Lower Palaeozoic

1 Introduction

The Baltic Basin is an intracratonic Phanerozoic sedimentary basin situated at the western margin of the East European Craton (Fig. 1a). The sedimentary succession in the Baltic Basin is largely Palaeozoic with a thin Mesozoic–Tertiary cover. The Caledonian stage was crucial for petroleum source rock maturation with grey-black mudstones being present within the Upper Ordovician–lower Silurian fine-grained sediments. This study focuses on the results of our recent studies on the kerogen content, composition and thermal maturity within these lower Palaeozoic mudstones along with a discussion on factors governing the maturation of organic matter in the Baltic Basin.

A. Cichon-Pupienis (✉) · J. Lazauskienė
Institute of Geosciences, Vilnius University,
21/27 M. K. Čiurlionio Street, 03101 Vilnius, Lithuania
e-mail: anna.cichon-pupienis@gf.vu.lt

R. Littke · F. Froidl
Institute of Geology and Geochemistry of Petroleum and Coal, Energy and Mineral Resources Group (EMR), RWTH Aachen University, Lochnerstr. 4-20, 52056 Aachen, Germany

2 Material and Methods

A set of mudstones core samples (174 samples) was collected from the Cambrian–Silurian interval with special focus on the Silurian due to the considerable thickness and organic richness. The analytic studies involved a wide range of methods: elemental analysis, organic petrography, vitrinite reflectance measurements, Rock-Eval pyrolysis and molecular geochemical analysis. Additional data were collected from industrial reports.

3 Results and Discussion

The results of the study revealed that the amount of organic matter varies from rich (TOC up to 22.0 wt%) to poor (TOC < 0.5 wt%). Three several metres thick clayey organic-rich horizons of the Upper Ordovician and Llandovery demonstrate good and excellent source rocks. Fair source rocks (avg. TOC of 1.3 wt%) are the upper lower Silurian calcareous mudstones (Fig. 1b). Despite changes in TOC content and age of the samples, kerogen within the studied section is oil-prone marine-derived Type II (Fig. 2).

The organic matter composition of Ordovician and Silurian samples is rather similar: zooclasts, amorphous organic matter (bituminous groundmass), algal bodies (telalginite and lamalginite), liptodetrinite, solid bitumen and vitrinite-like particles (Fig. 2).

M. Meghraoui et al. (eds.), *Advances in Geophysics, Tectonics and Petroleum Geosciences*,
Advances in Science, Technology & Innovation, https://doi.org/10.1007/978-3-030-73026-0_88

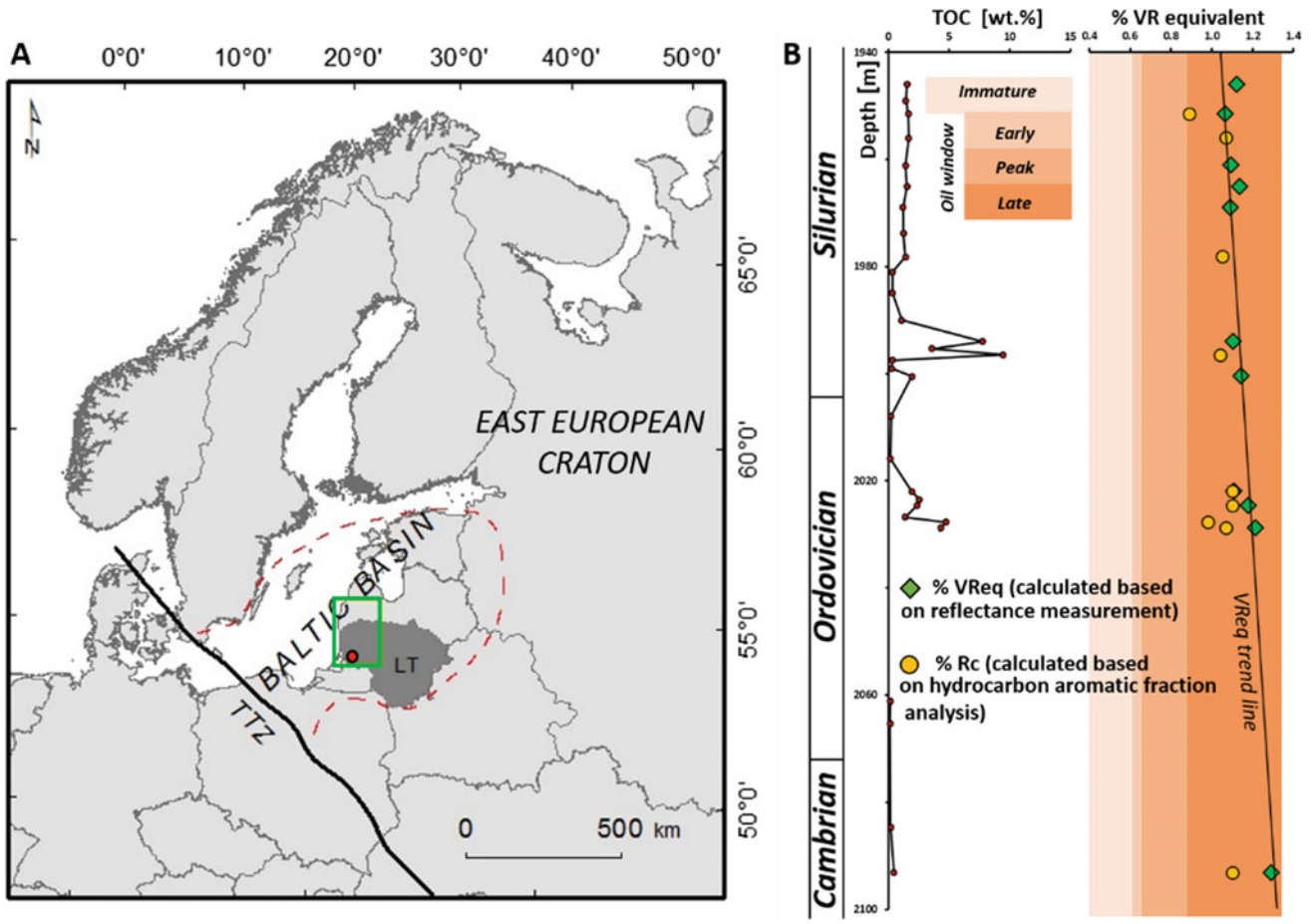

Fig. 1 **a** Sketch map of the East European Craton and **b** thermal maturity profile in a selected reference borehole showing a slightly increasing trend in maturities with burial depth within the Cambrian—lower Silurian succession (**b**). Dark grey—territory of Lithuania (LT), red line—boundary of the Baltic Basin, green line—study area, black line—SW boundary of the Baltic Basin–TTZ (Teisseyre-Tornquist Zone), red dot—reference borehole

Vitrinite reflectance equivalents (VR_{equiv}) calculated on the basis of measurements of the reflectance of the "vitrinite-like" macerals and hydrocarbon aromatic fraction analysis showed the reflectance values varying from 0.6 to 1.3% VR_{equiv}. The maceral composition changes with increasing thermal maturity. The samples of lower maturities (0.6% VR_{equiv}) are dominated by liptodetrinite and discrete alginite as well as zooclasts in transmitted light strew slides. With progressing kerogen transformation, solid bitumen becomes more abundant. In places, for samples with thermal maturities ~0.7 to 0.8% VR_{equiv}, the continuum of transformation from alginite to solid bitumen was recorded (Fig. 2d) (Littke et al. 1987; Stock et al. 2017; Hackley and Cardott 2016). At the higher maturities (1.0–1.3% VR_{equiv}), alginite was not present. Samples close to peak oil stage still host particles with a wide reflectance range that well illustrates different courses of particle maturation (Hackley and Cardott 2016). Generally, the lower Palaeozoic succession is within the immature-peak oil window stage which is in good agreement with a NE–SW increasing maturity trend in the Baltic Basin (Fig. 3). Maximum paleotemperatures exceeded present temperatures significantly. The maturity parameters imply paleotemperatures of 80–130 °C probably due to deep tectonic subsidence in Silurian, which might be explained by the progressing flexural foreland basin development at the SW basin margin and gradual migration of the foredeep rim to the east (Lazauskienė et al. 2002). This trend is overprinted by local effects, leading to increased maturities (late oil window) in the SW Lithuania, where paleotemperatures of 160–180 °C could have been reached. An additional source of heat could be associated with granitoid intrusions and increased mantle heat production.

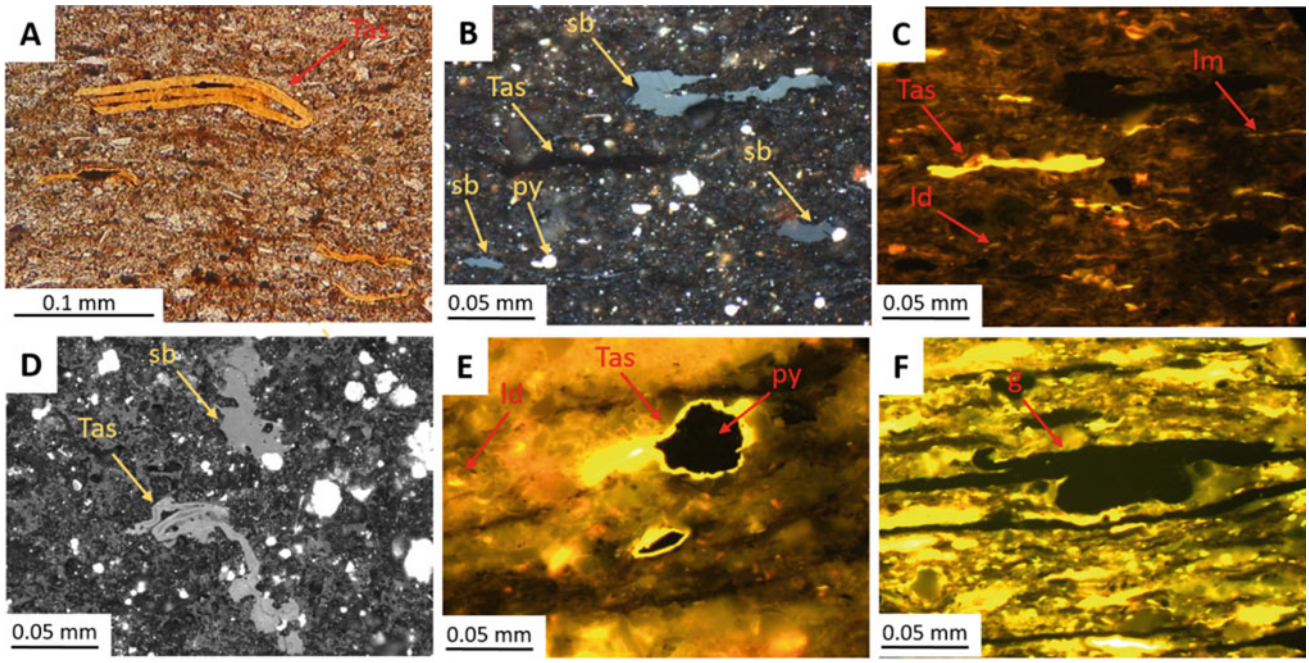

Fig. 2 Organic matter composition shown in photomicrographs. **a** Alginite bodies *Tasmanite* (Tas), thin-section, plane-polarized light; **b–f** solid bitumen (sb) *Tasmanite* (Tas), pyrite (py), lamalginite (lm), liptodetrinite (ld), graptolite (g); reflected white and UV light in oil immersion

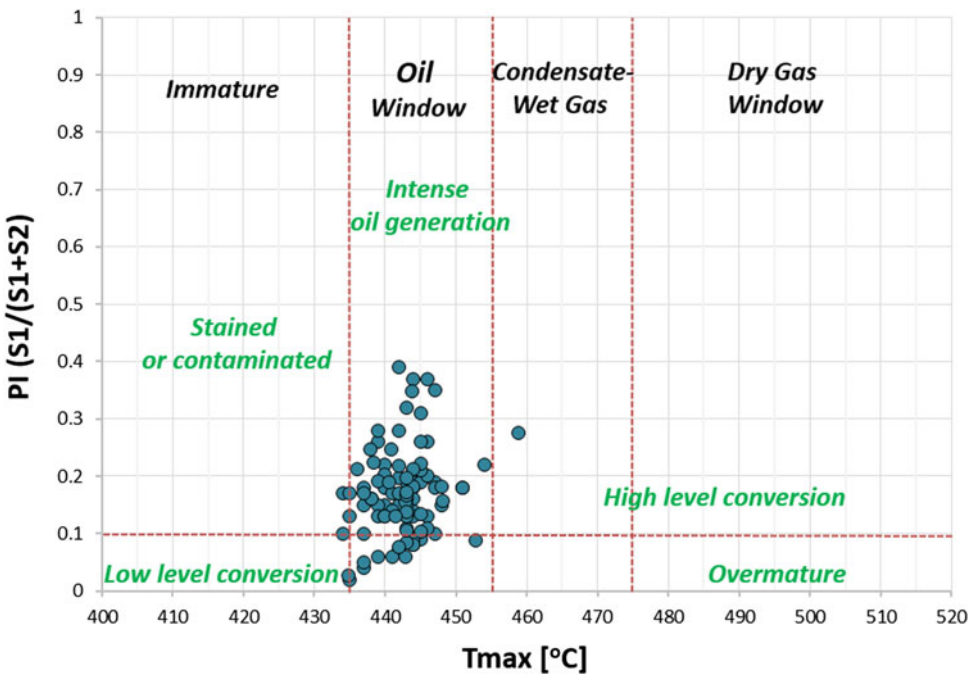

Fig. 3 Cross-plot of Tmax and PI (Production Index) showing the range of hydrocarbon generation potential. Applied TOC values cut-off—TOC > 0.5 wt%

4 Conclusions

Organic matter in the lower Palaeozoic fine-grained sediments is of marine origin with good oil generation potential. Kerogen composition involves macerals from the liptinite group, zooclasts and solid bitumen, being a by-product of kerogen transformation to petroleum. The studied succession could be buried to the depths corresponding up to 80–130 °C and generate liquid petroleum. Deep burial was probably the dominant mechanism leading to high paleotemperatures, but local factors (granitoid intrusion, increased mantle heat production) overlapped resulting in alteration of organic matter up to the level of late phase oil generation in the SW part of the studied area.

References

Hackley, P.C., Cardott, B.J.: Application of organic petrography in North American shale petroleum systems: a review. Int. J. Coal Geol. **163**, 8–51 (2016)

Lazauskienė, J., Stephenson, R., Šliaupa, S., van Wees, J.D.: 3-D flexural modelling of the Silurian Baltic Basin. Tectonophysics **346**, 115–135 (2002)

Littke, R., Baker, D.R., Leythaeuser, D.: Microscopic and sedimentologic evidence for the generation and migration of hydrocarbons in Toarcian source rocks of different maturities. In: Mattavelli, L., Novelli, L. (eds.) Adv. Org. Geochem. 1987. Org. Geochem., vol. 13, pp. 549–559, Pergamon Press, Oxford (1988)

Stock, A.T., Littke, R., Schwarzbauer, J., Horsfield, B., Hartkopf-Fröder, C.: Organic geochemistry and petrology of Posidonia Shale (Lower Toarcian, Western Europe)—The evolution from immature oil-prone to overmature dry gas-producing kerogen. Int. J. Coal Geol. **176–177**, 36–48 (2017)

Organic Matter in Condensed Section of Oligocene Shales in CuuLong Basin, Vietnam

Quan Vo Thi Hai

Abstract

Oligocene sediments are the main and very good source rocks in the CuuLong basin. The aim of this study was to investigate the variation in organic matter richness, thermal maturity and combine it with palynofacies data for more information about factors controlling source potential in condensed section of Oligocene shales (2760–2930 m). All samples contain very high TOC contents of 2.14 to 5.01 wt %, very high S2 values of 12.30 to 31.69 mg HC/g rock, indicating very good to excellent source rocks with type I-II kerogens, which are capable of generating oil. The source rocks fall into mature stage with Tmax ranging from 436 to 441 °C and poor-quality vitrinite reflectance values of 0.38 to 0.52%. The only shale sample in the condensed section (2800–2810 m) comprises a very low TOC value of 0.14%, S2 of 0.68 mg HC/g rock, HI of 486 mg HC/g TOC, Tmax of less than 435 °C and Ro value of 0.39%. This section is characterized by the abundance of phytoclast group. The ratio of opaque to translucent phytoclasts increases abruptly, and the palynomorph preservation decreases towards the maximum flooding surface (MFS).

Keywords

Condensed section • CuuLong basin • Palynofacies • Rock-Eval

1 Introduction

Rock–Eval (RE) parameters are often used for source rock evaluation. However, it is difficult for interpretation due to abnormal values of pyrolysis parameters in case of an unexpected decrease of total organic carbon content (TOC) in anoxic to oxic conditions. Therefore, a combination of Rock–Eval and palynofacies data is needed for better understanding of such sections where the total organic content of sediments is very low (<0.2 wt%).

Palynofacies are useful for distinguishing between well-preserved or highly degraded palynofacies in condensed intervals and provide valuable information on the depositional environments. A sample from a condensed interval (2800–2810 m) in Oligocene was studied in the A-1X well. This study showed a good relationship between geochemical and palynofacies data in interpreting abnormal geochemical data that has not been studied before in Vietnam.

2 Materials and Methods

Eight cuttings from the A-1X well were selected for Rock–Eval (RE), vitrinite reflectance analyses that provide organic richness, type of kerogen and thermal maturity of organic matter. The analyses were conducted at the VPI-Labs in Vietnam.

Rock–Eval pyrolysis: All shales were subjected to RE pyrolysis using Rock–Eval 6. Temperature was increased up to 850 °C with a rate of 25 °C/min; parameters such as TOC, S1, S2, HI, PI and Tmax were obtained.

Vitrinite reflectance: Kerogen containing vitrinite particles were measured under incident reflectance light of spectrometry microscope CRAIC 308 PV™.

Q. V. T. Hai (✉)
Geosystem Exploration & Petroleum Geoengineering Program, School of Engineering and Technology, AIT, Bangkok, Thailand
e-mail: quanvth@vpi.pvn.vn

M. Meghraoui et al. (eds.), *Advances in Geophysics, Tectonics and Petroleum Geosciences*, Advances in Science, Technology & Innovation, https://doi.org/10.1007/978-3-030-73026-0_89

Defining condensed sections (CS): CS are intervals that deposited on a landward-stepping shoreline (Roger 2006). It is common that the upper layer of a transgressive systems tract forms a condensed section, which is associated with the maximum flooding surface (MFS).

3 Results

The TOC contents vary from 2.17 to 5.01% in shale samples. The thermally extracted and generated hydrocarbons S1 and S2 range from 0.97 to 6.85 mg HC/g rock and from 12.30 to 31.69 mg HC/g rock, respectively. The S2 yields showing a good correlation with TOC contents indicate that these shales have very good to excellent source potential. The HI values ranging from 552 to 665 mg HC/g TOC, PI values of 0.07 to 0.18 and plot of HI versus Tmax indicate very good to excellent potential sources that derived from type II and I kerogens, which are favourable for generating oil (based on guideline for source rock interpretation by Peters and Cassa 1994). These shales fall into mature stage with a Tmax ranging from 436 to 441 °C. The low Ro values (0.38–0.52%) are due to the sparse presence of vitrinite particles with cavings in some samples, resulting in low accuracy of measurements. The only shale sample in the interval 2800–2810 m comprises a very low TOC value of 0.14%, S2 of 0.68 mg HC/g rock, HI of 486 mg HC/g TOC and Ro value of 0.39%. Tmax of this sample (347 °C) is not reliable due to the low S2 peak. The result indicates that the sample is in immature stage and contains very poor organic matter of type II/I kerogen (Table 1 and Figs. 1, 3a). These unusual results were integrated with stratigraphic data to define factors that affect an anomalous decrease in TOC content.

A condensed section is defined in the interval 2800–2810 m (MFS) from palynofacies data (Fig. 3b). The organic facies in this section are characterized by the abundance of phytoclast group; meanwhile, amorphous organic matter is almost absent. Moreover, very high proportions of Bossedinia and Dinoflagellates in organic matter indicate well-preserved assemblages in freshwater and lagoonal brackish environments above and below this condensed section. Towards the MFS, the ratio of opaque to translucent phytoclasts increases abruptly, and the palynomorph preservation decreases. It records a depositional environment quite unfavourable to organic matter preservation in this condensed section. Therefore, the TOC content of this condensed section is very low (<0.2%), which may affect the reliability of Rock–Eval pyrolysis parameters (Figs. 2 and 3a).

4 Discussion

Palynofacies data are effectively used as an additional technique together with geochemical data for interpretation abnormal TOC value in this condensed section and also for defining depositions of the organic matters in oil- or gas-prone based on the different groups of palynological elements.

This study provides evidence that depositional environments control the quality and quantity of organic matter in the condensed section, which helps to understand the good relationship between organic matter sources and palynofacies. The results show the high quantity and good quality of lacustrine and lagoonal brackish algae from type II and I kerogens present in overlying and underlying sediments of the condensed section. Therefore, oils derived from these source rocks are predominantly waxy. This study will be expanded later on for well-to-well correlation based on palynological data and geochemical properties to provide changes of kerogen macerals, paleoenvironments and apply the data for petroleum system modelling.

Table 1 Rock–Eval pyrolysis

Depth (m)	TOC (wt%)	S1 (mgHC/g rock)	S2 (mgHC/g rock)	HI (mgHC/g TOC)	PI	Tmax (°C)	Ro (%)
2760	2.14	0.97	12.30	575	0.07	437	–
2780	2.35	1.76	12.97	552	0.12	436	0.38
2800–2810	0.14	0.46	0.68	486	0.40	347	0.39
2860	3.20	2.09	21.28	665	0.09	441	0.35
2880	5.01	6.85	31.69	633	0.18	436	0.40
2900	3.14	3.30	20.24	645	0.14	437	0.42
2920	2.17	2.00	12.40	571	0.14	436	–
2920–2930	2.62	2.61	15.77	602	0.14	436	0.52

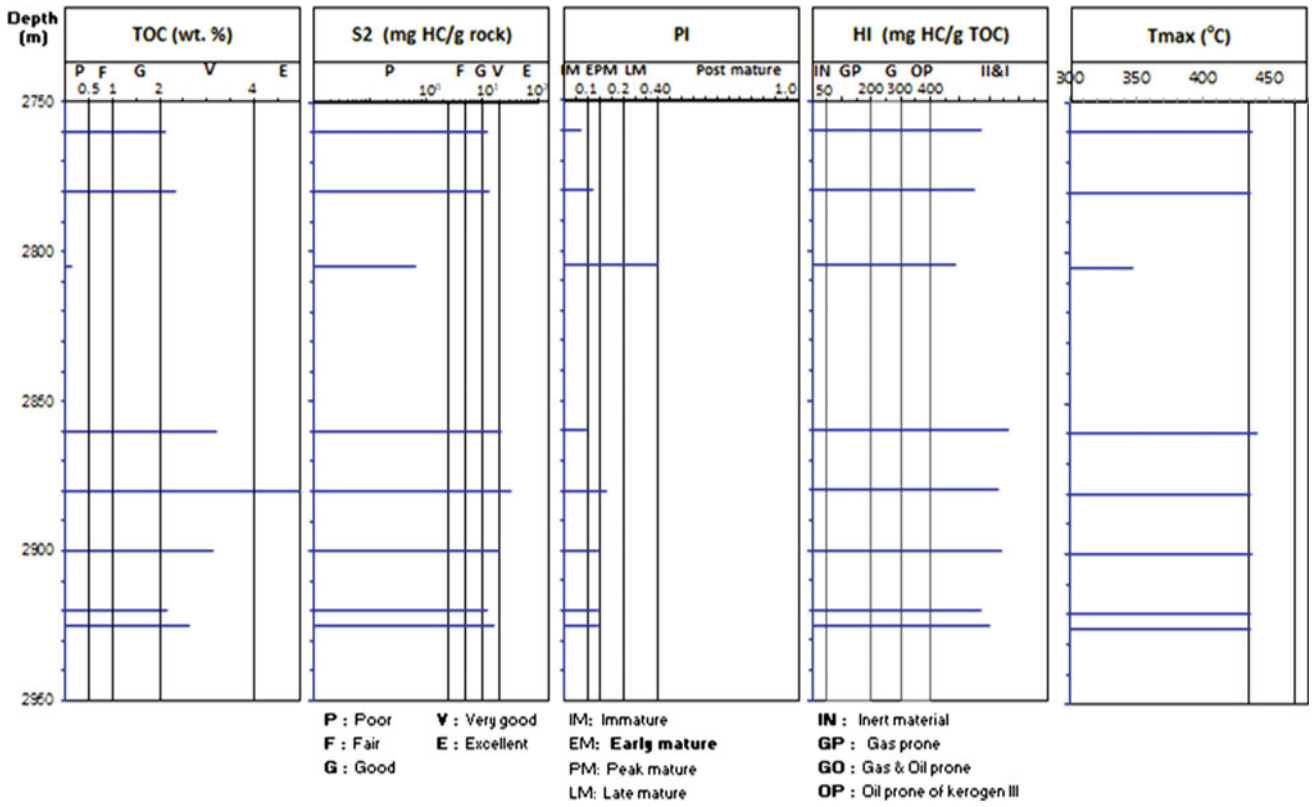

Fig. 1 Changes of Rock–Eval parameters with depth

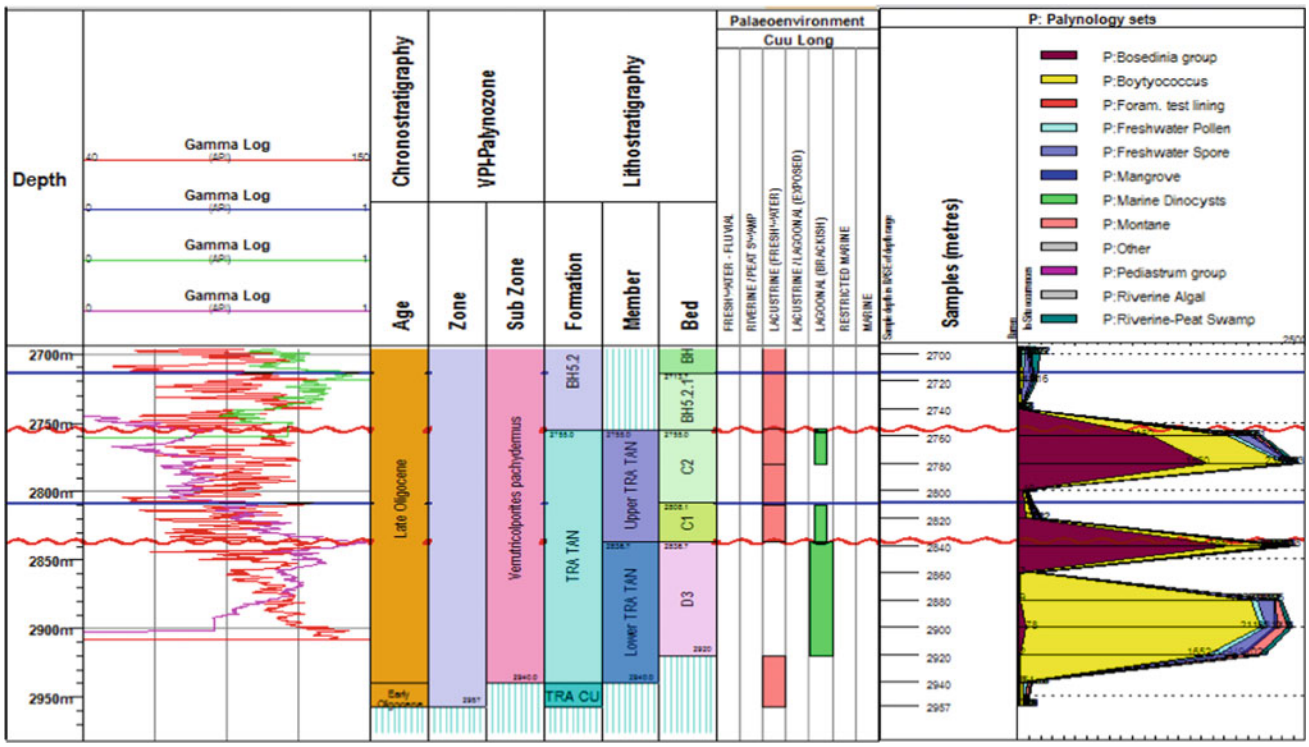

Fig. 2 Palynological distribution chart

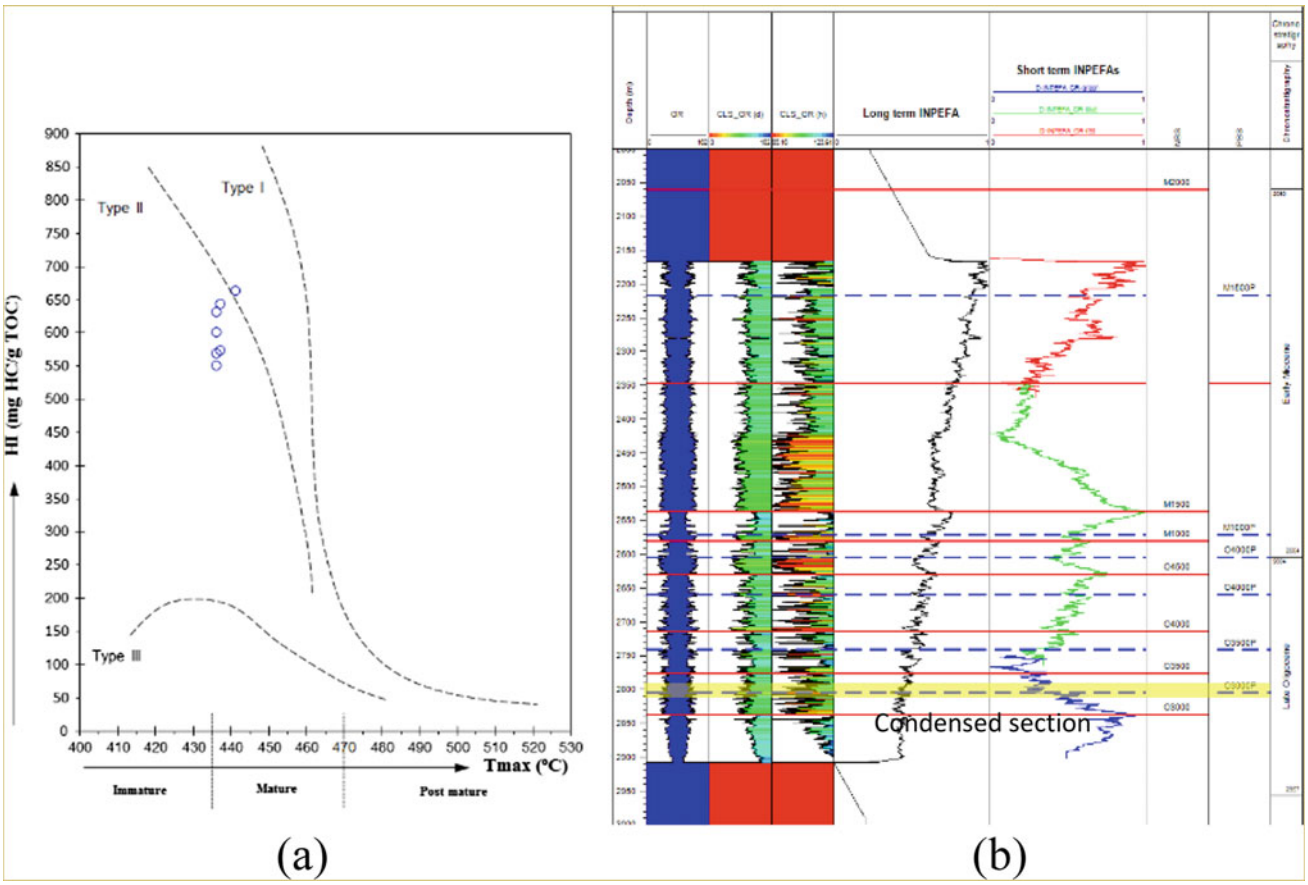

Fig. 3 **a** Types of organic matter; **b** cyclolog composites

5 Conclusions

The palynofacies show predominance of freshwater and brackish water algae in organic matter contributing to lacustrine and estuarine deposits. These are favorable conditions for the preservation of organic matters in Oligocene shale source rocks that contain very rich in organic matters, very good to excellent hydrocarbon generation potential of type-II and type-I of oil-prone kerogens. The shales are thermally mature with a Tmax range from 436 to 441 °C and vitrinite reflectance of less than 0.55%. The commercial quantities of oil in the intervals 2760–2930 m are expected from these source rocks. Moreover, the source rocks in deeper depths could reach to oil window and are expected to accumulate more hydrocarbons. Exception of a sample at condensed section is not considered as a source rock.

References

Peters, K.E., Cassa M.R.: The petroleum system-from source to trap. Applied source rock geochemistry. AAPG Memoir 60 (1994)
Roger, M.S.: Stratigraphic Reservoir Characterization for Petroleum Geologists, Geophysicists and Engineers, 1st edn. Elsevier B. V. Publisher, UK (2006)

The Geochemical Characterization of the Pelagian Domain, North-Eastern Tunisia Near Lampedusa: Oil–Oil and Oil-Source Rock Correlations

Mehdi Attia, Anis Belhaj Mohamed, Ibrahim Bouazizi, and Firas Ben Hamdene

Abstract

Due to the importance of the petroleum discoveries in the Pelegian domain and the poor knowledge of the hydrocarbon systems, a geochemical evaluation based on samples collected from different wells and layers—Aptian (Serdj formation), Albian (Lower Fahdene formation) and Yprisian (Bou Dabbous formation) drilled in the Pelagian province, offshore north-eastern Tunisia—should be done to better understand the petroleum system and identify source rock types. The geochemical study aimed to characterize source rock potential and to determine the origin of oil shows recorded in the Serdj Formation through the correlation of extracted oils with the different oils and source rocks present in the neighbouring provinces. This study is based on pyrolysis analysis using the RockEval 6 and on oil characterization using the gas chromatography/mass spectrometry. The present study has shown that the two extracted oils—FI-1 and SE-1—were generated from the Fahdene source rock (Gulf of Hammamet), and that there is no relationship between those oils and the IS oil (Bouddabous source rock, Gulf of Gabes) based on their biomarker distributions (Oil–Oil and Oil-Source Rock Correlations).

Keywords

Pelagian province • Rock–Eval • Gas chromatography/mass spectrometry • Oil/oil correlation • Oil/source rock correlation • Biomarkers

1 Introduction

The drilling in our area of interest (see Fig. 1) resulted in the identification of at least five potential reservoir formations: The Ain Grab Limestones (Langhian), the Riccio Formation (upper Eocene), the Bouddabous carbonates (Ypresian), the Abiod chalky fractured limestones (Upper Cretaceous), the Serdj Formation (Aptian) and the Lower Cretaceous sandstone beds such as the Sidi Aich Formation. The main source rock in the area is represented by the Early Cretaceous (Fahdene Formation). The Rock–Eval pyrolysis was carried out to identify the oil-bearing zones.

Oil extracts belonging to different reservoir layers were analyzed by gas chromatography/mass spectrometry to identify the main oil families and determine their origin.

2 Settings/Materials and Methods

The geochemical evaluation is based on the cuttings samples recovered from four exploration wells in the study area (see Fig. 1).

For the Oil–Oil correlation, we used three samples: FI-1 (lower Fahdene extracted oil), SE-1(Aptian Serdj Formation) and IS (El Garia Ypresian oil).

For Oil-Source Rock correlations, we used the Early Cretaceous Fahdene source rock (FAH-SR) as a reference biomarker distribution.

In this study, we used the Rock–Eval pyrolysis (RE6) to confirm the presence of oil stains, and the samples that show a high S1 value are chosen for extraction and fractionation (saturates, aromatics and NSO compounds).

Then, we used the gas chromatography/mass spectrometry to identify the biomarkers' distribution of each fraction.

2.1 Rock–Eval Pyrolysis

The Rock–Eval pyrolysis result for the Fahdene source rock shows a TOC higher than 1% with Tmax equal to 439 °C and a high hydrogen index (337). For FI-1-3030 and SE-1-3285 m, the Rock–Eval pyrolysis results are shown in Table 1.

M. Attia (✉) · A. B. Mohamed · I. Bouazizi · F. B. Hamdene
Entreprise Tunisienne d'Activités Pétrolières, Tunis, Tunisia

M. Meghraoui et al. (eds.), *Advances in Geophysics, Tectonics and Petroleum Geosciences*,
Advances in Science, Technology & Innovation, https://doi.org/10.1007/978-3-030-73026-0_90

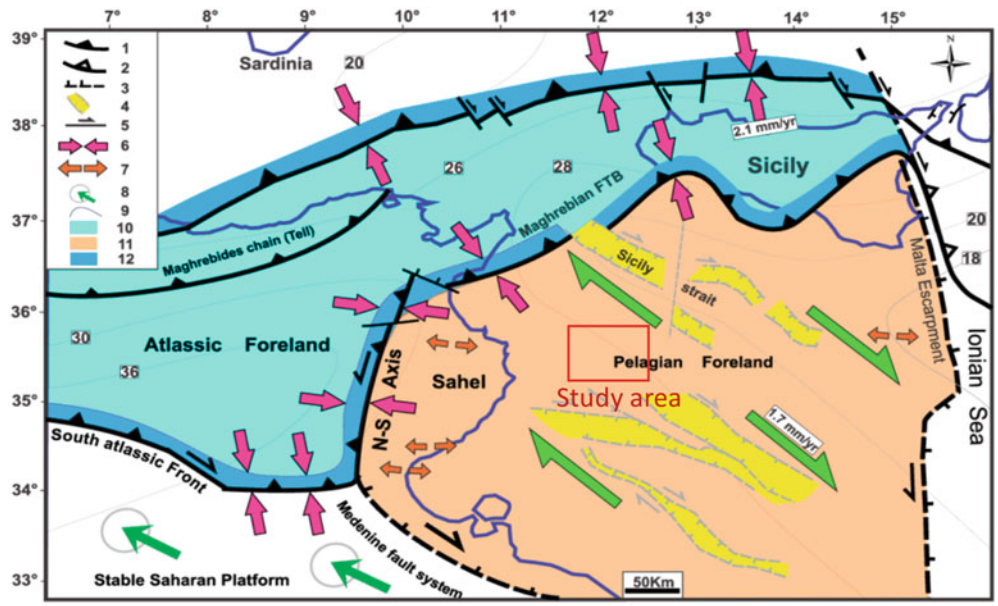

1: soft collision/thrust and reverse faults, 2: oceanic subduction, 3: normal fault, 4: neogene graben, 5: strike-slip fault, 6: compressional direction, 7: extensional direction, 8: the motion vectors of points south of the seismically active belts in northern Africa [Serpelloni et al., 2007], 9: depth to the Moho discontinuity [Grad and Tiira, 2009], 10: compressional to transpressional area, 11: strike-slip to trantensional area, and 12: compressive belt. Maghrebian FTB: Maghrebian fold-and-thrust belt.

Fig. 1 Tectonic map of the Pelagian province and the study area location (Soumaya 2015)

Table 1 Summary of Rock Eval pyrolysis results

	FI-1-3030 m	SE-1-3285 m
S1(mg/g) (Free hydrocarbon)	0.94	0.14
PI (Production index)	0.21	0.11

2.2 Oil–Oil and Oil-Source Rock Correlations

First, FI-1 and SE-1 oils were compared based on the biomarkers distribution of IS oil. Then, they were compared to FAH-SR (reference biomarkers of the source rock belonging to the study area) (see Fig. 2).

3 Discussion

The Rock–Eval results confirm that the Fahdene source rock has mixed types of organic matter (Type II and Type III), terrestrial matter and marine organic materials. Moreover, the source rock is considered early mature to mature based on the Tmax (higher than 435 °C).

The biomarkers' distribution of the extracted oils FI-1 and SE present in reservoir levels for the studied wells was similar and correlated with FAH-SR.

However, the IS oil belongs to a different oil family and shows no correlation with FAH-SR. These results are in accordance with a previous study (Gmiha et al. 2015), which has demonstrated that the IS oil originates from mixed source rocks (Bou Dabbous, Bahloul).

4 Conclusions

This study demonstrated that FI-1 and SE oils (extracted from different reservoirs) were identical and generated from the Albian source rock (Fahdene Formation located in the Gulf of Hammamet).

The IS oil was proven to be different from them and sourced from a distinct source rock level. In fact, the IS oil was sourced from allochtonous oils cogenerated by mixed facies between the Bahloul and the Bou Dabbous formations (Gmiha et al. 2015).

For a better understanding of the complex petroleum system in the Pelagian domain, supplementary studies should be done (comparison with other source rock extracts, isotope analysis, etc.).

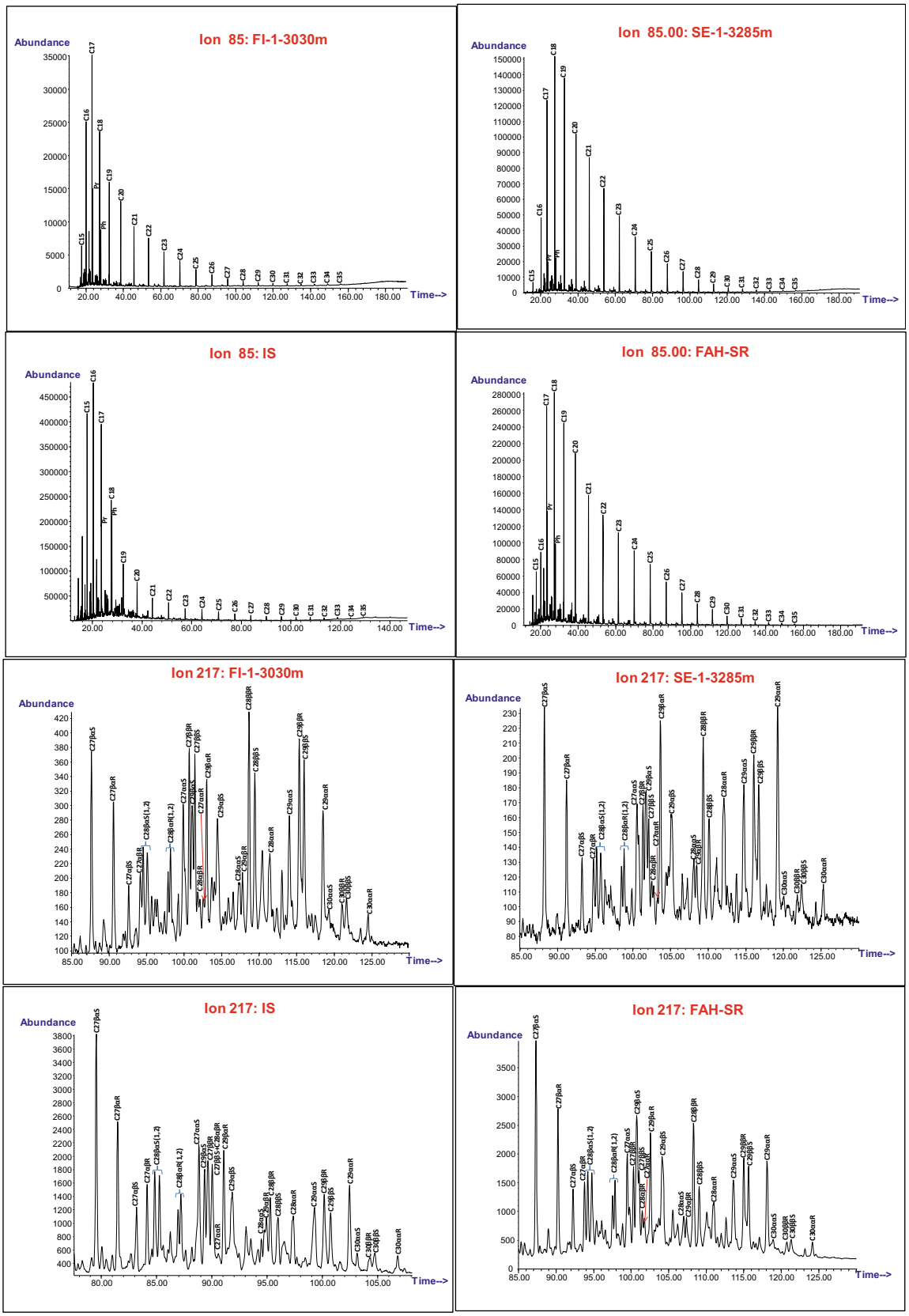

Fig. 2 Mass chromatograms m/z 85 and m/z 217 of FI-3030 m, SE-3285 m, IS and FAH-SR

References

Gmiha, S., Saidi, M., Mabrouk El Asmi, A., Belhaj Mohamed, A., Bouazizi, B.: Petroleum systems assessment of the ISIS Permit: from source rock and oil characterization to 1D modeling of hydrocarbon generation (EPC 2015)

Soumaya, A.: Spatial variation of Present-day stress field and tectonic regime in Tunisia and surroundings from formal inversion of focal mechanisms: geodynamic implications for Central Mediterranean (2015)

Origin of Oil Stains in a Well Located in Hammamet Gulf in the Sicily-Tunisia Channel

Firas Ben Hamdene, Anis Belhaj Mohamed, Mehdi Attia, and Ibrahim Bouazizi

Abstract

The studied well is located in the Gulf of Hammamet area in northern Tunisia, where important oil findings were recorded within the Miocene Birsa reservoir. This formation mainly consists of sand beds with shale intercalations and some minor limestones beds (Mejri et al. in Enterprise Tunisienne d'Activités Pétrolières, pp 108–109, 2006). Other oil stains were also recorded within the Late Cretaceous Abiod Formation which consists of chalky fractured carbonates. The presence of these oil stains is an indication of an active petroleum system in this area, and the objective of this study is to determine the origin of these oil stains linking them to the main source rocks identified in the gulf of Hammamet which are mainly the Fahdene Formation (Albian-Cenomanian), and secondly, the Bahloul horizon (Cenomanian- Turonian). Our study was based on oil stains extracted from core samples from both the Birsa and the Abiod reservoirs recovered from an exploration well. Oil–oil correlations proved that the two oil extracts (Birsa and Abiod) are different based on biomarkers distribution. Oil–source rock correlations proved the two oils to have been generated by the same source rock (Fahdene Formation, argillaceous), suggesting the existence of two distinct charging phases and/or that the two oils have undergone different reservoir conditions.

Keywords

Hammamet gulf • Birsa • Abiod • Oil stains • Biomarkers • Oil–oil correlation • Oil–source rock correlations • Charging

1 Introduction

This study is based on a well located in the Gulf of Hammamet area, in the Sicily-Tunisia channel where several oil and gas discoveries were made; the major part was within the Middle Miocene Birsa sands (Tazarka, Birsa, Zelfa …). Other proven reservoirs exist in the study area such as the Langhian Ain Grab limestones (Halk el Manzel field) and the Abiod chalky fractured limestones (The Zinnia gas field, onshore equivalent, Maamoura field) (Mejri et al. 2006). The main source rocks present in the area are, primarily, the Fahdene Formation (Albian-Cenomanian) and, secondarily, the Bahloul horizon (Cenomanian- Turonian). The aim of this work is to compare the biomarkers distribution and determine the origin of both the Birsa Formation and the Abiod Formation oil stains through oil–oil and oil–source rock correlations using oil extracts from the core samples available in our core facilities that were recovered from an exploration well drilled in the area.

2 Settings/Materials and Methods

Our study is based on core samples recovered from an exploration well located in gulf of Hammamet in the Sicily-Tunisia channel (see Fig. 1). Three core samples were collected from the reservoir sections (see Fig. 2). The first and the second ones were collected within two different sandstone layers in the Birsa Formation (B1 and B2) separated by a 15 m thick clay unit, and the third one in the Abiod Formation limestones (AB). Rock Eval pyrolysis (RE6) was then carried out to confirm the presence of oil stains within these samples. Three oil samples were then extracted using a solvent and fractioned (mini column separations) into saturate and aromatic fractions. The biomarkers distribution was then determined through a GCMS analysis, leading to oil–oil and oil–source rock correlations.

F. B. Hamdene (✉) · A. B. Mohamed · M. Attia · I. Bouazizi
Entreprise Tunisienne D'activités Pétrolières, Tunis, Tunisia

M. Meghraoui et al. (eds.), *Advances in Geophysics, Tectonics and Petroleum Geosciences*,
Advances in Science, Technology & Innovation, https://doi.org/10.1007/978-3-030-73026-0_91

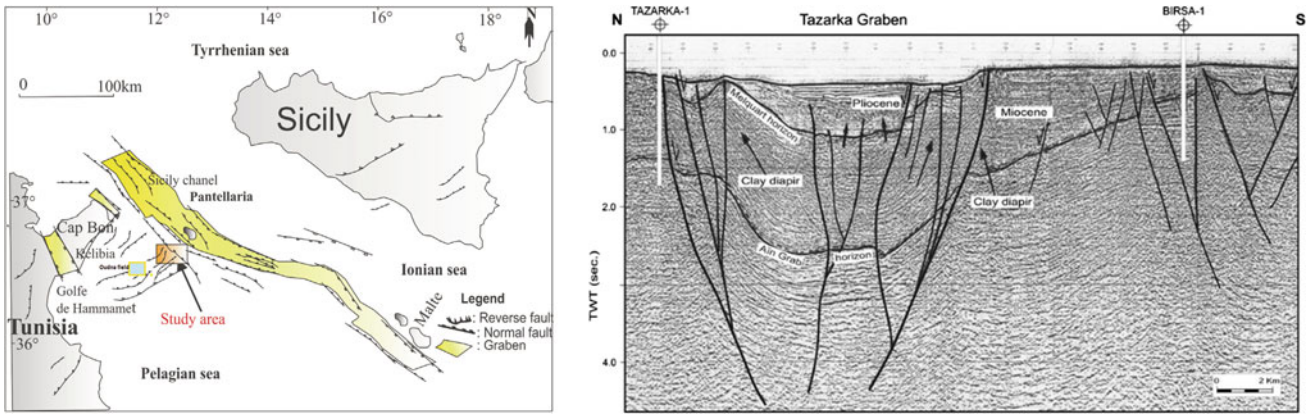

Fig. 1 Tectonic map of the central Mediterranean with main offshore structural features; study area location (Casero and Roure 1994); and seismic line across the study area (Zouaghi et al. 2011)

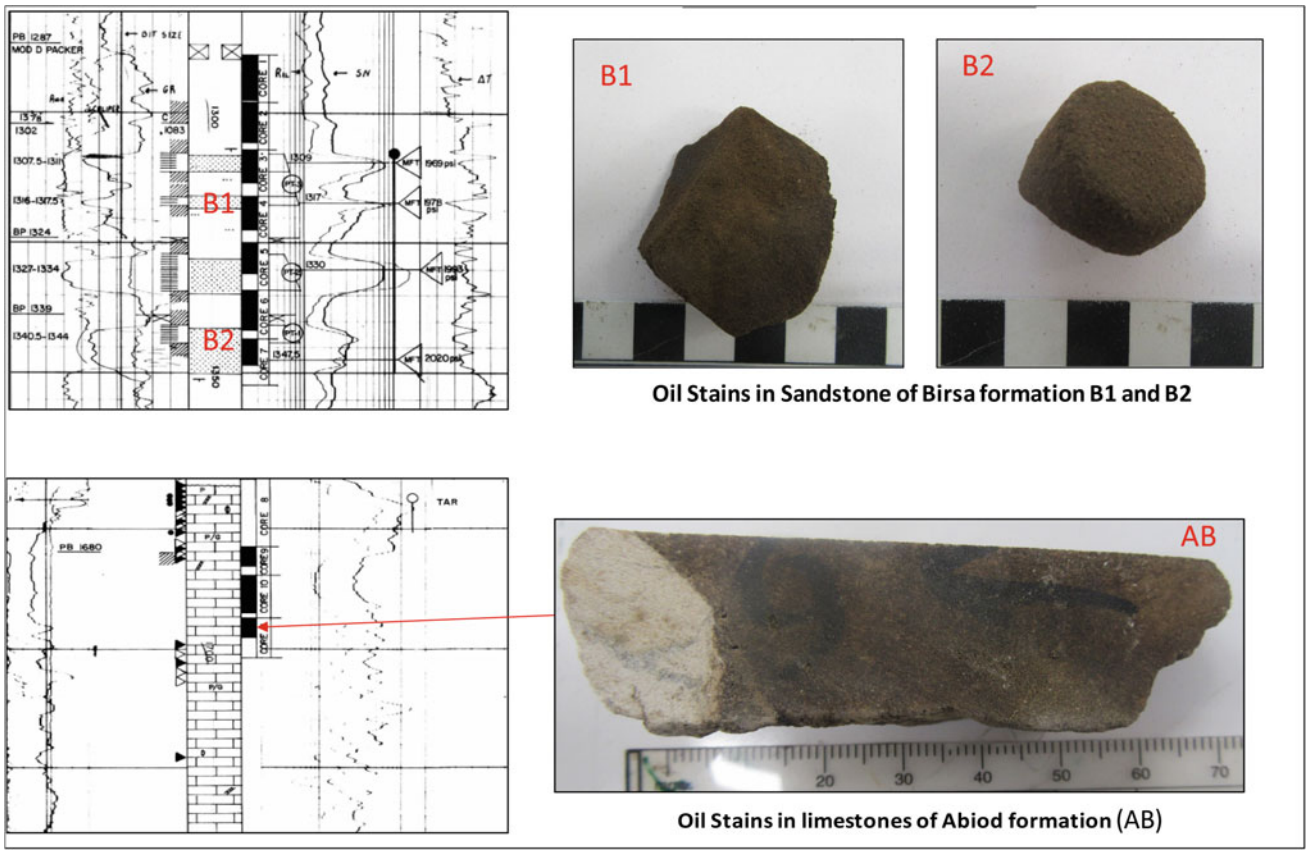

Fig. 2 Oil stains observed in the Birsa (B1&B2) and Abiod (AB) Formations in the studied well

3 Results

3.1 Rock Eval Pyrolysis

A small quantity from the three core samples (B1, B2 and AB) was crushed and analysed by Rock Eval pyrolysis. All the samples proved to be oil bearing, considering the high values of S1 which indicates a contamination with allochthonous oils and production indexes higher than 0.4. Considering that no source rock levels were encountered in the studied well and in the neighbouring wells due to their high structural position, reference sections for the source rocks in the Gulf of Hammamet (Fahdene and Bahloul Formations) were used.

3.2 Oil–Oil and Oil–Source Rock Correlations

The two oil samples recovered from the Birsa reservoir layers (B1 and B2) were first compared based on the biomarkers distribution and were found to be identical. Then, one of these two samples (B1) was compared with the oil sample extracted from the Abiod limestones (AB). They were different in terms of biomarker distributions (see Fig. 3). Peak identification and calculated reports between biomarkers used for correlations were selected according to the biomarkers guide (Peters et al. 2005). The two different oil extracts were then compared to source rock extracts of the Fahdene and the Bahloul source rocks available in our databases. Results showed a positive correlation with the Fahdene argillaceous source rock.

4 Discussion

The oil stains that were present within the reservoir sections of the studied well (Birsa and Abiod) were different in terms of biomarker distributions, but originated from the same Fahdene source rock. This can imply that they have undergone different reservoir conditions that can lead to differences in molecular properties. However, when considering, on the first hand, that the difference in depth is relatively not very high (300 m) and that the maturity and aromatic fractions that are the most conserved and resistant were also different, this scenario seems not to be plausible. Therefore, these results can be explained by the presence of at least two charging phases that occurred within the Fahdene Formation leading to the generation of two different oils.

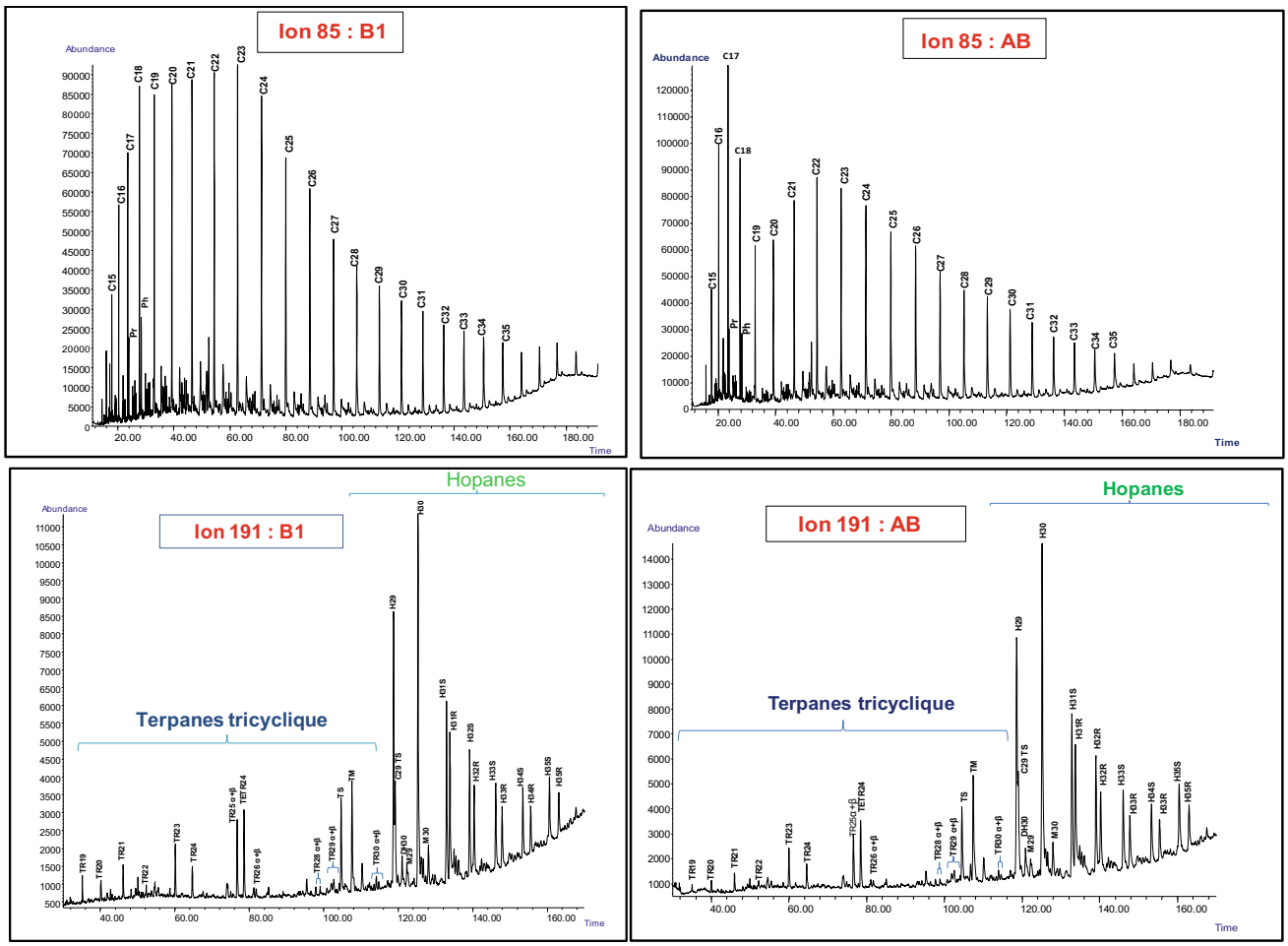

Fig. 3 Mass chromatograms m/z 85, m/z 191 (Tricyclic terpanes and hopanes) of B1 AB showing the differences in biomarker distributions

The main charging phase in the nearest wells [Birsa concession, south of the studied well (see Fig. 1)] has started in the beginning of the Paleocene (Bouhlel et al. 2000) leading to oil accumulations within the Miocene reservoir. Oil stains in the Abiod Formation (Upper Cretaceous) that were not studied in the Birsa concession—because this reservoir section was not reached by the drilling—may have been generated from another charging phase from the same source rock facies.

5 Conclusions

The present study suggests that the oil stains present in the two separate reservoirs (Birsa and Abiod) were generated from the Fahdene source rock through separate charging phases, leading to differences in terms of biomarker distributions both in saturate and aromatic fractions. Since previous studies link the oil accumulation within the Birsa Formation in the nearby Birsa concession to a main Paleocene charging phase (Bouhlel et al. 2000), the existence of another charging phase at the origin of the Abiod reservoir (Upper Cretaceous) is to be proved through a basin modelling study using more wells and the newly obtained results.

References

Bouhlel, A., Saidi, M., Fourati, L., Meskini, A.: Hydrocarbon Generation and Expulsion Histories in Hammamet Basin-Eastern Offshore Tunisia. In: 62nd EAGE conference & exhibition, Scotland, vol. 381, pp. 321–330 (2000)

Casero, P., Roure, F.: Neogene deformations at the Sicilian-North African plate boundary. In: Peri-Tethyan Platforms, pp. 27–50. EditionsTechnip, Paris (1994)

Mejri, F., Burollet, P.F., Ferjani, A.B.: Petroleum geology of Tunisia: a renewed synthesis. In: Enterprise Tunisienne d'Activités Pétrolières, pp. 108–109 (2006)

Peters, K.E., Walters, C.C., Moldowan, J.M.: The Biomarker Guide, 2nd edn. Cambridge University Press (2005).

Zouaghi, T., Bédir, M., Melki, F., Gabtni, H., Gharsalli, R., Bessioud, A., Zargouni, F.: Neogene sediment deformations and tectonic features of northeastern Tunisia: evidence for paleoseismicity. Arab. J. Geosci. **4**(7–8), 1301–1314 (2011)

Investigation of Rheological Properties of Heavy Oil Deposits

Sudad Al-Obaidi

Abstract

High viscosity of heavy oils at reservoir conditions is one of the main causes of the low production rates of producing wells, and sometimes even their complete absence when trying to develop a field on a natural mode. The rheological properties of heavy oil deposits in a wide temperature range were studied in this work. Special attention was paid to the study of viscous and elastic components of oil viscosity as a function of temperature to justify the optimal conditions for the development of heavy oil fields. Heavy oil samples collected from Pechersky oil field (Russia) were used in this research. Dynamic viscosity tests were carried out on the heavy oil of this field. It was noticed that high values of viscous and elastic components of oil viscosity were observed over the entire temperature range. It has also been remarked that the values of oil viscosity components are inversely proportional to the temperature increase.

Keywords

High viscosity oil • Bitumen • Elastic viscosity component • Rheological properties • Oil deposits

1 Introduction

Due to the steady depletion of reserves of light, low-viscosity oils in the oil industry, it is becoming increasingly important to launch onto the development of deposits of hard-to-recover reserves like high-viscosity oil and natural bitumen.

Most of the deposits of hard-to-recover reserves are located in Canada, Venezuela, and Russia. In the Russian Federation, more than 70% of high-viscosity oils are confined to five regions: Perm region (more than 31%), Tatarstan (12.8%), Samara region (9.7%), Bashkortostan (8.6%), and Tyumen region (8.3%) (Yu and Yashchenko 2005).

Oil deposits of this type are usually characterized by small depths of oil-bearing beds and, often, low reservoir temperatures, while the oil or bitumens lying in them have Non-Newtonian properties (Roshchin et al. 2015). Such properties are due to the high content of paraffin of asphaltenes and resins (Zinoviev et al. 2013). With a high content of heavy components in the oil, viscoelastic properties appear in the oil composition. These viscoelastic properties were first discovered in the 1970s (Devlikamov et al. 1975).

At the present time, the effect of using thermal methods or technologies on the productive formation is most widely used in the development of deposits of such hydrocarbons (Pierre et al. 2004).

Among these technologies, we may cite the cyclic steam injection and the areal steam injection. These two technologies are the most common methods of extracting and intensifying the oil flow rate in Russia, whereas the steam and gravity drainage (SAGD—steam assisted gravity drainage) is widely used abroad (Roshchin 2014).

To study the properties of high-viscosity oil, located in a complex carbonate reservoir, the Pechersky field, located on the bank of the Volga River, near the village of Pechersky was selected.

Earlier, rock (limestone and dolomite) saturated with heavy oil was mined at this field for subsequent extraction of raw material for the production of bitumen mastic.

2 Experimental Study

The author organized field visits to this field to collect information about the structure of the reservoir and to gather samples to study the rheological properties of oil and the void space of the reservoir.

S. Al-Obaidi (✉)
Department of Petroleum Engineering, College of Engineering, Knowledge University, Erbil, Iraq
e-mail: sudad.alobaidi@knowledge.edu.krd

M. Meghraoui et al. (eds.), *Advances in Geophysics, Tectonics and Petroleum Geosciences*,
Advances in Science, Technology & Innovation, https://doi.org/10.1007/978-3-030-73026-0_92

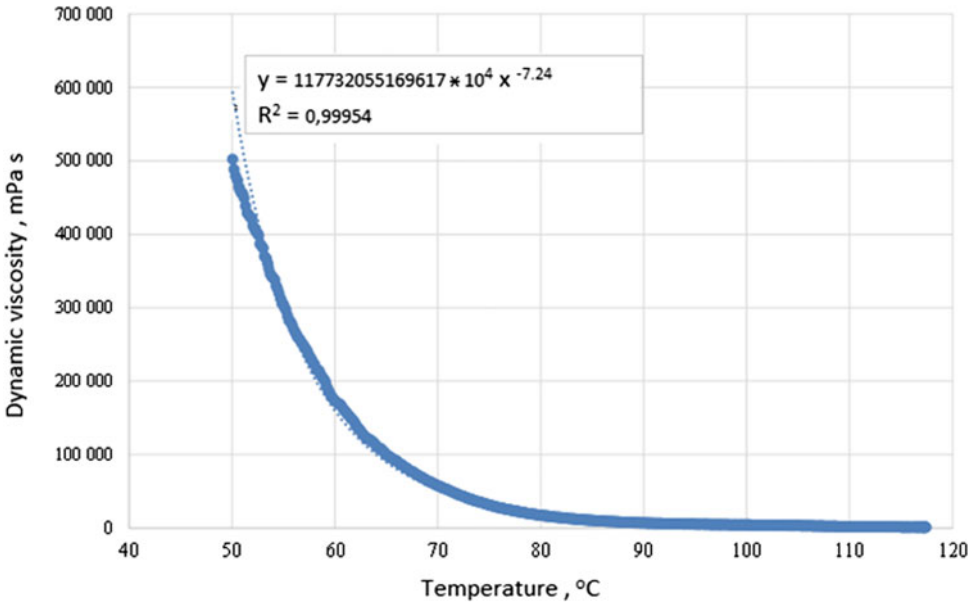

Fig. 1 Dependence of dynamic viscosity of high-viscosity oil on temperature

In this work, we studied the effect of temperature on the rheological properties of oil. For this case, a modern high-precision rotational viscometer with air bearings was used.

An experiment to study the dependence of the dynamic viscosity on temperature was carried out as follows: a drop of oil with a volume of 1 ml was placed on the heated to 70 °C viscometer platform, then the drop was pressed by the rotor while the temperature increased to 110 °C.

The angular velocity was set at 5 S-1 on the viscometer, after which the temperature gradually dropped to 50 °C. This temperature was proposed as a limiting temperature to prevent excessive overload of the viscometer motor (see Fig. 1).

In this figure, it can be clearly observed that when the temperature increases the dynamic viscosity decreases. Which means, that the viscosity of oil as a liquid is related inversely proportional to the increasing temperature.

The figure shows that the dynamic viscosity of oil can be described by a power function of the form

$$y = 117732055169617 \times 10^4 X^{-7.24} \quad (1)$$

with a value of approximation reliability $R^2 = 0.99554$.

R-squared represents the determination coefficient, and it is the fraction by which the variance of the errors is less than the variance of the dependent variable.

Oil in the entire range of temperatures presented is highly viscous (viscosity at 110 °C is 2003 mPa s, and at 50 °C it is 502,343 mPa s).

At this stage of the test, it was not possible to measure the viscosity of the oil at a reservoir temperature of 20 °C due to the limited capabilities of the viscometer.

For a deeper study of the rheological properties of this oil, additional specialized dynamic tests were carried out to determine the elastic and viscous components of the oil viscosity. In the course of the experiments, the effect of decreasing temperature on the elastic component of viscosity (dynamic shear modulus, also called storage modulus) and viscous component of viscosity (flexibility or loss modulus) were studied (Roshchin 2014). The oil of the Pechersky field, used in this research, was cooled in a selected temperature range from 90 to 50 °C.

The experiment was carried out as follows: a drop of oil with a volume of 1 ml was placed on the heated to 70 °C platform of the viscometer, then the drop was pressed by the rotor, and the temperature increased to 90 °C, after which it gradually decreased to 50 °C with data recording. The dynamic load was represented by the oscillatory motion of the rotor at a frequency of 1 Hz and a load of 100 Pa. The results are shown in Fig. 2.

The figure shows the dependency of both components (elastic and viscous) of oil viscosity of Pechersky field on temperature. It shows how both values of these components decreased with the increase of temperature. The figure shows that the elastic viscosity component of oil (storage modulus) can be described by a power function of the form

$$y = 130226893597931 \times 10^4 X^{-10,723} \quad (2)$$

with a value of approximation reliability $R^2 = 0.99554$.

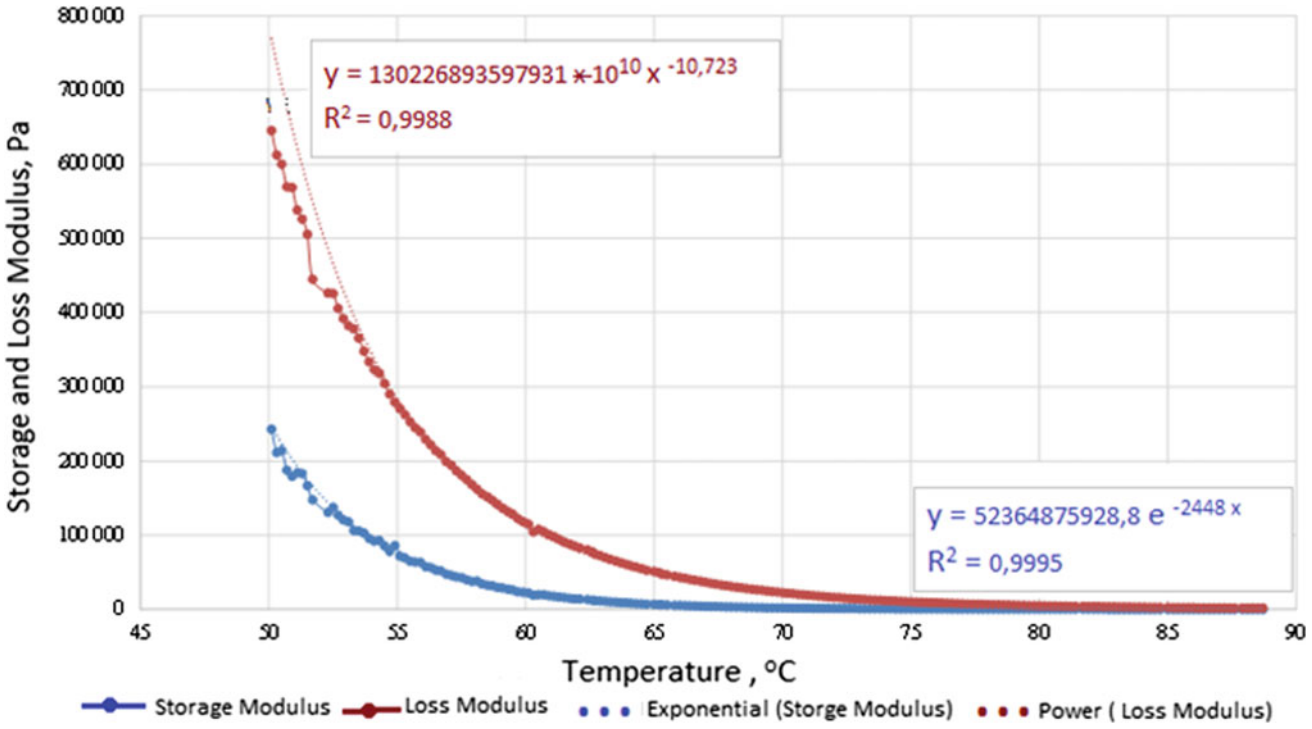

Fig. 2 Dependence of the elastic (storage modulus) and viscous (loss modulus) viscosity components of high-viscosity oil of the Pechersky field on temperature

Figure 2 also shows that the viscous component of oil viscosity (loss modulus) can be described by a power function of the form

$$y = 52364875928,8\,e^{-2448X} \quad (3)$$

with a value of approximation reliability $R^2 = 0.99554$.

3 Discussion

Analyzing the presented dependences, Fig. 2, it is quite possible to conclude that both viscous and elastic components of oil viscosity decrease with the increasing temperature and reach relatively small values at 80 °C, which proves the need for the use of thermal energy in the development of this field. It is also noticeable that at the studied temperature range oil has elastic properties, which, although reduced with the increasing temperature, reach significant values: 23.54 Pa.

It is well known that the fluid mobility represents the ratio of effective permeability to phase viscosity, and the well productivity is directly proportional to the mobility product. Therefore, the fluid viscosity represents a dominating factor affecting the mobility of any fluid. Therefore, any small reduction in oil viscosity will defiantly lead to a big increase in oil mobility which in its turn has a positive impact on the oil recovery. This will lead us to the fact that the use of thermal treatment in the oil fields with heavy oils (high viscosities) will enhance the viscous characteristics of these oils and make them more mobile.

4 Conclusions

Based on the results of the research, it is possible to draw the following conclusions:

1. High viscosity oil of the Pechersky field is characterized by an abnormally high viscosity; the measured dynamic viscosity at 50 °C is 502343 mPa s.
2. Based on the fact that the oil viscosity decreases from 502,343 mPa s to 2000 mPa s with the increasing temperature from 50 to 110 °C, the thermal treatment is necessary to extract oil from the rock of this field.
3. The studied oil has complex rheological properties, probably due to the high content of asphaltenes and resins characteristic of the near-surface deposits of the Samara region. High values of viscous and elastic components of viscosity are observed over the entire temperature range at which the dynamic tests were carried out. These high values of the components will undoubtedly have a negative impact on the process of extracting oil from the reservoir.

4. Once the feasibility study of the development process for any oil field containing heavy oils is conducted, the use of thermal treatment is recommended to enhance the viscous characteristics of these oils and bring many of the abandoned producing wells back to life.
5. It is highly recommended for further tests aimed at substantiation of effective technologies of extraction of such anomalous oils from productive formations, for example, technologies with the use of complex effects of thermal agents and solvents.

References

Devlikamov, V.V., Habibullin, Z.A., Kabirov, M.M.: Abnormal oil, p. 168. M: Nedra, 1975

Pierre, C., et al.: Composition and heavy oil rheology. In: Oil & Gas Science and Technology, pp. 489–501 (2004)

Roshchin, P.V.: Substantiation of complex processing technology of bottom-hole formation zone on deposits of high-viscosity oils with fractured-pore reservoirs: PhD. Technical Sciences. SPb., p. 112 (2014)

Roshchin, P.V., Zinoviev, A.M., Pods, I.A., Kalinin, E.S., Dziwornu, K.K.: Solvent selection based on the study of the rheological properties of oil. Int. Res. J. **6–1**(37), 120–122 (2015)

Yu, M., Yashchenko, I.G.: High viscosity oils: analysis of spatial and temporal changes in physicochemical properties. Electron. Sci. J. "Oil and Gas Business``. 2005№1 [Electronicresource]: http://ogbus.ru/authors/PolishukYu/PolishukYu_1.pdf. Appeal date 11/15/2015

Zinoviev, A.M., Olkhovskaya, V.A., Maksimkina, N.M.: Designing systems for the development of high-viscosity oil fields using the non-Newtonian flow model and the results of well testing for inflow. Oilfield Bus. **1**, 4–14 (2013)

Petroleum Engineering

Swelling Performance of Paraffinic Crude Oil Under Carbon Dioxide Injection

Muslim Abdurrahman, Asep Kurnia Permadi, Wisup Bae, Ivan Efriza, Shabrina Sri Riswati, and Adi Novriansyah

Abstract

Paraffinic crude reservoir is one of an attractive options for co-implementation of CO_2-EOR and CO_2-storage activities. The effectiveness of oil recovery is affected by an oil swelling mechanism. The swelling performance of CO_2 in paraffinic crude is essential to be studied due to the difficulties to pursue miscible condition. This mechanism was investigated through the analysis of the swelling factor value from the swelling experiment. Moreover, the equation of state calculation (EOS) using Peng–Robinson equation was performed to predict the minimum miscibility pressure (MMP) of the crude sample for investigating swelling trends toward this point. Results from the experimental test reveal a slow process of oil swelling due to CO_2 injection, which is implied from the low swelling factor value. The EOS calculation shows a large MMP value, which was impossible to reach under reservoir condition. Extrapolating extraction-condensation trend indicates no occurring extraction which means that the main mechanisms for this crude type was dominated by viscosity and interfacial tension reduction. Although it was impossible to pursue the MMP, the utilization of CO_2 in paraffinic crude may bring a positive impact on the oil recovery process.

Keywords

CO_2 • Paraffinic oil • Immiscible displacement • Swelling factor • Minimum miscibility pressure

1 Introduction

As an alternative option to store carbon dioxide (CO_2), main component of greenhouse gas (GHG), oil reservoir is an attractive storage candidate because CO_2 can be used as an enhance oil recovery (EOR) agent, known as CO_2-EOR (Gozalpour et al. 2005). For over two decades, CO_2-EOR has successfully recovered residual light oil (Zhang et al. 2019). As CO_2 is well known to solve wax problem in production facilities (Yang et al. 2019), CO_2 capability in paraffinic crude oil reservoir should be tested. Paraffinic oil contains a large amount of wax. This oil type has gravity more than 25° API or still in the range of medium to light oil, where CO_2 flooding is still acceptable. High wax content is the reason of the time consumed by CO_2 solubilization process (Abdurrahman et al. 2019). This is similar to mechanisms of CO_2 injection in heavy oil. (Li et al. 2013). Even though the mechanism is similar, viscosity of paraffinic crude is lower than that of heavy crude in reservoir conditions. Therefore, the strategy to implement CO_2 in this type of crude should be different, including its swelling performance.

The objective of this paper was to study CO_2 swelling performance of paraffinic crude under CO_2 injection. This parameter was analyzed by interpreting CO_2-Oil swelling factor, a ratio of observed oil level at specific injection pressure to initial oil level. The swelling factor is useful in the condensation-extraction analysis and MMP estimation (Abdurrahman et al. 2015). Peng–Robinson equation of state (EOS) calculation was used to predict the MMP and analyze the possibility of an extraction mechanism to occur in miscible condition.

M. Abdurrahman (✉) · A. Novriansyah
Universitas Islam Riau, Pekanbaru, Indonesia

A. K. Permadi
Institut Teknologi Bandung, Bandung, Indonesia

W. Bae · S. S. Riswati · A. Novriansyah
Sejong University, Seoul, Republic of Korea

I. Efriza
PT SPR Langgak, Jakarta, Indonesia

S. S. Riswati
Universitas Trisakti, Jakarta, Indonesia

M. Meghraoui et al. (eds.), *Advances in Geophysics, Tectonics and Petroleum Geosciences*,
Advances in Science, Technology & Innovation, https://doi.org/10.1007/978-3-030-73026-0_93

2 Methodology

This experimental study utilized a crude oil sample from central Sumatra basin. The sample has an API gravity of around 30 or included to the medium-light oil. The bubble point pressure, pour point temperature, wax, and asphaltene contents are 113 psi, 105–110 °F, 33 wt%, and 13 wt%, respectively. The percentage of heptane plus ($C_7H_{16}^+$) was around 90 mol% at reservoir condition (Table 1). The crude was sampled at 1200 ft. depth, and the reservoir pressure was approximately 500 psi (Abdurrahman et al. 2019).

The swelling factor apparatus consists of a syringe pump for CO_2 injection, high-pressure-high-temperature (HPHT) optical cell, camera, and PC for observation. Crude oil is placed inside the optical cell which was located in the air-bath. The temperature inside the air bath was maintained constant by adjusting a heater temperature to reservoir condition (136 °F). CO_2 was injected continuously into the cell at constant pressure. Crude level inside the optical cell was recorded by using camera and recorded into numerical data by computer. The experiment was repeated for certain injection pressure, starting from 300 to 3300 psi.

Before predicting the MMP under EOS calculation, the fluid should be modeled and verified by matching the bubble point pressure and reservoir temperature with the previously reported data (113 psi; 136 °F). A simulation study was performed to estimate the sample MMP. EOS by Peng–Robinson was used under WINPROP module in CMG software. (CMG software 2014). Hydrocarbon composition in Table 1 and reservoir temperature were needed as an input parameter for this module. The MMP determination was performed by selecting multiple contact miscibility modules in the software. For a designated solvent, i.e., pure CO_2 and range of pressure, the MMP was determined at a certain temperature. In MMP, no mix envelope was found in the ternary diagram.

3 Results and Discussion

Figure 1 shows the swelling factor plot over the injection pressure where two trends of swelling factor data were recorded in this test, i.e., the swelling factor tends to increase with 0.14% per 1000 psi at low pressure region (300–1900 psi) and to decrease with 6.5% per 1000 psi in the range of 2000–3300 psi, which is lower than light crude oil swelling factor (Abdurrahman et al. 2015). These trends are similar to condensation and extraction-condensation phenomena (Wang 1986). The MMP was not achieved in this experiment based on definition by Abdurrahman et al. (2015).

Figure 2 displays the bubble point pressure of the crude sample in the fluid model phase envelope from the WINPROP module, where the generated fluid model was

Table 1 Hydrocarbon composition of the crude sample in this study

Component	Mole%	Component	Mole%
Hydrogen sulfide (H_2S)	0.00	Iso-Butane (i-C_4H_{10})	0.90
Carbon dioxide (CO_2)	0.56	n-Butane (n-C_4H_{10})	1.57
Nitrogen (N_2)	0.00	Iso-Pentane (i-C_5H_{12})	1.56
Methane (CH_4)	0.67	n-Pentane (n-C_5H_{12})	1.50
Ethane (C_2H_6)	0.67	Hexanes (C_6H_{14})	0.35
Propane (C_3H_8)	1.51	Heptane plus ($C_7H_{16}^+$)	90.71

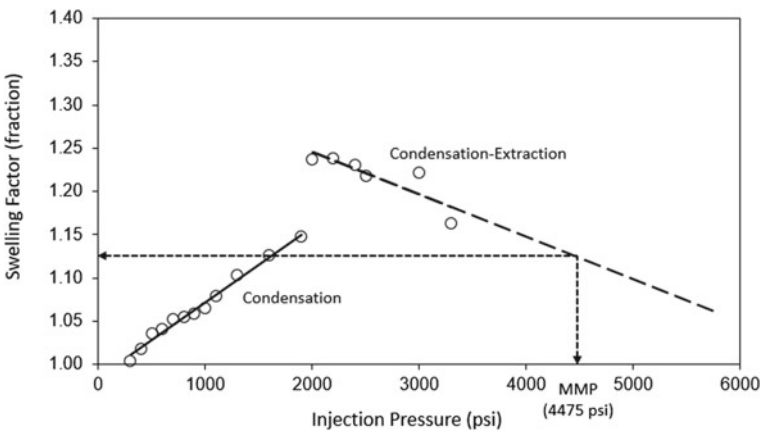

Fig. 1 Oil swelling factor at various injection pressure values

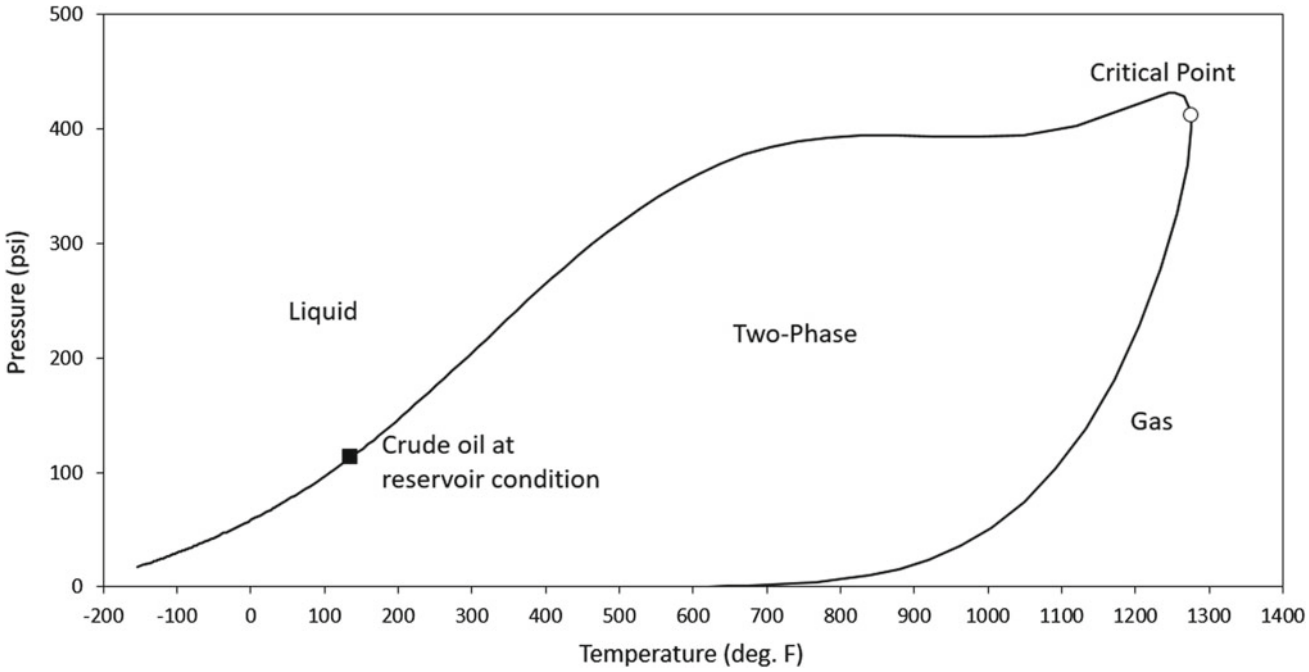

Fig. 2 Pressure–temperature diagram of crude oil sample

matched with the crude oil sample. The MMP calculation by Peng–Robinson EOS in WINPROP module yielded a large value (4475 psi), which means a displacement scenario is under immiscible condition with its reduction of oil viscosity and oil swelling due CO_2 dissolution mechanisms (Li et al. 2013). The ternary diagram in Fig. 3a indicates the change of the liquid line toward a vapor line by increasing the injection pressure. High pressure improves CO_2 solubility into oil, resulting high swelling factor (Abedini and Torabi 2014). In MMP condition (Fig. 3b), the vapor and liquid lines vanished, indicating miscibility already achieved, leaving a small portion of heavy component (represented as black dot in the ternary component) and Oil-CO_2 mixture (red dot in ternary diagram).

By referring to the swelling test result, the crude has a long extraction-condensation stage to pursue the MMP condition. Extrapolating the extraction-condensation trends to the expected MMP value from EOS calculation (Fig. 1)

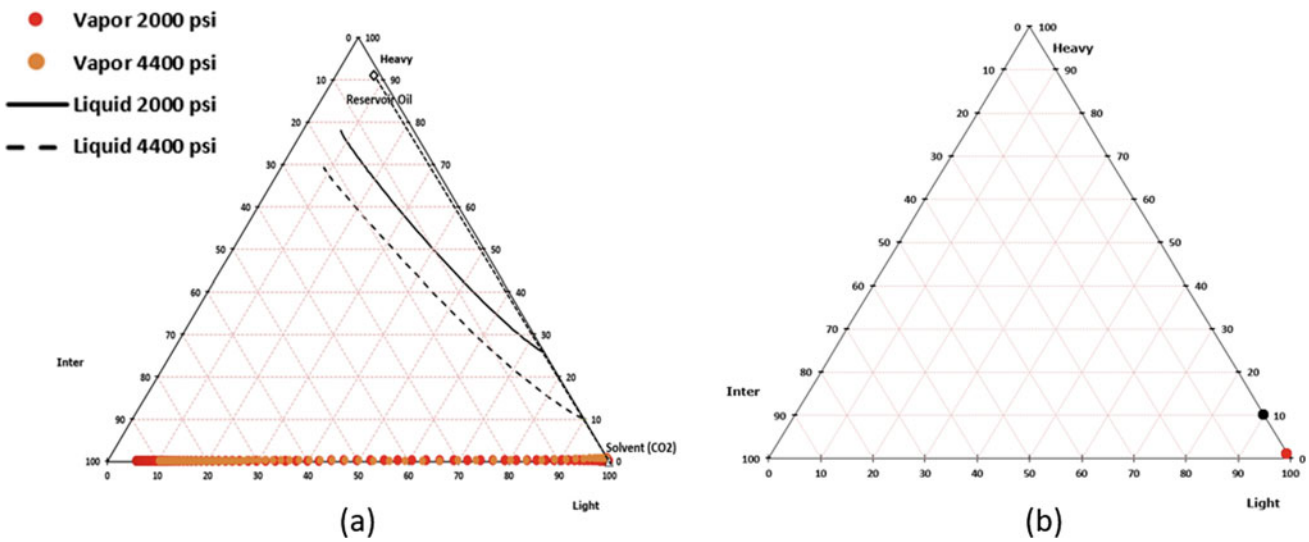

Fig. 3 Ternary diagram of fluid model at **a** 2000 and 4400 psi; **b** 4475 psi

results, the oil swelling factor was reduced from 1.24 to 1.12 (around 10% declined), which is still higher than the initial condition (1.00). Hence, the hydrocarbon extraction might not happen during CO_2 injection until the estimated MMP, and as a result, a CO_2 gas dissolves into oil, inducing the oil volume to increase. This phenomenon reduces the interfacial tension and viscosity, and the crude flows easier in porous medium (Li et al. 2013).

4 Conclusions

This paper combines the experimental and simulation work to study the swelling performance of paraffinic oil CO_2 injection. The swelling test led to two kinds of swelling factor trends which describe condensation and extraction-condensation phenomena. Both trends reveal low oil swelling factor, indicating the low capability of CO_2 dissolution. The MMP calculation by Peng–Robinson EOS limits the displacement process into immiscible scenario if the reservoir constraints are concerned. Long stages of extraction-condensation stage may have happened in the sample if the MMP from simulation was considered as MMP from the experiment. The CO_2 injection into this paraffinic crude may have ended in a CO_2 dissolution phenomenon.

References

Abdurrahman, M., Permadi, A.K., Bae, W.S.: An improved method for estimating minimum miscibility pressure through condensation–extraction process under swelling tests. J. Petrol. Sci. Eng. **131**, 165–171 (2015)

Abdurrahman, M., Permadi, A.K., Bae, W., Riswati, S.S., Dewantoro, R.A., Efriza, I., Novriansyah, A.: Effect of CO_2-oil contact time on the swelling factor and viscosity of paraffinic oil at reservoir temperature. In: Banerjee, S., Barati, R., Patil, S. (eds.) Advances in Petroleum Engineering and Petroleum Geochemistry, vol. 1, pp. 55–57. Springer, Cham (2019)

Abedini, A., Torabi, F.: Oil recovery performance of immiscible and miscible CO_2 huff-and-puff processes. Energy Fuels **28**(2), 774–784 (2014)

CMG (software): WinProp users Guide. Computer Modelling Group, Calgary, Alberta, Canada (2014)

Gozalpour, F., Ren, S.R., Tohidi, B.: CO_2 EOR and storage in oil reservoir. Oil Gas Sci. Technol. **60**(3), 537–546 (2005)

Li, H., Zheng, S., Yang, D.T.: Enhanced swelling effect and viscosity reduction of solvent (s)/CO_2/heavy-oil systems. SPE J. **18**(04), 695–707 (2013)

Wang, G.C.: A study of crude oil composition during CO_2 extraction process. In: Society of Petroleum Engineer California Regional Meeting (1986)

Yang, S., Li, C., Yang, F., Li, X., Sun, G., Yao, B.: Effect of Polyethylene-Vinyl Acetate (EVA) Pour Point Depressant on the Flow Behavior of Degassed Changqing Waxy Crude Oil before/after scCO_2 Extraction. Energy Fuels **33**(6), 4931–4938 (2019)

Zhang, N., Yin, M., Wei, M., Bai, B.: Identification of CO_2 sequestration opportunities: CO_2 miscible flooding guidelines. Fuel **241**, 459–467 (2019)

Polymer-Coated Silica Nanoparticles for Enhanced Oil Recovery in Water-Wet Berea Sandstone Core Plugs

Alberto Bila, Jan Åge Stensen, and Ole Torsæter

Abstract

Innovative enhanced oil recovery (EOR) technologies are needed to ensure a more economical oil production to meet the growing energy demand. Silica nanoparticles have been widely studied for EOR applications due to their unique physical and chemical properties. Recent studies have proposed a renewed application of polymer-coated silica nanoparticles (PSiNPs) to overcome stability issues induced by ionic strength in injection water; however, their effect on the EOR process has not been fully addressed. In this work, we evaluated four types of PSiNPs as additives to injection water for EOR in water-wet rocks through measurements of interfacial tension (IFT), wettability index and core flood experiments. The experimental results showed that PSiNPs, at 0.1 wt%, can increase oil recovery up to 15% point compared with 40% of original oil in place (OOIP) from water flood, in secondary mode. In tertiary EOR mode, the incremental oil recovery is varied from 4.6 to 10% of OOIP. Moreover, the PSiNPs altered the wettability of the rock surface to a more water-wet condition, decreased the IFT between oil and water, and increased the injection pressure.

Keywords

Polymer-coated silica nanoparticles • Core flood • Light oil recovery • Interfacial tension • Wettability index • Log-jamming

A. Bila (✉) · J. Å. Stensen · O. Torsæter
PoreLab Research Center, Department of Geoscience and Petroleum, Norwegian University of Science and Technology (NTNU), S. P. Andersens veg 15a, 7031 Trondheim, Norway
e-mail: alberto.bila@ntnu.no

J. Å. Stensen
Sintef Industry, S. P. Andersens veg 15a, 7031 Trondheim, Norway

1 Introduction

New technologies are required to increase oil production from existing oil-fields in order to meet the world energy demand (Khalil et al. 2017; Shamsijazeyi et al. 2014). Enhanced oil recovery by using silica nanoparticles in injection water is a promising technology. However, its application at a large scale is still hampered by many problems associated with nanoparticle stability, especially at high pressure and temperature, and high salinity environment (Khalil et al. 2017). One approach to overcome the stability issues and tailor the nanoparticle properties for a particular application is to covalently attach polymer chains to the nanoparticle surface, resulting in polymer-coated silica nanoparticles (Khalil et al. 2017; Shamsijazeyi et al. 2014). The surface-active polymers attached to the particle surface can improve the interfacial and surface properties, which make the PSiNPs prime candidates to stabilize emulsions and be injectables in porous media with low retention (Khalil et al. 2017; Shamsijazeyi et al. 2014; Alvarez et al. 2012). At present, few studies were carried out using these types of nanomaterials to assist water flood in enhancing oil recovery. It has been suggested that PSiNPs increase oil recovery by reducing the interfacial tension between oil and water and wettability alteration (Behzadi and Mohammadi 2016; Choi et al. 2017) and by lowering the injection pressure (Behzadi and Mohammadi 2016). Most of the previous studies evaluated PSiNPs mixed with low ionic strength aqueous solution (only Na^+) in their experiments, which may hinder a proper understanding of the behavior of PSiNPs in a typical reservoir water.

In this work, we investigated oil recovery efficiency of PSiNPs dispersed in water with typical seawater composition (Mg^{2+}, Ca^{2+}, etc.) and crude oil from a specific oilfield. The underlying oil recovery mechanisms of the nanoparticles were also studied.

M. Meghraoui et al. (eds.), *Advances in Geophysics, Tectonics and Petroleum Geosciences*, Advances in Science, Technology & Innovation, https://doi.org/10.1007/978-3-030-73026-0_94

2 Materials and Methodology

2.1 Fluids Properties

Four types of polymer-coated silica nanoparticles used in this work were supplied as AERODISP®, which are AEROSIL® particles in liquid solution by Evonik Industries.

The NPs size varied 32 to 218 nm. The concentrated solutions of nanoparticles were diluted with synthetic North seawater (38.318 ppm) to 0.1 wt. % concentration. The density and viscosity of the new solution or nanofluid were 1.023–1.028 g/cm^3 and 1.022–1.057 cP, respectively, at 22 °C. A light crude oil (28°API, 34 cP, at 22 °C) which is obtained from a field in the North Sea and n-decane was used for flooding and wettability experiments.

2.2 Experimental Procedure

Sixteen flooding tests were conducted with water-wet Berea sandstone rocks (length: 4.5 to 6 cm and diameter: 3.75 cm) at ambient conditions. The core porosity and permeability are ranged from 16.7–18.5% and 277–400 mD, respectively. A standard flooding experimental setup described in our previous work was used (Bila et al. 2019). The drainage was conducted by injecting oil at 0.5, 1.0, and 3 ml/min to establish initial water saturation (S_{wi}) and OOIP. Then, the nanofluid was directly injected into the core to displace oil to mimic secondary EOR process. In tertiary mode, water flood (WF) was conducted until there was no oil production for 1–2 pore volumes (PVs). After which, the injection was switched to nanofluid until there was no more oil production. In both injection schemes, a constant flow rate of 0.2 ml/min was used. The oil production was collected every 1/4 PV and corrected for the flooding system dead volume. The pressure and oil recovery were recorded versus PVs injected. The IFT of the fluids was measured with a pendant drop method, while the effect of NPs on rock wettability was characterized by the Amott test.

3 Results and Discussion

3.1 Evaluation of Oil Recovery

Polymer-coated silica nanoparticles were evaluated for oil recovery in secondary and tertiary core flood processes. To measure the experimental repeatability, two tests were carried out for each nanofluid system, and the results were compared with a reference WF. The average oil recovery of WF was 39.7% OOIP, and it is varied from 35.1 to 43.1% OOIP (Table 1). The variation in WF recoveries is attributed to differences in core properties and fluid viscosities ($\mu_o/\mu_w \approx 34$). This is because high core permeability zones and low water viscosity can induce water fingering and snap-off oil in the pores, resulting in variable oil recovery performance, even if the tests are carefully repeated.

In secondary mode, PSiNPs increased oil recovery by factors ranging from 8.3 to 14.8% point, on average, (from 48 to 54.5% OOIP) compared to 39.7% OOIP achieved by plain water flood. Figure 1 shows that ultimate recoveries were achieved with large PVs of injected PSiNPs compared to the plain WF. This is consistent with the delayed water breakthrough and continual oil production observed during nanofluid injection.

In tertiary mode, the PSiNPs at 0.1 wt% could mobilize residual oil. At initial stages of the injection (1 PV), the recoveries varied from null to 3.3% (Table 1), which showed that the injection equilibrium was not reached during WF stage for some tests. All core plugs produced the main oil at the expense of large volumes of injected nanofluids. This observation concurs with the notion that nanoparticles induce oil production through a prolonged physicochemical interactions with the rock system (Adil et al. 2018). The main parameters used to measure the viability of tertiary nanofluid floods are given in Table 1. The nanofluids increased oil recovery from 35.1 to 43.1% OOIP, in the case of WF, to 44.6–49.4% OOIP. An example of oil recovery profile is presented in Fig. 3 for NF-3, and it is resulted in the highest oil recovery and differential pressure increase.

Table 1 Oil recoveries (expressed as % of OOIP) achieved after WF and nanofluid flooding

Core #	PV (ml)	S_{wi} (%)	Nanofluid 0.1 wt.%	Water flood		Nanofluid flood			Total RF
				RF_1	S_{or1}	RF@1PV	RF2	S_{or2}	
M1	11.81	33.93	NF-1	43.07	37.61	3.33	4.61	35.55	47.69
M2	12.00	24.22		38.91	46.29	0.00	7.25	40.83	46.15
M3	11.68	24.68	NF-2	41.70	43.91	2.16	7.39	38.36	49.09
M4	12.23	20.68		39.42	48.05	0.00	7.01	42.52	46.43
M5	11.42	27.34	NF-3	40.72	43.07	0.00	8.67	36.78	49.39
M6	11.10	20.73		37.91	49.22	0.00	9.77	41.47	47.68
M7	8.02	23.97	NF-4	35.08	49.35	0.00	9.51	42.14	44.59
M8	8.33	18.41		40.58	48.48	0.00	6.62	43.09	47.20

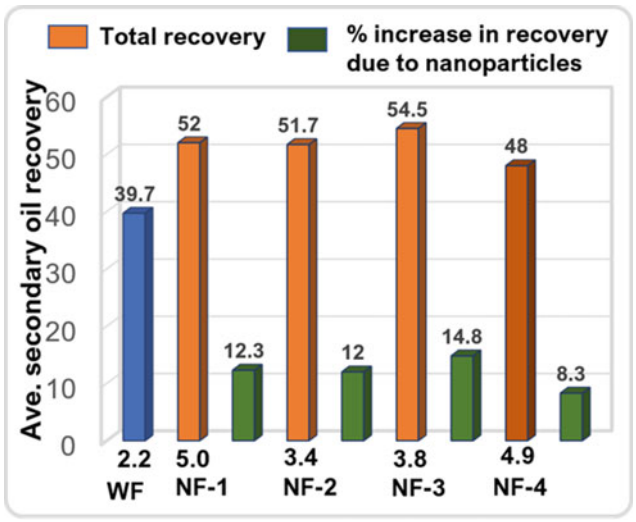

Fig. 1 Recovery factors versus injected PVs (*X*-axis). The results are reported on averaged: eight tests for WF and two tests for each nanofluid type

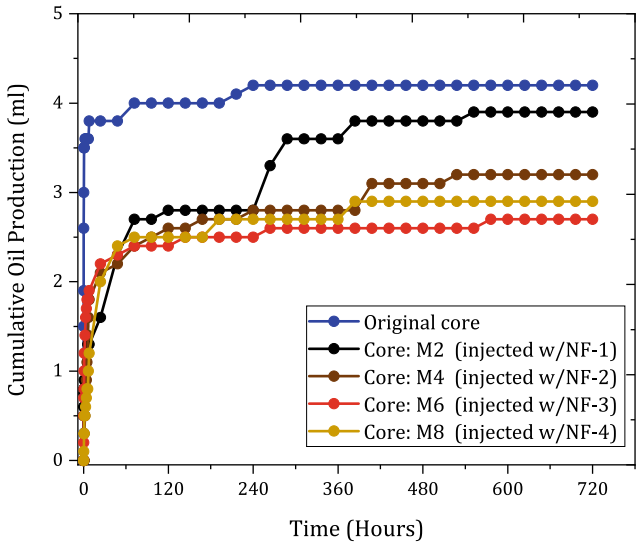

Fig. 2 Spontaneous imbibition behavior on core plugs before and after nanofluid injection

Comparing the results presented in Fig. 1 and those presented in Table 1, we see that the recoveries are low in tertiary recovery mode, suggesting that PSiNPs were relatively efficient in enhancing oil recovery in secondary mode. Additionally, the highest oil recovery was achieved with NPs with large diameter size, and no clear correlation was found between oil recovery and IFT reduction. The twin cores used for each NP type produced small variations (<5%), which proved the reproducibility of the experimental results and the ability of NPs to extract oil from water-wet reservoirs.

3.2 Interfacial Tension and Wettability Tests

A drop shape analyzer was used to measure the IFT between the reservoir flowing fluids at ambient conditions. The IFT between water and oil (w/o) was measured at 10.6 mN/m, and it was decreased to 6.8–4.1 mN/m with added PSiNPs. Alvarez et al. (2012) ascribed this phenomenon to the surface-activity of the polymers attached on the particle surface. It is well recognized that the IFT should be on orders of $<10^{-3}$ mN/m for a significant production of capillary trapped oil. The current results show that the surface-modified silica NPs with polymers molecules did not affect dramatically the IFT. Therefore, the PSiNPs may not induce oil recovery by solely decreasing the tension between w/o. Moreover, the results show how difficult it is to design highly stable NPs, especially in a high ionic strength aqueous solution. Nevertheless, the polymers attached to the NPs still play a significant role for the stabilization of emulsions (Shamsijazeyi et al. 2014). In this work, this hypothesis was tested by increasing flow rate at the end of a low rate injection. This provided an extra energy for the formation of emulsions such that fractions of oil-in-water emulsions were produced at core outlet. Phase separation of emulsion occurred within a couple of hours in an effluent separator. The conditions under which PSiNPs influence the behavior of the reservoirs fluids still needs further investigation to comprehend their production mechanisms.

In addition to IFT reduction, the NPs can change the wettability to a more favorable EOR condition. For this purpose, Amott wettability index (WI) was determined on post- nanofluid flooded cores. The first cycle of spontaneous imbibition (SI) was conducted for 30 days, and the rate of water imbibition was decreased on the treated cores as compared to original ones (not injected with NPs) as shown in Fig. 2; while in the second cycle of SI, the oil did not imbibe in the cores. Thus, Amott water index, I_w, was $0.54 < I_w < 0.78$.

The WI measured on the original cores was 0.86 (Bila et al. 2019). If the initial wettability was altered during the drainage and WF processes, the imbibition results suggest that it was reversed back to more water-wet condition by PSiNPs. The structuring of the particles during nanofluid injection was likely responsible for developing new hydrophilic layered surfaces on the pore spaces (Wasan and Nikolov 2003), which continuously improved the oil recovery while changing the wettability.

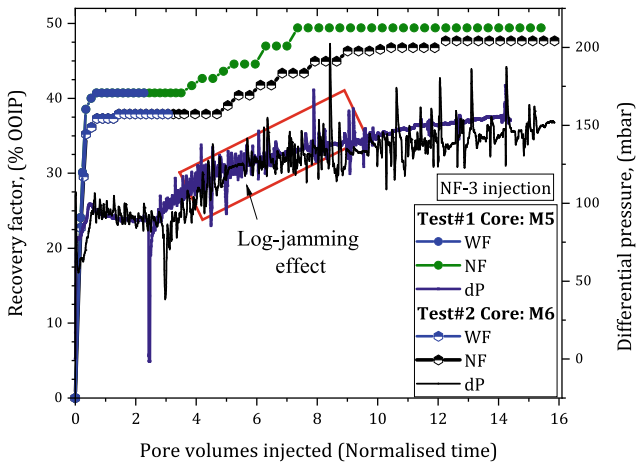

Fig. 3 RFs and dP recorded versus PVs during water and nanofluid injection. Oil production occurred after ~1.2 PV and the pressure increased with nanofluid injection

3.3 Differential Pressure Analysis

The differential pressure (dP) was recorded during flood tests to realize the migration behavior of the NPs across the cores. It was observed that the pressure increased with nanofluid injection and was higher with increasing nanoparticle diameter size. Accordingly, the largest permeability reduction was observed on cores flooded with large NPs size. The permeability reduction is ranged from 14 to 25%. The results were probably affected by the core preparation step for wettability evaluation. This was because the measurement of WI involved applying high pressure through the core to set S_{wi}. During this step, NPs and rock grains may be removed from the surface, thus increasing the rock pore connectivity. Figure 3 shows oil recovery and dP profiles recorded during the injection of NF-3 sample. During WF stage, the pressure across the core increased steadily, and it dropped after water breakthrough (see Fig. 3). Upon the NPs injection, the pressure progressively climbed, and at some point, it was spiky. This indicated an occurrence of jammed NPs within the pores. The rise in pressure could force injected water to find new paths and likely mobilize some of the by-passed oil in the adjacent pores and increase oil recovery. It is believed that log-jamming effect could be the main recovery mechanism of PSiNPs under the experimental conditions.

4 Conclusions

This study demonstrated that polymer-coated silica nanoparticles can increase the oil recovery in water-wet reservoirs. The secondary ultimate recoveries are varied from 48 to 55% OOIP with PSiNPs injection compared with 39.7% OOIP from water flood. After water flood, PSiNPs injection added 4.6 to 9.8% OOIP. The PSiNPs were more efficient in displacing oil as secondary EOR agents. Moreover, the nanoparticles with a large diameter size gave the highest incremental oil recovery and achieved the largest differential pressure due to the clogging of the rock pores. No clear correlation was found between the interfacial tension reduction and oil recovery. Overall, the results showed that PSiNPs can increase oil recovery by a synergistic effect of the IFT reduction and wettability alteration to more water-wet condition and log-jamming effect.

References

Adil, M., Lee, K., Zaid, H.M., Latiff, N.R.A., Alnarabiji, M.S.: Experimental study on electromagnetic-assisted ZnO nanofluid flooding for enhanced oil recovery (EOR). PloS ONE **13**(2), e0193518 (2018)

Alvarez, N.J., Anna, S.L., Saigal, T., Tilton, R.D., Walker, L.M.: Interfacial dynamics and rheology of polymer-grafted nanoparticles at air–water and xylene–water interfaces. Langmuir **28**(21), 8052–8063 (2012)

Behzadi, A., Mohammadi, A.: Environmentally responsive surface-modified silica nanoparticles for enhanced oil recovery. J. Nanoparticle Res. **18**(9), 266 (2016)

Bila, A., Stensen, J.Å., Torsæter, O.: Experimental Evaluation of Oil Recovery Mechanisms Using a Variety of Surface-Modified Silica Nanoparticles in the Injection Water, Society of Petroleum Engineers, Bergen, Norway, p. 19 (2019)

Choi, S.K., Son, H.A., Kim, H.T., Kim, J.W.: Nanofluid enhanced oil recovery using hydrophobically associative zwitterionic polymer-coated silica nanoparticles. Energy Fuels **31**(8), 7777–7782 (2017)

Khalil, M., Jan, B.M., Tong, C.W., Berawi, M.A.: Advanced nanomaterials in oil and gas industry: design, application and challenges. Appl. Energy. **191**, 287–310 (2017)

Shamsijazeyi, H., Miller, C.A., Wong, M.S., Tour, J.M., Verduzco, R.: Polymer-coated nanoparticles for enhanced oil recovery. J. Appl. Polym. Sci. **131**(15) (2014)

Wasan, D.T., Nikolov, A.D.: Spreading of nanofluids on solids. Nature **423**(6936), 156–159 (2003)

Experimental Analysis of Low Salinity Waterflooding in Tertiary Recovery Mode in Geleki Oil Field of Upper Assam Basin, India

Nayan Medhi and Minati Das

Abstract

Low salinity waterflooding (LSW) is an emerging enhanced oil recovery (EOR) technology where the salinity of the injection water is reduced/controlled to improve oil recovery by reservoir rock wettability alteration. Earlier studies have shown that tertiary oil recovery associated with low salinity water injection is very high (20–25% pore volume) in the near wellbore region which is as high as that in the laboratory (Li in Transp Porous Media 90:333–362, 2011). The oil recovery efficiency by LSW in tertiary recovery mode was investigated in this work. A set of experiments was performed using different high and low salinity brine for the tertiary recovery mode where oil saturated core plugs were flooded with high salinity brine followed by low salinity brine. The oil recovery efficiency after the high salinity waterflooding and additional oil recovery efficiency after LSW were determined. An additional oil recovery efficiency with low salinity brine up to 04.46% was observed of the original oil in place (OOIP). The wettability alteration of the core plugs toward more water-wet state (contact angle up to 40.04°), an increase in pH of the bulk fluid (up to 0.58) and a reduction of oil–water interfacial tension (IFT) (up to 01.5465 mN/m) were observed after the LSW. This work contributed with a systematic study on four different LSW experiments and determined the optimum salinity that gave the highest improvement of oil recovery efficiency by wettability alteration.

Keywords

Low salinity waterflooding • Tertiary recovery mode • Wettability • Interfacial tension • Contact angle

N. Medhi (✉) · M. Das
Dibrugarh University, Dibrugarh, Assam, India
e-mail: nmedhi.duiet@dibru.ac.in

1 Introduction

LSW is a new low-cost, environment-friendly EOR technique to sweep the residual oil left behind by secondary recovery. It is observed that the injection water having different ionic composition than formation brine can change the initial chemical equilibrium of the crude oil/brine/rock (COBR) system in the presence of polar organic compounds in crude oil and clays in reservoir rock and establish a new chemical equilibrium that alters the wetting properties of the reservoir rock (Tang and Morrow 1997, 1999). Experiment shows that LSW increases the oil recovery efficiency in either secondary or tertiary recovery modes (Webb et al. 2005). A very high tertiary oil recovery (20–25% pore volume) associated with low salinity water injection was observed in the near wellbore regions (Li 2011).

The present work aimed to find out the optimum salinity of the injection brine which gives the maximum oil recovery in the tertiary recovery mode of LSW in Geleki Oil Field of Upper Assam Basin, India.

2 Materials and Methods

In this study, fifteen liters of crude oil, four conventional core samples and some analytical data on formation brine (ONGC unpublished report) were collected from the study area.

The crude oil analysis was performed to determine the polar organic compounds. The petrographic analysis was achieved to study the mineralogical composition of the reservoir rock with the help of X-ray diffraction (XRD) analysis and scanning electron microscopic (SEM) study. For the coreflooding experiments, a total of six core plugs were prepared. The injection and formation brines were prepared by mixing KCl, $CaCl_2.2H_2O$ and $MgCl_2.6H_2O$ in required proportions with distilled water. For this study,

M. Meghraoui et al. (eds.), *Advances in Geophysics, Tectonics and Petroleum Geosciences*,
Advances in Science, Technology & Innovation, https://doi.org/10.1007/978-3-030-73026-0_95

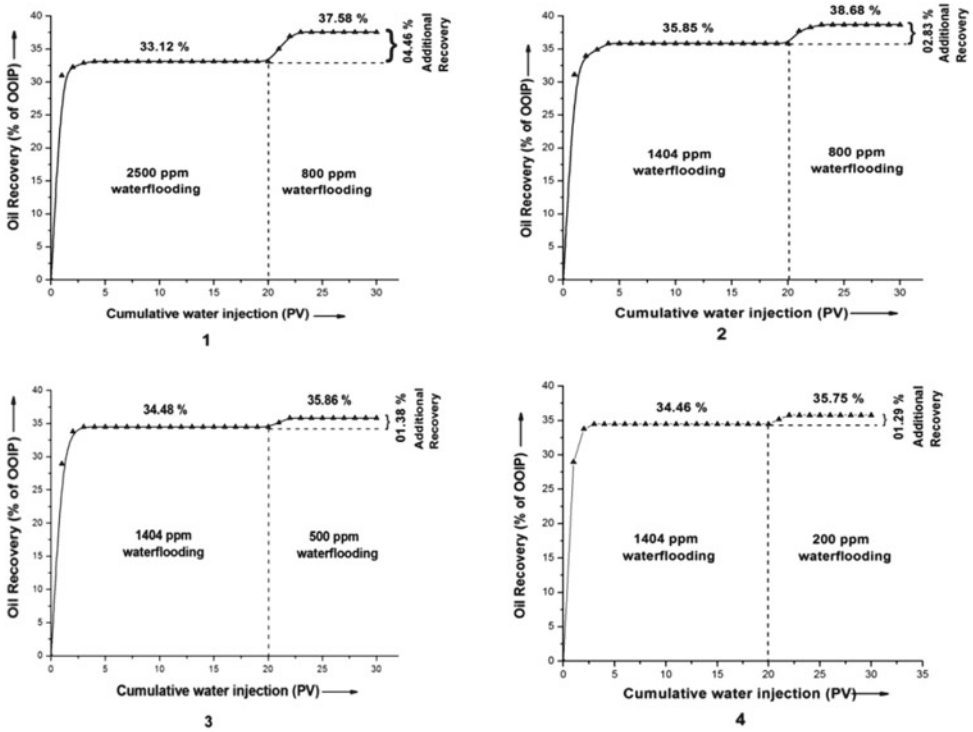

Fig. 1 Oil recovery by high salinity brine and additional oil recovery by low salinity brine in tertiary recovery mode

2500 ppm, 1404 ppm, 800 ppm, 500 ppm and 200 ppm (as NaCl) brine samples were prepared. The core flooding experiments were conducted at a constant injection rate of 01.87 cc/min at ambient temperature and pressure. Each core plug was first flooded with 20 pore volume (PV) of 1404 ppm brine at 200 psi confining pressure to make the core plugs fully saturated. The core plugs were then flooded with 20 PV oil and kept in the core holder for 13–15 days (aging time) with the confining pressure to achieve the equilibrium condition by COBR interaction. The oil saturated core plugs were then flooded by 20 PV high salinity brine (2500 and 1404 ppm) followed by 10 PV low salinity brine (800, 500 and 200 ppm). To know the wettability states of the flooded core plugs, the contact angles of each core plugs were determined using DSA100 Drop Shape Analysis System. pH of the injected low saline water before and after flooding was determined with a pH meter. The effect of LSW on oil–water IFT was determined with spinning drop tensiometer.

3 Results

3.1 Crude Oil, Brine and Rock Analysis

The analysis of the crude oil shows the presence of 15.49% (w/w) resin and 0.55% (w/w) asphaltene (polar organic compound). The analytical data on the formation brine having a salinity of 1404 mg/l (as NaCl) shows the presence of 6 mg/l Ca^{2+} and 8 mg/l Mg^{2+} ion. From the petrographic analysis, it is found that smectite, kaolinite and illite clays are present in the reservoir rock matrix of the study area (Medhi and Das 2015).

3.2 Coreflooding

After the injection of 20 PV high salinity brine into the oil saturated core plugs 1–4, 33.12, 35.85, 34.48 and 34.46% of OOIP was observed as shown in Fig. 1. The injection of 10 PV low salinity brine into the above cores in tertiary mode shows additional oil recovery efficiency of 04.46, 02.83, 01.38 and 01.29% of OOIP.

The oil saturated core plugs 5 and 6 were flooded by 2500 ppm and 1404 ppm brine, respectively. The experiments show 33.58% and 34.95% of oil recovery efficiency from the 2500 ppm and 1404 ppm brine, respectively.

3.3 Wettability, pH and IFT

The wettability states of the core plugs were determined after the LSW by measuring the contact angles which are found to be 40.25°, 40.04°, 40.97° and 41° for core plugs 1, 2, 3 and 4, respectively. The contact angles of the flooded core plugs 5 and 6 are 43.36° and 41.99°, respectively. The increase in pH of the injected water is found to be more (0.58 and 0.47) during 800 ppm flooding than 500 ppm and 200 ppm flooding (0.10 and 0.19). Also, the reduction of oil–water IFT is higher (1.3762 and 1.3764 mN/m) during 800 ppm

and 500 ppm flooding compared to 200 ppm flooding (0.9687 mN/m).

4 Discussion

The analysis of crude oil, formation brine and reservoir rock shows the presence of polar organic compounds, divalent cations and clays, respectively which are important for improving oil recovery by different LSW mechanisms (Tang and Morrow 1999; Lager et al. 2006). In the core flooding experiments, it was observed that LSW in the tertiary recovery mode gives additional oil recovery efficiency up to 04.46% of OOIP. The 800 ppm brine gives the highest additional oil recovery efficiency (04.46 and 02.83%) (Fig. 1). The study of wettability of the core plugs 1–4 flooded by low salinity brine shows lower contact angles then the core plugs 5 and 6 flooded by high salinity brine. This indicates that the wettability is shifted to more water-wet state after LSW (Zolotuchin and Ursin 2000). The lowest contact angle (40.25° and 40.04°) was observed in the core plugs flooded by 800 ppm brine. The study also showed an increase in pH of the injected water and reduction of oil–water IFT after LSW which was also observed by earlier researchers (McGuire et al. 2005; Morrow et al. 1998). This indicates that the pH increase mechanism is acting in the study area during the LSW (McGuire et al. 2005). All the above experiments have shown the influence of wettability alteration, pH increase and IFT reduction on the improvement of oil recovery in tertiary recovery mode of LSW.

5 Conclusions

From the above discussion, it can be concluded that LSW in the tertiary recovery mode enhances the oil recovery in the study area. During LSW, the reservoir rock wettability alteration occurs toward a more water-wet state. The pH increase and reduction of oil–water IFT occurs during the LSW which contributes to the additional recovery of oil. Out of the different salinity brines, 800 ppm is the optimum salinity of injection water which yields the highest additional oil recovery during the LSW.

References

Lager, A., Webb, K.J., Black, C.J.J., Singleton, M., Sorbie, K.S.: Low salinity oil recovery—An experimental investigation. In: SCA2006–36, International Symposium of the Society of Core Analysis, 12–16 Sept, Trondheim, Norway (2006)

Li, Y.: Oil recovery by low salinity water injection into a reservoir: a new study of tertiary oil recovery mechanism. Transp. Porous Media **90**(2), 333–362 (2011)

McGuire, P.L., Chatham, J.R., Paskvan, F.K., Sommer, D.M., Carini, F.H.: Low salinity oil recovery: an exciting new EOR opportunity for Alaska's North Slope. SPE 93903, 2005 SPE Regional Meeting, 30 Mar–1 Apr, Irvine, U.S.A. (2005)

Medhi, N., Das, M.: A study on the low salinity waterflooding (LSW) in a part of depleted oil field of Upper Assam Basin. J. Petrol. Eng. Technol. **5**(3), 1–9 (2015)

Morrow, N.R., Tang, G.Q., Valat, M., Xie, X.: Prospects of improved oil recovery related to wettability and brine composition. J. Petrol. Sci. Eng. **20**(3), 267–276 (1998)

Tang, G.Q., Morrow, N.R.: Salinity, temperature, oil composition and oil recovery by waterflooding. SPE Reserv. Eng. **12**(4), 269–276 (1997)

Tang, G.Q., Morrow, N.R.: Influence of brine composition and fines migration on crude oil/brine/rock interactions and oil recovery. J. Petrol. Sci. Eng. **24**(2), 99–111 (1999)

Webb, K.J., Black, C.J.J., Tjetland, G.: A laboratory study investigating methods for improving oil recovery in carbonates. In: IPTC 10506, International Petroleum Technology Conference, 21–23 Nov, Doha, Qatar (2005)

Zolotuchin, A.B., Ursin, J.R.: Introduction to Petroleum Reservoir Engineering, 2nd edn. Norwegian Academic Press, Norway (2000)

Performance of Oil-Based Demulsifier and Water Clarifier for Treating Oil Emulsion Stabilized by Fine Sands in Oilfield Under Low Salinity Waterflooding

Annur Suhadi and Darmapala

Abstract

Asphaltenes can cause water-in-oil emulsion, which can be stabilized by produced fine sands. Selecting proper demulsifiers and water clarifiers is critical in order to meet the required specification of commercial oil and injection water. The effects of combining a demulsifier with a water clarifier at various dosages were investigated with the bottle test method. The speed of water coalescence and settling to the bottom of the test bottle was evaluated. The obtained dosage was then implemented in a gathering station. Increasing the demulsifier dosage increases the break rate. However, increasing the demulsifier dosage on its critical dosage decreases the quality of injection water. The study found that the demulsifier DMO 21031 of 13 ppm, in combination with the water clarifier RBW 83000 of 1.5 ppm, was the most capable of resolving water-in-oil emulsion, containing 2.86% asphaltenes. The demulsifier-molecular formula of dodecylbenzene sulphonic acid was indicated by sulphonic acid and substitute benzene 1:3 at the wave numbers of 1184 cm^{-1} and 699–784 cm^{-1}, respectively. Alkyl benzene sufonate, used as an active content in the water clarifier, was indicated by benzene ring overtone stretching at wave number of 1701 cm^{-1} and sulfonic acid stretch mode at 1184 cm^{-1}.

Keywords

Dodecylbenzene sulphonic acid • Water-in-oil emulsion • Demulsification • Anionic latex • Fine sands

1 Introduction

The Zamrud field is located in the central Sumatra basin, in the province of Riau, Indonesia. The block covers an area of 9135 km^2 and has been exploited since 1975. In order to recover additional oil following the primary recovery, the main formation sands have been peripherally waterflooded starting from 1993. The reservoir is mixed-wet. The salinity and pH of formation water are 5100 ppm and 9.5. The primary and waterflood recovery factors were 15% and 24% by the end of 2018, respectively. The estimated ultimate recovery of this reservoir is 42%; therefore, there is a need for effective EOR techniques after waterflooding such as water-CO_2 mixture injection (Sun et al. 2018), CO_2-soluble surfactant injection (Sagir et al. 2014), ASP chemical injection (Flaaten et al. 2008), etc.

Waterfloods could produce fine solids, consisting mainly of kaolinite, contributing to the success of LSWF, in addition to a water-wet or mixed-wet reservoir condition (Tang and Morrow 1999). The formation of Zamrud field is a sandstone; as a consequence, the produced fine solids are quartz, feldspar, pyrite, and plagioclase. However, kaolinite, illite, calcite, and siderite are less common. Due to the high differential pressure between injection water and reservoir pressure, the formation brines often cause the suspended fine solids (such as loose sand and clays) to migrate, which can stabilize water-in-oil (W/O) emulsion at a certain inorganic salt content (Angle et al. 2007). Pointdexter et al. (2006) investigated the effect of solid content, ranging from 96 to 1090 lbm/1000 barrels of crude oil, on the stability of emulsion by avoiding asphaltene and other crude oil parameter stabilizing emulsions. The content of this fine solid in crude oil shall be reduced to meet the required sediment and water $\leq$ 0.5% and salt content $\leq$ 7 PTB before transportation.

Using a demulsifier from a previous vendor, the day-to-day operations face water-in-oil emulsions, which has not been completely resolved and cause a thick rag layer

A. Suhadi (✉) · Darmapala
BOB PT, BSP-Pertamina Hulu, Riau, Indonesia
e-mail: annur_suhadi@bobcpp.co.id

M. Meghraoui et al. (eds.), *Advances in Geophysics, Tectonics and Petroleum Geosciences*,
Advances in Science, Technology & Innovation, https://doi.org/10.1007/978-3-030-73026-0_96

between the oil and the water in the wash tank, hindering oil–water separation. The rag layer contains 12 wt% kaolinite, 15 wt% calcite, 6 wt% siderite, 6 wt% pyrite, 1 wt % feldspar, 1 wt% plagioclase, 43 wt% quartz, and other minerals.

Ultra-fine (nano-size) aluminosilicate clays of 100–200 nm in diameter, causing crude oil emulsions, were previously reported by Kotlyar et al. (1998). In the Zamrud oilfield, fine sands with a diameter ranging between 1 and 63 μm tend to stabilize the emulsions. To prevent the sale of off-specification crude oil and ensure clean effluent water for waterflooding, some new demulsifiers were tested. To obtain the best oil quality and water clarity, some demulsifier intermediates, which function as water drop settling, solid wetting, and coalescing demulsifiers, were combined. The effects of different dosages of the demulsifier, combined with the water clarifier, on resolving the emulsion and water clarification, were tested.

2 Materials and Methods

2.1 Materials

2.1.1 Demulsifier and Water Clarifier

The demulsifiers of TETROLITE DMO 21041, DMO 85394, and DMO 86334 were used in this bottle test. The water clarifiers of TRETOLITE RBW 83000, RBW 6560, and RBW 6060 were also tested in combination with some demulsifiers. All of them are products of Baker Hughes.

2.1.2 Field Emulsion

Field emulsions obtained from the Zamrud area are free of demulsifier, and any free water found is drained from the sample before bottle test was started. The Zamrud crude oil is classified as a light crude oil based on its API gravity.

2.2 Methods

2.2.1 Bottle Test

Prior to the bottle test, field emulsions were homogenized for 5–10 min. The oil/water ratio used was 30/70, representing the current condition in the field. Formation water as an aqueous phase and mixed with oil from the field to study the sediment effect in emulsion stabilization. The methods for determining the oil/water interface level (or grind-out), water drop, oil quality, and water quality were according to procedures reported by Pointdexter et al. (2003). The water drop (or settling time) readings were taken at time intervals of 5, 20, 30, 60 min.

3 Results

3.1 Effect of Dosage on S&W, Oil Content, and Turbidity

To obtain sediment and water (S&W) $\leq$ 0.5% and turbidity $\leq$ 10 NTU, several dosages of the demulsifier DMO 21041 and the water clarifier RBW 83000 were tested. Turbidity is measured as a standard water quality for injection water.

3.2 Fourier Transform Infra-Red of Demulsifier

Sulphonic acid at wave number of 1184 cm-1 where substitute benzene either 1:3 or 1,2,3 was read 699-784 cm-1 (See Fig. 1).

3.3 Interfacial Tension of Demulsifier

To explore the possible demulsification mechanism by the demulsifier DMO 21041 the interfacial tension (IFT) was tested. (Fig. 2) showed the image of crude oil-formation water interfacewith the presence of demulsifier in a spinning drop tensiometer, model TX500 C (KINO, USA). It was found that the IFT of the oil–water interface was 11.57 mN/m when the demulsifier was dosed at 13 ppm. The DMO 21,041 is a less polar demulsifier, proved by its better solubility in crude oil rather than in water. It can be concluded that a less polar demulsifier is suitable for crude oil, which has a high polar fraction.

4 Discussion

Table 1 shows that increasing the demulsifier dosage reduces S&W. Otherwise, the increase of the water clarifier dosage at the same dosage as the demulsifier results in a more turbid water and an increasing S&W. Reducing turbidity will carry less suspended solid to injection water.

Sulphonic acid at wave number of 1184 cm^{-1} where substitute benzene either 1:3 or 1, 2, 3 was read 699–784 cm^{-1} (see Fig. 1). The usage of dodecylbenzene sulphonic acid to first emulsify asphaltenes is correct since asphaltenes content in this crude oil is 2.86 wt%, although the crude oil is categorized as having a lower polarity. Asphaltene, which has stabilized the water droplet in water/oil emulsions, can be reduced in fraction, so that the emulsifying film can rupture. Then, the water droplet can grow large enough to settle out as a separate phase. Larger

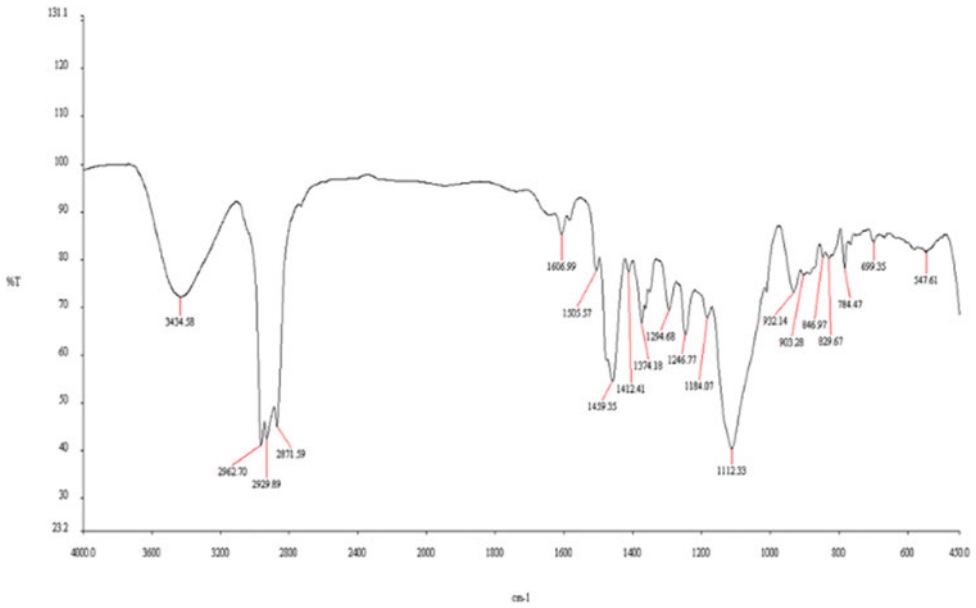

Fig. 1 FT-IR spectra for oil-based demulsifier DMO 21041

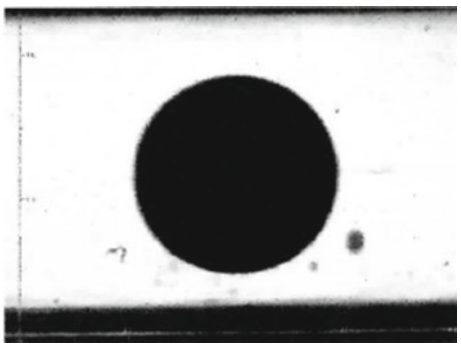

Fig. 2 Photograph of crude oil drop shape, containing demulsifier and formation water after 1.5 × lens magnification

droplets have less interfacial tension, so anything that can increase the droplet size will help in the separation process.

Water wetting agents (i.e. ethylene glycol monobutyl ether) are used to convert solids to water-wetted and become associated with free water. Ethylene glycol monobutyl ether, which is miscible with water and oil, is indicated by the peaks at 1374 cm^{-1} (–C–CH_3), 1412–1505 cm^{-1} (–CH_2), 2871–2962 cm^{-1} (–CH_3), and 3434 cm^{-1} (–OH). The transmittance of ester, whose function is to prevent asphaltic sludging which probably occurs after an acidizing stimulation, is read at wave number ranging from 1246 to 1294 cm^{-1}. Ester also functions as a wetting agent. Another wetting agent, which is used in combination with ester, is

Table 1 Effect of various dosages of demulsifier and water clarifier on oil content, turbidity, and S&W

No.	Sample code	Dosage (ppm)		Settling time of sample				Water quality		Water quality		Oil quality
								Interface @ 60 min		Oil content	Turbidity	
		DMO 21041	RBW 83000	5″	20″	30″	60″	Interface	Water quality	ppm	NTU	S&W
1	Blank	–	–	80	85	85	88	3	3	15.0	47.8	2.2
2	A	12	1.5	90	90	90	90	2	2	9.0	14.0	0.1
3	B	13	1.5	90	90	90	90	2	1	6.3	10.2	0.05
4	C	14	1.5	90	90	90	90	2	1	8.4	13.0	0.05
5	D	12	2	90	90	90	90	2	1	8.8	13.7	0.15
6	E	13	2	90	90	90	90	1	1	8.5	13.2	0.15

sulfonate. Sulfonate is the conjugate base of sulfonate acid, which is read at a wavelength of 1184 cm^{-1}. Sulfonate is very useful for wetting the surface of inorganic solids such as clay, sulphide minerals, or iron hydroxides. The solids will be displaced from the emulsions and will be removed with free water. The peak at 903–932 cm^{-1} wave number shows COOH of R.COOH, which has been derived to produce acid radical and reacts with P-amine at peak of 1606.99 cm^{-1} to synthesis material, to resolve (W/O) emulsion. Complexes with functional polyamine derivatives are capable of producing good "brightening" properties of oil and excellent desalting. This type of active content is for flocculation of small individual water droplets in w/o emulsion. If polyamine derivatives are mixed with resin, they will give fast water drop.

The water clarifier of RBW 83000 consists of anionic latex, which is a coagulant, aqueous solvent, and some additives. One additive, alkyl benzene sulfonate (ABS), is shown by benzene ring overtone stretch mode at 1701 cm^{-1} and stretching sulfonic acid, which is read at 1184 cm^{-1}. A tiny dosage of ABS is aimed at emulsifying an oil film dispersed in water, resulting in a reduction in the oil content. Reducing the oil content will correlate to reducing the oil loss and increasing the oil revenue.

5 Conclusions

The best dose for resolving water-in-oil emulsions is the 13 ppm demulsifier DMO 21031 and 1.5 ppm water clarifier RBW 83000. The interfacial tension of the oil–water interface was 11.57 mN/m, which shows a good demulsifier function. The active content of dodecylbenzene sulphonic acid was indicated by sulphonic acid and substitute benzene 1:3 at the wave numbers of 1184 cm^{-1} and 699–784 cm^{-1}, respectively. The water clarifier contains alkyl benzene sulfonate. Anionic latex, which was added to the water clarifier, is useful to improve water quality. It also reduces the load on filtration unit in water cleaning plants.

References

Angle, C.W., Dabros, T., Hanza, H.A.: Demulsifier effectiveness in treating heavy oil emulsion in the presense of fine sands in the production fluids. Energy Fuels **21**(2), 912 (2007)

Flaaten, A.K., Nguyen, Q.P., Zhang, J., Mohammadi, H., Pope, G.A.: ASP chemical flooding without the need for soft water. In: Annual Tech. Conf. and Exhibit. Denver, Colorado, 21–24 Sept 2008

Kotlyar, L.S., Sparks, B.D., Woods, J.R., Raymond, S., LePage, Y., Shelfantook, W.: Distribution and types of solids associated with bitumen. Pet. Sci. Technol. **16**, 1–19 (1998)

Pointdexter, M.K., Chuai, S., Marble, R.A., Marsh, S.C.: Classifying crude oil emulsions using chemical demulsifiers and statistical analyses. In: SPE Annual Tech. Conf. and Exhibit. Denver, Colorado. 5–8 Oct 2003

Pointdexter, M.K., Chuai, S., Marble, R.A., Marsh, S.C.: The key to predicting emulsion stability: solid content. SPE Prod. Oper. **21**(3), 357–364 (2006)

Sagir, M., Tan, I.M., Mushtaq, M., Nadeem, M.: CO_2 mobility and CO_2/brine interfacial tension reduction by using a new surfactant for EOR applications. J. Dispersion Sci. Technol. **35**(11), 1512–1519 (2014)

Sun, F., Yao, Y., Li, X., Li, G., Chen, Z., Chang, Y., Cao, M., Han, S., Chaohui, I., Feng, D., Sun, Z.: Effect of flowing seawater on supercritical CO_2-superheated water mixture flow in an offshore oil well considering the distribution of heat generated by the work of friction. J. Petrol. Sci. Eng. **162**, 460–468 (2018)

Tang, G.-Q., Morrow, N.R.: Influence of brine composition and fines migration on crude oil brine rock interactions and oil recovery. J. Petrol. Sci. Eng. **24**, 99–111 (1999)

Application 4D-Microtomography for Oil Displacement Experiments

Rail Kadyrov, Evgeny Statsenko, and Mikhail Glukhov

Abstract

This work demonstrates the capabilities of the serial 4D-microtomography in oil displacement experiments. The advantages of this method are high accuracy of volume measurements in comparison with standard filtration tests, proximity to natural PT-conditions, a wide range of obtaining experimental data, which includes the characteristics of the reservoir's porous system structure, permeability, the spatial distribution of oil and displacement fluid relative to pore camera sizes, 3-phase contact wetting angles and finally oil recovery. The presented results indicate the high potential of the 4D-microtomography method for studying filtration characteristics, verifying the effectiveness of enhanced oil recovery methods and mathematical models.

Keywords

4D-microtomography • Serial microCT • Oil displacement • Wetting angle • Fluids distribution in porous space

1 Introduction

4D X-ray computed tomography is a temporary three-dimensional image of dynamic processes, where "time" is considered as the 4th dimension. This subject appeared and began to develop in the late 1990s–early 2000s in medicine, where it became a solution to the problem of segmentation of objects at various stages of cyclic movements in the human body (for example, breathing or heartbeat) (Van Dyk 1999). The use of 4D tomography to study filtration processes in oil production (in particular, using physicochemical enhanced oil recovery methods) can provide not only new information on the physical features of these processes but also develop new methods for testing and modelling them (Kadyrov et al. 2018).

4D tomography can be divided into two varieties. First, the processes are suspended during tomography. The result of this study resembles an animation, where the individual stages of the dynamic process are displayed. The advantage of this approach is the high quality of the resulting tomography. In the second, the processes occur continuously. This requires a fast, continuous selective shooting and a slow dynamic process relative to the shooting time (Bultreys et al. 2016). The advantage of this approach is in the continuous study of the dynamic process. However, this method inevitably leads to a decrease in the quality of tomography, the appearance of noise and artifacts. This work demonstrates the application of the first approach to assess oil recovery during the displacement of water.

2 Method Description

Filtration experiments are carried out in a special radiolucent tube in which a cylindrical sample with a diameter of 5 mm is placed (Fig. 1). The sample is compressed with water to simulate confining pressure (up to 20 MPa). In addition, a mobile oven can be installed to heat up to 100 °C. Contrast fluid is led to the end of the sample, and filtration begins at a constant flow rate. The filtering process is suspended during the scan. Microtomography is performed after each injection step because the changing of liquid volumes is established by differences among obtained 3D models.

R. Kadyrov (✉) · E. Statsenko · M. Glukhov
Kazan Federal University, Kazan, Russia420008

M. Meghraoui et al. (eds.), *Advances in Geophysics, Tectonics and Petroleum Geosciences*,
Advances in Science, Technology & Innovation, https://doi.org/10.1007/978-3-030-73026-0_97

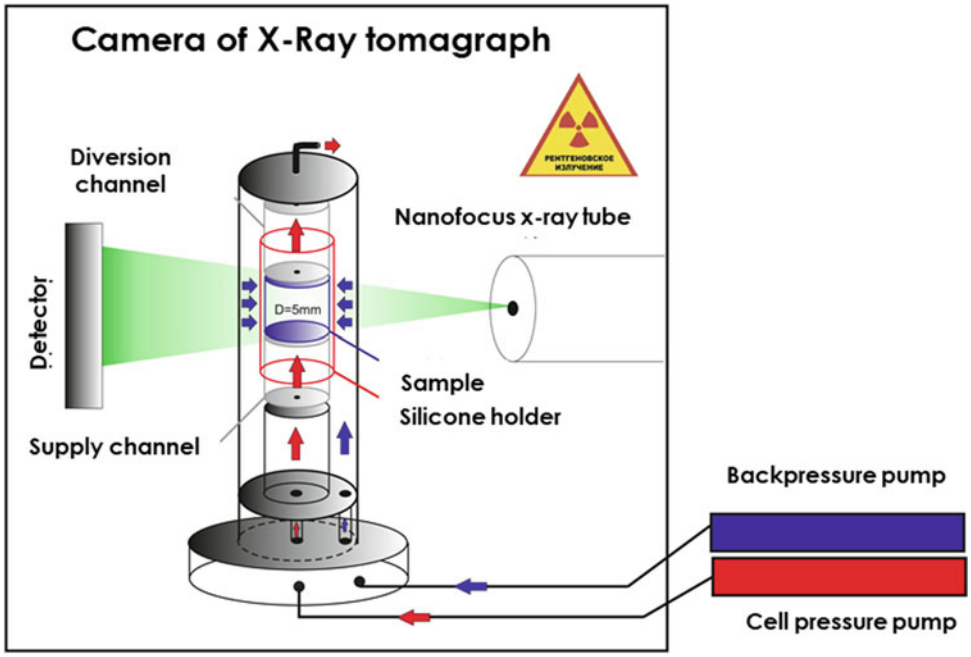

Fig. 1 The scheme of filtration system with special radiolucent tube in the tomographic camera

3 Results

Microtomography of the original sample before filtration allows observing sedimentological features and the structure of the porous space, the distribution of pore size, and the evaluation of the absolute and connected porosity (Bultreys et al. 2016). For example, the sample in Fig. 2-1 has the coefficient of absolute porosity equal to 18.45% and the coefficient of connected porosity 17.66%.

Then, the sample is saturated with brine, contrasted with potassium iodide. As a result, the black porous space of connected porosity becomes white in the volume where contrasted water invades the pore space (see Fig. 2-2).

After pumping oil into the sample, it is possible to measure the residual water and the initial oil saturation. Not-contrasted oil replaces the contrasted water in the connected porosity volume. The segmentation of these two phases gives their volumes. The initial oil saturation is 61%, and the residual water saturation is 39% for the sample in Fig. 2-3.

Additionally, it is possible to evaluate the hydrophobicity and hydrophilicity of the pore surfaces and measure their contact angles. Figure 3 demonstrates the results of measuring the contact angle for oil on the contact with water in the pore space of the sample. In addition, it shows the joint hydrophobicity and hydrophilicity of pores surfaces in the same sample.

Finally, after displacement with potassium iodide contrasted brine, the residual oil saturation and the oil displacement ratio can be estimated. They are 33% and 0.54, respectively, for the sample in Fig. 2-4.

4 Conclusions

The presented results demonstrate the high potential of the presented 4D microtomography approach in the study of filtration characteristics and testing the effectiveness of enhanced oil recovery methods. The advantages of this method include two general positions. The first is the high accuracy of measurement of the volumes obtained in comparison with standard filtration tests, which is associated with the high resolution of microtomography. The second is in the possibility of obtaining a large amount of data in one experiment at natural PT-conditions: from values of porosity and permeability to contact wetting angles and oil containing pore sizes distribution. In addition, 4D-microtomography results are experimental and can be used to check the mathematical models.

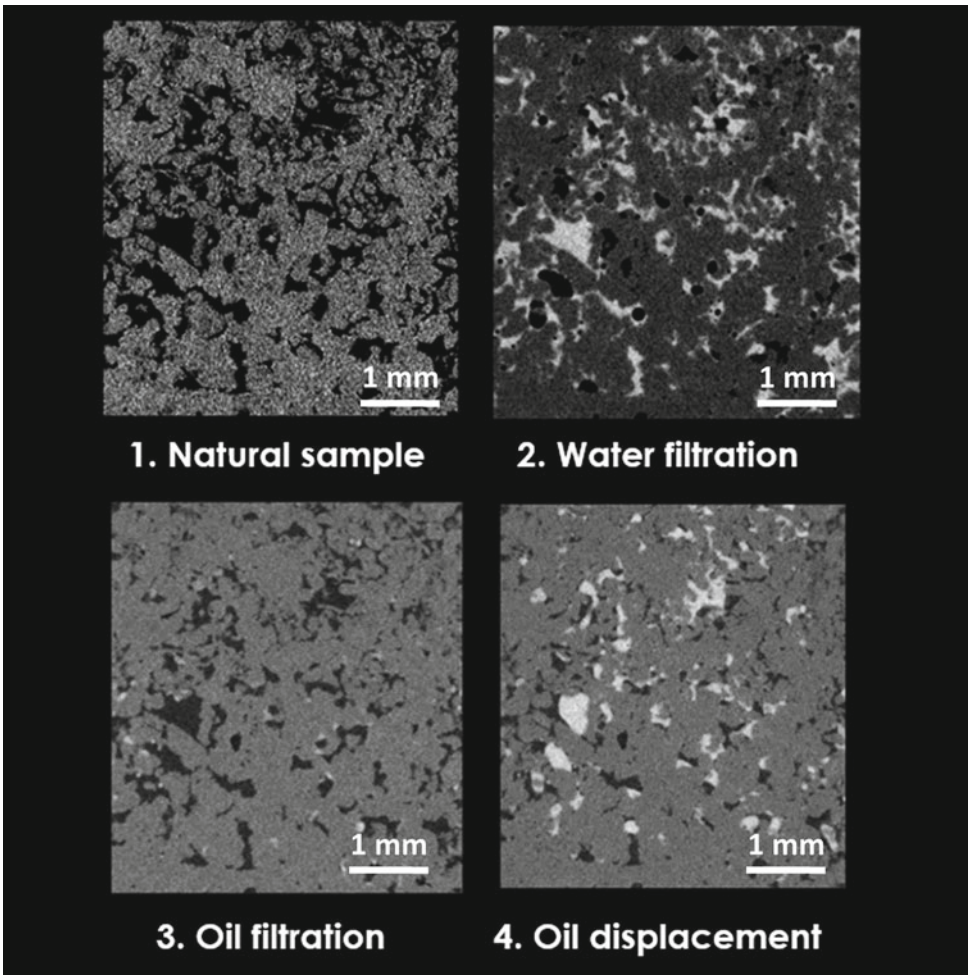

Fig. 2 The changes in X-ray slices in the XZ plane at various stages of the experiment

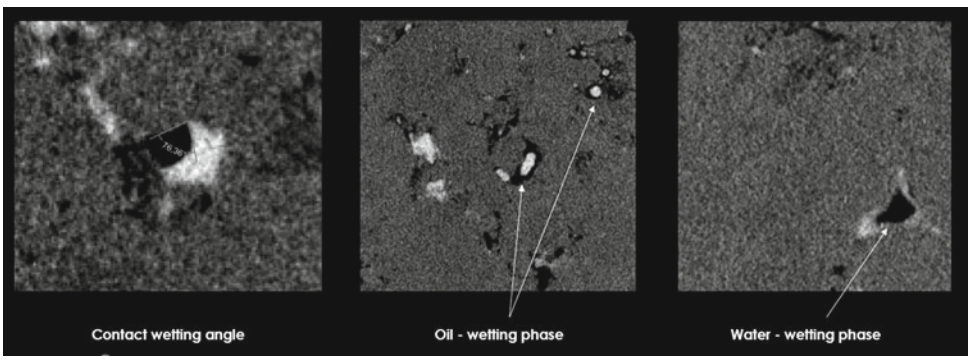

Fig. 3 Contact wetting angle measured for oil on contact with water in the pore space of the sample (on the right); hydrophobicity (middle) and hydrophilicity (right) of the pore surfaces in the carbonate sample

Acknowledgements This work was funded by the subsidy allocated to Kazan Federal University for the state assignment in the sphere of scientific activities (Project No 0671-2020-0048 of State Assignment No 075-00216-20-05 of 04.06.2020 (Part II Section 1)).

References

Bultreys, T., Boone, M.A., Boone, M.N., De Schryver, T., Masschaele, B., Van Hoorebeke, L., Cnudde, V.: Fast laboratory-based micro-computed tomography for pore-scale research: Illustrative experiments and perspectives on the future. Adv. Water Resour. **95**, 341–351 (2016)

Kadyrov, R., Glukhov, M., Statseuko, E., Galiulliu, B.: Structural transformation of the void-pore space of a lime reservoir during HCL treatment. Chem. Technol. Fuels Oils **54**(3), 307–318 (2018)

Van Dyk, J. (ed.): 4D CT extension of CT simulation. In: Modern Technology of Radiation Oncology (Chap. 5), pp. 131–168. Medical Physics Publishing, Madison (1999)

The Numerical Simulation of Effects of Porosity, Permeability and Fluid Saturation on Heat Dissipation in an Oil Reservoir

Atif Zafar, Yuliang Su, Wendong Wang, Lei Li, Syed Ghufran Alam, Asif Mehmood, Muhammad Usman Tahir, and Jingang Fu

Abstract

Heat dissipation into a petroleum reservoir has gained a significant attention due to the increasing trend of steam injection and thermal recovery of oil. Even geothermal energy extraction from abandoned oil and gas wells has also been under discussion. Therefore, a more detailed study of the factors affecting the heat dissipation mechanism within a petroleum reservoir was needed. In this paper, a reservoir numerical model of an actual oil field was generated and simulated with steam injection. Different parameters of thermal properties of geologic formations were discussed and adopted as per the actual geology of the study area for a more realistic simulation of heat storage, dissipation, and losses. The transmission of heat through conduction and convection mechanisms in the porous media, and through advective, dispersive, and diffusive processes in the fluid was modeled. The results revealed that heat dissipation increases with either a decrease in porosity or an increase in permeability, at a constant water saturation, whereas an increase in water saturation at the same porosity and permeability values results in more and faster heat dissipation. These correlations are very useful in order to design steam injection in an oil reservoir, as well as for heat extraction from a geothermal reservoir.

Keywords

Heat extraction • Permeability • Porosity • Saturation • Steam injection

1 Introduction

New developments in methods for exploiting potential resources have gained increased attention to enhance oil production. In petroleum engineering, where unconventional oil and gas reservoirs are getting more and more attention, the enhanced and optimum methods of developing the conventional reservoirs have also been studied and applied (Wang 2019).

Steam flooding is one of the thermal recovery methods of producing heavy crude oil. Conceptually, it is identical to a water flooding method, in which steam is injected into the reservoir where it is condensed by heating up the fluid and surrounding rocks which increases the mobility of heavy crude oil (Liu 2013, 1998).

The usage of abandoned petroleum wells for extraction of geothermal energy has also been investigated (Mehmood 2017a, b; Davis 2009). Even the current progress in the usage of enthalpy production to generate the electricity shows that low-enthalpy production resources are also conventional now (Li 2013). Therefore, there is a need for a thorough exploration of heat dissipation within a petroleum reservoir.

2 Reservoir Numerical Simulation

In this study, a numerical simulation model of a reservoir is generated by using a commercial software having thermal and compositional options. Since the overall actual study area of the oil field reservoir is very large, only a section of around 2 acres is simulated as the working reservoir

A. Zafar · Y. Su (✉) · W. Wang · L. Li · J. Fu
Key Laboratory of Unconventional Oil and Gas Development, China University of Petroleum (East China), Ministry of Education, Qingdao, 266580, China
e-mail: suyuliang@upc.edu.cn

A. Zafar · Y. Su · W. Wang · L. Li · A. Mehmood · M. U. Tahir · J. Fu
School of Petroleum Engineering, China University of Petroleum (East China), Qingdao, 266580, China

A. Zafar · S. G. Alam
Department of Petroleum Technology, University of Karachi, University Road, Karachi, 75250, Pakistan

M. Meghraoui et al. (eds.), *Advances in Geophysics, Tectonics and Petroleum Geosciences*, Advances in Science, Technology & Innovation, https://doi.org/10.1007/978-3-030-73026-0_98

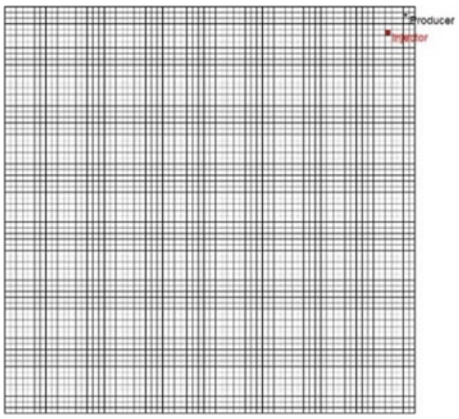

Fig. 1 2D grid model of whole reservoir

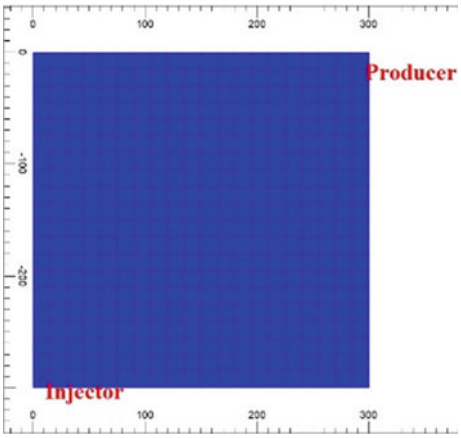

Fig. 2 2D grid model of simulated volume

simulation model (Figs. 1 and 2). Thickness is the same as per actual. The Cartesian Grids modeled as $20 \times 20 \times 15$ with $300 \times 300 \times 500$ feet dimensions like a quarter of inverted five spot well pattern having one injection well and one production well.

This is a sandstone reservoir. For accuracy, the thermal properties of the reservoir rock, the over-burden and under-burden rocks, were set as per the actual geology of the study area. Steam injection was started from the beginning of the simulation till the end (10 years). The steam quality was set as 0.8.

3 Results

Three sensitivity cases were run for porosity variations by taking the values as 10, 20, and 30%. The other parameters were kept the same. Figure 3 shows the comparison of the results of heat dissipation in the reservoir after 10 years of steam injection by using different porosity values.

Figure 4 shows the comparison of results of heat dissipation in the reservoir after 10 years of steam injection by using different permeability values. Three sensitivity cases were run for permeability variations by taking the values as 100md, 500md, and 1000md. The other parameters were kept constant.

To study the influence of water saturation on heat dissipation, three cases were run by taking the values of water saturation as 25%, 50%, and 100%. The other parameters were kept unchanged. Figures 5 and 6 show the comparison of the results of heat dissipation in the reservoir after 10 years of steam injection at different water saturation values.

4 Discussion

The results demonstrated that heat dissipation into the reservoir increases with either a decrease in porosity or an increase in permeability, at a constant water saturation. This is due mainly to connectivity of the mediums of heat transfer, i.e., rock and fluid. The lesser the porosity is, and the more connected the rock volume is. The higher the permeability translates to more connected fluid and pore volumes. From Fig. 5, it can be seen that the higher the water saturation, and the higher the heat dissipation, and the final temperature at the production well are greater because of the higher thermal heat capacity and conductivity of water.

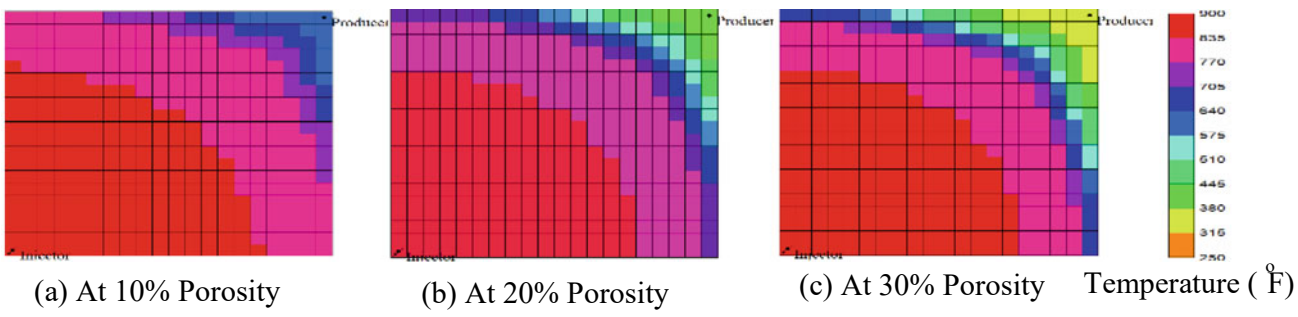

Fig. 3 Effects of increasing the porosity (from left to right **a**–**c**) on heat dissipation

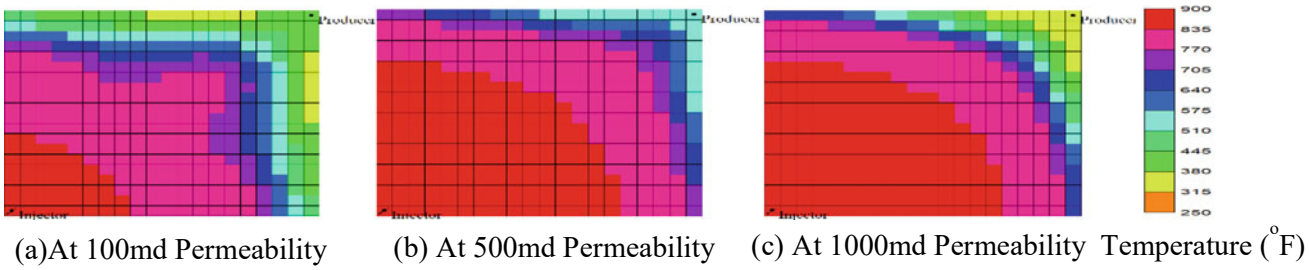

Fig. 4 Effects of increasing the permeability (from left to right **a**–**c**) on heat dissipation

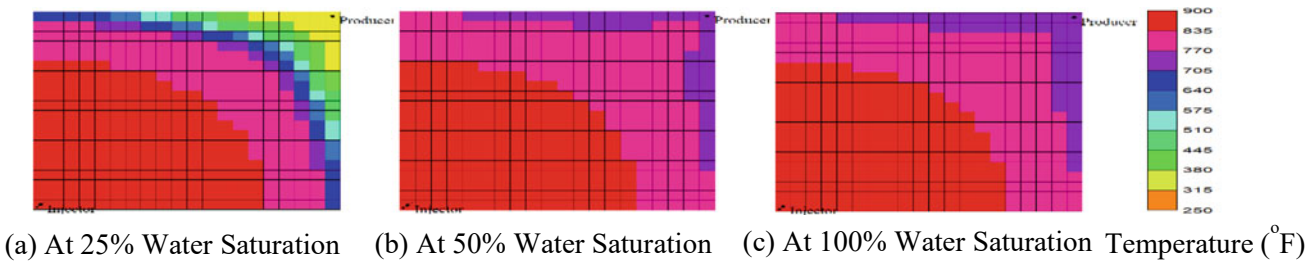

Fig. 5 Effects of increasing the water saturation (from left to right **a**–**c**) on heat dissipation

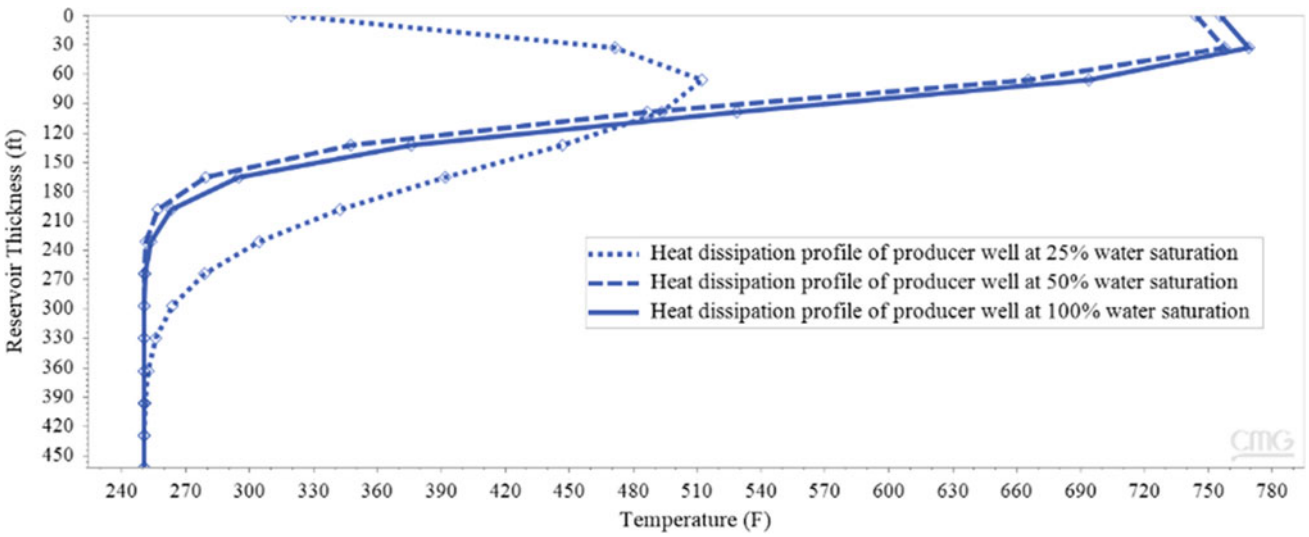

Fig. 6 Heat dissipation profiles at different water saturation levels

5 Conclusions

A comprehensive study of a reservoir numerical simulation of heat dissipation in a petroleum reservoir is carried out by using actual field data. It revealed three qualitative correlations based on porosity, permeability, and water saturation, regarding the heat transfer within a reservoir.

1. The higher the porosity, the lower the heat dissipation will be
2. The higher the permeability, the higher the heat dissipation will be
3. The higher the water saturation, the higher the heat dissipation will be

These correlations are very useful to select the suitable reservoir, well, region or even well spacing for heat injection in an oil well. These correlations are also very useful for other means of heating the reservoir that are in practice nowadays, i.e., in-situ combustion and hydraulic fracture heating technology. Beside the oil and gas production, the

results are also applicable for heat extraction from an oil field geothermal reservoir where the final temperature at the production well has great importance. These outputs provide screening criteria for an optimal zone or well for heat extraction from an oil field geothermal reservoir on the basis of the properties discussed in this study.

References

Davis, A.P.: Geothermal power production from abandoned oil wells. Energy **34**(7), 866–872 (2009)

Li, K.: Comparison of geothermal with solar and wind power generation. In: Thirty-Eighth Workshop on Geothermal Reservoir Engineering, pp. 1–10 (2013)

Liu, W.Z.: The Development Modes of Heavy Oil Reservoirs by Thermal Recovery. Petroleum Industry Press, Beijing (1998)

Liu, H.Q.: Principle and Design of Thermal Oil Recovery Processes. Petroleum Industry Press (2013)

Mehmood, A.: Geothermal energy potential of Pakistan on the basis of abandoned oil and gas wells. J. Pet. Environ. Biotechnol. **8**(3) (2017)

Mehmood, A.: Future electricity production from geothermal resources using oil and gas wells. Open J. Yangtze Gas Oil **2**, 191–200 (2017b)

Wang, W.: A review of analytical and semi-analytical fluid flow models for ultra-tight hydrocarbon reservoirs. Fuel **256**, 115737 (2019)

Unconventional Reservoir Characterization: Permeability Prediction in Shale Gas Reservoirs from Well-Logs Data Using Neural Network. Application to the Barnett Shale (USA)

Leila Aliouane, Sid-Ali Ouadfeul, and Amar Boudella

Abstract

Here, we suggest the use of the artificial neural network for permeability prediction in horizontally drilled well in unconventional shale gas reservoirs. Prediction of Permeability in shale gas reservoirs is a complicated task that requires new models where Darcy's fluid flow model is not suitable. The proposed idea is based on the training of neural network machine using the set of well-logs data as an input and the measured permeability, from Javadbour model, as an output. In this case, the multilayer perceptron neural network machine was used with Levenberg Marquardt algorithm. Application to two horizontal wells drilled in the Barnett shale formation exhibits the power of the neural network model to enhance unconventional reservoir characterization.

Keywords

Artificial neural network • Permeability • Shale gas • Unconventional reservoir • Well-logs

1 Introduction

Currently, unconventional reservoir characterization is an important task and challenge in the petroleum domain. It requires advanced technologies for their evaluation and extraction (Zee Ma and Holditch 2016; Aliouane and Ouadfeul 2013). Shale gas unconventional reservoirs and their permeability are still poorly understood where unconventional gas is found in reservoirs with relatively low permeabilities (less than 1 mD) and hence cannot be extracted via conventional methods. For that, we suggest the use of artificial intelligence such as neural network (ANN) for permeability prediction. Since, the ANN's techniques have been widely used to estimate conventional permeability (Aliouane et al. 2018). These techniques need just to be trained by training data. In our study, the well-logs of two horizontal wells, H1 and H2 in the Barnet shale from the Worth Basin, were used as input of neural network MLP model both for training and generalization. The obtained results will be compared to those obtained by Javadbour's relationship.

L. Aliouane (✉)
Laboratoire Physique de La Terre, Faculté des Hydrocarbures et de la Chimie, Université M'hamed Bougara de Boumerdes, 35000 Boumerdes, Algeria
e-mail: l.aliouane@univ-boumerdes.dz

S.-A. Ouadfeul
University M'hamed Bougara, 35000 Boumerdes, Algeria

A. Boudella
USTHB, Bab Ezzouar, Algeria

2 Data Description and Permeability Estimation Using Javadbour's Model

The raw well-logs data of two horizontal wells drilled in the Barnett shale located in the Ft Worth basin are exploited: total natural gamma (GR), bulk density (RHOB), neutron porosity (NPOR), transit time of P wave (DTCO), and transit time of S wave (DTSM). Figure 1 shows the raw well-logs data in tracks 2, 3, 4, 5, and 6. The recordings show that this reservoir is radioactive and tight by its low values of DTCO and DTSM.

Concerning the permeability computation, many authors have proposed many empirical relationships considering that the permeability in shale gas reservoirs is thought to be analogous to very tight sandstones (Moore et al. 2016). Such reservoirs consist of extremely tight formations through which transport of gas occurs by different mechanisms depending on the flow and porous formation conditions (Javadpour 2009; Civan et al. 2011; Haghshenas et al. 2013). Jenkins (2015) has shown the difficulty to estimate this parameter, mainly, in anisotropic permeability due to reservoir pressure change where it requires the confining stress method. In our study, permeability has been estimated using

M. Meghraoui et al. (eds.), *Advances in Geophysics, Tectonics and Petroleum Geosciences*, Advances in Science, Technology & Innovation, https://doi.org/10.1007/978-3-030-73026-0_99

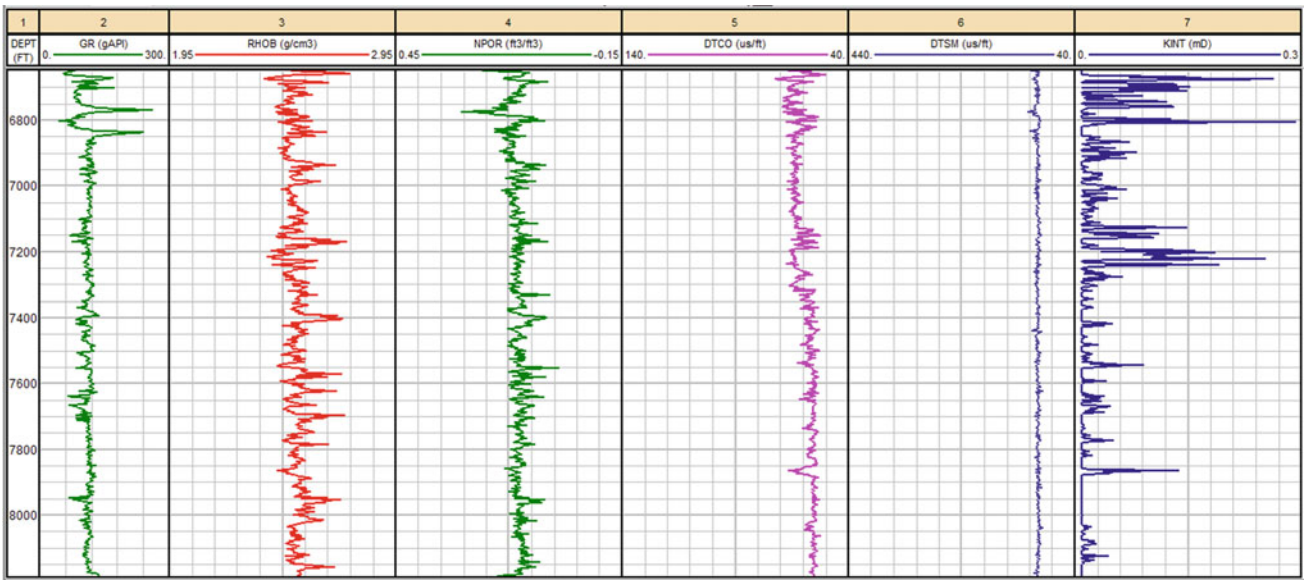

Fig. 1 Recorded well-logs data in the horizontal well H01 and the estimated permeability using the Javadbour model. Track 1: Depth (ft), track 2: GR (API), track 3: RHOB (g/cc), track 04: NPOR (%), track 05: DTCO (ms/ft), track 06: DTSM (ms/ft), track 07: estimated permeability using Javadpour model

the Javadbour equation (Javadpour 2009) in the Barnet shale of the two horizontal wells. The results of one well (H01) are shown in Fig. 1 track 7.

3 Permeability Prediction by Multilayer Perceptron Neural Network

The multilayer perceptron neural network machine (Aminian and Ameri 2005) with Levenberg Marquardt training algorithm (Aliouane et al. 2014) has been implemented for the prediction of the permeability in shale gas reservoirs. The 05 raw well-logs data, cited below, are used as an input in the input layer with 05 neurons, and the estimated permeability from Javadbour's equation is used as an output to train a neural network MLP for the output layer with one neuron (K_Predicted). The neural machine is trained in a supervised mode, and weights of connections are calculated during the training stage. The raw well-logs data are then injected in this machine, and an output is calculated using the weight of connections (Fig. 2).

4 Results Analysis and Conclusion

We can observe that the proposed MLP machine is able to provide very good results that are very close to the reality (Fig. 2). It is clear that the implanted machine is able to provide very good and realistic results.

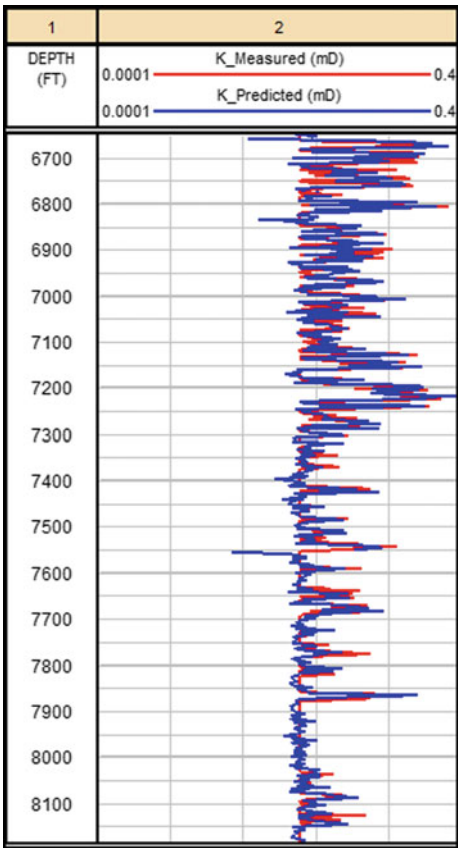

Fig. 2 Estimated permeability using the MLP with Levenberg Marquardt training algorithm (red color) compared with the estimated the Javadbour model (blue color) for the generalized well 01H

The implantation of this neural network machine enabled us to predict the permeability without the need to use Javadpour's relationship or another mathematical relationship that requires laboratory measurements of many rock parameters which are expensive and require financial support. We suggest testing the multilayer perceptron neural network machine to data of other horizontal wells drilled in the Barnett shale and that are close to the pilot well 01H to check its efficiency and generalize to weights of connection.

References

Aliouane, L., Ouadfeul, S, Djarfour, D., Boudella, A.: Permeability prediction using artificial neural networks. A comparative study between back propagation and Levenberg–Marquardt learning algorithms. In: Pardo-Igúzquiza, E., et al. (eds.) Mathematics of Planet Earth, Lecture Notes in Earth System Sciences. Springer, Berlin (2014)

Aliouane, L., Ouadfeul, S.: Sweet spots discrimination in shale gas reservoirs using seismic and well-logs data. A case study from the Worth basin in the Barnett shale. Energy Procedia (2013)

Aliouane, L., Ouadfeul, S.D., Boudella, A.: Back propagation and hidden weight optimization algorithms neural network for permeability estimation from well-logs data in Shaly Sandstone petroleum reservoirs: application to Algerian Sahara. In: Advances in Petroleum Engineering and Petroleum Geochemistry, Proceedings of the 1st Springer CAGJ, pp. 25–27. Tunisia (2018)

Aminian, K., Ameri, S.: Application of artificial neural networks for reservoir characterization with limited data. J. Petrol. Sci. Eng. **49**, 212–222 (2005)

Civan, F., Rai, C.S., Sondergeld, C.H.: Shale permeability determined by simultaneous analysis of multiple pressure-pulse measurements obtained under different conditions. SPE paper 144253 presented at SPE North American Unconventional Gas Conference and Exhibition, The Woodlands, Texas (2011)

Haghshenas, B., Clarkson, C.R., Chen, S.: Multi-Porosity, Multi-Permeability Models for Shale Gas Reservoirs. SPE Unconventional Resources Conference-Canada, SPE 167220 (2013)

Javadpour, F.: Nanopores and apparent permeability of gas flow in Mudrocks (shales and siltstone). J. Can. Pet. Technol. **48**, 16–21 (2009)

Jenkins, W.: Porosity and Permeability in tight rock. Thesis, Charles Darwin University (2015)

Moore, W.R., Zee Ma, Y., Pirie, I., Zhang, Y.: Tight Gas Sandstone Reservoirs, Part 2: Petrophysical Analysis and Reservoir Modeling. Elsevier (2016)

Zee Ma, Y., Holditch, S.A.: Unconventional Oil and Gas Handbook. Evaluation and Development. Elsevier (2016)

Shale Volume Estimation in Unconventional Tight Sand Reservoir from Well-Logs Data Using Neural Network Enhanced by the Spectral Mineralogical Neutron Measurements with an Application to Algerian Sahara

Sid-Ali Ouadfeul, Leila Aliouane, Amina Cherana, and Amar Boudella

Abstract

The main goal of this paper is to show the contribution of the neural network to predict the shale volume in an unconventional tight sand gas reservoir. Shale volume is, usually, estimated using the natural gamma log, which can give bad results in case of the presence of non-clayey radioactive minerals in the reservoir. Our purpose is to implement a multilayer neural network machine to predict clay volume using the conventional well-logs data as an input and the measured mineralogical component as desired output with a hidden weight optimization algorithm (HWO). Application to two reservoir intervals of a borehole located in the Algerian Sahara shows the contribution of spectral mineralogical well-logs and the power of the implemented neural network machine in unconventional tight sand reservoirs characterization.

Keywords

Shale volume • Tight sand • Unconventional reservoir • Mineralogical spectral tool • Neural network • Well-logs

1 Introduction

The shale volume is very useful in unconventional reservoirs characterization. It can be used to estimate porosity, to locate the sweet spots (Aliouane and Ouadfeul 2013), and to make completion decisions for the hydraulic fracturing. Using conventional logs data alone to estimate clay volume is prone to uncertainties (Moore et al. 2016). For that, the interpretation can be enhanced by advanced well-logs such as neutron spectral mineralogical recordings (Everett 2014). In case the latter are not available, neural network can be proposed since it is very popular in geosciences and in petroleum reservoir characterization from well-logs data.

In this paper, we propose to use the spectral mineralogical well-logs to enhance the unconventional tight reservoir characterization by implementing a neural network machine able to predict the shale volume in the Ordovician tight sand gas from the Algerian Sahara.

2 Data Analysis of Ordovician Tight Sand Reservoir

Petrophysical recordings, sensitive to shale, of Ordovician tight sand reservoir located in the Algerian Sahara have been exploited for shale volume estimation (Fig. 1): total natural gamma ray (GR), deep resistivity (RT), neutron porosity (NPHI), and transit time of P wave (DT). The tight character is shown with low porosity logs (NPHI and DT), and this kind of reservoirs can be radioactive where the radioactivity is not related to clay content (Ma et al. 2014). Due to shallow invasion in many tight gas sands, neutron porosity deficit can be a very good indicator of gas formation.

3 Shale Volume Estimation by Conventional Methods and Neural Network

In the traditional method, the shale volume is usually computed from GR, porosity logs, and combination of logs (Moore et al. 2016). Many analysts use density porosity alone calculated from the bulk density with a variable grain matrix to correct for mineral composition (pyrites and clay

S.-A. Ouadfeul (✉)
University of Khemis Miliana, Khemis Miliana, Algeria
e-mail: s.ouadfeul@univ-dbkm.dz

L. Aliouane · A. Cherana
Laboratoire Physique de La Terre, Faculté des Hydrocarbures et de la Chimie, Université M'hamed Bougara, 35000 Boumerdes, Algeria

A. Boudella
USTHB, Bab Ezzouar, Algeria

M. Meghraoui et al. (eds.), *Advances in Geophysics, Tectonics and Petroleum Geosciences*,
Advances in Science, Technology & Innovation, https://doi.org/10.1007/978-3-030-73026-0_100

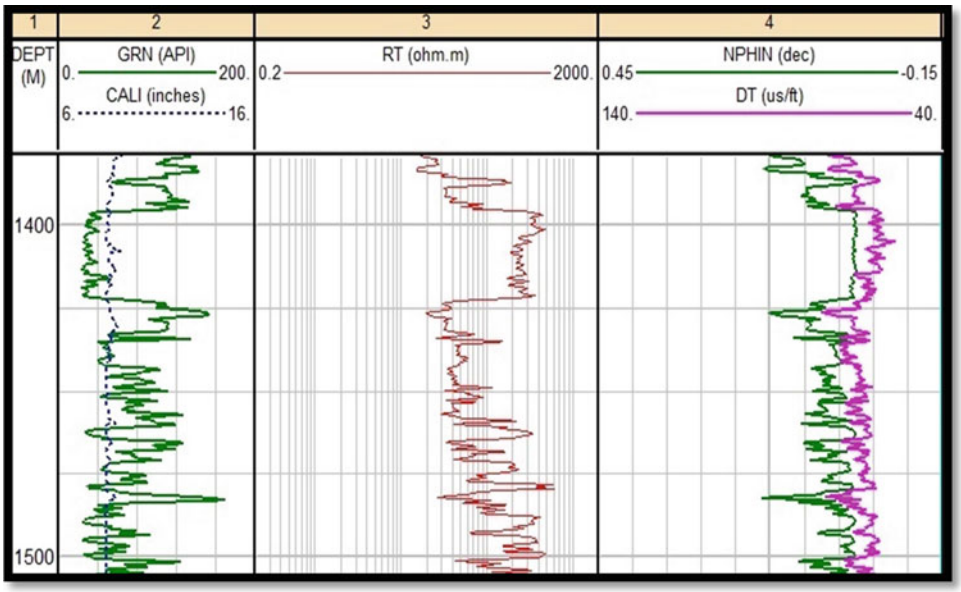

Fig. 1 Petrophysical recordings of Ordovician tight sand of a well-A (Algerian Sahara)

minerals) and a fluid density lower than 1 to compensate for incomplete flushing in the measurement zone. Using conventional log data alone to estimate shale volume suffers from uncertainties. For that, the spectral mineralogical neutron log can give better shale volume providing the percentage of aluminum (Al) which is the common element of all clay minerals (Everett 2014). This is the case of ECS which can estimate (Al) volume from (Ca), (Si), and (Fe) (Everett 2014).

A neural network machine with a multilayer model has been implemented to calculate the clay volume using the whole well-logs data of two intervals of an Ordovician tight reservoir of one well located in the Algerian Sahara (Well-A). Well-logs data of the first interval are used for learning and the second for generalization with a supervised learning using a hidden weight optimization algorithm (Aliouane et al. 2018).

The input layer is constituted by four neurons corresponding to four conventional well-logs data: gamma ray (GR), neutron porosity (NPHI), bulk density (RHOB), and sonic travel time (DT). The output layer presents only one neuron corresponding to the clay volume (Vsh-ANN)). The desired output is represented by volume computed by spectral mineralogical by elementary capture spectroscopy tool (ECS) (Vsh-ECS) data. Elemental spectroscopy tools can be used to determine the percentage of minerals in the rock composition so that porosity and clay volume can be calculated more accurately (Moore et al. 2016).

Figure 2 shows the clay volume computed from conventional well-logs data: from gamma ray (Vsh_GR), from neutron density (Vsh_ND, from density sonic (Vsh_DS), from the spectral neutron well-logs (Vsh_ECS), and from neural network (Vcl_ANN).

4 Results Analysis and Conclusion

Advanced well-logs data, such as spectral mineralogical recordings, when available, provide a better clay volume estimation. However, when advanced well-logs are not available, neural network can provide good results.

By implementing our method, we have demonstrated that it is possible to provide an accurate petrophysical interpretation within a short time in order to take completion decisions and to enhance unconventional tight sand gas reservoir characterization.

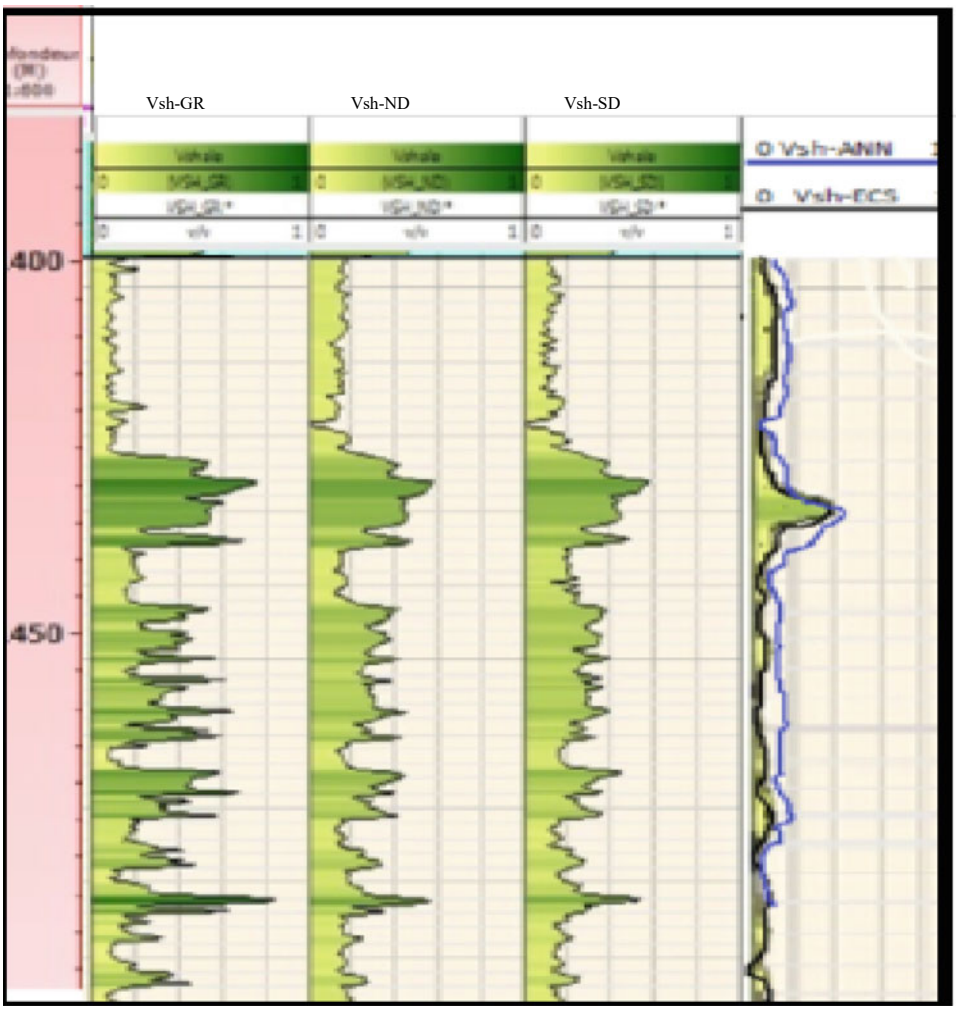

Fig. 2 Shale volume computed from conventional well-logs data (Vsh_GR, Vsh_ND, and Vsh_SD); spectral mineralogical (Vsh_ECS) and neural network (Vsh_ANN)

References

Aliouane, L., Ouadfeul, S.: Sweet spots discrimination in shale gas reservoirs using seismic and well-logs data. A case study from the Worth basin in the Barnett shale. Energy Procedia (2013)

Aliouane, L., Ouadfeul, S.D., Boudella, A.: Back propagation and hidden weight optimization algorithms neural network for permeability estimation from well-logs data in Shaly Sandstone Petroleum Reservoirs: application to Algerian Sahara. In: Advances in Petroleum Engineering and Petroleum Geochemistry, Proceedings of the 1st Springer CAGJ, pp. 25–27. Tunisia (2018)

Everett, R.V.: Three Methods for Log-Derived Mineralogy Primarly Used for Shales (Silts) and Tight Formations SWLS, pp. 19–35. Springer (2014)

Ma, Y.Z., et al.: Identifying Hydrocarbon Zones in Unconventional Formations by Discerning Simpson's Paradox. Paper SPE 169496 presented at the SPE Western and Rocky Regional Conference, Apr 2014

Moore, W.R., Zee Ma, Y., Pirie, I., Zhang, Y.: Tight Gas Sandstone Reservoirs, Part 2: Petrophysical Analysis and Reservoir Modeling. Elsevier (2016)

Development of a Local Correlation Between Static and Dynamic Elastic Properties for Three Main Carboniferous Carbonate Reservoir Rocks in the Volga-Ural Region

Ilmir Nugmanov and Andreas Henk

Abstract

This study aims to develop a new local correlation between dynamic and static elastic properties of carbonate rocks as part of the mechanical earth model building. Carboniferous carbonate reservoirs are the main source of hard-to-recover reserves in the Volga-Ural petroleum province. Knowledge of geo-mechanical (elasticity and strength) properties of carbonate rocks can help to reduce engineering risks in heavy crude oil production. The core samples taken from six wells were used as the base data for the study. Dynamic elastic properties were determined by ultrasonic testing. Static elastic properties were determined by the uniaxial compression testing. The rocks were classified according to the results of the petrographic analysis. The study has made it possible to obtain a linear correlation between dynamic and static elastic properties. The results were then compared with the data on carbonate rocks available in the literature. The obtained correlation could be used for log-based hydro-fracturing design for vertical and horizontal wells.

Keywords

Elastic properties • Young's modulus • Ultrasonic velocity • Unconfined compression strength • Carbonate reservoir

1 Introduction

Modern experimental studies of elastic properties of rocks cover a scale range from tens of micrometers (Saenger et al. 2016) to hundreds of meters (Cai et al. 2004). In geological terms, this means a scale ranging from grain aggregates to rock massifs. Reliable and consistent values of Young's modulus and uniaxial compressive strength are crucial for solving any engineering problems associated with rock mechanics, be it tunneling (Ajalloeian et al. 2017), hydropower and geothermal projects (Cai et al. 2004; Gegenhuber et al. 2017), selection of building materials (Martinez-Martinez et al. 2012), mining (Madhubabu et al. 2016), or petroleum geomechanics (Fjar et al. 2008).

Most researchers (Najibi et al. 2015; Brotons et al. 2016; Al-Shayea 2004) note that the estimation of elastic properties (static Young's modulus, Poisson Ratio, etc.) under loading conditions presents huge challenges: strict sample preparation requirements, highly accurate measuring systems, impossibility of sampling in highly fractured zones, and small number of intact rock specimens. Despite the fact that the laboratory tests are all standardized, the obtained values of the elastic properties may differ depending on the chosen technique (Al-Shayea 2004). However, ultrasonic tests providing data on dynamic elastic properties do not require sample destruction, and velocity properties can be up-scaled to log data and seismic data. These features have motivated the researchers to look for a relationship between dynamic and static properties, both in general (for different types of rocks and/or geological regions) and specific (for a specific sedimentation basin, a single stratigraphic unit or rock type) forms. Brotons et al. (2016), Najibi et al. (2015), and Gegenhuber et al. (2017) provided the most frequently used relationships between petro-physical and elastic properties. This study aims to develop a local correlation between static and dynamic elastic properties for three main Carboniferous carbonate reservoir rocks of the Volga-Ural region and to compare the results with the data available in the literature.

2 Geological Settings and Laboratory Testing Methods

The core samples were taken from 6 wells drilled in different oilfields located within the East European Carbonate Platform which is part of the Volga-Ural anteclise. The sampling

I. Nugmanov (✉) · A. Henk
Technische Universität Darmstadt, 64287 Darmstadt, Germany

M. Meghraoui et al. (eds.), *Advances in Geophysics, Tectonics and Petroleum Geosciences*,
Advances in Science, Technology & Innovation, https://doi.org/10.1007/978-3-030-73026-0_101

covered three main carbonate reservoirs. They include the Lower Mississippian and the Lower and Middle Pennsylvanian stratigraphic series (international stratigraphic scheme) and are represented by carbonate sediments of the Upper Tournasian stage, the Bashkirian stage, and the Lower Moskovian stage.

Elastic properties and uniaxial compressive strength were determined in accordance with procedures described in ASTM D2845-08 and ASTM D7012-14. Cylindrical (height-to-diameter ratio—2:1) samples were used for the tests. The sample was placed in the uniaxial compression measurement device between the plunger-retainer plates. Two LVDT-sensors were installed along the load axis to measure linear deformations. In the middle part of the sample, a single radial deformation sensor was installed to measure the change in circumference. Ultrasonic velocities were measured using the impulse technique. End-faces of the samples were used for petrographic thin section optical analysis and X-ray diffractometry.

3 Results

3.1 Mineralogical and Petrographic Analysis

According to the petrographic analysis conducted on thin sections, the carbonate rocks under study are limestones of different structural and genetic types. The reservoir rocks consist of grainstone and packstone, and the cap rocks are represented by wackstone and mudstone (Dunham's classification (Ajalloeian et al. 2017)). Rudstone and boundstone compose thin layers (their oil saturation depends on diagenetic processes). According to X-ray powder diffraction analysis, limestone is almost entirely composed of calcite, with minor inclusions of dolomite, quartz, pyrite, and mica.

3.2 Mechanical and Ultrasonic Tests

The mechanical and petro-physical properties of three main Carboniferous carbonate reservoirs are available via external link (Data Storage 2019). The cross-plot in Fig. 1 shows a correlation between dynamic and static elastic properties of carbonate.

The linear regression fitted model was obtained in the form of:

$$0.43E_{\mathrm{d}} - 2.17 = E_{\mathrm{s}}, \quad R^2 = 0.72 \tag{1}$$

4 Discussion

Dynamic and static elastic moduli are non-equivalent. Values of the elastic moduli determined under the load (static) are significantly lower than those obtained from the acoustic tests. Among the many possible reasons for this are fracturing, surfaces of weakness, weathering and epigenetic changes in rocks, the influence of which increases when upscaling from a rock sample to a rock mass. Gregor et al. 2003 (Data Storage 2019) stated that the porosity (its distribution and pore size) is the main factor directly affecting the elastic moduli. In carbonate rocks, the pore distribution reflects both the environmental conditions of sedimentation and the subsequent diagenetic transformations. The studies conducted by Yan et al. (Data Storage 2019) showed that dynamic and static bulk moduli (measure of bulk elastic state) become equal at depths at which pore stiffness is above 6 GPa. Croizet et al. (2013) (Data Storage 2019) indicates that at depths of more than 6 km, the porosity is almost zero, and the rock can be considered an isotropic medium.

5 Conclusions

The local correlation between static and dynamic elastic properties for three main Carboniferous carbonate reservoir rocks of the Volga-Ural region obtained in this study makes it possible to infer accurate values of Young's modulus from acoustic-log data combined with density-log data. The results of the laboratory tests are commensurate with the data available in the literature and can be further adapted for larger geographical areas. The variations in the results may be due to secondary changes in rocks and differences in mineralogical composition.

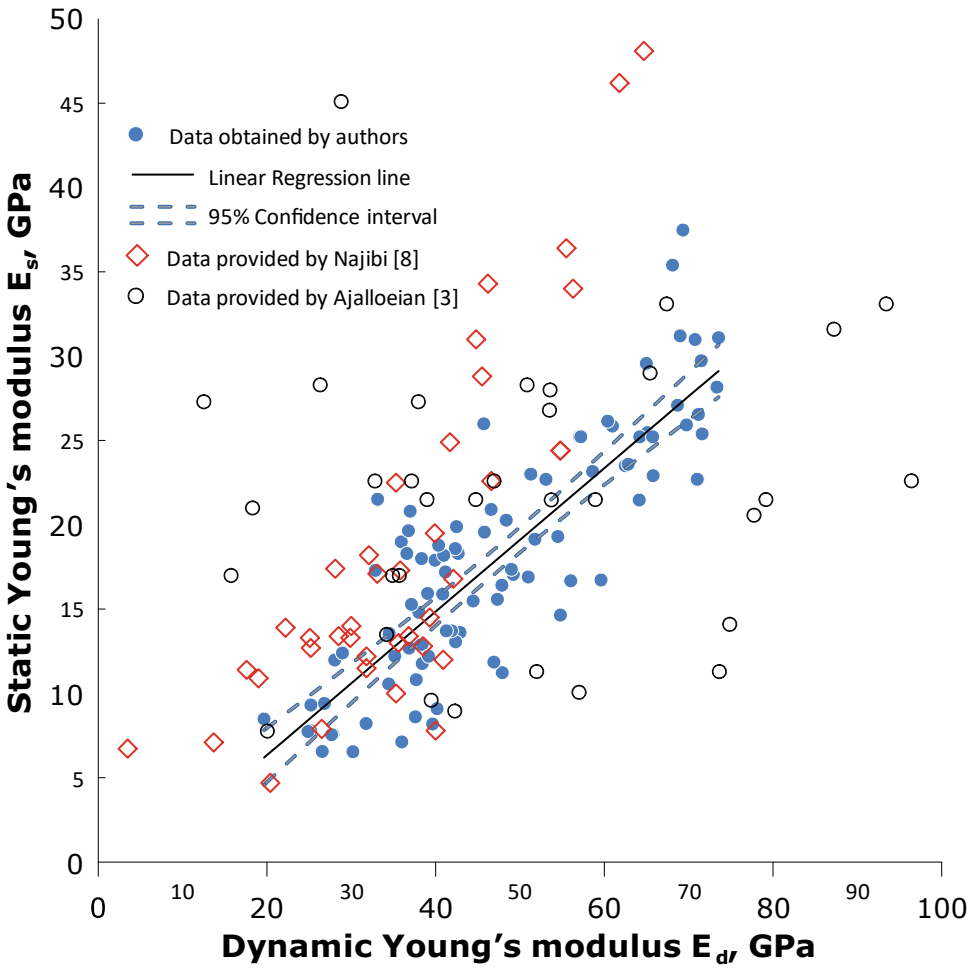

Fig. 1 Results of experimental rock mechanics test for core samples taken from six wells (blue dots). Cross-plot shows the relationship between static and dnamic elastic modulus in the studied carbonate samples and comparison to other data provided in the literature (red and black colored symbols)

References

Ajalloeian, R., Mansouri, H., Baradaran, E.: Some carbonate rock texture effects on mechanical behavior, based on Koohrang tunnel data. Iran. Bull. Eng. Geol. Environ. **76**(1), 295–307 (2017)

Al-Shayea, N.: Effects of testing methods and conditions on the elastic properties of limestone rock. Eng. Geol. **74**(1–2), 139–156 (2004)

Brotons, V., Tomas, R., Ivorra, S., et al.: Improved correlation between the static and dynamic elastic modulus of different types of rocks. Mater. Struct. **49**(8), 3021–3037 (2016)

Cai, M., Kaiser, P., Uno, H., et al.: Estimation of rock mass deformation modulus and strength of jointed hard rock masses using the GSI system. Int. J. Rock Mech. Min. Sci. **41**, 3–19 (2004)

Data Storage. https://github.com/INugmanov/CAJG_DATA.git. Last accessed 2019/06/14

Croizet, D., Renard, F., Gratier, J.-P.: Compaction and porosity reduction in carbonates: A review ofobservations, theory, and experiments. Advances in Geophysics, Elsevier **54**, 181–238 (2013). https://doi.org/10.1016/B978-0-12-380940-7.00003-2insu-00799787

Fjar, E., Holt, Horsrud, P., Raaen, A., Risnes, R.: Petroleum Related Rock Mechanics. 2nd edn. Elsevier Science, Hungary (2008)

Gegenhuber, N., Schifko, T., Pittino, G.: Petrographic coded model concept for the correlation between geomechanical and elastic properties and its application on log data for Alpine rocks. Austrian J. Earth Sci. **110**(1), 101–108 (2017)

Gregor, P., Eberli Gregor, T., Baechle Flavio, S., Anselmetti Michael, L., Incze.: Factors controlling elastic properties incarbonate sediments and rocks. Leading Edge **22**(7), 654–660 (2003). https://doi.org/10.1190/1.1599691

Madhubabu, N., Singh, P., Kainthola, A., et al.: Prediction of compressive strength and elastic modulus of carbonate rocks. Measurement **88**, 202–213 (2016)

Martinez-Martinez, J., Benavente, D., Garcia-del-Cura, M.: Comparison of the static and dynamic elastic modulus in carbonate rocks. Bull. Eng. Geol. Environ. **71**(2), 263–268 (2012)

Najibi, A.R., Ghafoori, M., Lashkaripour, G.R., Asef, M.R.: Empirical relations between strength and static and dynamic elastic properties of Asmari and Sarvak limestone's, two main oil reservoirs in Iran. J. Petrol. Sci. Eng. **126**, 78–82 (2015)

Saenger, E., Vialle, S., Lebedev, M., et al.: Digital carbonate rock physics. Solid. Earth **7**, 1185–1197 (2016)

Ecofriendly Lubricant Solutions for the Exploration and Exploitation of Oil and Gas Resources

Md Amanullah, Jothibasu Ramasamy, and Mohammad K. Al-Arfaj

Abstract

Readily biodegradable, virtually non-toxic, and highly ecofriendly lubricants were developed using waste vegetable oil to explore and exploit oil and gas resources without causing any damage and/or degradation to other terrestrial and marine resources. The low-cost raw material and the significantly lower development cost of waste vegetable oil-based ecofriendly lubricants compared to pure vegetable oil-based ecofriendly lubricants currently available in the market will provide higher economic benefits and much better return on investment. The performance of the lubricants was evaluated using the industry standard lubricity test method and apparatus for comparison with the performance of traditional lubricants. Their lubricating performances were also compared with a commercial green lubricant. Experimental results indicate that the newly developed lubricants provide desirable and comparable performance with respect to an equivalent commercial lubricant, and thus, demonstrate their suitability as the viable substitutes for this lubricant and for other similar products. Some lubricants showed good lubricating potential in a clay-based mud system, some in muds containing monovalent salts, and some for all of them due to the variation in the lubricants' composition. However, all of them showed good lubricating performance in their application domains, which, therefore, demonstrates their technical significance in reducing the torque and drag, while drilling.

Keywords

Ecofriendly lubricants • Waste vegetable oil • Lubricating potential • Bio-based lubricants • Renewable lubricants

M. Amanullah (✉) · J. Ramasamy · M. K. Al-Arfaj
Saudi Aramco, Dhahran, 31311, Saudi Arabia
e-mail: md.amanullah@aramco.com

1 Introduction

Poor lubricating potential of water-based drilling muds frequently creates various drilling problems including high torque and drag, while drilling for exploration and exploitation of oil and gas resources to meet the global energy demand. Hence, there is a need to add suitable lubricants in water-based muds to fulfill their functional tasks properly and complete the drilling operation safely and economically. The lubricating potential of drilling mud is one of the major critical factors for efficient drilling operations in deviated, horizontal, extended-reach and multilateral wells, and vertical wells with high-dogleg severity. Hence, the oil and gas industry use various types of chemicals and additives to improve the lubricating potential and other mud properties. Some of these additives and products are not ecofriendly and, thus, have a high restriction in their applications due to their detrimental impact on surrounding environments, ecosystems, habitats, water resources, surrounding faming lands, population, rig-site workers, and professionals, etc. (Davies et al. 1989; Dann and Mulder 1994; Friedheim and Conn 1996). Due to the lack of adequate ecofriendly lubricants, there is a push in the industry to develop more ecofriendly lubricants to be in the forefront of best drilling practices. According to the chemical market report described by Guzman (2002), there is an expected annual growth 32 of 7–10% ecofriendly lubricants in the US market over the next few years compared to an overall 2% growth rate of conventional lubricants. This is reflected in the increasing research to develop green additives and lubricants to replace or reduce the use of less ecofriendly additives and products (Amanullah 2005; Peresich et al. 1991; Bland et al. 1993).

To contribute to the development of ecofriendly lubricants, a pioneering research was conducted by EXPEC ARC to develop ecofriendly lubricants using waste vegetable oil as raw material due to its several positive characteristics both from the technical and environmental points of view. For

M. Meghraoui et al. (eds.), *Advances in Geophysics, Tectonics and Petroleum Geosciences*,
Advances in Science, Technology & Innovation, https://doi.org/10.1007/978-3-030-73026-0_102

example, the high fire and flash points of waste vegetable oil ensure a significantly lower risk of causing fire hazards, which makes it highly suitable for HTHP drilling environments to reduce the probability and the likelihood of causing a fire during handling, mixing, transporting, etc. Due to the absence of any toxic materials in waste vegetable oil composition, it has no/negligible occupational health issues, and is, thus, highly OHSE friendly. The high OHSE friendly nature of the waste vegetable oils and their derivatives dramatically reduces the risk of creating any occupational health hazards. Amanullah and Arfaj (2017), and How et al. (2012) have provided a comprehensive description of the advantages of vegetable or waste vegetable oil-based fluid additives over diesel and mineral oil-based products.

2 Lubricant Development Process

The huge volume of waste vegetable oil generated by the food and catering industry has no aromatic oil content, is virtually non-toxic, and readily biodegradable, thus, it is a potential source of renewable raw material for the development of ecofriendly lubricants. Hence, it was used as the raw material to develop several ecofriendly lubricants. Traditional esterification and hydrogenation methods of processing were used in the development of the lubricants. Figure 1a, b shows the chemical processes used in the development of the ecofriendly lubricants.

3 Results

The experimentally determined COF values of the base muds and the muds in the presence of the newly developed ecofriendly lubricants, ARC Ecolube, ARC Ecolube HP, ARC Ecolube HPL, ARC Vege Lube, and a commercial green lubricant are given in Fig. 2. Several frequently used water-based muds such as bentonite mud, LSND mud, KCl-Polymer Mud, and $CaCl_2$ mud were used as the base muds that have no lubricant in the mud systems to benchmark the performance of the lubricants.

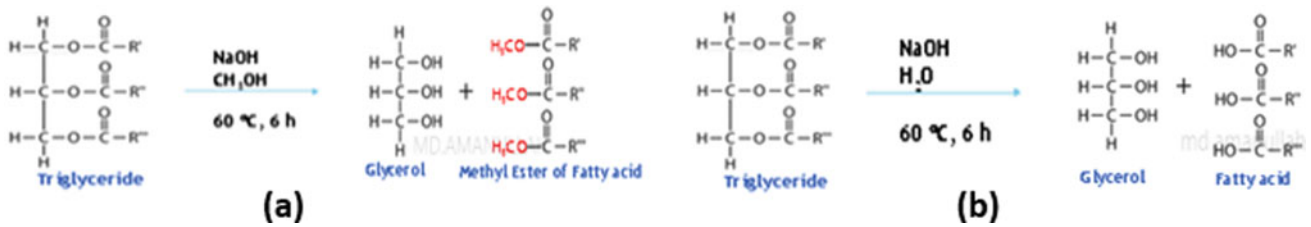

Fig. 1 Chemical processes used in the development of ecofriendly lubricants. **a** Esterification process and **b** hydrogenation process (Amanullah et al. 2019—modified)

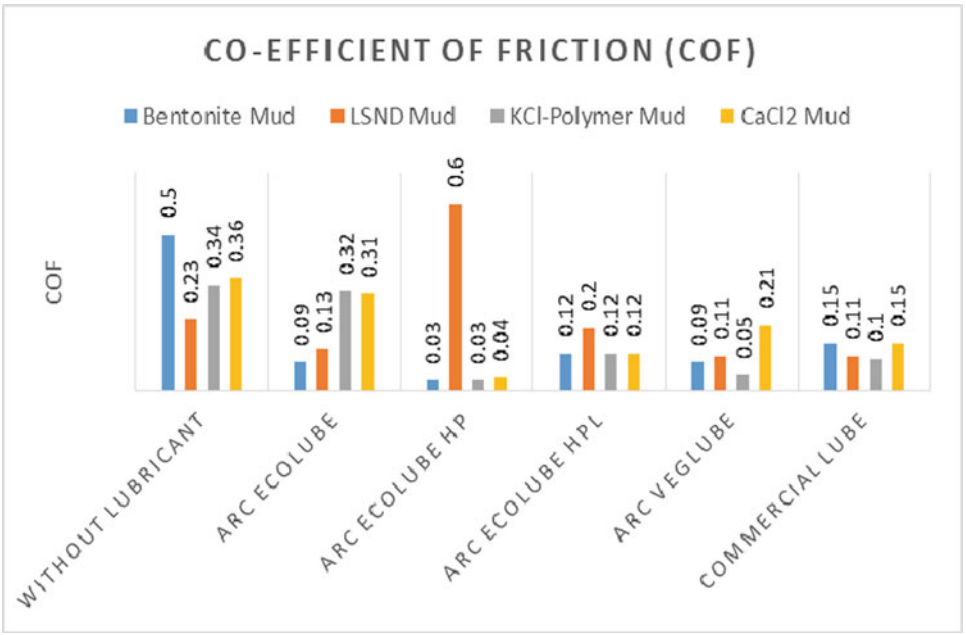

Fig. 2 COF values of various water-based muds in the presence of the newly developed ecofriendly lubricants and a commercial green lubricant

4 Discussion

Figure 2 shows the effect of the newly developed ecofriendly lubricants along with a commercial lubricant on the bentonite mud lubricity enhancement. As compared to the original mud, the co-efficient of friction values dropped significantly upon the addition of lubricants. In most cases, the COF values were reduced by more than 50% upon lubricant addition. Among the four lubricants developed and tested, ARC Ecolube HPL and ARC Veglube have an excellent lubricating property, followed by ARC Ecolube HP which shows an excellent COF reduction, except for the case of LSND mud system. ARC Ecolube shows a very good lubricating effect with bentonite and LSND muds. However, it does not show a huge impact on monovalent and divalent salts containing water-based mud systems. Except for the ARC Ecolube, all of the other newly developed lubricants have shown an excellent lubricating property with routinely used water-based mud systems including monovalent and divalent salt systems. Moreover, a similar or better lubricating performance has been observed compared to the commercially available ecofriendly lubricant.

5 Conclusions

The lubricants developed using the cooking waste oil demonstrated similar or better performance results compared to a commercially available equivalent green lubricant. Hence, the green lubricants developed using waste vegetable oil as raw material could provide a viable alternative to imported green lubricant products, and can, thus, significantly reduce the additive import cost. The renewable nature of waste vegetable oils provides a sustainable source of raw materials for the development of ecofriendly lubricants.

References

Amanullah, Md.: Physio-chemical characterization of vegetable oils and preliminary test results of vegetable oil-based muds. In: SPE/IADC Middle East Drilling Technology Conference and Exhibition, Dubai UAE. September, SPE-97008-PP (2005)

Amanullah, Md., Arfaj, Mohammed, Ramasamy, Jothibasu.: Waste cooking oil—a potential source of raw material for localization of green products development. Saudi Aramco J. Technol., Spring (2019), Lead Article (2019)

Amanullah, Md., Arfaj. K.M.: Novel method and apparatus for sticking fluid performance evaluation. In: SPE Kingdom of Saudi Arabia Annual Technical Symposium and Exhibition, Dammam, Saudi Arabia, 24–27, SPE-KSA-8278 (2017)

Bland, R.G., Clapper, D.K., Fleming, N.M., Hood C.A.: Biodegradation and drilling fluid chemicals. In: SPE/IADC Drilling Conference, Amsterdam, SPE/IADC 25754, 23–25 February (1993)

Davies, J.M., Bedborough, D.M., Blackman, R.A.A., Addy, J.M., Appelbee, J.F., Grogan, W.C., Parker, J.G., Whitehead, A.: The environmental effect of oil-based mud drilling in the North Sea. In: Engelhardt, F.R., Ray, J.P., Gillam, A.H. (eds.) Drilling Wastes, Elsevier Applied Science, London (1989)

Dann, R., Mulder, M.: Long-term effects of OBM cutting discharges in the sandy erosion area of the Dutch continental shelf. Netherlands Institute for Sea Research, Report NIOZ Rapport 1994–10 (1994)

Friedheim, J.E., Conn, H.L.: Second generation synthetic fluids in the North Sea: are they better? In: IADC/SPE Drilling Conference, New Orleans, LA, March 12–15. IACD/SPE 35061. Proceedings pp 215–228 (1996)

Guzman, D.: Chemical market. Report. **261**(23), 11 (2002)

How, H.G., Teoh, Y.H., Masjuki, H.H., Kalam, M.A.: Impact of coconut oil blends on particulate-phase PAHs and regulated emissions from a light duty diesel engine. Energy **48**, 500–509 (2012)

Peresich, R.L., Burrell, B.R., Prentice, G.M.: Development and field trial of a biodegradable invert emulsion fluid. In: SPE/IADC Drilling Conference, Amsterdam, SPE/IADC 21935, 11–14 March (1991)

Development and Rheological Properties of a Local (Nigerian) Organophilic Clay as a Constituent of Oil-Based Drilling Fluid

Bala Usman, Suleiman Shuwa, and Bilal Sabiu

Abstract

Nigerian bentonitic clays are mostly calcium-based and have shown poor rheological, filtration and thixotropic properties when mixed with water or oil due to low-swelling capacity. They are also incompatible with water-sensitive shales when used for oil-based mud due to their low-swelling capacity. This prompts the introduction of cationic surfactant aimed at replacing the calcium ions of the clay and its free surface to develop organophilic clay which has shown improved properties. The clay sample in this study was sourced from Fika formation from Yobe state, Nigeria. Cation exchange capacity (CEC) analysis was carried out to characterize the clay sample. There was an increase in CEC after soda ash activation from 37.5 to 40.5 meq/100 g clay. The soda ash activated sample was used to develop water in oil emulsion drilling mud. Rheological and thixotropic properties of muds formulated from the clay samples for oil-to-water ratios of 90:10, 80:20, 70:30 and 60:40 formulation were investigated using FANN 35SA viscometer by determining the plastic viscosity (PV), apparent viscosity (AV) and gel strength (GS). The 90:10 formulation has shown PV of 17 cP, AV of 18 cP, GS of 5 lbf/100 ft^2 and 6 lbf/100 ft^2 for 10 s and 10 min, respectively. 80:20 formulation has PV and AV of 18.5 cP and 26.5 cP, respectively, with GS of 4 lbf/100 ft^2 and 6 lbf/100 ft^2 for the 10 s and 10 min GS while the 70:30 formulation has shown PV and AV of 25 cP and 26.5 cP, respectively, with GS of 6.5 lbf/100 ft^2 and 8 lbf/100 ft^2 for 10 s and 10 min, respectively. The 60:40 formulation has PV and AV of 28.5 cP and 47.75 cP, respectively, with GS of 8 lbf/100 $ft^2$and 9 lbf/100 ft^2 for 10 s and 10 min, respectively. All the formulations compare very well with their respective formulations formulated from organophilic clay developed from API grade Wyoming bentonite clay sample.

Keywords

Bentonitic clays • Rheological properties • Water-sensitive shales • Plastic viscosity • Apparent viscosity

1 Introduction

Drilling fluid is a mud used in drilling operations which is circulated or pumped from the surface, down the drill string, through the bit and back to the surface via the annulus (Bilal 2016). It is a fluid which comprises a multitude of additives. It consists of fluid, solid and chemical components. The type and amount of additives are based on the drilling method employed and the type of reservoir to be drilled. The drilling mud can be broadly classified as water-based mud (WBM) when water is the continuous phase, oil-based mud (OBM) when oil is the continuous phase, synthetic-based mud (SBM) when synthetic material is the continuous phase. Other types are emulsions, invert emulsions, air, foam fluids, etc. (Subhash et al. 2010)

The need to move oil fields into new technology frontiers coupled with ever increasing global demand for energy brought the need for a more efficient and robust technology, especially where adverse conditions like water-sensitive reservoirs (most common in offshore environment), high temperature, and/or high-pressure environments are being encountered (SPE 2013). Furthermore, as the demand for energy increases, so does the need for more cost effective and environmentally friendly ways to tap resources. The drilling process accounts for 80% of the cost of the drilling phase, with drilling fluid representing 15–25% (Bourgoyene et al. 1991).

B. Usman (✉) · S. Shuwa · B. Sabiu
Department of Chemical Engineering, Ahmadu Bello University, Zaria, Nigeria

M. Meghraoui et al. (eds.), *Advances in Geophysics, Tectonics and Petroleum Geosciences*,
Advances in Science, Technology & Innovation, https://doi.org/10.1007/978-3-030-73026-0_103

Nigeria is blessed with more than 700 million metric tons of bentonitic clay in the North East region alone, with an annual average consumption of 100,000 tons for the drilling fluid formulation alone (RMRDC 2010). This clay is mostly calcium-based which is considered to be low grade since it has shown poor rheological, thixotropic and filtration property. However, when this clay is modified by the introduction of cationic surfactants based on CEC of the raw clay, organophilic clay is developed with resultant increase in interlayer spacing. This clay has high-swelling capacity in oil or emulsion of oil and water, with good rheology, thixotrophy and low-filtrate loss. It is characterized by its oil-wet composition, which makes it compatible with water-sensitive shales.

In this work, organophilic clay was developed, characterized, and used to formulate water in oil emulsion drilling mud. The mud was tested based on rheology, thixotrophy and filtration property, and the properties were compared with formulation from organophilic clay developed from API Wyoming bentonite.

2 Materials, Equipment and Methods

The materials used are bentonitic clay, sourced from Fika formation in North East Nigeria, API grade Wyoming bentonite, Hexadecyltrimethyl ammonium bromide (CTAB), Sorbitan mono Oleate, water, diesel, and 200 mesh size sieves.

The clay sample was physically beneficiated by dissolving about 20 g of the clay in 500 ml of water. The mixture was stirred for 20 min and allowed to sit for 24 h. The lower layer containing sand and quartz was discarded, and the upper layer was collected. It was then sun-dried, ground and used for organophilic clay development.

Chemical beneficiation was done by adding about 12 wt % soda ash to the physically beneficiated sample and allowing it to sit for 24 h so that cation exchange will take place (Bilal 2016). The clay mud sample was then filtered, dried, ground to the required particle size and sieved using 200 mesh size sieve before modification to organophilic clay.

The organophilic clay was developed by dissolving about 20 g of physically beneficiated clay in 1 L of water at 70–80 °C and homogenized at 250 rpm for 90 min. A calculated amount of CTAB, based on CEC of the clay, was added to 500 ml of water containing about 4 ml of con HCl. The two were mixed together and further homogenized for another 250 rpm for 90 min. The precipitated sample was then filtered using a suction pump with continuous washing to remove halides that may be present as a result of treatment with CTAB. After filtration, the residue was collected, sun-dried, ground and sieved to 63 μm using 200 mesh size sieves.

Drilling mud was formulated by 350 ml of a mixture containing water-to-oil ratio by volume of 90:10, 80:20, 70:30 and 60:40.

Constituents were added by firstly dissolving about 7 wt % of the total fluid phase as organophilic clay in the oil phase, followed by about 4 wt% of the oil phase sorbitan monooleate as emulsifier and viscosifier, followed by the aqueous phase.

Rheological properties were obtained using dial readings at 600 rpm and 300 rpm using Eqs. 1 and 2 below

$$\mathrm{PV} = \Theta_{600} - \Theta_{300} \tag{1}$$

$$\mathrm{AV} = \Theta_{600}/2 \tag{2}$$

The yield point was determined using Eq. 3

$$\mathrm{YP} = \Theta_{300} - \mathrm{PV} \tag{3}$$

Thixotropic property was determined by obtaining the gel strength. The sample was subjected to shear at 600 rpm for 10 s and the gear was then set to neutral position. The motor was shut off and waited for 10 s, and the deflection at 3 rpm was recorded as 10 s gel strength in $lb_f/100\ ft^2$. This procedure was repeated for the 10-min gel strength.

3 Result

XRF and CEC analyses were done to determine the elemental composition and cation exchange capacities of the local and API grade clay samples as shown in Table 1.

The rheological and thixotropic properties for 90:10, 80:20, 70:30 and 60:40 oil–water ratios formulations for modified (organophilic) API grade Wyoming, raw local organophilic sample formulation, viscosifier treated local organophilic sample formulation and soda ash pre-treated (activated) local organophilic sample formulation are shown in Figs. 1, 2, 3 and 4, respectively.

4 Discussion

4.1 XRF and CEC Analyses

Table1 shows the elemental composition of the API grade Wyoming bentonite, raw local sample and soda ash activated (pre-treated) sample. The API grade sample showed silica-alumina ratio of 0.33, while the local sample has a value of 0.25 but was found to increase to 0.34 when activated with soda ash. The local sample has also shown an increase in sodium oxide concentration from 2.51 to about 5.56 wt% with a decrease in the CaO composition, this implies that the sodium ion has actually replaced the calcium

Table 1 Elemental composition and CEC of the clay samples

Oxide	API grade[a]	Raw local clay[b]	Activated local clay
Na_2O	3.22	2.508	5.559
MgO	2.4	5.620	3.025
Al_3O_2	14.2	14.320	15.911
SiO_2	43.6	57.809	47.397
BaO	11.0	–	–
K_20	3.22	1.7 0	1.539
CaO	7.05	1.683	1.160
TiO_2	1.30	0.831	0.814
Fe_2O_3	14.5	5.151	5.255
CEC (meq/100 g)	86	37.5	40.5

[a]Shuwa (2019)
[b]Bilal (2016)

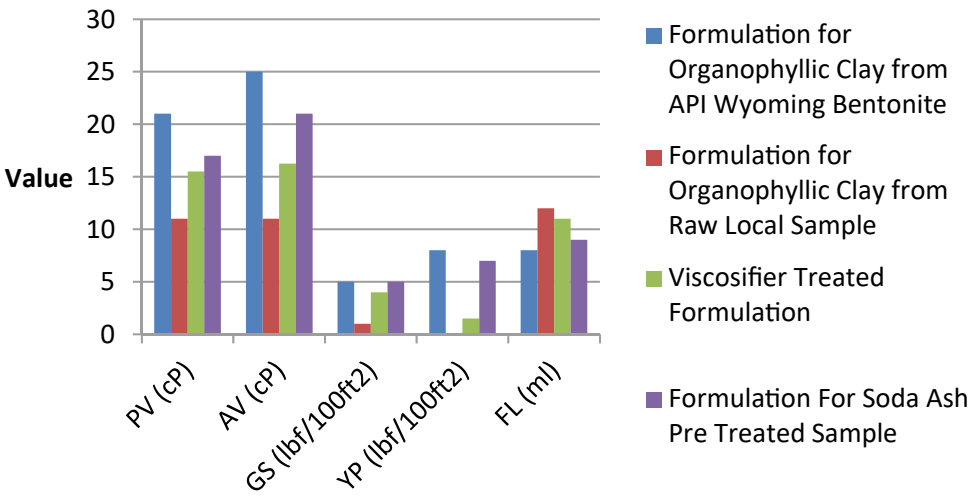

Fig. 1 Rheological and thixotropic properties of 90:10 formulations

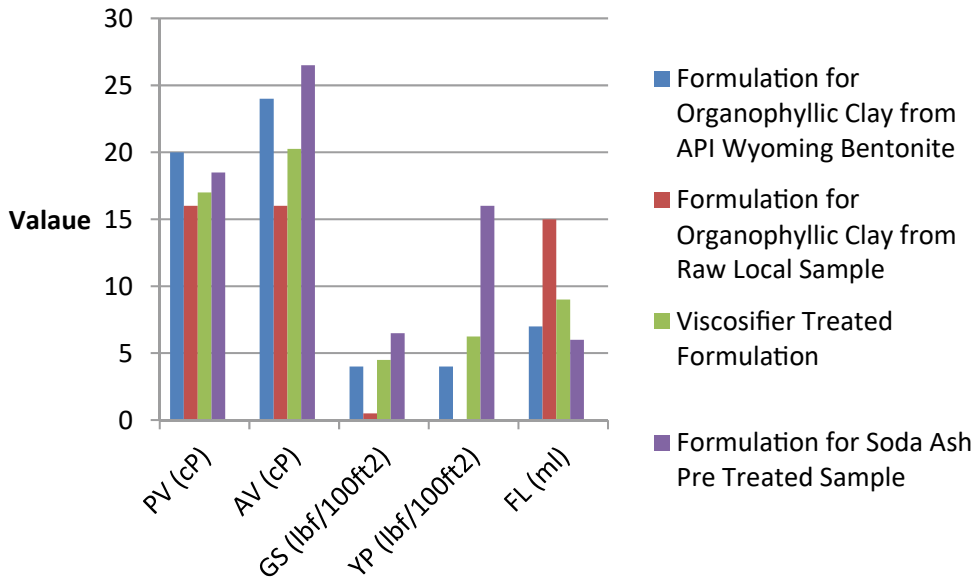

Fig. 2 Rheological and thixotropic properties of 80:20 formulations

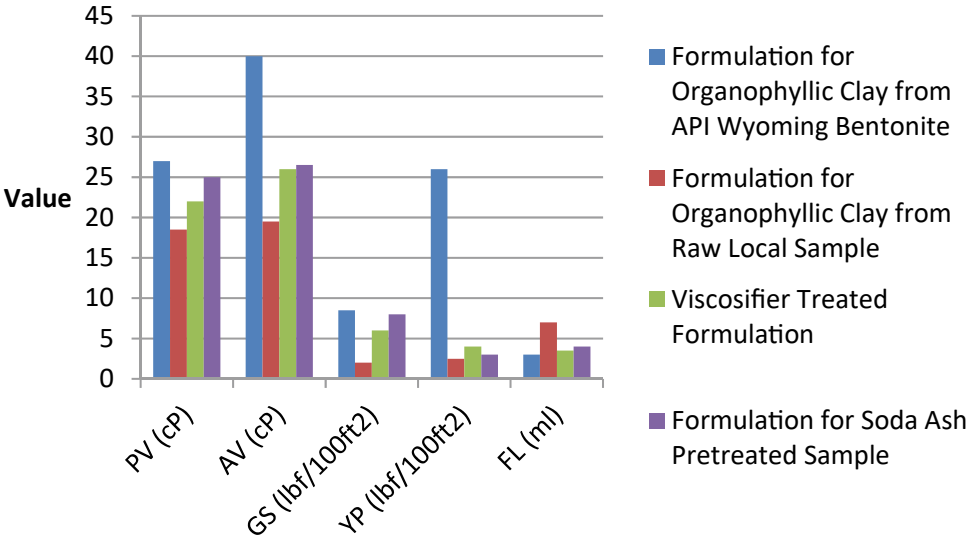

Fig. 3 Rheological and thixotropic properties of 70:30 formulations

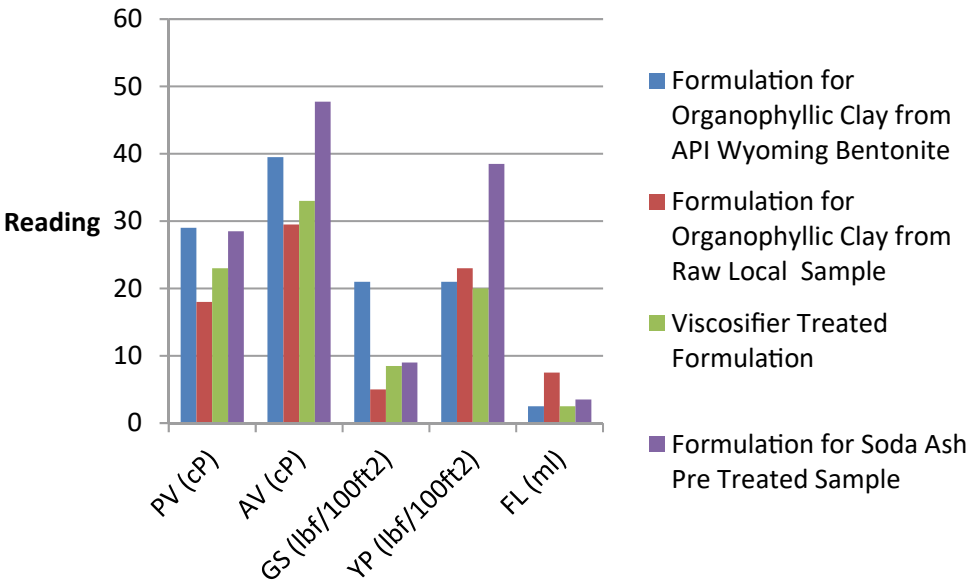

Fig. 4 Rheological and thixotropic properties 60:40 formulation

ions in the clay, hence a better rheology is expected as explained by Shuwa (2019). Furthermore, the cation exchange capacity (CEC) of the clay was found to increase from about 37.5 to 40.5 meq/100 g clay. This increase could be as a result of more negative charges at the surface after replacement of calcium ions. This could result into better rheological and thixotropic properties. This could translate into more CTAB consumption and, subsequently, better organophilic clay.

4.2 Rheological and Thixotropic Properties

The rheological and thixotropic properties for raw local organophilic sample formulation, viscosifier treated sample formulation and soda ash pre-treated with viscosifier addition were investigated. The 90:10 raw local organophilic sample formulation has shown a plastic viscosity (PV) of 11 cP, while the modified API formulation has shown a PV of 22 cP, a value twice that of the raw local organophilic sample formulation. The value has improved to 13.5 cP after viscosifier addition, and 17 cP after viscosifier addition with soda ash pre-treatment. There was also improvement in apparent viscosity (AV) in the soda ash retreated sample formulation to AV of 18 cP which is just close to the modified (organophilic) API sample's AV of 25 cP. Gel strength has also improved to 5 lb/100 ft^2 for both API and soda ash pre-treated organophilic sample for both 10 s and 10 min gel strength as shown in Fig. 1.

For the 80:20 formulation, a similar trend was noticed where the modified API grade Wyoming bentonite has shown a PV and AV of 20 cP and 24 cP, respectively, while

the formulated mud after soda ash pre-treatment showed PV and AV of 18.5 cP and 26.5 cP, respectively, with equal gel strength for 10 s and 10 min as shown in Fig. 2. Figures 3 and 4 show comparisons of mud properties for 70:30 and 60:40 formulations, respectively. For all formulations, the soda ash activated and viscosifier treated sample formulation has shown better properties indicating that soda ash pre-treatment improves the rheology and cutting carrying capacity of the mud.

5 Conclusions

The modified (organophilic) clay was developed using local Nigerian bentonitic clay sample and API grade Wyoming bentonite procured commercially. Results of the experiment have shown improved properties in terms of rheology and thixotrophy after soda ash activation with better properties as the aqueous phase concentration increases. The formulated mud compares very well with formulations developed from organophilic clay from API Wyoming bentonite.

References

Bilal, S.: Investigation and enhancement of quality of Nigerian bentonitic clay samples for oil and gas drilling operation. Unpublished Ph.D. Thesis, Department of Chemical Engineering, Ahmadu Bello University, Zaria, Nigeria (2016)

Bourgoyene, A.T.Jr., Milheim, K.K., Chenevert, M.E., Young, F.S. Jr.: Applied Drilling Engineering, Richardson TX, SPE (1991)

RMRDC: Non-Metallic Mineral Endowments in Nigeria: Bentonite. Abuja: Raw Materials Research and Development Council, Abuja, Nigeria (2010)

Shuwa, S.: Suitability of Nigerian (Warsale) bentonitic clay for oil well drilling fluid formulation. J. Exp. Res. **7**(1), 16–26 (2019)

SPE: Society of Petroleum Engineers. Functions of Drilling Fluid, available online at http:www petrowiki.spe.org/functions of drilling fluid (2013)

Subshash, N., Shah-Narayan, P.E.,Shanker, H., Oguguwe, C.C.: Future challenges of drilling fluid and their rheological measurements. A conference paper presented at the 2010 American Association of Drilling Engineers (AADE) Fluids conference and exhibition held at the Hilton Houston North, Houston, Texas, Texas AADE-10-DF-HO-41, 1–16 (2010)

Potential of a Blend of Low-Grade Nigerian and Commercial Grade (Wyoming) Bentonitic Clays as Constituents of Water-Based Drilling Fluids

Suleiman Shuwa, Bala Usman, and Ibrahim Mohammed-Dabo

Abstract

Nigerian bentonitic clays are principally Ca-based and unsuitable for use as a constituent of oil well drilling fluid. Recently, many research works were carried out to upgrade the low-grade Nigerian bentonitic clays so that they can be applied in drilling fluid formulation. Slight improvement was made in that respect and some of the clays were found to have little potentials to be used as a constituent of oil well drilling fluid. Despite improvement in their rheological properties, the drilling fluids formulated from the upgraded local clays are inferior to commercially available Wyoming clays. This research characterized two local bentonitic clays from the Dikwa formation in north eastern Nigeria and a standard commercial grade (Wyoming) bentonite (XRD, XRF, CEC and particle size distribution). The local clays were beneficiated using Na_2CO_3 as activating agent and blended with the commercial grade, and then drilling fluids were formulated from the clays. The XRD results confirmed the presence of montmorillonite mineral an indication that the clay is bentonite. The CEC results also showed increase in CEC of Na_2CO_3-beneficiated clay from 33 to 50 Meq/100 g, an indication of successful beneficiation. Rheological and filtration properties of the sample drilling fluids formulated from the blend of local clays and commercial Wyoming bentonite were found to be excellent (plastic viscosity = 8 cP, yield point = 20 lb/100 ft^2, gel strength = 50 lb/100 ft^2). The blends performed even better than the commercial (Wyoming) bentonite and fall within the API standards. This behaviour was attributed to the synergistic effects of the minerals present in the local and commercial clay samples. Although the XRD and CEC characterization showed that the local clays are inferior to the commercial grade, this study shows that the blend of our local clays and commercial varieties form excellent drilling fluid formulation.

Keywords

Low-grade Nigerian bentonitic clays • Dikwa formation • Na_2CO_3-beneficiated clay • Blend of local and commercial clays • Rheological properties

1 Introduction

Drilling is the major activity in the upstream sector, and the major component in the success of a drilling operation is the performance of the drilling fluid. The importance of clay and clay minerals in the drilling industry is evident from the fact that clays are added to drilling fluids to build viscosity, thixotropy and contribute wall building properties. The most commonly used clay in drilling fluid formulation is bentonite. Bentonitic clays exist in the north-east quadrant of Nigeria, where a probable reserve of more than 700 million tonnes has been estimated (RMRDC 2010). Nigerian bentonitic clays are principally calcium-based and unsuitable for use as a constituent of oil well drilling fluid due to their low-swelling capacities and poor rheological properties. Recently, many research works have been carried out to upgrade the low-grade bentonitic clays so that they can be applied in drilling fluid formulation (Folade et al. 2007; Apugo-Nwosu et al. 2011; Dewu et al. 2011, 2012; Ajugwe et al. 2012; Bilal et al. 2015, 2016).

Significant improvement was made in that respect, and some of the clays were found to have the potentials to be used as a constituent of oil well drilling fluid. Despite this reported improvement in the capacities of these local clays, they were found to be inferior to commercial grade type such as the Wyoming (API Standard). Most of the clays have poor filtration properties and low-gel strength which are amongst the required properties for water-based oil well

S. Shuwa (✉) · B. Usman · I. Mohammed-Dabo
Department of Chemical Engineering, Ahmadu Bello University, Zaria, Nigeria
e-mail: smshuwa@abu.edu.ng

M. Meghraoui et al. (eds.), *Advances in Geophysics, Tectonics and Petroleum Geosciences*,
Advances in Science, Technology & Innovation, https://doi.org/10.1007/978-3-030-73026-0_104

drilling fluid formulation as required by the American Petroleum Institute (API). This trend was observed even after the clays were upgraded. In this work, the potentials of a blend of a standard commercial grade (Wyoming) bentonite and two local clays were evaluated. Rheological and filtration properties of the drilling fluids formulated from the blend and pure standard commercial grade were compared.

2 Materials and Methods

The raw clay samples were collected from a pit dug to a depth of about 3ft at Warsale and Kaza villages of Dikwa province of Borno State of Nigeria. The raw samples were crushed and grinded, then shaken with a test sieve shaker to obtain 63 μm particle size to suit API specifications for bentonite. Chemical and mineralogical compositions of the raw and the commercial clay samples were determined using X-ray fluorescence, XRF (model Pan analytic B.V PW4030/45B) and X-ray Diffractometer (model Schmadzu 6000), respectively. Wyoming bentonitic clay was used as the standard (control), hence, it was equally characterized for the chemical and mineralogical composition. The hydrometer method was used for *particle size distribution analysis* of the clay samples, whereas the methylene-blue test method was used for cation exchange capacity (*CEC)* determination for the three clay samples. Chemical activation was carried out on the 63 μm fraction obtained above, and the predominant calcium bentonite was converted to sodium bentonite through ion exchange using sodium carbonate as the activating agent.

In order to formulate the sample mud, 24.5 g of the mixture of beneficiated and commercial clays (at different ratios) were weighed with the aid of an electronic weighing scale. The samples were poured into the mixer cups containing 350 ml of water, thoroughly mixed and then agitated vigorously with the aid of Hamilton Beach Mixer for 10 min to obtain a homogeneous mixture. Ofite 900 model viscometer was used for the measurement of apparent viscosity, plastic viscosity, gel strength and yield point, whilst a low-pressure API filter press was used for fluid loss determination.

3 Results

3.1 Mineralogical Analysis

The Wyoming bentonite sample is composed mainly of smectite (montmorillonite), sanderite, barite, morimotoinite and muscovite (Table 1). Other minerals detected in trace amounts are zinc arsenate, behierite and ammonium chlorate. The smectite dominates the Wyoming bentonite (about 50%) as expected. The smectite clay mineral is responsible for the swelling and high rheological and filtration properties of the drilling fluids. The Wyoming bentonite also shows high amounts of barite (about 20%), and a non-clay mineral used in drilling fluids as a weighting agent to increase the density of the drilling fluids. This could indicate that the Wyoming bentonite might have been treated with barite. It was also observed that the local bentonitic clay samples are composed mainly of smectite, quartz, kaolinites, gismondine and serpentine.

3.2 CEC Analysis

The CEC is the total amount of cations adsorbed expressed in milliequivalents per 100 g of dry clay. High CEC will have a positive impact on the hydration and swelling capability of the clay suspensions. Table 2 shows the CEC values of the investigated samples. The CEC of the Wyoming bentonite was found to be 86 meq/100 g which falls within the general range of (80–100) meq/100 g. This agrees with the values reported by Falode et al. (2007). It can be seen from table that the untreated local bentonitic clay samples have low CEC, but when treated with 6% Na_2CO_3, about 50% increase in CECs was observed. This is still much less than the CEC value of Wyoming bentonite. The CEC of clay and the species of cations in the exchange positions are a good indication of the colloidal activity of the clay. Clay such as smectite that has high CEC swells greatly and forms viscous suspensions at low concentrations of clay, particularly when sodium is in the exchange positions.

Table 1 Summary of mineral composition of the clay samples

Wyoming bentonite		Warsale clay		Kaza clay	
Mineral	Composition (%)	Mineral	Composition (%)	Mineral	Composition (%)
Smectite	50	Smectite	33.26	Smectite	26.67
Barite	19.4	Quartz	9.43	Quartz	7.39
Sanderite	10	Kaolinite	5.35	Kaolinite	4.04
Morimotoinite	7.9	Gismondine	35.31	Gismondine	41.5
Muscovite	6.9	Serpentine	6.09	Serpentine	5.40
Others	5.8	Others	10.56	Others	15

Table 2 Cation exchange capacities (Meq/100 g) of the clay samples

Warsale clay		Kaza clay		Wyoming clay
Untreated	Treated	Untreated	Treated	
33	50	30	46	86

3.3 Rheological and Filtration Properties of the Sample Muds

The sample muds prepared from a blend of local and Wyoming bentonitic clays displayed good rheological and filtration properties that compare favourably with the mud formulated from Wyoming bentonite. The results are shown in Figs. 1 and 2.

4 Discussion

Drilling muds formulated from a mixture of Wyoming and local clays displayed good rheological properties. For example, a blend of 70 wt% Wyoming and 30 wt% local clay (for both Kaaza and Warsale) gave a better result than the mud formulated using 100% Wyoming bentonite in

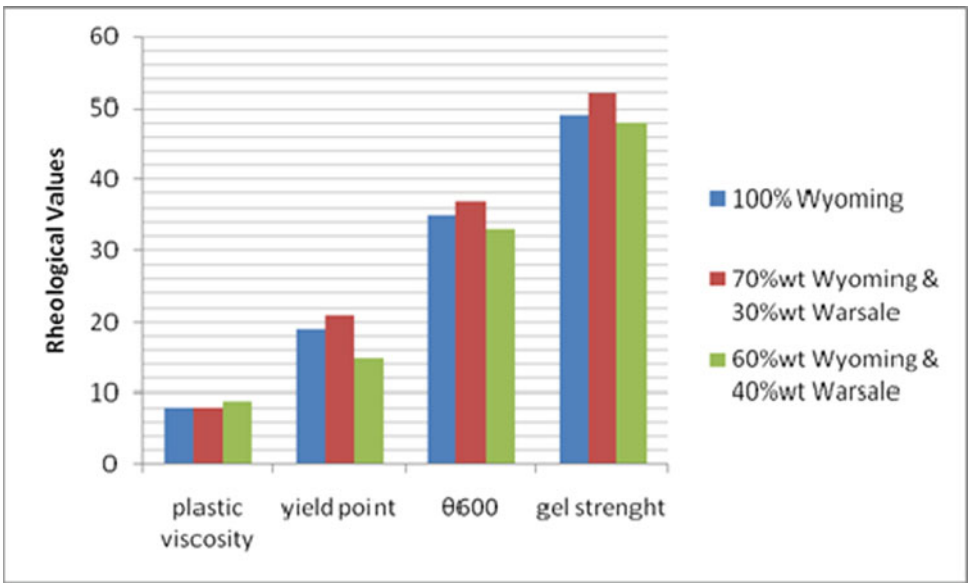

Fig. 1 Rheological properties of sample muds formulated from a blend of Wyoming and Warsale clay

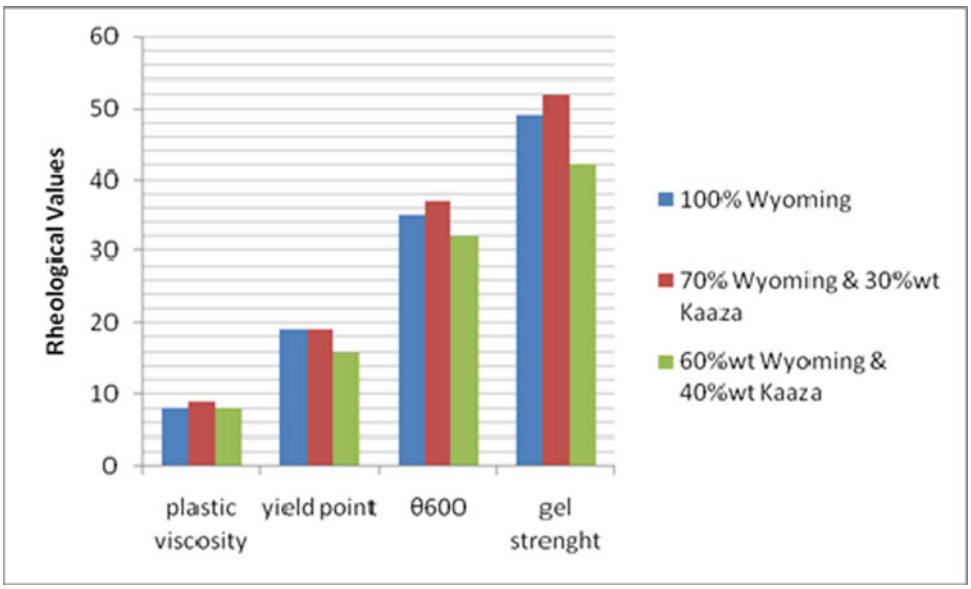

Fig. 2 Rheological properties of sample muds formulated from a blend of Wyoming and Kaza clay

terms of the yield point, gel strength and plastic viscosity. Figures 1 and 2 illustrate this behaviour for both Wyoming and local bentonitic clays. Even the sample drilling fluids prepared from a blend of 60 wt% Wyoming and 40 wt% local bentonitic clays displayed a good result that falls within the API specification. The fluid loss value of the muds formulated from Wyoming bentonite, and local clays were 21 ml and 22 ml, respectively. These values are above the API standard of a maximum of 15 ml per 30 min. But, when the muds were treated with 0.5 g of CMC, the fluid loss was reduced to values below the API standard of 15 ml. This confirmed that CMC is a good filtration control agent.

Rheological properties of the sample drilling muds formulated from a blend of local and commercial (Wyoming) met the international (API) specification required of a water-based drilling mud as evident from Figs. 1 and 2. The presence of a smectite mineral as shown by XRD and the increase in CEC due to the chemical activation of the local clays are responsible for the observed enhancement of the properties.

5 Conclusions

Results from the experimentation investigations showed that a low-grade local Nigerian bentonitic clay was successfully upgraded by beneficiating with Na_2CO_3 and enhancement in its CEC observed. Combination of local clays and commercial grade proved to be excellent material for drilling fluid formulation. Drilling fluids formulated from a blend of local clays and commercial clay performed even better than drilling fluids from standard commercial alone in terms of thixotropic, filtration and rheological properties. This unusual behaviour could be attributed to the synergy between the minerals present in the local and commercial clays as shown in XRD results.

References

Ajugwe, C., Oloro, J., Akpotu, D.: Determination of the rheological properties of drilling fluid from locally sourced clay from various geographical areas. J. Eng. Appl. Sci. **4**, 38–49 (2012)

Apugo-Nwosu, T.U., Mohammed-Dabo, I.A., Ahmed, A.S., Abubakar, G., Alkali, A.S., Ayilara, S.I.: Studies on the suitability of ubakala bentonytic clay for oil well drilling mud formulation. Br. J. Appl. Sci. Technol. **1**(4), 152–171 (2011)

Bilal, S., Mohammed-Dabo, I.A., Dewu, B.B.M., Momoh, O.R., Aminu, A.H., Abubakar, U., Adamu, M.S., Mashi, A.H.: Determination of morphological features and molecular interactions of Nigerian bentonytic clays using scanning electron microscopy (SEM). Bayero J. Pure Appl. Sci. **9**(2), 279–285 (2016)

Bilal, S., Mohammed-Dabo, I.A., Dewu, B.B.M., Momoh, O.R., Funtua, I.I., Oladipo, M.O.A., Arabi, A.S., Muhammad, T.: Effect of quartz (free silica) removal on the quality of Nigerian bentonytic clays for application in drilling fluid formulation. J. Exp. Res. **3**(2), 98–101 (2015)

Dewu, B.B.M., Oladipo, M.O.A., Funtua, I.I., Arabi, A.S., Mohammed-Dabo, I.A., Muhammad, A.M.: Evaluation of rheological and other physical properties of bentonitic clays from fika formation in parts of North-Eastern Nigeria. Pet. Technol. Dev. J. **1** (2012)

Dewu, B.B.M., Oladipo, M.O.A., Funtua, I.I., Arabi, A.S., Mohammed-Dabo, I.A., Muhammad, A.M., Hamidu, I.: Evaluation and beneficiation of bentonytic clays from pindiga formation in Benue trough. Am. J. Eng. Appl. Sci. **4**(4), 497–503 (2011)

Falode, O.A., Ehinola, O.A., Nebeife, P.C.: Evaluation of local bentonytic clay as oil well drilling fluids in Nigeria. Appl. Clay Sci. **39**, 19–24 (2007)

RMRDC: Non-metallic mineral endowments in Nigeria: bentonite. Raw Materials Research and Development Council, Abuja (2010)

Presence of NaCl as Strategy for Improving the CO_2 Replacement Process in Natural Gas Hydrate Reservoirs

Alberto Maria Gambelli and Federico Rossi

Abstract

Natural gas hydrates represent a valid opportunity in terms of energy supplying, carbon dioxide permanent storage and climate change contrast. Research is more and more involved in performing CO_2—replacement competitive strategies. In this context, the inhibitor effect on the hydrate formation process of sodium chloride needs to be investigated in depth. The present work shows the inhibitor effect produced by salt, dissolved in pure demineralized water with a concentration of 37 g/l, on the carbon dioxide hydrate formation process. Results proved how the formation trend is very similar between tests realized with salt and tests realized without it; the only difference stays in the equilibrium curve that, in case of salt presence, is shifted to higher pressure and/or lower temperature. The distance between equilibrium curves obtained in the absence of salt and in its presence is strongly dependent on its concentration. The present paper represents the first step of a wider scientific investigation, where the main goal consists in verifying if the inhibitor effect of sodium chloride might have a selective behaviour in function of the 'guest' species and if that phenomenon is related to its concentration. A comparison between CO_2 and CH_4 equilibrium curves, realized both in the presence and in absence of salt, has been provided. The feasibility of a carbon dioxide replacement process is directly related to the respective equilibrium curves distance. Thus, the influence of salt on their behaviour (and so on their distance) might determine the replacement process efficiency.

Keywords

Natural gas hydrate • NaCl inhibitor effect • CO_2 replacement efficiency • Inhibitors selective behaviour • Depressurization

1 Introduction

Gas hydrates are ice-like crystalline solid compounds, where small gaseous molecules, also called 'guests', are trapped inside a hydrogen-bonded network of water molecules, called 'hosts' (Sloan and Koh 2008). Both the scientific and industrial interests in gas hydrates were born from their several possible applications, in terms of gas storage, energy production, carbon dioxide sequestration, gas separation and desalination (Sun et al. 2018a, b). The scientific research is particularly involved in performing the CO_2 replacement process (Sun et al. 2018c). Several strategies for realizing the CO_2 replacement have been performed; from these, the most known are: depressurization, thermal stimulation, chemical inhibitor injection and a combination of them (Gambelli 2018). All these solutions are based on the major stability of the CO_2 hydrate rather than the CH_4 one. Carbon dioxide hydrates' formation and stability need lower pressures and higher temperatures than methane hydrates, so the exchange process naturally occurs, even if it is limited by the kinetics of the reaction (Gambelli et al. 2019a). Depressurization methods consist in decreasing the local pressure, keeping the temperature constant, in order to move the thermodynamic conditions out of the methane hydrate stability zone and provoke the replacement process (Ye and Liu 2012). In thermal stimulation methods, the contrary occurs (Sun et al. 2018d). The presence of chemical inhibitors shifts the hydrate stability condition to lower temperatures and higher pressure and so provokes their dissociation at the local thermodynamic conditions (Wang et al. 2014). In this work, we investigated the effect produced by sodium chloride

A. M. Gambelli (✉) · F. Rossi
Engineering Department, University of Perugia, Via G. Duranti 93, 06125 Perugia, Italy
e-mail: albertomaria.gambelli@unipg.it

M. Meghraoui et al. (eds.), *Advances in Geophysics, Tectonics and Petroleum Geosciences*,
Advances in Science, Technology & Innovation, https://doi.org/10.1007/978-3-030-73026-0_105

presence on carbon dioxide hydrate formation. If the disadvantageous effect of salt presence for hydrate is well known and documented in literature (Yu et al. 2018), the possibility that it could make the CO_2 replacement process more feasible or not need to be deepened. The feasibility of the CH_4/CO_2 exchange is due to the presence of a region between the CO_2 and the CH_4 equilibrium curves, in which the local condition are suitable only for CO_2 hydrate formation and stability (Gambelli and Rossi 2019). In our previous work (Gambelli 2019b), we illustrated how the application of a CO_2 replacement process, on a CH_4 hydrate core, with salt presence, leads to a higher percentage of CO_2 into water cages than in case of pure demineralized water. Thus, we analysed the CO_2 hydrate formation process in a solution of demineralized water and 37 g/l of sodium chloride and, then, compared results with what was obtained in the absence of salt.

2 Materials and Methods

Experimental Apparatus The experimental apparatus was designed for reproducing a sea bed natural gas hydrate deposit and then recovery methane contained into clathrates via CO_2 replacement strategies. In this section, only the most important information about the experimental apparatus is given; in an article by Rossi et al. (2019), a more detailed description is available. The reactor is made of 316SS stainless steel and has an internal volume, suitable for hydrate formation, of about 949 cm^3. The reactor is inserted in a thermostatic bath, model GC-LT, where temperature is regulated using a chiller. Pressure is regulated directly with the gas injection. In Fig. 1, a schematization of the whole experimental apparatus and a picture of the reactor are shown.

The whole apparatus was equipped with sensors, for monitoring the most important parameters involved in the process. Methane and carbon dioxide flow rates are monitored with two flow meters, model EL-FLOW F112AC. Temperature is measured with four Type K thermocouples, having class accuracy 1. Pressure is measured using a digital manometer, model MAN-SD, with accuracy equal to ±0.5% of full scale. All sensors are connected to a data acquisition system (LabVIEW software).

Materials In these experiments, ultra-high purity CO_2 was used (purity of 99.97%). The sea bed structure was designed with demineralized water (0.236 l), sodium chloride (37 g/l) and sand (0.744 l). This last element is composed by quartz spheres, having a 0.2 mm diameter and a porosity of 34%, measured with a porosimeter, model Therrno Scientific Pascal 140.

Experimental Procedure The experimental section of this work is composed by six tests, divided in two groups based on the presence, or the absence, of salt. In both cases, tests were carried out with the same procedure. The first step consists in reducing temperature until reaching values suitable for hydrate formation; those values range from 2 to 4 °C. Then, the CO_2 injection starts, and consequently, the pressure is increased to the desired value. As soon as the thermodynamic conditions are suitable, the process starts. The hydrate formation is characterized by its exothermic nature, which causes a sudden temperature increase. That peak coincides with the beginning in case of a spontaneous pressure decrease, due to gas entrapping into solid water cages. Pressure continues decreasing until it reaches the equilibrium value and stabilizes. Moles of CO_2 involved in the hydrate formation process are then calculated using the following equation:

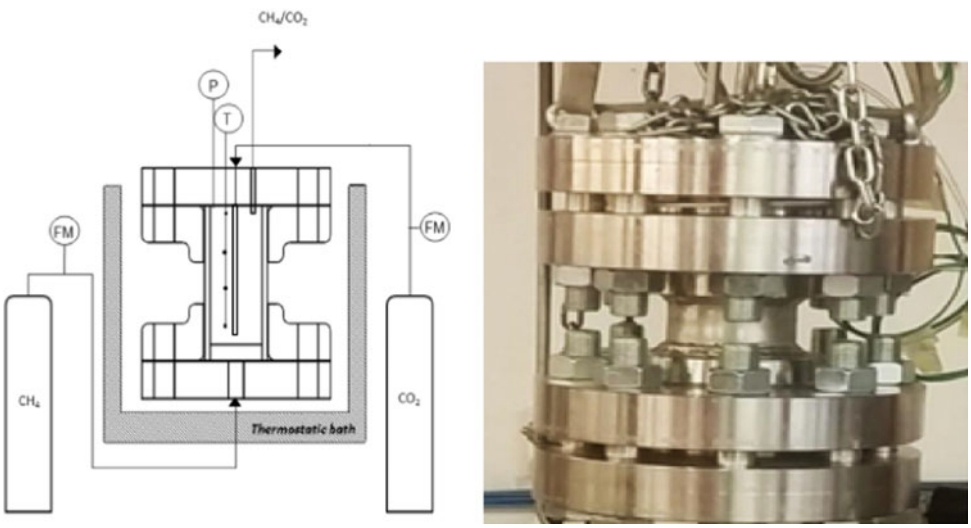

Fig. 1 Scheme of the complete experimental apparatus (left) and a picture of the hydrate reactor (right)

$$n_{\text{hyd}} = \left[V_{\text{pore}}\left(p_i \times Z_f - P_f \times Z_i\right)\right] / \left[Z_f \times \left(RT - P_f / p_{\text{hyd}}\right)\right] \quad (1)$$

where n_{hyd} is the CO_2 moles entrapped into hydrates, Z is the compressibility factor, calculated using the Peng–Robinson equation, V_{pore} represents the sand pores volume and ρ_{hyd} is the hydrate ideal molar density.

3 Results and Discussion

The experimental section consists of two CO_2 hydrate formation tests realized in the presence of salt water (37 g/l of sodium chloride) and, then, compared with two other tests performed in pure demineralized water. The most relevant parameters, about the tests carried out without salt, are shown in Table 1, while the same information for tests realized in the presence of salt is in Table 2.

In Tables 1 and 2, P and T represent pressure and temperature, respectively, while subscripts ‘ " and ‘f’ describe the moment in which the hydrate formation process began and the moment in which it ended, respectively. Finally, parameter $CO_{2\text{hyd}}$ shows the quantity (in moles) of carbon dioxide involved in hydrates. As the gas used in this work is CO_2, its capability to dissolve in water cannot be neglected. For this reason, the quantity of carbon dioxide involved in hydrates was calculated considering both the total amount of gas injected inside the reactor and the quantity dissolved in water, which was evaluated using the Henry Law. In particular, this last value can be considered in the hydrate counter. In fact, the presence of suitable thermodynamic conditions makes sure that, with the passage of time, dissolved carbon dioxide will be entrapped into water cages (Rossi et al. 2019). The following figures show a comparison between tests carried out in the presence of salt, with tests realized in pure demineralized water.

The black arrows indicate the time direction. The presence of sodium chloride clearly shifts the CO_2 hydrate equilibrium curve to regions characterized by higher pressure and/or lower temperature. The same effect is produced on methane hydrates and has been already tested in previous works (Rossi et al. 2019). While the salt function as hydrate inhibitor has been widely investigated in the literature, the possibility that it assumes a different behaviour in function of the gaseous specie involved in hydrate needs to be deepened. The comparison of CH_4 and CO_2 hydrate equilibrium curves, with the same salt percentage, leads to a diagram equal to Figs. 2 and 3 (but with different values). In this work, the effect of salt presence during the CO_2 hydrate formation process has been explored. The aim of future works is to analyse the evolution of CH_4 and CO_2 equilibrium curves in function of the water salinity, in order to establish what is explained above. In Fig. 4, the proposed two methane formation tests are realized in the presence (37 g/l) and in the absence of salt, respectively, which have been compared with tests 1 and 3 of the present work (already shown in Fig. 2).

The present comparison allows to make some further considerations. First of all, the experimental equilibrium curve better approximates the theoretical one for lower pressure value. It depends on different factors. Considering the reactor dimensions (typical of a lab-scale apparatus), a greater pressure value may trigger the hydrate formation reaction in different points of the experimental environment and in different time periods. That phenomenon is observed in the P–T diagrams with a temporary deviation from the trend and can also be observed in Fig. 4: the left side of CO_2 curve realized in presence of salt clearly describes that. This phenomenon was observed in several scientific works: Shagapov et al. (2017) explained how kinetics has a key role in experiments carried out in small-size reactors (Shagapov et al. 2017). In particular, pressure is directly linked to the sand pore saturation degree, and the experimental process is nearer to the theoretical one for lower sand saturation values. The thermodynamic area usable for the carbon dioxide replacement process is the strip between CH_4 and CO_2 P–T diagrams. In function of pressure, temperature, gas concentration, sand porosity and others, these two diagrams may show some different behaviours (Sloan and Koh 2008). Our experiments suggest that water salinity is also part of the previous list of factors. While the NaCl inhibitor effect is well-known, the possibility that its effect may be stronger or weaker depending on pressure, temperature, porosity and, mostly, in function of the guest species needs to be deepened more. Experiments shown in Fig. 4 suggest that, during hydrate formation, the CH_4 and CO_2 diagrams, due to the presence of salt, may undertake different variations from each other. If that variation leads to a curves removal, the greater spaces between curves will guarantee a higher CO_2 replacement process efficiency. The present work clearly represents a preliminary step in verifying if sodium chloride may be considered an allied for natural gas hydrate

Table 1 Pressure, temperature and moles values related to tests realized in absence of salt

	P_i [bar]	T_i [°C]	P_f [bar]	T_f [°C]	$CO_{2\text{hyd}}$ [mol]
Test 1	27.43	7.33	17.48	1.57	0.102
Test 2	25.23	6.51	17.09	2.86	0.083

Table 2 Pressure, temperature and moles values related to tests realized in presence of salt

	P_i [bar]	T_i [°C]	P_f [bar]	T_f [°C]	CO_{2hyd} [mol]
Test 1	32.01	6.66	26.34	1.68	0.068
Test 2	29.93	6.59	24.26	3.60	0.058

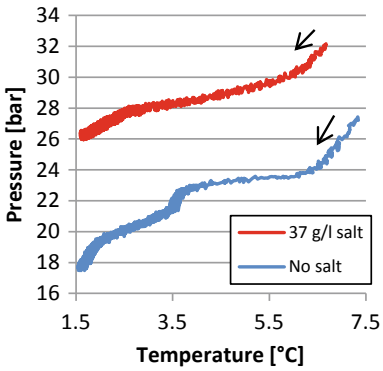

Fig. 2 Pressure versus temperature: a Comparison between Test 1 (blue) and Test 3 (red)

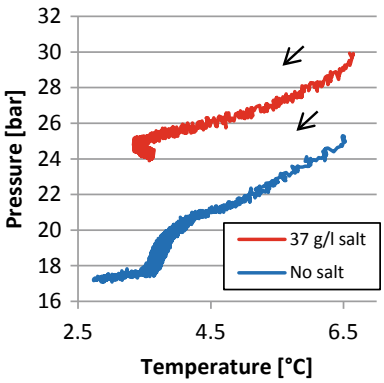

Fig. 3 Pressure versus temperature: a Comparison between Test 2 (blue) and Test 4 (red)

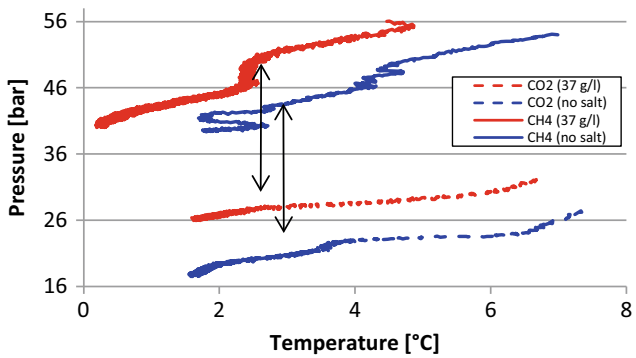

Fig. 4 Comparison between four different hydrate equilibrium curves: CO_2 is represented with the blue colour, while CH_4 with the red one; tests realized without salt are dashed, while the continuous line describes the test carried out in presence of 37 g/l sodium chloride

reservoirs exploitation and for carbon dioxide storage; the experimental purpose highlighted in this paper needs to be supported with further experimental considerations (also with different salt concentrations) in future works.

4 Conclusions

In the present work, the CO_2 hydrate formation process was investigated both in the presence and in absence of NaCl. Results were then compared, in order to establish the entity of the inhibition effect provided by salt. The same typology of experiments was carried out for CH_4 hydrate (and was shown in previous works (Gambelli et al. 2019c)). Then, in the final considerations of this work, we were encouraged to further investigate the possibility that the inhibitor effect of salt has a selective behaviour in function of the gaseous species involved in the hydrate formation process. A different influence, depending on gaseous species characteristic, could improve the CO_2 replacement methods efficiency and so make them more reliable for performing the CH_4 recovery and the CO_2 storage.

References

Gambelli, A.M.: Natural gas recovery from hydrate compounds using CO_2 replacement strategies: experimental study on thermal stimulation. Energ. Procedia **148**, 647–654 (2018)

Gambelli, A.M., Rossi, F.: Natural gas hydrates: comparison between two different applications of thermal stimulation for performing CO_2 replacement. Energy **172**, 423–434 (2019)

Gambelli, A.M., Castellani, B., Nicolini, A., Rossi, F.: Experimental study on natural gas hydrate exploitation: optimization of methane recovery, carbon dioxide storage and deposit structure preservation. J. Petrol. Sci. Eng. **177**, 594–601 (2019a)

Gambelli, A.M.: An experimental description of the double positive effect of CO2 injection in methane hydrate deposits in terms of climate change mitigation. Chem. Eng. Sci. 233, 116430 (2021)

Gambelli, A.M., Filipponi, M., Nicolini, A., Rossi, F.: Natural gas hydrate: effect of sodium chloride on the CO_2 replacement process. In: The 19th International Multidisciplinary Scientific Geo Conference SGEM 2019—Albena, Bulgaria, 28 June–06 July (2019)

Rossi, F., Gambelli, A.M., Sharma, D.K., Castellani, B., Nicolini, A., Castaldi, M.J.: Experiments on methane hydrates formation in seabed deposits and gas recovery adopting carbon dioxide replacement strategies. Appl. Therm. Eng. **148**, 371–381 (2019)

Shagapov, V.S., Khasanov, M.K., Musakaev, N.G., Duong, N.H.: Theoretical research of the gas hydrate deposits development using the injection of carbon dioxide. Int. J. Heat Mass Transf. **107**, 347–357 (2017)

Sloan, E.D., Koh, C.A.: Clathrate Hydrates of Natural Gases, 3rd edn. CRC Press, Taylor and Francis Group, New York (2008)

Sun, F., Yao, Y., Li, G., Li, X.: Geothermal energy development by circulating CO_2 in a U-shaped closed loop geothermal system. Energ. Conver. Manage. **174**, 971–982 (2018a)

Sun, F., Yao, Y., Li, G., Li, X., Li, Q., Yang, J., Wu, J.: A coupled model for CO_2 and superheated steamflow in full-length concentricdual-tube horizontal wells to predict the thermophysical properties of CO_2 and superheated steam mixture considering condensation. J. Petrol. Sci. Eng. **170**, 151–165 (2018b)

Sun, F., Yao, Y., Li, G., Li, X.: Performance of geothermal energy extraction in a horizontal well by using CO_2 as working fluid. Energ. Convers. Manage. **171**, 1529–1539 (2018c)

Sun, F., Yao, Y., Li, G., Li, X.: Geothermal energy extraction in CO_2 rich basin using abandoned horizontal wells. Energy **158**, 760–773 (2018)

Wang, Y., Li, X.S., Li, G., Huang, N.S., Feng, J.C.: Experimental study on the hydrate dissociation in porous media by five-spot thermal huff and puff method. Fuel **117**, 688–696 (2014)

Ye, Y.G., Liu, C.L.: Natural Gas Hydrate: Experimental Techniques and Their Applications. Springer, Berlin (2012)

Yu, D., Zhao, J., Sun, S.: Dissociation enthalpy of methane hydrate in salt solution. Fluid PhAse Equilib. **456**, 92–97 (2018)

Simulation on the Dynamic Variation of Properties During Deflagration Fracturing in Screen Completed Well

Zheng Liming, Li Guanghui, Wu Feipeng, and Zhang Tong

Abstract

A deflagration fracturing technique, also referred to as high-energy gas fracturing (HEGF), was used to create several fractures radiating from a wellbore to improve reservoir conductivity. Theoretical studies of deflagration fracturing were mainly focused on open-hole or perforated well completions. In this study, the deflagration fracturing technique was used in a screen completed well because conductivity was enhanced in a variety of reservoir types. A simulation on the dynamic variation of gas pressure in a screen completed well was required to avoid destroying the tool because of the structural difference between the screen pipe and casing pipe. A model was built to describe the deflagration fracturing process in a screen completed well. The equation for fluid flowing through screened pipe was introduced along with the traditional equations for perforated wells. Then, a numerical simulation was run to validate the equations. The simulated accuracy approached 80% when compared to the real production-increasing ratio. The simulated maximum pressure was 50.3 MPa with safe parameters for a screen completed well. The maximum length of a symmetric semi-fracture was 4.18 m, and the maximum width was 5.47 mm. The maximum gas pressure was lower for a higher density of holes and larger screen pipe size. Results of the simulations can be used to choose proper screen pipe for deflagration fracturing.

Keywords

Deflagration fracturing • Screen completed well • Modeling • Gas pressure • Sensitivity

1 Introduction

A deflagration fracturing technique, also referred to as high-energy gas fracturing (HEGF) technique (Li et al. 1995), is a low-cost and low-pollution technique for creating multiple cracks downhole after one fracturing event. HEGF is commonly used in open-hole and perforated wells. Sun et al. (2017) conducted a trial with a sand control screen completed well (HZ 26-1-20sb, China). After HEGF was finished, oil was produced from the well after a long period of being shut in. Even though the field trial was successfully completed, there is some concern about the safety of the downhole tool that requires further research. A model is needed to describe the dynamic variation of properties during HEGF in a screen completed well.

Previous research is limited to a few studies (Tian 2017; Zhang et al. 2018) that use qualitative analysis or experiments to investigate the dynamic mechanism of deflagration fracturing in a screen completed well. Because of the structural difference between the screen pipe and casing pipe, pressure drops during deflagration fracturing, and the stress distribution around the downhole pipe differs. A traditional mathematic model for HEGF results in an error when simulating a screen completed well and may correspond to a hazardous condition for the use of the tool. A model for deflagration fracturing in screen completed well was derived by combining the motion equation of fluid passing the screen pipe and the traditional mathematical model for HEGF simulation in a perforated well. A numerical simulation was then carried out with the parameters of HZ 26-1-20sb well to validate the model against field data. A sensitivity analysis was completed to investigate the

Z. Liming (✉) · L. Guanghui
College of Vehicles and Energy, Yanshan University, Qinhuangdao, 066004, Hebei, China
e-mail: upczlm@sina.cn

Z. Liming
Mechanical Engineering Postdoctoral Station in Yanshan University, Qinhuangdao, 066004, Hebei, China

W. Feipeng · Z. Tong
College of Petroleum Engineering, China University of Petroleum (East China), Qingdao, 266580, Shandong, China

M. Meghraoui et al. (eds.), *Advances in Geophysics, Tectonics and Petroleum Geosciences*, Advances in Science, Technology & Innovation, https://doi.org/10.1007/978-3-030-73026-0_106

influence of hole density and size of screen pipe on the gas pressure.

2 Mathematical Model for Deflagration Fracturing in Screen Completed Well

The traditional model for the deflagration fracturing included a model of the stress distribution around the wellbore, a model of the propellant deflagration, a model of pressurized liquid column movement, a model of perforation discharge, a model of fracture initiation (Lanari and Fakhimi 2015), a model of fracture extension, mass conservation equation and the energy conservation equation.

Modeling deflagration fracturing in a complex structured well has to consider the influence of deviation angle on the pressurized liquid column and in-situ stress near the wellbore as well as the pressure drop through the downhole tool. Differences between the equations used in the models are explained below.

(1) Influence of deviation angle on the movement of pressurized liquid column

Wu et al. (2010) gave a solution for liquid column movement in a vertical well with a wire rope operation. For the liquid column movement in a deviated well with downhole pipe string operation, the equation calculating the column displacement was given as Eq. (1):

$$\begin{cases} -A_1\dfrac{1}{K_\mathrm{f}}\dfrac{\partial \boldsymbol{h}_{l1}^2}{\partial x^2}+\rho_\mathrm{w}A_1 g\cos\psi \\ \quad +\dfrac{\rho_\mathrm{w}\lambda}{4R_\mathrm{sin}}\left(\dfrac{\partial \boldsymbol{h}_{l1}}{\partial t}\right)^2=\rho_\mathrm{w}A_1\dfrac{\partial \boldsymbol{h}_{l1}^2}{\partial t^2}, \text{ inside the pipe string} \\ -A_2\dfrac{1}{K_\mathrm{f}}\dfrac{\partial \boldsymbol{h}_{l2}^2}{\partial x^2}+\rho_\mathrm{w}A_2 g\cos\psi+\dfrac{\rho_w\lambda}{4(R_\mathrm{cin}-R_\mathrm{sout})}\left(\dfrac{\partial \boldsymbol{h}_{l2}}{\partial t}\right)^2 \\ \quad =\rho_\mathrm{w}A_2\dfrac{\partial \boldsymbol{h}_{l2}^2}{\partial t^2}, \text{ in the annulus} \end{cases} \tag{1}$$

wherein K_f is the bulk modulus of fluid; $\boldsymbol{h}_\mathrm{l}$ is the displacement of pressurized liquid column; x is the position of micro-element; ρ_w is the liquid density; ψ is the deviation angle; λ is the friction coefficient; A_1 is the cross section area of flow inside the pipe, $A_1=\pi R_\mathrm{sin}^2$(upward flow) and $A_1=\pi R_\mathrm{cin}^2$ (downward flow, which was often ignored); R is the pipe flow radius, $R=R_\mathrm{sin}$ (inner radius of pipe string) or R_{cin}(inner radius of casing pipe); A_2 is the cross section area of flow in the annulus, $A_2=\pi\left(R_\mathrm{cin}^2-R_\mathrm{sout}^2\right)$(upward flow); R_sout is the external radius of pipe string.

Before or after the shock wave arrived at the top of the column, the analytical solutions for liquid displacement are given as Eqs. (2) and (3)

$$S(t)_i=\frac{c}{K_\mathrm{f}}\sum\left(p_i^j-p_i^{j-1}\right)\left(t-t^{j-1}\right),\quad t<t_\mathrm{m}; \tag{2}$$

$$\begin{aligned} S(t)_i=\frac{c}{K_f}&\left[-p_0H_{well}/c+\int_0^t pdt-\int_{t_m}^t p(t-H_\mathrm{well}/c)\mathrm{d}t\right] \\ &+\int_{t_m}^t\int_{t_m}^t\left[\frac{p(t-H_\mathrm{well}/c)}{\rho_wH_{well}}-g\cos\psi-\lambda\frac{v(t)^2}{4gAR}\right]\mathrm{d}t, \\ &t>t_m \end{aligned} \tag{3}$$

wherein $S(t)$ is the liquid displacement; c is the wave speed in the liquid; P is the gas pressure; the subscript i refers to the liquid in the annulus or inside the pipe string; j is the node during calculation; t_m is the time shock wave arriving at the top of liquid column, $t_\mathrm{m}=H_\mathrm{well}/c$; H_well is the deviated depth of well; p_0 is the initial pressure downhole; $v(t)$ is the general velocity of fluid at time t.

(2) Influence of deviation angle on the in-situ stress

The stress around the deviated well could refer to the equation in Zeng et al. (2018). For a screen completed well or an open hole, the radial, circumferential and vertical stresses were calculated by substituting the gas pressure into the equations. The maximum and minimum horizontal stress around the open-hole screen well was 51.3 and 41.8 MPa, respectively. For the deflagration fracturing process in a horizontal well, the vertical principal stress was directly used to compare with the fracturing pressure to evaluate the formation of cracks.

(3) Pressure drop through the screen pipe

The pressure drops during flow in screen completed wells (Fig. 1) differed depending on the completion methods. The pressure drop passing the screen pipe was given in Eq. (4), which was based on Yang (2015). The expression for other pressure drop could be found in Wu et al. (2018). When the operating well was not filled with gravel packs, the terms ΔP_nD and S_nD could be omitted. Gao et al. (2017) gave an empirical formula for the pressure drop of the screen pipe through experiments with a skin factor of about 1.0–3.0:

$$\begin{aligned} \Delta P_\mathrm{h}&=\Delta P_\mathrm{nD}+\Delta P_\mathrm{s}+\Delta P_\mathrm{sk} \\ &=\frac{Q_\mathrm{g}B_\mathrm{g}\eta_\mathrm{g}}{2\pi h}\left(\frac{S_\mathrm{nD}+S_\mathrm{p}}{k_\mathrm{pack}}+\sum_{j=1}^{N-1}\frac{1}{k_j\ln\left(r_{j+1}/r_j\right)}\right). \end{aligned} \tag{4}$$

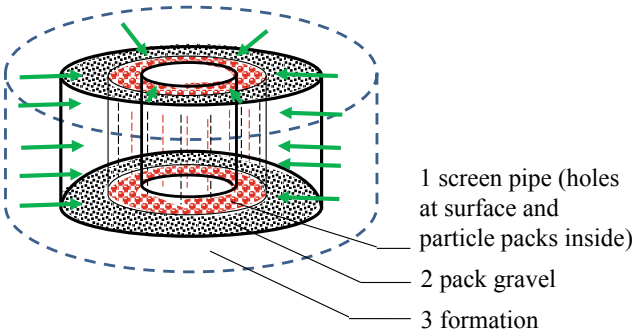

Fig. 1 Diagram of fluid flow in screen completed well

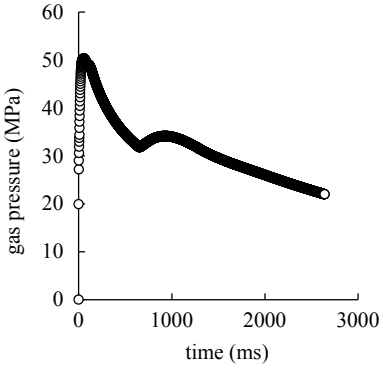

Fig. 2 Gas pressure in screen completed well

wherein ΔP_h is the pressure drop from the internal wall of casing pipe to the internal wall of screen pipe; ΔP_{nD} is the pressure drop through pack gravel between the casing tube and the screen pipe; ΔP_s is the pressure drop through the surface holes of the screen pipe; ΔP_{sk} is the pressure drop through the particle packs in the screen pipe; Q_g is the gas flow rate; B_g is the volume factor; η_g is the gas viscosity; h is the height of screen pipe; S_{nD} is the skin factor representing through the gravel pack; S_p is the skin factor representing through the surface holes of the screen pipe; k_{pack} is the permeability of the gravel pack; N is the axial numbers of particle packs; k_j is the permeability of No. j particle pack; r_{j+1} and r_j are the external and internal radii of No. j particle pack.

3 Numerical Simulation

The numerical parameters for deflagration fracturing in a screen completed well were obtained from Sun et al. (2017).

The gas volume in an open-hole screen completed well included volumes between the well and the screen pipe, between the screen pipe and the powder gun, for the deflagrated propellant of the remaining liquid column and for the fracture volumes. The simulated maximum value was 50.3 MPa (Fig. 2), which was less than the internal pressure strength of the screen pipe.

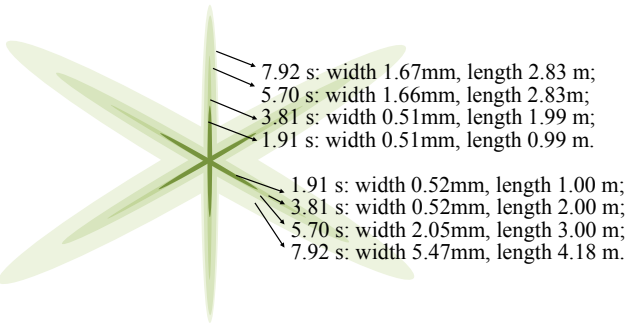

Fig. 3 The cracks at 0°, 60°, 120° azimuth angles

The simulated pressure increased sharply in the first 53 ms, then decreased rapidly at 1.95 s because of the upward movement of pressurized liquid column and the formation of cracks. Pressure increased again because of the backward movement of pressurized liquid column at 2.86 s and decreased in the final stage because of heat dissipation and gas flowing into the formation. Simulations showed that the screen pipe was safe during operation and agreed with the conclusions from the field trial. Three fractures were

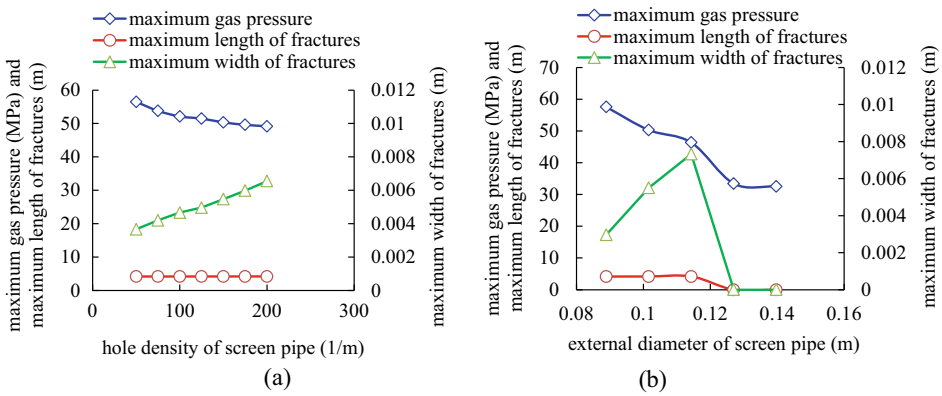

Fig. 4 Variation of the maximum values of gas pressure, crack width and crack length

formed with a maximum length of 4.18 m and a maximum width of 5.47 mm. The diagram for the distribution of fractures is shown in Fig. 3. The shape of a crack at 60° azimuth angle was the same as the shape of a crack at 120°, with the angle being the angle between the fracture and the principal stress. The production increase ratio was calculated to be 1.31 using Eq. (4) in Li et al. (1995). The simulation showed that the screen pipe was safe during the operation and agreed with the conclusion from the field trial.

A parametric study was used to analyze the influence of hole density and size of screen pipe on the variation of gas pressures (Fig. 4). The deflagrated gas flowed easily into the formation when the drainage area in the screen pipe increased. The maximum value of gas pressure and time had lower maximum values when there was a higher hole density. Higher screen pipe sizes had correspondingly lower maximum gas pressures, but the gas pressures were still large enough to form fractures. Fractures did not form, and the maximum gas pressure tended to be stable when the screen pipe was larger. Hole density or size of screen pipe had a negligible effect on the maximum length of fractures. There is a linear relationship between the maximum width of fractures and the hole density or external diameter of screen pipe.

4 Conclusions

The model for deflagration fracturing in a screen completed well differed from that of a traditional model in a perforated well. We evaluated the influence of deviation angle on the pressurized liquid column and in-situ stress nearby the wellbore as well as the pressure drop through the downhole screen pipe. The sensitivity study can be used to identify a proper screen size and hole density that forms multiple radial fractures and offers downhole safety and sand control.

Acknowledgements The authors would like to thanks the Doctoral Funds of Yanshan University (BL17024), Scientific and Technological Research Project of Higher Education Institutions in Hebei Province (QN2019163).

References

Gao, H., Wang, Z.M., Wang, X.Q., et al.: Study on friction coefficient and model of astropyle sand control screen. China Petrol. Mach. **45** (11), 12–17 (2017)

Lanari, M., Fakhimi, A.: Numerical study of contributions of shock wave and gas penetration toward induced rock damage during blasting. Comput. Part. Mech. **2**(2), 197–208 (2015)

Li, D., Zhao, G., Yang, W.Y.: High energy gas fracturing (HEGF): mechanism and practice. SPE 29992 (1995)

Sun, L., Yang, W.Y., Yi, F., et al.: Feasibility research on liner-completion deflagration fracturing technique. Spec. Oil Gas Reservoirs **24**(4), 161–165 (2017)

Tian, P.: The Feasibility Study on Screen Completion with Deflagration Fracturing. Xi'an Shiyou University, Xi'an (2017)

Wu, F.P., Pu, C.S., Wu, B.: A dynamic model of the pressurized liquid column movement in the high energy gas fracturing process. Explos. Shock Waves **30**(6), 633–640 (2010)

Wu, F.P., Wei, X.M., Chen, Z.X., et al.: Numerical simulation and parametric analysis for designing high energy gas fracturing. J. Nat. Gas Sci. Eng. **53**, 218–236 (2018)

Yang, Y.H.: Study on Segment and Screen Completion of Horizontal Well in Bottom Water Reservoir. China University of Petroleum (Huadong), Qingdao (2015)

Zeng, F.H., Cheng, X.Z., Guo, J.C., et al.: Investigation of the initiation pressure and fracture geometry of fractured deviated wells. J. Petrol. Sci. Eng. **165**, 412–427 (2018)

Zhang, J., Huang, L.P., Zhou, J.Y., et al.: Simulation study on high energy gas fracturing in screen completed wells. Drill. Prod. Technol. **41**(4), 66–68 (2018)

Risk Analysis of Gas Pipeline Laid in Permafrost

Galina Struchkova, Tamara Kapitonova, and Maria Nikolaeva

Abstract

This paper reviewed the safety and reliability of the operation of underground pipelines laid in the cryolithozone. As examples considered accidents and failures on the main gas pipeline Mastakh–Bergeh–Yakutsk. The paper presents the statistical analysis of the causes of accidents and failures on the linear part of the main gas pipeline (MG). Using Pareto chart a set of reasons that lead to the greatest losses of gas and time to eliminate an accident has been defined. On the basis of a probabilistic and statistical method of estimation of the damage probabilities, we have carried out the task of risk prediction. The accidents and failure analysis indicate the feasibility and need to consider pipelines in the permafrost zone as a single natural–technical system. This kind of data is of interest when deciding measures on reducing the accident risk degree probabilities at the facilities.

Keywords

Emergency • Main gas pipeline • Probabilistic and statistical methods • Analysis of causes of accidents and refusals • Permafrost soil

1 Introduction

Safety and reliability of underground main pipelines laid in the cryolithozone depend on a number of natural-technogenic factors. Risk analysis is a well-known methodology for risk assessment related to any industrial activity, and in this respect, it is a powerful tool to solve the problem of transportation of hazardous materials through pipelines. The problem of cause analysis of accidents and failures, risk assessment and prediction of catastrophic changes of a state of natural and technical systems are among the most relevant, priority areas of fundamental and applied research whether in Russia or abroad (Lepikhin et al. 2003; Revazov 2010; Khan et al. 2015; Bubbico 2018; Shan et al. 2018; Tchórzewska-Cieślak 2018).

The main pipeline structures of the Sakha Republic (Yakutia) have been constructed and operate in the area of permafrost. The Mastakh–Bergeh–Yakutsk gas pipeline is almost completely transferred to the underground version of laying. The underground scheme is about 98% of the total length of the constructed gas pipelines. The main oil and gas pipelines on the territory of the Sakha Republic (Yakutia) include the most dangerous objects, and ensuring their safety and uninterrupted functioning is a vital task.

2 Materials and Methods

The collection and processing of statistical data on failures of the Mastakh–Bergeh–Yakutsk gas pipeline have been achieved in the IPTPN SB RAS since being in service. In the studies carried out on the problem of the effects of natural and man-made disasters in the route of Middle–Vilyuisk gas condensate field (GCF)—Mastakh–Bergeh–Yakutsk, it is noted that the main reasons of accidents occurrence and development are: low temperatures, the possibility of flooding, permafrost; thermoerosive thermokarst phenomena; a large number of river crossings; the

G. Struchkova · T. Kapitonova (✉)
V.P. Larionov Institute of Physical-Technical Problems of the North Siberian Branch of the Russian Academy of Science, Yakutsk, Russia
e-mail: kapitonova@iptpn.ysn.ru

M. Nikolaeva
M.K. Ammosov North-Eastern Federal University, Yakutsk, Russia

M. Meghraoui et al. (eds.), *Advances in Geophysics, Tectonics and Petroleum Geosciences*,
Advances in Science, Technology & Innovation, https://doi.org/10.1007/978-3-030-73026-0_107

extended length of the main pipe; non-design plots of pipelines in non-cohesive areas (waterlogging of places of the route of a gas pipeline laying); high probability of formation of gas condensate and hydrate plugs; a low level of automation; substantial volume of process pipelines that have exhausted their resources; forest fires; a human factor (Kraidi et al. 2019; Sleptsov et al. 2008,2007). A pipeline, which has lost soil stability in permafrost terrain changes, is under seasonal alternating load which leads first to the development of micro- and then of macro-cracks (Levin 2002). The analysis of the most typical causes for failures of the gas pipeline Middle–Vilyuisk gas condensate field—Mastakh–Bergeh–Yakutsk MG revealed that more than 50 percent of failures accounted for welded annular seams with a formation of a through crack-blowhole (Kapitonova et al. 2013). The identified main causes of failures in the analysis result were combined into the enlarged groups as follows: natural phenomena (including geocryological); mechanical damage of pipes by mechanisms during excavation works; metallurgical pipe defects among others. For each cause group, the contribution to the total number of accident cases (percentage of cases) and the distribution of damage for each emergency situation from this group of causes were calculated. Using Pareto chart, the analysis of causes that lead to the greatest losses of gas and time to eliminate the accident was carried out. On the basis of probabilistic-statistical method of estimating damage probabilities, we carried out the task of risk forecasting (Lepikhin et al. 2003; Bolshakov 2010; Pugachev 2002). The results were obtained from a specific database of accidents and failures associated with a particular pipeline network. Therefore, they should be adapted for use in other conditions.

3 Results and Discussion

Let us consider the distribution of accidents depending on the causes of their occurrence for each time period of operation separately (Table 1).

For the operation period 1968–1978, there were emergency situations related to three main causes: natural phenomena (27% of the total share of emergency situations that occurred during the first period of operation—geocryological ones related to the activation of cryogenic processes as a result of construction works) and metallurgical (46%) related to the defects of construction and installation works and others (23%) related to hydrate formation and a human factor.

Over the past period of time (2000–2017), emergencies were mainly due to metallurgical defects (62%) related to the defects of construction and installation works and long service life of pipelines, mechanical damage of pipes during excavation (9%), natural phenomena (11%). The share of accidents related to the loss of stability at permafrost changes of soils significantly decreased as compared to previous periods. This is probably related to a decrease in the activity of cryogenic processes, and other reasons (18%) related to the violation of requirements in operation and errors of personnel. For each group of reasons, the contributions to the total number of emergency cases (percentage of all cases) and the distribution of damage for groups of reasons were calculated. The analysis results are presented in Table 2.

Table 1 The structure of causes of failures and for accidental damage Mastakh-Berge-Yakutsk pipelines in 1968 – 2016 are presented

Reasons	1968–1978 year (%)	(1) 1979–1989 year (%)	1990–1999 year (%)	(2) 2000–2017 year (%)
Natural phenomenon	27	26	6	11
Mechanical	4	–	13	9
Metallurgical	46	45	56	62
Others (hydrated plugs, presence of liquid, etc.)	23	29	25	18

Table 2 Ranking of factors that lead to the greatest losses of gas and time to eliminate failures and accidents

Factors	Share (in %) of cases	Factors	Percentage damage (gas loss)	Factors	Percentage of time spent on repairs
3	39.47	4	54,475	5	32,619
1	28.95	3	31,515	3	28,393
4	15.79	1	13,933	1	26,524
5	13.16	5	0.075	4	11,379
2	2.63	2	0.002	2	1084

4 Conclusions

For the operation period 1968–1978, emergency situations were characterized; the share of accidents related to natural phenomena was up to 27% of the total number, which is related to the activation of geocryogenic processes as a result of construction works. For the last period of time, the share of emergency situations caused by loss of sustainability at permafrost changes of soils markedly decreased as compared to previous periods, which may be due to the stabilization of the geocryogenic processes near the pipelines. However, it was still high (11%), which indicates the feasibility and need to reconsider pipelines laid in the cryolithozone as a single natural and technical system. These data are of interest when deciding about risk reduction measures of accidents.

References

Bolshakov, A.M.: Analysis of damage and defects in the main gas pipelines and tanks North. J. Gas Ind. **5**, 52–52 (2010)

Bubbico, R.: A statistical analysis of causes and consequences of the release of hazardous materials from pipelines. The influence of layout. J. Loss Prev. Process Ind. **56**, 458–466 (2018)

Kapitonova, T.A., Struchkova, G.P., Tarskaya, L.E., Efremov, P.V.: Main geological risks for pipelines in cryolithozone conditions. In: VI Eurasian Symposium on problems of strength of materials and machines for cold climate regions EURASTRENCOLD—2013, vol. 3, pp. 126–141 (2013)

Khan, F., Rathnayaka, S., Ahmed, S.: Methods and models in process safety and risk management: past, present and future. Process Saf. Environ. Prot. **98**, 116–147 (2015)

Kraidi, L., Shah, R., Matipa, W.: Fiona Bortwick analyzing the critical risk factors associated with oil and gas pipeline projects in Iraq. Int. J. Crit. Infrastruct. Prot. **24**, 14–22 (2019)

Lepikhin, A.M., Makhutov. N.N., Moskvichev, V.V., Chernyaev A.P.: Probabilistic risk analysis of structures of technical systems. Novosibirsk: Sci. 174 (2003)

Levin, A.I.: Cold resistance and reliability of pipelines of the Far North. Dissertations for the degree of doctor of technical Sciences, 32 (2002)

Pugachev, V.S.: Theory of Probability and Mathematical Statistics. Training Allowance, 2nd edn. Fizmatlit 496 (2002)

Revazov, A.M.: Analysis of emergency and emergency situations on the objects of the main gas pipeline transport and measures to prevent their occurrence and mitigate the consequences. Qual. Manag. Oil Gas Complex **1**, 68–70 (2010)

Shan, Ke., Shuai, J., Kui, Xu., Zheng, W.: Failure probability assessment of gas transmission pipelines based on historical failure-related data and modification factors. J. Nat. Gas Sci. Eng. **52**, 356–366 (2018)

Sleptsov, O.I., Lyglaev, A.V., Kapitonova, T.A., Struchkova, G.P.: Study of technogenic accidents and anthropogenic impacts on the environmental safety of the Republic of Sakha (Yakutia). Saf. Emerg. Probl. **4**, 88–94 (2007)

Sleptsov, O.I., Levin, A.I., Struchkova, G.P., Semenova, T.I.: Safety of technical systems in the Republic of Sakha (Yakutia). In: Fridovsky, V.Y., Prokhorov, V.A. (eds.) Novosibirsk, Nauka, Part. 4, pp. 249–257 (2008)

Tchórzewska-Cieślak, B.: Approaches to methods of risk analysis and assessment regarding the gas supply to a city. Energies **11**(12), 3304 (2018)

Implementation of a Process for the Treatment of Hydrocarbon-Contaminated Soil Using Petroleum Produced Water

Wajdi Ibn Haj Ali, Hassan El Gharbi, Fatma Aloulou, Subrata Borgohain Gogoi, and Monem Kallel

Abstract

Oil-Pipeline and Oil-Well accidents, and leaky underground storage Oil-tanks can all permanently contaminate massive areas of soil, making them economically useless as well as dangerous to the human health, biological resources, and ecosystems. There are many methods of treatment of these contaminated soils by hydrocarbons (Stegmann R et al. in Fondamentals analysis applications. Springer, Berlin, 658 p, 2001): stabilization/solidification, bioremediation (Suthersan et al. in Remediation engineering: design concepts. CRC Press, 2016), incineration, soil washing, etc. The present work focuses on the treatment of the contaminated soil by the hydrocarbons with soil washing process using oilfield produced water (PW). The methodological approach consists of researching the optimum conditions of soil washing based on the optimum of moisture's parameters between PW and contaminated soil such as Liquid/Solid contact time and Liquid/Solid ratio. Another parameter was analyzed; it is the successive wash test. The contaminated soil before applying the treatment has 1900 ppm of Total Petroleum Hydrocarbons (TPH). After six washing tests, the optimum parameters of test were fixed as follow: The optimum of Liquid and Solid contact time was 5 min, and the optimum of Liquid/Solid ratio was 100 mL/100 g. With these optimum conditions and after three successive soil washing, we succeeded to reduce the percentage of residual TPH in contaminated soil from 1.9% (1900 ppm) to 0.3% (300 ppm).

Keywords

Petroleum industry • Produced water (PW) • Contaminated soil • Total Petroleum Hydrocarbons (TPH) • Soil washing • Oil and gas activity

1 Introduction

In a context of very strong environmental, energy and societal pressures, including the need for the protection of water resources and the limitation of gas emissions, water management and decreasing the quantity of contaminated soil by hydrocarbons have become a major challenge for the oil industry.

In order to remove these contaminants, many different in-situ or ex-situ remediation technologies have been developed throughout the years to mitigate the risk imposed by soil contamination such as stabilization/solidification, bioremediation, incineration, soil washing, etc., (EPA 2007).

On the other hand, large volumes of produced water (PW) are generated with oil pumping operations. This PW can be used to clean contaminated soil by hydrocarbons with soil washing process. Washing tests have been executed in laboratory scale followed by analyzes to evaluate the release of TPH content from soil to the aqueous phase and determine the optimum conditions for an effective washing.

W. I. H. Ali (✉)
La Compagnie Franco-Tunisienne Des Pétroles CFTP; QHSE, Sfax, Tunisia

H. E. Gharbi · M. Kallel
Laboratoire de Génie de L'Environnement Et Echo-Technologie GEET, Ecole Nationale D'Ingénieurs de Sfax, Université de Sfax, Sfax, Tunisia

F. Aloulou
Laboratoire de Génie de L'Environnement Et Echo-Technologie GEET; Faculté Des Sciences de Sfax, Université de Sfax, Sfax, Tunisia

S. B. Gogoi
Department of Petroleum Technology, Dibrugarh University, Dibrugarh, India

M. Meghraoui et al. (eds.), *Advances in Geophysics, Tectonics and Petroleum Geosciences*, Advances in Science, Technology & Innovation, https://doi.org/10.1007/978-3-030-73026-0_108

2 Methodological Approach

The main factors controlling soil washing by chemical extraction using water are flushing number, Liquid and Solid contact time, Liquid/Solid ratio, and water temperature as reference to leaching column test (Jeannot et al. 2000). From which, we have chosen to study the effect of the first three factors on the removal of TPH at ambient temperature in order to determine the optimum conditions for an efficient soil washing process.

The soil washing treatment was based on the following steps to reduce the amount of hydrocarbons stored in the soil:

1. We have tried to select the optimum Liquid and Solid contact time for dissolving hydrocarbons in produced water at ambient temperature: 5, 10, and 20 min.
2. After having selected the optimum Liquid and Solid contact time, we limited the Liquid/Solid ratio at 100/100, 200/100, 300/100 (mL/g), respectively, to see the optimum ratio for dissolving hydrocarbons in produced water.
3. A series of successive washes were carried out in compliance with the optimum contact time and the optimum Liquid/Solid ratio in order to reduce the concentration of residual TPH in the soil (Fig. 1).

2.1 Soil Washing Process

2.1.1 Soil Sampling

Ten samples were collected from different locations at ambient temperature and were relatively homogenous representing the dominant type of soil at each location and depth.

Surface samples were collected from a maximum depth of 1 m and at depth intervals (0.4, 0.5, 0.84, or 1.0 m intervals).

In order to fill the sample bags, the top layer of soil was removed to the desired sample depth with Trax or spade. Then, we collected the soil and scraped it into the sample bag with a spatula.

2.1.2 The Stages of Soil Washing

Soil Preparation

A mixture of homogeneous soil was prepared by manual mixing and breaking of large aggregates. Then, we put the amount of soil that will be treated into a container, which was exposed to the sun and was dried without any moisture inside.

Chemical Extraction by Produced Water

Once the soil has been prepared, washing tests were carried out in the laboratory scale by produced water as an aqueous solvent.

Washing protocol:

- Weigh 100 g of homogenized soil sample to which washing water will be added according to Liquid and Solid ratio.
- When a mixture of contaminated soil and water was placed in a beaker, it was continuously stirred at 100 rpm within a specific contact time.
- Let the sample settle for about 20 min, then filter it to properly recover the soil sample and water separately.

2.2 Analytical Methods

2.2.1 Soil Analysis Before Treatment

Soil Water Retention Capacity

Procedure:

- 50 mL of soil and 25 mL of water were taken.
- We poured the water into the beaker containing the soil and shook it.
- A funnel covered with filter paper was placed in a graduated cylinder to pour the mixture into the funnel.

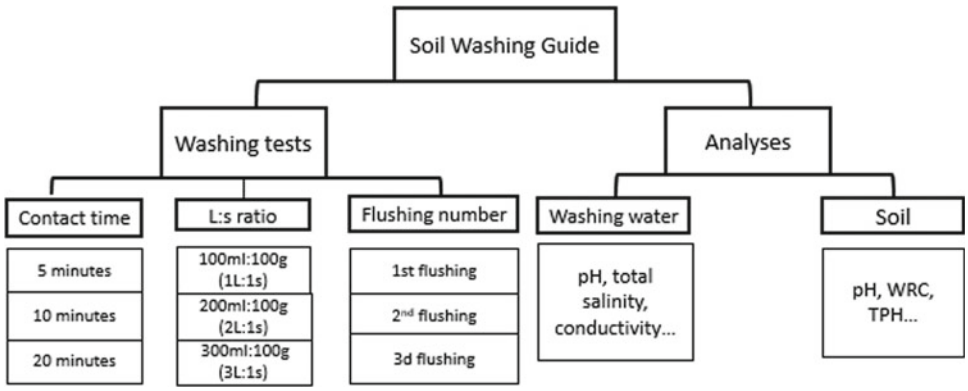

Fig. 1 Guide of soil washing application

- We waiting patiently for the water to drip and then the volume of water collected was noted.

Porosity

"Soil porosity" refers to the amount of pores, or open space, between soil particles.

Procedure and calculations:

- 100 mL of water was poured into a cup with a line drawn where the water was going,
- We noted that 100 mL was the total volume in a sheet data,
- We drained the water from this cup so that it could be filled with the soil sample up to the drawn line,
- The water was slowly and carefully poured into this cup using a graduated cylinder until it reached the top of the soil sample,
- The volume of water remaining in the graduated cylinder was recorded.

The porosity can be calculated using the following formula:

$$\text{Porosity}(\%) = \text{pores\_volume}/\text{total\_volume}$$

PH of Soil

The procedure of soil Hydrogen potential is as follows:

- 10 g of soil was mixed with 50 mL of distilled water to shake them up for an hour
- After their equilibrium for 16 h, the pH was measured by a pH-measuring device

Moisture Content

Definition:

Moisture by weight W of a soil is defined by the ratio of the mass of the liquid phase to that of the solid phase:

$$W = M_{\text{w}}/M_{\text{s}}$$

- W: weight humidity (100%)
- M_{w}: mass of the liquid phase (kg)
- M_{s}: mass of the solid phase (kg)
- $M_{\text{w}} = M$ (wet soil) − M (dry soil)

Procedure:

- 10 g of wet soil sample taken was weighed. Then, it air-dried to determine their dry weight

Organic Matter Percentage

The organic matter of soil is determined after calcinations of the dried soil at 105 °C sample in the oven at 550 °C for 2 h in order to obtain a weight of P_{550}

$$\text{OM}\% = (P550 - P105)/(P105 - P0)$$

2.2.2 Washing Water Analysis

We took a produced water sample from the production center of Oil field in order to determine their characteristics such as:

The electrical conductivity of produced water was measured by conduct meter at 22 °C.

Similarly, a pH-measuring device was used to determine their pH.

To determine the total salinity of produced water sample, an empty capsule previously dried in the oven at 105 °C and cooled to room temperature in a desiccator was weighted. Then, we poured 10 mL of produced water into the capsule. This capsule was placed in the agitator until the salts precipitated.

After that, we put the {capsule + salts} in the Oven at 105 °C for one hour, after that it was cooled to room temperature in a desiccator in order to weigh it.

The density was determined using a Density meter in a graduated cylinder containing 500 mL of produced water.

As well as, the hardness (Ca and Mg) was also determined using Digital Titrator.

2.2.3 Hydrocarbon Analysis

Liquid: Solid Extraction

In order to determine the quantity of Total Petroleum Hydrocarbons "TPH" according to (ISO TR 11046) at each wash test. We have included the mechanical agitation method which is based on Liquid: Solid extraction and consists in mechanically agitating the sample in the presence of an extracting solvent at atmospheric pressure and at room temperature.

It appears very simple and nevertheless interesting because it gives results at least as good as those obtained by the soxhlet technique (Jeannot et al. 2000). The organic solvent, which has to be used for extraction sample is DCM (Methylene dichloride (CH2Cl2)) (Zhang et al. 2013).

This method was processed by several steps to extract hydrocarbons from the contaminated soil which are detailed in the following extraction protocol:

Extraction Protocol:

- 10 g of contaminated soil was put in a beaker.
- 30 mL of organic solvent was taken by pipette to add it to the beaker containing the soil sample.

- Shake this mixture for 5 min using a mechanical shaker, then we let it settle to filter and recover the {hydrocarbons + organic solvent} into a new dried beaker.
- In order to separate TPH from the organic solvent, it is recommended to use Rotary evaporator at 40 °C.
- The concentration of hydrocarbons obtained after solvent evaporation was put into a dried carrycot to be weighed.

To calculate the quantity of extracted hydrocarbons, we may use this formula:

$$\mathrm{TPH} = (P - P0) * 100$$

- $P0$: Weight of the empty Carrycot (g)
- P: Weight of the Carrycot + the extracted Hydrocarbons (g)

To get the hydrocarbons concentration in 1 kg of contaminated soil, we need to multiply the result by 100.

Liquid Chromatography

It is a quantitative, qualitative and separative analytical technique mainly used in the field of analytical chemistry as a major scientific tool but also in various fields such as organic chemistry and biochemistry.

In this project, we choose liquid chromatography on solid phase since it allows us to separate compounds with different polarities as reference to Nouha (2006).

Analytical protocol:

As a first step, we have to prepare the separation column such that:

- Silica with a particle size of 70–230 mesh is activated by cleaning it with a mixture of dichloromethane and cyclohexane, once these two solvents have evaporated, the silica is vacuum-packed at 140 °C for one hour and then placed in an oven at 120 °C for one night.
- A Pasteur pipette is used in which a small quantity of glass wool is introduced to prevent the silica from leaving the column and then activated silica is added on which about 1 cm of Florisil is placed, which ensures the retention of polar compounds.

The next step consists of the elution of organic compounds by organic solvents as follows;

- The first elution was carried out with hexane (low polarity), which makes it possible to separate the less polar compounds (aliphatic hydrocarbons) from the polar compounds.

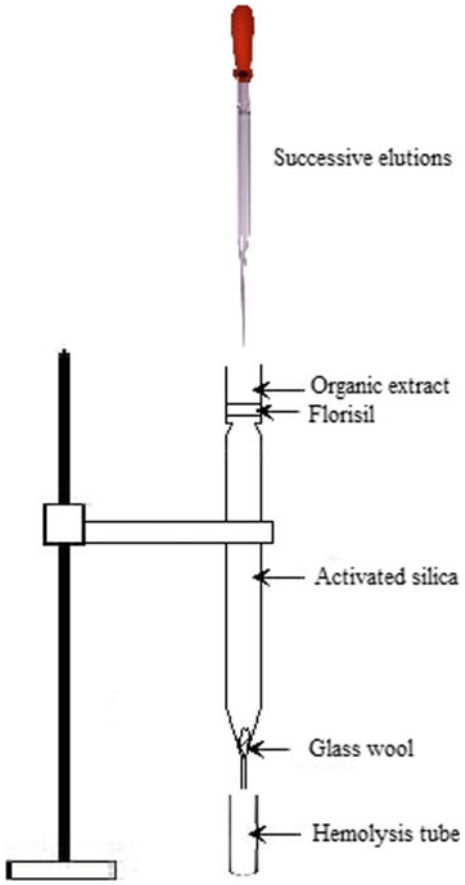

Fig. 2 Chromatographic separation column

- Then a mixture of hexane/Dichloromethane in the proportions (2/3, 1/3) is finally injected to recover the polar compounds (aromatic hydrocarbons). Actually, the presence of Dichloromethane in this mixture is for increasing the polarity of the hexane.

In the last step, these two fractions (aliphatic and aromatic hydrocarbons) are collected in identified hemolytic tubes and weighed after drying the elutes, the tubes are torn again, and the relative proportions of each of the fractions can thus be calculated for each sample by the difference between the mass of the empty and full tubes.

The following scheme represents the chromatographic column (Fig. 2).

3 Results

3.1 Untreated Soil Characterization

Some characteristics of studied soil before treatment have been identified that are important for understanding the interactions of petroleum hydrocarbons with this soil:

3.1.1 Water Retention Capacity

The soil used in this project has the capacity to retain about 80% of the water.

This content is a determining factor for the distribution of the pollutant in the three phases in the soil.

Indeed, if the pollutant is present in the gas phase, the presence of water on the surface of the adsorbent may reduce the adsorption of hydrophobic pollutant (by repulsion) or increase its retention if it is hydrophilic (hydrogen bonds with water molecules or dissolution in still water) (Gourdon 1997).

Therefore, the important water retention capacity of contaminated soil limits the adsorption phenomenon of hydrophobic pollutants.

3.1.2 Soil Porosity and pH

Soil contamination by hydrocarbons limits its porous space. Hence, the soil is air-dried in order to keep the hydrocarbons compounds into the soil system to accurately determine its porosity.

After executing the porosity test, the porous space occupied by air and water represents 41%, which enhances the distribution of wash water in the contaminated soil and their pH = 7.67.

3.1.3 The Moisture Content

The weight humidity of soil before treatment corresponds to 10% while the use of water to clean-up the soil causes the increase of this moisture to 32% and may reduce the adsorption of organic pollutants.

3.1.4 Organic Matter Percentage

8.7% is the percentage determined through the designed test this percentage is very high compared with the following figure in the non-contaminated soil gathered from an agriculture zone nearby the contaminated zone which is only 1.9% that is because the percentage of the hydrocarbons stored into the contaminated soil which exceeds 5% of the soil dry weight.

From the study of Gourdon (1997), this content plays a role in the soil's ability to retain organic pollutants, such low-polar, non-ionizable organic molecules have a greater affinity for hydrophobic elements than for water in the soil. This partition can be described by a solvation phenomenon that occurs in soils rich in organic matter since this latter has a significant role for hydrophobic interactions provides by its aliphatic chains.

As a result, the high percentage of organic matter limits the receptivity of soil for being treated by washing.

3.1.5 Soil Granulometry

The granulometric analysis of soil by wet sieving (63 µm sieve) shows that:

The coarse mineral fraction, which is sandy, represents 72% of total soil mass.

The percentage of fine particles, which are silt and clay, is 28%.

This parameter is very important since the soil rich in sand and silt is characterized by its high permeability to water. Moreover, these two fractions do not intervene practically in the adsorption of organic pollutants in the soil, unlike clays that have a very high adsorption capacity (Gourdon 1997).

Therefore, this significant percentage of sand improves the efficiency of water scrubbing.

3.2 Washing Water Characterization

Generally, most produced waters have salinities greater than that of seawater and, therefore, are denser than seawater (Collins 1975) while it contains the same salts as seawater, with sodium and chloride the most abundant ions.

This type of water is used as washing water and then their characteristics are well determined and recorded in Table 1:

From this table, produced water is characterized by high salinity and conductivity, which enhance the ionic strength of water and it has a low acidity (pH = 6.23).

3.3 Categories of Removed Hydrocarbons

3.3.1 Quantitive and Qualitative Analysis Result

In order to identify, and to qualify hydrocarbons types removed by the process of water leaching, we have set up an analytical program based on the liquid chromatography characterization. Thus, liquid chromatography (on silica column) allowed the identification of the class of removed hydrocarbons according to the analysis result of the following soil samples:

S0: Untreated soil sample.

SW1: Soil washed for once.

SW2: Soil washed for twice.

SW3: Soil washed for three times.

The obtained results are recorded in Fig. 3 and in Table 2.

The Total Petroleum Hydrocarbons is composed of three major fractions:

- Saturated hydrocarbons (SAT)
- Aromatic hydrocarbons (AROM)
- Nitrogen Sulfur Oxygen (NSO) compounds.

The polar compounds (NSO) were found to be the most abundant in the untreated soil sample S0, which represents 1150 ppm, following by the saturated hydrocarbons

Table 1 Physico-chemical properties of produced water

Physio-chemical characteristics	Produced water
Electrical conductivity (ms/cm)	270
Total salinity (g/L)	137
pH	6.23
Density (Kg/L)	1.01
Calcium (mg/L)	1820
Magnesium (mg /L)	6200
Chloride (mg /L)	76.58
Sodium (mg/L)	52.28
Nitrate (mg/L)	12
Barium (mg/L)	40
Sulfide (mg/L)	10
Sulfate (mg/L)	220

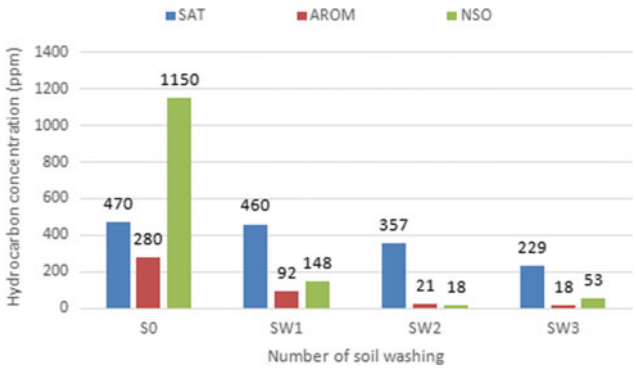

Fig. 3 Soil hydrocarbons evolution after different washing number with initial TPH = 1900 ppm; TPH: Total Petroleum Hydrocarbons; SAT: Saturated hydrocarbons; AROM: Aromatic hydrocarbons; NSO: Nitrogen Sulfur Oxygen compounds

(SAT) with a content of 470 ppm While the aromatic hydrocarbons (AROM) are the least abundant which correspond only to 280 ppm. This may indicate that the origin of hydrocarbons is heavy crude oil according to the composition of the following Ternary diagram (Fig. 4).

These concentrations of residual hydrocarbons in soil change considerably after three successive washings. In fact, there is a great release of NSO compounds, which decreases from 1150 to 53 ppm. Thus, the removal efficiency of these compounds is about 95%.

Similarly, the aromatic hydrocarbons know also a significant decrease from 280 to 18 ppm. Thus, their removal efficiency is about 93%.

However, the release of saturated hydrocarbons is carried out slowly to reach 229 ppm at the end of washing series from 470 ppm with a removal efficiency of 51%.

Relatively, saturated compounds appear to be less affected by washing process than other hydrocarbons. This result can be explained by the dissolution of saturated compounds in the produced water.

As a conclusion, polar compounds and aromatic hydrocarbons are the most removed hydrocarbons (elimination is around 95%) from soil to water, unlike saturated hydrocarbons (with elimination around 50%).

A detailed review of the total extracts composition in the different samples and after three washings by water shows that the proportions in NSO are changed significantly. In fact, the percentages decrease from 60 to 15%.

Similarly to the aromatic hydrocarbons which have decreased from 15 to 8% in percentage terms.

Unlike, the fraction of saturated hydrocarbons that occupied the majority of residual hydrocarbons in the soil with percentages greater than 60% (Fig. 5).

Table 2 Soil hydrocarbon rate evolution after different washing number

Studied soil	TPH (ppm)	SAT (%)	AROM (%)	NSO (%)
S0	1900	25	15	60
SW1	700	66	13	21
SW2	500	71	11	18
SW3	300	77	8	15

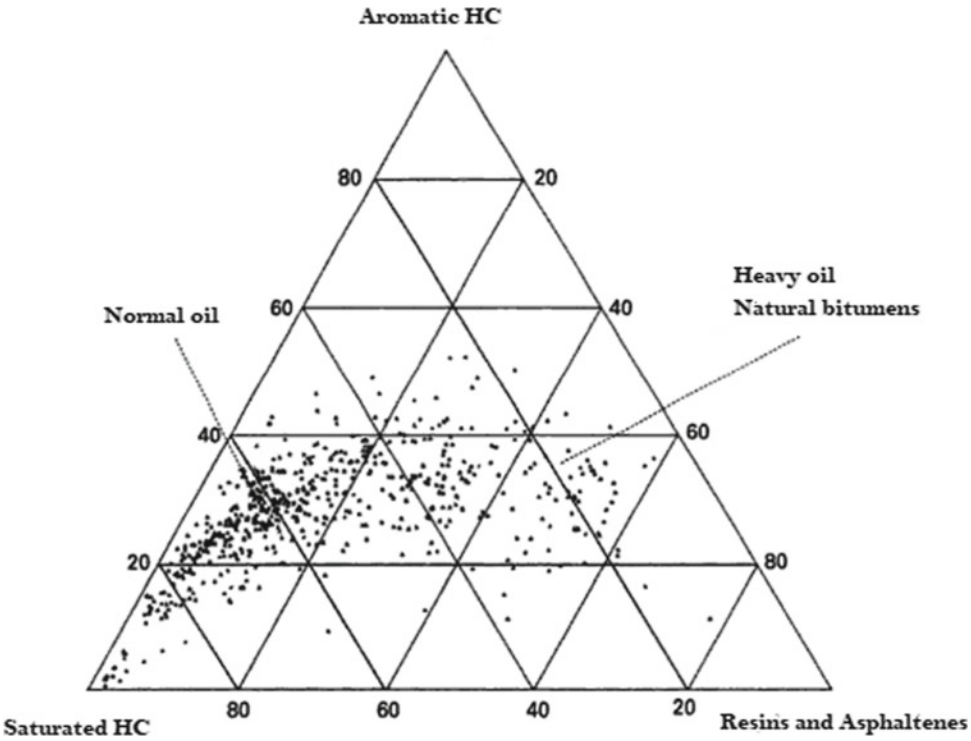

Fig. 4 Ternary diagram showing the composition of 636 crude oils into saturated crude hydrocarbons, aromatic hydrocarbons, and resins + asphaltenes. From Tissout and Welte (1984)

3.3.2 Interpretation

The tendency to dissolve and remove, preferably, the majority of aromatic hydrocarbons and polar compounds from soil to water are due to the difference of polarity between the different classes of Total Petroleum Hydrocarbons.

In fact, NSO compounds (resins and asphaltenes) are the most polar compounds followed by aromatic compounds, which are moderately polar, and finally, the aliphatics, which are apolar (Jane 2016). And, the high polarity enhances the hydrocarbons dissolution phenomenon into water, which is already a polar solvent.

Similarly, the dissolution defined by Nicholas (2015) mainly affects polar and low molecular weight aromatic compounds (mainly compounds lower than C15).

In addition to that, the solubility of petroleum hydrocarbons in water decreases as their size (molecular weight) increases; aromatic hydrocarbons are more water-soluble than saturated hydrocarbons with the same molecular weight (Jerry et al. 2011).

As well as, the evaporation phenomenon must be taken into consideration that may affect lighter volatile compounds with low molecular weight during soil drying before analysis at 40 °C.

In addition, the wide range of natural surfactant molecules in produced water provides the solubilization of hydrophobic compounds, especially the polycyclic aromatic hydrocarbons.

3.4 Liquid and Solid Contact Time Optimization

The washing conditions are:

- The volume of produced water is 100 mL
- Liquid/Solid ratio is 100/100 (mL/g)
- Liquid and Solid contact time is 5, 10, 20 min, respectively.

Table 3 summarizes the removal and residual TPH in soil after washing test.

3.5 Liquid/Solid Ratio Optimization

The washing conditions are:

- The volume of produced water is 100, 200, 300 (mL), respectively.
- Liquid/Solid ratio: 100/100, 200/100, 300/100 (mL/g), respectively.
- Liquid and Solid contact time is 5 min.

The removal and residual TPH in soil and after washing test is registered in Table 4

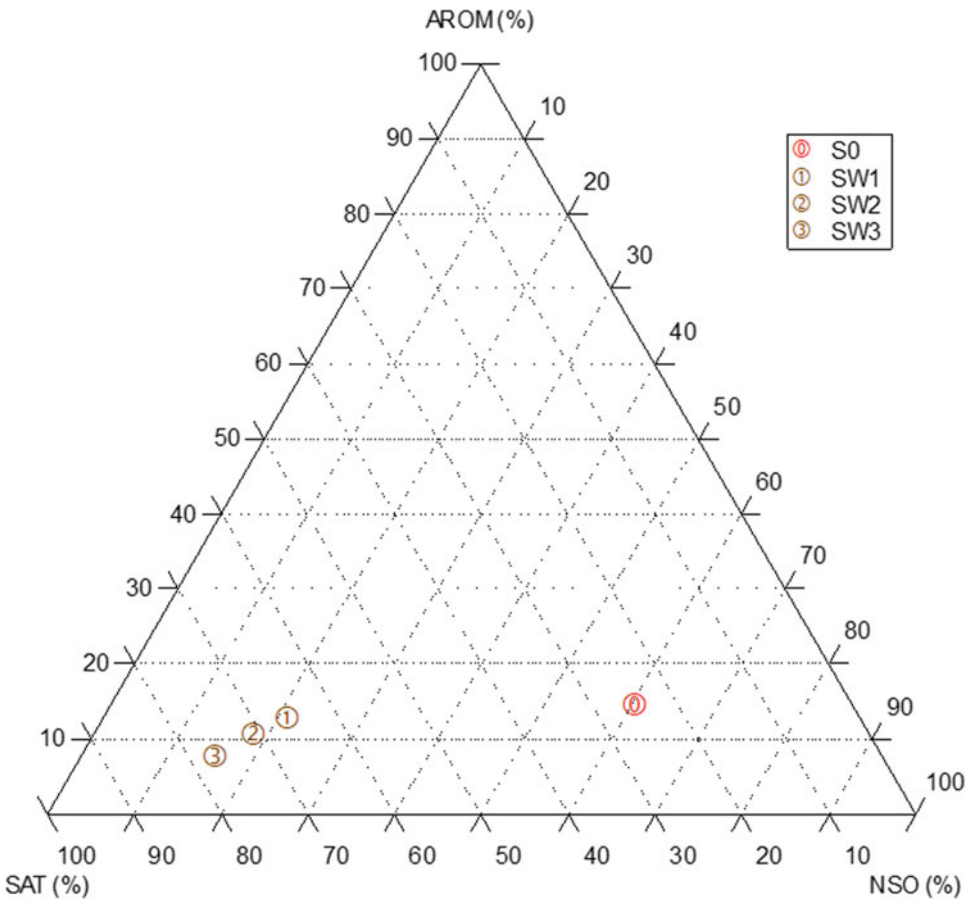

Fig. 5 Ternary diagram of soil samples

Table 3 Variation of TPH as a function of Liquid and Solid contact time

Sample name	Liquid and solid contact time (min)	Residual TPH (ppm)	Removal TPH (%)
S1	5	810	57
S2	10	690	64
S3	20	480	75

Table 4 Variation of TPH as a function of liquid/solid ratio

Sample name	Liquid/solid ratio (mL/g)	Residual TPH (ppm)	Removal TPH (%)
S4	100/100	880	53
S5	200/100	610	68
S6	300/100	224	88

3.6 Successive Wash Test

Successive washing consists of three consecutive washes on the same sample in order to produce three different extracts under the following conditions:

- Liquid and Solid contact time is 5 min
- Liquid/Solid ratio is 100/100 (mL/g)

Table 5 summarizes the removal and residual TPH in soil after each water rinse.

4 Discussion

4.1 Liquid and Solid Contact Time Optimization

The soil sample S0 represents the initial state of the soil records a TPH concentration of 1900 ppm. This concentration decreases rapidly after the first rinse. This drop in TPH concentration clearly shows that a significant proportion of the hydrocarbons have been removed about 57% as proven by the curve above.

Table 5 Variation of removal and residual TPH as a function of successive washing

Flushing number	Residual TPH (ppm)	Removal TPH (%)
1	700	63
2	500	73
3	300	84

At this point, a quick and significant dissolution of hydrocarbons with high solubility may carry out in produced water.

Table 3 shows that the increase of the contact time between liquid and solid phase provides a slight decrease in the remaining TPH in the soil. Indeed, residual TPH concentration is 810 ppm (for 5 min) while it is 480 ppm (for 20 min).

As a deduction, hydrocarbons proportions in the water are increased since the removal TPH comes to 74% for 20 min while it is about 57% for 5 min.

Thus, increasing the contact time between water and soil has an effect on TPH Removal efficiency.

From a profitability point of view, it is better to wash the soil for 5 min and reach to 57% of TPH Removal than to regulate the contact time up to 20 min (=increase of electricity) to reach to 74% of TPH removal. For that, an optimal washing time is 5 min.

4.2 Liquid/Solid Ratio Optimization

As found in the previous study of the Liquid and Solid contact time effect, washing the soil initially for 5 min in accordance with the Liquid/Solid ratio (100/100) transferred a significant amount of hydrocarbons from the soil to the water where the removal of TPH is about 53%.

Table 4 indicates that the increase of the Liquid/Solid ratio provides a decrease in the quantity of hydrocarbons remaining in the soil. In fact, the proportions of TPH removed from soil have been increased to 88% (300/100) from 53% (100/100).

Even though, the release of hydrocarbons becomes more important with the increase of the Liquid/Solid ratio. The amount of water used is considered very high while its removal efficiency compared to 100/100 ratio is low. Therefore, washing the soil according to the 100/100 ratio is cost efficient than washing it with high quantity of water. Thus, the optimal Liquid/Solid ratio has been selected is 100/100 ratio.

4.3 Successive Wash Test

From Table 5, a significant decrease for TPH in the soil is observed after the first flushing. Following by a gradual decrease after each successive washing until it comes to 300 ppm.

Indeed, the proportion of TPH removal for the first wash is important since it reaches to 63% from 100% of TPH in contaminated soil. This proportion increases considerably after the following successive washings since it reaches to 84%.

As a result, an important transfer of hydrocarbons from the contaminated soil to produced water can be achieved after this washing series.

Thus, increasing the number of flushing provide the increase of TPH removal efficiency.

5 Conclusion(s)

As a result, the application of soil washing with produced water as a method of treating hydrocarbon-contaminated soil has allowed us to reduce the percentage of residual TPH in soil from 1.9% (1900 ppm) to 0.3% (300 ppm). These results were obtained with the washing conditions below:

- Ambient temperature: between 19 and 21 °C
- Liquid and Solid contact time: 5 min
- Liquid/Solid ratio: 100 mL/100 g
- Flushing number: 3 successive washes

These optimum conditions can provide a TPH removal efficiency about 84%.

In the detail, the qualitative analysis of Total Petroleum Hydrocarbons indicated that this process has affected essentially the aromatic and polar fractions (NSO's) with an elimination rate exceeding 90% while the removal of saturated fraction does not exceed 50%.

Therefore, a washing process based on three successive washings using a ratio of 2 m^3 of water for 1 m^3 of soil. The water will be treated in wastewater treatment plant before the reuse (or water re-injection).

Thus, it's possible to reduce the quantity of hydrocarbon present in the Oil field contaminated soil with a low-cost technique and a minimum impact on the environment. Further essays should be conducted (in larger scale: semi-industrial) to calculate exactly the cost of this process.

References

Stegmann, R., Brunner, G., Calmano, W., Matz, G.: Treatment of contaminated soil. In: Fondamentals Analysis Applications. Springer, Berlin, 658 p (2001)

Suthersan, S.S., Horst, J., Schnobrich, M., Welty, N., McDonough, J.: Remediation Engineering: Design Concepts. CRC Press (2016)

EPA, E: Treatment technologies for site cleanup. Annual Status Report, Washington (2007)

Jeannot, R., Lemière, B., Chiron, S.: Guide méthodologique pour l'analyse des sols pollués. Rap. BRGM R 50128, 110 p., 44 fig, 3 ann (2000)

Zhang, J., Li, J., Thring, R., Liu, L.: Application of ultrasound and Fenton's reaction process for the treatment of oily sludge. Procedia Environ. Sci. **18**, 686–693 (2013)

Nouha, B.: Traitement d'un sol pollué par les hydrocarbures par le procedé de Landfarming. Tunisie. Master (FST), 101 p (2006)

Gourdon, R.: Etude de l'adsorption – desorption de polluants organiques dans les sols. Approche methodologique et application au pentachlorophenol et aux hydrocarbures polycycliques aromatiques. RECORD. 223 p, n°94-0404/3A (1997)

Collins, A.G.: Geochemistry of Oilfield Waters, p. 496. Elsevier Scientific Publishers, New York (1975)

Tissout, B.P., Welte, D.H.: Petroleum Formation and Occurrence. Springer, Berlin (1984)

Jane, F.: Chemistry for land contamination. Yorkshire Contaminated Land Forum (2016)

Nicolas, G.: Hydrocarbures pétorliers: caractéristiques, devenir et criminalistique environnementale, Études GENV222 et GENV23, Évaluation environnementale stratégique globale sur les hydrocarbures. Ministère du Développement durable, de l'Environnement et de la Lutte contre les changements climatiques, 41 p. et annexes (2015)

Jerry, M.N., Kenneth, L., Elisabeth, M.D.: Produced water: overview of composition, fates and effects, pp. 3–54. Springer, New York (2011). https://doi.org/10.1007/978-1-4614-0046-2_1

Structural Geology, Tectonics and Geodynamics, Petroleum Geology (T15): Structural Geology, Basement Architecture and Potential Data

Reconstruction of Late Hercynian Paleostress from Vein Data; Case Study of the Panasqueira Mine, Portugal

Christophe Pascal, Luís Jaques, and Atsushi Yamaji

Abstract

The quantification of tectonic forces or, alternatively, stresses represents a significant step toward the understanding of the natural processes governing plate tectonics and deformation at all scales. However, paleostress reconstructions based on the observation and measurement of natural fractures are traditionally limited to the determination of four out of the six parameters of the stress tensor. In the present study, we tried to reconstruct full paleostress tensors by extending the methodologies advanced by previous authors. We selected Panasqueira Mine, Central Portugal, as a natural laboratory, and focused on the measurement of subhorizontal quartz veins, which are favorably exposed in three dimensions in the underground galleries of the mine. Inversion of the vein data allowed for quantifying the respective orientations of the stress axes and the shape ratio of the stress ellipsoid. In order to reconstruct an additional stress parameter, namely pressure, we extensively sampled the vein material and combined fluid inclusion analyses on quartz samples with geothermometric analyses on sulfide minerals. Finally, we adjusted the radius of the obtained Mohr circle with the help of rupture laws and obtained the six parameters of the paleostress tensor that prevailed during the vein formation. Our results suggest a NW–SE reverse stress regime with a shape ratio equal to ~0.6, lithostatic pore pressures of ~300 MPa, and differential stress lower than ~20 MPa.

Keywords

Paleostresses • Quartz veins • Fluid inclusions • Geothermometry • Late Hercynian

C. Pascal (✉) · L. Jaques
Ruhr University Bochum, 44780 Bochum, Germany
e-mail: christophe.pascal@rub.de

A. Yamaji
Kyoto University, Kyoto, 606-8502, Japan

1 Introduction

Paleostress determination represents a step toward to quantification and modeling of tectonic processes and natural deformation of rocks. Traditional paleostress reconstruction methods are, however, limited to the quantification of four out of the six parameters of the stress tensor, in general. The present work introduced an integrated method to reconstruct full paleostress tensors that were later applied to the subhorizontal quartz veins found in the mines of Panasqueira, Central Portugal.

2 Geological Setting and Methods

The mines of Panasqueira (Fig. 1) are located in the Central Iberian Zone (CIZ), the southern arm of the Ibero-Armorican Arc, consolidated during the latest stages of the Hercynian Orogeny (i.e., ~310–295 Ma, e.g., Ribeiro et al. 1990). The economic deposits are found inside an extensive network of subhorizontal quartz veins hosted mainly in Ediacaran (?) to early Paleozoic schists and psammites, the Beira Schists (Thadeu 1951).

The subhorizontal vein network appears to be centered on a greisenized cupola of the underlying late Hercynian Panasqueira Granite and occasionally cuts through it (Kelly and Rye 1979). The veins consist of quartz (>90%) and, accessory, of wolframite, cassiterite, and chalcopyrite at sufficiently high concentrations for commercial exploitation; other sulfides such as arsenopyrite and sphalerite are also present. The extensive network of galleries and the particular "stope-and-pillar" type of operation of the economic deposits allows for excellent conditions of observation, measurement, and sampling of the mineral veins.

As a first step, we measured the attitudes of ~600 quartz veins and used the original inversion method of Yamaji and Sato (2011) to determine the orientations of the stress axes and the shape ratio of the stress ellipsoid, Φ. In addition, the

M. Meghraoui et al. (eds.), *Advances in Geophysics, Tectonics and Petroleum Geosciences*,
Advances in Science, Technology & Innovation, https://doi.org/10.1007/978-3-030-73026-0_109

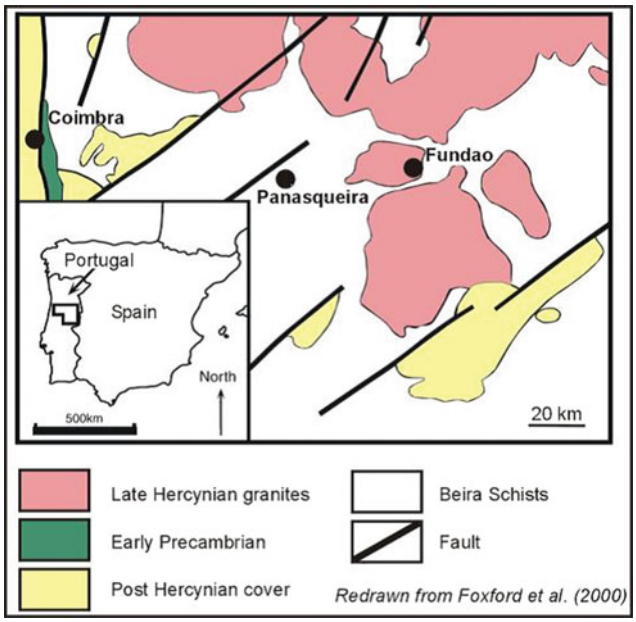

Fig. 1 Location and geological setting of the mine of Panasqueira

method provides a "relative pore pressure" value (i.e., the relative position of pore pressure in the obtained unscaled Mohr circle). Nevertheless, additional constraints were needed in order to determine the full paleostress tensor. We, therefore, analyzed fluid inclusions contained in the quartz of 16 selected veins and derived a collection of isochores from the data. The results from arsenopyrite geothermometry analyses on 10 samples were finally used in combination with the found isochores to determine the most probable range of paleopressures. The sixth parameter, needed to fully determine the paleostress tensor, was provided by means of adjusting the unscaled Mohr circle using a Mohr–Coulomb rupture law.

3 Results

The inversion of the ~600 vein data resulted in a reverse paleostress regime with σ_1 trending NW–SE, $\Phi \sim 0.6$ and a relative pore pressure of ~0.3. The inversion method was also designed to detect and separate distinct stress states through cluster analysis. The cluster analysis showed that the best fit was found for one single cluster of data, comforting our starting hypothesis that all the measured veins belong to a single tectonic event.

The analyzed fluid inclusions in quartz samples revealed a homogeneous aqueous-rich fluid with low to moderate salinity and variable CO_2, CH_4, and N_2 contents in the gaseous phase (Jaques and Pascal 2017). An "average" isochore was determined from the statistical analysis of the obtained isochores (Fig. 2). In order to better constrain paleopressure conditions, we analyzed the atomic percentage of ten samples to derive crystallization temperatures. The gathered information resulted in average pore pressures of ~300 MPa, corresponding to formation depths of ~10 km.

Finally, we scaled the previously obtained Mohr circle using as constraint a Mohr–Coulomb rupture law. The scaling resulted in the determination of a sixth parameter of the stress tensor and suggested a differential stress lower than 20 MPa.

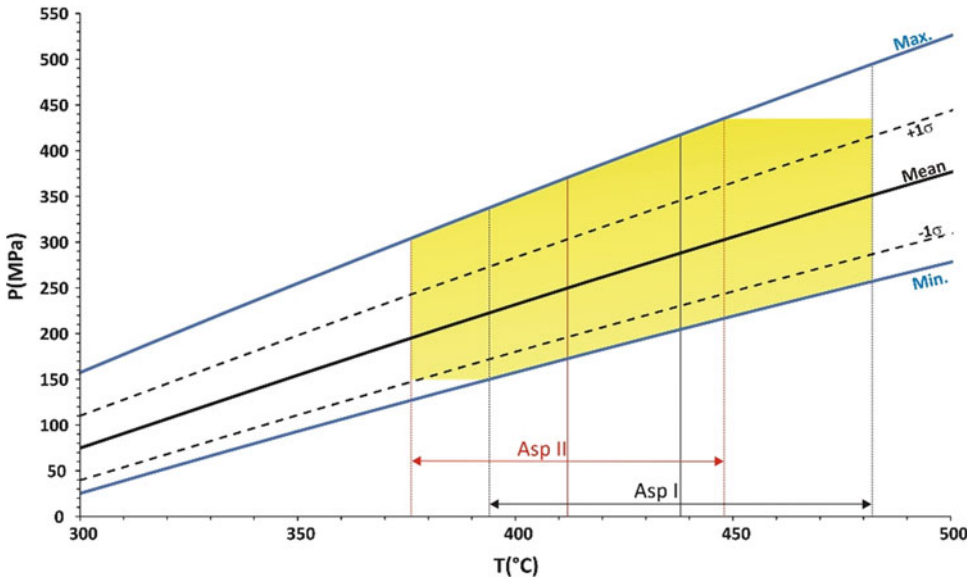

Fig. 2 Determination of paleopressure from fluid inclusion analyses and arsenopyrite geothermometry. The mean isochore is depicted as a dark bold line, min., max, and $+1\sigma$ and -1σ curves are also shown. The temperature ranges from geochemical studies of two arsenopyrite generations are given. The yellow field depicts the collection of probable P–T conditions prevailing during the vein formation

4 Discussion

The found NW–SE compression appears to be in contradiction with the inferred NE–SW shortening in the latest stages of the Hercynian orogeny in Central Portugal (Ribeiro et al. 1990). However, the stress field at the location of the present-day Panasqueira was also influenced by the intrusion of the Panasqueira granite. We may conclude that the reconstructed paleostress tensor is not representative of the regional stress field but reflects the interaction of the latter with local stress sources.

Our paleopressure determination resulted in a relatively high value of $\sim$300 MPa, suggesting formation depths of $\sim$10 km for the veins. This depth value is at odds with the very shallow depths proposed by Kelly and Rye (1979). Jaques and Pascal (Jaques and Pascal 2017) used in addition sphalerite geobarometry and analyzed mineral assemblages of the Panasqueira granite and of its contact metamorphic realm. The results were remarkably in-line with the pressure value advanced in this paper.

5 Conclusions

We tried to determine the full paleostress tensor, which prevailed during the formation of the (sub)horizontal quartz veins operated in the mines of Panasqueira, Central Portugal. We combined stress inversion of the measured veins with fluid inclusion analysis, sphalerite geothermometry and Mohr circle adjustment using rupture curves. Our study resulted in a NW–SE reverse stress regime with a shape ratio equal to $\sim$0.6, lithostatic pore pressures of $\sim$300 MPa and differential stress lower than $\sim$20 MPa. These results seem to be in agreement with the formation of the veins relatively deep in the crust and with the obvious absence of shear deformation.

References

Jaques, L., Pascal, C.: Full paleostress tensor reconstruction using quartz veins of Panasqueira Mine, central Portugal; part I: paleopressure determination. J. Struct. Geol. **102**, 58–74 (2017)

Kelly, W.C., Rye, R.O.: Geologic, fluid inclusion and stable isotope studies of the tin-tungsten deposits of Panasqueira, Portugal. Econ. Geol. **74**, 1721–1822 (1979)

Ribeiro, A., Pereira, E., Dias, R.: Structure of the Northwest of the Iberian Peninsula. In: Dallmeyer, D., Martinez Garcia, E. (eds.) Pre-Mesozoic geology of Iberia, pp. 220–236. Springer, Berlin (1990)

Thadeu, D.: Geologia do Couto Mineiro da Panasqueira. Comunicações dos Serviços Geológicos de Portugal **32**, 5–64 (1951)

Yamaji, A., Sato, K.: Clustering of fracture orientations using a mixed Bingham distribution and its application to paleostress analysis from dike or vein orientations. J. Struct. Geol. **33**, 1148–1157 (2011)

Stratigraphy and Structural Style of the Maghrebides Belt Foreland: Souk Ahras Sellaoua Unit Case (External Domain, NE Algeria)

Abdallah Chabbi, Asma Chermiti, and Stéphane Brusset

Abstract

The Sellaoua Unit is part of the foreland of the Maghrebides belt in northeastern Algeria and develops in the footwall of Tellian and Numidian thrusts sheets. A detailed geological mapping of Souk Ahras Sellaoua Unit (North–East of Algeria) supported by micro-paleontological and structural data allow us to reappraise the stratigraphy and the structural style of such area and characterize its relationship with the northern adjacent thrusts sheets. Data were collected from a sampling and observations along with four profiles for biostratigraphic study and five for structural constructions.

The obtained results show that the Sellaoua Unit of Souk Ahras area is made of carbonate marine formations ranging from Turonian to Paleocene unconformably overlain by detrital Miocene strata. Complex thrust systems have occurred during the Tertiary until the middle Miocene.

Keywords

Magrebides belt • Sellaoua unit • Stratigraphy • Structural style • Souk Ahras

A. Chabbi (✉)
Mohamed Cherif Messaadia University, Souk Ahras, Algeria
e-mail: a.chabbi@univ-soukahras.dz

Geodynamics and Natural Resources Laboratory, Badji Mokhtar University, Annaba, Algeria

A. Chermiti
Water Researches and Technologies Center, Ecopark of Bordj Sedria, Soliman, Tunisia

S. Brusset
Geosciences Environment Toulouse (GET), Paul Sabatier University–Toulouse III, Toulouse, France

1 Introduction

In northeastern Algeria, the external domain of the Maghrebides belt (Vila 1980) is characterized by an imbricate fan of thrust sheets over a detached and folded unit (Chabbi et al. 2016, 2019) which is called "Sellaoua Unit" (Vila et al. 1995). This complex structure is the result of several tertiary compressional phases (Leprêtre et al. 2018).

In the Souk Ahras region (Fig. 1a, b), the stratigraphy of the Sellaoua Unit and its relationships with the surrounding units are poorly known with the exception of a few regional or unpublished studies (David 1956). The northern part of Souk Ahras area (Fig. 1a, b) exhibits excellent outcrops for the Sellaoua Unit. Geological mapping has been performed together with micro-paleontological and structural studies, which allowed us to characterize the stratigraphy and structure of Sellaoua Unit in the Souk Ahras area.

2 Materials and Methods

The Sellaoua unit is part of the Maghrebides belt foreland series, in northeastern Algeria (Vila 1980). It outcrops between the Tunisian border and Souk Ahras city, and it continues westward to Ain Fakroune city (south of Constantine). It mostly consists of whitish carbonate formations outcropping below the allochthonous units (Tellian and Numidian thrust sheets) and in tectonic contact with the Triassic formation.

The present work is based on geological mapping supported by geological cross sections, using micro-paleontological, tectonic and structural data. More than sixty samples of marl, taken from four sections (Fig. 1b), have been dated. The sections are spread over three sectors in the region. From the west to the east, we distinguish the following sections: Oued Djedra section (OJ section), Dj. Bouallegue section (DB section), Ouled Driss section (OD section) and Chaabet el Ballout section (CB section). Five

M. Meghraoui et al. (eds.), *Advances in Geophysics, Tectonics and Petroleum Geosciences*,
Advances in Science, Technology & Innovation, https://doi.org/10.1007/978-3-030-73026-0_110

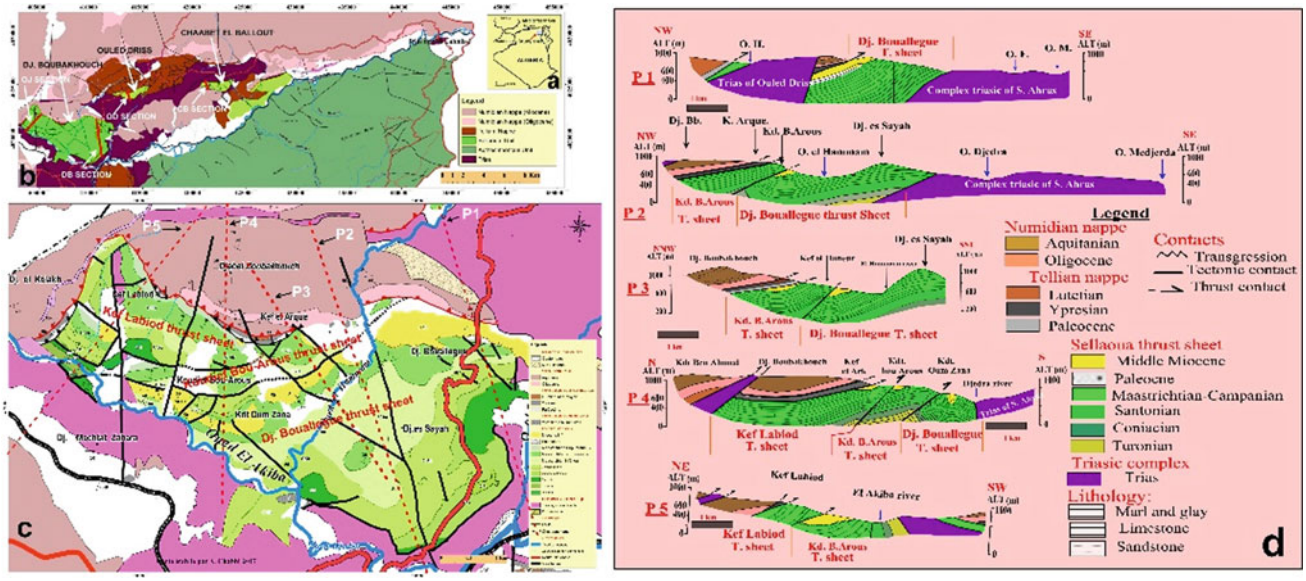

Fig. 1 **a** Schematic situation map, **b** regional geological map showing the structural Souk Ahras units and sampling cross-sections location, **c** study area geological map showing the structural cross-sections location, **d** geological cross sections

other structural sections exhibit the geological structure and tectonic style of the study area (Fig. 1c, d).

3 Results

3.1 Stratigraphical Results

The lithological analysis and micro-paleontological determinations of different samples taken from the Sellaoua outcrops, between (OJ) in the west of Dj. Boubakhouch and Chaabet el Ballot (CB) in the east, allowed us to define the stratigraphy of the Sellaoua Unit of Souk Ahras region and characterize its depositional environments. The stratigraphy and distribution of benthic, planktic foraminifera and ostracoda are summarized in table (Fig. 2). From base to top, the following succession was identified:

3.1.1 Turonian

Turonian is the oldest documented age in Sellaoua Unit of Souk Ahras region. It is cropping out on the right bank of Oued el Akiba (OJ.). It exhibits about fifty meters (50 m) of yellow limestone (beds of 30–40 cm) alternating with gray marl levels. It is defined by a rich association of planktic foraminifera (*Marginotruncana marianosi*, *Dicarinella primitiva, Marginotruncana sinuosa, Dicarinella concavata*) with the presence of rare benthic foraminifera (Fig. 2).

3.1.2 Coniacian

Outcropping only at Oued Akiba and is represented by about 150 m of gray marls and limestone containing exclusively planktic foraminifera of the *Marginotruncana sinuosa* biozone. They include *Marginotruncana coronata, Marginotruncana scheegansi* and *Marginotruncana primitiva*.

3.1.3 Santonian

Outcrops in Dj. Boubakhouch and is dominated by a series of gray marl, with rare decimetric levels of marl-limestone with yellowish patina. It is about 200 m thick, characterized by rich planktic foraminifer assemblage of *Dicarinella concavata* and *D. asymetrica* biozones associated to a benthic foraminifera and ostracoda (Fig. 2).

3.1.4 Campanian

Campanian is characterized by a 100-m thick package of grayish marls with abundant planktic foraminifera of *Globotruncanita elevate* biozone. The middle and upper Campanian is represented by 80 m alternating marl and marly calcairous surmounted by a bar of 60 m of chalky limestone containing Inocerames and ending with 10 m of marl and limestone. The planktic foraminifera contained in these series belongs to *Globotruncana ventricosa and G. calcarata* biozones. The benthic foraminifera and ostracoda exist but are not dominant (Fig. 2).

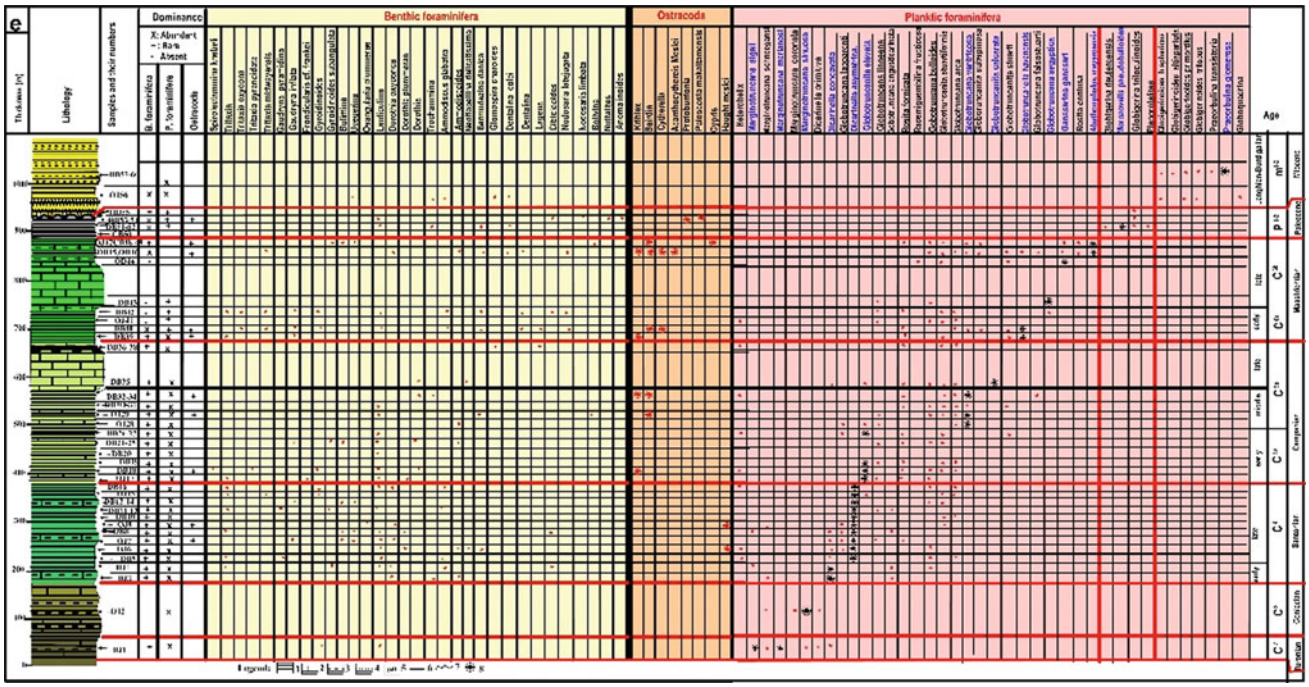

Fig. 2 Stratigraphic log showing the distribution of major foraminifera and ostracoda and sample locations, DJn: sample taken from OJ section and its number, DBn: sample taken from DB section, …). Legend: (1) marl and glay, (2) limestone, (3) marl-limestone, (4) sandstone, (5) sample number, (6) tectonic contact, (7) discontinuity, (8) biozone

3.1.5 Maastrichtian

Maastrichtian is characterized by three terms; the lower term is dominated by gray marl of lower Maastrichtian age determined by planktic foraminifera of *Globotruncanella havanensis* biozone. The middle and the third terms are upper Maastrichtian in age, they are represented by a bar of chalky white limestone with Inocerames (100 m thickness) topped by an alternation of limestone and gray marl (60 m). These terms are rich with planktic foraminifera of *Globotruncana aegyptiaca*, *Gansserinagansseri* and *Abathomphalus mayaroensis* biozones. The benthic foraminifera and ostracoda are diversified but less dominant than planktic (Fig. 2).

3.1.6 Paleocene

The Cretaceous—Paleocene transition is represented by a thick marly layer without any clear discontinuity. The Paleocene formation shows 120 m of dark gray marl. These are dated by planktic foraminifera of the early Paleocene (*Morozovella pseudobulloides* biozone), *Globigerina triloculinoides*, *Globigerina daujergensis* (Fig. 2) and rare Planorotalites. The thickness of the series is about 60 m.

3.1.7 Miocene

Miocene is unconformably overlying the previous series. It includes conglomerates, brown and greenish marls, sandstones and glauconitic sandstones. The thickness of the Miocene series varies from place to place and may exceed 200 m. The Planktic foraminifera association belonging to the *Praeorbulina glomerosa* biozone documents a Burdigalian—Langhian age (Fig. 2).

3.2 Structural Results

The structure and the tectonic style of the Sellaoua Unit are illustrated by the construction of five geological cross sections (P1 to P5, Fig. 1c, d). They show that the northern thrust sheets are a duplex constituted by a sole thrust in the Paleocene mudstones and a roof thrust in the Oligocene argillites. In the footwall of this duplex, the Sellaoua Unit displays thrust-related anticlines involving Mesozoic and Cenozoic strata. Triassic remnants are present in this thrust-wedge arrangement as witnesses of pre- or syncontractional salt tectonics (Fig. 1d: P2, P3, P4). The **faults** are dominated by a **reverse faults** trending E-W to NE-SW.

4 Discussion and Conclusion

Stratigraphic and biostratigraphic analyses of Sellaoua Unit in the Souk Ahras region show 950 m of carbonate series rich in planktic foraminifera associated with benthic foraminifera and ostracoda, ranging from Turonian to Paleocenein age, overlaid by a detrital Miocene series. The base of the

Sellaoua Unit remains unknown in the Souk Ahras region, while in the western part of the Sellaoua basin, the series begins in Jurassic age (Vila 1980). The dominance of planktic foraminifera on benthics in Sellaoua deposits reveals that it is a marine deposition environment of internal platform. The absence of Eocene- Oligocene deposits under the lower Miocene probably indicates that the Sellaoua basin was uplifted during this period and then it was deformed and eroded. This phase corresponds to the Atlasic phase. The transgression of the Miocene on the Sellaoua series indicates the subsidence of the Sellaoua basin during the Burdigalian—Langhian period.

The structure of the Sellaoua unit is characterized by the presence of thrust sheets, folds and reverse faults NE-SW to E-W trending, dipping to the north, involving Miocene formations attributed to Burdigalian—Langhian, which indicates a compressive N-S phase that probably corresponds to the Tortonian phase. This phase led to the folding and thrusting of Sellaoua Unit and the setting up of Tellian and Numidian thrust sheets which are overthrusted on the Sellaoua Unit in this area (Chabbi et al. 2019).

Acknowledgements We thank all those who participated in the production of this paper and its improvement in particular the anonymous reviewers and Mr. Abdelmadjid Dammak for its language editing.

References

Chabbi, A., Chouabbi, A., Chermiti, A., Ben Youssef, M., Kouadria, T., Ghanmi, M.: La mise en évidence d'une nappe de charriage en structure imbriquée: Cas de la nappe tellienne d'Ouled Driss, Souk-Ahras, Algérie. Courrier Du Savoir **21**, 149–156 (2016)

Chabbi, A., Chermiti, A., Chouabbi, A., Benyoussef, M.: The external domain of Maghrebides belt on the North–East of Algeria, Souk Ahras segment: definition of structural units, block structure and timing of thrusts setting. In: Rossetti, F., et al. (eds.) The Structural Geology Contribution to the Africa-Eurasia Geology: Basement and Reservoir Structure, Ore Mineralisation and Tectonic Modelling, pp. 237–41. Springer Nature, Cham (2019)

David, L.: Etude géologique de la haute Medjerda. Bulletin Service de la carte géologique de l'Algérie, n° 11, Algérie (1956)

Leprêtre, R., Frizon de Lamotte, D., Combier, V., Gimeno-Vives, O., Mohn, G., Eschard, R.: The Tell-Rif orogenic system (Morocco, Algeria, Tunisia) and the structural heritage of the southern Tethys margin. BSGF Earth Sci Bull **189**(2):10 (2018)

Vila, J.M.: La chaîne alpine d'Algérie nord oriental et des confins Algéro-tunisiens. Thèse de doctorat d'état en science. Université Pierre et Marie Curie, France. 665p (1980)

Vila, J.M., Feinberg, H., Lahondère, J.C., Gourinard, Y., Chouabbi, A., Magné, J., Durand-Delga, M.: The sandy uppermost Oligocene channel and the Miocene of Sidi-Affif area in their East Algerian structural setting -the Saharan Origin of the Numidian and the calendar of the Miocene overthrusts. Comptes Rendus De l'Academie Des Sciences Serie 2, **320**(10), 1001–1009 (1995)

Underlying Geological Structure of the Northern Edge of the Mitidja Basin and the Sahel Fold Near Tipasa Town (Algiers, Algeria) Using Magnetotellurics: First Results

Naïla Kerbadj, Abderrezak Bouzid, Walid Boukhlouf, Sofiane Saïd Bougchiche, Aboubakr Deramchi, Mehdi Amine Guemache, Hamou Djellit, and Abdeslam Abtout

Abstract

Magnetotelluric data were collected at seven stations in the northern edge of the Algerian Mitidja basin (around Sidi Rached in Tipasa town,Northern Algeria). MT stations are roughly aligned along a 5-km N-S trending profile, perpendicular to the main geological structures. Dimensionality analysis indicates that the resistivity structure is globally 2D, with small 3D local features. The geoelectric strike of N80°E agrees with the surface geological structures. Data, from 2D inversion, were collected in order to image the underlying deep Mitidja electrical structures and are also in agreement with these surface data. The Mitidja basin and the Sahel fold are still characterized by active tectonics; their present geological knowledge leads to natural risks, particularly seismic hazards. The resistivity model along the profile exhibits a significant deep resistive structure overlying a very conductive body rising up toward the north as related to the inverse fault separating the syncline of Mitidja basin from the Sahel anticline.

Keywords

Mitidja basin • Tipasa • Magnetotellurics • Inversion • Algeria

1 Introduction

Magnetotellurics (MT) is a passive electromagnetic method allowing the investigation of the electrical resistivity structure from the near surface to the upper mantle (Jones et al. 1989). A 5-km long N-S trending profile was studied at Sidi Rached, near Tipasa, on the northern border of the Mitidja basin (Fig. 1a). The depth and the nature of the substratum of the Mitidja basin as well as the thickness of the recent (from the Late Miocene) sediments remained unknown (Heddar et al. 2013). The subject of this study was to image the underlying geoelectric structures beneath Mitidja basin. To this end, we presented an MT data analysis and the corresponding 2D isotropic modeling.

2 Geological Settings

The Mitidja basin is located in the central part of Northern Algeria. It extends, between longitudes 2.00° E and 3.80° E and latitudes 36.20° N and 37.00° N, from east to west over hundred km (Fig. 1a). It is a large flat syncline in structure filled with sediments and volcanic rocks. Its sedimentary filling consists of Miocene to Pliocene marine marls, calcareous and sandstones covered by quaternary heterogeneous continental deposits (Heddar et al. 2013). It is bordered to the north by the Sahel anticline with a maximum elevation not exceeding 200 m. To the south, the basin is dominated by the Blida Mounts of the Tell Atlas. The basin cover was deformed along faults like those at the limit with the Tell Atlas and the Sahel fold (Heddar et al. 2013). In particular, the southern border of the Sahel anticline is underlined by a flexure corresponding to a deep basement fracture not apparent on the surface. This area is characterized by low to moderate seismicity but contains significant active structures at the origin of several natural hazards (earthquakes and flooding (Meghraoui 1989) that disturbed the topography of the studied MT sites.

N. Kerbadj (✉) · A. Bouzid · W. Boukhlouf · S. S. Bougchiche · A. Deramchi · M. A. Guemache · H. Djellit · A. Abtout
CRAAG, BP 63, Route de l'Observatoire, Bouzaréah, 16340 Algiers, Algeria
e-mail: neila.kerbadj@craag.edu.dz

N. Kerbadj · A. Deramchi
USTHB, BP 32, El Alia, Bab Ezzouar, 16111 Algiers, Algeria

M. Meghraoui et al. (eds.), *Advances in Geophysics, Tectonics and Petroleum Geosciences*,
Advances in Science, Technology & Innovation, https://doi.org/10.1007/978-3-030-73026-0_111

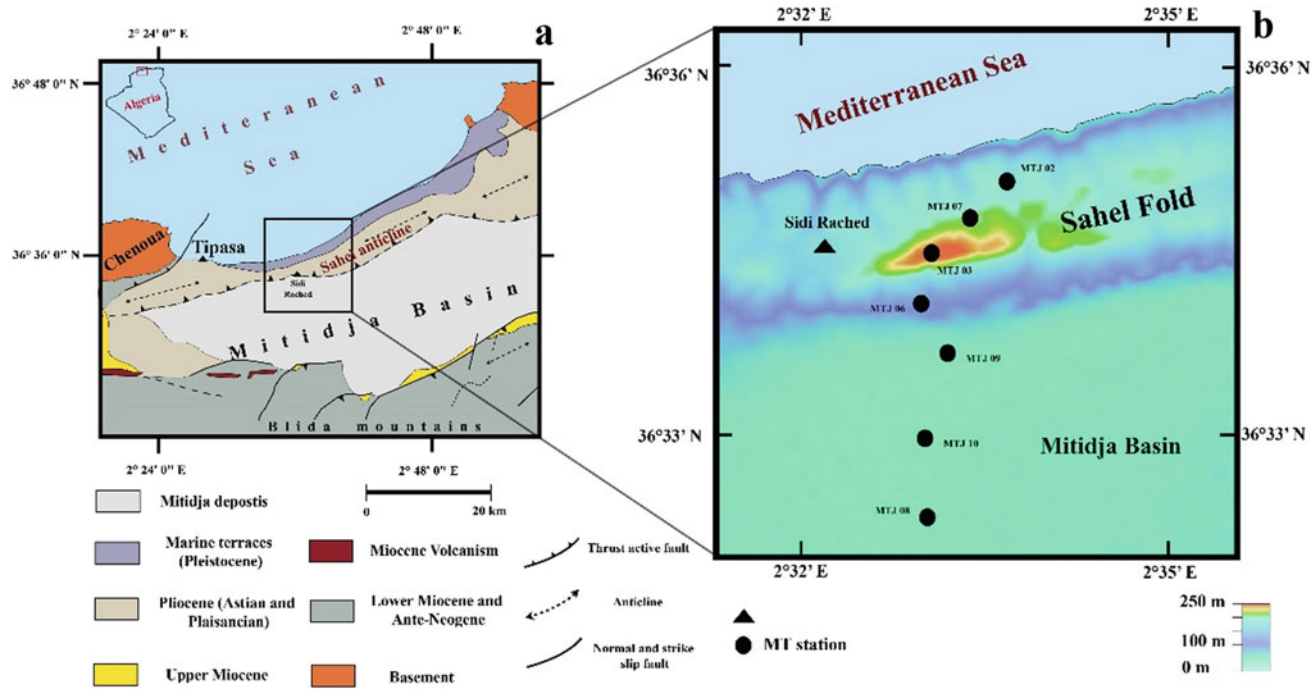

Fig. 1 **a** Simplified geological map modified from Maouche and Harbi (2018). **b** MT sites distribution plotted in black circle along a N–S profile (SRTM topo image, http://srtm.csi.cgiar.org)

3 Magnetotelluric Data

3.1 Data Acquisition and Processing

The MT data were collected between 2008 and 2015 from seven sites, located along a N-S profile (Fig. 1b). This 5-km long profile was chosen perpendicular to the main structural direction defined on the geological map. The distance between the sites varies from 0.5 to 1.2 km. The broadband measurements were made using V5 system 2000 of Phoenix Geophysics. The audio-magnetotelluric (AMT) recordings were performed during $\sim$1 h, whereas the MT ones were carried out over a time range of 3–24 h. The time series data were processed to give estimates of the impedance tensor and induction vectors using a code provided by the manufacturer, in the period range 0.0001–1000 s.

3.2 Dimensionality Analysis

The phase tensor method was applied to obtain information about the dimensionality of the regional structure (Caldwell et al. 2004). The dimensionality is shown (Fig. 2a) by the color that represents the skew angle (β): Most values for frequency range 0.1–0.001 Hz are distributed within a 5° interval, relatively close to 0°. This confirms that the resistivity structure can be assumed as 2D (Fig. 3). Some values, exceeding 5°, highlight small local features. In a next step, the geoelectric strike angle was calculated using phase tensor (Caldwell et al. 2004) in the whole period range. Figure 2b shows the rose diagram values for all frequency ranges. The estimated direction of N170° E was, however, subjected to 90° ambiguity; the latter was solved by referring to the geological structures. The assumed regional strike here was then fixed to N80° E.

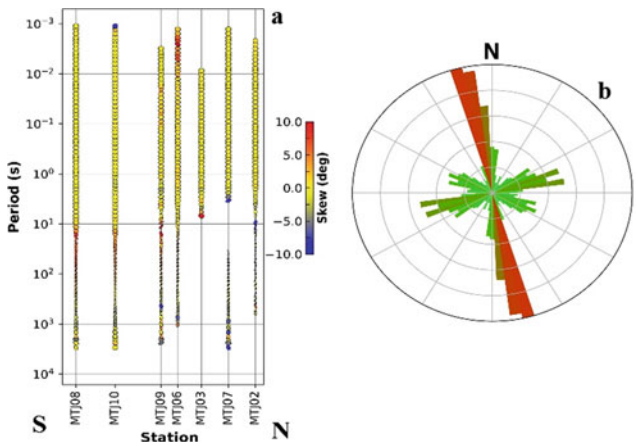

Fig. 2 **a** Skew angle β plot along the profile. **b** Rose diagram of strike angles obtained by the phase tensor method for all sites and all periods

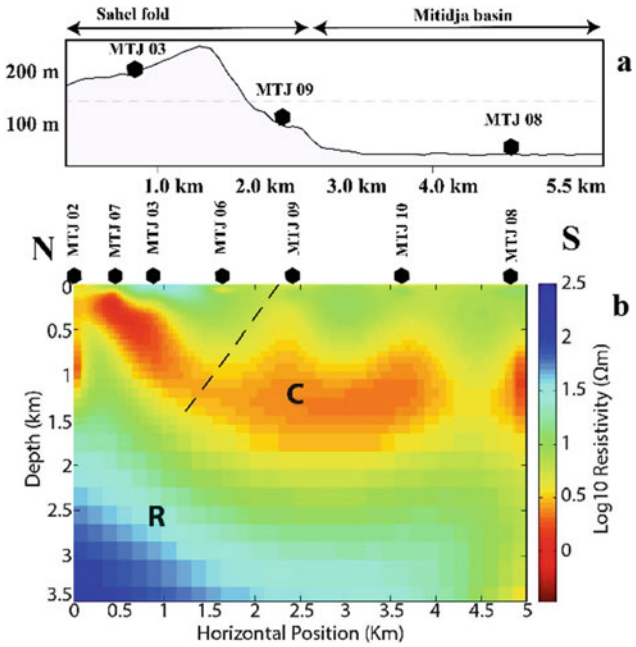

Fig. 3 **a** Topographic profile. **b** 2D resistivity model profile obtained with an rms of 1.86. Dash line refers to an inverse fault deduced from geological studies (Heddar et al. 2013; Maouche et al. 1999)

3.3 Two-dimensional Inversion

Several 2D inversion models have been carried out using Occam inversion code (Degroot-Hedlin and Constable 1990). The seven sites were used for the inversion using a period range of 0.001–01 s. The model shown in Fig. 3 was obtained by inverting apparent resistivity and phase data of both transverse electric (TE) and transverse magnetic (TM) modes, using a 100 Ω m homogenous half space as a starting model. An error floor of 10% was set for the apparent resistivity and 2.87° for the phase for both modes. The inversion process converged finally with an rms of 1.86.

4 Results and Discussion

Figure 3B shows the model obtained by the inversion of MT data of both modes TE and TM down to 3.5 km in depth. The model illustrates the transition from the Mitidja basin to the Sahel anticline that corresponds to the rising of the structures going northward. A first conducting layer (3 Ω m to 15 Ω m) consists of the ancient alluvium covering the Mitidja basin. Consisting of Plio-quaternary formations, it overlays a very conductive anomaly **C** (0.5 Ω m to 4 Ω m) that reaches the surface to the north (the Plio-quaternary formation is completely eroded toward the Sahel fold). The high conductivity might be related to fluid content within these marine Pliocene formation. Hence, from 2.5 km depth, a resistive structure **R** appears to the north of the profile with resistivity values >100 Ω m, which can correspond to Miocene deposits. The rise of structures toward the profile is related to the presence of the reverse fault that separates the Sahel fold from Mitidja basin (Fig. 3b). The resistivity model (Fig. 3b) is consistent with the geological cross-sections of the Sahel ridge (Aymé et al. 1954; Maouche et al. 1999).

5 Conclusions

The Sahel fold outlines the main upper marine Pliocene outcrops. The Mitidja basin contains the Villafranchian and alluvial layers of the recent quaternary. Nowadays, the latter is characterized by brittle deformation illustrated by several earthquakes. Other Plio-quaternary tectonic movements are not directly observable, but deep structures can be evidenced by the MT modeling. The result of the inversion shows an elongation of the structure in agreement with the surface geological data of the study area. This highlights strong compression at the limit, between the Mitidja syncline and the Sahel fold anticline, underlined by a reverse fault.

References

Aymé, A., Aymé, J.-M., Magne, J.: Etude des terrains Néogènes de la cluse du Mazafran Sahel d'Alger). Bulletin n°1, Fascicle **11**, 129–150 (1954)

Caldwell, T.G., Bibby, H.M., Brown, C.: The magnetotelluric phase tensor. Geophys J Int **158**, 457–469 (2004)

Degroot-Hedlin, C., Constable, S.: Occam's inversion to generate smooth two dimensional models from magnetotelluric data. Geophysics **55**(12), 1613–1624 (1990)

Heddar, A., Authemayou, C., Djellit, H., Yelles, A.-K., Déverchère, J., Gharbi, S., Boudiaf, A., Van Vliet Lanoe, B.: Preliminary results of a paleoseismological analysis along the Sahel fault (Algeria): new evidence for historical seismic events. Quatern. Int. **302**, 210–223 (2013)

Jones, A.G., Chave, A.D., Egbert, G., Auld, D., Bahr, K.: A comparison of techniques for magnetotelluric response function estimation. J. Geophys. Res. **94**, 14201–14213 (1989)

Maouche, S., Harbi, A.: The active faults of the Mitidja basin (North Central Algeria): what does the seismic history of the region tell us? A review. Euro-Mediterranean J. Environ. Integr. **3**, 21 (2018)

Maouche, S., Meghraoui, M., Morhange, C., Belabbes, S., Bouhadad, Y., Hddoum, H.: Active coastal thrusting and folding, and uplift rate of the Sahel Anticline and Zemmouri earthquake area (Tell Atlas, Algeria), 2nd edn. (1999). Tectonophysics **509**, 69–80 (2011)

Meghraoui, M.: Blind reverse faulting system associated with the Mont Chenoua-Tipaza earthquake of 29 Oct 1989 (north-central Algeria). Terra Nova **3**, 84–93

Subsurface Structural Trends from Gravity Data Analysis (Northern Tunisian Atlas)

Imen Hamdi Nasr, Benen Sarsar Nawali, Mohamed Hedi Inoubli, Oussama Abidi, Adnen Amiri, and Haifa Boussiga

Abstract

Detailed gravity data in conjunction with available geological data are analyzed to better understand the underlying structures in the area. The gravity data analysis includes the construction of gravity anomaly maps, upward continuations, residual and derivative maps, and Euler deconvolution. The comparison of gravity, geological and structural maps allows the identification of major structural directions and trends of the study area. It confirms some structural elements gathered from outcrops and defines new ones. The interpretation of the gravity data indicates that the study area is affected by many subsurface structural trends. The NE–SW is the major trend direction, related to J. Chehid and Bled TejraAkseb trend. The NW–SE is the second dominant trend bordered to the North of Bled El Ghorfa. Other trends defined through the interpretation of gravity data include the N–S direction, related to Lakouat fault trend. This interpretation led to the establishment of a structural map of the area.

Keywords

Euler deconvolution • Faults • Gravity anomaly • Positive anomaly • Tilt angle • Tunisia

1 Introduction

The North of Tunisia pertains to the northeastern edge of the African plate. It is bordered by the Mediterranean Sea and the Straight of Sicily to the North and northeast, with an uppermost crust bearing Meso–Cenozoic prevalent sedimentary packages that have long suffered Alpine and Atlassic orogenies.

The present configuration of the Tunisian margin is the result of the convergence and collisional movement between the African and European plates including the Tethys geological domain. In the concerned region, an Early Mesozoic rifting phase has structured basin sunk salt dominated Triassic deposits and was seconded by a passive margin tectonic basin style during the entire Meso–Cenozoic times.

The present paper aims to understand the subsurface structural trends within the northwestern Tunisia using gravity data.

The main goal of this work is to analyze gravity anomaly data to identify possible lineaments in the Western Tunisia area. Our pattern recognition criteria are based specially on the enhanced horizontal gradient (EHG), tilt angle method (TAM), and the Euler deconvolution (ED). All three methods closely agree on determining the horizontal locations of contacts; the last two also give similar results for source depths.

2 Gravity Data Analysis

A detailed high-resolution land gravity survey was carried out entailing a total of 660 stations of the acquired data over an area of approximately 640 km^2, in an average of almost one station per squared kilometer. Free-air and Bouguer gravity corrections were performed using sea level as a datum and a reduction density of 2.4 g / cm^3. Bouguer and terrain corrections were calculated automatically using a

I. H. Nasr (✉) · B. S. Nawali · M. H. Inoubli · O. Abidi · A. Amiri · H. Boussiga
URGAMM, University of Tunis-El Manar, Tunis, Tunisia

I. H. Nasr
Faculty of Science of Bizerte, Carthage University, Tunis, Tunisia

B. S. Nawali
ETAP Entreprise Tunisienne D' Activités, Tunis, Tunisia

M. Meghraoui et al. (eds.), *Advances in Geophysics, Tectonics and Petroleum Geosciences*,
Advances in Science, Technology & Innovation, https://doi.org/10.1007/978-3-030-73026-0_112

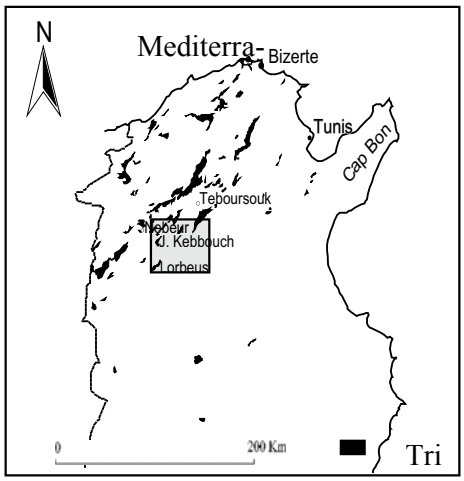

Fig. 1 Location of the study area

digital terrain model obtained by digitizing 1/50,000 topographic maps.

The complete Bouguer gravity anomaly values range from −15 mGal to the southeast in the Bled Elgorfa, to +2 mGal in J. Boukhil to the northwest and in J. Aksab to center-east of the map. Positive anomalies are situated in the central-eastern part of the map; they coincide with Triassic and Cretaceous outcrops at Jebel El Zitoun, Sidi el Mahdi, Jebel Argoub Naoua and Jbel Sfa Boubakrer, J. Aksab, J. Cheid, J. Touila zones. The maximum amplitude occurs over the lower cretaceous outcrops (Fig. 1).

The positive anomaly, distinguished by its higher amplitude, corresponds to the cretaceous series with marls and limestone characterized by a significant density contrast.

Negative anomalies correspond mainly at Quaternary outcrops; they are located in the North in Krib plain and synclinal of Gaafour, in the southwestern part of the map in Bled El Gorfa plain. Eocene series is also characterized by negative gravity response in the synclinal of OuedGaafour in the southwestern part of the map.

Residual gravity anomaly maps exhibit the combined effects of geologic bodies of distinctive densities, which may have varying shapes, dimensions, and burial depths. Thus, the gravity field is caused by the superposition of signals from many different bodies at different depths.

3 Data Enhancement and Interpretation

To help differentiate various gravity signals, we have implemented a three-stage analysis. First, residual gravity anomalies were computed by removing the regional anomalies from the complete Bouguer anomalies . Second, the enhanced horizontal gradients were calculated. Finally, the TAM image was provided to illustrate the recognition of the horizontal location and depth of geologic contacts as shown in Fig. 2

In order to highlight the shallow source anomalies, we applied a continuation filtering process designed to obtain a separation of long-wavelength anomalies from the short ones.

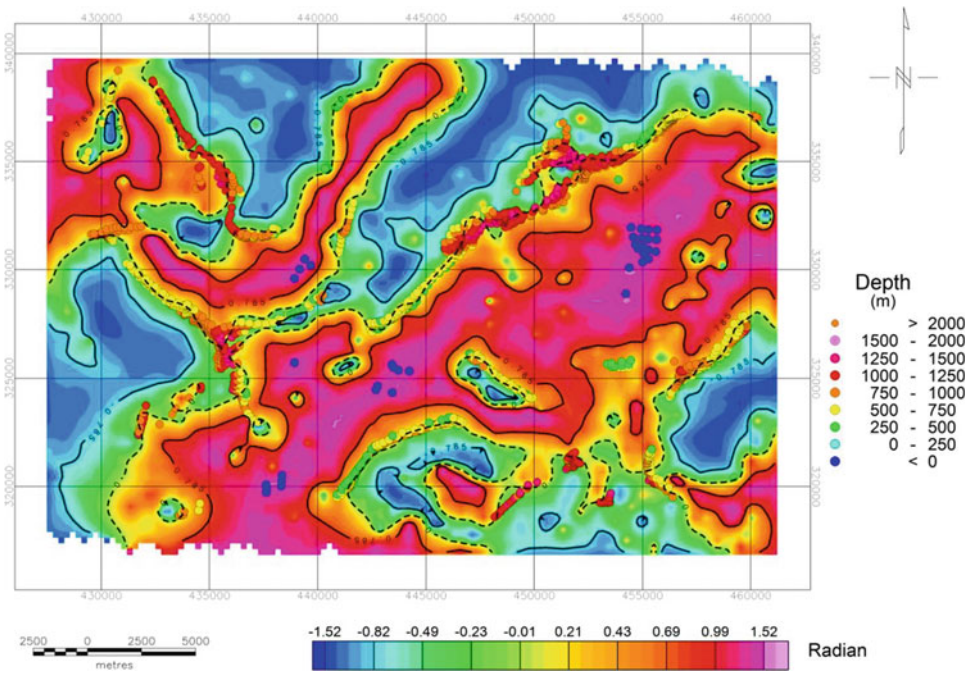

Fig. 2 Comparison of TAM images (dashed lines show the 0 rad contour of the tilt angle. Solid lines are contours of the tilt angle for $-\pi/4$ and $+\pi/4$ radians) and ED results; the source depths and locations from TAM and ED methods are well correlated

The gravity field is the superposition of signals in close connection with the above-defined parameters. In order to accentuate the shallow source anomalies, a designed continuation filtering process was applied leading to a separation of long-wavelength anomalies from the short-wavelength ones.

In the present case study, the regional component (Jacobsen 1987) was computed through upward continuing the Bouguer gravity grid to 25 km (average crustal thickness; Buness et al. 1992); it is relevant to indicate that for higher continuation levels, the extracted map shape is almost unchanged.

Therefore, a residual gravity map was computed by subtracting the regional grid from the Bouguer gravity grid. Derivative maps were also computed in order to enhance the short-wavelength features that usually correspond to shallow geological elements.

This map expresses shorter-wavelength anomalies with values ranging between −3 and +3 mGal. High amplitude maxima are located in the center-east and occur over the lower cretaceous of the big anticline of Bled Tejra-Aksab, to the north they correspond to the southern part of J. Cheid-Lakouat with a lateral extension to the south. The northwestern part corresponds partially to the Triassic outcrops of J. Boukhil, which also provided high response amplitude. In contrast, low amplitude anomalies are superimposed to Quaternary and Eocene deposits. The NE–SW trending lineaments in the study area are also supported by the residual gravity contours. The interpretation reveals the particular usefulness of these data spatially for mapping shallow faults. Longer wavelength features, typically the major tectonic elements such as basin bounding faults, and relative sediment thickness are also well expressed. Comparisons of various gravity Bouguer anomalies and their bounded components showed to be powerful to delineate subsurface geometry and distribution and locate promising areas (Hamdi Nasr et al. 2010).

The comparison between surface geology and Bouguer anomaly maps helps show that Triassic terrains of Lorbeus Bougrine do not express specific Bouguer anomaly responses. Over Cretaceous outcrops, in general, gravity Bouguer anomaly response is positive. The Tertiary series are associated with low Bouguer anomaly responses. The Quaternary series are associated with low, or even the lowest gravity responses. The low gravity response of synclines and troughs contrasts clearly with higher response of the anticline structures.

The tilt angle map of the study area highlights a short wavelength and reveals the presence of main gravity trends, NE–SW, which coincide with the main regional structural lineaments. One can conclude that there are more local uplifts in the northern edges of central uplift than those of the others. It is interesting to note that the TAM tends to convey the edge detection from uplifts at all scales and depths showing that the simple form of the TAM only displays the contours -π/4, 0, and +π/4 radians. The zero contours estimate the location of abrupt lateral changes in the density of deeper materials. This map shows short wavelength and reveals the presence of main gravity trends.

In the northwestern part, the southeast of J. boukhil is characterized by two parallel NW–SE lineaments in the tilt derivative, with the distance between the $-\pi/4°$ and $+\pi/4$ contours typically less than 2–2.5 km. This distance is twice the source depth (assuming contact source geometry), so sources indicated by the tilt contours are predominantly beneath the surface, the southern one is deeper than the other. This lineament borders Bled El Ghorfa region to the northwest.

Within the Aksab anticline, the tilt contours are much more widely spaced. These contours define gravity lineaments as well as areas of more chaotic contours which in part could be due to anomaly interference.

4 Conclusions

The integrated interpretation of the geological outcrops together with the near-surface gravity responses enabled a direct correlation between gravity anomalies and subsurface sources. The identified features constitute themselves new constraints to better understand the geological architecture of the area. This information can be used to better establish the structural model in order to infer the tectonic evolution of the region which is strongly linked to the western Mediterranean geodynamic evolution. Indeed, the interpretation of the gravity maps allowed gathering a synthetic overview of the underlying structures in the area that is largely destroyed by the activity of the existing multi-directional fault systems. The positive anomalies of, Lakouat, next to J. Boukhil, Bled TejraAkseb, which are interpreted as resulting from positive density contrast, are generally associated with the NE-directed faults.

The identified faults bordering Bled El Gorfa anomaly help to clarify its structure. It consists of a NW-directed negative anomaly, already well expressed in all gravity maps (residual, EHD, TAM, and Euler deconvolution). NW-directed faults are well-known in northern Tunisia and are characterized by an extensional movement, which is responsible for the partition of the region into blocks (Hamdi Nasr 2008, Amiri et al. 2011). Thus, the NW-directed faults limit graben structure; here, the idea that Bled El Ghorfa pertains to a depressed structure can be argued.

Fault systems disposition is expressed by the coexistence of compressive and extensive structures due to the occurrence of a compressive regime in the overall area.

The presented gravity analysis clarifies the identified inherited dislocations in the fault systems, some of which were sealed by the Quaternary.

References

Amiri, A., Chaqui, A., Hamdi Nasr, I., Inoubli, M.H., Ben Ayed, N., Tlig, S.: Role of prexisting faults in the geodynamic evolution of Northern Tunisia, insights from gravity data from the Medjerda valley. Tectonophysics **506**, 1–10 (2011)

Hamdi Nasr, I., Amiri, A., Inoubli, M.H., Ben Salem, A., Chaqui, A., Tlig, S.: Structural setting of Northern Tunisia insights from gravity data analysis, Jendouba Case Study. Pure Appl. Geophys. (2010)

Hamdi Nasr, I., Ben, S.A., Inoubli, M.H., Dhifi, J., Alouani, R., Chaqui, A., Perthuisot, V.: Apports de la gravimétrie dans la caractérisation des structures effondrées dans la région de Nebeur (Nord Ouest de la Tunisie). Swiss J. Geosci. **101**, 17–27 (2008)

Hamdi-Nasr, I., Inoubli, M.H., Ben Salem, A., Tlig, S., Mansouri, A.: Gravity contributions to the understanding of salt tectonics from the Jebel Cheid area (dome zone, Northern Tunisia). Geophys. Prospect. **57**, 719–728 (2009)

Jacobsen, B.H.: A case for upward continuation as a standard separation filter for potential field maps. Geophysics **52**, 1138–1148 (1987)

Najd-Related Transpressional Deformations in the Atalla Shear Zone (Eastern Desert, Egypt)

Zakaria Hamimi, Wael Hagag, Samir Kamh, and Asmaa El-Araby

Abstract

The Atalla Shear Zone (ASZ) is a NW-oriented mega-shear that belongs to the Najd-Shear Corridor in the Central Eastern Desert of Egypt. The present study focused on the structural and tectonic evolution of the ASZ throughout integrated space-born optical-based mapping and structural-field work. The ASZ area comprises a Neoproterozoic rock succession including serpentinites, island-arc assemblage of metasediments and metavolcanics, Dokhan Volcanics, Hammamat Sediments, and granitoids. A lithological mapping was carried out using Landsat-8 (ETM+) and ASTER, and the image processing techniques included false color composites (FCC), principal component analysis (PCA), and RGB band ratios (BR). The predominant trends were ENE-WSW and NE-SW. The transcurrent shearing related to ENE-WSW shortening in the ASZ resulted in prominent transpressive shear structures among which we find shear-related folds, imbricated fans and antiformal stacks, and passive-roofed- and domino-style-thrust duplexes. A reasonable structural history involving four successive deformation phases (D1–D4) was established. D_1 was recorded within the amphibolitic enclaves found at Um Baanib area. D_2 was a syn-accretion shortening stage, concurrent with the E–W assembly of Gondwanalands, and responsible for the W- and WSW-propagated thrusts and thrust-related folds. D_3 and D_4 were post-accretion phases that resulted in formation of the Najd-related ASZ with sinistral sense of shearing. The emplacement and exhumation of the Meatiq Gneiss Dome, and also the deposition of the Hammamat Volcanosedimentary Sequence in fault-controlled sags and pull-apart, are believed to be post-accretion and associated with the D_3 phase.

Keywords

Atalla shear zone • Najd-related transpression • Pan-African belt • Arabian-Nubian shield

1 Introduction

In the Eastern Desert of Egypt, the Najd Shear System (NSS) still has problematic issues that need to be addressed. The time, sense, and scale of shear are the most important of these issues. The present work was an integrated study using remote sensing techniques and structural-field mapping to investigate the shear criteria and discuss the deformation history; another objective was to set up a model depicting the tectonic evolution of the Atalla Shear Zone (ASZ; Fig. 1). Structurally, the study area can be classified into three main domains (e.g., Akaad and El-Ramly 1960, Akaad and Noweir 1980, Abd El-Wahed 2010): Meatiq Domain (MD); Atalla Shear Zone Domain (ASZD); and Wadi Hammamat Domain (WHD). The processing of remote sensing data enabled high-resolution discrimination for the different lithologies and structural elements, hence constructing a modified geological map for the ASZ. Furthermore, the structural setting and tectonic evolution of the ASZ would be addressed within the frame of the NW–SE-oriented Najd Shear System, which crosses the central part of the Arabian Shield for 1300 km and passes through the Eastern Desert of Egypt forming the so-called Najd Shear Corridor.

2 Materials and Methods

The remote sensing data used in the present study include both ASTER and Landsat-8. These images are preprocessed and processed using different remote sensing techniques

Z. Hamimi (✉) · W. Hagag · A. El-Araby
Department of Geology, Faulty of Science, Benha University, Banha, 13518, Egypt

S. Kamh
Department of Geology, Faculty of Science, Tanta University, Tanta, 31527, Egypt

M. Meghraoui et al. (eds.), *Advances in Geophysics, Tectonics and Petroleum Geosciences*, Advances in Science, Technology & Innovation, https://doi.org/10.1007/978-3-030-73026-0_113

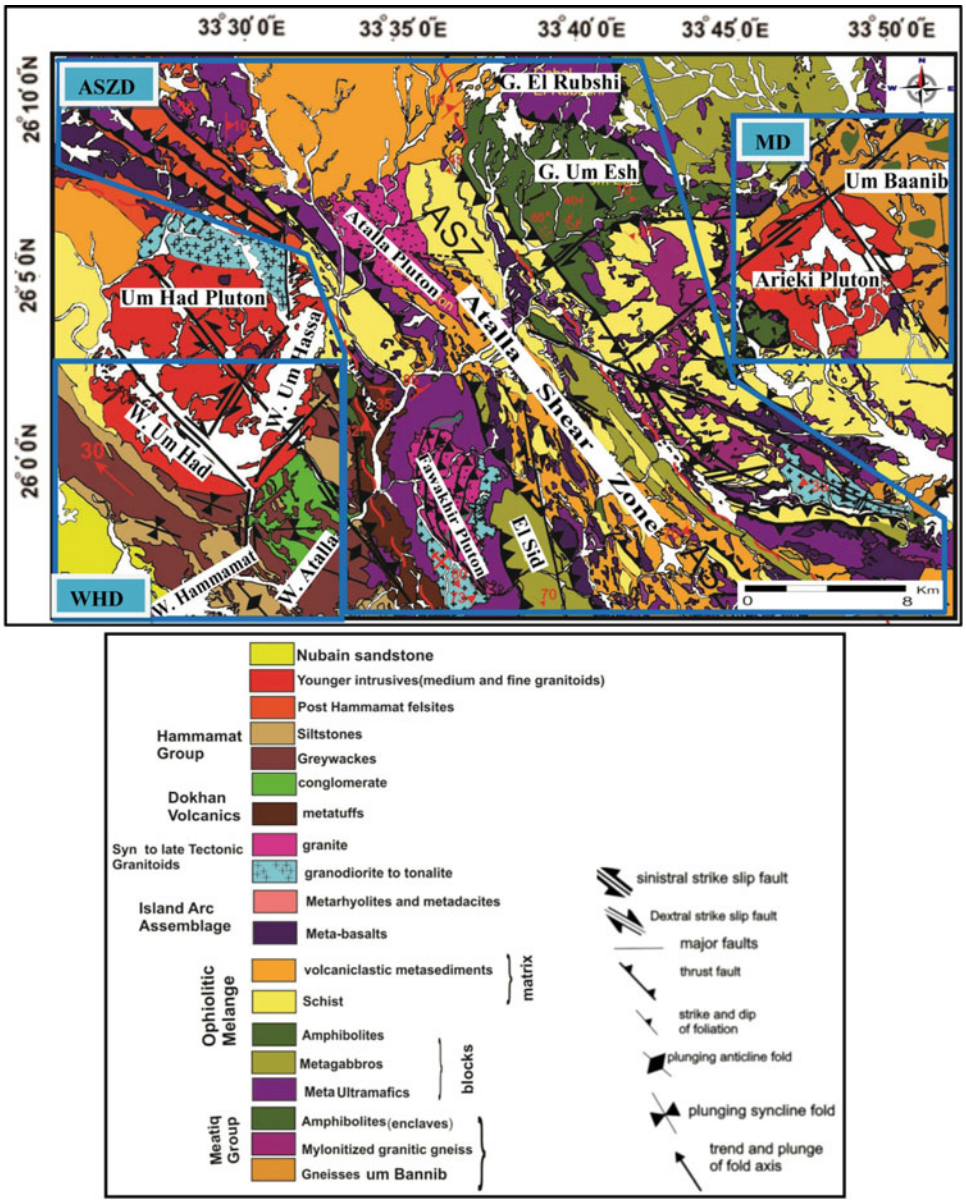

Fig. 1 Geological map of the Atalla Shear Zone and its environs (this study); MD: Meatiq Domain, ASZD: Atalla Shear Zone Domain, and WHD: Wadi Hammamat Domain

such as false color composite (FCC), principal component analysis (PCA), minimum noise fraction (MNF), and band rationing (BR). The satellite images were analyzed and processed using different software including ENVI 5.1, Erdas Imagine 9.2 and ArcGIS (10.1). For lineament extraction, some software, such as PCI Geomatica, were used. Rock Work, Steronet, surfer and Global Mapper software have also been applied during the study. Such techniques allowed us to discriminate various lithologies in the study area including gneisses, ophiolitc mélange, island-arc assemblage, Dokhan volcanics, Hammamat Sediments, Atalla felsites, and different granitoids. During the field work, lithological and structural contacts were checked, as well as many representative field photographs were taken. All the data collected were integrated to define the structural elements and describe the nature of tectonic movements deforming the Atalla Shear Zone. About 120 thin sections were prepared for the petrographic investigation of the different rock units. Based on the previous geological maps published on the study area and the remote sensing images, modified geological and structural maps were constructed. Some structural cross sections and sketches, as well as a 3D tectonic model, were made to depict the deformational stages and tectonic evolution of the study area.

3 Results and Discussion

The present study is an attempt to reappraise the geological and structural setting of the Atalla Shear Zone and its surroundings including Meatiq, Fawakhir, Um Had and Hammamat areas (located in the central Eastern Desert, Egypt) aided by remote sensing and GIS techniques. Remote sensing data were used to discriminate between the different rock units in the study area. This distinction between the rocks was accompanied by a detailed structural-field investigation of the base for a modified map compared to the previous maps (e.g., Akaad and El-Ramly 1960; Amer et al. 2010; Hassan et al. 2017). The remote sensing results were verified through the field work and petrographic investigation. The processes of image enhancement include different techniques. True color composite (TCC), false color composite (FCC), principal component analysis (PCA), minimum noise fraction (MNF) and band ratioing (BR) were applied to enhance the discrimination rate between the different rock units. As a consequence, the Neoproterozoic basement succession exposed in the study area was classified into eight groups including different rock units complemented by the field work and petrographic study. The groups include Meatiq Group, Ophiolitic Melange, island-arc assemblage, Syn- to late-tectonic granitoids, Dokhan Volcanics, Hammamat Sediments, post-Hammamat Felsites, and younger intrusives. Meatiq Group includes Gneisses (Gn), Mylonitized Granitic Gneiss (MGn) and Amphibolites. Ophiolitc Mélange includes blocks and matrix where blocks include metaultramafics, metagabbros, and amphibolites while matrix includes schists (talc schist, actinolite schist, tremolite talc schist, muscovite schist, and graphite schist), and volcaniclastic metasediments. Island-arc assemblage is represented by metabasalts. Syn- to late-tectonic granitoids represented by different plutons include Abu Ziran, Um Sheqila, Fawakhir, and Atalla Plutons. Dokhan Volcanics are represented by metatuffs and metabasalts. Hammamat Sediments include metaconglomerates, metagreywackes, and metasiltstones. Post-tectonic intrusives are represented by Arieki and Um Had granitic plutons.

As the ASTER channels are more continuous in the (SWI) bands than of Landsat-8, ASTER is the best for the minerals identification (Crosta et al. 2003). Several spectral indices were used for the mineral detection and among them are b7/b6 to distinguish muscovite and b5/b4 to distinguish biotite, chlorite, and amphiboles (ferrous silicates) (Hewson et al. 2001, 2005) while b5/b3 used to distinguish mafic minerals (ferrous iron, Fe 2+) (Rowan and Mars 2003). In the present study, the automatic methods for lineament extraction based on the edge filtering techniques were applied. Shaded relief images extracted from digital elevation model (DEM) are used by applying eight sun azimuths including 0°, 45°, 90°, 125°, 180°, 225°, 270°, and 315°, and the image resulting from combining the eight angles was used for the lineament extraction. In the case of 0° and 180° angles, the E–W, NW–SE, and NE-SW trends are detected, and E–W trend is the dominant. In the case of 45° and 225° angles, NW–SE trend is the dominant trend. In the case of 90° and 270° angles, N–S, NW–SE, and NE–SW trends are recorded and the dominant trend is N–S. In the case of 135° and 315°, NE–SW and E–W trends are recorded, and the dominant trend is NE–SW. In the case of combined shaded relief image, NE–SW, N–S, and NW–SE trends are recorded and NE–SW is the dominant trend.

In the Meatiq Domain, foliations associated with thrusts are deflected, folded, and transposed into the foliation within the high strain zone of the NW–SE striking ASZ. Foliations in the Meatiq Domain are moderately SE dipping parallel to the axial plane of NE–SW trending folds. Different types of lineations were recorded plunging gentle to moderate to NW and SE. Thrusts in the Meatiq Domain are directed toward the Um Baanib Area. The NW–SE ASZ is the major and most important shear zone in the study area. The main foliations in the ASZ strike NW–SE and dip mainly to NE. Several kinematic indicators, including S-C fabrics and asymmetric boudins, isolated a symmetric objects, folds and mica fish were recognized and reflect sinistral sense of shearing. In the Um Esh Area, the earlier NE–SW dextral shear is overprinted by NW–SE sinistral shear. Within the Wadi Hammamat Domain, foliations strike NW–SE and dip mainly to NE. Thrust faults and folds with NE–SW trend were recorded and associated with NW–SE compression that prevailed just after the deposition of the Hammamat Sediments (Greilling et al. 1994; Abdel Wahed 2010). Strike-slip faults cut all structures in the study area and can be considered as the youngest phase of deformation and the latest event of brittle deformation. Strike-slip faults occur in two sets. The first one is right-lateral NE–SW strike-slip faults cut by the youngest NW–SE left-lateral strike-slip faults. The two sets of strike-slip faults are not conjugate. Within the Atalla Shear Zone, transpression is very common especially in the Fawakhir area within the Fawakhir Granite and Fawakhir Serpentinites. Transpression is represented in the form of strike-slip duplexes and a positive flower structures.

Four deformation phases (D_1–D_4) can be defined in the study area. D_1 is the oldest and documented within the xenoliths of amphibolites at Um Baanib area. D_2 is accretion-related stage that was associated with the general E–W convergence between East and West Gondwanan lands. D_3 represents a phase of extensional collapse formed due to N–S to NW–SE orogen-parallel extension and associated with the deposition of molasses sediments and exhumation of the Meatiq Core Complex. After the deposition of Hammamat Sediments, a short phase of

compression was recorded and led to form NW-directed thrusts and NE trending synclines. D_4 is characterized by NW–SE sinistral transpression followed by NW–SE transcurrent shearing in relation to the Najd Shear Deformation.

4 Conclusions

- Detailed geologic mapping were obtained for the ASZ and its environs based on the integration of remote sensing data and intensive field work (Fig. 1).
- Four deformation phases (D_1–D_4) were documented from the structural analysis of the study area. D_1 is pre-accretion, D_2 is accretion-related, and D_3 and D_4 are post-accretion and Najd-related phases.

References

Abd El-Wahed, M.A.: The role of the Najd Fault System in the tectonic evolution of the Hammamat molasses sediments Eastern Desert, Egypt. Arab. J. Geosci. **3**, 1–26 (2010)

Akaad, M.K., El-Ramly, M.F.: Geological history and classification of the basement rocks of Central Eastern Desert of Egypt. Geol. Surv. Cairo, Egypt **9**, 1–24 (1960)

Akaad, M.K., Noweir, A.M.: Geology and lithostratigraphy of the Arabian Desert orogenic belt of Egypt between latitudes 25° 35 and 26° 30 N. Inst. Appl. Geol. Jeddah Bull. **3**, 127–135 (1980)

Amer, R., Kusky, T., Ghulam, A.: Lithological mapping in Central Eastern Desert of Egypt using ASTER data. J. Afr. Earth Sci. **56**, 75–82 (2010)

Crosta, A.P., Souza Filho, C.R., Azevedo, F., Brodie, C.: Targeting key alteration minerals in epithermal deposits in Patagonia, Argentina, using ASTER imagery and principal component analysis. Int. J. Remote Sens. **23**, 4233–4240 (2003)

Greilling , R.O., Abdeen, M.M., Dardir, A.A., EL Akhal, H., El Ramly, M.F., Kamal El Din, G.M., Osman, A.F., Rashwan, A.A., Ries, A. H., Sadek, M.F.: A structural synthesis of the Proterozoic Arabian Nubian shield in Egypt, vol 83, pp. 484–501. Springer, Berlin (1994)

Hassan, S.M., El-kazzaz, Y.A., Taha, M.M.N., Mohammed, A.T.: Late-Neoproterozoic basement rocks of Meatiq area, central Eastern Desert, Egypt: petrography and remote sensing characterizations. J. Afr. Earth Sci. **131**, 14–31 (2017)

Hewson, R.D., Cudahy, T.J., Huntington, J.F.: Geological and alteration mapping at Mt Fitton, South Australia, using ASTER satellite-borne data. IEEE Trans. Geosci. Rem. Sens. 724–726 (2001)

Hewson, R.D., Cudahy, T.J., Mizuhiko, S., Ueda, K., Mauger, A.J.: Seamless geological map generation using ASTER in the BrokenHill–Curnamona province of Australia. Rem. Sens. Environ. **99**, 159-172 (2005)

Rowan, L.C., Mars, J.C.: Lithologic mapping in the Mountain Pass, California area using Advanced Spaceborne thermal emission and reflection radiometer (ASTER) data. Remote Sens. Environ. **84**, 350–366 (2003)

Role of Pre-existing Structures During the Opening of the Red Sea, Western Saudi Arabian Margin

Abdulaziz Samkari, Richard Walker, and Marc Reichow

Abstract

Reactivation of continental basement structures during rifting can control fault patterns and basin architecture. Recent studies have shown that the obliquity of pre-existing anisotropies is critical to the style of overprinting. Here we investigated the role of a major Precambrian terrane boundary in controlling Cenozoic age Red Sea (RS) rifting: The Ad-Damn Shear Zone (ADSZ), western Saudi Arabian margin, separating the lowlands of the Jeddah terrane to the NW, from Asir terrane highlands to the SE. Regional lineaments analysis coupled with field observations reveals three major trends of Cenozoic fault- and dyke-sets that strike (i) RS-parallel (NW–SE), (ii) RS-oblique (N-S ±10°), and (iii) RS-normal (NE–SW), that record extension (i) E–W (ii) NW–SE, (ii) and (iii) NE–SW, respectively. Cenozoic structures (dykes and faults) are largely parallel to Precambrian foliations, resulting in abrupt changes in the dominant orientation of rift structures across the ADSZ. Measured fault kinematics and dyke opening directions show that structural reorientation also corresponds to abrupt changes in the principal strain axes. Within the ADSZ and Asir terranes, the extension is dominantly orthogonal to the main Red Sea rift, suggesting that the pre-existing structure has acted as a primary control on rift evolution.

Keywords

Tectonic inheritance • Reactivated structures • Red Sea rift system

A. Samkari (✉)
King Abdulaziz University, Jeddah, Saudi Arabia
e-mail: Asamkari@KAU.edu.sa

A. Samkari · R. Walker · M. Reichow
University of Leicester, Leicester, UK

1 Introduction

Understanding the role of inherited basement structures—such as foliation and shear zones—is critical to rift architecture of continental margins (Dixon et al. 1987). In many cases, like the Red Sea (RS) rift system, the orientation of the pre-existing structures and geometry of the rift axes are oblique to the regional rift trend and do not follow the far-field tectonic stresses (Rosendahl 1987). Here, we investigated the role of the Neoproterozoic Ad-Damm shear zone (ADSZ) on the western-central part of the Arabian Shield. The RS offers an excellent opportunity to study rift evolution. Unlike most other ocean-forming rifts, the Red Sea passive margins are largely accessible onshore; basement outcrops along much of the length of the Red Sea, allowing direct access to the Neoproterozoic basement structures along the flanks of Arabian-Nubian shields (Fig. 1) (Al-Saud 2008).

In general, rift stages comprise two main processes: (1) the formation of newly, oriented faults and fractures that form in a predictable range of orientations relative to the far-field stress state and (2) the reactivation of mis-oriented (here, Precambrian) fabrics, such as faults, fractures and foliations. Such reactivation along old-basement structures may require a rotation of the principal stress and strain axes relative to the far-field tectonic (first-order) stress and strain axes. Lithospheric flexure and buoyancy forces related to crustal thickness variation may also contribute to a (first-order) rotation of σ_3 along large Precambrian fabrics (Molnar et al. 2017). Furthermore, (second-order) σ_3 rotation occurs due to: fractures interactions with rift segments (e.g. rift-parallel faults), magma overpressure—when magma pressure ratio is >1, and strength contrast across different terranes, (Dixon et al. 1987). However, pre-existing relatively weak fabrics may promote rotation of the principal strain axes without corresponding rotation of the principal stresses, particularly

M. Meghraoui et al. (eds.), *Advances in Geophysics, Tectonics and Petroleum Geosciences*,
Advances in Science, Technology & Innovation, https://doi.org/10.1007/978-3-030-73026-0_114

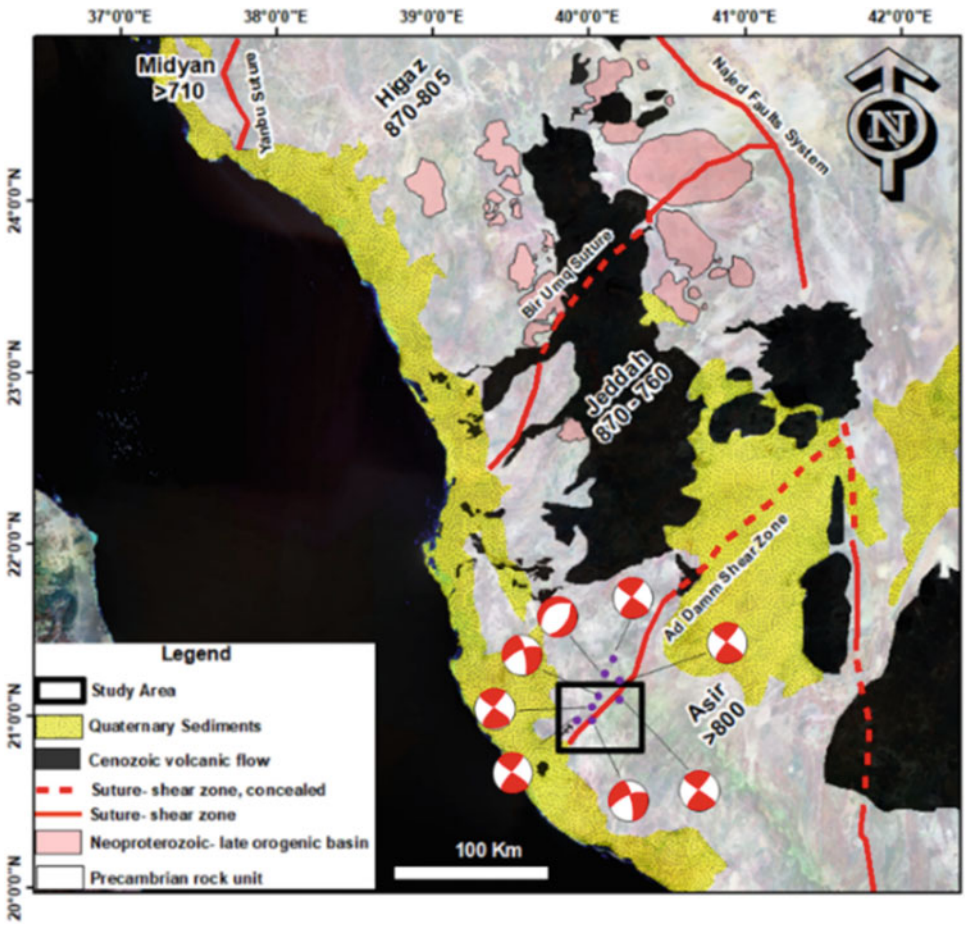

Fig. 1 Tectonic map of the western-central part of the Arabian shield, displaying the boundaries and ages of several terranes. Focal mechanism solution (FMS) recorded along ADSZ by Al-Saud (2008)

in cases where the fluid pressure approaches lithostatic to supralithostatic values.

2 Geologic Setting

In the RS, large-scale pre-existing structures are defined as discontinuous-tectonic boundaries (e.g. shear/transfer zones) that formed during the amalgamation of Precambrian terranes in the Neoproterozoic (e.g. Bir Umq suture) (Fig. 1). Onshore, rift geometry in the central part of the Arabian shield (east to the Red Sea) is controlled by the Ad-Damm Shear Zone (ADSZ) which bounds Jeddah terrane to the NW and Asir terrane to the SE (Hamimi et al. 2014) (Fig. 2). The Jeddah terrane is intruded by Neoproterozoic granites in meta-volcanic host rocks. The Asir terrane consists of a massive plutonic intrusion (mainly gneissic granite). Parallel to the Red Sea margins, the coastal plain is covered with Quaternary sediments (Hamimi et al. 2014).

3 Methods and Results

3.1 Fractures and Volcanic Lineaments

Shuttle Radar Topography Mission (SRTM) 30 m resolution images were converted to RGB for fracture/volcanic lineaments extraction (Fig. 3a). Lineament analyses along with ground-trothing during fieldwork indicate three major sets of features (Fig. 3b) that strike NW–SE, N–S, or NE–SW, and concentrate along the ADSZ and surrounding areas. Such areas suggest an extensive fracture development.

3.2 Fault Kinematic Data Analyses Results

A total of 159 fault zones were studied for fault kinematics analysis (Fig. 4). Three dominant extensional directions were identified across the study area. In the Jeddah terrane, fault planes lie parallel and subparallel to RS-rift-bounding

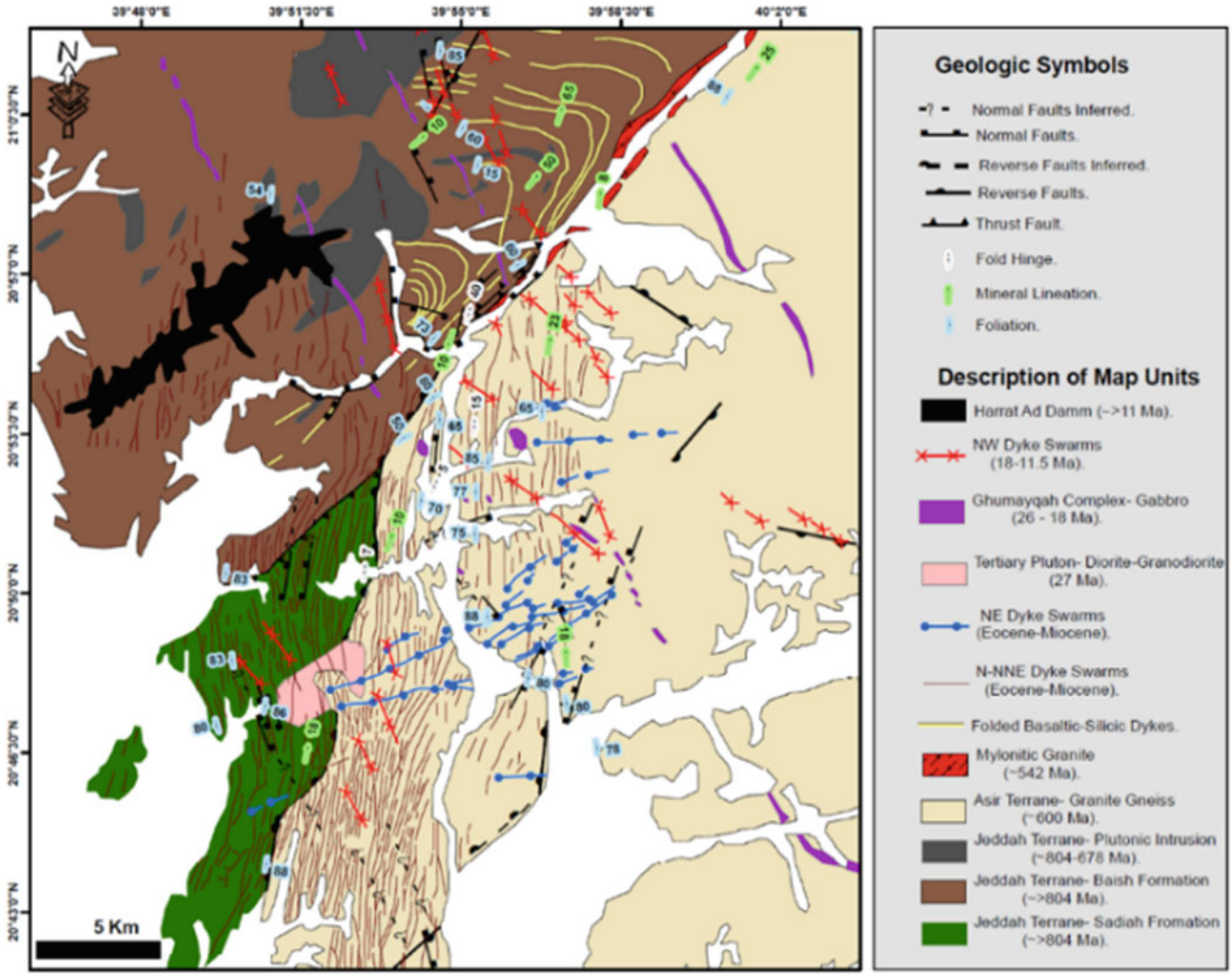

Fig. 2 Simplified geologic and structural map of the study area (Fig. 1), displaying the boundaries between Jeddah and Asir terranes and ADSZ

faults (*T*-axis ≈ 57°NE). In contrast, south of the ADSZ oblique normal faults displays approx. E–W extension (T-axis ≈ 102°–259°), accommodating extension oblique to the RS. Faults along the ADSZ-strike NE-indicate NW–SE extension (*T*-axis ≈ 333°NW).

4 Discussion

To build a kinematic-conceptual model about rift architecture and distribution of Neotectonic fabrics across the ADSZ, it is crucial to consider the spatial geometry of the Red Sea and propagation of modern structures. Cross-cutting relationships indicate an initial regional (first-order) extension, forming new RS-parallel faults (NW–SE). This supports a NW-propagation (towards 340°) model for the Red Sea rift system, originating at the Afar hotspot (Fig. 5a). Once the rift tip approached the ADSZ, the extensional strain axis (T) rotated from originally NE–SW, to ESE, as it became easier to exploit the pre-existing N–S foliation and reverse faults; this resulted in the formation of a number of RS-oblique (N–S ±10°) dykes and normal faults. Close to the ADSZ, where N–S weak zone becomes poorly defined, the extensional strain axis (*T*) deflected locally to NW–SE, resulting in RS-normal (NE–SW) dykes and faults which cut across N–S Neotectonic fabrics. Such observation is well correlated with other extensional-tectonic settings (e.g. Gulf of Suez, and Aden) and suggests that the ADSZ potentially acted as a transfer zone during reactivation (e.g. Bellahsen et al. 2013). Subsequently, as the NE-striking weak zone ends, the NW-propagation of the rift axis resumed and formed NW striking faults, which, in turn, cut across the NE and N–S fabrics. On the opposite side of the Red Sea, within the

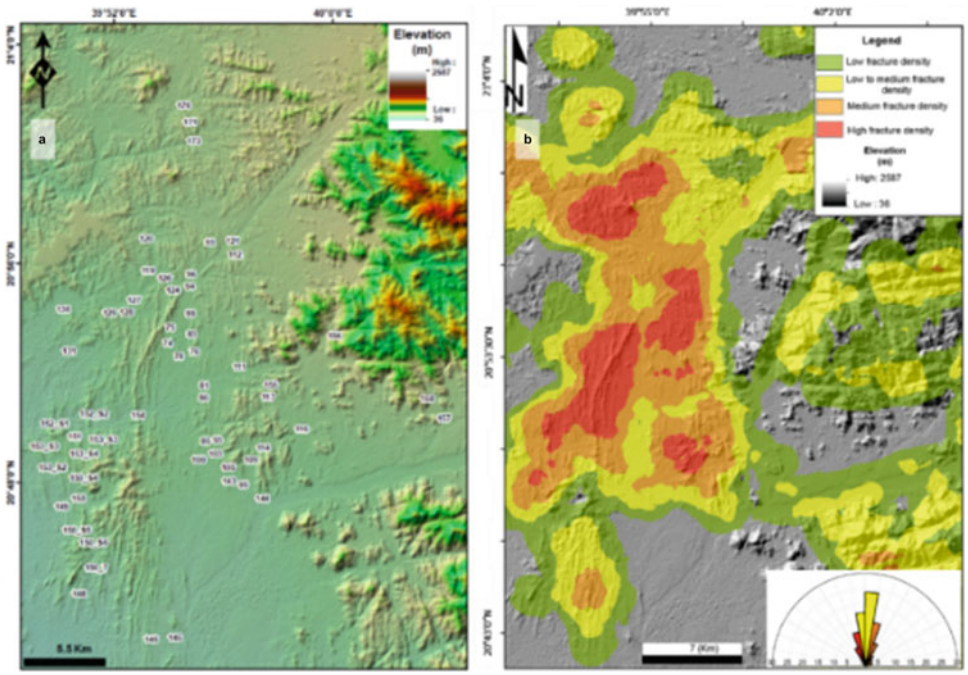

Fig. 3 **a** SRTM in (RGB) illustrates the fractures lineaments across the study area. White-masked numbers represent field localities. **b** The lineaments density map highlights areas of weakness zones. Rose diagram outlines three major lineaments trends (N-S, NW and NE)

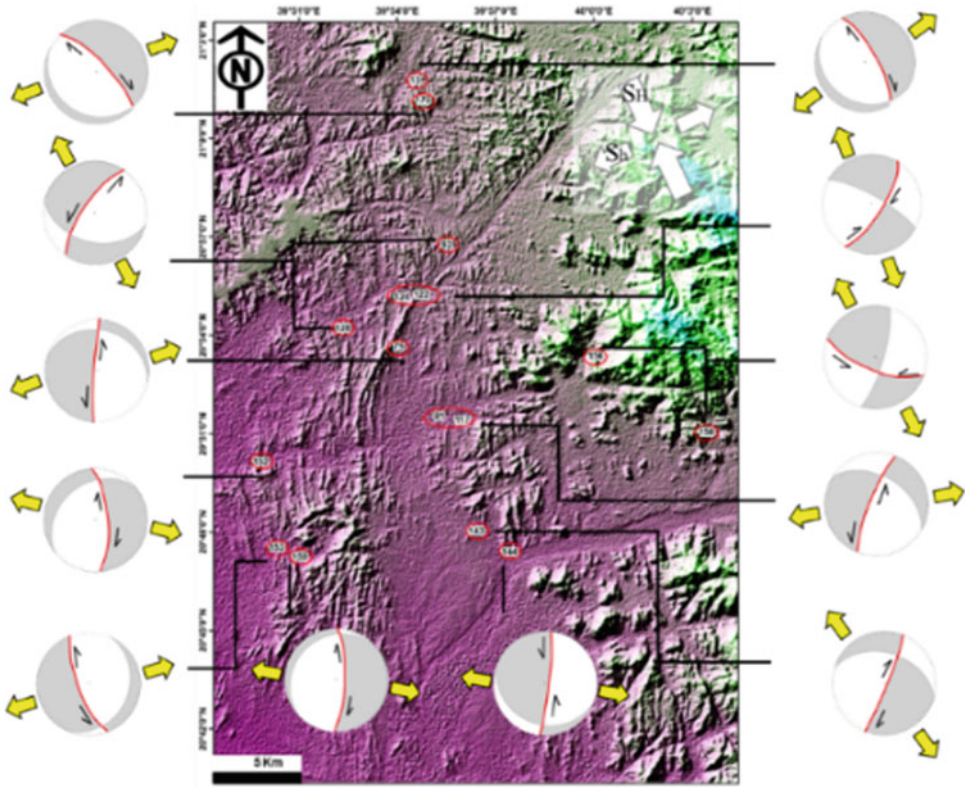

Fig. 4 Fault-plane solutions (FPS) map. Red lines within FPS indicate fault-nodal planes. Yellow arrows are the orientation of (*T*) axes (extension direction)

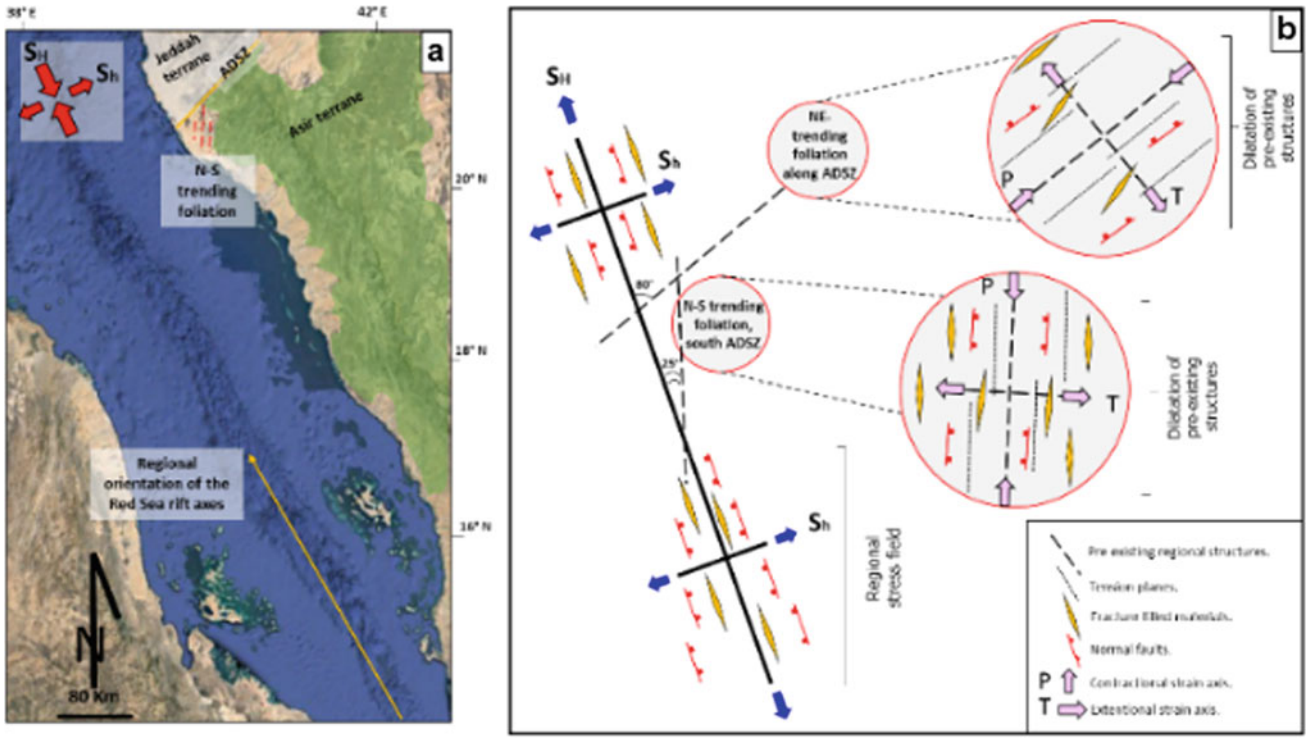

Fig. 5 **a** Annotated google satellite image displays the location of Precambrian structures. **b** A kinematic-conceptual model illustrates the effect of pre-existing structures on rift geometry

Nubian Shield, a similar deformation pattern was recorded and coincides with recent seismic activities (Dixon et al. 1987, Hamimi et al. 2014).

5 Conclusions

1. Rift-related structures on the RS margin inherited their geometry from ancient structures. New Cenozoic structures formed at various angles to the main rift, following existing Precambrian fabrics.
2. South of the ADSZ, Cenozoic structures were generally controlled by N–S foliation, forming an oblique E–W extension to the main RS rift, whereas structures in the ADSZ and Asir terrane show extension normal to the axial trough of the RS.

References

Al-Saud, M.M.: Seismic characteristics and kinematic models of Makkah and central Red Sea regions. Arab. J. Geosci. **1**(1), 49–61 (2008)

Bellahsen, N., Leroy, S., Autin, J., Razin, P., d'Acremont, E., Sloan, H., Khanbari, K.: Pre-existing oblique transfer zones and transfer/transform relationships in continental margins: new insights from the southeastern Gulf of Aden, Socotra Island, Yemen. Tectonophysics **607**, 32–50 (2013)

Dixon, T.H., Stern, R.J., Hussein, I.M.: Control of Red Sea rift geometry by Precambrian structures. Tectonics **6**(5), 551–571 (1987)

Hamimi, Z., El-Sawy, E.S.K., El-Fakharani, A., Matsah, M., Shujoon, A., El-Shafei, M.K.: Neoproterozoic structural evolution of the NE-trending Ad-Damm shear zone, Arabian shield, Saudi Arabia. J. Afr. Earth Sci. **99**, 51–63 (2014)

Rosendahl, B.R.: Architecture of continental rifts with special reference to East Africa. Annu. Rev. Earth Planet. Sci. **15**(1), 445–503 (1987)

Subsurface Structure of Saudi Cross-Border City of NEOM Deduced from Magnetic Data

Essam Aboud, Ahmed Ismail, and Faisal Alqahtani

Abstract

Saudi Arabia government announced the $500 billion mega project "NEOM City." It is located on the eastern side of the Gulf of Aqaba with the Sinai Peninsula on its western side. The selected site is geographically remarkable; nevertheless, it needs detailed geological and geophysical investigations. The current study aimed to understand the subsurface structure and tectonic setting of the vicinity of the NEOM City to address the potential seismic hazard and indicate geological attractions within and around the city. We used the available magnetic data in the analysis. From these data, the geological information and thermal system can be obtained. Preliminary results indicate that there is geological similarity between the southern part of Sinai Peninsula and northern part of the Arabian Shield. This is because the Gulf of Aqaba separates what was once a continuous Neoproterozoic crust. Results had shown the presence of prominent lineaments on both sides of the Gulf of Aqaba; hence, selecting a site of the NEOM City to be east of the gulf needs to be guided by careful understanding of potential seismic hazard. The Gulf of Aqaba separates the Sinai Peninsula from the northern Arabian Shield, and some of these lineaments might represent faults that can be still active. Future work will use a remote-sensing tool to get more insights into surface kinematics of these lineaments. It is expected that the combination of the magnetic and remote sensing results will produce a clearer picture about the neotectonics of the study area.

Keywords

NEOM City • Seismic hazards • Magnetic techniques • Remote-sensing techniques

1 Introduction

Geophysical surveys are routinely used to image the ground subsurface to explore for resources at the surveyed site or for site characterization for potential seismic hazards. Among these, geophysical surveys are the gravity and magnetic surveys, which are non-invasive methods that measure the rock density and susceptibility. The spatial changes in gravity and magnetic parameters are usually associated with subsurface geological features (Telford et al. 1976, Seigel 1995).

In 1995, a 7.3 MW magnitude earthquake occurred in the Gulf of Aqaba. The epicenter of this earthquake was determined at the central part of the Gulf, which represents together with the northern extension the Dead Sea Transform (DST), the active plate boundary between the Arabian Peninsula and the Arabian Plate (Fig. 1). The DST fault, also known as the Levant fault, extends for a ~1000 km from north of the Red Sea through the Gulf of Aqaba. The seismic data indicate that the DST is an active fault in this region. It is characterized by occasional large-scale destructive earthquakes. The 7.3 MW magnitude earthquake was the strongest seismic event recorded in the region in recent history. It is suggested that this event has also triggered a series of small to moderate earthquakes 500 km to the north of the epicenter.

The Saudi government is planning to launch a mega project to establish the NEOM City along the eastern shorelines of the Gulf of Aqaba (Fig. 1). This project will involve Saudi Arabia, Egypt and Jordon and will be conducted entirely on renewable energy.

E. Aboud (✉)
Geohazards Research Center, King Abdulaziz University, Jeddah, Saudi Arabia

A. Ismail
Boone Pickens School of Geology, Oklahoma State University, Oklahoma City, USA

F. Alqahtani
Faculty of Earth Sciences, King Abdulaziz University, Jeddah, Saudi Arabia

M. Meghraoui et al. (eds.), *Advances in Geophysics, Tectonics and Petroleum Geosciences*,
Advances in Science, Technology & Innovation, https://doi.org/10.1007/978-3-030-73026-0_115

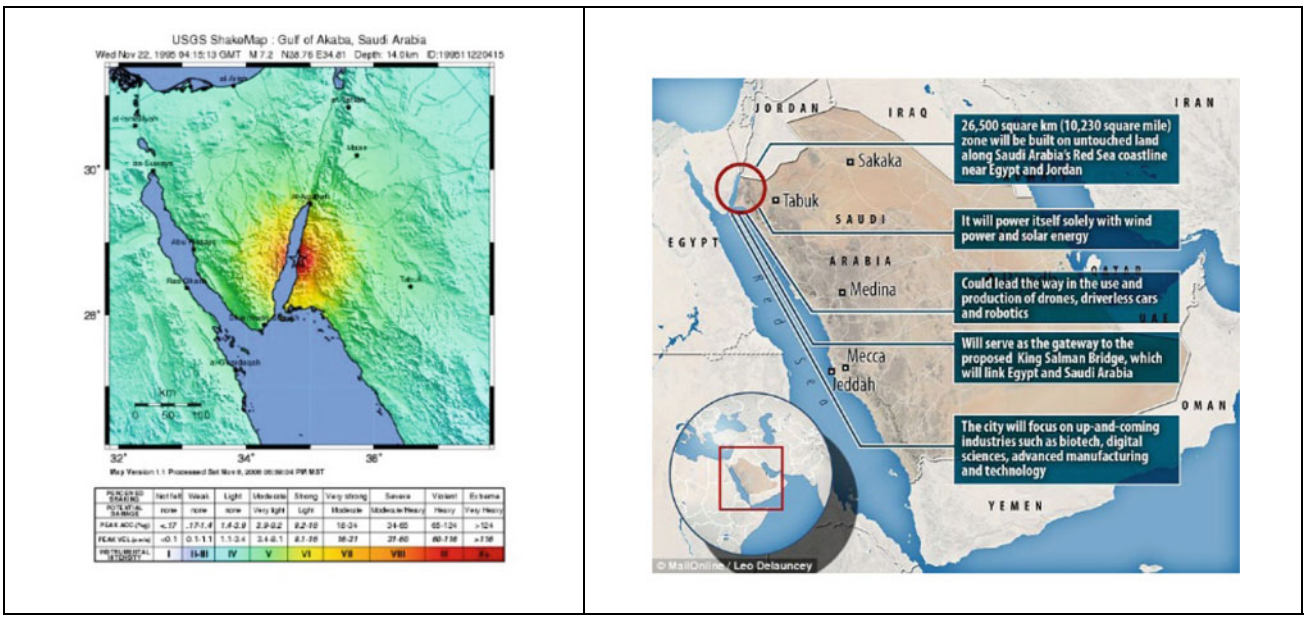

Fig. 1 Gulf of Aqaba on 7.3 MW earthquake and its relation to DST fault (left panel) and location of the NEOM City project (right panel)

2 Data and Methods

The current research used the magnetic data to image the subsurface structural features of the future site of the NEOM City (Fig. 2). These data were extracted from the global Earth Magnetic Anomaly Grid (EMAG2), compiled from satellite, ship and airborne magnetic surveys (Maus et al. 2009). Two techniques were applied to enhance the interpretability of these data and extract thermal information of the study area. These include the CET technique (Kovesi 1991, 1997; Lam et al. 1992; Holden et al. 2008, 2010) which helps map the edges of geological features such as the geological contacts and the Curie Point Depth (CPD), which assist in locating heat flow anomalies. The CET filter has been proven effective in highlighting the subsurface geological features of beneath the future site of the NEOM City.

3 Results

Figure 3 shows the CET filter results of the EMAG2 data. It illustrates a pattern of polygonal features defined by high nT/m closely hexagonal features surrounding regions of low nT/m. It is not clear to us what these magnetic features entirely represent. However, it is possible that these features represent NW-trending geological features with high magnetic susceptibility, and this dominant NW-trend is transected by geological features with high magnetic susceptibility at different orientations. One explanation for this pattern would be a set of NW-trending fractures and faults that are transected by a secondary set of fractures and faults that have various orientations and that these subsurface discontinuities are filled with a geological material that has high magnetic susceptibility. Regardless of any geological interpretation, it is clear to us that this magnetic anomaly pattern persists across the Gulf of Aqaba, in Sinai Peninsula and its eastern side. We can see some similarity in ridges or lineaments. The CPD (Fig. 3) shows that it is shallower in depth within a zone that crosses the Gulf of Aqaba from its eastern side to the southern part of the Sinai Peninsula.

4 Discussion and Conclusion

The analysis of the magnetic data indicates that there is a similarity in the dominant subsurface geological features between Southern Sinai Peninsula and the eastern side of the Gulf of Aqaba. It is not clear how these features is related to the Gulf of Aqaba trend since we interpreted that these magnetic features are NW-trending, and this trend is at high angle to the Gulf of Aqaba (Fig. 3). We also observed that the shallower CPD anomaly is found within a NW-trending zone that crosses the Gulf of Aqaba (Fig. 3). Curiously, the NW-trending magnetic and shallower CPD magnetic anomalies are parallel to the trend of the western shore of the Red Sea and its Gulf of Suez continuation. Hence, it can be stated that the region of the Red Sea, Gulf of Aqaba and Gulf of Suez will be our future site of the NEOM city in terms of structural and tectonic setting.

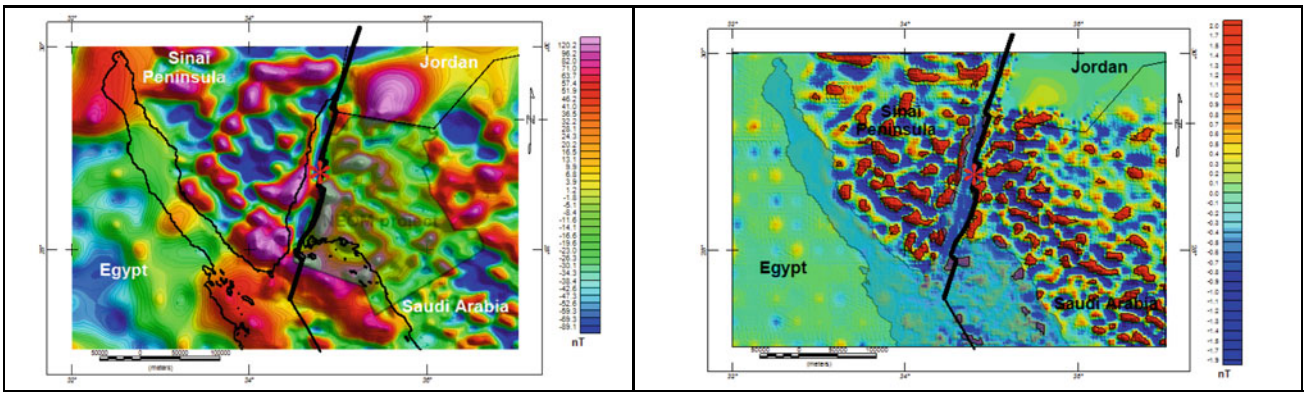

Fig. 2 Magnetic anomaly map around the future site of the NEOM City (left panel). Residual magnetic anomaly map (right panel). Black solid thick line indicates the DST. Red star shows the location of 1995 earthquake. Transparency area shows the location of the future site of the NEOM City

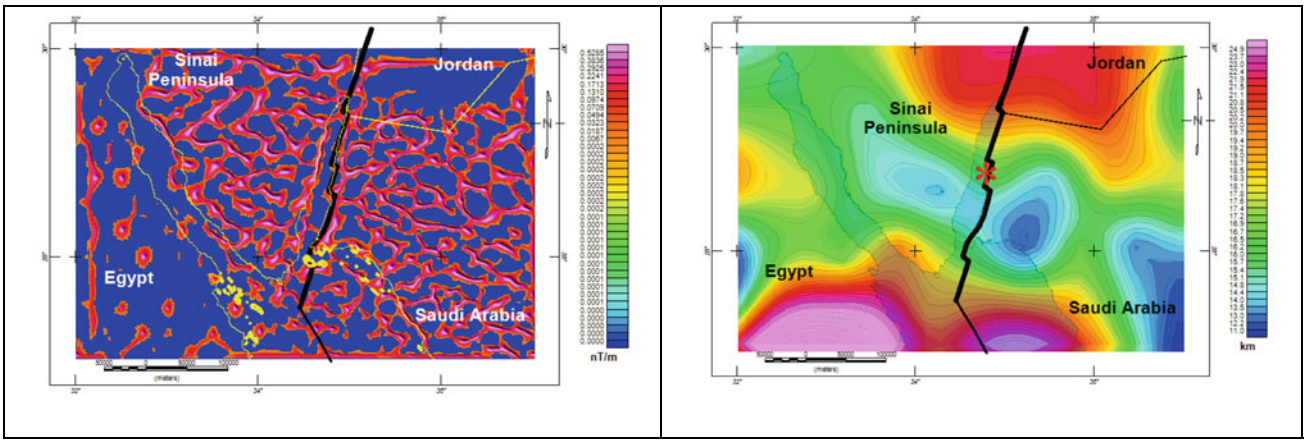

Fig. 3 CET technique results (left panel) and CPD map (right panel) of the region surrounding the future site of the NEON City. Black solid thick line marks the DST

References

Holden, E., Dentith, M., Kovesi, P.: Towards the automatic analysis of regional aeromagnetic data to identify regions prospective for gold deposits. Comput. Geosci. **34**(11), 1505–1513 (2008)

Holden, E., Kovesi, P., Dentith, M., Wedge, D., Wong, C., Fu, S.C.: Detection of regions of structural complexity within aeromagnetic data using image analysis. In: Twenty Fifth International Conference of Image and Vision Computing New Zealand, 8–9 Nov 2010

Kovesi, P.: Image features from phase congruency. Videre J. Comput. Vis. Res. **1**(3) (1991)

Kovesi, P.: Symmetry and asymmetry from local phase. In: AI'97, Tenth Australian Joint Conference on Artificial Intelligence. 2–4 Dec 1997

Lam, L., Lee, S.-W., Suen, C.Y.: Thinning methodologies—a comprehensive survey. IEEE Trans. Pattern Anal. Mach. Intell. **14** (9), 879 (1992)

Maus, S., et al.: EMAG2: A 2–arc min resolution Earth magnetic anomaly grid compiled from satellite, airborne, and marine magnetic measurements. Geochem. Geophys. Geosyst. **10**, Q08005 (2009). https://doi.org/10.1029/2009GC002471

Segal, N.: Mideast Trembler Rocks Region, Causing Several Deaths, Damage. Jewish Telegraphic Agency (1995)

Telford, W.M., Geldart, L.P., Sheriff, R.E., Keys, D.A.: Appl. Geophys. (1976)

Structural Evolution for AJJAJ Shear Zone, Northwestern Arabian Shield, Saudi Arabia

Osama Kassem, Yousef Alamri, Faisal Zaidi, Abdel Aziz Al Bassam, and Mansour Al-Hashim

Abstract

The Ajjaj shear zone is part of the regional-scale Quazaz-Ajjaj-Hamadat (QAH) shear zone that controls the structure of the northwestern Arabian shield. It consists of a sequence of volcanic rocks and sedimentary detrital, which is characterized by a difference in metamorphism facies with intruded granitoid bodies. Our work dealt with the structural characteristics of Ajjaj shear zone, accomplished through field reconnaissance and finite strain analysis, and microstructural investigation for understanding the tectonic evolution for studied area. R_f/φ and Fry techniques were applied to quartz and feldspar with some mafic minerals such as biotite and hornblende. The finite strain data show that the axial ratios average from 2.55 to 4.54 using the R_f/φ method and 1.95 to 4.33 using the Fry method in the *XZ* sections for the gneisses, metavolcanic, metasedimentary, and schist rocks. The finite strain direction for the long axes displays clustering along a NWN–SES trend with slight to moderate plunging. The Z axes are subvertical and associated with a subhorizontal foliation. The majority of data reveals oblate strain symmetry (flattening) with minor of prolate strain symmetry (constructional) and the strain magnitudes show no considerable increase toward the tectonic contacts. The volume change in the different lithologies was not associated with the accumulation of finite strain in the studied area. Furthermore, the subhorizontal foliation was parallel to the thrusting and illustrated mainly the same attitudes of tectonic contacts with the overlying nappes. It is concluded that the field observations and finite stain data resulted from simple-shear deformation for nappes in the orogeny.

Keywords

Finite strain • Microstructural analysis • Ajjaj shear zone • Arabian shield • Saudi Arabia

1 Introduction

The Arabian Shield is characterized by neoproterozoic basement complex. Dobrich et al. (2007) that subdivided the Arabian Shield into eight Regions (see Fig. 1). They include Jiddah, Asir, Hijaz, Midyan terranes in western Arabia, Ar Rayn, Afif, Ad Dawadimi, and Hail terranes in eastern Arabia. Many authors suggested that the small plates in the Arabian Shield are separated from each other by sutures or shear zones (Vail 1983; Camp 1984; Al-Shanti and Abo Omar 2003). In the studied area, the Midyan and Hijaz regions are separated by Yanbu belt that was effected by the tectonic movement (Dobrich et al. 2007).

The Ajjaj shear zone is one of the major structural elements in the region. It is a northwest-trending belt of distinctively styled shearing and has a consistent sinistral sense of displacement. The southern boundary is south of the Al Wajh region, and the northern boundary, 90–100 km away, is the wrench fault running between the Ash Shab complex and the warid complex.

An investigation of the finite strain and microstructures is important to determine the tectonic setting. The form of the finite strain ellipsoid is necessary for studying the shearing. The strain measurement methods such as R_f/φ and Fry depend on strain ratios required for various applications. Otherwise, the finite strain ratios may be known if rocks have objects of recognized shape or distribution. Deformed rocks were used as part of a strain measurement technique (Kassem and Ring 2004; Ring and Kassem 2007; Kassem

O. Kassem (✉) · Y. Alamri · F. Zaidi · A. Aziz Al Bassam · M. Al-Hashim
Department of Geology and Geophysics, Faculty of Science, King Saud University, P.O. Box 2455 Riyadh, 11451, Kingdom of Saudi Arabia

O. Kassem
Department of Geology, National Research Center, Al-Behoos str., Dokki, Cairo, 12622, Egypt

M. Meghraoui et al. (eds.), *Advances in Geophysics, Tectonics and Petroleum Geosciences*, Advances in Science, Technology & Innovation, https://doi.org/10.1007/978-3-030-73026-0_116

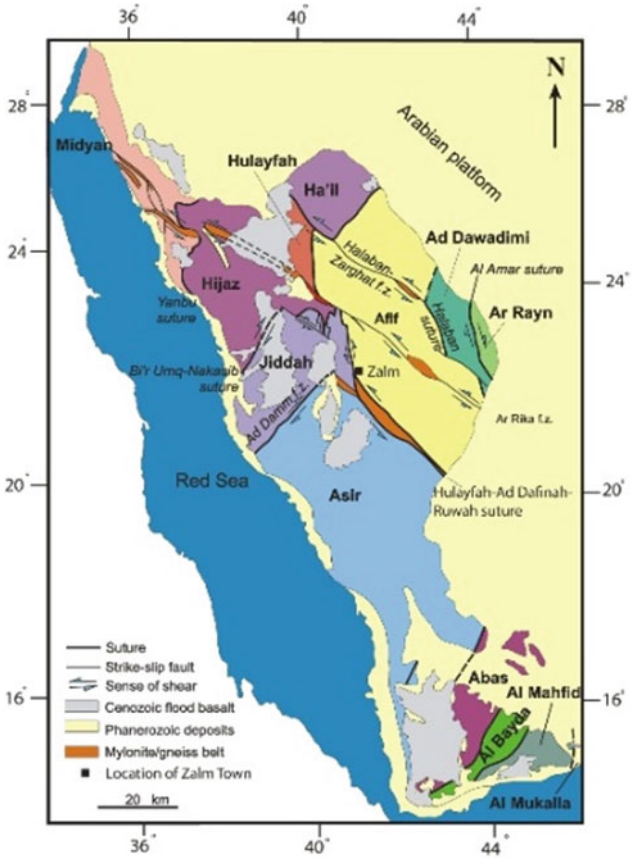

Fig. 1 Tectonic map terranes for Arabian Shield (Johnson and Woldehaimanot 2003)

and Abd El Rahim 2010). The aim of the present work was to evaluate a relationship between different lithologies in the Ajjaj shear zone with mineralogy description and tectonic setting. Also, it elucidated the post-accretionary thrusting and thrust-related structures in the Ajjaj shear zone.

2 Geological Setting

The Neoproterozoic Midyan terrane of the Arabian shield is characterized by unconformably overlying Phanerozoic sandstone and flood basalt, and a narrow strip of coastal plain and Red Sea half-graben. The Midyan terrane includes varied volcanic and sedimentary assemblages of the Zaam, Bayda, Thalbah and other groups, several suites of Neoproterozoic intrusive rocks, and large, through-going shear zones created by pervasive sinistral shear. The shear zone is characterized by sinistral subhorizontal shear, amphibolite facies metamorphism (Fig. 2).

Some details of the Ajjaj shear zone geology are given in Fig. 2. The Ajjaj shear zone is part of the regional-scale Quazaz-Ajjaj-Hamadat (QAH) shear zone that consists of amphibolites-grade, well banded, strongly foliated and lineated ortho- and para-gneiss. It trends west-northwest; the Hamadat shear zone along strike to the east has a more northerly trend. It is part of the only Najd shear zone that trends northwest across the entire Arabian shield. In the study area, the Ajjaj shear zone is the southernmost of the set of shears that make up the QAH (Fig. 2).

3 Sampling and Techniques

Twenty four samples were collected from study area, which represented gniesses rocks, metasedimentary, metavolcanic, and schist rocks. These samples are oriented into NW–SE trending with shallow dip in the Ajjaj shear zone. They included eight gniesses, six metavolcanics, six metasedimentary, and four schist. All different rock units were used to quantify the finite strain in the Ajjaj shear. The collected samples were prepared by cutting into thin sections through three perpendicular axes planes, which were subparallel to the *XZ*, *YZ* and *XY* principal axes planes. Many authors suggested that the three-dimensional strain geometry (principal planes) were prepared on *XY*, *XZ* and *YZ* sections ($X \geq Y \geq Z$, finite strain axes) to detect the kinematic vorticity and finite strain (Ramsay 1967; Ramsay and Huber 1983; Ring and Kassem 2007).

4 Structural and Deformation Analysis

Most of the Precambrian rocks of the Arabian Shield were regionally metamorphosed to the low and middle greenschist facies. However, amphibolites-grade metamorphism took place in the Ajjaj shear zone, Quazaz-Baladiyah complexes and schist zones of the Bayda group. The Ajjaj shear zone consists of quartzo-feldspathic schist with or without biotite, hornblende, and garnet. A broad antiformal zone of gneissic granite and granodiorite en-echelon with the Quazaz complex is flanked by the almandine-amphibolite schist phase. The Ajjaj shear zone forms the schistose envelope of the gneissic granite and granodiorite, flank the Baladiyah complex, and locally occur adjacent to the Quazaz complex. The growth of idioblastic garnet and hornblende on the schistosity and foliation planes of both the schist and country rock indicates that metamorphism outlasted the tectonic deformation. Metamorphism decreased to greenschist facies toward the southern end of the antiform. The Ajjaj shear zone was characterized by the development of Land L-S tectonites, and abundant kinematic indicators.

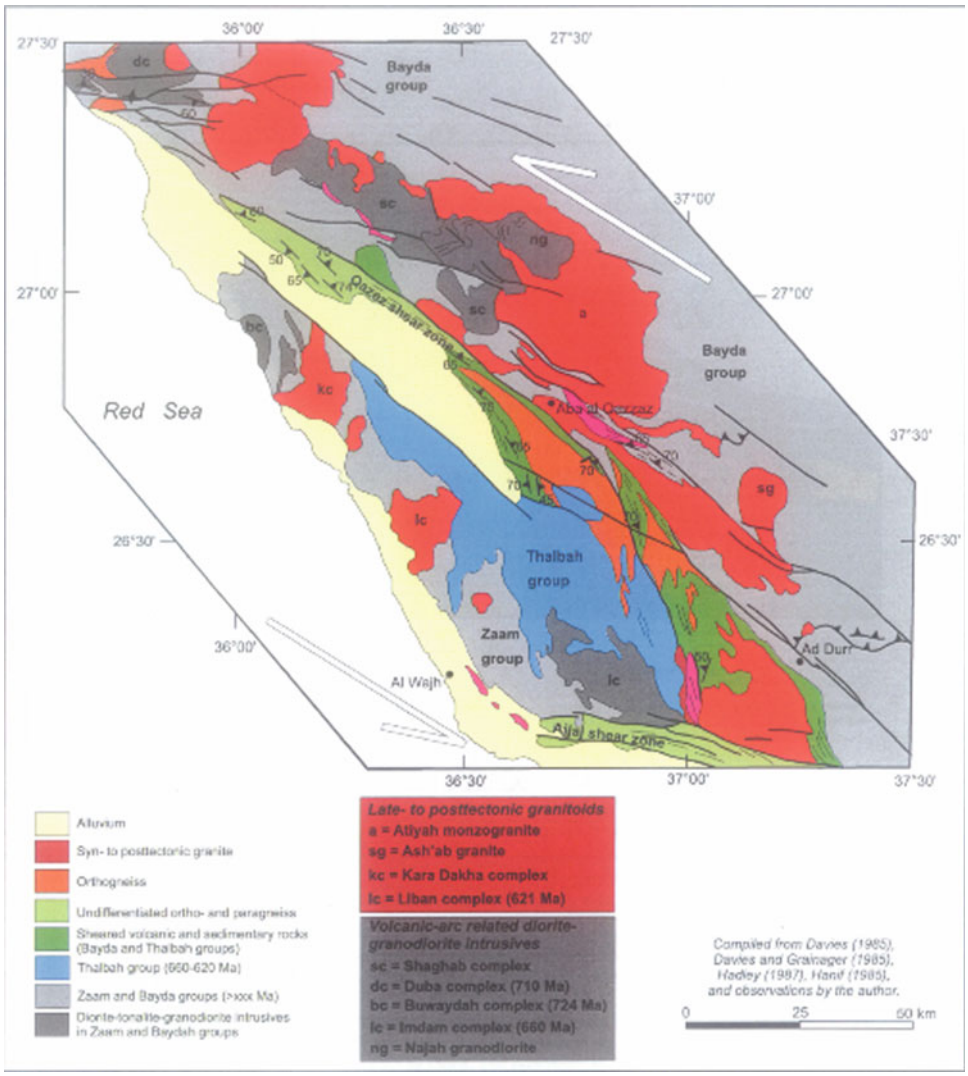

Fig. 2 Sketch map of the regional-scale, brittle-ductile Qazaz-Ajjaj-Hamadat shear zone

5 Results of Finite-Strain Analysis

The result of strain data shows that the axial ratios (*XZ*) for the R_f/φ method are on average from 2.55 to 4.54 for gniesses rocks, metasedimentary, metavolcanic, and schist rocks. In other cases, the axial ratios (*XZ*) for the Fry technique are on average from 1.95 to 4.33 for the same type of rocks. Furthermore, the axial ratios (*YZ*) for the R_f/φ method vary from 1.78 to 3.86 and the axial ratios (*YZ*) for the Fry technique are on average from 1.54 to 3.99. Also, the axial ratios (*XY*) for the R_f/φ technique average from 1 to 1.49, and the axial ratios (*XY*) for the Fry method are on average from 1 to 3.48.

The data for the stretch axes (S_X) are on average from 2.18 to 3.58 for the R_f/φ technique and from 2.01 to 2.97 for the Fry technique. The stretch axes (S_Y) range from 1.06 to 1.42 for the R_f/φ technique and from 0.85 to 1.45 for the Fry technique, which indicates both contraction and extension in this stretch. In addition, the stretches axes range from 0.5 to 0.74 in (S_Z) and show vertical shortening of 25–95% for the R_f/φ technique. In addition, the strain data for the Fry technique shows S_Z averages from 0.39 to 0.82 with vertical shortening of from 11 to 33%. Our strain data indicates no difference in the deformation behavior, which was obtained for the R_f/φ and Fry techniques.

6 Discussion

The different lithologies in the Ajjaj shear zone are products of the superimposition of dynamic metamorphism, which represented the major structural feature on the regional metamorphism. South of the Baladiyah complex, near the southern margin of the Ajjaj shear zone, rocks of the Nasrah formation of the Zaam group were strongly deformed and recrystallized.

Plutonic rocks, such as the Abu Suar complex, within the Ajjaj shear zone, are deformed and schistose. The Abu Suar

complex is surrounded by metamorphosed country rock and an intense schistosity is common to its margin; thermal metamorphic effects are limited. Granitic plutons intruded outside the Ajjaj shear zone produced few contact metamorphic effects other than the hydrothermal introduction of epidote. Even where large plutons, such as the Ash Shab complex, intrude argillaceous sedimentary rocks, the only obvious contact-metamorphic products are rare cordierite hornfels patches and magnetite cubes. Many of the clastic stratiform country rocks in contact with the intrusions still obviously contain original lithic and crystal fragments. Thermal effects of the granites appear to have been brief and subdued by the refractory nature of most of the country rocks and by low levels of fluid migration and metasomatism.

Foliation and mineral lineation are well developed, and structurally the rocks vary from L-S tectonite to L-tectonite. Foliation dips are moderate to steep, and lineations plunge gently NW and SE, with a preponderance toward the SE. The Ajjaj and Quazaz shear zones are linked by a wide NNW-trending shear zone that deforms large granite intrusions and Thalbah group rocks. A distinctive feature of this linking shear zone is a north-trending antiform of gneiss immediately north of the Ajjaj shear zone. The antiform termed the Baladiyah complex (676 $\pm$ 4 Ma) is reminiscent of gneiss domes exposed in the Eastern Desert.

Systematic strain variations and changes in metamorphic grade occur across the Ajjaj shear zone, and these exert a major influence on the location of granite intrusions in the structure. Arcuate folds associated with late-stage wrench faults exhibit systematic variations in orientation across the zone; the dihedral angles between axial surfaces and the wall of the shear zone decrease from about 60° at the margin of the zone to about 15°, at the center of the zone.

7 Conclusion

The finite stain data and microstructural analysis show the following concluding remarks:

- The majority of strain ellipsoids have oblate strain symmetry.
- No significant differences in the deformation behavior between Rf/φ and Fry methods were remarked.
- The finite strain in various lithologies has the same order of magnitude in the investigated lithologies.

The obtained finite strain data conflicts with the suggestion that nappes in orogens resulted from simple-shear deformation.

References

Al-Shanti, H.A., Abo Omar, J.M.: Effect of olive cake on layers' performance and egg quality. J. Al-Azhar Univ. Gaza (Nat. Sci.) **6** (1) (2003)

Camp, V.E.: Island arcs and their role in the evolution of the western Arabian shield. Geol. Soc. Am. Bull. **95**, 913–921 (1984)

Doebrich, J.L., Al-Jehani, A.M., Siddiqui, A.A., Hayes, T.S., Saleh, Y., Wooden, J.L., Johnson, P.R., Kattan, F.H., Shaikan, B., Basahel, M., Zahran, H., Al-Shammari, A.: Geology and mineral resources of the Ar Rayn Terrane, Eastern Arabian Shield, Kingdom of Saudi Arabia. Precambr. Res. **158**, 17–50 (2007)

Johnson, P.R., Woldehaimanot, B.: Development of the Arabian-Nubian Shield: perspectives on accretion and deformation in the northern East African Orogen and the assembly of Gondwana. Geol. Soc. London, Special Publications **206**(1), 289–325 (2003)

Kassem, O.M.K., Abdel Raheim, S.: Finite strain analysis for the Metavolcanic-sedimentary rocks in the Gabel El-Mayet region, Central Eastern Desert, Egypt. J. Afr. Earth Sc. **58**, 321–330 (2010)

Kassem, O.M.K., Ring, U.: Under plating-related finite-strain patterns in the Gran Paradiso massif, Western Alps, Italy: heterogeneous ductile strain superimposed on a nappe stack. J. Geol. Soc. London **161**, 875–884 (2004)

Ramsay, J.G.: Folding and fracturing of rocks. McGraw-Hill, New York, 568 pp (1967)

Ramsay, J.G., Huber, M.: The Techniques of Modern Structural Geology. Strain Analysis, vol. 1. Academic Press, London (1983)

Ring, U., Kassem, O.M.K.: The nappe rule: why does it work? J. Geol. Soc. **164**, 1109–1112 (2007)

Vail, J.R.: Pan-African crustal accretion in northeast Africa. J. Afr. Earth Sci. **1**, 285–294 (1983)

Interpretation of Aeromagnetic and Geochemical Data for Tectonic and Structural Setting of Granitic Rocks Around Bishewa Area, Southwestern Nigeria

Ajadi Jimoh and Olasunkanmi K. Nurudeen

Abstract

High resolution aeromagnetic data of Bishewa area has been analyzed to establish the geometry of its lithologic settings. Magnetic residualization of the total magnetic intensity (TMI) and derivative of resulting magnetic anomalies were enhanced using the fast Fourier transform of Oasis montaj geo-software. The reduced to equator residual anomaly varies within −174.9 to 111.9 nT which revealed the contrasting lithologic units viz: sedimentary and basement complex. The negative magnetic intensities (lows) in the southern and sparsely within the northwestern regions are associated with rocks of lower content of ferromagnetic minerals and are attributable to underlying igneous and metamorphic rocks or intrusive bodies within the schist. The positive anomalies coincide with the predominant migmatite-gneiss complex. Structural relationships between the granites and metasedimentary host rocks suggest that the emplacement of the granitoids is associated with early, large-scale thermotectonic regional deformation within the Nigerian basement complex. This study also revealed a transpressional regime that is characterized by WNW-ESE shortening and large-scale sinistral strike-slip faults associated with the regional NE-SW structural grains in the basement rocks of the area. Regional geologic features and structural correlation show that the area is underlain by the northwestern extension of the Ilesha schist belt in the western sector of the Nigerian basement complex.

Keywords

Aeromagnetic data • Fourier transform • Structural relationships • Regional deformation • Transpressional regime

1 Introduction

The geology of Bishewa area forms part of the northern limit of the migmatite-gneiss complex in the southwestern sector of the Nigerian Basement Complex bordered in the north by the Cretaceous sediments of the Bida Basin which overlies the basement complex rocks. This complex lies within the African crystalline shield believed to be part of the Late Proterozoic to Early Paleozoic Pan African mobile belt, which is bordered to the west by the West African cratonic plate and to the southeast by the Congo craton. The study area lies between latitudes 8° 39′ N and 8° 46′ N, and longitudes 5° 03′ E and 5° 11′ E, underlying an area of about 220 km^2. This area is located in the northwestern sector of the 1:50,000 Lafiagi southwest sheet 203. The main lithologies outcropping in the area have been classified into four major groups. These include early metamorphic tectonites (biotite gneiss and migmatitic gneiss), metasedimentary rocks (quartz-biotite-muscovite schist, tremolite-talc schist, quartzite and amphibolite), the Pan African (Older) Granite (medium-coarse grained biotite granite and pegmatite) and minor intrusives rocks (granodiorite, porphyritic granite, lamprophyre, aplite and quartz vein). The geochemistry and petrogenetic evolution of these rocks have been described in some detail (Ajadi 2017) (Fig. 1).

A. Jimoh (✉)
Geology and Mineral Sciences Department,
Kwara State University, Malete, Nigeria
e-mail: jimoh.ajadi@kwasu.edu.ng

O. K. Nurudeen
Physics and Materials Science Department,
Kwara State University, Malete, Nigeria

M. Meghraoui et al. (eds.), *Advances in Geophysics, Tectonics and Petroleum Geosciences*,
Advances in Science, Technology & Innovation, https://doi.org/10.1007/978-3-030-73026-0_117

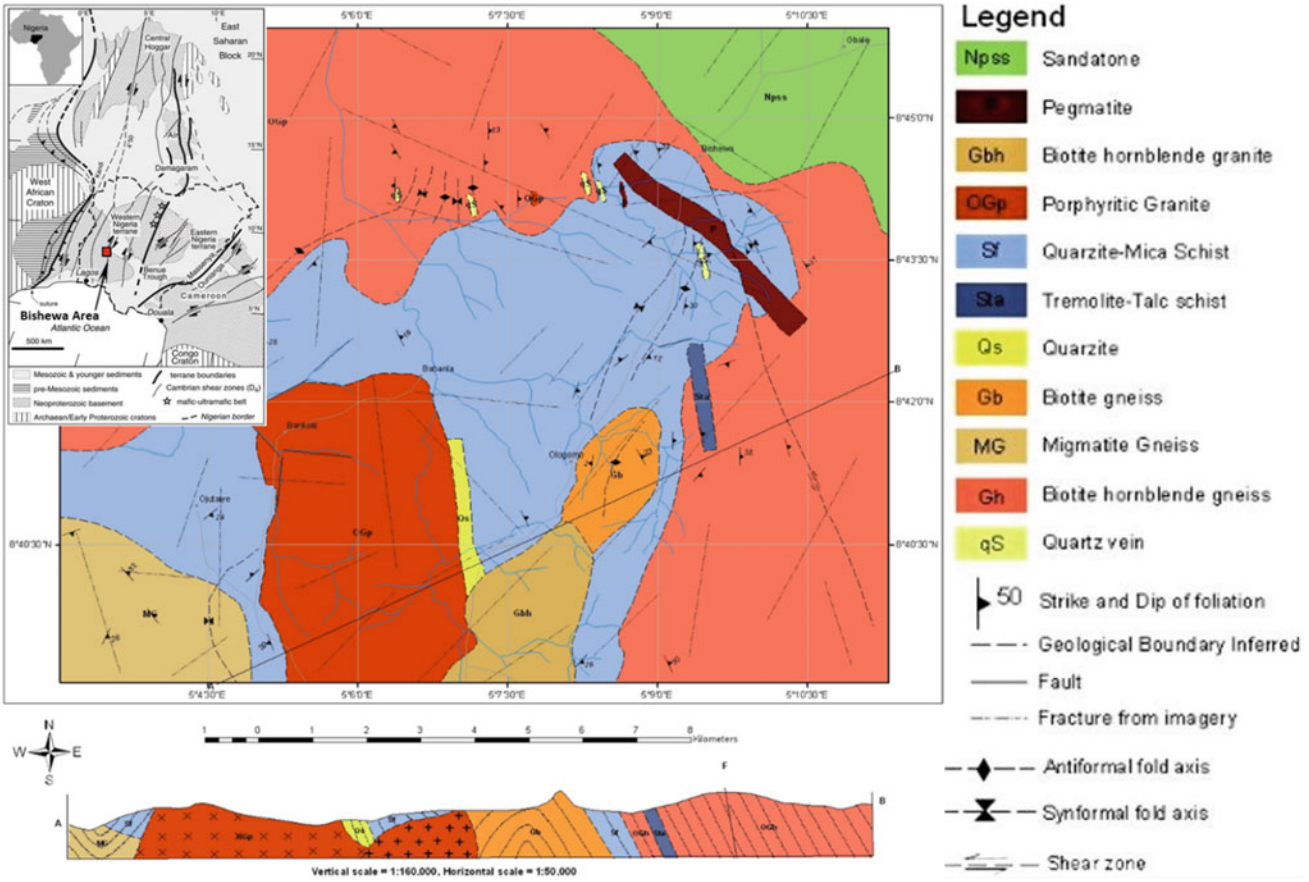

Fig. 1 Geological map of Bishewa area showing lithological distributions (Ajadi 2017)

2 Materials and Methods

2.1 Data Set and Procedure

Total field aeromagnetic intensity (TMI) data of Bishewa were extracted from data sheets 202 and 203 published by Nigeria Geological Survey Agency (NGSA), from high resolution airborne magnetic survey carried out within 2003 to 2006, with a view to using magnetic anomalies to map contrasting lithologies and associated structural elements (Fig. 2). The data were acquired at traverse line spacing of 500 m and tie line of 2 km in NW–SE and NE–SW orientations respectively and at flight height of 200 m. The TMI data was reduced to the magnetic equator using the geomagnetic inclination and declination of −8.59° and −1.69° respectively, in order to correct the asymmetric and lateral shift of measured magnetic total filed, and that maximum magnetic anomalies lies in the middle above the magnetized body. RTE was accomplished by using the step-by-step fast Fourier transform (FFT) filtering procedure on Oasis Montaj software to remove the inclination effects from the grid data and produce magnetic anomalies that seems calculated at the equator.

The derivatives (tilt and total horizontal derivative) take the form (Eqs. 1 and 2) to normalize the signatures in images of residual magnetic data so that weak, small amplitude anomalies can be amplified relative to stronger ones. Normalized derivatives also help to define the locations of magnetic edges, show which side of each edge is likely to have a higher magnetization, and give a qualitative indication of the dip of contacts (Fairhead and Williams 2006). The analytic signal (/*A*/) used the total magnetic gradient, to approximately estimate positions of magnetic contacts and obtain some depth estimates from the gridded data. The /*A*/ served as the basis for the definition of the derivatives; where *M* is total magnetic field. The relationship of normalized gradients are expressed as Eq. 2; where vertical gradient is denoted by VDR and total horizontal gradient as THDR.

$$|A| = \sqrt{\left|\frac{\mathrm{d}M}{\mathrm{d}x}\right|^2 + \left|\frac{\mathrm{d}M}{\mathrm{d}y}\right|^2 + \left|\frac{\mathrm{d}M}{\mathrm{d}z}\right|^2} \tag{1}$$

$$\text{Tilt Derivative} = a\tan\frac{\text{VDR}}{\text{THDR}} \tag{2}$$

Depth to magnetic sources was estimated from the magnetic source parameter imaging (SPI) and Euler deconvolution

at structural indices of zero and one. The Euler deconvolution technique analysis potential field data using Euler's relation for homogenous functions (Eq. 3). With the regional value of the total magnetic field (B) and the position (x_o, y_o, z_o) of the magnetic sources, which produces the total field (T) measured at (x, y, z), the deconvolution employs first order (x, y, z) derivatives to determine location and depth for various idealized targets (sphere, cylinder, thin dyke, contact), each characterized by a specific structural index (Thompson 1982). The SPI automatically calculates source depths from total magnetic field (Thurston et al. 2002; Nabighian 1972).

$$(x - x_o)\frac{dT}{dx} + (y - y_o)\frac{dT}{dy} + (z - z_o)\frac{dt}{dz} = N(B - T) \quad (3)$$

Rock samples were crushed and reduced to 1 mm size using a Geocrusher and pulverizer, and 200 g of samples were ground to −200 mesh using a disk mill. Sample contamination was prevented by carrying out air cleaning at each stage. Hot digestion of 0.5 g of the sample in a mixture of HNO_3, $HClO_3$ and HF was carried out before the XRF analysis for chemical composition of the 20 selected samples. 50 mg of the pulverized rock sample was also subjected to hot digestion in a mixture of HNO_3, $HClO_3$ and HF before being fed into the ICPMS machine for trace element analysis.

2.2 Data Processing

The TMI was reduced to magnetic equator (RTE), since there are no appreciable remmanence effects within low latitude (Paananen 2013) having low geomagnetic inclination value −8.59. THDR has been established as a better edge detection tool as it gives resolution of both vertical derivative (VDR) and horizontal derivative (HDRx and HDRy) (Foss 2011). The RTE residual magnetic anomaly map was further enhanced using fast Fourier transform for total horizontal derivative (THDR), Analytic Signal (AS) and Euler deconvolution at structural index of zero (SI = 0); to reveal the edges/geometry of various geologic models. The geochemistry of the rocks was analyzed and interpreted using Petrograph software to determine the tectonic and structural setting of emplacement of the granitic rocks around Bishewa area.

3 Results

Three groups of structural features have been recognized within the Basement Complex around the study area. These include relict sedimentary structures as well as the ductile and brittle structures. Most of these structures occur on outcrop scale, an interplay of some of which were used to infer a few large-scale features observed in Fig. 1. Most of the fractures encountered in the study area frequently occur as variably oriented joints. The open to tight NNE-SSW trending minor folds in the area particularly in the north central part is suggestive of a transpressional force. Figure 2 shows the rosette plots of joint trends, indicating a NW–SE transpressional force with minor faults and NNE-SSW folds which created the dominant NE-SW fractures in the study area with subordinate complimentary NNW-SSE and WNW-ESE fracture trends. About 40% of the joints in the study area are healed with quartz or pegmatitic materials which are simple or complex in composition (Garba et al. 2019) and trend mostly in the NNW-SSE directions (Fig. 2c, d). These main structural trends are also observable on the reduced to equator residual magnetic anomaly and analytic signal amplitude maps of Bishewa (Fig. 3).

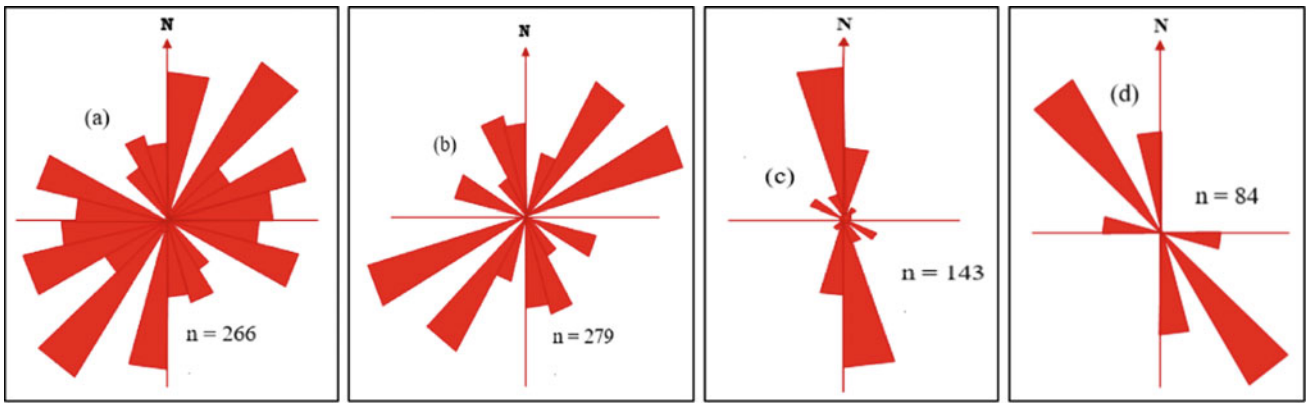

Fig. 2 Rosette plots of joints in the **a** granitic gneisses **b** granites **c** pegmatites **d** vein quartz around Bishewa

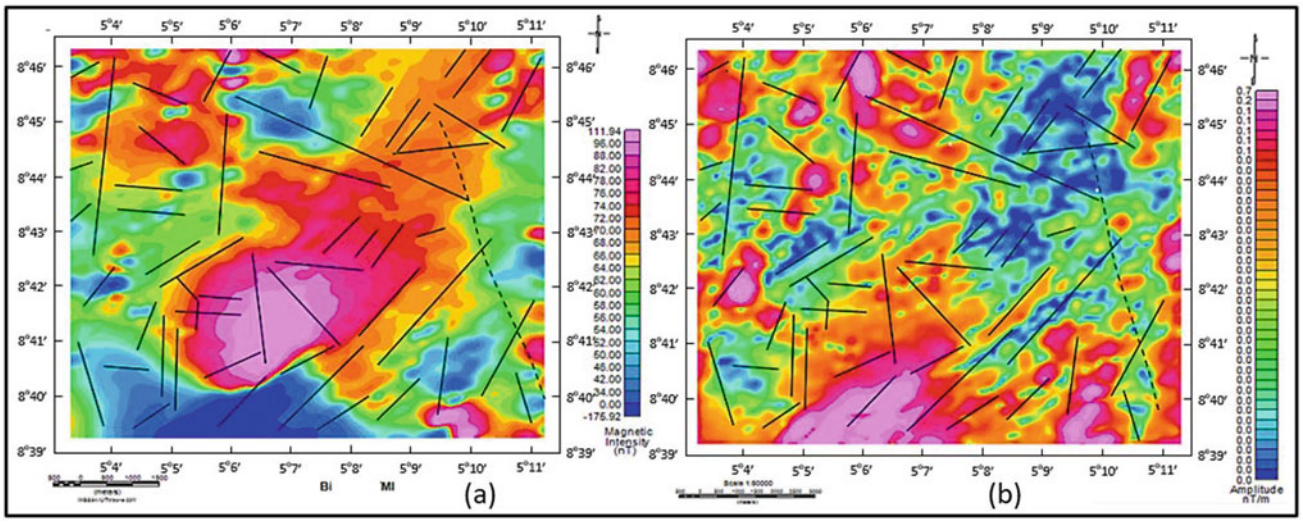

Fig. 3 **a** Reduced to equator residual magnetic anomaly and; **b** analytic signal amplitude maps of Bishewa

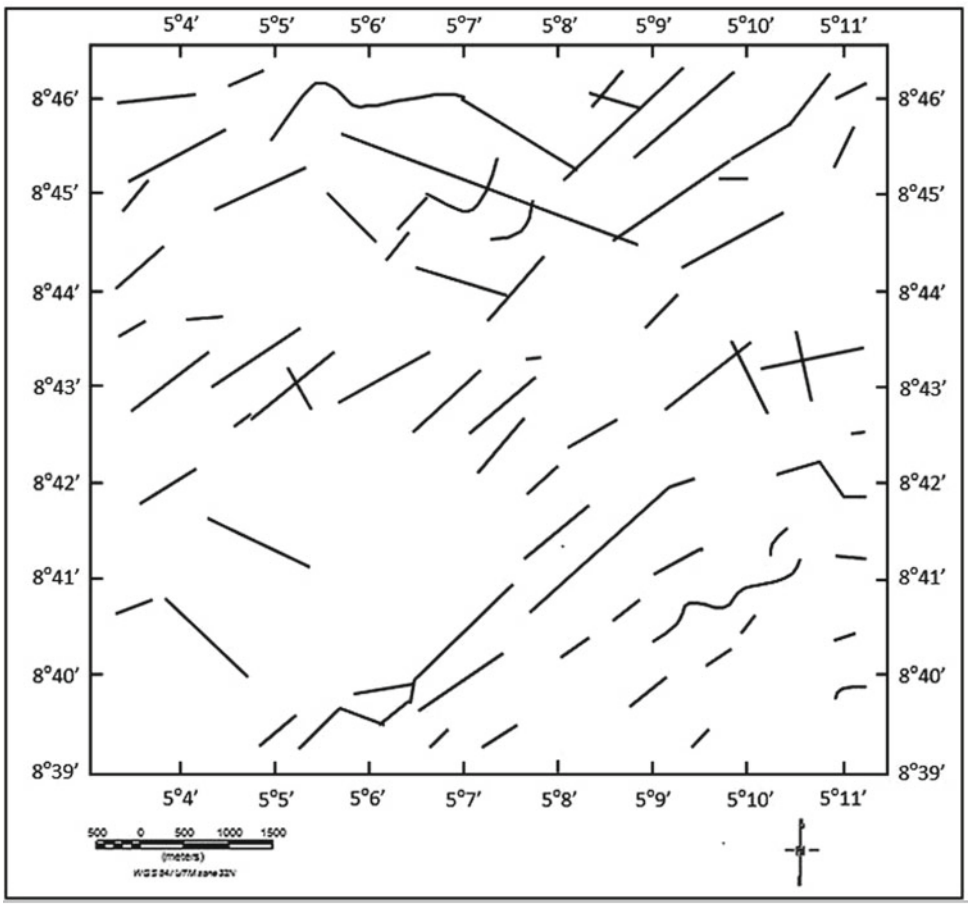

Fig. 4 Lineament extracted from normalized derivative of the reduced to equator magnetic anomalies of the area

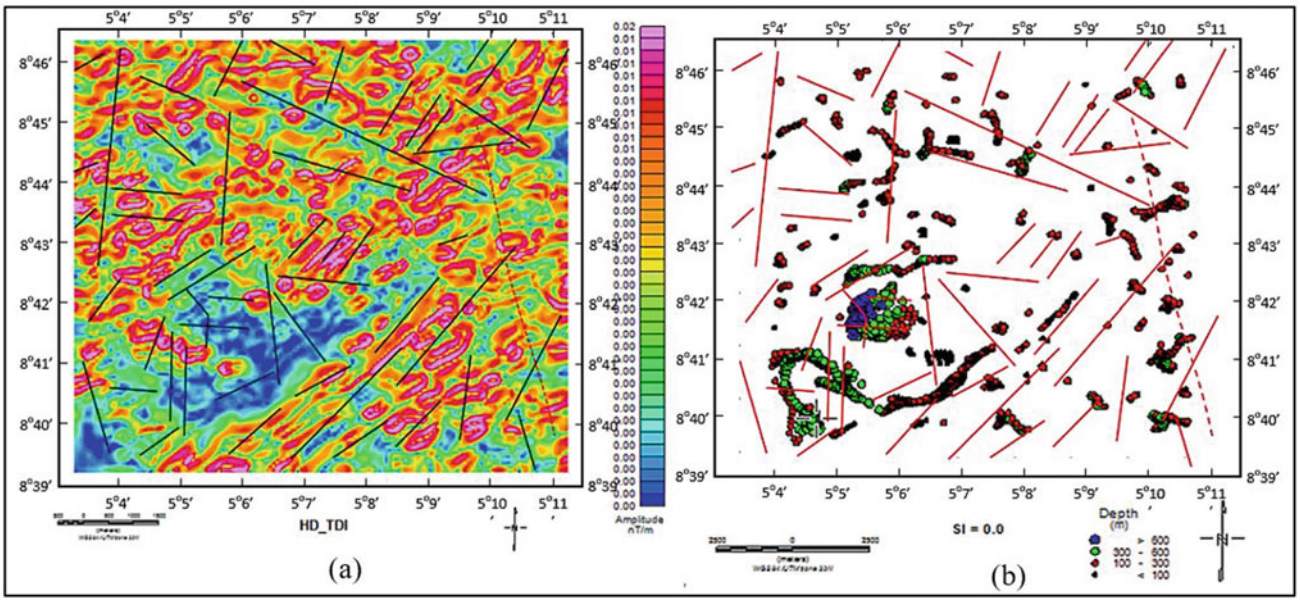

Fig. 5 **a** Total horizontal derivative and; **b** Euler deconvolution maps of Bishewa

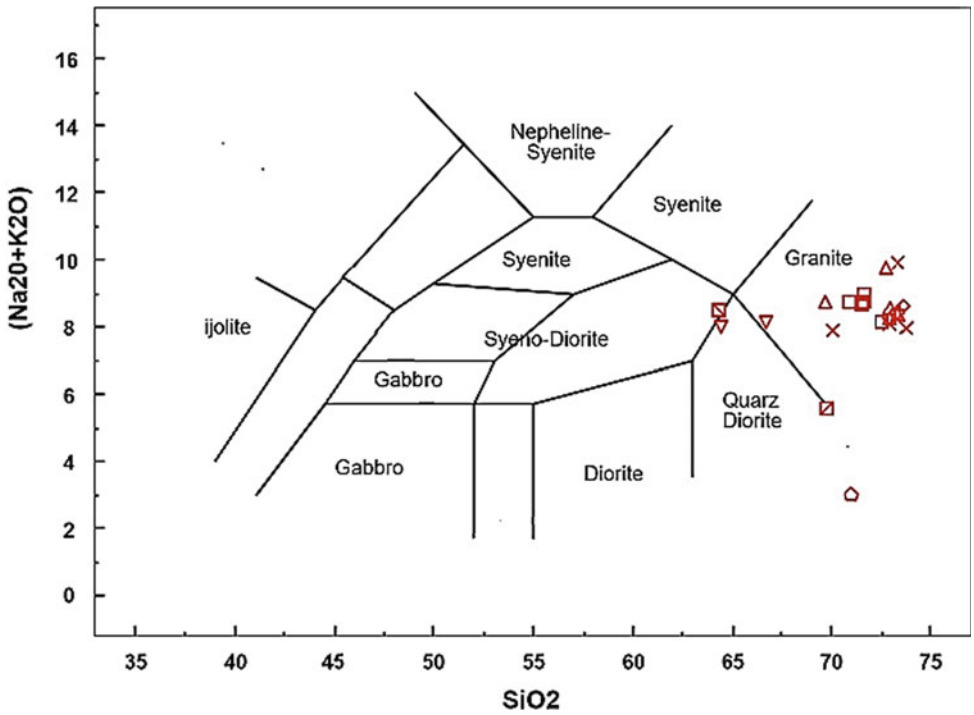

Fig. 6 TAS discriminatory plot for plutonic rocks in Bishewa area (Caby 1989)

4 Discussion

The residual magnetic anomalies (Figs. 3a and 4) obtained from reduction to magnetic equator through fast Fourier transform (FFT) of the TMI map range from −174.9 to 111.9 nT while the corresponding AS amplitude (Fig. 3b) range from 0 to 0.7 nT m^{-1}. The negative (low) anomalies in the southern region correspond to the high amplitude of analytic signal attributable to granitic intrusion (Mume 1964) comprising biotite hornblende granite and porphyritic granite (Neoproterozoic). The relatively high anomalies coincide with the presence of relict amphibolite lenses outcropping within the massive hornblende-bearing schist (Lower Proterozoic) in the southcentral and the sandstone in the northeastern areas while the intermediate anomalies

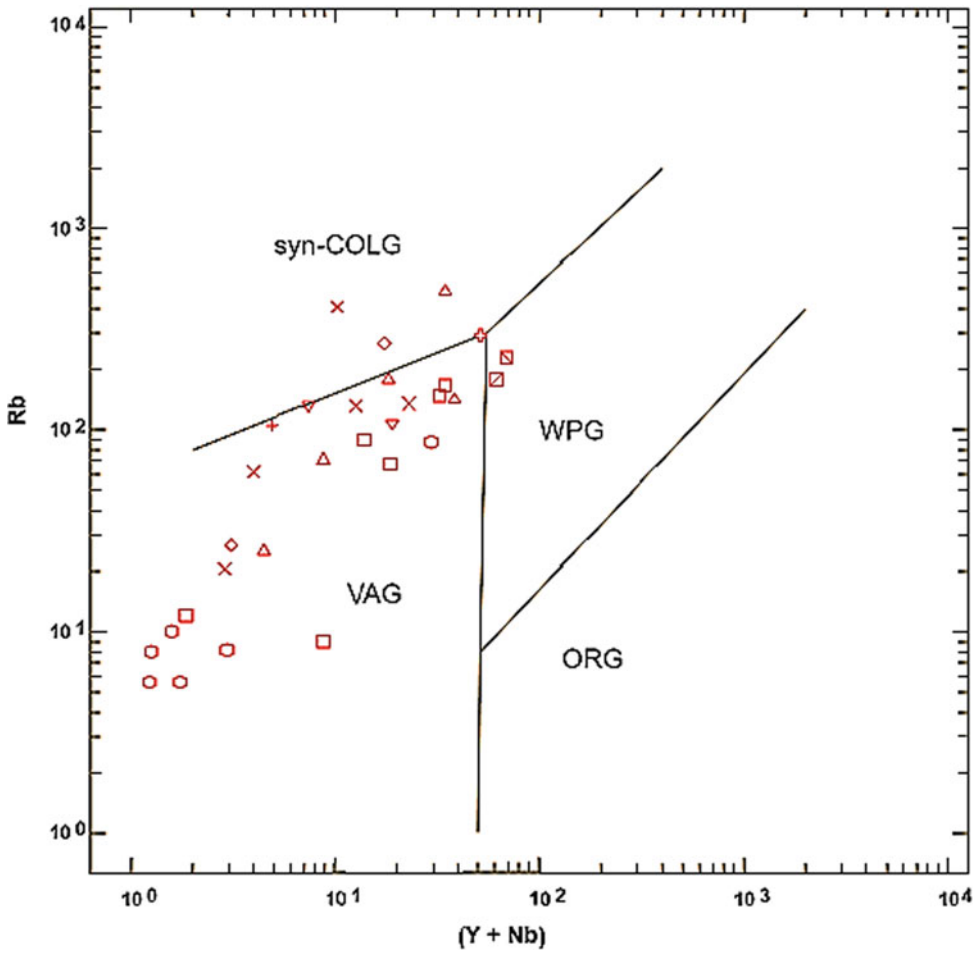

Fig. 7 Rb versus Y + Nb discrimination diagram for granitic rocks in Bishewa area (Cox et al. 1979)

depict the predominant migmatitic gneiss rocks. The THDR model (Fig. 5a) depicts the dominantly NE–SW structural grains of the Nigerian basement complex which lies between the Neoproterozoic Trans-Saharan Fold Belt (Ajadi 2017) formed between 750 and 500 Ma by accretion of terrains between the converging Archaean blocks of the West African Craton, the Congo Craton and the East Saharan Block (Caby 1989). The Euler deconvolution at SI = 0 for a contact (Foss 2011) (Fig. 5b), corresponds to the linear trend revealed on THDR and estimated depth to magnetic source ranges from 100 to 600 m. Total alkali versus silica discriminatory plot for the plutonic rocks (Cox et al. 1979) in the study area (Fig. 6) shows granitic affinity with few being dioritic while the trace element tectonic discrimination plot of Rb versus Y + Nb for the granitic rocks in the area (Pearce et al. 1984) (Fig. 7) suggests an intra-continental volcanic arc origin that is spatially related to the established easterly dipping subduction zone in the eastern part of West African craton (see Fig. 1 inset) (Caby 1989).

5 Conclusions

Interpretation of the high resolution aeromagnetic data of Bishewa area has revealed the contrasting lithologic units with associated structural grains. Structural relationships between the granites and metasedimentary host rocks suggest that the emplacement of the granitoids are associated with early, large-scale thermotectonic regional deformation associated with transpressional regime that is characterized by WNW-ESE shortening and a large-scale NE-SW trending fractures within the Nigerian basement complex. Structural relationships between the metasedimentary host rocks and the intruding granites suggest an emplacement within early, large-scale thermotectonic regional deformation of the Nigerian basement complex. Geochemical plots revealed that the granitic rocks of the study area are structurally emplaced within a subduction-related volcanic arc environment.

References

Ajadi, J.: Geochemistry and petrogenetic evolution of rocks around Bishewa-Ologomo area, part of Lafiagi Sheet 203, Northcentral Nigeria. Int. J. Sci. Eng. Res. **8**(4), 1333–1343 (2017)

Caby, R.: Precambrian terranes of Benin-Nigeria and Northeast Brazil and the late Proterozoic South Atlantic fit. Geol. Soc. Am. Spec. Pap. **230**, 145–158 (1989)

Cox, K.J., Bell, J.D., Pankhurst, R.J.: The Interpretation of Igneous Rocks, 450 pp. Allen and Unwin, St Leonards (1979)

Fairhead, J.D., Williams, S.E.: Evaluating normalized magnetic derivatives for structural mapping. SEG 2006 New Orleans Extended Abstract. SEG (2006)

Foss, C.: Magnetic data enhancement and depth estimation. In: Gupta, H.K. (ed.) Encyclopedia of Solid Earth Geophysics. Springer Science+Business Media B.V. (2011)

Garba, A.A., Adekeye, J.I.D., Akande, S.O., Ajadi, J.: Geochemistry and rare-metal bearing potentials of pegmatites of Gbugbu, Lema and Bishewa areas of North Central Nigeria. J. Environ. Earth Sci. **9**(3), 170–186 (2019)

Mume, W.G.: Negative total-intensity magnetic anomalies in the southeast of South Australia. J. Geophys. Res. **69**(2), 309–315 (1964)

Nabighian, M.N.: The analytic signal of two-dimensional magnetic bodies with polygonal cross-section: its properties and use for automated anomaly interpretation. Geophysics 507–517 (1972)

Paananen, M.: Completed lineament interpretation of the Oikiluoto region. Posiva (2013).

Pearce, J.A., Harris, N.B.W., Tindle, A.G.: Trace element discrimination diagrams for the tectonic interpretation of granitic rocks. J. Petrol. **25**(4), 956–983 (1984)

Thompson, D.T.: EULDPH-new technique for making computer-assisted depth estimates from magnetic data. Geophysics, 31–37 (1982)

Thurston, J.B., Smith, R.S., Guillion, J.C.: A multi-model method for depth. Geophysics, 555–561 (2002)

Effect of the Movement Across a Surface Breaking, Inclined, Locked, Finite Strike-Slip Fault in Visco-elastic Medium of Burger's Rheology

Piu Kundu and Seema Sarkar Mondal

Abstract

Seismically active regions are associated with fault systems and the movement of these faults influences the nature of stress accumulation/release in that region. For an in-depth analysis of the effect of such movement, we here developed a mathematical model by considering a surface breaking, inclined, finite strike-slip fault in the visco-elastic medium of Burger's rheology. The caused deformation in the medium was then considered. Analytical expressions for displacements, stresses and strains were derived using Green's function technique and Laplace transform. The variation of displacements, stresses and strains due to the locked fault was studied. These variations are graphically depicted for different inclinations of the fault with the free surface and for different fault movement velocities using MATLAB. Such studies may shed some light on the nature of stress and strain accumulation/release due to fault movement in Burger medium.

Keywords

Finite strike-slip fault • Locked fault • Aseismic period • Burger's rheology • Green's function technique

1 Introduction

Earthquake is the shaking of the surface of the earth, resulting in the sudden release of energy in the earth's lithosphere that creates seismic waves. Tectonic earthquakes occur when there is sufficiently stored elastic strain energy to drive fracture propagation along a fault plane. Recently, researchers have shown an increasing interest in the study of the nature of stress and strain accumulating/release due to fault movement in seismically active regions. While analyzing the dynamics of the earthquake process in that region, the study must be carried out not only during seismic periods (when an earthquake takes place) but also during the apparently static aseismic periods which involve slow, subsurface movements. These phenomena stimulated us to develop a mathematical model during aseismic periods to study the stress–strain accumulation/release due to seismic event.

A pioneering work on earthquake fault including static ground deformations in elastic media was started by Steketee (1958a, b). Okada (1986) presented an analytical expression for the surface displacements, strains and tilts due to inclined faults in a half-space for point and finite rectangular sources. Further, Okada (1992) calculated the internal displacements, strains and tilts for the same model as explained in 1986. In his book, Paul Segal (2010) has vividly described the elastic solution in continuum mechanics including the basics of volcano deformation and some advanced topics including visco-elasticity, elastic gravitational coupling and friction. Mondal et al. (2018) developed the effect of movement of an infinite, buried, inclined fault in visco-elastic half-space of Burger's Rheology.

In most of these cases, the material is taken as elastic or visco-elastic half-space of Maxwell type or layered medium of standard linear solid representing the lithosphere-asthenosphere system. To the best of our knowledge, no theoretical model has been previously developed with finite fault in the visco-elastic half-space of Burger element type to represent earthquake faults. Hu (2016) suggested that Burger's type visco-elastic material may be a suitable representation of the lithosphere-asthenosphere system in the seismically active region during aseismic periods. Also, Burger's rheology has been used to describe post-seismic deformations as found in Pollitz (2003) and Hetland and Hager (2005). The Burger model which is the combination of Kelvin-Voiget and the Maxwell type material gives a

P. Kundu · S. S. Mondal (✉)
Department of Mathematics, National Institute of Technology Durgapur, Durgpur, 713209, India

M. Meghraoui et al. (eds.), *Advances in Geophysics, Tectonics and Petroleum Geosciences*,
Advances in Science, Technology & Innovation, https://doi.org/10.1007/978-3-030-73026-0_118

comprehensive model for deriving time-dependent solutions for displacements, stresses and strains.

2 Model Description

In this paper, a theoretical model of a finite, strike-slip fault in the lithosphere-asthenosphere system in visco-elastic medium of Burger's rheology was considered. The fault was taken to be inclined to the free surface, and the nature of displacements, stresses and strains was analyzed. Graphical representation of displacements, stresses and strains for different inclinations of the fault and various fault movement velocities was depicted from the analytical study.

A three dimensional theoretical model of a finite, locked, surface breaking, inclined, strike-slip fault of length $2L$ (L-finite), width D and inclination θ with the free surface was taken in the lithosphere-asthenosphere system. To represent this, we introduced a rectangular Cartesian co-ordinate system (y_1, y_2, y_3) with plane free surface as $y_3 = 0$, y_3 axis points to the half-space, y_1 is on the free surface parallel to the upper edge of the fault, y_2 axis is perpendicular to y_1–y_3 plane. For convenience, we introduced a new co-ordinate system (y'_1, y'_2, y'_3) as shown in Fig. 1 which is related to (y_1, y_2, y_3) via the following relations;

$$y'_1 = y_1, \quad y'_2 = y_2 \sin\theta - y_3 \cos\theta, \quad y'_3 = y_2 \cos\theta + y_3 \sin\theta$$

To determine the displacements, stresses and strains, we considered the constitutive laws in the Burger medium which gave a relation between stress and strain including time derivatives. If the inertial forces are too small for a small deformation then the acceleration can be taken to be negligible and the body forces will not act in the system during our consideration. Under such situation, we considered the quasi-static equilibrium equations for the visco-elastic half-space. Along with the constitutive equation and stress equation of motion, suitable boundary conditions on stresses and initial conditions were taken. We started with a situation when the system is in an aseismic state. In this case, the displacements, stresses and strains are continuous throughout the system and their solutions can be found by using Laplace transform w.r.t time t to get a boundary value problem. Finally, inverse Laplace transform was considered to get the solutions for displacements, stresses and strains in the absence of any fault movement. It is to be noted that due to the sudden movement across the fault, the accumulated stress will be released at least to some extent and the fault becomes locked when the shear stress near the fault has been sufficiently released. For a comparatively short period of time during and after sudden fault movement, the inertial forces are not small and cannot be neglected. We leave out this short period of time during and immediately after sudden fault movement and consider the model after the restoration of the aseismic state which occurs when the seismic disturbances near the fault gradually disappear. We determined the displacements, stresses and strains during this second phase of aseismic state which is restored in the system after the sudden fault movement. The solutions of displacements, stresses and strains of this phase can be obtained using Laplace transform and Green's function technique (Maruyama 1966; Rybicki 1971). Hence, the final solutions for displacements, stresses and strains can be obtained by taking the sum of displacements, stresses and strains before and after the fault movement.

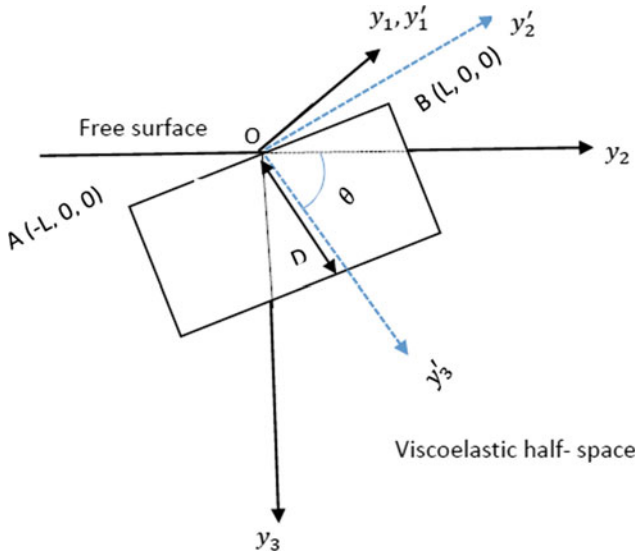

Fig. 1 A finite, surface breaking, inclined, locked strike-slip fault in visco-elastic half-space of Burger medium

3 Discussion

Some graphical representations of analytical expressions for displacements, stresses and strains against variation in depth, distances from the fault, inclinations and time were plotted which can depict the pattern of displacement, stress and strain accumulation/release due to fault movement in a Burger medium. Such representation may help develop an earthquake prediction program.

4 Conclusions

The explicit expressions for displacements, stresses and strains for a surface breaking, locked, inclined, finite strike-slip fault in visco-elastic half-space of Burger's rheology have been obtained. These analytical solutions are useful in modeling the lithospheric-asthenospheric deformation associated with strike-slip faulting in the earth.

Graphically, it was observed that the nature of displacements, stresses and strains were affected by the variation of inclination of the fault with free surface, velocity of the fault movements. The model was validated numerically and computed using suitable values of the model parameters. It was observed that the total displacement due to an infinite fault in a Burger medium (Mondal et al. 2018) is greater than that of a finite fault in the same medium. Permanent surface deformations which occur as a result of faulting can be measured by geodetic survey carried out before and after an earthquake. It was also observed that there are stress accumulation and release due to fault movement. The nature and the rate of stress accumulation/release near the fault may be used to study the behavior of the medium.

References

Hetland, E.A., Hager, B.H.: Postseismic and interseismic displacements near a strike-slip fault: a two dimensional theory for general linear viscoelastic rheologies. J. Geophys. Res. **110**, B10401 (2005). https://doi.org/10.1029/2005JB003689

Hu, Y., Burgmann, R., Banerjee, P., Feng, L., Hill, E.M., Ito, T., Tabei, T., Wang, K.: Asthenosphere rheology inferred from observations of the 2012 Indian Ocean Earthquake. Nature **538**, 368–372 (2016)

Maruyama, T.: On two dimensional dislocations in an infinite and semi-infinite medium. Bull. Earth-quake Res. Inst. Tokyo Univ. **44** (part 3), 811–871 (1966)

Mondal, D., Sarkar (Mondal), S., Sen. S.: Effect of movement across a long, inclined, buried, creeping, strike-slip fault in the visco-elastic medium of burger's rheology. J. Eng. Appl. Sci. **14**(3), 965–974 (2018)

Okada, Y.: Surface deformation due to shear and tensile fault in a half-space. Bull. Seismol. Soc. Am. **75**(4), 1135–1154 (1986)

Okada, Y.: Internal deformation due to shear and tensile fault in a half-space. Bull. Seismol. Soc. Am. **82**(2), 1018–1040 (1992)

Pollitz, F.F.: Transient rheology of the uppermost mantle beneath the Mojave desert, California. Earth Planet. Sci. Lett. **215**, 89–104 (2003)

Rybicki, K.: The elastic residual field of a very long strike-slip fault in the presence of a discontinuity. Bull. Seis. Soc. Am. **61**, 79–92 (1971)

Segal, P.: Earthquake and Volcano Deformation. Princeton University Press (2010)

Stekeetee, J.A.: On Volterra's dislocations in a semi-infinite medium. Can. J. Phys. **36**, 192–205 (1958a)

Stekeetee, J.A.: Some geophysical applications of the theory of dislocations. Can. J. Phys. **36**, 1168–1198 (1958b)

Tectonics and Geodynamics

Major Kinematic Revolutions: The Underside of the Maps

Daniel Aslanian, Maryline Moulin, Marina Rabineau, Philippe Schnürle, Estelle Leroux, Romain Pellen, and Joseph Thompson

Abstract

Earth's surface features, on land surface and ocean floor, are intimately related to the dynamics of the Earth's interior. Large-scale topographic features, such as seafloor spreading ridges, plateaus, volcanic eruptions, mountain ranges, cratonic basins, pediments, and alluvial/fluvial/deltaic/slope/deep systems, are the product of numerous parameters interacting in various ways: tectonic history, lithosphere and mantle segmentation, vertical and lateral crustal movements, mantle convection, heat fluxes, lithospheric composition, the presence of fluids, and even the core's dynamo. Subsidence and isostatic rebound, uplift, climatic variation, and fluid escape are closely connected to the processes of erosion, sedimentary mass transfer, and ultimately, deposition and storage of material in deep basins. These processes are at the heart of the sedimentary cycle, and at the same time responsible for generating sedimentary archives of Earth's past geodynamic and climatic activity and landform evolution.

Despite the great influence of these parameters on Earth's surface features and the people, the complex nature of their interactions still needs to be understood.

We proposed here a kinematic reading grid of some events that may give a new view of these interactions.

Keywords

Kinematic phases • Geodynamic • Tectonics • Kimmeridgian • Messinian

D. Aslanian (✉) · M. Moulin · P. Schnürle · E. Leroux
IFREMER, REM/GM/LGS, Centre de Brest,
29280 Plouzané, France
e-mail: daniel.aslanian@ifremer.fr

M. Rabineau · R. Pellen
CNRS, UMR6538, Domaines Océaniques, IUEM,
29280 Plouzané, France

J. Thompson
University of Accra, P.O Box LG 25 Legon, Accra, Ghana

1 Introduction

Mountains building and their erosion and peneplanation, sediment, and nutriment transfer trough river into continental plate-form and deep ocean and are deeply connected with the growth cycle of the Earth, the birth and the evolution of the oceans, the paleo-climate, and the paleo-oceanography variations, which are all linked with deep Earth processes. Mantle evolution and tectonic forces are thought to constitute the engine of the ocean floor, creating and destroying ocean basins, and driving complex structural and sedimentological evolution at ocean margins. Despite this general assumption, lots of questions still remain unanswered; among them: What drives horizontal and vertical movements of the crust, what are the nature and history of these movements in different geodynamic contexts, and how do these movements drive landform evolution, basin subsidence, and erosion? What processes control the evolution of sedimentary basins, from tectonic drivers deep inside the Earth to surface conditions driving physical and chemical weathering, and how are they linked? How have landforms evolved in response to the combination of vertical and horizontal movements, sediment erosion, and deposition, and how will they evolve going forwards? How do sedimentary archives preserve a history of these processes, as well as Earth's history of catastrophic events, such as earthquakes, tsunamis, landslides, and volcanic eruptions? Probing the strong correlation between deep and surface processes in order to understand the Earth's growing and to model forecasts, needs indeed a multidisciplinary approach.

Published data sets of the past ~250 Ma show several worldwide events, such as mass extinctions, sea-level lows, continental flood-basalt eruptions, mountain-building events, abrupt changes in seafloor spreading, ocean-anoxic and black-shale events, or large evaporite deposits (Rampino and Caldeira 1992). These events present a cyclicity which may be related to the geodynamic changes as illustrated by the dislocation of Pangea in three main episodes: Triassic (195–

M. Meghraoui et al. (eds.), *Advances in Geophysics, Tectonics and Petroleum Geosciences*,
Advances in Science, Technology & Innovation, https://doi.org/10.1007/978-3-030-73026-0_119

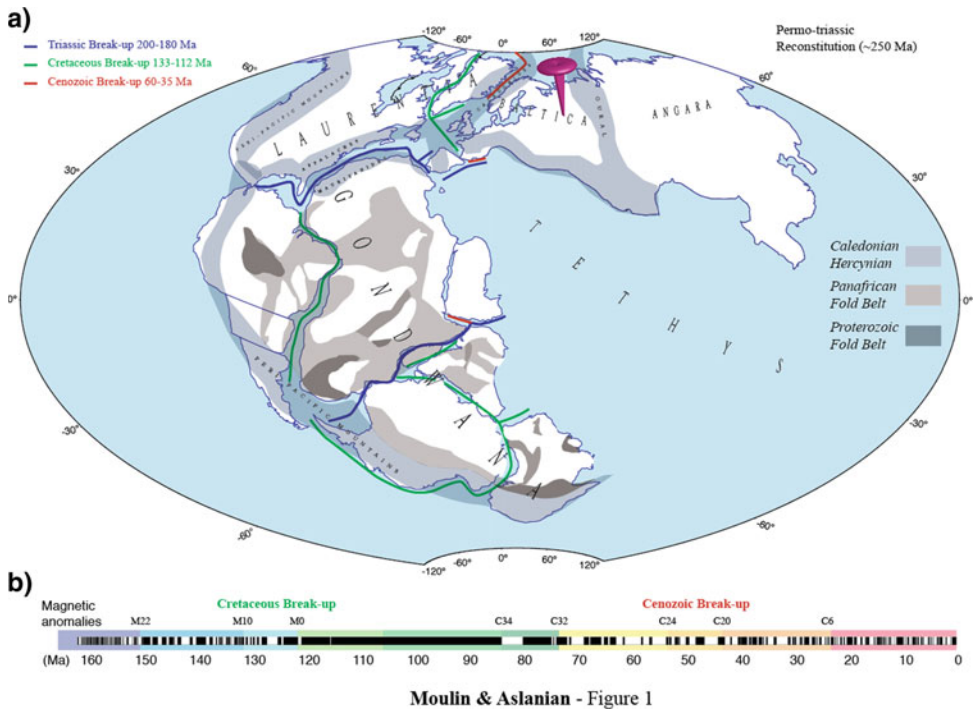

Fig. 1 **a** Reconstruction at Permo–Triassic time just before the break-up of the mega-continent Pangea. This break-up occurred in three main episodes separated by about 60 Ma. The Upper Triassic episode separated the Pangea in three equivalent blocks. The second episode (in green) occurred during the Early Cretaceous, and the last episode (in red) during the Tertiary. Note the almost general coincidence between the different break-ups and older orogenic belts. The block is considered as the fixed plate. Hammer Projection. **b** Magnetic anomalies inversions. Note the change of the pattern around the Cretaceous and Cenozoic break-ups, after Moulin and Aslanian (2010)

185 Ma), Early Cretaceous (135–125 Ma), and Tertiary (75–65 Ma), that can also be recognized at first order on the time distribution of Earth's magnetic field, which suggests the possibility of a link between biological extinction, magnetic reversal, large body impact (Raup 1985) and global kinematic phases (Moulin and Aslanian 2010) (Fig. 1).

The tectonic events, oceanic and subduction evolution, transpression, and basin inversions were investigated by Matthews et al. (2012) who show that the reorganization which occurred between 105 and 100 Ma was global in scale and affected all major plates.

We presented here two recent studies covering two different periods: Kimmeridgian and Messinian times.

1.1 Kimmeridgian Revolution

There are very few parts of the oceans that are old enough to record this period on the Earth, but all of them were impacted by this event (Thompson et al., Submitted—Fig. 2).

The Central Atlantic shows, at chron M25 (Oxfordian–Kimmeridgian boundary), an increase in the spreading rate (to 2.7 cm/y) (Labails et al. 2010), which corresponds to a structural change in the basement observed on seismic lines (Klingelhoefer et al. 2009; Labails et al. 2009). As noticed by Labails et al. (2010), in the Central Atlantic Ocean. The Oxfordian–Kimmeridgian boundary appears to be the time of a major tectonic event.

In the Pacific Ocean, this Kimmeridgian tectonic event was recorded in the evolutions of the Pacific–Izanagi–Farallon and the Pacific–Farallon–Phoenix triple junctions. The first triple junction exhibits an 800 km-eastward ridge jump, forming the Shatsky Rise (Nakanishi et al. 1989; Nakanishi and Sager 1996; Sager et al. 1999; Mahoney et al. 2005) which will end at Barremian time (~125 Ma). During the same period, the Central Pacific Basin (CPB) saw the birth of the Trinidad microplate as the result of a reorganization of the plate boundaries (Nakanishi and Winterer 1998), recorded in the change in the trend of the Phoenix lineations: two triple junctions (TJ) appeared, the Ridge–Ridge–Ridge Pacific–Farallon–Trinidad TJ and the Fault–Fault–Ridge Pacific–Trinidad–Phoenix TJ. Synchronous with the birth of the Trinidad microplate, the nearby Magellan Rise was formed (Winterer et al. 1973) as probably the Mid-Pacific Mountains (Nakanishi et al. 1999).

In the Indian Ocean, the north-western Australian margins began to form, with the onset of seafloor spreading along Argo Ridge at 155 Ma (Veevers et al. 1985; Fullerton et al. 1989; Gibbons et al. 2012), and the oceanic spreading

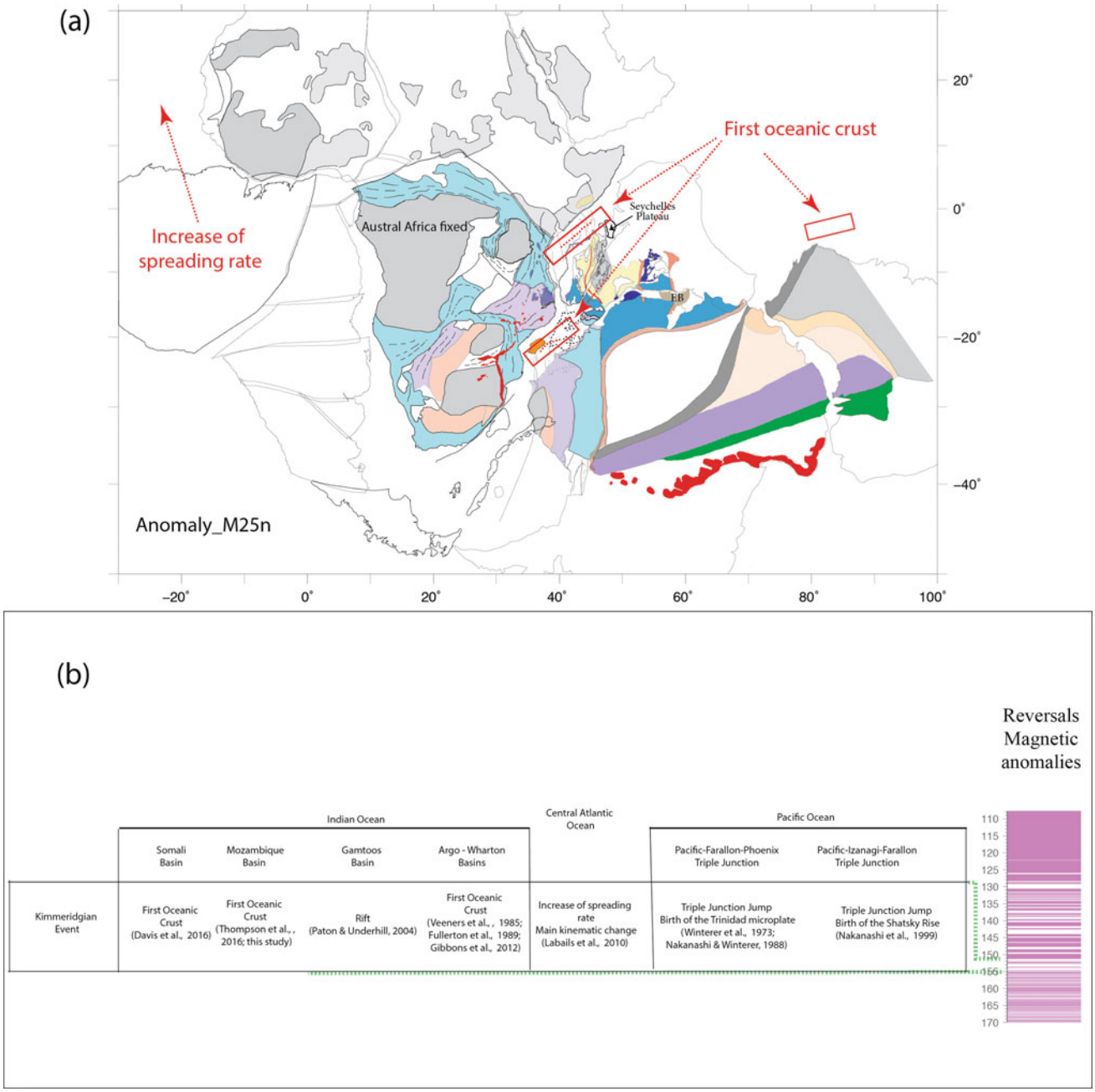

Fig. 2 **a** Reconstructions at anomaly M25, after Moulin et al. (2010) and Thompson et al. (2019); highlighting the relationship between the first break-up of East Gondwana, with the major increase in spreading rate in the Central Atlantic Ocean (Labails et al. 2010). **b** Expressions of Kimmeridgian event in the Oceans and Basins (Thomspon et al., submitted). Time scale from Ogg et al. (2016)

started at the same time in the Somalia Basin (Davis et al. 2016) and Mozambique Basin (Thompson et al. , 2019).

Due to these global observations and the coincidence with the magnetic reversals pattern, Thompson et al. (submitted) proposed that this first break-up of the Gondwana super plate is the result of a global kinematic revolution at Kimmeridgian period, which reactivated the old rift structures allowing the initiation of the Mozambique and the Somali basins.

1.2 Messinian Revolution

The catastrophic Messinian event is famous in the Mediterranean Sea. This event is widely regarded as one of the most dramatic episodes of oceanic changes over the last 20 million years. It started 5.97 million years ago, when vast amounts of evaporite began to be deposited in the Mediterranean area, leading to a significant drop in Global Ocean salinity (Adams et al. 1977).

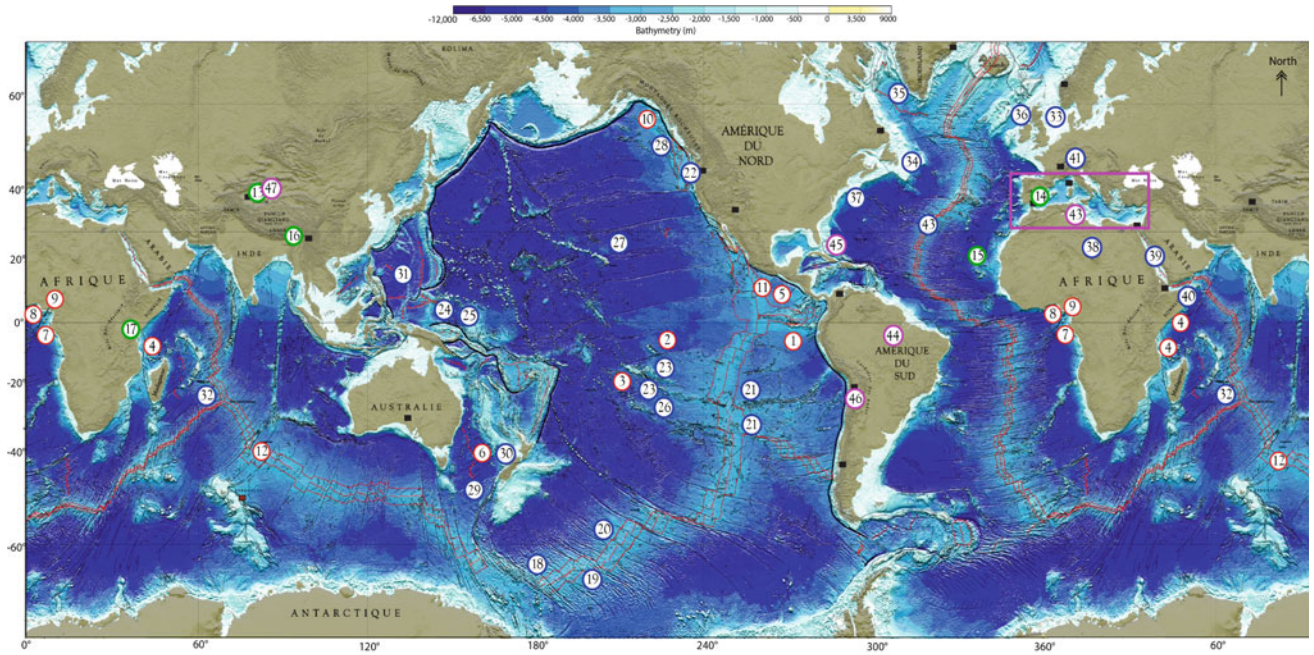

INCREASED RELIEF

■ location of increased relief area since 6 Ma

MAGMATISM

Rejuvenated Magmatism (5.9 Ma-5 Ma)

1. Galapagos (Eastern Central Pacific)
2. Cook Austral (Central Pacific)
3. Marquesas plateau (Central Pacific)
4. Mayotte & Comores islands & Somali Basin (Indian Ocean)
5. Bowland & Rosencrands (Central Panama)
6. Tasmantid Seamounts (South Pacific)
7. Annobon Island (Central Atlantic)
8. Cameroon & Guinea (Central Africa)
9. Biu Plateau & Cameroon Volcanic line (Central Africa)

Rejuvenated Magmatism (4 -3.6 Ma)

10. Dickins & Pratt-Welker Islands (Gulf of Alaska)
11. Mathematicians Seamounts (Pacific Ocean)

Decrease in the ridge crustal production

12. Saint-Paul and Amsterdam (Indian Ocean)

CARBONATITE

13. Yuli (China), age: 6 Ma-5 Ma
14. Calatrava (Spain), age: 6 Ma-5 Ma
15. Sao Vicente (Cap Verde), age: 6 Ma-5 Ma
16. Namjagbarwa (China), age: 6 Ma-5 Ma
17. Main Sadiman (Tanzania), age: 4 Ma

Some Ecological events

44. Onset of the Amazonian rainforest of present-day dimensions
45. Change in sediment architecture in the Bahamian platform
46. Onset of present-day hyper-aridity in the Atacama desert
47. Onset of present-day hyper-aridity in the Taklimakan desert

KINEMATICS

Major reorganizations in the Pacific-Antarctic & Indian plates around 5.9 Ma

18. Abrupt clockwise rotation along the Pitman fracture zone (South Pacific)
19. Rift propagators or linkage of ridge segments (Pacific plate)
20. Initiation of giant overlapping spreading centers (Pacific)
21. Formation of the Juan Fernandez and Easter microplates (East Pacific Rise)
22. Changes (rotation and spreading rate) in Juan de Fuca spreading center (Pacific)
23. Sharp change in the direction along Tahiti hotspot track (Pacific)
24. Sharp change in the direction along Mokil Atoll hotspot track (Pacific)
25. Sharp change in the direction in the Carolin Chain hotspot track (Pacific)
26. Sharp change in the direction in the MacDonald Seamount hotspot track (Pacific)
27. Sharp change in the direction in the Hawaii hotspot track (Pacific)
28. Sharp change in the direction in the Bowie Seamount hotspot track (Pacific)
29. Change in the rheologic behaviour of the Macquarie Plate (South-Western Pacific)
30. Change in tectonics of the Alpine Fault Zone of New Zealand
31. Change of motion of Philippine Sea Plate
32. Profound change in the geometry of the Indian Ocean Triple Junction with sharp increase in spreading velocity

Major reorganizations in the Atlantic and Arctic domains around 5.9 Ma

33. Induced subsidence increase along Central North Sea (North Atlantic)
34. Induced subsidence increase along Labrador Grand Banks (North Atlantic)
35. Induced subsidence increase off West Greenland (North Atlantic)
36. Induced subsidence increase along Scotian shelf (North Atlantic)
37. Induced subsidence increase along US Atlantic margin (North Atlantic)

Change in the Absolute motion of Africa relative to North America and Pacific plates

38. Change in the absolute motion of Africa relative to the hotspots ■ Location of the rotation pole
39. Geological evidences in the Red Sea (African plate boundary)
40. Geological evidences in the Gulf of Aden spreading sytems (African plate boundary)
41. Geological evidences in the Alpine deformation zone (African plate boundary)
42. Geological evidence in the Central and Southern Mid-Atlantic Ridge (African plate boundary)

Catastrophic event

43. Messinian Salinity Crisis (whole Mediterranean Area)

Fig. 3 Non-exhaustive compilation of observations showing the main tectonic changes in the World around 6–5 Ma. Topography and bathymetry from satellite data. See Leroux et al. (2018), for further bibliographic references

This event left indelible signs in the present terrestrial and marine landscapes through intense erosion associated with a Mediterranean >1000 m sea-level drop (Clauzon 1982; Bache et al. 2009; Pellen et al. 2019) and the accumulation of large volumes of clastic (Lofi et al. 2005; Gorini et al. 2005; Leroux et al. 2017) and evaporitic rocks, mainly gypsum and halite (Hsü et al. 1973; CIESM 2008).

As introduced by Pérez-Asensio (2013), "the general consensus is that the Mediterranean was isolated from the Atlantic due to the closure of the Betic and the Rifian corridors (Strait of Gibraltar) and that this led to the deposition of the Lower and Upper Evaporite". There are still key issues under intense debate. One of these concerns the main mechanisms that led to the isolation of the Mediterranean.

A recent review of geological and geophysical observations (Leroux et al. 2018) shows that Messinian time is marked by a number of important events of different types (Fig. 3): (1) A magmatic World peak is thus observed (red circles) with a reactivation of activity within a large number of volcanic plateaus; (2) At the same time, the oceans are recording the consequences of a global kinematic reorganization (blue circles); (3) It is also the period of an increase in landforms all over the World (black squares); (4) Besides the occurrence of very rare events, such as the formation of carbonatite, which appear in different parts of the World (green circles) and which, with magmatic rejuvenation, suggest deep geodynamic processes such as mantle plumes, asthenospheric upwelling, delamination of the sub-continental mantle and crust, convection of the deep mantle; (5) Finally, it is a period of severe and important ecological events (pink circles).

This review points towards a worldwide kinematic change at around 6 Ma. The synchronicity of many manifestations (tectonics, magmatism, kinematics, ecological events among others) at ~6 Ma, similar to those recognized from time to time on geological timescale, argues for a global geodynamic event that had led to many regional consequences on the Earth's surface. In particular, we proposed that it was the main trigger for the threefold increase in sediment deposits in the World Ocean over the last ~5 Ma, and also for the onset of the Messinian Salinity Crisis in the Mediterranean area, one of the most severe ecological crises in the Earth history.

The Mediterranean Messinian thus represents only one manifestation of a World event that we may call the Messinian revolution. This global nature gives a new perspective on the controversy we mentioned in the introduction. Given its almost closed sea situation, it is not surprising that this global kinematic revolution produces consequences exacerbated by a near closure of the strait located at Gibraltar level which links the Mediterranean to the global ocean and leads to its drying up. It has also been able to produce uplift movements at Mediterranean thresholds, in particular between Tunisia in the south and Calabria and Sicily in the north, which separates the Western and Eastern Mediterranean (marked by different evaporitic records), or the uplift of the "hot line of Morocco" which connects the Canary Islands to the east of the Alboran Sea and could contribute directly to containment.

2 Conclusions

The Earth geological history exhibits several global revolutions, which present striking correlations with mass extinctions, radiometric dates, frequency of geomagnetic reversals, and meteorites impacts (Pal and Creer 1986; Rampino 2015). These kinematic revolutions produced changes in the lithospheric stress field on very large wavelengths which may have used the tectonic heritage, as old sutures and rifts, producing large uplifts (as in South Africa), exhumation, break-up, erosion, impacting the sedimentary cycle. The origin of horizontal movements remains debatable (subduction pull, ridge push, mantle convection, etc.) but the correlation between large global revolutions and the changes in magnetic reversal patterns suggest a very deep origin. These revolutions appear to be cyclic with the Messinian revolution as the last member of these global event series.

References

Adams, C.G., et al.: The Messinian salinity crisis and evidence of late Miocene eustatic changes in the world ocean. Nature **269**(5627), 383–386 (1977)

Bache, F., et al.: Messinian erosional and salinity crises: view from the Provence Basin (Gulf of Lions, Western Mediterranean). Earth Planet. Sci. Lett **286**(1), 139–157 (2009)

Clauzon, G.: Le canyon messinien du Rhône: une preuve décisive du "desiccated deep basin model" [Hsü, Cita et Ryan, 1973]. Bull. Soc. Géol. France **7**(3), 597–610 (1982)

Davis, J.K., et al.: New Somali Basin magnetic anomalies and a plate model for the early Indian Ocean. Gondwana Res. **34**, 16–28 (2016)

Fullerton, L., et al.: Late Jurassic-Early Cretaceous evolution of the Eastern Indian Ocean adjacent to Northwest Australia. J. Geophys. Res. **94**(83), 2937–2953 (1989)

Gibbons, A.D., et al.: Constraining the Jurassic extent of Greater India: tectonic evolution of the West Australian margin. Geochem. Geophys. Geosyst. **13**(5) (2012). https://doi.org/10.1029/2011GC003919

Gorini, C., et al.: The Late Messinian salinity crisis and Late Miocene tectonism: interaction and consequences on the physiography and post-rift evolution of the Gulf of Lions margin. Mar. Petr. Geol. **22** (6), 695–712 (2005)

Hsü, K.J., et al. The origin of the Mediterranean evaporates. In: Initial Report of Deep Sea Drilling Project, 13, 2, Washington, D.C., U.S. Government Printing Office, pp. 1203–1231 (1973)

Klingelhoefer, F., et al.: Deep crustal structure of the SW-Moroccan margin from wide-angle and reflection seismic data (The DAKHLA experiment). Part A: Wide-Angle seismic models. Tectonophysics, Special issue: Role of the magmatism **468**(1–4), 63–82 (2009)

Labails, C., et al.: Deep crustal structure of the SW-Moroccan margin from wide-angle and reflection seismic data (The DAKHLA experiment). Part B: the tectonic heritage. Tectonophysics, Special issue: Role of the magmatism (2009)

Labails, C., et al.: An alternative early opening scenario for the Central Atlantic Ocean. Earth Planet. Sci. Lett. **297**, 355–368 (2010)

Leroux, E., et al.: High-resolution evolution of terrigenous sediment yields in the Provence Basin during the last 6 Ma: relation with climate and tectonics. Bas. Res. **29**(3), 305–339.

Leroux, L., et al.: The late Messinian event: a worldwide tectonic revolution. Terra Nova **30**(3), 207–214 (2018). Publisher's official version: https://doi.org/10.1111/ter.12327. Open Access version: https://archimer.ifremer.fr/doc/00422/53362/

Lofi, J., et al.: Erosional processes and paleo-environmental changes in the Western Gulf of Lions (SW France) during the Messinian Salinity Crisis. Mar. Geol. **217**(1), 1–30 (2005)

Mahoney, J.J., et al.: Jurassic-Cretaceous boundary age and mid-ocean-ridge–type mantle source for Shatsky Rise. Geology **33**(3), 185–188 (2005). https://doi.org/10.1130/G21378.1

Matthews, K.J., et al.: A global scale reorganization event at 105–100Ma. EPSL **355–356**, 283–298 (2012). https://doi.org/10.1016/j.epsl.2012.08.023

Moulin, M., Aslanian, D.: Corrigendum to: a new starting point for the South and Equatorial Atlantic Ocean. Earth Sci. Rev. (2010)

Moulin, M., Aslanian, D., Unternher, P.: A new starting point for the South and Equatorial Atlantic Ocean. Earth Sci. Rev. **98**(1), 1–37 (2010). https://doi.org/10.1016/j.earscirev.2009.08.001

Nakanishi, M., et al.: Magnetic lineations within Shatsky Rise, northwest Pacific Ocean: implications for hot spot–triple junction interaction and oceanic plateau formation. J. Geophys. Res. **104**, 7539–7556 (1999)

Nakanishi, M., Sager, W.W.: Formation of the Jurassic oceanic plateau, Shatsky Rise, northwestern Pacific Ocean. Eos Trans. AGU **77**(46), Fall Meet. Suppl., F705 (1996)

Nakanishi, M., Winterer, E.L.: Tectonic history of the Pacific-Farallon-Phoenixtriple junction from late Jurassicto Early Cretaceous: An abandoned Mesozoic spreading system in the Central Pacific Basin. J. Geophys. Res. **103**(B6), 12453–12468 (1998)

Nakanishi, M., et al.: Mesozoic magnetic anomaly lineations and seafloor spreading history of the northwestern Pacific. J. Geophys Res. **94**, 15437–15462 (1989)

Ogg, J.G., et al.: A Concise Geologic Time Scale. Elsevier, 240 p (2016). https://doi.org/10.1016/C2009-0-64442-1

CIESM: The Messinian salinity crisis from mega-deposits to microbiology—a consensus report. N° 33. In: Briand, F. (ed.) CIESM Workshop Monographs, 168 p, Monaco (2008)

Pal, P.C., Creer, K.M.: Geomagnetic reversal spurts and episodes of extraterrestrial catastrophism. Nature **320**(6058), 148–150 (1986)

Pellen, R., et al.: The Messinian Ebro River incision. Global Planet. Changes **181** (2019). https://doi.org/10.1016/j.gloplacha.2019.102988

Pérez-Asensio, J.N., et al.: Glacio-eustatic control on the origin and cessation of the Messinian salinity crisis. Global Planet. Change **111**, 1–8 (2013)

Rampino, M.R.: Disc dark matter in the Galaxy and potential cycles of extraterrestrial impacts, mass extinctions and geological events. Monthly Notices R. Astron. Soc. **448**(2), 1816–1820 (2015)

Rampino, M.R., Caldeira, K.: Episodes of terrestrial geologic activity during the past 260 million years: a quantitative approach. In: Dynamics and Evolution of Minor Bodies with Galactic and Geological Implications, pp. 143–159. Springer, Netherlands (1992)

Raup, D.M.: Magnetic reversals and mass extinctions. Nature **314**, 341–343 (1985)

Sager, W.W., et al.: Bathymetry of Shatsky Rise, Northwest Pacific Ocean: implications for ocean plateau development at a triple junction. J. Geophys. Res. **104**, 7557–7576 (1999)

Thompson, J.O. et al.: Submitted to Geology, Aug 2019. The opening of the Indian Ocean: a consequence of a major kinematic reorganization?

Thompson, J.O., et al.: New starting point for the Indian Ocean: Second phase of breakup for the Gondwana. Earth Sci. Rev. **191**, 26–56 (2019)

Veevers, J.J., et al.: Magnetic expression of the continent-ocean boundary between the western margin of Australia and the Eastern Indian Ocean. J. Geophys. Res. **56**, 106–120 (1985)

Winterer, E.L., et al.: Initial report of the deep-sea drilling project, vol. 17, 930 p. U.S. Gov. Print Off., Washington D.C. (1973)

Exhumed Lower Continental Crust and Proto-oceanic Crust Interactions? The BasAlg and ArcMal Deep Seismic Projects

Philippe Schnürle, Daniel Aslanian, Maryline Moulin, Alexandra Afilhado, Mikael Evain, Afonso Loureiro, Angélique Lepretre, and Nuno Dias

Abstract

The exhumed lower continental crust appears to be omnipresent in the intermediate domain of passive margins. However, the first oceanic crust seems to be essentially atypical in nature, herein called proto-oceanic, before the establishment of a homogeneous and stable oceanic crust. The interaction between these two domains suggested nearly 50 years ago (Bott in Tectonophysics 11:319–337, 1971) seems to be a crucial phenomenon in the genesis of passive margins; it has major consequences on the thermal and tectonic evolution of the margin, as well as on the geodynamic paleo-reconstructions of the system. In the Mediterranean, the Provençal Basin has already highlighted this relationship (Moulin et al. in BSGF 186:309–330, 2015; Afilhado et al. in BSGF, ILP Special volume 186:331–351, 2015) but some areas remain unresolved. We proposed two experiments, on either side of the Strait of Sicily: in the Algerian Basin (Western Mediterranean) and in the Levantine Basin (Eastern Mediterranean). In both places, the nature and geometry of the different segments of the Earth's crust, their boundaries and links are of crucial importance for a precise geodynamic evolution, which remains controversial.

Keywords

Proto-oceanic crust • Lower continental crust • Passive margins • Wide-angle seismics • Levantin Basin • Algerian Basin • Mediterranean Sea

1 Introduction

The transition from the so-called intermediate domain of passive continental margins located between the continental necking and the first true oceanic crust is still under debate and the exact boundary of the first true oceanic crust may be difficult to define in many, if not all, passive margins. The nature of the intermediate domain, after a more or less rapid and narrow continental thinning zone, is also the subject of debate and exhibits lateral variations. Over twenty years, Ifremer with its academic and industrial partners have imaged this transition zone in the Mediterranean Sea (Provençal Basin), the Central Atlantic (Morocco margins), the Equatorial Atlantic (Berrenhinhas-Maranão-Ceara margins), the central segment of the South Atlantic (Angola Margin, Santos Basin, Jequitinhonha-Almada-Camamu-Sergipe-Alagoas margins) and the Indian (Mozambique margins) oceans. The forwarded modeling of the wide-angle seismic profiles acquired at sea and on land during these experiments reveals an evolution from the continental necking zone to the true (but usually thin) oceanic crust, with a domain of exhumed material, most generally exhumed lower continental crust, and the existence of a proto-oceanic crust. Lateral and longitudinal variations were also described. In the Santos Basin for instance, the central segment presents strong lateral variation, showing a passage of a thin exhumed lower continental crust to an anomalous and probably heterogeneous crust, which can be inferred as proto-oceanic crust on a failed rift (Moulin et al. 2012; Evain et al. 2015). On the Ceara-Maranhão Margin, the 4–5 km thick intermediate domain is interpreted as exhumed lower continental crust. Seawards and parallel to the coast, an

P. Schnürle (✉) · D. Aslanian · M. Moulin · M. Evain · A. Lepretre
IFREMER, REM/GM/LGS, Centre de Brest, 29280 Plouzané, France
e-mail: Philippe.Schnurle@ifremer.fr

A. Afilhado
Instituto Superior de Engenharia de Lisboa, Lisboa, Portugal

A. Loureiro · N. Dias
Instituto Dom Luis, Faculdade das Ciencias da Universidade de Lisboa, Lisboa, Portugal

M. Meghraoui et al. (eds.), *Advances in Geophysics, Tectonics and Petroleum Geosciences*, Advances in Science, Technology & Innovation, https://doi.org/10.1007/978-3-030-73026-0_120

about 50 km-wide band of proto-oceanic crust is described before reaching a more normal but only 5 km thick oceanic crust (Aslanian et al. 2016). Lastly, in the Provençal Basin, wide-angle data and seismic 3D-grid, drilling and numerical stratigraphic modeling allow identifying a segmentation in three domains of different crustal nature: continental crust, exhumed lower continental crust and proto-oceanic crust (Moulin et al. 2015; Afilhado et al. 2015; Leroux et al. 2018). However, the nature and the evolution of some domains in the Mediterranean sea, as the Algerian and the Levantine basins, remain subject of debate. Opposite hypotheses are proposed, implying opposite geodynamic evolutions.

2 BasAlg Project

The opening of the Algerian Basin remains controversial regarding its kinematic evolution (north–south vs. east–west extension—Fig. 1), crustal nature (oceanic vs. thinned continental) and geodynamic process (slab roll-back vs. continental delimination-driven). Recent evolution (Ethève et al. 2016; Leprêtre et al. 2018) favors a two-step opening scenario including a first westward migration and a second one toward the edges of the basin, which is accompanied by detachment or delamination. Last, while the roll-back process is the most widely accepted mechanism to explain the coincidence of compression and expansion in this region, other models such as the collapse of the previously thickened continental crust during the Alpine stage (Dewey 1989; Platt and Vissers 1989) or lithospheric delamination (Roure et al. 2012) are also proposed. This great variety of evolution hypotheses arises from the differences in study scale, chosen approach and type of data, in particular the geological and/or geophysical, onshore and/or offshore data.

This leads to very different positions of the same element when the Cenozoic evolution of the Western Mediterranean system proposed by different authors is compared. This is illustrated with the position of the AlKaPeCa metamorphic units at 33 Ma (Fig. 2) and even the proposal of the absence of the Alboran Terrane in its pre-drift position (Carminati et al. 2012).

At the same time, the kinematic and amount of displacement between the different segments of the AlKaPeCa terrane are key data to determine origin and role of the observed limit between each onshore and offshore domain developed during the opening of the Western Mediterranean.

This basin presents a strong E-W segmentation which may play an important geodynamic role and must be studied in detail.

3 ArcMal Project

In the Eastern Mediterranean, models involving the opening and closing of the Neo-Tethys still depend largely on determining the nature, age and deformation of the crust forming the Cyprus, Herodotus and Levant basins, and many questions remain to be discussed. Thus, according to different authors, the opening of the Eastern Mediterranean began at the end of the Paleozoic (Stampfli et al. 1991; Stampfli and Borel 2004) or even in the Cretaceous (Dercourt et al. 1993; Ricou 1994). Granot (2016) proposes that the floor of the Herodotus Basin is of oceanic nature and 340 Ma in age, based on magnetic anomalies. Nevertheless, was rifting facilitated by a mantelic plume in the Lower Cretaceous, and followed by the accretion of an ocean floor during the period of magnetic calm between CM10N (~122 Ma) and C34N (~84 Ma, Segev et al. 2018)? The opening direction of these basins is also debatable and one may face the following question: is the Levant Margin a transform margin in direct connection with Neo-Tethys (Stampfli et al. 1991; Keeley 1994; Stampfli and Borel 2004) or a combined normal margin of the micro-continental block of Eratosthenes and Cyprus (Garfunkel 1998; Barrier and Vrielynck 2008; Gardosh et al. 2010)?

Schattner and Ben-Avraham (2007, 2012) propose that the Carmel Structure south of the Galilean Graben separates a basin to the north (Phoenician) from the Levantine Basin to

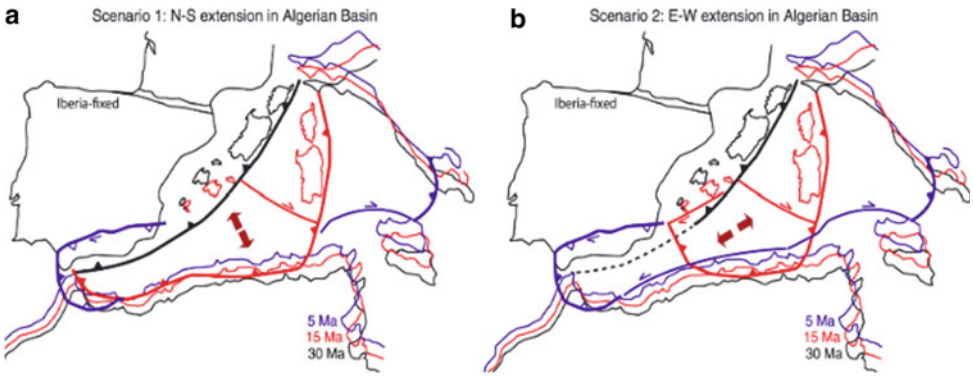

Fig. 1 Two types of scenarii for the opening of the Algerian Basin (Van Hinsbergen et al. 2014)

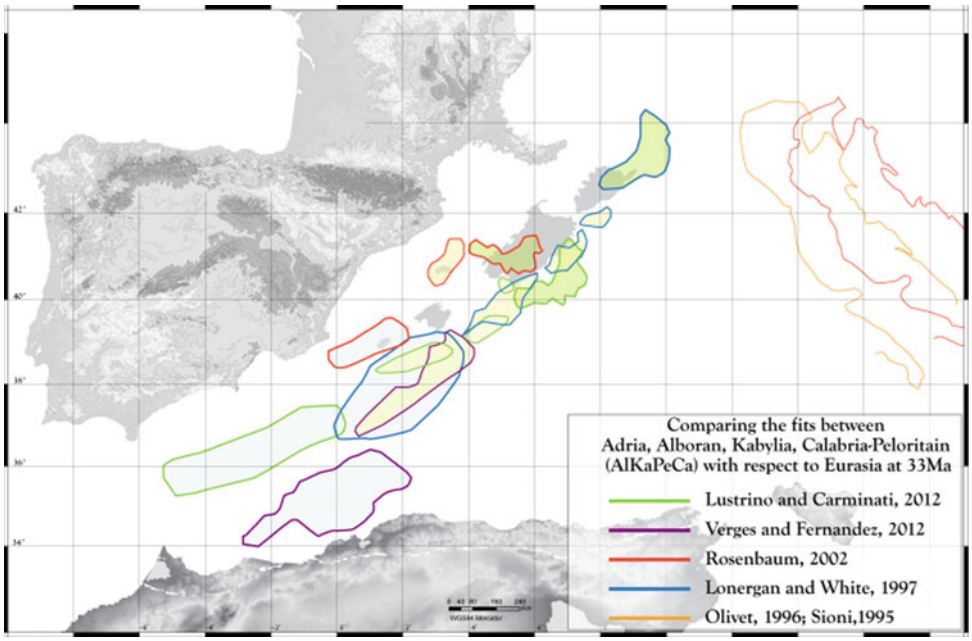

Fig. 2 Different positions of the AlKaPeKa blocks according to various author

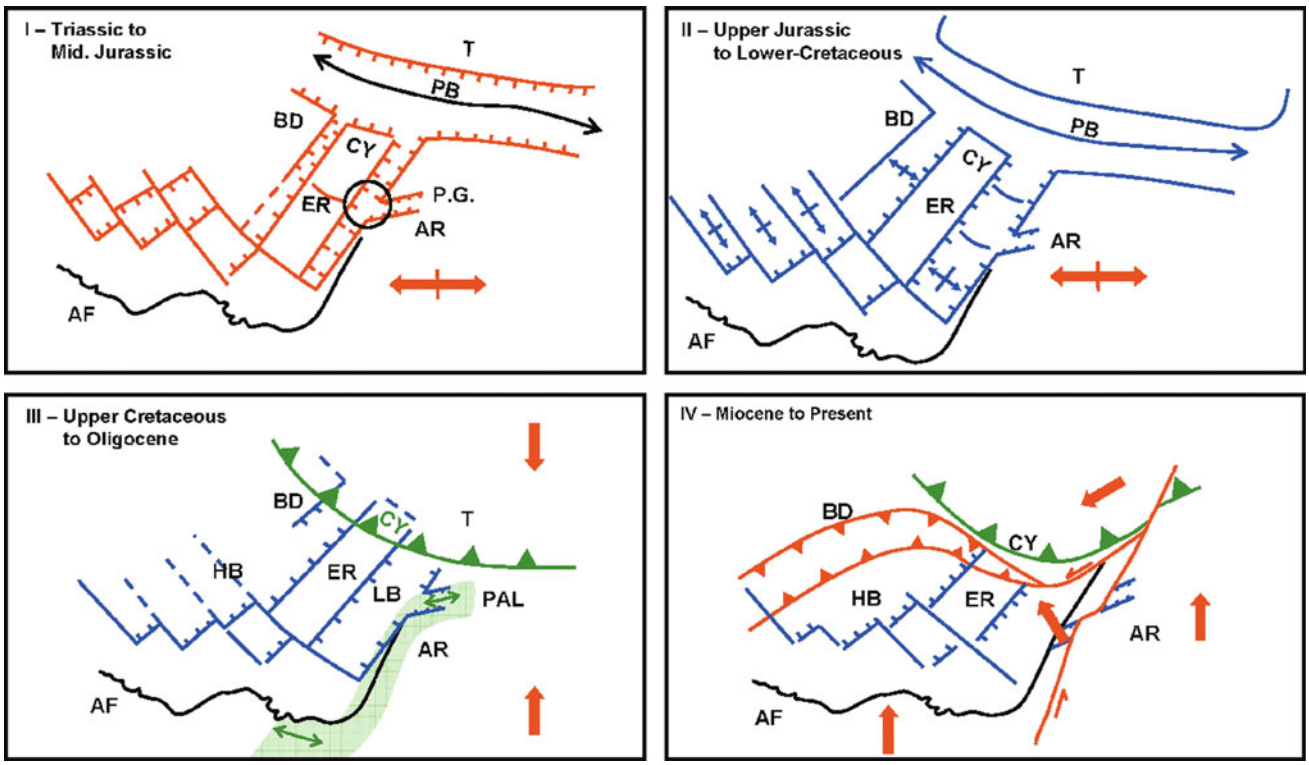

Fig. 3 Paleo-tectonic evolution of the Eastern Mediterranean from the Triassic (ER = Continental Block of Eratosthenes, CY = Cyprus, BD = Bey Daglari, HB = Herodot Basin, PB = Pamphyliein Basin, T = Taurus, AR = Arabia, AF = Africa: MR = Mediterranean Ride). (I) Rift from Triassic to Middle Jurassic. (II) Oceanic extension and accretion from the Upper Jurassic to the Cretaceous. (III) Upper Cretaceous: formation of the Cyprus Arc and its ophiolitic belt, subduction continues during the Paleogene. (IV) Miocene to the Present, activity of the Mediterranean Ridge, Latakia Ridge, and the transform fault of the Levant. According to Montadert et al. (2014)

the south. The northern basin would be rifted in Permian times from the Eratosthenes Block and followed by an oceanic N-S accretion, forming a sliding margin on its continental edge of north Levant (Galileo and Lebanese); the southern basin is derived from the NW migration of the Eratosthenes Block. Montadert et al. (2014) propose a paleo-tectonic scheme common to all basins in the Eastern Mediterranean, separated by transfer/transforming faults (Fig. 3).

Is the Levantine Basin rather a back-arc basin formed by the subduction of the Meso-Tethys (the Herodotus Basin) during the Senonian-Maastrichtian period (Segev and Rybakov 2010)? Has this extension been followed by a rift and accretion of oceanic crust (Frizon de Lamotte et al. 2011)? Active processes during rifting, such as crust thinning, exhumation of lower crust and/or upper mantle are poorly characterized, and the location of the ocean-continent transition in these basins also remains uncertain (Gardosh et al. 2010).

While the Levant Margin and Levantine Basin south of the Carmel Structure, the Eratosthenes Seamount, the Cypriot Arc and the Hecataeus Ridge have been the subject of several wide-angle seismic surveys, it is not the case of the Herodotus and North Levant basins, the Latakia Ridge and the Lebanese Margin. These structures identify areas where tectonic events are numerous and diverse, and structural boundaries are still poorly constrained.

4 Conclusions

We proposed to conduct two wide-angle and multi-channel reflection seismic surveys, which would allow determining the geometry, structure, and acoustic velocity of the different segments of the Algerian and Levantine basins, their bases and the underlying lithospheric mantle.

Characterizing the sequence of processes that lead from continental rifting to oceanic drifting during the genesis of passive margins is a key to our fundamental knowledge of the structure and history of the earth. Clarifying the nature and behavior of the first oceanic crust contributes to understanding the processes presently active at mid-oceanic ridges and transform faults. The respective role and behavior of the lower crust and upper mantle between rift and drift remain to be established.

Furthermore, the dynamic of the upper mantle is responsible for topography building, leading to consecutive erosion, subsidence and isostatic rebound, and is therefore connected to the quantification of global sedimentary mass transfer through time (Source to Sink). Finally, continental margins are the most populated and developed areas on earth. Deep Earth dynamics (topography, erosion, tectonics) are strongly related to naturals hazards such as earthquakes, slope instabilities, and tsunamis and mass transfers have important consequences on geo-resources and geothermal energy. The ability to read and understand the link between deep Earth dynamics and surface processes has therefore important societal impacts.

Thanks to these new cruises, this rather unique data set will cover most of the geological and geodynamical settings and hopefully establish the nature and geometry of the different segments, their limits and their connections, and to replace this new information in a geodynamic context in order to fully resolve the kinematic history of the Western and Eastern Mediterranean seas.

References

Afilhado A et al (2015) Deep crustal structure across an young passive margin from wide-angle and reflection seismic data (The SARDINIA Experiment)—II. Sardinia's margin. BSGF, ILP Special volume **186**, 331–351 (2015). https://doi.org/10.2113/gssgfbull.186.4-5.331

Aslanian, D., et al.: Seismic structure of the Maranhão-Barreirinhas--Ceará margin, NWBrazil, from the MAGIC wide-angleseismic, SBGF, Porto Alegre 2016.

Bott, M.H.P.: Evolution of young continental margins and formation of shelf basin. Tectonophysics **11**, 319–337, 1971

Barrier, E., Vrielynck, B.: Paleotectonic maps of the Middle East: atlas of 14 maps. Comm. de la Carte Geol. du Monde, Paris (2008)

Carminati, E., et al.: Geodynamic evolution of the central and western Mediterranean: tectonics versus igneous petrology constraints. Tectonophysics **579**, 173–192 (2012)

Dercourt, J., et al.: Atlas Tethys of Paleoenvironmental Maps. Gauthier-Villars, Paris (1993)

Dewey, J., et al.: Kinematics of the western mediterranean: In: Coward, M.P., Dietrich, D. (eds.) Alpine Tectonics, Geological Society of London Special Publication, vol. 45, pp. 265–283 (1989)

Etheve, N., et al.: Extensional versus contractional Cenozoic deformation in Ibiza (Balearic Promontory, Spain): integration in the West Mediterranean back-arc setting. Tectonophysics **682**, 35–55 (2016)

Evain, M., et al.: Deep structure of the Santos Basin-São Paulo Plateau System (SSPS). Geophys. J. Int. (2015). https://doi.org/10.1002/2014JB011561

Gardosh, M.A., et al.: Tethyan rifting in the Levant region and its role in Early Mesozoic crustal evolution. Geol. Soc. Spec. Publ. **341**, 9–36 (2010)

Garfunkel, Z.: Constrains on the origin and history of the Eastern Mediterranean basin. Tectonophysics (1998)

Granot, R.: Palaeozoic oceanic crust preserved beneath the eastern Mediterranean. Nat. Geosci. **9**(9), 701–705 (2016). https://doi.org/10.1038/ngeo2784

Keeley, M.L.: Phanerozoic evolution of the basins of northern Egypt and adjacent areas. Geol. Rundsch. **83**(4), 728–742 (1994). https://doi.org/10.1007/BF00251071

Leprêtre, R., et al.: The Tell-Rif orogenic system(Morocco, Algeria, Tunisia) and the structural heritage of the southern Tethys margin. BSGF Earth Sci Bull **189**, 10 (2018)

Leroux, E., et al.: Sedimentary markers in the Provençal Basin (western Mediterranean): a window into deep geodynamic processes. Terra Nova **27**, 122–129 (2015)

Leroux, E., et al.: Atlas of the stratigraphic markers in the western Mediterranean sea with focus on the Gulf of Lion. Commission de la Carte Géologique du Monde (2018)

Montadert, L., et al.: Petroleum systems offshore Cyprus. AAPG Mem. **106**, 301–334 (2014)

Moulin, M., et al.: Kinematic keys of the Santos-Namibe Basins. In: Mohriak, W.U., et al., (eds.) Conjugate Divergent Margins. Geological Society, London, Special Publications, vol 369 (2012). https://doi.org/10.1144/SP369.3

Moulin, M., et al.: Deep crustal structure across an young passive margin from wide-angle and reflection seismic data (The SARDINIA Experiment)—I Gulf of Lion's Margin. BSGF **186**, 309–330 (2015). https://doi.org/10.2113/gssgfbull.186.4-5.309

Platt, J.P., Vissers, R.L.M., Extensional collapse of thickened continental lithosphere: a working hypothesis for the Alboran Sea and Gibraltar Arc. Geology **17**, 540–543 (1989)

Ricou, L.E.: Tethys reconstructed: plates continental fragments and their boundaries since 260 Ma from Central America to south-eastern Asia . Geodin. Acta **7**, 169–218 (1994)

Roure, F., et al.: Alpine inversion of the North African margin and delamination of its continental lithosphere. Tectonics **31**, TC3006

Schattner, U., Ben-Avraham, Z.: Transform margin of the northern Levant, eastern Mediterranean: From formation to reactivation. Tectonics **26**(5) (2007). https://doi.org/10.1029/2007TC002112

Schattner, U., Ben-Avraham, Z.: Tectonic development of the Levant continental margin, eastern Mediterranean. Researchgate (2012). https://www.researchgate.net/publication/281763542

Segev, A., Rybakov, M.: Effects of Cretaceous plume and convergence, and Early Tertiary tectonomagmatic quiescence on the central and southern Levant continental margin. J. Geol. Soc. London **167**(4), 731–749 (2010). https://doi.org/10.1144/0016-76492009-118

Segev, A., et al.: Age and structure of the Levant basin, Eastern Mediterranean. Earth Sci. Rev. **182**, 233–250 (2018). https://doi.org/10.1016/j.earscirev.2018.05.011

Stampfli, G., et al.: Tethyan margins in space and time. Palaeogeogr. Palaeoclimatol. Palaeoecol. **87**, 373–409 (1991). https://doi.org/10.1016/0031-0182(91),90142-E

Stampfli, G.M., Borel, G.D.: The TRANSMED transects in space and time: Constraints on the paleotectonic evolution of the mediterranean domain. In: Cavazza, W., et al. (eds.) The TRANSMED Atlas: the Mediterranean Region from crust to mantle, vol. 1, pp. 53–80. Springer, Berlin (2004)

Van Hinsbergen, et al.: Origin and consequences of western Mediterranean subduction, rollback, and slab segmentation. Tectonics **33**, 393–419 (2014)

Seismo-stratigraphic Mapping Guided by Magnetic Anomalies Stripes: Assessing Opening Models for the Eastern Algerian Oceanic Domain

Shaza Haidar, Jacques Déverchère, Mohamed Arab, Frauke Klingelhoefer, David Graindorge, and Mourad Medaouri

Abstract

The Eastern Algerian basin (EAB) occupies a key position at the eastern tip of the Western Mediterranean. Although clear triangular-shaped magnetic anomalies (MA) are well identified since long, the way seafloor spreading occurred during the middle Miocene is still debated. In this work, a new seismo-stratigraphic interpretation of deep penetration seismic data correlated to reduced to the pole MA was used in order to specify the distribution of the oldest sedimentary deposits in the oceanic domain, and thus to assess the best opening models matching the MA fan-shaped pattern. According to this pattern, our results reveal that the seafloor spreading of EAB has occurred along an NW–SE-oriented accretion system giving birth giving birth to six magnetic inversions spanning ca. 2 Myr in Langhian Serravallian times. The oldest units overlying the oceanic floor are of Langhian, i.e., younger than the syn-rift deposits identified on the stretched continental crust further south. We discussed the implications of our findings on the current opening models of the Western Mediterranean Sea.

Keywords

East Algerian oceanic basin • Magnetic anomalies • Seismic interpretation • Opening model

1 Introduction

A multi-phase evolutionary scheme was proposed for the tectonics history since the Oligocene for the Western Mediterranean basin and gave rise to several basins (Fig. 1) (Alboran Sea, Algerian basin, Liguro-Provencal Basin, Tyrrhenian Sea and Valencia Trough). The Algerian basin is an Oligo-Miocene oceanic domain formed by back-arc extension induced by rollback of the Tethyan slab south of the European forearc (Frizon de Lamotte et al. 2000). It is suspected that its western and central oceanic domains are younger than the eastern ones, implying the formation of two different types of margins: transform-type to the west and rifted-type to the east. Moreover, the Lesser Kabylia (LK) block displays (1) a collision zone (south) and (2) a passive-type margin (north) bearing the oldest sedimentary units identified off Algeria, supporting an SE-ward drift of the block (Arab 2016). However, from the initial stage of the migration of LK (upper Oligocene) until its final collision with Africa (>17 Ma, Abbassene 2016), the published kinematic models fail to accurately explain both the geophysical data offshore and geological evidence on land, favoring either N–S or E–W dominant directions of opening (Cohen 1980; Driussi 2015; Martin 2006; Schettino and Turco 2006), even within the well-identified sphenochasm-shaped area to the east (Fig. 1). In this work, we addressed this issue by correlating MA with the first seismo-stratigraphic units deposited on the seafloor.

2 Correlation of Seismo-acoustic Units with MA

The MA data interpretation was attempted for the first time in this region thanks to a reduced to the pole (RTP) processing (Fig. 2). RTP processing allows us to convert magnetic anomaly to a symmetrical pattern corresponding to a vertical magnetization (e.g. Cooper & Cowan, 2005).

S. Haidar (✉) · J. Déverchère · D. Graindorge
IUEM, Géosciences Océan, Université de Brest, 29200 Brest, France
e-mail: Shaza.Haidar@univ-brest.fr

M. Arab · M. Medaouri
SONATRACH Exploration Division, 3029 Boumerdes, Algeria

F. Klingelhoefer
IFREMER Centre de Brest, Géosciences Marines, 29200 Brest, France

M. Meghraoui et al. (eds.), *Advances in Geophysics, Tectonics and Petroleum Geosciences*,
Advances in Science, Technology & Innovation, https://doi.org/10.1007/978-3-030-73026-0_121

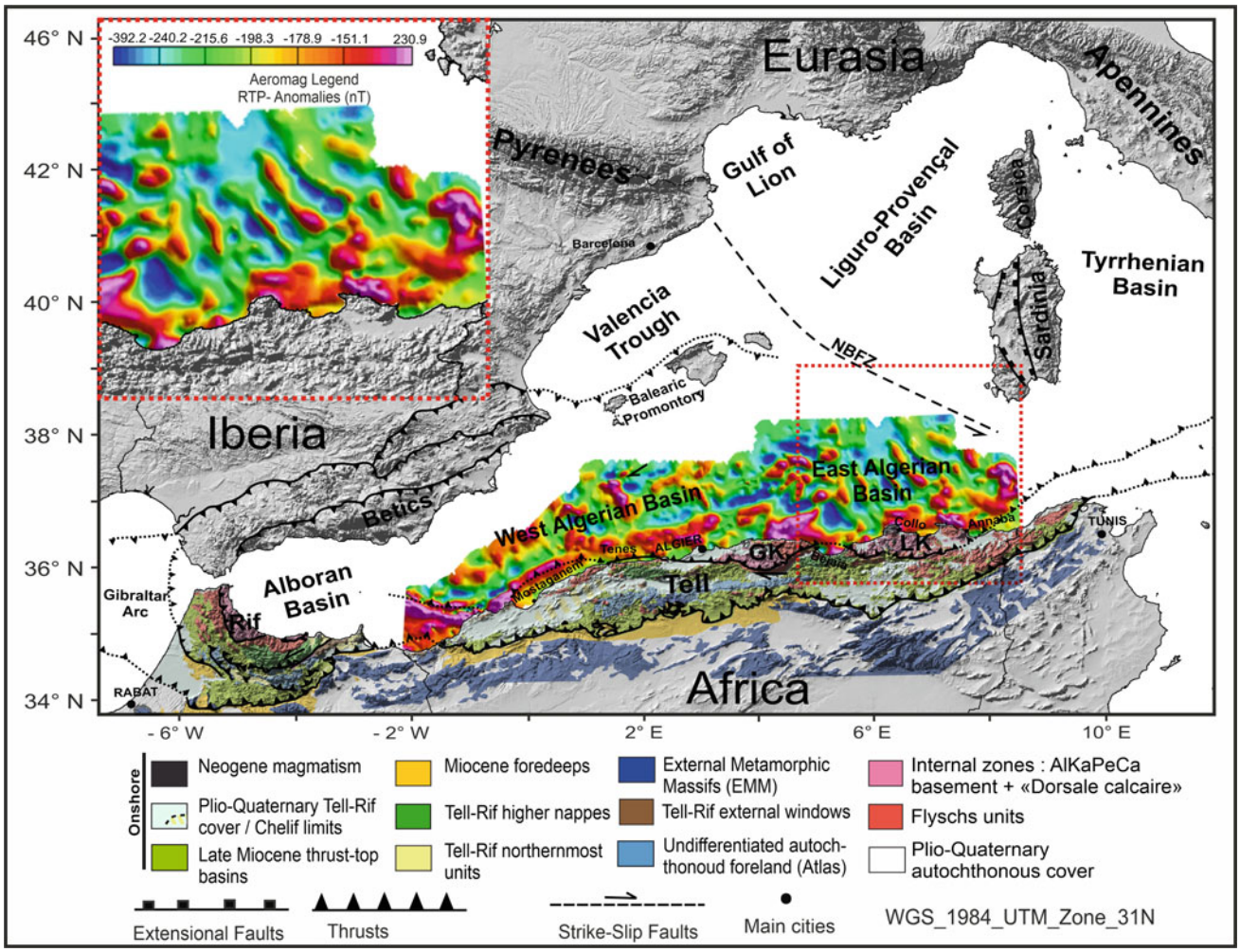

Fig. 1 Map of the Western Mediterranean region with the main basins superimposed on the reduced to the pole (RTP) magnetic anomaly map (values in nT) (Reproduced after Medaouri 2014) and the structural scheme of the distribution of different units and Kabyle or AlKaPeCa domain on land. Red frame: location of the inset that displays regularly organized NW–SE magnetic anomalies in the central part of the EAB. LK and GK: Lesser and Great Kabylia, respectively, and NBTZ: North Balearic Transform Zone

These anomalies provide fundamental constraints for determining the oceanic spreading modes and timing.

Firstly, we interpreted the RTP map to describe the MA shapes, directions and extensions. Then, a representative magnetic profile (Fig. 2) was drawn across the MA, which allowed us to compare amplitudes and wavelengths and made their comparison easy on both sides of a probable central axis. From this profile, we tried to build an interpretative model (Fig. 3) according to a magnetic reversal scale which helps to correlate MA inversions with the geomagnetic time scale (GMTS) (Gee and Kent 2007) in order to predict a mean time interval and a rate for seafloor spreading. We finally attempted to fit an opening model according to the normal and reverse identified anomalies.

Using available seismic profiles, mainly from WesternGeco (2000–2002) and the Spiral (2009) cruises, we mapped the changes of the top basement (depth, shape) and the distribution of the first sedimentary deposits over the oceanic crust. A seismo-stratigraphic interpretation was used for deep seismic reflection lines on the basis of the land–sea correlation of Miocene sedimentary units (Arab 2016). Sub-Messinian units were identified by their seismic facies and reflector configurations on the seismic sections of which the limits were interpreted as chronostratigraphic time lines. This interpretation was made using the "IHS Kingdom" software.

3 Results

Based on the RTP-MA map and the magnetic profile plotted across the triangular zone (Figs. 2 and 3), we assumed an opening centered on a pole of rotation A (Fig. 2) and we identified 13 subparallel positive–negative magnetic strips including a central axis characterized by a negative anomaly

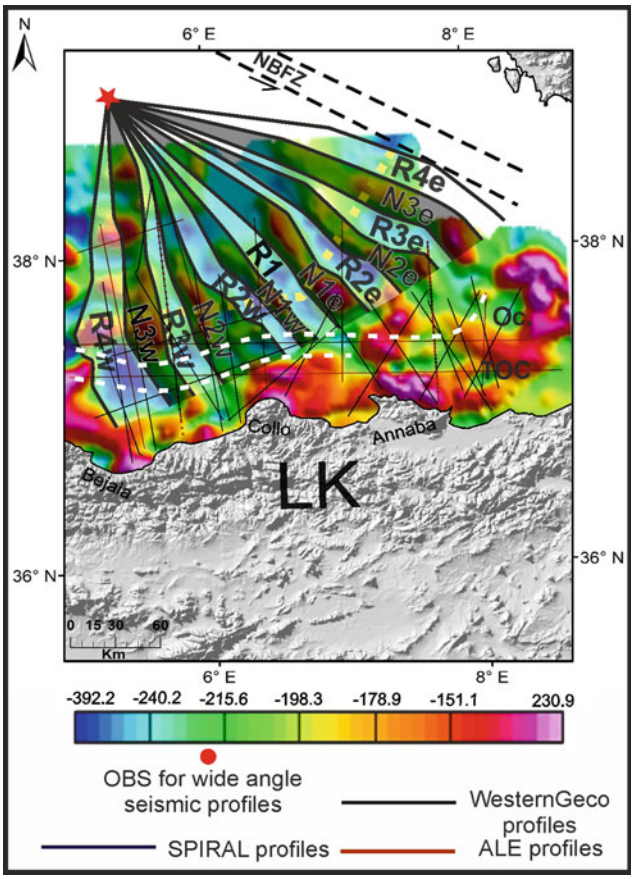

Fig. 2 RTP magnetic anomalies map (values in nT) for the EAB. Colored lines: location of data set of the seismic lines available in this zone. LK: Lesser Kabylia. Black and white strips represent intervals of normal and reverse polarity anomaly, respectively. The R4O strip to the west is interpreted as a reverse polarity anomaly assumed to be overprinted by late magmatic intrusions. A is the pole of rotation assumed to best fit the pattern of MA identified. Dashed yellow line is the position of the magnetic cross-section of Fig. 3. Dashed white lines locate the limits of the ocean-continent transition from wide-angle seismic profiles

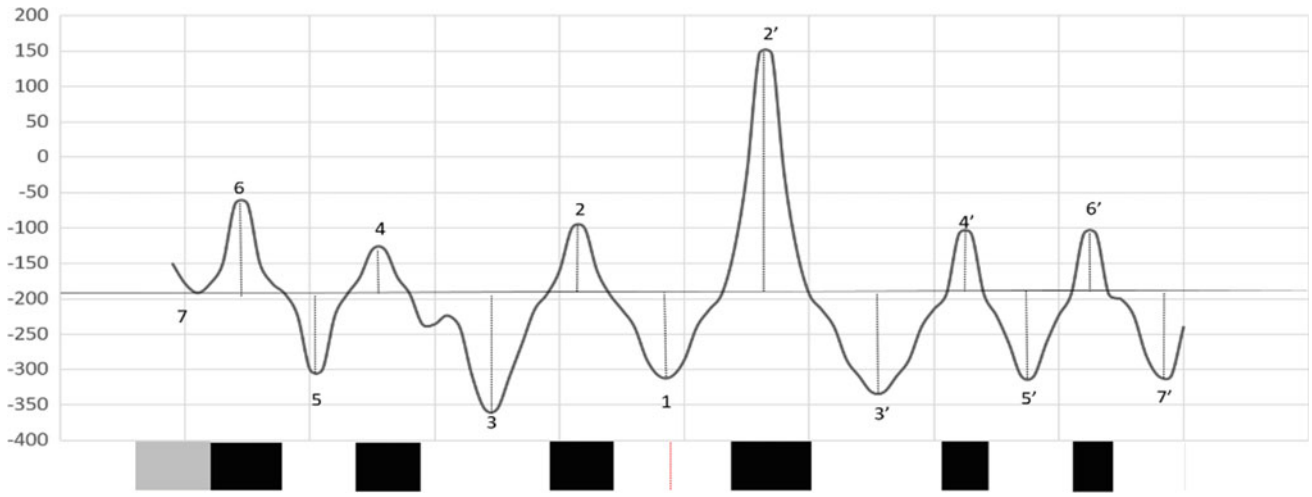

Fig. 3 Top: magnetic anomalies profile (values in nT) plotted along the triangular zone (dashed yellow line on Fig. 2). Bottom: interpretative model where the black and white blocks represent normal and reverse polarities of the magnetic field. The gray block is interpreted as the symmetrical anomaly of 7′/R4E anomaly and thus as a reverse polarity anomaly assumed to be overprinted by late magmatic intrusions which gave the positive signature

of −356 nT of amplitude (Fig. 3). In contrast with the hypothesis of Bayer (1973), this magnetic model, therefore, implies six magnetic polarity reversals besides the final central accretion of negative polarity.

It is worth noting that the negative anomaly (R4E) is continuous with the North Balearic Transfer Zone (NBTZ), and its westernmost symmetrical negative anomaly (R4O) is affected by the magnetic signature of a post accretion magmatism which gave its positive signature. All of this was assessed by seafloor topography on seismic lines (Arab 2016).

We used the geomagnetic polarity timescale (GPTS) (Gee and Kent 2007) in order to build a time interval for seafloor spreading in the EAB. To this end, we computed an average accretion period from the GMTS, counting six inversions and starting from a central inverse anomaly. An arithmetic average time interval of ca. 2 Myr was obtained using a time window between 16 Ma and ∼11 Ma (Gee and Kent 2007). We finally used the basement depth and the first pre-Messinian deposits identified in our set of seismic sections crossing the MA to ascribe an approximate age of the seafloor and discuss the ability of published opening models (S–N, E–W or combined) to explain this match.

Using the age model (Arab 2016), we have shown that the oldest seismic units laying over the top of the oceanic basement are likely of Langhian (15.97–13.65 Ma) age, i.e., younger than the syn-rift deposits identified on the stretched continental crust further south (Arab 2016).

4 Conclusions

Based on magnetic and seismic data, we revisited the opening of the EAB during Miocene time and showed that this basin opened during a period lasting about 2 Myr in Langhian time (15.97–13.65 Ma) or even Serravallian (13.65–11.608 Ma) time, i.e., later than generally assumed, i.e., when the anticlockwise rotation of Sardinia to the east and the collision of Lesser Kabylia with Africa to the south were ending. The pattern of magnetic anomalies represents the first evidence of oceanic-type crust and suggests an opening around a close rotation pole that is likely related to the onset of the westward motion of the Alboran domain driven by the Tethyan slab segment retreat toward Gibraltar (Hinsbergen et al. 2014).

References

Abbassene, F., et al.: A 17 Ma onset for the post-collisional K-rich calc-alkaline magmatism in the Maghrebides: evidence from Bougaroun (northeastern Algeria) and geodynamic implications. Tectonophysics **674**, 114–134 (2016)

Arab, M., et al.: Tectonostratigraphic evolution of the eastern Algerian margin and basin from seismic data and onshore-offshore correlation. Mar. Pet. Geol. **77**, 1355–1375 (2016)

Bayer, R., et al.: Magnetic Anomaly Pattern in the Western Mediterranean, vol. 19, pp. 168–176. Elsevier, Amsterdam (1973)

Cohen, C.: Plate tectonic model for the Oligo-Miocene evolution of the Western Mediterranean. Tectonophysics **68**, 283–311 (1980)

Driussi, O., et al.: Evidence for transform motion along the South Balearic margin and implications for the kinematics of opening of the Algerian basin. Bulletin De La Société Géologique De France **186**, 353–370 (2015)

Frizon de Lamotte, D., et al.: The two main steps of the Atlas building and geodynamics of the western Mediterranean. Tectonics **19**, 740–761 (2000)

Gee, J.S., Kent, D.: Source of Oceanic Magnetic Anomalies and the Geomagnetic Polarity Timescale, vol. 5, pp. 455–507. Elsevier B.V. (2007)

Martin, A.K.: Oppositely directed pairs of propagating rifts in back-arc basins: Double saloon door seafloor spreading during subduction rollback. Tectonics **25**, TC3008. https://doi.org/10.1029/2005TC001885 (2006)

Medaouri, M.: Origine de la segmentation de la marge Algérienne et implications sur l'évolution géodynamique et les ressources pétroliers. Thesis, Brest University (2014)

Schettino, A., Turco, E.: Plate kinematics of the Western Mediterranean region during the Oligocene and Early Miocene. Geophys. J. Int. **166**, 1398–1423 (2006)

van Hinsbergen, J.J., et al.: Origin and consequences of western Mediterranean subduction, rollback, and slab segmentation, Tectonics **33** (2014). https://doi.org/10.1002/tect.20125(2014)

Vertical Movements and Source-to-Sink Systems of the Rifted Margin of NW Africa: Surprises Continue

Giovanni Bertotti, Remi Charton, Mohamed Gouiza, Emmanuel Roquette, James Lovell-Kennedy, and Jonathan Redfern

Abstract

Rifted continental margins are generally considered as very well studied and understood. Extensive use of low-T geochronological tools has shown, however, that rifted margins experienced upward and downward vertical movements completely unpredicted by available models. New erosion-sedimentation systems are developed as a response. The margin of NW Africa is no exception. Triassic to Jurassic exhumation occurred in the Anti-Atlas and Regibat domains of Morocco and Mauritania feeding large amounts of terrigenous sediments to the W and E. In North Morocco, a stage of Triassic to Early Jurassic subsidence was followed by Middle Jurassic to Early Cretaceous exhumation associated with the delivery of terrigenous sediments in the offshore domain. Constraining tectono-sedimentary systems in Morocco, Mauritania and Senegal are in full development and will bring fundamentally new insights about the evolution of NW Africa.

Keywords

NW Africa • Passive continental margin • Exhumation • Erosion • Source-to-sink

The original version of the chapter has been revised: The author name "Emmanuel Roquette" has been corrected. A correction to this chapter can be found at https://doi.org/10.1007/978-3-030-73026-0_149

G. Bertotti (✉) · R. Charton
Delft University of Technology, Delft, The Netherlands
e-mail: g.bertotti@tudelft.nl

R. Charton · M. Gouiza
University of Leeds, Leeds, UK

E. Roquette · J. Lovell-Kennedy · J. Redfern
University of Manchester, Manchester, UK

G. Bertotti · M. Gouiza · E. Roquette · J. Lovell-Kennedy · J. Redfern
North Africa Research Group (NARG), Manchester, England, UK

1 Introduction

Around ten years ago, it was discovered that substantial parts of the Moroccan rifted margin experienced Jurassic to Cretaceous, i.e., during the post-rift phase, km-scale exhumation with associated erosion, sediment production and dispersal. This finding provided the first explanation for the enigmatic terrigenous sands documented by ODP wells and which are known all along the NW Africa margin from Morocco to Senegal where they form attractive reservoirs (Davison 2005; Castell et al. 2019). More in general, exhumation, erosion and sediment dispersal studies are key to assess Source-to-sink sedimentary systems and help define the characteristics of potential hydrocarbon reservoirs (e.g., Helland-Hansen et al. 2016).

Following these initial discoveries, we (North Africa Research Group) have analyzed in details the exposed parts of sedimentary successions of the Agadir-Essaouira basin and, further, to the S in the coastal regions of central Morocco (Arantegui et al. 2019). We have expanded our focus to Mauritania and Senegal producing the first low-T geochronology data from the region and reconstructing the tectono-sedimentary evolution of the region using a large set of seismic data. Our findings, especially those on the Triassic evolution, have important implications for the understanding of sedimentary systems and related hydrocarbon plays in Eastern Morocco and elsewhere (Helland-Hansen et al. 2016).

The low-T geochronology data we presented are based on Fission Track analysis and (U-Th)/He measurements on apatite. Like most authors, we interpreted the resulting time–temperature curves as resulting from exhumation, that is, from vertical movement with respect to the earth surface. Thermal effects such as those related to the CAMP magmatic event (e.g., Nomade et al. 2007) are considered as of secondary importance as documented by (i) the widespread occurrence of pre-CAMP ages and (ii) the age pattern which is clearly related to tectonic structures and not to the alleged shape of the CAMP anomaly.

M. Meghraoui et al. (eds.), *Advances in Geophysics, Tectonics and Petroleum Geosciences*,
Advances in Science, Technology & Innovation, https://doi.org/10.1007/978-3-030-73026-0_122

2 Exhumation and Sedimentation in Morocco

Low-T geochronology time–temperature curves from the Meseta and High Atlas (N Morocco) are converted to time-depth curves using a variety of geothermal gradients, document Late Triassic to Early Jurassic subsidence followed by a Middle Jurassic to Early Cretaceous phase of exhumation (Ghorbal et al. 2008; Leprêtre et al. 2015; Gouiza et al. 2016; Charton 2018). Triassic subsidence calls for a reconsideration of Triassic paleogeography, which would exclude the Massif Ancien de Marrakech (Moroccan arch) as a source for the widespread fluvial sediments (Fig. 1). On the contrary, Middle Jurassic to Early Cretaceous exhumation in the Massif area resulted in terrigenous sands found in the Agadir-Essaouira basin and offshore. Dispersal of sediments toward the west was influenced by roughly E–W trending folds resulting from tectonics and salt tectonics (e.g., Luber 2017).

Vertical movements in the Anti-Atlas and Reguibat massifs are significantly different from those of the Meseta and High Atlas and are characterized by prolonged exhumation from 150 Ma (Anti-Atlas) and from 220 Ma in the Reguibat massif (Fig. 2) (Charton 2018). Neither timing nor spatial distribution of vertical movements bears clear links with rifting and drifting kinematics and exhumation in both massifs follows a "whale-back" geometry elongated in a WSW-ENE direction. The persistent exhumation of the two areas provides a potential source of sediments of regional importance. The Anti-Atlas, for instance, could be the source of Triassic sediments in N and E Morocco and further to the E (Fig. 1).

3 Mauritania and Senegal

In the last two years, we have produced the first low-T geochronological ages from Mauritania. Samples suitable for low-T geochronology can only be found in the Mauritanides Hercynian belt which stretches in a N–S direction separating the coastal basins to the W from the Taoudeni Basin to the E. Preliminary t-T curves suggest subsidence at 300–200 Ma followed by gentle exhumation between 200 and 50 Ma (Fig. 3) confirming the occurrence of syn- to post-rift exhumation along the entire margin. The major Permian-Cretaceous sedimentary gap documented in the Taoudeni basin by Martin-Monge et al. (2016) could be related to these movements resulting in a very wide source area, larger than the presently visible one.

In Senegal, we took samples from the Bakel area (Fig. 4), in the few remnants of the Mauritanides belt; the results are expected in 2019. Interestingly, onshore seismic sections document a pre-Early Cretaceous stratigraphic gap in a large area to the *W* of the outcropping basement, thus pointing to a large source area.

4 Conclusions

Up to a few years ago, rifted continental margins were considered as well understood geological structures. The increasingly widespread quantitative reconstruction of vertical movements (upward and downward), however, is providing a very different picture calling for a thorough reconsideration of the evolution of these margins and of the associated sedimentary systems. Rifted continental margins

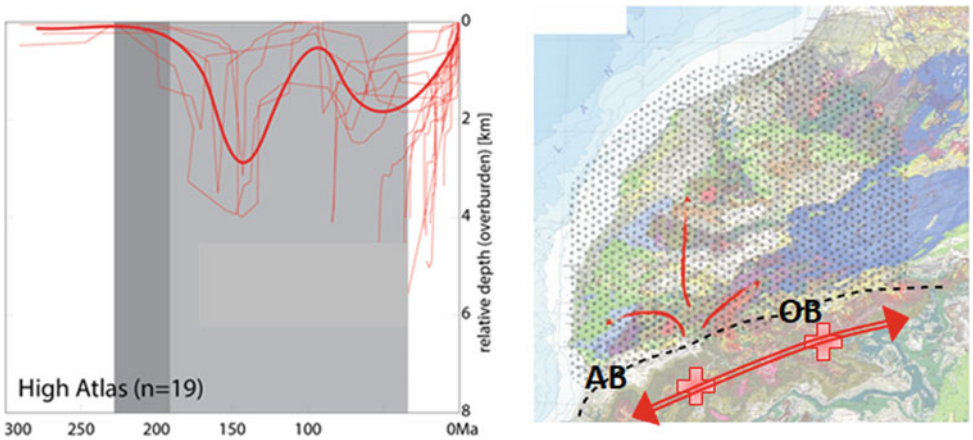

Fig. 1 Time temperature curve in the Meseta (from Charton, 2018) and new sedimentary model for the Triassic. AB=Argana basin, OB=Oukaimaden basin

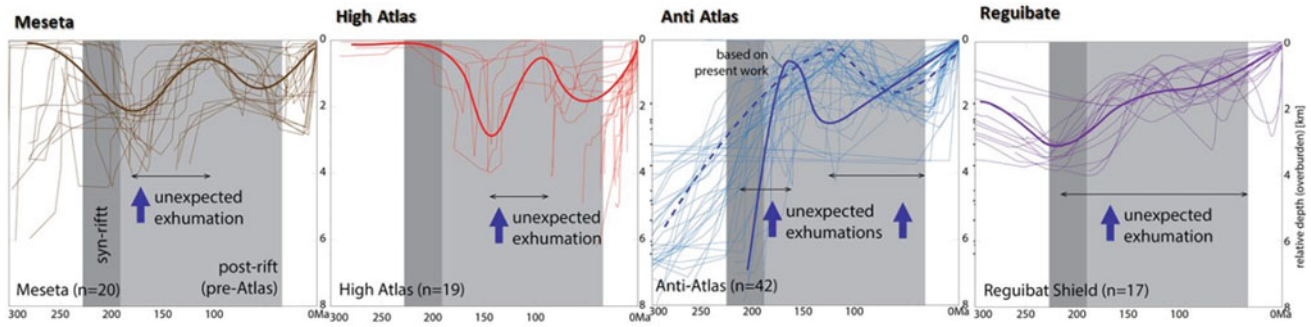

Fig. 2 Exhumation curves from different domains of Morocco (from Charton 2018)

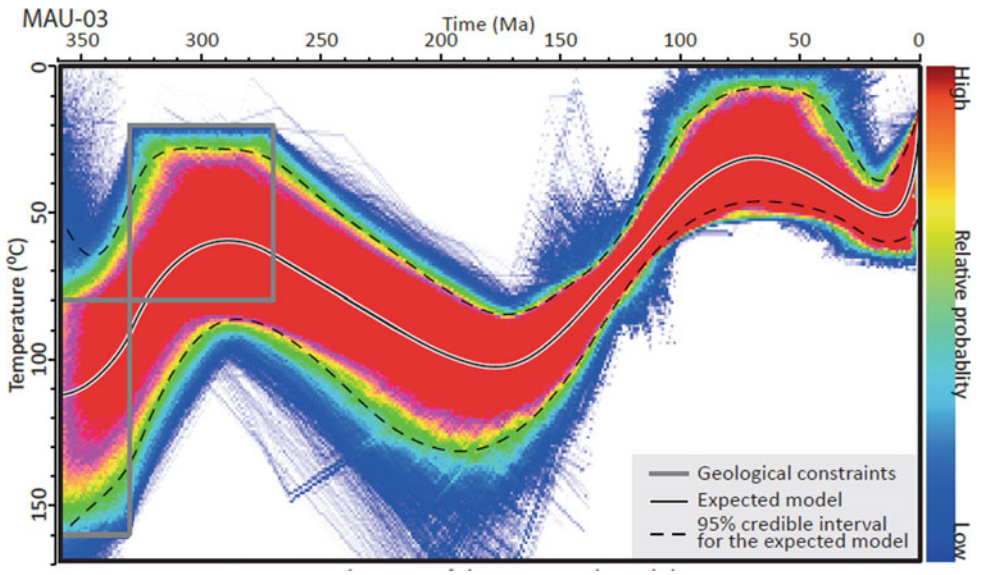

Fig. 3 Time–temperature curve for the Mauritanides (from Gouiza et al., submitted)

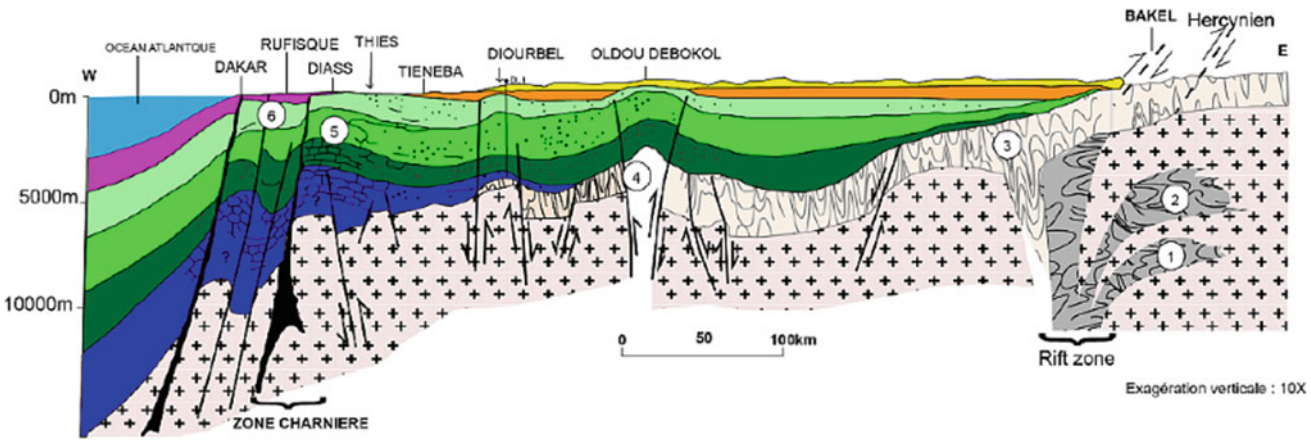

Fig. 4 E–W section across Senegal (Ndiaye et al. 2016)

experienced at different stages vertical movements are not predicted by quantitative models. The margin of NW Africa is not an exception and is becoming one of the best settings to document these movements and the resulting source-to-sink systems.

References

Arantegui, A., Jerrett, R., Schröder, S., Bulot, L.G., Gatto, R., Monari, S., Redfern, J.: Constraining Mesozoic early post-rift depositional systems evolution along the eastern Central Atlantic margin. Sed. Geol. **386**, 31–51 (2019). https://doi.org/10.1016/j.sedgeo.2019.03.005

Castell, J.D., Scotchman, J., Butt, T.: Lessons learnt from recent dry wells in northwest Africa. First Break **37**, 53–58 (2019)

Charton, R.J.G.: Phanerozoic Vertical Movements in Morocco. Delft University of Technology (2018)

Davison, I.: Central Atlantic margin basins of North West Africa: geology and hydrocarbon potential (Morocco to Guinea). J. Afr. Earth Sci. **43**, 254–274 (2005). https://doi.org/10.1016/j.jafrearsci.2005.07.018

Ghorbal, B., Bertotti, G., Foeken, J., Andriessen, P.: Unexpected Jurassic to Neogene vertical movements in 'stable' parts of NW Africa revealed by low temperature geochronology. Terra Nova **20** (2008). https://doi.org/10.1111/j.1365-3121.2008.00828.x

Gouiza, M., Charton, R., Bertotti, G., Andriessen, P., Storms, J.E.A.: Post-Variscan evolution of the Anti-Atlas belt of Morocco constrained from low-temperature geochronology. Int. J. Earth Sci. **106**, 1–24 (2016). https://doi.org/10.1007/s00531-016-1325-0

Helland-Hansen, W., Somme, T.O., Martinsen, O.J., Lunt, I., Thrmond, J.: Deciphering Earth's natural hourglasses: perspectives on source-to-sink analysis. J. Sediment. Res. **86** (2016)

Leprêtre, R., Missenard, Y., Barbarand, J., Gautheron, C., Saddiqi, O., Pinna-Jamme, R.: Post-rift history of the eastern Central Atlantic passive margin: insights from the Saharan region of South Morocco. J. Geophys. Res. **120**, 1–22 (2015). https://doi.org/10.1002/2014JB011549

Luber, T.L.: Integrated Analysis of Lower Cretaceous Stratigraphy and Depositional Systems: The Essaouira-Agadir Basin of Morocco. University of Manchester (2017)

Martin-Monge, A., Baudino, R., et al.: An unusual Proterozoic petroleum play in Western Africa: the Atar Group carbonates (Taoudeni Basin, Mauritania). Geol. Soc. Spec. Publ. **438** (2016)

Ndiaye, M., Mgom P.M., Gorin G., Villenueve M., Sartori M., Medou J.:A new interpretation of the deep-part of Senegal-Mauritanian Basin in the Diourbel-Thies area by integrat-ingseismic, magnetic, gravimetric and borehole data: Implication for petroleum exploration.J. African Sci. **121**, 330–341 (2016)

Nomade, S., Knight, K.B., Beutel, E., Renne, P.R., Verati, C., Féraud, G.: Chronology of the Central Atlantic Magmatic Province: implications for the Central Atlantic rifting processes and the Triassic—Jurassic biotic crisis. Palaeogeogr. Palaeoclimatol. Palaeoecologyeogeog. Pleoclimatol. **244**, 326–344 (2007). https://doi.org/10.1016/j.palaeo.2006.06.034

Evolutionary Geological Models of the Central-Western Peri-Mediterranean Chains

Francesco Guerrera, Manuel Martín-Martín, and Mario Tramontana

Abstract

Two main groups of geological models on paleogeographic and kinematic Alpine evolution of the central-western Mediterranean area presented in the last decades were compared. One interpretation provides for a single Mesozoic Tethyan Ocean, located between Africa and Europe and from which both Eo-Alpine and Neo-Alpine chains derived during Cretaceous to Miocene time span. Another interpretation considers the presence of at least two Tethyan oceanic branches separated by one or more microplates. Starting from these different approaches, progressive innovations and improvements to the different interpretative models were proposed over time and sometimes the resulting interpretations do not integrate easily. The proposed discussion tries to update the state of knowledge.

Keywords

Central-western Mediterranean chains • Tethys • Geological models

1 Introduction

The central-western Mediterranean area is bordered by three main Neo-Alpine orogenic systems: Betic Cordillera, Maghrebian Chain (Rif, Tell, Sicily and Calabria) and Apennines (BMA). These chains are linked by the Gibraltar Arc to the west and the Calabria-Peloritani Arc to the east. The involved Mesozoic-Tertiary successions deposited in three major paleogeographic domains from which internal, intermediate (Maghrebian Flysch Basin/MFB, and its lateral extension) and external tectonic units were generated. A general view of their geological evolution based on studies of classical geology is due to Durand Delga (1980) and Durand Delga and Fontboté (1980). Successively, many authors developed models at a larger scale (e.g., Guerrera et al. 1993,2005; Doglioni 1992; Doglioni et al. 1999; Michard et al. 2006; Schettino and Turco 2010; Critelli et al. 2017; Vitali and Ciarcia 2013; Guerrera and Martín-Martín 2014; Bouyahiaoui et al. 2015; Leprêtre et al. 2018). The aim of the paper was to present the different interpretations, considering the general geological framework in order to clarify the paleogeographic setting and update the state of knowledge, starting from the main basic models.

2 State of the Art

One of the first paleogeographic and paleotectonic interpretations of the central-western Mediterranean area (Bouillin 1986; Bouillin et al. 1986) considered the occurrence of a single ocean (Jurassic Tethys) closed by means of a transform fault and from which generated progressively both the northern Eo-Alpine (Alps; Cretaceous-Paleocene orogeny) and southern Neo-Alpine (Betics, Maghrebids and Apennines; Miocene orogeny) chains. Successively, a different and more complex evolutionary model considered the occurrence of two ocneanic branches separated by one or more microplates. The two main approaches differ in the interpretation of the Jurassic paleogeography inherited from the Hercynian orogeny. Often successive models that do not consider the presence of intermediate microplate(s) between African and European Plates were considered equivalent to those providing for microplates, thus generating confusion and implying different geodynamic reconstructions.

F. Guerrera · M. Tramontana (✉)
Università degli Studi di Urbino Carlo Bo, 61029 Urbino, Italy
e-mail: mario.tramontana@uniurb.it

M. Martín-Martín
Universidad de Alicante, 03080 Alicante, Spain

M. Meghraoui et al. (eds.), *Advances in Geophysics, Tectonics and Petroleum Geosciences*,
Advances in Science, Technology & Innovation, https://doi.org/10.1007/978-3-030-73026-0_123

3 Results

The Jurassic-Cretaceous paleogeographic interpretations of the central-western Mediterranean area can be roughly summarized into two main groups of geological models that consider a different Jurassic paleogeography: (1) absence of microplates between African and European Plates (Type A); (2) presence of microplate(s) between African and European Plates (Type B). Moreover, other literature models show different features and complexities that are not easily referable to one or the other type. According to the Type A the shortening of the Tethyan oceanic space (Ligurian-Piemontese Basin and Maghrebian Basin) was controlled by the relative movements of the African and European Plates, generating two orogenic systems (Eo-Alpine and Neo-Alpine) with an opposite vergence. During this evolution, a fragment of the European Margin usually identified as the AlKaPeCa (as an acronym of Alboran-Kabylian-Peloritan-Calabrian, Internal Zones of alpine units) detached, which is incompatible with the existence of a Jurassic intermediate microplate because this detachment occurred after the Eo-alpine closure. The European and African-Adria Margins represented the external domains of the two chain systems. The Type B considers the occurrence in the Jurassic-Cretaceous paleogeography of an independent microplate (Mesomediterranean Microplate/MM) located between African and European Plates and separating at least two oceanic branches of the western Tethys experiencing successive and differently oriented subductions. The closure of the northwestern branch of the Tethys Ocean (Nevado-Filabride and Ligurian-Piemontese Ocean), whose southern margin was represented by the MM, caused the formation of the Eo-Alpine Chain (Cretaceous-Paleocene). The other oceanic (MFB) space, located between the MM and the African-Adria Margins, deformed during the Miocene (Neo-Alpine orogeny), during a subduction below the southern continental margin of the MM and the consequent continental collision. The internal units of this chain system originated from the migration toward the external zones of MM fragments (Alboran, Kabylides, Peloritani and Calabria blocks). Therefore, the intermediate microplate participated as an internal domain both first in the Eo-alpine history (toward SE subduction; NW-vergence of the chain) and successively in the Neo-Alpine evolution (toward NW to NE subduction; SE to SW-vergence of the chain).

4 Discussion

The following features are considered important for a comparison between models.

1. The ophiolite suite of the Nevado-Filabride Units (Betics) is considered the SW extension of the Ligurian-Piemontese Ocean (e.g., Puga et al. 2017). This implies the presence of a northern Tethyan oceanic branch separating the Iberian margin from a southern continental margin different from the African-Adria Margins.
2. The Internal units of the BMA show very similar features due to a common origin from the same continental element, differently located by authors: (a) European Margin and (b) MM.
3. The main orogenic phases of the BMA system started not before the middle-late Miocene and showed a rough diachronism from Gibraltar Arc to Apennines (e.g., Guerrera and Martín-Martín 2014). The external units of the BMA derived from the deformation of African-Adria Margins. Differently from the internal units, the external units show differences from one area to another, as for example in the Gibraltar Arc where the external units of the Betic Cordillera are very different from those of the Rif Chain, so evidencing different paleogeographic margins.
4. A consistent latest Chattian-Langhian orogenic calc-alkaline magmatism occurring in different sectors of the central-western Mediterranean area generated a pene-contemporaneous high amount of volcaniclastites interbedded within sedimentary marine successions (cfr. Guerrera et al. 2015, 2016; Martín-Martín et al. 2020). According to Type A, the Internal Units of the Miocene BMA orogenic system result from the collision between African and European Plates, while the Type B considers that they derive from the collision between African-Adria Plate and a microplate(s) constituting the northern margin of the MFB and its lateral extents in Betides and Apennines. Therefore, the more complex Type B interpretation expects for the occurrence of an intermediate microplate(s), participating in the Alpine Chain building, and whose northern margin was docked to the European Margin already in the Paleogene. This interpretation implies paleogeographic and paleotectonic differences between Alpine and BMA orogenesis

especially concerning vergence, subduction direction, and oceanic branches involved. The internal units of the two systems (Alpine and BMA systems) resulted from a complex development of tectonic events that first determined the closure of the Nevado-Filabride/Ligurian-Piemontese oceanic branch and later of the Maghrebian oceanic branch and its lateral extensions. This reconstruction implies a double involvement of a microplate(s) to constitute the internal zone of the chains both during the Eo-Alpine orogeny (alpine vergence) and in the successive Neo-Alpine orogeny (Apennine-Maghrebian vergence).

For a wider discussion (not possible in the present abstract) involving also models at a more general scale, based on different methodological approaches, it is necessary to consider other papers (e.g., Stampfli and Borel 2002; Golonka 2004; Seton et al. 2012).

5 Conclusions

Two different evolutionary geodynamic interpretations based on different approaches were presented for the central-western Mediterranean area. In our opinion, the presence of an independent microplate(s) located since Jurassic between European and African Plates and inherited from the Hercynian orogeny, appears the more likely paleogeographic scenario for the Alpine and BMA evolution. This reconstruction involves at least two main subduction zones and related ocean closure generating, at different times, two orogenic systems (Alps and BMA) and the

Table 1 Evolutionary stages and geodynamic events in the Eo-Alpine and Neo-Alpine systems (central-western peri-Mediterranean chains)

Age	Eo-Alpine Evolution	Neo-Alpine Evolution			Basin evolutionary stages, Geodynamic events
		Betic-Rif-Tell	Peloritani	Apennines	
Late Miocene -Pliocene	Molassic and/or intramontane basins				Extension and strike-slip deformation (Post-orogenic phase)
Middle Miocene	Thrust-top basin	Thrust-top basin	Piggy-back basin	Piggy-back basin	Late-orogenic phase (continental collision)
			Foredeep	Foredeep	
Early Miocene	Post-Eo-Alpine deformation	Foredeep	Pre-foredeep		Siliciclastic supply with volcaniclastites (subduction; syn-orogenic phase)
Paleogene					
Cretaceous	Thrust-top basin ? Foredeep	Pre-foredeep	Drifting		Terrigenous supply after tectonic inversion (compressional phase with blind-thrusts and gentle folding)
	Pre-foredeep	Drifting			Marine pelagic depositional stage (extensional phase)
	Oceanization				
Jurassic	Rifting		Rifting		
			Pre-rifting		
Triassic	Pre-rifting				Continental depositional stage (start of extension)

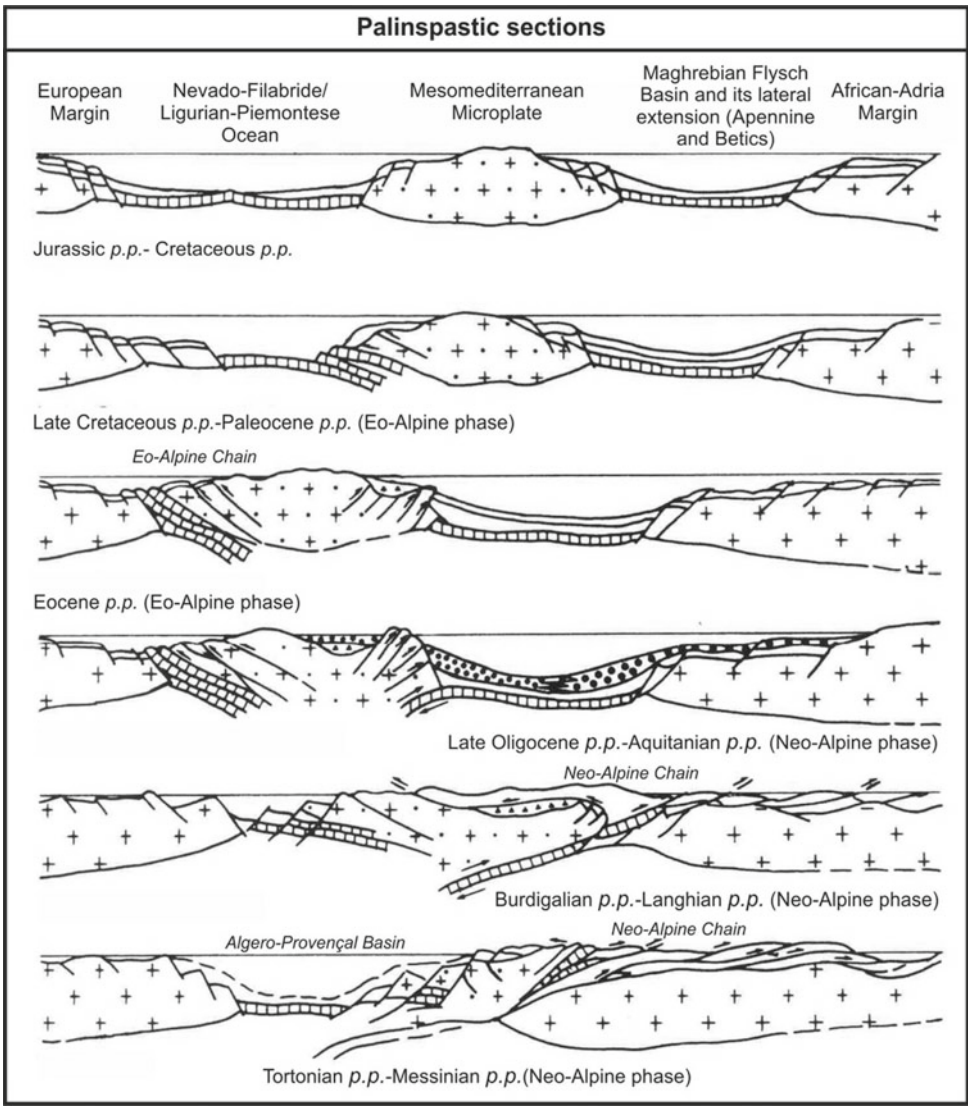

Fig. 1 Schematic palinspastic sections showing the Jurassic *p.p.*-Messinian *p.p.* evolution of the central-western Mediterranean area (after Guerrera et al. 1993, modified)

successive opening of the central-western Mediterranean area (Alboran, Algerian-Provençal and Tyrrhenian Basins). The main evolutionary stages and geodynamic events are listed in Table 1 and Fig. 1.

The presence of microplates between European and African Plates seems to have played an important geodynamic role in the development of the central-western peri-Mediterranean chains.

References

Bouillin, J.-P.: Le "bassin maghrébin": une ancienne limite entre l'Europe et l'Afrique à l'ouest des Alpes. Bull. Soc. Géol. Fr. **2**, 547–558 (1986)

Bouillin, J.P., Durand-Delga, M., Olivier, Ph.: Betic-Rifian and Tyrrhenian Arcs: distinctive features, genesis and development stages. In: Wezel, J.F. (ed.) The origin of arcs, pp. 281–304. Elsevier Publ, Amsterdam (1986)

Bouyahiaoui, B., Sage, F., Abtout, A., Klingelhoefer, F., Yelles-Chaouche, K., Schnu ̈rle, P., Marok, A., Déverchère, J., Arab, M., Galve, A., Collot, J.Y.: Crustal structure of the eastern Algerian continental margin and adjacent deep basin: implications for late Cenozoic geodynamic evolution of the western Mediterranean. Geophysical J. Intern. **201**, 1912–1938 (2015)

Critelli, S., Muto, F., Perri, F., Tripodi, V.: Interpreting provenance relations from sandstone detrital modes, southern Italy foreland region: Stratigraphic record of the Miocene tectonic evolution. Marine Petroleum Geol. **87**, 2–14 (2017)

Doglioni, C.: Main differences between thrust belts. Terra Nova **4**, 152–164 (1992)

Doglioni, C., Fernandez, M., Gueguen, E., Sabat, F.: On the interference between the early Apennines-Maghrebides back-arc extension and the Alps-Betics orogen in the Neogene geodynamics of the Western Mediterranean. B.S. Geol. It. **118**, 75–89 (1999)

Durand Delga, M.: La Méditerranée occidentale: étapes de sa genèse et problèmes structuraux liés à celle-ci. Livre Jub. Soc. géol. Fr., Mém. h.s. **10**, 203–224 (1980)

Durand Delga, M., Fontboté, J.M.: Le cadre structural de la Méditerranée occidentale. Mém. B.R.G.M. **115**, 67–85 (1980)

Golonka, J.: Plate tectonic evolution of the southern margin of Eurasia in the Mesozoic and Cenozoic. Tectonophysics **381**, 235–273 (2004)

Guerrera, F., Martín-Martín, M.: Geodynamic events reconstructed in the Betic, Maghrebian, and Apennine chains (central-western Tethys). Bull. Soc. Géol. Fr. **185**(5), 329–341 (2014)

Guerrera, F., Martin-Algarra, A., Perrone, V.: Late Oligocene-Miocene syn-/-late-orogenic successions in Western and Central Mediterranean Chains from the Betic Cordillera to the Southern Apennines. Terra Nova **5**, 525–544 (1993)

Guerrera, F., Martín-Martín, M., Perrone, V., Tramontana, M.: Tectono-sedimentary evolution of the southern branch of the Western Tethys (Magrebian Flysch Basin and Lucanian Ocean). Terra Nova **17**, 358–367 (2005)

Guerrera, F., Martín-Martín, M., Raffaelli, G., Tramontana, M.: Volcaniclastites as a key for geodynamic constraints in the evolution of the central-western Mediterranean region: an overview. Asian Acad. Res. J. Multidiscip. (AARJMD) **3**(10), 179–217 (2016)

Guerrera, F., Martín-Martín, M., Raffaelli, G., Tramontana, M.: The early Miocene "Bisciaro volcaniclastic event" (northern Apennines, Italy): a key study for the geodynamic evolution of the central-western Mediterranean. Int. J. Earth Sci. (Geol. Rundsch.) **104**, 1083–1106 (2015). https://doi.org/10.1007/s00531-014-1131-5

Leprêtre, R., Frizon de Lamotte, D., Combier, V., Gimeno-Vives, O., Mohn, G., Eschard, R.: The Tell-Rif orogenic system (Morocco, Algeria, Tunisia) and the structural heritage of the southern Tethys margin. BSGF Earth Sci. Bull. **189**, 10 (2018). https://doi.org/10.1051/bsgf/2018009.

Martín-Martín, M., Guerrera, F., Tramontana, M.: Geodynamic implications of the latest Chattian-Langhian Central-Western Peri-Mediterranean volcano-sedimentary event: a review. J. Geo. **128**, 29–43 (2020)

Michard, A., Negro, F., Saddiqi, O., Bouybaouene, M.-L., Chalouan, A., Montigny, R., Goffé, B.: Pressure-temperature-time constraints on the Maghrebides mountain building: evidence from the Rif transect (Morocco), Kabylian correlations (Algeria) and geodynamic implications. C. R. Geosci. **338**, 92–114 (2006)

Puga, E., Díaz de Federico, A., Fanning, M., Nieto, J.M., Rodríguez Martínez-Conde, J.A., Díaz Puga, M.A., Lozano, J.A., Bianchini, G., Natali, C., Beccaluva, L.: The betic ophiolites and the mesozoic evolution of the western tethys. Geosci. **7**, 31 (2017)

Schettino, A., Turco, E.: Tectonic history of the western Tethys since the Late Triassic. Geol. Soc. Am. Bulletin **123**, 89–105 (2010)

Seton, M., Müller, R.D., Zahirovic, S., Gaina, C., Torsvik, T., Shephard, G., Talsma, A., Gurnis, M., Turner, M., Maus, S., Chandler, M.: Global continental and ocean basin reconstructions since 200 Ma. Earth-Sci. Rev. **113**, 212–270 (2012)

Stampfli, G.M., Borel, G.D.: A plate tectonic model for the Paleozoic and Mesozoic constrained by dynamic plate boundaries and restored synthetic oceanic isochrons. Earth Planet. Sci. Lett. **196**, 17–33 (2002)

Vitali, S., Ciarcia, S.: Tectono-stratigraphic and kinematic evolution of the southern Apennines/Calabria–Peloritani Terrane system (Italy). Tectonophysics **583**, 164–182 (2013)

Pliocene to Quaternary Tectonic Inversion of the Algerian Margin Along the Spiral Transect of Kabylies (North Central Algeria)

C. Aidi, M. Beslier, A. K. Yelles-Chaouche, and F. Klingelhoefer

Abstract

The Algerian margin is frequently seen as the seat of moderate to strong seismic activity as shown by the major Mw 6.9 May 21, 2003, Boumerdes earthquake that occurred close to the Great Kabylia block. This offshore seismic activity is occurring along active faults at seafloor. We presented here the tectonic structures associated to the Pliocene–Quaternary (PQ) tectonic inversion of the central part of the Algerian margin offshore Great Kabylia using new deep multichannel seismic (MCS) lines acquired during the Algerian-French SPIRAL cruise (September 2009, R/V L'Atalante). The seismic profile offshore Kabylia shows that the inversion is expressed by the presence of perched basin along the slope with south-dipping blind thrust which is parts of a flat-ramp system developed in the basement.

Keywords

Tectonic inversion • Flat-ramp system • Seismic data • Boumerdes

1 Introduction

Slow convergence rate ~4.5–5 mm year^{-1} (Bourgrine et al. 2019) between the Africa and Eurasia plates is expressed by seismicity along the Algeria continental margin. This activity is mainly controlled offshore by sub-marine active faulting, as shown by the major MW = 6.9 May 21, 2003, Boumerdes earthquake that occurred in the eastern part of the Mitidja basin, close to the western boundary with the Great Kabylian block (Fig. 1). Along the margin, inversion-related shallow structures were already described through high-resolution seismic reflection lines of the MARADJA survey, blue line in Fig. 2, (e.g., Domzig 2006, Strzerzynski et al. 2010). Taking into account new MCS lines acquired during the spiral cruise, we focused on the tectonic inversion process along the Kabylian margin.

2 Data Processing

During the Algerian-French SPIRAL survey (September 2009 R/V Atalante), five multichannel reflection seismic (MCS) lines were acquired in the study area (Fig. 1). Four lines were acquired using 3040 cu.in. air-gun array and 4.5 km 360 channel digital streamer. The fifth MCS line and one coincident wide angle seismic WAS were acquired using 8350 cu.in. source to facilitate deep penetration. All profiles presented here are pre-stack times migrated. Processing seismic lines allowed the understanding of the deep seismic structure of the crust and the deformation pattern from the abyssal plain to the margin slope.

3 Results

In the Eastern part of the study area, from the interpreted section shown in Fig. 2, the south-dipping reflector at 5–6 stwtt (CMP 650-800) is interpreted as blind thrust on the top of which the sedimentary series is bent in an antiform that uplifts the base of the Messinan series. A second antiform prolongates this uplift 20 km northward (to CMP 300) beneath which another blind thrust is supposed to exist (Fig. 2). The tow blind thrust described may join at depth

C. Aidi (✉) · A. K. Yelles-Chaouche
Centre de Recherche en Astronomie Astrophysique Et Geophysique, CRAAG, Algeris, Algeria
e-mail: c.aidi@craag.dz

M. Beslier
Université de Nice Sophia-Antipolis, CNRS (UMR 7329), Observatoire de La Côte D Azur, Valbonne, France

F. Klingelhoefer
Insitut Français de La Recherche Pour L'exploitaion de La Mer, Brest, France

M. Meghraoui et al. (eds.), *Advances in Geophysics, Tectonics and Petroleum Geosciences*,
Advances in Science, Technology & Innovation, https://doi.org/10.1007/978-3-030-73026-0_124

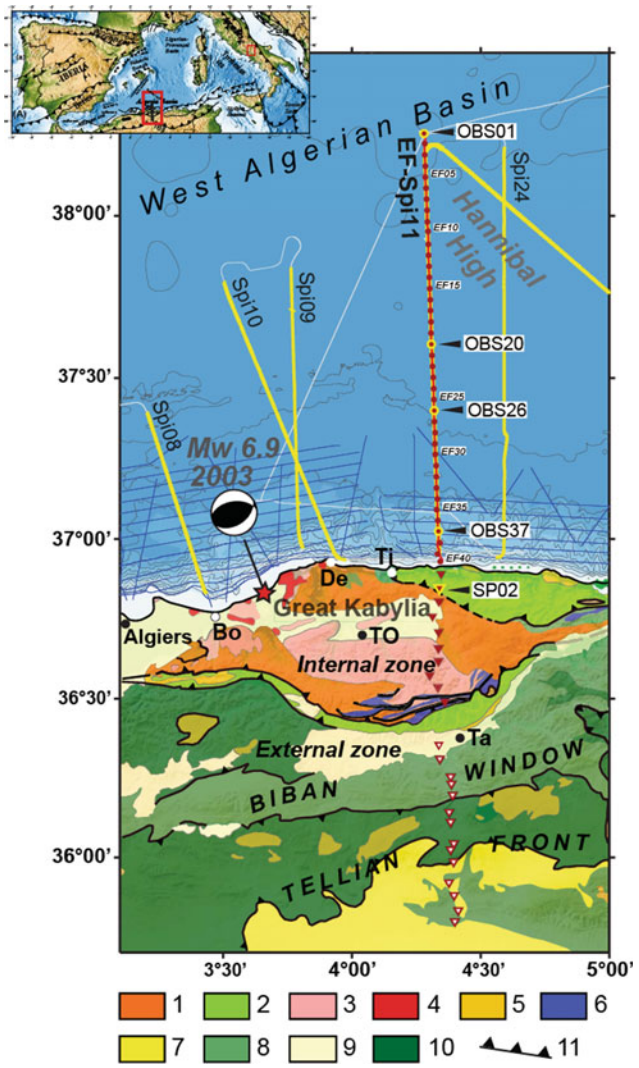

Fig. 1 Location map of the seismic lines across the north Algerian margin (Aïdi et al. 2018). Red dots: OBS station, red triangles: land stations (unfilled symbols for stations that did not record the offshore shots), red star: location of the 2003 Boumerdès earthquake from and its focal solution from Harvard Global CMT, Bo: Boumerdès, Ti: Tigzirt, De: Dellys, TO: Tizi-Ouzou, Ta: Tazmalt. Simplified geological map onland; 1: Kabylian Oligo-Miocene, 2: Flysch nappe, 3: Basement (Paleozoic included), 4: Calc-alkaline magmatism, 5: Numidian nappes, 6: Trias and Jurasic limestones, 7: Tellian for-chain (Miocene), 8: Autochtonous formations, 9: Post-Miocene formations, 10: Tellian nappes, 11: Major anormal contact. In the inset: map of the Mediterranean basin showing the location of the study area with red rectangle

along a high-amplitude, low-dipping to subhorizontal reflector (±7 stwt) (Fig. 2). They are part of a flat-ramp system developed in the acoustic basement of the deep margin. These antiforms delimit two asymmetric sub-basins at the margin toe filled with a southward thickening PQ wedge. Below the slope, reverse faults could develop (at 2–3 stwt) as expressed by south-dipping reflectors (dashed lines). They intersect the north dipping, rough lithological bedding marked in the chaotic units that warp the acoustic basement. This interpretation is supported by the convex shape in the Pliocene–Quaternary basin (PQ), where numerous superficial normal faults accommodate the destabilization of the Pliocene–Quaternary sediments and may control the formation of the upper slope of the Pliocene–Quaternary (PQ) basin.

In the central part of the study area (Fig. 3), tectonic inversion is expressed under the deep margin as a flat-ramp compressive system (FRS), black thick lines in the deep sedimentary series, which emerge at the foot of the continental slope and mark the seaward limit of the PQ basin perched at mid-slope. The flats use two inherited lithologic discontinuities, the top of the basement (red), and the base of the Messinian evaporitic series (light orange). More deeply, a southward dipping reflector in the pre-Messinan series (mio) defines the deeper neo-formed ramp (CMP 250-400) which connects the two faults (F1,F2). If we take into account the slight uplift of the base of the Messinian evaporitic series at the foot of the margin (CMP 350-450) and the apparent deformation of the underlying pre-Messinian series, we can suggest the existence of deeper ramp (s) in the acoustic basement (thick dashed lines at 6 s twt), where the ramp (s) could intersect older Oligocene–Miocene syn-rift normal faults (blue dashed line).

4 Discussion and Conclusion

Tectonic inversion is expressed on all profiles at the deep margin of the central Algerian margin offshore Great Kabylia. The western lines, offshore Boumerdes region display south-dipping blind thrusts which are part of a flat-ramp system developed in the basement. These deep structures delimit two sub-basins at the margin toe filled with southward thickening of PQ wedge. Eastward offshore Tigzirt (Ti in Fig. 1), inversion occurs at a shallower structural level as a flat-ramp system in deep sedimentary cover that emerges at the foot of the continental slope and marks the seaward limit of PQ perched basin at mid-slope. Both inherited lithological discontinuities (flats) and south-dipping ramps control the geometry on the inversion-related structures.

Previous mapping of these basins in the western part of the study area from the interpretation of HR seismic data shows that these basins form continuous belt of discontinuous and imbricated sub-basins along the foot of the margin and at mid-slop (Figs. 2 and 3). The SPIRAL deep seismic data show that (1) these basins are delimited at depth by south-dipping blind thrusts with flat-ramp geometry (2) the compressive system stretches eastward toward Bejaia. In this area, the inversion-related structures are

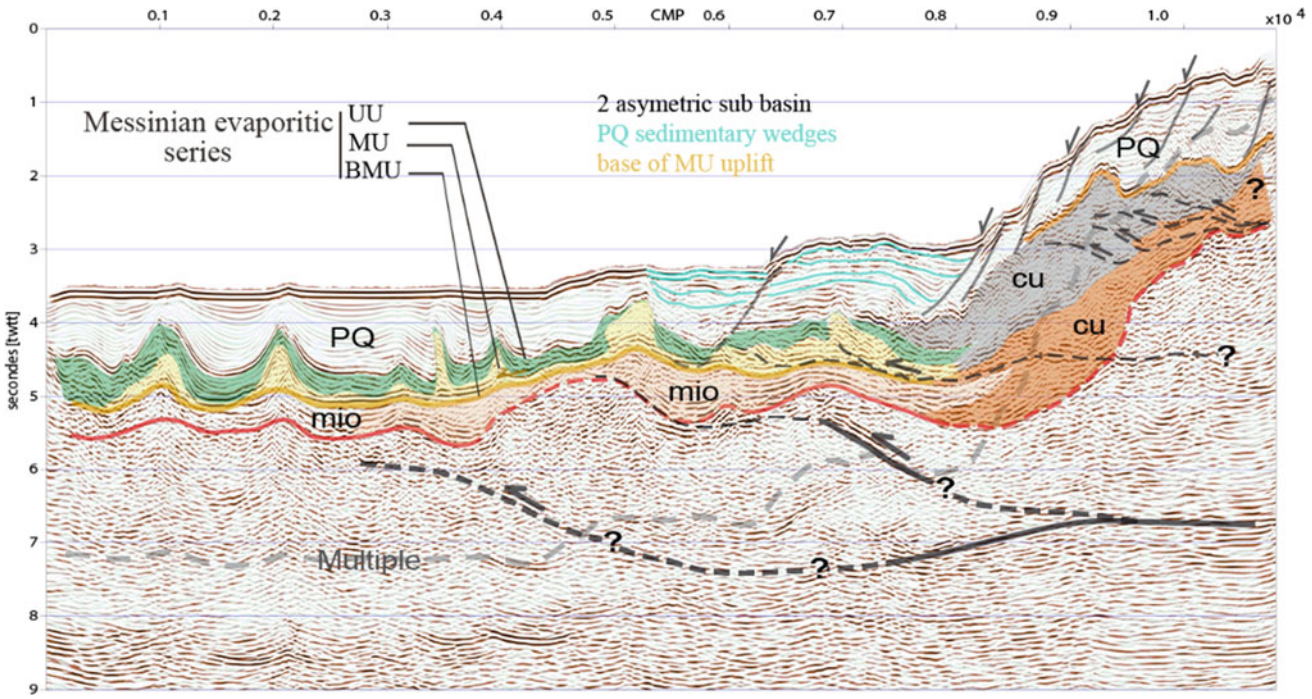

Fig. 2 Interpretation of the Spi08 section, see location on Fig. 1

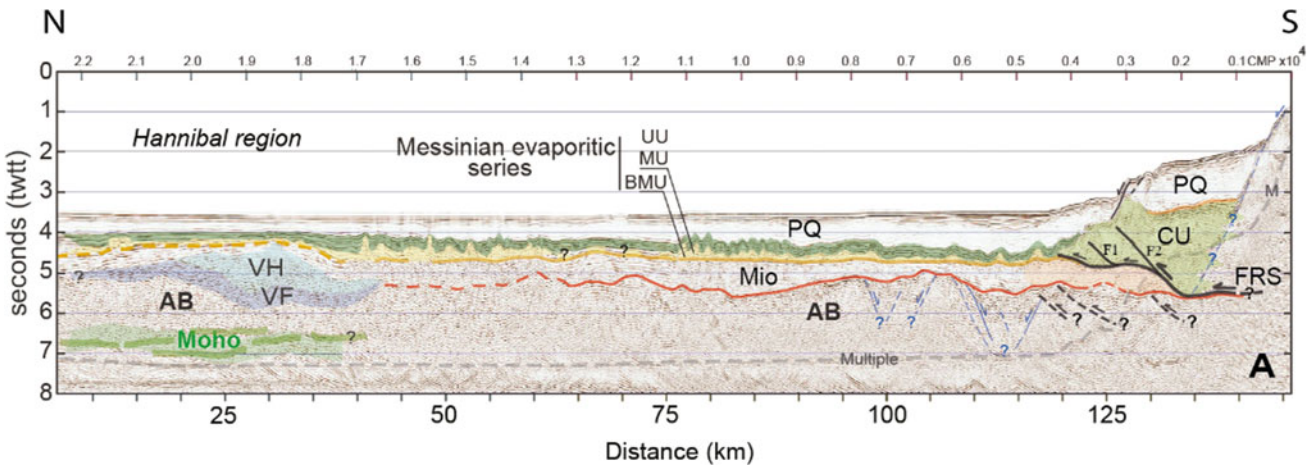

Fig. 3 Interpretation of the Spi11 located on the central part of study area (Aïdi et al. 2018), see location on Fig. 1

shallower under the margin, with development of mid-slope perched basin over flat-ramp system in a deep sedimentary cover. As a whole, the geometry of the reverse structures supports fault-bend fold model which are likely to participate in large uplifts such as the coastal one related to Boumedres earthquake located at the foot of the margin at 10 km depth causing an average uplift of 55 cm along the 50 km coastal shoreline with maximum of 85 cm in the epicentral area.

References

Aïdi, C., Beslier, M.O., Yelles-Chaouche, A.K., Klingelhoefer, F., Bracene, R., Galve, A., Djellit, H.: Deep structure of the continental margin and basin off Greater Kabylia, Algeria-New insights from wide-angle seismic data modeling and multichannel seismic interpretation. Tectonophysics **728**, 1–22 (2018)

Bougrine, A., Yelles-Chaouche, A.K., Calais, E.: Active deformation in Algeria from continuous GPS measurements. Geophys. J. Int. **217**(1), 572–588 (2019)

Domzig, A.: Déformation Active et Récente, et Structuration Tectonosédimentaire de la Marge Sous-marine Algérienne. PhD Thesis. Université Bretagne Occidentale, p. 332 (2006).

Strzerzynski, P., Déverchère, J., Cattaneo, A., Domzig, A., Yelles, K., Mercier de Lepinay, B., Babonneau, N., Boudiaf, A.: Tectonic inheritance and Pliocene-Pleistocene inversion of the Algerian margin around Algiers: insights from multibeam and seismic reflection data. Tectonics 29, TC2008 2010. https://doi.org/10.1029/2009TC002547.ASTI. http://www.springer.com/ASTI, Last accessed 2016/11/21

Early Exhumation of the Beni Bousera Peridotite-Granulite Unit (Internal Rif, Morocco) Inferred from Its Metasedimentary Cap; A New View on Some Marbles and Regional Implications

André Michard, Omar Saddiqi, Ahmed Chalouan, and Aboubaker Farah

Abstract

The exhumation of the Beni Bousera peridotites of the Internal Rif is currently ascribed to the Neogene tectonics of the Alboran Domain. Here we report on marbles included in a fault zone surrounding the Beni Bousera peridotite-granulite unit and overlain by the Filali gneiss and schists. They should derive from a sedimentary cap overlying unconformably the Beni Bousera unit. Their metamorphic evolution would have occurred beneath the Filali thrust burial. We examined the possible correlations with the Beni Malek serpentinites (External Rif) and the Ronda peridotites massifs (Betic Cordilleras), and infer a post-Permian, pre-Neogene exhumation of the Beni Bousera unit.

Keywords

Infracontinental Peridotites • Mantle exhumation • Hyper-extended margin • Gibraltar Arc • Rif Belt

1 Introduction

The largest complex of orogenic peridotites on Earth crops out in southern Spain (Ronda, Alpujarrides nappes) and northern Morocco (Beni Bousera, Sebtides nappes) within the Alboran Domain at the core of the Gibraltar Arc (Fig. 1).

Their exhumation up to the surface is currently ascribed to the Neogene tectonics of the Alboran Domain (Gueydan et al., in press and references therein). An early exhumation of the mantle rocks and juxtaposed granulites (kinzigites) up to the middle crust depth is supposed to have occurred during the Jurassic rifting of the Alpine Tethys, based on scarce geochronological data (Michard et al. 2002; Hinsbergen et al. 2014). However, recent field studies of the southern Ronda massif have suggested that it was exhumed up to the surface as early as the Permian (Sanz de Galdeano and Ruiz Cruz 2016).

2 Geological Setting

The Beni Bousera massif stands to the SE of the Rif Internal Zones (Figs. 1 and 2); it is cored by the peridotites and their kinzigites envelope, which form together the Beni Bousera unit characterized by high-pressure, high-temperature mineral associations (Chalouan et al. 2008; Kornprobst 1971). The Beni Bousera unit is overlain by the Filali unit where mineral associations belong to the high-temperature, low-pressure metamorphic facies. Both units are shaped by a late, NW–SE trending antiform truncated obliquely by normal faults along its northeastern flank (Ras Araben fault system). These high-grade units (Lower Sebtides) are overlain by two sets of lower grade thrust units, from bottom to top, (i) the Federico units (Upper Sebtides) that include Permian–Triassic terrains likely detached from the Filali unit, and (ii) the Ghomarides-Malaguides nappes mainly constituted by Paleozoic terrains and their Mesozoic-Cenozoic non-metamorphic cover. The "Dorsale calcaire" detached units are pinched at the front of the Ghomarides-Sebtides nappe stack. They altogether form the southern part of the Alboran Domain thrust onto the Maghrebian Flyschs nappes (Fig. 1b). The latter nappes are made up of Cretaceous-Cenozoic deep marine turbiditic and clayey beds regarded as the infilling of the Alpine Tethys, which connected with the Central Atlantic from the Middle Jurassic to the Eocene (Frizon de Lamotte et al. 2011). The southern Alboran terrains are interrupted southeastward by the Jebha sinistral fault; they crop out again further to the east in the Bokkoya massif (Fig. 1b).

A. Michard (✉)
Paris XI University, 91405 Orsay, France

O. Saddiqi · A. Farah
Hassan II University, Casablanca Aïn Chock, Morocco

A. Chalouan
Mohamed V University, Rabat Agdal, Morocco

M. Meghraoui et al. (eds.), *Advances in Geophysics, Tectonics and Petroleum Geosciences*,
Advances in Science, Technology & Innovation, https://doi.org/10.1007/978-3-030-73026-0_125

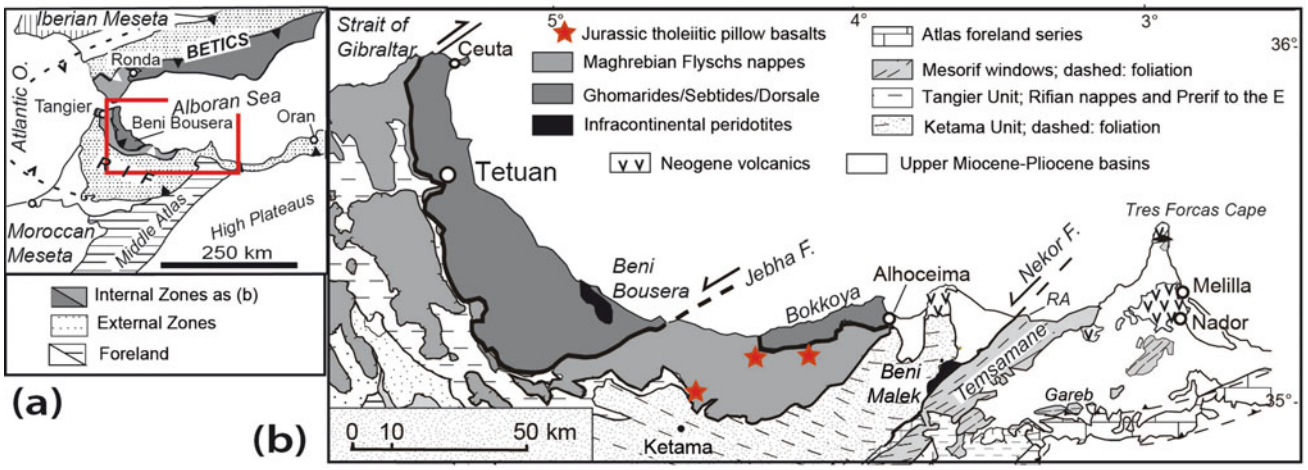

Fig. 1 **a** Sketch map of the Betic and westernmost Maghrebides (Rif-Tell) Alpine belts, after (Durand-Delga et al. 2000). **b** Structural map of the northern Rif after (Chalouan et al. 2008)

The Flysch nappes are in turn thrust upon the External Zones that derive from the inversion of the North African hyper-extended margin (Michard et al. 2007). The Beni Malek serpentinites and associated metabasalts are pinched between the Lower Cretaceous sandstones of the Ketama unit (Intrarif) and the Temsamane Jurassic-Miocene stacked units (Mesorif); they record an oceanic area of exhumed serpentinized mantle during the Upper Jurassic (Michard et al. 2007). The Oligocene–Miocene suturing of this area was associated with a medium-pressure, low-temperature metamorphism. The same "Mesorif suture zone" can be recognized further to the east in the Oran Mountains (Michard et al. 2007).

3 Methods

A detailed mapping of the marble outcrops was carried out on both sides of the Oued Amter valley, which cuts across the southeastern pericline of the Beni Bousera antiform (Figs. 2 and 3). In the marble outcrops, the structural analysis classical methods were implemented. Samples were collected for petrography. At the present stage of our work, thin sections have been studied only under the optical microscope (Christian Chopin courtesy, ENS Paris). Other samples are being processed for geochronological purposes.

4 Results

4.1 Mapping

Marbles have been mapped in detail over >1 km along the northeastern flank of the Beni Bousera antiform on both sides of the Oued Amter valley, and observed on the southwestern flank of the pericline in the Oued Jouj (Fig. 3).

On the northeastern flank of the antiform (Fig. 4), the marbles occur in the form of dismembered, 10–30 m thick minor units in a fault zone whose thickness varies from ~300 m near Taza-village to only ~30 m or less at Inoualine.

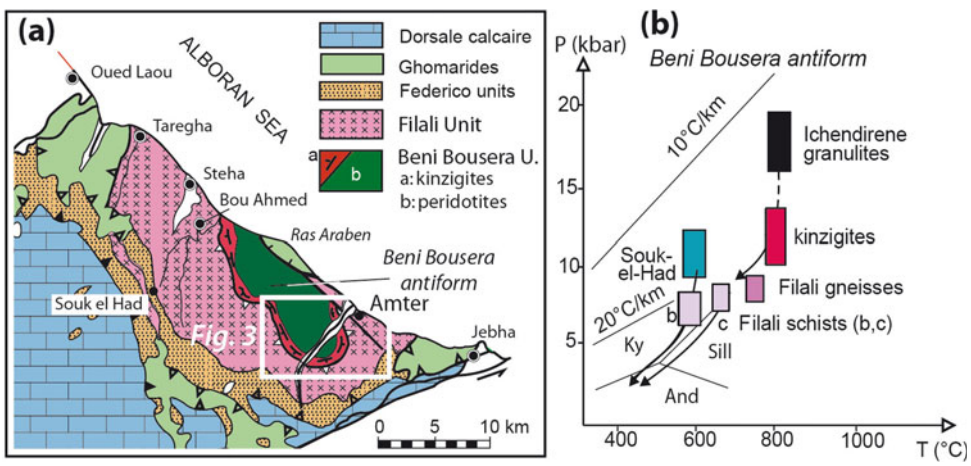

Fig. 2 **a** Structural map of the Beni Bousera massif and juxtaposed units of the southern Alboran Domain, after (Chalouan et al. 2008). **b** P–T paths of the southern Sebtides units after (Chalouan et al. 2008)

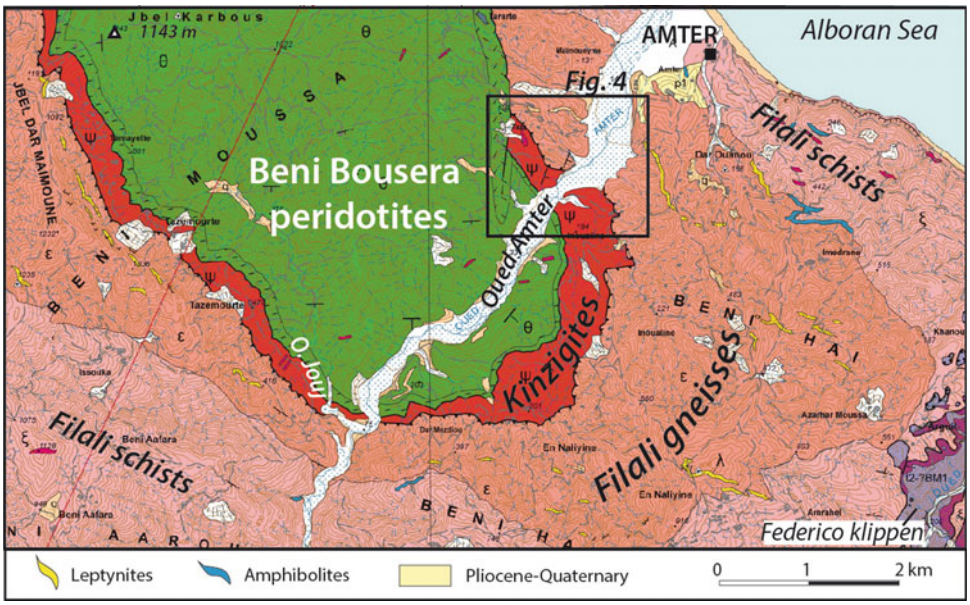

Fig. 3 SE pericline of the Beni Bousera antiform after (Kornprobst 1971) in the Geological map of Morocco, scale 1:50,000, Bab Berred sheet, modified. Framed: location of Fig. 4

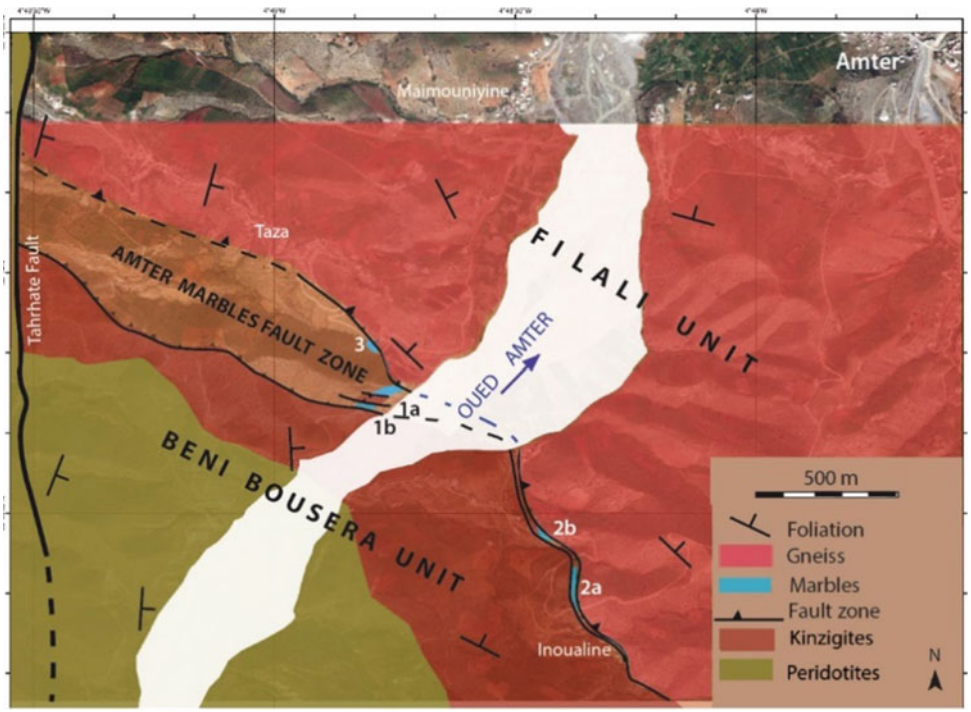

Fig. 4 Geological map of the Amter Marbles Fault Zone (a mix of marbles, kinzigite and gneiss spalls) along the NE flank of the Beni Bousera Unit. Location: Fig. 3

4.2 Lithology, Structure, Mineralogy

The marbles frequently display alternating beds of pure and silicate-rich facies or of thinly bedded marble and green phyllitic facies (Saddiqi 1988), which demonstrates unequivocally their sedimentary origin (Fig. 5a–c). Locally (outcrop 2a, Fig. 4), thinly layered meta-clastites are interleaved within the marbles. Two outcrops (1b and 2b, Fig. 4) suggest a primary unconformity onto the kinzigites (Fig. 5a). In contrast, the upper limit of the marbles at the bottom of the Filali unit is a NW-verging thrust fault involving a meter-thick calc-mylonite with fractured fragments of the overlying gneiss (Fig. 5d).

Within each marble elementary unit of the "Amter Marbles Fault Zone", NNE-trending folds are conspicuous. Locally two generations of folds can be observed (Fig. 5b, c). The second-order faults within the fault zone exhibit either the characters of northwestward ductile thrusts (Fig. 5a) or that of northward dipping, brittle normal faults.

The marbles exhibit varied metamorphic minerals either scattered or arranged in foliation planes within the recrystallized calcite ground mass. Pending the results of

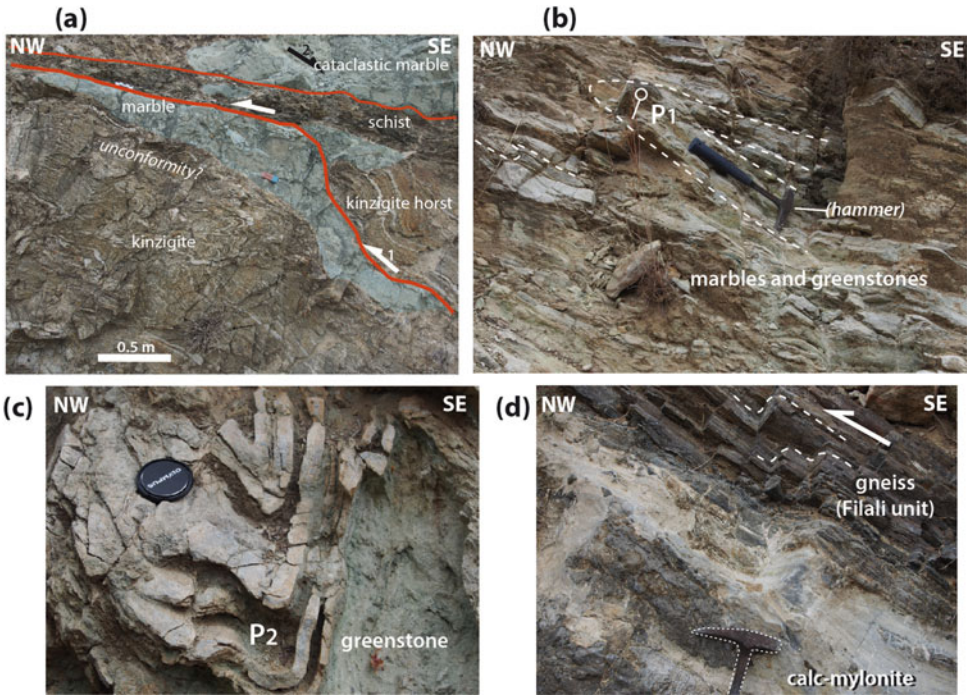

Fig. 5 **a** Basal contact of Inoualine marbles (location 2b, Fig. 4). **b, c** Thinly bedded marbles with alternating phyllitic beds showing superimposed folds P1, P2 (location 3, Fig. 4). **d** Calc-mylonite with gneiss spalls on top of the marbles beneath the Filali unit (location as b, c)

micro-chemical analyses, we confirm the occurrence of diopside, scapolite, K-feldspar, and titanite, already noticed by Kornprobst (1971). We also observed abundant phlogopite lamellae and late talc, likely recording an evolution of the conditions of metamorphism of magnesian limestones or dolostones. Detrital minerals include quartz, K-feldspar and zircon grains. Rounded phyllitic aggregates could derive from peridot (Kornprobst 1971) or pyroxene of detrital origin.

5 Discussion

5.1 Amter Marbles Significance

Kornprobst (1971) considered the marbles as intercalations within the kinzigites series. Our results show that the Amter marbles are not intercalated within the kinzigites, but concentrated in a relatively thin fault zone between the kinzigite envelope of the Beni Bousera unit and the overlying Filali unit. Moreover, it seems that the marbles only suffered high-temperature, low-pressure metamorphism (Kornprobst 1971), similar to that of the Filali unit and contrasting with that of the granulite-facies kinzigites. Therefore, we assume that the Amter marbles derive from marine, basically carbonate deposits with scarce clay fraction and detrital input that initially capped the kinzigites. This implies that the Beni Bousera unit was exhumed up to the seafloor at the time when these calcareous facies were deposited. The metamorphism of the marbles was presumably acquired together with that of the Filali unit and beneath the same burial, judged on a broad estimate of their conditions of recrystallization.

5.2 Early Exhumation of the Gibraltar Arc Peridotites

Pending the results of datings, we propose to correlate the Amter marbles either to the Triassic (?) marbles described over the SE part of the Ronda peridotites (Sanz de Galdeano and Ruiz Cruz 2016) or to the Jurassic (?) marbles that overlie the Beni Malek serpentinites in the Mesorif Suture Zone (Michard et al. 2007, 1992, 2018) (Fig. 1). In both cases, the exhumation of the Beni Bousera-Ronda peridotites up to the land surface or to a few hundred meters (the average thickness of the granulite envelope) beneath the seafloor appears as a post Variscan event, linked to the Permian–Triassic rifting of Pangea and subsequent opening of the Central Atlantic—Alpine Tethys realm. This is consistent with the Early Jurassic-Early Cretaceous U–Pb SHRIMP zircon ages previously measured from a Ronda pyroxenite (Sánchez-Rodriguez and Gebauer 2000).

The Beni Malek serpentinites were exhumed at the toe of the hyper-extended African margin (Michard et al. 2007; Gimeno-Vives et al., in press). The Beni Bousera and Ronda peridotites-granulites belong to the Alboran Domain, which was located at the southeastern margin of Iberia until the Late Eocene onset of the Tethyan crust subduction (Fig. 6a; Jabaloy Sánchez et al. 2019) and references therein). The

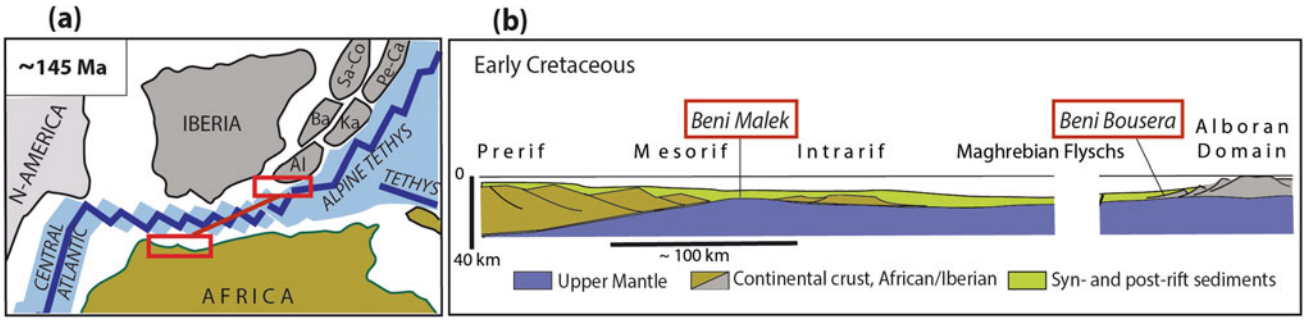

Fig. 6 **a** Plates setting by the end of Jurassic times, after (Sallarès et al. 2011). Crustal blocks partly detached from of Iberia: Al, Alboran; Ba, Balearic Isl., Ca, Calabria; Co, Corsica; Ka, Kabylias; Pe, Peloritani; Sa, Sardinia. Framed: conjugate margins shown in profile (**b**). **b** Conceptual profile of the conjugate African and Alboran margins and intervening Tethyan corridor (Maghrebian Tethys) between the Central Atlantic and the Alpine Tethys. After Michard et al. (2007), modified

African and Iberian conjugate margins were affected coevally by the prolonged extensional tectonics of the Alpine Tethys (Michard et al. 2002; Frizon de Lamotte et al. 2011), which triggered upper mantle exhumation up to or very close to the Earth surface (Fig. 6b). Accordingly, the Neogene exhumation that occurred by the end of the subduction and orogenic thickening of the Alboran Domain (Gueydan et al., in press; Gervilla et al. 2019) should be now regarded as a secondary process with respect to the Triassic-Jurassic exhumation of the Gibraltar Arc mantle rocks.

5.3 Beni Bousera—Filali Units Relationships

A metamorphic gap occurs between the granulites and kinzigites of the Beni Bousera unit and the gneisses and schists of the Filali unit (Chalouan et al. 2008; Kornprobst 1971 and references therein). A similar gap is noticed in the Betic branch of the Gibraltar Arc between the granulitic gneisses above the Ronda peridotites and the Jubrique migmatitic gneisses and schists. This has been explained by ductile thinning of the intermediate crustal rocks in the context of crustal extension (see Chalouan et al. 2008; Jabaloy Sánchez et al. 2019) and references therein).

The occurrence of the Amter marbles in between the Beni Bousera and Filali units makes us reconsider this interpretation. As a working hypothesis, we might assume that thinning actually operated via a ductile low-angle normal fault during the early exhumation of the mantle and lower crust rocks, but that this structure inherited from the Triassic-Jurassic evolution has been inverted as a ductile thrust fault during the Cenozoic contractional events. As reported above, the thrust fault structures (locally observable today: Fig. 5d) are superimposed by late normal faults, which operated in brittle conditions, likely during the Miocene rifting of the Alboran Basin.

6 Conclusion

Our map of the Amter marbles on top of the Beni Bousera peridotite-unit brings a strong geological argument in support of an early exhumation of the mantle rocks and juxtaposed lower crust granulite virtually up to the seafloor.

This early exhumation would have occurred during the Triassic-Jurassic rifting and drifting evolution that gave birth to the Alpine/Maghrebian Tethys. As such, the exhumation of the Beni Bousera and Ronda mantle rocks of the Alboran Domain could be older than or coeval with that of the Beni Malek serpentinites at the toe of the African margin.

The Beni Bousera granulites-kinzigites preserved on top of the peridotites are separated from the overlying mid-upper crustal Filali gneisses by a mylonitic thrust contact, which could originate from the Neogene inversion of a former extensional low-angle ductile fault associated with the early exhumation of the mantle rocks.

References

Chalouan, A., Michard, A., El Kadiri, K., Negro, F., Frizon de Lamotte, D., Soto, J.I., Saddiqi, O., The Rif belt. In: Michard, A., Saddiqi, O., Chalouan, A., Frizon de Lamotte, D. (eds.), Continental evolution: the geology of morocco: structure, stratigraphy and tectonics of the africa–atlantic–mediterranean triple junction. Lect. Notes Earth Sci. **116**, 203–302 (2008)

Durand-Delga, M., Rossi, P., Olivier, P., Puglisi, D.: Situation structurale et nature ophiolitique de roches basiques jurassiques associées aux flyschs maghrébins du Rif (Maroc) et de Sicile (Italie). C. r. Acad. Sci. **331**, 29–38 (2000)

Frizon de Lamotte, D., Raulin, C., Mouchot, N., Wrobel-Daveau, J.C., Blanpied, C., Ringenbach, J.C.: The southernmost margin of the Tethys realm during the Mesozoic and Cenozoic: initial geometry and timing of the inversion processes. Tectonics **30**, TC3002 (2011). https://doi.org/10.1029/2010TC002691

Gervilla, F., González-Jiménez, J.M., Hidas, K., Marchesi, C., Piña, R.: Geology and metallogeny of the upper mantle rocks from the Serranía de Ronda, pp. 11–122. Soc. Esp. Mineral. Publ, Granada (2019)

Gimeno-Vives, O., Mohn, G., Bosse, V., Haissen, F., Zaghloul, M.N., Atouabat, A., Frizon de Lamotte, D.: The Mesozoic margin of the Maghrebian Tethys in the Rif belt (Morocco): Evidence for poly-phase rifting and related magmatic activity. Tectonics, in press. https://doi.org/10.1029/2019TC005508 (2019)

Gueydan, F., Mazotti, S., Tiberi, C., Cavin, R., Villaseñor, A.: Western Mediterranean sub-continental mantle emplacement by continental margin obduction. Tectonics, in press (2019). https://doi.org/10.1029/2018TC005058

Jabaloy Sánchez, A., Martín-Algarra, A., Padrón-Navarta, J.A., Martín-Martín, J.A.M., Gómez-Pugnaire, M.T., López Sánchez--Vizcaíno, V., Garrido, C.J.: Lithological successions of the internal zones and flysch trough units of the Betic chain. In: Quesada, C., Oliveira, J.T. (eds.) The geology of Iberia: a geodynamic approach. Regional Geol. Rev. (2019). https://doi.org/10.1007/978-3-030-11295-0_8

Kornprobst J.: 1971–1974. Thèse Doct. ès-Sci. Univ. Paris (1971) and Notes Mém. Serv. Carte géol. Maroc 251, pp. 1–256 (1974)

Michard, A., Feinberg, H., Elazzab, D., Bouybaouene, M.L., Saddiqi, O.: A serpentinite ridge in a collisional paleomargin setting: the Beni Malek massif, External Rif, Morocco. Earth Planet. Sci. Lett. **113**, 435–442 (1992)

Michard, A., Chalouan, A., Feinberg, H., Goffé, B., Montigny, R.: How does the Alpine belt end between Spain and Morocco? Bull. Soc. Geol. Fr. **173**, 3–15 (2002)

Michard, A., Frizon de Lamotte, D., Negro, F.: Serpentinite slivers and metamorphism in the external maghrebides: arguments for an intra-continental suture in the African paleomargin (Morocco, Algeria). Rev. Soc. Geol. España **20**, 173–185 (2007)

Michard, A., Mokhtari, A., Lach, P., Rossi, P., Chalouan, A., Saddiqi, O., Rjimati, E.C.: Liassic age of an oceanic gabbro of the External Rif (Morocco): Implications for the Jurassic continent–ocean boundary of Northwest Africa. C. r. Geosci. **350**, 299–309 (2018)

Saddiqi, O.: Tectonique de la remontée du manteau: les péridotites des Beni Bousera et leur enveloppe métamorphique, Rif interne, Marocco Unpublished Thesis, University Louis-Pasteur Strasbourg, pp. 1–172 (1988)

Sallarès, V., Gailler, A., Gutscher, M.A., Graindorge, D., Bartolome, R., Grácia, E., Díaz, J., Dañobeitia, J.J., Zitellini, N.: Seismic evidence for the presence of Jurassic oceanic crust in the central Gulf of Cadiz (SW Iberia margin). Earth Planet. Sci. Lett. **311**, 112–123 (2011)

Sánchez-Rodriguez, L., Gebauer, D.: Mesozoic formation of pyroxenites and gabbros in the Ronda area (southern Spain), followed by early Miocene subduction metamorphism and emplacement into the middle crust: U-Pb sensitive high-resolution ion microprobe dating of zircon. Tectonophysics **316**, 19–44 (2000)

Sanz de Galdeano, C., Ruiz Cruz, M.D.: Late Paleozoic to Triassic formations unconformably deposited over the Ronda peridotites (Betic Cordilleras): evidence for their Variscan time of crustal emplacement. Estud. Geol. **72** https://doi.org/10.3989/egeol.42046.368 (2016)

van Hinsbergen, D.J.J., Vissers, R.L.M., Spakman, W.: Origin and consequences of western Mediterranean subduction, rollback, and slab segmentation. Tectonics **33**, 393–419 (2014)

Magnetotelluric Modelling of the Central Hoggar (Tuareg Shield, NW Africa) Lithospheric Structure

Abderrezak Bouzid, Aboubakr Deramchi, Abderrahmane Bendaoud, Riad Ben El Khaznadji, Nouredine Akacem, Abdeslam Abtout, Abdelhamid Bendekken, and Mohamed Hamoudi

Abstract

The Hoggar massif (southern Algeria) with Aïr and Adrar des Iforas is part of the Touareg shield. The present study attempted to model lithospheric structure of its central part using Magnetotelluric (MT) data. MT data were collected from 17 sites in 2005. The stations form two nearly parallel NW–SE profiles approximately 200 km long. The distance between the MT sites of the order of 40 km allowed resolving the geological regional structure of the lower crust and the lithospheric mantle down to 80 km deep. The lower crust contains a number of small conductive structures probably associated with inter and intra-terrane faults. One of the most important observations that can be deduced from the MT model is that the Cenozoic volcanic districts of Manzaz/Atakor of Central Hoggar are underlain by a deep lithospheric conductive structure. This structure was interpreted as being the path taken by the magmas to go up from the base of the lithosphere to the surface.

Keywords

Hoggar massif • Tuareg shield • Cenozoic volcanism • Lithosphere • Magnetotellurics

1 Introduction

The lithospheric geological structure of the Hoggar massif, which is part of the Tuareg shield with Aïr in Niger and the Adrar des Iforas in Mali, remains rather poorly known because of the lack of high-resolution geophysical data (Bouzid et al. 2015; Liégeois 2019). This has been the source of controversy over the interpretation of the presence of Cenozoic volcanism coupled with a topographic bulge and a strong negative gravity anomaly. Electrical resistivity can be a good geological marker. It can change depending on the nature of the rock, its porosity, the presence of magma, fluids or mineralization and the geodynamic conditions to which the rock is subjected. Some geological structures generally have an electrical signature that manifests itself in a strong drop in resistivity such as faults, magmatic chambers, or the existence of partial melt or fluid/mineralization within the lithosphere. Being sensitive to the distribution of electrical resistivity in the earth, the Magnetotellurics is a good tool to constrain the structure of the lithosphere. Its depth of investigation increases with the duration of the recording at a measurement site reaching several tens of km, even a hundred km or more with an acceptable spatial resolution. In this work, we presented the results of the processing and modelling of two reconnaissance profiles carried out at Central Hoggar.

2 Magnetotelluric Data Collection, Analysis and Modelling

Magnetotelluric data were collected in February 2005 along the major Hoggar reconnaissance profiles with ~40 km measurement step. The data were completed by hog12 collected in 1993, and hog23 and hog24 in 2003. The whole forms two NW–SE profiles approximately 200 km long, intersecting Serouanout and Egéré-Aleksod terranes (Fig. 1). In each site, the time series were recorded during about twenty hours using the Phoenix Geophysics 5-component device. The time series were processed using robust code provided by the manufacturer. The impedance tensor and tipper data were extracted over a period range of 0.003–1000 s.

In order to determine the geometry (dimensionality) of the geo-electric structure and the direction of its elongation

A. Bouzid (✉) · A. Deramchi · A. Abtout
CRAAG, BP 63, Route de l'Observatoire, 16340 Algiers, Algeria
e-mail: a.bouzid@craag.dz

A. Deramchi · A. Bendaoud · R. B. E. Khaznadji · M. Hamoudi
USTHB, BP 32 El Alia, 16111 Algiers, Algeria

N. Akacem · A. Bendekken
U.R. Tamanrasset, CRAAG, BP 32, 11000 Tamanrasset, Algeria

M. Meghraoui et al. (eds.), *Advances in Geophysics, Tectonics and Petroleum Geosciences*,
Advances in Science, Technology & Innovation, https://doi.org/10.1007/978-3-030-73026-0_126

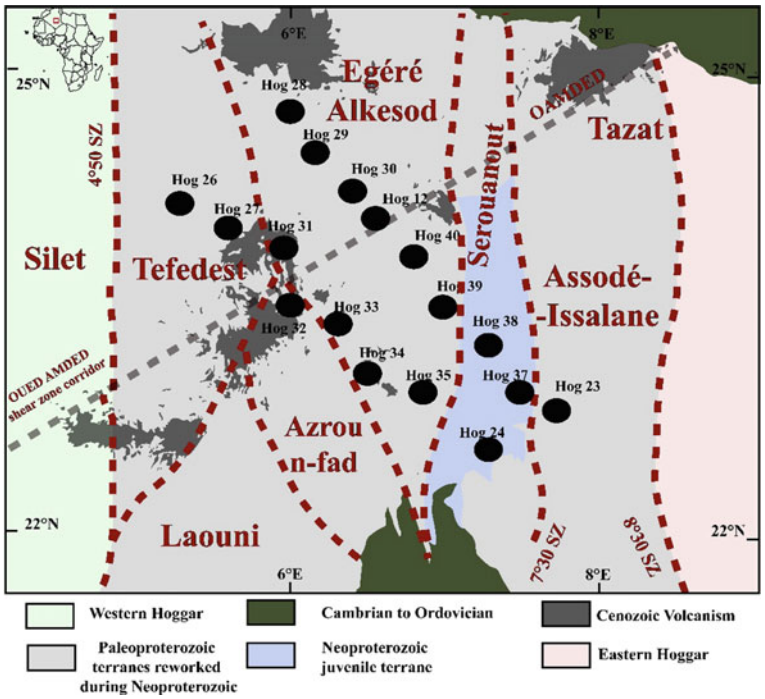

Fig. 1 Location of MT sites (solid circles) on a simplified geological map of Central Hoggar (Liégeois 2019; Bertrand et al. 1977)

(or strike), the magnetotelluric impedance data were analysed using the phase tensor (PT) technique (Caldwell et al. 2004). The dimensionality analysis shows that the geo-electrical structure can be considered 2D in the whole (β skew <5°). However, it is rather 3D for some stations and certain frequencies (Fig. 2a, b). The strike direction calculated from impedance data using Z-invariant (Weaver et al. 2000) and PT method (Caldwell et al. 2004) for both profiles is sub-meridian. To remove the 90° ambiguity on the direction of the strike, we took into account the geological

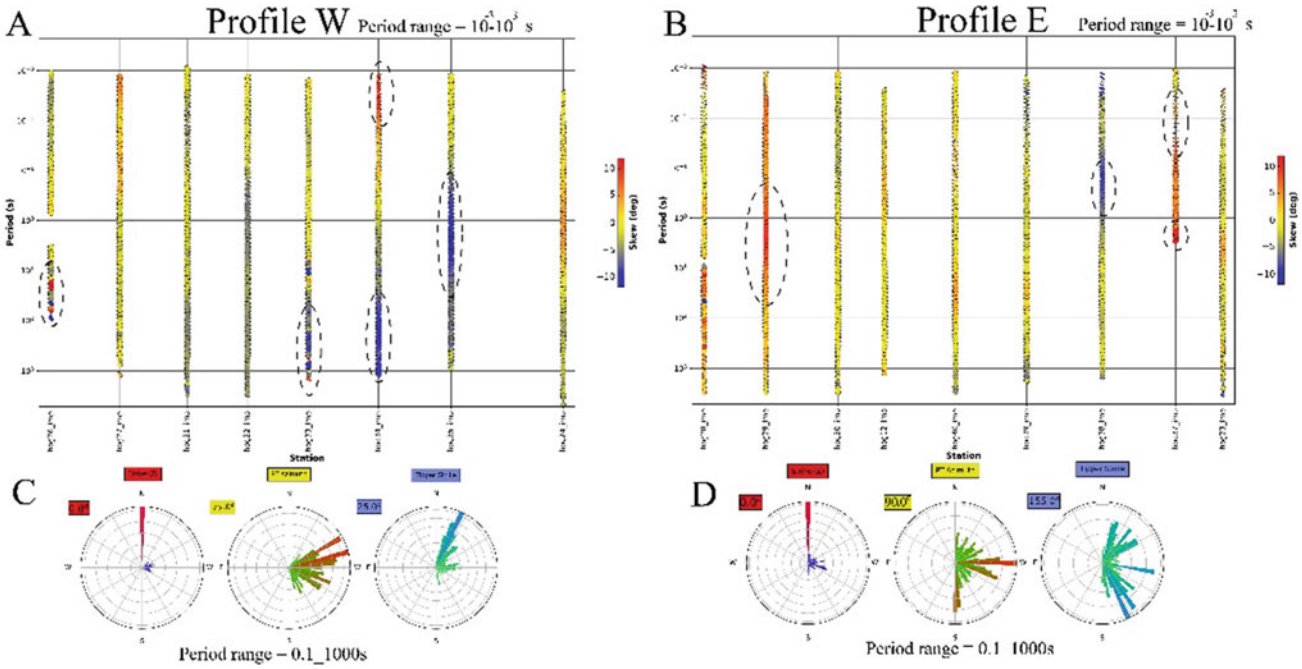

Fig. 2 Beta phase tensor ellipses cross-sections (**a** and **B**) and rose diagrams of strike obtained from the impedance, phase tensor and tipper, respectively (**c** and **d**), for the two MT profiles. Figures have been plotted thanks to MTPY (Kirkby et al. 2019)

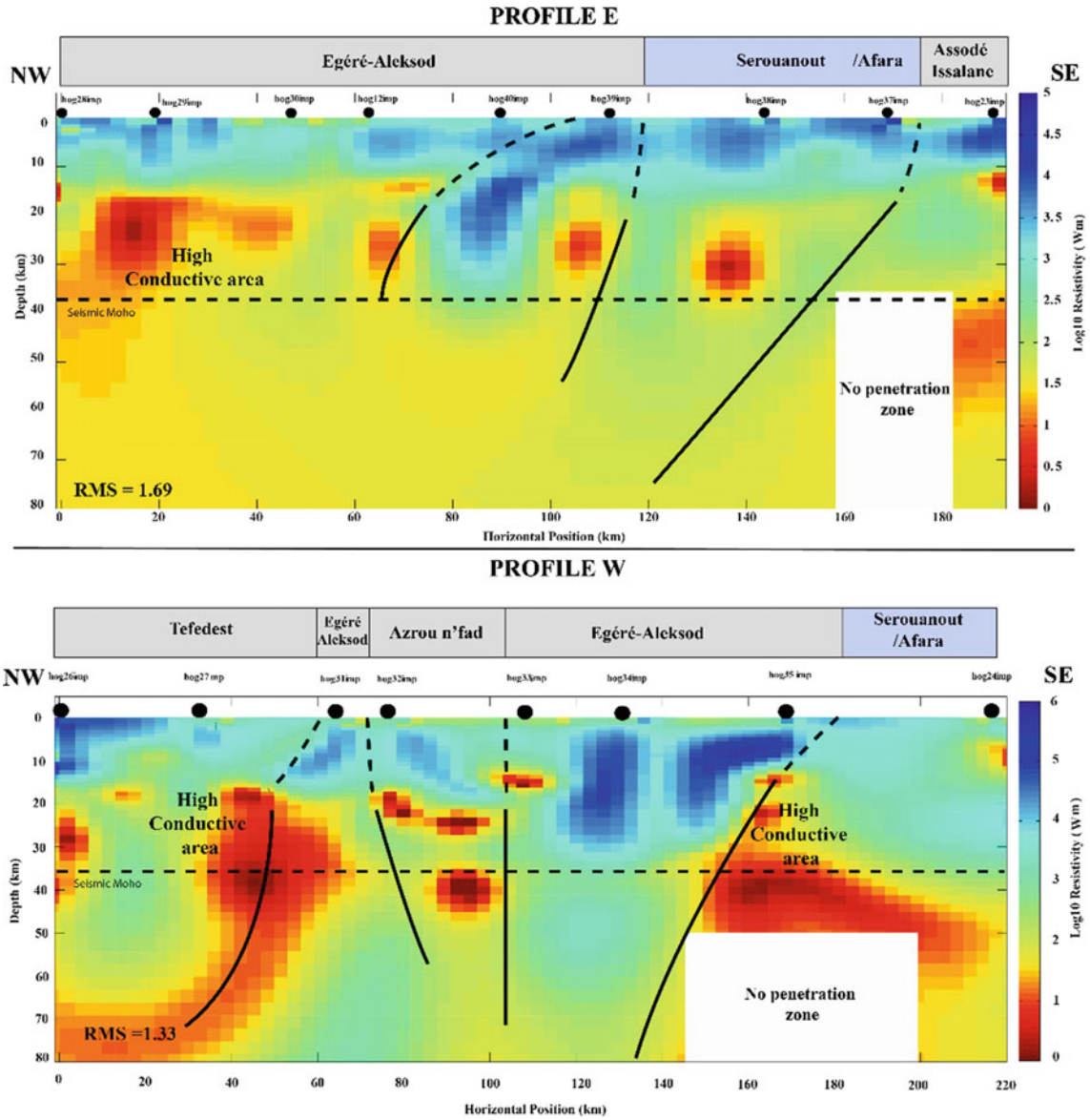

Fig. 3 2D isotropic models of the eastern profile (Top) and western profile (Bottom)

map that shows an extension of the major geological structures in the NS direction. Moreover, the tipper strike suggests an oblique angle to that obtained from impedance (Fig. 2c, d). Thus, the electric polarization or TE mode (respectively, magnetic polarization or TM mode) was obtained by the NS component (EW component) of the electric field and the EW component (NS component) of the magnetic field.

The 2D inversions were carried out using the Occam2d algorithm (deGroot-Hedlin and Constable 1990). Several data combinations have been tested to obtain a 2D model with the lowest RMS and more consistent electrical structures. It turns out that the combination of TM mode data (apparent resistivity and phase) with the TE mode phase only and the tipper is the one that gives the best result. The TE apparent resistivity seems to be affected by some 3D effects generating several artefact. The two preferred models (Fig. 3) were obtained with a starting model consisting of a 100 Ω m homogeneous isotropic half-space. The mesh used consisted of 141 × 76 nodes and 159 × 76 for the profile E and W, respectively, and extend to ∼120 km each side of the profile and to a depth of ∼400 km. Data in a period range of 0.1–900 s have been inverted using an error floor of 5% on apparent resistivity, 1.43° on both phases and 0.015 on tipper. The two models were obtained with an RMS of 1.69 for the eastern profile (Fig. 3, top) and 1.33 for the western profile (Fig. 3, bottom). "No penetration zones" not constrained by the data have been blanked out.

3 Geological Interpretation

The spacing between the measuring stations (~40 km) and the range of periods used for the inversion of the MT data allows obtaining relatively better spatial resolution for the lower crust and the upper mantle to a depth of approximately 80 km. Moreover, the resistivity models calculated without geological constraints show a typical resistive upper crust resting on an inhomogeneous lower crust and a lithospheric mantle of moderate resistivity around a hundred Ω m for the eastern profile and high conductive large bodies on the western one. Most of the anomalies situated at a depth of ~35 km are coherent with the seismic Moho (Liu and Gao 2010). The lower crust shows several small conductive structures that can be associated with faults separating or/and affecting different terranes. In addition, Egéré-Aleksod seems to have not only a resistive upper and lower crust but also shows a resistive lithospheric mantle in the western profile. It should be noted that the north-western part of the western profile exhibits a significant deep conductive body (until 80 km) which is consistent with the known negative gravimetric anomaly affecting central Hoggar (Lesquer et al. 1988).

Other earlier MT studies have already shown the existence of a lithospheric conductive structure under the Cenozoic volcanic districts of Manzaz/Atakor (Bouzid et al. 2015). This conductive structure probably corresponds to the path taken by the magma when it rises to the surface. The electrical signature could be due to trapped fluids released by the magma and/or deposits of mineralization and/or rocks in partial melting or to high temperature zones.

4 Conclusions

Magnetotelluric data collected at 17 stations forming two nearly parallel profiles of about 200 km in length were modelled. The distance between the MT sites of the order of 40 km allowed resolving the geological structure of the lower crust and the lithospheric mantle down to 80 km deep. The lower crust contains a number of small conductive structures probably associated with inter and intra-terrane faults. The volcanic districts of Manzaz/Atakor of Central Hoggar are underlain by a lithospheric conductive structure. This structure is interpreted as being the path taken by the magma to go up from the base of the lithosphere to the surface.

References

Bertrand JM, Caby R, SONAREM Geologists, Compilers Carte géologique du Hoggar (Algeria). SONAREM, Algiers, scale 1:1,000,000, 2 sheets (1977)

Bouzid A, Bayou B, Liégeois J-P, Bourouis S, Bougchiche SS, Bendekken A, Abtout A, Boukhlouf W, Ouabadi A (2015) Lithospheric structure of the Atakor metacratonic volcanic swell (Hoggar, Tuareg Shield, southern Algeria): electrical constraints from magnetotelluric data. In: Foulger, G.R., Lustrino, M., King, S. D. (eds.) The Interdisciplinary Earth: A Volume in Honor of Don L. Anderson. Geological Society of America Special Paper 514 and American Geophysical Union Special Publication 71, pp. 239–255 (2015)

Caldwell, T.G., Bibby, H.M., Brown, C.: The magnetotelluric phase tensor. Geophys. J. Int. **158**, 457–469 (2004)

deGroot-Hedlin, C., Constable, S.: Occam's inversion to generate smooth two-dimensional models from magnetotelluric data. Geophysics **55**(12), 1613–1624 (1990)

Kirkby, A.L., Zhang, F., Peacock, J., Hassan, R., Duan, J.: The MTPy software package for magnetotelluric data analysis and visualisation. J. Open Source Softw. **4**(37), 1358 (2019)

Lesquer, A., Bourmatte, A., Dautria, J.M.: Deep structure of the Hoggar domal uplift (Central Sahara, South Algeria) from gravity, thermal and petrological data. Tectonophysics 152, 71–87 (1988)

Liégeois, J.-P.: A new synthetic geological map of the Tuareg Shield: an overview of its global structure and geological evolution. In: Bendaoud, A., et al. (eds.) The Geology of the Arab World—An Overview, pp. 83–107. Springer Geology (2019)

Liu, H.L., Gao, S.S.: Spatial variations of crustal characteristics beneath the Hoggar swell, Algeria, revealed by systematic analyses of receiver functions from a single seismic station. Geochem. Geophys. Geosyst. **11**, Q08011 (2010)

Weaver, J.T., Agarwal, A.K., Lilley, F.E.M.: Characterization of the magnetotelluric tensor in terms of its invariants. Geophys. J. Int. **141**, 321–336 (2000)

Tectonophysics Modeling of Baimka Ore Zone (Western Chukotka)

Natalya Frolova, Taras Kara, and Andrey Chitalin

Abstract

Baimka ore zone (BOZ) containing the greatest in Russia Au-Cu-porphyry deposit "Peschanka" located in Alazey–Oloy fold belt and associated with Late Jurassic–Early Cretaceous volcanic belt complex. Ore zone originated in regional Aluchin fault, which controlled localization of intrusive bodies, Cu-porphyry systems, Au-Ag-polymetallic occurrences and placer gold deposits. Different-scaled paragenesis examinations led to interpret of these faults as right-hand shear, at the same time, to evidence a reverse movement by these shear zones with the left-hand shear preceding the right-hand shear movement. Ore localization controlled by deformation and several deformation phases results in heterogeneity of the environment that leads to complication of stress fields. The deformation process physical modeling in ore zone is an actual challenge, and experiments for shear zones with several intersecting sinuous faults and reverse movement have not been described so far. Tectonophysics modeling of Baimka ore zone performed at Moscow State University tectonophysics laboratory using modeling table with special modeling tool was constructed: a rectangular box made of four blocks that can be rotated over each other changing the form of the box from rectangle to parallelogram. Structural pattern of BOZ corresponds to two-phase reverse model of shear zones. Main faults were created in a left-hand shear and reactivated in right-hand shear conditions. Ore stock works and veins are concentrated in sites of local tension of right-hand shear. Modeling data can be used for the prognostication of ore zones. The main model fissures correspond to poorly studied potential ore fields allocated formerly in BOZ.

Keywords

Baimka ore zone • Tectonophysics modeling • Au-Cu-porphyry Peschanka deposit • Alazey–Oloy fold belt • Okhotsk–Chukotka magmatic belt

1 Baimka Ore Zone Structural Position

Baimka ore zone (BOZ) containing the greatest Au-Cu-porphyry deposit "Peschanka" in Russia is located in Alazey–Oloy fold belt and associated with Late Jurassic–Early Cretaceous volcanic belt complex (Fig. 1). The ore zone extended more than 170 km in NW direction parallel to South Anyuy suture and originated from deep regional Aluchin fault, which controlled the localization of Early Cretaceous ore-forming intrusive bodies and Cu-porphyry systems, Au-Ag-polymetallic occurrences and placer gold deposits associated with them. BOZ is about 20 km in width on the SE overlain by Late Cretaceous volcanic rocks of Okhotsk–Chukotka magmatic belt. Hypabyssal intrusive of diorite and monzodiorite complexes burst folded volcanic–sedimentary Late Jurassic–Early Cretaceous deposits. The main deformation structures near the surface are several subparallel to BOZ slightly sinuous crossing faults (Fig. 2).

2 Tectono-Physical Modeling of Fault Structure Zone

Tectonophysics modeling of Baimka ore zone performed in collaboration of Moscow State University tectonophysics laboratory as an experiential equipment base, Polyus Gold LCC as an exploration company, interested in ore structure survey for BOZ and Institute of GeoTechnology as

N. Frolova
MSU, Moscow, Russia

T. Kara (✉)
Polyus Gold LLC, Moscow, Russia

A. Chitalin
Geotechnology Institute, Moscow, Russia
e-mail: a.chitalin@igeotech.ru

M. Meghraoui et al. (eds.), *Advances in Geophysics, Tectonics and Petroleum Geosciences*,
Advances in Science, Technology & Innovation, https://doi.org/10.1007/978-3-030-73026-0_127

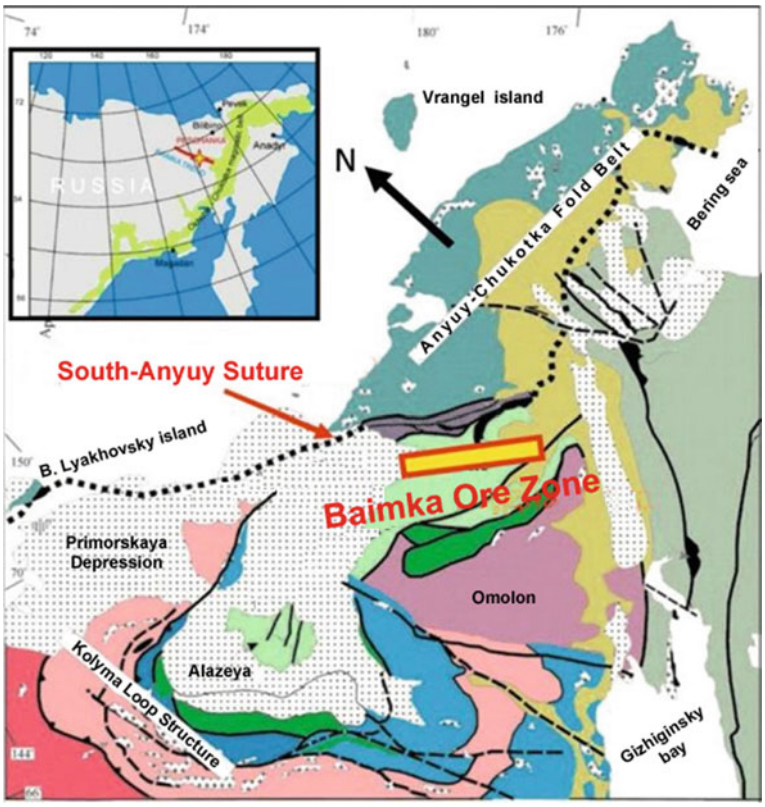

Fig. 1 Baimka ore zone in North-East Eurasia structure (Chitalin et al. 2013)

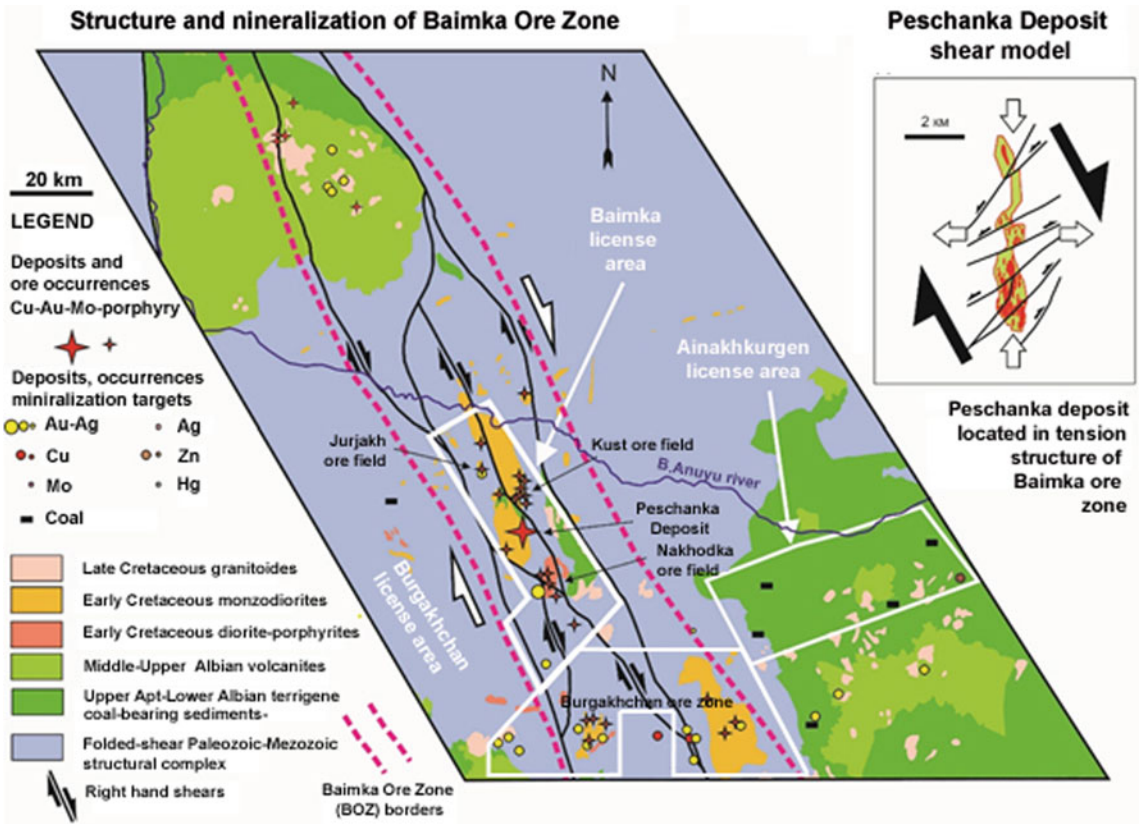

Fig. 2 Main fault structures of Baimka ore zone (Chitalin et al. 2013)

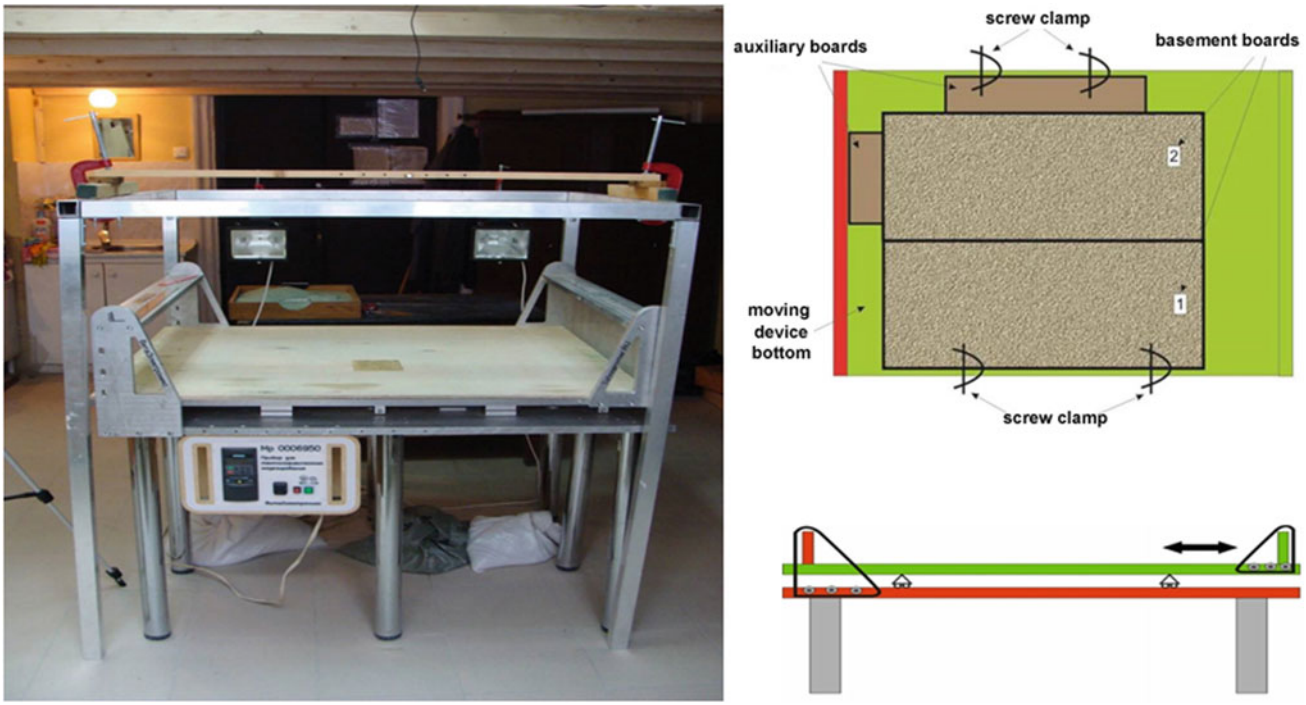

Fig. 3 Modeling table scheme in MSU tectonophysics lab. (Frolova 2017–2018)

expert organization in Baimka zone structures, explored "Peschanka" deposit for a long time (Fig. 3).

The modeling was performed on original tectonophysics instrumentation—modeling table with two borders, one of which is moving together with a tabletop. The device was equipped with an engine that kept the necessary speed conditions. For BOZ modeling, special modeling tool constructed: rectangular box made of four blocks that can be rotated over each other changing form of box from rectangle to parallelogram. On the bottom of the Box 31 Plexiglas rails of 1 cm width. This construction mounted to main tectonophysics instrumentation in a way that allows us to equally show all the zone in one and opposite directions for modeling reverse right-hand and left-hand shears. Silicone layer was

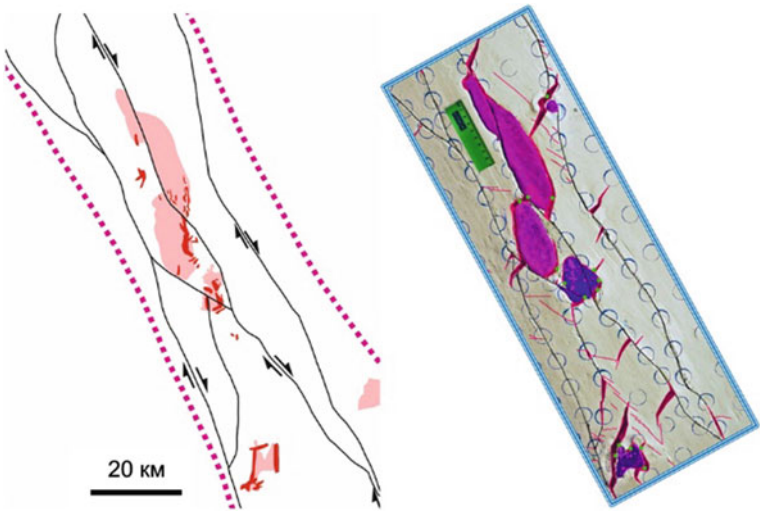

Fig. 4 Structural pattern and results of modeling BOZ (Frolova 2018)

placed on the rails under wet clay or sand sample that contains faults modeling real BOZ fault system (made by pattern). Experiments were performed with one- and two-layer models on wet clay and sand samples, as suitable equivalent material for analog deformation modeling (Atmaoui et al. 2006).

3 Results and Models

Using the equipment, serial of experiments performed including

- Right-hand shear in viscous bedrock under homogeneous covering;
- Right-hand shear and reverse left-hand shear in viscous bedrock without dividing bedrock and covering using clay and sand material;
- Viscous clay, one-stage deformation;
- Minor viscous clay, one-stage deformation;
- Minor viscous clay, two-stage reverse deformation;
- Minor viscous clay, one-stage deformation with model of intrusive bodies.

More than 30 experiments totaling about 600 hours of modeling time were conducted (Fig. 4).

Structural pattern of BOZ corresponds to two-phase reverse model of shear zones. The main faults were created in a left-hand shear and reactivated in right-hand shear conditions.

Ore stock works and veins were concentrated in the sites of local tension of the right-hand shear. The modeled data can be used for the prognostication of ore zones. The main model fissures correspond to poorly studied potential ore fields allocated formerly in BOZ.

References

Atmaoui, N., Kukowski, N., Stöckhert, B., König, D.: Initiation and development to pull-apart basin swith Riedel shear mechanism: insights from scaled clay experiments. Int. J. Earth Sci. **95**(2), 225–238 (2006). https://doi.org/10.1007/s00531-005-0030-1

Chitalin A.F, Usenko V.V., Fomichev E. V. Baimka ore zone—cluster of large, deposits of non-ferrous and precious metals at the East of Chukotka. Mineral recourses of Russia. Econ. Manage. Sci. Tech. J. **6**, 68–73 (2013)

Geotectonics and Geodynamics of Kazakhstan Paleozoides from the Plume Tectonics Position (Kazakhstan)

A. B. Baibatsha

Abstract

According to the seismic tomography, the lithosphere formation of Kazakhstan has a plume origin. In the Paleozoic, Kazakhstan was a separate continent and consisted of three concentric rings of bounded geometry sutures. The rings made a vertical movement under the active influence of mantle plume, and their axes made a horizontal movement. The development of variously oriented lineaments led to the formation of a clumpy-block structure. The modern structure of Kazakhstan was formed during the interaction with Europe, Siberia and southern continents during the Paleozoic–Cenozoic. The proposed geodynamic model of the Kazakhstan development explains the features of the localization of active zones of sedimentation, intrusions and effusive magmatism and metamorphism of the geological formations, ophiolitic zones, availability and promising metallogenic zones and areas with large and unique mineral deposits, oil and gas fields.

Keywords

The geology of Kazakhstan • Deep structure • Continents and oceans • Mantle plumes • Ring structures • Geological formations • Oil and gas fields

1 Introduction

New data on the deep structure of the crust and upper mantle of the continents during complex studies on the international geotraverse system were collected. Some of them are laid on the territory of Kazakhstan. On their basis, models of the lithosphere to a depth of 100–200 km were constructed in the republic, revealing a heterogeneous-block structure of the upper mantle. At depths of about 200 km, the electrical resistance of the mantle substance decreases sharply, which is presumably linked to the elevation of the roof of the asthenospheric layer. The structure of the crust in some cases continues in the upper mantle. The asthenosphere in the geosuture zones rises to the level of 80–100 km, and the asthenoliths penetrate above the Moho border into the Earth's crust.

2 Settings

Advances in studying the structure of the earth's crust over the past fifty years, in particular, the revival and improvement of mobilistic views, led to reconsider many traditional ideas on the dynamics of the lithosphere, both in general and for individual regions. The foregoing can be regarded as an attempt to recreate the chain of events of geological history that led to the formation of modern geotectonics. However, some researchers, mechanically transferring the geodynamics of the lithospheric plates of our planet and the evolution of its structural elements, on the territory of microcontinent Qazaqia, find the same structural elements of geotectonics and explain their geodynamics in accordance with the global theory of plate tectonics. Accordingly, the geodynamics of individual continents and oceans within the territory of the «microcontinent Kazakhstan» is described, which, in our opinion, is not entirely correct.

With the emergence of the mobile belt of the Proto-Tethis, Pangea-I was split into two parts—Rodinia in the north and Gondwana in the south. Nevertheless, these two continental masses also soon, if not simultaneously, were also split. It is assumed that because of the split of the Rodinia, independent continents, namely Siberia, Qazaqia, Katazia and others formed. Already at the end of the Proterozoic, Kazakhstan began to exist independently.

A. B. Baibatsha (✉)
Kazakh National Research Technical University named after K.I. Satpaev, Almaty, Republic of Kazakhstan

M. Meghraoui et al. (eds.), *Advances in Geophysics, Tectonics and Petroleum Geosciences*,
Advances in Science, Technology & Innovation, https://doi.org/10.1007/978-3-030-73026-0_128

3 Results and Discussion

According to modern geophysical data, the introduction of a plume and the penetration of the mantle and asthenosphere into the lithosphere led to a local rise and the formation of a fixed nuclear in the form of a ring structure—the prototype of the Qazaqia continent. The diameter of the nuclear-ring structure was approximately 2.5–3.0 thousand km. The formation of such a peculiar geological structure is associated with the action of the superplume in the Paleozoic and is clearly visible on the geological and tectonic maps of Kazakhstan (Golonka et al. 2006; Baibatsha 2017a,b).

With the adoption of plate tectonics, which is well coordinated with the geotectonics and geodynamics of planetary-scale structures, an attempt was made to correlate the tectonic structure of Kazakhstan with its main elements. However, the mechanical transfer of plate tectonic elements evident on a planetary scale (rifts, spreading, island arcs, collisions, etc.) did not find confirmation in practical geology and caused confusion in the geotectonics and geodynamics of the republic. The sophistication of the application of the principles of plate tectonics is particularly clearly visible on the maps, where, within the limits of essentially a microcontinent Qazaqia began to distinguish «continents» and «oceans», which are, respectively, only geological blocks (terranes) and bays and/or straits of the seas of neighboring Paleozoic oceans, for example, the Paleoasian, Ural, and Tetis.

Modern geophysical data claimed that the introduction of the plume and the picked materials from the mantle and the asthenosphere into the lithosphere led to local rising and the formation of a fixed nuclei in the form of ring structure (Yuen et al. 2007; Joachim et al. 2007; Pirajno 2000). In the modern geological structure of Kazakhstan, the inner and middle ring structures are fairly fully preserved. The inner ring became elongated in the northwestern direction, and its northwestern edge was straight, sometimes even concave. Due to the pressure of the above-mentioned lithospheric plates and the formation of a collision zone, the middle ring from the south and southeast sides became close to the inner ring, and the deformed northeast edge is traced along the Altai collapse zone. The outer ring also became flattened and crumpled into mountain-folded structures from the south and southeast, joining the Ural mountain-folded belt and the West Siberian plate from the north, and a shear-collision zone between Siberia is cut off from the northwest (Fig. 1).

The proposed geodynamic model of the development of Kazakhstan explains the localization features of active sedimentation zones, intrusive and effusive magmatism and metamorphism of geological formations, ophiolitic zones and olistostromes and the location of productive and promising metallogenic zones and areas with large and unique mineral deposits. In general, the main geological structures were laid in the early stage of the territory development, and they acquired a modern look in the form of the Ural–Mongolian belt in the Mesozoic–Cenozoic. In the Cenozoic under the influence of the drifting southern continents, in particular, the Indian plate, the lineaments of the northwestern direction laid, which in some places cut through the annular and geosuture zones.

Research to determine the laws that affect the deployment areas hydrocarbon reserves and resources of oil and gas, source rocks, formations and series, with which they are

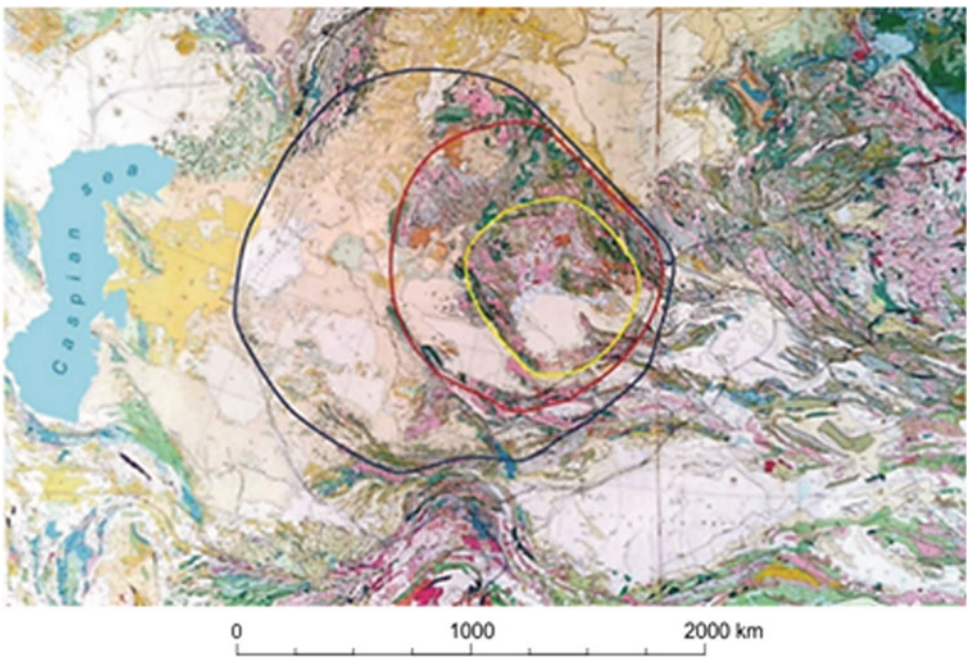

Fig. 1 Scheme of ring structures on a modern tectonic basis

associated, and their spatial and temporal characteristics; the type and degree of thermal transformation of organic matter; predominant type of hydrocarbons generated by certain source rocks; identified analog connection between the source rocks. These studies are among the main criteria both in exploration and in the operation of oil and gas fields. These studies are urgently needed because of the depletion of hydrocarbon reserves and resources within the land on the territory of Kazakhstan. The research results will help to identify both new oil and gas accumulation zones and deposits, local congestion, deposits, land, fields and blocks of oil and gas.

4 Conclusions

The proposed geodynamic model of development of Kazakhstan explains the localization features of active sedimentation zones, intrusive and effusive magmatism and metamorphism of geological formations, ophiolitic zones and olistostromes and the location of productive and promising metallogenic zones and areas with large and unique mineral deposits. A new model may serve as a theoretical basis for the forecast of mineral deposits perspective oil and gas sedimentary basins.

In general, the main geological structures were laid in the early stage of development of the territory, and they acquired a modern look in the form of the Ural–Mongolian belt in the Mesozoic–Cenozoic. In the Cenozoic, under the influence of the drifting southern continents, in particular, the Indian plate, lineaments of the northwestern direction are laid, which in some places violate the ring geosuture zones.

Acknowledgements This work was supported by the scientific program BR05233713 «Comprehensive geological study of subsurface resources for the development of resource base and mining exploitation of new sources of ore raw materials in Kazakhstan».

References

Baibatsha, A.: Relationship of paleozoides and mineral deposits of Kazakhstan with the Paleozoic Superplume. In: 17th International Multidisciplinary Scientific GeoConference SGEM 2017, vol. 17, Issue 11, pp. 479–486. Albena, Bulgaria (2017)

Baibatsha, A.B.: Plumetectonics nature forming geological structures of Kazakhstan with large deposits and basins. In: Plate Tectonics at 50. William Smith Meetings. p. 104. London (2017)

Franco, P.: Ore Deposits and Mantle Plumes, 556 p.. Kluwer Academic Publishers, Dordrecht/Boston/London (2000)

Golonka, J., Krobicki, M., Pajak, N., Zuchiewicz, W.: Global Plate Tectonics and Paleogeography of Southeast Asia, 128 p. Krakow (2006)

Joachim, R.R., Ritter, R., Ulrich, C.: Mantle Plums. 502 p. Springer (2007)

Yuen, D.A., Maruyama, S., Karato, S.I., Windley, B.F.: Superplumes: Beyond Plate Tectonics. 569 p. Springer (2007)

Post-Mesozoic Evolution of the Eastern Flank of the Mongol–Okhotsk Orogenic Belt

Inna Derbeko and Varvara Kichanova

Abstract

The axial structure of the Central Asian fold belt (CAFB)—the Mongol–Okhotsk orogenic belt (MOOB)—is divided into western and eastern links. We examined the eastern flank of the belt. Over the recent years, geochronological, isotopic, and geochemical data have become available, which made it possible to take a fresh look at the development of this region. It was stated that synchronous geodynamic processes took place along the eastern flank of the belt in the Late Mesozoic, accompanied by the formation of synchronous magmatic complexes. Their distribution is limited in the west by the Selengino-Stanovoy superterrane (SSS) along the northern framing of the belt. The superterrane northern border is represented by the zone of the Dzheltulak fault. In the south, the superterrane is bordered by the belt. Zone of tectonic melange is established along this boundary. It consists of rocks which age relates to the Mesozoic—early Precambrian. The obtained data show that the evolutional processes in the frames of MOOB and its framing continued during the late Mesozoic time after the final formation of the belt. This research was dedicated to the salvation of the problem. Authors assume that the position of the superterrane in the Late Mesozoic did not correspond to the modern location. And that the location of the western fragment of the joint of the CAFB structures and the Siberia craton in Cenozoic was formed under the influence of collisional processes occurring between the Indian and Eurasian plates. This phenomenon was the "driving force" of the superterrane movement in the post-Mesozoic time.

Keywords

Mongol–Okhotsk orogenic belt • Suprterrane • Subduction • Craton

1 Introduction

The MOOB is the axial structure of the CAFB (Parfenov et al. 1999). It extends from Inner Mongolia to the shores of the Pacific Ocean for 3000 km (Fig. 1). The formation of the belt is due to the approach of the Siberian and North China cratons and the closure of the Mongol–Okhotsk basin of the same name in the Late Mesozoic. MOOB has a binominal structure: the western and eastern links. We examined the eastern flank of the belt. The northern margin of the eastern flank (MOOB) is represented by two superterranes: SSS and Dzhugdzhuro-Stanovoy superterrane (DSS). They are the south-eastern components of the southern frame of the Siberia Craton.

Along the southern boundary of the MOOB, the Argun and Bureya-Jiamusi superterranes are distinguished, separated by the South Mongol-Khingan orogenic belt (Fig. 2a). These structures contain early Precambrian complexes, which were subjected to tectonic reorganizations and magmatic renewals, which were the most pronounced in the late Mesozoic. Long-term studies of this geological object did not lead to an unambiguous representation of its evolution. Geochronological, isotope, and geochemical data obtained in recent years made it possible to take a fresh look at the development of this complex region.

2 Methods and Materials

To identify the kind of geological events affecting the post-Mesozoic evolution of MOOB, not only the original data of the authors were used (Derbeko 2018, 2012; Derbeko

I. Derbeko (✉) · V. Kichanova
Institute of Geology and Nature Management Far Eastern Branch, Russian Academy of Sciences, Amure region, Blagoveschensk, 675000, Russia

M. Meghraoui et al. (eds.), *Advances in Geophysics, Tectonics and Petroleum Geosciences*,
Advances in Science, Technology & Innovation, https://doi.org/10.1007/978-3-030-73026-0_129

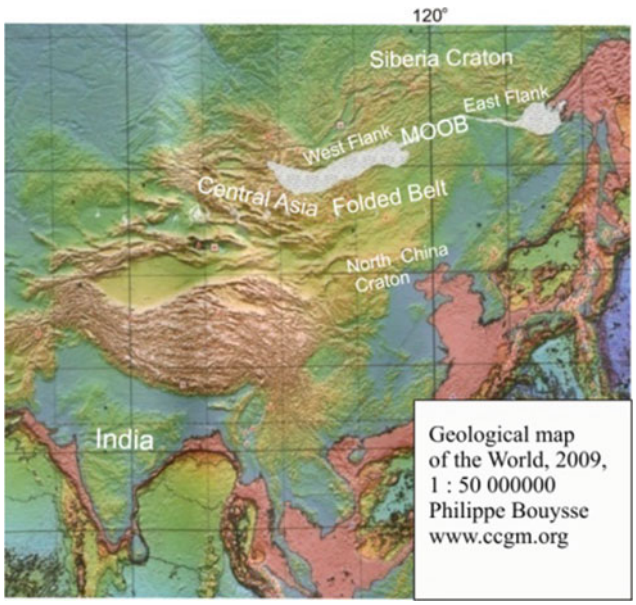

Fig. 1 Dislocation of the MOOB among the main structures of the region

and Markevich 2013), but also the results of geochronological, isotopic, and geochemical studies of igneous complexes accompanying the evolution of the MOOB in the Late Mesozoic, published in recent years (Arkhangelskaya et al. 1993; Velikoslavinsky et al. 2012). The results of geophysical studies, the Skovorodino—Tommot profile transect, passing through the MOOB (Didenko et al. 2013, 2010), were also used.

3 Results

As a result, it was established (Derbeko 2018) that, synchronous geodynamic processes occurred during the Late Jurassic - Early Cretaceous in the frame of the east flank of the MOOB. They were accompanied by the formation of coeval magmatic complexes with the same geochemical characteristics that took place (Fig. 2a). The active magmatism began 145–138 Ma with the formation of the adakite-like volcano–plutonic complexes (Derbeko 2018). In the interval 140–122 Ma, differentiated volcanic–plutonic complexes were formed. According to their geochemical characteristics, these rocks correspond to the suprasubduction formations of calc-alkaline series of active continental Andean type margins (Derbeko 2018). Later on the formation of bimodal complexes began 119–97 Ma. The complexes accompanied the final formation of MOOB (Derbeko 2012). The formation of the intraplate riftogenic magmatism, represented by trachyandesites and absarokites, has occurred already 94–88 Ma (Derbeko and Markevich 2013). The spreading of all the rocks listed above along the southern framing of the MOOB is clipped in the east by the Bureya-Jiamusy superterrane structure (Fig. 2).

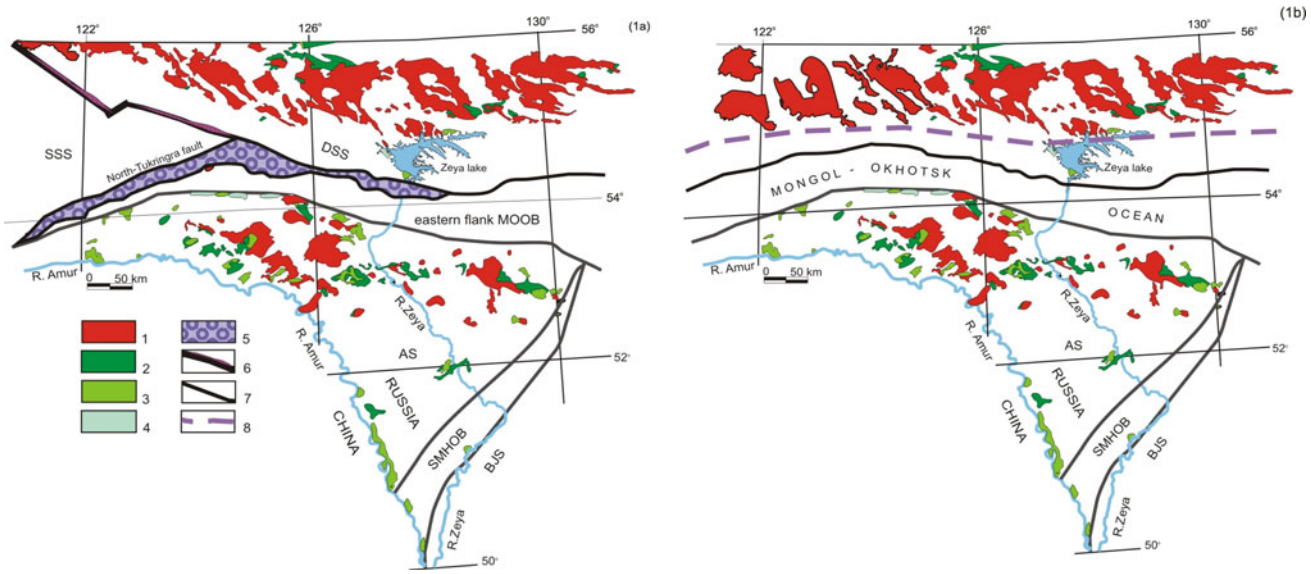

Fig. 2 Scheme of the Late Mesozoic tectonic zoning of the east flank of the MOOB (Parfenov et al. 1999) and the location of magmatic formations in its frame: after (**a**) and before (**b**) Cenozoic tectonic restructuring. Magmatites (1–3): 1 calc-alkaline granitoids (145–126 Ma); 2 calc-alkaline volcanics (130–122 Ma); 3 bimodal series (119–97 Ma); 4 trachyandesites, absarokites of rifting (94–88 Ma). Melange zone (Derbeko 2018) 5 Dzheltulak fault zone; 6 structure-forming tectonic boundaries; 7 the border of spreading of Late Mesozoic magmatic complexes before tectonic restructuring in Cenozoic; 8 abbreviations not indicated in the text: Bureya-Jiamusy superterrane (BJS), Argun superterrane (AS); South Mongol-Khingan orogenic belt (SMHOB)

Within it, the Late Mesozoic magmatites are asynchronous in time to the formation of rocks of the above complexes (Derbeko 2018, 2012; Derbeko and Markevich 2013). The distribution of the above-mentioned rocks is clipped in the west by the structure of the SSS along the northern framing of the belt. Magmatites are widely developed within this structure. They are known as the Selengino-Vitimsky volcano–plutonic belt in the literature (Gordienko and Kuzmin 1999). Rocks of calc-alkaline and bimodal volcano–plutonic series were formed in the early stages of its development (C_2–P_2). Formations of the bimodal magmatic series (Gordienko and Kuzmin 1999) occurred at the late stage (T).

4 Discussion

The northern boundary between the SSS and DSS is represented by the Dzheltulak crust fault zone (Didenko et al. 2010). Mylonites, blastomylonites, blastocataclasites, schist zones, silica-alkaline metasomatism are widely developed within the zone of the Dzheltulak fault. The age of zircons from blastomylonites determined by the U–Pb method showed that there are formations of various ages: 1960–1930, 1750–1700, 1600–1500 Ma (determination by zircons), 2000–1350 Ma (determination by pyrochlore) (Arkhangelskaya et al. 1993). Paleozoic magmatic complexes are widely developed in the SSS frames. But the complexes are absent at the north of the Dzheltulak fault. Late Mesozoic magmatism is widely manifested here: Late Jurassic - Early Cretaceous volcano-plutonic complexes, which are similar to the formations developed along with the southern framing of the MOOB (Derbeko 2012). In the south, the territory of the east flank of the SSS borders the MOOB along the North-Tukuringra fault. The fault consists of sedimentary and volcanogenic rocks metamorphosed in the amphibolite facies that form a structure with a length of 800 km and a width of up to 50 km (Fig. 2a). Geochronological U–Pb and isotope geochemical (Sm–Nd) studies of the rocks (Velikoslavinsky et al. 2012) indicate the presence of volcanic rocks with an age of 193 ± 1 Ma; granitoids with an age of 370 Ma, which are characterized by a minimum tNd (DM) = 1.1 Ga. According to the values of tNd (DM), the metamorphic rocks of the sequence are divided into two groups with tNd (DM) = 1.1–1.9 and tNd (DM) = 2.5–3.1 Ga. The authors of Velikoslavinsky et al. (2012) note that there is no clear spatial distribution of the formations with the Late Archean and Proterozoic tNd (DM). These data allowed them to come to the following conclusions (Velikoslavinsky et al. 2012): (1) rocks of different ages were combined into the zone; (2) the zone is a tectonic melange composed of metamorphosed rocks of Mesozoic, Paleozoic, and Early Precambrian age; (3) the formation of this zone occurred in the Mesozoic, during the Late Jurassic—Early Cretaceous collisional processes between the North Chinese and Siberian cratons. This thesis is refuted by the findings of the early Cretaceous rocks of the zone. As the magmatic processes in the northern and southern framing of the MOOB occurred synchronously and were associated with the closure of the Mongol–Okhotsk basin (Derbeko 2012), it should be assumed that the magmatites were equidistant from the assumed border of subduction by the end of late Mesozoic (Fig. 2b). The position of the SSS at that period of time differed from its current location. It can be stated that SSS "wedged in" between the MOOB and the southern framing of the Siberian craton after the completion of the Late Mesozoic magmatism (Fig. 2a). According to the data of geophysics (Didenko et al. 2013), the base of SSS is a heterogeneous layered structure of the lithosphere, which is a feature of horizontal movements in the earth's crust and sub-crustal area (Didenko et al. 2013). Within the zone, there are deep sloping faults of late Cenozoic and earlier formation. Late Cenozoic faults have a southward slope, and paleo-faults have a northward slope (Didenko et al. 2013). Paleo-faults occurred as the result of late Mesozoic subduction processes: oceanic crust of the Mongol–Okhotsk basin subducted under the continental margin of the southern framing of the Siberian craton. Late Cenozoic faults confirm the presence of the tectonic restructuring during this period. It is believed that the western fragment of the joint region of the structures of the Central Asian belt and the Siberian platform was affected by collisional processes occurring between the Indian and Eurasian plates in the Cenozoic (Buslov et al. 2017).

5 Conclusions

Magmatic activity in the frame of the east flank of the MOOB was completed at the beginning of the Late Cretaceous. In fact, from that time on, the territory was in a state of immobility: platform formations occurred. But it was during this period that the tectonic restructuring of the region took place. Ancient continental blocks "met" and "swallowed" about 200 km of the belt in the region of 120 meridian. The belt was divided into two flanks: west flank and east flank. An SSS wedged between the southern border of the Siberian craton and MOOB. These events coincide in time with the collision processes occurring between the Indian and Eurasian plates, when the Indian plate moved in the northeast direction. The interdependence of geological objects allows us to suggest that the collision processes occurring between the Indian and Eurasian plates was the "driving force" of the SSS movement.

References

Arkhangelskaya, V.V., Kazansky, V.I., Prokhorov, K.V., Sobachenko, V.N.: Geological structure, zoning and formation conditions of the Katuginsky Ta–Nb–Zr deposit. Russ. Geol. Geophys. **54**(2), 115–131 (1993)

Buslov, M.M., Travin, A.V., Abildaeva, M.A., Rubanova E.S.: Late Paleozoic surface-shear tectonics of the Altai-Sayan fold region: the effect of long-range effects of the convergence of continental plates. In: Meeting Materials. Issue 15. Institute of the Earth's Crust, SB RAS, Irkutsk, 20–23(2017)

Derbeko I.M.: Bimodal volcano-plutonic complexes in the frames of Eastern member of Mongol-Okhotsk orogenic belt, as a proof of the time of final closure of Mongol-Okhotsk basin. In: Francesco S (eds) Updates in Volcanology—A Comprehensive Approach to Volcanological Problems, 5, 99–124. Tech, Croatia, Rijeka (2012)

Derbeko I.M.: Magmatism as an indicator of synchronous geodynamic events in the frame of the Mongol-Okhotsk orogenic belt. In: Lth Tectonic Proceedings of the Meeting. V. 1, pp. 142–146. GEOS, Moscow (2018)

Derbeko, I.M., Markevich, V.S.: Late Mesozoic subalkai volcanism of the south framing of the east flank of Mongol-Okhotsk orogenic belt. Nat. End. Tech. Sci. **2**(64), 135–143 (2013)

Didenko, A.N., Kaplun, V.B., Malyshev, Yu.F., Shevchenko, B.F.: Lithospheric structure and mesozoic geodynamics of the Eastern Central Asian orogen. Russ. Geol. Geophys. **51**(5), 492–506 (2010)

Didenko, A.N., Efimov, A.S., Nelyubov, P.A., et al.: Structure and evolution of the earth's crust in the region of junction of the Central Asia fold belt and the Siberia platform: skovorodino–tommot profile. Russ. Geol. Geophys. **54**(10), 1583–1599 (2013)

Gordienko, I.V., Kuzmin, M.I.: Geodynamics and metallogeny of the mongol-Transbaikalian region. Russ. Geol. Geophys. **40**, 1545–1562 (1999)

Parfenov, L.M., Popeko, L.I., Tomurtogoo, O.: The problems of tectonics of the Mongol-Okhotsk orogene. Russ. J. Pacific Geol. **18** (5), 24–43 (1999)

Velikoslavinsky, S.D., Kotov, A.B., Salnikova, E.B., et al.: On the age of the Ustygilyuya stratum of the Mill Selengin-Stanovoy superterrane complex of the Central Asian fold belt. Dokl. Earth Sci. **444** (4), 402–406 (2012)

Fission Track Cooling Ages in the Brazilian Central Plateau Linked to Orogenies and Continental Break-Up

Marco Antonio Caçador Martins-Ferreira, Airton Natanael Coelho Dias, Farid Chemale Jr., and José Eloi Guimarães Campos

Abstract

Fission-track analysis in zircon and apatite detrital grains from Mesoproterozoic sedimentary sequences show evidence of two main cooling episodes in central Brazil and indicate the possibility of four distinct events. Apatite fission track reveals a main cooling episode during the Late Cretaceous (at ca. 64 Ma), providing important clues on cooling by uplift and denudation during drifting of South America and Africa. The event can be directly correlated to the intraplate tectonic deformation due to flexural subsidence at the Atlantic margin and Andes orogeny and development of intracratonic basins. Zircon fission track data indicate a main cooling event at 375 Ma interpreted as related to the Famatinian orogeny. Zircon data also suggest three distinct cooling events: (i) a Neoproterozoic-Cambrian event, probably related to the thermal decay of West Gondwana assembly, (ii) a Devonian-Carboniferous event, probably related to the late Famatinian orogeny, and (iii) an early Permian to Triassic event, linked to the late Gondwanide orogeny. These results indicate that the processes of assembly and break-up of supercontinents, might significantly affect the plate interior, especially along ancient orogenic belts.

Keywords

Zircon fission-track • Apatite fission-track • Thermochronology

1 Introduction

The region known as the Brazilian Central Plateau is located in a central portion of the South American Plate (Fig. 1a and e). The Plateau is mainly comprised by the elevated areas of the Brasília Belt (Pimentel 2016). In this region, the topography varies from 100 to 1676 m above sea level (Fig. 1c). The higher surfaces (above 900 m) generally dips slight to the south. Erosion is generating intermediate surfaces (between 900 and 600 m), usually forming abrupt escarpments, that separate the higher and intermediate surfaces from the lower surfaces (between 600 and 200 m), as shown in Fig. 1d. The studied area is located in the central portion of this elevated area, in a region known as Chapada dos Veadeiros (Veadeiros Plateau), where the altitude is the highest (up to 1676 m) and the topographic contrast is also most abrupt (Fig. 1c). These abrupt escarpments and the deep incisions made by local rivers (Fig. 1f) suggest uplift of this region (Pazzaglia 2003), but the mechanisms and timing of the tectonic events responsible for landscape modeling are not well constrained. In this study, we used zircon and apatite thermochronology to constrain the cooling ages and the events related to the evolution of the Brazilian Central Plateau.

2 Geological Setting

The investigated area in this study is located in the northern portion of the Brasília Belt (central Brazil), an orogenic belt formed during the Neoproterozoic Brasiliano-Pan Africano orogeny in the western margin of the São Francisco Craton

M. A. C. Martins-Ferreira (✉)
Faculdade de Ciências e Tecnologia, Univ. Federal de Goiás, Ap. de Goiânia, GO 74968755, Brazil

A. N. C. Dias
Departamento de Física, Química e Matemática, UFSCar, Sorocaba, SP 18052780, Brazil

F. Chemale Jr.
Programa de Pós-Graduação em Geologia, Unisinos, São Leopoldo, RS 93022000, Brazil

J. E. G. Campos
Instituto de Geociências, Universidade de Brasília, Brasília, DF 70910900, Brazil

M. Meghraoui et al. (eds.), *Advances in Geophysics, Tectonics and Petroleum Geosciences*, Advances in Science, Technology & Innovation, https://doi.org/10.1007/978-3-030-73026-0_130

(Fig. 1d) (Pimentel 2016). The Brasília Belt external zone, the focus of this study, is a foreland fold-and-thrust belt and sampling area that comprises metasedimentary rocks from Mesoproterozoic basins, locally metamorphosed up to low-greenschist facies, but generally anchimetamorphic.

After the Brasiliano orogeny [peak at ca. 630 Ma (Pimentel 2016)] the region occupied an intracontinental position, and no other orogenic or intrusive events, that could be responsible for warming, have occurred in the region. However, in the plate margins, different orogenetic and taphrogenetic events occurred. The main of these events are the Famatinian (Devonian/Carboniferous), Gondwanide (Carboniferous/Permian), the Andean orogenies and the Pangaea break-up (Cretaceous).

3 Samples and Methods

Zircon Fission Track (ZFT) sample preparation and analysis involved handpicking grains and mounting in the PFA Teflon® with hot plate. The Mount was ground, polished and etched with 1:1 eutectic mixture of KOH and NaOH at

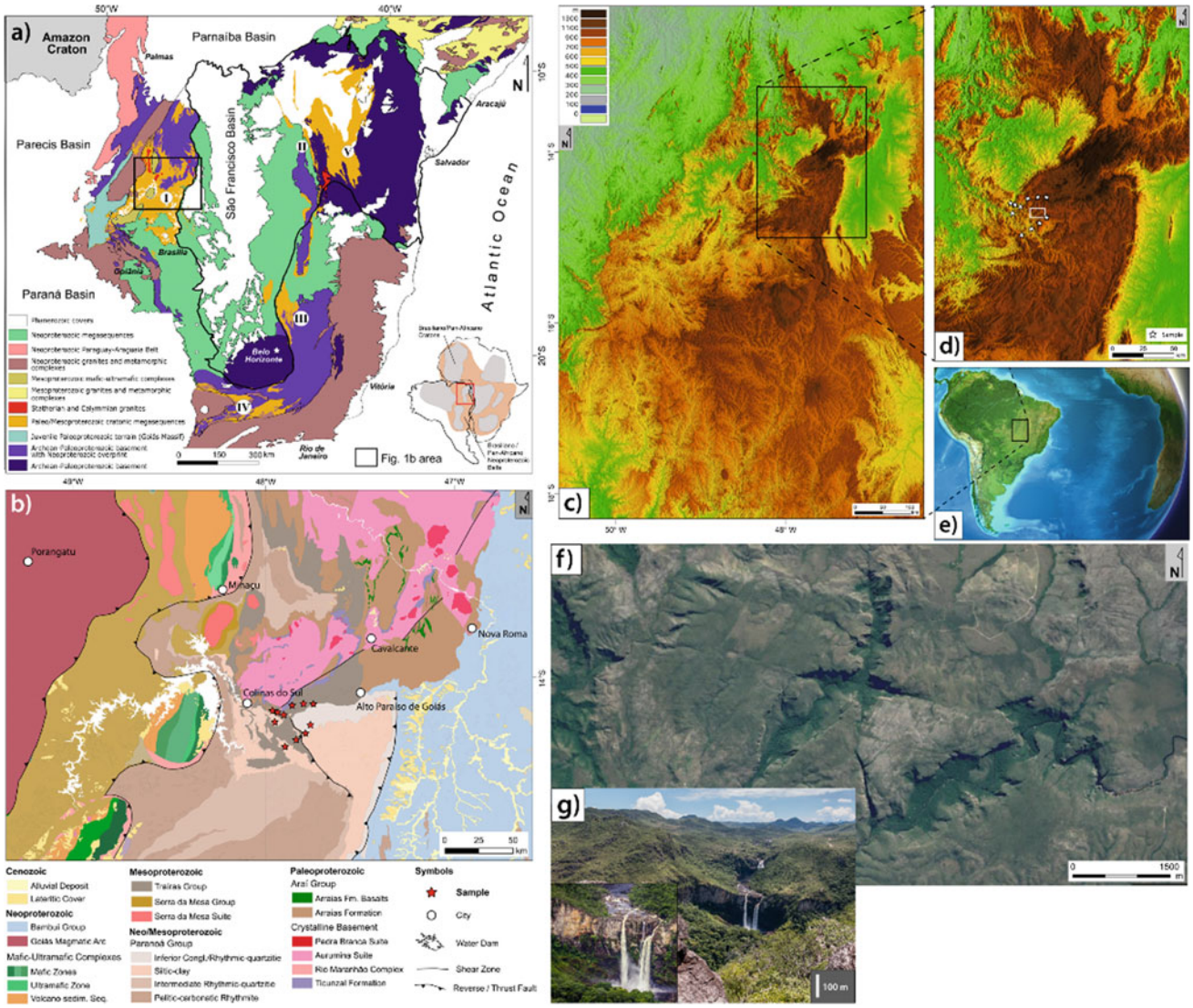

Fig. 1 **a** Geological map showing the São Francisco craton, surrounded by Phanerozoic basins, the black rectangle marks the area of Fig. 1b (modified from Martins-Ferreira et al., (2018)); **b** Simplified geologic map showing samples location (marked as red stars); **c**, **d**, **e** Digital Elevation Models showing **c** the uplifted region of the Brasília Belt; **e** the location of the Brasília Belt in the central portion of the South American plate; **d** the contrasting topography in the Chapada dos Veadeiros region and abrupt topographic variation up to 500 m. (sampling sites marked as white stars, white rectangle mark the area of Fig. 1f); **f** Satellite image showing river incisions in the higher surfaces (image location indicated by white rectangle in Fig. 1d); **g** Photographs showing the common occurrence of free-fall waterfalls higher than 100 m

225 ± 2 °C (Tagami et al., 1990) in periods of 2–4 h (Garver 2003). Fission track densities (ρS) were obtained using Leica DM2700 M microscope (dry, nominal increase 1500×). The U concentration was measured in a Thermo-Finnigan Neptune multi-collector ICP-MS coupled with a Photon-Machines 193 nm laser system with energy density of ca. 8 J/cm^2 at repetition rates of 10 Hz, and 20 µm spot diameter. The primary reference was the GJ-1 zircon (Jackson 2004) and second was the Plesovice zircon (Sláma et al., 2008).

Apatite Fission Track (AFT) sample preparation and analysis involved mounting in epoxy resin, grinding and polishing and etching with HNO_3 in 5 mol, 20 s at 21 °C. After etching, the samples were juxtaposed to white mica, used as an external detector method, previously etched with 48% HF at 15 °C for 90 min, and then sent to the IPEN/CNEN nuclear reactor for irradiation. Besides the micas, in each irradiation, uranium CN-5 doped glasses were used, U (CNs) to obtain the RM value and thin films of Th for the Th/U rate, with calibration factor $N_U^v \varepsilon_U^v$ = 0.4169 * 1014 (Jackson et al., 2004). The RM value and ages were calculated using the equation described in Dias et al., (2017) by absolute calibration (Iunes et al., 2004).

A total of 12 sedimentary samples were collected (Fig. 1b) in two different geological Mesoproterozoic units, the Calymmian Traíras and Stenian Paranoá groups (Martins-Ferreira et al., 2018). Zircon grains were found in 11 samples, but only five samples contained apatite grains.

4 Results

The zircon fission track (ZFT) age results obtained in this study are limited to ages older than the Mesozoic era. On the other hand, the apatite fission track (AFT) results are limited to ages between the upper Cretaceous and Paleocene epochs. Most of the ZFT ages fall in the 400–330 Ma interval, with the exception of three samples, a younger age of 289 Ma and two older of 549 and 519 Ma. The AFT results are less diversified, spanning from 77 to 65 Ma. Central ages calculated using all zircon samples yielded ca. 375 ± 8 Ma and for apatite ca. 64 ± 2 Ma (Table 1).

5 Discussion

Our results show evidence of at least two and maximum four distinct cooling episodes in central Brazil. AFT central age for all the samples indicates a main cooling episode at ca. 64 Ma. There are no records of magmatic or orogenic activities during this period of time; we thus interpret this cooling as a result of uplift and denudation by the end of the Cretaceous, as a consequence of thermal decay during and after the break-up of Pangaea. The event can be directly correlated to flexural subsidence and uplift at the passive margin of South Atlantic Ocean and orogenic processes in the western margin of the South American Platform during the Andean orogeny (Ramos and Alemán 2000). In response

Table 1 Results from zircon (orange) and apatite (blue) fission track central ages

Sample	**Zircon** FT Central Age	**Zircon** grains (n)	**Apatite** FT Central Age	**Apatite** grains (n)	**Lithology**	**Group**
TFC_01	398 ± 22 Ma	27	67 Ma±7 Ma	17	Conglomerate	Paranoá
TFC_02	366 ± 23 Ma	29	-	-	Greywacke	Traíras
TFC_03	382 ± 22 Ma	47	-	-	Sandstone	Traíras
TFC_04	364 ± 19 Ma	46	-	-	Sandstone	Traíras
TFC_05	549 ± 26 Ma	35	-	-	Sandstone	Traíras
TFC_06	289 ± 15 Ma	57	-	-	Sandstone	Traíras
TFC_07	350 ± 18 Ma	49	-	-	Conglomerate	Paranoá
TFC_08	333 ± 44 Ma	06	63 ± 2 Ma	61	Sandstone	Paranoá
TFC_09	-	-	63 ± 3 Ma	51	Siltstone	Paranoá
TFC_10	519 ± 41 Ma	18	77 ± 11 Ma	05	Conglomerate	Paranoá
TFC_11	328 ± 25 Ma	02	65 ± 4 Ma	43	Siltstone	Paranoá
TFC_12	369 ± 26 Ma	28	-	-	Sandstone	Paranoá
Central Age (All samples)	**375 ± 8 Ma**		**64 ± 2 Ma**		-	-

to these continental-scale processes, the São Francisco intracratonic basins developed by the end of the upper Cretaceous (Parecis, Bauru, Sao Francisco, etc., basins) while central Brazil was uplifted and provided sediment for these basins during erosion and consequent cooling.

ZFT central age for all the samples indicates a main cooling event at 375 Ma, possibly related to the Famatinian orogeny. The central ages for ZFT individual samples also suggest three possible cooling events: (i) a Neoproterozoic-Cambrian event recording those processes of the Brasiliano and Pampean orogenies, an evidence of thermal decay during West Gondwana assembly, (ii) a Devonian-Carboniferous event, probably related to the late Famatinian and early Gondwanides orogeny, and (iii) an early Permian–Triassic event, possibly related to the late Gondwanides orogeny. These results indicate that the processes of assembly as well as break-up of supercontinents, might significantly affect the interior plate, especially along ancient orogenic belts. These assumptions take us back to the old concept of "Mobile Belts" as old orogenic regions that represent weak portions of the continental crust, assumed to have greater tendency for mobility, when solicited. In this case, the Brasília Belt has shown to present great vertical mobility, accommodating tectonic far-field forces by uplift and subsidence as a result, feeding the Phanerozoic basins around it.

The AFT ages indicate that the studied region of the South American continent interior has been significantly affected by tectonic events happening at plate boundaries. These events, detected by AFT, can be directly correlated in time to the subsidence pulses of intercontinental basins and allow to infer uplift and erosion ages of the areas that acted as sediment sources.

6 Conclusions

The results reported in this paper indicate that the effects of the Famatinian and Gondwanide orogenies as well as the Mesozoic Pangaea break-up and Andean orogeny are recorded in central Brazil. Due to the lack of other thermal anomalies, these events can be interpreted to have been likely to promote uplift and denudation of the studied region.

Two main cooling episodes are constrained. AFT ages reveal a main cooling episode during the Late Cretaceous (at ca. 64 Ma). The event can be directly correlated to the intraplate tectonic deformation due to flexural subsidence at the Atlantic margin and Andes orogeny and development of intracratonic basins in the São Francisco basin system. ZFT ages indicate a main cooling event at 375 Ma interpreted as related to the Famatinian orogeny. ZFT from individual samples also suggest three distinct cooling events: (i) a Neoproterozoic-Cambrian event, probably related to the thermal decay of West Gondwana assembly, (ii) a Devonian-Carboniferous event, probably related to the late Famatinian orogeny, and (iii) an early Permian to Triassic event, linked to the late Gondwanide orogeny.

These results suggest that the processes of assembly as well as break-up of supercontinents, might have significantly affected the plate interior, especially along ancient orogenic belts. Moreover, the study indicates that low-temperature thermochronology conducted in intracontinental areas can be used to reveal information on the effects of the tectonic events happening at plate margins. Also, these studies can be useful to identify source areas for the sedimentary basins known to have formed during the revealed cooling ages.

References

Dias, A.N.C., et al.: A new approach for electron microprobe zircon fission track thermochronology. Chem. Geol. **459**, 129–136 (2017)

Garver, J.I.: Etching zircon age standards for fissiontrack analysis. Radiat. Meas. **37**, 47–53 (2003)

Iunes, P.J., et al.: Durango apatite fission-track dating using length-based age corrections and neutron fluence measurements by thorium thin films and natural U-doped glasses calibrated through natural uranium thin films. Chem. Geol. **187**, 201–211 (2002)

Iunes, P.J., et al.: Uranium and thorium film calibrations by particle track techniques. J. Radioanal. Nucl. Chem. **262**, 461–468 (2004)

Jackson, S.E., et al.: The application of laser ablation-inductively coupled plasma-mass spectrometry to in situ U-Pb zircon geochronology. Chem. Geol. **211**, 47–69 (2004)

Martins-Ferreira, M.A.C., et al.: Proterozoic intracontinental basin succession in the western margin of the São Francisco Craton: Constraints from detrital zircon geochronology. J. Am. Earth Sci. **81**, 165–176 (2018)

Pazzaglia, F.J.: Landscape evolution models developments in quaternary. Sciences **1**, 247–274 (2003)

Pimentel, M.M.: The tectonic evolution of the Neoproterozoic Brasília Belt, central Brazil: a geochronological and isotopic approach. Brazilian J. Geol. **46**, 67–82 (2016)

Ramos, V.A., Alemán, A.: Tectonic evolution of the Andes. In: Cordani, E.U.J., Milani, E.J., Thomaz Filho, A., Campos, D.A. (eds.) 31st International Geological Congress, pp. 635–685. Tectonic Evolution of South America, Río de Janeiro (2000)

Sláma, J., et al.: Plešovice zircon—a new natural reference material for U–Pb and Hf isotopic microanalysis. Chem. Geol. **249**, 1–35 (2008)

Tagami, T., et al.: Thermal annealing characteristics of spontaneous fission tracks in zircon. Chem. Geol. Isotope Geosci. Sect. **80**, 159–169 (1990)

Thermicity, Petroleum and Other Georesources

Tectonic and Geodynamic Controls on Petroleum Systems in Compressional Basins

François Roure

Abstract

Compressional systems still host huge amounts of hydrocarbon reserves, either in anticlinal and other structural traps in the foothills, or in stratigraphic and structural traps in the autochthonous foreland. Compressional basins are commonly considered as risky frontier areas for the exploration. Case studies in prolific HC provinces from the American Cordilleran basins, the Middle East and the Circum-Mediterranean Foreland Fold-and-Thrust Belts (FFTB) presented in this paper have elucidated the main tectonic and geodynamic controls exerted on their petroleum systems. Commonly, long-range migration pathways between the foredeep and the forebulge account for huge but biodegraded hydrocarbon accumulations in the foreland, as in the Orinoco and Athabasca tar belts, whereas short-range migration between underthrust synclines and adjacent anticlines still occur in recent tectonic wedges in Albania and the Carpathians. A good knowledge of the Wilson cycle, including the pre-orogenic rifting and passive margin stages, the collisional stage, and subsequent post-orogenic collapse is a pre-requisite before addressing realistic thermal and petroleum modelling, due to the important temporal and lateral variations of their lithospheric thickness and basal heat flow during alternative extensional and compressional stages.

Keywords

Foreland flexural basins • Fold-and-thrust belts • Petroleum systems • Wilson cycle • Lithospheric thickness • Thermal and petroleum modelling

1 Introduction

The American Cordilleran basins, the Middle East, and the Circum-Mediterranean Foreland Fold-and-Thrust Belts (FFTB) host huge oil and gas reserves in the complex structural traps of their foothills (Lacombe et al. 2007; Roure 2008,2013), as well as large tar sand accumulations in their adjacent forelands, i.e. the Athabasca and Orinoco heavy oils. Based on well-documented case studies, the aim of this paper was to describe the main petroleum habitats and exploration risks related to these compressional basins. Ultimately, a good knowledge of the Wilson cycle is a pre-requisite to (1) better predict their source rocks and reservoir distributions, which are derived from both the former passive margin and synflexural/synorogenic series, and to (2) address more realistic thermal and petroleum modelling, which must take into account both temporal and lateral heat flow variations during the successive stages of rifting and passive margin development, and subsequent collision and post-orogenic collapse (Swennen et al. 2004).

2 Petroleum Habitats in Classic Foreland Fold-and-thrust Belts

2.1 Source Rocks and Reservoirs Distribution

Most of the source rocks and carbonate reservoirs in Alpine/Tethyan and Cordilleran orogenic systems were already deposited in the autochthonous foreland before the onset of compression, either in the Paleozoic substratum or in Mesozoic rift and passive margin sequences (Callot et al. 2010,2017; Tarapoanca et al. 2010; Turrini et al. 2017; Ziegler and Roure 1999). Instead, younger sandstone reservoirs are usually productive in the synflexural and synorogenic piggyback sequences like in the Subandean basins in Eastern Colombia and Venezuela (Toro et al. 2004; Zoetemeijer et al. 1993). Worth noting, synflexural clastic

F. Roure (✉)
IFP Energies Nouvelles, Rueil-Malmaison, France

M. Meghraoui et al. (eds.), *Advances in Geophysics, Tectonics and Petroleum Geosciences*,
Advances in Science, Technology & Innovation, https://doi.org/10.1007/978-3-030-73026-0_131

reservoirs are locally impacted by tectonic compaction or Layer Parallel Shortening (LPS), their overall residual porosity/permeability depending on whether they became overpressured or not prior to their tectonic accretion (Roure et al. 2003,2005).

2.2 Tectonic and Stratigraphic Traps

Extensional and halokinetic tectonic traps inherited from the previous rift or passive margin stages are still worth prospecting in the foreland, whereas thrust anticlines are the dominant traps in the foothills. Stratigraphic traps involving growth strata or located along diachronous unconformity are also numerous in both the piggyback basins and foreland flexural basin (Fig. 1).

2.3 Short Range Versus Long Range Hydrocarbon (HC) Migration

Early oil was usually generated in the current units of the inner part of the foothills prior to their tectonic accretion, the lack of frontal anticline then allowing the migration of HC towards the distal part of the foredeep (Tarapoanca et al. 2010). Younger portions of the basin also contributed to the HC charge of the foreland before they also became tectonically accreted into the allochthonous wedge (Vilasi and Malandain 2009). In many cases, these early oils were biodegraded due to their thin sedimentary cover, resulting in the giant Orinoco and Athabasca tar belts in Venezuela and Alberta, respectively, (Faure et al. 2004). Late gas generated in the Zagros foredeep is also likely to charge laterally the giant fields in Qatar, updip the regional flexure.

By contrast, allochthonous units may still preserve an important oil and gas potential, especially when they had been detached early along an efficient decollement level (i.e. salt or overpressured shales). In this case, HC are generated in underthrust synclines, the oil then migrating for short distance towards adjacent or overlying anticlines. This is for instance the case in the Albanian foothills, the Romanian and Ukrainian Carpathians, and in the Potwar Basin in Pakistan (Grelaud et al. 2002; Roure et al. 2004,1993; Roure and Sassi 1995), where source rocks are still immature at the crest of the growth anticlines, whereas mature kitchens occur in adjacent synclines (Fig. 2).

2.4 Biogenic Versus Thermogenic Gas and Shale Gas

The synflexural siliciclastic sequence of recent Alpine-Tethyan orogens usually comprises organic-rich shales with TOC ranging from 1 to 3% and a Type III kerogen prone for biogenic gas generation. Therefore, biogenic gas is actively explored in the Po River Basin and other circum-Adriatic foredeeps. Thermogenic gas is also a major play in the Canadian Rockies (Faure et al. 2004) and portions of the Zagros and Suleiman mountains in Iran and Pakistan, respectively.

In older, Paleozoic orogens like the Appalachians, post-orogenic erosional unroofing allows the production of residual shale gas in relatively shallow source rock horizons, which are still too deeply buried in younger Alpine tectonic wedges and associated foredeeps.

3 Exploration Risks in Foreland Inverted Structures

Foreland inversion features reactivating former normal faults and tilted blocks are usually common in the autochthon, away from the more allochthonous foothills units, especially when a good coupling operated between the tectonic wedge and the adjacent foreland, allowing the deformation to propagate within the plate during the periods of reduced activity of the thrust system. Unfortunately, the related anticlinal traps may constitute a major risk for the exploration in areas where the adjacent rift or passive margin basins reached their maximum burial at an earlier stage of

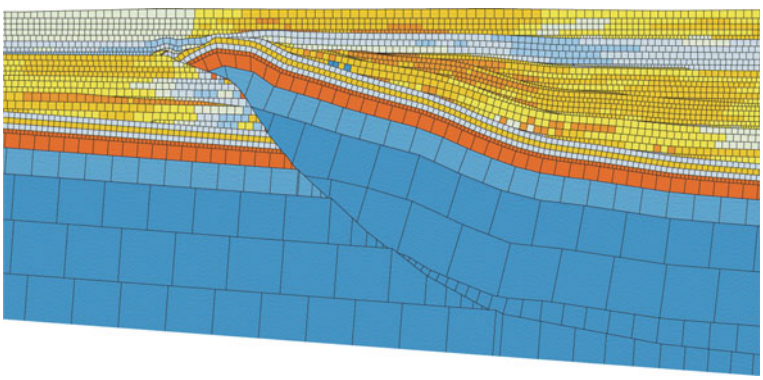

Fig. 1 Stratigraphic traps controlled by growth anticlines and foreland flexure. Passive margin sequences are in blue and orange, whereas synorogenic sequences are in yellow and white

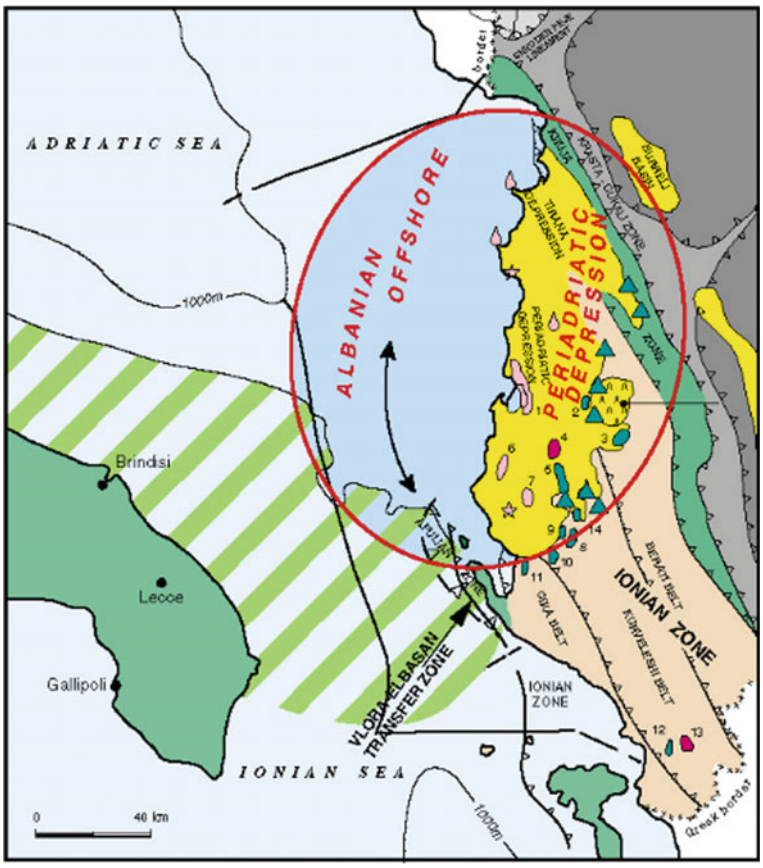

Fig. 2 The Adriatic foredeep kitchen has charged the Puglia margin, whereas short range migration accounts for local trapping in the Albanian tectonic wedge (Roure et al. 2004)

evolution, prior to the development of these compressional structural traps.

Worth noting, all the drilled Alpine anticlines in south-eastern France were dry, whereas former extensional tilted blocks of the adjacent Ardèche margin turned out to host residual HC and bitumen, accounting for early episodes of HC generation, migration and trapping during the Late Cretaceous, most accumulations being now biodegraded due to post-orogenic unflexing and unroofing (Fig. 3).

4 Exploration Risks in Collapsed Orogens

Slab detachments have been documented by mantle tomography in the Apennines, Sicily, and the Maghrebides (Arab et al. 2016; Cavazza Ziegler Spakman et al. 2004; Roure et al. 2012), whereas post-orogenic rise of the asthenosphere is well documented beneath the North American Cordillera from Mexico to Canada (Gonzales et al. 2012; Hardebol et al. 2012; Roure, et al. 2009). Such vertical motion of the lithosphere induced by mantle convection may generate a progressive unflexing and unroofing of foreland basins and the outer part of adjacent foothills (Khomsi et al. 2019), resulting in a drastic change in the migration pathways for the HC from kitchens to traps. This accounts for instance for the unusual HC charge of the Cordoba Platform in SE Mexico by hydrocarbon kitchens located in the Veracruz Basin, i.e. east of the tectonic front (Fig. 4).

5 The Wilson Cycle and Its Implications for Thermal and Petroleum Modelling of Compressional Systems

Post-orogenic collapse of the Hercynian thrust belt has been well documented in Western Europe. The Tyrrhenian and Western Mediterranean basins also result from back-arc extension and negative inversion of former Neogene thrusts in the Apennines and Maghrebides (Arab et al. 2016; Cavazza et al. 2004; Roure et al. 2012), and of former Eocene Pyrenean thrusts in the vicinity of the Gulf of Lions. Many rift basins and passive margins developed above former suture zones and orogenic systems, due to such pre-existing weakness zones. Because the source rocks are usually hosted by the former rift or passive margin sequences, thermal and petroleum modelling must take into account these temporal and lateral variations of basal heat flow induced by the post-rift cooling of the lithosphere, as well as by post-orogenic unroofing and crustal stretching associated with an asthenospheric rise.

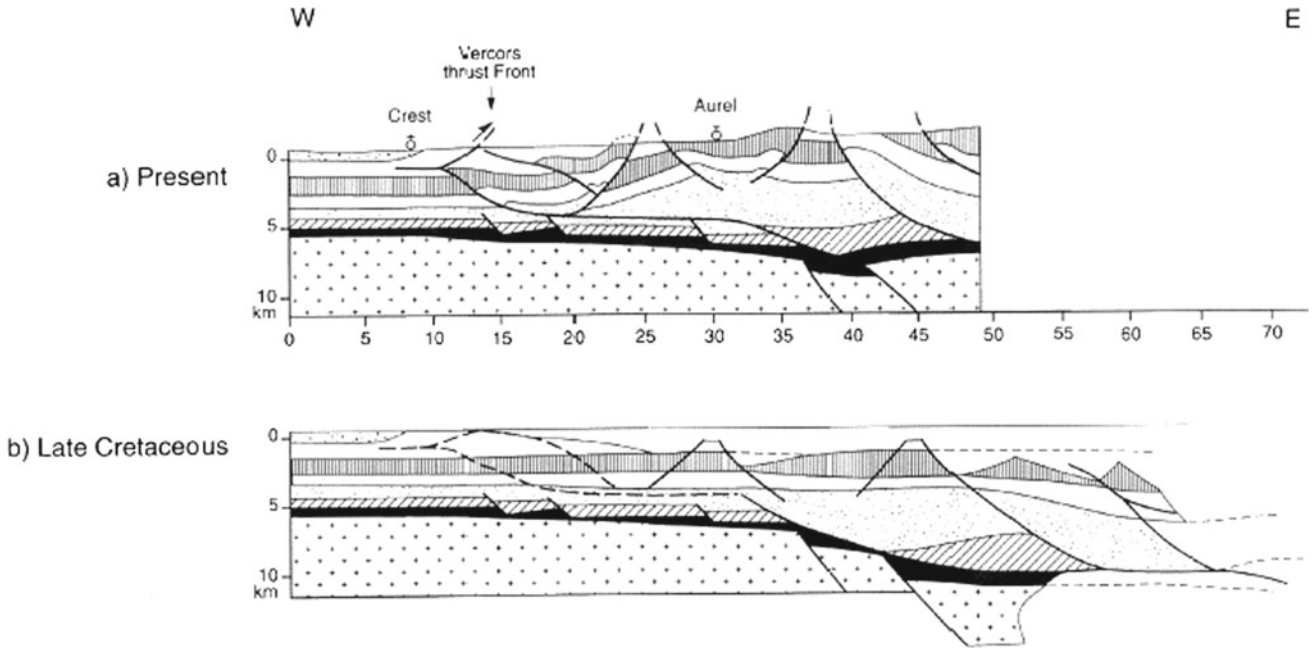

Fig. 3 Maximum burial of Jurassic source rocks occurred during the Late Cretaceous in the Alpine foreland of southeastern France, whereas compressional traps are Neogene and dry because they post-date the HC migration (Roure et al. 1994)

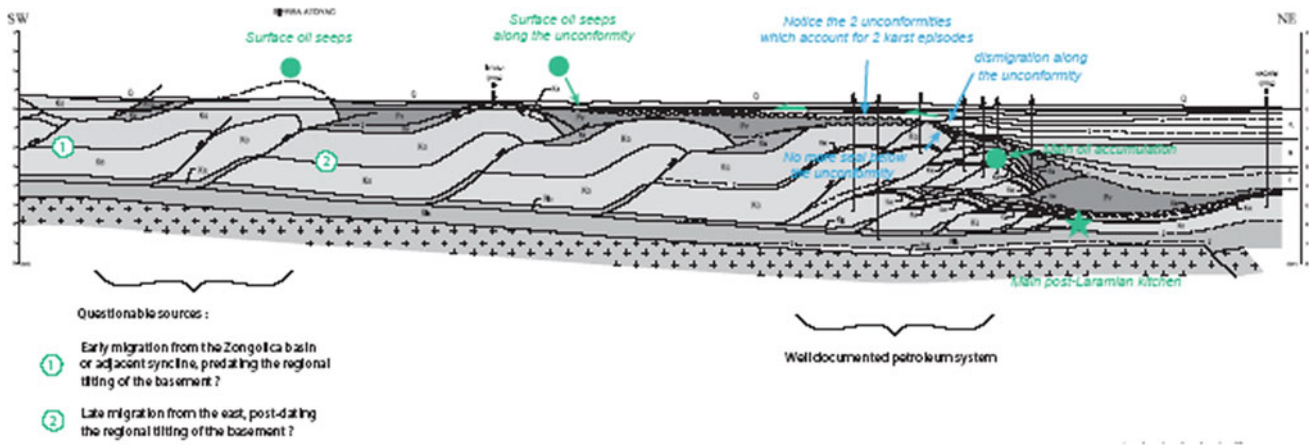

Fig. 4 Post-Laramian lithospheric unflexing has impacted the petroleum systems of the Cordoba Platform and Veracruz Basin in SE Mexico, the foothills being currently charged from the foreland kitchens (Gonzales et al. 2012)

Due to lateral changes in the burial of a distinct source rock or to the occurrence of different source rocks at different burial depths, the timing of HC generation is likely to vary from an area to another (Casero et al. 1991). However, calibration of thermal and petroleum modelling may sometimes be difficult even with the use of paleothermometers because of uncertainties on both the amounts of erosion and paleo-heat flow (Fig. 5).

6 Conclusions

An accurate prediction of the hydrocarbon potential in FFTB requires a good understanding of the Wilson cycle and its controls on the temporal and lateral variations of lithospheric thickness and basal heat flow (Roure et al. 2009). Actually, major efforts should be dedicated to the calibration of ero-

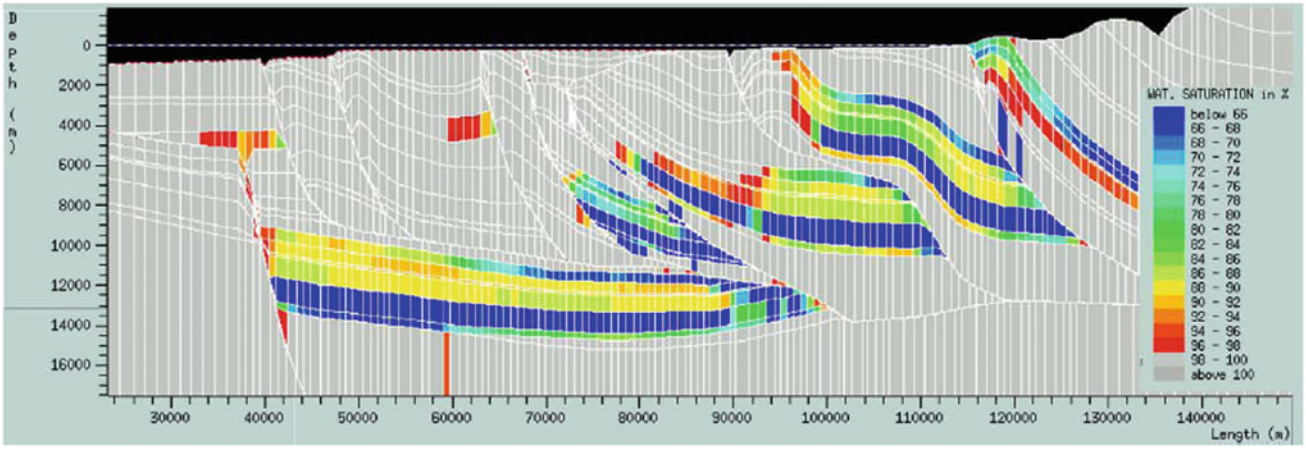

Fig. 5 Thermal and petroleum modelling of southern Albania, accounting for different kitchens and successive episodes of HC generation, migration, and trapping (Vilasi and Malandain 2009)

sions and paleo-burial, not only by means of paleothermometers but also by using paleo-barometers (Roure et al. 2010), as a same maturity rank could be reached with two very different burial and temperature paths (low burial and high thermal gradient versus large burial with low thermal gradient).

References

Arab, M., Granjeon, D., Roure, F., Arbeaumont, A., Rabineau, M., Belhai, D., Arezki, L., Sulzer, C., Bracène, R.: Coupling stratigraphic and petroleum systems modelling tools in complex tectonic domains: case study in the North Algerian offshore. Arabian J. Geosci. **9**(4) (2016). https://doi.org/10.1017/s12517-015-2296-3

Callot, J.P., Breesch, L., Guilhaumou, N., Roure, F., Swennen, R., Vilasi, N.: Paleo-fluids characterization and fluid flow modelling along a regional transect in the Northern Emirates. Arabian J. Geosci. **3**, 413–437 (2010)

Callot, J.P., Roure, F., Faure, J.L., Tarapoanca, M.: Kinematic, thermal and petroleum modeling of the Northern Emirates. In: Abu Ali, M., Moretti, I., Nordgärd-Bolås, H.M. (eds.) Petroleum Systems Analysis. Case Studies. American Assoc. Petrol. Geol., Memoir, **114**, pp. 135–164 (2017)

Casero, P., Roure, F., Vially, R.. Tectonic framework and petroleum potential of the Southern Apennines. In: Spencer, A. (ed.) Generation, Accumulation and Production of Europe's Hydrocarbons, pp. 361–387. European Assoc. Petrol. Geol., Oxford Univ. Press, Oxford (1991)

Cavazza, W., Ziegler, P., Spakman, W., Stampfli, G., Roure, F. (eds): The Transmed Atlas: the Mediterranean Region From Crust to Mantle, pp. 1–141. Springer, Heidelberg +CR-ROM (2004)

Faure, J.L., Osadetz, K., Benaouali, N., Schneider, F., Roure, F.: Kinematic and petroleum modelling of the alberta foothills and adjacent foreland, west of calgary. Oil Gas Sci. Technol. Revue De l'IFP **1**, 81–108 (2004)

Gonzales, E., Ferket, H., Callot, J.P., Guilhaumou, N., Ortuño, S., Roure, F.: Paleoburial, hydrocarbon generation and migration in the Cordoba Platform and Veracruz Basin: insights from fluid inclusion studies and two-dimensional (2D) basin modelling. In: Harris, N.B., Peters, K.E. (eds.) Analyzing the Thermal History of Sedimentary Basins: Methods and Case Histories, pp. 167–186. Publ, SEPM, Spec (2012)

Grelaud, S., Sassi, W., Frizon de Lamotte, D., Jaswal, T., Roure, F.: Kinematics of eastern Salt Range and south Potwar Basin (Pakistan) a new scenario. Marine Petrol. Geol. **19**, 1127–1139 (2002)

Hardebol, N.J., Pyskliwec, R.N., Stephenson, R.: Small-scale convection at a back-arc to continental transition. Application to the southern Canadian Cordillera. J. Geophys. Res. Solid Earth, **117**, B1, B01408. https://doi.org/10.1029/2011JB008431 (2012)

Khomsi, S., Roure, F., Khelil, M., Mezni, R., Echihi, O.: In: Lacombe, O., Fillon, C. (eds.) A review of the Crustal Architecture and Related Pre-Salt Oil/Gas Objectives of the Eastern Maghreb Atlas and Tell: Needs for Deep Seismic Profiling. Tectonophysics, Spec. Issue (2019)

Lacombe, O., Lavé, J., Roure, F., Verges, J. (eds).: Thrust Belts and Foreland Basins; from Fold Kinematics to Hydrocarbon Systems, pp. 1–491. Springer (2007)

Roure, F.: Foreland and hinterland basins: what controls their evolution? Swiss J. Geosci. **101**, 5–29 (2008)

Roure, F., Sassi, W.: Kinematics of deformation and petroleum systems appraisal in Neogene foreland fold-and-thrust belts. Petrol. Geosci. **1**, 253–269 (1995)

Roure, F., Roca, E., Sassi, W.: The Neogene evolution of the outer Carpathian flysch units (Poland, Ukraine and Romania). Sed. Geol. **86**, 177–201 (1993)

Roure, F., Brun, J.P., Colletta, B., Vially, R.: Multiphase extensional structures, fault reactivation and petroleum plays in the Alpine foreland of southeastern France. In: Mascle, A. (ed.) Hydrocarbon and Petroleum Geology of France, pp. 245–268. Springer-Verlag, European Assoc. Petrol. Geoscientists (1994)

Roure, F., Casero, P., Addoum, B.: Alpine inversion of the North African margin, and delamination of its continental crust. Tectonics (2012). https://doi.org/10.1029/2011TC002989

Roure, F.: Crustal architecture, thermal evolution and energy resources of compressional basins. André Dumont medallist lecture 2013. Geologica Belgica **17**(2), 182–190 (2014)

Roure, F., Nazaj, S., Mushka, K., Fili., I., Cadet, J.P., Bonneau, M.: Kinematic evolution and petroleum systems: AAN appraisal of the Outer Albanides. In: McKlay, K. (ed.) Thrusts Tectonics and Petroleum Systems, pp. 474–493. American assoc. Petrol. Geol., Memoir 82, Chapter 24 (2004).

Roure, F., Swennen, R., Schneider, F., et al.: Incidence and importance of tectonics and natural fluid migration on reservoir evolution in foreland fold-and-thrust belts. In: Brosse, E., et al., (eds.) Oil and Gas Technology, pp. 67–106. Revue de l'IFP, 60 (2005)

Roure, F., Cloetingh, S., Scheck-Wenderoth, M., Ziegler, P.: Achievements and challenges in sedimentary basins dynamics. In: Cloetingh, S., Negendank, J. (ed.) New Frontiers in Solid Earth Sciences, pp. 145–233. Springer (2009)

Roure, F., Andriessen, P., Callot, J.P., Faure, J.L., Ferket, H., Gonzales, E., Guilhaumou, N., Lacombe, O., Malandain, J., Sassi, W., Schneider, F., Swennen, R., Vilasi, N.: The use of paleo-thermo-barometers and coupled thermal, fluid-flow and pore-fluid pressure modelling for hydrocarbon and reservoir prediction in fold and thrust belts. In: Goffey, G.P., Craig, J., Neddham, T., Scott, R., (eds.) Hydrocarbons in Contractional Belts, pp. 87–114. Gel. Soc., London, Spec. Publ., 348 (2010)

Roure, F., Bordas-Lefloch, N., et al.: Petroleum systems and reservoir appraisal in the Subandean basins (Eastern Venezuela and Eastern Colombia foothills). In: Bartolini, C., Burke, K., Buffler, R., Blickwede, J., Burkart, B., (eds.) Mexico and the Caribbean Region; Plate Tectonics, Basin Formation and Petroleum Habitats, pp. 750–775. American Assoc. Petrol. Geol., Memoir, 79, Chapter 34 (2003)

Roure, F., Alzaga-Ruiz, H., et al.: Long lasting interactions between tectonic, loading, unroofing, post-rift thermal subsidence and sedimentary transfer along the western margin of the Gulf of Mexico: Some insights from integrated quantitative studies. In: Bertotti, G., Frizon de Lamotte, D., Teixell, A. (eds.) Tectonics of Vertical Movements, Tectonophysics, pp. 169–189. Spec. Issue (2009)

Swennen, R., Roure, F., Granath, J., (eds.): Deformation, Fluid Flow and Reservoir Appraisal in Foreland Fold and Thrust Belts, pp. 1–430. American Assoc. Petrol. Geol., Hedberg Series 1 (2004)

Tarapoanca, M., Andriessen, P., Broto, K., et al.: Forward kinematic modelling of a regional transect in the Northern Emirates, using geological and apatite fission track age constraints on paleo-burial history. Arabian J. Geosci. **3**, 395–411 (2010)

Toro, J., Roure, F., Bordas-Lefloch, N., Le Cornec-Lance, S., Sassi, W.: Thermal and kinematic evolution of the Eastern Cordillera fold-and-thrust belt, Colombia. In: Swennen, R., Roure, F., Granath, J. (eds.) Deformation, Fluid Flow and Reservoir Appraisal in FFTB, pp. 79–116. American Assoc. Petrol. Geol., Hedberg Series, 1 (2004)

Turrini, C., Bosica, B., Ryan, P., Shiner, P., Lacombe, O., Roure, F.: 3D structural and thermal modelling of Mesozoic petroleum systems in the Po Valley Basin, northern Italy. Petrol. Geosci. (2017). https://doi.org/10.1144/petgeo2017-031

Vilasi, N., Malandain, J., et al.: From outcrop and petrographic studies to basin-scale fluid flow modelling: the use of the Albanian natural laboratory for carbonate reservoir characterization. Topo-Europe Vol. Tectonophys. **474**, 367–394 (2009)

Ziegler, P.A., Roure, F.. Petroleum systems of Alpine-Mediterranean thrust belts an basins. In: Durand, B., Jolivet, L., Horvath, F., Séranne, M. (eds.) The Mediterranean Bain; Tertiary Extension Within the Alpine Orogen, pp. 517–540. Geological Society, London, Special Publ., 156 (1999)

Zoetemeijer, R., Cloetingh, S., Sassi, W., Roure, F.: Stratigraphic sequences in piggy-back basins: records of tectonic evolution. Tectonophysics **226**, 253–269 (1993)

The Crustal Configuration and Deep Structures Related to the Pre-salt Oil/gas Objectives of the Eastern Maghreb: Need for Deep Seismic Imaging

Sami Khomsi, François Roure, Gabor Tari, Mannoubi Khelil, Riadh Mezni, and Oussema Echihi

Abstract

Over the last decade, the major tectonic evolutionary steps of the Eastern Maghreb structures have been precisely constrained by shallow seismic Sects. (5 s TWT) interpretations and structural analyses. However, their overall configurations at depth, and their deep structural configuration controlled by the underlying basement, remain poorly understood because only few wells have succeeded to penetrate slightly deeper than the thick Triassic evaporites sequences in the Atlas and the foreland basins. Thus, this work focused on the deep structures affecting the Pan-African basement in the Eastern Maghreb by means of wide regional cross-sections passing through key structures of the Eastern Maghreb. Our purpose was to stimulate the exploration of deep hydrocarbon traps and stimulate the industry, universities, and other public research companies to launch a major research program on the deep crustal configuration in the Eastern Maghreb for the unlocking of deep oil/gas plays.

Keywords

Regional structural transects • Atlas • Tell • Oil/gas pre-salt traps and deep seismic profiles

1 Introduction

In Eastern Maghreb, only one single old refraction profile has been recorded in Tunisia (EGT, Geotraverse experiment). On the other hand, conventional industrial shallow reflection sections have been recorded in both of Tunisian and Algerian Tellian and Atlas foreland domains, but unfortunately, they cannot provide any structural information about the deep sedimentary sequences and structures configuration beneath the Triassic salt which is up to 4000 m thick beneath the Atlas (Khomsi et al. 2019). Thus, the lack of deep regional seismic reflection sections still precludes any characterization of deep potential hydrocarbon oil/gas plays (Khomsi et al. 2019). Therefore, deep seismic sections along the Eastern Maghreb margin from the Algerian basin in the north to the Pelagian-Sirt basins in the south throughout the Atlas and Tell belts would open new exploration perspectives for deep oil and gas plays, which are potentially seated in the Paleozoic structures buried beneath the Triassic evaporites of the Atlas and its foreland basins (Tari et al. 2017).

Our main objective was to present a set of predictive structural crustal sections issued from seismic interpretations in both the Tunisian and Algerian onshore segments of the Maghrebides as well as along and the Atlas fold thrust belts, in order to stimulate an ambitious North African crustal imagery project which would help unlock the pre-salt traps in the Tell and Atlas fold and thrust belts and their respective forelands.

S. Khomsi (✉)
Faculty of Earth Sciences, King Abdulaziz University KAU, Geo-exploration department, Jeddah, Kingdom of Saudi Arabia

F. Roure
IFP-Energies Nouvelles, Rueil-Malmaison, France

G. Tari
OMV, Exploration & Production, Vienna, Austria

M. Khelil · R. Mezni
Faculté Des Sciences de Tunis, Al Manar University, Tunis, Tunisia

M. Khelil · R. Mezni
Centre D'études Recherches Et Technologies Des Eaux CERTE, Labo Géoresources, Technopole Borj Cedria/University of Carthage, Tunis, Tunisia

O. Echihi
Reservoir Department, ETAP, Entreprise tunisienne des activités pétrolières, Tunis, Tunisia

M. Meghraoui et al. (eds.), *Advances in Geophysics, Tectonics and Petroleum Geosciences*, Advances in Science, Technology & Innovation, https://doi.org/10.1007/978-3-030-73026-0_132

2 The Paleozoic-Jurassic Composite Petroleum Systems: The Pre-Salt System

The Paleozoic petroleum systems (Tari et al. 2017; Mejri et al. 2006) are well productive in North Africa with major oil/gas fields situated along with the Saharan Platform (Tari et al. 2017; Tari and Kiely 2017; Aissaoui et al. 2016) charged by two known source rocks: the Silurian Tanezzuft Formation with TOC up to 17% (Mejri et al. 2006; Tari and Kiely 2017; Aissaoui et al. 2016) and Middle to Upper Devonian black shales which have entered the oil window since Permian times with an important expulsion phase since the Cretaceous and a peak during Late-Cretaceous continuing during Eocene (Aissaoui et al. 2016). They charged two major pre-salt reservoirs: the fluvial sand-rich Norian TriasArgilo-Gréseux Inférieur (TAGI) and the shaly Rhaetian Trias Argilo-Gréseux Supérieur (TAGS) (Tari and Kiely 2017). The main seals correspond to Triassic and Liassic salt and Cretaceous shales locally. Recently, some authors (Tari and Kiely 2017), have shown that the pre-salt basin beneath the Atlas has the potential for very large pre-salt petroleum fields associated to Paleozoic petroleum systems (Khomsi et al. 2019). From this point of view, the Atlas salt basin remains clearly unexplored for the pre-salt traps (Tari and Kiely 2017) which are not visualized on current, conventional shallow seismic sections. In line with (Tari and Kiely 2017), we think that the pre-salt traps are well developed underneath the Atlas belt and the foreland domain, where thick Triassic and Liassic evaporites series ensure seal for the potential Paleozoic petroleum reservoirs (Fig. 1). Obviously, the Atlas compressions events may have exerted a positive role in trapping hydrocarbon generated from Silurian and Devonian mature kitchens toward the potential reservoirs in apical parts of deeply buried anticlines and horsts below the Atlas belt and its foreland basins (Fig. 1).

3 Some Regional Structural Cross-Sections

3.1 Along the Sahara Platform

This structural cross-section goes from the Southern Atlas belt in the NW edge (Figs. 2 and 3), to the Chotts basin and then the Sahara Platform in the SW to the Gulf of Gabes (Khomsi et al. 2019) passing through the Jeffara Plain. It shows the Pan-African basement configuration, which presents highs and lows controlled by deeply seated basement faults (Fig. 3). These faults are inherited from the Paleozoic tectonic evolution (Khomsi et al. 2019). They were rejuvenated later on, during the Tethyan opening events starting by the Triassic rifting. The Mesozoic sedimentary sequences recorded the successive transgressions of the Paleo-Tethyan Sea above a wide and faulted Paleozoic sag platform (Khomsi et al. 2019). To the east, the Jeffara fault system represents a transitional tectonic domain to the Sirt basin (Khomsi et al. 2019), where the Meso-Cenozoic series are

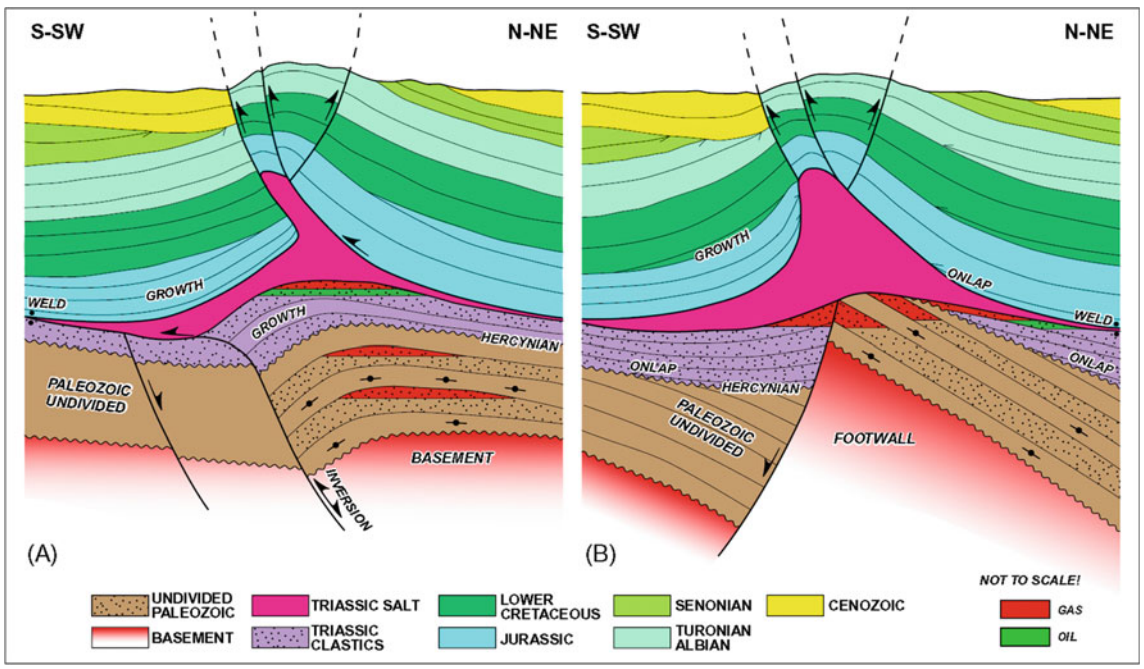

Fig. 1 Conceptual models for structural traps controlled by growth anticlines and foreland flexure underneath the Triassic salt in the Central Atlas of Tunisia. From (Tari and Kiely 2017). Notice the occurrence of potential plays underneath the Diapiric Triassic salt with possible oil/gas accumulations in the Paleozoic successions. Not to scale

highly subsiding. In this basin, important diapiric salt walls are observed on seismic sections (Fig. 3) and are mainly controlled by vertical movements of Liassic salt (Khomsi et al. 2019). The Liassic thick Diapric structures seal potential unexplored oil and gas traps seated in the Paleozoic structures (Fig. 3)..

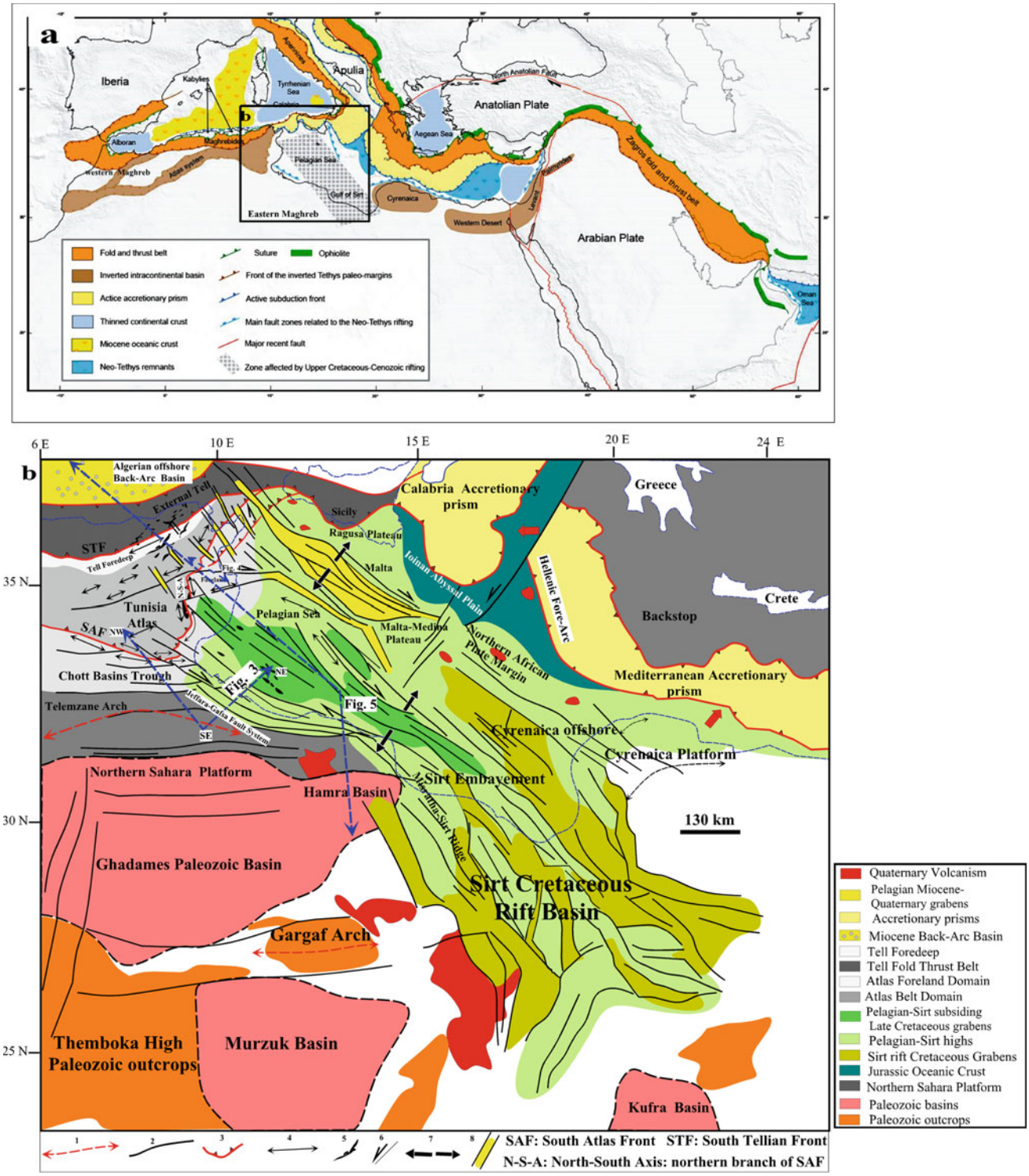

Fig. 2 Geotectonic maps of the Circum-Mediterranean and Central Mediterranean domains with the position of the regional transects. **a** Structural domains of the Mediterranean area (from Frizon de Lamotte et al. (2011)). **b** Detailed structural features of the Eastern Maghreb domain and its foreland basins from Khomsi et al. (2019); Khomsi et al. 2016) with the major structures in the Pelagian-Sirt domain (modified after (Fiduk 2009)). Captions: 1 major arche, 2 major faults, 3 major thrust, 4 major anticline, 5 salt bodies, 6 major strike-slip, 7 strike of stretching, 8 grabens

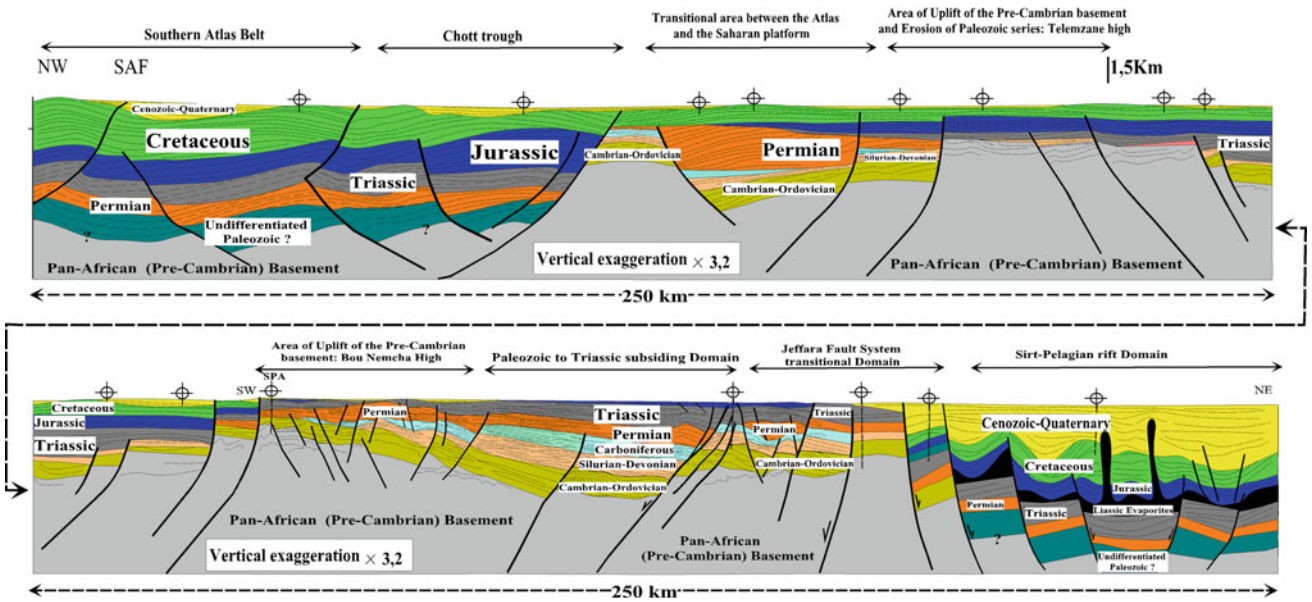

Fig. 3 Regional cross-section from South Atlas belt passing through the SAF to the Saharan Platform and then to the Sirt Rift Basin issued from seismic interpretations. Position on Fig. 2. Notice that the well SPA cross cuts the Precambrian basement. Notice also that diapirism in the Sirt Basin is essentially due to halokinetic motion of Liassic evaporites, after (Khomsi et al. 2019)

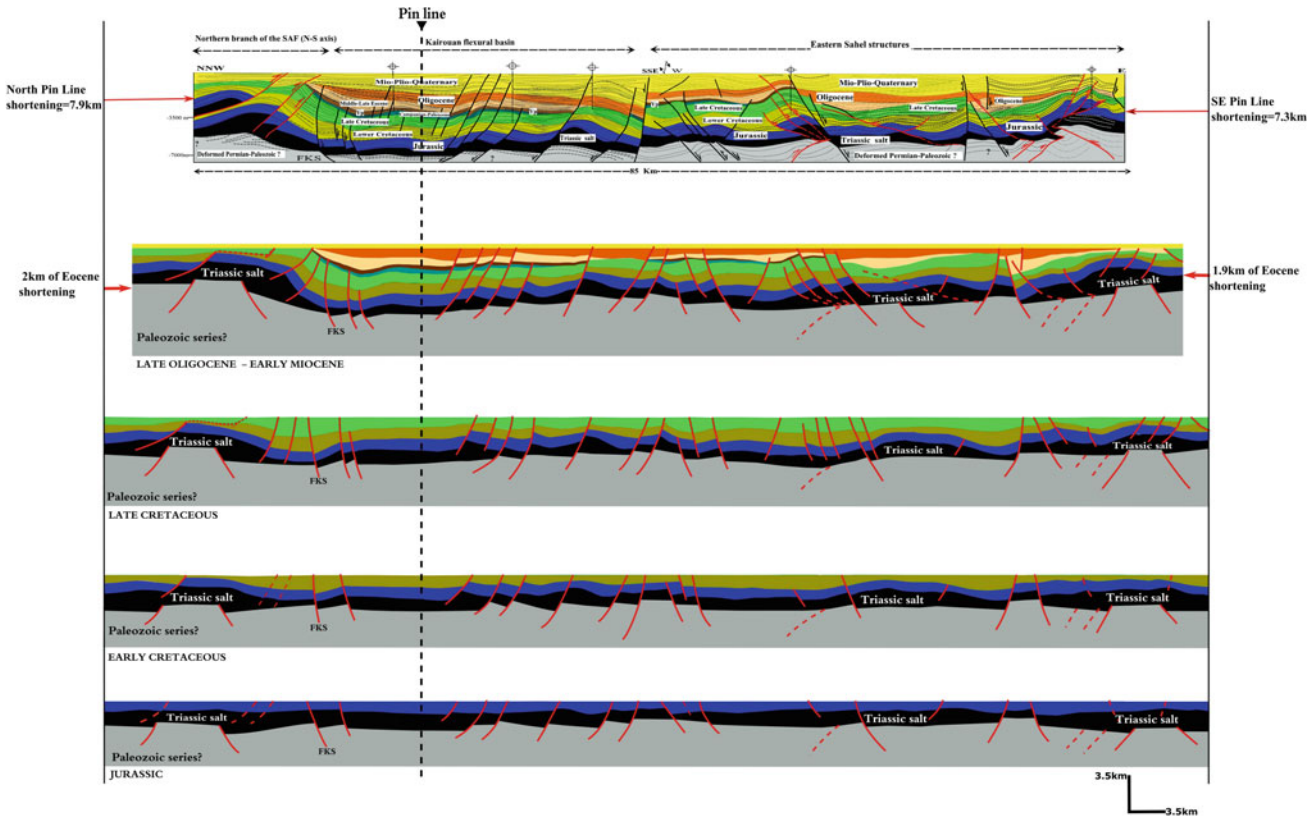

Fig. 4 Structural balanced cross-section from the Atlas belt to its eastern foreland basins through the Kairouan flexural basin with restorations through time since the Jurassic (from Khomsi et al. (2019))

3.2 Along the Atlas Belt and Its Foreland Basins

This structural cross-section shows the transition from the Atlas belt to the Sahel foreland basins, as well as the importance of the halokinesis of the Triassic salt, accounting for Late-Cretaceous-Paleogene diapirs (Khomsi et al. 2019). On the other hand, the flexural basin of Kairouan is clearly visualized and corresponds chiefly to a highly subsiding domain with an overall estimated total sedimentary thickness of more than 8500 m from the base of the Triassic to the Quaternary in the footwall of the Atlas belt.

The balanced cross-section (Fig. 4) was restored to the previous stages of deformation from the Jurassic to the Miocene-Quaternary (Khomsi et al. 2019) accounting for the major deformation steps and the deep configuration of the Post-Paleozoic cover, as well as the Paleozoic sequences underneath the Triassic salt (Fig. 4). According to Khomsi et al. (2019), the total amount of shortening for the Late Eocene and late Miocene compressions together is of 18% (15.2 km). The cross-section shows also that interesting potential oil/gas plays structures are situated underneath the Triassic salt in the Paleozoic structures, especially those on basement highs in the apical parts of some anticlines affecting the Paleozoic such as those on the western and eastern edges of the section (Fig. 4). These relatively shallow structures are not drilled and should be considered as future objectives for exploration.

3.3 A Regional Predictive Section

We presented two long interpretative cross-sections allowing underlining the overall structures of the Eastern Maghreb (Fig. 5). In the Tell, the tectonic style is thin-skinned with duplex anticlines (Khomsi et al. 2019; Roure et al. 2012) affecting the Post-Paleozoic sedimentary strata admitting the Triassic salt as major decollement level. In the southeast through the foreland basins, the tectonic style is predominantly thick-skinned (Mezni et al. 2019), mainly controlled by deep-seated faults both in the Atlas belt and in the foreland domain (Mezni et al. 2019). In the Tell as well as in the Atlas fold and thrust belts, we have no constraints on the Pre-Triassic structures and on the possible occurrence of oil and gas habitats in the Paleozoic series and structures beneath the thick Triassic evaporites sealing levels. Productive petroleum systems can occur there but are not understood nor characterized yet (Fig. 1). In the southeast, the two cross-sections reveal the Saharan Platform configuration mainly dominated by deep-seated faults anchored on the Precambrian basement. The Sahara Platform suffered the

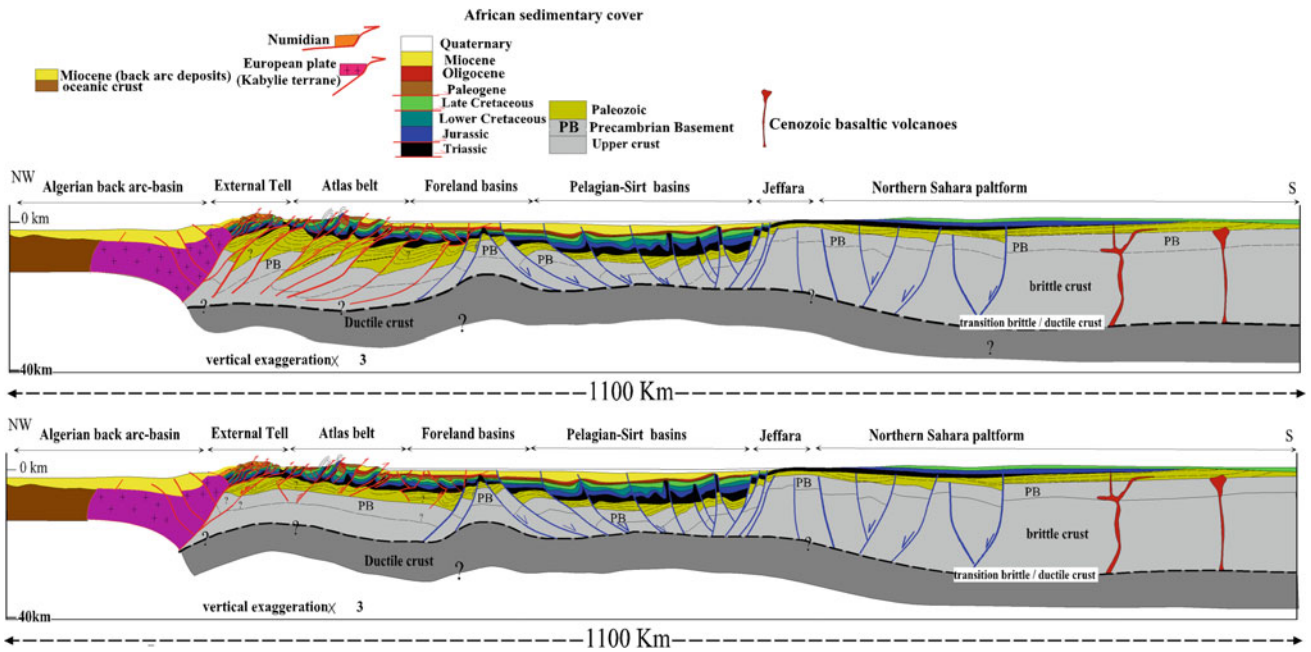

Fig. 5 Tentative regional cross-sections with two alternatives through the Eastern Maghreb from the Algerian back-arc basin in the northwest to the Sahara Platform in the south. Notice the Sirt-Pelagian subsiding basins. The depth of the Moho is issued from Grad et al. (2009). Cross-sections from Khomsi et al. (2019). Position on Fig. 2 The two cross-sections represent two possible alternatives for the foothills of the Tell and Atlas Fold and thrust belts. A deep seismic profile would unlock the deep configuration there

Cenozoic compressions and chiefly corresponds to a sag domain (Khomsi et al. 2019).

4 Concluding Remarks

Our presented cross-sections fully support the utility to record regional deep seismic reflection and wide angle profiles in a seismic North African Maghreban experiment, in order to visualize and characterize the deep structures beneath the Triassic evaporites. Infra-Triassic petroleum/gas systems may occur within the Paleozoic structures and sequences (Tari and Kiely 2017; Khomsi et al. 2019), but a better understanding on structures and basement faults could also guide prediction of hydrocarbon charge of shallower traps such as those in the Eastern foreland basin of the Atlas (Fig. 5). Such regional sections would not only give a better understanding of the basement configuration but also open new perspectives in oil exploration and activities for the coming years. The long regional cross-sections (Fig. 5) can serve for these purposes, but we think that it needs to be constrained by seismic deep sections which will allow characterizing the pre-salt traps which we think have very important potentials. On the other hand, it is clear that the potential deep seismic profiles will also open future exploration perspectives to characterize not only deep oil/gas plays but also deep geothermal aquifers, and mineral resources presumably seated and trapped along deep faults and deep Paleozoic reservoir successions. The conceptual model (Fig. 1) for oil/gas accumulations underneath the Triassic salt in the Atlas and its foreland is represented by a set of different types of structures buried beneath thick Triassic Diapirs and salt-pillows which ensure the sealing of potential Paleozoic charged reservoirs.

References

Aissaoui, M.N., Bédir, M., Gabtni, H.: Petroleum assessment of Berkine–Ghadames Basin, Southern Tunisia. AAPG Bull. **100**(3), 445–476 (2016)

Fiduk, J.C.: Evaporites, petroleum exploration, and the Cenozoic evolution of the Libyan shelf margin, central North Africa. Mar. Pet. Geol. **26**, 1513–1527 (2009)

Frizon de Lamotte, D., Raulin, C., Mouchot, N., Wrobel Daveau, J.C., Blanpied, C.,Ringenbach, J.C.: The southernmost margin of the Tethys realm during the Mesozoic and Cenozoic: initial geometry and timing of the inversion processes. Tectonics **30** (2011). TC3002. https://doi.org/10.1029/2010TC002691

Grad, M., Tiira., TESC Working Group: The Moho depth map of the European Plate. Geophys. J. Int. **176**(1), 279–292 (2009). https://doi.org/10.1111/j.1365-246X.2008.03919.x

Khomsi, S., Frizon de Lamotte, D., Bédir, M., Echihi, O.: The Late Eocene and Late Miocene fronts of the Atlas Belt in eastern Maghreb: integration in the geodynamic evolution of the Mediterranean Domain. Arab J. Geosci. **9**, 650–670 (2016). https://doi.org/10.1007/s12517-016-2609-1

Khomsi, S., Roure, F., Khelil, M., Mezni, R., Echihi, O.: A review of the crustal architecture and related pre-salt oil/gas objectives of the Eastern Maghreb Atlas and Tell: needs for deep seismic profiling. In: Lacombe, et al. (eds.) Tectonophysics, Spec. Issue, (2019). Tectonophysics, vol. 766, pp 232–248 (2019). https://doi.org/10.1016/j.tecto.2019.06.009

Mejri, F., Burollet, P.F., Ben Ferjani, A.: Petroleum geology of Tunisia. A renewed synthesis. ETAP Memoir **22**, 233 (2006)

Mezni, R., Khomsi, S., Bédir, M.: Structural styles, tectonic events, and deformation features along a surface–subsurface structural transect from the South Atlas Front(N–S axis) to the Eastern Sahel foreland basin of Tunisia. Arab. J. Geosci. **12**, 18 (2019). https://doi.org/10.1007/s12517-019-4366-4

Roure, F., Casero, P., Addoum, B.: Alpine inversion of the North African margin, and delamination of its continental crust. Tectonics (2012). https://doi.org/10.1029/2011TC002989

Tari, G., Kiely, J.: Is the Pre-salt sequence underexplored regionally in North Africa? AAPG Datapages/Search and Discovery Article #90313 ©2017 AAPG Africa Region GTW, Paleozoic Hydrocarbon Potential of North Africa, Marrakech, Morocco, November 1–4 (2017)

Tari, G., Flinch, J.F., Soto, J.I.: Petroleum systems and play types associated with permo-triassic salt in Europe. North Africa and the Atlantic Region. In: Soto, J.I., Flinch, J.F., Tari, G. (eds.) Permo-Triassic Salt Provinces of Europe, North Africa and the Atlantic Margins: Tectonics and Hydrocarbon Potential, pp. 129–156 (2017). https://doi.org/10.1016/B978-0-12-809417-4.00007-0; https://doi.org/10.1016/B978-0-12-809417-4.00038-0

New Structural and RSCM Thermometric Data from the Variscan Orogen of Morocco: Insight into the Extension-To-Compression Transition

André Michard, Abdeltif Lahfid, Lahssen Baidder, Christian Hoepffner, Hassan Ouanaimi, Abderrahmane Soulaimani, Aboubaker Farah, and Omar Saddiqi

Abstract

The Western Moroccan Meseta exposes in the Zaian region a pre-Visean, Eo-Variscan belt of inclined to recumbent folds detached from their Precambrian basement and embedded in the Variscan Orogen. Using the Raman Spectroscopy of Carbonaceous Material (RSCM) method, we obtained the first quantitative thermometric characterization of the Cambro-Ordovician and unconformable Upper Visean rocks in the area. The pre-Visean fold belt developed in relatively high-T conditions (mean value 323 ± 23 °C) compared to the juxtaposed Variscan folds that formed at lower T (209 ± 37 °C). The high geotherm of the Paleozoic series during folding is likely to be inherited from the Late Devonian extensional setting, but the fold belt emerged through compression, probably during the Devonian-Tournaisian transition.

Keywords

Polyphase folding • Extension • Compression • RSCM thermometry • Variscan • Morocco

1 Introduction

Here, we considered a polyphase folded belt exposed in the Zaian region of the Moroccan Meseta (Fig. 1), which belongs to the southern branch of the Variscides (Michard et al. 2010). The Moroccan Meseta was depicted as the former passive margin of the Saharan Platform, inverted during the Late Carboniferous-Permian due to the Laurussia-Gondwana collision (Michard et al. 2010; Frizon de Lamotte et al. 2013). So, one of the hot frontiers of the tectonic studies today, i.e., the importance of structural and thermal inheritance phenomena during the transition from extension to compression (Vacherat et al. 2016; Clerc et al. 2018), is illustrated there.

The present study was based on new field campaigns and laboratory analyses. Admittedly, we contradict here a previous conference paper (Ouanaimi et al. 2018), which was based on two fragmentary field observations and no thermometric measurements.

2 Geological Setting

The Zaian Mountains (Fig. 2a) stand to the East of the Western Meseta; they form the deepest part of the autochthonous units beneath the Variscan nappes that root at the front of the Eastern Meseta-Tazekka domain. The mountains are basically formed by folded siliciclastic Cambrian-Ordovician strata overlying Middle/Lower Cambrian greywackes and marbles and cored by Ediacaran meta-volcanics and granites (Fig. 2b). The folded Cambro-Ordovician quartzites and metapelites are unconformably overlain by Upper Visean-Serpukhovien deposits that in turn carry the Ordovician-Devonian material of the Eastern Nappes and are folded together during the late Variscan events.

Two opposite interpretations of the pre-Upper Visean folding have been debated; it was first described as the result of a Late Devonian compressional folding associated with a moderately dipping cleavage (Allary et al. 1976), then it was

A. Michard (✉)
Paris-Sud University, 91400 Orsay, France

A. Lahfid
BRGM/ISTO, Orléans University, 45060 Orléans, France

L. Baidder · A. Farah · O. Saddiqi
Hassan II University Aïn Chock, 5366 Casablanca, BP, Morocco

C. Hoepffner
Mohamed V University, Rabat, Morocco

H. Ouanaimi · A. Soulaimani
ENS/FSSM, Cadi Ayyad University, Marrakech, Morocco

M. Meghraoui et al. (eds.), *Advances in Geophysics, Tectonics and Petroleum Geosciences*,
Advances in Science, Technology & Innovation, https://doi.org/10.1007/978-3-030-73026-0_133

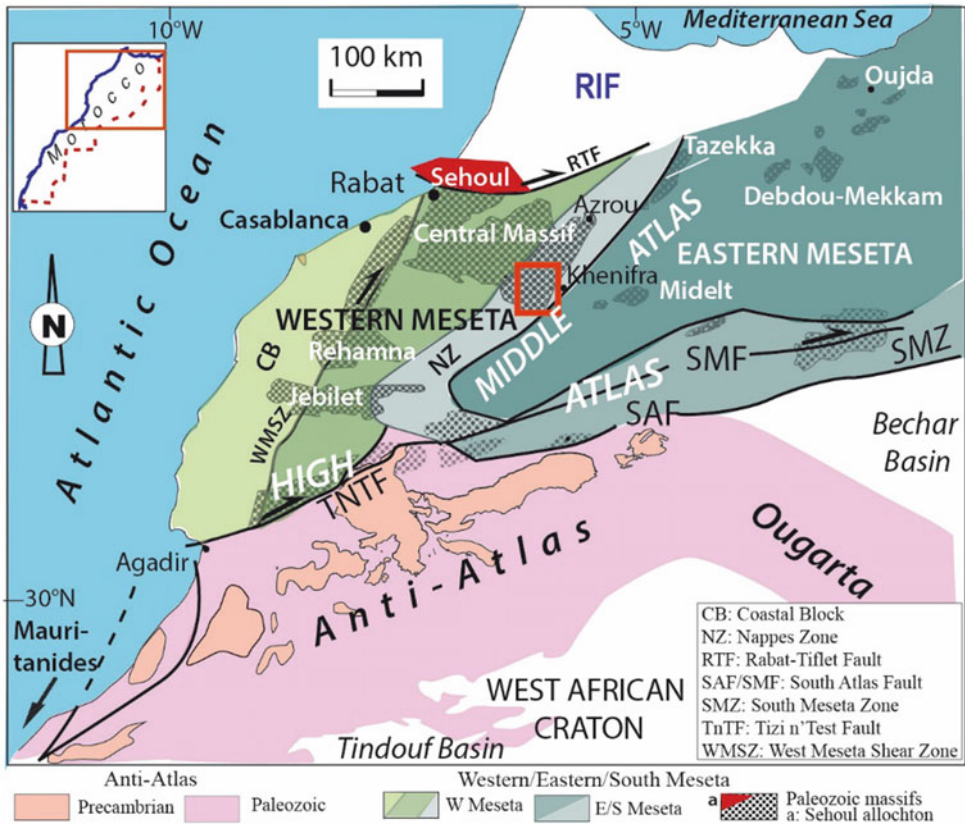

Fig. 1 Sketch map of the Moroccan Meseta Orogen at the northern margin of the Anti-Atlas foreland belt, after (Michard et al. 2010; Hoepffner et al. 2017). Triassic-Neogene cover terrains of the Atlantic plateaus or Atlas Domain not shown. Red box west of Khenifra: Fig. 2. Heavy black lines: major faults

regarded as due to gravity sliding in tilted pull-apart basins, and the quoted cleavage ascribed to the post Visean-Serpukhovian compression (Bouabdelli 1989).

3 Methods

In order to clarify the above uncertainties, we implemented two types of methods. First, we used the classical methods of structural analysis in the rock units on both sides of the Visean unconformity, at the kilometer to millimeter scale. Second, we collected samples on both sides of the unconformity for measurement of the maximum temperature (TRSCM) that the rocks suffered by the Raman Spectroscopy of Carbonaceous Material (RSCM) method (Beyssac et al. 2002; Lahfid et al. 2010; Delchini et al. 2016).

4 Results

4.1 Structures

We confirm the occurrence of inclined to recumbent folds associated with a slaty cleavage typical of a sub-greenschist metamorphic facies in the pelitic or shaly lithologies of the Zaian Cambrian-Ordovician series (Fig. 3b, c). This contrasts with the evolution of the overlying Carboniferous deposits in the diagenetic facies (Fig. 3e, f).

The pre-Visean folds are detached on the Lower-Middle Cambrian (Fig. 4).

During the Variscan compression, the Upper Visean unconformity was affected by large-wavelength folds and reverse faults (Fig. 5). Additionally, the unconformity surface is frequently reactivated as a shallow-dipping shear zone (Kef Nsour, Sidi Lhoussine, Tanayfout) and.

4.2 RSCM Temperatures

The Cambrian-Ordovician sites (Fig. 2a) from the Zaian Mts and Jebel Hadid yielded TRSCM values from 290 ± 9 °C to 365 ± 7 °C (mean value 323 ± 23 °C). The hottest TRSCM are observed in the Lower and Middle Cambrian samples of Goaida. The Upper Visean samples from the sites around or within (Goaida) the Zaian Mts yielded TRSCM values from 160 ± 20 °C to 260 ± 10 °C (mean value 209 ± 37 °C), except one sample from the Ment granite aureole and one from the Bouhssoussene shear zone (Fig. 2a).

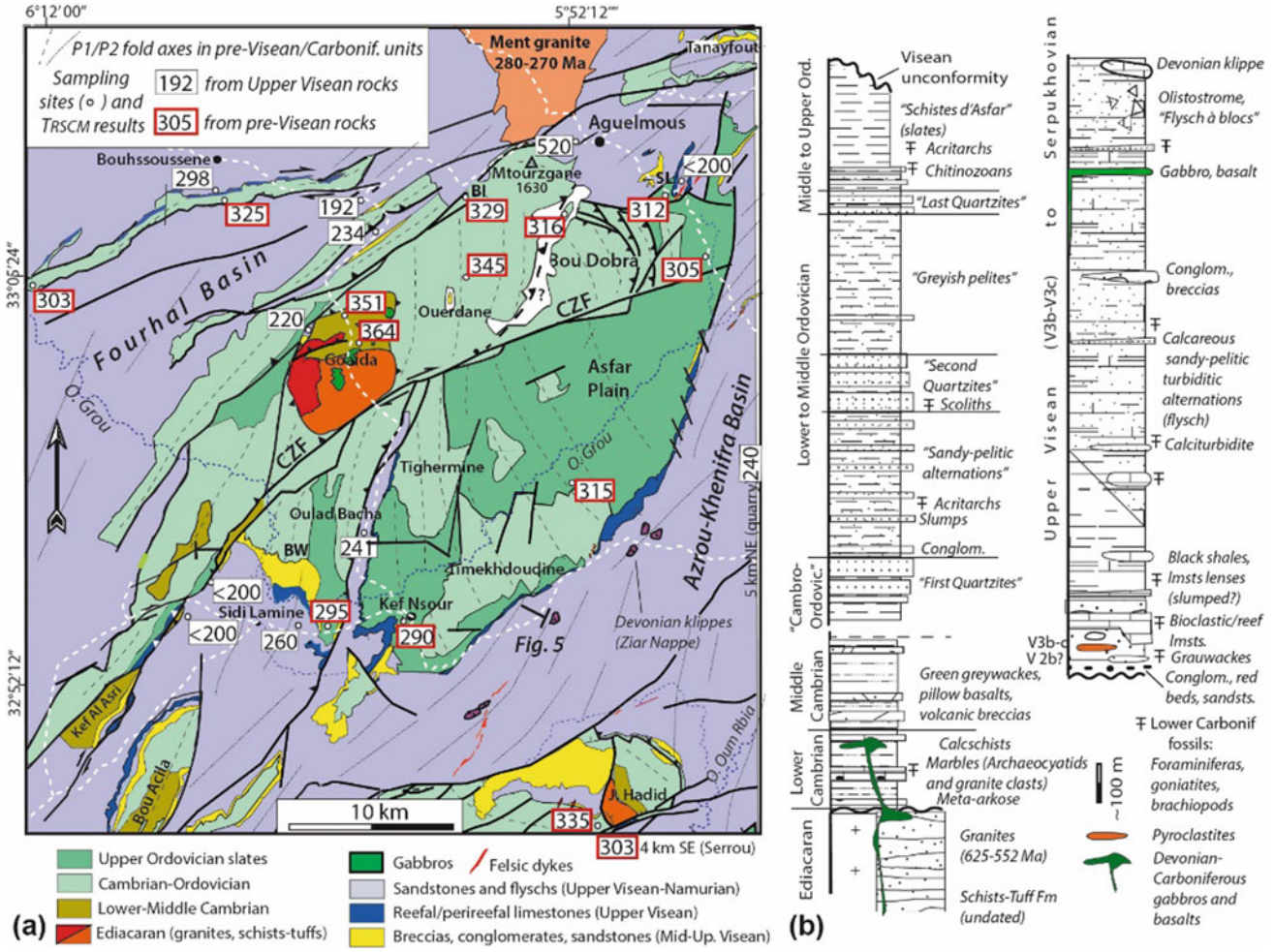

Fig. 2 **a** Geological map of the Zaian Mts and overlying Carboniferous basins, after (Ouanaimi et al. 2018; Allary et al. 1976; Bouabdelli 1989; Verset 1988) and this work, with the results of the present RSCM study. White: Quaternary. BI: Bou Issardene; BW: "Bird's wing"; CZF: Central Zaian Fault; SL: Sidi Lhoussine. **b** Stratigraphic columns, after (Bouabdelli 1989; Verset 1988; Ouabid et al. 2017; Houicha et al. 2018; Cailleux 1994). Black heavy lines: major faults (half arrows: strike-slip; teeth: thrusts); dotted white lines: roads

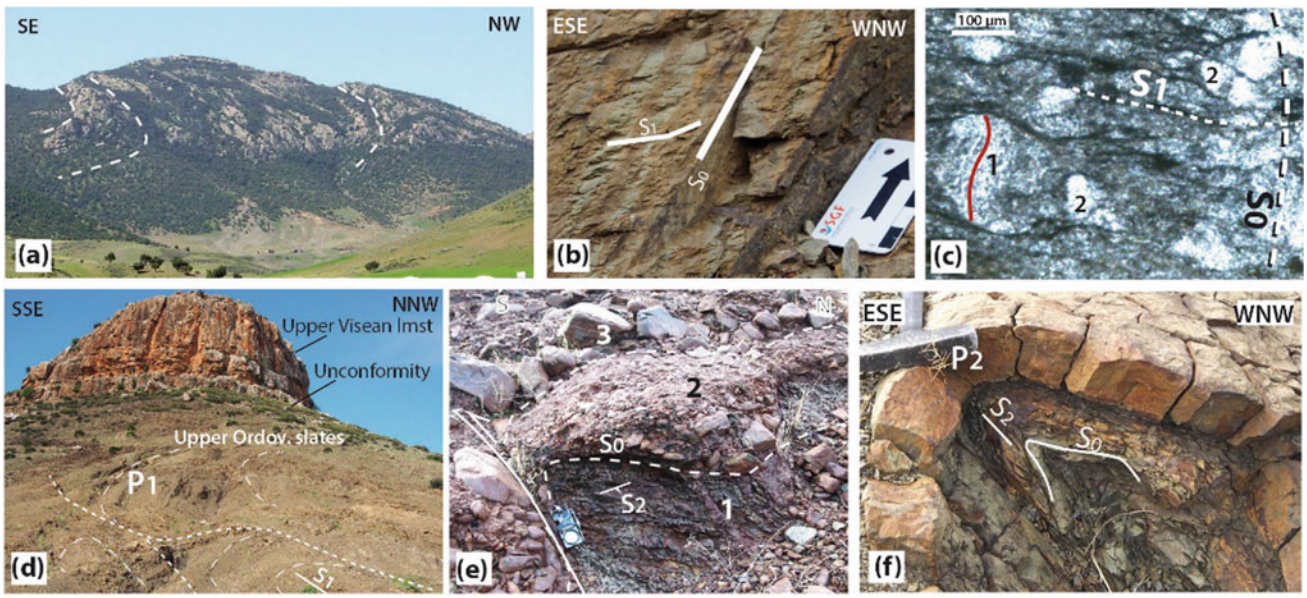

Fig. 3 **a** Recumbent fold in the Bou Dobra Ordovician quartzites. **b** Slaty cleavage (S1) in the Upper Ordovician metapelites, Sidi Lhoussine. **c** Micrography of Ordovician metapelites, Ouerdane. **d** Upper Visean unconformity, Kef Nsour. **e** Conglomeratic red beds (1–3), Bird's wing unconformity. **f** Non-penetrative pressure solution cleavage (S_2) in a P_2 hinge, Sidi Lhoussine. See Fig. 2 for location

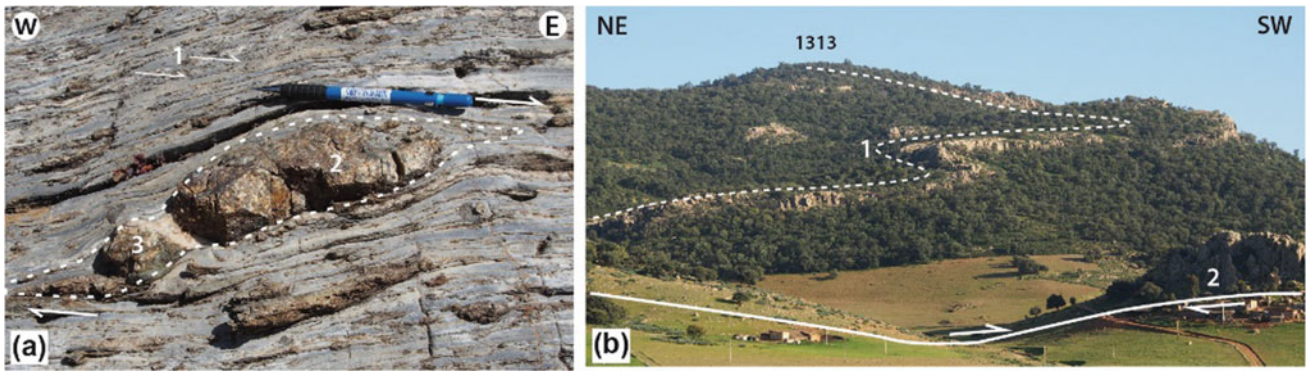

Fig. 4 **a** Strong shearing of the Lower Cambrian marbles, Goaida. 1 Boudinaged quartz vein; 2 Sigmoidal, boudinaged granite pebble; 3 Back-rotated fragment of (2). **b** Bou Issardene recumbent folds. 1 Inverted limb minor fold with N100-110E horizontal axis; 2 Quartzite sliver in the major fault bounding the folded unit

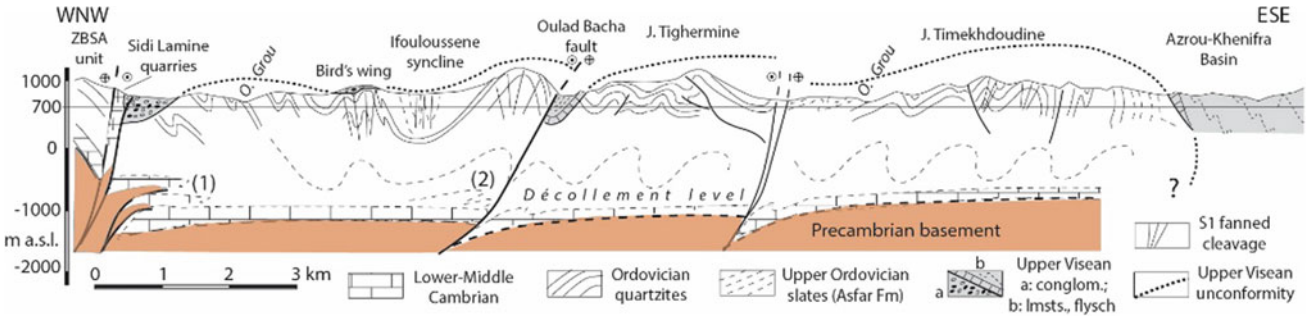

Fig. 5 Cross-section of the southern Zaian Mts (see Fig. 2 for location). The occurrence of basement slivers and the Lower Cambrian décollement level are shown after the Goaida massif (1) and the Bou Issardene folds (2) of the northern Zaian Mts (Fig. 4b)

5 Discussion

All the samples of the Zaian Mts and J. Hadid display TRSCM values higher than those of the surrounding Upper Visean samples, with a difference of around 100 °C in the TRSCM mean values. Hence, the Zaian pre-Visean fold belt acquired its thermal structure before that of the subsequent, lower grade Variscan belt. Our thermometric data fully confirm the structural observations that show the occurrence of an early fold belt embedded in the Variscan one and characterized by a sub-greenschist facies. The "hot" Visean sample (299 °C) from the Bouhssoussene shear zone belongs to the Fourhal Basin (Fig. 2). This structural domain exhibits superimposed folding episodes and opposite vergence of thrusts suggesting a strong Variscan shortening in a major flower structure.

The 310 °C mean temperature reached by the Upper Ordovician folded units before their pre- Upper Visean erosion cannot result from sedimentary burial only; regional considerations (see references in Michard et al. (2010)) suggest that this burial did not exceed 2 km of Silurian-Devonian compacted deposits. Admitting that the maximum temperature was reached in the Upper Ordovician rocks only after folding and then after tectonic thickening has occurred, we may hypothesize a burial of 3 km (after ~50% of tectonic shortening) and a shallow geotherm of ~100 °C/km. The deep geotherm measured for the ~3 km thick Cambrian-Ordovician folded pile is ~20 °C/km (hydrothermal advection). The linear geothermal gradient is estimated at 60 °C/km.

In the conceptual model below (Fig. 6), the hot linear geothermal gradient would be inherited from the overall extensional setting that characterizes the Meseta and Anti-Atlas domains during the Middle-Late Devonian (Michard et al. 2010; Frizon de Lamotte et al. 2013; Baidder et al. 2008; Becker et al. 2015). In the Meseta domain, mafic outflows were recorded in the Famennian-Tournaisian turbidites close to the WMSZ and RTF faults [Fig. 1; see (Michard et al. 2010)]. The onset of magmatism has been dated at 358–345 Ma in the Jebilet massif (Delchini et al. 2018), and the Debdou-Mekkam massifs of Eastern Meseta recently yielded a Late Devonian (~380 Ma) population of detrital zircons (Accotto et al. 2018). The crustal segment of the future belt is located above the subducting Rheic slab (not in view; (Baidder et al. 2008). During the Late

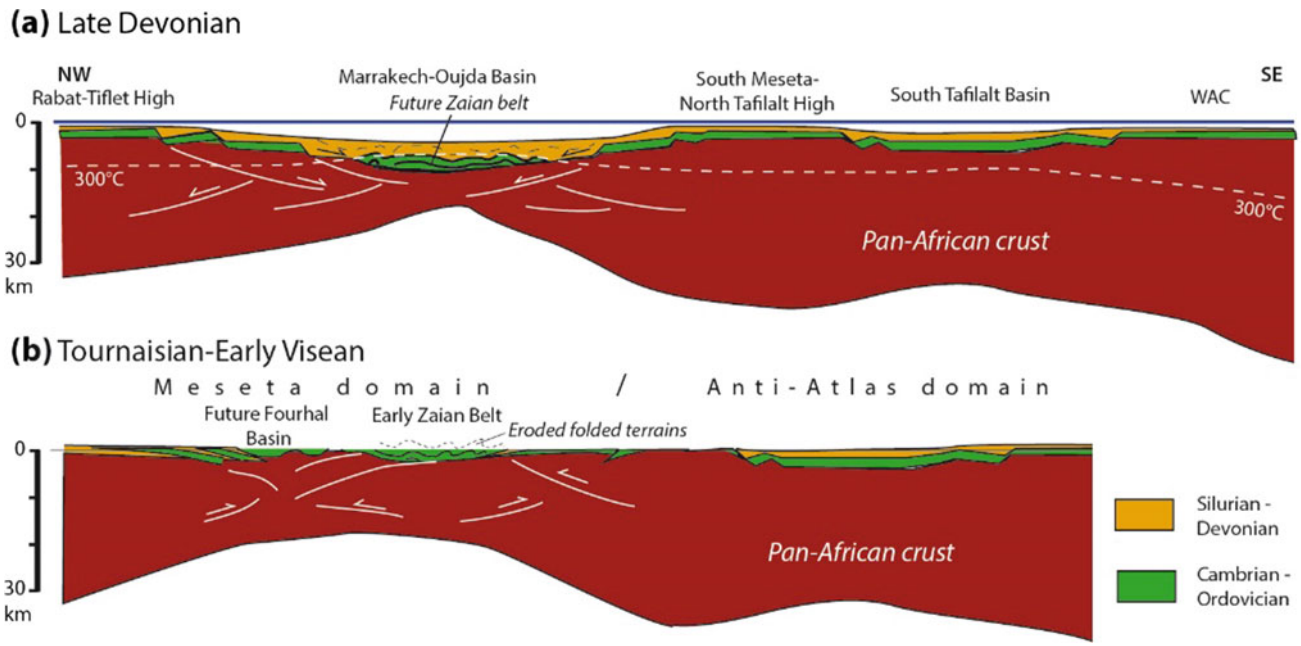

Fig. 6 Conceptual model for the formation of the Zaian pre-Visean belt. **a** Early detachment of the Paleozoic series in extensional setting. **b** Compression or transpression in inherited high-temperature conditions (~330 °C) resulted in the belt emersion; the uppermost folded terrains have been eroded in subaerial conditions

Devonian rifting climax, the Cambrian-Ordovician and overlying Silurian-Devonian series would have detached from the thinned Pan-African crust. Because of the mantle hot anomaly, the 300 °C isotherm would have climbed above the Cambrian-Ordovician formations and beneath the Devonian sedimentary blanket in the Marrakech-Oujda pelagic-turbiditic basin (stage a). Folding could have begun at that stage, but it was only achieved in a subsequent compression/transpression stage, which is necessary to explain the subaerial conditions of erosion prior to the Upper Visean transgression. The positive inversion of the crustal faults (stage b) caused incipient shortening of the most stretched part of the crust, the folding of the overlying, already detached Cambrian-Ordovician series, duplex formation further to the NW, and the emersion of the Meseta domain. By the Late Visean, the entire Meseta domain is prone to be covered by unconformable, subaerial, and shallow water deposits (not shown).

6 Conclusions

Using the RSCM method, we gave here the first quantitative geothermic characterization of the pre-Visean and Variscan events in the Zaian Mts area. The early, pre-Visean (Eo-Variscan) fold belt developed in high-temperature conditions (290 ± 9 °C to 365 ± 7 °C) under a 2–4 km sedimentary-tectonic burial (sub-greenschist facies). By contrast, the Variscan folds around and above the early fold belt formed under low-temperature conditions, < 200 to 260 ± 10 °C.

We proposed that the high geotherm, and probably the initial detachment and folding of the Zaian pre-Visean fold belt were inherited from the Late Devonian extensional setting. However, the Zaian early fold belt was only achieved during a compressional event, during the Devonian-Tournaisian transition.

This study offers a new conceptual framework for studies that should be undertaken in the numerous Meseta areas where the Upper Visean unconformity occurs.

References

Accotto, C., Martínez Poyatos, D., Azor, A., Jabaloy, A., Azdimousa, A., Tahiri, T., El Hadi, H.: First U/Pb detrital zircon age populations from the Eastern Variscan Moroccan Meseta. Geophys. Res. Abstr. **20**, EGU2018–14857 (2018).

Allary, A., Lavenu, A., Ribeyrolles, M.: Etude tectonique et microtectonique d'un segment de chaîne hercynienne dans la partie sud-orientale du Maroc central. Notes Mém. Serv. Géol. Maroc **261**, 1–170 (1976)

Baidder, L., Raddi, Y., Tahiri, M., Michard, A.: Devonian extension of the Pan-African crust north of the West African Craton and its bearing on the Variscan foreland deformation: evidence from eastern Anti-Atlas (Morocco). In: Ennih, N., Liégeois, J.P. (eds). The Boundaries of the West African Craton. Geol. Soc. London Spec. Publ. 297, pp. 453–465 (2008)

Becker, T., Aboussalam, Z.S., El Hassani, A., Hartenfels, S., Baidder, L.: The timing of Eovariscan block faulting, reworking and re-deposition in the Moroccan Meseta. Strata **1**(16), 14–15 (2015)

Beyssac, O., Goffé, B., Chopin, C., Rouzaud, J.N.: Raman spectra of carbonaceous material in metasediments: a new geothermometer. J. Metamorph. Geol. **20**, 859–871 (2002)

Bouabdelli, M.: Tectonique et sédimentation dans un bassin orogénique: le sillon viséen d'Azrou-Khénifra (Est du Massif hercynien central du Maroc). Unpubl. State Thesis Univ. Louis Pasteur Strasbourg, pp. 1–270 (1989)

Cailleux, Y.: Le Cambrien et l'Ordovicien du Maroc Central méridional. In: El Hassani, A., Piqué, A., Tahiri, A. (eds) Le Massif Central marocain et la Meseta orientale. Bull. Inst. Sci. Rabat 18, pp. 10–31 (1994)

Clerc, C., Ringenbach, J.C., Jolivet, L., Ballard, J.F.: Rifted margins: Ductile deformation, boudinage, continentward-dipping normal faults and the role of the weak lower crust. Gondwana Res. **53**, 20–40 (2018)

Delchini, S., Lahfid, A., Plunder, A., Michard, A.: Applicability of the RSC geothermometry approach in a complex tectono-metamorphic context: the Jebilet massif case study (Variscan Belt, Morocco). Lithos **256–257**, 1–12 (2016)

Delchini, S., Lahfid, A., Lacroix, B., Baudin, T., Hoepffner, C., Guerrot, C., Lach, P., Saddiqi, O., Ramboz, C.: The geological evolution of the Variscan Jebilet Massif, Morocco, inferred from new structural and geochronological analyses. Tectonics **37**, 4470–4493 (2018)

El Houicha, M, Chopin, F., Tessitore, L., Ghienne, J.-F, Jouhari, A., Vandenbroucke, T., Schulmann, K.: Revisiting the middle - late Visean unconformity in the SE Moroccan Massif Central: New data and perspectives. Int. Joint Congr. CAAWG9-ArabGU2, El Jadida, Abstr. 87–89 (2018)

Frizon de Lamotte, D., Shirazi-Tavakoli, S., Leturmy, P. et al.: Evidence for Late Devonian vertical movements and extensional deformation in Northern Africa and Arabia. Integration in the geodynamics of the Devonian world. Tectonics **32**, 107–122 (2013)

Hoepffner, C., Ouanaimi, H., Michard, A.: La Meseta, un terrain vagabond ou la marge fragmentée de l'Anti-Atlas ? Géologues (Soc. Géol. Fr.) **194**, 19–23 (2017)

Lahfid, A., Beyssac, O., Deville, E., Negro, F., Chopin, C., Goffé, B.: Evolution of the Raman spectrum of carbonaceous material in low-grade metasediments of the Glarus Alps (Switzerland). Terra Nova **22**, 354–360 (2010)

Michard, A., Soulaimani, A., Hoepffner, C., Ouanaimi, H., Baidder, L., Rjimati, E.C., Saddiqi, O.: The south-western branch of the Variscan Belt: evidence from Morocco. Tectonophysics **492**, 1–24 (2010)

Ouabid, M., Ouali, H., Garrido, C.J., Acosta-Vigil, A., Román-Alpiste, M.J., Dautria, J.-M., Marchesi, C., Hidas, K.: Neoproterozoic granitoids in the basement of the Moroccan Central Meseta: correlation with the Anti-Atlas at the NW paleo-margin of Gondwana. Precamb. Res. **299**, 34–57 (2017)

Ouanaimi, H., Soulaimani, A., Hoepffner, C., Michard, A.: The Eovariscan Synmetamorphic Phase of the Moroccan Meseta Domain revisited; a hint for Late Devonian extensional geodynamics prior to the Variscan orogenic evolution. In: Rossetti et al. (eds.), The Structural Geology Contribution to the Africa-Eurasia Geology: Basement and Reservoir Structure, Ore Mineralisation and Tectonic Modelling. Adv. Sci., Technol. Innov. **10**, 259–261 (2018). https://doi.org/10.1007/978-3-030-01455-1_56

Vacherat, A., Mouthereau, F., Pik, R., Bellahsen, N., Gautheron, C., Bernet, M., Daudet, M., Balansa, J., Tibari, B., Jamme, R.P., Radal, J.: Rift-to-collision transition recorded by tectonothermal evolution of the northern Pyrenees. Tectonics **35**, 907–933 (2016)

Verset, Y.: Carte géologique du Maroc au 1/100.000, feuille Qasbat-Tadla et Mémoire explicatif. Notes Mém. Serv. géol. Maroc 340–340bis (1988)

Reconstruction of the Hot Shale Distribution in Geological Outcrops Cross the Murzuq Basins, SW Libya

Nuri Mohamed Fello

Abstract

In Silurian outcrops of the Murzuq Basins, perform the amount of organic matter appears to be commonly heavily oxidised through weathering so that geochemical identification of the unit in the field is difficult. Weathering has also altered the black colour of the shales to reddish and greenish, so that rock colour cannot be used as evidence for or against the presence of the Silurian "Hot Shales" horizon in outcrops. Uranium and pyrite framboids appear to be less vulnerable to weathering and may be used to identify intervals of originally organic-rich shales in exposures. Framboids are discrete spheroidal aggregates of pyrite microcrystallites and their size distribution is thought to be controlled by Palaeo-depositional bottom-water redox-conditions.The "Hot Shales" marker of the basal Tanezzuft has a wide subsurface occurrence in the Murzuq Basin. All thesediments of the Tanezzuft Formation point to a sharp change in environment after the deposition of the hugeCambro-Ordovician sandstones blanket. The Silurian system records the first marine transgression in westernLibya. The Silurian source rock can be detected easily in well logs because of strong uranium-related naturalradiation leading to total gamma-ray values of up to 600 API. To better understand the regional distribution andanatomy of the Silurian "Hot Shales" it is necessary to integrate the subsurface data from the basin interiors with outcrop data from the basin margins. The early Silurian in North Africa and Arabia was characterised by widespread deposition of organic-rich "Hot Shales" in Palaeo-depressions, and the unit represents an important hydrocarbon source rock in the Murzuq Basin and other parts of northern Gondwana, such as Algeria, Jordon and Saudi Arabia. The "Hot Shale's" marker deposited in restricted to open marine conditions associated with an early Silurian marine transgression over a Taconic erosional surface. The sediments of the Tanezzuft Formation are rich in graptolites, especially the lowermost interval. The fauna is rich in individual forms but poor in species. Initial analyses of fresh Silurian organic-rich shales from a Murzuq Basin core reveal a close correspondence, for the most part, between TOC, total gamma-ray response, uranium content (as determined by spectral gamma ray) and framboid parameters.

Keywords

Silurian • Gamma-ray • Uranium • Petroleum source rock • Black shale • Libya

1 Introduction

The distribution of the black shale is now well-known for the subsurface of areas that have been intensely explored for hydrocarbons, such as parts of the western Libyan Ghadames and Murzuq Basins (Lüning et al. 2003). Information on the regional distribution of this unit is needed by the petroleum industry as this organic-rich shale represents an important source rock for rich oil reserves in many North African and Arabian basins, including the western Libyan basins. However, little is currently known about the occurrence of this lower Silurian "hot shale" in the less explored parts of the northern Gondwanan Palaeozoic basins where only few wells have been drilled. Here, we presented spectral gamma-ray data from the Ordovician–Silurian boundary interval in seven field sections in the Ghat outcrop belt at the western margin of the Murzuq Basin (Fig. 1). Weathering has also altered the black colour of the shales to reddish and greenish, so that rock colour cannot be used as evidence for or against the presence of the Silurian "hot shales" horizon in outcrops.

N. M. Fello (✉)
Nafusah Oil Operations B. V., Geosciences Department Manager, Tripoli, Libya
e-mail: Nuri.Fello@nafusah.com

M. Meghraoui et al. (eds.), *Advances in Geophysics, Tectonics and Petroleum Geosciences*,
Advances in Science, Technology & Innovation, https://doi.org/10.1007/978-3-030-73026-0_134

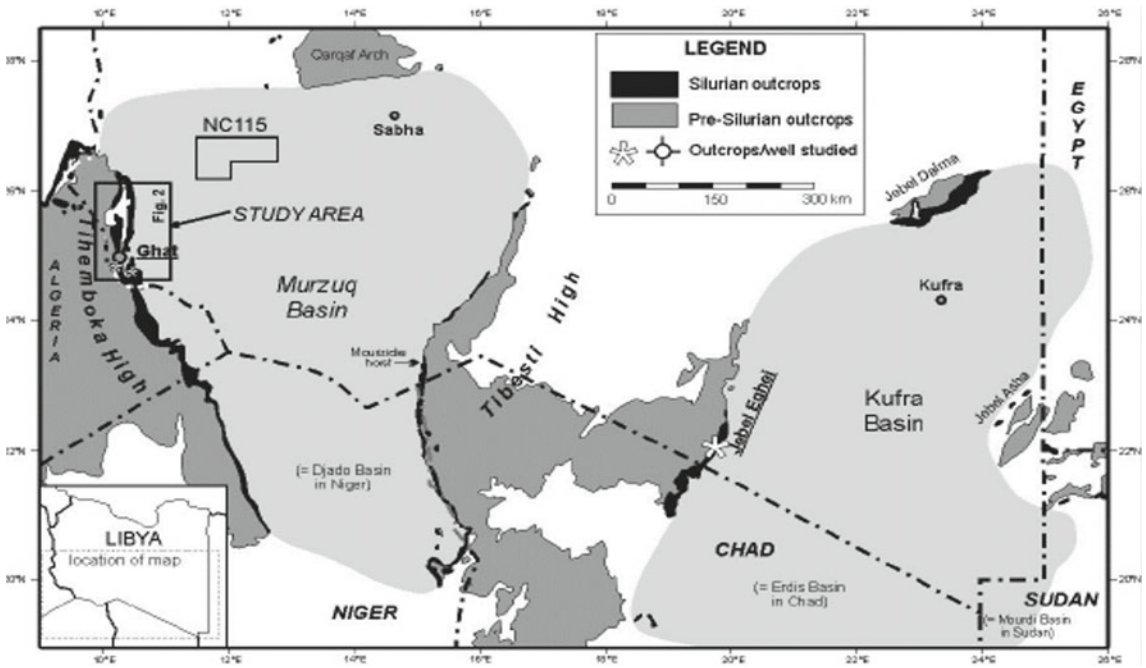

Fig. 1 Location map of the southern Libyan basins including the study area in the Ghat outcrop belt on the western margin of the Murzuq Basin

2 Structural Development

The Murzuq Basin is a Palaeozoic sag basin infilled by Cambrian to Cretaceous continental to shelfal sandstones, siltstones, and shales. Following late Neoproterozoic PanAfrican orogeny, Libya entered a tectonically quieter phase in the Cambrian. Intraplate processes dominated during the Cambrian to mid Silurian, including local transpressionalv/transtensional movements as evidenced on seismic from the subsurface of the Murzuq Basin. A major intraplate uplift phase affected the central parts of the Murzuq Basin during the late Silurian/early Devonian (the so-called "Caledonian" tectonic phase) leading locally to erosion cutting deep into the Silurian Tanezzuft shales (Davidson et al. 2000).

In Murzuq Basin, the "hot shales" member is the primary source rock for the basin. It is restricted to Taconic unconformity palaeotopographic lows and, therefore, is only present in certain areas of the basin. The early Silurian in North Africa and Arabia was characterised by widespread deposition of organic-rich "hot shales" in Palaeo-depressions, and the unit represents an important hydrocarbon source rock in the Murzuq Basin and other parts of northern Gondwana, such as Algeria, Jordon, and Saudi Arabia (Seilacher et al. 2002).

3 Material and Methods

In the Ghat study area (Fig. 2), the Tanezzuft shales are underlain by glacial to periglacial sandstones of the Ashgillian Mamuniyat Formation, or where absent, by shales and siltstones of the Caradocian to Ashgillian Melez-Shuqran Formation that was also affected by periglacial processes. Spectral gamma-ray measurements were carried out in seven Ordovician–Silurian boundary sections using a portable spectrometer (3″ × 3″ detector, GRS-2000, GF Instruments, formerly Geofyzika, Brno) with 10–46 measurements per section. A 3 min measuring interval was selected allowing quantitatively reproducible results.

The thickness of the lower Silurian organic-rich shale in exploration wells was measured in well logs based on its characteristically high gamma-ray signature. In this contribution, we defined hot shales as shales with gamma-ray values greater than 150 API corresponding roughly to TOC

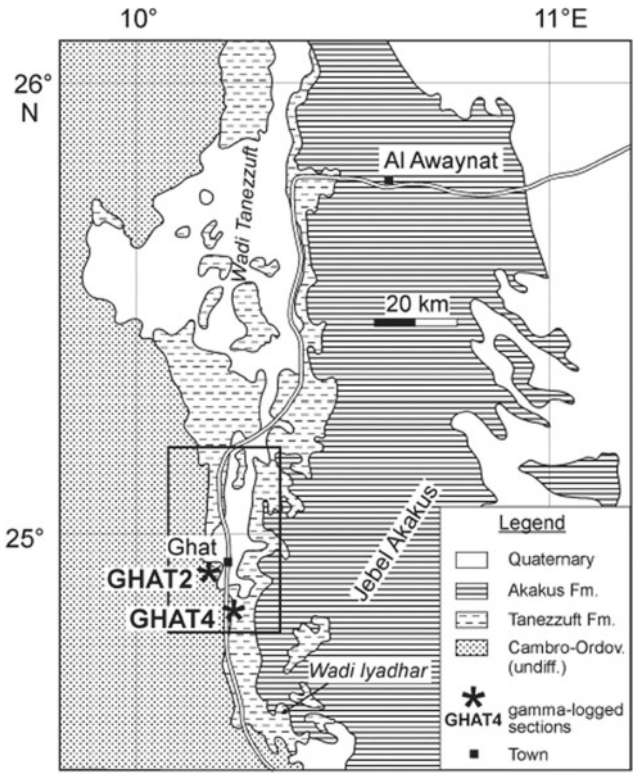

Fig. 2 Geological map of the Ghat study area and locations of logged sections

values of greater than 1% for oil window maturities (Fello et al. 2006).

4 Outcomes

4.1 Lithologies

Colours of the studied shales are ranged from red, light to medium grey, and in one case also dark grey. Black colours, as observed for the Silurian organic-rich shales in the subsurface of the Murzuq Basin, do not occur. In all the studied field sections, the shales are strongly weathered, with some of the shales having a very soft, flaky, and paper-like character. The shales are interbedded with wavy/rippled siltstone and fine sandstone beds that are mm- to a few cm-thick. Occasionally hummocky-cross stratification occurs in the coarser units.

4.2 Spectral Gamma-Ray

Spectral gamma-ray data from well H29-NC115 from the Murzuq Basin (Fig. 4) indicates that the high total gamma-ray signal of the lower Silurian hot shale is almost entirely due to an increase in uranium, while only a moderate to no increase occurs in the K and Th concentrations compared to the overlying organically lean shales. A similar radiation pattern occurs in five of the seven newly measured field sections where the basal Tanezzuft is characterised by elevated total gamma radiation which is also dominated by the uranium signal, with only small contributions by K and Th. In the studied Tanezzuft shale outcrop sections, the K values vary between 2 and 4%, and the Th values between 7 and 25 ppm. Maximum U concentrations in the basal U-enriched part of the Tanezzuft Formation are around 50 ppm (sections Ghat-2 and Ghat-7), while the shales above the U-enriched unit are characterised by U values ranging only between 4.5 and 7 ppm. A cut-off of 10 ppm was chosen to distinguish between the basal U-enriched shale unit and the overlying "normal" shales.

4.3 Biostratigraphy

The Graptolites were rather rare in the studied field sections, most probably due to poor preservation as a result of intense weathering. Graptolites were recovered from five sections; however, in many cases, only a rough generic identification was possible due to the poor preservation (Fig. 3). All the collected graptolites yielded Early Llandovery (Rhuddanian) ages although only in a few cases was it possible to interpret the biostratigraphic age on a more precise biozone level. The thick U-enriched interval in section Ghat-3 most probably includes the middle Rhuddanian *tariti-africanus* Zone. In section Ghat-4 where the U-enriched unit is nearly absent, the basal shales are dated as late Rhuddanian *fezzanensis* Zone based on the occurrence of *Neodiplograptus fezzanensis*.

In general, palynomorphs cannot be recovered from Saharan outcrop samples because weathering has usually fully destroyed the palynomorph fauna here. In fresh subsurface samples, palynomorphs often offer the only means of biostratigraphic dating because graptolites are destroyed in cutting samples. Nevertheless, the palynoflora from the

Silurian hot shale in core H29-NC115 turned out to be barren (Fello et al. 2006).

4.4 Subsurface Hot Shale Isopach

In general, palynomorphs cannot be recovered from Saharan outcrop samples because weathering has usually fully destroyed the palynomorph fauna here. In fresh subsurface samples, palynomorphs often offer the only means of biostratigraphic dating because graptolites are destroyed in cutting samples. Nevertheless, the palynoflora from the Silurian hot shale in core H29-NC115 turned out to be barren (Fig. 4). In contrast, a moderately diverse acritarch assemblage was found in the underlying Hirnantia Shale, dominated by mainly proximal morphotypes, indicating inner shelf conditions. The GR peak is almost entirely due to radioactive material an elevated Uranium Content. Feasibility tests of the concept are also carried out at exposures in the Murzuq Basin and may form the basis for improved Silurian organic-rich shale distribution maps and more precise age models for Silurian organic-rich depositional phases in northern Gondwana.

5 Results

The study shows that the lower Silurian hot shale can be identified in field exposures based on its uranium concentrations as measured by portable gamma-ray spectrometer. Traditional methods such as total organic carbon surveys fail in such environments because the intensive

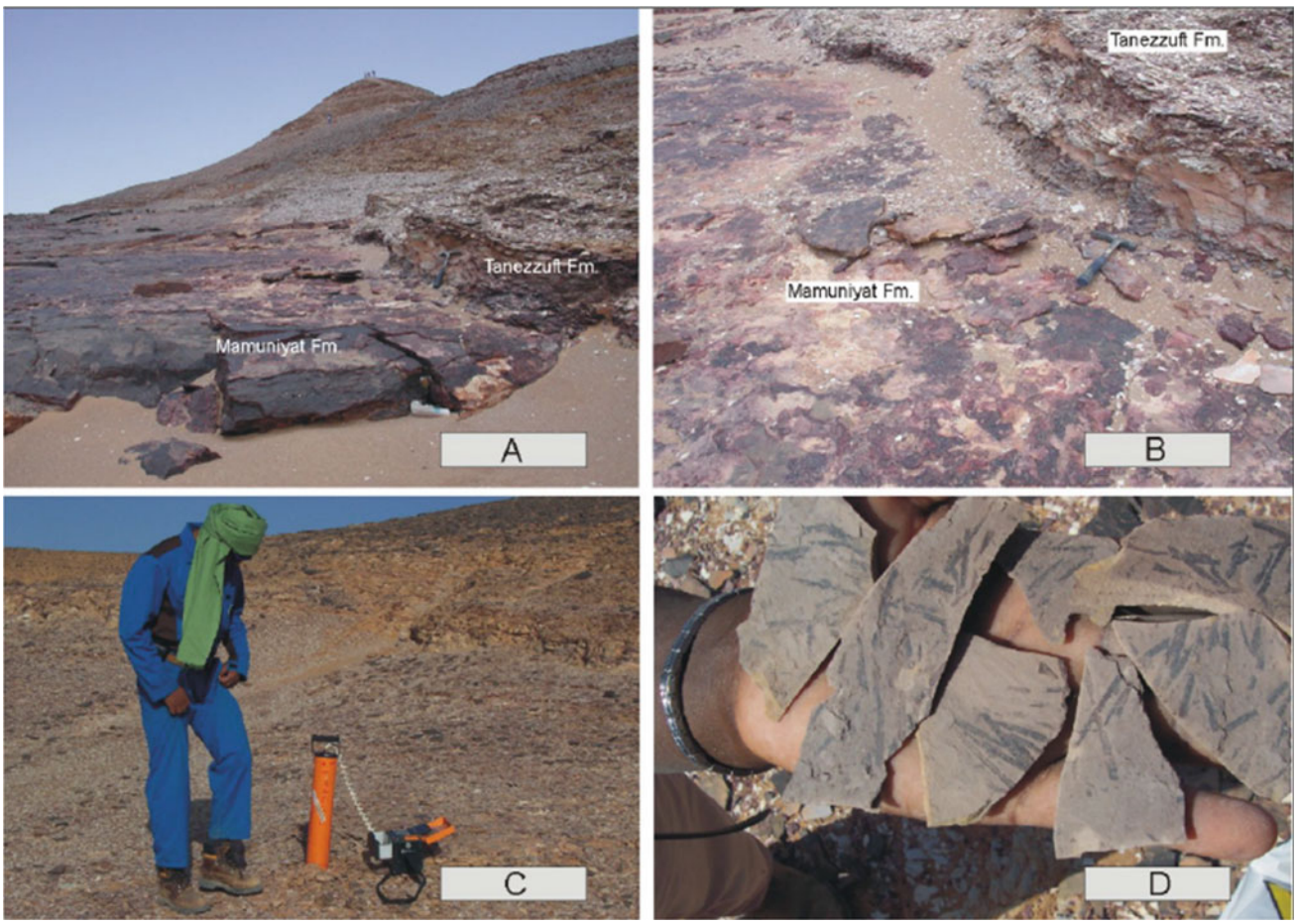

Fig. 3 **a**, **b** Section Ghat-4 exposing the contact between the uppermost Mamuniyat Formation and the lowermost Tanezzuft Formation (See Fig. 2 for location of section). **c** Spectral gamma-ray measurements in the field using the portable gamma-ray spectrometer GRS-2000. **d** Rhuddanian graptolites from the basal Tanezzuft Formation near Ghat

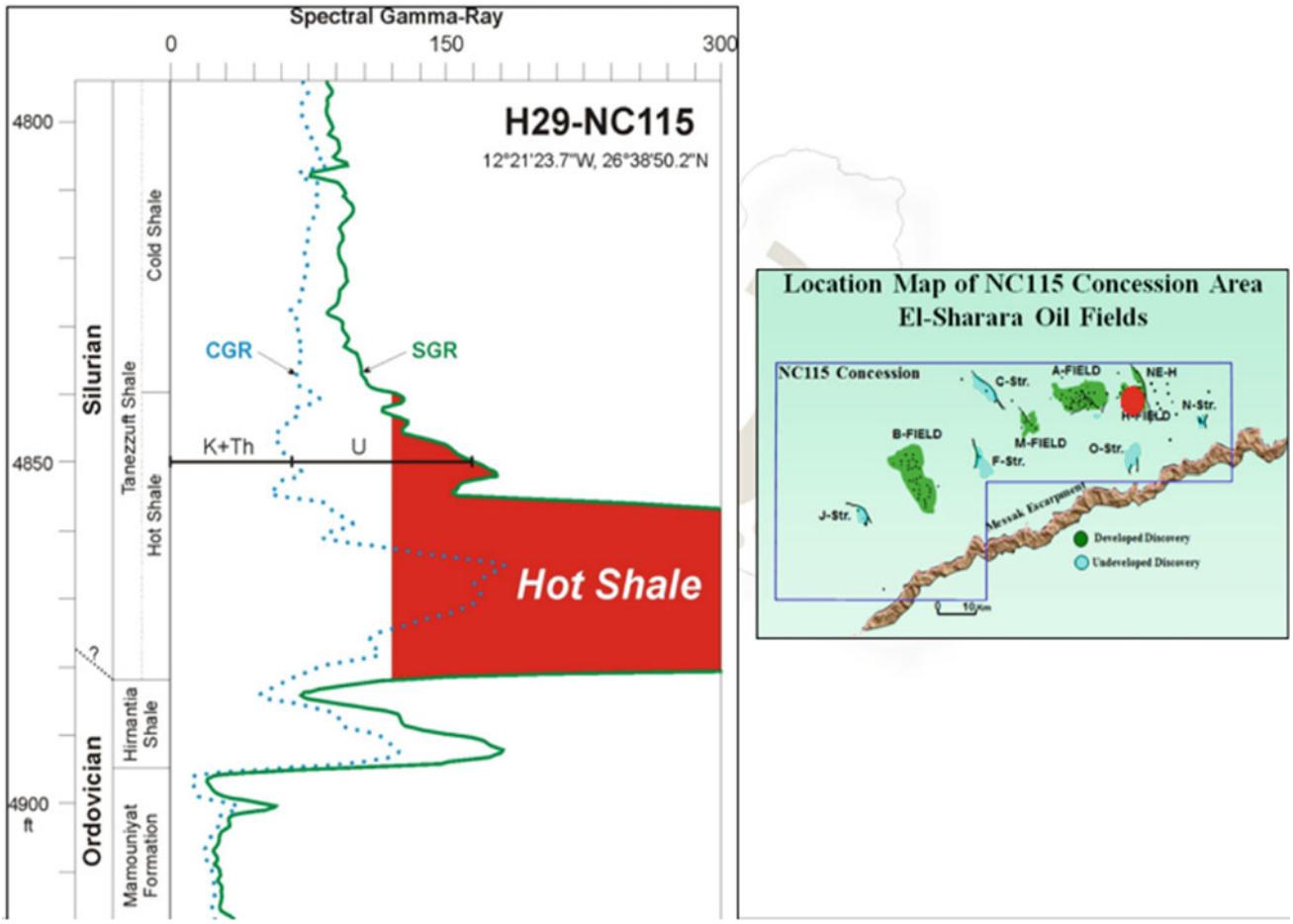

Fig. 4 Spectral gamma-ray data of the lowermost Silurian, called (lower hot shale) in typical well H29-NC115 located in NC115, Murzuq Basin, SW Libya

weathering under arid climate conditions has commonly destroyed the organic matter and palynomorphs and, furthermore, has changed the rock colour to red/green/light grey tones.

The technique described in this pilot study from the Ghat outcrop belt may help to compile a larger-scale, multi-section database around the Murzuq Basin to reconstruct large-scale trends in the distribution of the patchy lower Silurian hot shale across the basin. In particular, such outcrop data could allow better source availability/quality predictions in subsurface areas west of the existing well data in the western part of the Murzuq Basin.

The technique is also suitable for the Silurian outcrops along the eastern margin of the Murzuq Basin. Here, however, logistic preparations are substantially greater due to the remoteness of this area. The technique may also help to further clarify the source rock availability question in the Kufra Basin, SE Libya. This suitable Ordovician–Silurian boundary sections would need to be searched for in this basin. Unfortunately, previous fieldwork has shown that such sections are rarely exposed around the Kufra Basin (Lüning et al. 1999).

Acknowledgements We would like to thank the National Oil Corporation (NOC) and Nafusah Oil Operations (NOO) for their support to carry out this study. We are also grateful to Petr Štorch (Geological Institute of the Czech Academy of Sciences, Prague) for biostratigraphic graptolite determinations and discussions.

References

Davidson, L., Beswetherick, S., Craig, J., Eales, M., Fisher, A., Himmali, A., Jho, J., Mejrab, B., Smart, J.: The structure, stratigraphy and petroleum geology of the Murzuq Basin, southwest Libya. In Geological Exploration in Murzuq Basin, pp. 295–320. Elsevier Science BV (2000)

Fello, N.M., Luning, S., Storch, P., Redfern, J.: Identification of early Llandovery (Silurian) anoxic palaeo-depression as the western margin of the Murzuq Basin (southwest Libya), based on gamma-ray spectrometery in surface exposures. GeoArabia **11**(3), 101–118 (2006)

Lüning, S., Craig, J., Fitches, W.R., Gamudi, A., Mayouf, J., Busrewil, A., El Dieb, M., Loydell, D., McIlroy, D.: Re-evaluation of the petroleum potential of the Kufra Basin (SE Libya, NE Chad): does the source rock barrier fall? Mar. Pet. Geol. **16**, 693–718 (1999)

Lüning, S., Archer, R., Craig, J., Loydell, D.K.: The Lower Silurian 'Hot Shales' and 'Double Hot Shales' in North Africa and Arabia. In: Salem, M.J., Oun, K.M., Seddiq, H.M. (eds.) The Geology of Northwest Libya (Ghadamis, Jifarah, Tarabulus and Sabratah Basins), vol. 3, pp. 91–105. Earth Science Society of Libya, Tripoli (2003)

Seilacher, A., Lüning, S., Martin, M.A., Klitzsch, E., Khoja, A., Craig, J.: Ichnostratigraphic correlation of Lower Palaeozoic clastics in the Kufra Basin (SE Libya). Lethaia **35**, 257–262 (2002)

Assessing Net Rock of Oil Reservoirs by Combining the Morphology of Geological Units and Simulated Images of Rock Types: A Case Study

Lamia Boussa, José Almeida, Amar Boudella, and Zahia Benaissa

Abstract

The spatial characterization of the net rock index (volume of rocks with potential for hydrocarbon storage) in oil reservoirs is very important because it allows differentiating between the zones with higher and lower productive potential in a single image. In this case study, a geostatistical workflow encompassing sequential indicator simulation (SIS) method was applied on real data, and the net rock index was constructed at the end by combining the thickness of the reservoir geological units and the likelihood of occurrence of lithologies with medium–high porosity and permeability such as the sandstones. The resulting net rock image correctly combines the available seismic and well data and balance the local and regional uncertainty of the studied reservoir volume.

Keywords

Geostatistics • Sequential indicator simulation (SIS) • Rock types • Uncertainty • Spatial resolution

1 Introduction

Reservoir characterization and flow studies require accurate inputs of petrophysical properties such as porosity, permeability, water and residual oil saturation, and capillary pressure functions (Archer 1986). All these parameters are necessary to evaluate, predict, and optimize the production of a reservoir.

This study summarized the construction of a net rock aerial map by combining stochastic simulation of rock types (Almeida 2010) and processed seismic data. In this case study, seismic data were previously interpreted and allowed to model at high spatial resolution the top and bottom surfaces of the potentially productive reservoir units. Well data allowed the construction of a 3D model of lithologies (rock types) within the previously delimited geological units procured from seismic interpretation. For the construction of the 3D model of rock types, a geostatistical workflow encompassing the modelling of experimental variograms and sequential indicator simulation (SIS) was used (Journel and Albert 1988). The geostatistical methodologies of stochastic simulation such as SIS enabled the generation of several realistic scenarios of a categorical variable, such as rock types, within a volume, thus facilitating the association of local probabilities of occurrence of each rock type (Almeida 2010; Caers 2011).

2 Methods

In the present work, an aerial image of net rock was obtained using a stochastic workflow. The initial data consisting of top and bottom surfaces of several reservoir units obtained from seismic studies and rock types at well locations is obtained from composite logs.

The approach involves the following steps:

(1) Generate a 3D grid of blocks within the volume delimited by the top and bottom surfaces of the reservoir units;
(2) Transform the rock type at well locations to an indicator vector variable (Almeida 2010);
(3) Upscale the rock type data from the initial vertical resolution at well data to the size of the reservoir blocks. The result of this upscaling is the probability of a specific length of the well-being of a rock type.

L. Boussa (✉) · A. Boudella · Z. Benaissa
Department of FSTGAT, University of Sciences and Technology Houari Boumediene, BebEzzouar, Algeria

J. Almeida
Department of Earth Sciences and GeoBioTec, FCT-NOVA University of Lisbon, Lisbon, Portugal

M. Meghraoui et al. (eds.), *Advances in Geophysics, Tectonics and Petroleum Geosciences*, Advances in Science, Technology & Innovation, https://doi.org/10.1007/978-3-030-73026-0_135

(4) Compute experimental variograms of the probabilistic values obtained in (3) and fit a theoretical model of variogram (Almeida 2010);
(5) Generate n realizations (images) of rock types by SIS (Almeida 2010; Nunes and Almeida 2010; Quental et al. 2012; Soares 1998);
(6) Evaluate local entropy uncertainty metric (Almeida 2010);
(7) Generate the aerial image of net rock (NR), combining local reservoir units thicknesses (h_{xy}) and probability of each volume (p_{xy}) being a productive rock type, such as sandstone (Archer 1986).

The net rock (NR) of each aerial location (x, y) is computed by $NR_{xy} = h_{xy}.p_{xy}$ where

$$h_{xy} = Z_{xy}^{\text{Top of the reservoir units}} - Z_{xy}^{\text{Bottom of the reservoir unit}}$$

and

$$p_{xy} = \frac{\sum_{iz=1}^{nz}(\text{number of realizations with produtive rock type}/n)}{nz}$$

nz number of blocks in the vertical location (x, y).

3 Results

3.1 Reservoir Description and Morphological Model of Geological Units

The proposed methodology was applied on real data to generate an aerial image of the net rock index of a complex and heterogeneous tight reservoir in Algeria.

This reservoir is a sandstone sequence of Ordovician age deposited during glacial conditions. Composite logs from 15 wells drilled into the formation were used in this study.

The geological model interpreted from the seismic study involves four main units of Ordovician reservoir; each unit is subdivided on four main facies (shale, sandstone, mudstone and siltstone). The relationships between sub-units and facies have been established based on lithology extracted from the data analysis of well logs of each well.

A large reservoir grid of the blocks was generated in accordance with the top and bottom surfaces of the geological units. The size of each grid block is 300 by 300 m in the horizontal direction and 20 m in the vertical direction.

3.2 Stochastic Model of Rock Types by SIS

Well data rock types (shale, sandstone, mudstone and siltstone) were coded as indicator variables and then upscaled to the vertical resolution of the grid (20 m).Thus, the indicator variables were converted into probabilities of belonging to each rock type. The predominant rock type was sandstone, followed by shale, mudstone, and siltstone, the last two with minor proportions.

Experimental multiphase variograms of the rock types proportion variables were calculated for horizontal and vertical directions, and theoretical models were fitted (see Fig. 1). A significative anisotropy of 16.47 was obtained between horizontal and vertical ranges. The horizontal variogram is of poor quality due to the small number of wells (Fig. 2).

After fitting the variograms theoretical models, 100 realizations of rock types were produced by SIS for the reservoir region delimited by the seismic study. Each simulated image of rock types honours the variogram model, the experimental proportions of the rock types and the well data itself (Almeida 2010; Quental et al. 2012). The set of simulated images enabled the calculation of a local uncertainty measurement, and thus, the entropy metric was computed. Figure 3 shows two simulated images (scenarios) of the

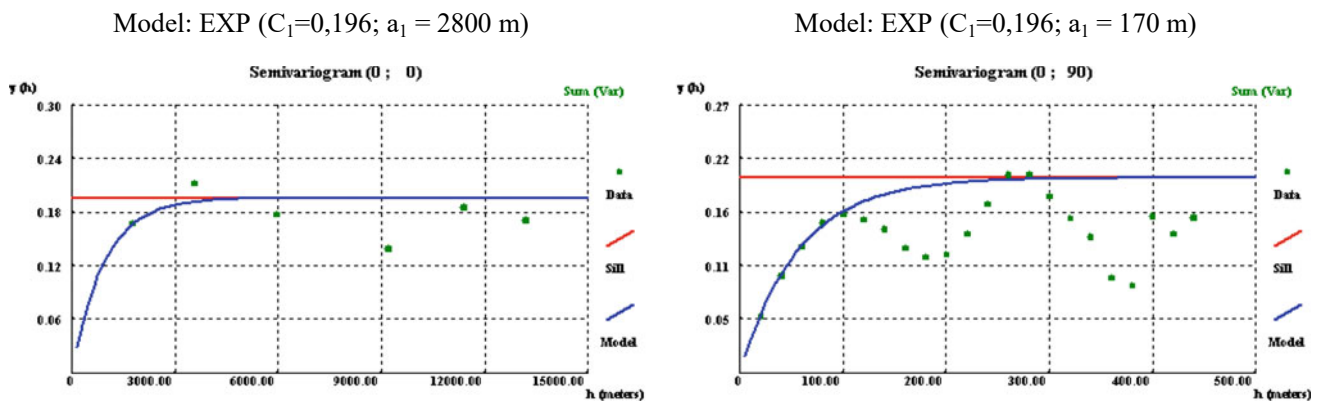

Fig. 1 Horizontal and vertical multiphase variograms of the rock types and theoretical models

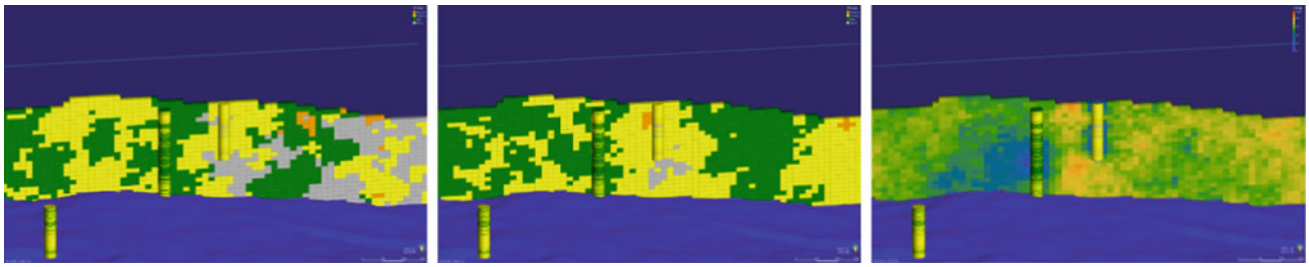

Fig. 2 Two simulated scenarios of rock types of an intermediate cross section and the entropy metric of uncertainty (images from Leapfrog Geo, v4.5)

rock types in an intermediate cross section and the wells nearby with rock types at the small scale. It was possible to confirm the match between the well data and the simulated images.

3.3 Generation of the Aerial Net Rock Image

To produce the final aerial net rock image, two intermediate aerial images were produced and then multiplied, and the first

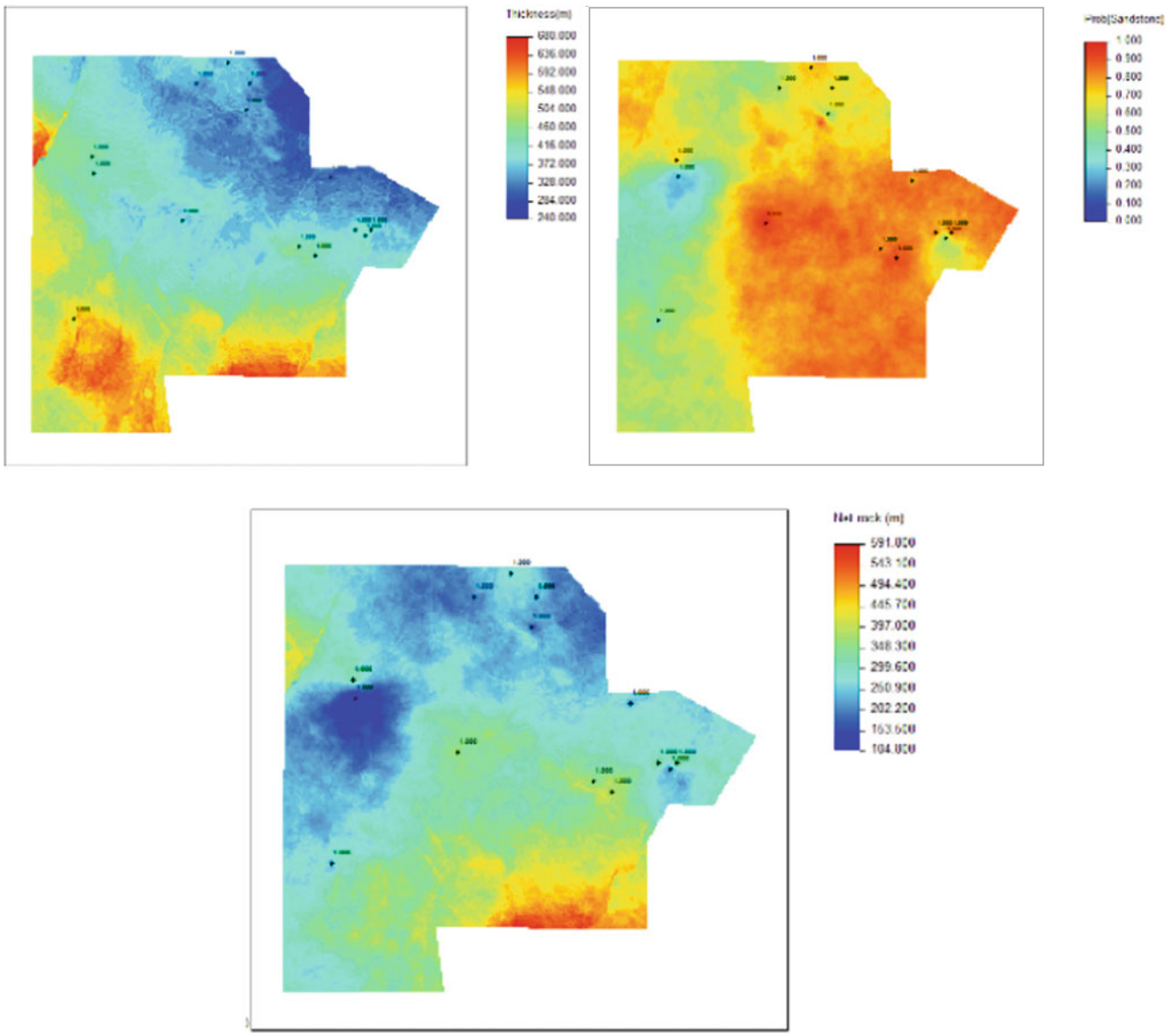

Fig. 3 Aerial images of the reservoir unit thickness, probability of being sandstone, and net rock index

image is the thickness of the reservoir units, and the second image is the probability of a specific location being of rock type sandstone. The thickness of the reservoir units was locally computed subtracting the top and the bottom Z coordinates of the unit surfaces derived from the seismic data. The probability of a specific location being of rock type sandstone was computed from the rock type simulations (see methods).

The net rock index image displays the potential quality of the reservoir and combines thickness with probability of being sandstone. The higher both variables are, the better the reservoir formation is. Figure 3 shows the aerial image of the thickness, the aerial image of the probability of being sandstone, and the product of both variables.

The images of Fig. 3 highlight the large area of the studied reservoir formation and the relatively small number of wells. The top/left image shows that the thickness of the reservoir is higher in southern areas than in the northern ones, and the structural accidents can be seen very clearly. The top/right image shows higher probability values on the right than on the left, but overall the probability of being sandstone is in average high, due to the high experimental proportion of 70%. The combination of both images highlights a bottom right region as a good reservoir; however, this is rather speculative due to lack of well data.

4 Conclusions

The results obtained inspire the continuation of the work by applying geostatistical tools suitable for the evaluation of geological uncertainty with the integration of petrophysical data. This is in order to further understand the intricacies of the methods and the impact of the technique on the resulting uncertainty profile.

Acknowledgements This paper is the contribution to GeoBioTec/NOVA (UID/GEO/04035/2019). The authors would like to express their gratitude to SEEQUENT - Owners of LeapfrogGeo software 3D based in Implicit modelling, and the geologist Carlos Alonso for his support and permission to use LeapfrogGeo®.

References

Almeida, J.A.: Stochastic simulation methods for characterization of lithoclasses in carbonate reservoirs. Earth-Sci. Rev. **101**(3–4), 250–270 (2010)

Archer, J.S.: Petroleum Engineering. Springer, Dordrecht (1986)

Caers, J.: Modeling Uncertainty in the Earth Sciences. Wiley (2011)

Journel, A.G., Albert, F.G.: Focusing on spatial connectivity of extreme valued attributes: stochastic indicator models of reservoir heterogeneities. SPE paper 18324 (1988)

Nunes, R., Almeida, J.A.: Parallelization of sequential Gaussian, indicator and direct simulation algorithms. Comput. Geosci. **36**(8), 1042–1052 (2010)

Quental, P., Almeida, J.A., Simões, M.: Construction of high-resolution stochastic geological models and optimal upscaling to a simplified layer-type hydrogeological model. Adv. Water Resour. **39**, 18–32 (2012)

Soares, A.: Sequential indicator simulation with correction for local probabilities. Math. Geol. **30**(6), 761–765 (1998)

Wellbore Stability Analysis Based on 3D Geo-Mechanical Model of an Algerian Southeastern Field

Said Eladj, Tanina Kenza Lounissi, Mohamed Zinelabidine Doghmane, and Mabrouk Djeddi

Abstract

The main objective of this study was to analyze wellbore stability of wells based on 3D geo-mechanical model obtained using seismic inversion in an Algerian South Eastern Field. The correlation between the inversion model and logging data was very good. Thus, the constructed geo-mechanical model was used to analyze the stability of the four drilled wells and propose the drilling mud weight window for well-5 that is going to be drilled. The reliability of the 3D geo-mechanical model allowed the optimization of drilling mud weight parameter so that stability of wellbore was ensured on the one hand, and reservoir damage was avoided, on the other. It is highly recommended to use the obtained model to propose new wells (like well-5 in this case study) and minimize exploration uncertainties in the region.

Keywords

Seismic inversion • 3D Geo-mechanical model • Wellbore stability analysis • Algerian field • Mud weight window

1 Introduction

Drilling wells is one of the steps of exploring new hydrocarbon fields. During the process, the drillers cross several formations with different rock properties, therefore, the drillers have to be cautious to ensure the stability of the well and avoid its collapse due to differential pressure variation. The best method is to have control over the drilling mud density that balances the well (McLean et al. 1990). The chosen field for this study is located in the South East of Algeria. The study included a seismic inversion and the construction of a geo-mechanical model was conducted. The first part consists of inverting the seismic data before summation in order to highlight the different lithologies, and thus to better understand the reservoir (Quogue et al. 2012). The AVO seismic inversion model was built using the iterative method of *Aki and Richard*, in which the wavelet is extracted using *Roy White* technique, volumes of Acoustic impedance, *Vp/Vs* ratio, and density have been obtained, the correlation values between the obtained model and logging data of the four existing wells ranged from 72 to 85%. The second part was for 3D geo-mechanical model construction (Trading et al. 2014); it was used to analyze the wellbore stability in order to carry out a new drilling and determine its preferential direction. Thus, it would minimize the drilling costs by mitigating drilling incidents and avoid reservoir damage by estimating the optimum density of drilling mud (McLean et al. 1990; Doghmane et al. 2019).

2 Seismic Inversion

The study was carried out using the seismic data. It contains four (4) cubes with four (4) different stack angles: 5–10°, 10–20°, 20–30°, 30–40°. Four (4) wells were drilled in the field. Eight (8) seismic horizons were defined: (1) *Maastrichtian*, (2) *Campanian*, (3) *Santonian*, (4) *Coniacien*, (5) *Turonian*, (6) *Cenomanian*, (7) *Albian*, and (8) *Aptian* (Doghmane et al. 2014). The good correlation between seismic inversion for density and density logs is shown in Fig. 1.

S. Eladj (✉) · T. K. Lounissi · M. Djeddi
University M'hamed Bougara of Boumerdes, labophyt, 35000 Boumerdes, Algeria
e-mail: s.eladj@univ-boumerdes.dz

M. Z. Doghmane
Department of Geophysics, FSTGAT, University of Sciences and Technologies Houari Boumediene, 16000 Bab Ezzouar, Algiers, Algeria

M. Meghraoui et al. (eds.), *Advances in Geophysics, Tectonics and Petroleum Geosciences*, Advances in Science, Technology & Innovation, https://doi.org/10.1007/978-3-030-73026-0_136

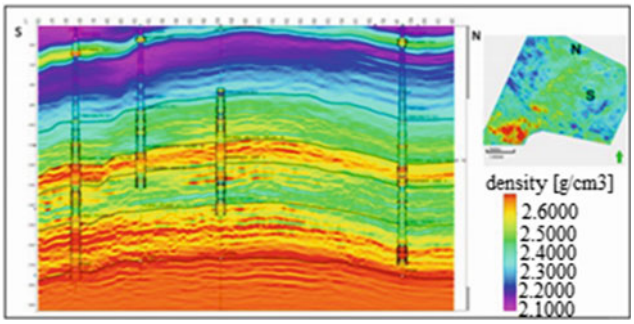

Fig. 1 Seismic inversion result for the density model

3 Reservoir Characterization

The characterization of the reservoir in terms of fluid content and lithological indication is a secondary objective; the main objective was to use the inversion results to construct a 3D geo-mechanical model (Quogue et al. 2012, 2014). Nevertheless, the reservoir is characterized by using the results provided by (Doghmane et al. 2014; Gironde et al. 2014); the lithology is defined for clay: *if Vshale > 0.2*, Tight Limestone: *if Vshale < 0.2 and PHI < 0.05*, Porous limestone: *if Vshale < 0.2 and PHI > 0.05*. Figure 2 shows the lithology cube generated using these conditions; and this model is used in determining the mud weight window selection.

4 Geo-Mechanical Modeling

In this study, 7 simulations were required to find the best correlation between the estimated data and the well data. The simulation aimed at modeling the distribution of the vertical, horizontal stresses as given in Fig. 3. Taking into account these stresses and the structures resulting from the seismic data interpretation, the optimum direction and orientation of new wells can be determined (Gray et al. 2012).

5 Well Design and Results Discussion

The usefulness of 3D geo-mechanical modeling and wellbore stability analysis was to determine the preferential direction of well-5 and determine the ideal mud density to minimize damages (Quogue et al. 2012). Figure 4 demonstrates the results of windows construction for the four existing wells. The constructed 3D geo-mechanical model allows us to estimate the mud density window to be used for well-5, where:

- **Gray block**: represents the values of the pore pressure, if it is higher than the density of mud a Kick could occur. The Kicks correspond to the shelling of the walls of the wells.
- **Yellow block**: represents the Shear Failure or Breakout. This occurs when the sludge density is below the maximum in-situ stress.
- **Light blue block**: represents the Fracture gradient due to the minimum horizontal stress in-situ. When the mud density is higher than the latter, this will lead to open the natural fractures.
- **Dark blue block**: Fracture limits called Breakdown. This occurs when the sludge density is greater than the maximum horizontal stress.

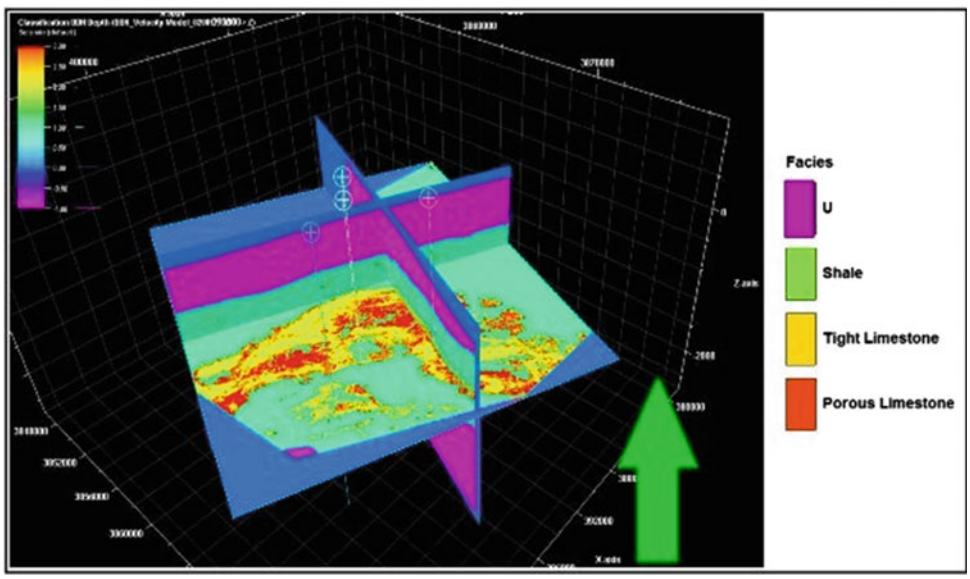

Fig. 2 Lithology classes for the whole seismic volume

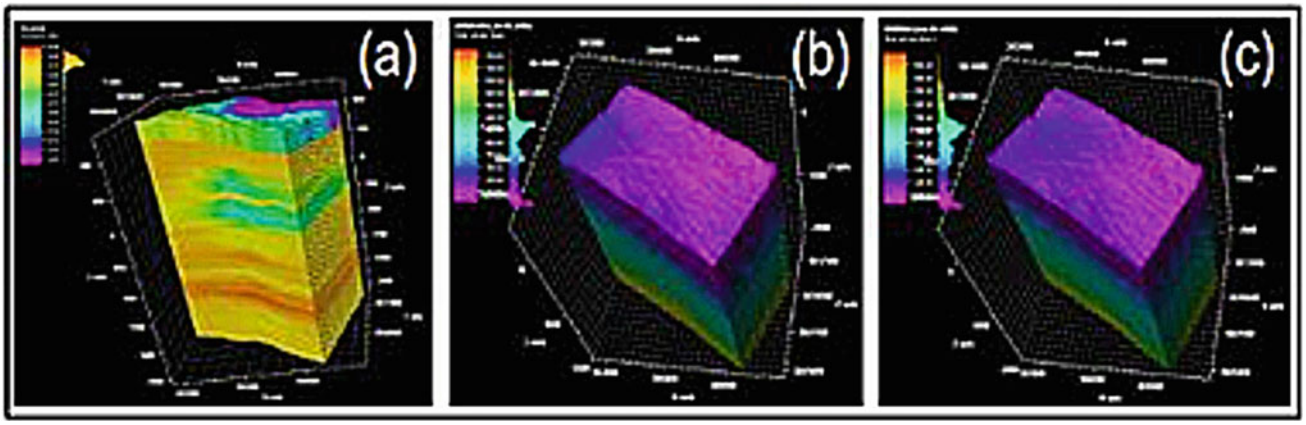

Fig. 3 Results of: **a** vertical stresses, **b** horizontal stress max, **c** horizontal stress min

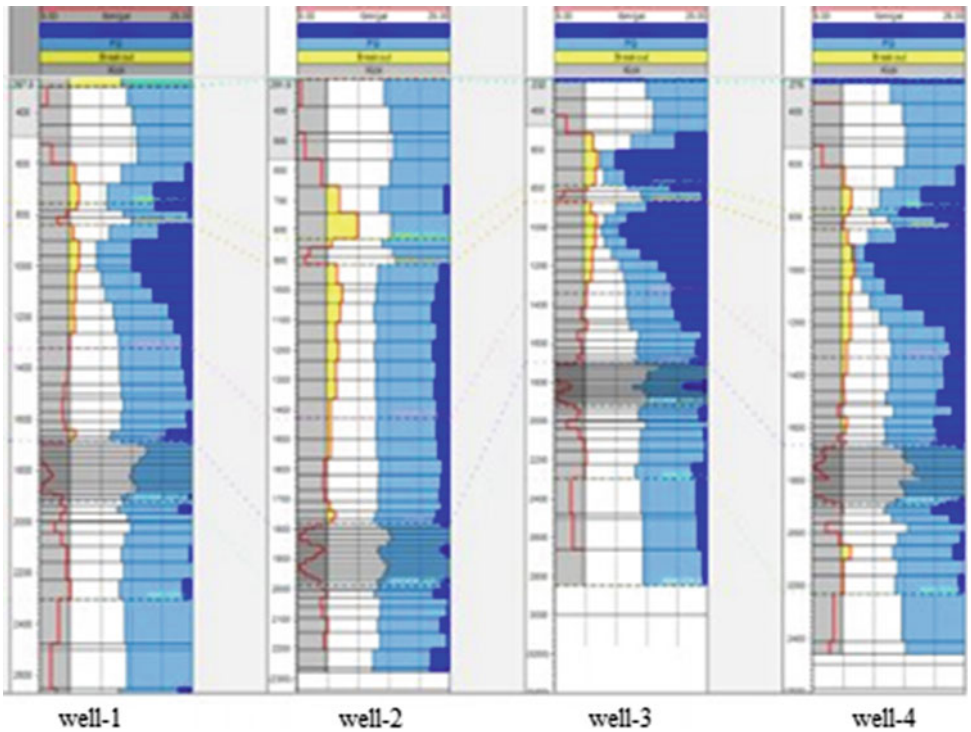

Fig. 4 Mud weight window for the four existing wells of the studied field

6 Conclusions

Based on the results of this study, mud density windows were designed for each drilling phase of well-5. The main novelty was to avoid damaging the borehole and creating artificial fractures (Quogue et al. 2012), where for *Maastrichtian* (0–600 m MD): MW = 1.05 g/m3 (WBM). For *Maastrichtian-Companion-Santonian* (600–1200 m MD): MW = 1.23 g/m^3 (OBM). For *Coniacian* (1200–1681 m MD): MW = 1.05 g/m^3 (OBM). For *Turonian-Cenomanian* (1681–2000 mMD): MW = 1.05 g/m^3 (OBM). These values will ensure the wellbore stability without damaging the reservoir at the level of well-5.

References

Doghmane, M.Z.: Classification Automatique des Faciés en Utilisant les Algorithmes d'intelligence Artificiels, Magister Thesis. The Algerian Petroleum Institute Boumerdes, Algeria (2014)

Doghmane, M.Z., Belhacen B., Kidouche M.: Application of Improved Artificial Neural Network Algorithm in Hydrocarbons' Reservoir Evaluation. In: Hatti M. (eds) Renewable Energy for Smart and Sustainable Cities. Lecture Notes in Networks and Systems 62.

Springer, Cham, 129–138 (2019). https://doi.org/10.1007/978-3-030-04789-4_14

Fernando, A.N., Al-Maroon, A., Jung, J.K., Nebrija, E.L.: Fracture characterization of deep tight gas sands using azimuthal velocity and AVO seismic data in Saudi Arabia. Lead. Edge **22**(5), 469–475 (2003). https://doi.org/10.1190/1.1579581

Gironde, L., Willock, B., Rodriguez-Herrera, A., Koutsabeloulis, N., Lowden, D.: Applications of broadband seismic inversion in the assessment of drilling and completion strategies: a case study from eastern Saudi Arabia. In: SEG Technical Program Expanded Abstracts, 3153–3156 (2014). https://doi.org/10.1190/segam2014-1358.1

Gray, D., Anderson, P., Logel, J., Welbeck, F., Schmidt, D., Schmidt, R.: Estimation of stress and Geomechanical properties using 3D seismic data. J. Name First Break **30**(3), 59–68 (2012). https://doi.org/10.3997/1365-2397.2011042

McLean, M.R., Addis, M.A.: Wellbore Stability: The Effect of Strength Criteria on Mud Weight Recommendations. SPE Annual Technical Conference and Exhibition, 23–26 September. New Orleans Louisiana, USA (1990). https://doi.org/10.2118/20405-MS

Quogue, L., Zhang, X., Al-Grammar, K. S., Labia, M.: 3-D Geomechanical Modeling and Wellbore Stability Analysis in Abu Babul Field. Abu Dhabi International Petroleum Conference and Exhibition, 11–14 November 2012 Abu Dhabi, UAE (2012). https://doi.org/10.2118/159091-MS

Trading, T., Garcia-Teixeira, X., Rodriguez-Herrera, A. and Khazanehdari, J.: Using Stochastic Seismic Inversion as Input for 3D Geomechanical Models. IPTC: International Petroleum Technology ConferenceEAGE (2014)

Vertical Movements and Petroleum System Modelling in the Southern Chotts Basin, Central Tunisia

Pierre-Olivier Bruna, Giovanni Bertotti, Salma Ben Amor, Ahmed Nasri, and Sondes Ouahchi

Abstract

The southern Chotts basin (SCB), Central Tunisia, has shown hydrocarbon potential since the end of the 1980s. This basin records a complex structural history which appears decoupled at the Hercynian or Variscan unconformity. The Paleozoic series is deformed by short to medium wavelength folds (kilometres-multi kilometres scale) and by steep normal faults. The Mesozoic series is largely less deformed. The evolution of the basin through time is still a matter of debate as the preserved Paleozoic series is fragmented (e.g. affected by erosions). In this paper, we proposed a reconstruction of the vertical movements affecting the basin and an evaluation of their magnitude. Using basin modelling techniques, we provided new insights on the possible thermal evolution of the basin that might be used in the future exploration phases. This study was completed by structural restorations allowing the reconstruction of the paleogeography of the basin at the time of deposition of principal reservoir formations.

Keywords

Southern Chotts basin • Vertical movements • Basin modelling • Structural restoration • Fractures

P.-O. Bruna (✉) · G. Bertotti
Department of Geoscience and Engineering, Delft University of Technology, Delft, The Netherlands
e-mail: p.b.r.bruna@tudelft.nl

S. B. Amor
Mazarine-Energy B.V, Lange Voorhout 31-33, 2514 EC The Hague, The Netherlands

A. Nasri · S. Ouahchi
Mazarine-Energy Tunisia, Rue de la Bourse, Zenith Building, 1053 Tunis, Tunisia

1 Introduction

The southern Chotts basin (SCB) is located in Central Tunisia, about 140 km southwest of the Gulf of Gabes. This area is a proven prolific oil and gas province since the early 1980s. In this area, the most important and productive reservoirs are located in the Ordovician mixed sandstone and siltstones of the El Atchane and of the Hamra formations and in the Triassic sandstone of the TAGI unit (Trias Argilo-Gréseux Inférieur), (Mejri et al. 2006). The principal source rock feeding these reservoirs is the Late Silurian to Early Devonian shale and siltstone of the Fegaguira Formation (Soua 2014). The Fegaguira shales also acts as a caprock for the Ordovician reservoir system. For the TAGI, the overlying Triassic anhydrites and salt are considered as the main reservoir caprock. The nature of the traps in the Ordovician is mainly of structural origin (system of horst and graben), whereas traps are more of stratigraphic origin for the TAGI (fluvial staked systems).

2 Geological Setting

Between the Cambrian and the Cretaceous, the SCB underwent a complex and polyphased tectonic history resulting in contrasted basin architecture before and after the so-called Variscan unconformity. Seismic data in the Pre-Variscan package showed folding of various wavelengths and a variable faulting intensity within the SCB. Between the Cambrian and the Permian, extensional tectonics and large scale inversions took place and resulted, respectively, in: the onset of an arch and basin configuration (Lüning et al. 2005) and (ii) major uplift phases marked by successive internal erosion within the Paleozoic series. The Post-Variscan package is quieter and displays a layer-cake configuration. Between the Jurassic and the Early Cretaceous a long phase of continuous subsidence occurred.

M. Meghraoui et al. (eds.), *Advances in Geophysics, Tectonics and Petroleum Geosciences*,
Advances in Science, Technology & Innovation, https://doi.org/10.1007/978-3-030-73026-0_137

3 Results

3.1 1D Subsidence and Basin Analysis

The present study focused on the evaluation of the timing and magnitudes of vertical movements affecting the SCB. A series of subsidence curves (based on an extensive literature synthesis and on seismic observations) was created based on 14 petroleum wells. The comparison of the subsidence curves (Fig. 1) showed a relatively stable subsidence history throughout the basin but a variable magnitude of the vertical movements from one well to another.

In addition, a 1D basin modelling was performed based on 6 of the 14 selected wells. This modelling used the geological history obtained from the subsidence curves. To complete these data, the geochemical properties of the principal source rocks were gathered from literature and from sampling and analyses available from the wells. The sediments-water interface conditions were obtained from Wygrala (1989) algorithms. The present-day heat flow was calibrated using the corrected bottom hole temperature, and multiple scenarios were proposed for the paleo heat (calibrated using vitrinite reflectance dataset). The results of our models allowed separating two groups of wells: (i) in wells 3, 8 and 9, the oil window is attained at the end of the Jurassic and (ii) in wells 5, 6 and 7, the oil window is entered at the beginning of the Devonian (to be related with the onset of the Caledonian uplift). Based on these results, we found that the Fegaguira formation is mature and started to produce hydrocarbon earlier than the Devonian and at least during the Jurassic. The migration occurred after these periods and probably at the beginning of the Paleocene (Kraouia et al. 2019).

3.2 2D Restoration

Sequential structural restorations based on 16 regional seismic transects permitted evaluating the structural style of the deformation observed in the area of interest and evaluated the initial amount of TAGI and Early Ordovician sediments deposited in the basin. Whilst compared with the present-day depth maps of the TAGI and Ordovician reservoir, the paleo-topographic maps revealed local vertical movements of the basin (Fig. 2).

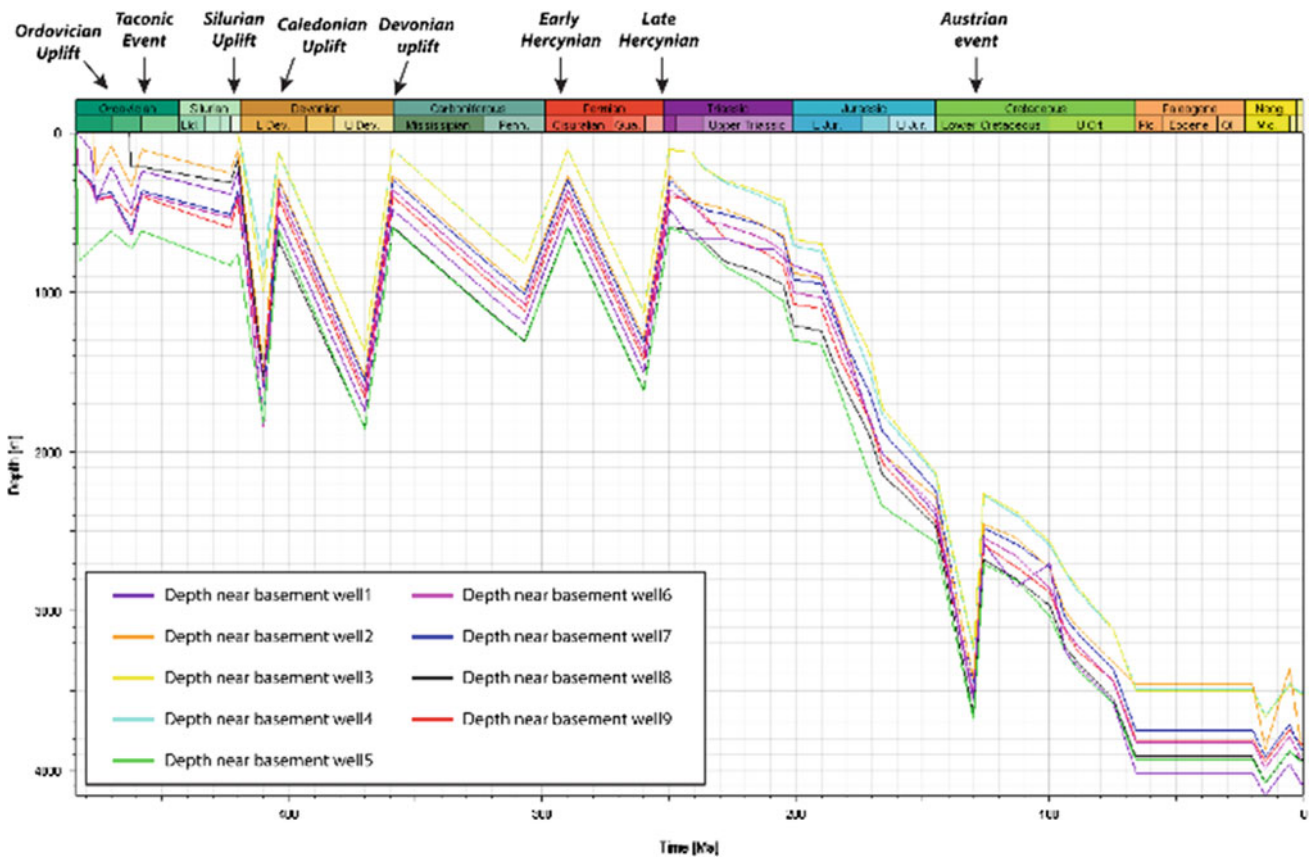

Fig. 1 Compared burial curves in wells located in the western part of the southern Chotts basin

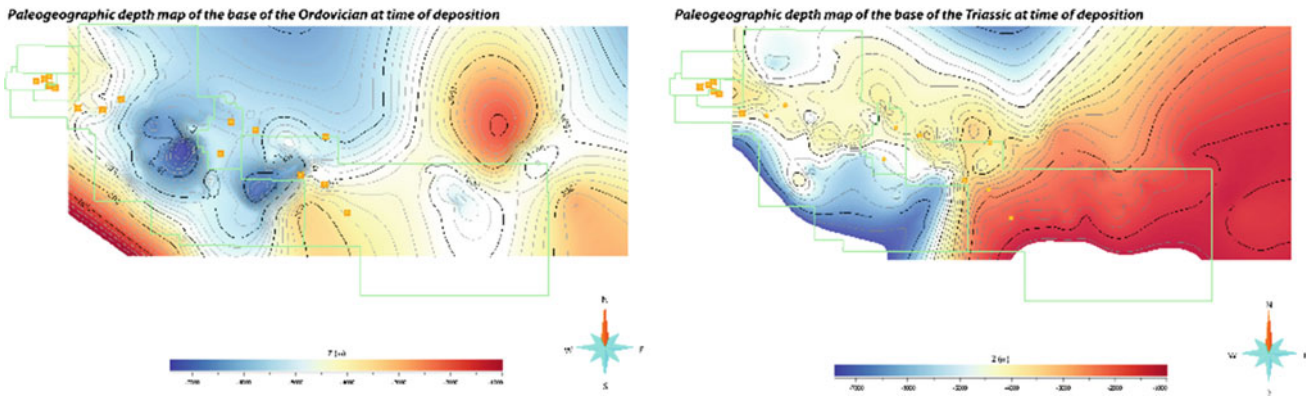

Fig. 2 Base of the Ordovician (left-hand side) and of the Triassic packages (right-hand side)

4 Discussion and Perspectives

The reconstructed subsidence history allowed proposing a possible renewed scenario of the vertical movements affecting the area of interest especially during the Paleozoic. Uncertainties about the burial history remain related to the timing of deposition and erosion phases. This has potential implications for petroleum system maturity and therefore for future exploration planning. A campaign of sampling for apatite fission track analyses (AFTA) conducted in selected wells and outcrops of the Jeffara escarpment are planned to be conducted in the coming months. These thermo-chronological data will greatly help to validate or adjust our structural history and to link it with the thermal maturation of the hydrocarbon systems in the SCB.

The sequential restoration allowed building paleogeographic maps showing the geometry of the basin at the time of deposition of the Ordovician and Triassic packages. The present-day base of the Ordovician show a high topography in the southern part of the model. The paleogeography of the Triassic highlighted the presence of a high (anticline) parallel to the Telemzane Arch and separated from it by a relative low (syncline?). This geometry has a strong implication for sand filling and provenance and will allow reducing the number of hypotheses concerning the dynamic of the sedimentary system in this area. For the future, 2D basin modelling (using PetroMod software) could be performed to evaluate the migration path within the basin and eventually evaluate where sweets spots can be located.

The perspective of this study is focused on natural fractures characterisation and on the establishment of the link between the large scale vertical movements and the small scale deformations. The Ghrib block, located in the western part of the area of interest, was chosen as a pilot to build discrete fracture network models of the Early Ordovician and Triassic reservoirs. The paleo-topographic reconstruction demonstrated that the area was located on the limb of an arch structure (during the Ordovician) and in a synclinal structure (during the Triassic). Consequently, these zones might be affected by different fracture types which can be related to variable strain conditions. During the same AFTA campaign, fracture analysis (geometrical characterisation, dating) will be performed in outcrops presenting similar configurations to evaluate the possible analogy between the Jeffara escarpment and the subsurface.

5 Conclusions

In this study, a combination of 1D basin modelling and 2D structural restorations was used to get new insights on the petroleum system history of the SCB. The 1D basin modelling served to test different scenarios of tectonic history and evaluate their impact on the thermal evolution of the SCB petroleum system. The restoration of the basin geometry was used to locate vertical movements' anomalies and evaluate the initial thicknesses of the Ordovician and Triassic reservoirs at the time of their deposition. Ongoing research aims to improve the preliminary results of this research on a large scale and to offer a better small scale structural characterisation in the SCB.

References

Kraouia, S., Mabrouk El Asmi, A., Ben Salem, A., Saidi, M.: Geopetroleum evaluation of the ordovician and triassic reservoirs in the Southern Part of Chotts Area (Southern Tunisia) and maturity modeling. In: Advances in Petroleum Engineering and Petroleum Geochemistry: Proceedings of the 1st Springer Conference of the Arabian Journal of Geosciences (CAJG-1), pp. 153–159 Tunisia (2018)

Lüning, S.: AFRICA|North African phanerozoic. In: Selley, R.C., Cocks, L.R.M., Plimer, I.R. (eds.) Encyclopedia of Geology, pp. 12–25. Elsevier, Oxford (2005)

Mejri, F., Burollet, P.F., Ben Ferjani, A.: Petroleum geology of Tunisa. Entreprise Tunisienne d'Activites Petrolieres (ETAP), Tunis (2006)

Soua, M.: Paleozoic oil/gas shale reservoirs in southern Tunisia: an overview. J. Afr. Earth Sci. **100**, 450–492 (2014)

Wygrala, B.P.: Integrated Study of an Oil Field in the Southern Po Basin, p. 217. University of Cologne, Cologne, Germany, Northern Italy (1989)

Salt Tectonics and Mineralization Processes in NE Algeria

Azzedine Bouzenoune

Abstract

In Tebessa area (NE Algeria) many extrusions of Triassic evaporites outcrop; they constitute privileged diapiric structures for mineral and oil exploration. These evaporites consist of a saliferous core (halite, sulfates, carbonates) surmounted by anhydritic and gypsiferous breccia formation. These extrusions are hosted in a thick (>6 km) sedimentary series, essentially clay-marly, with episodically carbonates. This lithostratigraphic arrangement has induced a polyphased salt tectonic. All the recent research findings have highlighted the close relationship between this salt tectonic and the genesis of mineralizations. The role of these structures in the evolution of the sedimentary basin dynamics has been revealed through several ways. From a sedimentological point of view, they have controlled the nature of the microfacies, while from a mechanical point of view they created the traps by fracturing and emersions they induced. On a chemical level, they supply sulfur and probably ores. As a heat source, they control the disposition of the isotherms and mineralizing fluids circulation.

Keywords

Salt tectonic • Diapir • Evaporite • Mineralizations • Tebessa

1 Introduction

The outcrops of Triassic evaporates in Tebessa region (northeastern Algeria) constitute diapiric structures (Aoudjehane et al. 1991) resulting from polyphased salt tectonics (Fig. 1). The economic importance of these structures was demonstrated both in Gulf Coast (U.S.A.) and in North Africa. Apart from the salt (NaCl) and sulfur, they also contain numerous polymetallic mineral concentrations of Fe, Pb–Zn, Cu, Ba, Sr, F. These structures also comprise hydrocarbons, particularly in the United States, and thus constitute privileged targets (Rouvier et al. 1985; Pohl et al. 1986; Kyle and Saunders 1996). This research focused on showing the polyphased salt tectonics directly or indirectly involved in the lithostratigraphic, sedimentological and structural history of the sedimentary basin as well as the ore mineralization genesis.

2 Geological Settings

Tebessa region consists of Triassic to Quaternary rocks. However, the Jurassic outcrops are missing (Fig. 2). The total thickness of the series exceeds 6 km, reflecting a strong subsidence especially during the Mesozoic (Dubourdieu 1956). Mainly three evaporate sets constitute the Triassic formations. A lower thick (>200 m) saliferous complex consists mainly of halite, anhydrite and magnesite (Bouzenoune 1993; Bouzenoune et al. 1995). A chaotic clay-gypsiferous upper formation constitutes all the outcrops of the region with a thickness traversed by borehole that can be up to 230 m. Anhydritic formation, absent as outcrop, was intersected only by borehole over a thickness of about twenty meters: it also includes polygenic breccias with mainly dolomitic elements.

The Cretaceous formations are dominated by clay-sandstone sedimentation for the lower Cretaceous and clay-marl for the Late Cretaceous with a significant episodic appearance of carbonate, particularly during the Aptian and Turonian. Thinner carbonate levels are also known in the Albian and Senonian (Fig. 2). The Cenozoic formations are essentially Paleocene marl overlaid by 35 m thick phosphates; they are carbonates in the lower Eocene and mainly

A. Bouzenoune (✉)
LGG, Jijel University, BP 98, Jijel, Ouled Aïssa, Algeria
e-mail: bouzenoune@univ-jijel.dz

M. Meghraoui et al. (eds.), *Advances in Geophysics, Tectonics and Petroleum Geosciences*,
Advances in Science, Technology & Innovation, https://doi.org/10.1007/978-3-030-73026-0_138

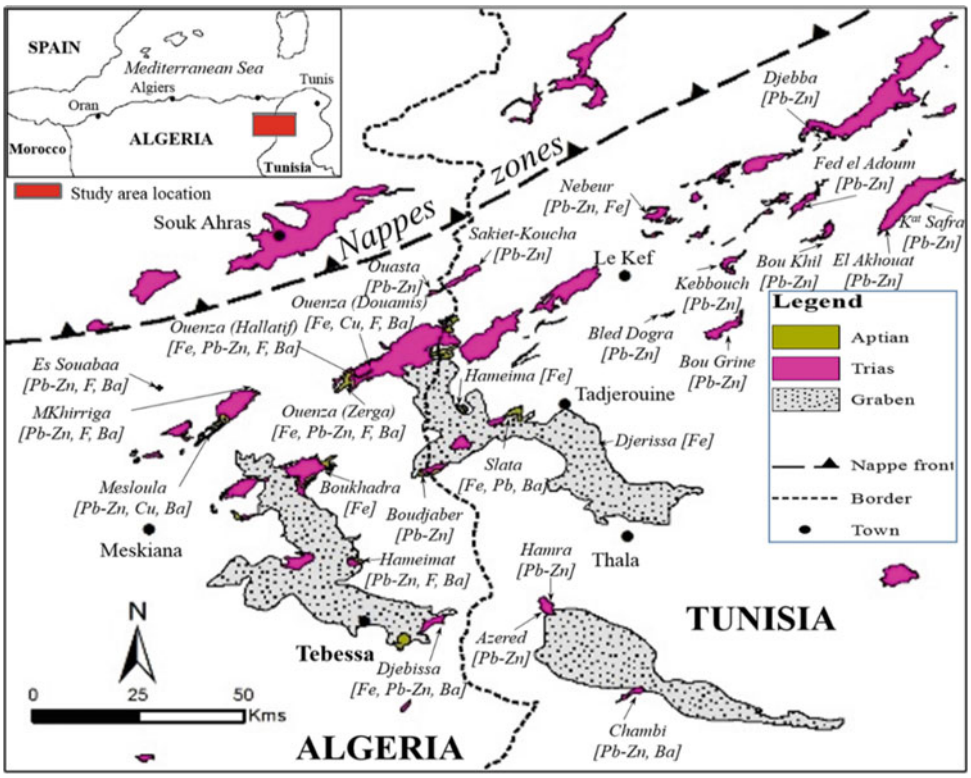

Fig. 1 Schematic geological map showing location of the main mineralization and their spatial relationship with the outcrops of Triassic evaporites

detrital formations in the Neogene. The different tectonic phases that affected this region generated two major tectonic directions (Fig. 1): the first direction NE–SW is materialized by the alignments of Triassic evaporite extrusions, which seem to be controlled by the set of deep accidents involving the ante-Triassic substratum and the orientation of the axes of the main folds generated by the so called Atlasic Eocene phase and complicated by the Miocene phase. The second direction NW–SE is represented by grabens whose bordering accidents are witness of the reactivation of old normal faults delimiting titled blocks as early as the lower Cretaceous (Aoudjehane et al. 1991). The polyphased salt mobilization, at least since the Aptian (Thibieroz and Madre 1976), was favored by the existence of the thick (>200 m) halitic formation (Bouzenoune 1993; Bouzenoune et al. 1995), the presence of deep accidents and the thick Meso-Cenozoic sedimentary series.

3 Mineralization

Two large groups of spatially distinct mineralization can be distinguished. Polymetallic Pb–Zn, Ba, Sr "intradiapiric" mineralization are hosted by Triassic formations in the cortical or "cap-rocks" zones that cover these structures, and Fe, Pb, Zn, Cu, Ba "peridiapiric" mineralization hosted by the sedimentary series covering these salt domes. The second ones are the most important economically.

4 Discussion

The close spatio-temporal relationship between ore deposits and saliferous diapirs (Figs. 1 and 2) reflects the role of multiphase diapirism of Triassic evaporites in the mineralization genesis. This role has been expressed on several levels: petrographic and sedimentological, mechanical, chemical, thermal and hydrological.

4.1 Salt Tectonic and Cap Rock Genesis

The salt domes are usually surmounted by a cortical formation, commonly called "cap-rock", that hosts significant Pb–Zn, Ba, Sr mineralization. The genesis of the different zones of these "cap-rocks," and the associated mineralization are closely linked to the upward movement of the salt-bearing body. The halokinetic intrusion of the halite formation in an unsaturated water seepage zone induced the dissolution of the salt and the accumulation of the insoluble residue consisting mainly of anhydrite and, incidentally, of carbonates, quartz and clay minerals.

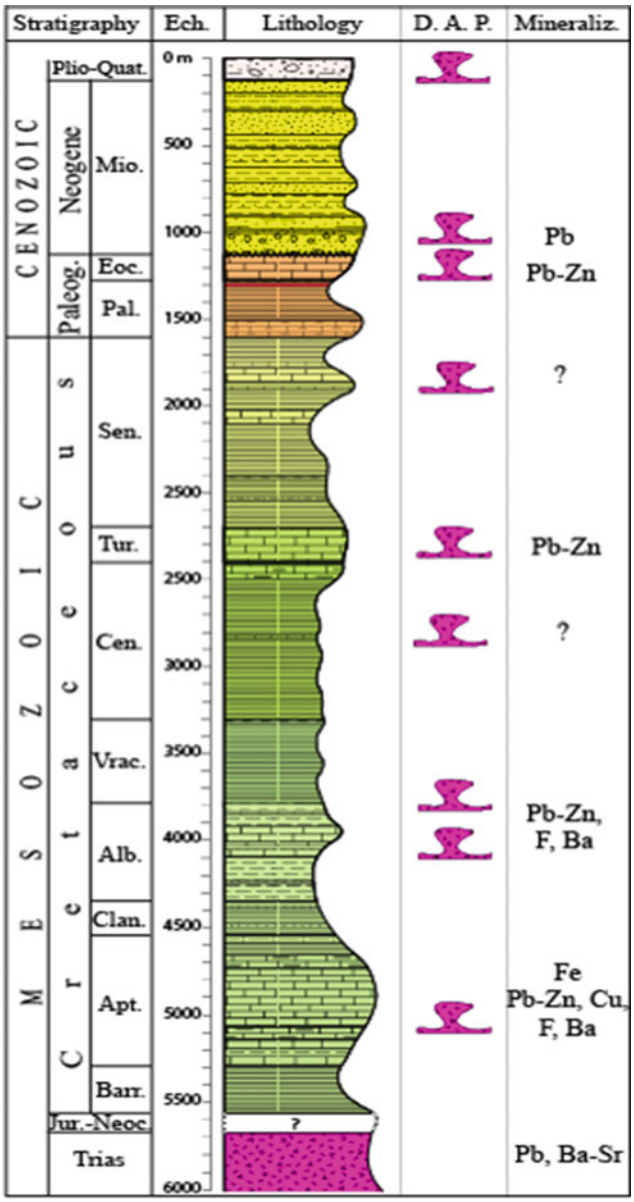

Fig. 2 Lithostratigraphic column showing the main diapiric activity periods and the ages of the host rocks of mineralization

4.2 Control of the Host Rocks Facies

Synsedimentary activity of diapirism, sometimes with extravasations (Aoudjehane et al. 1991), is an important feature that controls depositional carbonate facies hosting mineralization. The calcareous sedimentation is predominant in the proximal zones of the diapiric apices, and progressively leads to more and more clayey sedimentation while moving away from the diapirs. The carbonate rocks, especially Albo-Aptian, hosting mineralization, deposited on high and subsident zones related to the halokinetic rise of Triassic evaporites. Known for their reactive carbonaceous nature with mineralizing fluids, these host rocks, played a direct role in the modification of the pH of the fluids and caused the mineral precipitation.

4.3 Creation of Mineralizations Traps

Polyphased diapiric activity has created two types of traps for mineralization: paleogeographic traps such as discontinuities related to local emersion surfaces and tectonic traps such as fractures in the Albo-Aptian cover. The constraints generated by the halokinesis of Triassic evaporites have generated a multitude of fractures and faults, which gave to the host rocks porosity and permeability favorable to the circulation of the mineralizing fluids, on the one hand, and allowed the traps themselves for mineralization, on the other.

4.4 Source of Sulfur and Metals

The lithological nature of the Triassic evaporites (halite, sulfates, carbonates, clays) is a favorable factor to give the fluids the high salinities necessary for the dissolution and transport of the constituent metals of the minerals. In contact with evaporitic bodies, the fluids dissolve the salt (halite) and acquire the necessary salinities. Fluid inclusions contained in fluorite, sphalerite, and barite give salinities of the order of 10 to 22% eq. NaCl (Bouzenoune 1993; Salmi-Laouar 2004; Sami 2011). These evaporitic rocks are also an important source of sulfur for sulfides (sphalerite, galena) and sulfates (barite, celestine). The genetic affiliation between the sulfur of the sulfates of the Triassic evaporites and that of the sulfides and sulfates of the mineralization have also been demonstrated using stables isotopes of sulfur in all the minerals of the Tebessa area (Salmi-Laouar 2004; Sami 2011). In addition, the sedimentary series of the interdiapiric zones form by their thickness (>6 km) and by their nature (with argillaceous dominance) a potential source for metals.

4.5 Heat Source

The diapiric dome structures generated by the salt tectonics deformed the isotherms and induced the heat transfer from the depths to the superficial zones; this transfer was ensured by the good thermal conduction of the halite. In the presence of these diapirs, a geothermal gradient of the order of 30–40 °C/km would give temperatures of the order of 200–250 °C at depths of 6 km (average thickness of the post-Triassic sedimentary series). The high temperatures required for mineralizing fluids to dissolve and transport metals can therefore be acquired without the presence of magmatic bodies in the region.

4.6 Creation of Drains for Mineralizing Fluids Circulation

The temperature and pressure gradients generated by salt tectonics caused circulations of geo-pressurized hydrothermal fluids around these diapiric structures. The various tectonic accidents and particularly the contact of the diapiric bodies with their sedimentary cover (Triassic-cover edge contact) constituted the main hydraulic drains for these circulations. The poly-phased process of the diapiric activity also contributed to the creation of secondary porosities (fractures or dissolutions linked to emersions).

5 Conclusions

The strong spatial relationship between the mineralization and the extrusions of Triassic evaporites in this northeastern part of the Saharan Atlas of the Algerian-Tunisian border reflects the involvement of salt tectonics in the minerals genesis. The polyphased extrusion at different times (Aptian, Albian, Vraconian, Cenomanian, Senonian, Eocene, Miocene, Quaternary—Fig. 2) of these Triassic evaporitic rocks constituted topographic anomalies, which influenced the sedimentary dynamics. The lithofacies and discontinuities that have been generated form the main metallotects of so-called peridiapiric mineralization. The diapiric structures created by the salt tectonics allowed putting in contact the deep zones with the superficial ones by the transfer of the heat and the fluids mainly through the edge contact between the evaporites and their sedimentary cover. Owing to their saliferous and sulfated nature, evaporites, constituted a source for the salinity of the fluids and for the sulfur of sulfide and sulfated minerals of the mineralization. The essentially clayey sedimentation of the interdiapiric zones may have been a potential source for metals.

References

Aoudjehane, M., Bouzenoune, A., Rouvier, H., Thibiéroz, J.: Halocinèse et dispositifs d'extrusions du Trias dans l'Atlas saharien oriental (NE algérien). Géol. Médit, Marseille **XIX**, 273–287 (1991)

Bouzenoune, A.: Minéralisations péridiapirique de l'Aptien calcaire: les carbonates de fer du gisement hématitique de l'Ouenza (Algérie orientale). Thèse Doct, Univ., Paris VI, 206 p, France (1993)

Bouzenoune, A., Rouvier, H., Thibieroz, J.: Trias de l'Ouenza: contexte diapirique, zonation minéralogique et conséquences métallogéniques. Bull. Serv. Géol. Algérie **6**(1), 3–24 (1995)

Dubourdieu, G.: Etude géologique de la région de l'Ouenza (confins algéro-tunisiens). Thèse Sci. Paris. Publ. Serv. Carte géol. Algérie, n.s., Bull. **10**, 659 (1956)

Kyle, J.R., Saunders, J.A.: Metallic deposits of the Gulf-Coast basin: diverse mineralization styles in a young sedimentary basin. Soc. Econ. Geol. Spec. Publ. **4**, 218–229 (1996)

Pohl, W., Amouri, M., Kolli, O., Scheffer, R., Zachmann, D.: A new genetic model for the North African metasomatic siderite deposits. Miner. Deposita **21**, 228–233 (1986)

Rouvier, H., Perthuisot, V., Mansouri, A.: Pb-Zn deposits and salt bearing diapirs in southern Europe and North Africa. Econ. Geol. **80**, 666–687 (1985)

Salmi-Laouar, S.: Contribution à l'étude géologique et géochimie des isotopes stables (S, O, C) des minéralisations polymétalliques (Zn, Pb, F, Ba, Fe, Hg) de la «zone des diapirs» du nord de Tébessa (NE algérien). Nouvelle Thèse de Doctorat, Univ. Badji-Mokhtar. Annaba, Algérie, 190 p (2004)

Sami, L.: Caractérisation géochimique des minéralisations à Pb-Zn, F, Ba, Cu, Fe et Hg des confins Algéro-tunisiens. Thèse doctorat, FSTGA, USTHB Bab Ezzouar Alger, Algérie, 179 p (2011)

Thibieroz, J., Madre, M.: Le gisement de sidérite du Djebel El Ouenza (Algérie) est contrôlé par un golfe de la mer aptienne. Bull. Soc. Hist. Nat. Afrique du Nord, Alger **67**(3–4), 126–150 (1976)

New Insight on the Hydrocarbon Prospectivity of the Aptian-Albian Play in Central Tunisia

Makrem Harzali and Habib Troudi

Abstract

The Aptian Serj Formation has been considered of significant interest for oil and gas exploration, in the Central Tunisia, since the 1960s. The predominant structural trapping styles for hydrocarbons, within the area, involve fault-bounded anticlines and paleo-horst structures. 2D seismic mapping over the area of interest highlights numerous structures near the top Aptian. These latters are predominantly associated with salt tectonics, which might explain the sporadic development of reefal carbonates facies that prevailed during the Aptian. The oil has been generated from the excellent Albian Fahdene source rock that charges the underlying Serj reservoir by simple pressure differential (downward migration) and/or source/reservoir juxtaposition. Based on core and well log analysis, the Aptian carbonate reservoirs are observed to typically develop poor pore systems with porosity variations closely related to the thickness of the overburden (burial) and the intensity of mesogenetic alteration, such as recrystallization and early cementation. Above a reactive salt diaper, the Aptian Serj carbonates show a significant increase in reservoir parameters due to diagenetic processes, in particular dissolution and dolomitization, especially near unconformities. The evidence of substantial oil rates from some wells provide evidence of the contribution coming from the open fractures into the flow. Despite the poor reservoir characteristics, substantial oil rates have been recorded in several wells without any reservoir stimulation. This new insight into the Aptian/Albian play has been used to narrow down the exploration risk of this play in central Tunisia and particularly in the Pelagian Basin.

Keywords

Aptian • Salt tectonics • Diagenetic processes • Hydrocarbon charging • Central Tunisia

1 Introduction

In Central Tunisia, significant numbers of exploration wells encountered moderate to strong oil shows within Aptian carbonate reservoirs immediately below the Albian Fahdene rich source rocks. Several studies (Bédir et al. 2001; Chihaoui et al. 2010; Godet et al. 2014; Harzali et al. 2014; Jaillard et al. 2013; Kassaa 1998; M'Rabet 1981; Troudi et al. 2010) have made significant contributions with regard to our knowledge of the sedimentology, structural geology and regional tectonics of the Lower Cretaceous succession in Central Tunisia. A few works focus on carbonates diagenesis and petrophysical proprieties (Kassaa 1998; Troudi et al. 2002, 2010) of the Serj reservoir in Central Tunisia. However, the role of natural fracturing and late diagenesis on development of the Serj reservoir quality at great depth (over 3000 m) is not yet well understood.

The main aim of this study was to develop an integrated approach in order to have a clear idea about the remaining prospectivity of the Aptian-Albian play in Central Tunisia. The approach includes the analysis of three fundamental elements: (1) the role of the salt tectonics on the genesis of Aptian traps that can accommodate attractive hydrocarbon resources, (2) the impact of various diagenetic controls and natural fractures on Aptian carbonates reservoir and (3) the impact of salt tectonics on the distribution and maturation of the Albian source rocks.

M. Harzali (✉)
Water, Energy and Environment Laboratory, Engineering National School of Sfax (ENIS), University of Sfax, Sfax, Tunisia

H. Troudi
Entreprise Tunisienne d'Activités Pétrolières,,
54, Avenue Mohamed V, 1002, Tunis, Tunisia
e-mail: habib.troudi@etap.com.tn

M. Meghraoui et al. (eds.), *Advances in Geophysics, Tectonics and Petroleum Geosciences*,
Advances in Science, Technology & Innovation, https://doi.org/10.1007/978-3-030-73026-0_139

2 Geological Background

Central Tunisia, including the onshore Pelagian Basin (Fig. 1), is interpreted to be part of the foreland of the Tunisian Atlas fold belt and has a long hydrocarbon exploration history. Cretaceous petroleum systems (Fig. 2) are confirmed in this area and documented by numerous oil and gas accumulations trapped within Late Cretaceous and Eocene carbonate reservoirs (Bédir et al. 2001; M'Rabet 1981).

Despite the discovery of the Douleb-Semmama-Tamsemida fields in 1966 and the encouraging results of OBL-1, Lotus-1 and Madia 1 and 2 wells, the Aptian Serj carbonates reservoir is still underexplored in Central onshore/offshore Tunisia. The Aptian carbonates reservoirs are characterized by variable porosity but tends to be better towards the apex of paleo-structures characterized by a high vertical closure. Permeability is extremely low in the tight matrix and, therefore, oil flow from such carbonates is attributable to fracture-enhanced permeability. In the uplifted areas and/or near unconformities, the reservoir properties are enhanced by pervasive dolomitization and subsequent dedolomitization. The organic rich Albian Fahdene and Early Turonian Bahloul Formations are considered as the most prolific source rocks in Central Tunisia. These two source rocks are preferentially developed in the deep basins or within rim synclines adjacent to paleohighs, created by halokinesis. Both of these source rocks have good total organic carbon (TOC) values (2–8%).

3 Methodology

Approximately 1000 km of 2D seismic reflection profiles were interpreted in order to characterize the trapping mechanisms of the Aptian Serj reservoir and define the location of diapirs, their geometry and timing of growth. The spacing of the seismic grid is highly variable, locally making interpretation challenging.

Several wells have seismic velocity information and the seismic-to-well ties are generally of good quality for the Aptian and most of the Cretaceous reservoirs. The seismic data quality is moderate to good, except at the level of the Triassic autochthonous salt, where quality is generally poor to moderate. Confidence in seismic mapping of the salt was gained by the multiple loop correlations on all the available 2D seismic lines. The base salt surface and the pre-salt sequences are typically not imaged by the currently available seismic data in the study area.

4 Results and Discussion

Aptian Serj reservoir in the Central Tunisia basin is characterized by low matrix porosity and permeability. The long-term exposure unconformities and fractures, generated by superposition of multiple tectonic movements and prolonged fall of sea level, can significantly enhance permeability and connectivity of most carbonates reservoir intervals. In fact, dissolution porosity and fractures contribute in the formation of high-quality reservoir. Therefore, Aptian reservoir evaluation should take reefs and fractures into consideration. Various styles of traps have been observed near the top Aptian and most of them have a multi-age structural genesis. Based on current knowledges, most of Aptian discoveries in Central onshore/offshore Tunisia occurred in structural traps. Combined structural-stratigraphic trapping mechanisms are still speculative, but not excluded, especially in the area showing extensive salt tectonics (Troudi et al. 2010).

The Aptian carbonates have been affected by a variety of diagenetic processes (Fig. 3). With regard to reservoir quality, initial depositional porosity decreased with burial due to compaction and cementation, but subsequent

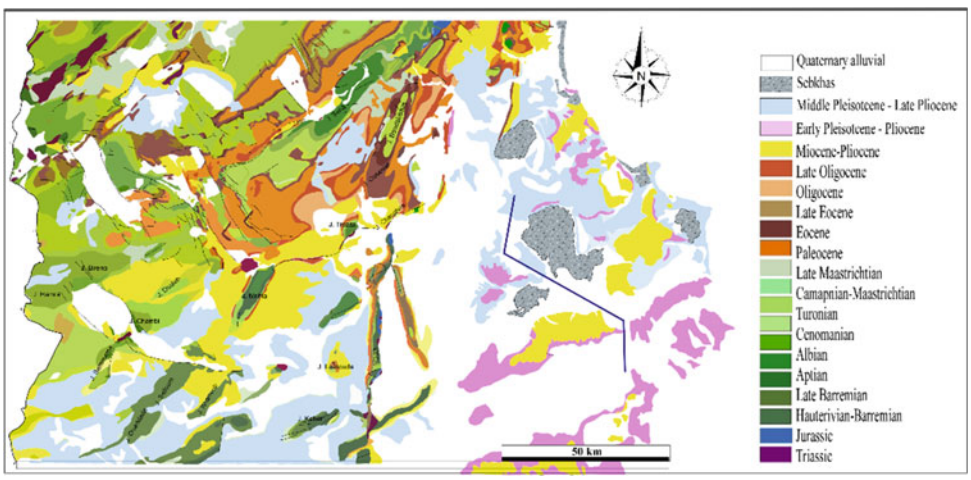

Fig. 1 Regional geology of Central Tunisia. Blue line shows the location of the interpreted seismic regional line (Fig. 5)

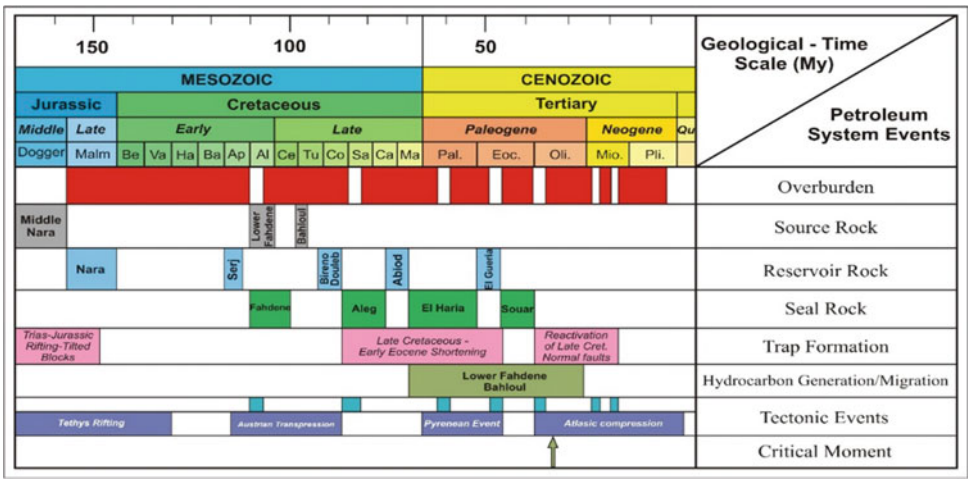

Fig. 2 Proven petroleum systems in Central Tunisia (Troudi et al. 2017)

dolomitization/dedolomitization processes and fracture-enhanced permeability has locally improved the reservoir quality.

The thick section of Albian-Cenomanian sediments accumulated in high subsiding areas could have excluded enormous quantities of water during its burial evolution due to compaction and dewatering. Interaction of dolomitizing fluids with evaporites along the faults and fractures is supposed to have occurred in the region (Fig. 4).

The dolomitizing fluids were heated during deep circulation (95–130 °C) and interacted with the salt-diapir-hosted magnesium rocks possible source for the hypersaline fluid (10–25 wt% NaCl equiv.) (Kassaa 1998). Dolomitization was pervasive and fabric destructive in zones near the fractures that acted as main hydrothermal conduits, showing complex structures and highly variable porosity. Outwards from these fractures, the dolomites bear primary structures and low-petrophysics proprieties.

The dolomitization/dedolomitization process has greatly affected the evolution of secondary porosity. The highest porosity (over 9%) is contained within the upper, pervasively dolomitized part of the Serdj reservoir beneath the Aptian-Albian unconformity. This process is mostly represented by secondary intercrystalline porosity related to several stages of dedolomitization. Porosity, formed by enlargement of intercrystalline pores, varies in size from several tens of millimeters vuggy porosity to submicroscopic (Troudi et al. 2002, 2010). Consequently, the quality of a potential dolomite reservoir is strongly controlled by the tectonic and diagenetic history of the host carbonates and future hydrocarbon exploration should focus

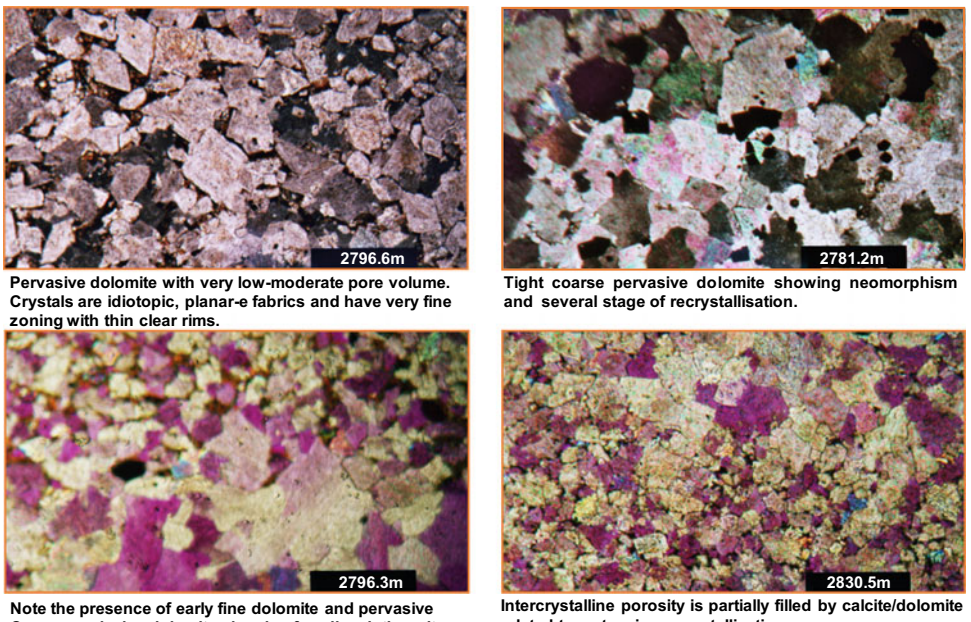

Fig. 3 Impact of diagenesis on Aptian carbonate reservoir, samples from MAH-1 well (Troudi et al. 2010)

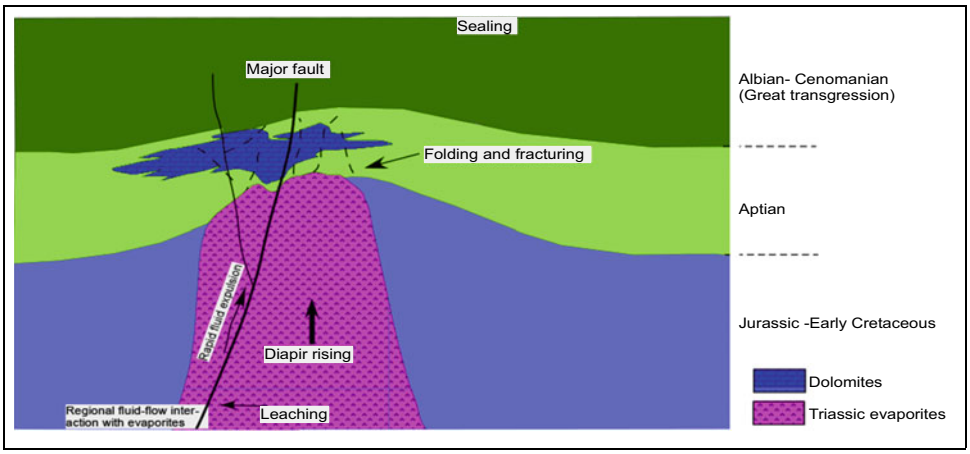

Fig. 4 Simplified dolomitization model

on structural highs, which have the best opportunities of showing significant porosity.

Based on interpretation of the 2D seismic lines (Fig. 5), most geoscientists postulate that Aptian structures are embryonic compressional basement uplifts with associated normal or high-angle deep-seated reverse faults (Bédir et al. 2001; Harzali et al. 2014 and 2019; Troudi et al. 2017).

The genesis and geometry of the Aptian structures appear to be also controlled by halokinetic activity. Subsurface mapping of the Triassic salt in Central Tunisia highlighted several salt structures separating sub-basins. A prominent WNW-ESE trending diapiric salt wall has been identified and was drilled by exploration wells without encountering any Cretaceous reservoirs. The dominant driver for salt tectonics is interpreted to be repeated periods of N–S to NE–SW directed extension, causing diapiric growth since the early Jurassic. Hydrocarbon charge is also controlled by the multiple phases of salt tectonics, which strongly affected the basin configuration and, therefore, the preservation and maturation of source rocks. With regard to reservoir quality, the initial porosity decreased due to compaction and cementation, with later dolomitization/dedolomitization processes and fracturing enhancing permeability resulting in improved reservoir quality.

Salt withdrawal and pillowing are responsible for the initiation of sub-basins in between the diapiric salt walls as early as the early Jurassic. The increasing thickness of sedimentary infill of these sub-basins promoted maturation of the Albian and Turonian source rocks. Hydrocarbon migration paths from the kitchen area to the Aptian Serj reservoir target range from rather simple cross-fault juxtapositions of mature source and reservoir, to cross-fault migrations combined with downward migrations. Besides the structural closures are a potential for as yet-undrilled more complex structural and stratigraphic traps against salt walls.

5 Conclusions

Aptian carbonate reservoirs in Central Tunisia basin are characterized by low matrix porosity and permeability. However, the long-term exposure unconformities and fractures, generated by superposition of multiple tectonic movements and prolonged fall of sea level, can significantly enhance permeability and connectivity of reservoir strata.

Dolomitization was pervasive and fabric destructive in zones near the fractures that acted as main hydrothermal

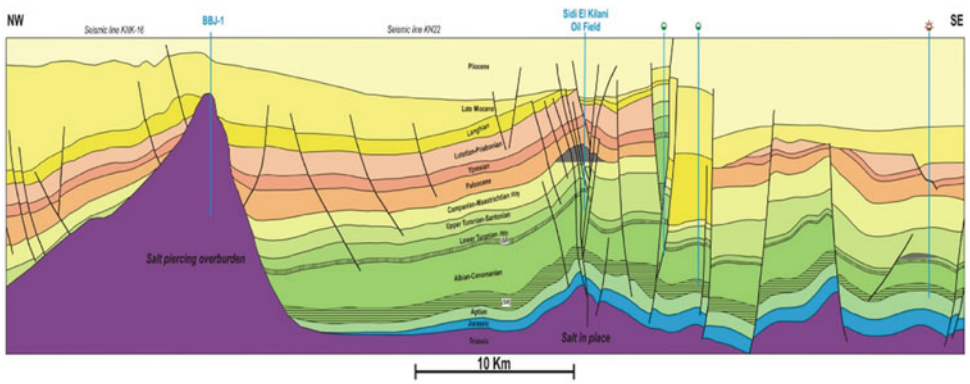

Fig. 5 Regional transect based on 2D seismic lines and wells, Troudi et al. (2017)

conduits, showing complex structures and highly variable porosity. Outwards from these fractures, the dolomites bear primary structures and higher porosity. We argue that the quality of a potential reservoir is influenced by tectonic and diagenetic history of host carbonates prior to burial. Future hydrocarbon exploration should focus on structural highs, which have the best opportunities of showing significant porosity. This study illustrates the importance of understanding the diagenetic and tectonic history of potential carbonate reservoir and helps to predict the model for the dolomite distribution in the subsurface and the distribution of reservoir to non-reservoir units.

References

Bédir, M., Boukadi, N., Tlig, S., Ben, T.F., Zitouni, L., Alouani, R., Slimane, F., Bobier, C., Zargouni, F.: Subsurface Mesozoic basins in the Central Atlas of Tunisia, tectonics, and sequence deposit distribution and hydrocarbon potential. Am. Asso. Petrol. Geol. Bull. **85**, 885–907 (2001)

Chihaoui, A., Jaillard, E., Latil, J.-L., Susperregui, A.-S., Touir, J., Ouali, J.: Stratigraphy of the Hameima and lower Fahdene formations in the Tajerouine area (Northern Tunisia). J. Afr. Earth Sci. **58**(2010), 387–399 (2010)

Godet, A., Hfaied, R., Arnaud-Vanneau, A, Zghal, I., Arnaud, H., Ouali, J.: Aptian palaeoclimates and identification of an OAE1a equivalent in shallow marine environments of the southern Tethyan margin: evidence from Southern Tunisia (Bir Oum Ali section, Northern Chott chain). Cretaceous Res. **48**(March 2014), 110–129 (2014)

Harzali, M., Troudi, H., Ben, B.K., Ouali, J.: Carbonate platform-margins and reefs distribution using 2-D seismic analysis, Central Tunisia. J. Afr. Earth Sci. **100**(2014), 109–120 (2014)

Jaillard, E., Dumont, T., Ouali, J., Latil, J.L., Arnaud, H., Arnaud-Vanneau, A., Zghal, I.: The Albian tectonic "crisis" in Central Tunisia: nature and chronology of the deformations. J. Afr. Earth Sci. **85**(September 2013), 75–86 (2013)

Kassaa, S.: Pétrologie des matériaux carbonatés, sulfurés et strontianifères dans leur cadre stratigraphique, holocinétique et structural à Geurn Halfoya et au J. Boukhil (domaine des Diapirss et des Glaciers de sel Tunisie du Nord-Ouest). Thèse 3ème cycle, Fac, Sci, Tunis, 373 p (1998)

M'Rabet, A.: Stratigraphie, sédimentation et diagenèse carbonatée des séries du Crétacé inférieur de la Tunisie centrale. Thèse ès Sciences, Université Paris sud, Centre d'Orsay, 540 p (1981)

Troudi, H., Acheche, M., Saidi, M.: Mid-Cretaceous platform carbonate play in Tunisia, North Africa: attributes evidence from producing fields. In: AAPG Conference, Houston, USA. Search and Discovery # 90007 (2002)

Troudi, H., Ouahchi, A., Saidi, M., Soussi, M.: Early Cretaceous clastic and carbonate reservoirs in central Tunisia: characteristics and prospectivity. In: Field Trip Guide Book, The 12th ETAP EPC, 2010, Memoir 30, 48 p (2010)

Troudi, H., Tari, G., Cantarella, G., Alouani, W.: Styles of salt tectonics in central Tunisia: an overview. In: Elsevier Book, Permo-Triassic Salt Provinces of Europe, North Africa and the Atlantic Margins, Chap. 25, pp. 543–561 (2017)

Harzali, M., Troudi, H., Alexis, G., Ouali. J.: Seismic stratigraphy and hydrocarbon prospectivity of the Aptian–Albian succession along the Oued Bahloul Basin, Central Ouest Tunisia. Journal of Iberian Geology, 45, 383–399 (2019)

The Cenomano-Turonian Facies Through the Algerian-Tunisian Confines (Region of Tebessa): Correlations, Subsidence and Source Rock

Imen Chairat, Fouad Djaiz, and Mabrouk Boughdiri

Abstract

The Algero-Tunisian confines (Tebessa region) belong to the southern Tethyan domain and the Monts Mellegue. This region is partly composed of Cenomano-Turonian carbonate outcrops; therefore, the investigated sections highlight the black shale levels reported over a short period, around the Cenomanian-Turonian boundary. The lithostratigraphic study designated a depositional environment that emphasized a relatively deep, calm, and often confined ocean environment significantly shallower on the northern part of the study area. The facies lithology and distribution leads to underline the pelagic influences during the upper Cretaceous and neritic throughout the lower Cretaceous period. The maximum thickness of the Cenomano-Turonian (1000 m) was recorded in the southern zones and the minimum (100 m) occurred further north. This palaeogeographic organization persists laterally in Tunisia as the extension of the Constantine mole. The geochemical analyses reveal that the maturity of the Cenomanian source rock is variable. Nevertheless, the Turonian source rock seems to be at the beginning of the oil phase.

Keywords

Cenomanian-Turonian • Source rock • Tebessa • EAO-2 • Subsidence

1 Introduction

The study area is a part of a vast palaeogeographic province extended on both sides of the Algero-Tunisian border called the Algero-Tunisian Atlasic basin (Fig. 1).

In North-Eastern Algeria, the Cenomano-Turonian series is not studied in detail; it is only after the oil exploration program launched by Sonatrach in SE Constantinois region that the Cenomano-Turonian were studied in detail with regard to lithobiostratigraphy has become scientifically and economically interesting. The purpose of this paper was to focus on a characterization of the Cenomano-Turonian facies and source rock, its extension and the relationship between subsidence and the geodynamic context of the region.

2 Materials and Methods

This paper is based on several studies: a stratigraphic analysis based on field data, drilling data and descriptions of thin sections to establish correlations and iso-thickness maps. A structural analysis based on the interpretation of surface data (field measurements, geological maps) and subsurface was also used. A geochemical analysis was intended for the petroleum potential characterization of the source rock levels (TOC and PP values as well as the maturity).

3 Results

A field campaign allowed to specify the palaeoenvironment during the Cenomano-Turonian in the region of Tebessa. At the time, the region was in a relatively deep, calm and often confined ocean environment, significantly shallower to the north of the study area Ruault-djerrab et al. (2012), Vila (1980). The lithological variations recognized, including the bioturbation surfaces and the microfossil content (foraminifers or echinoderms), reflect sea level fluctuations.

I. Chairat (✉) · F. Djaiz
Laboratory of Mobilization and Management of Water Resources, Institute of Earth and Universe Sciences, University of Batna 2, Batna, Algeria

M. Boughdiri
Department of Geology, Faculty of Sciences of Bizerte, University of Tunis Carthage, Tunis, Tunisia

M. Meghraoui et al. (eds.), *Advances in Geophysics, Tectonics and Petroleum Geosciences*,
Advances in Science, Technology & Innovation, https://doi.org/10.1007/978-3-030-73026-0_140

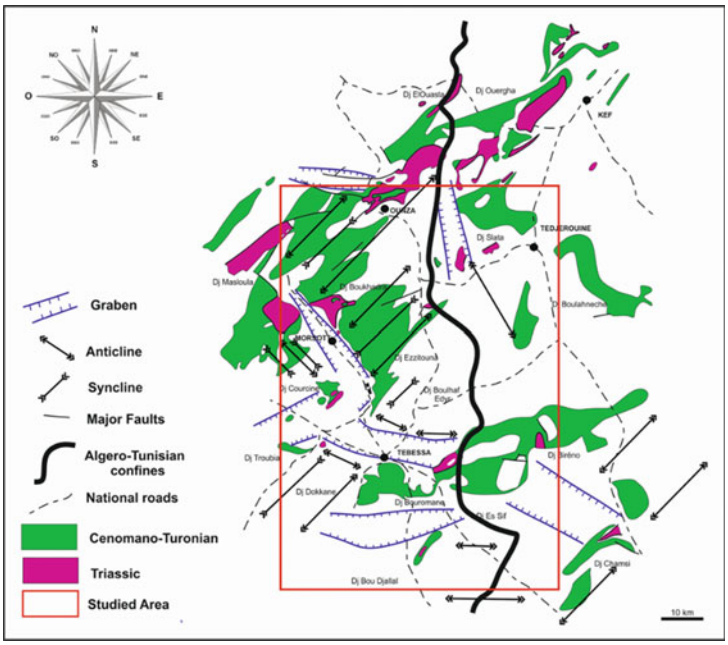

Fig. 1 The Cenomano-Turonian outcrops in the studied area

Periods of low sea level generally coincide with a detrital flow (marl) whereas periods of high sea level are generally characterized by a significant production of carbonate (limestone) or silica and low detrital flow under conditions of hot and humid climate (Fig. 2).

The Lower Cenomanian is characterized with marls, clays and bituminous marl. The measured values are distributed according to their geographical situation on both sides of the Saharan flexure. South of the Saharan flexure, the geochemical analyses show the following values: 0.5% < TOC < 3.25% and 0.38 < PP < 5.08 kg HC/tons of rock. Regarding the maturity, the Cenomanian is in oil phase with a conversion rate of 25%. North of the Saharan flexure, the values obtained are 0.5% < TOC < 2.05% and 0.3 < PP < 3 kg HC/tons of rock. The maturity is variable; it range from the immature phase/beginning of the oil phase, to the gas phase/condensate zone.

The Lower Turonian consists of marls, limestones and marl-limestones in platelets, and bituminous. South of the Atlasic flexure, the values vary from 0.5% < TOC < 11.5% and 0.5 < PP < 35 kg HC/tons of rock. The degree of maturity of this zone translate oil phase. North of the Atlasic flexure, the values vary from 0.5% < TOC < 8.08% and 0.45 < PP < 47 kg HC/tons of rock. The zone is at the beginning of the oil phase.

4 Discussion

The lithology and the distribution of the facies in the region recognize the pelagic influences during the upper Cretaceous and neritic during the lower Cretaceous period (Vila, 1980). We record the maximum thickness of the Cenomano-Turonian (1000 m) in the southern zones and

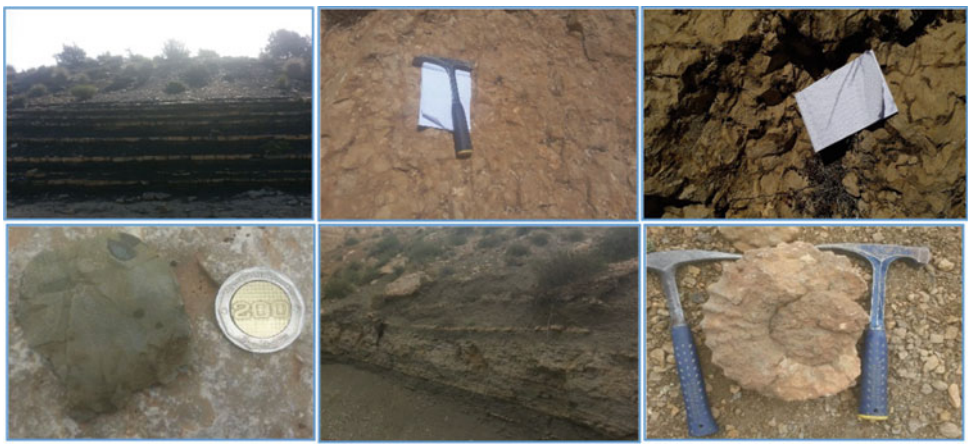

Fig. 2 Field aspects: 1 = blackshales, 2 = oxidized bioturbations, 3 = hard ground surface, 4 = echinoderm, 5 = marl-limestone alternation, 6 = "giant" ammonite (Cenomanian)

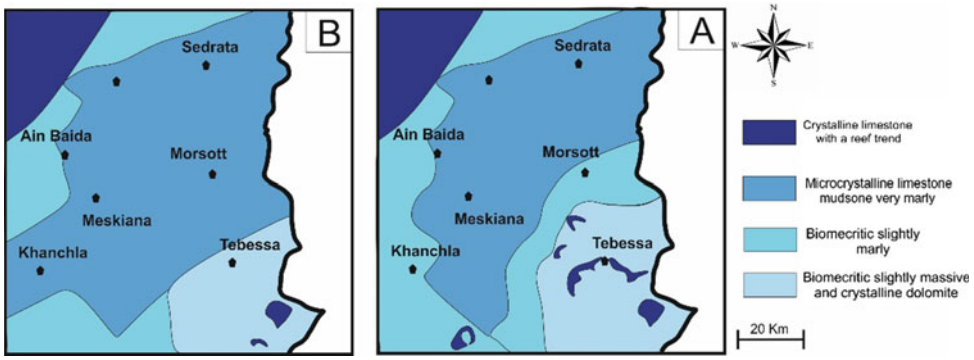

Fig. 3 Cenomanian and Turonian palaeogeographic maps (A = Turonian, B = Cenomanian)

the minimum (100 m) appears further to the north. This Palaeogeographic organization continues laterally in Tunisia as the extension of the Constantine mole (Fig. 3).

The Cenomano-Turonian series of the northern part of the Algero-Tunisian (Masloula-souk Ahras) borders compared to those more meridian as well as with those hosted in the Algerian domains reveal a clear variation of the thicknesses in N–S direction. The Cenomanian-Turonian facies, generally marly and calcareous, preserve the same lithology over large areas, becoming rich in carbonate in the West direction, that of the Constantine neritic mole, and becoming thicker, contrasting with those of the South (Fig. 4).

A large thickness of the Cenomano-Turonian series of the subsiding zone of the north of the study area continues towards East Tunisia in the region of Kef, where it fades. Then a thick umbilical field of sedimentation makes this area continue down to the Tunisian Dorsal. Further north from this E–W to NE–SW direction band, the thickness reduction is clear. This repetitive N-S thickness decrease, from the lower Cretaceous to the Upper Cretaceous, suggests that there is a stable mole in Tunisia between the Mejerda range and the present coast, which could be a continuity of Constantine mole (Fig. 5).

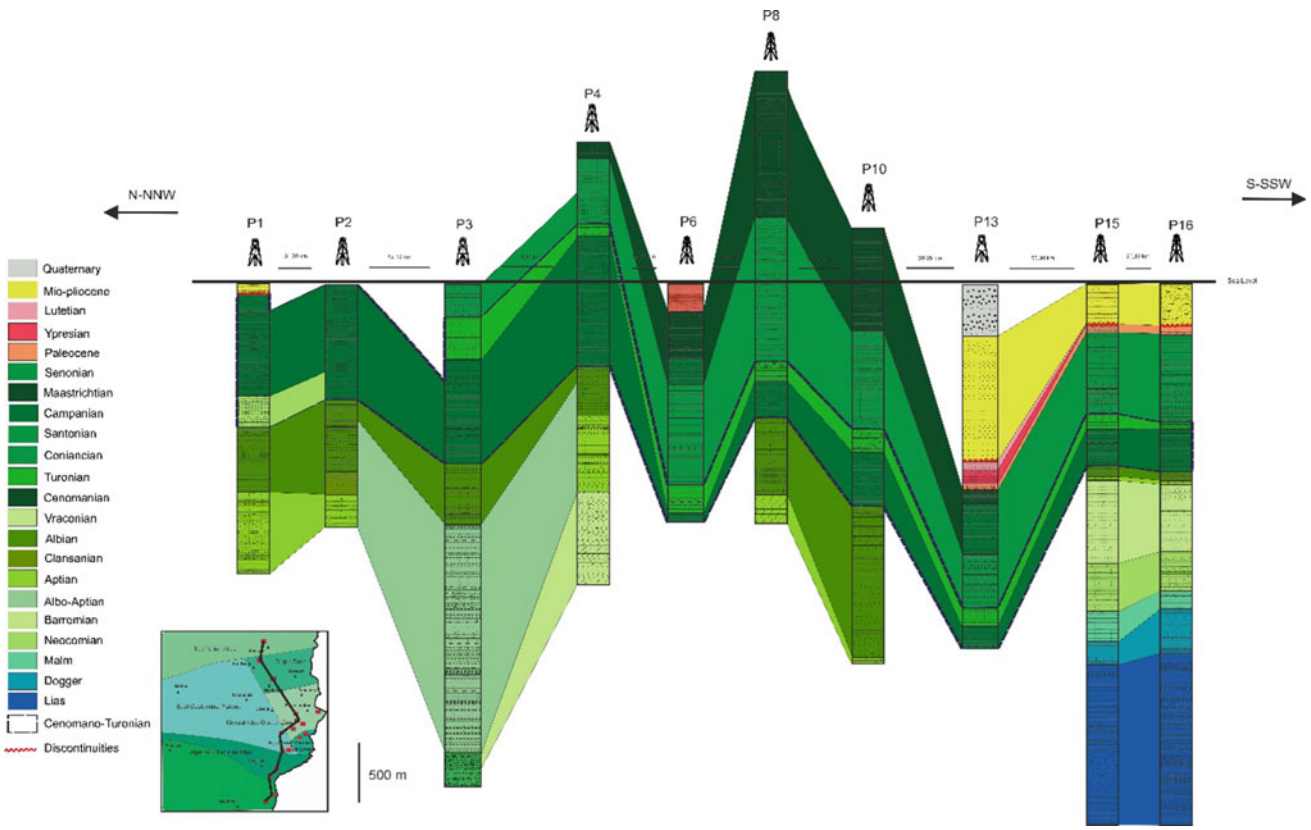

Fig. 4 N–S correlation of wells in the study area

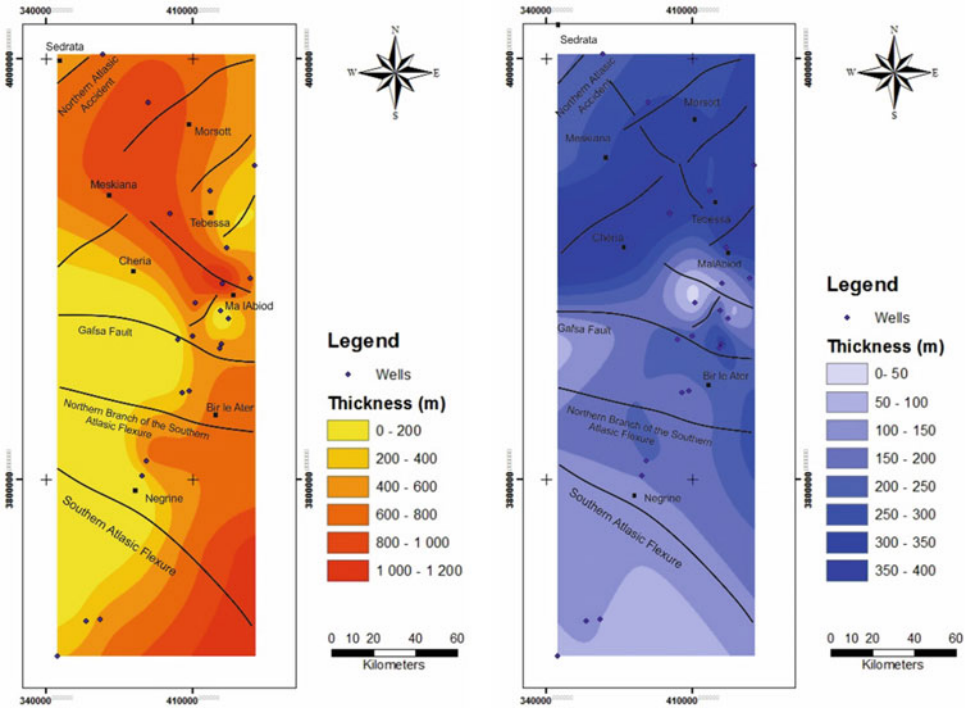

Fig. 5 Iso-thicknesses maps of Cenomanian (red) and Turonian (blue)

The basement collapses induced depression of the Algerian-Tunisian confine that took place from the Barremian to the end of the Cretaceous period was filled a sediment accumulation up to 4 to 5,000 m in thickness. This subsidence was not constant but interrupted by sporadic Aptian shoals on which sub-reefal carbonate sedimentation onset.

Some authors suggest that the appearance of these shallows isrelated to the diapiric activity of the Triassic formations. The latter would have been determined by the replay of Hercynian accidents oriented NNE–SSW or the Aptian NE–SW extension (Herkat and Guiraud, 2006).

5 Conclusions

The Cenomanian marly deposits experience a subsidence activity as characterized by their remarkable thickness. However, the Turonian successions are progressively enriched in carbonated which can be inferred to a subsidence slowdown of a shallower trend.

A sequential analysis leads to reconstruct a characteristic external platform-to-basin depositional environment, with local reefs in the central part of the study zone and the 'Cenomanian-Turonian' series has endured variations in the deposition environment in the lower partdefined as a closed environment towards the extern. The appearance of the shallows in the northern part of the studied area is related to the diapirism activity of the Triassic formations.

The geochemical characterization attests that the maturity of the Cenomanian source rock is variant from the immature phase/beginning of the oil phase, to the gas phase. Regarding the Turonian source rock, interpreted results indicate a source rock at the beginning of the oil phase.

References

Herkat, M., Guiraud, R.: The relationships between tectonics and sedimentation in the late Cretaceous series of the eastern Atlasic domain (Algeria). J. Afr. Earth Sci. **46**, 346–370 (2006)

Ruault-djerrab, M., Ferre, B., Kechid-benkherouf, F.: Etude micropaléontologique du Cénomano-Turonien dans la région de Tébessa (NE Algérie): implications paléoenvironnementales et recherche de l'empreinte de l'OAE2. Revue de Paléobiologie, Genève **31**(1), 127–144 (2012)

Vila, J.M.: La chaîne alpine d'Algérie orientale et des confins algéro-tunisiens. Thèse de doctorat, Université Paris VI, 665 p (1980)

Characterization of the Fractured Eocene Carbonate Reservoir of Dyr Syncline (Tebessa, North-Eastern Algeria)

Nihad Bouroudi, Azzedine Bouzenoune, Riad Benzaid, Kamel Boufaa, and Eric Mercier

Abstract

One of the most studied fields for water resource development is the characterization of fractured reservoirs. Although the role of matrix porosity is important as it controls water storage, fractures also play a key role as they transport water and determine reservoir production. This study was carried out on a multi-scalar characterization of the fractured carbonate reservoir of the Dyr massif (Tebessa, North Eastern Algeria). It is a perched syncline oriented NE–SW and formed of ypresian limestone rocks. The samples taken from the Dyr on a cross-section show a generally low total porosity, except at the hinge, where this porosity is relatively high in Nummulite limestones and bioclastic limestones. The reservoir capacities of the ypresian limestones of the Dyr are therefore mainly dependent on the fracturing state of these carbonates. The fracturing state of the Dyr was approached by a multi-scale analysis (terrain, photo-aerial). The results obtained on both scales show three families of fractures in NE–SW, E–W and NW–SE directions. These three families show variable frequencies depending on the structural position (flanks and hinge) and on the scale. The spatial distribution of the fracturing density on the massif, established from the photo-aerial appears heterogeneous. The most densely fractured areas near water sources appear to be controlled by major tectonic accidents.

Keywords

Dyr • Reservoir • Ypresian • Porosity • Fractures

N. Bouroudi (✉) · A. Bouzenoune · R. Benzaid · K. Boufaa
Geological Engineering Laboratory (LGG), University of Mohamed Seddik Benyahia, Jijel, Algeria

E. Mercier
Laboratory of Planetology and Geodynamics (LPG), University of Nantes, Nantes, France

1 Introduction

The Dyr syncline is located in North Eastern Algeria, 12 km North-East of Tebessa city and 09 km from the Algerian-Tunisian border. It is a NE–SW perched syncline whose skeleton is mainly provided by the biomicritic limestones of the Ypresian (Bouroudi 2014). It is one of the fractured carbonate aquifers exploited for its water resources.

2 Methodology

The microscopic analysis of the microfacies and porosity was carried out on about ten samples taken according to a NW–SE cross-section located in the north-eastern part of the syncline (because accessible). The thin blades were pre-treated with methylene blue resin impregnation.

The measures of fracturing on the outcrops were taken from six stations on the same NW–SE section.

The method we used for sampling field measurements is the so-called quantitative method. It consists in determining a dimensioned area over which as many of the existing fracture directions and dips as possible are measured. This was complemented by a lineament study on photo-aerial images (scale 1/20,000). The measured parameters are directions and lengths.

3 Microfaciological and Porosity Analysis

The achieved microfaciological study allowed us to identify three microfacies: a Nummulite microfacies, a bioclastic microfacies with debris of undissolved Molluscs and a bioclastic microfacies with debris of dissolved Molluscs (Bouroudi 2014).

Two types of porosity were observed (Fig. 1): matrix porosity and crack porosity (Bouroudi 2014). The matrix

M. Meghraoui et al. (eds.), *Advances in Geophysics, Tectonics and Petroleum Geosciences*,
Advances in Science, Technology & Innovation, https://doi.org/10.1007/978-3-030-73026-0_141

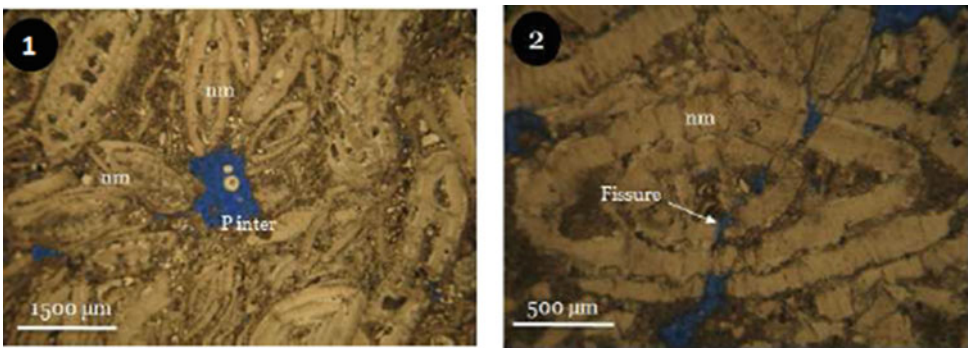

Fig. 1 Photos illustrating examples of porosities affecting ypresian limestones of Dyr syncline (blue color) in the Nummilite microfacies. Photo 1: inter-particle porosity (P inter); Photo 2: crack porosity, nm: Nummulite

porosity is represented by the types: intra- and inter-particle (Choquette and Pray 1970).

The total matrix porosity shows small percentages with an average not exceeding 3%, variable in space. The highest matrix porosities were found at the syncline hinge in the Nummulite microfacies and the dissolved Mollusc bioclastic microfacies (Bouroudi 2014). These low rates of matrix porosity indicate that the reservoir capacities of the Eocene carbonate rocks of the Dyr are mainly controlled by the porosity of fractures.

4 Fracture Network Characterization

From the fractures measured on the outcrops and the fractures analyzed in the photo-aerial we found the presence of two families of dominant fractures: «d1» of direction near E–W whose orientations vary between N80E and N110E and «d2» NW–SE steering whose fractures have orientations between N120E and N170E. A third submeridian family less expressed "d3" in NNE–SSW direction with orientations varying between N10E and N30E (Bouroudi 2014; Benabbas 2016; Bles 1969). The frequencies and lengths of these different families of fractures vary in space by passing from the flanks to the hinge of the fold and according to the scale (outcrop, aerial photo). At the aerial photo scale, the families of fractures with the most dominant orientations are the same as the most important lengths (resolution of the means of investigation) (Bouroudi 2014).

The fracturing density established from the aerial photographs reveals a high concentration of fractures around the large tectonic accidents that cut the massif and coincide with the resurgence zones of the waters (Bouroudi 2014) (Fig. 2).

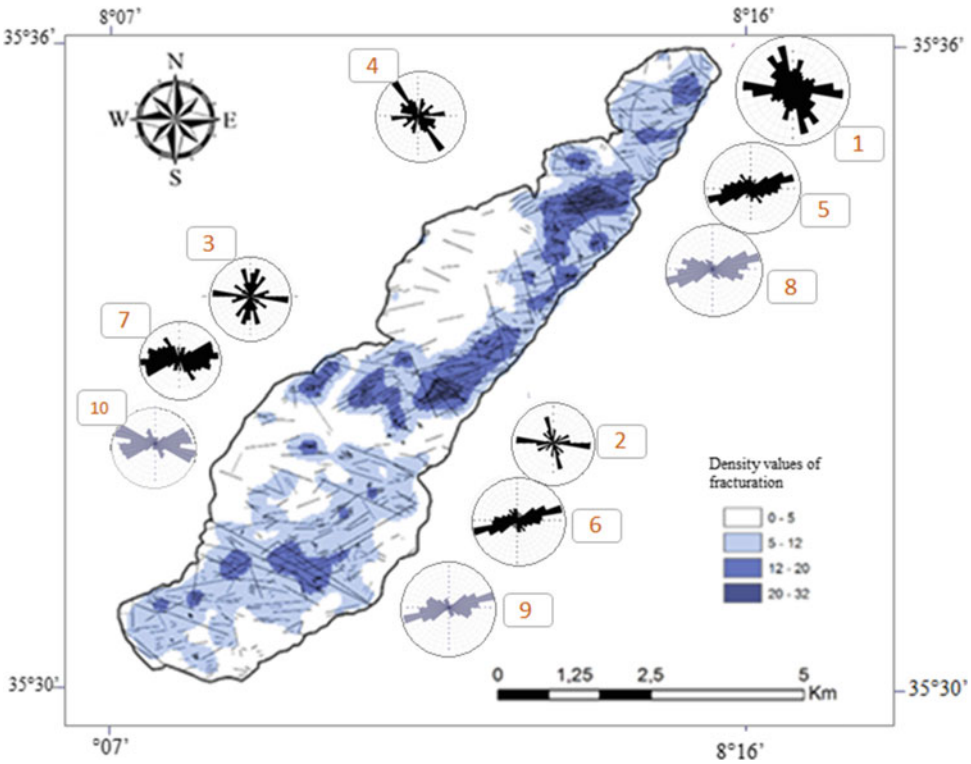

Fig. 2 Representation of fracturing measurement results (Bouroudi 2014). (1, 5) global frequency, (2, 6) NE flank frequency, (3, 7) SW flank frequency, (4) hinge frequency, (8) global length, (9) NE flank length, (10) SW flank lengths. Diagrams 1–4 taken from the outcrop measurements and 5–10 from the fracturing derived from the aerial photographs

5 Conclusions

In light of these results, it appears that the Dyr syncline is weakly porous (total matrix porosity around 3%). The porosity depends on the type of facies and the position in the structure (flanks, hinge). The function of the reservoir is thus fulfilled by the presence of a network of conjugated fractures that allow both storage and transfer of water. There are three main directions: E–W, NW–SE, NNE–SSW. These three directions are found at all scales and show slight variations in orientation in relation to the structural position (flanks, hinge). However, the relative abundance of fractures of a given orientation may vary depending on the scale. The orientation is therefore an independent parameter of the observation scale but dependent on the structural position within the fold.

References

Benabbas, Ch.: Evaluation Mio-Plio-Quaternaire des bassins continentaux de l'Algérie Nord-orientale; apport de la photo géologie et analyse morphostructurale, Phd thesis. Univ. Mentouri Constantine, 256 p (2016)

Bles, J.L.: Contribution à l'étude des déformations cassantes de la feuille de Morsott (SE Constantinois, Algérie). Les microfractures et leurs relations avec les failles et les plis. Publ. Serv. Carte géol. Algérie, N. S., Bull. n°39, 7–17 (1969)

Bouroudi, N.: Caractérisation du réservoir carbonaté fracturé éocène du Djebel Dyr (Tébessa, Algérie Nord Orientale). Master thesis, Univ. Mohamed Seddik Benyahia, Jijel, Algérie, 140 p (2014)

Choquette, P.W., Pray, L.C.: Geologic nomenclature and classification of porosity in sedimentary carbonates. AAPG Bull. **54**, 207–250 (1970)

Effects of Aptian–Albian Tectonic Instabilities on Sedimentation and Petroleum Systems in Northwestern Tunisia

Asma Meftahi, Mohamed Hedi Negra, Radhouane Khouni, and Mohamed Sabri Arfaoui

Abstract

During the lower Cretaceous, the southern margin of the Tethys was marked by an extensional tectonic activity expressed as a reactivation of previous rift faults that developed during the opening of Tethys. This tectonic instability acted on the salt triggering a halokinesis which was at the origin of the tilting processes resulting in blocks inclined in various directions. The present work aimed at highlighting remarkable and rapid variations in thicknesses and facies of lower Cretaceous deposits in northwestern Tunisia. Our approach based on comparative surface and subsurface geological investigations shows rapid lateral variations of Cretaceous reservoir and source rocks. The significance and style of these variations sharply change from the Aptian–lower Albian M'Cherga deposits to the late Albian Fahdene black shales and younger series. A regional unconformity identified for the first time in the study area marked by the non-deposition of lower-middle Albian series, provides a direct contact between Aptian reservoir rocks and upper Albian «black shales» which are considered as excellent source rocks in Tunisia. Subsidence inversions are found immediately above this regional unconformity. In fact, the subsident areas which received thick Aptian deposits were transformed, since the late Albian, into relatively paleohighs. Conversely, the latters were covered, since the late Albian, by thick sedimentary package, often starting with black shales. Overall, the use of a multidisciplinary approach, both incorporating subsurface and outcrop data, offers improved subsurface interpretations and hydrocarbon exploration modeling.

Keywords

Aptian–Albian • Tectonics • Sedimentation • Subsidence • Inversions

1 Introduction

The study area, located in Northwestern Tunisia, part of the northern Atlas "salt outcrops area," is marked by numerous Triassic-Cretaceous outcrops, the majority of which are aligned in a NE-SW trending (Chikhaoui et al. 1998). The high quality of the surface exposed series facilitates outcrop studies, whereby lateral correlations and comparisons with subsurface data could be properly achieved. In order to reconstruct the depositional environments and assess a geological model that helps to better understand the potential relationship between sedimentation and tectonics/salt activity. To this end, we used a multidisciplinary approach based both on surface and subsurface data and results.

2 Materials and Methods

Our study is based first on a bibliographic synthesis of previous works on the study area. Three studied sections of lower Cretaceous series are scattered throughout the study area (OM1, TG, Nb; Fig. 1). This work is also based on the interpretation of the NE-SW trending seismic line L1 with medium to good quality and calibrated using an oil well located approximately 5 km South of the el Kef city.

In order to understand the tectono-sedimentary history of the study area, we carried out sedimentological and stratigraphical analyses. The analysis of Aptian–Albian facies and measurements of thickness led to establish correlations between the surveyed lithostratigraphic sections.

A. Meftahi (✉) · M. H. Negra · R. Khouni · M. S. Arfaoui
University of Tunis El Manar, 2092 Tunis, Tunisia

R. Khouni · M. S. Arfaoui
PRIMOIL SA Campany, Emeraude Building, 3rd Floor, Les Berges du Lac 2, 1053 Tunis, Tunisia

M. Meghraoui et al. (eds.), *Advances in Geophysics, Tectonics and Petroleum Geosciences*, Advances in Science, Technology & Innovation, https://doi.org/10.1007/978-3-030-73026-0_142

3 Results

3.1 The Aptian Deposits and Their Correlation

Starting from the Oued Mellegue area (OM1 section), the Aptian series is about 1000 m in thickness and directly overlies Triassic deposits. It has claystones at the base, intercalated with siltstones and fractured hard sandstone beds. Above, a predominantly carbonate sedimentation is expressed by two carbonate units separated by a marly unit. Carbonates consist of highly fractured micritic limestone beds and appear to have been deposited immediately after an episode of terrigenous detrital input, in an outer-ramp environment. Laterally, 4 km to the SE, in the Nebeur area (Nb section), a sharp change is marked by a the total pinch out of the 1000 m thick Aptian deposits, suggesting the existence of a paleohigh, on which Triassic deposits are directly overlain by upper Albian black shales.

Toward the NE, in the Tell el Ghozlane area (TG section), the Aptian series is obviously thicker (about 2300 m) and shows different and particular facies. These are rather concordant, and mainly represented by "basinal" claystones, admitting the intercalation of fine-grained sandy lens-shaped "bars," Bedoulian to Gargasian in age. They are overlain by claystones and marlstones, Clansayesian in age, with rare intercalated thin beds of clayey-carbonates. The depositional environment consists of a distal outer-ramp area. During the Bedoulian–Gargasian, this area has recorded an abundant detrital input in relation with erosional processes preferentially affecting highs such as horsts.

The spectacular Aptian deposits thickening and deepening in Tell el Ghozlane area may be related to blocks tilting toward the NE. In fact, the border faults activity (NW–SE F1 fault; Fig. 2) in the Nebeur–Mellegue block is interpreted to have given rise to tilting of the basin toward the East and NE, giving way to considerable thickening and deeper depositional environment of Aptian series. Similarly, tilting processes also appear to be active toward the South, in direction of the drilled well (Fig. 2).

3.2 The Late Albian Deposits and Their Correlation

The Albian series is essentially composed of carbonates and black shales. The deep marine character of the latter suggests a clear tilting and/or a sea-level rise during the late Albian. Regional and global correlations confirm this transgressive event (Chihaoui et al. 2010).

In contrast to the Aptian deposits, the late Albian and younger series show a completely different feature. The areas, which acted as subsiding sectors during the Aptian, constitute paleohighs since the late Albian. This spectacular "subsidence inversion" can be recognized both on surface correlations and seismic profiles (Figs. 2 and 3). This inversion appears immediately above the Aptian/late Albian unconformity, which has, at least, a regional extent (Chihaoui et al. 2010).

The tilting processes related to faulting activity, rather toward the West and SW, are associated with a thickening of

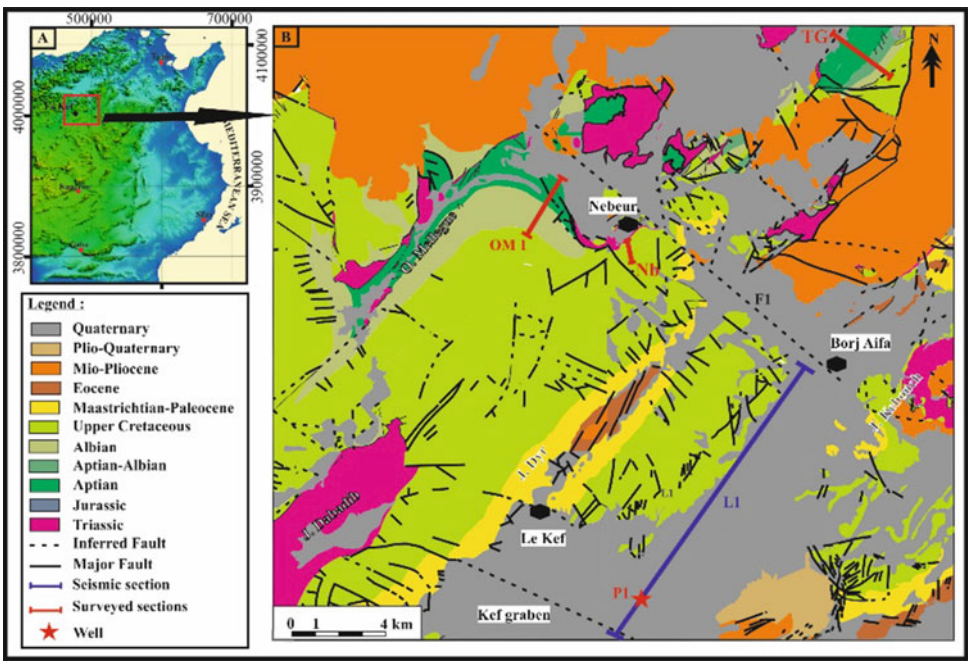

Fig. 1 **A** DEM of Northern Tunisia showing area of interest. **B** Location of the studied sections (OM1, TG, Nb) and the P1 well on the study area redrawn from public (1/50,000) geological maps

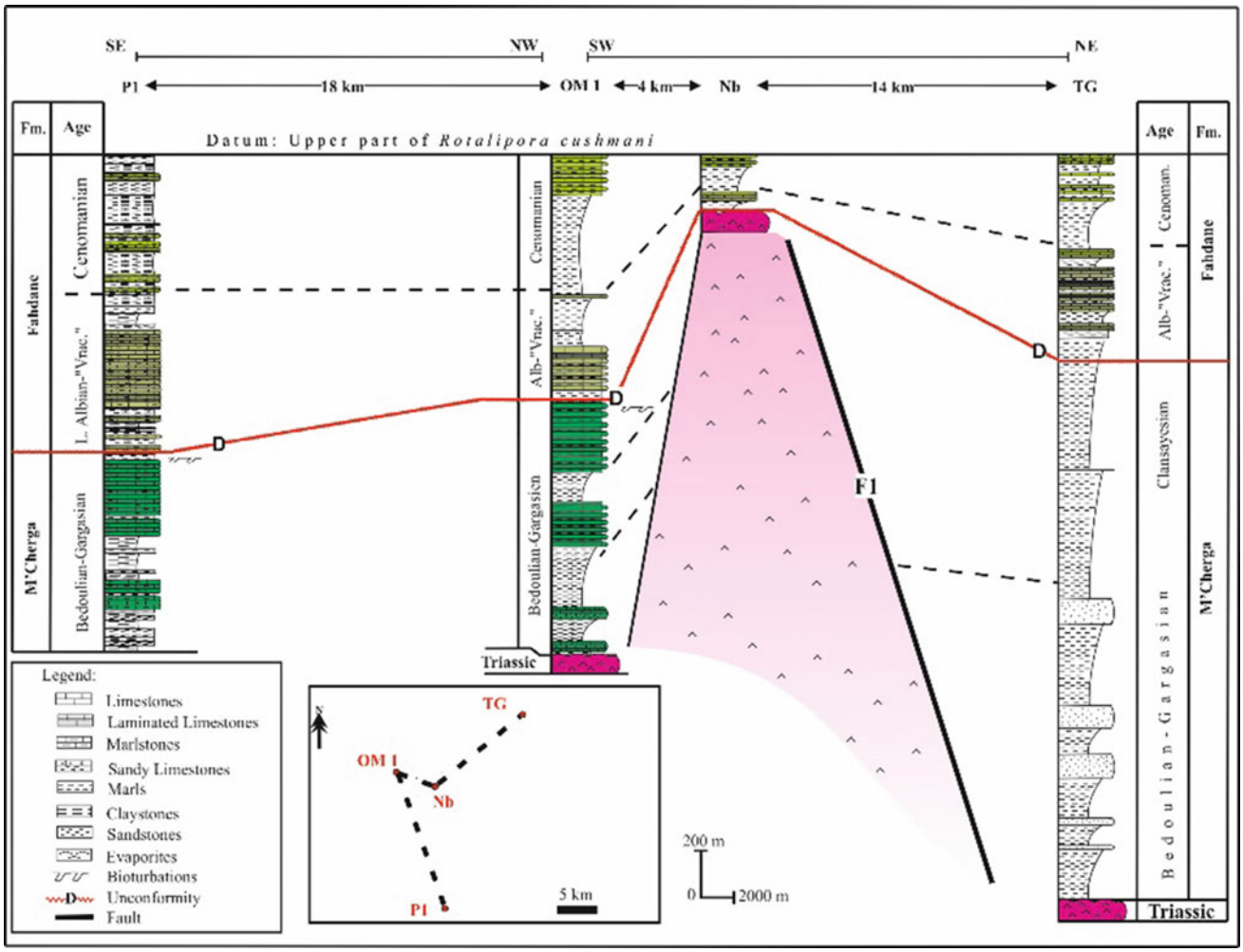

Fig. 2 SE–NW and SW–NE lithostratigraphic correlations of P1, OM1, Nb, and TG sections

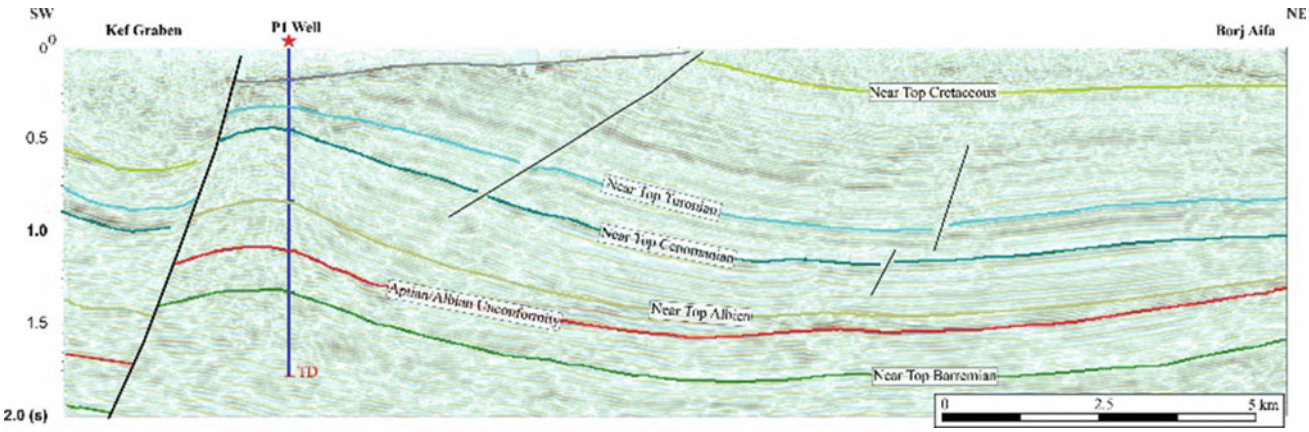

Fig. 3 NE–SW regional migrated seismic line L1 showing data from P1 well to Borj Aifa domain

the late Albian black shales in the Mellegue area (OM1 section) and to the South, toward the well.

4 Discussion

The correlations between the lithostratigraphic logs, petroleum well, and seismic profiles provided a clear picture of the evolution of the Mellegue–Nebeur–Tell el Ghozlane sedimentary basin during the Aptian–Albian times which can be proposed. The facies and thickness variation thus identified are interpreted to be related to at least two main interacting factors: Contemporaneous tectonics and Triassic salt instability induced by the migration of salt along major faults.

The main fault system F1, trending NW–SE (Figs. 1 and 2), bounds the Nebeur–Mellegue area, and appears to have been active during the Aptian–Albian, with an extensional regime favoring tilting and subsiding processes. However, from the Aptian to the late Albian, an obvious shift occurs in terms of directions and style of tilting and subsidence.

During the Aptian, the extensional regime was mainly expressed by normal to listric faults, which triggered a block tilting toward the NE and consequently the formation of a subsiding basin in the Tell el Ghozlane area (TG section) and an uplifted horst toward the W (Nebeur–Mellegue area) and the SW (P1 well). Following NE-SW tectonics, coupled with loading by the sedimentary overburden, induced halokinetic movements of the plasticity of the predominantly Triassic salt, especially to the NE of the study area. Since the late Albian onward, the picture changed completely. Tilting and subsidence were rather active toward the W and SW. This picture may be due to a tectonic regime probably in relation with the collapse of Aptian "diapirs."

Concerning the petroleum prospects of the area, the study area is part of the northern margin of Tunisia, where Aptian siliciclastics and carbonates are among the main reservoir rocks. Our study of the tectonic-sedimentary processes allowed us to reconstruct the regional paleogeography during the Aptian. The tilting of the Nebeur–Mellegue block toward the NE was accompanied by a significant detrital input favoring sandstone rather than calcareous sedimentation and consequently better quality of reservoir rocks than that detected to the SW in the Mellegue area (OM1).

5 Conclusions

During the Aptian–Albian interval, the study area appears constituted of several blocks separated by faults. At least, a main NW–SE fracturing trend was detected. During the Aptian, normal to listric faults induced blocks tilting toward the NE, favored the creation of depocenters. Parallel to tilting, subsiding resulted in the deepening of the basins. These depocenters mainly received detrital input forming potential reservoir rocks. The combined effect of overburden loading associated with subsidence and Aptian extensive tectonics contributed to the triggering halokinetic activity, particularly during the Albian, giving rise to "subsidence inversion" in places and tilting of blocks towards the SW. This shows that both tectonics and halokinetic activity played a crucial role in the control of tectono-sedimentary evolution in Aptian and Albian times in northwestern Tunisia. The approach used in this study may help in subsurface interpretations and hydrocarbon exploration modeling and could be transposed to other areas in the southern Tethyan margin.

References

Chihaoui, A., Jaillard, E., Latil, J., Zghal, I., Susperregui, A.S., Touir, J., Ouali, J.: Stratigraphy of the Hameima and lower Fahdene Formations in the Tajerouine area (Northern Tunisia). J. Afr. Earth Sci. **58**, 387–399 (2010)

Chikhaoui, M., Maamouri, A.L., Salaj, J., Turki, M.M., Ben Youssef, M., Ghanmi, M., Zarbout, M.: Blocs basculés au Crétacé inférieur dans la région du Kef (Tunisie nord-occidentale). C. R. Acad. Sci. Ser. IIA Earth Planet. Sci. **327**, 265–270 (1998)

Comparative Surface–Subsurface Studies of Upper Cretaceous Carbonates in Central Tunisia. Erosion, Resedimentation Processes, and Petroleum Implications

Akrem Soltani, Fares Khemiri, and Mohamed Hédi Negra

Abstract

Detailed lithostratigraphical studies of Turonian–Coniacian sedimentary records from three sections outcropping to the SE of Sidi Bouzid city, central Tunisia, close to an exploration well in the "Sahel domain" (Sfax onshore), allowed us to provide new data about the facies pattern in the area. The upper Cenomanian–early Turonian platform carbonates of the Gattar Member, well developed in central Tunisia, are predominantly composed of rudist-rich limestones changing to tidal-flat-open lagoonal facies. Around the Boudinar–Boudouaou area, the Gattar carbonates are marked by emersion and erosion features. The erosion product material, which is resedimented in neighboring depressions, constitutes the Rouana breccia that is only encountered at Boudinar and Boudouaou outcrops. Above, the lower-middle Turonian Bireno carbonates are also rich in rudists associated to peloids and lithoclasts. During this time, erosion features and resedimentation processes occur in Khsham el Artsouma outcrop and the studied well. During the Coniacian, the Douleb oolitic shallow marine limestones, which are well represented and encountered at the eastern studied outcrops and in subsurface, appear more homogeneous and relatively well correlatable. During the late Cenomanian–Turonian, the identified facies changes may reflect topographic irregularities of the sea floor, in relation with contemporaneous tectonic movements. This predominantly extensive faulting has created paleohighs and subsiding blocks. This architecture is at least suggested by three features: the significant thickness and facies variations; the frequency of gravity structures such as slump marks; the local frequency of mass-flow deposits such as debris-flow conglomerates.

Keywords

Late Cretaceous • Carbonate platforms • Central Tunisia • Resedimentation • Gravity deposits

1 Introduction

During the Turonian–Coniacian, the Tethyan domain was characterized by the development of carbonate platforms on shallow shelves (Khemiri et al. 2014). Spectacular tectonic activities were marked by the beginning of the Cenomanian–Turonian "rifting" allowing the opening of five intra-Pangean basins. In Tunisia, as part of the southern Tethyan margin, the onset of this event (rifting) allowed the development of upper Cenomanian–early Turonian rudist-rich carbonates known as the "Gattar Member" and widely extended in central Tunisia. Immediately above the Gattar carbonates, polygenic mega-breccia known as the Rouana Member (Khessibi 1978) and paleosoils were locally developed in central Tunisia. Regarding their origin, some authors consider it related to sedimentary processes while others suggest tectonic activities. Toward the eastern part ("Sahel domain"), there is no evidence of resedimentation processes. The upper Cenomanian–lower Turonian Gattar carbonates are directly overlain by the Annaba marls and the rudist-rich carbonates of the Bireno Member. Above, the upper Turonian–Coniacian Douleb carbonates consist of oolitic-rich shallow marine carbonates. The present work was undertaken for a better understanding of upper Cretaceous facies pattern, lateral variations, and carbonate platform evolution through time in response to eustatic and tectonic factors.

A. Soltani (✉) · M. H. Negra
Département de Géologie, FST, Université de Tunis El Manar, Tunis, Tunisia

F. Khemiri
Entreprise Tunisienne des Activités Pétrolière (ETAP), CRDP, Charguia, Tunisia

M. Meghraoui et al. (eds.), *Advances in Geophysics, Tectonics and Petroleum Geosciences*,
Advances in Science, Technology & Innovation, https://doi.org/10.1007/978-3-030-73026-0_143

2 Materials and Methods

This study relied on surface and subsurface data gathered from three outcrop sections, described, logged, and sampled at bed-scale in Sidi Bouzid-Mezzouna area (Central Tunisia) and one subsurface section selected from an exploration well, is located in the onshore "Sahel domain" of the Sfax area (eastern Tunisia; Fig. 1). More than 550 thin sections of carbonate rocks were studied under binocular polarizing microscope and described. Thus, clay and marl samples were washed through sieves of 200, 355, and 800 µm then oven dried at a temperature less than 50 °C. The obtained residues were used to identify planktonic foraminifera specimens and other associated species. The biostratigraphical studies provide a precise age for the studied series and the following correlations.

3 Results

In the Boudouaou section, (Fig. 1), the Gattar Member mainly consists of a rudist-rich dolomitic unit (Razgallah et al. 1994) locally showing laminated and silicified beds at its upper part. Above, the conglomeratic Rouana Member (Khessibi 1978) is clearly thicker (45 m) and qualified as a mega-breccia unit. In terms of lithology, contains poorly sorted angular to sub-angular, dolomitic, sandy, and siliceous elements. The latter range from centimeter-sized pebbles to decimeter-scale blocks (0, 1 to 0.8 m) floating within a yellowish dolomicritic matrix (Fig. 3a, b). The overlying Bireno Member is composed of marls, tidalitic laminated dolostone, and limestone containing benthic foraminifers, peloids, and gastropods. It is overlain by upper Turonian–Coniacian Douleb marls and carbonates. The latter consist of

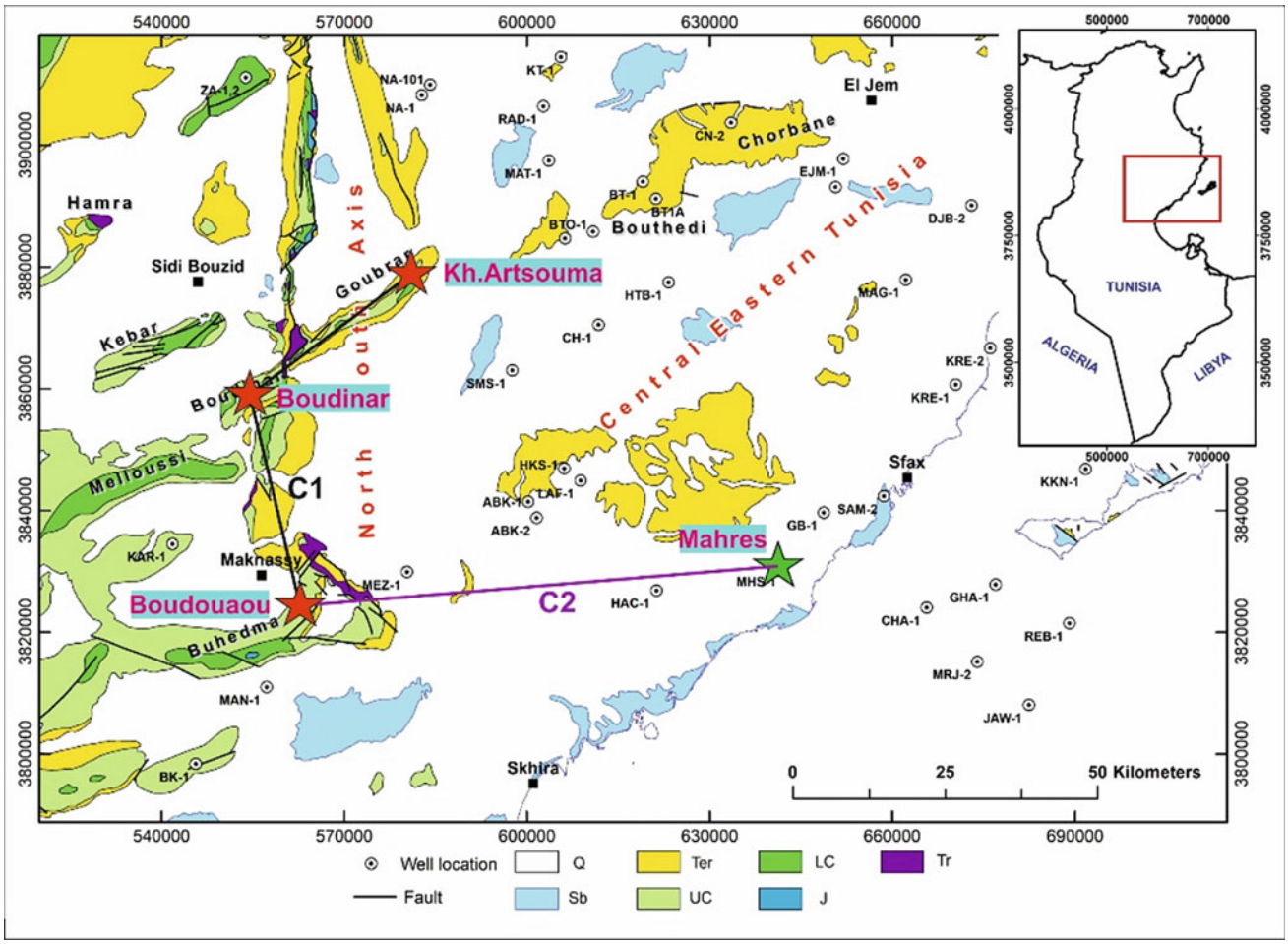

Fig. 1 Location of the studied sections on the extract map portion from the geological map of Tunisia at a 1.500000

stromatolites-rich laminated dolostones and limestones composed of wackestones rich in benthic foraminifers (miliolids) and peloid-rich packstones (Fig. 2c). This unit shows metric slump marks, suggesting sliding features on slopes, triggered in relation with tectonic instabilities. Laterally, in the Boudinar section, the Gattar Member shows a comparable composition (rudist dominant facies) where the summital part is marked by erosional features expressed by micro-breccia deposits and red silts of continental aspect. The Rouana breccia and conglomerates form a layer thinner than that encountered in the Boudouaou section. In addition, the resedimented elements are dominated by poorly sorted angular and sub-angluar, non-fossiliferous dolomitic blocks, enveloped by a red silty matrix (Figs. 2a and 3a). Above, the resedimented elements are rather sub-rounded, well sorted, and enveloped by a white to beige matrix. They probably reflect an aquatic reworking and transportation. To the east, in Sfax onshore, the Cenomanian–Turonian Zebbag and Bireno units associate carbonates and anhydrites. Carbonates, which are mainly represented by dolostones, are composed of bioclasts and oolites, suggesting shallower depositional environments comparatively to the outcrops sector (toward the west). However, the clear thickening, at least locally, in Sfax onshore, suggests an active subsidence related to contemporaneous extensive faulting. The absence of conglomeratic deposits confirm the relatively elevated position of this area during the late Cenomanian—early Turonian. Above, the lower-middle Turonian Bireno facies are comparable and correlatable from the Boudinar area to the Boudouaou section. They are mainly formed of massive burrowed bioclastic dolostones topped by algal-rich laminated carbonates. However, in Khshem Artsouma, the Bireno facies (Razgallah et al. 1994) change to more open marine facies formed of thin marly layers alternating with rudist-rich dolostones and oolite-rich dolomitic limestones. Above, in the Boudinar section, the Coniacian Douleb series are made up of marls alternating with tidal-flat dolostones containing stromatolites and showing bird's eyes structures.

Laterally, in Khshem Artsouma section, the Douleb Member consists of three lithologic units: The lower unit formed of nodular, lumachellic marls alternating with burrowed limestone beds containing bryozoans, dasyclads, echinoderms, and peloids (Fig. 2d); The middle unit is formed of thick oolitic to bioclastic grainstone–packstone; The upper unit is made of thin limestone beds alternating with marly lumachellic layers at the top (Khemiri et al. 2014). It contains echinoderms, dasyclads, benthic foraminifera (miliolids), and other bioclasts (Fig. 1). Comparable facies were encountered in the studied well, with a dominance of oolitic limestones suggesting high-energy shoal environments.

4 Discussion

During the late Cenomanian–early Turonian, lateral changes from a shelf setting (in the central part) to a more open marine to outer shelf facies (Fig. 3b) are obvious. At early to

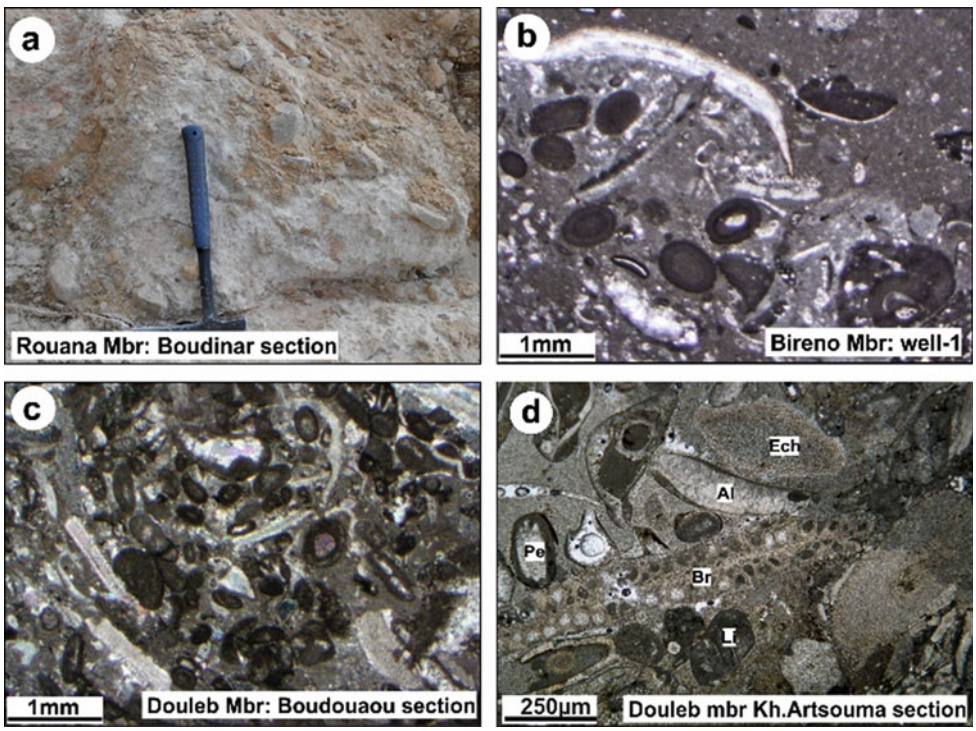

Fig. 2 Turonian–Coniacian facies association in central-eastern

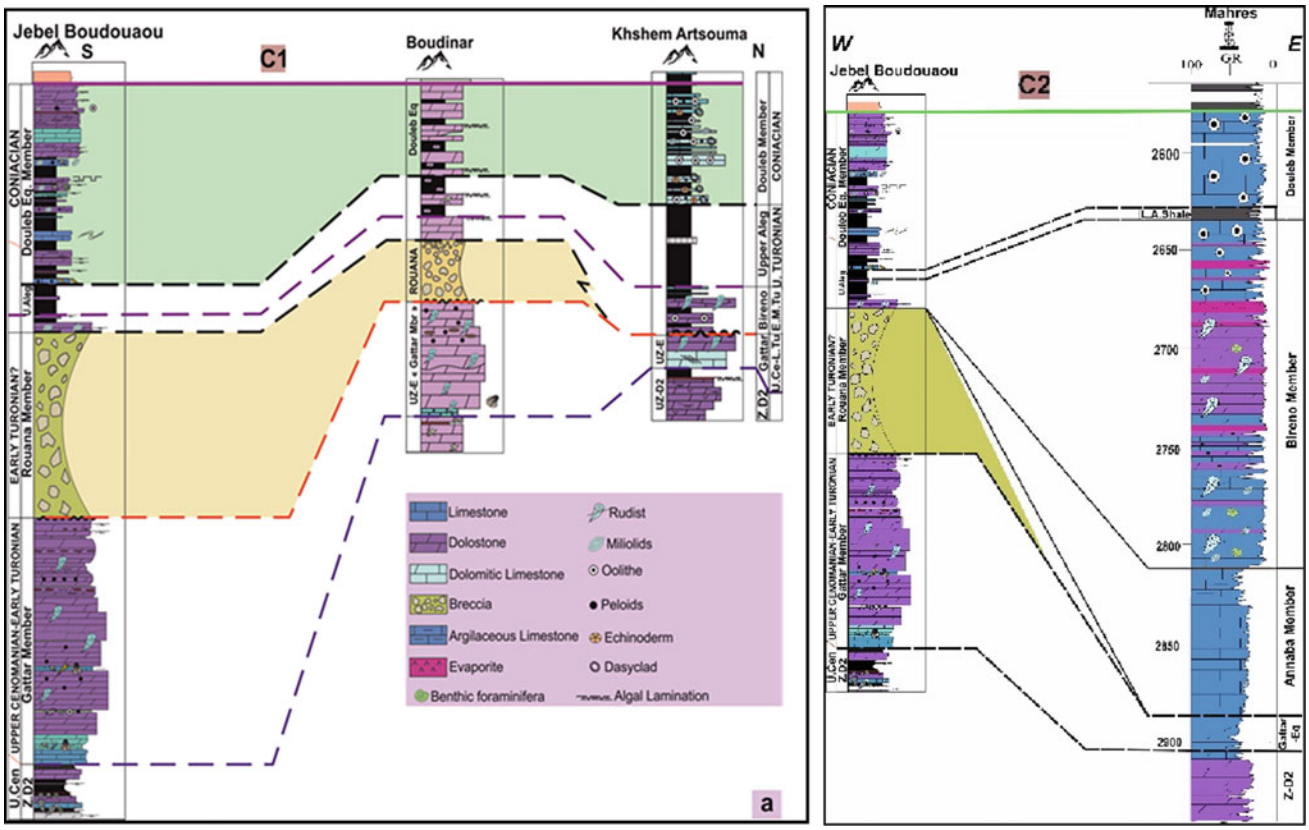

Fig. 3 S–N and W–E correlations of the surveyed sections

middle Turonian timeline, a major regression occurred. The sea level dramatically fell reached a trough in earliest Turonian (Razgallah et al. 1994; Haq 2014) causing an emersion of the Gattar platform in the central part. Concerning the Rouana Breccia, the difference in size, shapes, and roundness of elements and blocks across the two-outcrop sections suggests its deposition at different positions from the source. These features suggest that this breccia seems to be located in more distal setting (Fig. 3a).

5 Conclusions

In central-eastern Tunisia, during the upper Cenomanian–Coniacian, sedimentological investigations have led to the identification of varied facies associations. Lateral variations within the succession is controlled by tectonic movements and sea level fluctuations. The existence of gravity structures such as slump marks, debris-flow deposits (Rouana conglomerates), in addition to thicknesses variations, are in favor of resedimentation processes following erosion and transportation of the erosion product material on slopes. The sudden beginning of the erosion processes could be rather related to contemporaneous tectonic movements. Mid-late Cretaceous tectonic movements were common in other areas of central Tunisia (Chihi et al. 1984; Kadri et al. 2015).

References

Chihi, L., Dlala, M., Ben Ayed, N.: Manifestations tectoniques synsédimentaires et polyphasées d'âge crétacé moyen dans l'Atlas tunisien central (région de Kasserine). C.R. Acad. Sci. (Paris) **298/II** (4), 141–146 (1984)

Haq, B.: Cretaceous eustasy revisited. Global Planet. Change **113** (2014), 44–58 (2014)

Kadri, A., Essid, M., Merzeraud, G.: "Kasserine Island" boundaries variations during the Upper Cretaceous-Eocene (Central Tunisia). J. Afr. Earth Sci. **111**, 244–257 (2015)

Khemiri, F., Meskini, A., Maazaoui, A., Soussi, M.: Coniacian Douleb carbonate member at Khsham El Artsouma, Central Eastern Tunisia. Reservoir Characterization and Subsurface Analogue, Search and Discovery Article #51042 (2014)

Khessibi, M.: Etudes géologiques du secteur Maknassy- Mazzouna et du Jebel Kebar (Tunisie centrale). Thèse d'Université, Lyon (1978)

Razgallah, S., Philip, J., Thomel, G., Zaghbib-Turki, D., Chaabani, F., Ben Haj Ali, N., M'Rabet, A.: La limite Cénomanien-Turonien en Tunisie centrale et méridionale: biostratigraphie et paléoenvironnements. Cretac. Res. **15**, 507–533 (1994)

Tectono-Sedimentary Evolution of the Uranium Deposits in the DASA Graben (Northern Niger)

Abdoulwahid Sani, Moussa Konate, Karimou Dia Hantchi, and Peter Wolenberg

Abstract

This study presented the structural evolution of the N70° Paleozoic–Mesozoic DASA graben which is considered as a sub-basin of the Tim Mersoï basin located in the northern part of Niger. The DASA graben is a uranium-rich trough discovered in recent exploration surveys. A tectono-sedimentary analysis of the DASA graben is implemented with a combined use of satellite imagery, field observations, borehole data analysis, and available literature. The DASA graben was affected from Carboniferous to Early Cretaceous by two major tectonic periods. The first period corresponds to uplifting stage (Carboniferous to Permian) and the second one to a rifting stage (Triassic to Early Cretaceous). The particularity of the DASA graben is its very high uranium grade. We have established that those lithological and tectonic factors control the setting up of the uranium mineralization in the DASA graben. The successive fracturing phases that affected the DASA graben associated with a greater circulation of hydrothermal fluids would have favored higher grades of uranium mineralization. Compared to the Tim Mersoï basin, the DASA graben is characterized by its very high uranium grade due to the intense fracturing favoring fluids flow.

Keywords

DASA graben • Tectono-sedimentary • Uplifting stage • Rifting stage • Uranium deposit

A. Sani (✉) · M. Konate
Département de Géologie, Université d'Agadez Niger, PO Box 199 Agadez-Niger, Niger

K. D. Hantchi
Université de Maradi, PO Box 465 Maradi, Niger

P. Wolenberg
Global Atomic Corporation, Toronto, Canada

1 Introduction

The Tim Mersoï basin, located in the western edge of the Aïr, is well known due to its uranium mineralization, hosted in the carboniferous and Jurassic formations (Fig. 1a). This basin corresponds to the northeastern part of the Iullemmeden basin (Fig. 1b). It is bounded to the West by In Guezzam Ridge and to the East by the Aïr Mountain. Toward the North, it penetrates the Hoggar Massif to Algeria where it is known as the syncline of Tin Séririne (Fig. 1b) (Yahaya 1992; Konaté et al. 2007).

Recent exploration surveys have highlighted a highly mineralized graben corresponding to DASA (Dajy Surface Anomaly) graben. The latter is the object of this study. It has a singular position between the Arlit mining area to the North and the Anou Araren coal trough to the South (Fig. 2a). The main objective of this study was to determine the factors favoring uranium concentrations in the DASA graben.

2 Geological Settings

The Paleo-Mesozoic Tim Mersoï basin is characterized by a detrital infilling which rests unconformably on the ante-Cambrian basement.

The DASA graben is a sub-basin of the Tim Mersoï basin. It is bounded by the N70° trending fault (Azouza fault) along which the Azelik deposit is located. Geologically, all the sedimentary series recognized in the Tim Mersoï basin are represented at the DASA area (Fig. 1a). The use of satellite images, combined with survey and field data, delineated the DASA graben (Fig. 2b). The main faults observed are: the Azouza N70° trending fault which marked the border of the trough, Adrar-Emoles N30° striking fault, and secondary faults N130° to N150° trending and E–W striking (Fig. 2b).

M. Meghraoui et al. (eds.), *Advances in Geophysics, Tectonics and Petroleum Geosciences*, Advances in Science, Technology & Innovation, https://doi.org/10.1007/978-3-030-73026-0_144

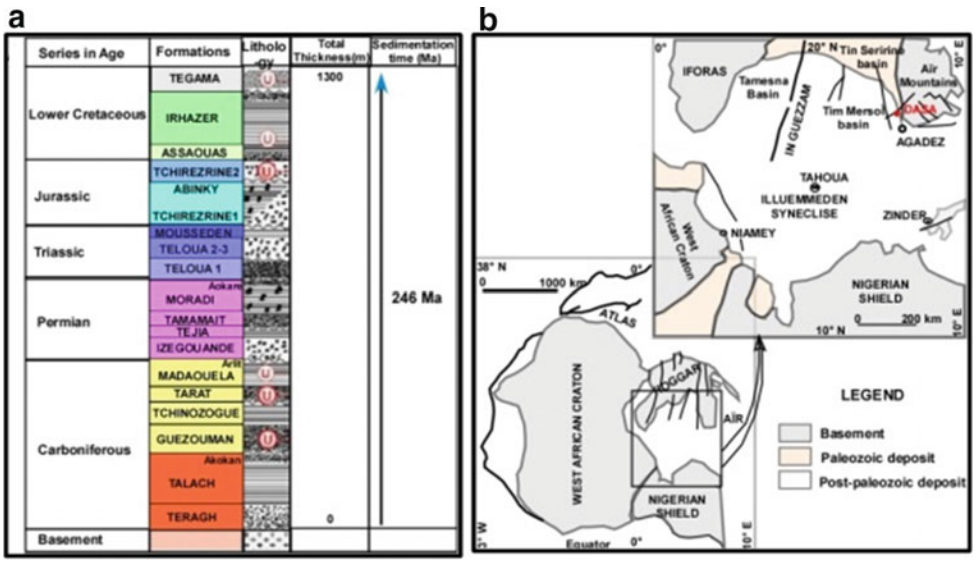

Fig. 1 **a** Simplified stratigraphic log of the geological series of the Tim Mersoï basin (modified after Cazoulat 1984), mean subsidence = 5.28 m/Ma. **b** Geographical location of the Tim Mersoï Basin in the Iullemmeden syneclise (modified after Konaté et al. 2007)

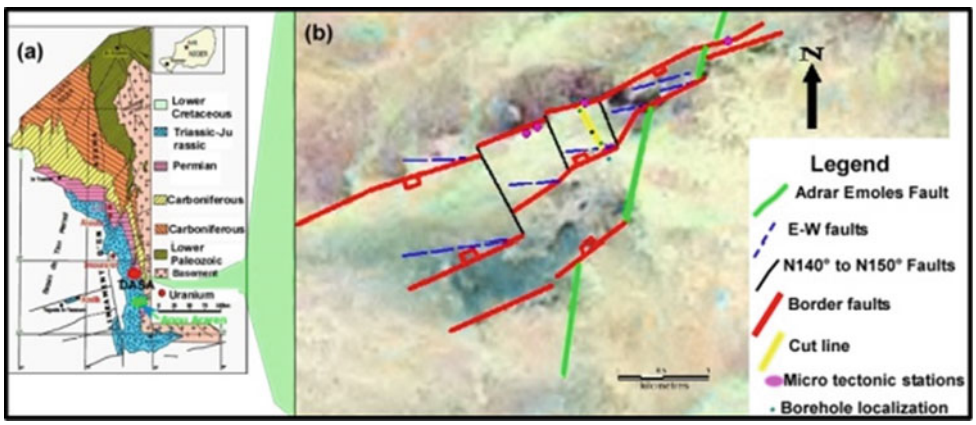

Fig. 2 Location of the DASA trough in the Tim Mersoï Basin: in **a** simplified geological map of the eastern part of the Tim Mersoï Basin (modified after Gerbeaud 2006) and **b** DASA graben

3 Materials and Methods

In this study, a multidisciplinary approach involving various tools (e.g., seismic profiles, satellite images, drilling cores), software (e.g., MapInfo 11.5, Surfer 11, Canvas 11), and techniques (e.g., seismic interpretation, well logs correlation, microtectonics analysis, and geochemical analysis) has enabled us to:

(1) make a tectono-sedimentary analysis;
(2) determine the spatial arrangement of uranium deposits;
(3) characterize the basin geometry.

4 Results

4.1 Relationship Between Tectonics and Sedimentation

To better understand the DASA graben structuration, we have achieved synthetic cross-sections from well logs correlation (Fig. 3). This approach allowed us to show the lateral and vertical succession of the different facies and establish the relationships between tectonics and sedimentation. The geological cross section obtained shows, that in the axial zone of the DASA graben, the maximum thickness of the deposits is about 805 m (according to the borehole data), for a

sedimentation period of 246 Ma (according to the lithostratigraphic column). This implies a lower subsidence of about 3.22 m/Ma (Fig. 3) compared to that of the Tim Mersoï basin whose subsidence is on average of 5.3 m/Ma (Fig. 1a). Most sedimentary series of the DASA graben exhibit variations in thickness on both sides of the border faults (Fig. 3). However, according to the stratigraphic series (Fig. 3), these variations are more or less marked in thickness.

The sedimentary infilling of the DASA graben is marked by two periods of subsidence:

- A first period characterized by a low subsidence rate (3.75 m/Ma on average), which extends from the Carboniferous to the Permian. The Permian series are particularly marked by a strong reduction in thickness in the axial zone of the graben (30 m), compared to the edge zones (188–215 m) (Fig. 3).
- A second period marked by a strong subsidence rate (4.11 m/Ma) from the Triassic to the lower Cretaceous (Fig. 3). The strongest subsidence rate occurred during lower Cretaceous in the axial zone (6.52 m/Ma), while in the border zones the subsidence rate is very low (1.17–1.65 m/Ma) (Fig. 3).

The subsidence inversions between the axial zone of the DASA graben and the edge zones reflect a morphological inversion related to a change in the tectonic regime.

During the first period, from Carboniferous to Permian, the axial zone of the DASA graben was affected by an uplift stage. During the second one, from the Triassic to the lower Cretaceous, the highest thicknesses of the deposits are observed in the axial zone of the graben, whereas the thicknesses are lower on the border zones. The DASA sector was affected by a rifting stage.

4.2 Mineralogy and Uranium Distribution in DASA Graben

Uranium mineralization in the DASA graben is hosted in organic matter and/or pyrite rich sandstones or in analcime-rich sandstones. The chemical analyzes performed on the core samples yielded six types of uranium minerals which are: Carnotite; Uranophane; U-rich titanite; Coffinite; Torbernite; Autunite. For mineralization distribution at the DASA graben, the highest concentrations are on the Southeastern part (Fig. 4). This sector corresponds to the most faulted area of the DASA graben.

4.3 Microtectonic Analysis

In the DASA graben, Paleo-Mesozoic sedimentary deposits are affected by normal microfaults (syn- and post-sedimentary). These locally determine a microhorts and microgaben structure (Fig. 5A). Figure 5C(a) shows syn-sedimentary microfaults affecting carboniferous deposits while Fig. 5C(b) corresponds to syn-sedimentary microfaults affecting Jurassic deposits. Figure 5B shows a post-sedimentary microfault affecting Jurassic deposits.

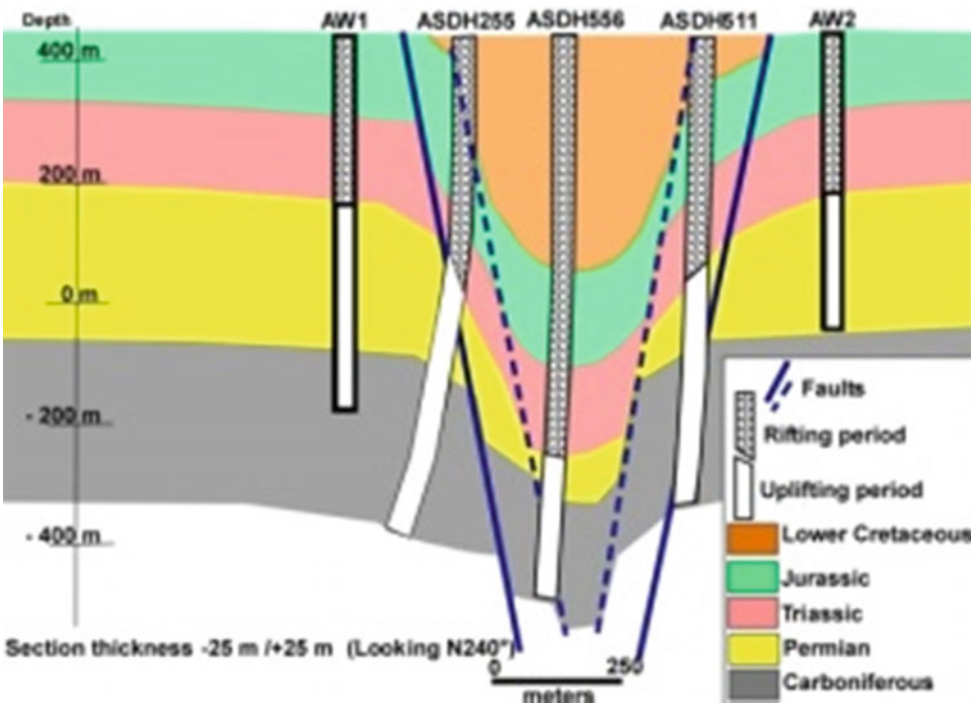

Fig. 3 Geological section of the DASA graben made from survey data

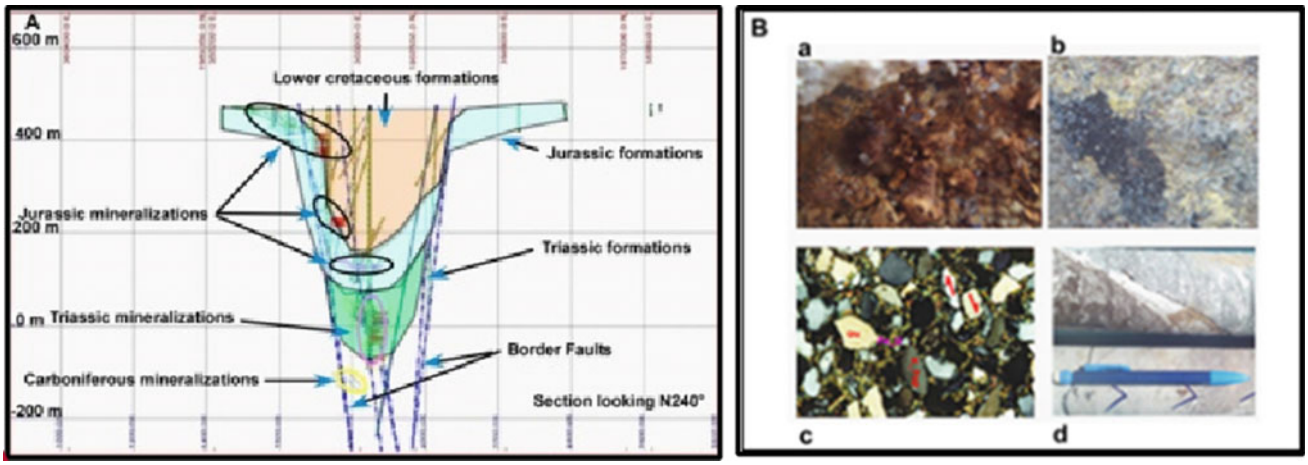

Fig. 4 Uranium distribution in DASA graben (**A**), **B** (**a**) Oxidize sandstone, (**b** and **c**) occurrence of uranium in DASA sandstone, (**d**) microfault infilling with calcite

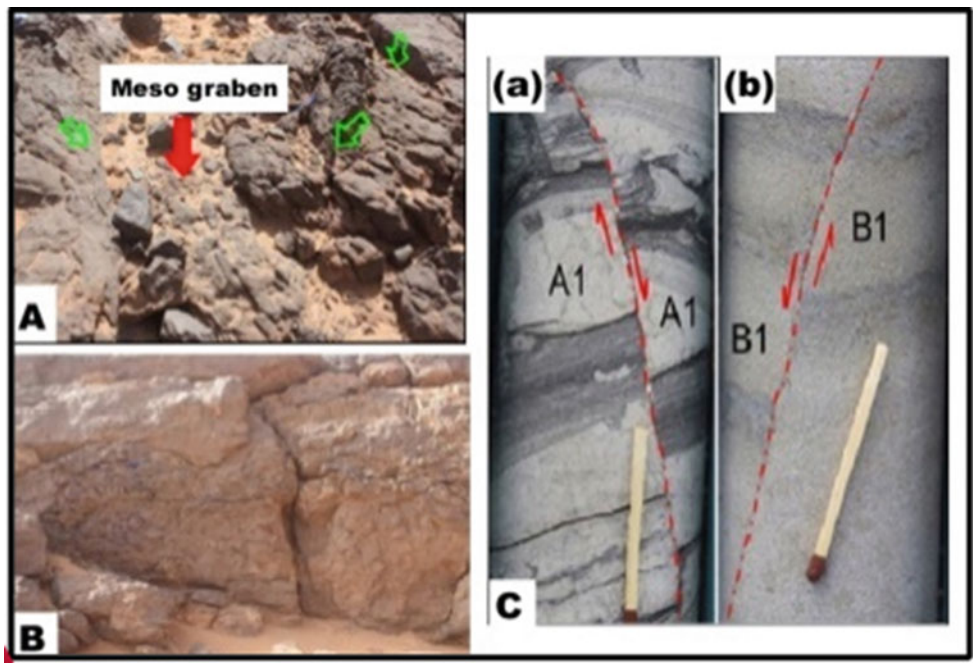

Fig. 5 **A** Meso-graben, **B** cataclazed area in DASA and **C** syn-sedimentation microfault on the DASA core. Two criteria are used to distinguish the syn-sedimentary tectonics. These are, on the one hand, the thickness level variations on both sides of the microfault and, on the other hand, lateral facies variations (**a** in the Carboniferous formation of Tarat and **b** in the Jurassic formation of Tchi2)

5 Discussion

To explain the succession of the two phases of the DASA graben structuring (uplift/rifting) over time, the results of this study are compared to those achieved in other African basins, such as Tim Mersoï, Téfidet (North Niger), Benue trough (Nigeria), and Muglad basin (Sudan).

An N40° Visean compression phase has been highlighted in Algeria in the Ougarta area by Blès (1969), in the Béchar Basin by Conrad and Lemosquet (1984), in the Illizi Basin by Boudjema (1987), and in the Ahnet Basin by Zazoun (2001). In Tim Mersoï basin, too, a N25° horizontal shortening, upper Visean in age, was highlighted by Konaté et al. (2007). During the Visean period, the uplifting observed in the DASA graben indicates that the strike-slip sinistral reactivation of the N70° trending faults has a reverse component. An ~N70° transpressive regime would have affected the DASA graben during this period.

The structural evolution of the DASA graben during the Jurassic–Cretaceous period is compared to those of the West and Central African Rift Systems. During the lower Cretaceous, these rift systems were affected by extensive to transtensive tectonics regime (Guiraud et al. 1993; Ye 2016), favoring a strong rate of subsidence (54 m/Ma for the Termit basin (Liu et al. 2015), 65 m/Ma for the Muglad Basin

(Yassin 2016), 43 m/Ma for the Benue trough (Guiraud 1992) and 13 m/Ma for the Téfidet trough (Konaté et al. 2019)). Unlike those Cretaceous rift systems, the DASA graben has a lower subsidence rate (about 6.52 m/Ma). Given to the geodynamic context during the Cretaceous period, these extensional tectonic regimes affecting the DASA graben could be associated with the opening of the South Atlantic that occurred during this period (Genik 1992; Guiraud et al. 2005; Ye 2016).

Uranium mineralizations, recognized in the Carboniferous and Jurassic–Cretaceous formations of the Tim Mersoï Basin, are also found in the DASA Graben. Six types of uranium minerals were identified on samples from the Jurassic sediments of the DASA graben. These are the following minerals: Carnotite, Uranophane, Titanite, Coffinite, Torbernite, and Autunite. In addition to these Carboniferous and Jurassic–Cretaceous mineralizations, the DASA graben also contains uranium mineralizations in the Triassic formation.

In the DASA graben, many factors are involved in the control of the uranium mineralization. These are:

- Lithological factor: uranium is mainly hosted within the coarser-grained microconglomeratic facies of grayish to greenish color containing sulfides and organic matter.

This characteristic was mentioned by Forbes (1989) who shows that organic matter and pyrite bearing sandstones would be a preferential trap for uranium mineralization. Moreover, in the case of the DASA deposit, it also seems that analcime-rich sediments (Triassic to Cretaceous in age) could be a favorable lithology to the uranium mineralization concentration. This last observation is in agreement with the results obtained by Billon (2014) in Tim Mersoï basin.

- Tectonic factor: microfractures mineralized in uranium are observed in several core samples. Quartz and feldspar contain microfractures partially filled with U-rich oxide. Some samples are intensely cataclastically deformed by a high hydrothermal fluid pressure that gives the rock a granitic appearance. In the Tim Mersoï basin, this hydrothermal fluid flow has been mentioned by Salze (2008). According to Forbes (1989), the acting of the Arlit fault would have favored to put some reduced carboniferous formations in contact with oxidized Permian formations. This spatial arrangement would have favored the concentration of uranium in the Arlit area Carboniferous formations. A similar arrangement has been observed in the DASA graben, where faults have put into contact the Triassic–Jurassic formations with the Permian formations (Fig. 3).

Unlike other deposits in the Tim Mersoï basin (0.04–0.05% of uranium grade), in the DASA graben, the higher fracturing density associated with a greater circulation of hydrothermal fluids would have favored higher grades (1% on average) of uranium mineralization (Global Atomic Corporation 2018).

6 Conclusions

The tectono-sedimentary analysis suggests that the DASA graben was affected by two major structuring periods.

- The first period is an uplifting stage, which prevailed during the Carboniferous–Permian times. It was marked by a ~N70° transpressive tectonic regime.
- The second one is a rifting stage that occurred during the period ranging from Triassic to Lower Cretaceous. This period was mainly characterized by a ~N160° extensional regime.

Several factors have controlled the establishment of uranium mineralization in the DASA graben. These are lithologic and tectonic.

From a lithological point of view, uranium is mainly hosted within coarse-grained sediments, including sulfides and organic matter in Carboniferous deposits or analcime in Triassic to Cretaceous deposits.

This study also shows that the successive fracturing phases which affected the DASA graben played an important role in the emplacement of the mineralization. In addition, this intense fracturing observed in some core samples is associated with fracture infilling by sediments with a higher grade of uranium mineralization.

References

Billon, S.: Minéraux argileux dans le gisement uranifère d'Imouraren (Bassin de Tim Mersoï, Niger): Implications sur la genèse du gisement et sur l'optimisation des processus de traitement du minerai. Thèse Terre solide et enveloppes superficielles. Poitiers: Université de Poitiers, (2014)

Blès, J.L.: Les relations des microfractures avec le plissement dans la région du Djebel Ben Tadjine et au 'km 30' (Chaînes d'Ougarta--Sahara occidental, Algérie). Publication Service Géologique Algérie 39,193-204 (1969)

Boudjema, A.: Évolution structurale du bassin pétrolier 'triasique' du Sahara Nord Oriental (Algérie). Thèse Doctorat Etat, Paris XI-Orsay, France, 290p (1987)

Cazoulat, M.: Geologic environment of the uranium deposits in the Carboniferous and Jurassic sandstones of the Western margin of the Aïr mountains in the Republic of Niger. In: Geological environments of sandstone-type uranium deposits. IAEA-TECDOC 328, Vienna, Pp.247-263 (1985)

Conrad, J., & Lemosquet, Y.: Du craton vers sa marge; evolution sedimentaire et structurale du bassin Ahnet- Timimoun-Bechar

(Sahara algerien) au cours du Carbonifere; donnees paleoclimatiques. Bulletin de la Société Géologique de France, 7(6), 987-994 (1984)

Forbes, P.: Rôles des structures sédimentaires et tectoniques, du volcanisme alcalin régional et des fluides diagénétiques-hydrothermaux pour la formation des minéralisations à U-Zr- Zn-V-Mo d'Akouta (Niger): mémoire édité par le Centre de Recherches sur la Géologie de l'Uranium (CREGU), Nancy, 376p (1989)

Genik, G. J.: Regional framework, structural and petroleum aspects of rift basins in Niger, Chad and the Central African Republic (CAR). Tectonophysics, 213(1-2), 169-185 (1992)

Gerbeaud, O.: Evolution structurale du Bassin de Tim Mersoï: Déformations de la couverture sédimentaire, Relations avec la localisation des gisements d'uranium du secteur d'Arlit (Niger). Thèse de doctorat Université de Paris-Sud UFR scientifique d'Orsay, 270 p (2006)

Global Atomic Corporation. Rapport interne d'exploration, (2018)

Guiraud, R., Bosworth, W., Thierry, J., & Delplanque, A.: Phanerozoic geological evolution of Northern and Central Africa: an overview. Journal of African Earth Sciences, 43(1- 3), 83-143 (2005)

Guiraud, M.: Late Jurassic rifting-early Cretaceous rifting and late Cretaceous transpressional inversion in the upper Benue basin (NE Nigeria). Bulletin des centres de recherches exploration-Production Elf-Aquitaine, 17(2), 371-383 (1993)

Guiraud, R., Maurin, J. C.: Early Cretaceous rifts of Western and (1992)

Konaté, M., Ahmed, Y., & Harouna, M.: Structural evolution of the Téfidet trough (East Aïr, Niger) in relation with the West African Cretaceous and Paleogene rifting and compression episodes. Comptes Rendus Geoscience, 351(5), 355-365 (2019)

Konaté, M., Denis, M., Yahaya, M., Guiraud, M.: Structuration extensive au devono-dinantien du bassin de Tim Mersoï (Bordure occidentale de l'Aïr, Nord Niger). Publié dans: Université de Ouagadougou, Annales, Série C, v. 005, 32 p (2007)

Liu, B., Wan, L., Mao, F., Liu, J., Lü, M., & Wang, Y.: Hydrocarbon potential of Upper Cretaceous marine source rocks in the Termit Basin, Niger. Journal of Petroleum Geology, 38(2), 157-175 (2015)

Salze, D.: Etude des interactions entre uranium et composés organiques dans les sys245tèmes hydrothermaux. Thèse de l'université de Nancy, 316p (2008)

Yahaya, M.: Dynamique sédimentaire du Guézouman et des formations viséennes sous-jacentes en liaison avec la tectonique, le volcanisme et le climat, paléomilieux des gîtes uranifères d'Arlit (Niger). Thèse Doctorat troisième cycle, Université de Dijon, 357 p (1992)

Yassin, M. A., Hariri, M. M., Abdullatif, O. M., Korvin, G., Makkawi, M.: Evolution history of transtensional pull- apart, oblique rift basin and its implication on hydro carbon exploration: A case study from Sufyan Sub-basin, Muglad Basin, Sudan. Marine and Petroleum Geology, 79, 282-299 (2017)

Ye, J.: Evolution topographique, tectonique et sédimentaire syn-à post-rift de la marge transformante ouest Africaine (Doctoral dissertation, Université de Toulouse, Université Toulouse III-Paul Sabatier), (2016)

Zazoun, RS.: La tectogenese hercynienne dans la partie occidentale du bassin de258 l'Ahnet et la region de Bled El-Mass, Sahara Algerien: un continuum de deformation. Jour259nal of African Earth Sciences, 32(4), 869-887 (2001)

Impact of Bioturbation on Quality of Early-Middle Miocene Shoreface Reservoirs, Coastal Swamp Depobelt, Niger Delta Basin (Nigeria)

Ayonma Wilfred Mode, Christopher Jackson, Ogechi Clementina Ekwenye, and Sunny Chibuzor Ezeh

Abstract

Core sections from two wells (M-11 and M-22) from the lower Miocene interval, in the Coastal Swamp Depobelt, Niger Delta Basin, were studied to determine the depositional environments and the impact of bioturbation on the reservoirs. Plots of average porosity and permeability values against the bioturbation intensity (BI), for the upper shoreface (USF) and lower shoreface (LSF) sections in each well, indicate that the burrowed intervals in the USF sections show a decline in porosity values with an increase in bioturbation intensity, reaching a maximum of 12% in M-11 well and 51% in M-22 well. The burrowed LSF section in M-11 well showed an increase in porosity with an increase in bioturbation intensity reaching a maximum of 38%, while the burrowed LSF section in M-22 exhibited a decline in porosity value to 45%. However, the burrowed USF and LSF sections in both M-11 and M-22 cores, showed a general decline in porosity/permeability with an increase in bioturbation intensity. The trends between bioturbation intensity and porosity/permeability in this study suggests that intervals with: (i) Moderate and rare bioturbation (BI: 2–3) have better reservoir quality, probably due to limited impact on the sediment fabrics (ii) Intense bioturbation (BI: 4–5), affected reservoir quality negatively due to the decrease in grain sorting resulting in porosity/permeability loss in the USF. However, in the LSF the reduction of porosity and permeability may be, related to siderite cementation.

Keywords

Bioturbation intensity • Shoreface reservoirs • Reservoir quality • Niger delta Basin

1 Introduction

Several studies have shown that sediment texture created by biogenic reworking (bioturbation) significantly affects the porosity and permeability trends in aquifers and petroleum reservoirs. In some cases, they may represent the only evidence available to develop a reasonable picture of depositional conditions and estimate reservoir heterogeneity. Bioturbation can enhance or reduce porosity/permeability, depending on trace fossil morphology, composition of burrow linings/fills, burrow size and bioturbation intensity (La Croix et al. 2012. Gingras et al. 1999, 2002, 2004, 2007; Pemberton and Gingras 2005; Cunningham et al. 2009; Tonkin et al. 2010).

Although burrowing is common in some Niger Delta reservoirs, studies of the impact of biogenic reworking on reservoir quality in the basin are very limited (Egbu et al. 2009; Mode 2012; Jackson et al. 2013; Ezeh et al. 2016).

The present study was performed on cores from two wells (M-11 and M-22), in the Coastal Swamp Depobelt of the Niger Delta Basin (Fig. 1), to determine the sedimentary environments and the impact of burrowing on the quality of the reservoirs.

2 Methodology

Core sections obtained from two wells "M-11" and "M-22" in OML 11 in the Coastal Swamp Depobelt were described and delineated into lithofacies. Depositional environments of the sediments were interpreted by integrating the lithofacies and ichnological data.

A. W. Mode (✉) · O. C. Ekwenye · S. C. Ezeh
Department of Geology, University of Nigeria, Nsukka, Enugu State, Nigeria
e-mail: wilfred.mode@unn.edu.ng

C. Jackson
Sterling Oil Exploration and Energy Production Company Ltd, Lagos, Nigeria

M. Meghraoui et al. (eds.), *Advances in Geophysics, Tectonics and Petroleum Geosciences*, Advances in Science, Technology & Innovation, https://doi.org/10.1007/978-3-030-73026-0_145

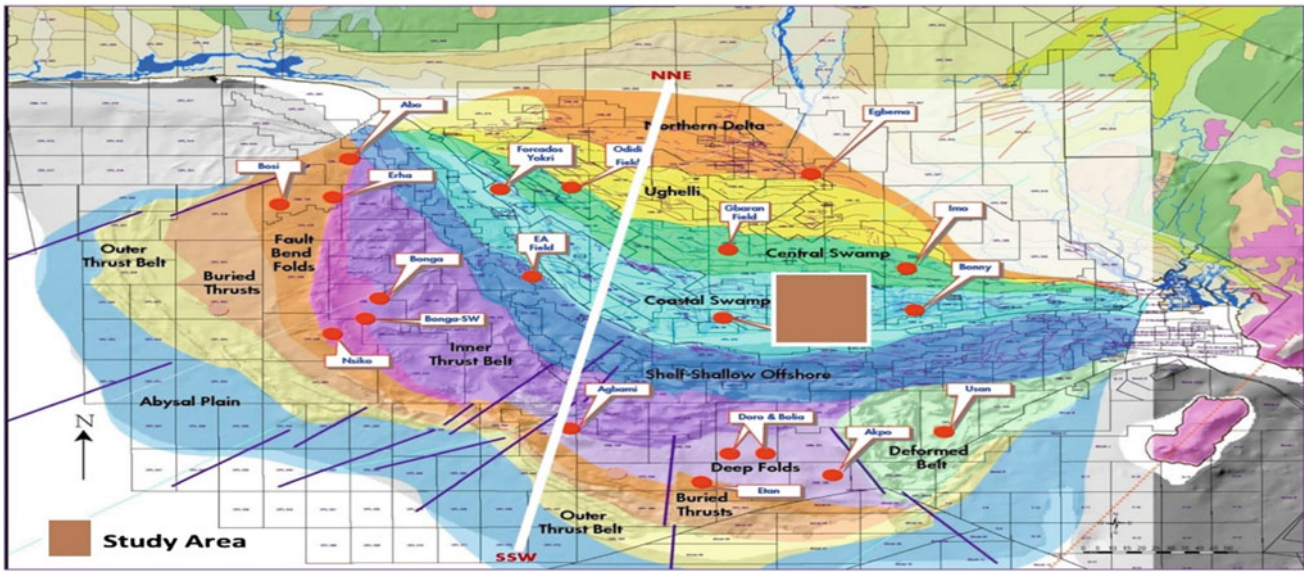

Fig. 1 Depobelt map with the structural play segments, Niger Delta Basin showing the study area in the Costal Swamp Depobelt (modified after Dim and Onuoha 2017)

The Ichnofabric index of Drosser and Bottjer (1986, 1989) was used to quantify the bioturbation intensity for each foot of core described in this study. Porosity and permeability values were obtained from core plugs at I foot interval in the core sections. Bioturbation index (BI) values, ranging from 1 (no burrows), 2 (up to 10%), 3 (10–40%), 4 (40–60%), and 5 (60–100%), were assigned to each foot of the core sections. The BI values were grouped into four classes representing the intensity of biogenic reworking as follows: 1 (BI: 1; no bioturbation); 2 (BI: 2; rare bioturbation), 3 (BI: 3; moderate bioturbation), and 4 (BI: 4–5; intense bioturbation). Porosity and permeability values corresponding to the four BI classes were averaged for the upper shoreface (USF) and lower shoreface (LSF) sections in each well (Tables 1 and 2). The porosity and permeability values were plotted against the BI values as histograms and charts to visualize the relationship between the ichnofabric and the petrophysical parameters; and to determine the impact of biogenic reworking on the shoreface reservoir sections in each well.

3 Results

Well M-11: Ichnofabric analysis of this core indicates the USF section is 59% burrowed with varying degrees of intensity (rare = 14%, moderate = 18%, and intense 27%). The LSF section is 81% burrowed also with varied intensity (rare = 14%, moderate = 14%, and 53% intense) (Fig. 2).

There is a general decrease in porosity values with an increase in BI, in the burrowed intervals in the USF section ranging from 5.63 to 12%. However, a similar plot for the LSF section showed a significant increase in porosity values with increased BI for the burrowed intervals ranging from 22.56 to 38% (Table 1). Permeability values in the USF consisting of sandstones are generally higher than in the LSF which consists of heteroliths. There is also a general decline in permeability values with an increase in bioturbation intensity in the burrowed intervals of both the USF (212.22–896.75 md) and the LSF (146.33–77.86 md) (Table 1).

Table 1 Ichnofabric index and porosity permeability relationship of M-11 core

Depositional environment	Upper shoreface (USF)			Lower shoreface (LSF)		
Bioturbation index (BI)	Average porosity (Θ) %	% Θ Decrease	Average permeability (md)	Average porosity (Θ) %	% Θ increase	Average permeability (md)
1- Absent	29.46	–	2017.42	20.48	–	147.33
2-Rare	27.55	6.5	258.35	28.26	38.00	146.33
3-Moderate	27.8	5.63	896.75	25.1	22.56	77.86
4–5-Intense	25.92	12	212.22	28.2	37.70	140

Table 2 Ichnofabric index and porosity permeability relationship of M-22 core

Depositional environment	Upper shoreface (USF)			Lower shoreface (LSF)		
Bioturbation index (BI)	Average porosity (Θ) %	% Θ Decrease	Average permeability (md)	Average porosity (Θ) %	% Θ Decrease	Average permeability (md)
1-Absent	28.10	–	4451.4	11.57	–	161.7
2-Rare	–	–	–	6.78	41.40	43.71
3-Moderate	–	–	–	6.32	45.37	14.23
4–5-Intense	13.72	51	112.6	–	–	–

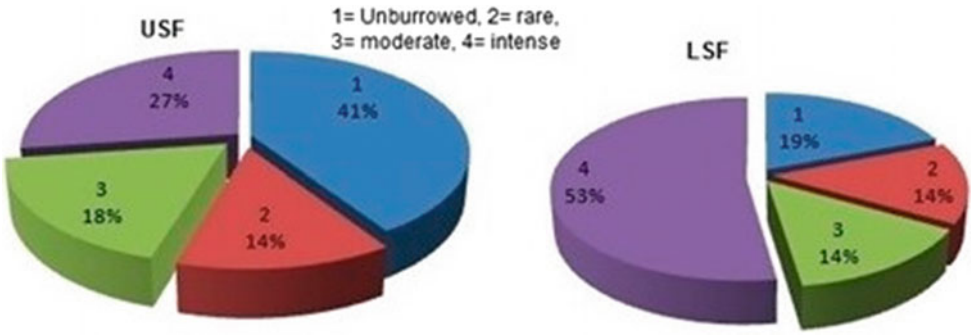

Fig. 2 Chart showing % burrowed/burrowed and burrow intensity in the USF and LSF sections of the M-11 core

Well M-22: the USF section in this core is 50% intensely burrowed, while the LSF section is also 50% burrowed with varying intensities (32% rare and 18% moderately burrowed, Fig. 3).

There is significant decrease in porosity noted in the burrowed intervals in both the USF and LSF sections with an increased bioturbation intensity (51% (USF) and 41.40–45.73 (LSF)). There is also a marked decrease in the permeability with an increase in BI in both the USF and LSF sections (Table 2).

4 Discussion

Porosity and permeability are two key petrophysical parameters that determine the quality of a reservoir rock. These parameters determine the ability of the reservoir to store fluids (porosity), allow their migration and ease their extraction (permeability) from an accumulation. Bioturbation or biogenic reworking disrupts the fabric and texture of sediments. It may result in enhanced or reduced porosity and permeability (Tonkin et al. 2010). The enhanced porosity/permeability often results from sediment cleaning bioturbation style, while the reduced porosity/permeability is a product of sediment packing, and mixing styles. In this study, these two styles of bioturbation influenced the observed relationship between bioturbation intensity and porosity/permeability trends. The USF sections are *Ophiomorpha* dominated fabrics; concentration of the clay-silt grade material into laminae, burrow linings, and fill within sandstone may have reduced the porosity/permeability by decreasing grain sorting. The LSF section however, is dominated by *Cruziana* icnofacies and is commonly siderite cemented. We therefore suggest that porosity/permeability loss in the LSF may be related to siderite cementation.

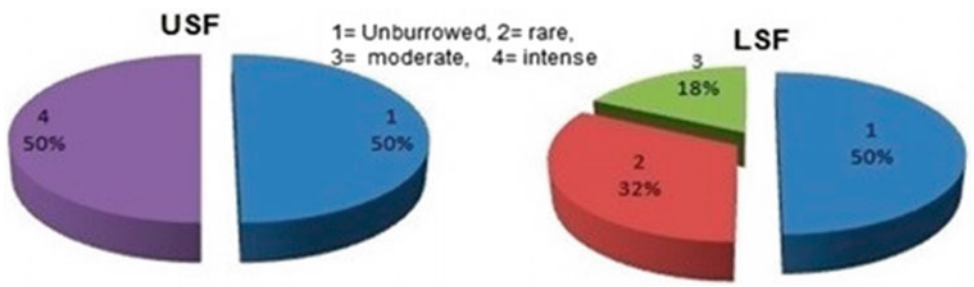

Fig. 3 Chart showing % unburrowed/burrowed and burrow intensity in the USF and LSF sections of the M-22 core

5 Conclusion

A general decline in porosity/permeability was observed in the USF and LSF sections with increased bioturbation intensity in the studied cores (Fig. 3). The trends between bioturbation intensity and porosity/permeability in this study suggest that intervals with: (i) Moderate and rare bioturbation (BI: 2–3) have better reservoir quality, probably due to limited impact on the sediment fabrics (ii) Intense bioturbation (BI: 4–5), affected reservoir quality negatively due to decrease in grain sorting resulting in porosity/permeability loss in the USF. However, in the LSF, the reduction of porosity and permeability may be related to siderite cementation. Understanding the impact of bioturbation on porosity and permeability may reduce uncertainties and improve reserve estimation in burrowed shoreface reservoirs in the Niger Delta Basin.

References

Cunningham, K.J., Sukop, M.C., Huang, H., Alvarez, P.F., Curran, H. A., Renken, R.A., Dixon, J.F.: Prominence of ichnologically influenced macroporosity in the karst Biscayne aquifer: Stratiform "super-K" zones. Geol. Soc. Am. Bull. **121**, 164–180 (2009)

Dim, C.I.P., Onuoha, K.M.: Insight into sequence stratigraphic and structural framework of the onshore Niger Delta Basin: integrating well logs, biostratigraphy, and 3D seismic data. Arab. J. Geosci. **10**, 300 (2017). https://doi.org/10.1007/s12517-017-3070-5

Droser, M.L., Bottjer, D.J.: A semiquantitative field classification of ichnofabric. J. Sediment. Res. **56**, 558–559 (1986)

Droser, M.L., Bottjer, D.J.: Ichnofabric of sandstones deposited in high-energy nearshore environments: Measurement and utilization: PALAIOS, v. 4, p. 598-604 (1989)

Egbu, O.C., Obi, G.C., Okogbue, C.O., Mode, A.W.: Ichnofacies and Reservoir Properties of Shoreline Deposit in the Coastal Swamp Depobelt of the Niger Delta. American Association of Petroleum Geologists: Search and Discovery. Article #40412 (2009), 7 p (2009)

Ezeh, S.C., Mode, A.W., Adejinmi, K., Ozumba, M.B.: Ichnological characteristics and variability of Miocene deposits in the Cenozoic Niger Delta: examples from cores in the Coastal Swamp and Offshore depobelts. Palaeogeogr. Palaeoclimatol. Palaeoecol. **454**, 89–201 (2016)

Gingras, M.K., Pemberton, S.G., Mendoza, C.A., Henk, F.: Assessing the anisotropic permeability of Glossifungites surfaces. Pet. Geosci. **5**, 349–357 (1999)

Gingras, M.K., MacMillan, B., Balcom, B.J., Saunders, T., Pemberton, S.G.: Using magnetic resonance imaging and petrographic techniques to understand the textural attributes and porosity distribution of Macaronichnus burrowed sandstone. J. Sediment. Res. **72**, 552–558 (2002)

Gingras, M.K., Mendoza, C.A., Pemberton, S.G.: Fossilized worm burrows influence the resource quality of porous media. AAPG Bull. **88**, 875–883 (2004)

Gingras, M.K., Pemberton, S.G., Henk, F., MacEachern, J.A., Mendoza, C.A, Rostron, B., O'Hare, R., Spila, M., Konhauser, K.: Applications of ichnology to fluid and gas production in hydrocarbon reservoirs. In: MacEachern, J.A., Bann, K.L., Gingras, M.K., Pemberton, S.G. (eds.) Applied Ichnology: SEPM Short Course Notes, vol. 52, pp. 129–143 (2007)

Jackson, C.A., Mode, A.W., Oti, M.N., Adejinmi, K., Ozumba, B., Osterloff, P.: Effects of bioturbation on reservoir quality: an integration in reservoir modeling of selected fields in the Niger Delta Petroleum Province. Niger. Assoc. Pet. Explor. Bull. **25**, 29–42 (2013)

La Croix, A.D., Gingras, M.K., Dashtgard, S.E., Pemberton, G.S.: Computer modeling bioturbation: the creation of porous and permeable fluid-flow pathways. AAPG Bull. **96**, 545–556 (2012)

Mode, A.W.: Ichnology and depositional environments of selected wells from OMLs 11, 18, 22, 24 & 35, Niger Delta, Basin. Technical report submitted to the Geological Services Dept, Shell Petroleum Development Company Ltd, Warri, 46 p (2012)

Pemberton, G.S., Gingras, M.K.: Classification and characterizations of biogenically enhanced permeability. AAPG Bull. **89**, 1493–1517 (2005)

Tonkin, N.S., McIlroy, D., Meyer, R., Moore-Turpin, A.: Bioturbation influence on reservoir quality: a case study from the Cretaceous Ben Nevis Formation, Jeanne d'Arc Basin, offshore Newfoundland, Canada. AAPG Bull. **94**, 1059–1078 (2010)

Orientation of Maximum Horizontal Stress in Pilot Well of Akan Oilfield, Russia

Ilmir Nugmanov, Karsten Reiter, and Andreas Henk

Abstract

Reconstructing the stress field at a local scale for the South Tatar Arch and adjacent basin areas (The East European Craton, Russia) is of particular interest for the evaluation in the context of tight oil reservoir management. Recently, the key players of the oil and gas industry (Gazprom, Rosneft, Tatneft) have begun to introduce geomechanical models into their exploration and field development practice. The state of stress (the orientations and magnitudes of the three principal stresses) constitutes a crucial element of the geomechanical model that forms the basis of reservoir management. This study aimed to estimate local stress state for Akan oilfield located within the Volga-Ural petroleum province. Stress regime has been estimated using stress polygon approach. According to the processing of acoustic borehole scanner images and the direction of the fast shear wave propagation, northeast orientation of the maximum horizontal stress axis has been obtained. Normal faulting stress regime was determined for the depths to range from 700 to 900 m below sea level. Knowledge of the principal stress orientation alone can be applied to improve reservoir drainage, water floods, and hydraulic fracture operations and is a critical element in all petroleum geomechanics studies.

Keywords

Stress state • Image log analysis • Shear wave anisotropy • Hydraulic fracturing • Carbonate reservoir

1 Introduction

Knowledge of the orientation and magnitude as well as the spatial variation of stress in the crust can be combined with mechanical, thermal, and rheological constraints to examine a broad range of geological processes (Zoback 2007). Geological and geophysical methods of paleo-stress state assessment can be used to reconstruct tectonic stress fields in a wide stratigraphic range (Rebetsky 2007). However, on a practical level, information on modern tectonic fields remains the most reliable (can be verified using various methods, characterized by high repeatability) and meaningful data source. The term "modern" means that the tectonic processes are currently active in the region. In most cases, data that are from Quaternary till present-day age are used to represent the youngest episode of deformation in an area.

Sbar and Sykes (1973) showed that there are large regions of the earth characterized by consistent orientations of principal stresses as determined by both earthquake mechanisms and a variety of in situ measurements. Such consistency strongly argues for a tectonic origin for such stresses. Later, Zoback and Zoback (1980) showed that it was possible to define specific stress provinces that correlate with physiographic provinces defined by the topography, tectonics, and crustal structure. This paper became the basis for regional (Zoback and Zoback 1989) and later global studies of the present-day stress field (Zoback et al. 1989), which resulted in the World Stress Map (WSM) project (Heidbach et al. 2018).

The best-estimated stress model approach was described in detail by Heidbach et al. (2016). They advocated that this approach should be used to minimize uncertainties before the estimation of the final rock stress model of a site. The link between different stress tensor estimation sources and numerical modeling should be considered as a strength of that approach.

I. Nugmanov (✉) · K. Reiter · A. Henk
Technische Universität Darmstadt, 64287 Darmstadt, Germany

M. Meghraoui et al. (eds.), *Advances in Geophysics, Tectonics and Petroleum Geosciences*,
Advances in Science, Technology & Innovation, https://doi.org/10.1007/978-3-030-73026-0_146

2 Geological Settings and Stress State Determination Methods

The object of the research, known as Akan oilfield, is located in the southeastern part of the Volga-Ural petroleum province in the eastern flank of the Melekess Basin. A long process of sedimentation (beginning in the mid-Devonian) under the platform conditions, ever-changing sedimentation stages, and alternating tectonic movements resulted in structural complexity of the sedimentary cover. In this region, oilfields are confined to small high-amplitude anticlinal structures of the Paleozoic era with inherited development and multi-layer deposits.

Establishes of the stress orientation was performed for well no. 2403 This well contains acoustic borehole scannerlogs and cross-dipole acoustic logging. Acoustic borehole image and cross-dipole acoustic logging were acquired over the intervals 988.5–1071.5 m using the Borehole Acoustic Scanner (SAS-90, JSC «Bashneftegeofizika») and VAK-32 acoustic wireline tool. Data cover Lower Carboniferous stratigraphic intervals.

The resulting information from SAS-90, travel time, and amplitude of the pulse reflected off the borehole were analyzed with software WellCAD. The oriented data, amplitude and travel time converted to radius, are displayed as a function of depth and azimuth as unwrapped images of the borehole wall. The images of the reflectivity of the wellbore wall and the exact shape of the well allow the determination of the orientation and characteristics of natural and drilling-induced fractures and of wellbore enlargements such as pipe wear and breakouts (Stephansson and Zang 2012). Our primary goal was to detect the stress-induced wellbore breakouts, which are the result of localized failure around the borehole in response to asymmetrical horizontal compression. This compression creates spalling in diametrically opposed zones around the azimuth of minimum horizontal stress S_{hmin}, where the circumferential compressive stress is greatest. In this case, maximum horizontal stress S_{Hmax} orientation will be perpendicular to S_{hmin}.

Cross-dipole acoustic logging data processing is based on the work of Alford (1986), who proposed a method for estimating the azimuth of fast and slow shear wave propagation for seismic data. Azimuthal shear wave anisotropy analysis was carried out according to Kozak et al. (2014). The magnitudes of minimal horizontal stress have been measured within several oil wells with hydraulic fracturing method. The total vertical stress, given by the overburden, has been estimated using density log data and vertical seismic profiling.

3 Results

The results of the processing Borehole Acoustic Scanner image logs show wellbore site problems in the intervals of Moscovian deposits. Limestones or dolomites with sub-horizontal beddings present most of the sediments. In the image logs, incipient borehole breakouts and several drilling-induced tensile fractures were observed. Azimuthal distribution of the wellbore breakouts using stereonet chart and rose diagrams shows clear evidence of the active present-day stress field triggered by the plate tectonics. Cumulatively, 7 incipient borehole breakout zones with total length of 25.1 m were observed on the amplitude and travel time images. The standard deviation for the azimuth of picked breakouts has been about 11°.

Orientation of S_{Hmax} axis is lying in azimuth of 65.96 ± 10.6° (Fig. 1a).

As a result of the cross-dipole acoustic log processing, it was revealed that the direction of propagation of the fast

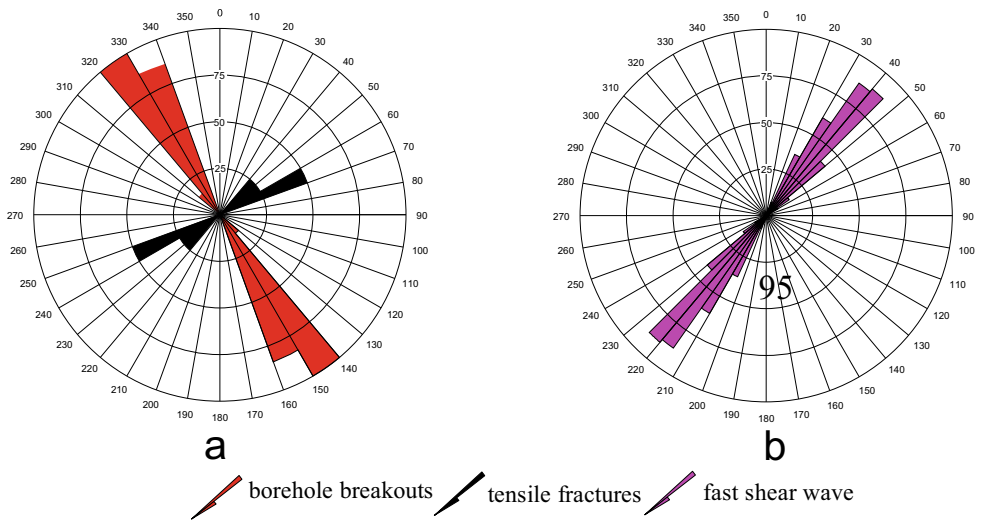

Fig. 1 Rose diagram shows S_{Hmax} orientation: **a** image log analysis and **b** azimuthal shear wave anisotropy analysis

wave in the entire research interval has a close pattern with image log analysis results (Fig. 1b). However, the observed differences in the orientation of acoustic anisotropy could be explained owing to past tectonic events.

4 Discussion

The data on crustal present-day stress field may be obtained from different sources. However, the occurrence and origins of small-scale stress fields in sedimentary basins remain poorly understood, primarily because of the lack of data from sedimentary basins, especially for Russia which is currently a white spot in the WSM (http://www.world-stress-map.org). The most accessible sources of information about the minimum horizontal stress magnitude and direction aremicroseismic monitoring during hydrofracturing. Borehole images data also provides valuable information about therocks mechanical properties and stress anisotropy, especially in the depths range associated with the reservoir.

5 Conclusions

Lower Carboniferous carbonate rocks of the Akan oilfield were investigated with the aim of the state of stress determination. In situ, stress orientation has been obtained using borehole image log and azimuthal shear wave anisotropy analysis. According to WSM quality ranking scheme, events documented from image logs of the well No. 2043 correspond to "C" quality and S_{Hmax} axis is lying in azimuth of 65.96° and believed to be within ±20–25°. The acoustic anisotropy (azimuth of the fast shear wave propagation) shows a similar pattern documented from image logs. Differences in the orientation of maximal horizontal stress, observed between two independent results in the same depth interval, should be explained due to previous active tectonics and long period of uplift of the Volga-Ural region from the Late Permian period.

References

Alford, R.M.: Shear data in the presence of azimuthal anisotropy. In: 56th SEG Annual Meeting, pp. 476–479. SEG, Houston (1986)

Heidbach, O., Rajabi, M., Reiter, K., Ziegler, M., WSM Team: World Stress Map Database Release 2016. GFZ Data Services (2016). https://doi.org/10.5880/WSM.2016.001

Heidbach, O., Rajabi, M., Cui, X., Fuchs, K., Müller, B., Reinecker, J., Reiter, K., Tingay, M., Wenzel, F., Xie, F., Ziegler, M.O., Zoback, M.-L., Zoback, M.: The World Stress Map database release 2016: crustal stress pattern across scales. Tectonophysics **744**, 484–498 (2018)

Kozak, M., et al.: Azimutal shear wave anisotropy analysis, guided in time domain. In: SPWLA 55th Annual Logging Symposium 2014, pp. 1–13. UAE, Abu Dhabi (2014)

Rebetsky, Yu.L.: Tectonic Stresses and Rock Strength of Natural Mountainous Massifs. Akademkniga Press, Moscow (2007)

Sbar, M.L., Sykes, L.R.: Contemporary compressive stress and seismicity in eastern North America: an example of intra-plate tectonics. Geol. Soc. Am. Bull. **84**, 1861–1882 (1973)

Stephansson, O., Zang, A.: ISRM suggested methods for rock stress estimation. Part 5: Establishing a model for the in situ stress at a given site. Rock Mech. Rock Eng. **45**, 955–969 (2012)

The World Stress Map Project. A Service for Science and Earth System Management. http://www.world-stress-map.org. Last accessed 2019/07/01

Zoback, M.L.: Reservoir Geomechanics. Cambridge University Press, New York (2007)

Zoback, M.L., Zoback, M.D.: State of stress in the conterminous United States. J. Geophys. Res. **85**, 6113–6156 (1980)

Zoback, M.L., Zoback, M.D.: Tectonic stress field of the conterminous United States. Geol. Soc. Am. Memoirs **172**, 523–539 (1989)

Zoback, M.L., Zoback, M.D., et al.: Global patterns of tectonic stress. Nature **341**, 291–298 (1989)

Geological Structure and Hydrocarbon Bearing Prospects of the Northwestern Part of the Persian Gulf Basin (The Western Desert of Iraq)

Kostantin Osipov and Enver Ablya

Abstract

Before the 1990s, exploration in the Western Desert (WD) of Iraq was focused on Mesozoic-Cenozoic section. As of today there are prospects for the discovery of hydrocarbons (HC) in deep sections—Proterozoic and Paleozoic deposits. Through the literature Analysis, two-dimensional basin modeling and maturity maps of source rocks were provided to identify the HC bearing prospects of three petroleum systems: Vendian-Cambrian (V-Cm), Paleozoic (PZ), and Mesozoic-Cenozoic (MZ-CZ). V-Cm salt sections were detected based on gravity data. It may contain all elements of petroleum system similar to play Ara in Oman. Based on seismic data, there is an angular unconformity apparently between Ordovician and Silurian deposits. This unconformity creates PZ stratigraphic traps filled with HC. In MZ-CZ section, there are mature Jurassic source rocks (SR) to the west of Abu Jir fault system. Their maturity was proved by pyrolysis data from well Merjan-1. Although the MZ-CZ section has a monoclinal slope to the east, it is possible to detect small-sized closed structural traps filled with HC.

Keywords

Western Desert of Iraq • Petroleum systems • Hydrocarbon bearing prospects • Basin modeling

1 Introduction

Until the 1990s, the WD of Iraq was an unpromising region due to the fact that only the upper, Mz-Cz monoclinally lying part of the section was considered. Lack of prospects was associated with both the lack of evaporite seals of the Jurassic Gotnia formation (Fm) (analogous to Hith Fm in Saudi Arabia) and the Middle Eocene Lower Fars Fm (Jassim and Goff 2006; Sabah 2006), and with the presence of seeps along Abu Jir fault zone (Al-Ameri 2014). These facts indicate the cessation of long-term lateral migration of HC from the kitchen of Jurassic SR (Baniasad et al. 2017)—the Mesopotamian depression. In 1987–93 years fields were discovered in Pz section of W Iraq and E Jordan (Akkas, S and N Risha fields) (Al-Ameri 2010; Ahlbrandt 2010). These discoveries have breathed new life into the exploration of the region. It is possible that in the Pz deposits of this area there are accumulations of HC similar to those found in other parts of the Persian Gulf Basin (HC in Unaizah Fm and in Khuff Fm in Saudi Arabia). In addition, salt basins, probably of the V-C age, were found in the study area according to the gravity and seismic data (Jassim and Goff 2006). They can also be an exploration target by analogy with the Ara play in Oman (Aqrawi et al. 2012). According to recent geochemical data, it was revealed that the WD of Iraq may have its own mature Jurassic SR that could generate some amount of HC for Cretaceous reservoirs.

2 Geological Settings, Materials, and Methods

The WD of Iraq is located in the northern part of the Arabian Peninsula, in the SW Iraq. The geological section is represented by three complexes—metamorphosed pre-Vendian basement, salt deposits of the V-Cm transition complex, and Phanerozoic sedimentary cover. The basin model (as per MSU methodology) was built along the West Kifl 1 (WK-1) deep well (TD around 5.8 km, age of borehole deposits—Permian). Materials for the model include thickness of deposits that was not penetrated by well (Jassim and Goff 2006; Al-Hadidy 2007), well tops, lithology, age of deposits (Pitman et al. 2004), deposition environments (Jassim and Goff 2006), vitrinite reflections from the nearest published well Misaib, temperatures at the bottom of the well

K. Osipov (✉) · E. Ablya
Lomonosov Moscow State University, Moscow, 119234, Russia

M. Meghraoui et al. (eds.), *Advances in Geophysics, Tectonics and Petroleum Geosciences*,
Advances in Science, Technology & Innovation, https://doi.org/10.1007/978-3-030-73026-0_147

Table 1 Source rocks geochemical data in the Western Desert of Iraq for basin modeling

Age	Formation	Composition	Thickness, m	Kerogen type	TOC, wt %	HI, mgHC/gTOC
J3-K1	Sulaiy	Carbonates	40–50	I	0.7	770
J3	Najmah	Carbonates	10–20	IIS	3.4	550
J	Sargelu	Carbonates	Up to 210	IIS	0.8	430
P1	Razzaza	Shales	50–82	III	1	200
D3-C1	Ora	Shales	250–280	III	2.2	200
S	Akkas	Shales	60–65	II	8.5	430
O	Khabour	Shales	Up to 100	II	2.3	370

(Al-Ameri 2014), data on rift periods (Jassim and Goff 2006), data of SR within the Western Desert of Iraq and its neighborhood (https://www.academia.edu/2343876; Al-Hadidy 2007; Pitman et al. 2004; Grabowski 2014; Aqrawi and Badics 2015; Baniasad et al. 2017) (Table 1). For the construction of maturity maps, the following data was used: the depths of the oil and gas windows, seismic data (tying well WK-1 to seismic; velocity model) within the eastern part of the Western Desert.

Based on seismic data, there is an angular unconformity apparently between Ordovician and Silurian deposits. This unconformity creates stratigraphic trap that may be filled with hydrocarbons. Migration pathways from D3-C1 (Ora Fm) and P (Razzaza) SRs are mainly lateral as overlying Triassic deposits are mainly thick seals composed of shales and salts. Traps are small-sized structural. Migration routes from Jurassic mature SR are lateral and vertical. Traps are also small-sized structural.

3 Results

Oil window is placed on depths from 2.4 to 5.3 km (%Ro 0.55–1.3%) and gas window—from 5.3 km (%Ro > 1.3%). In well WK-1 transformation ratio (TR) increased from 5 to 70% in lower-middle Triassic for Akkas Fm, from 5 to 60–70 in lower Cretaceous for Ora and Razzaza Fm, from 5 to 20–25 in upper Cretaceous-Tertiary for Sargelu and Najmah Fm. So all of mentioned SRs are mature and there was expulsion from each. The expulsion threshold for II type of kerogen is up to 10% of TR; for III type of kerogen is fluctuating from 30 to 50% of TR. Boundaries between oil and gas window, between oil window and immature rocks, have N–S trend as W D of Iraq has monoclinal slope to the east. The position of these boundaries relative to well WK-1 is presented on Table 2.

Migration pathways and traps. Faults mainly has sub-meridional extension and do not reach Ordovician deposits so migration from Silurian hot shales (Akkas Fm) is downward and lateral to underlying Ordovician sandstones (Khabour Fm) (see Fig. 1).

4 Discussion

Hercinian erosion that destroyed many hundreds of sediments within Salman zone is not supported by seismic data within the research area. The Monoclinal slope of seismic reflections are observed under Permian deposits (Chia Zairi Fm) instead of angular unconformity. Moreover, the angular unconformity is recognized apparently between Ordovician and Silurian deposits on the central part of W D of Iraq. The mentioned features were not well documented and are crucial not only for understanding the Pz section of Western Desert of Iraq but also for a rational exploration.

5 Conclusions

The Vendian-Cambrian petroleum system lies quite deep (7–9 km) and is of future exploration interest. The Pz petroleum system has prospects in the lower part (the Silurian and Ordovician sandstones of the Khabor Fm in stratigraphic traps) and in the upper part (the Permian carbonates of the

Table 2 Position of maturity boundaries for source rocks relative to well WK-1

Age of source rock	Formation	Gas and oil window boundary (distance west of WK-1, km)	Oil window and immature rocks boundary (distance west of WK-1)
J	Sargelu	–	20
P1	Razzaza	40	150
S	Akkas	100	230

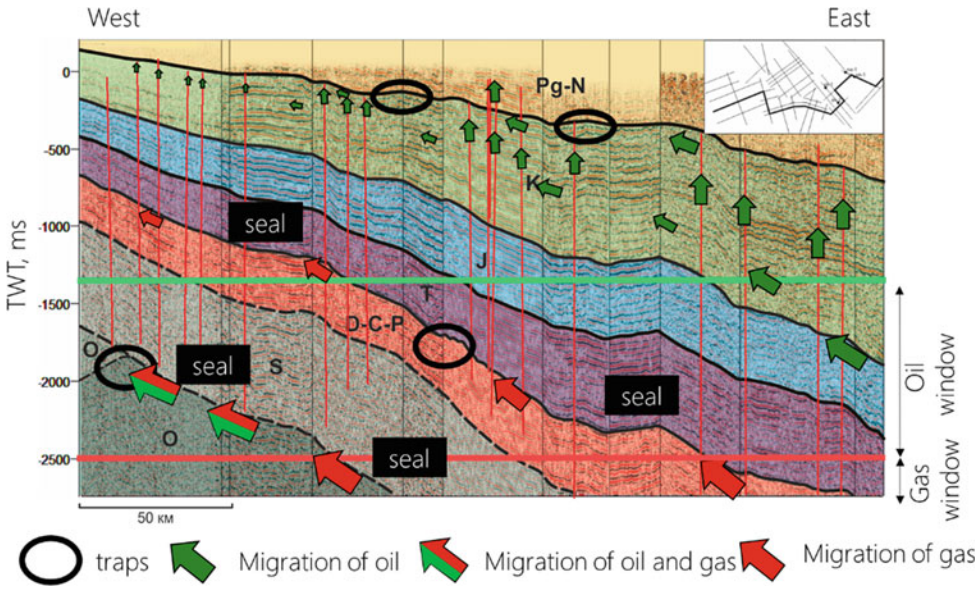

Fig. 1 Seismic section through the eastern part of Western Desert of Iraq with horizon interpretation, traps, major seals, oil and gas windows, and migration pathways

Chia Zairi Fm in small-sized structural traps). Paleozoic SRs are mature and they are able to fill exploration targets with both oil and gas. The predominant migration path is lateral. In the Mz-Cz, it is possible to detect small structural traps in which HCs are possible due to the presence of mature Jurassic SR (migration path is lateral and vertical).

References

Ahlbrandt, T.: The Petroleum Endowments of the Total Petroleum Systems in the Middle East and North Africa Tethys. Search and Discovery Article #10244 (2010)

Al-Ameri, T.: Palynostratigraphy and the assessment of gas and oil generation and accumulations in the lower Pz, W Iraq. Arab. J. Geosci. **3**(2), 155–179 (2010)

Al-Ameri, T.: Oil biomarkers, isotopes, and palynofacies are used for petroleum system type and migration pathway assessments of Iraqi oil fields. Arab. J. Geosci. **8**(8), 5809–5831 (2014)

Al-Hadidy, A.: Pz stratigraphic lexicon and HC habitat of Iraq. GeoArabia **12**(1), 63–130 (2007)

Al-Khafaji, A., Al-Ameri, T.: The OG of the Middle Euphrates Region (Kifl, W Kifl, Musaiyab and other), Middle Iraq. https://www.academia.edu/2343876

Aqrawi, A., Badics, B.: Geochemical characterisation, volumetric assessment and shale-oil/gas potential of the Middle Jurassic-Lower Cretaceous SR of NE Arabian Plate. GeoArabia **20**(3), 99–140 (2015)

Aqrawi, A., Skarpnes, O., Scotchmer, J., Masri, A.: Lower Palaeozoic Petroleum Systems of Western Iraq with Reference to Jordan. Search and Discovery Article #50590 (2012)

Baniasad, A., Rabbani, A.R., Moallemi, S.A., Soleimany, D., Rashidi, M.: Petroleum system analysis in NW part of Persian Gulf, Iranian sector. Org. Geochem. **107**, 69–85 (2017)

Grabowski, G.: Iraq. In: Marlow, L., Kendall, C., Yose, L. (eds.) Petroleum Systems of the Tethyan Region, AAPG Memoir, vol. 106, pp. 379–467. AAPG, Tulsa (2014)

Jassim, S., Goff, J.: Geology of Iraq, 1st edn. Dolin, Prague (2006)

Pitman, J., Steinshouer, D., Lewan, M.: Petroleum generation and migration in the Mesopotamian Basin and Zagros Fold Belt of Iraq: results from a basin-modeling study. GeoArabia **9**(4), 41–72 (2004)

Sabah, M.: Megaseismic section across the northeastern slope of the Arabian Plate, Iraq. GeoArabia **11**(4), 77–90 (2006)

The Glacial Episodes of the Arabian Peninsula

Abdulaziz Laboun

Abstract

The Arabian Peninsula is one of the few regions in the world where sediments of at least seven main global glacial episodes are well preserved and exposed in the Proterozoic Arabian Shield and the Phanerozoic Arabian Shelf. Global glaciations in the earth's geologic history are well recorded in the Arabian Peninsula. The four glaciations in the Proterozoic (the Gaskiers, Miranoan, Sturtian, and Kaigas glaciations) are represented by the glacial deposits of the Jabalah Group, Silasia Formation, Za'am Group, and Mahd Group, respectively. The three glaciations of the Phanerozoic took place during the Late Ordovician (Hirnantian), Permo-Carboniferous, and Pleistocene glaciations. The Hirnantian glaciation is represented by the Saqiyah, Sarah, and Hawban Formations (Tabuk Group) in Central and Northwestern Saudi Arabia and Sanamah Formation in the southwest. The Carboniferous-Early Permian glaciation is represented by the Juwayl Formation in Southwest Saudi Arabia, Akbarah Formation in Northwest Yemen, and Al Khlatah Formation in Southeast Oman. The Pleistocene glaciation "Ice Age" is represented by the Midyan and Ajfar Formations in Northwestern Saudi Arabia and Jabal ar-Rassyss in the Arabian Shield. Porous and permeable glacial and periglacial deposits are becoming hydrocarbon exploration target in different parts of the Arabian Peninsula. The Hirnantian and Permo-Carboniferous glacio-fluvial and glacio-marine sandstones are oil-bearing reservoirs in Saudi Arabia and Oman.

Keywords

Arabian Peninsula • Saudi Arabia • Yemen • Oman • Geology • Glaciation

A. Laboun (✉)
Ibnlaboun Geological Consultants, P.O. Box 63280 Riyadh, 11516, Saudi Arabia

1 Introduction

This abbreviated paper is an attempt to document the glacial episodes that occurred in the geologic history of the Arabian Peninsula and place them in the context of the global glacial episodes. Proterozoic igneous and metamorphic rocks and thick Phanerozoic sedimentary rocks are well exposed in the Arabian Peninsula. Geologic field investigations have proven that glaciogenic deposits of different glacial facies have been identified in well-preserved outcrops at various parts of the Arabian Peninsula (Fig. 1).

Spectacular glacial deposits and related structures include tillite, diamictite, and dropstones, and associated sedimentary structures; striations, grooved and striated pavements (Fig. 2), U-shaped valleys, and overturned drag-folds are well documented in the outcrops. Glaciogenic deposits are recognized in the subsurface as well.

2 Methods

Extensive geologic field investigations have been carried out to identify the glaciogenic deposits. Selected representative localities were measured, described, and photographed. Ancient Arabian glacial facies were correlated with recent glacial depositional environments through two visits to Antarctica. Surface and subsurface data were used to establish stratigraphic relationships of the glacial deposits with underlying and overlying lithostratigraphic units.

3 Results

Detailed regional and global correlations have indicated that seven glacial events took place in the Arabian Peninsula; four in the Proterozoic, two in the Paleozoic, and one in the Cenozoic (Fig. 3).

M. Meghraoui et al. (eds.), *Advances in Geophysics, Tectonics and Petroleum Geosciences*,
Advances in Science, Technology & Innovation, https://doi.org/10.1007/978-3-030-73026-0_148

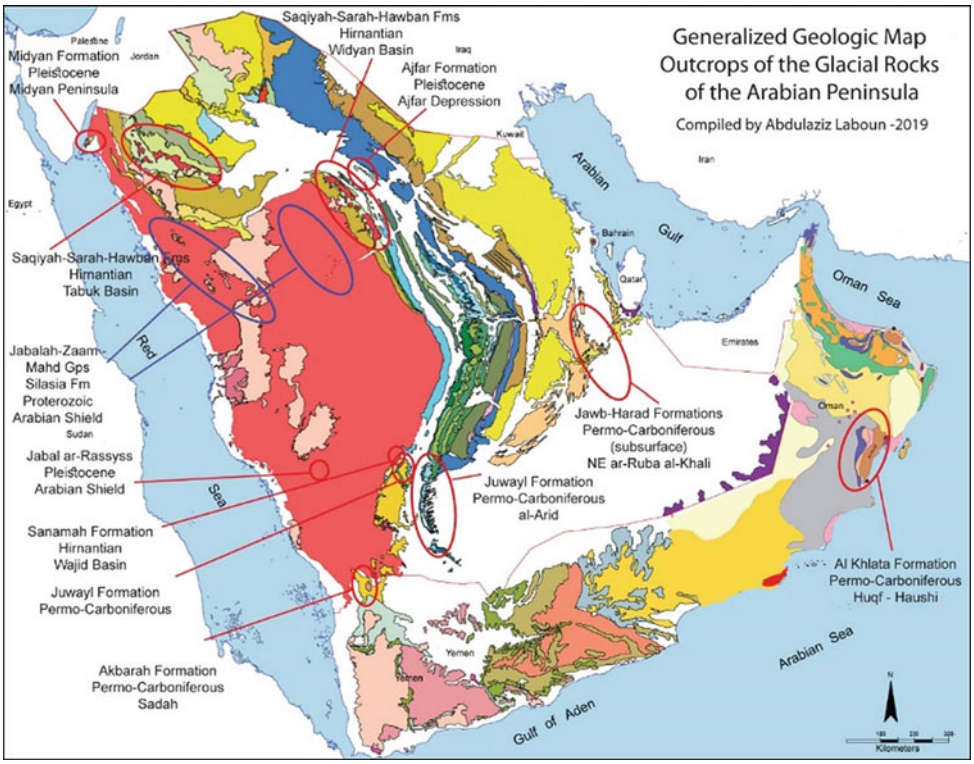

Fig. 1 Generalized geologic map of the Arabian Peninsula showing the main outcrops of glacial deposits in Saudi Arabia, Yemen, and Oman

Fig. 2 Late Ordovician glacial grooved and striated pavement exposed in al-Qassim region, Central Saudi Arabia

Porous and permeable glacial and periglacial deposits are becoming hydrocarbon exploration target in different parts of the Arabian Peninsula. The Hirnantian and Permo-Carboniferous glacio-fluvial and glacio-marine sandstones are oil-bearing reservoirs in Saudi Arabia and Oman.

4 Discussion

Evidence of the glaciations in the Arabian Peninsula has grown since 1958 (Fig. 4). Four identified global glacial episodes during Neoproterozoic time; Kaigas, Sturtian, and

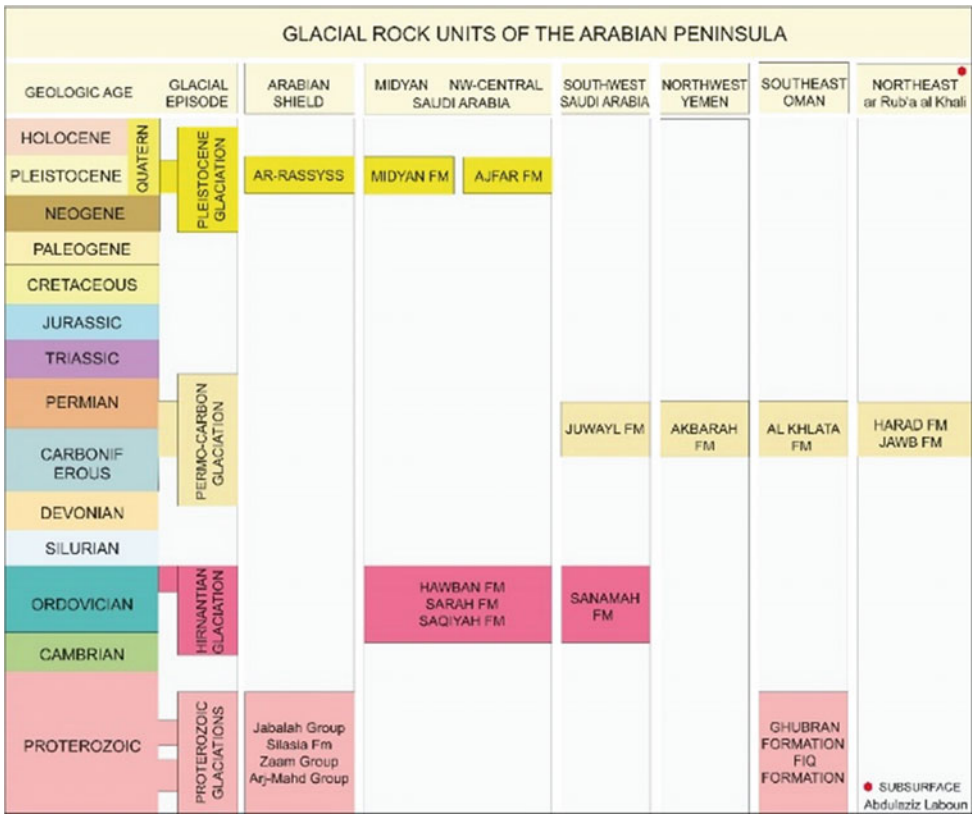

Fig. 3 Generalized stratigraphic column showing the main episodes of glaciations in the Arabian Peninsula; Proterozoic, Late Ordovician (Hirnantian), Permo-Carboniferous, and Pleistocene. The column shows representative glaciogenic rock units and subsurface glacial Jawb and Harad formations in Northeastern ar-Rub'a al-Khali

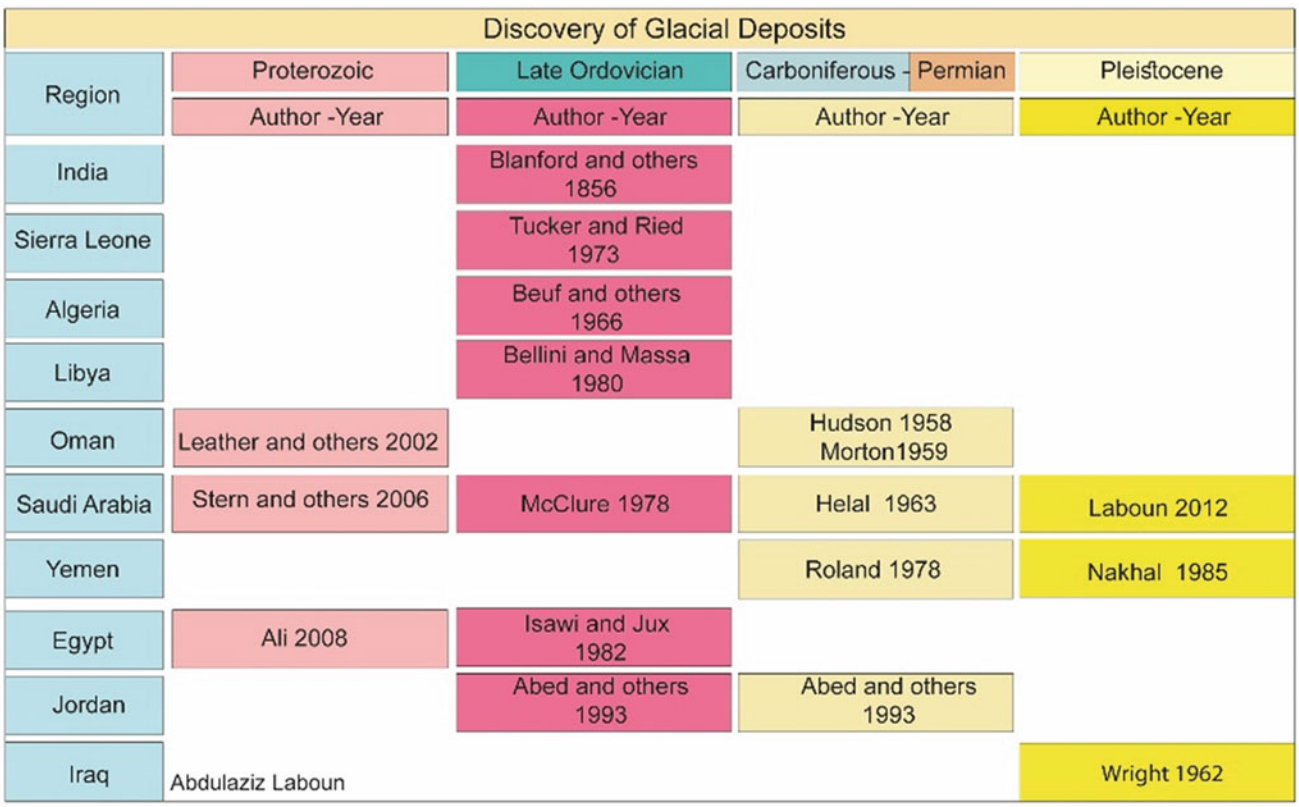

Fig. 4 Discovery of glacial deposits in the Arabian Peninsula and adjacent regions

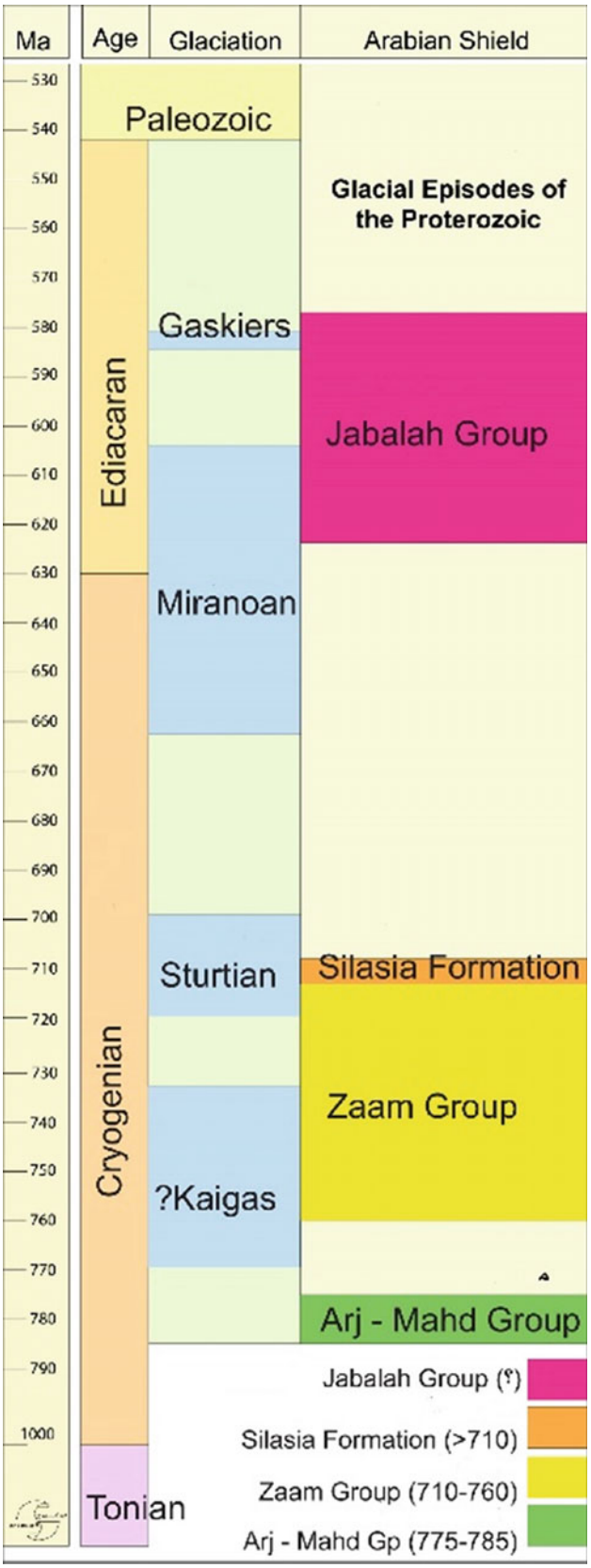

Fig. 5 Generalized column showing the main glacial episodes of the Proterozoic and glacial rock units of the Arabian Shield

Merinoan (Cryogenian Period) and one; Gaskiers (Ediacaran Period) (Fig. 5). Proofs supporting the Snowball Earth hypothesis have been identified at many Neoproterozoic rocks in the Arabian Shield. The glaciations in the earth's geologic history are represented in the Arabian Peninsula by four rock units in the Proterozoic. The Gaskiers, Miranoan, Sturtian, and Kaigas glaciations are most probably represented by the glacial deposits of the Jabalah Group, Silasia Formation, Za'am Group, and Mahd Group (Johnson 2006; Stern et al. 2006), respectively.

The three Phanerozoic glaciations took place during Late Ordovician (Hirnantian) (McClure 1978), Permo-Carboniferous (Helal 1963), and Pleistocene (Laboun 2012). The Ordovician glaciation is represented by the Saqiyah, Sarah, and Hawban Formations (Tabuk Group) in Central and Northwestern Saudi Arabia and Sanamah Formation in the southwest. The Carboniferous-Early Permian glaciation is represented by the Juwayl Formation in Southwest Saudi Arabia, Akbarah Formation in Northwest Yemen, and Al Khlatah Formation in Southeast Oman. The Pleistocene glaciation "Ice Age" is represented by the Midyan and Ajfar Formations in Northwestern Saudi Arabia and Jabal ar-Rassyss in the Arabian Shield (Laboun 2012).

5 Conclusions

Evidence supporting the Snowball Earth hypothesis is growing. Recent studies show that the hypothesis has been proven thanks to many Neoproterozoic rocks in the Arabian Peninsula. The identification of deposits of seven glacial episodes makes the Arabian Peninsula one of the few regions in the world where the main global glacial episodes are well preserved and exposed. The glacial episodes are well documented in excellent outcrops in the Proterozoic Arabian Shield and the Phanerozoic Arabian Shelf.

References

Ali, K.A.: Age and significance of Neoproterozoic Diamictite and Metavolcanic Rocks in Egypt and Saudi Arabia, Richardson, Texas, University of Texas at Dallas Ph.D. Dissertation, 219 p (2008)

El-Nakhal, H.A.: Observations on Polygonal Patterns in a Jurassic Sandstone, Kohlan, Yemen Arab Republic. Cold Reg. Sci. Technol. **11**, 237–240 (1985)

Helal, A.H.: Jungpalaozoische glazialspuren auf dem Arabischen Schild, (short notice on the occurrence and stratigraphic position of Permo-Carboniferous tillites in Saudi Arabia) published in Eiszeit und Gegenwart, vol. 14, pp. 121–123 (1963)

Hudson, R.G.S., Sudbury, M.: Permian Brachiopods from South-east Arabia. In: Dubertret, M.I. (ed.) Notes et Memoires sur le Moen-Orient; Museum National D'Histoire Naturelle, vol.7, pp. 19–55 (1959)

Johnson, P.R.: Explanatory notes to the map of Proterozoic geology of western Saudi Arabia. Technical Report, Saudi Geological Survey, SGS-TR-2006-4 (2006)

Laboun, A.A.: Did glaciers exist during Pleistocene in the Midyan Region, Northwest Corner of the Arabian Peninsula? Arabia. Arab. J. Geosci. **5**(6), 1333–1339 (2012)

McClure, H.A.: Early Paleozoic glaciation in Arabia. Palaeogeogr. Palaecoclimatol. Palaeoecol. **25**, 31–36 (1978)

Stern, R.J., Avigad, D., Miller, N.R., Beyth, M.: Evidence for the snowball Earth hypothesis in the Arabian-Nubian Shield and the East African Orogen. Geological Society of Africa Presidential Review, No. 10. J. Afr. Earth Sci. **44**, 1–20 (2006)

Correction to: Vertical Movements and Source-to-Sink Systems of the Rifted Margin of NW Africa: Surprises Continue

Giovanni Bertotti, Remi Charton, Mohamed Gouiza, Emmanuel Roquette, James Lovell-Kennedy, and Jonathan Redfern

Correction to:
Chapter 122 in: M. Meghraoui et al. (eds.), *Advances in Geophysics, Tectonics and Petroleum Geosciences*, Advances in Science, Technology & Innovation,
https://doi.org/10.1007/978-3-030-73026-0_122

In the original version of the book, the author name "Emanuel Roquette" has been changed to "Emmanuel Roquette" in the Frontmatter and in Chapter 122. The correction to this chapter have been updated with the changes.

The updated version of this chapter can be found at https://doi.org/10.1007/978-3-030-73026-0_122

M. Meghraoui et al. (eds.), *Advances in Geophysics, Tectonics and Petroleum Geosciences*,
Advances in Science, Technology & Innovation, https://doi.org/10.1007/978-3-030-73026-0_149